

PROCEEDINGS

THIRTIETH WORKSHOP GEOHERMAL RESERVOIR ENGINEERING

JANUARY 31 - FEBRUARY 2, 2005



**STANFORD GEOTHERMAL PROGRAM
WORKSHOP REPORT SGP-TR-176**

TABLE OF CONTENTS

PREFACE

INTRODUCTION

RESERVOIR ENGINEERING

FIELD STUDIES

TRACERS

MODELING

PRODUCTION ENGINEERING

INJECTION

HOT DRY ROCK / ENHANCED GEOTHERMAL SYSTEMS

GEOCHEMISTRY

GEOPHYSICS

GEOLOGY

EMERGING TECHNOLOGY

PARTICIPANT LIST

AUTHOR LIST

SUBJECT INDEX

PREFACE

The Thirtieth Workshop on Geothermal Reservoir Engineering was held at the Fisher Conference Center on the Stanford University campus on January 31-February 2, 2005. There were 120 registered participants, from 13 countries: Canada, Costa Rica, France, Germany, Japan, Mexico, New Zealand, Norway, Philippines, Switzerland, Turkey, United Kingdom, and the United States.

Professor Roland N. Horne opened the meeting and welcomed visitors. The keynote speakers were L. Roy Mink, who gave an overview of the research and development activities of the Department of Energy, John Lund who gave a history of the 100 years of development of geothermal electrical generation, and Tonya “Toni” Boyd who gave an overview of geothermal web sites.

65 papers were presented in the technical sessions of the workshop. Technical papers were organized into 18 sessions, on the topics of reservoir engineering, tracers, enhanced geothermal systems (EGS), geochemistry, field studies, modeling, geophysics, production, injection and emerging areas.

Session chairmen were major contributors to the workshop, and we thank: Kewen Li, Roland Horne, Pete Rose, John Garnish, Mike Shook, Joe Moore, Paul Moya, Susan Petty, Phil Wannamaker, Chih-Ying Chen, Ann Robertson-Tait, John Pritchett, Subir Sanyal, David Blackwell, Keisuke Ushijima and Kit Bloomfield.

The entertainment for the evening of the banquet was the outstanding Taiko drum group from Stanford University. The show brought the audience to their feet in recognition of their tremendous performance.

The Stanford Geothermal program faculty, staff, and graduate students organized the Workshop. We wish to thank our students who operated the audiovisual equipment.

The Thirtieth Workshop was dedicated to the memory of Noel Urmeneta. Noel was an MS graduate of the Stanford Geothermal Program in 1997, and worked in the geothermal developments of the Philippines and Indonesia. He died suddenly and unexpectedly in December 2004, while still at the peak of his technical career. He will be remembered and missed by many in the worldwide geothermal community.

Roland Horne, Laura Garner, Sandy Costa, and Kewen Li, were the Workshop Coordinators.

Introduction

Geothermal Websites

Tonya "Toni" Boyd

[5](#)

100 Years of Geothermal Power Production - Trends and the Future

John W. Lund

[10](#)

GEOHERMAL WEBSITES

Tonya "Toni" Boyd

Geo-Heat Center
3201 Campus Drive
Klamath Falls, OR, 97601, USA
E-mail: boydt@oit.edu

ABSTRACT

The Internet has become such an important part of our every day life. It can be used to correspond with people across the world, a lot faster than to send a letter in the mail. The Internet has a wealth of information that is available to anybody just by searching for it. Sometimes you get more information than you ever wanted to know and sometimes you can't find any information.

This paper will only cover a small portion of the websites and their links that have geothermal information concerning reservoir engineering, enhanced geothermal systems, hot dry rock and other aspects of geothermal. Some of the websites below are located in the US others international, such as, geothermal associations, and websites where you can access publications. Most of the websites listed below also have links to other websites for even more information.

STANFORD GEOHERMAL PROGRAM

<http://ekofisk.stanford.edu/geotherm.html>

This website provides information on their program and their graduate study. They also have a section for their downloadable reports and publications. Some of the technical reports they have available go back to 1973. There are overview reports from 1990 on including Quarterly reports. As you all probably know they have information on their upcoming Geothermal Workshop. All the proceeding from the Geothermal Workshops from 1997 to the current can be searched for on their website. The database can be search by any word in the title, author name, keyword, year or session.

GEO-HEAT CENTER

<http://geoheat.oit.edu>

The Geo-Heat Center provides dissemination of geothermal information and technology transfer. The transfer of technological information to consultants,

developers, potential users, and the general public is an important element in the development of direct heat utilization of geothermal energy. Their main focus is on the use of low to moderate temperature resources and small-scale power. Their website includes an interactive direct-use map, information on co-located resources, and a database on geothermal wells and springs for 16 western states. They also have downloadable technical papers and bulletin articles on all types of geothermal applications and resources, plus a geothermal heat pump newsletter.

GEOHERMAL RESOURCES COUNCIL

<http://www.geothermal.org/index.html>

The Geothermal Resource Council (GRC) has a searchable library containing bibliographic information of articles from a variety of publications on all aspect of geothermal worldwide. This database will inform you on where the publication is located and if you do not have the publication how you can order it. A new addition to their website for GRC members is access to all the GRC Transactions volumes 1 through 27 and GRC Special Reports volumes 1 through 19 as downloadable PDF files. If you are a member of the GRC you can download papers free of charge. The non-member section of the library database allows the same searches and a preview of the above publications only. They also provide information on becoming a member of the organization and their Annual Meeting.

INTERNATIONAL GEOHERMAL ASSOCIATION

<http://iga.igg.cnr.it/index.php>

They provide information on geothermal energy use around the world, world conferences on geothermal, and links to related web sites. They have an interactive map of the geothermal of the world, plus a table of electrical generation and direct use applications for each country. There is also a summary of each country's applications that have

been summarized from the World Geothermal Congress proceedings papers, which will be updated after the WGC2005 conference. They also have a link to where you can search for IGA Geothermal Conference Papers database (hosted on the Stanford Geothermal Program website). This database search covers World Geothermal Congress proceedings from 1995 and 2000, European Geothermal Congress 2003, Iceland Geothermal Conference 2003, International Geothermal Workshop, Russia 2003, Beijing International Geothermal Symposium, 2002, Geothermal Energy in Underground Mines, Ustron, Poland 2001, and Stanford Geothermal Workshops 1997 – 2004. There is also a database to search for Past IGA newsletters from Issue 1 to 49.

WORLD GEOTHERMAL CONGRESS 2005

<http://www.wgc2005.org>

This website contains information on the World Geothermal Congress 2005 meeting. Some of the links includes information on their short courses, technical program, organizing committee, calendar and deadlines and accommodation.

ENERGY & GEOSCIENCE INSTITUTE - UNIVERSITY OF UTAH

<http://egi-geothermal.org/>

Under the links on their main page they have a link to the popular “Red Brochure” and a link to GIS Projects. The “Red Brochure” is a publication that has some general information on geothermal and is a great publication to inform people about geothermal. The link for GIS Projects includes a Geothermal Internet map server, which was created by using ArcIMS. This map server has several layers, which can be visible or active. As you zoom into the map you are presented with more layers. Some of the layers include thermal springs; geothermal study areas/fields, faults and surface geology, county boundaries just to name a few that can be viewed. You can also get information about areas they have studied – an example would be the Dixie Valley area. After getting information about the area, a link is provided to another page which provides some publications on the area, raster data for the area, plus some of the ArcView files are available. Of course at the time I looked at the pages not every area had all this information.

SOUTHERN METHODIST UNIVERSITY GEOTHERMAL LABORATORY

<http://www.smu.edu/geothermal/>

They have a couple of databases on their website. The Regional Geothermal Database of US is a database of primarily regional or background wells

that has been used to determine the heat flow for the United States. The Western Geothermal Areas Database is a database of over 5000 wells in mainly high temperature geothermal areas from the Rockies to the Pacific Ocean; all wells within a geothermal area are located where available; the majority of the data are from company documents, well logs and publications. Many of the wells were not previously accessible to the public. They have also produced a Geothermal Map of North America and they explain where the information came from to produce the map. They also have some publications that are downloadable from their website and links to other websites and information.

THE GLOBAL HEAT FLOW DATABASE OF THE INTERNATIONAL HEAT FLOW COMMISSION

<http://www.heatflow.und.edu/index2.html>

This website provides information on heat flow for all over the world. They have maps and databases in either Excel or ASCII format for most of the world. The data presented on the maps use a color-coded format using the visible light spectrum so that warm colors (reds) indicate high heat flow and cool colors (violet) indicate low heat flow. The spectral range for each data map is 0 to 200 mW/ m² in intervals of 10 mW/ m². Heat flows greater than 200 mW/ m² are assigned the warmest color.

DEPARTMENT OF ENERGY - GEOTHERMAL ENERGY PROGRAM

<http://www.eere.energy.gov/geothermal>

Describes the U.S. DOE Geothermal Energy Program and provides information and news on geothermal energy. They also have a link on their website under their tab “Information Resources” which provides links to all the National Labs publications that are available for downloading or information on how to request the publications on their respective websites.

NATIONAL RENEWABLE ENERGY LABORATORY (NREL) GEOTHERMAL TECHNOLOGIES PROGRAM

<http://www.nrel.gov/geothermal/>

The information on this website is organized by topics such as technology description, program summary, research and development projects, and publications. The publications listed are downloadable PDF files.

DEPARTMENT OF ENERGY - GEOTHERMAL ENERGY TECHNICAL SITE

<http://geothermal.id.doe.gov/>

This website is maintained by Idaho National Engineering and Environmental Laboratory (INEEL). They have links to several publications including their research program annual reports, articles and a recent Dixie Valley Workshop. They also provide information on the geothermal resource maps they have produced and links to download the maps.

**SANDIA NATIONAL LABORATORIES:
GEOHERMAL RESEARCH DEPARTMENT**

<http://www.sandia.gov/geothermal/>
<https://cfwebprod.sandia.gov/cfdocs/GPI/>

Sandia provides information on the different projects they are working on and an email link to the person in charge of the project. They also provide links to several downloadable publications with more to be added at a later date.

GEOHERMAL ENERGY ASSOCIATION

<http://www.geo-energy.org>

The Geothermal Energy Association website includes information on existing and planned power plants. Some of that information includes contact information and where they are located. Also includes information on the next Geothermal Energy Trade Show that runs in conjunction with the Geothermal Resources Council Annual Meeting.

GEOHERMAL-BIZ.COM

<http://www.geothermal-biz.com/home.htm>

This website provides development information for the geothermal entrepreneur. They have information on financing geothermal direct use and small-scale power projects. They also provide information on why geothermal energy should be used for state agencies, electric power companies and environmental groups. Their calendar of events is the most comprehensive that I have found.

**THE UNITED NATIONS UNIVERSITY -
GEOHERMAL TRAINING PROGRAMME**

<http://www.os.is/page/unugtp>

This website explains what the United Nations University does and explains about their program plus what training they provide and the selection process for becoming a candidate.

A significant part of the practical training is done in connection with the research projects of the Fellows. In many cases the participants bring with them data from geothermal projects in their home countries, but sometimes the research projects are integrated with

geothermal exploration or utilization projects that are in progress in Iceland at the time of training. The project topic is always selected with respect to the conditions of the home country of the participant. Many of the project reports are written in such a way that they serve as manuals for performing certain measurements or interpretations dealt with in respective reports.

The Training Programme publishes all the project reports. Since 1994, the reports have been published in the annual book "Geothermal Training in Iceland" which has an international publishing code (ISBN 9979). Copies can be obtained upon request. The reports are mailed regularly to former UNU Fellows and many of the leading geothermal institutions in the developing countries. UNU-GTP reports from the years 1999 to 2003 are now available for downloading from their website.

**EUROPEAN GEOHERMAL ENERGY
COUNCIL – EGEC**

http://www.geothermie.de/egec_geothernet/menu/frameset.htm

This website has a tremendous amount of information on their website, but it is easy to forget where you are in their website. They have three different levels that you can enter into (Beginners, Professional and Scientist), but once you enter into a level you can access information in all the levels.

The Beginners level includes information on what is geothermal, why we should use it, geothermal short course and basic information on the countries with geothermal. The Professional level has information on country overviews, project information, applied technology, geological information, research overview and future potential and developments. The Scientists level includes information on research projects, scientific papers and congress information.

**GREAT BASIN CENTER FOR GEOHERMAL
ENERGY**

<http://www.unr.edu/geothermal>

CALIFORNIA ENERGY COMMISSION

<http://www.energy.ca.gov>

**CALIFORNIA DEPARTMENT OF
CONSERVATION – DIVISION OF OIL, GAS
AND GEOHERMAL RESOURCES**

<http://www.consrv.ca.gov/DOG/index.htm>

NEW ENERGY AND INDUSTRIAL TECHNOLOGY DEVELOPMENT ORGANIZATION (NEDO) - GEOTHERMAL ENERGY DEVELOPMENT DEPARTMENT

<http://www.nedo.go.jp/chinetsu/indexe.htm>

This website provides information on the types of projects that NEDO are involved in.

HOT DRY ROCK

Swiss Deep Heat Mining Project

<http://www.dhm.ch/dhm.html>

The website includes information on the Hot Dry Rock geothermal energy program in Switzerland. There is also information about the technology and the ongoing development program, including photos, maps, and diagrams.

European HDR project, Soultz-sous-Forets, France

<http://www.soultz.net/>

This website provides basic information on the HDR Soultz project and status of the current phase of the project.

Stadtwerke Bad Urach (German)

http://www.geothermie.de/bad_urach.htm

This website is in German, but they provide pictures and graphics of the project, plus there are links to other HDR projects in the world.

CADDET

They provided information on full-scale commercial geothermal energy projects and case studies.

<http://www.caddet.co.uk/html/geo.htm>

INTERNATIONAL DISTRICT ENERGY ASSOCIATION

<http://www.districtenergy.org/>

WASHINGTON STATE UNIVERSITY ENERGY PROGRAM

<http://www.energy.wsu.edu/projects/renewables/geothermal.cfm>

PUBLICATIONS AVAILABLE ONLINE

Geopubs – USGS Western Region Geologic Publications

<http://geopubs.wr.usgs.gov/>

This webpage provides links to geologic publications by the USGS on Scientific Investigation Reports and Maps, Fact Sheets, Geologic Investigations Series Maps, Circulars and Open-File Reports from 1988 to 2005, which can be viewed sorted by state or topic.

USGS Open-File Report 99-425 Geothermal Industry Temperature Profiles from the Great Basin

<http://wrgis.wr.usgs.gov/open-file/of99-425/webmaps/home.html>

This webpage provides a link to the database produced from this report on the Great Basin and an interactive map to access the well data including a temperature log.

Geothermics

<http://www.elsevier.com/locate/geothermics>

This webpage link provides information on the publication Geothermics. Information is also included on how to submit a paper and how to subscribe to the Journal. The table of contents and abstracts to articles is provided free.

DOE's Scientific and Technical Information - Information Bridge

<http://www.osti.gov/bridge/>

The website provides information on Department of Energy research and development reports for such topics as environmental sciences, energy technologies, renewable energy and other topics.

Office of Scientific and Technical Information - Geothermal Energy Technology

<http://www.osti.gov/get/gethome.html>

This website allows you to search for publications from several different databases including Energy Information Administration, Environmental Protection Agency and National Technical Information Service. I found the search mechanism, though, on their website is a little hard to get the publications you are trying to access.

Proceedings for Multiple Integrated Uses of Geothermal Resources - International Geothermal Conference - 2003

<http://www.jardhitafelag.is/igc/nytt/>

They have provided a website where the proceeding of the conference can be downloaded. They can be looked at by session or by author.

WEBSITES WITH PICTURES OR SLIDES

Geothermal Education Office

<http://geothermal.marin.org/>

The Geothermal Education Office has produced a slide presentation with 122 slides. These can be viewed on their website and they provide information on the use of the slides.

National Renewable Energy Laboratory - Photographic Information Exchange

http://www.nrel.gov/data/pix/searchpix.cgi?query=GEO_THERMAL&display_type=tiled&max_display=20&search_home=searchpix_visual.html

This website has 620 pix images concerning geothermal which can be viewed at 20 pictures on a page with a description of each picture.

GEO_THERMAL ASSOCIATION WEBSITES

Most countries have some type of Geothermal Association below are the ones that I have come across in my research for this paper. I am sure there are other association websites, but they might be in their native language only and not English. Some of the websites below are in both their native language and English.

Australian CRC for Renewable Energy Ltd
<http://acre.murdoch.edu.au/refiles/geo/text.html>

Canadian Geothermal Energy Association
<http://www.geothermal.ca/>

German Geothermal Association Welcome to GtV
<http://www.geothermie.de/>

Hungarian Geothermal Association
<http://www.deltasoft.hu/mgte/indexa.htm>

Iceland Geothermal Association
<http://www.jardhitafelag.is/english/index.shtml>

Indonesian Geothermal Association
<http://www.api.or.id/>

Ireland Geothermal Association
<http://www.feasta.org/documents/wells/contents.html?seven/connor.html>

Mexican Geothermal Association
<http://www.ugm.org.mx/agm/>

New Zealand Geothermal Association
<http://www.nzgeothermal.org.nz/>

Polish Geothermal Association
<http://www.pga.org.pl/>

Swiss Geothermal Society _SVG-SSG
<http://www.geothermal-energy.ch/fr/svg/svg.htm>
Turkish Geothermal Association
<http://www.jeotermaldernegi.org.tr/>

HEAT PUMP WEBSITES

Geothermal Heat Pump Consortium
<http://www.geoexchange.org/>

International Ground Source Heat Pump Association
<http://www.igshpa.okstate.edu/>

European Heat Pump Association
<http://www.ehpa.org>

GeoCool Lab - Department of Mechanical Engineering - University of Alabama
<http://bama.ua.edu/~geocool/>

Earth Energy Society of Canada, Ground Source Heat Pumps
<http://www.earthenergy.ca/>

The IEA Heat Pump Centre (HPC)
<http://www.heatpumpcentre.org/>

100 YEARS OF GEOTHERMAL POWER PRODUCT

John W. Lund

Geo-Heat Center
3201 Campus Drive
Klamath Falls, Oregon, 97601, USA
e-mail: lundj@oit.edu

ABSTRACT

Electricity from geothermal energy had a modest start in 1904 at Larderello in the Tuscany region of northwestern Italy with an experimental 10 kW generator. Today, this form of renewable energy has grown to 8904 MW in 25 countries producing an estimated 56,831 GWh/yr. These “earth-heat” units operate with an average capacity factor of 73%; though, many are “on-line” over 95% of the time, providing almost continuous base-load power. This electricity production is serving an equivalent 63 million people throughout the world, which is about one percent of our planet’s population. The development of worldwide geothermal power production can be seen in Figure 1. The large downward spike in the production is the result of the destruction of the Italian field at the end of World War II – discussed later. Since WWII, geothermal power has grown at a rate of 6.2% annually. Electric power from geothermal energy, originally using steam from resources above 150°C, is now produced from resources down to 100°C using the organic Rankine cycle process in binary power units in combination with a district heating project.

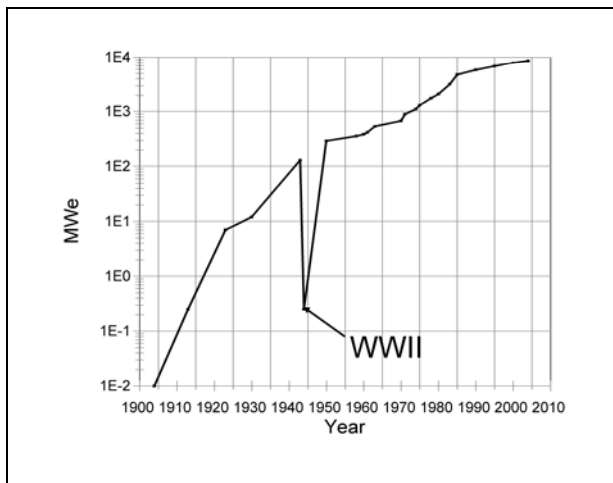


Figure 1. World geothermal power production 1904-2004.

THE EARLY YEARS – DRY STEAM DEVELOPMENT

Geothermal energy was not new to the Larderello area in 1904, as sulfur, vitriol, alum and boric acid was extracted from the hot spring areas and marketed at least since the 11th century. In the late 18th century, boric acid was recognized as an important industry in Europe, as most was imported from Persia. Thus, by the early 1800s, it was extracted commercially from the local borate compound using geothermal heat to evaporate the borate waters in *lagoni* or *lagone coperto* -- a brick covered dome (Figure 2). Wells were also drilled in the early 1800s in the vicinity of fumaroles and natural hot pools to access higher boron concentrations.

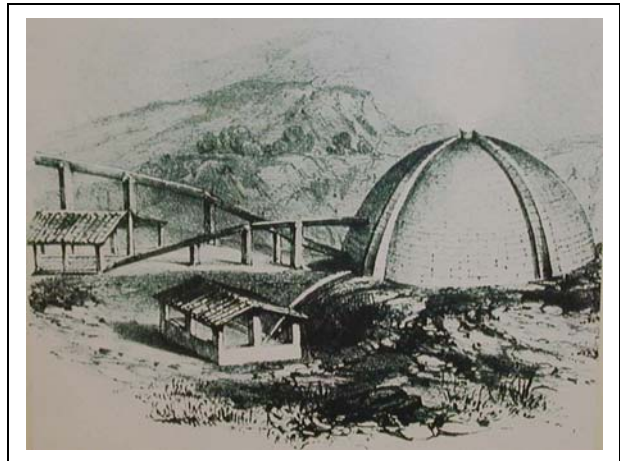


Figure 2. Covered lagoon (“lagone coperto”), Larderello, Italy (courtesy of ENEL), 18th century.

In the beginning of the 19th century, the Larderello chemical industry came under the direction of Prince Piero Ginori Conti. He experimented with the use of geothermal steam as an energy source for electrical production. He carried out his investigations for several years and was rewarded with success in 1904, when five light bulbs were lighted using geothermal power. He used a piston engine coupled with a 10-

kilowatt dynamo; the engine was driven by pure steam produced in a small heat exchanger fed with wet steam from a well near Larderello (Figure 3). This engine used an “indirect cycle” – that is the geothermal fluid heated a secondary pure water to produce steam that turned the piston-generator set. This was the first binary cycle – using a secondary working fluid. The “indirect cycle” protected the piston from the potential harmful affects of chemicals in the geothermal fluid.

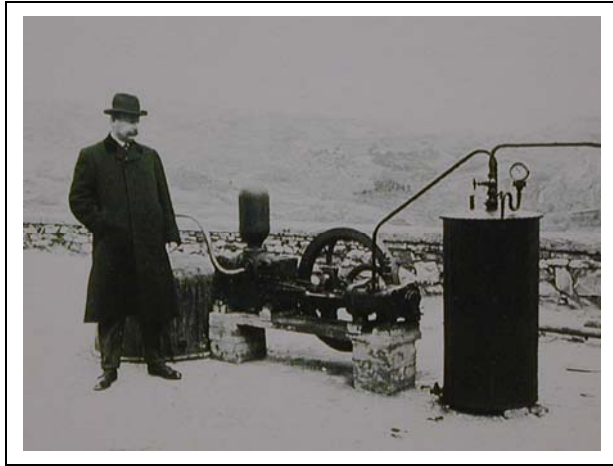


Figure 3. Prince Ginori Conti and the 10 kW experimental power plant, Larderello, Italy, 1904 (courtesy of ENEL).

Encouraged by the results from this “first” experiment, Prince Conti developed the “first” prototype of a geothermal power plant, which went into operation in 1905. This Cail reciprocating engine connected to a 20-kilowatt dynamo along with a Neville Reciprocating engine coupled to a second 20-kilowatt dynamo in 1908 enabled the electrification of Larderello’s most important industrial plants and the main residential buildings. In 1913, the “first” commercial power plant, named Larderello 1, was equipped with a turbine generating 250 kilowatts of electricity (Figure 4). It was designed and built by the Tosi Electromechanical Company to operate with wellhead fluid pressures of up to three atmospheres. The turbine was driven with pure steam obtained from a heat exchanger supplied by geothermal fluids from two wells at 200 to 250°C. The energy from this plant was fed into a network serving all the chemical production plants and the main buildings of Larderello, and the villages of the region.

By 1923, two 3.5-megawatt turbo alternators units using the “indirect cycle” were installed, equaling most of the world’s installed hydroelectric and thermal power plants of the time. The “first” pilot turbine fed directly with natural steam produced from the wells or “direct cycle,” with a capacity of 23

kilowatts was installed at Serrazano in 1923 (Figure 5). Other “direct cycle” plants at Castelnuovo (600 and 800 kW) and at Larderello (3.5 MW) followed in the late 1920s. Thus by 1930, the installed capacity of this Boraciferous region was 12.15 MW of which 7.25 MW used the “indirect cycle” and 4.90 MW the “direct cycle.” The “indirect cycle” plants remained popular, as the natural steam produced by the wells at Larderello was more valuable to extract valuable chemical by-products.

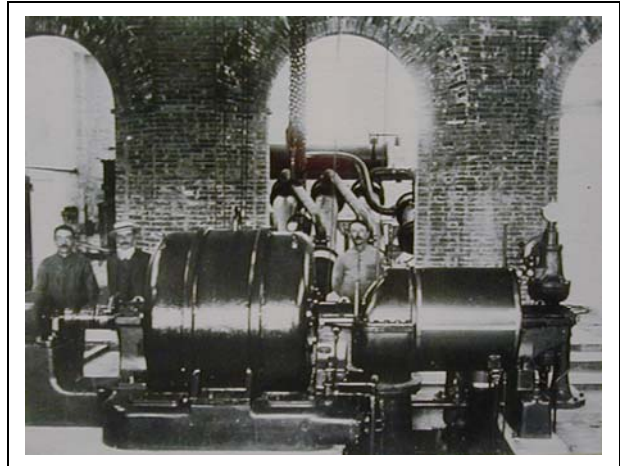


Figure 4. First commercial geothermal power plant, 250 kW, Larderello, Italy, 1913 (courtesy of ENEL).

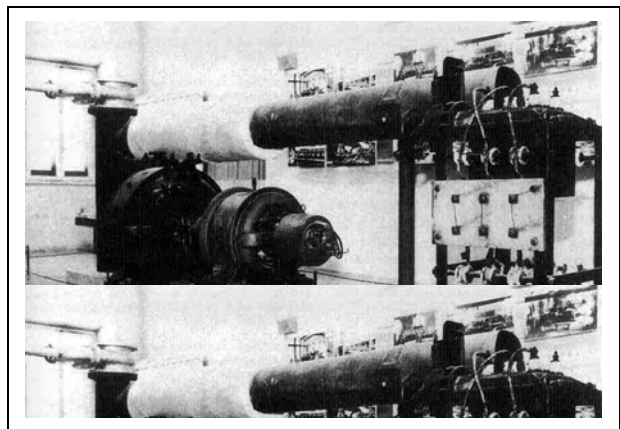


Figure 5. First “direct cycle” power plant, Serrazano, Italy, 1923 (courtesy of ENEL).

At the end of 1943, the total installed capacity in the Boraciferous region was 132 MW of which 107 MW used the “indirect cycle.” The others were exhausting-to-atmosphere units or “direct cycle.” Unfortunately in 1944, the Larderello region was directly involved in World War II. The Larderello power plants were strategically important because they provided electricity to the whole railway

network of central Italy. In the spring of 1944, not far from Larderello, the retreating armies then in Italy formed the “Gothic Line” which separated the two warring groups. All the geothermal power stations and chemical plants in the area were heavily bombed and destroyed (Figure 6), and almost all the production wells were blown up by charges placed at the base of the master valve. Only the 23-kW “direct cycle” plant survived – which has been used at the company school to train technical personnel since 1925.



Figure 6. Geothermal plant at Larderello, destroyed in WWII, 1944 (courtesy of Ian Thain).

With hard work, the capacity of the region was reconstructed and reached almost 300 MW by 1950, and has continued to increase over the years to the present installed capacity of 790.5 MW (699 MW operating capacity) producing 5.3 billion kWh in 2003. Many of these earlier plants have natural draft cooling towers that dominated the landscape. However, the newer plants are designed to have a low profile with forced draft cooling towers and are architecturally pleasing in appearance (Figure 7). Most of these plants are supplied by “dry steam” wells that produce only high-temperature steam – thus, eliminating the need to separate steam from water.

THE NEXT STAGE – WET STEAM DEVELOPMENT

A major geothermal resource with surface manifestations occurs at Wairakei, in the volcanic region of North Island of New Zealand. Thus, during World War II, New Zealand government scientists arranged for army engineers serving with the British 8th Arm, in the Italian campaign, to visit, inspect and report on the Larderello geothermal power development. Unfortunately, when they got to the plant in June 1944, it had been total destroyed.

Further interest in the development of the Wairakei field came in 1947 from severe electricity shortages

following two dry years which restricted hydro generation and a desire by the government for the New Zealand electricity supply to be independent of imported fuel. Thus in 1948, New Zealand engineers were again sent to Larderello where, they found rebuilt power plants producing over 140 MW and another 142-MW station under construction.



Figure 7. Geothermal power plant at Larderello today (courtesy of ENEL).

These observations of the power plants and geothermal use at Larderello were important; however, the New Zealand engineers faced a more complicated problem. Whereas, the Larderello resource was of the “dry steam” type, Wairakei was a “wet steam” resource. This meant that New Zealand technology had to be developed to separate the steam from the high-temperature hot water, produced at 13.5 barg (approximately 200°C). Thus, encouraged by the enthusiasm of the Italian engineers for geothermal power production, New Zealand decided to proceed with the development of Wairakei.

Drilling started in 1949, with some spectacular results (Figure 8), and 20 MW of power was proven by 1952. The initial plans for Wairakei was a combined power station and a heavy water plant. Conceptual designs in 1954 provided for a 47-MW power plant and production of 6 tonnes per year of heavy water. However, the heavy water plant idea was abandoned in 1956, and thus the electric power station, Wairakei “A,” was redesigned for two high pressure (HP) units of 6.5 MW, two intermediate pressure (IP) units of 11.2 MW, and three low pressure (LP) condensing units of 11.2 MW, giving a total installed capacity of 69 MW. The HP units used flashed steam at the wellhead of 13.5 barg, the IP units used 4.5 barg, and the LP units used a pressure of just above one barg. Due to increased output from the wells, two addition HP units of 11 MW and one LP unit of 11 MW were added to Wairakei “A” Station. Additional generating capacity was added through a “B” Station, which brought the entire development to 192.6 MW.

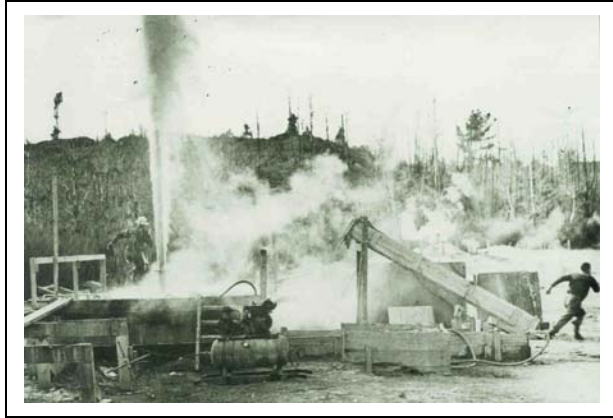


Figure 8. Drilling at Wairakei, New Zealand, 1950s (courtesy of Ian Thain).

In November of 1958, the first turbine-generator sets in “A” Station were synchronized to the national grid – the first geothermal electrical development in the world using “wet steam.” High-temperature and pressure well water of five HP and two IP wells was fed into a flash plant; where, the pressure was reduced and a fraction of the water (15 to 20%) is flashed to steam in successive stages. The Wairakei Separator was developed for this task, which used a tangential entry bottom outlet tank. The center of the production field is approximately 3.5 km from the power station, and the steam is transmitted to the power station via three 760 mm and five 508 mm diameter pipelines (Figure 9). The power station is located adjacent to the Waikato River; where, the water is used for the direct contact condensers (Figure 10). Condensing the steam with river water exiting from the turbine reduces the pressure to a vacuum, thus increasing the pressure drop across the turbine, which in turn increases the output efficiency by as much as 100% compared to atmospheric exhaust plants.



Figure 9. Wairakei, New Zealand geothermal field.



Figure 10. Wairakei power plant with Waikato River in background, New Zealand.

With time, both double flash and triple flash turbines were installed to take advantage of the three-pressure levels of steam. Due to steam decline, the HP systems were derated and only IP and LP steam are only used today. Other fields at Ohaaki, Rotokawa, Mokai, Kawerau and Ngawha have been added to the geothermal power generating network with a total installed capacity of 435 MW (403 MW operational) of which 162 MW are at Wairakei. These plants, producing 2774 GWh/yr, operate with a capacity of around 80%, providing the country with about 5.5% of its installed electricity capacity and 6.7% of the energy generated.

EARLY DEVELOPMENTS IN THE AMERICAS

United States

The surface geothermal manifestations at The Geysers geothermal field in northern California, was used by Indians who cooked with the stream and hot water at thermal features, and basked and bathed for pleasure and cures. In the mid-1880s, European settlers “discovered” the area and referred to them as the “Gates of Hades.” The area was then developed for tourists with the construction of The Geysers Hotel. By the 1880s, the hotel had earned an international reputation as a resort and spa. By the early 1920s, the resource was being considered for electrical power generation. Well No. 1 was drilled in 1921 and at a shallow depth “...the well blew up like a volcano.” A second well, also called No. 1, was drilled in 1922 and controlled, but not before it blew out “...mud, tools, rocks, and steam” -- the world’s first successful geothermal well drilled for electrical power generation outside of Larderello. Steam was found at about 60 meters – a second “dry steam” field. Well No. 2 was completed in 1923 to a depth of 97 m with a temperature of 153°C and 4 barg pressure.

John Grant constructed the first power plant at The Geysers in the early 1930s near wells No. 1 and 2 (Figure 11). It was a 35-kilowatt power plant containing two reciprocating, steam-engine-driven turbine generators from General Electric. Various metal alloys were heated to determine the best composition for the turbine blades – as the steam was used directly in the turbine – unlike the early “indirect steam” plants at Larderello. A contract was signed to sell the energy to nearby Healdsburg City; however, an oil glut hitting the West Coast of the U.S., made electricity generated from this fuel more attractive. The contract was cancelled in 1934 and at least one of the two original generators was moved to The Geysers Resort. Here, electricity was generated for the hotel, cottages, bathhouse and grounds into the 1950s.

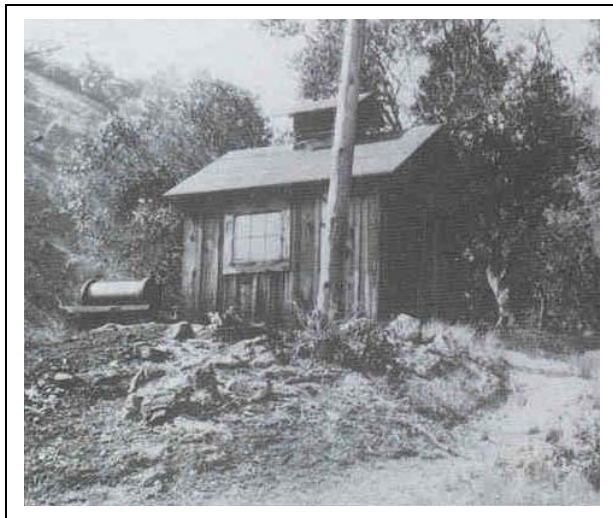


Figure 11. First power plant at The Geysers, USA, early 1930s (courtesy of Geothermal Resources Council).

B.C. McCabe who had created Magma Power Company drilled the first modern well, Magma No. 1, in 1955. Dan McMillan Jr. created Thermal Power Company in 1956, and together these two companies began drilling five wells over the next two years, the deepest at 427 meters. In 1958, Pacific Gas & Electric Company (PG&E), a major public utility in Northern California, signed a contract to purchase steam from the Magma-Thermal venture, the first modern commercial agreement for geothermal electrical power generation in the United States. PG&E built power plant Unit 1 and began operating in 1960 – the first modern power plant to generate electricity from geothermal steam in the U.S.

By 1968, the capacity of the field increased to 82 MW and wells reach to depths of 600 meters. In 1967, Union Oil Company of California became the field operator. By 1989, 29 units had been

constructed with an installed capacity of 2,098 MW. Today, Calpine Corporation and Northern California Power Agency (NCPA) operate the field with a gross capacity of 936 MW from 22 units (Figure 12). The reduction in capacity is due to the dismantling and retirement of a number of units and a reduction in steam production due to “too many straws sucking from the reservoir” and only about 20% of the produced fluid being injected back into the reservoir. This reduction is being reversed in several units by the Southeast Geysers effluent recycling system (SEGEP). This project and the more recent one from the city of Santa Rosa injects recycled wastewater into the reservoir to recover more steam for power production. A total of 820 liters/second is being injected through two large pipelines. To date, the inject water from SEGEP has brought back 77 MW and another 100 MW increase is expected from the Santa Rosa project.

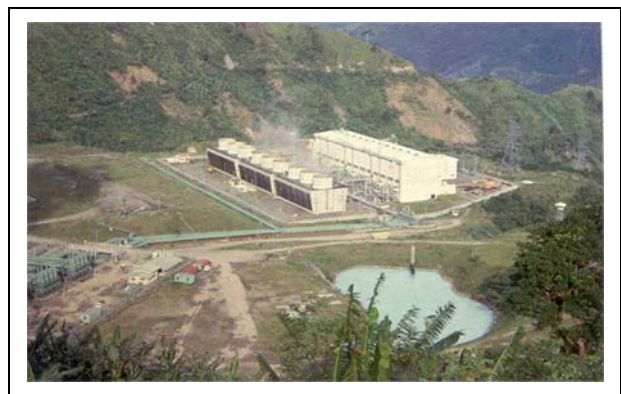


Figure 12. Modern 110 MW plant at The Geysers, California.

The total installed capacity in the U.S. is now about 2534 MW (2000 operating) generating about 17,840 GWh/yr for a capacity factor of 80%.

Mexico

Another “dry steam” field was developed at Pathé in central Mexico. It was the first geothermal zone explored in the country between 1950 and 1955. In 1955, the first exploration well was drilled. Over 24 wells, to depths of 195 to 1288 meters, were drilled over the next four years, with three successful one used to supply steam to a geothermal power plant of 3.5 MW in 1959. The geothermal plant, the first commercial one on the American Continent was operated until 1972, when it was abandoned and dismantled.

Later fields at Cerro Prieto, just over the U.S. border near Mexicali, and at Los Azufres, between Mexico City and Guadalajara were developed. They, with two other smaller fields, now have an installed

capacity of 953 MW producing 6,282 GWh/yr (2003) for a capacity factor of 75%.

DEVELOPMENTS IN ASIA

Japan

Small geothermal test plants were made in Beppu (1925) and Otake (1926) geothermal fields on the southern island of Kyushu. These tests were based on the idea that "... volcanoes have enormous heat energy as seen in volcanic explosions." However, these trials were not successful.

The first commercial power plant was put online at Matsukawa on northern Honshu in 1966. This 23-MW condensing power plant uses a "dry steam" resource. Like Larderello and The Geysers, this is one of the few sites in the world where "dry steam" is available. This plant is the result of drilling in 1953 in the hope of discovering a source of hot water to supply a health spa. Instead, many of the wells produced steam at a depth of 160 to 300 meters. Before the power station was constructed, tests were run for 18 months on a 450-kW atmospheric exhaust (back-pressure) turbine to assess the corrosion effects on various materials from exposure to geothermal steam and its condensate. Five wells now provide superheated steam at a pressure of 4.4 barg and temperatures ranging from 153 to 190°C. A natural draft tower, the only one of its type in Japan, provides water for the direct-contact condenser (Figure 13).

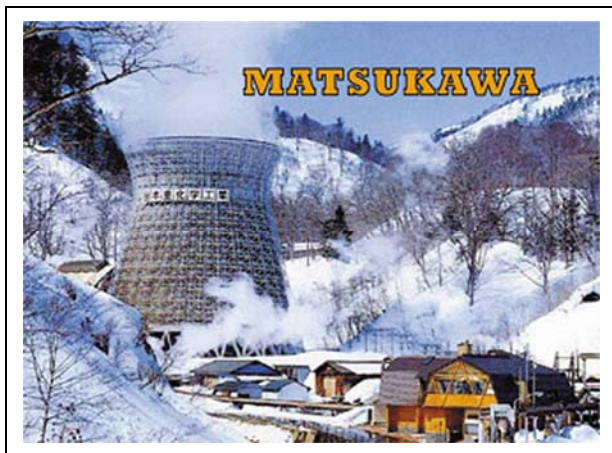


Figure 13. First power plant in Japan – 23 MW "dry steam" at Matsukawa.

Japan now has an installed capacity of 535 MW with plants distributed over 14 fields producing 3467 GWh/yr (1999-2000) for a capacity factor of 74%.

Russia

The Paratunka geothermal power plant, located on the Kamchatka peninsula in eastern Siberia, was an attempt to provide cascaded energy for use in both electric power generation and direct-use. The power plant began operation in 1967 (Figure 14), and was the first to use an organic binary fluid in the power cycle, R-12 refrigerant, as the working fluid heated so that it vaporized by geothermal water at 81°C – which is the lowest record geothermal fluid temperature recorded for electric power generation!

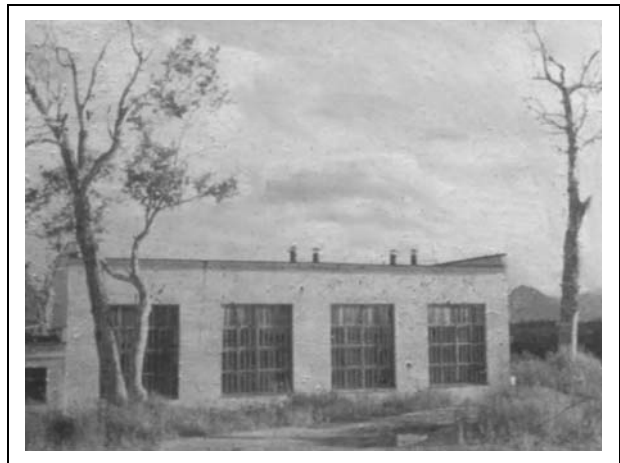


Figure 14. First binary plant using 81°C water at Paratunka, Kamchatka, Russia, 1967.

The power from the plant served a small village and several Soviet state farms. The geothermal water, after leaving the plant, was cooled to 45°C and used to heat the soil in a series of greenhouses. Finally, the cooling water leaving the condensers of the power plant was used to water the plants in the greenhouse, as the water from the local river was too cold to use. The power plant has since been shut down and dismantled, mainly due to leaks in the refrigerant piping.

A second plant at Pauzhetka in the same region was also put into production in 1967. This plant is a flash steam type using a cyclone separator, consisting of two units combining to 5 MW capacity. Nine wells are used to supply the plant, providing 2 to 4 barg pressure at 127°C. Another 11 MW have been added at Pauzhetka, along with 12 MW at the Severo-Mutnovka field. Presently, a 50-MW plant at Mutnovsky is operating at about 36 MWe net. Several smaller plants have been constructed on the Kuril Islands producing about 11 MW of power.

The total installed capacity of geothermal power plants in Russia, all located in the Kamchatka and Kuril Islands area, is 79 MW. These plants are critical, as all power in this area has to be produced

for local plants. Due to heavy snowfalls in the area, the new plant at Mutnovsky, is designed to be remotely operated, however six meter of snow depth limited the capacity of the cooling tower in winter.

Peoples Republic of China

In the early 1970s, recognizing the importance of geothermal energy as an alternative source of electrical power, small experimental power units were established along the east coast of China at Fengshun in Guangdong Province in 1970 (0.3 MW flash steam), followed by small binary plants, around 0.3 MW capacity, using temperatures between 80 and 100°C as Wentang and Huailai in 1971, Huitang in 1975 and Yingkou in 1977. It was found that these units were too small and the efficiency too low due to the low temperature of the geothermal water, that all have been shut down. In 1977, a geothermal power plant was put online at Yangbaijing in Tibet supplying power to Lhasa. The installed capacity was 3 MW using 202°C fluid of which 5 to 20% was flashed to steam. Today, the installed capacity, all located in Tibet, is 28 MW supplying over 30% of the electric power to Lhasa.

ICELAND

The first geothermal power plant was placed online in 1969 at Namafjall in northern Iceland (also known as Kisilidjan). This 3-MW non-condensing (back-pressure) plant was purchased second-hand from England to reduce construction time (Figure 15). The energy is supplied to diatomaceous earth drying plant located next to Lake Myvatn. Diatomaceous earth, with moisture contents at 80%, is dried in rotary drum driers and shipped to Germany to be used as a filter in beer production. Since it is a non-condensing plant, the efficiency is quite low, estimated around 14%; however, it is still in operation today.

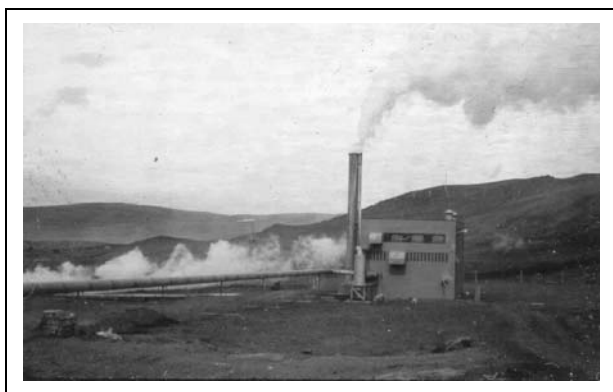


Figure 15. First geothermal plant in Iceland at Namafjall, 1969 – 3 MW non-condensing plant.

More recently, a combined heat and power plant has been built at Svartsengi in southwestern Iceland. The

plant using 240°C fluid, provides 45 MW of electricity (8.4 MW of which is from binary units) and 200 MW of thermal energy to the surrounding community. The waste brine, high in silica content, is run into the adjacent lava field, sealing the bottom, thus providing a large heated pond. This pond today is famous as the Blue Lagoon, used by local and tourists (Figure 16).



Figure 16. Combined heat and power plant at Svartsengi, Iceland – Blue Lagoon on right (courtesy of Haukur Snorrason, Rekkjavik, Iceland).

RECENT DEVELOPMENTS

With the successes through the 1960s and early 1970s, geothermal power plant construction took off:

- 1975 – 30 MW at Ahuachapan, El Salvador
- By 1980 – plants in Indonesia, Kenya, Turkey, the Philippines and Portugal (Azores) were online.
- By 1985 – plants in Greece (Milos), France (Guadeloupe) and Nicaragua online.
- By 1990 – plants in Thailand, Argentina, Taiwan and Australia on line – the plant in Greece shut down.
- By 1995 – plant in Costa Rica online.
- By 2000 – plants in Austria, Guatemala and Ethiopia online – the plant in Argentina shut down.
- By 2004 – plants in Germany and Papua New Guinea online.

Binary cycle plant using the organic Rankin cycle, became more popular – as they can use lower temperature water – down to 100°C. Since efficiencies are low and economics questionable (high parasitic loads) at these temperatures, these plants are often constructed in concert with a district heating system. These plants are also modular, generally in sizes less than one megawatt, thus, allowing for rapid installation. Examples of these new installations are as follows:

Austria

A one-megawatt binary unit at Altheim using 106°C fluid at 100 liters/second from a 2,270-meter deep well, also supplied 10 megawatts of thermal energy

to the local district heating network (Figure 17). A second power plant-district heating project is at Bad Blumau in eastern Austria providing 250 kW of electric power from a binary plant using 110°C water, and then supplies 2.5 MW of thermal power with the waste 85°C water to the hotel and Spa Rogner.

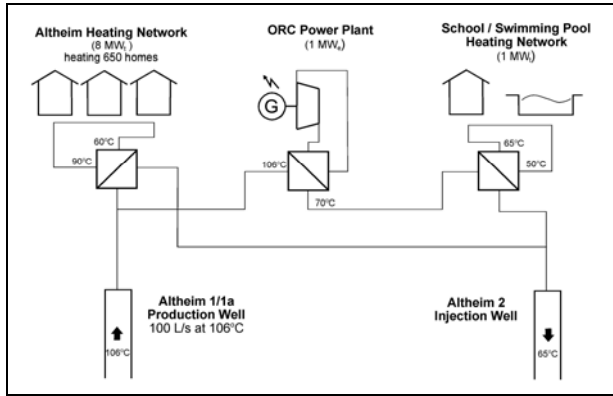


Figure 17. Combined heat and power plant at Atheim, Austria.

Thailand

A 300-kW binary plant using 116°C water provides power to the remote village of Fang (Figure 18). In addition hot water is also used for refrigeration (cold storage), crop drying and a spa. The power plant provides electric energy at a rate of 6.3 to 8.6 US cents per kWhr, replacing a diesel generator that cost 22 to 25 US cents per kWhr.



Figure 18. Binary power plant, 300 kW, at Fang, Thailand.

Germany

At Neustadt Glewe in north Germany a well at 100°C provides energy for a 210 kW_e binary plant and 11 MW thermal to a district heating system (Figure 19). This is the lowest temperature binary plant operating in the world at present.

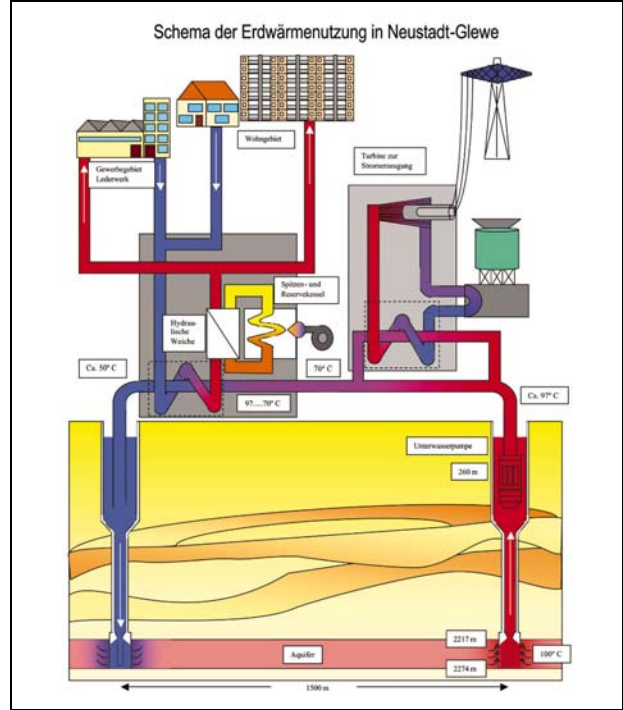


Figure 19. Combined heat and power at Neustadt Glewe, Germany.

Mexico

In the northern state of Chihuahua, an isolated village, Maguarichic, relied on a 90-kW diesel generator to provide electricity for only three hours in the evening. The villagers rarely had meat, cheese or milk, and they were not aware of national events since no television was available. The federal government in 1997 provided a 300-kW_e binary plant using 150°C water for US\$3000/kW (Figure 20). The villagers now have street lights, refrigerators and have established a small cottage industry using electric sewing and tortillaria machines. Best of all, the children now have ice cream!



Figure 20. 300 kW binary plant at Maguarichic, Mexico.

United States

Near Susanville in northern California, two 375-MWe binary plants operated by Wineagle Developers provide a net power output of 600 kW (Figure 21). The plants used 63 liters per second of 110°C waters. The plant is completely automated. The entire plant, including the well pump, is controlled by either module. By pushing one button on the module control panel, the plant will start, synchronize to the power line and continue operation. If the power line goes down, the module and downhole pump immediately shut down, since no power is available for its operation. When the power line is re-energized, the modules restart the downhole pump, and then bring themselves on line. Operation can be monitored remotely, with a service person alerted by an alarm system.



Figure 21. Wineagle binary plant of 2X375 kW in northern California, USA.

SUMMARY

The following figures are based on reports for the World Geothermal Congress 2005 (Turkey) (Bertani, 2004). The figures for capacity is the installed number, as the operating capacity may be less, and the energy produced, in many cases are estimated, as data is often not available.

CONCLUSIONS

With 100 years of experience, reservoir engineers, and plant operators have learned the importance of giving more attention to the resource, including the injection of spent fluids. With proper management the resource can be sustained and operated for many years. Geothermal fields have been operated for over 50 years and probably can be for over 100 years. The cost of power has been declining, and in many cases is competitive with fossil fuel plants at 4 to 5 US cents per kWh.

Binary cycle plants are becoming more popular, as they can use lower temperatures – down to 100°C – and the economics of the system is improved if the wastewater is used in a direct-use project such as district heating. Modular units are available in both binary and flash steam models, which allows for rapid installation. This will allow geothermal power to be extended to many “low-temperature” geothermal resource countries. I predict, that in the next 20 years we will see 25 new countries added to the list of geothermal power producers.

Table 1. Installed (gross) Geothermal Power Worldwide (2004).

<u>Country</u>	<u>Installed MW</u>	<u>Est. Energy Produced (GWh/a)</u>
Argentina	(1)	not operating
Australia	0.2	0.5
Austria	1	3.2
China	28	95.7
Costa Rica	163	1145
El Salvador	151	967
Ethiopia	7	30
France (Guadalupe)	15	102
Germany	0.2	1.5
Greece	(2)	not operating
Guatemala	33	212
Iceland	202	1406
Indonesia	797	6085
Italy	790	5340
Japan	535	3467
Kenya	127	1088
Mexico	953	6282
New Zealand	435	2774
Nicaragua	77	207.7
Papua New Guinea	6	17
Philippines	1931	9419
Portugal (Azores)	16	90
Russia	79	85
Taiwan	3	3.3
Thailand	0.3	1.8
Turkey	20	105
<u>United States</u>	<u>2534</u>	<u>17840</u>
TOTAL	8904	56831

Finally, the importance of geothermal power production in some countries is significant in contributing to the electrical energy mix as presented in Table 2 (Bertani, 2004).

ACKNOWLEDGEMENTS

I would like to acknowledge the support of Dr. Burkhardt Sanner and Dr. Werner Bussmann of Geothermische Vereinigung e. V. (German Geothermal Association), and the International Geothermal Association of Pisa, Italy for their support in making the original presentation of this

subject at the "Day of Geothermal Power" of the International Conference for Renewable Energies, Bonn, Germany, 2 June 2004.

Table 2. National Geothermal Contribution to the Electric Power Utilization (2004)

<u>Country</u>	<u>% of National Capacity (MW)</u>	<u>% of National Energy (GWh/yr)</u>
El Salvador	14.0	24.0
Kenya	11.2	19.2
Philippines	12.7	19.1
Iceland	13.7	16.6
Costa Rica	8.4	15.0
Nicaragua	11.2	9.8
New Zealand	5.5	7.1
Indonesia	2.2	6.7
Italy	1.0	1.9
USA	0.3	0.5
Tibet (China)	30	30
San Miguel (Azores)	25	25
Lihir Is. (Papua NG)	11	11
Guadeloupe (France)	9	9

REFERENCES

Bertani, R., 2004. "World Geothermal Generation 2001-2005: State of the Art," prepared for the World Geothermal Congress 2005, Turkey, 19 p.

Burgassi, P. D., 1999. "Historical Outline of Geothermal Technology in the Larderello Region to the Middle of the 20th Century," Chapter 13 in: *Stories from a Heat Earth – Our Geothermal Heritage* (R. Cataldi, S. F. Hodgson, and J. W. Lund,

editors), Geothermal Resources Council, Special Report 19, Davis, CA, pp. 195-220.

Thain, I. A., 1998. "A Brief History of the Wairakei Geothermal Power Project," *Quarterly Bulletin*, Geo-Heat Center, Klamath Falls, OR, pp. 1 – 4.

Hodgson, S. F., 1997. "A Geysers Album – Five Eras of Geothermal History," California Department of Conservations, Division of Oil, Gas, and Geothermal Resources, Sacramento, CA.

Lund, J. W., 2003. "The USA Geothermal Country Update," *Geothermics*, Vol. 32 (4/6), Elsevier Ltd., Oxford, UK, pp. 409-418.

Gutiérrez-Negrin, L. C. A, Garduño-Monroy, V. H., and Z. Casarrubias-Unzueta, 2000. "Tectonic Characteristics of the Geothermal Zone of Pathé, Mexico," *Proceedings*, World Geothermal Congress 2000, International Geothermal Association, Pisa, Italy, pp. 1189-1193.

Sato, K., 1970. "The Present State of Geothermal Development in Japan," *Proceedings* of the United Nations Symposium on the Development and Utilization of Geothermal Resources, Geothermics, Pisa, Italy, pp. 155-184.

DiPippo, R., 1980. Geothermal Energy as Source of Electricity, U.S. Department of Energy, U.S. Government Printing Office, Washington, D.C.

Kononov, V., Polyak, B., and B. Kozlov, 2000. "Geothermal Development in Russia: Country Update Report 1995-1999," *Proceedings*, World Geothermal Congress 2000, International Geothermal Association, Pisa, Italy, pp. 261-275.

Reservoir Engineering

Sustainable Heat Mining. A Reservoir Engineering Approach	<u>21</u>
<i>Miklos Antics, Maria Papachristou and Pierre Ungemach</i>	
High Temperature Plug Formation with Silicates	<u>35</u>
<i>S. Bauer, P. Gronewald, J. Hamilton, A. Mansure</i>	
Multiphase Flow Properties of Fractures	<u>43</u>
<i>Chih-Ying Chen and Roland N. Horne</i>	
Well Performance Estimation from Brief Discharge Using Heuristic Decline Analysis	<u>53</u>
<i>Malcolm A Grant</i>	
Inferring Relative Permeability from Resistivity Well Logging	<u>58</u>
<i>Kewen Li and Roland N. Horne</i>	
First Eleven Years of Exploitation at the Miravalles Geothermal Field	<u>64</u>
<i>Paul Moya and Antonio Yock</i>	
Tracer Test Analysis for Characterization of Laugaland Geothermal Field	<u>72</u>
<i>Gopi Nalla, G. Michael Shook, G.Axelsson</i>	
Why Well Monitoring Instruments Fail	<u>80</u>
<i>Randy Normann, Bernie Hubner, Harold Snyder</i>	
Classification of Geothermal Systems - A Possible Scheme	<u>85</u>
<i>Subir K. Sanyal</i>	
Pore Network Modeling of Adsorption Effects in Geothermal Reservoirs	<u>93</u>
<i>Ilkay Uzun and Serhat Akin</i>	

SUSTAINABLE HEAT MINING, A RESERVOIR ENGINEERING APPROACH

Miklos Antics⁽¹⁾, Maria Papachristou⁽²⁾ and Pierre Ungemach⁽¹⁾

⁽¹⁾Geoproduction Consultants (GPC), Paris Nord 2, 14 rue de la Perdrix, Lot 109,
BP 50030, 95946 ROISSY CDG CEDEX, France

m.antics@geoproduction.fr , pierre.ungemach@geoproduction.fr

⁽²⁾Aristotle University of Thessaloniki, Department of Geology, 54124 Thessaloniki, Greece
mariap@geo.auth.gr

ABSTRACT

Given that geothermal sources cannot be regarded as renewable, but exhaustible instead, heat mining prevails in any exploitation undertaking whatsoever.

Optimum heat recovery, pressure maintenance and waste disposal concerns make (re)injection of the heat depleted brine into, preferably, the source reservoir a major engineering and environmental concern.

This poses the problematic of reservoir life, assessed from production well thermal breakthrough times, and of sustainable resource extraction and reservoir management, which ambition at mining heat over significantly long, say at least fifty year, times.

In so doing, it should be borne in mind that geothermal operators need to reconcile this farsighted objective with severe constraining factors, such as well lifetime and drill site limitations, the latter particularly acute in city geothermal district heating environments.

The foregoing are discussed and illustrated in a case study addressing the following issues:

- (i) elaboration of the early system conceptual model and related breakthrough predictions;
- (ii) matching forecasted vs. actual breakthrough times, and model redesign and calibration by:
 - comparing 2D (single layer equivalent) and 3D (multilayered) reservoir structures,
 - assessing proper bed and cap rock thermal boundary conditions,
 - quantifying (analytically and numerically) interbedded impervious layers, stationary and transient, heat transfers and their impact on reservoir cooling kinetics;
- (iii) enhancement of system and reservoir life via appropriate production/injection multiwell (doublet/triplet) arrays and novel, long lasting, completions;

- (iv) last but not least, elaboration of relevant future heat demand and offer scenarios securing the sustainable management outcome.

Keywords: sustainability, reservoir engineering, reservoir management, district heating

INTRODUCTION

Low grade heat geothermal deposits are exhaustible. Heat within the geothermal reservoir is resupplied by conduction and abstracted, for commercial development purposes, by convection, at least an order of magnitude higher, an imbalance, which causes heat to be mined.

How to reconcile this “fatal” issue with sustainable heat mining strategies, aimed at securing well and reservoir longevities, is what geothermal engineering and further resource management are all about.

The foregoing will be illustrated and discussed in a case study addressing the Paris Basin geothermal district heating scheme, initiated in the late 1960’s by the completion, South of Paris, of the doublet concept of heat mining, combining a production and an injection well, the latter pumping the heat depleted brine into the source reservoir, followed by 54 replicates, of which 34 remain operating to date.

The exercise will elaborate on the following issues:

- (i) early reservoir conceptual models and related production well thermal breakthrough predictions;
- (ii) matching forecasted vs. actual breakthrough times and redesigning/calibrating modelling features by:
 - comparing 2D (single layer) and 3D (multilayered) reservoir structures;
 - assessing relevant bedrock/caprock thermal boundary conditions;
 - quantifying (analytically and numerically) interbedded impervious layer heat transfers

- and subsequent impacts on production well cooling kinetics;
- (iii) enhancement of well and reservoir life via appropriate production/injection multiwell arrays and novel, long lasting, well completions;
 - (iv) relevant future heat demand and offer scenarios meeting sustainability requirements.

SCOPE

Resource and reservoir setting

The Paris area belongs to a large intracratonic sedimentary basin, stable and poorly tectonised, whose present shape dates back to Jurassic age.

The Mid-Jurassic (Dogger) carbonate rocks were soon recognised as the most promising development target. The Dogger limestone and dolomite are typical of a warm sea environment associated to thick oolitic layers (barrier reef facies). They host a dependable reservoir, of regional extent, and display reliable reservoir properties as evidenced by the present development status.

Reservoir depths and formation temperatures range from 1400 to 2000 m and 56 to 80°C respectively.

A thorough survey of the Paris Basin geothermal reservoir can be found in the comprehensive review edited by Rojas (1989).

Development status

The location of the geothermal district heating sites is shown in fig. 1. Of the fifty five well doublets (mostly deviated from a single drilling pad), completed between 1971 and 1986, thirty four remain on line as of late 2004. They supply heating proper and sanitary hot water, via heat exchange, to ca. 120,000 equivalent dwellings. The total distributed heat amounts to 1,100 GWh/yr. (Ungemach et al, 2005)

Heat extraction

It was based, since exploitation start-up, on the doublet concept of heat mining pioneered by Gringarten and Sauty (1975), which provided a means for improved designs of well locations, bottomhole spacings and subsequent reservoir/well lifetimes.

The latter, assuming convective heat transfer alone, in a 2D homogeneous reservoir of constant thickness, upper and lower bounded by hydraulically impervious and thermally insulated bed and caprocks, is formalised by the thermal breakthrough time formula:

$$t_B = \frac{\pi \gamma_t d^2 e}{3 \gamma_f q} \quad (1)$$

where:

- t_B = thermal breakthrough time (h)
- d = bottomhole (top reservoir) well spacing (m)
- e = reservoir thickness (m)
- q = production (-)/injection (+) flowrate (m³/h)
- γ_t = reservoir heat capacity (J/m³ K)
= $\phi \gamma_f + (1 - \phi) \gamma_r$
- γ_f = fluid heat capacity (J/m³ K)
- γ_r = rock heat capacity (J/m³ K)
- ϕ = porosity

The Gringarten/Sauty analytical approach accounts for conductive recharge from the confining caprock, assumed at constant temperature, thus improving from 5 to 7%, breakthrough time assessed from (1).

It can also accommodate multiple production/injection well arrays in order to optimise heat recovery and reservoir lifetime, provided the reservoir remains homogeneous (Gringarten, 1979).

Most, if not all, well doublet arrays were designed, as to locations and spacings, according to this procedure. Since completion (the latest in 1986), no production well has undergone (premature) cooling yet, although there has been evidence of hydrodynamic interferences between neighbouring doublets, as one would normally infer from the dense well concentrations noticed in the Southern part of the reservoir (see fig. 1).

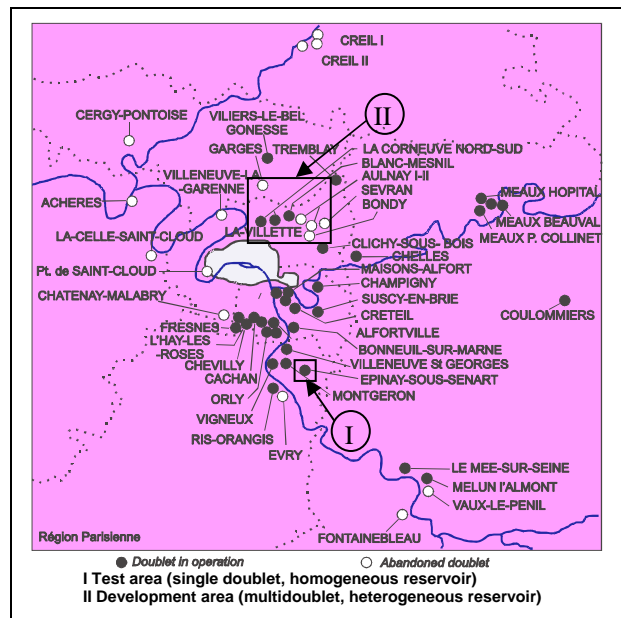


Figure 1. Location of the geothermal district heating sites in the Paris Basin

Recently, there has been renewed interest, among the public, toward reservoir simulation matters, as a result of growing clean air concerns, particularly acute in large city sensitive environments, such as the Paris suburban areas. These highlighted the environmental merits of geothermal district heating, which were merely rediscovered whereas the technology proved mature and reliable during the past decades.

Sustainability is becoming a key issue. In this respect, it should be borne in mind that ongoing district heating doublets are aging to the stage they should soon meet their expected 20 to 25 year well and reservoir longevity deadline.

This background has initiated several actions supporting sustainable resource and reservoir development prospects. Among those, it is worth mentioning the implementation of an interactive Dogger geothermal database and of long term oriented reservoir models commented and developed by Ungemach and Antics (2003) and Ungemach et al. (2005), aimed at achieving reliable reservoir management tools.

PROCEDURE

In order to assess sustainable reservoir development routes, prolonging the longevity of the existing heat

mining sites and facilities, the methodology flowcharted in fig. 2 has been designed.

It is basically aimed at (i) improving the previously exercised simulations (Ungemach and Antics, 2003; Ungemach et al., 2005), deemed to have simplified the actual reservoir features by portraying a 2D equivalent structure whereas it displays a multilayered suite of alternating interbedded permeable and impervious sublayers, (ii) investigating the impact of the latter in sustaining conductive heat resupply, and (iii) assigning adequate boundary conditions to the confining bed and caprocks.

It also proposes a parameter interpolation (usually performed via a geostatistical – Kriging – method) criterion, substituting to the former single well distributions doublet averaged figures (unless otherwise dictated by lithological considerations at locations close to lateral boundaries exhibiting fast facies changes) instead, thus smoothing the process.

It ought to be stressed that, in spite of the huge amount of doublet exploitation data recorded to date, the reservoir monitoring status lacks observation wells, tracer (Tritium for instance) injection surveys and reliable (production vs. injection well) interference tests. In no way does this ease the model calibration process.

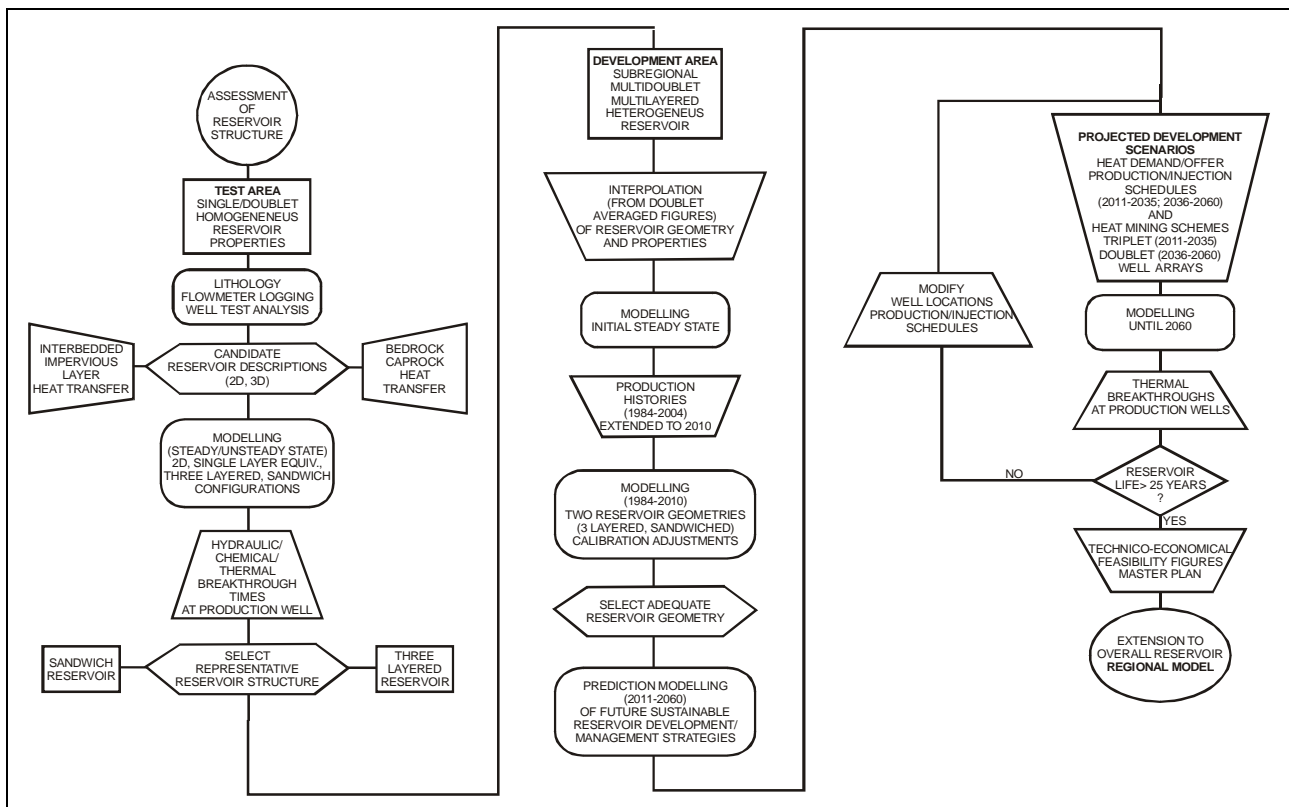


Figure 2. Sustainable reservoir development procedure

Summing up, the fig. 2 flowchart emphasises three main sequences, namely:

Assessment of reservoir structure

It addresses the single layer doublet/homogeneous reservoir case study, implemented on the so called test area, selected due to its remote location avoiding undue interferences from neighbouring doublets and homogeneous reservoir properties (uniform transmissivities and porosities) evidenced by well testing.

The simulations, run with SHEMAT (Clauser, 2003), screen four candidate reservoir configurations (i) 2D, i.e. single layer equivalent, stacking the individual producing layers identified from flowmeter logging (fig. 3a), bounded by hydraulically and thermally inert cap and bed rocks; it corresponds to the setting

formalised by equation (1), (ii) single layer equivalent, bounded by thermally active bed (constant terrestrial heat flow supply) and caprocks (constant mid point temperature), (iii) three layered reservoir including three productive and two intermediate impervious layers (fig. 3b), the latter storing heat eligible to conductive heat (re)supply of confining reservoir layers, and (iv) the “sandwich” reservoir, which reduces the previous layering to a single (stacked) impervious layer bounded by two symmetric (geometrically and hydraulically) reservoir layer setting (fig. 3c).

Configurations (iii) and (iv) comply to the bedrock and caprock conditions applied to (ii).

The foregoing are illustrated in fig. 3 sketches.

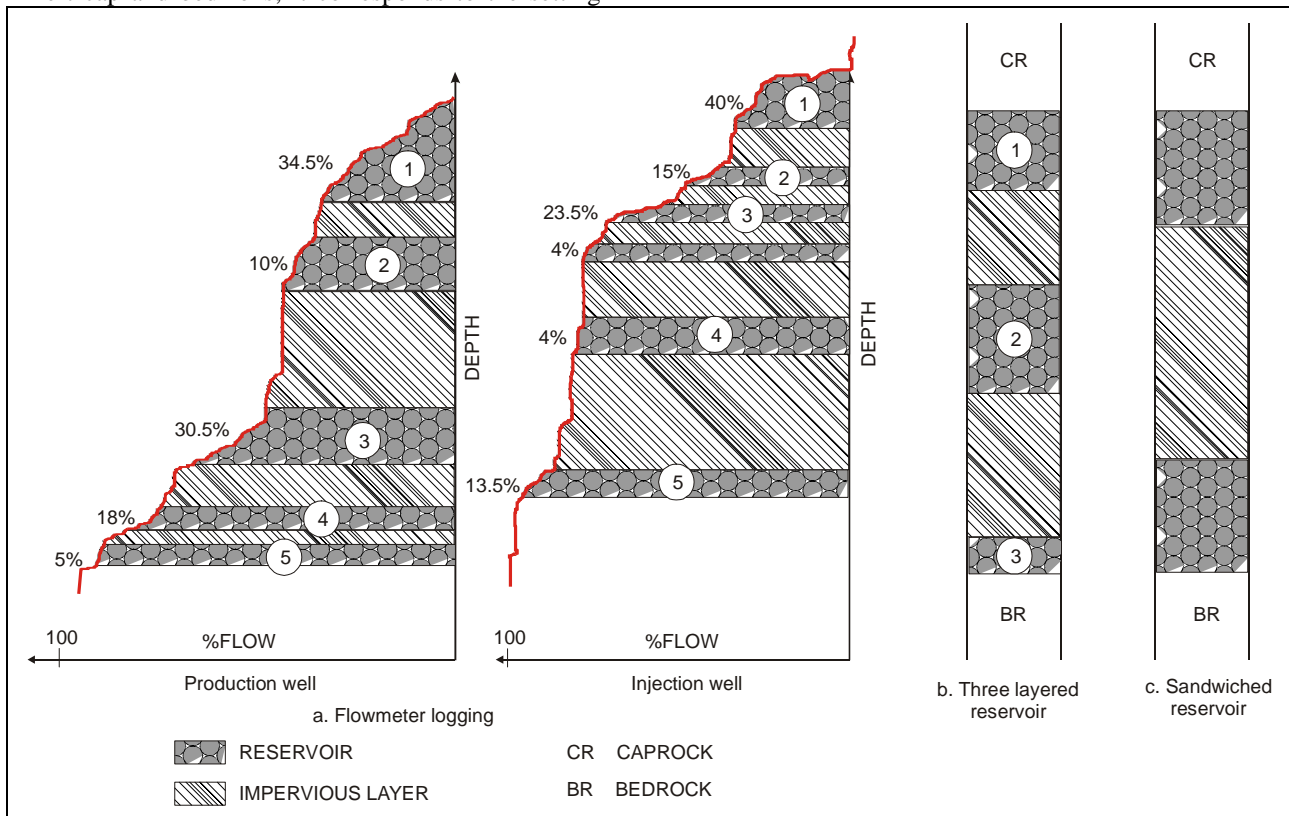


Figure 3. Test area. Flowmeter logs and productive/impervious layer assessment

The impact of heat transfer through and from the interbedded impervious layers, deemed to significantly delay reservoir cooling kinetics and production well thermal breakthroughs owing to their large amounts of stored heat, are analysed in Appendix. This mathematical, somewhat academic, exercise may nevertheless help in appraising critical, threshold type, impervious layer thicknesses while dealing with large simulation time scales.

Subregional reservoir simulation

It deals with the simulation, over the so called development area, of a multidoublet heterogeneous reservoir case, meeting the requirements of farsighted sustainable reservoir development/management objectives.

The reservoir model contemplates two eligible structures, three layered and “sandwich” types respectively, using TOUGH2 (Pruess, 1991), widely applied throughout the geothermal community.

Reservoir geometry (three layered structure) and hydrodynamic parameters, interpolated from target (3) and neighbouring (4) doublet averaged values, are described in a later section (fig. 6, layering, and 7, parameters and initial pressure temperature patterns).

Further to past exploitation schedules, extended until year 2010, two future well arrays and production/injection demand schedules, each lasting 25 years, are investigated and thermal breakthroughs appraised accordingly.

The rationale behind the exercise consists of assuming a 25 year well life, starting from year 2011, with, first, triplet well (two injectors, the former reconditioned/lined doublet wells and a new, suitably located, large diameter anticorrosion/fibreglass lined, producing well) and, second, a doublet (the previous production well complemented by a new, similarly designed, anti-corrosion injection well) well arrays.

The objective aims at securing, for each 25 year period, an equivalent well/reservoir life avoiding any undue cooling whatsoever.

Production/injection schedules will contemplate two issues, a demand and an offer model respectively, the latter optimising the maximum extractable heat, eligible to district heating/cooling uses.

Overall regional simulation

The previously validated rationale and protocol should ultimately be extended to the overall basin and operated interactively with the exploitation database, according to users' requests and reservoir management requirements. These issues remain, at this stage, far beyond the scope of the present paper.

RESULTS

Test Area

The four candidate reservoir configurations, derived from flowmeter logging, on both production and injection wells, are sketched in fig. 3 and the corresponding model input data files listed in table 1.

Table 1A. THREE-LAYERED RESERVOIR

	CAP ROCK	RES-1	IMP-1	RES-2	IMP-2	RES-3
Depth (m)	1393	1593	1601.5	16011.5	1624	1636
Midpoint (m)	1493	1597.25	1606.25	1617.75	1631.5	1641.25
Thickness (m)	200	8.5	10	12	15	4.5
Temperature (°C)	71.4	75	75	75	75	75
Pressure (bar)	163.40	173.94	174.88	176.02	177.41	178.39
Head (m)	179.46	186.91	187.59	187.78	188.29	188.59
Permeability (D)	1E-30	2.24E-12	1E-40	1.81E-12	1E-40	1.77E-12
Porosity	0.001	0.16	0.001	0.16	0.001	0.16
Thermal Conductivity (W/m°C)	2.1	2.5	2.1	2.5	2.1	2.5
Thermal Capacity (MJ/m ³ K)	2.7	2.7	2.7	2.7	2.7	2.7
Flow-Rate (m ³ /s)	-	0.0186	-	0.0225	-	0.0078

Table 1B. SANDWICH TYPE MODEL

	CAP ROCK	TOP RES	IMP-1	BOTT. RES
Depth (m)	1393	1593	1605.75	1630.75
Midpoint (m)	1493	1599.4	1618.25	1637.125
Thickness (m)	200	12.75	25	12.75
Temperature (°C)	71.4	75	75	75
Pressure (bar)	163.40	174.16	176.07	177.98
Head (m)	179.46	186.95	187.8	188.78
Permeability (D)	1E-30	2E-12	1E-40	2E-12
Porosity	0.0001	0.16	0.0001	0.16
Thermal Conductivity (W/m°C)	2.1	2.5	2.1	2.5
Thermal Capacity (MJ/m ³ K)	2.7	2.7	2.7	2.7
Flow-Rate (m ³ /s)	-	0.0245	-	0.0245

Simulations were run for 65 years over a domain, 42 km² in area (rectangular grid 6×7 km uniform, 100×100 m, mesh size). Lateral boundary conditions were set at constant heads and temperatures respectively.

Model outputs are displayed, as production well temperature decay curves (fig. 4a, b and c) and head and temperature fields calculated 17 years after doublet start-up (fig. 5a, b, c and d).

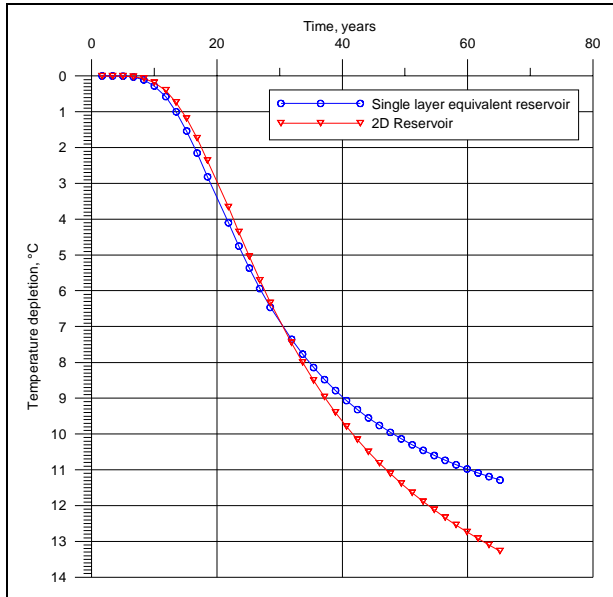


Figure 4a. Temperature depletion at production well. 2D and single layer equivalent reservoir models

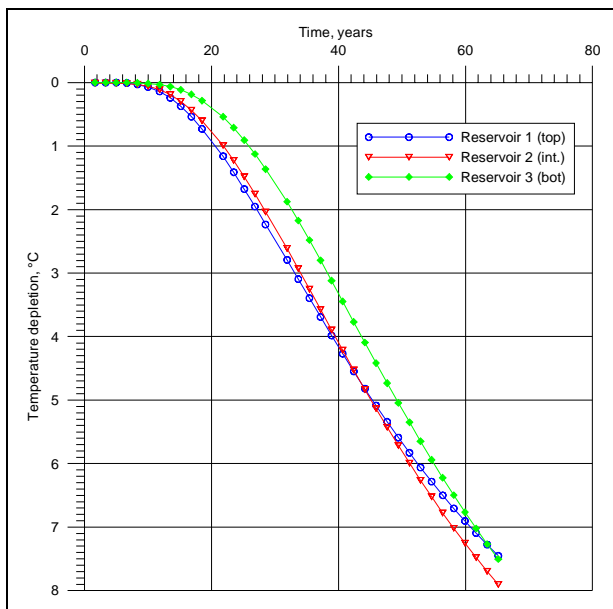


Figure 4b. Temperature depletion at production well. Three layered reservoir model.

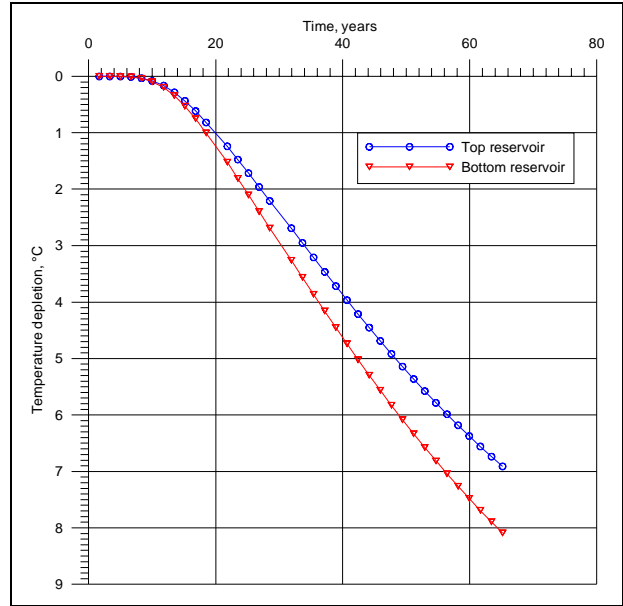


Figure 4c. Temperature depletion at production well. Sandwiched reservoir model.

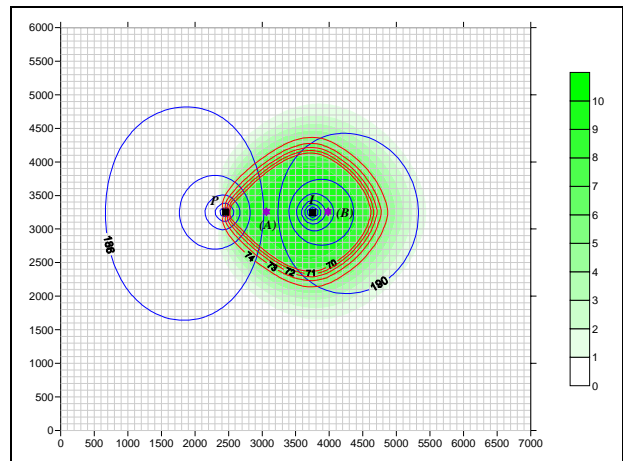


Figure 5a. 2D Model – Transient simulation. Simulation time=17 years.

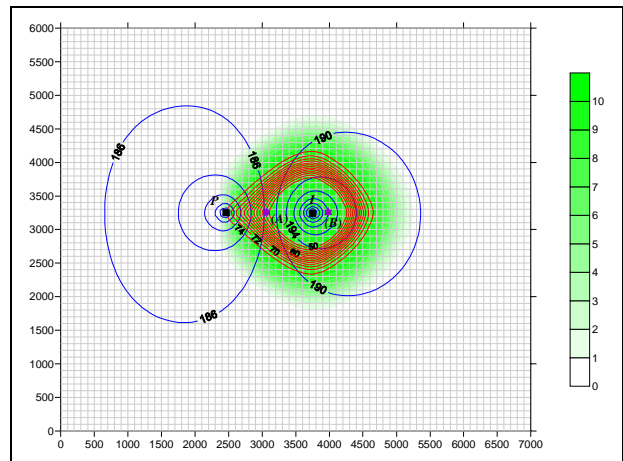


Figure 5b. Equivalent reservoir model – Transient simulation. Simulation time=17 years.

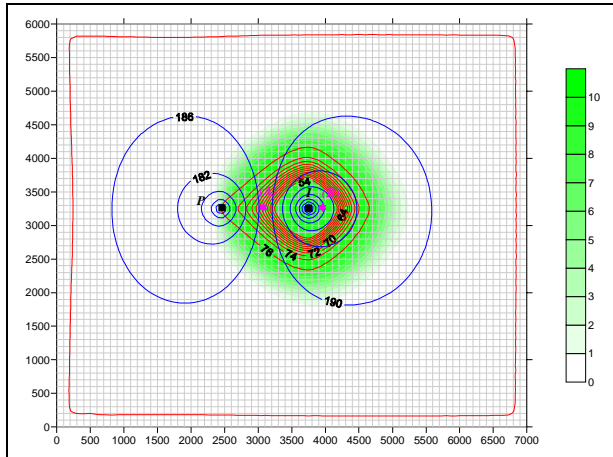


Figure 5c. Three layered reservoir model – Transient simulation. Simulation time=17 years. Reservoir 2.

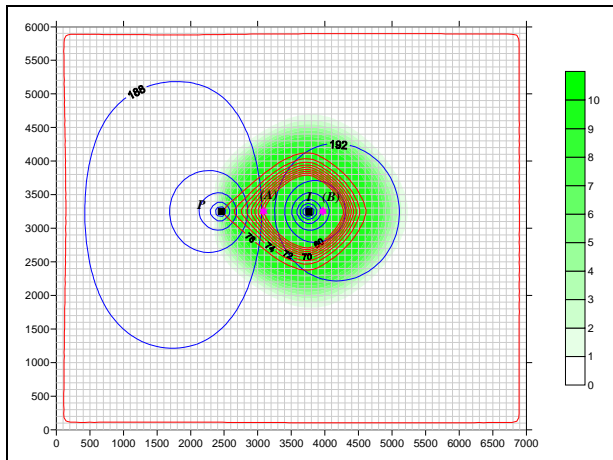


Figure 5d. Sandwiched reservoir model – Transient simulation. Simulation time=17 years. Bottom Reservoir.

■ injected water concentration

These results suggest the following comments:

- cooling kinetics shape faster than initially anticipated. This is particularly obvious for the 2D single layer equivalent reservoir case. Here, the thermal breakthrough (assumed equal to a 1°C temperature drop), occurs after ca. 14 years a figure significantly lower than the one inferred from equation (1), as exemplified hereunder:

$$d = 1270 \text{ m}$$

$$e = 25 \text{ m}$$

$$q = 0.049 \text{ m}^3/\text{s} \text{ (176 m}^3/\text{h)}$$

$$\gamma_r = 2.7 \text{ MJ/m}^3\text{K}$$

$$\gamma_f = 4.18 \text{ MJ/m}^3\text{K}$$

$$\phi = 0.16$$

$$\gamma_t = \phi\gamma_f + (1 - \phi)\gamma_r = 2.94 \text{ MJ/m}^3\text{K}$$

$$t_B \approx 19 \text{ yrs}$$

- actual thermal breakthroughs can be appraised from hydraulic breakthroughs, given that the arrival of

the thermal front is delayed by a factor equal to the reservoir to fluid heat capacity ratio, i.e. $\frac{1}{\phi} \frac{\gamma_t}{\gamma_f}$.

Here, the hydraulic breakthrough could be estimated, based on chemical evidence (sulphide ion increase caused by the insemination from the injection well of sulphate reducing bacteria), at 5.4 years, a figure further backed up by tracer simulation trials.

Numerical application:

$$\gamma_r = 2.7 \text{ MJ/m}^3\text{K}$$

$$\gamma_f = 4.18 \text{ MJ/m}^3\text{K}$$

$$\phi = 0.16$$

$$\gamma_t = \phi\gamma_f + (1 - \phi)\gamma_r = 2.94 \text{ MJ/m}^3\text{K}$$

$$\frac{1}{\phi} \frac{\gamma_t}{\gamma_f} \cong 4.4$$

$$\phi \gamma_f$$

thus leading to a ca. 24 year estimated thermal breakthrough time.

- this figure is fairly well matched by the three layered model which yields a ca. 23 year breakthrough time (within a 1°C allowance) (fig. 4b).
- noteworthy is that the three layered and “sandwich” reservoir cooling patterns trend almost identical, which tends to validate the latter approach, thus achieving significant computational time savings.
- it should be, however, borne in mind that the foregoing are based on the stacking of individual impervious layers whose thicknesses are in excess of five meters, a matter discussed in Appendix.

Development Area

It deals with the subregional domain, 80 km² in area, located North of Paris (fig. 1). It includes three operating doublets, GLCS, GLCN, GBMN, from which averaged reservoir geometric and hydrodynamic features were extrapolated, via Kriging, making use of the figures assessed on the surrounding, nowadays abandoned, doublets.

The reservoir is structured according to the five (two pervious) layer stack depicted in fig. 6.

Overall reservoir transmissivities and initial pressure/temperature patterns (assigned to all interbedded layers) are displayed in fig. 7. Constant vertical bedrock and caprock heat/temperature and lateral pressure/temperature boundary conditions were assigned accordingly.

Table 2 summarises the production/injection schedule, from 1983 to 2060. It is subdivided into three main periods: 1983-2010, 2011-2035, 2036-2060, each corresponding to well and, initially anticipated, reservoir lifetimes.

Table 2. Subregional reservoir simulation. Production/injection schedule. 1983-2060

WELL NAME	TYPE	1983-1989		1990-1997		1998-1999		2000-2001		2002-2003		2004-2010		2011-2035		2036-2060	
		Q (m ³ /h)	Ti (°C)	Q (m ³ /h)	Ti (°C)	Q (m ³ /h)	Ti (°C)	Q (m ³ /h)	Ti (°C)	Q (m ³ /h)	Ti (°C)	Q (m ³ /h)	Ti (°C)	Q (m ³ /h)	Ti (°C)	Q (m ³ /h)	Ti (°C)
Scheme		Doublet ⁽¹⁾												Triplet ⁽²⁾		Doublet ⁽³⁾	
GLCS1	P	-132		-132		-132		-90		-90		-80		57.5	38		
GLCS2	I	132	42	132	42	132	42	90	42	90	42	80	40	57.5	38		
GLCS3	P													-115		-118	
GLCS4	I															118	32
Scheme		Doublet ⁽¹⁾												Triplet ⁽²⁾		Doublet ⁽³⁾	
GLCN1	I	156	43	156	43	156	43	156	43	156	43	160	42	77	38		
GLCN2	P	-156		-156		-156		-156		-156		-160		77	38		
GLCN3	P													-176		-154	
GLCN4	I															154	32
Scheme		Doublet ⁽¹⁾												Triplet ⁽²⁾		Doublet ⁽³⁾	
GBMN1	P	-163		-152		-145		-145		-130		-80		65	48		
GBMN2	I	163	48	152	50	145	52	145	52	130	53	80	45	65	48		
GBMN3	P													-130		-110	
GBMN4	I															110	40
DOUBLET		YEARLY HEAT PRODUCTION (MWh _a)															
GLCS		18000		18000		18000		14250		14250		12500		20200		27600	
GLCN		22800		22800		22800		22800		22800		25000		34300		39000	
GBMN		31800		26700		22600		22600		19000		18000		25400		30000	
TOTAL		72600		67500		63400		59650		56050		55500		79900		96600	

⁽¹⁾ initial doublet: 2 deviated wells (steel cased 9"5/8)

⁽²⁾ intermediate triplet: 2 injection wells (initial reconditioned doublet, 7" steel lining), 1 new anticorrosion (steel/fiberglass lined), large diameter deviated well

⁽³⁾ final doublet: 3 anticorrosion (steel/fiberglass lined), large diameter deviated (existing producer and newly completed injector) wells.

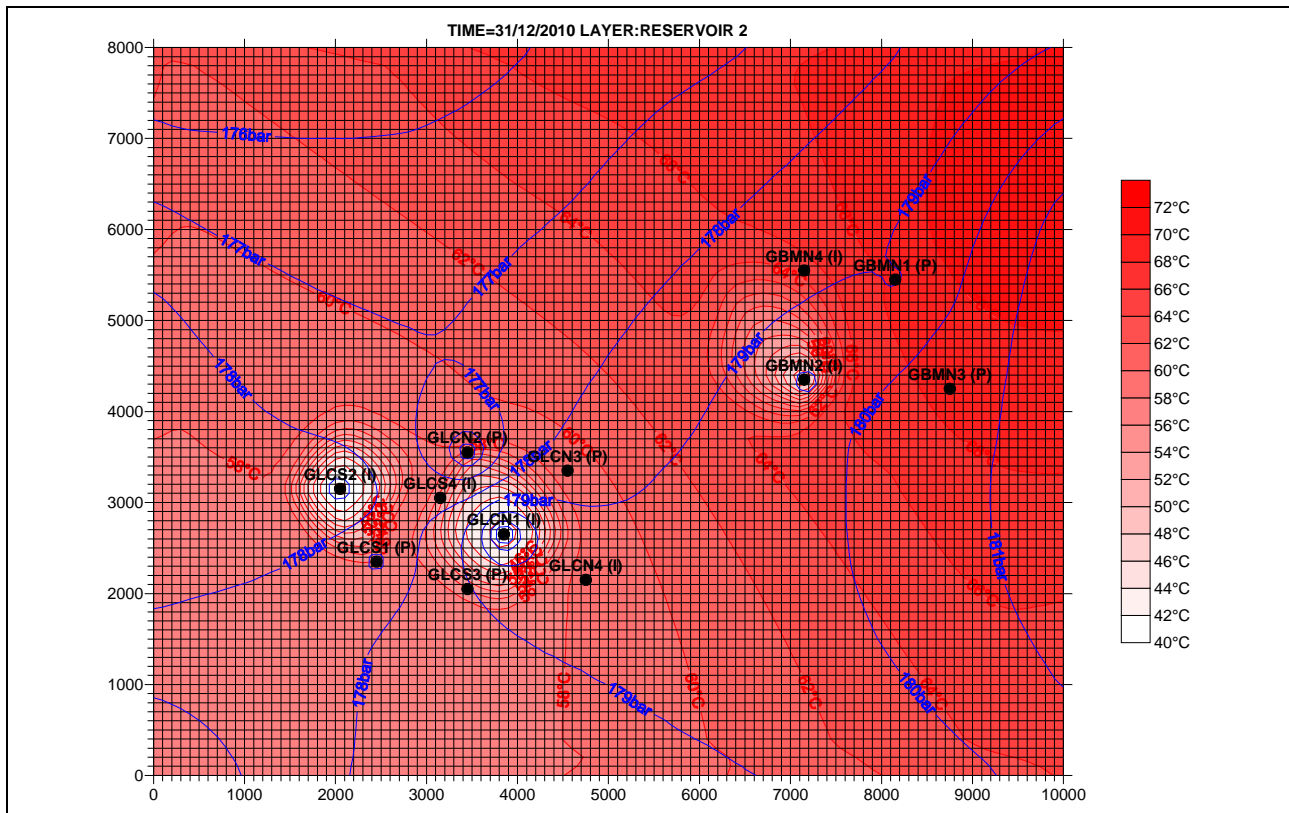


Figure 8a. Subregional model. Transient simulation. Simulation time=27 years. Reservoir 2.

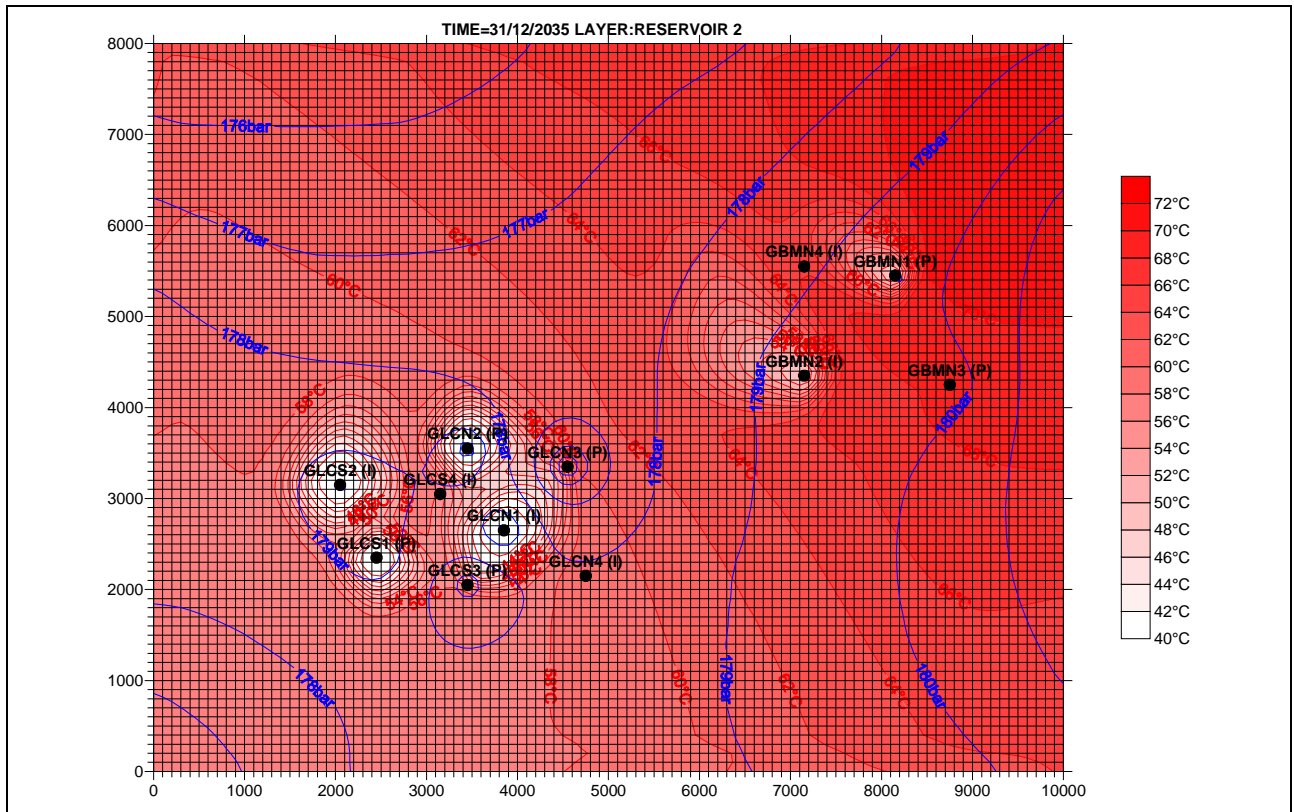


Figure 8b. Subregional model. Transient simulation. Simulation time=52 years. Reservoir 2.

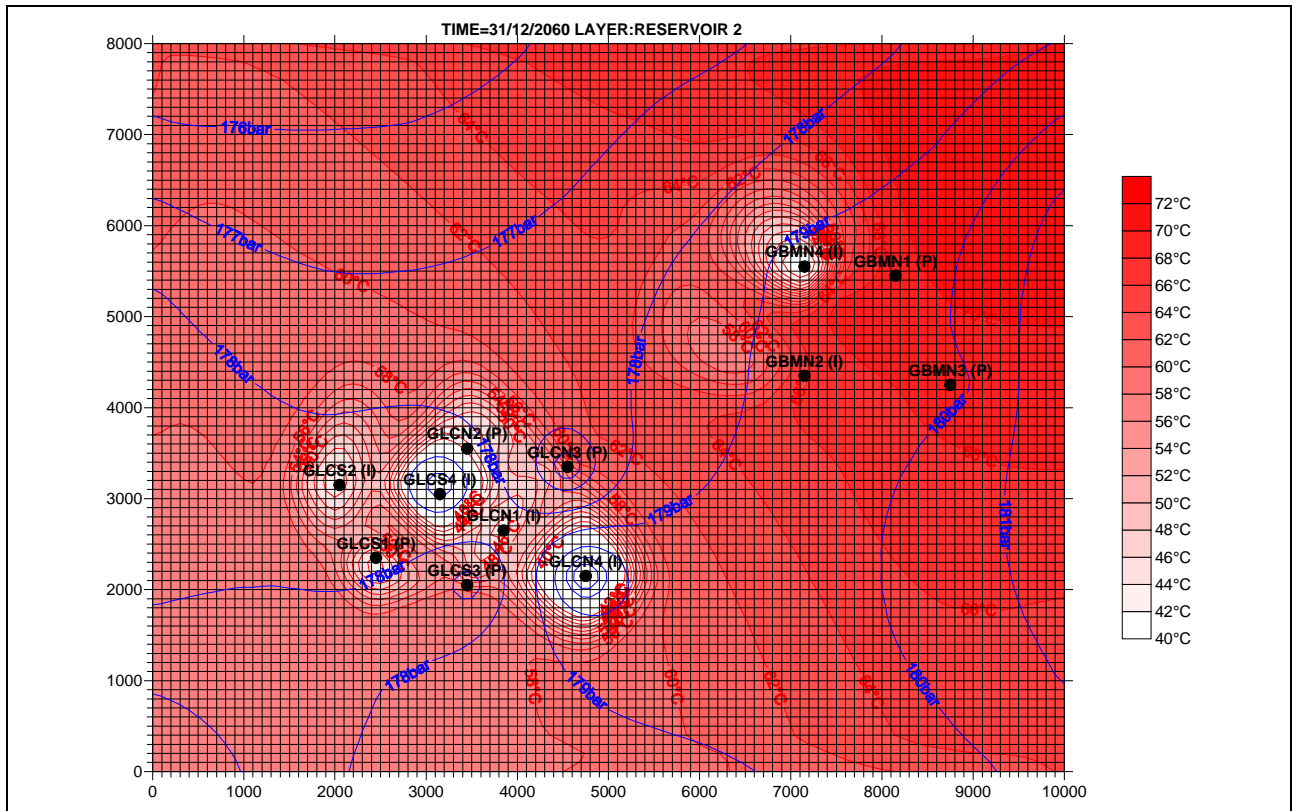


Figure 8c. Subregional model. Transient simulation. Simulation time=77 years. Reservoir 2.

DISCUSSION

It addresses chiefly reservoir assessment and simulation issues.

Reservoir Assessment

The local modelling definitely pointed out the limitations of the 2D and single layer equivalent structures in matching actual temperature depletion kinetics. This led us to advocate the (quasi)3D, either three layered or sandwich configurations instead, which achieved better matching to the thermal breakthrough times (≈ 24 years) inferred from chemical breakthrough monitoring.

The multilayered reservoir configuration is elsewhere backed by lithological analyses, which individualised three main lithofacies. It evidenced the impact of conductive heat (re)supply from interbedded impervious layers, in delaying the migration of the, injection induced, cold water front. Not to the extent initially anticipated so far. The analytical and semi-analytical heat transfer and storage approaches, elaborated in Appendix, provided in this respect some useful clues, emphasising the cooling kinetics and heat exhaustion from thin (metric size) interbedded impervious layers, therefore constraining the interbedding stacking process.

Reservoir Simulation

It has been previously stated that the Dogger geothermal reservoir enjoys among the best documented background knowledge recorded to date. It lacks, however, observation wells and tracer surveys enabling to monitor the pressure/temperature patterns and sample the fluids away from the exploited doublets and to directly assess actual thermal breakthrough times, easing accordingly model calibration. Unfortunately, neither abandoned doublets could be reconvered into piezometers nor tritium injection experiments be implemented; still the need remains.

This obviously imposes somewhat stringent model calibration protocols, a constraint which could be (partly) overcome thanks to the preliminary local area modelling segment. It set the bases for securing the further, subregional development area, predictive simulation stages.

The latter accounted for twenty five year well physical and reservoir thermal life sequences, an assumption deemed realistic based on field practice. The pros and cons of TOUGH2 and SHEMAT simulators will not be discussed here. Both produced pressure/temperature patterns consistent with recorded data, within the aforementioned limitations

(no observation wells and no actual tracer transit times).

Both were bench tested on simple case studies eligible to analytical solutions.

CONCLUSIONS

Owing to the exhaustible nature of geothermal resources, sustainable heat mining is of utmost importance in designing and implementing relevant exploitation strategies aimed at reconciling users' demands with reservoir longevity concerns.

The latter require (i) dependable reservoir properties, (ii) reliable heat extraction technologies, and (iii) appropriate databases and representative, calibrated, reservoir simulation tools.

These issues were illustrated on a case study, borrowed to the well documented Paris Basin district heating scheme, which benefits from a thirty year exploitation record and thirty four ongoing district heating well doublets.

The modelling, on a purposely selected area (remote location, locally uniform reservoir transmissivity), of a single doublet/homogeneous reservoir setting aimed at screening four candidate reservoir structures (2D, single layer equivalent, three layered, sandwiched) assessed from flowmeter logging, well testing and lithological investigations. Related reservoir layering and confining bedrock/caprock features were assigned as doublet averaged figures/conditions, and not interpolated from individual (production/injection) well values as previously practiced.

The exercise enabled to validate two eligible reservoir structures, three layered and sandwich respectively, which proved consistent in achieving a good match between calculated and field inferred thermal breakthrough times.

The previous rationale was extended to the simulation of a multidoublet/heterogeneous reservoir configuration (the so called subregional development area) in view of investigating long term sustainable exploitation routes. This exercise was far from academic as it addressed the future of the existing geothermal district heating facilities and the problematic of well (physical) and reservoir (thermal) life.

As a matter of fact, while approaching the twenty five year deadline assigned to geothermal district heating projects and to well life, the question arose as whether there was a life after. Or, would the geothermal route be abandoned and natural gas fired systems, already coexisting with geothermal heat

exchange on twenty cogenerated grids, be substituted instead.

Modelling dealt with a three layered reservoir structure and data interpolation (via Kriging) from doublet averaged figures, over a 80 km² area and 77 years period. It included three operating doublets.

Simulations of future trends in heating/cooling demand, together with adequately spaced/located triplet/doublet designs, proved consistent with expectations as no significant thermal breakthroughs occurred over a fifty year life, extending from year 2011 to 2060.

The next step (in progress), designed as a thorough reservoir management tool, focuses on regional, basin wide, reservoir simulations operated online with an exploitation database.

Summing up, here, as already noticed from the geothermal exploitation record scored worldwide, lifetimes nearing one hundred years should not be any longer regarded as unrealistic, but meeting sustainable development and resource management requirements instead.

REFERENCES

Clauser, C. Ed. (2003): Numerical Simulation of Reactive Flow in Hot Aquifers. SHEMAT and Processing SHEMAT. Springer Publ. Co. Berlin..

Gringarten, A. C., and Sauty, J. P. (1975): A Theoretical Study of Heat Extraction from Aquifers

with Uniform Regional Flow. *J. Geophys. Res.*, **80**, 4956-4962.

Gringarten, A. C. (1979): Reservoir Lifetime and Heat Recovery Factor in Geothermal Aquifers Used for Urban Heating. *Pure and Applied Geophysics*, **80**, 297-308.

Pruess, K. (1991): TOUGH2. A General Purpose Numerical Simulator for Multiphase Fluid and Heat Flow. Lawrence Berkeley Laboratory, Berkeley, CA.

Rojas, J. (Ed) (1989): Caractérisation et Modélisation du Réservoir Géothermique du Dogger, Bassin Parisien, France. *Rapport Final*. R&D contract EN 3G-0046-F(CD) supported by the EU Commission, Brussels, Belgium.

Ungemach, P. (1976): Leakage Schemes in Hydrogeological Investigations of the Al Wasia Aquifer in the Eastern Province of Saudi Arabia. Regional Study. *Final Report (Appendix 10)*. Report 76AGE006-BRGM, Orleans, France.

Ungemach, P., and Antics M. (2003): Insight into Modern Geothermal Reservoir Management Practice. *Text Book*, International Geothermal Days Turkey, Seferihisar, Turkey.

Ungemach, P., Antics, M., and Papachristou, M. (2005): Sustainable Geothermal Reservoir Management. *Paper 0517* accepted for oral presentation. World Geothermal Congress (WGC2005). Antalya, Turkey, 15-19 April 2005.

APPENDIX

The interbedded reservoir configuration depicted in fig. can be treated, regarding one dimensional vertical conductive heat transfer, within the “sandwiched” impervious layer as the two point boundary value problem summarised hereunder:

$$\frac{\partial^2 \theta(z, t)}{\partial z^2} = \frac{1}{\alpha^2} \frac{\partial \theta(z, t)}{\partial t} \quad (1)$$

with:

θ = temperature

z = vertical coordinate

t = time

$$\alpha^2 = \frac{\lambda'}{\gamma'}$$

γ' = heat capacity

λ' = thermal conductivity

$$\begin{cases} \theta(0, t) = \theta_1(t) \\ \theta(e', t) = \theta_2(t) \end{cases} \quad t > 0 \quad (2)$$

$$\theta(z, 0) = 0 \quad z > 0$$

The solution of equation (1), subject to boundary and initial conditions (2), is given by (Ungemach, 1976):

$$\theta(z, t) = \theta_1 + \frac{z}{e'} (\theta_2 - \theta_1) - \frac{2}{\pi} \sum_1^{\infty} \left\{ \frac{(-1)^{n+1}}{n+1} e^{-\left(\frac{n\pi}{e'}\alpha\right)^2 t} + \left[\theta_1 \sin\left(n\left(1 - \frac{z}{e'}\right)\pi\right) + \theta_2 \sin\left(n\pi \frac{z}{e'}\right) \right] \right\} \quad (3)$$

From (3) can be derived the interfacial, reservoir vs. sandwiched impervious layer, crossflows Q :

$$Q(z, t) = -\lambda' \frac{\partial \theta(z, t)}{\partial z} = -2 \frac{\lambda'}{e'} \left\{ \sum_1^{\infty} (-1)^{n+1} \cdot \left[\theta_2 \cos\left(n\pi \frac{z}{e'}\right) - \theta_1 \cos\left(n\pi \left(1 - \frac{z}{e'}\right)\right) \right] e^{-\left(\frac{n\pi}{e'}\alpha\right)^2 t} \right\} \quad (4)$$

(3) and (4) at selected locations become:

- “sandwiched” layer mid-point

$$\begin{aligned} \theta\left(\frac{e'}{2}, t\right) &= \left(\frac{\theta_1 + \theta_2}{2}\right) - \\ &- \left\{ \frac{2(\theta_1 + \theta_2)}{2} \sum_0^{\infty} \frac{(-1)^p}{2p+1} e^{-\left[\frac{2(2p+1)}{e'}\pi\alpha\right]^2 t} \right\} \end{aligned} \quad (5)$$

- lower and upper reservoir interfaces

$$Q(z=0) = \frac{\lambda'}{e'} \left\{ \theta_1 \left[1 - 2 \sum_1^{\infty} e^{-\left(\frac{n\pi}{e'}\alpha\right)^2 t} \right] - \right. \quad (6)$$

$$\left. \theta_2 \left[1 - 2 \sum_1^{\infty} (-1)^{n+1} e^{-\left(\frac{n\pi}{e'}\alpha\right)^2 t} \right] \right\}$$

$$Q(z=e') = \frac{\lambda'}{e'} \left\{ \theta_2 \left[1 - 2 \sum_1^{\infty} e^{-\left(\frac{n\pi}{e'}\alpha\right)^2 t} \right] - \right. \quad (7)$$

$$\left. \theta_1 \left[1 - 2 \sum_1^{\infty} (-1)^{n+1} e^{-\left(\frac{n\pi}{e'}\alpha\right)^2 t} \right] \right\}$$

Note that, for large values of time, (3) and (4) reduce to:

$$\theta(z, t) \cong \theta_1 + \frac{z}{e'} (\theta_2 - \theta_1) \quad (8)$$

and

$$Q(z, t) \cong -2 \frac{\lambda'}{e'} (\theta_2 - \theta_1) \quad (9)$$

Conductive drainage of the heat stored in confining impervious layers.

All, permeable and impervious, layers are assumed initially at thermal equilibrium ($\theta = \theta_0$), before cold waters are pumped into the injection well at constant temperature θ_1 .

- Heat stored, per unit volume $\Delta x \Delta y e'$, in the interbedded impervious layer:

$$W(J) = \gamma_r \Delta x \Delta y e' \quad (10)$$

with:

γ_r = rock heat capacity ($J/m^3 K$)

$\Delta x \Delta y$ = unit simulation cell area (m^2)

e = layer thickness (m)

- Heat withdrawn, per unit area $\Delta x \Delta y$, confining reservoir layers:

$$Q(W) = \lambda_i \frac{\Delta \theta}{\Delta z} \Delta x \Delta y \quad (11)$$

with:

λ_i = interface thermal conductivity ($W/m^2 C$)

$$= \frac{2}{(e' + e)} (e' \lambda_t + e \lambda_r)$$

λ_r = reservoir thermal conductivity ($W/m^2 C$)

$$= \phi \gamma_f + (1 - \phi) \gamma_r$$

λ_f = fluid thermal conductivity ($W/m^2 C$)

λ_r = rock thermal conductivity ($W/m^2 C$)

e = reservoir thickness (m)

$$\frac{\Delta\theta}{\Delta z} = \frac{\theta_0 - \theta}{\Delta z} = \text{temperature gradient measured}$$

between impervious layer and reservoir mid point locations (°C/m)

θ =reservoir temperature (°C)

$$\Delta z = \frac{(e + e')}{2}$$

The time Δt required to mine by 1°C the impervious layer temperature layer verifies:

$$Q\Delta t = W \quad (12)$$

Hence:

$$\Delta t = \frac{\gamma_r}{\lambda_i} \frac{\Delta z}{\Delta\theta} e' \quad (13)$$

Numerical application:

$$\gamma_r = 2.7 \text{ MJ/m}^3\text{K}$$

$$\lambda_i = 2.2 \text{ W/m}^\circ\text{C}$$

$$e = 15 \text{ m}$$

$$e' = 25 \text{ m}$$

$$\Delta z = 20 \text{ m}$$

$$\theta_i = \text{injection temperature} = 45^\circ\text{C}$$

$$\theta_0 = \text{impervious layer initial temperature} = 75^\circ\text{C}$$

$$\Delta\theta = \theta_0 - \theta_i = 30^\circ\text{C}$$

$$\Delta t(30^\circ\text{C}) = 2.05 \times 10^7 \text{ s} \approx 0.65 \text{ yr}$$

$$\Delta\theta(^\circ\text{C}) = 1$$

For a 5 m thick impervious layer:

$$\Delta t(30^\circ\text{C}) \approx 0.13 \text{ yr} (\approx 1 \text{ month})$$

Elsewhere, equation (13) can be extended towards investigating the heat mining kinetics within the impervious layer, by calculating the time required by the confining reservoirs to exhaust the heat stored in the sandwiched impervious rocks. As a matter of fact the time at which the impervious layer mid point temperature stabilises at cold water injection temperature can be estimated, assuming constant vertical conductive heat transfer over unit (say 1°C) temperature depletion increments, via the following summation process, derived from equation (13):

$$t_E = \frac{1}{2} \frac{\gamma_r}{\lambda_i} \Delta z e' \sum_{i=1}^N \left[\frac{1}{\Delta\theta - (i-1)} \right] \quad (14)$$

Application to the symmetric sandwich reservoir structure, using the previous numerical values (25 m thick impervious layer), would lead on the injection well cell to a heat exhaustion time close to 38 years according to the temperature depletion curve, based on 30 (N) increments, displayed in fig. 1.

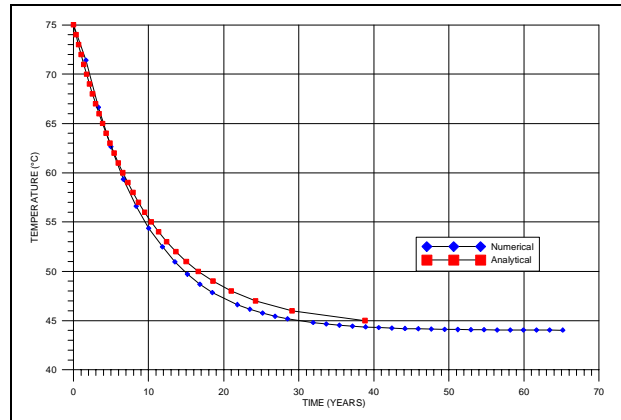


Figure 1. Impervious layer heat mining. Sandwich reservoir structure. Numerical and analytical cooling kinetics. Injection well cell.

Of interest to note is that the process achieves, at least on the injection well cell, a close match with model simulated cooling kinetics.

Equation (14) may allow also to assess the critical impervious layer thickness, which in this instance could be assigned to metric size.

In no way do the foregoing apply to the lower (bedrock) reservoir boundary which supplies a constant intake, set equal to the terrestrial heat flow density (0.09 W/m²). Neither do they address the upper confining caprock, owing to its thickness (200m), which secures the constant mid-point temperature condition assigned to reservoir simulation.

HIGH-TEMPERATURE PLUG FORMATION WITH SILICATES

Stephen Bauer¹, Patrick Gronewald¹, Janice Hamilton², Arthur Mansure¹

¹Sandia National Laboratories
Geothermal Research, Dept. 6211, MS 1033
Albuquerque, NM, 87185, USA
sjbauer@sandia.gov

²National Silicates
27 Coronet Road Unit 11/12
Toronto ON M8Z 2L8
janice.hamilton@silicates.com

ABSTRACT

A grouting system is being developed that is applicable to water shutoff, steam flooding, and high-temperature grouting/plugging for lost circulation. This grouting system uses silicate hydrates as the plugging material. We describe a means to introduce sodium silicate and an activator through a single tubular by encapsulating the activator in a material that is temperature sensitive, thus delaying the initiation of the reaction. The formation of silicate hydrate plugs has been studied over the range of 80°C to 300°C as well as the chemical stability of silicate hydrate for 10-12 weeks.

INTRODUCTION

This work describes a chemical solution of exploiting silicates' unique gelling properties in an environmentally friendly and cost-effective way to form plugs for use in water shutoff strategy, steam flooding, and high-temperature grouting/plugging for lost circulation. Silicates have been used to form stable grouts and cements for over 50 years because of their ability to gel and polymerize. This reaction has also been used successfully for water shutoff and to solve lost-circulation problems in oil and gas drilling that require a plug to be formed at various weak spots in a well formation. The reaction happens in seconds to minutes (generally controlled by the mixing rate). In addition to their gelling action, silicates will also react with soluble metal salts, such as calcium chloride, to produce insoluble metal silicate hydrate plugs.

The need for this work arose primarily from geothermal drilling research wherein we are faced with severe lost-circulation problems, often at elevated temperatures. This paper summarizes current laboratory-based advances in developing high-temperature plugs for lost-circulation zones. The purpose of this research includes developing emplacement systems and determining the temperature limits of reactive plugs for cross flow. Sandia National Laboratories, with support by the Geothermal Technologies Program of the U.S. Department of Energy has studied wellbore integrity in geothermal environments. A portion of wellbore integrity research has been directed towards developing materials and methods of solving lost circulation problems in a cost-effective way. Geothermal environments are hot, with temperatures in the range of 80°C to 300°C, and are possibly laden with water, brine, etc. In severe lost-circulation situations, cross flow may be experienced, in which pressure-induced fluid flow may occur through a borehole. When lost circulation of drilling fluid is experienced in geothermal wells, cement plugs are a common initial solution to the problem. A typical procedure would be to stop drilling, place the cement plug and allow the cement to cure, and then re-drill. However, high cross-flow rates and/or large voids, many fractures, and high porosity/permeability zones can present difficult circumstances for conventional cement plug deployment. For example, cement can be washed out or migrate away from the zone of interest due to unbalanced hydrostatic pressures before it has set, or the amount of placed cement may not fill all of the voids present.

As background, lost circulation occurs when formation-fluid pressure is less than the fluid column pressure in the wellbore, so that some or all of the

drilling fluid escapes into the formation instead of recirculating back up the well annulus. Lost circulation is often accompanied by further loss of wellbore integrity including sloughing, caving, washing out, or bridging. These phenomena are persistent in geothermal drilling and are very expensive – often accounting for 10-20% of the total cost for drilling a typical geothermal well – and cause many additional drilling problems such as stuck drill pipe, damaged bits, slow drilling rates, and collapsed boreholes.

Lost circulation is particularly difficult to plug when it includes cross flow. Cross flow occurs when the wellbore encounters permeable zones whose pore pressures are not hydrostatically balanced (Figure 1). This often occurs when alluvial deposits are separated from underlying volcanics by an impermeable layer. The fluid level in the borehole may fall hundreds of feet below the surface (significant lost circulation/cross flow) when drilling penetrates the volcanics. Therefore, if the surface casing shoe is not set in the impermeable zone, the well can have cross flow from one zone to another sufficient to wash away all cement plugs and primary cement.

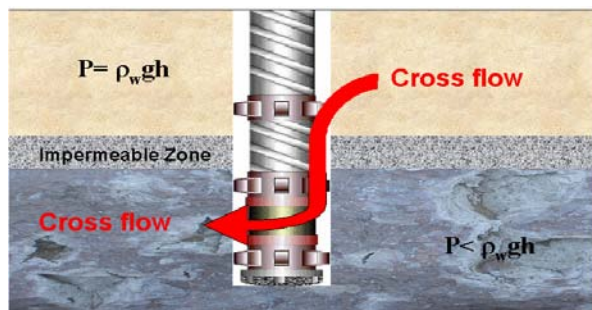


Figure 1: Cross flow occurs when two formations have unbalanced pore pressure (P), where ρ_wgh is the weight of a water column back to surface.

For a geothermal short circuit, water shutoff and to control flow in steam flooding, the problem is slightly different. In these situations, the grout must flow into fractures or into a permeable zone, filling it, and set up in an intelligent manner to affect a seal. This concept implies that timing or reactivity of the plug material must be considered as part of the grout system.

We envision a system which works as follows. When a loss zone is encountered, the drilling would be stopped and the drill string backed off one to two stands. A reactive grout material would be injected through the drill string to the hole bottom and allowed to flow into the loss zone and the immediate

vicinity. There it would react, gel/harden quickly, and allow for continued drilling almost immediately.

In order for this concept to become functional, we have been studying reactive plug systems for geothermal (hot and wet) environments.

Through a systems approach, we are investigating materials that can be created and will survive in a geothermal environment without degrading. The chemistry as well as the “mechanical survivability” of the materials at geothermal conditions has been studied, initially through lab and planned bench-scale and field-testing. Awareness of a reasonable downhole deployment scheme must be factored into early material development work. Materials considered must be environmentally suitable and the total costs of the material’s deployment process must be economic, realizing that down time caused by lost circulation is very costly.

Recognizing the importance of minimizing trouble time caused by severe lost circulation in geothermal wells, we have studied the chemical stability of potentially viable silicate plugging material. The material satisfies multiple needs, namely: (1) no special handling requirements and considered non-hazardous by the DOT and EPA; (2) low cost (3) readily pumpable; (4) controllable gel time- the reaction rate needs to be adjustable for varied conditions both at the surface and downhole; (5) controllable placement such that it has minimal water solubility and adheres well to rock surfaces through a single delivery hose; (6) hydrothermally stable for 8 weeks at geothermal temperatures; and (7) once placed, the grout is sufficiently stiff, to allow drilling with conventional means, and no unanticipated problems with drill bit plugging. These criteria were used because the initial situation we wished to address was that of geothermal lost circulation.

SILICATE CHEMISTRIES STUDIED

Silicates have the ability to polymerize and form gels, or plugs, with other chemicals. Several chemicals were screened for their plug forming ability with silicates. The stability of these plugs was studied at temperatures of 25°C to 300°C.

Water shutoff and lost circulation (Heaven et al, 1999; Lakatos et al, 2001; Samari et al, 1998; Viddick et al, 1988) applications require a plug to be formed at various weak spots in a well formation. Silicates are very stable and do not have the adverse environmental effects associated with other gel-forming chemicals (Heaven et al, 1999; Lakatos et al, 2001; Samari et al, 1998; Viddick et al, 1988). Soluble silicates contain three components: silica, alkali and water. Although silicates have been described as the metal salts of silicic acid, they

actually exist as polymeric forms in solution. The fundamental building block of silicate solutions is the silicon atom at the centre of an oxygen-cornered, four-sided tetrahedral pyramid (Figure 2). In sodium silicate, typically, each oxygen atom is associated with a sodium or hydrogen atom, or it may be linked to another silica tetrahedron. The silica tetrahedra can link to form chains (Figure 2), cyclic and larger polymeric structures.

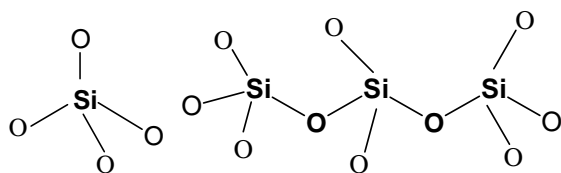
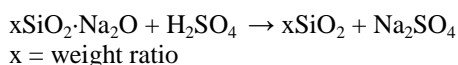


Figure 2: Silicate Monomer, Silicate Trimer.

Regarding sodium silicate, the $\text{SiO}_2:\text{Na}_2\text{O}$ ratio plays a major role in polymerization. The distribution of various polymers is described as speciation and can be affected by concentration and temperature. Below a 0.05 ratio, monomers dominate the distribution. Three-dimensional anions are most abundant in 2.48 and higher ratios. For a 3.22 ratio at increased temperature, the larger cyclic anions are relatively stable, while dimers and monomer increase (PQ, 2004; Iler, 1979; Patterson, 1994). Further additions cause interactions with large silica oligomers and polymers to yield precipitates and gelation. For example, mineral acids will react with sodium silicate as follows:



Another example of this precipitation/gelling phenomenon is the reaction of silicates with polyvalent metal ions to produce metal silicate precipitates that are less soluble across a broader pH range than the metal hydroxides produced by non-silicate processes. Thus, calcium salts react with sodium silicate to form calcium silicate hydrate. This reaction is fundamental in cementing and grouting. The foregoing discussion impacts downhole placement, because the composition ratios will dictate whether a gel or a hard plug is formed.

This ability of calcium salts to form gels and precipitates with metal silicates has been exploited to produce silicate plugs in water shutoff applications. Calcium chloride is a good example of an activator in the formation of stable silicate plugs (PQ, 2004; Iler, 1979).

The work summarized in this paper describes a way of exploiting silicates' unique gelling properties in an environmentally friendly and cost-effective way to form plugs for use in geothermal applications.

Lab Evaluations

Previous studies have shown the potential for using silicates with activators to form plugs for water shutoff (Heaven et al, 1999; Lakatos et al, 2001; Samari et al, 1998; Viddick et al, 1988). New geothermal applications for this technology require the plugs to be able to withstand temperatures of 150° – 300°C.

The screening study was undertaken to assess the potential of several chemicals known to react with N sodium silicate¹ to form plugs and then determine the stability of these plugs at 200°C. Stainless steel bombs were used, which became pressurized at high temperatures. Initial experiments determined whether and how much dilution of the silicate was appropriate to obtain the hardest, most solid plug that retained stability and integrity over time. Table 1 summarizes dilution requirements of the sodium silicate for each activator.

Table 1. Activators & Silicate Dilution Assessments

Activators with N Sodium Silicate without dilution	Activators with Diluted N Sodium Silicate (~ 25% v/v)
Calcium Chloride 10%	Calcium Sulfate – 7.5 % Plaster of Paris Powder
Sulfuric or Nitric Acid 20%	Citric Acid 20%
Hydrochloric Acid 20%	Hydrochloric Acid 50%
Sodium Bicarbonate 10%	Acetic Acid 20%

Table 2 summarizes the initial screening test matrix with the starting materials at room temperature and pressure. All of the activators cause plug material to form in a brief time period, often as quickly as one mixed the solutions. The plug material is of a consistency that can plug holes in rock, and i.e. the material is hard, stiff and cohesive. At room temperature and pressure mixing conditions, it appears that all of these chemical combinations are options. However, additional criteria were invoked to further define the screening. First, the plugs were sealed in a pressure vessel and placed in an oven set at 200°C for 16 hours, then cooled to room temperature and pressure. Some of the plug materials were physically broken down by the heating and cooling process, thus were not tested further. The nitric and sulfuric acids were not tested further because they are not common chemicals at drill sites

¹ The N sodium silicate used in all the experimentation is obtained as a 37.5% solution in water and has a silicate to alkali ($\text{SiO}_2:\text{NaO}_2$) weight ratio of 3.22. In this paper it will be referred to as N sodium silicate or sodium silicate.

and are strong acids, requiring careful handling; the HCl, although a strong acid, is more common at drill sites and was tested further.

Table 2. Initial Screening Test Matrix

Activator	Time to Form Plug	Appearance and Visual Strength Assessment	
		Initial RT	16 Hours at 200°C
Nitric Acid	30 Seconds	Smooth solid plug	Very hard, smooth solid plug with aqueous layer
Sulfuric Acid	30 seconds	Uneven solid plug	Smooth solid plug with aqueous layer
Hydrochloric Acid	45 seconds to 1 minute	Smooth solid plug	Hard, uneven solid plug
Acetic Acid	15 – 30 seconds	Smooth solid plug	Plug breaks down into watery liquid and fine precipitate
Citric Acid	8 – 10 minutes	Smooth solid plug	Plug breaks down into watery liquid and fine precipitate
Calcium Chloride	30 seconds	Uneven solid plug	Hard, uneven solid plug
Calcium Sulfate	2 – 3 minutes (can be longer)	Smooth solid plug	Fine granular mass – easy to press into available space
Sodium Bicarbonate	1 – 2 minutes	Smooth solid plug	Liquid – viscosity increases on cooling but does not reform into plug

The following activators were chosen for further study based on customer interest and availability in the field.

1. Calcium chloride – 10% w/w solution with undiluted N sodium silicate
2. Calcium sulfate – 7% by weight (CaSO₄ is insoluble) with diluted N sodium silicate
3. Hydrochloric acid – 20% w/w solution with undiluted N sodium silicate

All solutions were acclimatized to the testing temperature before mixing.

Effect of Temperature on Plug Formation

For geothermal and steam flood applications, study of plug formation at temperature and pressure is a necessary reality which must be evaluated, as the formation is hot. However, local and transient cooling in a borehole may be realized through

circulation to cool the injection area from ambient temperatures. After plug placement, plug and formation temperatures could again increase. In order to best replicate actual downhole conditions, a step-wise experimental program was developed.

For the beginning of this program, tests were completed in which the sodium silicate and activator were heated in an oven to a specified temperature. The two components were then mixed in the oven and results obtained. Stable plug formation was monitored at temperatures of 25°, 65°, 100° and 150°C (Table 3). (Note: In this lab work we are attempting to observe what happens in a geothermal well. The oven and mixing container are at the stated temperature; the materials mixed were placed in the oven and reached maximum temperatures of boiling when mixed in the oven, while observing the gel time.)

Increasing temperature led to an increase in plug formation time. Once formed, plugs were stable at formation temperature and room temperature.

Table 3. Summary of Bench-Scale Test Matrix

Activator	Gel Time 25°C	Gel Time 65°C	Gel Time 100°C	Gel Time 150°C
CaCl ₂ (10% w/w solution)	≤ 10 s Uneven hard mass	10 – 15 s Hard smooth mass	15 – 30s Hard smooth mass	≥ 30s Hard smooth mass
CaSO ₄ (Solid Plaster of Paris)	3 min. Amorphous mass, can be pressed into shape of container	7 min. Amorphous mass, hardens to a solid granular mass over 12 – 24 hours	12 min. Amorphous mass, hardens to a solid granular mass over 12 – 24 hours	30 min. Initially softer amorphous mass & increased ppt., becomes solid, hard, granular
HCl (20% w/w solution)	≤ 10 s Uneven hard mass	10 – 15 s Hard smooth mass	15 – 30s Hard smooth mass	≥ 30s Hard smooth mass

Long Term Stability Testing

From Table 3, each of the assessments produced materials that we feel should be considered as a plug material at least for short-term plugging needs. We chose to pursue using calcium chloride as an activator, making calcium silicate hydrate as plug material because of cost, ease of use and it is relatively benign.

The next series of tests evaluated the long-term stability of calcium silicate hydrate at elevated temperature and pressure of water. For these tests, samples were placed in a pressure vessel with excess tap water, and heated for times up to 12 weeks and

temperatures up to 300°C. The water pressure resulting from heating the contained water was sometimes measured, but generally the pressures were assumed to be those obtained from the steam tables. The samples were cooled and depressurized weekly, and observed and photographed. No visible changes were observed. All samples, heated at temperatures ranging from 80°C to 300°C and pressures from 14.5 to 1250 PSI, were stable (for example, Figure 3).



3 a. 3 b.
 Figure 3: Calcium silicate hydrate (a) 16 hours at 250 °C, $P_{H_2O} = \sim 680\text{PSI}$ (b) 7 days at 250 °C, $P_{H_2O} = \sim 680\text{PSI}$

Effect of Temperature and Pressure on Plug Formation

As stated above, geothermal and steam flood environments, which are hot and often water laden, motivated sample fabrication in a manner representative of downhole conditions. A set of experiments was designed to simulate at-depth temperature and pressure conditions at the time of the chemical reaction. Because the sodium silicate and calcium chloride have to remain separated (to prevent a reaction), methods were devised to keep the reactants separated until they are exposed to a hot and wet environment.

These methods involve tests with (1) injection of separate component materials into a hot vessel, (2) encapsulation of one of the components, the calcium chloride, and (3) or combinations of injection and encapsulation.

For (1) injection of separate component materials tests, a pressure vessel with a beaker partially full of water is heated. After achieving the test temperature and pressure, the two reactants are separately injected (at a pressure slightly in excess of the internal pressure of the vessel) forming a plug.

For static bulk encapsulation tests, calcium chloride solid was placed at the bottom of a beaker and covered with a layer of wax or thermoplastic to form a permeability barrier. Sodium silicate and water were poured on top of the permeability barrier. The beaker was placed in a pressure vessel and then in an oven already at temperature. At specific

temperatures, the barrier melts and the reaction takes place.

The bulk encapsulation method was refined through encapsulation of individual calcium chloride pellets. The individual pellets can float in N sodium silicate, and will react when heated to a sufficient temperature (at which point the encapsulant melts). (Note: the density of N sodium silicate is 1.39 g/cm³ which can be decreased by dilution with water, and the density of the encapsulated calcium chloride pellets is about 1.3 g/cm³. The process, wherein an encapsulated activator of N sodium silicate is exposed to the silicate through downhole heating allowing a plug-forming reaction to occur, can be extended to downhole geothermal placement (see emplacement scenarios).

Different melting points of the encapsulant enabled observations of the calcium silicate hydrate plug having been formed at different temperatures. Addition of small excess amounts of water to the N sodium silicate did not have detrimental effects on plug formation (some water is in fact needed for a complete reaction). Because calcium chloride is readily soluble in water, when the calcium chloride is exposed through melting of the encapsulant, it dissolves and the calcium reacts with the N sodium silicate. The dissolution of the calcium chloride at room conditions is observed to be exothermic, further facilitating mixing of the reactants in relatively static conditions. This is important because the emplacement scenarios envisioned amount to injecting the two components at the well bottom, thus allowing for the injection and convection of the fluid to effectively cause the mix.

Plug materials formed in this manner were initially studied at two temperature ranges, 80°-90°C and 170°-195°C, the melt temperatures of the encapsulants. However, we extended this experimental program to study the chemical reaction at many temperatures between 90°C and 195°C through injection tests. In the first series of tests, sodium silicate and encapsulated calcium chloride pellets were injected into a hot and pressurized water or water and gravel container. The temperature of the interior of the vessel only has to be equal to or greater than the melt temperature of the encapsulant for the reaction to proceed. When the reactants are injected, they heat up quickly, causing the encapsulant to melt, allowing the calcium chloride to dissolve and then react with the sodium silicate, forming a calcium silicate hydrate solid. Injection testing was further extended to inject into hot and pressurized water-laden gravels with a differential pressure (Figure 4). In this example, formed and kept at relatively low temperature, a stiff gel is observed to form.



Figure 4. Gravel and calcium silicate hydrate agglomerate formed at 90°C.

Adhesion to Rock

The grout must have a finite strength and adhere to rock. No specific mechanical properties tests have been completed on the grout. It is observed that grouts adhere to gravel when the components are mixed in their presence, or when the reactants are injected into hot-wet gravel. When the test system is disassembled, the grout-gravel agglomerate retains cohesion and strength (Figure 4).

Simulated Geothermal Drilling Conditions

Recent tests have focused on injections into gravel while circulating hot water (Figure 5 is a longitudinal section of a completed test, in which the gravel is red and the grout material is white). In these tests an assembly consists of the flow configuration shown (Figure 5) potted in a large thermal mass within an oven set for 120° to 150°C. By flowing a closed loop of water through the assembly, the temperature within the gravel can be maintained at 80° to 90° C. This is meant to simulate the near well bore situation in a geothermal well, wherein drilling fluids are circulated to cool the drill bit and remove cuttings. At a specific time flow is momentarily halted, then the grout reactants are injected, then flow is restarted. Typically no flow is observed, thereby demonstrating the effectiveness of the plug. To further evaluate the plug integrity, the upstream end has been pressurized up to about 300 PSI with little to no flow observed. The results have thus far consistently produced a plug material that adheres to the gravel. The plugging action is observed to clog the pores in the gravel and decrease flow rates by orders of magnitude.



Figure 5. A gravel-packed pipe sample (post test). Arrows indicate water flow and grout injection direction.

Chemical Analyses

A limited number of chemical analyses of samples were completed using X-ray diffraction and Raman Spectra methods, with consistent and sensible results. First, the plug material composition in all samples is calcium silicate hydrate; this composition is consistently found with increasing time at a given temperature of formation. Second, with increasing time and temperature, the crystallinity of the calcium

silicate hydrate increases from amorphous to glass to ordered structures. This appears to indicate the plug will become more stable chemically and mechanically with time (and not degrade under adverse conditions). Also, important to geothermal applications, calcium silicate is acid resistant.

Downhole Placement Considerations

Given the current lack of direct experience with this type of plug in a geothermal environment one can only suggest the following emplacement scenarios for calcium silicate hydrate plugs based on lab and bench-scale testing. In beakers, the plug material is observed to form immediately on mixing. Within a pressure vessel, with only “static mixing” the plug material forms on the bottom, side, and center of the container. In the injection tests the plug material forms when exposed to the hot wet gravel. Consequently, at least two potential emplacement scenarios are envisioned.

Method 1: Upon encountering an extreme loss zone, the drilling could be stopped and the drill-string removed from the hole. The first method is similar to twin streaming. It is unknown at present if a mixing nozzle is required; based on static mixing experiments it appears unlikely. Two hoses would be strapped to the drill pipe and lowered to within 60 ft of the hole bottom. The sodium silicate and activator (calcium chloride 10% w/w solution) would need to be separately prepared in a volume sufficient to fill the bottom 40 ft in preparation for separate pumping from the surface. The two components would be pumped through two separate pipes, and chased with water to help drive the plug a short distance into the formation. We envision that this placement method will allow the plug to travel only a very short distance into the formation, because the mixing and plug solidification will occur in the hole. Filling the hole with water would confirm closure of the loss zone. Twin coil tubing could similarly be used. The use of a drillable tail pipe at the bottom of the drill pipe may be desirable to minimize the potential for cementing the drill pipe in the hole (Figure 6).

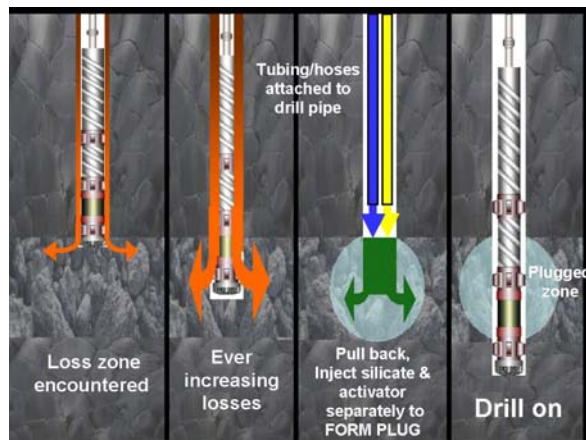


Figure 6. Placement scenario using tubing attached to drill pipe.

Method 2: In the second method, the calcium silicate hydrate plugs would be placed as follows. A measured amount (for the volume determined from the hole diameter and stand-off height) of the mixture for filling the backed off section of hole, with encapsulated CaCl_2 and N sodium silicate could be placed by pumping the constituents down the interior of the drill pipe. The size of coated pellets must be less than 1/3 the drill-bit port diameter. Alternatively if particle size risked bridging the nozzles, the drill pipe could be tripped and runback in open-ended with a drillable tailpipe if deemed necessary. (Note: Some of our encapsulation studies included encapsulation of powders, so encapsulated activator can be quite fine.) The pumping/flow rate would have to be such that all of the plug mix exited the drill bit before melting of the encapsulant occurred. Temperature determinations, coupled with pumping/flow rates would need to be part of this grout system such that the plug forming reaction did not happen inside the drill string. If the downhole conditions had been determined to be excessively hot, perhaps water could be pumped down the drill string for a short time period to cool the drill pipe. The mixture, once delivered, would be heated (by the downhole heat), the encapsulant would melt, and the plug would be formed, sealing the loss zone (Figure 7). It may be necessary to chase this mixture with water (or another fluid) to provide a backpressure to drive the plug a short distance into the formation. It is envisioned that this plug material would flow a short distance into the formation, because the plug-forming reaction is thermally activated. If the drill hole already has water in it, the calcium silicate hydrate plug material will sink to the hole bottom, because it is more dense than water. The drilling could commence in a short time because the plug sets immediately. Each of the methods described should be evaluated through bench-scale and field-testing.

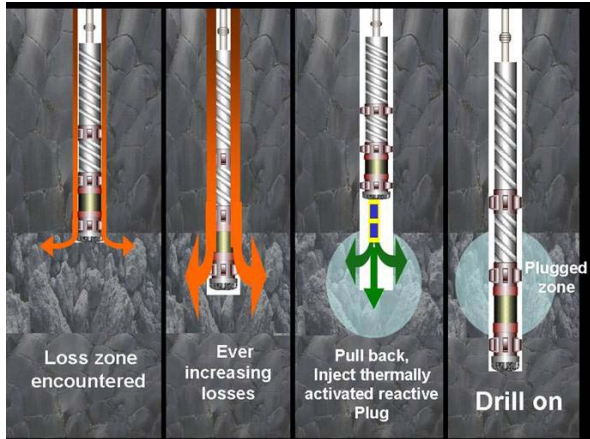


Figure 7. Placement scenario using through drill string delivery system.

DISCUSSION AND CONCLUSIONS

Recognizing the importance of minimizing trouble time caused by severe lost circulation in geothermal wells, water shutoff and steam flooding, we have studied a high temperature grout system that uses silicates. The synthesis and chemical stability of viable high-temperature silicate plugging materials, as well as, placement of the grout material in a hot water laden environment were part of this study. The material complies with the initial needs, namely (1) no special handling requirements and considered non-hazardous by the DOT and EPA; (2) low cost; (3) readily pumpable; (4) controllable gel time; the reaction rate needs to be adjustable for varied conditions both at the surface and down-hole; (5) controllable placement such that it has minimal water solubility and adheres well to rock surfaces through a single delivery hose; (6) hydrothermally stable for 8 weeks at geothermal temperatures (7) once placed, the grout is sufficiently stiff, to drill with conventional means, and no unanticipated problems with drill bit plugging.

Because of their ability to form fast-setting stable gels, we are reintroducing silicates to geothermal applications. There exists the potential to solve high-temperature lost-circulation problems through the use of these fast-setting silicate plugs. The laboratory study has shown that silicate hydrate plugs solidify quickly and maintain their integrity for extended time periods at high temperatures (300°C). In principle, the material should survive at greater temperatures. Encapsulation of one of the plug components allows emplacement at 80°C to 300 °C (and, in principle, at higher temperatures). Simple deployment schemes are presented which may decrease drilling downtime that has resulted from lost circulation.

ACKNOWLEDGEMENTS

This work was completed primarily at Sandia National Laboratories, which is a multiprogram laboratory operated by Sandia Corporation, a Lockheed Martin Company, for the United States Department of Energy under Contract DE-AC04-94AL85000. Initial screening and stability work was carried out at the National Silicates Technical Centre in Toronto, Canada, an affiliate of PQ Corporation.

REFERENCES

- Heaven, W.J., Anderson G.E., Gaudet D.R., Thomas F.B., Bennion D.B. (1999), "Resin Technology for Water Control in Production Wells", Presented at the 5th International Conference on Water Conformance Profile – Water and Gas Shutoff, November 8–10 1999, Houston, TX.
- Iler, R.K. (1979), "The Chemistry of Silica"; Wiley: New York, pp 582, 558-590.
- Lakatos, J., Lakatos-Szabo J., Tromboecky S., Munkacsi I., Kosztin B., Palasthy G. (2001), "Potentials of Silicates in Treatment of Oil Producing Wells", Oil and Gas Business Journal, December 11, 2001.
- Patterson R.E. (1994), "Preparation and Uses of Silica Gels and Precipitated Silicas, Chapter 32 of "The Colloid Chemistry of Silica", Horacio E. Bergna, Editor; Advances in Chemistry Series 234, American Chemical Society, Washington DC.
- PQ, (2004), Technical Bulletins 24-1, 12-31, 52-53.
- Samari E., Scott D.L.T., Dalrymple D. (1998), "Water Shutoff Treatments in Eastern Alberta: Doubling Oil Production, Decreasing Water Cut by 20%", SPE 39617 presented at SPE/DOE Eleventh Annual Symposium on Improved Oil Recovery, April 19-22, 1998, Tulsa OK
- Vidick B., Yearwood, J.A., Perthuis H. (1988), "How to Solve Lost Circulation Problems", SPE 17811 presented at The SPE International Meeting on Petroleum Engineering, November 1-4 1988, Tianjin China.

MULTIPHASE FLOW PROPERTIES OF FRACTURED GEOTHERMAL ROCKS

Chih-Ying Chen and Roland N. Horne

Stanford Geothermal Program, Stanford University, Stanford, California 94305, USA

alnchen@stanford.edu; horne@stanford.edu

ABSTRACT

The understanding of the properties of two-phase flow in fractured rocks is central to the prediction of geothermal reservoir performance. In this study, we suggest an alternative approach to describe the two-phase relative permeability behavior in rough-walled fractures based on the two-phase flow structures. This approach lumps the microscale physical mechanism (viscous and capillary forces) into an apparent observable parameter, *channel tortuosity*, which was found to dominate the reduction of the relative permeabilities from the values that would be expected based on the X-curve. Three artificial fractures, smooth-walled, homogeneously rough-walled and randomly rough-walled fractures, were studied to represent distinct surface geometry and heterogeneity. The experimental results from these three fractures could be described successfully by the proposed model. Furthermore, we found that the magnitude of the channel tortuosity increases when the heterogeneity of the fracture surface increases. Although only three simplified fractures were studied and the relationship between the flow-based heterogeneity and the channel tortuosity is not fully developed yet, we were able to derive an empirical, tortuous channel model generalized from all channel tortuosities from these three fractures. This model can represent the current experimental data and as well as observations from earlier studies with good agreement.

1. INTRODUCTION

Rock fractures or joints often form high-permeable flow pathways and therefore dominate single- or multiphase fluid transports in fractured porous media in geothermal reservoirs. Multiphase flows in fractured media are of great importance and engineering interest in geothermal development and environmental protection. In the last two decades, single-phase flow in fractures has been widely studied experimentally, numerically and theoretically. Several models have been proposed to describe the single-phase hydraulic properties in rough fractures (Witherspoon et al., 1980; Zimmerman and

Bodvarsson, 1996; Meheust and Schmittbuhl, 2001; Lomize, 1951). However, limited studies have been done to determine the fundamentals of multiphase flow behavior in fractures, especially the effects of fracture geometry on relative permeabilities.

Chen et al. (2004a) suggested a phenomenological approach, the tortuous channel approach (TCA), to describe the air-water relative permeability behavior in a smooth-walled fracture. A method to evaluate the mutual tortuosities induced by the blocking phase, namely the *channel tortuosity*, was proposed from observations of the flow structure images. With verification from laboratory experiments and visualizations, it was concluded that in smooth-walled fractures the coefficients of channel tortuosity dominate the reduction of the relative permeability values from the X-curve (i.e. relative permeability equals saturation). The results also indicated that the X-curve relative permeability cannot be reached for two-phase flows in fractures even if their surfaces are smooth. Instead, an upper bound for the air-water relative permeability in fractures was proposed. Despite the successful representation of the experimental results in the smooth-walled fracture, the feasibility of using TCA to describe the relative permeabilities in rough fractures was not studied – the rough-walled fracture represents a flow configuration much close to that expected in real rocks.

This research extended and modified the TCA to include rough-walled fractures. Existing and newly measured experimental data from two rough fractures with distinct surface roughness, randomly rough (RR) and homogeneously rough (HR), were used to evaluate and generalize this modified approach. Finally, a more general model deduced from these data was proposed to describe two-phase relative permeabilities in both smooth and rough fractures.

2 MODEL DESCRIPTION

The diversity and variability of the geometry of a single, natural fracture and the complexity of the two-phase interaction and interference have made it difficult to

reach a unique and accurate model to describe the two-phase flow behavior by means of the relative permeability concept. With the development of the visualization and surface measurement techniques, it has become possible to observe the multiphase flow behavior dynamically and to quantify the geometrical heterogeneity in fracture space. Nicholl et al. (2000) studied the effect of the immobile phase on the flowing-phase relative permeability in the saturated condition and developed a conceptual model for flowing-phase relative permeability by using the effective medium approach suggested by Zimmerman and Bodvarsson (1996). In the conceptual model of Nicholl et al. (2000), an in-place tortuosity induced by the immobile phase was used as a correction term to decrease the effective hydraulic gradient. The flowing-phase (water) relative permeability is then obtained as:

$$k_{rw} = S_w \tau_{ip} \underbrace{\left[\frac{\langle b_f \rangle^2}{\langle b \rangle^2} \right] \left[\left(1 + \frac{9\sigma_b^2}{\langle b \rangle^2} \right)^{1/2} \left(1 + \frac{9\sigma_{bf}^2}{\langle b_f \rangle^2} \right)^{-1/2} \right]}_A \quad (1)$$

where k_{rw} and S_w are the wetting-phase (water) relative permeability and saturation respectively, $\langle b \rangle$ and σ_b^2 are the mean and variance of the aperture field, the subscript (f) refers to parameters for the region occupied by the flowing phase, and τ_{ip} (range from 0 to 1) is the in-place tortuosity. From their definition, the smaller the value of τ_{ip} , the more tortuous the flowing phase structure behaves. Since their experiment was conducted in the saturated condition, nonwetting (air) phase remained entrapped. Nonwetting relative permeability was therefore always zero. From the experimental data, Nicholl et al. (2000) concluded that the in-place tortuosity is the dominant factor controlling the flowing phase relative permeability. However, the in-place tortuosity could not be measured in their study. Instead, in-place tortuosity was estimated independently by further simulating flow on the measured phase geometries under some simplified assumptions.

Chen et al. (2004a) conducted drainage (nonwetting phase displaces wetting phase) air-water cocurrent flow experiments in a smooth-walled fracture and defined a similar but measurable tortuosity coefficient for the channel flow regime, called channel tortuosity; τ_c , and used this coefficient to characterize the morphology of flow structures. The definition of this apparent parameter is based on the area of the channel and the smallest bounding rectangle that covers the whole channel for a specific phase. By using digital video recording and image-processing techniques, thousands of continuous flow images were analyzed automatically, and different flow structures were recognized and separated. It was found that the channel flow was the major flow structure spanning most of the water

saturation (S_w) range, except for extremely small or large values of S_w . The channel area, A_c , length and width of the smallest bounding box, L_x and L_y , were computed for channels of each phase. The channel tortuosities for gas and water were then defined as:

$$\tau_{c,g} = \left(\frac{L_x L_y}{A_c} \right)_g \quad \text{and} \quad \tau_{c,w} = \left(\frac{L_x L_y}{A_c} \right)_w \quad (2)$$

where the subscripts (g) and (w) denote the gas and water phases respectively.

The detailed methodology and an illustration of the computation of τ_c can be found in Chen et al. (2004a). Similar to the definition in porous media, the coefficient τ_c for each phase varies from 1 to infinity, with the two end cases representing respectively a homogeneous straight channel (no dispersed phase) and an extremely tortuous channel for each phase. This coefficient is related to the interfacial area and, consequently, allows quantification of the shear stress at the interface between the two fluids. From the experimental data, Chen et al. (2004a) found that the coefficients of channel tortuosity dominate the reduction of relative permeability in comparison to the X-curve, and that the following relative permeability relationship could replicate the experimental data with good accuracy:

$$k_{rw} = \frac{S_w}{\tau_{c,w}} \quad (3)$$

$$k_{rg} = \frac{S_g}{\tau_{c,g}} \quad (4)$$

It is worth noting that because of their different definitions of the tortuosity, the τ_{cw} in Equation (3) and τ_{ip} in Equation (1) should be close to reciprocal. Therefore, for smooth-walled fractures ($\langle b \rangle = \langle b_f \rangle$ and $\sigma_b^2 = \sigma_{bf}^2$), and Equation (1) can be simplified to Equation (3).

For the drainage relative permeabilities in rough-walled fractures, a major factor that was not considered in Equations (3) and (4) was the residual water, which was observed to be negligible in the smooth-walled case. The significant capillary force due to local aperture field variation can entrap considerable amounts of water phase, and some of it will contribute to the residual water saturation (S_{wr}) ultimately. To this end, a more rigorous approach by separating different phase structures was developed. Figure 1 illustrates the principle and concepts of this rough-walled tortuous channel approach. The two-phase flow structures were separated into three major parts, namely the flowing channels, the entrapped phases and the water film flowing along the fracture surfaces.

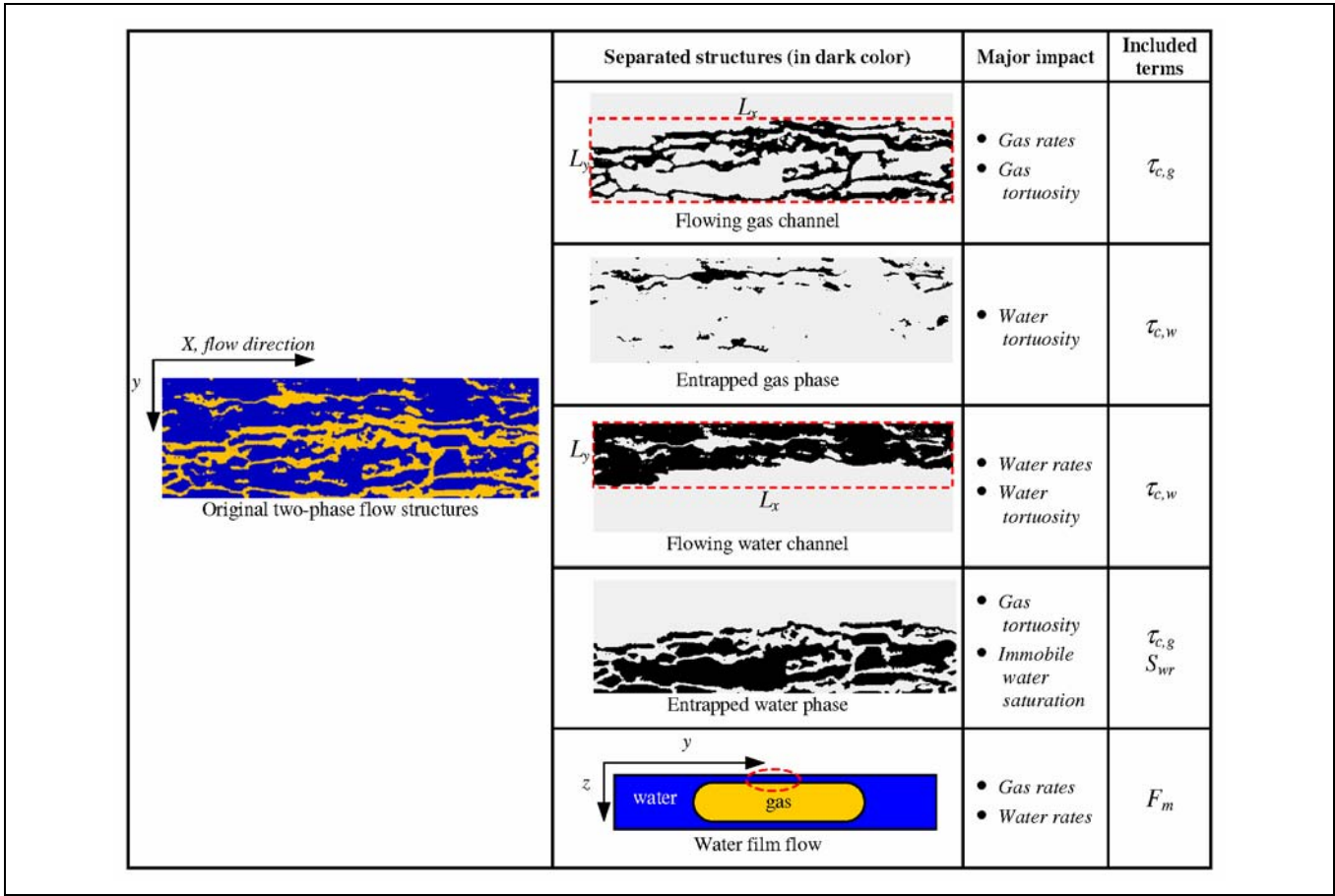


Figure 1: Illustration of separating the two-phase flow structures and the major impact parameters in each separated structure considered in the rough-walled TCA for drainage process.

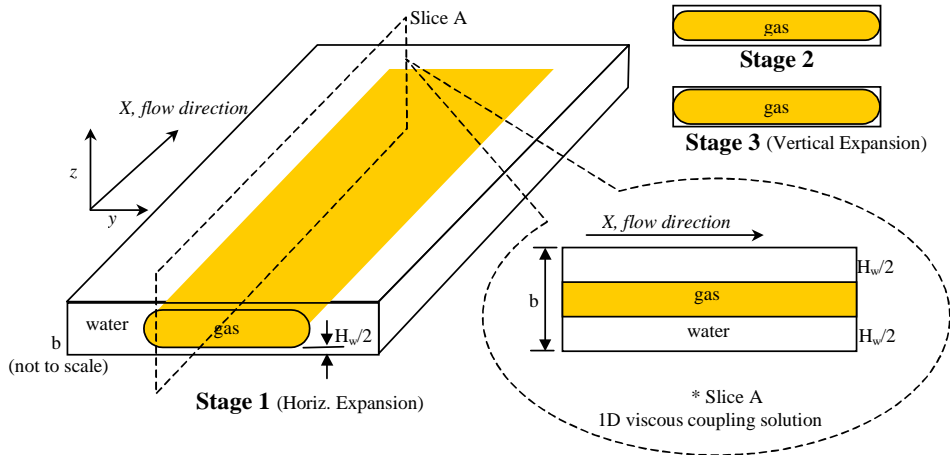


Figure 2: A simple superposition method for integrating one-dimensional viscous coupling model to two-dimensional viscous coupling model. The water film thickness, H_w , was assumed being constant during stage 1 and 2. After Stage 2, the H_w starts decreasing and the corresponding relative permeabilities approximately follows one-dimensional viscous coupling. (b and H_w are not to scale)

During the steady-state drainage process, the first two parts were fully or partially included in the channel tortuosity terms, except for the considerable immobile and residual water phase. In analogy to earlier studies of relative permeability modeling in porous media (Brooks and Corey, 1966; van Genuchten, 1980), the immobile and residual phases were taken into account by normalizing the water saturation. For the drainage process, the normalized water saturation is:

$$S_w^* = \frac{S_w - S_{wr}}{1 - S_{wr}} \quad (5)$$

where subscript (r) refers to residual saturation. Regarding the water film flow along the fracture surfaces, an extended two-dimensional viscous coupling model was used to evaluate the effect of film thickness on relative permeabilities. The one-dimensional viscous coupling model was obtained by integrating Stoke's equations under parallel-plate assumption. The one-dimensional model was then defines as:

$$k_{rw} = \frac{S_w^2}{2} (3 - S_w) \quad (6)$$

$$k_{rg} = (1 - S_w)^3 + \frac{3}{2} \mu_r S_w (1 - S_w) (2 - S_w) \quad (7)$$

where $\mu_r = \mu_g/\mu_w$ is the viscosity ratio.

Since the one-dimensional viscous coupling model has poor representation of the real two-phase flow behaviors in fractures, the simplified but more practical geometrical consideration of the drainage process in an ideal fracture space is shown in Figure 2. The gas channel was initially assumed to be in a round-ended rectangular column with constant height, H_w , which is close to but always smaller than the fracture aperture, b . The relative permeability was computed by using either the superposition or integration of the one-dimensional solution in each vertical slice as shown in Figure 2. After the gas channel reaches the fracture boundaries (Stage 2), the gas phase starts to expend vertically and the corresponding relative permeability approximately follows one-dimensional viscous coupling in Stage 3. By setting different values of the water film ratio, H_w/b , and assuming the fracture width was much larger than its aperture, the effect of water film thickness on air-water relative permeabilities is shown in Figure 3. The water film ratio affects the relative permeabilities almost linearly because the scale of the fracture aperture is relatively small. In addition, the effect on gas-phase relative permeabilities is stronger than on the water phase. Consequently, film flow correctors, F_{mw} and F_{mg} , were suggested as corrections to the relative permeabilities to account for the water film flow. Combining all factors in Figure 1, the modified TCA for describing the relative permeabilities of the rough fractures can be written in the following form:

$$k_{rw} = \frac{S_w^*}{\tau_{c,w}} F_{mw} \quad (8)$$

$$k_{rg} = \frac{S_g}{\tau_{c,g}} F_{mg} \quad (9)$$

Comparing Equation (8) to Equation (1) and examining the definition of the channel tortuosities, we can see that part A in Equation (1) has inherently contributed to the coefficients of $\tau_{c,w}$, and S_w^* .

Generally, the water film in partially saturated rock surfaces is attributed to adsorptive forces on flat surfaces of minerals or by capillary effects within the surface roughness. The metric potential is the major parameter that controls the thickness of the film. By considering the fracture-matrix interaction in fractured porous media, Tokunaga and Wan (1997) measured average surface film thickness ranging from 2 to 70 μm . However, for a single fracture with an impermeable matrix as in our cases, earlier studies indicated that the water film ratio was less than 1% (Romm, 1966; Pan et al., 1996) for smooth-walled fractures. However this ratio may increase for the rough-walled fractures since surface roughness and pits on the surface increase capillary and absorption forces. To the best of our knowledge, no practical methods exist to estimate the H_w in accordance with different surface geometry for a single fracture with impermeable surfaces. Judging from the study by Romm (1966) and the corresponding result in Figure 3, the water film ratio should be small and F_m should be close to 1, which means that the film effect on the relative permeabilities may be insignificant. Following this result, Equations (8) and (9) can be further simplified to:

$$k_{rw} = \frac{S_w^*}{\tau_{c,w}} \quad (10)$$

$$k_{rg} = \frac{S_g}{\tau_{c,g}} \quad (11)$$

In these simple equations, only two measurable parameters are needed. The residual saturation is readily obtained in the laboratory; however, the channel tortuosity has to be obtained by the aid of tomography or visualization techniques during two-phase flow experiments, unless some correlation between channel tortuosities and fracture geometry can be built to predict the channel tortuosity. To this end, several experiments were conducted to explore this issue and verify the model.

3 EXPERIMENTS

The fractures for the experiments were made by transparent silica glass with dimensions around 30cm

(L) x 10cm (W). Two fractures with distinct surface roughness, randomly rough (RR) and homogeneously rough (HR) fractures, were used in the steady-state air-water cocurrent drainage experiments to represent two distinct surface geometries and heterogeneities. The experiment of the RR case was conducted during this study while the data from the HR case were provided by an earlier experiment (Chen et al. 2004b). Details of the experimental apparatus and procedures can be found in Chen et al. (2004a). The three-dimensional profile of the RR fracture and the two-dimensional surface pattern of the HR fracture are shown in Figure 4.

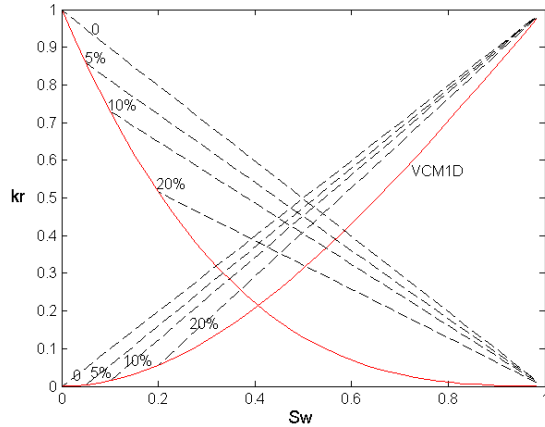
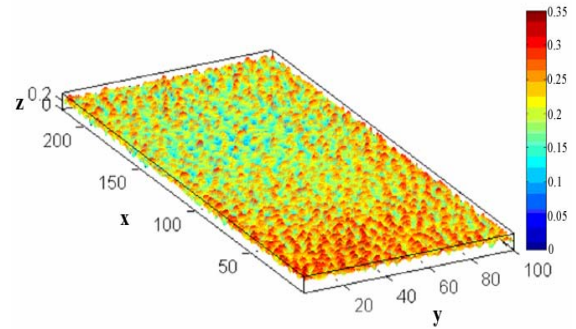


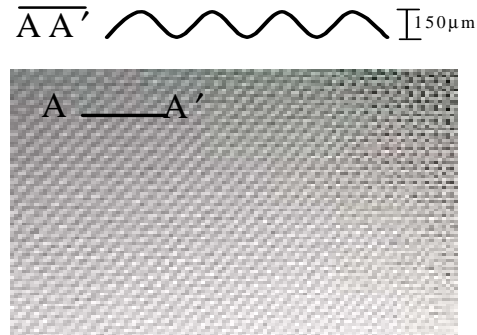
Figure 3: Effect of water film thickness on air-water relative permeabilities. VCM1D is the one-dimensional viscous coupling model. The percentage means the water film ratio (H_w/b).

The RR fracture has a hydraulic aperture of around $240 \mu\text{m}$ (~ 4800 darcy in permeability). The three-dimensional surface profile was measured by Leitz PMM 12106 CMM Stylus Machine (20 microns resolution, ~ 2 microns precision). The HR fracture has repeatable wedge-shaped pattern with hydraulic aperture of around $145 \mu\text{m}$ (~ 1750 darcy in permeability).

Initially, the fractures were fully saturated with deionized water. The drainage process was controlled by adjusting water and gas injection rates to decrease the water saturation. First, the water rate was kept constant while increasing gas rate to decrease the water saturation through the fracture until the water saturation was no longer sensitive to the increase of the gas rates. Then, the water rate was decreased further and the previous procedure was repeated. To avoid the dissolution of the gas phase and evaporation of the water phase, the water was equilibrated with air and the nitrogen gas was saturated with water-vapor. During each designated input rate of gas and water, the data were acquired when a stable or repeatable flow structure had been reached. After finishing one run (one pair of prescribed water and gas rates), the flow structures were destroyed by rapidly flushing water through the fractures, and then another run was commenced.



(a) Randomly rough fracture (Max. aperture variation $\sim 350 \mu\text{m}$)



(b) Homogeneously rough fracture (Max. aperture variation $\sim 150 \mu\text{m}$)

Figure 4: Surface profile of the rough-walled fractures: (a) three-dimensional profile of the RR fracture; (b) two-dimensional surface pattern of the HR fracture.

According to air-water experiments reported by earlier studies (Persoff and Pruess, 1995; Diomampo, 2001; Chen et al. 2004a), the fracture flow experiments are unsteady by nature. While input rates of water and gas were fixed, considerable pressure fluctuations accompanied by corresponding saturation changes occurred, which made flow rates through the fractures vary. A traditional time-average data processing was deemed to be infeasible and unrepresentative since every datum fluctuation may indicate a corresponding fluctuation of flow structure and saturation. To overcome these issues, all instantaneous data were acquired in a period less than or equal to one second. The high-speed data acquisition system gathered instantaneous pressure and flow rate, while instantaneous gathering of saturation and flow structure data was accomplished by the use of the digital video camcorder and automatic image processing techniques.

4 RESULTS AND DISCUSSION

Around 3000 data points were obtained in each experiment within a period of 1 second. The information of pressure, rates and saturation were then used to compute relative permeabilities using generalized two-phase Darcy equations. These experimental results

served as the reference relative permeabilities to validate the suggested model (Equations (10) and (11)). Continuous flow images from these experiments were analyzed. Phase channels were recognized, and the $\tau_{c,w}$ and $\tau_{c,g}$ values were then computed. Figure 5 shows several representative images extracted from these two experiments as well as the smooth-walled images replicated from Chen et al. (2004a). Snapshots in each row in Figure 5 have similar water saturation but are from different type of fractures. Clearly, the channel tortuosity increases when the heterogeneity of the fracture surface increases. The phase channels in RR fracture are always the most tortuous among these three cases. In general, for a specific fracture, the channel tortuosity of one phase has a countertrend to the saturation of that phase. In other words, the water (gas) channel tortuosity increases when the water (gas) saturation decreases. With increasing surface heterogeneity, the nested behavior of flow structures was increasingly apparent. Even though the flow structures were destroyed before changing the input rates, the gas phase had some stationary preferential pathways in the rough fractures, particularly in the RR fracture. When the gas saturation increased further, the gas channels expanded from these base pathways or branched from them. This behavior may demonstrate the likely flow structure evolution in natural fractures.

After analyzing thousands of images, the channel tortuosities of each phase were evaluated, and then the relative permeabilities were computed using the proposed TCA in Equations (10) and (11). Figures 6 and 7 compare these results to the reference experimental relative permeabilities from the generalized Darcy equations for the RR and FR fractures respectively. Due to the unstable nature of the flow, the experimental relative permeabilities are scattered. For the RR fracture, the result from TCA fits the experimental result with good accuracy. The gas-phase relative permeabilities seem to be overestimated slightly. Close agreement was also obtained in the HR fracture case. However, the gas-phase values from TCA were larger than the experimental result. The overestimation in gas-phase relative permeability may be attributed to the water film flow effect as demonstrated in the previous section (but neglected in the current study), or the experimental and image processing errors. The major source of the image processing errors was from the recognition of the channel connectivity, particularly for the rough-walled fractures. Because of the local aperture variation, some phase channels were connected via thin threads that were too narrow to be recognized in the images in a few cases. This led to the less accurate calculation of tortuosity.

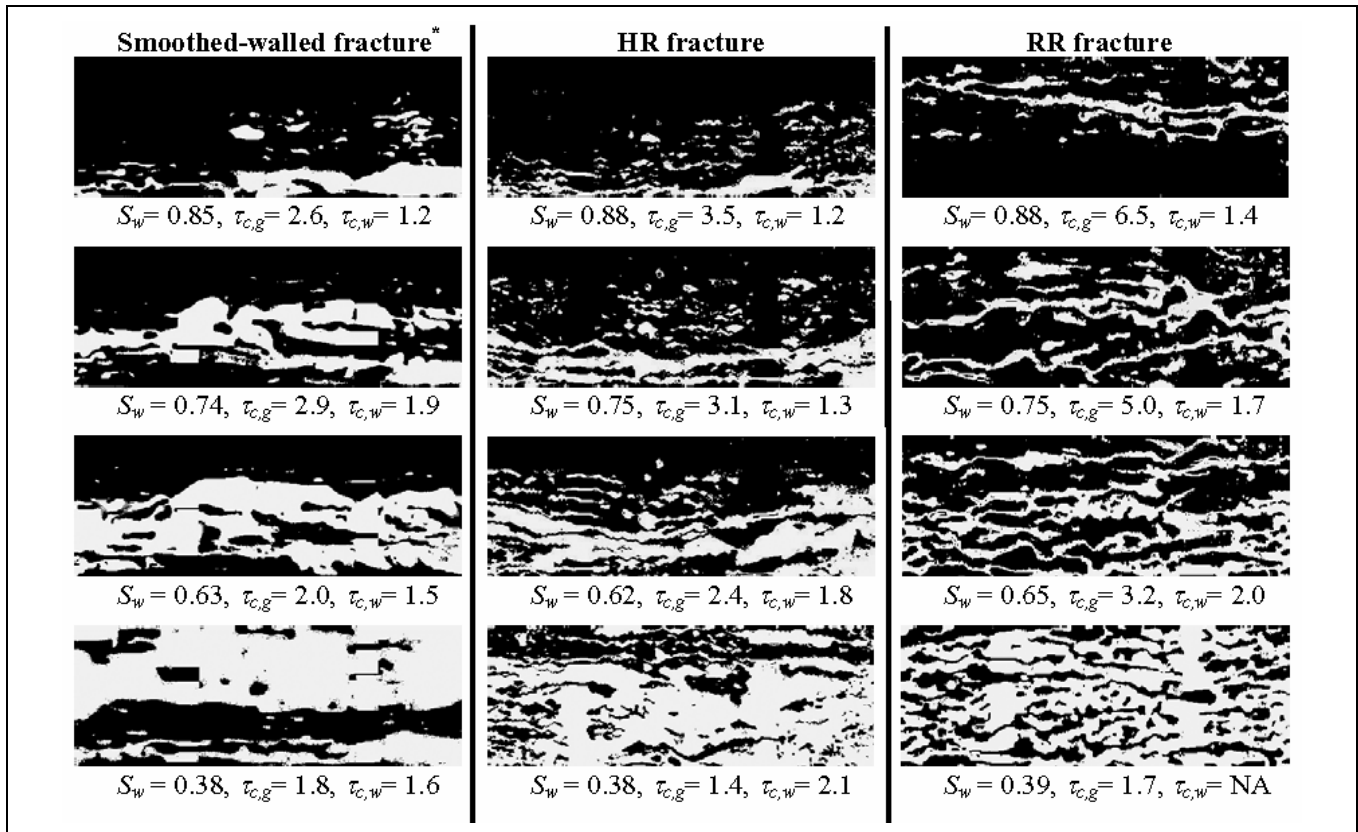


Figure 5: Representative images extracted from the image-processing program of channel recognition for the smooth and rough fractures and corresponding channel tortuosities evaluated. (Gas phase is white and water is black. *Smooth-walled images are from Chen et al., 2004a)

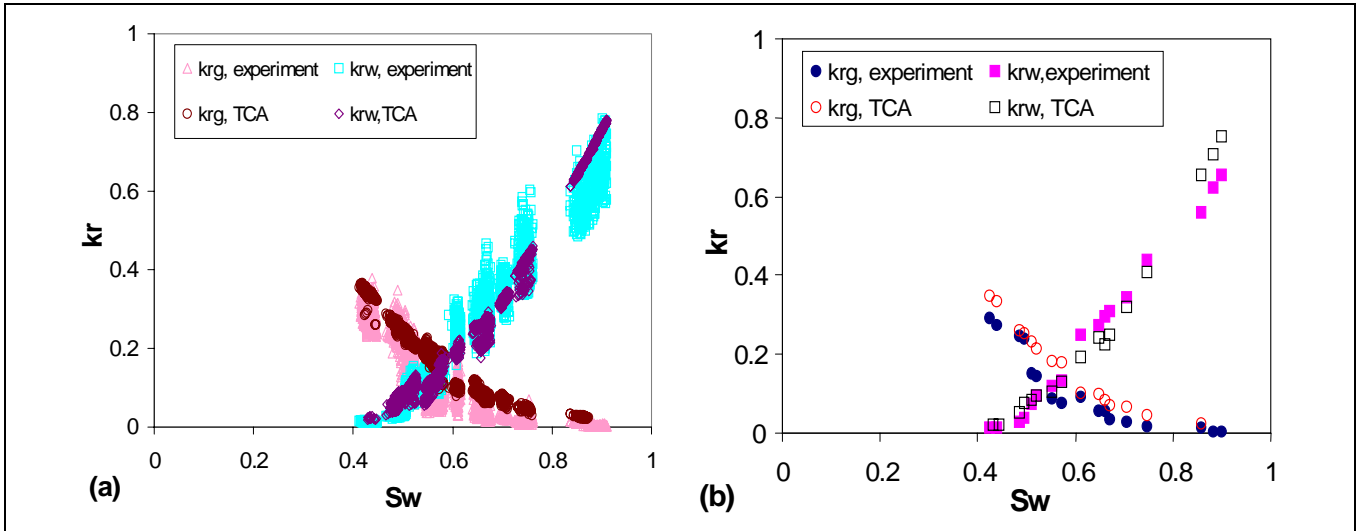


Figure 6: Relative permeabilities from tortuous-channel approach and its comparison with the experimental result for the RR fracture: (a) all data points (~3000 points), (b) averages of each runs in (a).

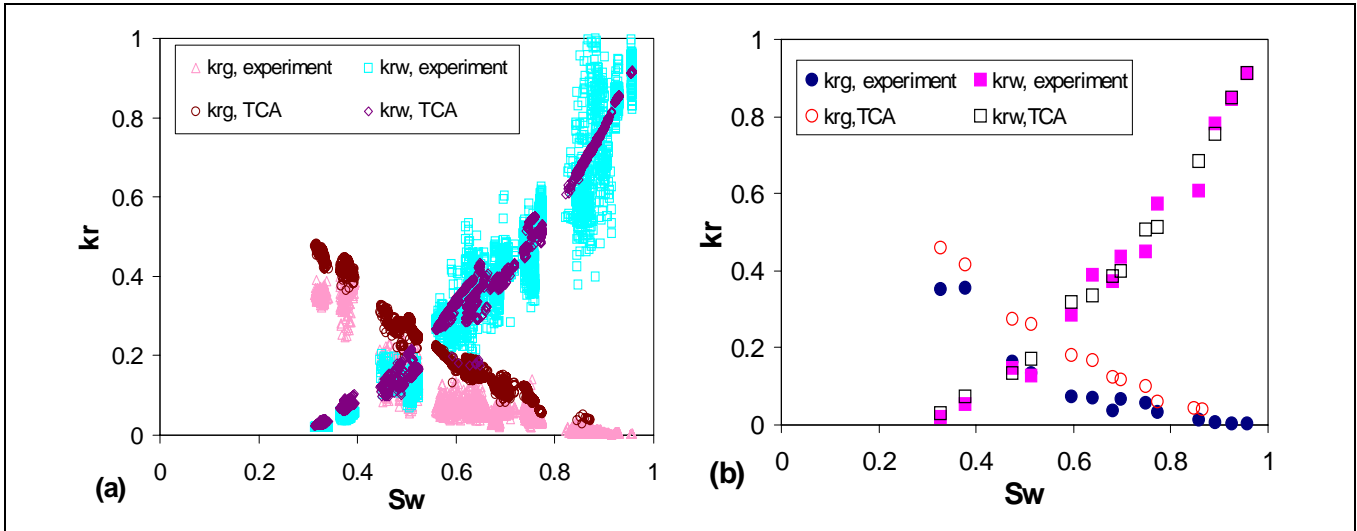


Figure 7: Relative permeabilities from tortuous-channel approach and its comparison with the experimental result for the HR fracture: (a) all data points (~3000 points), (b) averages of each runs in (a).

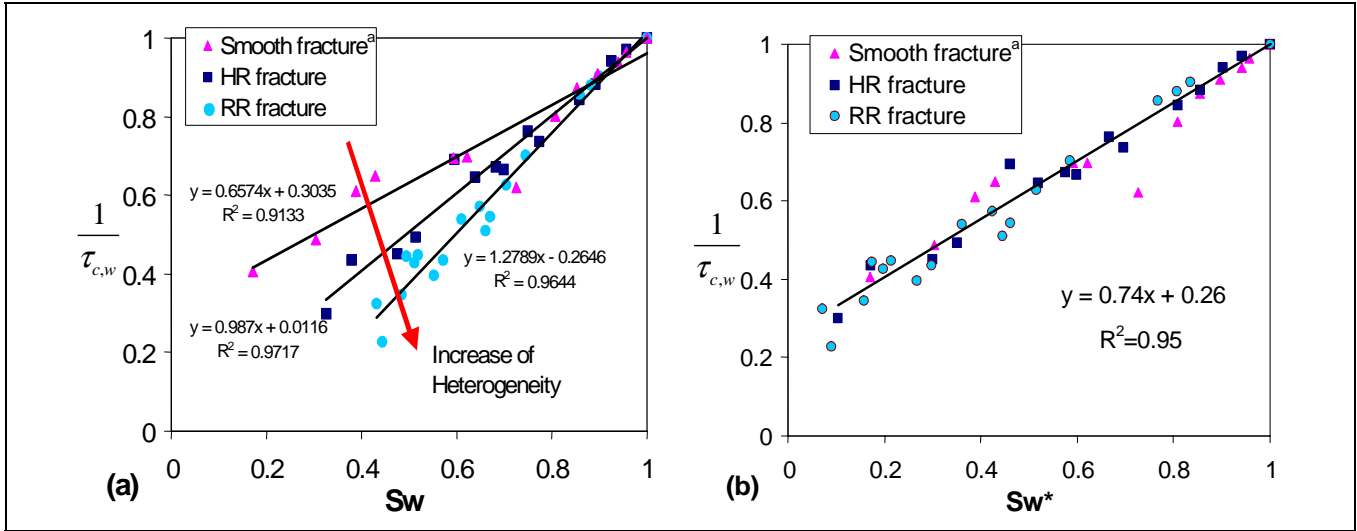


Figure 8: Reciprocal of average water channel tortuosity versus (a) water saturation and (b) normalized water saturation for smooth and rough fractures. (^a: from Chen et al., 2004a)

The evolution of phase channels shown in Figure 5 may reveal the correlation between the channel tortuosity and the surface geometry and heterogeneity of fractures. Earlier studies also suggested that relative permeabilities in fractures are sensitive to the nature and range of spatial correlation between apertures (Pruess and Tsang, 1990). Combining current results with the smooth-walled results from Chen et al. (2004a), Figure 8a shows the reciprocal of average water-phase tortuosity versus water saturation for all of the fractures studied. A straight channel has a value of reciprocal of tortuosity equal to 1. As can be seen in this figure, acceptable linear trends can be found in these three cases, while their slopes increase when the heterogeneity of the fracture surfaces increases. Interestingly, these data seem to collapse to a single linear trendline when plotted in normalized water saturation as shown in Figure 8b. On the other hand, the average gas channel tortuosities show similar trends in the smooth and the HR fractures while the RR fracture results demonstrate a slightly more tortuous trend as shown in Figure 9. However, most of the deviated points in Figure 9 were close to the end point of the gas saturation, which has a less significant inference on the Equations (10) and (11). All of these gas-phase tortuosities can be expressed approximately in a second-order relationship with respect to gas saturation.

Generalizing from these three specific types of fractures, preliminary and empirical correlation equations between the channel tortuosity and saturation can be obtained as shown in Figures 8b and 9. Substituting these equations into Equations (10) and (11), the tortuous channel model (TCM) for the three fractures we studied is then obtained as:

$$k_{rw} = 0.74S_w^{*2} + 0.26S_w^* \quad (12)$$

$$k_{rg} = 0.43S_g^3 + 0.38S_g^2 + 0.19S_g \quad (13)$$

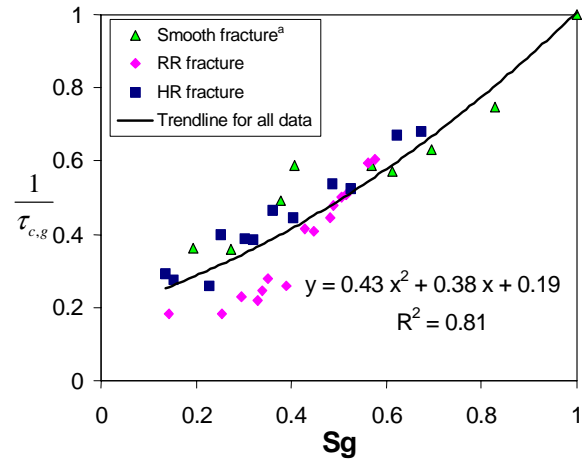


Figure 9: Reciprocal of average gas channel tortuosity versus gas saturation for smooth and rough fractures. (^a: from Chen et al., 2004a)

Fitting this model to the experimental results is shown in Figure 10. Close agreement was obtained between this tortuous channel model and the experimental measurements. Using measured values of residual water saturation S_{wr} from the experiments of the rough fractures, this model can describe the water-phase relative permeabilities with good accuracy, accounting for the residual phase. The gas-phase curve generalized from all gas-phase tortuosities seems to overestimate k_{rg} slightly compared to the experimental result; nevertheless the model curve can still capture the trend of the experimental data.

Nicholl and Glass (1994) conducted experiments to measure flowing-phase (water phase) relative permeabilities in the presence of entrapped gas phase

in a homogeneous, isotropic fracture. The corresponding in-place tortuosities were inferred from simulated flow rates using measured phase geometries (Nicholl et al., 2000). Although their experiments were conducted in saturated condition (water was the only flowing phase) and the final residual water saturation was not reported, Equation (10) still shows an acceptable fit to their flowing relative permeabilities by using their simulated tortuosities and setting a reasonable value for S_{wr} (0.36), as illustrated in Figure 11. In addition, most of the simulated tortuosities fall on the linear trendline suggested in this study (Figure 12). Pruess and Tsang (1990) predicted fracture relative permeabilities from numerical simulation of conceptual and heterogeneous fracture geometries. The phase occupancy and permeability were derived by assuming a parallel-plate model for small subregions in the fracture plane. Although only qualitative applications were suggested and the nonwetting phase relative permeabilities were deemed to be less physical in their simulated results, the wetting-phase relative permeabilities did follow a conventional pattern. As shown in Figure 13, these numerical results can be interpreted by the proposed tortuous channel model by setting a reasonable value for S_{wr} .

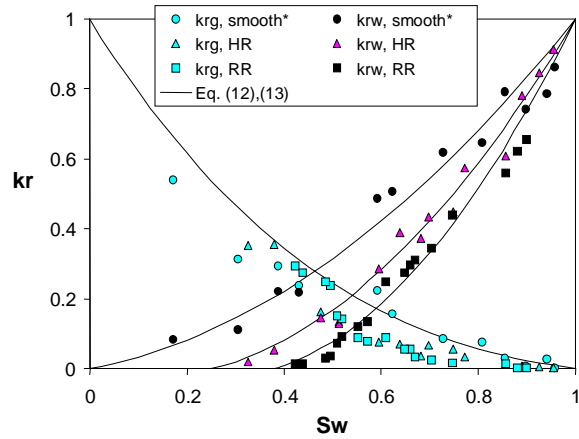


Figure 10: Comparison of the experimental relative permeabilities with the TCM using Equations (12) and (13) for the smooth-walled, HR and RR fractures. The S_{wr} for HR and RR fractures is 0.25 and 0.39 respectively determined from the experiments. (*: from Chen et al., 2004a)

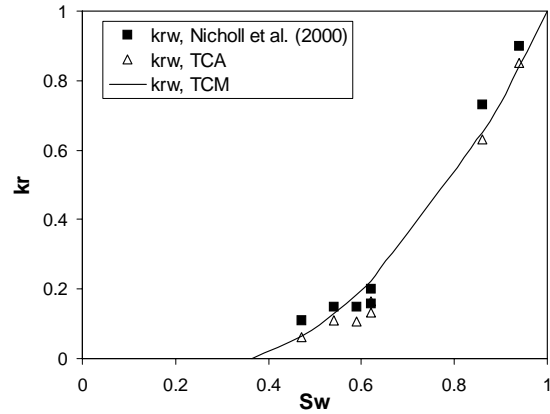


Figure 11: Using proposed TCA and TCM to interpret flowing-phase relative permeabilities from Nicholl et al. (2000) by setting $S_{wr} = 0.36$.

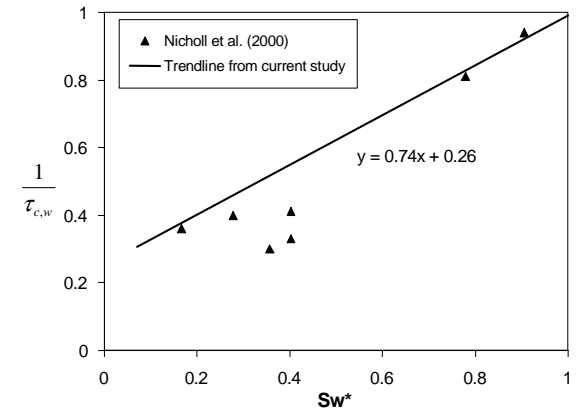


Figure 12: Plot of reciprocal of in-place tortuosities from Nicholl et al. (2000) versus normalized water saturation by setting $S_{wr} = 0.36$.

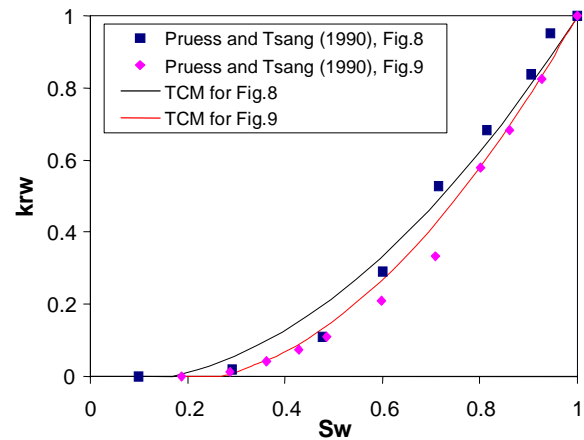


Figure 13: Using proposed tortuous channel model (Equations (12) and (13)) to interpret the water-phase relative permeabilities from earlier numerical study done by Pruess and Tsang (1990). (S_{wr} was set to be 0.27 and 0.17 respectively)

5 CONCLUSIONS

This study has demonstrated the possibility of using a flow-structure model to predict the corresponding relative permeabilities in rough-walled fractures. The proposed approach can represent the experimental data from current and earlier studies with good agreement. By studying three fractures with different surface roughness, we found that the magnitude of the flow channel tortuosity increases when the heterogeneity of fracture surface increases. Generalizing from all the channel tortuosities measured in these three fractures, we suggested an empirical, tortuous channel model. Although some successful descriptions of relative permeabilities in rough-walled fractures using the proposed tortuous channel approach and model were achieved, it is very important to emphasize the limitations. At this moment, the method of evaluating the coefficient of tortuosity and the feasibility of using the tortuous-channel approach were only validated in specific artificial fractures made of silica glass. To account for the complex connectivity and flow structures in full-scale naturally-fractured media, the algorithm to evaluate τ_c and the methodology to characterize the flow-based heterogeneity may have to be developed further. Characterizing the flow-based heterogeneity of the fractures is believed to be the major challenge of the future application. The tortuous-channel model (Equations (12) and (13)) was developed from current results empirically. The characteristics of heterogeneity in natural fractures are certainly much more complex and variable. Therefore more studies of the relationship between tortuosity and fracture geometry may be needed to gain rigorous models for predicting fracture relative permeabilities accurately. If such work can be achieved, perhaps the relative permeabilities of natural fractures can be predicted simply by measuring S_{wr} and the geometry of the fracture surface or by using tomographic technology to determine channel tortuosity.

REFERENCES

Brooks, R.H. and Corey, A.T.: "Properties of Porous Media Affecting Fluid Flow," *J. Irrig. And Drain. Div.*, Proc. ASCE, IR2 (1966), Vol. 92, p. 61-88.

Chen, C.-Y., Horne, R.N., and Fourar, M.: "Experimental Study of Liquid-Gas Flow Structure Effects on Relative Permeabilities in a Fracture," *Water Resources Research*, (Aug 2004a), Vol. 40, No.8, W08301.

Chen, C.-Y., Li, K., and Horne, R.N.: "Experimental Study of Phase Transformation Effects on Relative Permeabilities in Fractures," paper SPE 90233, presented in SPE 2004 Annual Technical Conference and Exhibition, Houston, TX, USA, September.26-29, 2004b.

Diomampo, G.P.: *Relative Permeability through Fractures*, MS thesis, Stanford University, Stanford, California (2001).

Lomize, G.M.: *Flow in Fractured Rocks*, (Gosenergoizdat, Moscow, 1951).

Meheust, Y., Schmittbuhl, J.: "Geometrical Heterogeneities and Permeability Anisotropy of Rough Fractures," *Journal of Geophysical Research*, (Feb. 2001); Vol.106, No.B2, p.2089-2102.

Nicholl, M.J. and Glass, R.J.: "Wetting Phase Permeability in A Partially Saturated Horizontal Fracture," Proc. 5th Ann. Int. Conf. On High Level Rad. Waste Mgmt., 2007-19, American Nuclear Society, Las Vegas, Nevada, May 22-26,1994.

Nicholl, M.J., Rajaram, H. and Glass, R.J.: "Factors Controlling Saturated Relative Permeability in a Partially Saturated Horizontal Fracture," *Geophysical Research Letters*, (Feb. 2000), Vol.27, No.3, p.393-396.

Pan, X., Wong, R.C. and Maini, B.B.: "Steady State Two-Phase Flow in a Smooth Parallel Fracture," presented at the 47th Annual Technical Meeting of the Petroleum Society in Calgary, Alberta, Canada, June 10-12, 1996.

Persoff, P. and Pruess, K.: "Two-Phase Flow Visualization and Relative Permeability Measurement in Natural Rough-Walled Rock Fractures," *Water Resources Research* (May 1995) Vol. 31, No. 5, p. 1175-1186.

Pruess, K. and Tsang, Y. W.: "On Two-Phase Relative Permeability and Capillary Pressure of Rough-Walled Rock Fractures," *Water Resources Research* (Sept. 1990) Vol. 26 No. 9, p. 1915-1926.

Romm, E.S.: *Fluid Flow in Fractured Rocks*, "Nedra" Publishing House, Moscow (Translated from the Russian) (1966).

Tokunaga, T.K. and Wan, J.M.: "Water Film Flow along Fracture Surfaces of Porous Rock," *Water Resources Research*, (Jun 1997), Vol.33, No.6, p.1287-1295.

van Genuchten, M.T.: "A Closed Form Equation for Predicting the Hydraulic Conductivity of Unsaturated Soils," *Soil Science Society of America Journal*, (1980), Vol.44, No.5, p.892-898.

Witherspoon, P.A., Wang, J.S.W., Iwai, K. and Gale, J.E.: "Validity of Cubic Law for Fluid Flow in a Deformable Rock Fracture," *Water Resources Research*, (1980), Vol. 16, No. 6, pp 1016-1024.

Zimmerman, R.W. and Bodvarsson, G.S.: "Hydraulic Conductivity of Rock Fractures," *Transport in Porous Media*, (Apr 1996), Vol.23, No.1, p.1-30.

WELL PERFORMANCE ESTIMATION FROM BRIEF DISCHARGE USING HEURISTIC DECLINE ANALYSIS

Malcolm Alister Grant

MAGAK
208D Runciman Rd
RD2 Pukekohe 1800, New Zealand
magak@xtra.co.nz

ABSTRACT

Traditionally stable well outputs have been determined by extended discharge: flowing the well to waste for a period of weeks or months. This has become increasingly difficult because of environmental constraints, resulting in well testing requiring injection wells and pipelines in order to allow extended flow periods, and this means that tests cannot be carried out routinely in the exploration program. Brief vertical or horizontal discharges to waste are still possible, and indeed a brief discharge is required to clear the well of debris. Data from a period of several hours of open flow has been used for a decline analysis. The analysis is an heuristic adaptation of flow at constant pressure. For wells, which were reasonably well warmed up before discharge, such decline analysis has given acceptable estimates of ultimate stabilized flow, even though it involves extrapolation well beyond the accepted limit of validity. Examples from Mokai are used to illustrate the application of the method.

1. INTRODUCTION

Mokai geothermal field is located in the Taupo Volcanic Zone of New Zealand. It was first drilled in the early 1980s, and developed in the late 1990s. Menzies et al. (2001) describe the power project.

After drilling a new production well, a figure for its future production capacity is desired. This is sometimes not straightforward. Completion testing gives a reasonable measure of the well's permeability, and from this an estimate of its production; but because cold water is used there remains some uncertainty. An initial discharge is usually short and will contain a greater or lesser amount of rundown.

It has usually been considered that the only reliable way to measure a well's output is to actually discharge it for some period, at least a few weeks.

However environmental constraints often prevent this. In a new field there is no injection system and even in an established one extra pipework may be needed to connect.

For these reasons the current development at Mokai was never able to discharge new wells other than briefly, with a maximum length of eight hours. During such a blow, the well runs down to a greater or lesser extent. Clearly the greater the rundown in this short time, the more may be expected in a longer time. Conversely, a very permeable well such as MK5 shows little rundown during its brief blow, and little more in longer time.

Therefore these brief discharges were examined for possible extrapolation to longer time.

2. THEORY

A convenient reference is the behaviour of a well flowing at constant pressure. Normal transient analyses examine the change in pressure when a well flows at constant rate. However if the flowing pressure is held constant, there is a transient in the flow. For a well in a homogeneous aquifer, the reciprocal of the flow rate will produce a linear plot when plotted against the time, on a semilog plot (Grant et al., 1983 eq (A1.47)):

$$\frac{1}{W} = \left(\frac{\nu}{4\pi kh} \right) \left(\frac{1}{\Delta P} \right) [2.303 \log_{10}(t) + const.]$$

where W is mass flow, ν the kinematic viscosity, kh the transmissivity, t the time flowing and ΔP the flowing pressure drop. The slope is inversely proportional to the aquifer's transmissivity. The use of semilog plots is also appealing since the rundown is initially rapid, and then becomes increasingly slow. The logarithmic time scale compresses the longer time period.

3. APPLICATION AT MOKAI

Semilog decline plots were made for all the Mokai wells and used as the basis for estimating the expected flow after a longer period. There was also available some discharge data for the old wells, from longer tests in the early 1980s.

In general, when extrapolating from the brief discharges to stable flow, which was taken to be the flow at several months or a year, there was an extrapolation over 3-3½ log cycles, far beyond the

validity of any semilog plot. Notwithstanding, the estimates were the best available and were used. Now that Mokai has been producing for several years these decline estimates can be compared with subsequent performance.

Figure 1 below shows a typical vertical discharge. As only lip pressure is available, an assumed enthalpy was used. MK15 was blown in August 2004 for seven hours. There is four hours rundown with the well wide open, followed by several steps of throttling. Transient changes in flow rate and wellhead pressure are apparent in each stage.

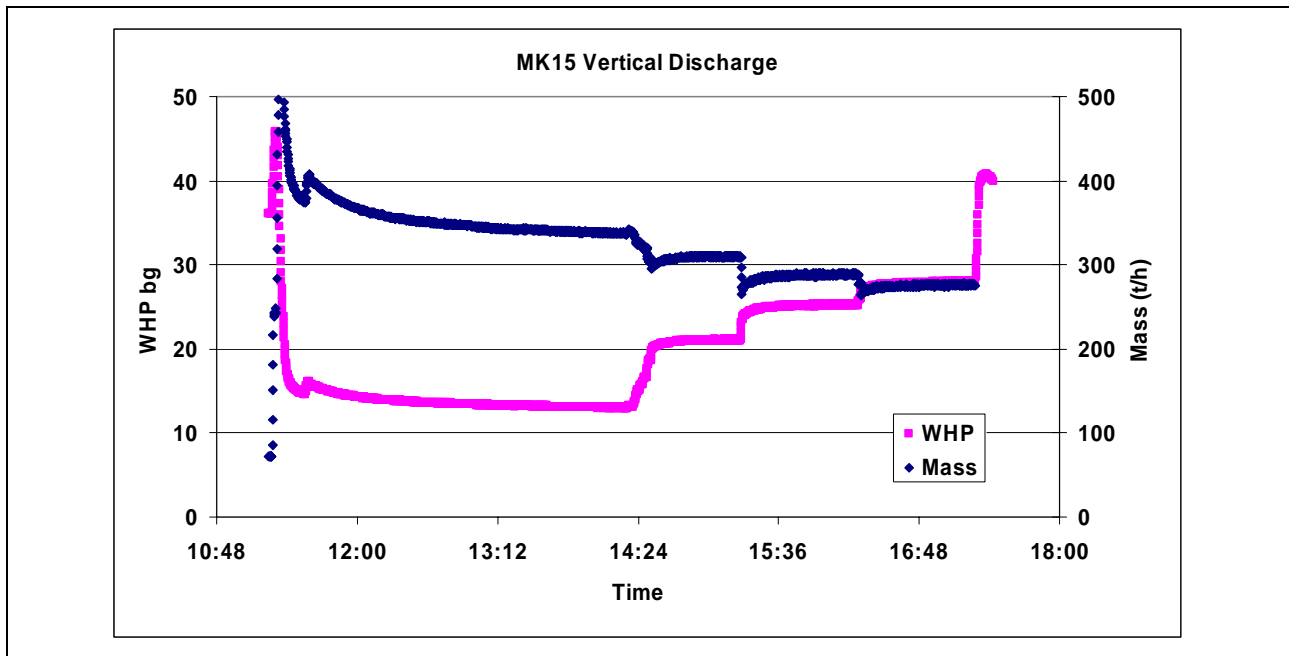


Figure 1. First blow of MK15

A nominal output curve can be defined using the last flow and wellhead pressure at each setting, but clearly these are not stable values. The first period shows considerable rundown. When the well is throttled, there is some recovery due to the throttling, superimposed upon continuing rundown.

To estimate at stable flow, the initial decline is analyzed.

There is a further complication that the wellhead pressure was running down. The nominal output curve using the last output at each setting was fitted to an ellipse. It defines an MDP of 45.6 bar, which is also near the maximum WHP observed during the test. Using this MDP and an assumed elliptical output curve, the flow during the first blow (up to 14:20) was corrected to a production WHP of 20 bar gauge. This was then plotted as a decline of the reciprocal of the flow rate against time on a semilog plot. This is shown in Figure 2 below. A straight line is fitted to

the latter part of the data. This line was then extrapolated to 1 year, 3½ log cycles.

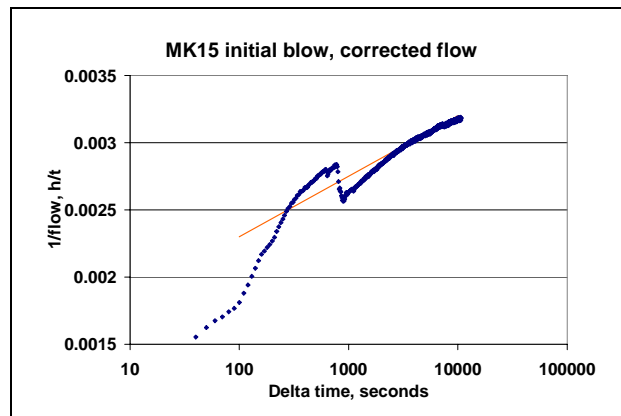


Figure 2. Decline analysis of initial blow of MK15

The extrapolated value was $1/W = .0051$ h/t, or a flow rate of 195 t/h. This was the estimate of the stable flow of the well at production pressure. The observed flow rate during the test at this pressure was around 300 t/h. Clearly the stable flow would be less. How good is this estimate of the future rundown? The next section reviews estimates made on earlier wells and compares with later performance.

4. EXPERIENCE AT MOKAI

4.1 MK3

MK3 was blown in 1997. Figure 3 shows the decline plot of this blow, as it was then reported and analysed, with the addition of production data for 2000-2003. This production data is plotted based upon a start time of 1 January 2000.

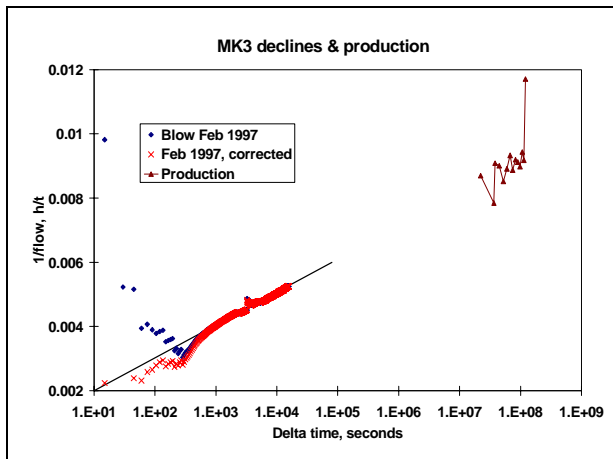


Figure 3. MK3 blow and subsequent production.

During the initial blow, the wellhead pressure was running down, although it was near to 20 bar gauge during most of the period, but was higher during the first section. The flow data is replotted with an estimated corrected flow. The flow was corrected by assuming an output curve as an ellipse, with MDP 64 bar gauge. It can be seen that there is little difference except in the early period, and the fitted line is a better fit. The fit also provides a good estimate of the subsequent production flows.

Figure 4 shows data from a two-week discharge in 1983. This is very interesting. It does not replicate the 1997 results. There is an early straight line and then a flattening to a later line. This later line extrapolates to the production performance. Had only the early data been available, it would have given an extrapolation to a production flow of 50-60 t/h, an underestimate by 50% or 60 t/h.

There is no obvious reason why the 1983 test does not replicate the 1997 results. The valve control was

different. In 1997 the valve was set so that most of the test occurred near 20 bar gauge. (This was also the case for MK5, 6 & 7.) The 1983 test was at significantly higher wellhead pressures, so that very considerable correction is involved. It is possible this causes a problem, but the same anomaly is present in corrected and uncorrected data.

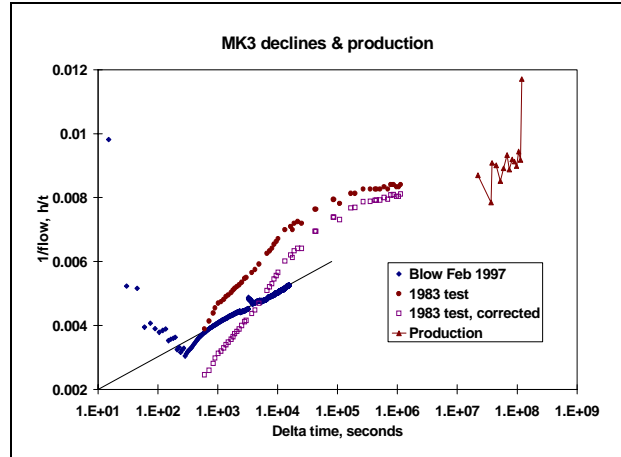


Figure 4. MK3 blow and 1983 discharge.

4.2 MK5

Figure 5 shows the blow of MK5 and subsequent production. It can be seen that the extrapolation lies below the subsequent production, which means that there has been more rundown than estimated from the extrapolation. The extrapolation overestimates production flow by about 10%, or 50 t/h.

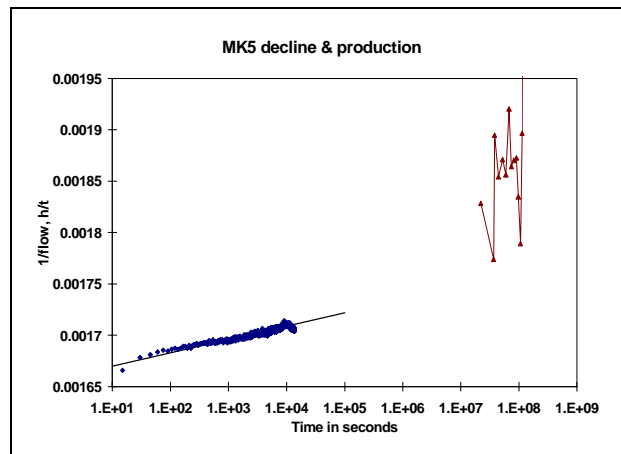


Figure 5. MK5 blow and production

MK5 is of course highly permeable ($kh = 50-70$ dm) and there is little rundown either during the blow or under production. This well is expected to run down in response to the drawdown of the reservoir as a whole rather than any local restriction of permeability.

4.3 MK6

Figure 6 shows MK6. The extrapolation provides a good estimate of subsequent production performance.

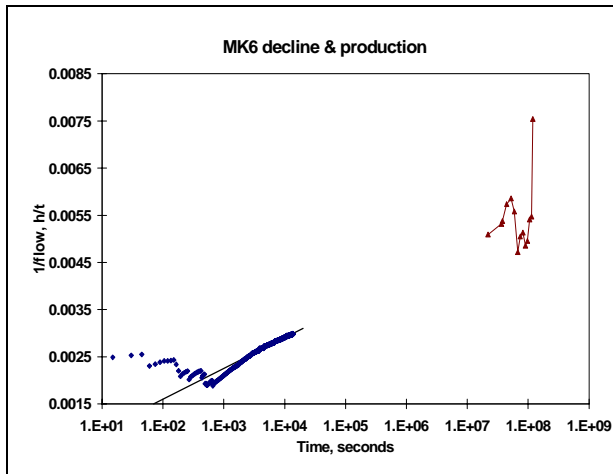


Figure 6. MK6 blow and production

4.4 MK7

This well is a more difficult case, due to the changes in performance that occurred. The well was tested in 1998. Its performance was unsatisfactory, with flow surprisingly small and continued production of rubble. The lower part of the well was obstructed by a lost fish. On retest in 2000, decline was much greater than in 1998, so that: “*kh value in 2000 is estimated at one-third of the 1998 value.*” Based upon the change in the decline slope, and the known obstruction of the wellbore, it was concluded that the lower part of the well had been blocked off. By contrast, had there been a restriction in the wellbore, but all zones still open, a decline plot would have the same slope but be displaced upwards. The decline plot is able to identify a total blockage of the lower part of the well.

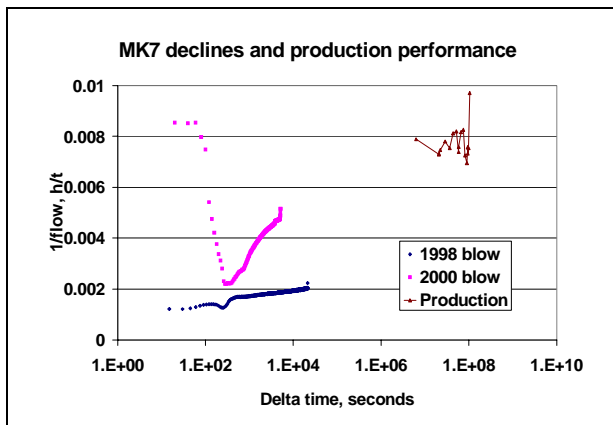


Figure 7. MK7 blows and production

An estimate was made of 110 t/h as the stable flow at 20 bg, but this was just by visual comparison of the “output” curve, not by extrapolation. Average of the production flows is 130 t/h, so this estimate was an underestimate by 20%, or 20 t/h. No attempt was made at the time to extrapolate from the semilog plot, because of the problems with the data and well. An extrapolation of the “2000 blow”, fitting to the latter part of the plot, would give a production flow of around 90 t/h.

5. DISCUSSION

5.1 Utility of the method

For wells MK3 & 6, the extrapolation provides a production estimate with negligible error – it lies within the range of the production measurements. For MK5, there is an overestimate of 10% or 50 t/h, and for MK7 an underestimate of 40% or 40 t/h.

For the total flow of the four wells (which was the purpose of the original estimate), the total flow of MK3+5+6 was accurate to 50 t/h or 6%, and the total flow of MK3+5+6+7 was accurate to 1%.

Whatever the theoretical weaknesses, the method was effective in practice. The method was also helpful in diagnosing changes in MK7 performance.

While the analysis is partly heuristic, the transient decline in flow rate contains as much information, in principle, as a transient of equal length. The practical limitation is that the changes in flowing pressure are not known. Given an adequate model for the relationship between flowrate and downhole pressure, the same information about reservoir permeability could be extracted as from a conventional transient.

It is concluded that this decline extrapolation technique has provided, at Mokai, acceptable estimates of long-term production performance, despite the very long extrapolation involved. The estimates were sufficiently close that it was not justified to carry out longer term tests, and the decision to use only the short discharge test was correct.

Comparison of an earlier test of MK3 raises questions about whether the method can be reliably replicated. It may be that significant variation in wellhead pressure is a problem, not solved by simple corrections. The recent tests of new wells at Mokai have all been done wide-open, so that wellhead pressure falls well below 20 bg. This may be less of a problem, since there is little variation of flow with wellhead pressure in the low part of the range.

It is also the case that the recent tests have been carried out on new wells, which may be still heating. In general this should not be a major problem, as with aerated drilling there has been little drilling loss, as shown by the rapid warming. For the recent wells, these past results provide support for the method but do not fully validate it because of these two changes in conditions.

If a well had been drilled with water or mud, with considerable losses, there is an additional transient effect, the warming of the well. This effect was largely absent at Mokai, as the wells had either been drilled long ago, or more recently, drilled with underpressured aerated fluid.

5.2 Theoretical basis

The decline measured in the blow reflects the permeability near the well. With longer time the permeability at greater distance controls the response, so the well tends to reflect average reservoir performance. Thus it could be expected that the long-term decline would be overestimated for low permeability wells (ie MK3, 7) and underestimated for high permeability wells (ie MK5). It would also be expected that with a group of wells, containing a range representative of reservoir permeability, these errors would cancel out. This does appear to be the case in the relatively small number of wells tested.

If we consider each well to contain a local near-well region of permeability distinctive to the well, surrounded by a reservoir of uniform “average” permeability, Figure 8 shows the decline trends expected of each well. There is an early period reflecting the local permeability, whereas at later time the average reservoir permeability controls the decline. Only the first period is observed in the brief tests discussed above.

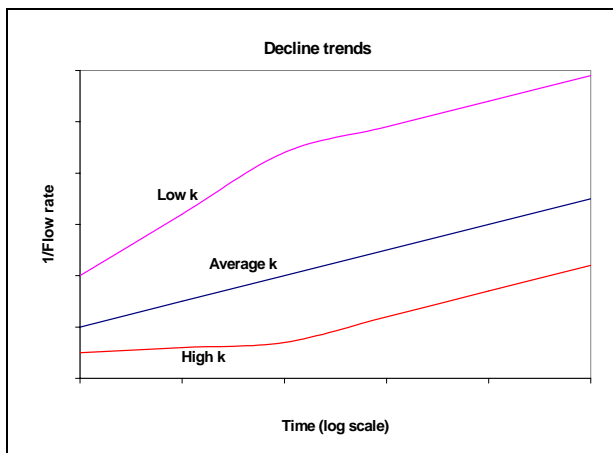


Figure 8. Expected trends with different local permeabilities

A well whose local permeability is the same as the reservoir average, will simply show a steady decline.

A well with low local permeability will show an initial more rapid decline, followed by a decline reflecting the average permeability, at later time when its drainage radius has reached beyond the local zone. It will then show the same decline slope as the average well, but displaced by the effective skin created by the extra local resistance.

A well with locally high permeability similarly shows an initial smaller trend, and later an average slope with a negative skin.

5.3 Possible refinements

The method could readily be made more rigorous by the use of a coupled wellbore and reservoir simulator. Ignoring the very first part of a well blow, which reflects the unloading of the wellbore, it would be acceptable to regard the wellbore column as quasi-steady. Only local reservoir structure is relevant, so the aquifer could be modeled as uniform. Thus a model of a uniform aquifer and quasi-steady wellbore flow could be fitted to the observed well performance during the brief discharge. This provides a calibration for the reservoir permeability near the well. Using these local parameters within a general reservoir model could then give long-term estimates of well performance.

If one knew the downhole pressure history, the plot could be improved by plotting $\Delta P/W$ rather than $1/W$. But the drawdown is not known. Fitting a wellbore and reservoir model to the decline is the best way of bringing the variations in flowing pressure into the analysis.

6. ACKNOWLEDGEMENTS

I thank Tuaropaki Power Company for permission to publish data and results.

7. REFERENCES

- Grant, M.A., Donaldson, I.G., & Bixley, P.F., 1983 “Geothermal reservoir engineering” Academic Press, New York
- Menzies, A.J., Brown, P., Searle, J., & King, R., 2001 “The Mokai geothermal power plant, New Zealand: Analysis of performance during the first year of operation” Transactions, Geothermal Resources Council V25, pp535-542.

INFERRING RELATIVE PERMEABILITY FROM RESISTIVITY WELL LOGGING

Kewen Li and Roland N. Horne

Stanford Geothermal Program, Stanford University
Green Earth Science Building, 367 Panama St.
Stanford, CA 94305-2220, USA
e-mail: kewenli@stanford.edu

ABSTRACT

Steam-water relative permeability can be calculated from capillary pressure. However this technique still requires measurement of capillary pressure. In this study, a semianalytical model was developed to infer relative permeability from resistivity data. Although it would still be necessary to conduct experimental measurements of resistivity, these are easier than measuring capillary pressure. On the other hand, resistivity data are commonly available from routine well logging. The semianalytical model was tested against experimental data. The results demonstrated that the relative permeabilities calculated from resistivity data using the new model were close to those calculated from capillary pressure data. The model developed in this study may also provide an approach to estimate permeability using both the resistivity well logging and well testing.

INTRODUCTION

One important parameter in geothermal reservoir engineering is steam-water relative permeability. Yet it is difficult to measure steam-water relative permeability because of mass transfer and phase transformation as pressure changes. Previously, Li and Horne (2002, 2004) reported that steam-water relative permeability could be calculated from capillary pressure data. These models provide an easier and more economical approach to obtain steam-water relative permeability, compared to the experimental technique. The disadvantage is the need to measure steam-water capillary pressure, which can also be difficult and time consuming in many cases. It would be helpful for engineers and scientists to have a method to infer steam-water relative permeability from resistivity data because it is easier to measure and resistivity data may be available from well logging. In this study, a semianalytical model was developed to infer relative permeability from resistivity data.

MATHEMATICAL MODELS

The relationship between relative permeability and resistivity index is derived in this section. The main theory behind this is the similarity between fluid flow in a porous medium and electricity flow in a conductive body.

Calculation of the Wetting-Phase Relative Permeability

The conductance of a porous medium at a water saturation of 100% is:

$$G_a = 1/R_o \quad (1)$$

where R_o is the resistivity at a water saturation of 100%, G_a is the conductance of a porous medium at a water saturation of 100%.

The conductance of a porous medium at a specific water saturation of S_w is:

$$G_w = 1/R_t \quad (2)$$

where R_t is the resistivity and G_w is the conductance at a specific water saturation of S_w .

According to the similarity theory between fluid flow and electric flow, the relative permeability of the wetting phase can be calculated using the following equation:

$$k_{rw} = \frac{G_w}{G_a} = \frac{R_o}{R_t} = \frac{1}{I} \quad (3)$$

where I is the resistivity index, k_{rw} is the relative permeability of the wetting phase.

According to the Archie's equation (1942), the following equation applies:

$$I = \frac{R_t}{R_o} = (S_w)^{-n} \quad (4)$$

Where n is the Archie's saturation exponent.

At a water saturation of 100%, it is known that $I=1$, so the value of k_{rw} calculated using Eq. 3 would be equal to 1, which is true. At the residual water saturation, it is known that $k_{rw}=0$, which implies that I approaches infinity according to Eq. 3. But it is known that the value of I does not approach infinity at the residual water saturation. So the value of k_{rw} calculated using Eq. 3 is greater than zero, which is not consistent with physical observation.

One can also expect that the relative permeability of the wetting phase calculated using Eq. 3 will be greater than the true value. The reason is that the resistivity counts the average volumetric properties of the pore bodies in a porous medium while permeability counts the properties of pore throats. This is also why resistivity well logging can obtain porosity but not permeability.

Considering these problems, Eq. 3 is modified as follows:

$$k_{rw} = \frac{S_w - S_{wr}}{1 - S_{wr}} \frac{1}{I} \quad (5)$$

where S_{wr} is the residual saturation of the wetting phase. According to Eq. 5, $k_{rw}=1$ at $S_w=100\%$ and $k_{rw}=0$ at $S_w=S_{wr}$, which is reasonable.

Eq. 5 can also be expressed as follows:

$$k_{rw} = S_w^* \frac{1}{I} \quad (6)$$

S_w^* is the normalized saturation of the wetting phase and is expressed as follows:

$$S_w^* = \frac{S_w - S_{wr}}{1 - S_{wr}} \quad (7)$$

Relative permeability of the wetting phase can be calculated using Eq. 6 from resistivity index data once the residual saturation of the wetting phase is available. Note that the residual saturation of the wetting phase can be obtained from the experimental measurement of resistivity.

Calculation of the Nonwetting-phase Relative Permeability

According to Li and Horne (2002), the wetting-phase relative permeability can be calculated using the Purcell approach (1949):

$$k_{rw} = (S_w^*)^{\frac{2+\lambda}{\lambda}} \quad (8)$$

where λ is the pore size distribution index and can be calculated from capillary pressure data.

After the relative permeability curve of the wetting phase is obtained using Eq.6, the value of λ can be inferred using Eq. 8.

According to the Brooks-Corey model (1964) and the study by Li and Horne (2002), the relative permeability of the nonwetting phase can be calculated once the value of λ is available. The equation is expressed as follows:

$$k_{rnw} = (1 - S_w^*)^2 [1 - (S_w^*)^{\frac{2+\lambda}{\lambda}}] \quad (9)$$

One can see that the entire relative permeability set (both wetting and nonwetting phases) can be inferred from resistivity index data using Eqs. 6 and 9.

RESULTS

The experimental data of resistivity and capillary pressure measured by Sanyal (1972) in rocks with different permeability were used to test the models (Eqs. 6 and 9) developed in this study. Firstly the values of relative permeability were calculated using Eqs. 6 and 9. Secondly relative permeability data were calculated using capillary pressure data (Li and Horne, 2002). According to the study by Li and Horne (2002), relative permeability could be calculated accurately using the capillary pressure technique. Finally the results of relative permeability inferred from resistivity index and capillary pressure data were compared.

Berea Sandstone

The Berea sandstone sample used by Sanyal (1972) had a porosity of 20.4% and a permeability of 300 md. Fig. 1 shows the relationship between resistivity index and water saturation in Berea sandstone at a temperature of 175°F.

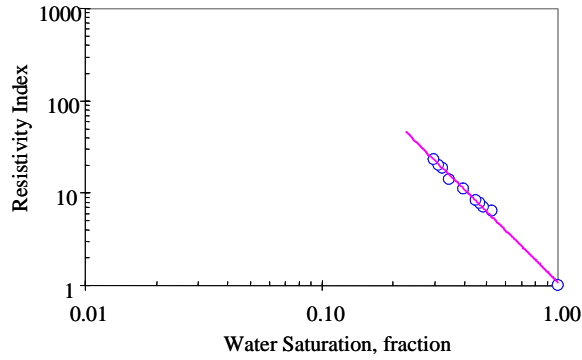


Figure 1. Relationship between resistivity index and water saturation in Berea sandstone at a temperature of 175°F (Sanyal, 1972).

The values of the resistivity index at different water saturation shown in Fig. 1 were measured in oil-water (water displaced by oil) systems. Fig. 1 also shows that the relationship between resistivity index and water saturation in Berea sandstone at a temperature of 175°F is linear on a log-log plot, which is consistent with Eq. 4.

Oil/water capillary pressure data were measured simultaneously with resistivity in the same core sample. The results are plotted in Fig. 2.

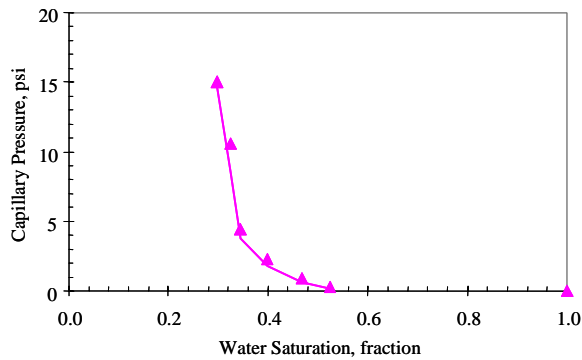


Figure 2. Capillary pressure data measured in Berea sandstone at a temperature of 175°F (Sanyal, 1972).

Oil/water relative permeability data were calculated from resistivity index (using Eqs. 6 and 9) and capillary pressure data (See Li and Horne, 2002) respectively. The results are compared and shown in Fig. 3.

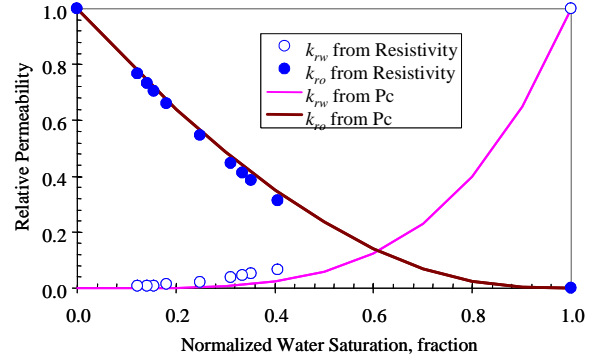


Figure 3. Relative permeability calculated from resistivity and capillary pressure data in Berea sandstone at a temperature of 175°F.

The results shown in Fig. 3 demonstrate that the relative permeability data inferred from the resistivity index data are close to those calculated using capillary pressure data. The oil relative permeabilities inferred from resistivity index data are almost equal to those calculated from capillary pressure data.

Sanyal (1972) also conducted the experimental measurements of resistivity index and capillary pressure at different temperatures in the same core sample. The resistivity index data at a temperature of 300°F are plotted in Fig. 4. One can see from Fig. 4 that the resistivity index data also follows the Archie's law (Eq. 4).

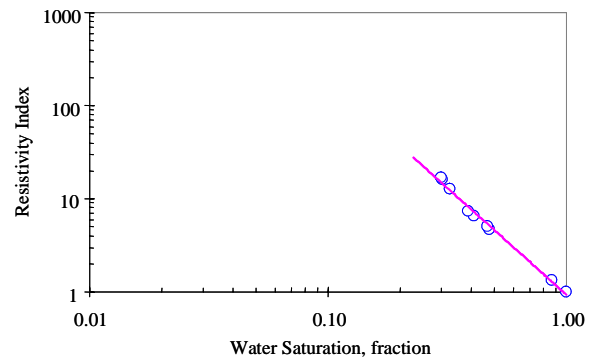


Figure 4. Relationship between resistivity index and water saturation in Berea sandstone at a temperature of 300°F (Sanyal, 1972).

Fig. 5 shows the oil/water capillary pressure data measured simultaneously with resistivity in the same Berea sandstone core sample at a temperature of 300°F.

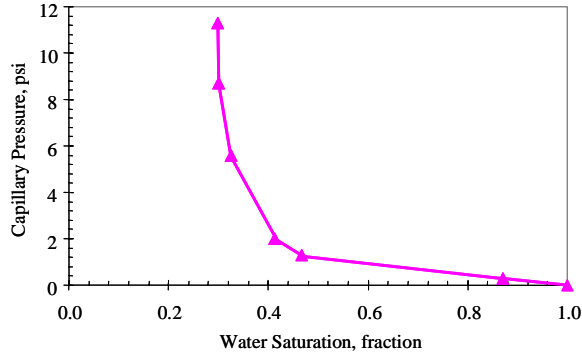


Figure 5. Capillary pressure data measured in Berea sandstone at a temperature of 300°F (Sanyal, 1972).

Fig. 6 demonstrates the relative permeability data calculated from both the resistivity index data shown in Fig. 4 (using Eqs. 6 and 9) and the capillary pressure data in Fig. 5 (see Li and Horne, 2002).

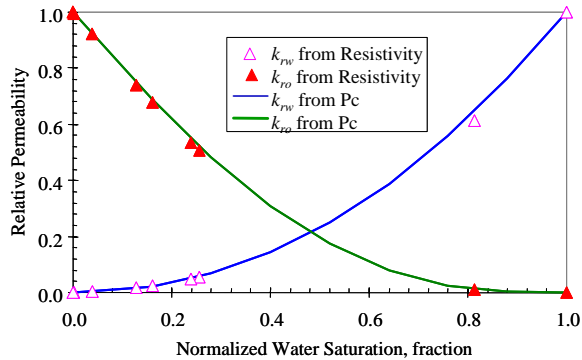


Figure 6. Relative permeability calculated from resistivity and capillary pressure data in Berea sandstone at a temperature of 300°F.

One can see in Fig. 6 that both the oil and water relative permeabilities inferred from the resistivity index data are almost equal to those calculated from the capillary pressure data.

Boise Sandstone

The Boise sandstone core sample had a porosity of 32% and a permeability of 960 md. The values of porosity and permeability are greater than those of Berea sandstone used by Sanyal (1972).

Figs. 7 and 8 show the resistivity index data and capillary pressure vs. water saturation in Boise sandstone at a temperature of 175°F.

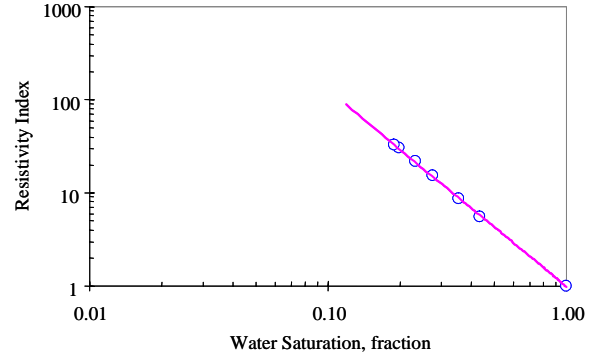


Figure 7. Relationship between resistivity index and water saturation in Boise sandstone at a temperature of 175°F (Sanyal, 1972).

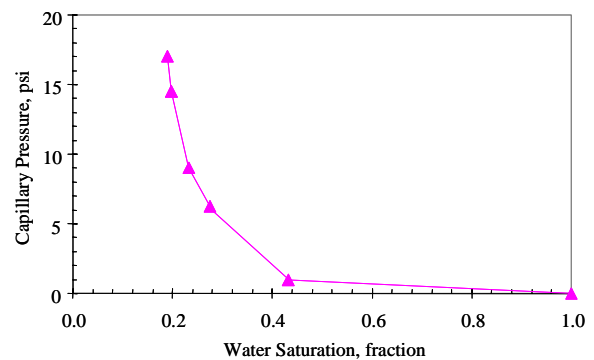


Figure 8. Capillary pressure data measured in Boise sandstone at a temperature of 175°F (Sanyal, 1972).

The relative permeability data calculated from both the resistivity index data shown in Fig. 7 (using Eqs. 6 and 9) and the capillary pressure data in Fig. 8 are plotted in Fig. 9.

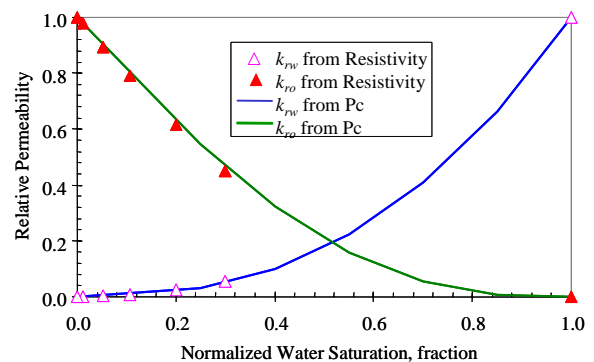


Figure 9. Relative permeability calculated in Boise sandstone at a temperature of 175°F.

Fig. 9 shows that the oil and water relative permeabilities calculated from the resistivity index data are close to those calculated from the capillary pressure data.

The results at a temperature of 300°F are demonstrated in Figs. 10-12. Fig. 10 shows the resistivity data and Fig. 11 shows the capillary pressure data. Fig. 12 plots the relative permeability calculated from the resistivity index shown in Fig. 10 (using Eqs. 6 and 9) and the capillary pressure in Fig. 11 respectively.

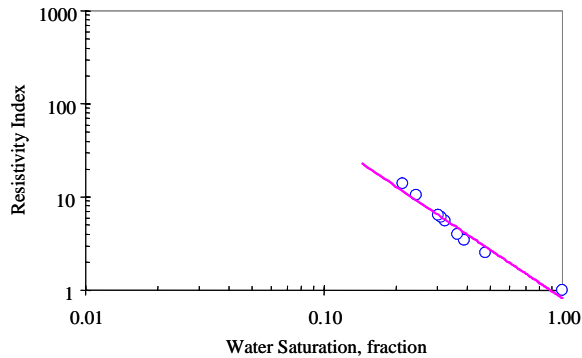


Figure 10. Resistivity index in Boise sandstone at a temperature of 300°F (Sanyal, 1972).

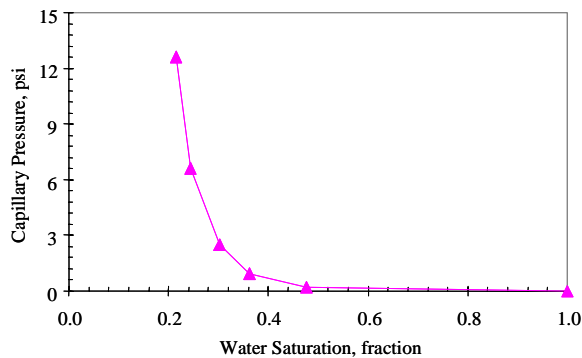


Figure 11. Capillary pressure data measured in Boise sandstone at a temperature of 300°F (Sanyal, 1972).

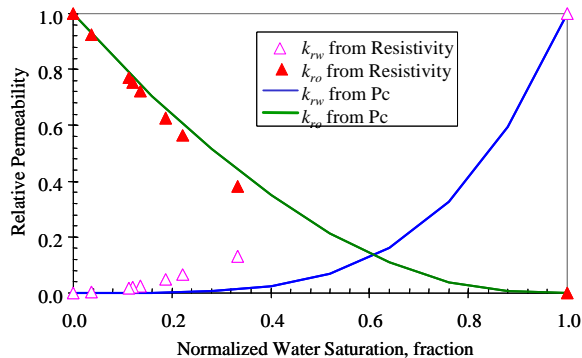


Figure 12. Relative permeability calculated from resistivity and capillary pressure data in Boise sandstone at a temperature of 300°F.

Fig. 12 shows that the oil relative permeability calculated from resistivity index is close to those inferred from capillary pressure. However the water relative permeability calculated from resistivity index data is smaller than those inferred from capillary pressure.

Limestone

The limestone core sample had a porosity of 19% and a permeability of 410 md.

The resistivity index and capillary pressure data at a temperature of 300°F are displayed in Figs. 13 and 14 respectively.

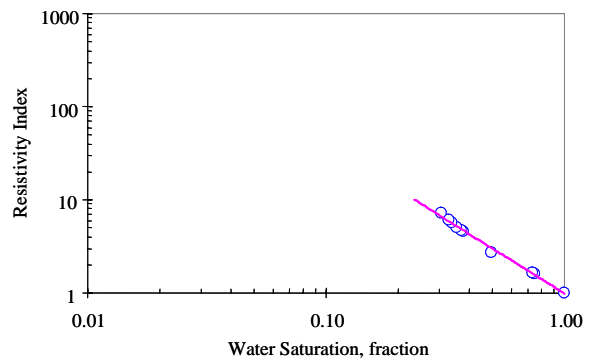


Figure 13. Resistivity index vs. water saturation in limestone at a temperature of 300°F (Sanyal, 1972).

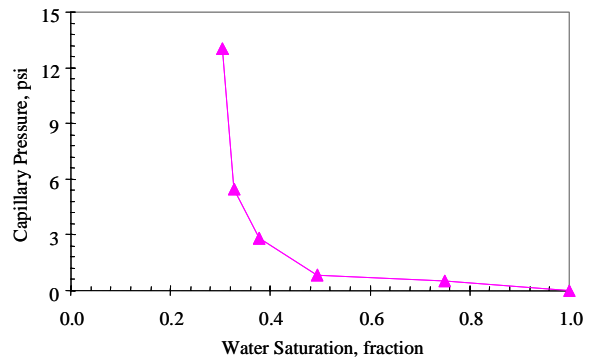


Figure 14. Capillary pressure data measured in limestone at a temperature of 300°F (Sanyal, 1972).

The results of relative permeability calculated from the resistivity index and the capillary pressure data are shown in Fig. 15.

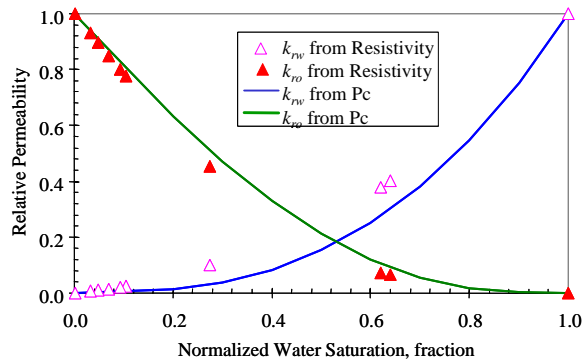


Figure 15. Relative permeability calculated from resistivity and capillary pressure data in limestone at a temperature of 300°F.

One can see in Fig. 15 that the oil relative permeabilities inferred from the resistivity index data are almost equal to those calculated from the capillary pressure data in limestone core sample. The difference between the relative permeability inferred from the resistivity index and those calculated from capillary pressure is acceptable in terms of reservoir engineering applications.

CONCLUSION

Based on the present study, the following conclusions may be drawn in the cases studied:

1. A semianalytical model was developed to infer relative permeability from resistivity index data.
2. The values of the nonwetting phase relative permeability inferred from the resistivity index data are almost equal to those calculated from capillary pressure data.
3. For the wetting-phase relative permeability, the values inferred from the resistivity index are close to those calculated from capillary pressure in most of the cases studied.

ACKNOWLEDGMENTS

This research was conducted with financial support to the Stanford Geothermal Program from the US Department of Energy under grant DE-FG07-02ID14418, the contribution of which is gratefully acknowledged.

REFERENCES

- Archie, G.E.: "The electrical resistivity log as an aid in determining some reservoir characteristics," *AIME Petroleum Tech.* (1942), 1-8.
- Brooks, R.H. and Corey, A.T.: "Hydraulic Properties of Porous Media," Colorado State University, Hydro paper No.5 (1964).
- Li, K. and Horne, R.N.: "Experimental Verification of Methods to Calculate Relative Permeability Using Capillary Pressure Data," SPE 76757, Proceedings of the 2002 SPE Western Region Meeting/AAPG Pacific Section Joint Meeting held in Anchorage, Alaska, May 20-22, 2002.
- Li, K.: "Generalized Capillary Pressure and Relative Permeability Model Inferred from Fractal Characterization of Porous Media," SPE 89874, presented at the 2004 SPE Annual Technical Conference and Exhibition, Houston, Texas, U.S.A., 27 – 29 September 2004.
- Purcell, W.R.: "Capillary Pressures-Their Measurement Using Mercury and the Calculation of Permeability", *Trans. AIME*, (1949), 186, 39.
- Sanyal, S.K.: *The Effect of Temperature on Electrical Resistivity and Capillary Pressure Behavior of Porous Media*, Ph.D. report, Stanford University, Stanford, Calif., 1972.

FIRST ELEVEN YEARS OF EXPLOITATION AT THE MIRAVALLES GEOTHERMAL FIELD

Paul Moya and Antonio Yock

Instituto Costarricense de Electricidad, UEN Proyectos y Servicios Asociados
C. S. Recursos Geotérmicos, Apartado Postal 10032-1000
San José, Costa Rica, Centro América
e-mail: pmoya@ice.go.cr , ayock@ice.go.cr

ABSTRACT

The Miravalles Geothermal Field has been producing electric energy since March 1994. It has provided steam for Unit 1 (55 MWe) since 1994, a Wellhead Unit (5 MWe) installed in 1995, Unit 2 (55 MWe) in 1998, Unit 3 (29 MWe) in 2000 and Unit 5 (19 MWe, a binary plant) in year 2004. The total installed capacity in Miravalles is therefore 163 MWe. The reservoir response during the eleven years of exploitation is described in the following sections. So far the field has successfully supplied the steam needed to maintain constant production over the first eleven years of exploitation. Field management policies as well as injection strategies have been implemented to minimize the pressure decline in the reservoir.

INTRODUCTION

The Miravalles geothermal field, located on the southern slope of the Miravalles volcano, is the most important Costa Rican geothermal development. The present field extends over an area of more than 21km², of which about 16 km² are dedicated to production and 5 km² to injection. The temperature of the water-dominated geothermal reservoir is about 240°C. Fifty-three geothermal wells have been drilled to date (Figure 1). They include observation, production and injection wells, whose depths range from 900 to 3,000 meters. Individual wells produce enough steam to generate between 3 and 12 MWe; injection wells accept between 70 and 450 kg/s of separated water each (Moya, 2003).

Commercial production of electricity from geothermal steam began at Miravalles in early 1994, when Unit 1, a 55 MWe single-flash plant, was commissioned. The following year, the Costa Rican Electricity Institute (ICE) completed the installation of a 5 MWe wellhead unit. Two temporary 5 MWe wellhead plants then came on line as part of an agreement between ICE and the Comisión Federal de Electricidad of Mexico (CFE). In January and

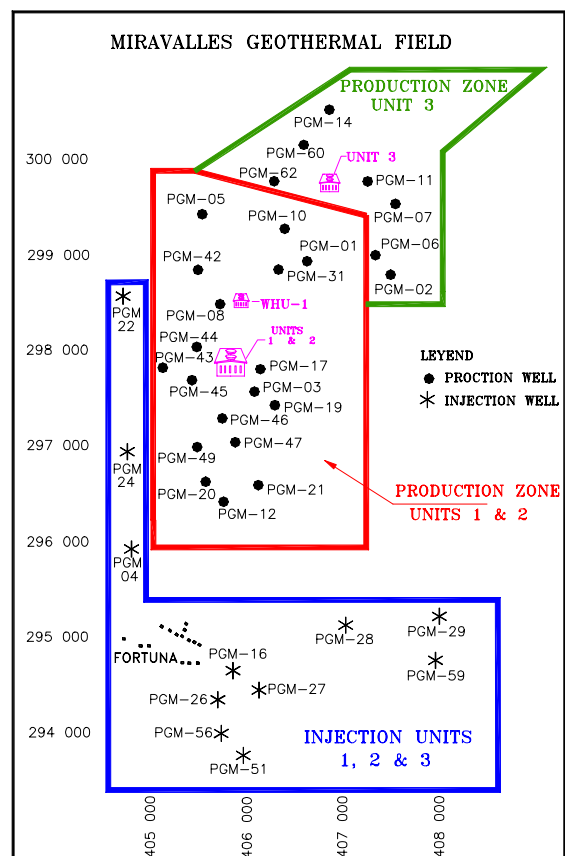


Figure 1. Miravalles Geothermal Field.

August 1998, the two temporary units were disassembled and returned to CFE.

Unit 2, the second 55 MWe plant, began production in August 1998. Finally, in March 2000, Unit 3, a privately owned 29 MWe single-flash plant began delivering electricity to the national grid, increasing the installed capacity at Miravalles to 144 MWe. This capacity was increased to 163 MWe when a bottoming-cycle binary plant came online in January of 2004. Table 1 summarizes the units that have been installed at the Miravalles geothermal field.

Plant Name	Power (MW)	Belongs to	Start-up Date	Final Date
Unit 1	55	ICE	3/1994	
WHU-1	5	ICE	1/1995	
WHU-2	5	CFE	9/1996	4/1999
WHU-3	5	CFE	2/1997	4/1998
Unit 2	55	ICE	8/1998	
Unit 3	29	ICE (BOT)	3/2000	
Unit 5	19	ICE	1/2004	

Federal de Electricidad (México); WHU - Wellhead Unit; and BOT – build-operate-transfer.

The history of the growth of capacity at the field is shown in Figure 2. Concurrent with growth in installed capacity at Miravalles, there was an even more important increase in the amount of electricity generated (Figure 3). Between 1994 and 2004, the installed capacity at the field grew from 55 to 163 MWe (a 196% increase), while generation grew from 341 to 1,144.3 GWh (a 235% increase).

Table 1. Units at the Miravalles Geothermal Field

In Table 1, the abbreviations stand for: ICE - Instituto Costarricense de Electricidad; CFE - Comisión

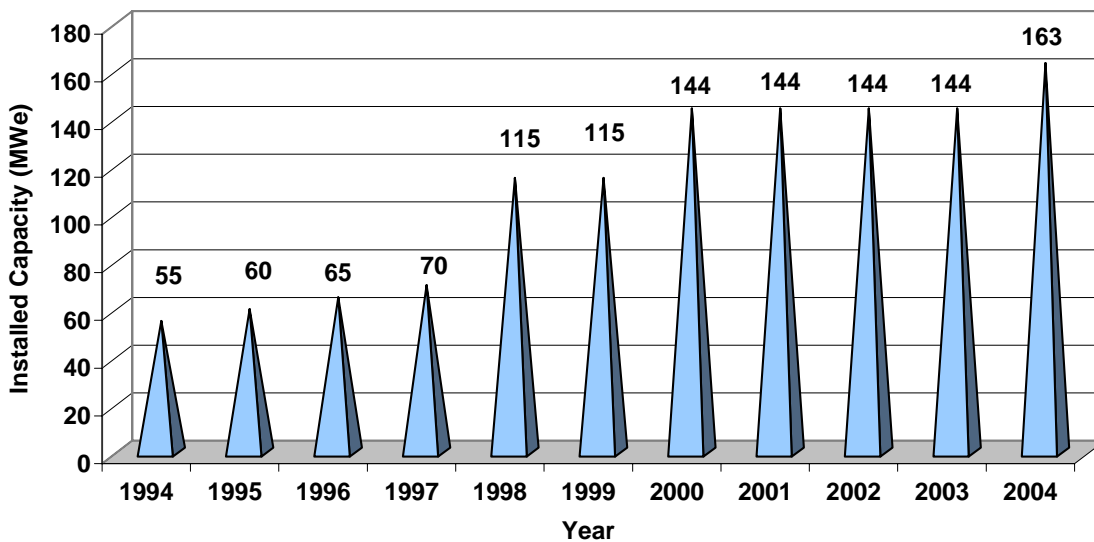


Figure 2. Installed Geothermal Capacity at Miravalles (1994 – 2004)

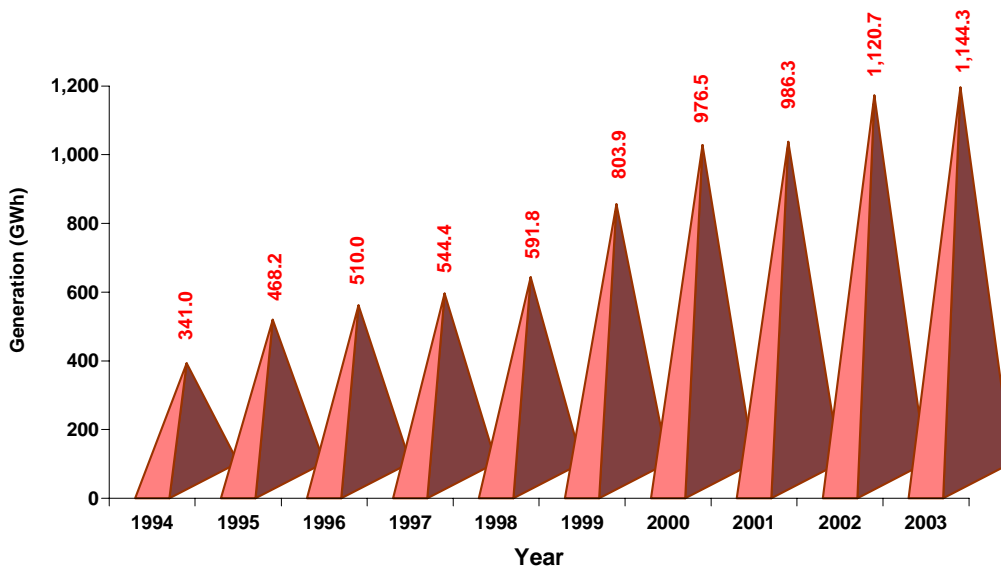


Figure 3. Geothermal Generation at Miravalles (1994 – 2003)

Steam for Units 1-3 and the wellhead unit is separated from the hot water at seven separation stations. Generally, two or three production wells send their two-phase fluids to one of these stations. Separation stations 2, 3 and 4 supply steam mainly to Unit 1; stations 1, 5 and 6 feed Unit 2, and station 7 sends its steam to Unit 3.

The mass produced from the reservoir since 1994 is shown in Figure 4. Incremental production increases accompanied each of the new units coming on line. The residual (separated) geothermal water is sent to the injection wells, which are distributed in four areas of the field: the northern, southern, eastern and southwestern sectors (Figure 5).

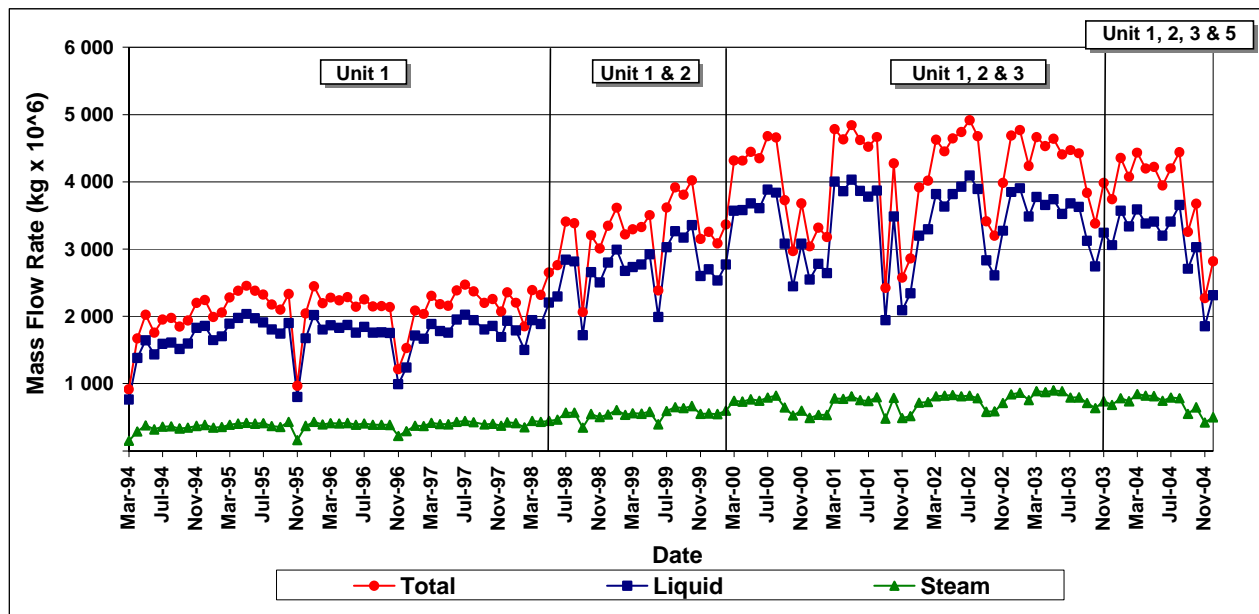


Figure 4. Mass Production at the Miravalles Geothermal Field (March 1994 – December 2004)

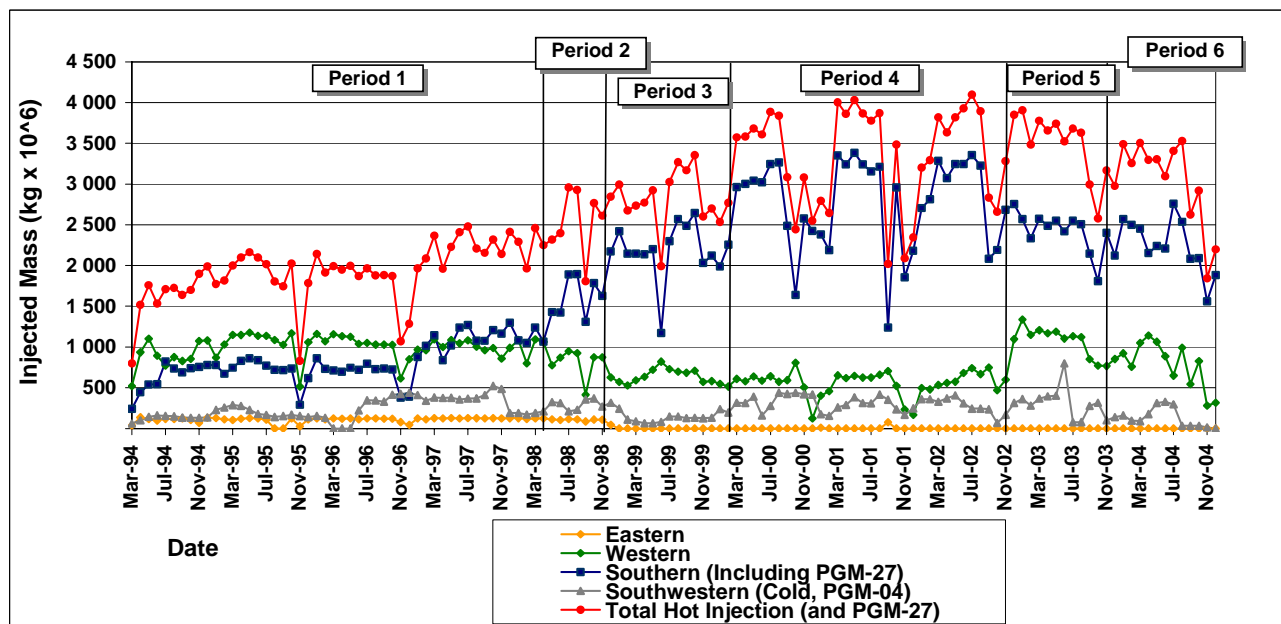


Figure 5. Injection at the Miravalles Geothermal Field (March 1994 – December 2004)

CHEMICAL AND THERMODYNAMIC CHANGES WITH TIME

Several parameters have been monitored at each production well to evaluate the behavior of the reservoir over the first eleven years of its exploitation. These parameters are: enthalpy, temperature, pressure, flow rate, wellhead pressure, and certain chemical species such as chloride, sulfate, bicarbonate, sodium, potassium, calcium,

magnesium, silica and non-condensable gases (Yock, 1998).

The production zone at the Miravalles geothermal field has been divided into six different sectors: northern-1, northern-2, western-central, central, central-southern and southern (Figure 6). Each production sector contains a group of wells and, for each well, the non-condensable gases, enthalpy and chloride concentration parameters have been graphed versus time (figures 7 to 12).

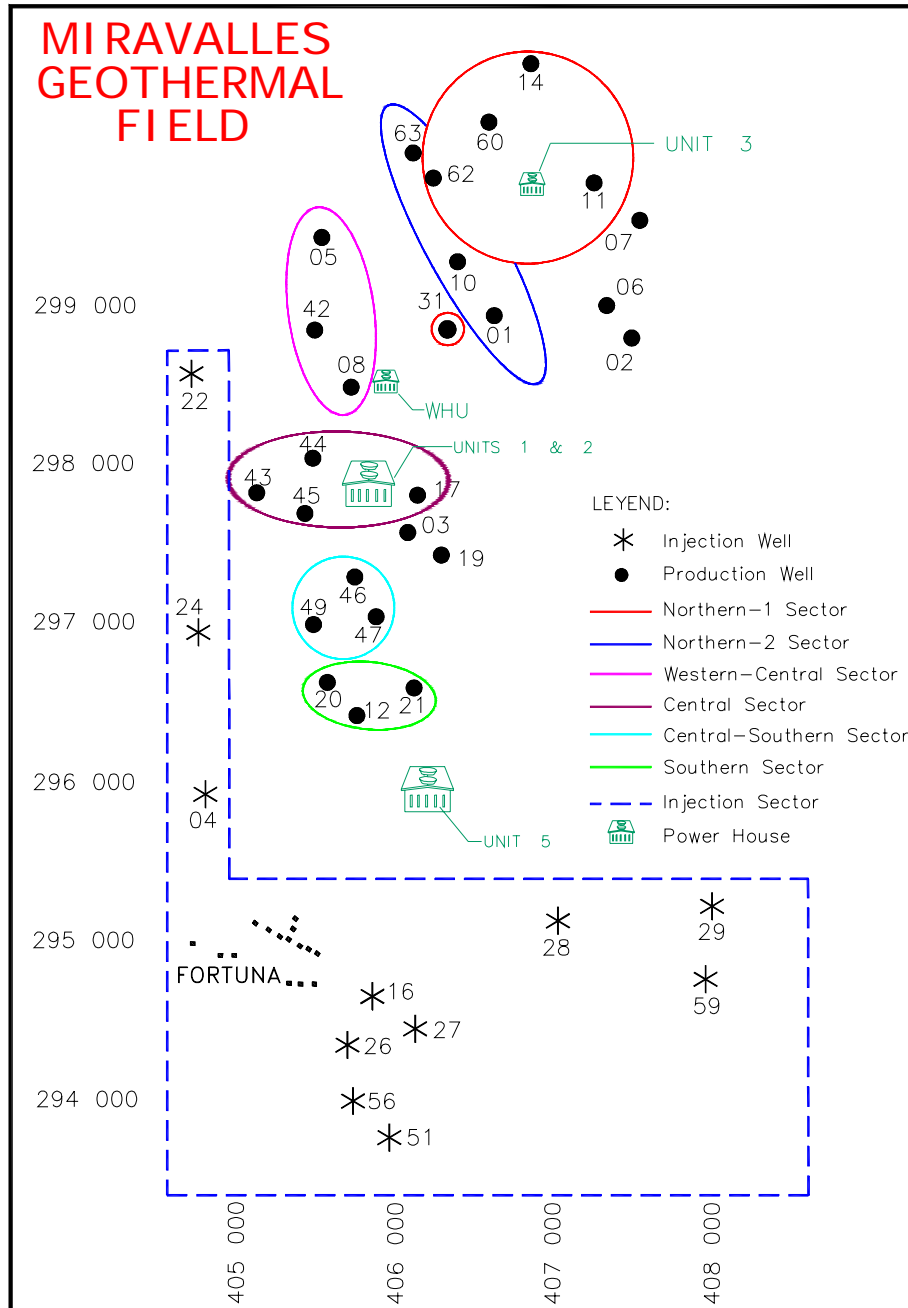


Figure 6. Production Sectors at the Miravalles Geothermal Field

Fluid injection at the Miravalles geothermal field has taken place mainly in two areas: the west and south of the production zone (Figure 6).

The vertical lines in figures 7 to 12 indicate the commissioning of Unit 1 (U-1), Unit 2 (U-2), Unit 3 (U-3) and Unit 5 (U-5). "IC" in these figures stands for "injection change".

Early in the year 2003, the injection rate in the western zone was increased by diverting some of the fluids that initially were sent to the southern zone.

Northern-1 Sector

The wells that belong to this sector are PGM-11, PGM-14, PGM-60, PGM-62 and PGM-31. Wells PGM-11 and PGM-31 began their production in 1994 with the commissioning of Unit 1. Wells PGM-14, PGM-60 and PGM-62 began producing when Unit 3 came online. The chloride concentration in all of these wells has been almost constant (around 4,100 ppm), with the exception of PGM-31, where the chlorides increased slightly until the year 2000 (Figure 7). After the commissioning of Unit 3, the chloride content in PGM-31 began to decrease slightly, reaching values close to 4,100 ppm. The enthalpy values for these wells are close to 1050 kJ/kg, and their non-condensable gases increased after the commissioning of Unit 3 in the year 2000.

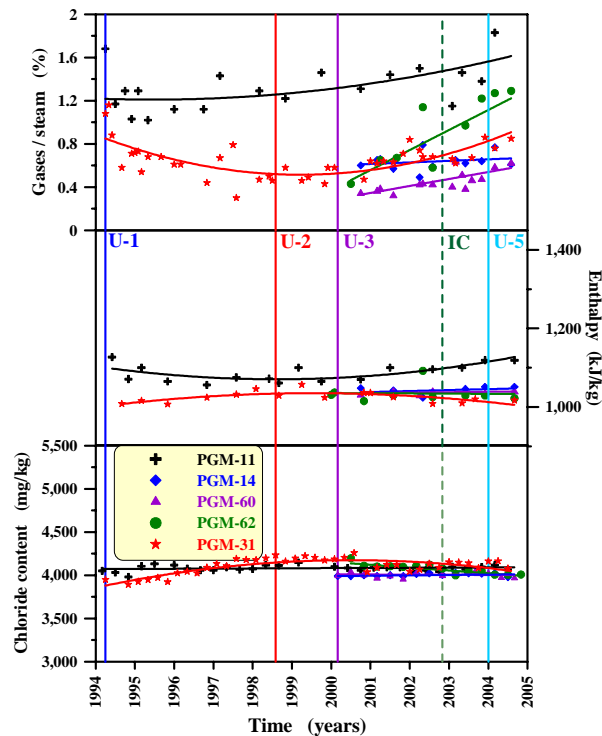


Figure 7. Monitoring results, Northern-1 Sector wells

Northern-2 Sector

The wells associated with this sector are PGM-01, PGM-10 and PGM-63. At present, all of these wells are non-productive. Wells PGM-01 and PGM-10 were in production from March 1994 to February 2003. Well PGM-63 produced from July 2002 to August 2003 (Figure 8).

For wells PGM-01 and PGM-10, the chloride concentration increased until Unit 2 came online in August 1998; thereafter, it decreased to values between 3,750 to 4,000 ppm. The enthalpy at PGM-01 remained constant until the end of 2002, but then it increased rapidly from 1,000 kJ/kg (end of 2002) to 1,200 kJ/kg (end of 2003). The enthalpy at PGM-10 has increased steadily since the middle of 1997. The non-condensable gas concentration began to increase in both wells (PGM-01 and PGM-10) after the commissioning of Unit 2.

At PGM-63 the chloride content decreased while the well was producing, but both the enthalpy and the non-condensable gases increased during the same period.

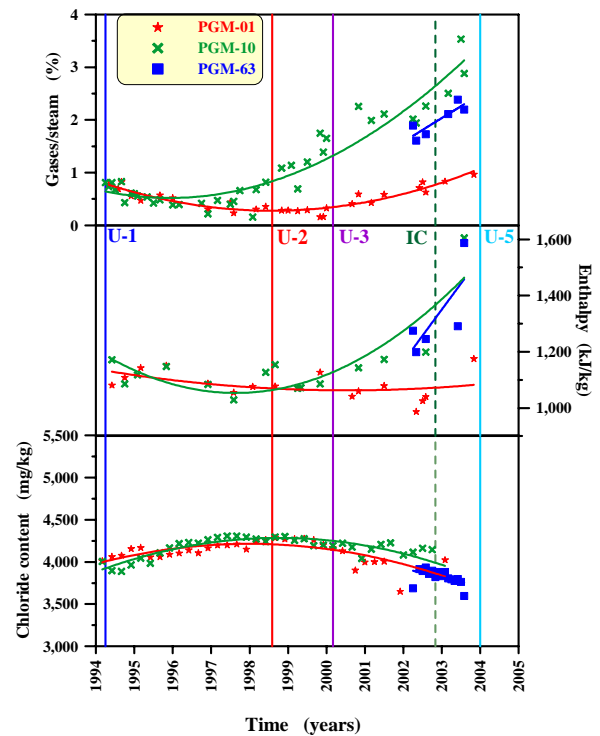


Figure 8. Monitoring results, Northern-2 Sector wells

Western-Central Sector

The wells that are part of this sector are PGM-05, PGM-08 and PGM-42. PGM-05 started producing in 1994, when Unit 1 came online. Wells PGM-08 and PGM-42 began production in 1998, when Unit 2

came online. The chloride concentration at PGM-05 increased from 1994 to the middle of 1998, then remained almost constant until the end of 2004. Since the commissioning of Unit 2, all the wells in this sector have maintained a constant chloride content of about 4,250 ppm (Figure 9). Enthalpy decreased at wells PGM-05 and PGM-42 during their production period, and remained constant at well PGM-08. Non-condensable gases have decreased in well PGM-05 ever since 1994, and stayed constant in wells PGM-08 and PGM-42 from the start of their production until the middle of 2001. After mid-2001, the non-condensable gases in all three wells have shown a slight tendency to increase.

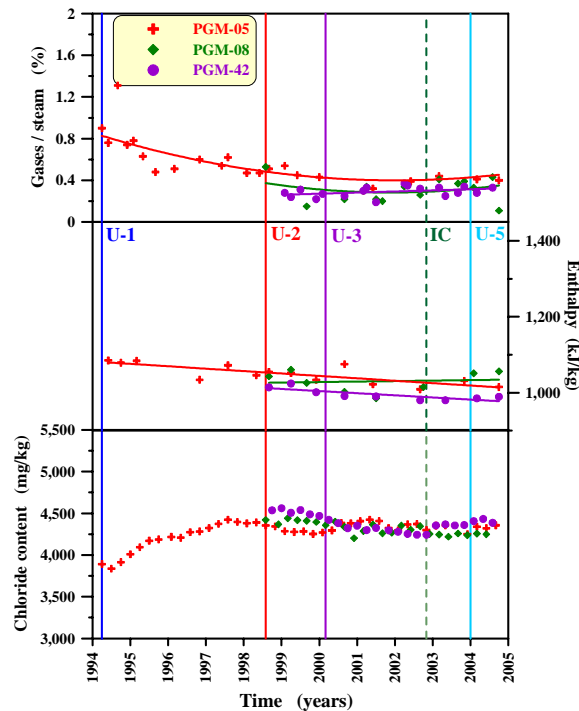


Figure 9. Monitoring results, Western-Central Sector wells

Central Sector

The wells that belong to this sector are PGM-17, PGM-43, PGM-44 and PGM-45. These wells are close to injection wells PGM-22 and PGM-24. PGM-17 started its production in 1994, PGM-45 in 1996, PGM-43 in 1998 and PGM-44 at the end of 1999. Even though all these wells were in operation in different years, all of them have experienced an increase in chloride content since their production began. The enthalpy slightly decreased or remained constant (at around 1,000 kJ/kg) in all the wells, with the exception of PGM-45, which has presented an anomalously high enthalpy from the middle of 2001 to the present (Figure 10). The non-condensable gases have remained constant in PGM-44, decreased in PGM-43, and increased PGM-45. In PGM-17 the

non-condensable gases have fluctuated and have tended to decrease since early 2003 (when injection into wells PGM-22 and PGM-24 was increased).

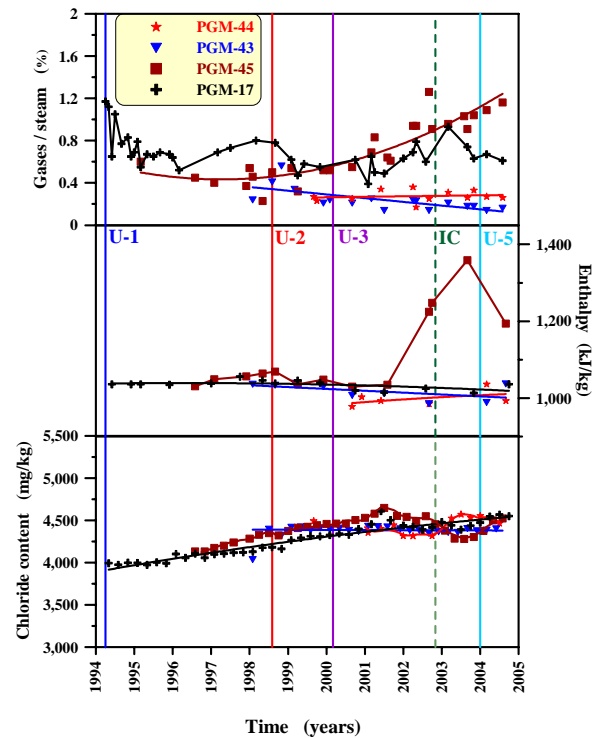


Figure 10. Monitoring results, Central Sector wells

Central-Southern Sector

The wells associated with this sector are PGM-46, PGM-47 and PGM-49. All of these wells are close to injection well PGM-24. PGM-46 started its production in 1994 and was deepened at the end of the year 2001. Wells PGM-47 and PGM-49 began their production in the middle of 1998 when Unit 2 came online.

The chloride content in all these wells has tended to increase, indicating that injected geothermal fluid is arriving in this sector. There was a decrease in the chloride concentration at PGM-49 by the middle of 2003, right after the rate of fluid injection in the western part of the production zone (PGM-22 and PGM-24) was increased. The chloride concentration at PGM-46 has remained constant since the well was deepened, and has also stayed constant at PGM-47 (Figure 11). The enthalpy at PGM-46 increased from 1994 to 2001, but after the well was deepened the enthalpy became constant. A similar behavior (constant enthalpy, around 1,000 kJ/kg) was seen at wells PGM-47 and PGM-49. The non-condensable gases in PGM-46 decreased until the year 2000, then increased until the well was deepened during 2001, and have kept increasing until the present. In contrast, in PGM-47 the non-condensable gases have shown a tendency to decrease slightly, while in

PGM-49 they have stayed constant (close to 0.4% w/w).

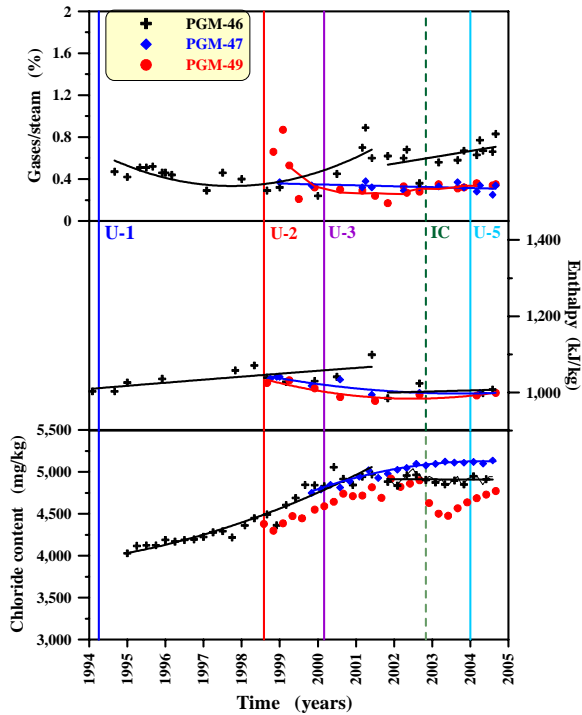


Figure 11. Monitoring results, Central-Southern Sector wells

Southern Sector

The wells that are part of this sector are PGM-12, PGM-20 and PGM-21. All of these wells began their production in 1994, when Unit 1 came online. The chloride concentration in all of the wells has increased since 1994 (Figure 12).

The enthalpy in PGM-20 and PGM-21 has been constant from 1994 to the present, but in well PGM-12 it has decreased slightly, to less than 1,000 kJ/kg. The non-condensable gases in wells PGM-20 and PGM-21 have decreased slightly, but in PGM-12 they decreased from 1994 to 2001, then have increased until the present.

DATA ANALYSIS

Analyzing the northern part of the production zone (northern-1 and northern-2 sectors, figures 7 and 8), it can be observed that the majority of the wells (producing since 1994) were receiving a small fraction of the injected fluids until Unit 2 came online (middle of 1998). After that, the chloride content at the wells started to decrease and their non-condensable gases began to increase.

Wells PGM-01, PGM-10 and PGM-63 became non-productive, probably because fluid withdrawal rapidly lowered the flashing depth in these wells due to low permeability in this part of the reservoir. Lowering the flashing depth causes calcium

carbonate deposition to take place, initially inside the production casing and then in formation fractures, reducing the permeability that allows the wells to produce.

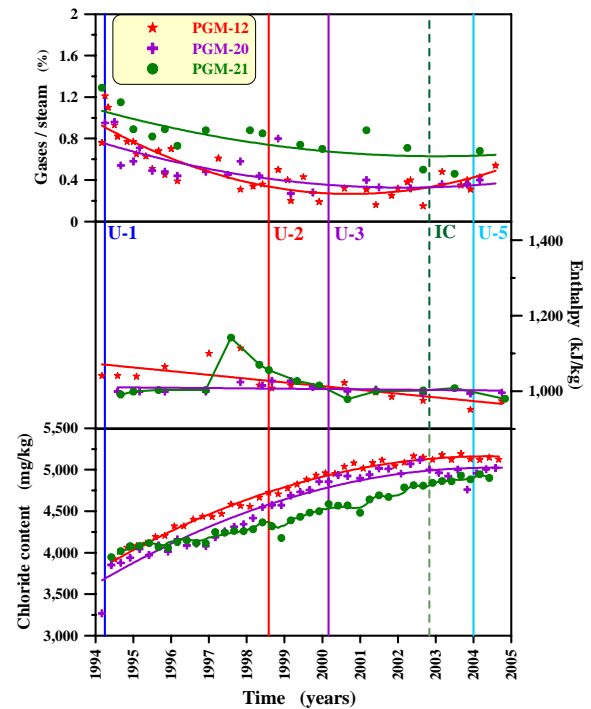


Figure 12. Monitoring results, Southern Sector wells

While calcium carbonate deposition is taking place, CO_2 moves from the liquid to the steam phase, following the reaction indicated by Equation 1:



When lowering the flashing depth, this reaction causes the precipitation of calcium carbonate and some shallow productive fractures may be affected.

In the central part of the production zone (Western-Central and Central Sectors) it can be observed that the chloride concentration has increased or stayed constant in all the wells (Figures 9 and 10). The enthalpies in all the wells have decreased slightly, to values close to 1,000 kJ/kg, with the exception of well PGM-45, which presents a high-enthalpy anomaly due to a shallow steam zone. This steam zone was initially observed also in nearby well PGM-46, but it disappeared as the well produced. It was necessary to deepen well PGM-46 to recover its productivity.

The non-condensable gases have decreased in the majority of the wells that belong to the central sectors. In PGM-17 the non-condensable gases fluctuated from 1994 to 2003, but began decreasing right after the western fluid injection was increased, and have continued to do so until the present. Of all the wells that are part of the Western-Central and

Central Sectors, the only one that has shown an increase (since 1997) in non-condensable gases is PGM-45.

In the Central-Southern and Southern Sectors of the field, the chloride concentration has increased in all the wells since they began production (Figures 11 and 12). In all of these wells it is noticed that, due to the increase in the western fluid injection (with a corresponding decrease in the southern injection), less injected fluid is reaching these wells, causing the chloride content to stop increasing and be fairly constant. The enthalpies in the wells of these two sectors have decreased or stayed constant at values around 1,000 kJ/kg.

The non-condensable gases decreased in the majority of these wells, except for PGM-12 and PGM-46. The non-condensable gases have been increasing in PGM-12 since the middle of 2001, and in PGM-46 since late 1997. The deepening of PGM-46 caused the rate of increase to lessen, but it has continued nonetheless.

FINAL REMARKS

On March 25, 2005, the Miravalles geothermal field will complete 11 years of continuous exploitation. During all these years, the field has been able to supply the steam and the separated brine required by the generating units, even though the installed capacity and the generation have increased ever since 1994.

At present, wells PGM-01, PGM-10 and PGM-63 are non-productive. It is probable that the natural low permeability in that part of the reservoir, combined with some calcium carbonate deposition in the reservoir fractures, has caused these wells to stop producing.

In the near future, injection into PGM-63 will be performed in order to evaluate the possibility of recovering the production within the northern sector of the field.

Chloride concentrations increased in wells PGM-01, PGM-10 and PGM-31 until Unit 2 came online, then decreased and remained constant. On the other hand, the chloride content has shown a tendency to increase in the central and southern part of the field. The northern sector of the reservoir benefits the least from return of injected fluids. The increase in the western fluid injection has had an impact mainly on the central and southern parts of the production zone. At present, no cool front has been detected, and therefore effect of the arrival of the injected fluids at some wells has been positive so far.

Enthalpies have tended to decrease slightly in the northern, central and southern parts of the field ever since production began.

The non-condensable gases have increased in the northern sectors and in some wells of the central part of the production zone. In the southern part of the

field, the non-condensable gases have been decreasing.

Since the northern sector of the reservoir has experienced the strongest productivity declines, the wellhead unit should be relocated to well PGM-29. By doing so, the steam requirements will decrease in the northern and central sectors of the production zone.

The generating units should be kept at their nominal capacities. Extra generation from these units will tend to over-exploit the reservoir, and might not be sustainable over the long term.

The current detailed program of monitoring the main reservoir parameters should be continued in order to detect any future negative impacts.

ACKNOWLEDGEMENTS

The authors thank Roger Henneberger (GeothermEx, Inc.) for editing and improving the manuscript.

REFERENCES

Moya, P., (2003), "The Costa Rican Geothermal Energy Development," *The IERE Central America Forum Transnational Electrical Interconnections and Sustainability in Central America*, Session 2, November 24-25, 2003. San José, Costa Rica.

Yock, A., (1998), "Chemical and Isotopic Studies in the Miravalles Geothermal Field, Costa Rica," *The United Nations University, Geothermal Training in Iceland, 1998*, Reports 1998, Number 17, pages 461-499.

TRACER TEST ANALYSIS FOR CHARACTERIZATION OF LAUGALAND GEOTHERMAL FIELD

Gopi Nalla¹, G. Michael Shook¹, Gudni Axelsson²

¹Idaho National Engineering and Environmental Laboratory
Idaho Falls, ID 83415-2107

²ÍSOR, Iceland GeoSurvey, Grensasvegur 9, IS-108
Reykjavik, Iceland
e-mail: nallg@inel.gov

ABSTRACT

This paper presents the tracer data analysis obtained from the single-phase, conservative tracer experiments conducted during a two-year reinjection project at Laugaland geothermal field in N. Iceland. Three tracer tests were conducted during the two-year period (1997-1999). The tracers injected were sodium fluorescein in Test 1 and Test 3 and potassium iodide in Test 2. We concentrated on Test 1 only, the reasons for which are explained in the paper.

Axelsson et al. (2000; 2001) have conducted a comprehensive analysis of the Laugaland reinjection project tracer test data, including both qualitative and quantitative aspects using multi-flow-channel models. In this study, we focus only on the quantitative analysis of tracer test data using analytical interpretation methods. It has been proved extensively that the first temporal moment analysis leads to an estimation of the tracer swept pore volume in a closed boundary with a balanced injection/production rate scenario. But in this paper, we prove that the first temporal moment does give the swept pore volume, even for open boundaries with an unbalanced rate scenario such as existed at the Laugaland geothermal field. The produced tracer concentration history was used to estimate the interwell reservoir relative flow capacity versus storage capacity (F-C plot). The F-C plot is a simple and powerful semi-quantitative tool to evaluate the conceptual model's relative flow and storage geometries. The relative flow and storage capacities calculated from the flow channel geometry obtained from multi-flow-channel modeling (Axelsson et al. 2001) for one production well LN-12 agreed well with the continuous F-C plot obtained from the tracer return data. The second temporal moment of tracer production history was used to derive an equivalent dispersion coefficient. The reservoir interwell heterogeneity was characterized using the Lorenz coefficient derived from the F-C plot. The Lorenz

coefficient for well pair LJ-08/LN-12 was 0.509, indicating that it is moderately heterogenous.

Reservoir information was obtained for interwell LJ-08/LN-12 and, to some extent, LJ-08/TN-04. The tracer data for other wells could not be analyzed, since the streamlines were not constant, and deconvolution techniques need to be developed to do meaningful interpretation. Recommendations for possible future Laugaland reservoir modeling are offered in order to obtain a better description of the reservoir.

INTRODUCTION

Tracer testing for reservoir description has been applied in the petroleum and geothermal industries and in environmental applications. Tracers are a useful tool for understanding the flow of fluids through reservoirs and contain valuable information about the reservoir properties hidden in its production history. In order to obtain reliable estimates of these reservoir properties, proper quantitative analysis is required. The preliminary information obtained from a tracer contains the flow direction, presence of barriers to the flow, and the relative interwell connectedness. But the tracer data has valuable hidden information about the reservoir properties that can be obtained through quantitative analysis. Several researchers in the petroleum, environmental, and geothermal industries have developed methods to correlate tracer history with reservoir properties. Allison et al. (1991) determined such important reservoir characteristics as layer permeabilities, thicknesses, dispersion, and oil saturation, based on history matching the interwell tracer results using a numerical model. Abbaszadeh-Dehghani et al. (1984) developed techniques to determine reservoir layering and the individual layer's porosity-thickness and permeability-thickness from well-to-well tracer flow.

The goal of tracer tests in geothermal reservoirs is to provide the reservoir operator with tools to better

understand the reservoir and to achieve optimal production/extraction of thermal energy from the geothermal rocks. Robinson et al. (1984) have developed methodologies for analyzing the internal flow characteristics of fractured geothermal reservoir using tracer-determined residence time distribution curves. Shook (1998) has shown that the moment method yields excellent approximations to the volume of a geothermal reservoir drained by the production well or supported by the injection well for closed boundary, single-phase heterogeneous reservoirs. Shook (2003) has also demonstrated that the production tracer history could be used to obtain a flow capacity versus storage capacity plot, which serves as a simple and fast tool to aid in estimating fracture geometry. It indicates relatively what fraction of flow paths occur through what fraction of pore volume.

The Laugaland geothermal field is located in North Iceland. Axelsson et al. (2001) have comprehensively analyzed the tracer data obtained from the two-year reinjection experiment conducted at the Laugaland field. Based on the tracer analysis, their conceptual model produced the theory that the tracer traveled through the area bedrock by two modes: along high permeability and low porosity fractures, and dispersed through the large volume of the reservoir. The tracer recovered was assumed to be flowing through the modeled channels, and the rest of the tracer was dispersed through the large reservoir volume. Axelsson et al. (2001) have conducted cooling predictions that would take place due to long-term reinjection based on their multi-flow-channel model analysis of tracer tests data. Their predictions showed that the reinjection experiment would cause a temperature decline of only 1–3°C in 10 years.

The reinjection experiment included three tracer tests, of which we have reanalyzed the data from the first test only and estimated inter-well reservoir parameters using analytical interpretation methods. No thermal drawdowns were investigated in our analysis. The estimated interwell reservoir parameters could be used in the future for developing the integrated numerical model that is representative of the Laugaland geothermal reservoir.

THE LAUGALAND GEOTHERMAL FIELD AND TRACER TESTS

The well layout for the Laugaland geothermal field is shown schematically in Figure 1; and the well details are schematically depicted in Figure 2. The whole reinjection project was conducted for two years, but Test 1 was identified as about the first two-month period, or 67.0 days.

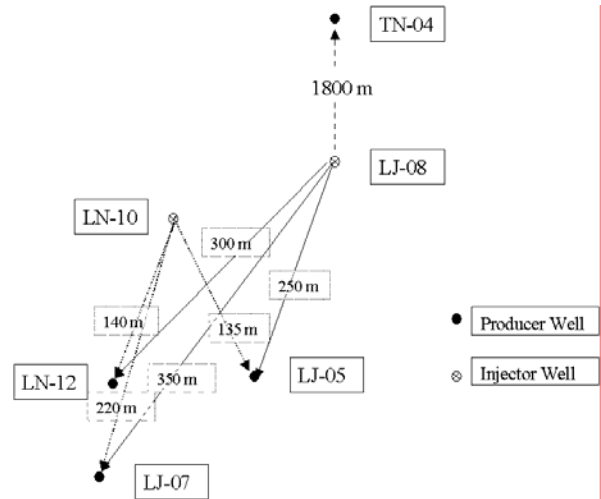


Figure 1. Schematic diagram of well layout in the Laugaland Geothermal System. [Interwell distances were inferred from Axelsson et al. (2001, Figure 2) and known distances].

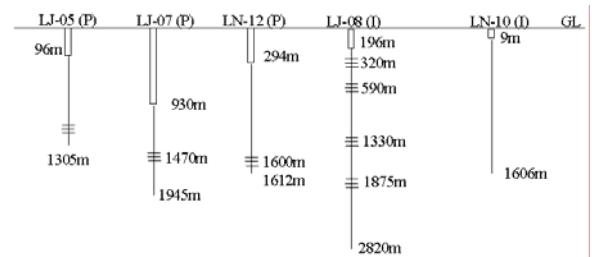


Figure 2. Schematic diagram of well depths, casings, and main feed-zones in the Laugaland geothermal field.

The first tracer test was started on September 25th, 1997 and continued for 67 days. The tracer used was sodium-fluorescein, which was injected into well LJ-08. Steady flow conditions were maintained during the Test 1 period, which would allow the streamlines from the injector to the producer during this period to be unaltered. The effect of temperature change on the mixing of injectate and in situ reservoir fluid may have a small effect on the change of streamlines, but for the purpose of this analysis, the flow conditions were considered as steady and controlled during the two-month period. The flow condition for tracer Test 1 was a constant injection rate maintained at 8.0 l/s in well LJ-08. The only production well on line during these two months was LN-12, at 41.0 l/s. The distance between these two wells, LJ-08 and LN-12, was 300 m.

Although LN-12 was the only production well on-line during the Test 1 period, the other production wells that had seen the injected tracer subsequently were LJ-05, LJ-07, and TN-04. The production data from well LN-12 during the 67 days was considered good because of the controlled and steady production conditions. Production from well LJ-05 was started only after the first 67 days, yet this well had produced the major fraction of the tracer at the end of two years (21%). The short distance from the injection well LJ-08 would imply that the tracer input function is not an impulse function. The interpretation could not be carried out with confidence for wells LJ-05, because the steady state flow regime was altered, implying the flow streamlines are being altered too. The tracer concentration history of well LJ-05 has to be deconvolved in some manner to be able to account for its dormant state within the first few months of nonproduction and subsequent rate variations and shut in periods during the two-year reinjection experiment. At present, the interpretation of tracer data from well LJ-05 has not been done, as information is insufficient about the distribution of tracer in the reservoir just before production of LJ-05.

An insignificant amount of tracer was produced from well LJ-07 (only 1% in two years) because the well was hardly used; hence, that tracer data was not interpreted. Approximately 6% of the injected tracer was produced during the 2-year period from well TN-04, which was 1800 m away from injection well LJ-08. Even in the case of well TN-04, the steady state flow regime was altered, and the injected tracer is no longer an instantaneous tracer concentration impulse function with respect to well TN-04. But the large distance between wells LJ-08 and TN-04 would allow the assumption that the perturbations in the flow conditions near the injector well are diminished in the larger scale. The declining portion of the tracer concentration was not captured in the time span of measurement for well TN-04, and, hence, extrapolation of the tracer tail was not possible. The tracer data from TN-04 was interpreted until the point of termination.

More detailed information about the tracer tests can be obtained from Axelsson et al. (2001).

QUANTITATIVE ANALYSIS

The quantitative analysis performed on the tracer data is described as follows:

1. Flow Capacity – Storage Capacity

Information about relative fraction of flow paths versus swept pore volume (Shook, 2003)

$$f_i = \frac{k_i A_i / L_i}{\sum_{j=1}^{\#frac} k_j A_j / L_j} \quad (1)$$

$$c_i = \frac{V_{pi}}{\sum_{j=1}^{\#frac} V_{pj}}$$

$$F_i = F_{i-1} + f_i \quad \text{for } i = 1, \#frac \quad (2)$$

$$C_i = C_{i-1} + c_i$$

$$C(t) = \frac{\int_0^t c_{out} d\tau}{\int_0^{\infty} c_{out} dt} \quad (3)$$

$$F(t) = \frac{\int_0^t c_{out} d\tau}{\int_0^{\infty} c_{out} dt}$$

$$\text{Lorenz Coefficient, } L_C = 2 \left\{ \int_0^1 F dC - \frac{1}{2} \right\} \quad (4)$$

$$2. \text{ Zero}^{\text{th}} \text{ Temporal Moment} = \int_0^{\infty} C_{out} \cdot dt \quad (5)$$

$$\text{Mass of tracer recovered} = q_{ext} \cdot \int_0^{\infty} C_{out} \cdot dt \quad (6)$$

$$3. \text{ First Temporal Moment, } \bar{t} = \frac{\int_0^{\infty} t \cdot C_{out} \cdot dt}{\int_0^{\infty} C_{out} \cdot dt} \quad (7)$$

$$\text{Mean Swept Pore Volume, } V_P = q_{inj} \cdot \bar{t} \cdot \left(\frac{m_{rec}}{M_{inj}} \right) \quad (8)$$

$$4. \text{ Second Temporal Moment, } \bar{t}_2 = \frac{\int_0^{\infty} t^2 \cdot C_{out} \cdot dt}{\int_0^{\infty} C_{out} \cdot dt} \quad (9)$$

$$\text{Variance, } \sigma^2 = \left(\frac{\int_0^{\infty} t^2 \cdot C_{out} \cdot dt}{\int_0^{\infty} C_{out} \cdot dt} \right) - (\bar{t})^2 \quad (10)$$

Equivalent Dispersion Coefficient,

$$D_L = \bar{U} x \left(\frac{\sigma_{out}^2 - \sigma_{in}^2}{\bar{t}^2} \right) \quad (11)$$

$$\text{Dispersion, } \alpha = \frac{D_L}{U} \quad (12)$$

A more detailed description of the flow capacity versus storage capacity can be obtained from Shook (2003). A brief description is given here. The flow capacity of any given fracture is proportional to the volume of fluid it carries and the fracture length itself. The incremental flow capacity of the i^{th} fracture is the ratio of that fracture's flow capacity to the total network's flow capacity. The fractional storage of the i^{th} fracture is pore volume of that fracture divided by the total fracture pore volume. The flow capacity, F, and storage capacity, C, are simple summations of the individual fracture f_i and c_i .

The equivalent dispersion coefficient (Neretnieks, 1983) was calculated from the second temporal moment. This is equivalent to the case when the tracer spreading has taken place in a one-dimensional infinitely long homogenous system between the injection and extraction points. The equivalent dispersion coefficient serves as a means of quantifying the tracer spreading.

Testing the Validity of First Temporal Moment for Unbalanced Rates, Open Boundary Porous Media

The hypothesis to be tested is that the first temporal moment of a producer tracer concentration history leads to the determination of inter-well swept pore volume in the case of unbalanced rates and an open boundary reservoir. A simple synthetic model was set up to test the validity of first temporal moment analysis for these conditions. In order to compare the tracer-deduced swept volume, the swept volume is also determined geometrically from the tracer concentration (binary data) contour and streamline velocity vector contours. The analysis of the binary tracer concentration data and streamline velocity vector contour are subject to interpretation error and therefore considered to give only approximate estimates. The schematic diagram of the 2D synthetic model with the well placement, rates, and boundary conditions is shown in Figure 3. The streamline velocity vector contour for this synthetic model is

shown in Figure 4. The results of comparison of the swept pore volume calculated from tracer concentration contour (282.0 m³) with the temporal moment method (280.1 m³) shows a difference of 0.7%, while the swept pore volume calculated from streamline velocity vector contour (245.6 m³) with the temporal moment method shows a difference of 14.0%. Hence, it is proved for the simple case that the first temporal moment gives the swept pore volume, even for unbalanced rates and open boundary system. Various other geometries, boundary conditions and flow rates were studied as well. All results confirmed that swept volume could be determined for tracer tests using Equation 8.

ANALYSIS OF LJ-08/LN-12 TEST1 TRACER DATA

We analyzed and interpreted the tracer data from well LN-12 in Test 1. The measured tracer concentration history for the first 67.0 days is shown in Figure 5. The assumptions of steady-state flow and pulse injection hold good during the first couple of months. The validity of applying the temporal moment analysis to an open boundary, unbalanced injection/production rate scenario was proved before proceeding to interpret the LJ-08/LN-12 tracer data. At 67.0 days, numerical integration shows the swept pore volume was 850.0 m³ and the tracer recovery was 4.7 %.

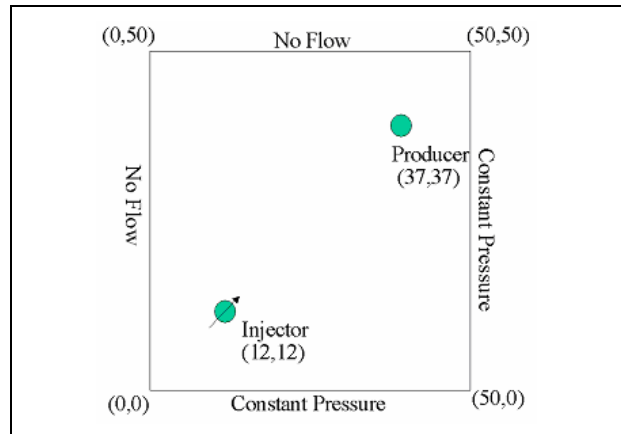


Figure 3. 2D synthetic model schematic diagram showing well locations and boundary conditions.

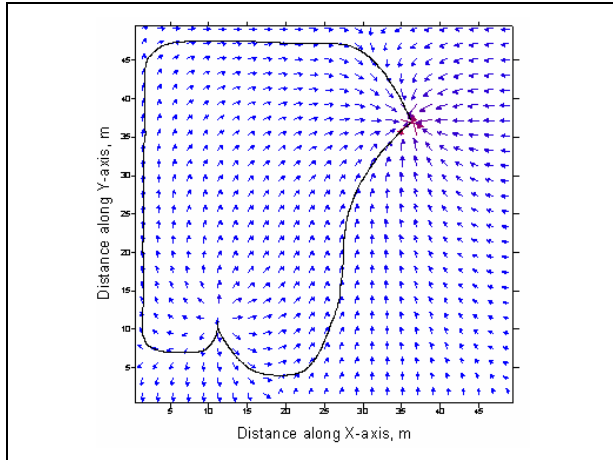


Figure 4. Streamline velocity vector contour from the synthetic model.

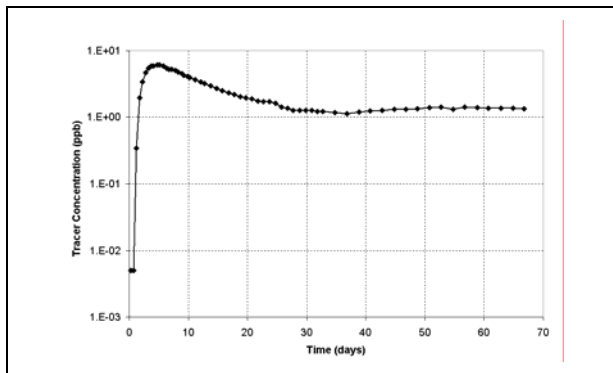


Figure 5. Tracer concentration history produced from well LN-12 during Test 1.

excellent agreement with the measured tracer concentration history. Based on the channel flow geometry, the discrete flow capacity and storage capacity values of the fractures were calculated, as shown in Table 1. The discrete fractional flow and storage capacity points were plotted on the continuous tracer-derived F-C curve. We were encouraged to see these discrete points fall closely on the F-C plot (shown in Figure 9), constructed from the production tracer history of well LN-12. The heterogeneity of the inter-well reservoir was characterized using the Lorenz coefficient. The Lorenz coefficient (Lake 1989) is one of the commonly used measures of reservoir heterogeneity and is defined as the area between the F-C curve and a 45° line (homogenous F-C curve) and normalized by 0.5, as given in equation (4). The extremes of the Lorenz coefficient

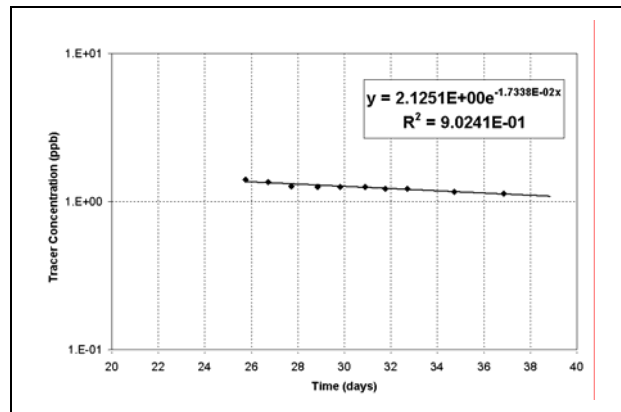


Figure 6: Tracer concentration data matched with an exponential curve.

The tracer concentration data from 26.0 to 37.0 days were matched with an exponential curve, as shown in Figure 6, to obtain the parameters describing the curve fit. Using the last available concentration measured at 67.0 days, the tail was extrapolated as shown in Figure 7.

At 23 months, the analysis based on the extrapolated tracer tail curve shows a total swept pore volume of 3181.6 m³. At infinite time, the swept pore volume did not change significantly and was 3181.9 m³, and the mean injectate residence time was 62.0 days. The cumulative tracer recovery history from the zeroth temporal moment is given in Figure 8. At the end of 23 months, the cumulative tracer recovered was 7.3%, whereas the analysis done by Axelsson et al. (2001) estimated 8.0 % recovery. The variance of the tracer concentration history was calculated to be 3801.0 day², the equivalent dispersion coefficient 1438.0 m²/day, and the equivalent dispersivity 297.0 m.

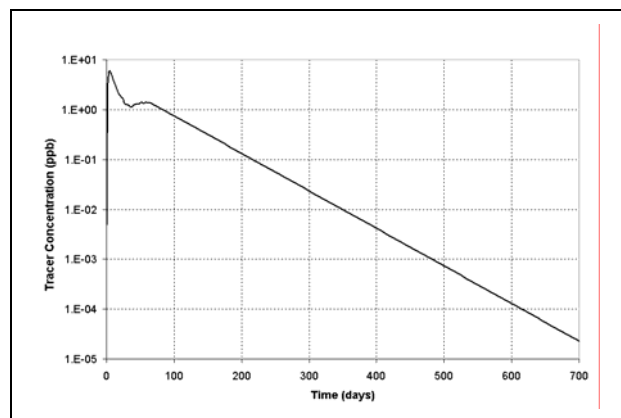


Figure 7: Extrapolated LN-12-produced tracer concentration history curve.

Axelsson et al. (2001) developed a three-channel flow model connecting wells LJ-08 to well LN-12 whose simulated tracer production history was in

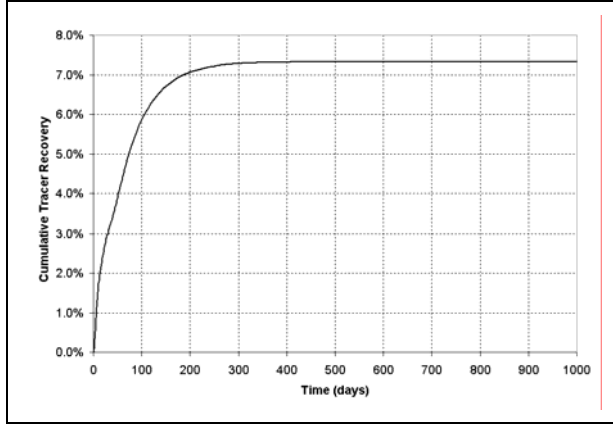


Figure 8: The cumulative tracer recovery calculated from the zeroth temporal moment.

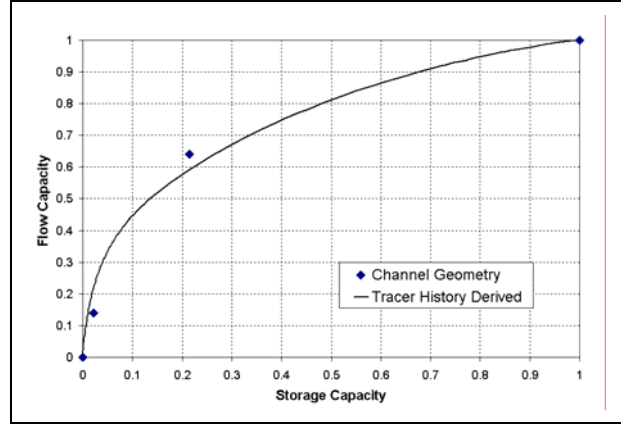


Figure 9: The flow capacity versus storage capacity derived from the tracer concentration history of well LN-12 (tracer Test 1) and the F-C discrete values obtained from Axelsson et al. (2001) channel geometry data.

Fracture #	Length (m)	Porosity	u (m/s)	A (m ²)	C _i = Frac V _p	F _i = u*A	R	C	F
								0	0
1	300	0.07	7.30E-04	1.40	29.4	1.02E-03	3.48E-05	0.021391	1.40E-01
2	500	0.07	4.80E-04	7.57	265	3.63E-03	1.37E-05	0.214203	6.40E-01
3	1000	0.07	1.70E-04	15.43	1080	2.62E-03	2.43E-06	1	1.00E+00

Table 1: F-C parameters calculated from the channel geometry data (Axelsson et al. (2001)).

are 0.0 for perfectly homogenous media and 1 for infinitely heterogenous media. The Lorenz coefficient for well pair LJ-08/LN-12 was 0.509, indicating a moderately heterogenous media.

The F-C plot can serve as a useful tool to obtain a semi-quantitative description of the fracture geometry. From the continuous F-C plot generated from the tracer history, discrete F-C points can be selected on the basis of which conceptualized fracture flow geometry could be constructed. By conducting this preliminary conceptual model development using the F-C plot, the numerical modeling is constrained further and the total number of numerical experiments could be reduced to minimal.

ANALYSIS OF LJ-08/TN-04 TEST 1 TRACER DATA

Well TN-04 is at a distance of 1.8 km from the injection well and, therefore, the perturbations in the flow field near the injector well are considered to be negligible. The tracer concentration history from well TN-04 is given in Figure 10. The tracer history in TN-04 had not begun declining, and hence could not be extrapolated to infinity.

The temporal analysis on the available data gave the following results. At the end of 23 months, the calculated mean residence time was 521.0 days, mean flow velocity 4.0×10^{-5} m/s, tracer recovery 5.6 %,

injectate/tracer swept pore volume $20,475 \text{ m}^3$, and equivalent dispersivity 109.6 m. Axelsson et al. (2001) developed a single flow-channel model connecting wells LJ-08 to well TN-04 whose simulated tracer production history was in excellent agreement with the measured tracer concentration history until the point of termination. The single flow-channel model analysis gave the results of mean flow velocity 3.5×10^{-5} m/s, flow-channel cross-sectional area 360 m² (assuming a porosity of 7%), dispersivity 97 m, tracer recovery 6.0% at 23 months and 7.2% at infinite time. In the single flow-channel model, the mean tracer residence time calculated from the interwell distance and mean flow velocity was 595.2 days and the flow-channel pore volume was $45,360 \text{ m}^3$. Axelsson et al. (2001) results agree reasonably well with our analysis results other than the tracer swept pore volume as compared to the single flow-channel pore volume. The reason for this difference could be explained due to the different approaches and the different time scales used. Our analysis was based on an analytical method (Equation 8) while Axelsson et al. (2001) adopted a channel-flow model approach that could be non-unique. Also, we used the tracer data only until the point of termination at which point the tracer concentration had not even begun declining, where as the channel model would simulate the produced tracer concentration history beyond the point of termination until infinite time. Because our analysis truncates the tracer history prematurely, our pore volume estimate

is low. The extent it is low cannot be inferred from the analysis. The extent to which Axelsson et al. (2001) obtain a good match of the tracer data suggests their model captures the character of the LJ-08 - TN-04 flow zone.

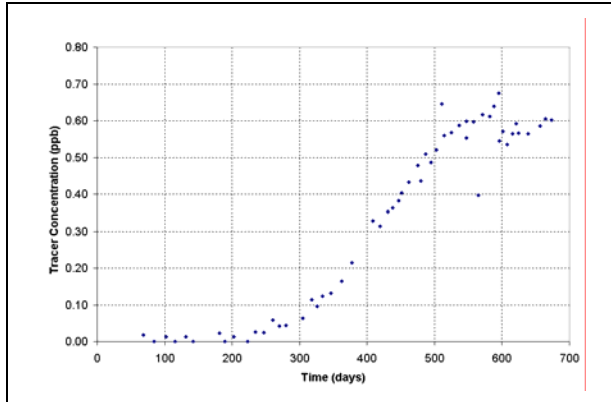


Figure 10: Tracer concentration history from well TN-04

SUMMARY AND CONCLUSIONS

The first tracer test period extended from September 25 to November 30, 1997 (about a 2-month period). Controlled and stable conditions were maintained in the reservoir. Analysis of the tracer concentration history using the temporal moments was conducted and useful reservoir information was obtained, which included the inter-well mean residence time, swept pore volumes, equivalent dispersion coefficients, flow-storage capacity plot, and Lorenz coefficient.

The flow-storage capacity plot obtained from tracer data for well LN-12 agreed well with the discrete F-C points calculated from the channel geometry estimated by Axelsson et al. (2001). The F-C data can be used to constrain a numerical model.

Well LJ-05 did not have steady flow conditions in the reservoir, as was maintained for LN-12, because of the unsteady production flow rates beyond the first two months. After two months, the flow streamlines would have changed, since the other wells started producing too. Hence, the tracer data were not interpreted using the moment analysis method.

No tracer concentration history data were available for well LJ-07.

Tracer breakthrough in well TN-04 occurred about May 1998. The declining portion of the tracer concentration history for well TN-04 was not measured, and, hence, the tail could not be extrapolated. The tracer data from TN-04 was interpreted until the point of termination. The mean residence time, mean flow velocity, and equivalent dispersivity estimates

obtained from the temporal analysis agreed reasonably well with the single flow channel model analysis by Axelsson et al. (2001).

The possible direction for future Laugaland reservoir description would be to develop a complex reservoir model based on data from all available sources, such as interwell tracer data, pressure tests, well logs, seismic data, and core analysis. This modeling approach would involve history matching of all production tracer histories even at unsteady state conditions. This numerical model could be used as a tool to predict the temperature drawdown history due to long-term reinjection.

NOMENCLATURE

A_i	Mean cross-sectional area of the i^{th} fracture
c_i	Incremental storage capacity of the i^{th} fracture
C	Storage capacity
C_{out}	Produced tracer concentration
D_L	Equivalent dispersion coefficient
f_i	Incremental flow capacity of the i^{th} fracture
F	Flow capacity
F_i	Cumulative flow capacity function of the fracture network
k_i	Permeability of the i^{th} fracture
L_c	Lorenz coefficient
L_i	Length of the i^{th} fracture
m_{rec}	Mass of tracer recovered
M_{inj}	Mass of tracer injected
q_{ext}	Production flow rate
q_{inj}	Injection flow rate
t	Time
\bar{t}	First Temporal Moment (Mean Residence Time)
\bar{t}_2	Second Temporal Moment
\bar{U}	Mean Flow Velocity
V_p	Swept pore volume
V_{pi}	Pore volume of the i^{th} fracture
x	Distance in flow direction
α	Dispersionivity
σ^2	Variance
σ_{in}^2	Injection tracer function variance
σ_{out}^2	Produced tracer function variance

REFERENCES

- Abbaszadeh-Deghani, M. and Brigham, W.E. (1984), "Analysis of Well-to-Well Tracer Flow to Determine Reservoir Layering," *Journal of Petroleum Technology*, 1753–1762.
- Allison, S.B., Pope, G.A. and Sepehrnoori, K. (1991), "Analysis of Field Tracers for Reservoir Description," *Journal of Petroleum Science and Engineering*, **5**, 173–186.
- Axelsson, G., Flovenz, O. G., Hauksdottir S., Hjartarson A. and Liu J. (2001), "Analysis of Tracer Test Data, and Injection-induced Cooling, in the Laugaland Geothermal Field, N-Iceland," *Geothermics*, **30**, 697-725.
- Axelsson, G., Hjartarson, A., Hauksdottir, S., Flovenz, O.G., Sverrisdottir, G., Arnason, F., Finnsson, M., Arnason, A. and Bodavarsson, R. (2000), "Demonstration of Improved Energy Extraction From a Fractured Geothermal Reservoir," Final Report for Thermie Project GE-0060/96
- Lake, L.W. (1989), "Enhanced Oil Recovery," Prentice Hall, NJ.
- Neretnieks, I. (1983), "A Note of Fracture Flow Dispersion Mechanisms in the Ground," *Water Resources Research*, **19**, 364–270.
- Robinson, B. A. and Tester, J. W. (1984), "Dispersed Fluid Flow in Fractured Reservoirs: An Analysis of Tracer-Determined Residence Time Distributions," *Journal of Geophysical Research*, **89**, 10374–10384.
- Shook, G.M. (1998), "Prediction of Reservoir Pore Volume from Conservative Tracer Tests," *Geothermal Resources Council Transactions*, **22**, 477–480.
- Shook, G. M. (2003), "A Simple, Fast Method of Estimating Fractured Reservoir Geometry from Tracer Tests," *Geothermal Resources Council Transactions*, **27**, 407–411

ACKNOWLEDGEMENTS

We gratefully acknowledge the support of the Nordurorka energy firm in N-Iceland in providing us with the data. This work was funded by the U.S. Department of Energy, Office of Energy Efficiency and Renewable Energy, Geothermal Technology Division, under contract DE-AC07-99ID13727, whose funding is gratefully acknowledged.

WHY WELL MONITORING INSTRUMENTS FAIL

Randy Normann
Joseph Henfling

Sandia National Labs
PO Box 5800
Albuquerque, New Mexico, 87185 USA
e-mail: ranorma@sandia.gov

ABSTRACT

This overview is intended to provide the reader with insight into basic reliability issues often confronted when designing long-term geothermal well monitoring equipment. No single system is looked at. General examples of the long-term reliability of other industries are presented. Examples of reliability issues involving electronic components and sensors along with fiber optic sensors and cables are given. This paper will aid in building systems where a long operating life is required. However, as no introductory paper can cover all reliability issues, basic assembly practices and testing concepts are presented.

BASIC INSTRUMENTATION OPERATING LIFE LIMITATIONS

There are a number of industries currently developing high-temperature (HT) instrumentation or control systems for a number of applications. Below is a short list of HT applications to give the reader a snapshot of the commercial HT instrumentation drivers and limitations.

Automotive

The automotive engineer designs are targeting 140-150°C with occasional temperature excursions to 170-200°C. The transmission is perhaps the hottest place for electronics. The transmission controller utilizes a microprocessor (16 bit), A/D (10 bit) and actuators.

Unfortunately, the automotive application only requires a lifetime of 150K miles/10 years of operation. The automotive industry targets transmission control electronics for 6Khrs (~8 months) of continuous service (150K/30miles/hr = 5Khrs). [Johnson (2003)]

Weapon Systems

Up until the 1990s, the weapon engineer designed systems using Mil-Spec components rated for long-

term 125°C operation. Unfortunately, the US military was unable to justify the cost of maintaining a 125°C component infrastructure to support weapon systems when the vast majority of those systems operate below 85°C. Today, there is virtually no support for Mil-Spec electronic ICs.

Aircraft Engines

Electronic controls systems for aircraft engines have been demonstrated but not yet commercially produced. Under programs as the USAF More Electric Aircraft [Weimer, 2004] there is a real expectation that future HT commercial versions will be developed.

The aircraft-engine controller electronics use a combination of SiC (Silicon-Carbide) and SOI (Silicon-On-Insulator) technology. These systems are designed to operate for 5 years at 225°C without failure. These systems are designed to fail “gracefully”. Gracefully means to fail by falling out of specification while continuing to operate. For comparison, drilling industry instrumentation is life-temperature rated to failure. HT aircraft electronics have a calculated operating life of 20 years at 150°C [Gingerich (1999)].

Unfortunately, aircraft engine control systems and automotive transmission controllers use low-resolution measurement components for an 8-to-12 bit resolution. Most logging tools require 16 to 24 bits of resolution to take well-data measurements.

Oil & Gas Industry

The fossil energy industry is operating wells at temperatures as high as 225°C [Rountree (2002)]. At temperatures of 200°C, Measurement-While-Drilling (MWD) tools are limited to <100 hrs [Rountree (2002)] before refurbishment. Wells being drilled at temperatures above 200°C are drilled “Blind”. Schlumberger reports target operating life times of 400 hrs for 175°C logging tools, and 5 years for 150°C intelligent-well completions called smart wells. [Parmentier (2003)]

Smart-well electronics are used to control valves deep within multi-completion wells. A multi-completion well is like a tree with one trunk and many roots. In order to enhance production, the well owner can control flow at each branch in the well. Here smart-well electronics are primarily interested in monitoring wellbore pressure, temperature and flow. These valves are either hydraulically controlled from the surface or via electric motors located at the valve.

To qualify a smart-well measurement system for a reliable multi-year operating life at elevated temperatures, the major commercial service companies must design the system and freeze the design for years of testing and commercial production. This includes the following costly activities:

1. Establishing multi-year (3-5) reliability requires time/testing
 - Accelerated life testing (or HALT) within the oil patch is difficult because systems are complex and may have a known failure mode only a few (<25°C) degrees above the targeted operating range.
 - Once oven and autoclave testing is completed, well testing is started.
 - Following successful initial testing, the engineers cannot continue changing the design without reevaluating the entire testing program.
 - For most systems, testing is the single greatest cost but not the only cost.

2. Perform a LIFE-OF-PROGRAM buy of system components and materials.

The vast majority of commercial electronics components have NO manufacturer-specified operating life. The service companies self-qualify electronic components.

- Historically, the electronics industry re-invents itself every six years, so service companies MUST buy self-qualified components at the time they qualify them because they may never get a second chance.
- Materials qualified for high-temperatures and a SLOW aging process must also be evaluated for potential well effects as fluid pressure, free hydrogen, potential HCl and other caustic fluids and gasses.

- In short, the major service companies tie up MILLIONS OF DOLLARS in life of program buys to support their intelligent well completion instruments.

HIGH TEMPERATURE TECHNOLOGIES

Electronic Components

There are two potential component temperature rating of interest here, Industrial Grade and HT SOI.

Industrial-grade electronics provide specified performance at 85°C. These are 'bulk' silicon devices using aluminum-to-silicon bonds and tinned aluminum leads connecting to the outside world.

The vast majority of these devices will not function above 125°C because of thermally generated leakage currents inside the silicon. These thermally generated currents are not normally destructive, allowing the circuits to return to operation after cooling.

Leakage currents cause analog circuits to develop excessive measurement errors. Hardest hit are the DC measurements as strain, temperature or tilt. The digital circuits will continue to operate until a point is reached where the low logic '0' in binary code can not be electrically produced. At that point, the digital system can not function.

Industrial-grade electronic devices that continue to function with increased leakage currents will exhibit a limited operating life of approximately 18 months at 150°C. The main failure mode of these devices is the electromigration of aluminum metallization into the silicon chip resulting in a failed electrical connection. [Gingerich (1999)]

Electromigration is a well known aging process. It is a function of junction temperature, current density and time. It is important to keep in mind that junction temperature is always greater than well ambient temperature. The junction refers to the transistor. Transistors generate heat. Transistors are small. Transistor junction temperature can easily run 10-to-20°C above ambient for small instrumentation devices to +100°C for power devices. Care must always be taken to insure that electronic devices have a means for removing self generated heat.

HT SOI is new. Most HT SOI devices from Honeywell called HTMOS® and were designed for aircraft engine control applications. HT SOI uses silicon-on-insulator (SOI) technology to reduce thermally generated leakage currents ~100 times.

The reduction of leakage currents allows most HT SOI devices to continue operating up to 250-300°C.

The electromigration process is better controlled using a 0.5 mA/um² current density where many Industrial Grade components use a 5 mA/um² design rule.[Gingerich (1999)]

Fiber Optic Sensor and Cables

Fiber optic systems and sensors offer a lot of advantages but also have some inherent disadvantages. A huge advantage of fiber sensors is the ability to connect fiber sensors in series, creating complete well sensor profile readings from a single fiber. Series fiber temperature and strain sensors have been demonstrated in a number of commercial applications.

The published operating life of fiber within oil wells has been very mixed. Fiber optic sensor and cable life appears to be highly dependent on well conditions and installation methods.

Fibers are normally installed within stainless steel tubing to protect it from wellbore fluids.

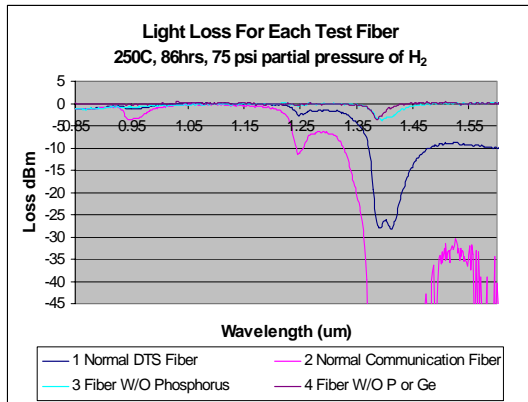


Figure 1. Hydrogen-induced light losses in four grades of fibers. These test fibers were only 50ft long. [Normann, (2001)]

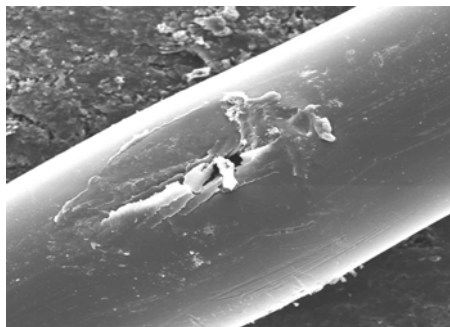


Figure 2. Water exploiting a fiber buffer defect. [Normann, (2001)]

Fiber is affected by hydrogen (creating light lossy HO bonds) and by crystal growth in unprotected glass. [Normann (2001)] The effects of HO in fiber can be seen in Figure 1. Figure 2 shows fiber glass damage caused by super heated water within a buffer defect. As such, the given well conditions along with fiber installation methods can greatly affect the fibers operating life.

EXAMPLES OF FAILED MATERIALS OR COMPONENTS

Wire Breaks

Wire breaks or failed solder joints are the most common types of well instrumentation failures. Figure 3 below shows a photo of a failed wire. The wire broke off a solder joint. Common solder is 60% tin and 40% percent lead. A common wire type is copper. In Figure 3, a manufacturer qualified 200°C silver plated copper wire was tested at 193°C. At elevated temperatures (>95°C), the copper migrates through the silver to react with the tin (found in the solder) resulting in intermetallic growth: in this case crystalline bronze. The resulting intermetallic growth is structurally very weak, easily broken.



Figure 3. Common solder and copper wire are subject to intermetallic growth, weakening the wire.

At Sandia, we are using high lead-solder and nickel plated copper wires to greatly reduce intermetallic grow up to +250°C. However, the instrumentation designer needs to validate their component selection. The capacitor shown in Figure 4 is 200°C rated for automotive use. As can be seen in Figure 5, the manufacturer has an intermetallic growth problem at the device lead. This device failed after 3 months at 193°C.

Ceramic Capacitors

Perhaps the most common electronic component ever produced is the ceramic capacitor; for example, the Sandia memory-based pressure, temperature and spinner tool uses over 30 ceramic capacitors.



Figure 4. The before photo of the after photo shown in figure 5.



Figure 5. The after photo of the capacitor was exposed to 193°C for ~7000hrs.

Ceramic capacitors have a deadly flaw called dielectric breakdown. Dielectric breakdown is a function of time, temperature and applied voltage. Dielectric breakdown is deadly for two reasons. First, ceramic capacitors are used to reduce power supply ripple and common 60 hertz. As such these capacitors are placed across the circuits supply voltage. Ceramic capacitors fail at electrical SHORTS. The short is so hard, that traces on the printed wiring board will be burned off. Figure 6 shows a cut-away view of a short inside a ceramic capacitor. The physical damage to the capacitor is obvious.

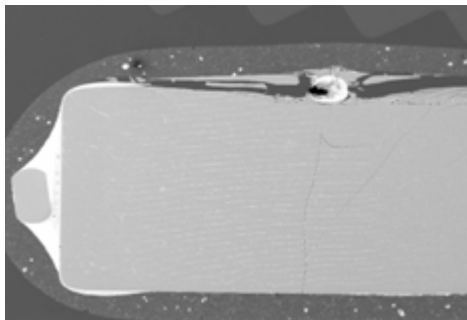


Figure 6. Cut-away view of a shorted ceramic capacitor.

The second deadly reason, extremely small defects within the ceramic capacitor's dielectric can lie in wait for hundreds of hours before creating a

dielectric-breakdown event. The majority of these defects are impossible to detect until millisecond before failing. Because of this fatal flaw, ceramic capacitors are not used on aircraft control systems.

Chemical Interactions

Geothermal wells contain more than hot water. They have a brine fluid containing dissolved minerals, noncondensable gasses and hostile chemicals. Among the more common notable hostile chemicals are chlorine (HCl), free hydrogen and H²S.

The image in Figure 7 is from a dissected quarter-inch 316L stainless steel tubing used to hold a fiber-optic cable. This damage was caused by a small amount of HCl found within a 250°C geothermal well. This damage occurred within 16 hours. The weld to the left of the image may have sensitized the steel even more than typical 316L steel.

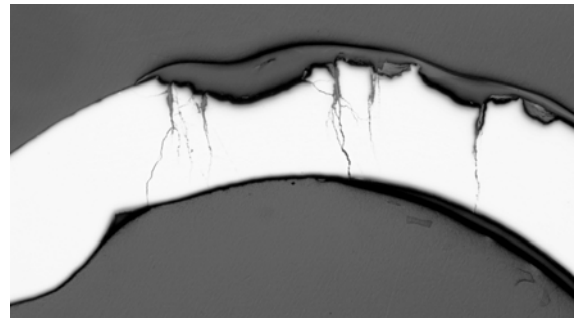


Figure 7. HCl damage to a 316L stainless steel tube.

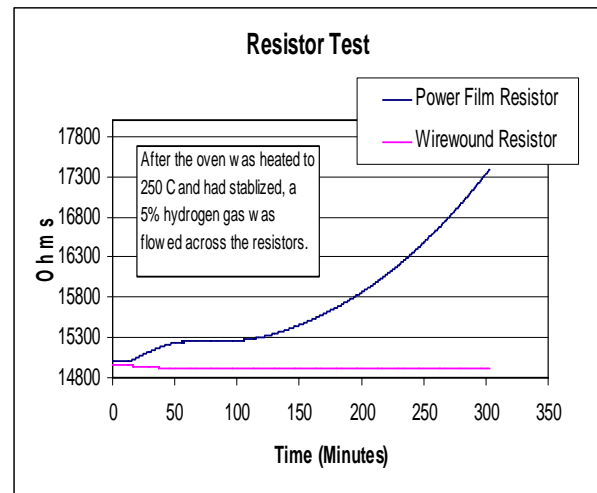


Figure 8. Both resistors are rated for 250°C by the manufacturer. The resistor showing an increase in resistance is a thin metal film resistor, the other is a wirewound resistor.

Free hydrogen affecting fiber has already been noted. However, it can also affect passive resistors used in electronics. The plot shown in Figure 8 shows the

effect of hydrogen on a manufacturer 250°C rated resistor.

FINAL COMMENT

This paper can not cover all the issues found when designing a new test or monitoring equipment needed for a hot well. This report can help a new researcher or developer get a head start and perhaps prevent a few costly mistakes.

To conclude, a “short” outline of the “current” Sandia practices will be given below. These are some of the activities the Sandia Geothermal Research Department undertakes before installing a tool for a long-term test. For more information, please contact the authors.

Outline of Sandia Installation Activities

1. All metal housing parts are baked out at 250°C for 48hrs to remove machining oils.
2. Electronics components are mounted on circuit boards while heated to a temperature about half the expected well temperature.
3. The assembled board is ‘burned-in’ under a constant vacuum to pull any VOC off during the curing process. The burn-in temperature is 10-to-25°C hotter than the expected well temperature.
4. The burn-in is conducted for 2 to 4 weeks.
5. The tool is fully assembled within the lab.
6. The tool is evacuated and filled with Argon three times to remove oxygen and moisture.
7. The tool is installed on the cable or tubing and placed within the well.

ACKNOWLEDGMENTS

Sandia is a multiprogram laboratory operated by Sandia Corporation, a Lockheed Martin Company, for the United States Department of Energy’s National Nuclear Security Administration under Contract DE-AC04-94AL85000.

REFERENCES

Gingerich, B.L.; Brusius, P.G.; Maclean, I. M. (1999) “Reliable Electronics for High-Temperature Downhole Applications”, Society of Petroleum Engineers, 1999, SPE 65438

Johnson, R. Wayne (2003), “High Temperature Automotive Electronics”, Report to Sandia National Laboratories, Geothermal Research Department, Aug. 26, 2003.

Normann, Randy; Weiss, Jonathan; Krumhansl, Jim, “Development of Fiber Optic Cables for Permanent

Geothermal Wellbore Deployment”, 2001 Stanford Geothermal Workshop.

Parmentier, Bernard; Vermesan Ovidiu; Beneteau, Lionel (2003) “Design of High Temperature Electronics for Well Logging Applications”; High Temperature Electronics Network, Oxford Eng, 2003. pp77-83

Rountree, S. P. (2002), “High Temperature MWD Systems”, High-Temperature Conference, Albuquerque, NM, May 2002

Weimer, Joseph A. (2004), “High Temperature Power Electronics for the More Electric Aircraft”, High-Temperature Electronics Conference, Invited Paper, Santa Fe, NM. May 2004

CLASSIFICATION OF GEOTHERMAL SYSTEMS – A POSSIBLE SCHEME

Subir K. Sanyal

GeothermEx, Inc.
5221 Central Avenue, Suite 201
Richmond, California 94804 USA
e-mail: mw@geothermex.com

ABSTRACT

At the request of the United States Department of Energy, the author was asked by the Geothermal Energy Association (Washington, D.C.) to prepare a white paper on the subject (in connection with a new national assessment of geothermal resources). This paper offers a possible scheme in which geothermal resources are classified into seven categories based on temperature: non-electrical grade (<100°C), very-low temperature (100°C to <150°C), low temperature (150°C to 190°C), moderate temperature (190°C to <230°C), high temperature (230°C to <300°C), ultra-high temperature (>300°C), and steam fields (approximately 240°C with steam as the only mobile phase). In the first four classes of reservoirs, liquid water is the mobile phase; in the “high” and “ultra-high” temperature reservoirs, the mobile fluid phase is either liquid or a liquid-vapor mixture.

This scheme is based not only on temperature but also according to a set of additional attributes important for practical utilization of geothermal energy: (a) steam fraction in the mobile fluid phase in the reservoir (a controlling factor in reservoir performance), (b) type of power generation technology applicable, (c) production mechanism and the state of the fluid at the wellhead (which influence operational economics), (d) factors other than temperature that control well productivity (these factors affect the optimization of field development and operation), and (e) unusual operational problems that impact power cost (such as scaling, corrosion, high content of non-condensable gases, etc.). The paper discusses the rationale for this scheme and why some other possible schemes were not considered. Finally, the paper considers the distribution of the identified geothermal systems in the United States *vis a vis* these categories. The author invites comments on this scheme that may lead to a generally accepted one.

INTRODUCTION

In June 2004, the United States Department of Energy (DOE) approached the Geothermal Energy Association (GEA), a U.S. trade organization based

in Washington (D.C.), to propose an approach to classification of geothermal systems. The need for such a classification scheme stems from the proposed national assessment of the geothermal resources in the United States. Based on a discussion between the DOE and GEA, the author was asked by the GEA to prepare a white paper that could serve as a basis for arriving at a formal classification scheme; this paper is the product.

A BASIS FOR CLASSIFICATION

Many possible criteria for such classification are available, but most would agree that for classifying geothermal resources, reservoir temperature should be the primary criterion. Table 1 offers 7 possible classes based on temperature as the primary criterion and steam fraction in the mobile fluid phase in the reservoir (but not necessarily steam saturation in the reservoir) as a secondary criterion. The reservoir temperature limits suggested in Table 1 can be shifted by 5° to 10°C without disrupting the logical structure of the scheme, which is summarized below. The scheme is illustrated on a pressure-enthalpy-temperature diagram for pure water on Figure 1. The attributes of the reservoirs in the various classes, as depicted in Figure 1 and listed in Table 1, reflect general industry experience.

Class 1 (less than 100°C): The boiling point of water at atmospheric pressure, 100°C, is a reasonable lower limit for power generation from a geothermal fluid; no commercial geothermal power project has been developed based on a resource cooler than 100°C. Therefore, a resource in this class is suitable only for non-electrical uses.

Class 2 (100°C to less than 150°C): The mobile fluid phase in these reservoirs is liquid water. Only three power projects (totaling about 6 MWe capacity) have been developed in the U.S. based on geothermal resources in the 100° to 150°C temperature range, and these projects have proven only marginally commercial. Well productivity for such a resource would be less than 5 MWe, the typical range being 2 to 4 MWe. Geothermal resources in this temperature

range call for pumped wells and binary-cycle power generation. Given the significant advances made in downhole pump and binary-cycle power generation technologies over the last two decades, power generation from resources in this temperature range is eminently commercial today. The 150°C temperature limit is somewhat arbitrary and may be moved either way by perhaps up to 10°C.

Class 3 (150°C to less than 190°C): The mobile fluid phase in these reservoirs is liquid water. A number of commercial power projects have been operated over the last two decades using geothermal resources in the 150° to 190°C range, the latter temperature being the limit of operation of commercially available downhole pumps today; geothermal water over most of this temperature range must be pumped because the fluid does not have sufficient energy for self-flow at a commercial rate. However, at the upper end of this temperature range wells may be either pumped or self-flowed (if the reservoir flow capacity is relatively large). Well productivity for such a resource would be less than 7 MWe, the typical range being 3 to 6 MWe. While temperature tolerance for commercial pumps may some day exceed 190°C, the higher vapor pressure at higher temperatures might reduce the available pressure drawdown sufficiently to make pumping less attractive than self-flow. Therefore, the 190°C limit for this range is reasonably well defined.

Class 4 (190°C to less than 230°C): The next higher resource temperature limit is chosen as 230°C, which is lower than the minimum initial resource temperature encountered in vapor-dominated reservoirs worldwide. Vapor-dominated reservoirs have such a unique set of characteristics that these have been grouped as a separate class as described below. Reservoirs above a temperature level of 230°C may have free steam saturation initially or develop steam saturation upon exploitation, but this would be unlikely for a reservoir below a 230°C temperature level. Thus, reservoirs in the 190° to 230°C range should have liquid water as the mobile fluid phase, and as such, this class is reasonably well constrained. The wells for this class would be too hot to pump and must be self-flowed. Therefore, the productivity of wells in this class would be more variable, typically in the range of 3 to 12 MWe.

Class 5 (230°C to less than 300°C): Above a temperature level of 230°C, the reservoir would be expected to become two-phase at some point during exploitation. The next higher temperature limit of 300°C is rather arbitrary; changing it by perhaps up to 20°C will not affect the classification. For this class of resource, as well as for classes 6 and 7, well productivity varies within an extremely wide range, depending on reservoir flow capacity as well as the extent of steam saturation in the reservoir, which,

together with the relative permeability characteristics of the reservoir, determines the steam fraction in the mobile fluid phase. Individual well productivities as high as 50 MWe have been reported for fields in classes 5 through 7.

Class 6 (greater than 300°C): Such reservoirs are characterized by rapid development of steam saturation in the reservoir and steam fraction in the mobile fluid phase upon exploitation. The performance of such reservoirs, specifically the evolution of production enthalpy, is generally difficult to forecast with any confidence. The upper temperature limit for this class may be considered the critical temperature of water (374.1°C). A temperature significantly higher than the critical is unlikely to be encountered in a productive well for a number of physical reasons.

Class 7 (Steam fields): This special class of resource needs to be recognized, its uniqueness being the remarkably consistent initial temperature and pressure (approximately 240°C and 33.5 bar-a) displayed by all such fields in the world: Kamojang (Indonesia), The Geysers (California), Lardanello (Italy), Matsukawa (Japan), Darajat (Indonesia), etc. Furthermore, the enthalpy of the resource in such a field is the maximum enthalpy possible for saturated steam (2,800 kJ/kg). Since a pervasively superheated steam reservoir is physically unlikely (notwithstanding occasional cases of superheated steam production at the wellhead), a Class 7 resource typically has the largest available energy per unit mass of all classes. Therefore, wells of 30 to 50 MWe capacity are not uncommon in such fields.

Ignoring geothermal resources in the National Parks, The Geysers is the only such field in the U.S. Given the pivotal importance of The Geysers to the U.S. geothermal industry, this class is recognized separately. It should be noted that the low-pressure steam reservoir exploited until recently at Cove Fort (Utah) is unique and such low-pressure steam reservoirs are generally “steam caps” over a liquid reservoir and do not represent a significant commercial resource. Incidentally, the plant at Cove Fort has been shut down and a new plant is planned to be operated using water occurring below the steam cap.

IS THE PROPOSED CLASSIFICATION REASONABLE?

A useful classification should be one that can ascribe a consistent set of practically useful attributes to each class; Table 1 lists these for the proposed scheme. From the viewpoint of power plant development and operation, the important attributes are the following: (a) steam fraction in the mobile fluid phase in the reservoir (a controlling factor in reservoir

performance), (b) type of power generation technology applicable, (c) production mechanism and the state of the fluid at the wellhead (which influence operational economics), (d) factors other than temperature that control well productivity (these factors affect the optimization of field development and operation), and (e) unusual operational problems that impact power cost (such as scaling, corrosion, high content of non-condensable gases, etc.).

As seen from Table 1, the proposed classification manages to pigeon-hole geothermal resources not only according to temperature (which uniquely determines, except for Class 7, the available MWe per unit mass production rate) but also according to the above set of additional attributes. Furthermore, this classification scheme leads to consistently increasing MWe reserves per identified field in the U.S. (Figure 2) as one considers progressively higher classes. Figure 2 is based on data shown in Table 2, which in turn draws upon the results of the last nationwide assessment of geothermal resources conducted by the U.S. Geological Survey in 1978 (Muffler, 1979). It is clear from Table 2 and Figure 2 that the number of identified fields declines but the MWe reserves per field increase, nearly exponentially in both cases, as one considers progressively higher temperature classes, the steam field category (Class 7) being, of course, an exception.

While progressively higher temperature classes are expected to show higher levels of power potential per unit mass production rate, the curious empirical fact of progressively higher reserves per field for higher temperature classes adds another dimension to the conceptual consistency of the proposed classification. As such, the scheme appears reasonable.

COULD WE CHOOSE SOME OTHER BASIS FOR CLASSIFICATION?

We could, but the above-described consistency would be lost. For example, one could consider geology as the main classification criterion. While it might be an interesting intellectual exercise, there is no consistent set of practically useful attributes that would characterize a geologic environment (volcanic, sedimentary, metamorphic, etc), or a geologic province (Basin and Range, Imperial Valley, etc in the U.S.). For example, within the Imperial Valley, Salton Sea is a far larger, hotter and more saline field than either East Mesa or Heber. Within the same Basin and Range province, the Dixie Valley field has entirely different reservoir characteristics than does Steamboat, and so on.

Similarly, consideration of reservoir depth or permeability (or any other petrophysical property, for that matter) as a classification criterion does not lead

to satisfactory pigeon-holing of the above-mentioned attributes. For example, there are numerous wells in Nevada and the adjoining region of California that consistently produce 3 to 4 MWe from a remarkably wide depth range (less than 150 m to greater than 2,500 m); and the permeability-thickness values of the exploited fields range from less than 300 to more than 300,000 millidarcy-meter without serving as a unique or ready indicator of commercial prospects of the fields. As regards depth, for example, The Geysers reservoir has seen commercial production from a depth range of 300 to 4,000 m. Then, to which class, in a depth-based classification, should The Geysers belong? Similarly, within the same reservoir, petrophysical properties can easily vary by orders of magnitude. How could one then pigeon-hole such a reservoir with a classification scheme based on a petrophysical property? In addition, the range of production depths or petrophysical properties of a field can only be defined after a significant amount of development drilling. Reservoir temperature, on the other hand, can be approximated from geochemical exploration and heat flow studies long before a field is confirmed by drilling or considered for commercial development. This is one more advantage of a temperature-based classification.

The choice of a basis for classification ultimately hinges on the purpose of such a classification. In this paper, we have assumed the purpose to be standardization of references to various geothermal systems (in a national inventory) as regards their commercial prospects; this is apparently what the wind industry has done. As such, this paper has disregarded the possibility of alternative schemes of classification based on criteria less relevant to the commercial world.

HOW CAN ENHANCED GEOTHERMAL RESOURCES BE CLASSIFIED?

There is no readily apparent logical basis to classify enhanced geothermal systems (EGS) or hot dry rock (HDR) resources other than perhaps considering temperature-based classes as discussed above; unfortunately, as shown below, even classification according to temperature may not be particularly meaningful. One can superimpose on such temperature classes some consideration of the *in-situ* stress regime to define sub-classes; but given the paucity of data on underground stress regimes this approach may prove illusory. Another possible approach could be to define two broad groups of EGS projects, those developed in purely conductive systems and those developed in tight parts of convective systems (Sanyal and Butler, 2004); EGS field demonstration projects, supported by the U.S. Department of Energy, at Coso and Desert Peak fall in the latter group, while the Fenton Hill (New Mexico) experiment conducted in the 1970s and

1980s involved the former. For either group, further classification based on temperature is an option; even the stress regime might be invoked for defining yet further subclasses.

Temperature is an unsatisfactory criterion for classifying EGS projects, because unlike a hydrothermal system, the characteristics of an EGS reservoir are largely engineered. Therefore, some of the attributes listed in Table 1 for the various temperature classes would not prove meaningful. For example, productivity of a well will depend more on the extent of artificial enhancement of reservoir flow capacity than on the intrinsic porosity or permeability or even temperature of the formation. For any specific temperature range, most of these attributes (applicable power generation technology, production mechanism, fluid state at the wellhead, etc.) are not expected to be unique but will depend also on the nature and extent of artificial enhancement of permeability and the injection/production configuration employed (doublet, triplet, 5-spot, etc.) and its dimensions. Therefore, the extent of permeability enhancement or injection/production scheme employed is as important a criterion for classification as is temperature.

Given the limited practical experience with EGS projects to date and the above-discussed conceptual limitations, it is too early to attempt to develop a classification scheme for EGS projects. Perhaps such a classification scheme should be considered after significant results from EGS experiments and field developments, at Coso and Desert Peak as well as in Australia and Europe, become available. In any case, the absence of a classification scheme should not hold up progress on the EGS front for the foreseeable future.

REFERENCE

Muffler, L. J. P., Editor, 1979. "Assessment of Geothermal Resources of the United States – 1978," Geological Survey Circular 790, United States Department of the Interior, 1979.

Sanyal, Subir K. and Steven J. Butler (2004), "National Assessment of U.S. Enhanced Geothermal Resources Base – A Perspective," Trans., Geothermal Resources Council, Palm Springs, California, Volume 28, August – September, 2004, pp 233-238.

ACKNOWLEDGEMENT

The author wishes to thank Allan Jelacic of DOE for raising the issue of classification, the GEA for giving the author the opportunity to prepare this white paper, Steven Butler of GeothermEx for his generous assistance in preparation of the graphics, author's colleagues at GeothermEx for their critical review of this paper, and the Board of Directors of GeothermEx for financing this study.

Table 1. A Possible Classification Scheme for Geothermal Resources

<u>Class of Resource</u>	<u>Reservoir Temperature</u>	<u>Mobile Fluid Phase in Reservoir</u>	<u>Production Mechanism</u>	<u>Fluid State at Wellhead</u>	<u>Well Productivity and Controlling Factors other than Temperature</u>	<u>Applicable Power Conversion Technology</u>	<u>Unusual Development or Operational Problems</u>
1. Non-electrical Grade	< 100°C	Liquid water	Artesian self-flowing wells; pumped wells	Liquid water	Well productivity dependent on reservoir flow capacity and static water level	Direct Use	
2. Very Low Temperature	100°C to < 150°C	Liquid water	Pumped wells	Liquid water (for pumped wells); steam-water mixture (for self-flowing wells)	Typical well capacity 2 to 4 MWe; dependent on reservoir flow capacity and gas content in water; well productivity often limited by pump capacity	Binary	
3. Low Temperature	150°C to < 190°C	Liquid water	Pumped wells; self-flowing wells (only at the higher-temperature end of the range)	Liquid water (for pumped wells); steam-water mixture (for self-flowing wells)	Typical well capacity 3 to 5 MWe; dependent on reservoir pressures, reservoir flow capacity and gas content in water; productivity of pumped wells typically limited by pump capacity and pump parasitic power need; productivity of self-flowing wells strongly dependent on reservoir flow capacity	Binary; Two-stage Flash; Hybrid	Calcite scaling in production wells and stibnite scaling in binary plant are occasional problems
4. Moderate-Temperature	190° to < 230°C	Liquid water	Self-flowing wells	Steam-water mixture (enthalpy equal to that of saturated liquid at reservoir temperature)	Well productivity highly variable (3 to 12 MWe); strongly dependent on reservoir flow capacity	Single-stage Flash; Two-stage Flash; Hybrid	Calcite scaling in production wells occasional problem; alumino-silicate scale in injection system a rare problem

Table 1. A Possible Classification Scheme for Geothermal Resources

<u>Class of Resource</u>	<u>Reservoir Temperature</u>	<u>Mobile Fluid Phase in Reservoir</u>	<u>Production Mechanism</u>	<u>Fluid State at Wellhead</u>	<u>Well Productivity and Controlling Factors other than Temperature</u>	<u>Applicable Power Conversion Technology</u>	<u>Unusual Development or Operational Problems</u>
5. High Temperature	230°C to < 300°C	Liquid water; Liquid-dominated two-phase	Self-flowing wells	Steam-water mixture (enthalpy equal to or higher than that of saturated liquid at reservoir temperature); saturated steam	Well productivity highly variable (up to 25 MWe); dependent on reservoir flow capacity and steam saturation	Single-stage Flash; Hybrid	Silica scaling in injection system; occasionally corrosion; occasionally high NCG content
6. Ultra High Temperature	300°C+	Liquid-dominated two-phase	Self-flowing wells	Steam-water mixture (enthalpy equal to or higher than that of saturated liquid at reservoir condition); saturated steam; superheated steam	Well productivity extremely variable (up to 50 MWe); dependent on reservoir flow capacity and steam saturation	Single-stage Flash	High NCG content; silica scaling in injection system; occasionally corrosion; silica scaling potential in production wells at lower wellhead pressures
7. Steam Field	240°C (33.5 bar-a pressure; 2,800 kJ/kg enthalpy)	Steam	Self-flowing wells	Saturated or superheated steam	Well productivity extremely variable (up to 50 MWe); dependent on reservoir flow capacity	Direct steam	Occasionally high NCG content or corrosion

Table 2. Distribution of Identified Hydrothermal Systems in the U.S. among the Resource Classes*

<u>Resource Class</u>	<u>Reservoir Temperature</u>	<u>No. of Identified Systems</u>	<u>Reserves in Identified Systems</u>
2. Very Low Temperature	100°C to < 150°C	134	8,000 MWe
3. Low Temperature	150°C to < 190°C	34	5,500 MWe
4. Moderate Temperature	190° to < 230°C	11	4,300 MWe
5. High Temperature	230°C to < 300°C	7	8,200 MWe
6. Ultra High Temperature	300°C+	1	2,000 MWe
7. Steam Field	230°C to 240°C	<u>1</u>	<u>1,000 MWe</u>
	Total:	188	29,000 MWe

* Excluding systems in National Parks

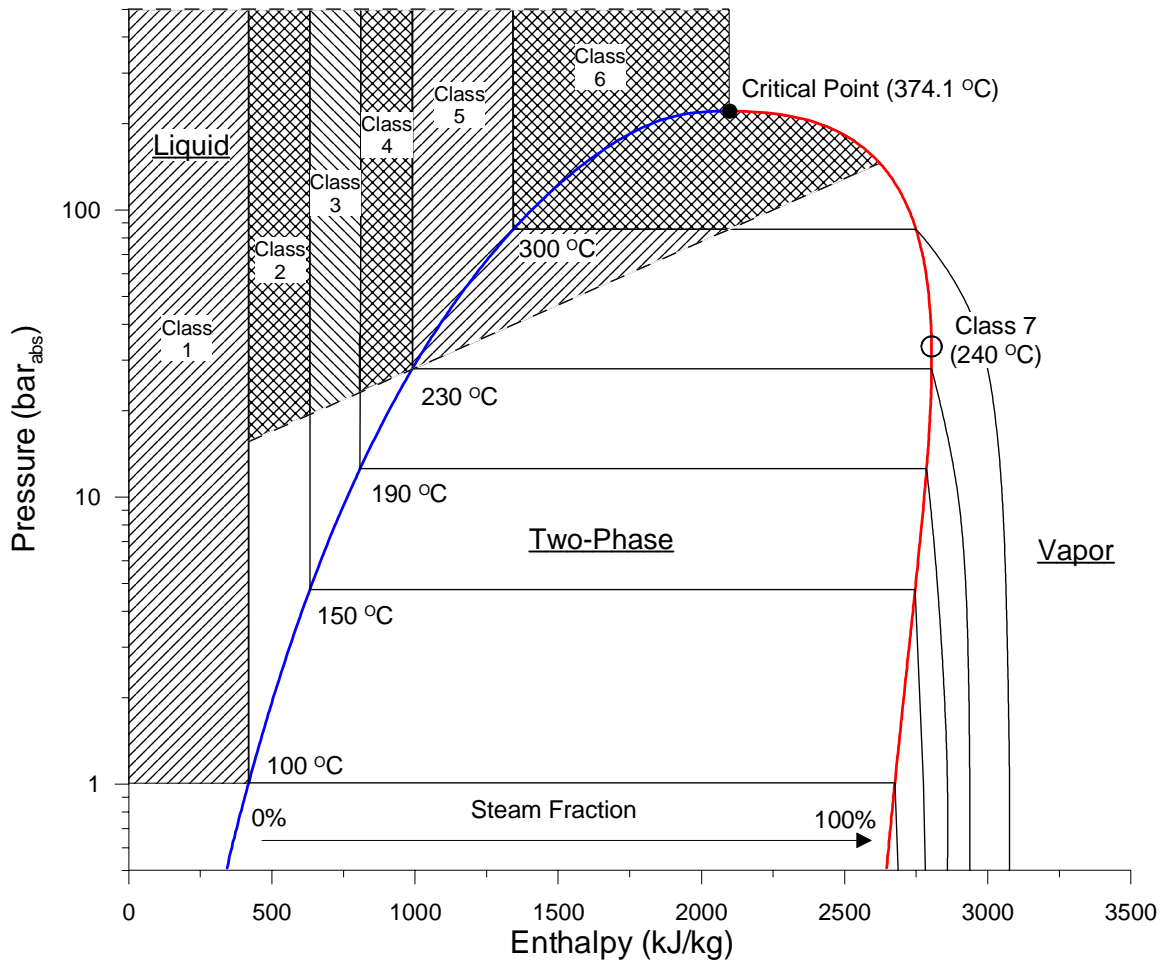


Figure 1: Classification Scheme on Pressure-Enthalpy-Temperature Diagram for Water.

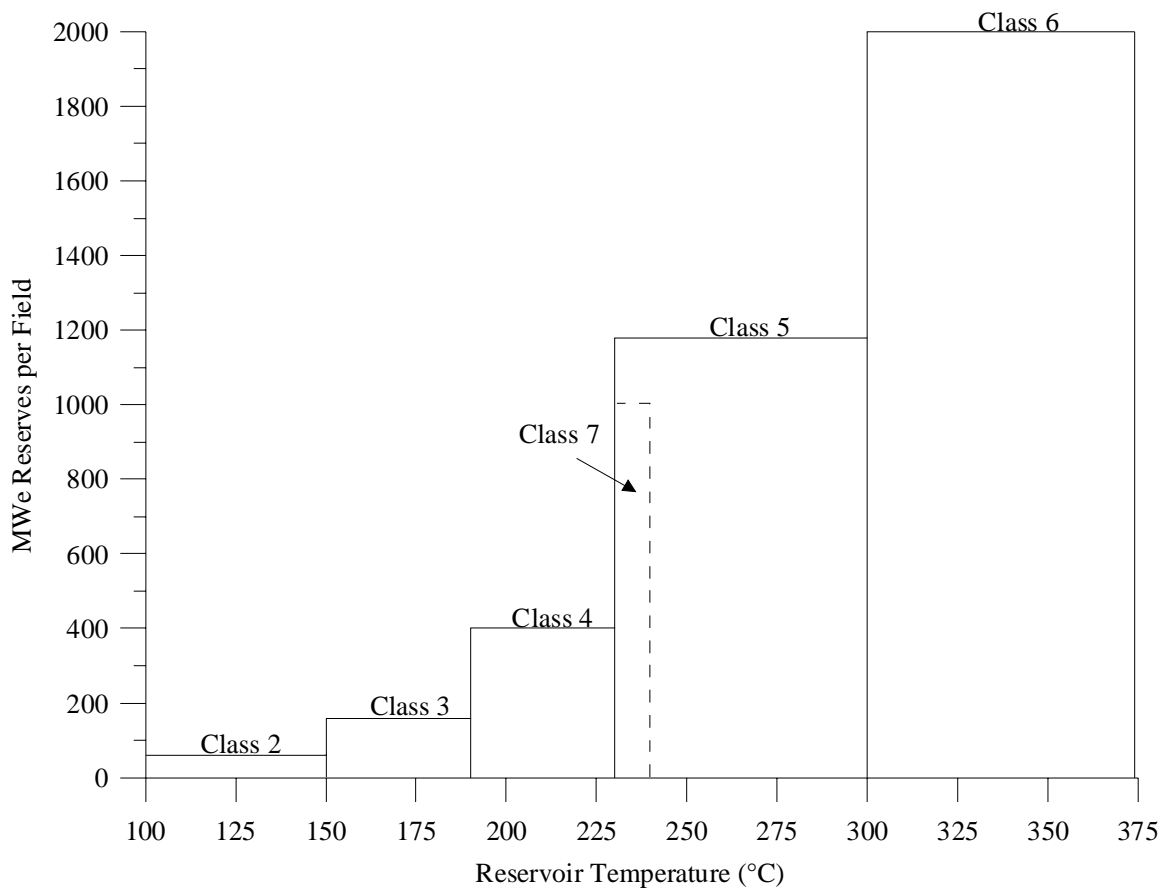


Figure 2. MWe Reserves per Identified Field for Various Resource Classes

PORE NETWORK MODELING OF ADSORPTION EFFECTS IN GEOTHERMAL RESERVOIRS

Ilkay Uzun and Serhat Akin

Middle East Technical University
METU Petroleum and Natural Gas Engineering Department
Ankara, 06531, Turkey
uilkay@metu.edu.tr , serhat@metu.edu.tr

ABSTRACT

Physical adsorption is a major factor governing the behavior of geothermal reservoirs. That is, adsorbed water on the rock surfaces in a geothermal field has been thought to provide a major source of fluid within the reservoir. In addition to this, the effect of carbon-dioxide flow through water is another main concern for geothermal reservoirs. A single pore model was developed to investigate adsorption considering CO₂ presence in water.

Using this model, adsorption effects with CO₂ presence is discussed at varying temperature and pressure. The model is run at temperatures ranging between 90-130°C at different relative pressures. Stanford experimental adsorption data were compared to the results of this developed model. It has been found that, there is a reasonable fit between the experimental data and the model. A critical pore radius that allows vapor molecule to enter the pore was calculated. It has been observed that the amount of CO₂ adsorbed as well as water in geothermal fields is considerable.

INTRODUCTION

Geothermal reservoirs which are especially vapor-dominated consist of porous or fractured rock, with the interstitial spaces filled with steam (*Horne et al.*). Because of the occurrences of the adsorption process, water molecules are stored on the surfaces of the pore spaces in a state that is more like that of a liquid than that of a vapor. It is accepted that the performance of a vapor-dominated geothermal reservoir is governed strongly by the effects of adsorption (*Horne et al.*).

The phenomenon of adsorption and desorption at solid/liquid interface is of major importance since it is generally accepted that the wettability of a reservoir can be changed by adsorption. Moreover, working with microporous materials has generally shown that the effects of adsorption are, in fact, important when the pore sizes become small and the

ratio of pore surface area to pore volume (PV) becomes large. Due to these facts, the rates of water adsorption and the rates of CO₂ adsorption miscible in water for geothermal fields were analyzed. It is accepted that the performance of a vapor-dominated geothermal reservoir is governed strongly by the effects of adsorption (*Horne et al, 1994*).

The pore network is a representation of the void space of the reservoir rock. Each pore was assumed to be cylindrical or spherical and hence contain just one phase. There are lots of studies concerning pore models in order to observe the permeability, saturation, multiphase flow in a pore network model (*Oren et al, 1997; Fenwick et al, 1997; Blunt, 2001*). Fundamentally, the geometry of the void space of a porous medium and the interactions of the multiple phases with the solid determine macroscopic properties such as porosity, relative permeability, capillary pressure and resistivity index (*Al-Gharbi et a, 2003*).

In this study, the network model idealizes a porous medium as a three-dimensional lattice of a spherical chamber. The network model is reduced to a single pore model which has a volume of approximately 329 μm³. Then using appropriate methods, adsorption effects on the rock are computed in the network modeling.

It is a fact that, Langmuir equation is the cornerstone of all theories of adsorption. Therefore, in this study, the amounts of adsorbed particles with respect to relative pressures are calculated using Langmuirian isothermal equations. With this approach, monolayer surface adsorption on an ideal surface can be understood. When examining the water adsorption Langmuir type is considered. On the other hand, when CO₂ flowing through water is under consideration, the BET (Brunauer *et al*, 1938 as cited in Do, 1998) isotherms are used to calculate the amount of adsorbents with respect to relative pressures. This is due to the fact that Langmuir type adsorption can not hold for the solution type systems.

BET equations are the extended version of the Langmuir equations for the mixture type systems. A large number of adsorption isotherm models presented in the literature are generally able to describe the adsorption of water, methane, ethane, propane, activated carbons, and etc. (Zhou *et al*, 2004; Busch *et al*, 2003; Do *et al*, 1991; Lucas *et al*, 2004); however there is a lack of study understanding both adsorption of water and adsorption of CO₂ in water for geothermal conditions.

The first task in this study was, therefore, to compare the existing experimental data on the adsorption of water in vapor-dominated geothermal fields. The next step was to implement calculation methods suitable for the CO₂ presence in water with the same conditions by using a single pore model. Issues to be discussed in this paper are: (1) Principles of the model (2) What is adsorption? (3) Adsorption on homogeneous solid surfaces by using Langmuir Equations (4) BET Isotherms (5) Comparison with the experimental data (6) CO₂-water adsorption

ADSORPTION

Adsorption is a process where molecules from the gas phase or from solution bind in a condensed layer on a solid or liquid surface. The molecules that bind to the surface are called the *adsorbate* while the substance that holds the adsorbate is called the *adsorbent*. The process when the molecules bind is called *adsorption*. Removal of the molecules from the surface is called *desorption* (Masel, 1996).

Adsorption is essentially an attraction of adsorbate molecules to an adsorbent surface. Interaction between adsorbate and the adsorbent consists of molecular forces embracing permanent dipole, induced dipole and quadrupole electrostatic effects. For reasons adsorption is nearly always an exothermic process (Crittenden *et al*, 1998).

There are two fundamentally different types of adsorption;

- *Multilayer adsorption* – Consists of several layers of adsorbate on the surface of the adsorbent.
- *Monolayer adsorption* – All the adsorbate is held in close proximity to the solid.

Multilayer adsorption is basically condensation process; attractive interactions between adsorbate molecules cause gases to condense into a liquid like film on top of the molecules in the first monolayer.

In order to quantify how much gas is adsorbed, adsorption isotherms, which are plots of the amount of gas that is adsorbed on a surface as a function of

the pressure of the gas at constant temperature, are used. The major adsorption models are: the Langmuir isotherm, Henry's law, the BET (Brunauer-Emmett-Teller) equation, and the Gibbs adsorption isotherm.

LANGMUIR ISOTHERMS

The Langmuir Adsorption Isotherm was derived by Irving Langmuir in 1918 (Do, 1998) in an attempt to describe the chemisorptions of atoms or molecules at a surface.

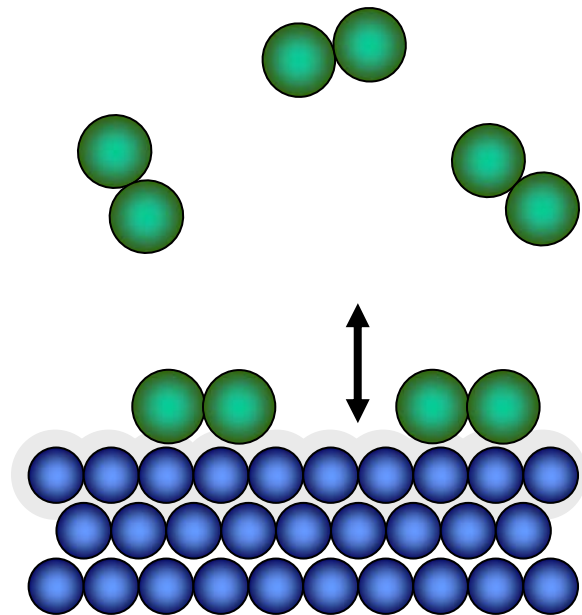


Figure. 1. Schematic diagram of Langmuir adsorption mechanism (Do, 1998).

The assumptions of the Langmuir model (Do, 1998)

1. The surface is homogeneous, that is the adsorption energy is constant over all sites
2. Adsorption on surface is localized, that is adsorbed atoms or molecules are adsorbed at definite, localized sites
3. Each site can accommodate only one molecule or atom

As it is indicated (Do, 1998), the Langmuir theory is based on a kinetic principle, that is the rate of adsorption (which is the striking rate at the surface multiplied by a sticking coefficient, sometimes called the accommodation coefficient) is equal to the rate of desorption from surface.

The rate of striking the surface, in mole per unit time and unit area, is:

$$R_s = \frac{P}{\sqrt{2\pi MRT}} \quad (1)$$

Where M is molecular weight, R is gas constant (8.314 J/mol K), π is spreading pressure, T is temperature and P is pressure.

The rate of adsorption, R_a in mole adsorbed per unit bare surface area per unit time when sticking coefficient α is considered is:

$$R_a = \frac{\alpha P}{\sqrt{2\pi MRT}} \quad (2)$$

The rate of adsorption on an occupied surface, that is when a molecule strikes the surface that is already occupied with adsorbed species, is:

$$R_a = \frac{\alpha P}{\sqrt{2\pi MRT}} (1 - \theta) \quad (3)$$

Where θ is the fractional coverage.

The rate of desorption, R_d from the surface is:

$$R_d = k_d \theta = k_{d\infty} \exp\left(-\frac{E_d}{RT}\right) \theta \quad (4)$$

Where E_d is the activation energy for desorption, that is the heat of adsorption for physically sorbed species and k_d and k_{∞} are constants.

Equating the rates of adsorption and desorption will yield the famous Langmuir isotherm in terms of fractional loading:

$$\theta = \frac{bP}{1 + bP} \quad (5)$$

Where b is Langmuir constant.

$$b = \frac{\alpha \exp(Q/RT)}{k_{d\infty} \sqrt{2\pi MRT}} = b_{\infty} \exp(Q/RT) \quad (6)$$

Where Q is heat of adsorption

When the pressure is very low ($bP \ll 1$), the Langmuir isotherm equation reduces to Henry's law isotherm, that is the amount of adsorbed increases linearly with pressure (Do, 1998).

If experimental data correlation is taken into account, there will be a need for an equation with amount of adsorbed species instead of fractional loading. In order to have a relation between amounts of adsorbed with pressure, let C_{μ} be the amount adsorbed phase μ

in mole per unit mass and $C_{\mu s}$ be the amount adsorbed concentration of phase μ corresponding to a complete monolayer coverage. Then the Langmuir equation written in terms of the amount adsorbed is (Do 1998):

$$C_{\mu} = C_{\mu s} \frac{b(T)P}{1 + b(T)P} \quad (7)$$

where

$$b(T) = b_{\infty} \exp(Q/RT) \quad (8)$$

BET (BRUNAUER, EMMETT AND TELLER) ISOTHERM

The BET theory was first developed by Brunauer et al. (1938) for a flat surface (no curvature) and there is no limit in the number of layers which can be accommodated on the surface. This theory made use of the same assumptions as those used in the Langmuir theory. Let s_0, s_1, s_2 and s_n be the surface areas covered by no layer, one layer, two layer, and n layers of adsorbate molecules, respectively (Do 1998).

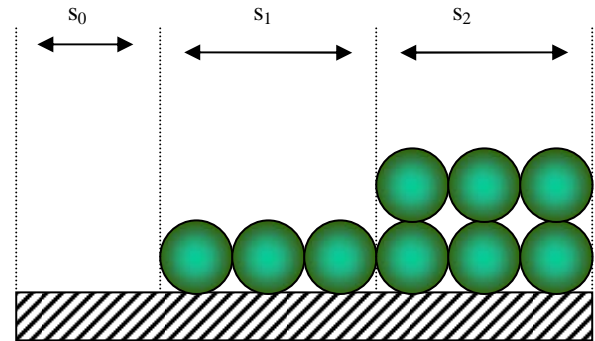


Figure. 2. Schematic Diagram of Multiple layering in BET theory. (Do, 1998)

The concept of kinetics of adsorption and desorption proposed by Langmuir is applied to this multiple layering process, that is the rate of adsorption on any layer is equal to the rate of desorption from that layer (Do 1998). So, in general:

$$A_i P s_{i-1} = b_i s_i \exp(-E_i / RT) \quad (9)$$

The total area of the solid is the sum of all individual areas, that is:

$$S = \sum s_i \quad (10)$$

The volume of gas adsorbed on the section of the surface having "i" layers is:

$$V_i = V_m \left(i \frac{s_i}{S} \right) \quad (11)$$

Hence, the total volume of gas adsorbed at a given pressure is the sum of all these volumes:

$$V = \frac{Vm}{S} \sum_{i=0}^{\infty} i s_i = V_m \frac{\sum_{i=0}^{\infty} i s_i}{\sum_{i=0}^{\infty} s_i} \quad (12)$$

An expression for s_i in terms of gas pressure is needed in order to obtain the amount of gas adsorbed as a function of pressure. Therefore, a further assumption should be made. That is the ratio of the rate constants of the second and higher layers is equal to each other:

$$\frac{b_2}{a_2} = \frac{b_3}{a_3} = \dots = \frac{b_i}{a_i} = g \quad (13)$$

According to Langmuir isotherms, it is assumed that the heat of adsorption of the second and subsequent layers are the same and also equal to the heat of liquefaction, E_L :

$$E_2 = E_3 = \dots = E_i = E_L \quad (14)$$

Therefore, the surface coverage of the section containing i layers of molecules is:

$$s_i = \frac{a_1}{b_1} s_0 g \exp(\varepsilon_1 - \varepsilon_L) \left[\left(\frac{P}{g} \right) \exp \varepsilon_L \right]^i \quad (15)$$

for $i = 2, 3, \dots$, where ε_L is the reduced heat of liquefaction

$$\varepsilon_L = \frac{E_L}{RT} \quad (16)$$

As a result,

$$\frac{V}{Vm} = \frac{Cs_0 \sum_{i=1}^{\infty} i x^i}{s_0 \left(1 + C \sum_{i=1}^{\infty} x^i \right)} \quad (17)$$

where the parameter C and the variable x are defined as follows:

$$y = \frac{a_1}{b_1} P \exp(\varepsilon_1) \quad (18)$$

$$x = \frac{P}{g} \exp(\varepsilon_L) \quad (19)$$

$$C = \frac{y}{x} = \frac{a_1 g}{b_1} e^{(\varepsilon_1 - \varepsilon_L)} \quad (20)$$

The equation then can be simplified in the following form:

$$\frac{V}{Vm} = \frac{Cx}{(1-x)(1-x+Cx)} \quad (21)$$

In order to relate this equation with pressure instead of x , the procedure is as follows:

This model is valid for infinite layers on top of a flat surface. Therefore, the amount adsorbed must be infinity when the gas phase pressure is equal to the vapor pressure, that is $P = P_0$ occurs when $x = 1$. Thus,

$$x = \frac{P}{P_0} \quad (22)$$

$$\text{where } P_0 = g \cdot \exp\left(-\frac{EL}{RT}\right) \quad (23)$$

So, the infamous BET equation containing two fitting parameters C and V_m becomes:

$$\frac{V}{Vm} = \frac{CP}{(P_0 - P)(1 + (C - 1)(P/P_0))} \quad (24)$$

Where P_0 is the vapor pressure.

PRINCIPLES OF THE MODEL

The single pore model is a perfect sphere which has a volume of approximately $329 \mu\text{m}^3$. The pore radius ($4.28 \mu\text{m}$) is a typical average value observed in sandstones. Initially, the pore is saturated with water. Initially water adsorption occurs. The amount of water adsorbed is calculated using the aforementioned Langmuir model. The vapor pressures for the working temperatures (90°C - 130°C) are gathered from literature. The next step is to compute the amount of adsorption due to the CO_2 in presence of water. Thus, CO_2 is introduced into the pore at a fixed rate. It is assumed that CO_2 is completely dissolved in water at the moment it is introduced into the pore. At this stage entire pore is

filled with the CO₂ – water mixture. Therefore, the amount of liquid and gas phase in the pore is known both for the water and the CO₂ – water mixture. It is assumed that BET equations are valid. The vapor pressure of the CO₂ – water solution is computed using Raoult’s equations. In both adsorption stages there are no chemical reactions that will lead to solution and deposition of silica. The final assumption is that the temperature of the pore does not change during the process.

COMPARISON OF THE CALCULATED AMOUNT OF ADSORBED WATER WITH THE EXPERIMENTAL DATA

In this part, the amount of adsorbed water from the literature was compared with the proposed model. The comparison was made with high pressures and temperatures.

Fig. 3 shows the trend of amount of adsorption of water with varying temperatures in a core from the Geysers MLM-3 (Horne et al, 1994). It can be seen that there is a linear behavior below relative pressures of 0.6.

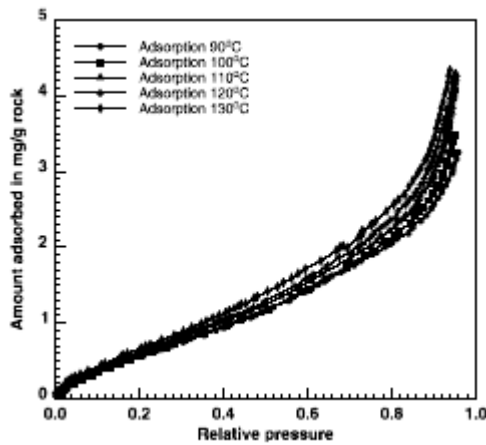


Figure 3: Adsorption Isotherms on Geysers MLM-3 Sample at Different Temperatures (after Horne et al, 1994)

Fig. 4 shows the amount of water adsorbed as a function of relative pressure calculated using the proposed single pore model. The total amount of water adsorbed increases as the temperature increases. This is expected as adsorption is an exothermic process. For relative pressure values below 0.6 the model results also show a linear trend. When the amounts of adsorbed values were compared, a reasonable fit was obtained. There is an error of less than %7 when the experimental data is compared with the proposed method. For relative pressures above 0.6, model adsorption values start to deviate and the error between the computed data and

the experimental data becomes significantly high (more than %25). Moreover, it is observed that when temperature and pressure increase the error becomes higher. This may occur due to the fact that Langmuir type isotherms assume monolayer coverage. However recent results show that at high pressures there may be more than just monolayer coverage (Knight et al.,2005).

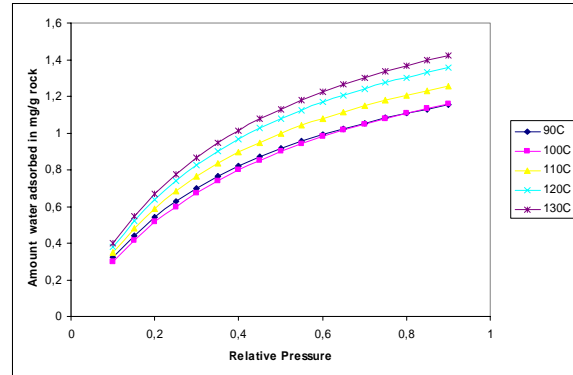


Figure 4: Calculated Adsorption Isotherms for Geysers MLM-3.

CO₂-WATER ADSORPTION

The next step is to investigate adsorption of CO₂ with presence of water since aqueous solutions that contain volatile (gas) components are one of the most important types of fluid in the Earth’s crust (Diamond, 2001). After primary adsorption of water the secondary adsorption of CO₂ in the same pore was investigated. CO₂ mole percent was fixed at 5 and the relative vapor pressure of the mixture was calculated according to this assumption. BET isothermal equations were used to calculate the amount of adsorbed values for both CO₂ and water.

The solubility of CO₂ decreases with rising temperature, but increases sharply with rising pressure up to the saturation pressure and a lesser rate thereafter (Spycher 2003). Qualitatively, the adsorption process of CO₂ follows the same trend. Fig. 5 shows the relationship between pressures ranging between approximately 5kPa to 44.5kPa. In this figure, a linear function up to a relative pressure of 0.2 was observed. But, after that point, there is a rapid increase in the amount of CO₂ adsorption. Since adsorption is an exothermic process, the amount of adsorbed CO₂ increases as the temperature increases.

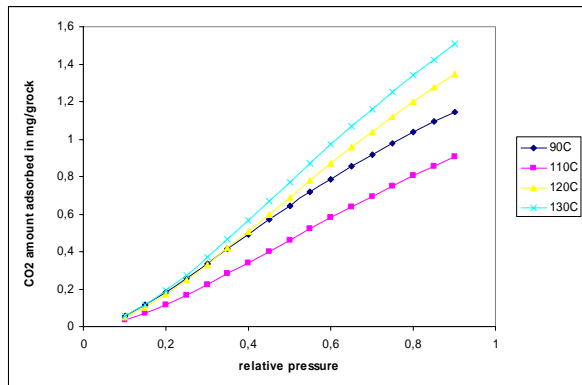


Figure 5: Calculated CO₂ Adsorption isotherms

Fig. 6 shows the comparison of the adsorption tendencies of water and CO₂-water solution at 90°C. It is easily observed that amount of adsorbed water is higher than that of CO₂ at the same temperature and pressure. The major dissimilarity between CO₂ and water adsorption arises from the fact that CO₂ molecules are large and non-polar, whereas H₂O molecules are small and dipolar.

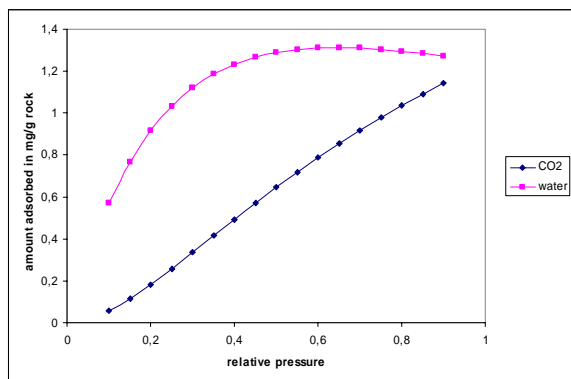


Figure 6: Comparison of adsorbed amounts at 90°C

Although there are dissimilarities between CO₂ and water in their physical properties, both water and the CO₂-water solution isotherms had increasing trends during adsorption processes. Fig. 7 shows the adsorption isotherm calculated at 130°C. When the trends both at 90°C and 130°C were compared, it is observed that both isotherms have the same trend; however, at the same pressures, the liquid amount adsorbed by the rock for the high temperature is more than the low temperature. Moreover, at the same pressures, the liquid amount adsorbed by the rock for secondary adsorption process was less than that of water in the primary adsorption. The adsorption behavior is determined by the ratio of the fluid-wall attractive interaction. For water this ratio is very small, due to the strong hydrogen bonding (H-bonding) between water molecules. (Brennan *et al.* 2001). The rapid increase of adsorbed molecules in mixture at higher pressures is due to the accuracy of

BET equations at higher pressures. This rapid increase is a result of capillary condensation.

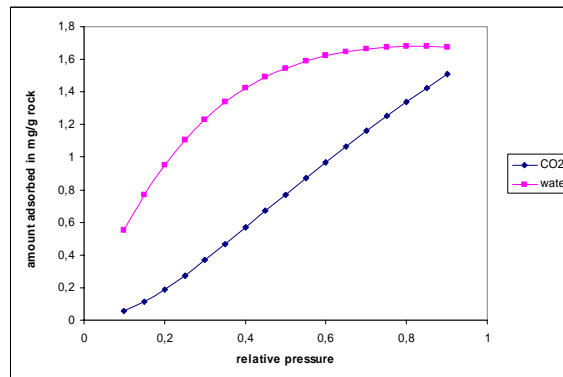


Figure 7: Comparison of adsorbed amounts at 130°C

Critical radius r_c , which is equivalent to the radius of space extended by a steam molecule, r_g , at a given temperature and pressure is a concern to be discussed in an adsorption process. Because of the fact that, this value of radius controls the entrance of the vapor molecule a pore with a radius smaller than r_c can not be filled with the vapor since capillary condensation cannot take place. In order to find out this critical radius, this procedure is used for several pore radii and it is obtained that, within this method the critical pore radius should be as 2.98 μm .

CONCLUSION

In this paper, a simple single pore model, taking advantage of Langmuir and BET isotherms has been presented to calculate the adsorption of water alone and in the presence of carbon dioxide. A comparison of the adsorption of water with the literature data and an approach which deals mainly with the tendency of adsorbed amounts of CO₂-water mixtures towards higher pressures and temperatures is presented. It was observed that for low relative pressures (<0.6) the model agrees well (less than %7) with the published data. For high relative pressures the difference was more than %25. It is concluded that water adsorption is more pronounced in a pore filled with water only when compared to a pore filled with both water and CO₂.

This article has stressed adsorption phenomenon to understand the fluid inclusion behavior and to interpret adsorption properties of water and carbon-dioxide. One of the keys to extracting this information lies in understanding the phase relations of the relevant fluid systems.

REFERENCES

- Al-Gharbi, Mohammed, S., Blunt, Martin, J., (2003): "A 2D dynamic pore network model for modeling primary drainage" Proceedings of the ESF Workshop on Recent Advances in Multiphase Flow and Transport in Porous Media, European Science Foundation, Delft.
- Blunt, Martin, J., (2001): "Flow in porous media--pore-network models and multiphase flow", Current Opinion in Colloid & Interface Science 6, pp.197-207.
- Brennan, John, K., Bandosz, Teresa, Thomson, Kendall, T., Gubbins, Keith, E., (2001): "Water in porous carbons", Colloids and Surfaces A: Physicochemical and Engineering Aspects 187-188, 539-568.
- Busch, A., Kross, B.M., Gensterblum, Y., van Bergen, F., Pagnier, H.J.M.(2003): "High-pressure adsorption of methane, carbon dioxide and their mixtures on coals with a special focus on the preferential sorption behavior", Journal of Geochemical Exploration 78-79, pp. 671-674.
- Crittenden, Barry and Thomas, W., John, Adsorption Technology & Design (1998), pp.1-7.
- Diamond, Larry, W., (2001): "Review of the systematics of CO₂-H₂O fluid inclusions", Lithos 55, pp. 69-99.
- Do, D., Duong (1998): "Adsorption Analysis: Equilibria and Kinetics".
- Do, D., Hu, X., and Mayfield, P., L., J., (1991) : "Multi-component adsorption of ethane, n-butane and n-pentane in activated carbon", Gas Separation & Purification, Vol. 5, Issue 1 , pp. 35-48.
- Fenwick, Darryl, H., Blunt, Martin, J., (1997): "Use of Network Modeling to Predict Saturation Paths, Relative Permeabilities and Oil Recovery for Three Phase Flow in Porous Media", SPE
- Hoory, S.E., and Prausnitz, J.M. (1967): "Molecular Thermodynamics of Monolayer Gas Adsorption on Homogeneous and Heterogeneous Solid Surfaces", Chemical Eng. Symposium, vol. 63.
- Horne, R.N., Ramey, H.J.Jr., Shang, S., Correa, A., Hornbrook, J.: "Improving Models of Vapor-Dominated Geothermal Fields: The Effects of Adsorption", New Zealand Geothermal Workshop, November (1994).
- Knight, A., Hauser, R., Oshier, J.: "Gas Adsorption" Chem. 4411L. , http://itl.chem.ufl.edu/4411L_f00/ads/sample/knight.html, Accessed on 24.01.2005
- Lucas, S., Calvo, M.P., Palencia, C., Cocero, M.J., (2004): "Mathematical model of supercritical CO₂ adsorption on activated carbon Effect of operating conditions and adsorption scale-up", J. of Supercritical Fluids 32 , pp. 193–201
- Masel, I., Richard, Principles of Adsorption and Reaction on Solid Surfaces, (1996), pp.108-122.
- Oren, P. E., Bakke, S., (1997): "Extending Predictive Capabilities to Network Models, SPE
- Spycher, Nicolas, Pruess, Karsten, and Ennis-King, Jonathan, (2003): "CO₂-H₂O mixtures in the geological sequestration of CO₂. I. Assessment and calculation of mutual solubilities from 12 to 100C and up to 600bar", Geochimica et Cosmochimica Acta, Vol 67, No. 16, pp.3015-3031.
- Zhou HS, Zhu SM, Honma I, Seki K, (2004): "Methane gas storage in self-ordered mesoporous carbon (CMK-3)", Chemical Physics Letters, 396 (4-6), pp. 252-255.

Field Studies

Geothermal Exploration at Fort Bidwell, California	<u>101</u>
<i>Ben Barker, Mack Kennedy, Mike Hoversten, M.C. van Soest and Ken Williams</i>	
Infrared Spectroscopy for Drillhole Lithology and Mineralogy	<u>106</u>
<i>Wendy M. Calvin, Chris Kratt, and Jim Faulds</i>	
Comparison of Acoustic and Electrical Image Logs from the Coso Geothermal Field, CA	<u>111</u>
<i>Nicholas C. Davatzes, Steve Hickman</i>	
Analysis of Workover Techniques in Geothermal Wells of Cerro Prieto Field, Mexico	<u>122</u>
<i>Juan De Dios Ocampo-Díaz, Jaime E. Vaca Serrano</i>	
Lessons Learned in Drilling DB-1 and DB-2, Blue Mountain, Nevada	<u>129</u>
<i>Susan Petty, Brian Fairbank, and Stephen Bauer</i>	
A Preliminary Evaluation of the Convective Energy Escaping from Hydrothermal Submarine Chimneys	<u>136</u>
<i>Mario César Suárez-Arriaga and Fernando Samaniego V.</i>	

GEOTHERMAL EXPLORATION AT FORT BIDWELL, CALIFORNIA

Ben Barker¹, Mack Kennedy², Mike Hoversten³, M.C. van Soest⁴ and Ken Williams⁵

¹Consultant, 237 Dartmouth Way, Windsor, CA 95492 USA

^{2,4}Center for Isotope Geochemistry, Lawrence Berkeley National Laboratory, Berkeley, CA 94720

^{3,5}Energy Resources Program, Lawrence Berkeley National Laboratory, Berkeley Ca, 94720

¹benbarker@earthlink.net; ²bmkenney@lbl.gov; ³gmhoversten@lbl.gov; ⁴mcvansoest@lbl.gov; ⁵khwilliams@lbl.gov

ABSTRACT

Preliminary geochemical and geophysical exploration has begun at the Fort Bidwell Indian Reservation (FBIR) which will lead to siting a 1500 m slim exploration well in the summer of 2005. Unusually enriched helium isotope values, geothermometry in nearby gradient wells and encouraging results from time-delay SP surveys are favorable indicators in the work to date.

BACKGROUND

The Gidutikad Band of the Northern Paiute, known as the Fort Bidwell Indian Community (FBIC), resides in the extreme northeast corner of California. This area, now known as the Fort Bidwell Indian Reservation, was established in 1866 as a military outpost to subdue the Paiute people. The Reservation is situated within the Tribe's aboriginal territory in Modoc County, 12 miles south and east of the Oregon and Nevada borders.

The FBIR lies on the high-desert, eastern slopes of the 10,000 ft Warner Mountain Range. It is bordered by the Modoc National Forest to the west, private ranch land to the north and south and the town of Fort Bidwell to the east. FBIR land totals 3,543 acres, about 2,600 of which are forested with stands of fir, pine and cedar at elevations ranging from 5,000 to 8,000 ft.

Like many rural communities, the FBIR suffers from a lack of local job opportunities, a lack of basic facilities (e.g., grocery and gasoline) and a declining population. The FBIC's unemployment and poverty rates are estimated by Federal agencies to be more than three times the national average for Indian Reservations. The tribal leadership has identified sustainable development of FBIR's natural resources as its preferred path of economic development, with

geothermal resources having a high priority. In June, 2004 the Tribal Council approved an application to the DOE's GRED III program for the project that is the subject of this report.

PRIOR EXPLORATION

Fort Bidwell is at the north end of Surprise Valley and has very little surface expression of the geothermal system beneath. A single natural hot spring is on a ranch north of the reservation. Shortly after the fort was established a hot water well was drilled to supply the soldiers' domestic needs. The rusted end of the well casing is still exposed and flow from it supplies a small bathing pool known as the reservation hot spring.

Geothermal direct use and small hydroelectric generation projects on the reservation were supported in the early 1980's by the California Energy Commission (CEC) with some success. Three wells were drilled and tested with modern equipment and the data from them tells a lot about the shallow aquifers. The wells were also planned to provide deeper temperature gradient information, and the third well, FB-3, provides very useful indications of deeper conditions.

The flow rates and geochemistry found in the wells drilled with CEC support are listed in Table 1. Well FB-1 is located near the reservation hot spring and produces substantially the same fluid as that issuing from the remains of the soldiers' well. The composition of the FB-2 fluid was reportedly more similar to that of the natural hot spring north of the reservation (Juncal, 1984). These results are consistent with a model of near-surface mixing of fresh water from precipitation in the Warner Range to the west and upwelling geothermal waters from a deep fault zone.

Table 1: Properties of 1981-1985 Wells

Well		FB-1	FB-2	FB-3
Completion data				
(m)	depth	155	396	890
(l/s)	flow rate	28	50	25
(C)	flow temp.	46.7	35.6	92.2
Water analysis				
(mg/l)	sodium	108	66	326
	potassium	9	6	8.55
	calcium	21	7	14
	magnesium	0.6	<0.49	0.05
	silica	91	76	138
	bicarbonate	68	133	184
	sulfate	84	35	370
	chloride	36	17	203
	TDS	348	250	1075
Geothermometry				
(C)	Na-K-Ca	n/a	n/a	143
(C)	chalcedony	105	94	132

Well FB-3 was fortuitously drilled deep enough to confirm the existence of a subhorizontal outflow from a significantly hotter source. FB-3 encountered an artesian flow of approximately 25 l/s (400 gpm) with a flowing temperature of 92 C (198°F). The inflow zone extends from 654 to 732 m depth, emitting from a layer of volcanic cinders. The maximum temperature was measured at 710 m and this was followed by a temperature reversal of 10 C in the next 100 m. The geothermometry indicates a temperature of at least 92 C, sufficient to consider binary electric generation technology.

CURRENT PROJECT PLANS

The project objectives as approved by the DOE under GRED III are divided into three phases.

- Phase I: Conduct geothermal exploration and evaluate the preliminary geologic model to assess the validity of the targeted drillsite on the FBIR and select an optimum drilling location. Conduct environmental field surveys, and agency consultations. Conduct environmental review and obtain permits for the well scheduled to be drilled in Phase II and tested in Phase III.
- Phase II: Drill a slim-hole geothermal well and perform preliminary testing.
- Phase III: Conduct testing to demonstrate commercial potential of the resource.

The contract between DOE and FBIC was signed at the end of September 2004. This allowed time for some preliminary work on Phase 1 before snow halted operations. The major geophysical work,

including a CSAMT survey, will be done when the ground clears in 2005.

Initial wellhead inspections of FB-1, -2 and -3 were conducted in early October 2004. Wellhead vandalism had been reported at FB-3 and the condition of all three wells' valves was unknown, so equipment was not mobilized for any extended flow. The wellhead valves were serviced as necessary for fluid sampling. In early November each well was produced long enough to obtain samples of formation fluids and record stable temperatures.

All three wells showed flow rates and temperatures near those reported in the 1980's. A modest amount of plumbing would be required for extended production, as in a time-delay SP survey or tracer test, but no major obstacles were found.

During the October inspection a self-potential (SP) survey that yielded interesting results was run in the vicinity of FB-3. Helium isotope analysis of the fluid samples also produced unusual results. The progress of field work and the survey results are very encouraging and will be discussed in turn.

SP Surveys

SP survey lines were run by LBL geophysicists on the same day as the FB-3 inspection in hopes the well could be produced, as it was. The locations of the survey lines are indicated by the lines of flags on Figure 1. Lines 1 and 2 were run from South-west to North-east with station 0 being the first station. Well FB-3 was opened approximately 12 minutes after SP measurements began. The well flowed continuously for the first 19 minutes and for several intervals thereafter. Over a total period of two hours and 38 minutes the well produced at full capacity for 57 minutes and at about one-third capacity for 15 minutes.

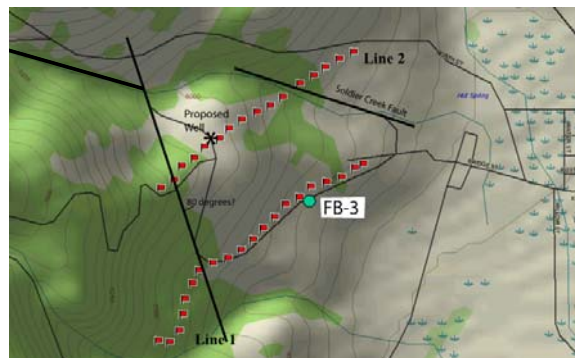


Figure 1: Site map for SP flow test.

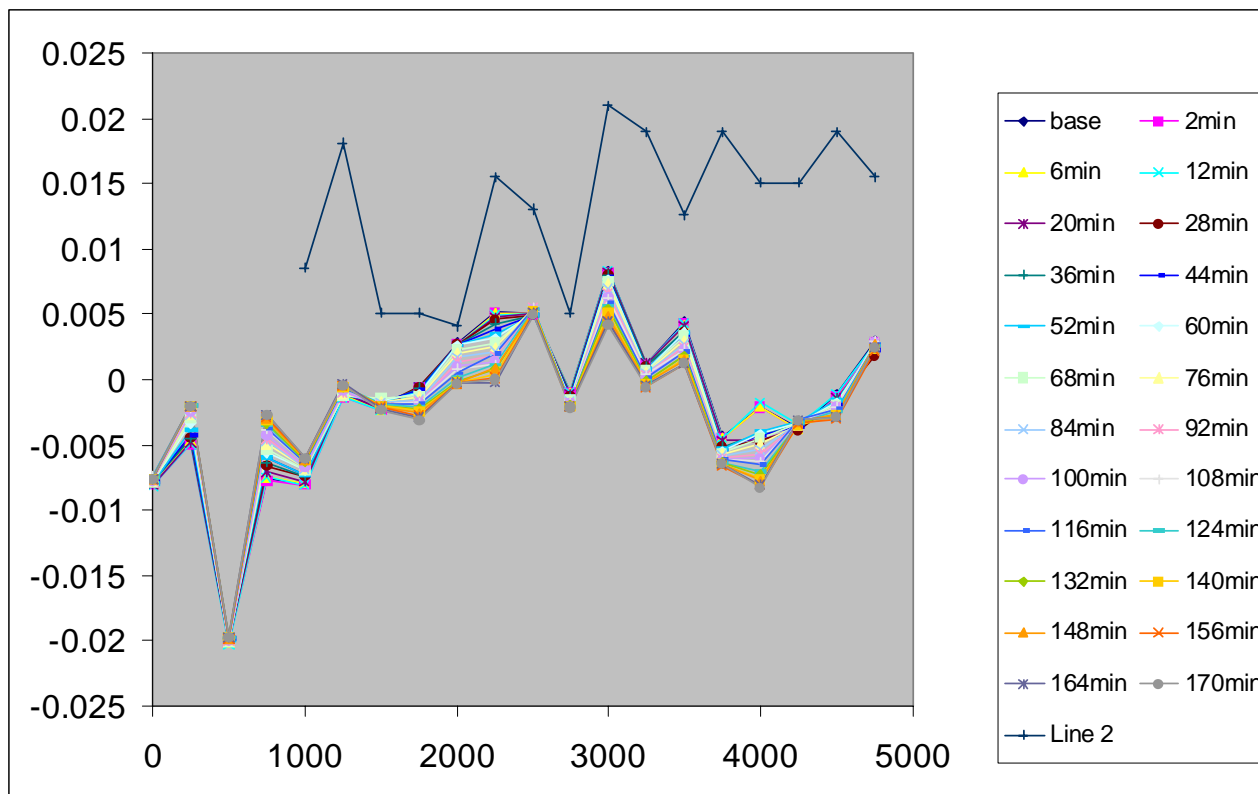


Figure 2: SP signal measured on Line 1 at time intervals shown in legend. FB-3 began flowing at 12 minutes into the SP measurements.

Figure 2 shows the voltage measured on SP line # 1. There are two areas of large deviation as a function of time. The first occurs between sites 7 and 11 and the second between sites 16 and 18. A major north-west to south-east fault is mapped between sites 7 and 8 and the well location is between sites 15 and 16. This preliminary data indicates that time-lapse SP measurements have the potential to map the spatial location of subsurface pathways that act as fluid conduits.

The plan for future work is to lay out a surface array of SP lines that covers the prospective area. With this array in place, measurements will be made for a week or so prior to any well flowing to establish a baseline for the time-varying SP signals. In addition, a monitoring magnetotelluric station will be set up to at some distance from the site to measure the electric fields induced by the MT signal.

Once the base line data is acquired the array will be monitored during a controlled set of well production periods. The test periods will be structured so that FB-3 creates a pre-defined flow signal. This signal will consist of a series of on-off flow periods with variable duration of the on and off intervals. This will allow time-series analysis of the SP data to extract signals in the SP data that correlate with the flow pattern and help to reduce the SP signal that is

not related to flow. The processed SP data will be used to interpret the flow pathways in the geothermal system at depth.

Helium Isotopes at Fort Bidwell

Water and gas samples were collected from FB-1, -2 and -3 and from the reservation hot spring during the October and November 2004 flow periods. They were analyzed for helium isotopes at the Center for Isotope Geochemistry, Lawrence Berkeley National Laboratory.

The Fort Bidwell geothermal resource appears to be a typical Basin and Range (B&R) style occurrence where deep circulation of fluids along a range front fault with large offset provides a conduit for the delivery of heat- and mantle-derived volatiles to the surface. Figure 3 shows the topography of the Fort Bidwell – Cedarville area with sampling points indicated. The presence of geothermal fluids at the surface in the Lake City area south of Fort Bidwell confirms that the range front fault along the east edge of the Warner Mountains acts as a permeable pathway for such fluids. More hot springs occur along this fault further to the south of Cedarville, while several can also be found along the east side of the Surprise Valley as indicated by the red dots on Figure 3.

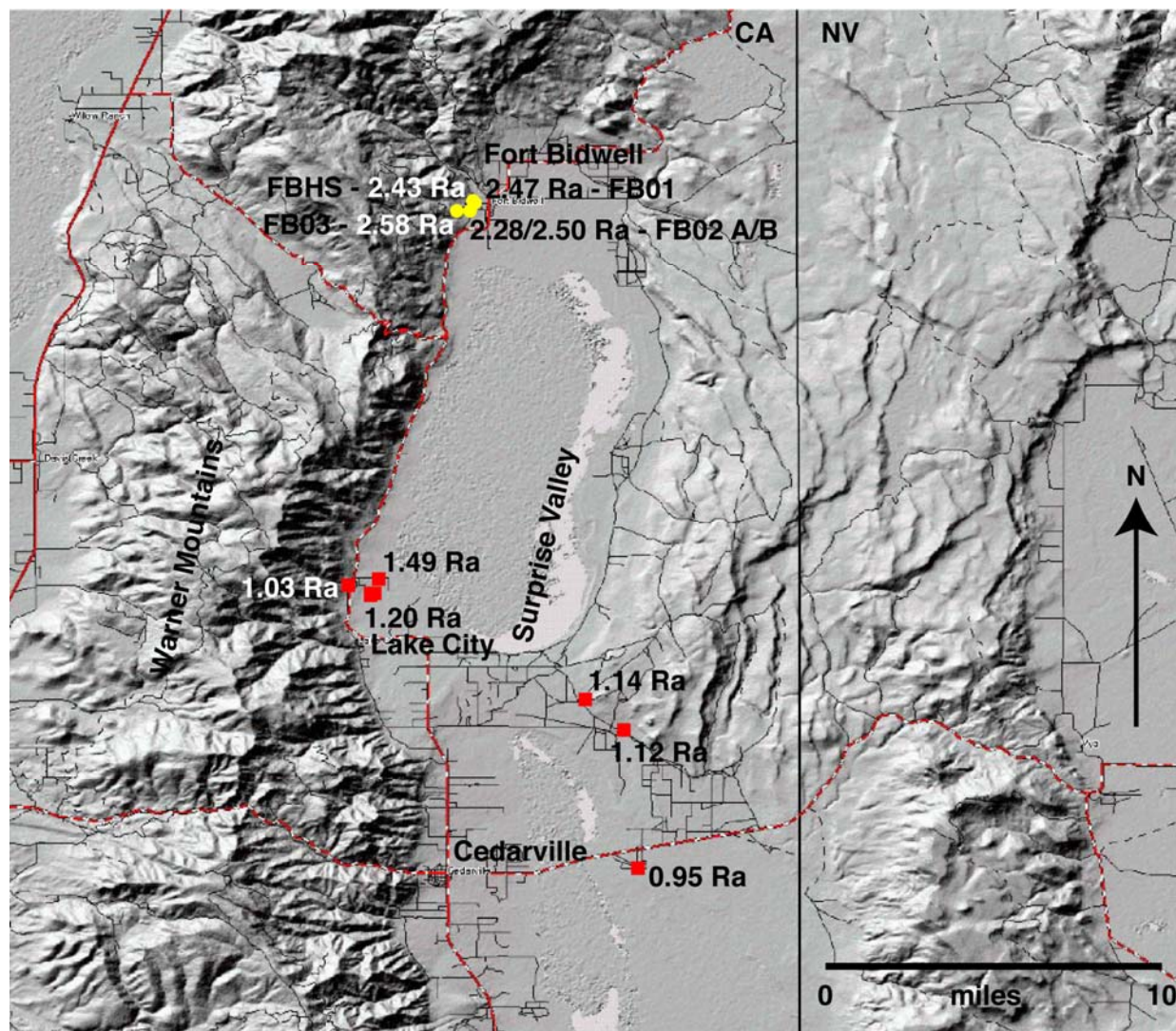


Figure 3: Relief map of Fort Bidwell and surrounding areas. Dots represent wells and springs sampled in this project; numbers are measured helium isotopic ratios (normalized to air, Ra).

Helium isotope results for the Fort Bidwell geothermal resource range from 2.28 Ra to 2.58 Ra (where Ra is the $^3\text{He}/^4\text{He}$ ratio in the atmosphere). These are the highest ratios observed to date in the B&R for what is believed to be a non-magma hosted geothermal resource. The Fort Bidwell area really stands out in comparison to the Lake City/ Surprise Valley area and to Dixie Valley. Lake City is about 22 km directly south of Ft. Bidwell and is characterized by R values of 0.95 to 1.49 Ra. The Dixie Valley system is 300 km southeast of Fort Bidwell and shows maximum ratios of 0.86 Ra (Kennedy and Van Soest, 2005).

There is also a trend of increasing mantle influence from south (Surprise Valley) to north (Ft. Bidwell), as shown by Figure 4 on the following page. It is

evident that all of the sampled geothermal features conform to the mantle-crust mixing model, except for a few which appear to be strongly influenced either by air contamination or air saturated water (ASW).

We do not have sufficient information to assess whether the higher helium isotope ratios at Ft. Bidwell reflect recent volcanism and, perhaps, the presence of a small shallow magma chamber or, more likely, the range front fault serves as a highly permeable fast path for the transport of heat and mantle volatiles from deep crust and/or mantle to the near surface (e.g., Kennedy and van Soest, 2005).

Either possibility bodes well for success of the planned well FB-4 if the upflow zone can be identified.

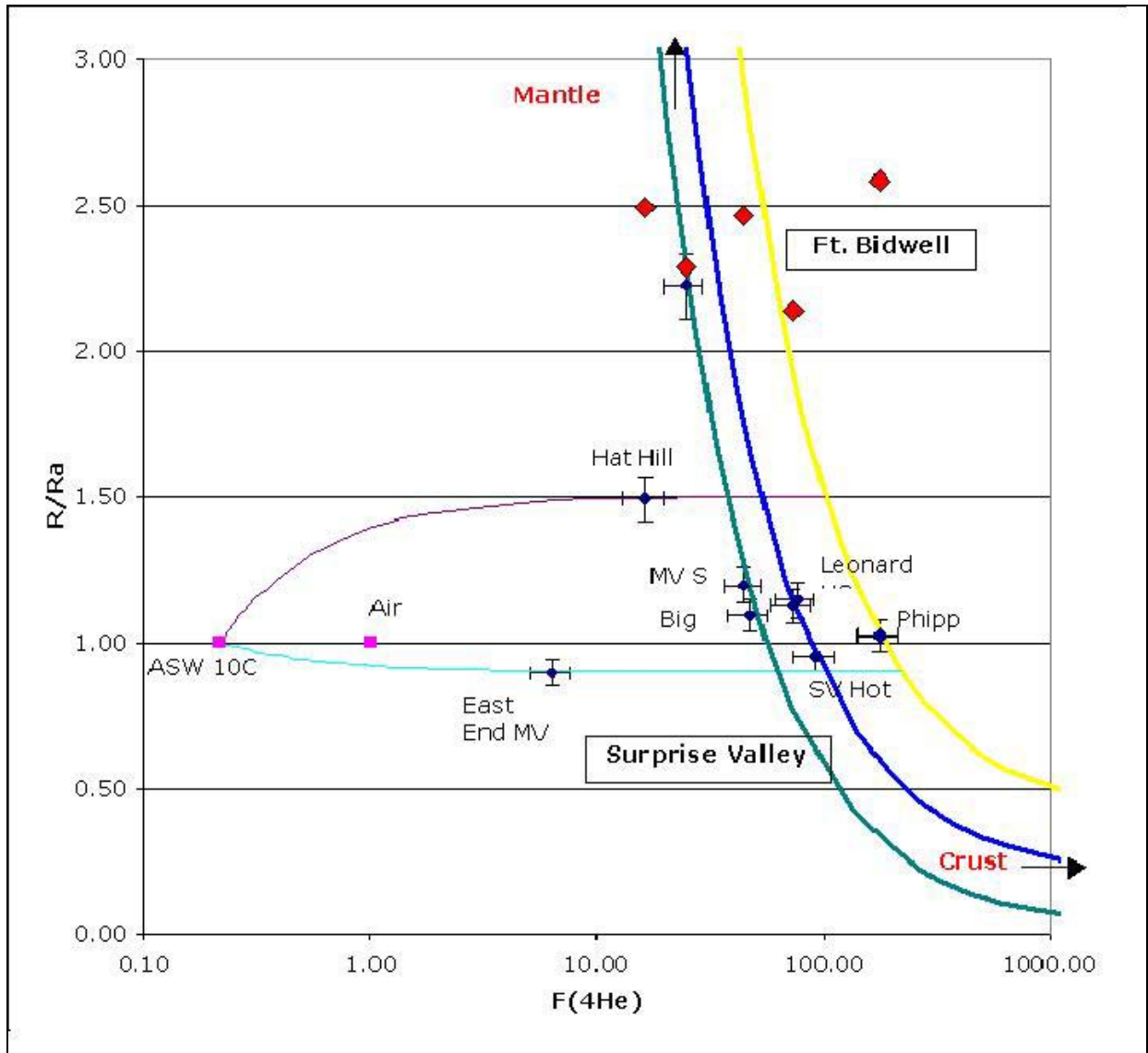


Figure 4: Helium isotopic compositions (R/R_a) plotted as a function of ^4He enrichment factors [$F(^4\text{He})$ refers to the $^4\text{He}/^{36}\text{Ar}$ ratio normalized to the ratio in air]. The Ft. Bidwell data are shown as red diamonds; the other data points are features to the south of the Ft. Bidwell area and predominately are from Surprise Valley. The Green, Blue, and Yellow lines are mixing lines between mantle and crustal end-member compositions.

ACKNOWLEDGEMENTS

The authors and the Fort Bidwell project team led by Joe LaFleur, P.I., gratefully acknowledge the support of the people of the FBIC and the Department of Energy under Contract No. DE-FC36-04GO14343. For this work Mack Kennedy and Thijs van Soest were supported by the U. S. Department of Energy, Office of Basic Energy Sciences and Office of Geothermal Technologies under Contract No. DE-AC03-76SF00098. The work of Mike Hoversten and Ken Williams was supported by the Assistant Secretary for Energy Efficiency and Renewable Energy, Office of Geothermal Technologies, of the

U.S. Department of Energy under Contract No. DE-AC03-76SF00098.

REFERENCES

- Juncal, R.W. (1984), "Technical Summary, Drilling and Testing of Exploratory Well FB-2," Fort Bidwell Indian Community Council report (049-9014).
- Kennedy, B.M. and van Soest, M.C., (2005), "A helium isotope perspective on the Dixie Valley, Nevada hydrothermal system," Submitted to *Geothermics*.

INFRARED SPECTROSCOPY FOR DRILLHOLE LITHOLOGY AND MINERALOGY

Wendy M. Calvin, Chris Kratt, and James E. Faulds

Geological Sciences, and the Great Basin Center for Geothermal Research
University of Nevada – Reno, MS 172
Reno, NV, 89557 USA
e-mail: wcalvin@unr.edu

ABSTRACT

Infrared spectroscopy has been used to identify rocks and minerals for over 30 years. The technique is sensitive to primary silicates as well as alteration products. Minerals can be uniquely identified based on multiple absorption features in reflected and emitted radiation. We are currently establishing methods and protocols in order to use the technique for rapid assessment of downhole lithology during drilling operations. Initial work performed includes spectral analysis of both chip cuttings and core sections from drill sites around Desert Peak, NV. We have recently performed laboratory measurements of 17 core sections from a variety of additional holes to examine spectral variability of ash-flow tuffs. We will describe the utility of the technique for lithologic and mineralogic discrimination as well as field methods that can be employed during drilling operations.

INTRODUCTION

Optical and infrared spectroscopy has been used since the 1960's to identify specific rocks and minerals (e.g. Farmer, 1974; Hunt, 1977). The technique hinges on the interaction of light with geologic materials that absorb specific wavelengths creating a fingerprint signature. The resulting spectrum contains information on both the primary elemental composition as well as crystallographic coordination. At shorter wavelengths, the optical and infrared (0.4 to ~ 2.5 μm), the resulting spectrum is most sensitive to iron (oxides, oxyhydroxides) and alteration cations (water, hydroxyl, carbonate) (e.g. Clark, 1999; Gaffey, 1997). In the infrared (5 to 50 μm) absorption features from various classes of silicates are apparent (Hook et al., 1999; Christensen et al., 2000). Instruments have been developed so the spectra of samples can be quickly and directly measured in the field, as well as in the lab (e.g. <http://www.asdi.com>; Korb et al., 1996).

APPLICATION TO DRILL HOLE SAMPLES

A number of geophysical techniques are used to characterize the borehole. Geologic typing is often carried out via quick assessment in the field and core sections or chips are logged as a function of depth. As many rocks are difficult to identify in hand sample, core samples are often warehoused for later detailed analysis using thin sections and petrographic microscope as well as XRD techniques. These tools are time consuming and require extensive sample preparation. We often use infrared spectroscopy as a tool for quick mineralogic assessment in the field and we undertook a pilot study to establish the utility of the technique for rapid assessment of samples for parameters of particular interest to the Geothermal Energy community. Of interest would be (a) quick analysis of lithology and geologic units related to those expressed at the surface, (b) identification of hydrothermal alteration zones and silicification, (c) identification of the presence of swelling clays (smectites, bentonite, i.e. montmorillonite and illite) at depth, (d) identify specific alteration minerals that may be used as rough geothermometers, or (e) correlate individual stratigraphic units separated by faults.

METHODS

For this "proof of concept" phase we made measurements of two types of drill hole products. Chip boards housed at the University of Utah, from the Desert Peak hole DP 23-1, covering 3000m down hole were measured in one afternoon. That analysis was described by Kratt et al. (2004). In summary, although there was some interference from the glue holding the chip samples onto the boards we were able to identify large alteration zones consistent with previous detailed analysis by Lutz (2003). We also have access to drill core samples from other holes in the Brady-Desert Peak geothermal fields but wanted to do a preliminary analysis of the best wavelength range to discriminate ash-flow tuff units that have been used as marker beds in geologic field mapping. The ability to correlate strata offset by faults allows

determinations to be made about the timing of tectonic events and the amount of offset. This is particularly true for ash-flow tuffs with potassium-argon dates (Faulds and Garside, 2003). This report describes the analysis of 17 core pieces for use in relating geologic structure across fault zones.

Samples

Initial analysis focused on samples from six different drill holes in the Bradys/Desert Peak region. Cores from holes BCH--2, --3, --5, --8, and --10 as well as hole 35--13 were measured. All of our samples come from volcanic strata that were subjected Cenozoic normal faulting. These include 3 fine-grained basalts with varying degrees of alteration, and the remaining samples from ash-flow tuff units, varying in degree of alteration, crystal content, and lithic fragments. Figure 1 illustrates the general visual variation of the cores.



Figure 1. Photo of representative core samples. Keys for scale.

Measurements

The samples were measured using an Analytical Spectral Devices (ASD) spectrometer using a small halogen source and a white halon calibration panel for correction to absolute reflectance. This instrument provides spectra from 0.4 to ~ 2.5 μm and is analogous to standard laboratory techniques for this wavelength range (e.g. Clark et al., 1990). The samples were also taken to the reflectance lab of the Earth Remote Sensing group at the Jet Propulsion Lab for measurement from 2 to 15 μm . In this set-up a Fourier Transform Infrared Spectrometer (FTIR) system is used and the samples are measured in reflectance relative to a diffuse gold plate and using an integrating sphere (e.g. Salisbury et al., 1994). This longer wavelength range provides information on the primary silicate phases as the Si-O fundamental vibration occurs near 10 μm and absorption features vary strongly with tetrahedral coordination.

RESULTS

Table 1 (following the References) summarizes the data by core hole and sample number. The table includes a brief geologic description of the hand sample inferred by eye under a hand lens, and the major features observed in both the short wavelength region (ASD) and longer wavelengths (FTIR). This initial assessment provides a quick view of the bulk constituents of the samples. More detailed analysis that focuses on minor and/or weak contributions to the spectra is ongoing.

The majority of the samples exhibit very similar spectral characteristics in both ASD and FTIR spectra. Figures 2 and 3 show the main spectral character of these samples. At shorter wavelengths the spectra are dominated by a strong downward slope, beginning approximately 0.8 μm . This is typical for basaltic samples, although the albedo of the tuffs is typically brighter than most basalts. Features are evident at 1.4, 1.9, and 2.2 μm that are characteristic of some alteration to clay minerals, especially montmorillonite, muscovite, or illite. The stronger the features the more alteration to clay minerals has occurred. Slope variations below 0.8 μm may be due in part to the geometry of the source illumination.

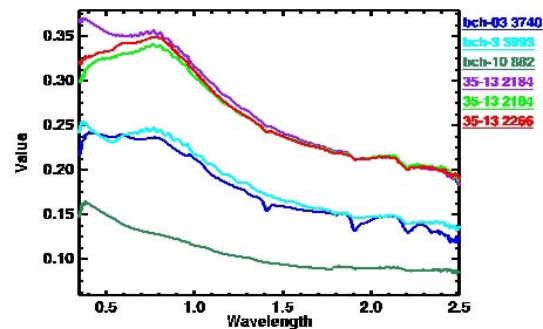


Figure 2. Spectra of typical samples from the ASD instrument. Features at 1.4, 1.9, and 2.2 μm suggest varying levels of clay alteration.

In the infrared, these same samples again show varying contributions from clay, exhibited now by a narrow peak near 9.3 μm (Fig. 3). This feature matches well with montmorillonite. The FTIR spectra also show clear evidence of quartz in these samples, by the absorption edge near 8 μm , by an extremely narrow, well-defined absorption at 8.6 μm , and twin peaks between 12 and 13 μm . All these samples have broad wings from 10 to 12 μm . These wings vary in width. Amphiboles, pyroxenes and potentially biotite can contribute to the shape of this wing. The samples do not show unique, narrow

features that would help discriminate among these additional potential silicates. Detailed modeling of the spectra can be performed and yield better estimates of contributions from other minor constituents (e.g. Ramsey and Christensen, 1998) and will be the subject of future analysis.

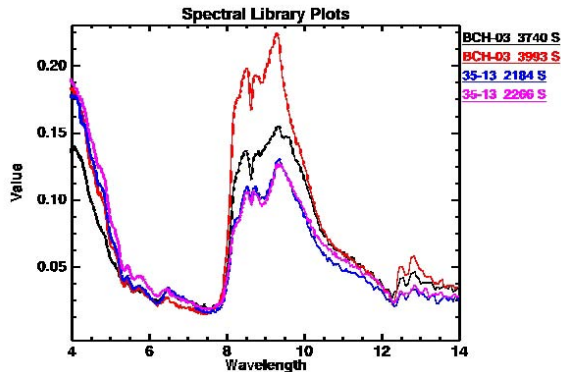


Figure 3. Spectra of typical samples from the FTIR instrument. The peak near 9.3 μm is associated with clays, especially montmorillonite and the very narrow absorption at 8.6 μm is due to quartz.

Additionally, a few samples show a shift in the clay peak to slightly longer wavelengths in the FTIR spectra. This is well matched by saponite from the mineral libraries, but not by either biotite or muscovite as might be expected based on the ASD spectra. Assignment of these features is still preliminary.

Two samples, BCH-03 4065 and 35-13 1947, showed very unique spectra in the optical and near infrared (Figure 4). However, their FTIR spectra are quite different, largely due to the stronger presence of quartz features in the spectrum of BCH-03 4065 (Figure 5). These spectra are consistent with either amphiboles and/or iron layer silicates such as chlorite or antigorite.

Only one sample, BCH-08 447, showed the diagnostic spectral features of carbonate. This was true for both the ASD and the FTIR spectra (Figure 6), and this sample shows almost no other features in either spectrum. Subtle band shifts are identified with cation substitution and the well-defined absorption and peak centers identify this sample as calcite dominated.

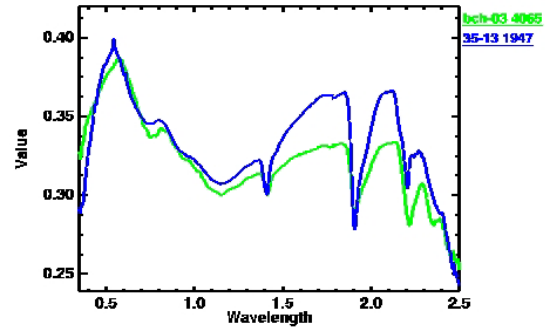


Figure 4. ASD spectra of two samples showing unique optical and near-infrared spectral character due to either amphiboles or iron bearing serpentine minerals.

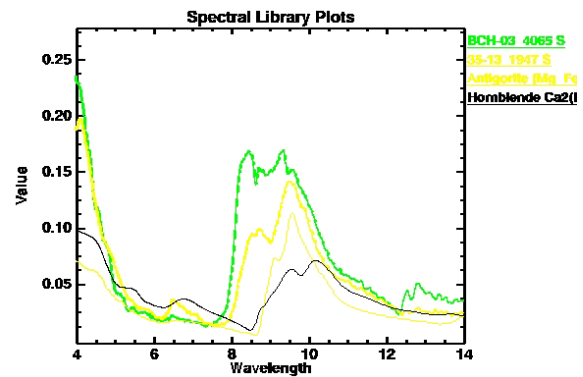


Figure 5. FTIR spectra of BCH-03 4065 and 35-13 1947, corresponding to Figure 4. These are compared with hornblende and antigorite from the JHU mineral library.

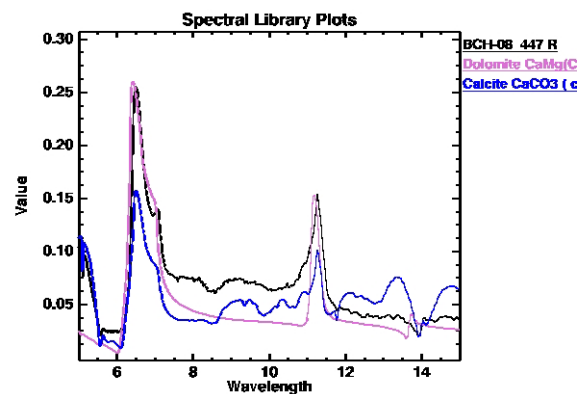


Figure 6. Sample BCH-08 447 (black line) is clearly identified as calcite when compared with library spectra of dolomite (purple) and calcite (blue).

SUMMARY

Infrared spectroscopy can identify both broad mineral similarities and differences among core hole samples rapidly and without extensive sample preparation. The technique shows promise for use in the field to quickly identify geologic and lithologic changes down hole. The technique is especially useful for identifying alteration zones and degree of alteration as well as correlating stratigraphy across fault zones.

Future work will emphasize detailed mineralogic identification of existing samples and pilot studies during actual field operations. Our ASD instrument is fully portable and can be run on battery power enabling spectral measurements at remote field sites. Chip or core samples can be monitored quickly during drilling operations to assist geologists in sample identification and characterization.

REFERENCES

- Christensen, P.R. et al. (2000) A thermal emission spectral library of rock-forming minerals. *Journal of Geophysical Research*, **105** (E4), 9735—9739.
- Clark, R.N. (1999) Spectroscopy of Rocks and Minerals and Principles of Spectroscopy. In *Remote Sensing for the Earth Sciences*, Manual of Remote Sensing, 3rd Edition, Vol. 3, Chapter 1.
- Clark, R.N., King, T.V.V., Klejwa, M., Swayze, G.A., and Vergo, N. (1990) High spectral resolution reflectance spectroscopy of minerals. *Journal of Geophysical Research*, **95** (B8), 12653—12680.
- Gaffey, S.J., McFadden, L.A., Nash, D. and Pieters, C.M. (1997) Ultraviolet, visible, and near-infrared reflectance spectroscopy: laboratory spectra of geologic materials. In *Remote Geochemical Analysis: Elemental and Mineralogical Composition*, Ch. 3, pp. 43-77.
- Faulds, J.E., and Garside, L.J. (2003) Preliminary geologic map of the Desert Peak-Brady geothermal fields, Churchill County, Nevada: Nevada Bureau of Mines and Geology Open-File Report 03-27.
- Farmer, V.C. Ed., (1974) *The Infrared Spectra of Minerals*. Mineralogical Society Monograph 4.
- Hook, S.J., Abbot, E.A., Grove, C., Kahle, A.B., Palluconi, F. (1999) Use of multispectral thermal infrared data in geological studies. In *Remote Sensing for the Earth Sciences*, Manual of Remote Sensing, 3rd Edition, Vol. 3, Chapter 2.
- Hunt, G. H. (1977) Spectral signatures of particulate minerals in the visible and near-infrared. *Geophysics*, **42**, no. 3, 501-513.
- Kratt, C., Calvin, W., and Lutz, S. (2004) Spectral Analyses of Well Cuttings from Drillhole DP23-1, Desert Peak EGS area, Nevada – preliminary study of minerals and lithologies by infrared spectrometry, GRC, Transactions, vol 28.
- Korb, A.R., Dybwad, P., Wadsworth, W., and Salisbury, J.W. (1996) Portable FTIR spectroradiometer for field measurements of radiance and emissivity. *Applied Optics*, **35**, 1679—1692.
- Lutz, S.J. (2003) Petrographic and X-Ray diffraction analyses of samples from corehole 35-13TCH and drillhole B23-1, Desert Peak Geothermal Field, Nevada: Report prepared for ORMAT Nevada Inc. under DOE Contract DE-FC07-02ID14406.
- Ramsey, M.S. and Christensen, P.R. (1998) Mineral abundance determination: quantitative deconvolution of thermal emission spectra. *Journal of Geophysical Research*, **103** (B1), 577—596.
- Salisbury, J.W., Wald, A., and D’Aria, D.M. (1994) Thermal infrared remote sensing and Kirchoff’s law I: Laboratory measurements, *Journal Geophysical Research*, **99** (B6), 11897—11911.

Table 1: Core samples from Bradys/Desert Peak. Brief description of hand samples and major spectral features.

Core name and depth	Brief Description	ASD		FTIR	
		Avg Albedo	Major Features	Reflectance Peak	Major Features
BCH-2, 2450'	Ash-flow tuff, light maroon/grey/green, rich in a variety of lithics, up to 2cm, minor quartz veining, some sanidine	0.29	Lots of structure. Curious spectrum in NIR. 0.7, 0.93, 1.16 features. Narrow 1.4. Large 1.9, 2.2; shoulder at 2.25, narrow 2.35, weak 1.8	0.18	Quartz + clay, secondary shoulder at 9.0um.
BCH-2, 3850'	Ash-flow tuff, light grey/maroon/green, rich in sanidine, up to 3mm	0.12	Large slope down. Modest 1.9, 2.2. Weak 1.4.	0.18	Strong quartz, broad wing 10 to 12um.
BCH-2, 3950'	Ash-flow tuff, light maroon, flamme rich, some lithics up 1cm	0.14	strong Iron oxide edge - strong 0.5, peak at 0.8, big slope down. Weak 2.2 and very weak 1.9	0.16	Qartz+clay, no shelf at 9.0 um
BCH-2, 3979'	Ash-flow tuff, pink, some biotite, some sanidine, up to 3mm, some lithics, up to 1cm	0.28	similar to 3950 - strong 0.5, peak at 0.8, another peak at 1.05 (wk Fe 0.85) slope down. Strong 1.9 and 2.2, weak and narrow 1.4	0.16	Quartz + clay, shelf rather than band at 9.0um.
BCH-03, 3740'	Ash-flow tuff, grey/white/green, rich in feldspar with lesser amounts of biotite	0.18	strong slope down, 1.4, .9, 2.2 - weak clay development possible subtle 2.35	0.15	Strong quartz plus clay, shoulder at 10.5 um. Possible feldspar 9.6um.
BCH-03, 3993'	Ash-flow tuff, light maroon/grey, some feldspar, up to 3mm, lithic-rich, up to 2cm	0.18	0.55, strong slope down, weak 2.2, and very weak 1.9	0.22	Strong qartz+clay, shoulder at 10.5um.
BCH-03, 4065'	Ash-flow tuff, very light grey/green, some sanidine, up to 2mm, abundant lithics up to 1.5cm, some lithics are dark	0.32	Olivine + clay (montm) broad 1um narrow 1.4, triangle 1.9 typ 2.2 for illite/mont. Also 2.3 ledge and narrow 0.75	0.17	Quartz, clay, feldspar. Narrow 9.3 and 9.55 peaks.
BCH- 5, 1878'	Basaltic andesite, black with tint of dark green, aphanitic	0.08	Apparent FeOx ledge, pk at 0.7. Strong 1.4, Very Noisy	0.20	Clay combination - peak matches saponite
BCH-05, 3044'	Ash-flow tuff, light grey/green, vitric, biotite-rich, up to 2mm	0.26	Strong slope down. Apparent FeOx 0.7, weak 1.9 broad and rounded 2.2	0.13	Quartz. Possible feldspars at 9.4 and 9.8 um. Broder wing at 11um.
BCH-8, 447'	Ash-flow tuff, tan, some quartz, aphyric	0.55	Carbonate, calcite dominant. Add'tl contribution at 1.4 and 1.9 broad Fe slope to 1um	0.26	Carbonate. Best match to calcite.
BCH-8, 565'	Basalt, dark green, aphanitic, abundant amygdules that have been altered to clay, up to 5mm	0.13	Fe3+ triangular 1.9, narrow 2.3, very weak 1.4	0.19	Clay. Quartz shoulder at 8.5, but no narrow 8.5 absorption. Good fit to saponite.
BCH-10, 882'	Basalt, black, aphanitic	0.12	Strong slope down. Maybe weak and broad 2.2	0.14	Distinct from others. More clay dominated, broader wing from 10 to 12 um.
35-13, 1947'	Ash-flow tuff, light grey/green groundmass, some quartz, rich in biotite, and feldspar altered to clay, up to 3mm	0.35	serpentine or amphiboles? Broad 1um with additional 0.75. Narrow and strong 1.4, 1.9 and 2.2 narrow peak at 0.55	0.14	Strong clay, including 6.5 um peak. Quartz
35-13, 2184'	Ash-flow tuff, light grey, rich in lithics of other tuffs and a few from basalt up to 1.5 cm, some biotite and feldspar, up to 1mm	0.25	strong slope down. Weak 1.9 and narrow pointy 2.2	0.12	Quartz + clay, secondary shoulder at 9.0um.
35-13, 2266'	Ash-flow tuff, medium grey, rich in lithics of other tuffs and a few from basalt < 0.5cm, some biotite and feldspar, up to 1mm	0.25	nearly identical to 2184	0.12	nearly identical to 2184'
35-13, 2436'	Ash-flow tuff, maroon/tan groundmass, rich in feldspar, up to 5mm, abundant green clay lithics	0.17	similar to 2266 and 2184 but lower albedo, stronger 1.4. 2.2 could be kaolinite well developed hematite+goethite .6 and .78 peaks (limonite)	0.15	Qartz + clay, clay peak shorter - montmorillonite
35-13, 2559.5'	Ash-flow tuff, medium maroon groundmass, rich in feldspar altered to clay, up to 3mm, biotite, up to 1mm, minor lithics	0.17	odd structure .4 to .8, large slope down. Good 1.4, 1.9 and 2.2 bands	0.15	Strong clay, including 6.5 um peak. Quartz

COMPARISON OF ACOUSTIC AND ELECTRICAL IMAGE LOGS FROM THE COSO GEOHERMAL FIELD, CA

Nicholas C. Davatzes and Steve Hickman

U.S. Geological Survey, Menlo Park, CA, 94025
e-mail: ndavatzes@usgs.gov

ABSTRACT

Electrical and acoustic image logs collected from well 58A-10 in crystalline rock on the eastern margin of the Coso Geothermal Field, CA, reveal different populations of planar structures intersecting the borehole. Electrical image logs appear to be sensitive to variations in mineralogy, porosity, and fluid content that highlight both natural fractures and rock fabrics. These fabric elements account for about 50% of the total population of planar structures seen in the electrical image log, but locally approach 100%. This fabric is unlikely to contribute to permeability in the reservoir. Acoustic image logs reveal a similar natural fracture population, but generally image slightly fewer fractures, and do not reveal rock fabric. Both logs also record textural properties of deformed materials within fractures; these textures can be related to variations in mineralogy, alteration, or porosity using the electrical log and can be used to infer slip history. In addition, locations of high fracture density occur adjacent to major faults, but also occur as zones confined within intervals of distinct rock type.

The acoustic image logs collected in Well 58A10 reveal large numbers of drilling-induced borehole wall tensile fractures and breakouts. In addition, previously un-recognized drilling-induced petal-centerline fractures are evident in images of the borehole wall from this well. These features are thought to form just ahead of the drill bit and provide additional constraint on the orientation of the minimum horizontal stress. Both breakouts and petal-centerline fractures are difficult to identify in electrical image logs because of the low percentage of the borehole wall imaged. Analysis of induced structures in acoustic image logs indicates that the minimum horizontal stress is oriented along an azimuth of $102^{\circ} \pm 18^{\circ}$. This orientation is consistent with the local strike of the Coso Wash normal fault that bounds the basin containing well 58A-10.

INTRODUCTION

Electrical and acoustic image logging tools provide an invaluable opportunity to characterize the fracture populations that typically control fluid flow in geothermal systems. However, these tools detect fractures by measuring different properties of the borehole wall. Fractures interpreted from electrical image logs are identified by contrasts in conductivity between the fracture and the adjacent borehole wall. By contrast, fractures in acoustic image logs are associated with changes in borehole wall surface roughness or acoustic reflectivity. In both types of logs, fractures with the largest apparent apertures are often—but not always—observed to dominate subsurface fluid flow in geothermal fields (Barton et al., 1998; Sheridan and Hickman., 2004). Similarly, other properties affecting subsurface permeability such as rock type variation, foliation, and potential hydrothermal alteration can also be detected through these methods.

Stress concentrations associated with drilling and the introduction of the borehole can produce structures such as petal-centerline fractures (Kulander et al., 1990; Lorenz et al., 1990), borehole wall tensile fractures and breakouts (Moos and Zoback, 1990). These structures are directly related to the current stress state and can be used to infer the orientations of the principal stresses. Small-scale rotations of the principal stresses revealed by changes in orientation of these structures can also indicate which faults have recently slipped. Currently slipping fractures, or those well oriented for slip in the current stress state, typically comprise the majority of permeable fractures in crystalline rocks (Barton et al., 1995; Barton et al., 1998; Sheridan and Hickman, 2004).

In this study, we analyzed populations of natural and induced fractures from well 58A-10 (Figure 1) in the Coso Geothermal Field using both electrical and acoustic image logs to: (1) determine how geologic features detected by each technique differ, (2) determine each technique's effectiveness in inferring the local stress state from drilling induced structures,

(3) relate natural fracture populations to the local state of stress and rock type variation, and (4) evaluate the use of these techniques for interpreting fracture-dominated fluid flow in geothermal systems.

GEOLOGIC SETTING

The Coso Geothermal Field is located along the western edge of the Eastern California Shear Zone, subjected to both strike slip and Basin and Range style normal faulting (Figure 1a). Unruh et al. (2002) suggested that Coso lies within the right (releasing) step between the right lateral Owens Valley fault to the north and the Airport Lake fault to the south. The field sits above a shallow heat source presumed to be a partially molten magma body as shallow as 4-5 km depth (Wicks et al., 2001).

Well 58A-10 is located in Coso Wash adjacent to the exploited geothermal field (Figure 1b), but outside the region impacted by current production or

injection. We analyzed both acoustic and electrical image logs from a measured depth of about 6800 to 10238 ft through diorite, quartz diorite, and granodiorite. In addition to providing a better understanding of image logging methods in geothermal wells, the analysis of fractures crossed by this well and the local state of stress inferred from drilling-induced structures provides a basis for comparison with the adjacent producing geothermal field. Previous studies in other Coso wells, such as 38C-9, have been based on the interpretations of electrical image logs. Thus this comparison between electrical and acoustic image logging methods also provides a necessary benchmark for the interpretation of these different data sets. In particular, this study will help combine insights from both techniques in preparation for the stimulation of well 34-9RD2 as part of the Enhanced Geothermal Systems (EGS) experiment in the Coso Geothermal Field.

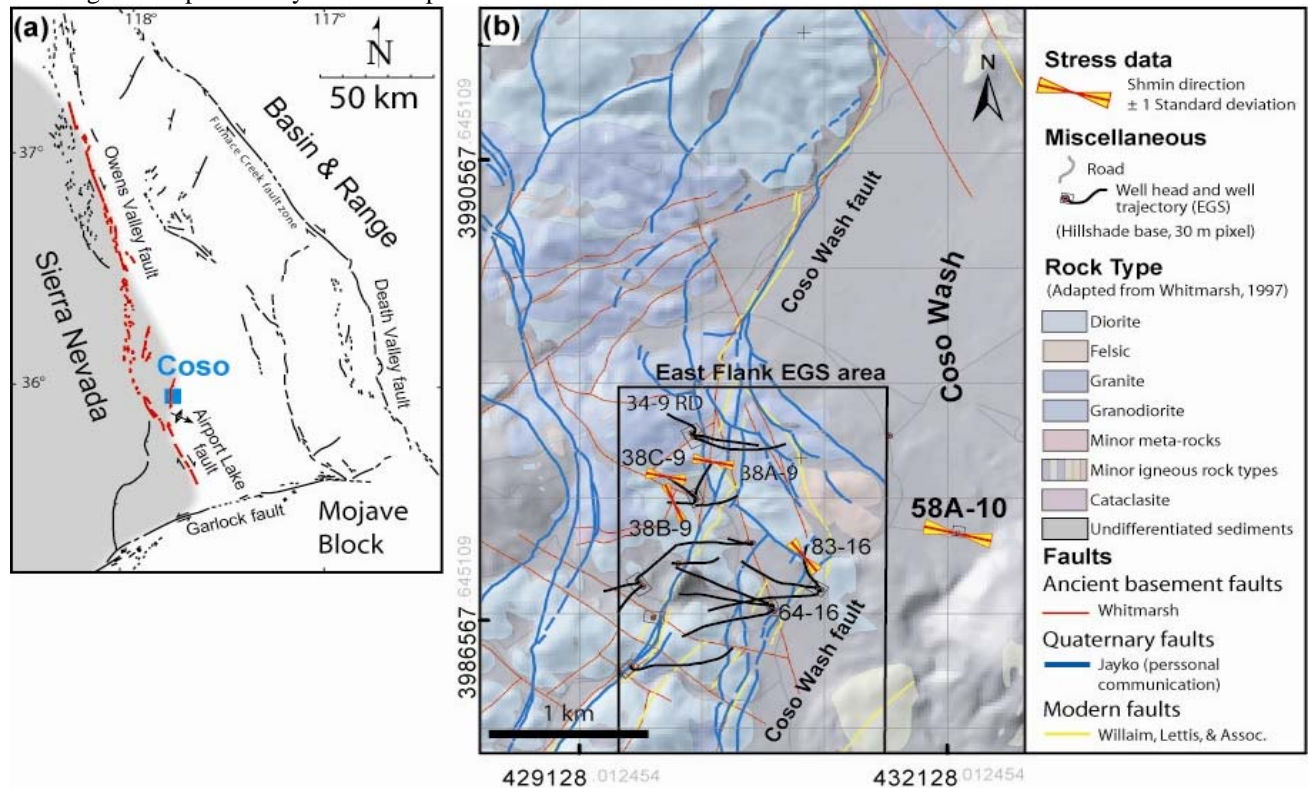


Figure 1: (a) Tectonic map of southern portion of Eastern California Shear zone modified from Unruh et al. (2002). (b) Simplified geologic map of basement crystalline rocks in the Coso Geothermal Field. Faults of different ages are shown, as are measured orientations of the minimum horizontal stress (S_{hmin}) from induced structures in well 58A-10 and based on observations by Sheridan and Hickman (2003) from wells 83-16, 38B-9, 38C-9, and 38A-9.

IMAGE LOGGING METHODS

Electrical image logs were obtained in well 58A-10 using Schlumberger's Hot Hole Formation Micro-Scanner tool (FMS) that has been used extensively throughout the Coso Geothermal Field. Electrical images are produced by placing pads with arrays of electrodes maintained at a constant electrical potential against the borehole wall, and measuring the current drop as the electrodes travel along the borehole wall (Ekstrom et al., 1987). Data from multiple electrodes are combined to produce electrical conductivity images. Because a current is being passed into the borehole wall, this technique actually measures the properties of a volume of rock within a few inches of the borehole wall. The azimuthal coverage of the image and its resolution is determined by the size and number of electrodes, their arrangement, the pad dimensions, and the borehole diameter. Resolution approaching 5 mm was attained in well 58A-10 with the FMS tool, and the image spanned about 40% of the borehole circumference within four equally spaced strips. Overall image quality is strongly related to pad contact and thus is sensitive to borehole shape and roughness, and to mud cake (Hearst et al., 2000). This tool can operate at temperatures up to 200° C for up to 1 hour, with longer operating times at lower temperatures.

The acoustic log used in this study was produced by a new state-of-the-art borehole televiewer (BHTV) built by Applied Logic Technologies (ALT) under joint funding from the Department of Energy and Navy Geothermal Program Office in collaboration with Sandia National Lab and the U.S. Geological Survey. The new BHTV is specifically designed for use in geothermal wells up to 300°C can operate at temperatures of 275°C for approximately 12 hours. This study combines results from two BHTV tools from ALT, the ABI85 which includes a combined temperature sensor, and the prototype

Acoustic image logs are produced by bouncing an ultrasonic acoustic pulse from the borehole wall (Zemanek et al., 1970). The tool uses a transducer that both emits and records the acoustic pulse. The travel time of the pulse from the transducer to the wall and back indicates the dimensions of the borehole and the relative position of the tool. The energy of the returning pulse, recorded as amplitude, is a function of the degree of scattering of the pulse due to the borehole shape and rugosity as well as the acoustic impedance contrast between the borehole fluid and wall. Complete azimuthal scans of the borehole wall are composed of 72, 144, or 288 acoustic pulses directed by a rotating mirror.

ABI88. Each pulse has an optimal footprint of 5 to 7 mm. Two images are available for analysis: (1) two-way travel time (proportional to borehole radius) and (2) amplitude. Image quality is sensitive to borehole shape and tool position. Smooth, cylindrical boreholes with a well-centered tool return maximum acoustic energy because of the resulting high incidence angle and low scattering of the acoustic beam. Departures from this ideal degrade the image quality. BHTV logs were collected in 58A-10 with vertical pixel dimensions of 5 to 7 mm and azimuthal pixel dimensions of 2.5°, about 3.5 mm. BHTV image logs were processed using two different programs: WellCad™ by ALT and Imager™ by Geomechanics International (GMI).

During FMS and BHTV log analysis we distinguished drilling-induced structures, natural fractures, rock fabric, rock type transitions, and indications of alteration wherever possible. The orientation of structures in both types of image logs was measured interactively within Imager™. In addition, we ranked the quality of natural fracture, fabric, and rock type transitions on a scale from A to C. A indicates the highest quality, least ambiguous pick which occurs in locations of good overall image quality, continuous fracture trace across the borehole and clearly defined orientation. Structures assigned a quality ranking of C required greater interpretation, usually resulting from connecting discontinuous or ambiguous line segments to define the structure trace. Conservative picking in this study probably underestimates the total number of fractures, but leads to a more reliable orientation analysis and relative distribution of structures. For high quality fracture picks we also measured the apparent aperture, or thickness of the feature, in the image of the borehole wall. To ensure an unbiased comparison of results from each image log, structures were initially picked independently in each log and subsequently followed up with detailed comparison. Interpreted image logs were cross-referenced with the cuttings log to correlate overall image log character with rock type. Future work includes incorporation of temperature and magnetic field strength recorded by the ABI85 into our structural and lithologic interpretations.

IMAGE LOG ANALYSIS AND COMPARISON

Natural fractures and fault rock texture

Planar fractures appear as sine waves when the 360° borehole images are unwrapped onto a flat plane. Fractures with large apparent aperture and distinct from neighboring fractures are easy to pick using both FMS and BHTV logs. However, in cases where

the fracture is slightly non-planar, or in locations of high fracture density, it becomes difficult to reliably pick fractures in the FMS because of incomplete azimuthal imaging. For the same reason crosscutting and abutting relations are far harder to distinguish in the FMS than in the BHTV. However, where large faults are evident from observations in the FMS log or cuttings log, or where caliper data suggests widening of the borehole, the BHTV typically provides poorer image quality than the FMS due to data loss resulting from scattering of the signal along rough borehole walls.

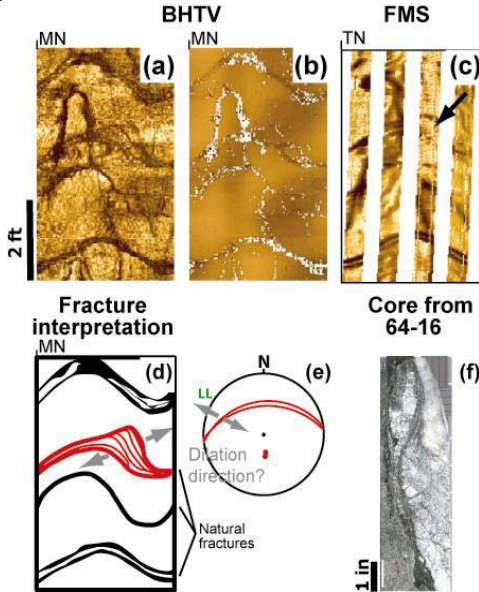


Figure 2: Natural fractures in BHTV (a) amplitude, (b) travel time, and (c) FMS image logs from a measured depth of 9857 ft. The BHTV and FMS logs are oriented with respect to magnetic North (MN) and true (TN), respectively, with a magnetic declination at this site of 14°E. Each image progresses from North, then through East, South, West, and back to North. (d) Sketch of natural fracture geometry and texture of fault rock seen in Figures 1a through 1c. (e) Stereogram of natural fracture colored red in (d). The gray arrows indicate the dilation direction inferred from the texture of the natural fracture. (f) Similar geometry to (a-d) is visible in core from 990 ft measured depth in well 64-16 (Figure 1). In this figure and all subsequent figures brighter images in the BHTV amplitude indicate greater signal strength and in two-way travel time indicate shorter times. Brighter images in FMS indicate lower conductivity. White in travel time data indicates signal loss.

In well 58A-10 both types of image logs revealed natural fractures with varying thickness or slightly non-planar geometry (Figure 2). For example, the fracture visible at center-depth in Figures 2a, b, and c has a large asperity along its surface. The basal trace is the most nearly sinusoidal, and successively less planar segments (less sinusoidal) in the un-wrapped image are associated with the “descending” limb of the sinusoid. The shape of the asperity suggests successive opening or shearing along multiple surfaces, possibly representing multiple crack-seal events (Figure 2d). Either geometry indicates apparent extension consistent with oblique normal slip across this fracture (Figure 2e). This geometry is similar to core from well 64-16 (Figure 1) from the East Flank of the field (Figure 2f), which contains multiple shear zones of foliated chlorite-smectite surrounded by brecciated host rock.

The BHTV clearly reveals fine scale geometry of the structure in Figure 2. The FMS log reveals less of the internal structure, but indicates variation in the conductivity of the fracture where more resistive zones are bright and more conductive zones toward the margins of the fracture are dark. In the BHTV image the locations corresponding to higher conductivity coincide, with signal loss (white areas in the travel time data) indicating a rough or recessed surface. Both the variation in the loss of data and varying conductivity indicate heterogeneous physical properties within the fracture that might be related to porosity production accompanying slip, the distribution of minerals with different conductivity, or preferential erosion of the fracture and adjacent wall rock during drilling.

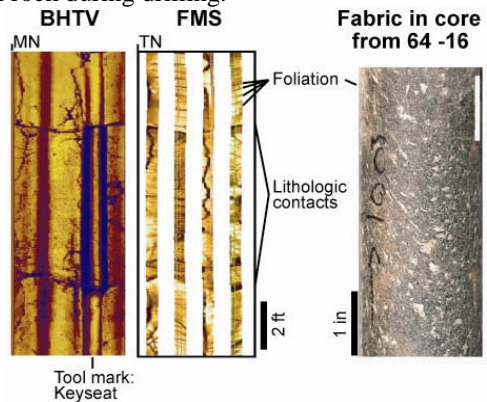


Figure 3: BHTV amplitude and FMS image logs of intervals containing two transitions in rock type indicated by changes in image log character and changing depth of wear caused by rubbing of the drill string (tool marks). The upper rock type contains a foliation, which is only visible in the FMS log and is similar to fabric visible in core from well 64-16.

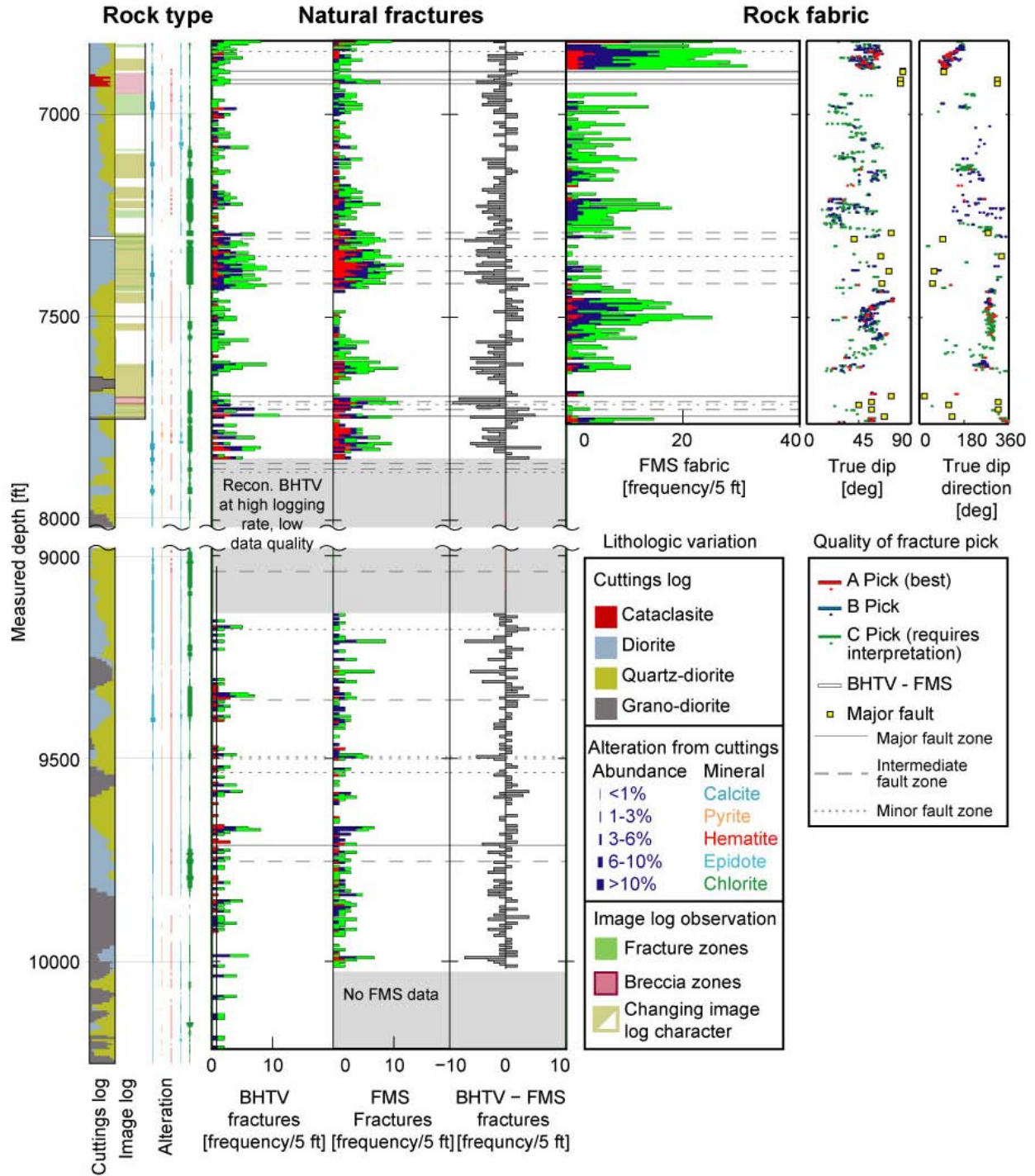


Figure 4: Plots of rock type variation indicated by the cuttings log and changes in image log character (as in Figure 3), natural fracture frequency, fabric frequency and true fabric orientation corrected for borehole deviation in the logged interval of well 58A-10 from 6820 to 10238 ft. Alteration was logged from the cuttings during drilling as part of the cuttings log.

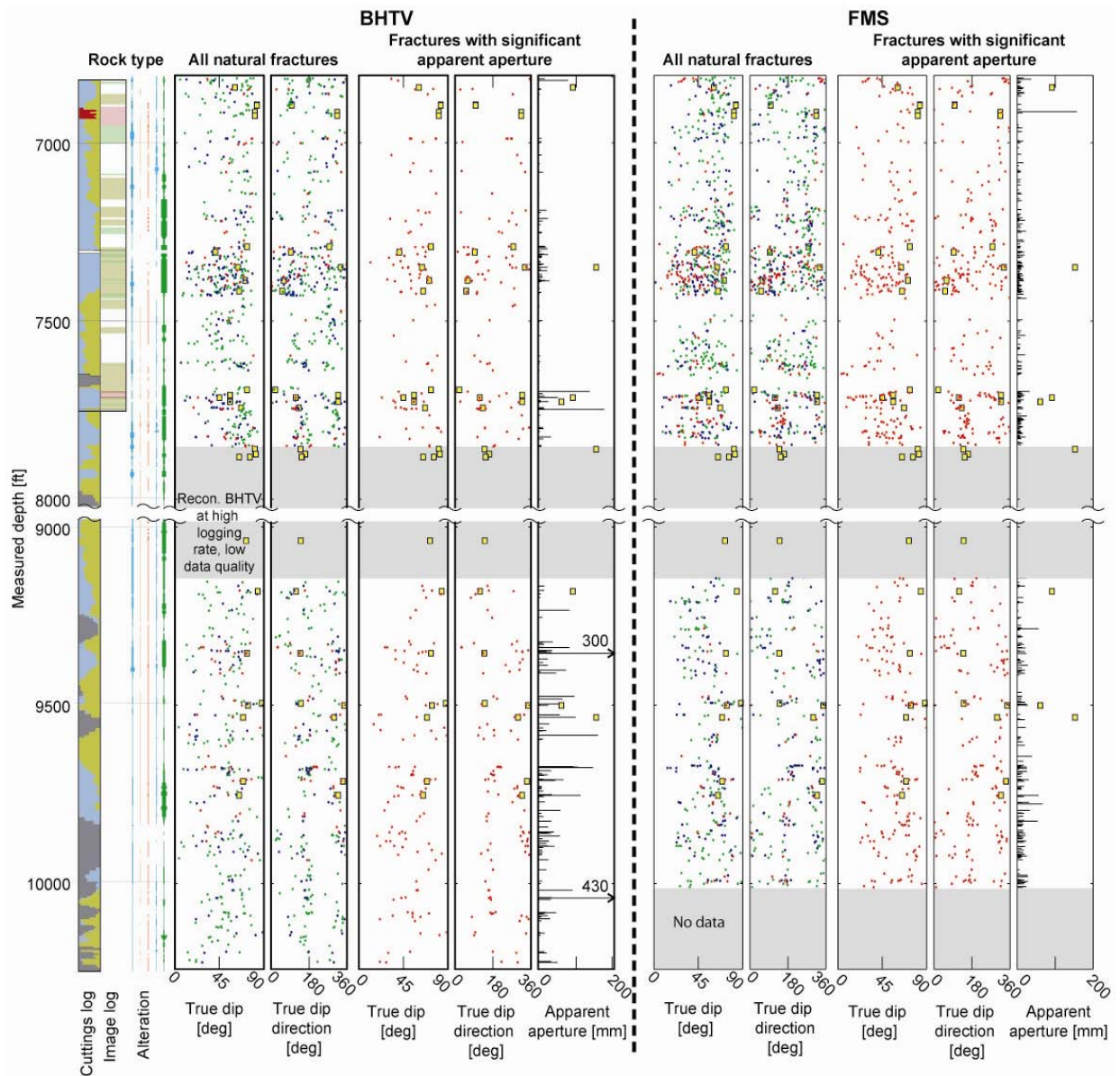


Figure 5: Natural fracture true dip and true dip direction for all fractures and for those with greater than 5 mm apparent aperture from FMS and BHTV logs for the interval from 6800 to 10238 ft. (5 mm is roughly equivalent to the minimum resolution of the FMS and BHTV.) Major faults are plotted as yellow boxes.

Rock type and rock properties

Both image logs show changes in image log character, image quality, and pipe-wear along the borehole wall that occur across abrupt near-planar transitions. Transitions that separate large (10^2 's of m) depth intervals of distinct image log character coincide with changes in rock type indicated by the cuttings log. Smaller depth intervals distinguished by distinct image log character in both BHTV and FMS (Figure 3) are not associated with distinct changes in cuttings mineralogy. However, as shown here, the depth of pipe-wear visible in BHTV images often

changes abruptly across such transitions, and qualitatively indicates differences in rock hardness or abrasion resistant. The FMS does not clearly distinguish the change in pipe-wear (although in some cases it might be detectable from the associated caliper log), but does suggest different conductivity of the borehole wall in this region. We interpret these changes in the physical properties of the borehole wall to suggest that either rock type or alteration vary rapidly over shorter distances than are resolved by cuttings analysis.

The depth interval above the first rock type transition at the top of the images in Figure 3 is also distinguished by a pervasive set of sub-parallel sinusoids only visible in the FMS image. This type of

nearly sub-parallel (over discrete depth intervals) and uniformly spaced planar structure consisting of alternating dark and bright bands characterizes broad regions of the FMS image log. Caliper logs indicate that these structures have little impact on the borehole wall geometry, consistent with their absence in the BHTV log (Figure 3). Crosscutting relationships with natural fractures always indicate that these structures are older. In addition, the boundaries of these regions generally coincide with fault zones and/or changes in image log character (Figure 3) consistent with changing rock types that are corroborated by the cuttings log (Figure 4). Most importantly, these characteristics are similar to core and surface outcrops elsewhere in the field that contain non-brittle fabrics (Figure 3). Therefore, we interpret these structures as non-brittle fabrics such as foliation that can be distinguished from natural fractures in image logs because of their consistent geometry (attitude and spacing) and absence in the BHTV log.

Distribution of geologic structures in depth

Comparison of FMS and BHTV logs from the same interval revealed differences in the populations of natural fractures and other planar structures imaged by the two techniques (Figure 4). In general, fabric elements comprise more than 50% of all planar structures measured in the FMS log, and locally approach 100%. This subset of planar structures shows consistent orientations over short depth intervals but systematic changes in dip and dip direction with depth (Figure 4). At any given depth, the orientation of foliation is clearly distinct from the orientations of the natural fracture population (Figure 5).

The residual fracture population left by subtracting these fabric elements from the total FMS data set is similar to the fracture population interpreted solely from the BHTV image log in frequency distribution (Figure 4) and orientation (Figure 5). However, the FMS data still indicates more fractures than the BHTV (Figure 4). Both data sets suggest that most fractures are associated with distinct zones of image log character, suggesting that there is a correlation between fractures density and specific rock types or alteration recorded in the cuttings log.

In general, apparent apertures estimated from the FMS logs are larger for small fractures, are smaller for large fractures, and show more fractures with

significant apparent aperture than the BHTV (Figure 5). In FMS data this “thickness” is a function of both the relative conductivity and the actual thickness of material defining the structure. The measured thickness could thus reflect the local mineralogy or fluid chemistry associated with the structure. In BHTV data this thickness is a function of the geometric irregularity of the borehole wall at its intersection with the structure and the footprint of the acoustic beam. Thus, FMS and BHTV estimates of apparent aperture do not directly measure the aperture or thickness of a fracture zone and are not directly comparable. Consequently, apparent aperture only provides insight into the relative importance of fractures and most likely over-estimates true thickness or aperture.

Drilling induced structures and stress state

In this study we distinguished three types of drilling induced structures: failure of the borehole wall as (1) breakouts and (2) tensile fractures, and failure of rock ahead of the drill bit as (3) petal-centerline fractures.

(1) Borehole wall breakouts

Introduction of a borehole concentrates the remote stresses at the unsupported free surface of the borehole wall. Where the hoop stress exceeds the compressive strength of the rock, compressive failure of the borehole wall produces breakouts (Zoback et al., 1985). In near vertical wells, where the overburden represents one of the principal stresses, the compressive hoop stress is greatest along the azimuth of the minimum horizontal stress (S_{hmin}). Thus, breakouts indicate the azimuth of S_{hmin} and will tend to occur in pairs 180° apart. The occurrence, width, and depth of breakouts are primarily a function of the rock strength, remote stress state (breakouts being favored in locations with large

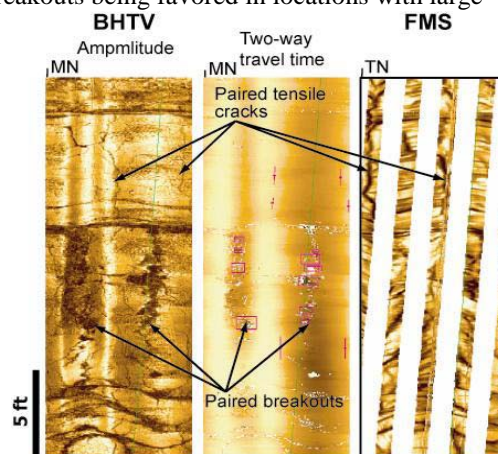


Figure 6: BHTV amplitude and two-way travel time, and FMS image logs of intervals containing borehole wall tensile fractures and breakouts.

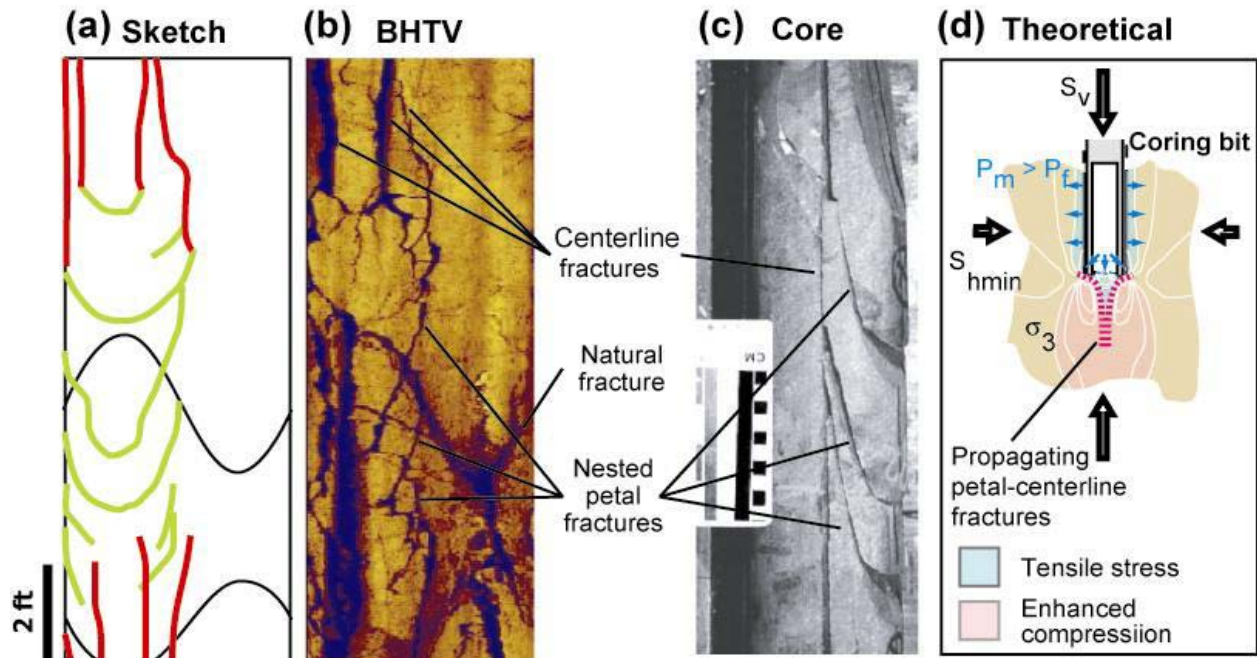


Figure 7: (a) Sketch of petal (green) and centerline (red) fractures visible in (b) borehole televiwer image log at ~7000 ft measured depth from well 58A-10. (c) Petal-centerline fractures are commonly observed in core (modified from a photo by Al Lacazette, www.naturalfractures.com). (d) Cartoon of stress concentration around the bottom of a borehole subjected to a mud pressure in excess of the formation pressure based on studies by Li and Schmitt (1997, 1998).

horizontal stress magnitudes), mud weight relative to formation fluid pressure and well bore orientation. Observations of breakout width in conjunction with estimates of rock strength can be used to constrain the range of horizontal stress magnitudes (Moos and Zoback, 1990).

In borehole cross section, breakouts typically have a “dog ear” geometry (Zoback et al., 1985) which is only visible in the BHTV log due to the ability of the acoustic signal to map the complete borehole shape. We limited our picks of breakouts to logged intervals where breakouts occurred as paired irregularly shaped patches 180° apart and where they could be clearly distinguished from any tool marks. In well 58A-10, breakouts are preferentially distributed within zones of distinct image log character (Figure 6), which are typically associated with deeper tool-wear than immediately adjacent regions. It is thus likely that these regions are distinguished by relatively low compressive strength.

(2) Borehole wall tensile fractures

Tensile failure of the borehole wall occurs where the hoop stress around the borehole is negative and exceeds the tensile strength of the rock (Moos and Zoback, 1990). For near-vertical wells, this failure produces vertical tensile fractures 180° apart and

oriented parallel to the maximum horizontal stress (S_{Hmax}). Tensile failure of the borehole wall is also promoted by high mud weights and thermal stress induced by cooling of the borehole wall during circulation of drilling fluids.

Borehole wall tensile fractures are common in both BHTV and FMS image logs of well 58A-10 (Figure 6). We identified this type of borehole wall failure in logged intervals where tensile fractures occurred as paired vertical lineations 180° apart or as an echelon lineations 180° apart.

(3) Petal-centerline fractures

Petal-centerline fractures are interpreted to form ahead of the drill bit due to the complex concentration of stress at the floor of the borehole (Kulander et al., 1990; Lorenz et al., 1990; Li and Schmitt, 1997, 1998). These induced fractures are favored in normal to strike slip faulting environments and are promoted by high mud weights and the rough geometry of the borehole floor (Li and Schmitt, 1998). They have long been recognized in core, and both empirical studies of oriented core (Kulander et al., 1990) and theoretical studies (Li and Schmitt, 1997, 1998, 1998) demonstrate that they strike parallel to S_{Hmax} . However, they have generally gone un-recognized in both types of image logs. In this

study we take advantage of these fractures and reaffirm that they provide stress orientations consistent with the other induced structures discussed above.

In image logs petal fractures appear as smoothly curving chevrons (pointing up or down). The tips of the chevrons merge with pairs of centerline fractures oriented parallel to the borehole axis (Figure 7a and b) consistent with examples in core (Figure 7c). Whereas the symmetrical stress concentration around the borehole free surface causes classic borehole wall tensile fractures to form 180° apart, petal-centerline fractures propagate through intact rock ahead of the drill bit as opening-mode fractures that open in the local direction of the least compressive principal stress (Figure 7d). The resulting fracture plane strikes parallel to S_{Hmax} , but does not necessarily lie along the borehole axis. Thus, once the bit has drilled through the induced fracture, the petal-centerline fracture will have variable azimuthal spacing along the borehole wall. The orientation of S_{hmin} can then only be reliably estimated by calculating the average azimuth of pairs of centerline fractures or paired measurements on both limbs of petal fractures.

In FMS images, pairs of centerline fractures are unlikely to be completely imaged because they need not form 180° apart and FMS pads are spaced at 90° increments (although greater coverage in other electrical imaging tools will reduce this limitation). As a result, centerline fractures spaced less than 180° could be misinterpreted as classic borehole wall tensile fractures (FMS image in Figure 8). Similarly, petal fractures might mistakenly appear to be parts of

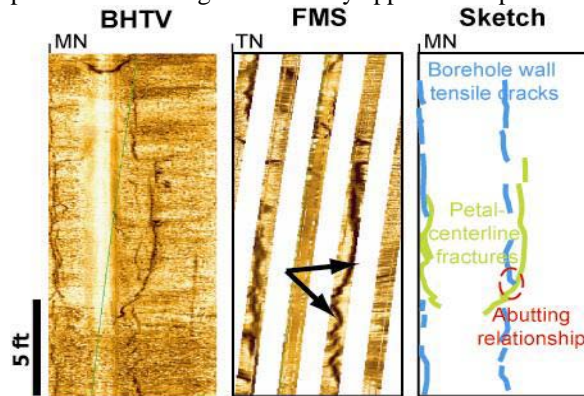


Figure 8: BHTV and FMS image logs of classic borehole tensile cracks (blue) abutting against a petal-centerline fracture (green). The abutting relationship circled in red in the sketch confirms that the petal-centerline fractures formed before the tensile failure of the borehole wall. This relationship is not visible in the FMS image, where one could easily

mistake a petal-centerline fracture for a true borehole wall tensile crack (arrows).

natural fractures in an FMS log. The potential for such misinterpretation is exacerbated where these fractures are nested (Figures 7b and c). Practically, use of an FMS log alone is thus prone to increased scatter in measured orientations of S_{hmin} . Using a BHTV log and applying the same averaging technique to all tensile fractures, including those produced by borehole wall failure, helps limit this pitfall.

Figure 8 illustrates an example where such confusion is likely in the FMS. This example also reveals an abutting relationship visible in BHTV log that confirms that classic borehole wall tensile fractures form after petal fractures.

Orientation of principal stresses

Analysis of breakouts, pairs of borehole wall tensile cracks and pairs of petal-centerline fractures from the BHTV logs (Figure 9) indicates that S_{hmin} near well 58A-10 is oriented along an azimuth of $102^\circ \pm 18^\circ$. A large proportion of the tensile fractures evident in these BHTV image logs are interpreted as petal-centerline fractures. Our analysis of the BHTV data shows that petal-centerline fractures provide comparable stress orientations to breakouts and borehole wall tensile fractures (summarized in Figure 9). In contrast, the FMS data shows considerably more scatter and fewer picks because of the poor azimuthal coverage of the borehole wall and the inability to distinguish petal-centerline fractures from borehole wall tensile cracks. The FMS mean S_{hmin} direction also departs by 13° from the BHTV analysis. Careful calibration (not presented here) between the logs demonstrates that they are well oriented with respect to each other. Thus, this difference is probably a result of the sampling bias resulting from FMS pad spacing and the much smaller population sampled (including lack of breakouts).

The average azimuth of S_{hmin} is consistent with the local orientation of the Coso Wash normal fault just to the west of the well and another similarly striking, but west dipping normal fault to the east (Figure 1). Inside the East Flank (boxed area in Figure 1), stress orientations show greater heterogeneity between wells separated by relatively short distances, presumably because of the proximity of active faults.

The depth distribution of induced structures visible in the BHTV data also shows one prominent stress rotation at ~9750 ft near the locations of several large

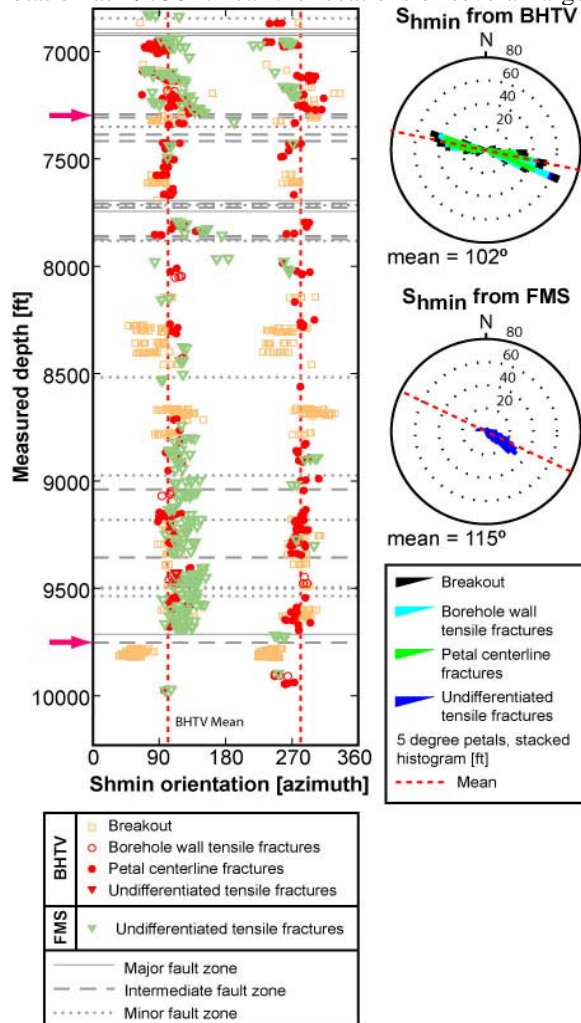


Figure 9: Orientation of S_{hmin} as a function of depth. The means S_{hmin} orientation shown as dashed red line in the depth section is derived only from analysis of the BHTV logs. Red arrow shows location of a significant stress rotation possibly related to slip on one or more active faults observed at this depth.

faults visible in the image logs (arrow in Figure 9). Other less prominent stress rotations, such as the potential rotation at ~7350 ft, are evident, but do not stand out as clearly from the scatter. These rotations probably indicate active slip on faults nearby or intersecting the borehole.

CONCLUSIONS

FMS logs generally reveal more planar structures than BHTV logs and are sensitive to characteristics like foliation, layering, or systematic variations in resistivity related to mineralogy or fluids. More than 50% of the planar structures imaged by FMS logs in well 58A-10 appear to be fabric elements not well imaged by BHTV logs. These fabric elements probably do not contribute to reservoir productivity. In contrast, BHTV logs preferentially record open or un-cemented fractures that are more likely to break the continuity of the borehole wall; thus it is unlikely to image fabric. As a result, FMS logs may provide a more complete record of the entire fracture population, possibly including healed fractures and foliation, while BHTV logs more selectively image “open” natural fractures that are expected to contribute to reservoir permeability.

FMS and BHTV logs to varying degrees reveal rock type transitions indicated by changes in image log character, image quality, and pipe-wear along the borehole wall and are generally consistent with the cuttings log. Fault zone textures potentially related to the slip history and relative ages of fractures are also revealed in both image logs, although the BHTV is better at revealing cross-cutting relationships and non-planar fracture step-overs by virtue of its greater azimuthal coverage. Combining both techniques allows a clearer characterization of fault texture that might reflect the distribution of minerals, fluids, or porosity.

Azimuthal coverage provided by the BHTV log reveals a much larger suite of stress state indicators than the FMS log. Pairs of petal-centerline fractures, and borehole wall breakouts and tensile fractures indicate imaged in the 58A-10 BHTV log an S_{hmin} azimuth of $102^{\circ} \pm 18^{\circ}$. This azimuth is generally consistent with image log analyses from other wells within the producing geothermal reservoir and is at high angle to the strike of the active Coso Wash normal fault.

ACKNOWLEDGMENTS

Steve Bjornstad and Frank Monastero of the Navy Geothermal Program Office provided data, insight, and review that greatly helped with this study. Other collaborators include: Coso Operating Company and the Energy and Geoscience Institute (U. Utah). Funding for N.C. Davatzes was provided by a U.S. Geological Survey Mendenhall Fellowship. Judith Sheridan and Dan Moos provided input on previous image log interpretations at Coso.

REFERENCES

- Barton, C.A., Zoback, M.D., and Moos, D. (1995), "Fluid flow along potentially active faults in crystalline rock," *Geology*, **23(8)**, 683-686.
- Barton C.A., Hickman, S., Morin, R., Zoback, M.D., and Benoit, D., (1998), "Reservoir-scale fracture permeability in the Dixie Valley, Nevada, Geothermal Field," PROCEEDINGS, Twenty-Third Workshop on Geothermal Reservoir Engineering, SGP-TR-158, Stanford University, Stanford, California, January 26-28, 1998. 8 p.
- Ekstrom M.P., Dahan, C.A., Chen, M.Y., Lloyd, P.M., and Rossi, D.J., (1987), "Formation imaging with microelectrical scanning arrays," *Log Analyst*, **28**, 294.
- Hearst, J.R., Nelson, P.H., and Paillett, F.L., (2000), Well Logging for Physical Properties: A Handbook for Geophysicists, Geologists and Engineers: Second Edition, John Wiley & Sons, Ltd, New York, NY, 483 p.
- Kulander, B.R., Dean, S.L., and Ward, B.J.Jr., (1990) Fractured Core Analysis: Interpretation, Logging, and Use of Natural and Induced Fractures in Core, American Association of Petroleum Geologists, Tulsa, OK. **AAPG Methods in Exploration Series, No. 8**, 88 p.
- Li, Y. and Schmitt, D.R., (1997), "Well-bore bottom stress concentration and induced core fractures," *AAPG Bulletin*, **81(11)**, 1909-1925.
- Li, Y. and Schmitt, D.R., (1998), "Drilling-induced core fractures and in situ stress," *J. Geophys. Research*, **103(B3)**, 5225-5239.
- Lorenz, J.C., Finley, S.J., and Warpinski, N.R., (1990), "Significance of coring-induced fractures in Mesaverde core, Northwestern, Colorado," *AAPG Bulletin*, **74(7)**, 1017-1029.
- Moos, D. and Zoback, M.D., (1990), "Utiliation of observations of well bore failure to constrain the orientation and magnitude of crustal stresses: Application to continental, deep sea drilling project, and ocean drilling program boreholes," *J. Geophys. Research*, **100(B)**, 12791-12811.
- Sheridan, J.M. and Hickman, S., (2004), "In situ stress, fracture, and fluid flow analysis in well 38C-9: An Enhanced Geothermal System in the Coso Geothermal Field," PROCEEDINGS, Twenty-Ninth Workshop on Geothermal Reservoir Engineering, SGP-TR-175, Stanford University, Stanford, California, January 26-28, 2004. 8 p.
- Unruh, J.R., Hauksson, E., Monastero, F.C., Twiss, R.J., and Lewis, J.C., (2002), "Seismotectonics of the Coso Range—Indian Wells Valley region, California: Transensional deformation along the southeastern margin of the Sierran microplate," in: Glazner, A.F., Walker, J.D., and Bartley, J.M., (eds), Geological evolution of the Mojave Desert and Southwestern Basin and Range: Boulder, CO, **Geological Society of America Memoir 195**, 227-294.
- Wicks, C.W., Thatcher, W., Monastero, F.C., and Hasting, M.A., (2001), "Steady-state deformation of the Coso Range, East-Central California, inferred from satellite radar interferometry," *J. Geophys. Research*, **106(B7)**, 13769-13780.
- Zoback, M.D., Moos, D., Mastin, L., and Anderson, R.N., (1985), "Well bore breakouts and in situ stress," *J. Geophys. Research*, **90(B7)**, 5523-5530.
- Zemanek, J., Glen, E.E.Jr., Norton, L.J., and Cardwell, R.L., (1970), "Formation evaluation by inspection with the borehole televiewer," *Geophysics*, **35**, 254-269.

ANALYSIS OF WORKOVER TECHNIQUES IN GEOTHERMAL WELLS OF CERRO PRIETO FIELD, MEXICO

Juan De Dios Ocampo-Díaz¹; Jaime E. Vaca-Serrano²

¹Universidad Autónoma de Baja California, Facultad de Ingeniería, Blv. Benito Juárez s/n, Mexicali, B. C., México,
Tel (686) 5-66-42-70 ext 1329, E-mail: juandios@telnor.net

²Comisión Federal de Electricidad, Gerencia de Proyectos Geotermoelectricos, Subgerencia de Perforación, Morelia
Michoacán, E-mail: jaime.vaca@cfe.gob.mx

ABSTRACT

The Cerro Prieto is one of the biggest geothermal fields on production stage in the world; to present day there are about 150 production wells located in 15 km² area, producing a different mixture (water-steam) ratio [1]. These wells supplying about 5,600 metric tons of steam per hour, to four power plants installed with 720 MWe of total capacity. There are several factors causing a steam production decline in wells, but in Cerro Prieto Field one of most common is the silica scaling in both reservoir and pipes [1], [2]. Therefore, each year is necessary to realize from 12-15 workovers, [3], [4].

Additionally to workovering jobs in wells, others tasks like drill new wells, are making to recover and keep the steam flow rate required by power plants. Some workover techniques are usually manage to workover wells, these are cleaning the production casing, deepening the production zone, sidetrack, under reaming, etc, the workover selection type, depend of several factors like: pipes and reservoir conditions, workover risk, workover time and cost. This paper analyzes and discusses the workover wells techniques used in Cerro Prieto geothermal field and results obtained of the application of these.

1. INTRODUCTION

The Cerro Prieto geothermal field is located in the south part of the Salton trough about 20 miles South of the United States-Mexico border in Baja California, Mexico (fig.1). More than 250 deep wells have been drilled in the area. Present there are about 150 production wells that are feeding from different depth aquifer. To date the installed electrical power generating capacity is 720 MWe [5].

Due to the capacity installed and the declining steam production shown by the wells it was necessary to workover some wells and to drill some additional

wells to make up for the lost steam production, the last task are realized constantly [3].

2. GEOLOGICAL ASPECTS OF CERRO PRIETO RESERVOIR

The Cerro Prieto geothermal field exploitation through 24 years of commercial operation has utilized the alpha (α) and beta (β) reservoir for the Cerro Prieto I area and mainly the beta reservoir for Cerro Prieto II and III areas.

Toward the east of the exploitation zones, some authors have identified a deep reservoir named gamma (γ) [7].

Cerro Prieto II and III derive production from the beta reservoir which is deeper, and to some extent underlines the alpha reservoir. The distribution and depth of production is controlled by a northeast trending structural high. Silica and epidote mineralization and high temperatures (300 °C+) which delineate the top of the reservoir are also related to this structure. The average thickness of the produced reservoir in these zones is about 380 m. A fundamental lithological characteristic in these zones is the silica cement in the production sandstone [8].

At greater depth the “transition zone” has sandstones which contain both calcite and silica cement. The calcite cement increases with depth in calcite zone [9], [10].

3. CERRO PRIETO WORKOVER WELLS

The workover wells in Cerro Prieto geothermal field began in 1973, since this about 383 wells have been repaired in the field, Fig. 2, shows the well numbers repaired each year in Cerro Prieto. Every year, averages of 12 wells are repaired in Cerro Prieto field, for different, but the main cause is due to decrease in their steam flow rate delivered. Most commonly, a production decrease in geothermal wells in Cerro Prieto field is due to:

- Surface pipeline scaling.
- Mechanical damage in the wellbore (pipes).
- Entrance of cooler fluids to the producing reservoir.
- Reservoir scaling.
- Well scaling.

4. DIAGNOSTIC TOOLS THAT ARE USE TO ANALYZE PROBLEMS IN CERRO PRIETO WELLS

Today, the Cerro Prieto reservoir is undergoing thermodynamic and chemical changes such as boiling condensation, dilution and mixing. These changes are natural response to exploitation and brine reinjection [4]. Successful new well location and workover require that reservoir engineering in Cerro Prieto uses classical tools such as pressure and temperature logs (mechanical tools), production and enthalpy analysis, geology and mineralogy inspections and new tools like chemical and isotopes analysis, and electronic instruments (TPS: temperature, pressure and spinner electronic logs). The most important characteristics that are considered to rehabilitation of a well in Cerro Prieto field are: Mechanical conditions of the well, geological conditions, behavior of the wellhead pressure enthalpy and geochemical production data and analysis of pressure and temperature logs [2].

5. WORKOVER TECHNIQUES THAT ARE USE IN CERRO PRIETO WELLS

The most common techniques used until now for rehabilitation of wells in Cerro Prieto geothermal field have been the following:

- Cleaning of the silica scaling in casing (Cleanout).
- Under reamed
- Sidetrack.
- Deepening

Occasionally, it is necessary to install a less diameter casing inside of damage casing of high diameter, because, it shows a mechanical damage, like casing collapse and failures.

The under reamed technique has been used when the permeable feeding reservoir strata near to the downhole is scaled, both calcite and silica or with metallic sulfides, however this techniques was used sporadically in the past.

Comision Federal de Electricidad (CFE), who has general management of the geothermal field, realized a statistical analysis of workover results in Cerro Prieto through 1988-1991, the data obtained showed that using mechanical cleaning of the scaling in the casing, the steam flow rate production recovers, after

the workover, the 45 % of the initial steam flow rate produced by the well [1].

A workover compare analysis, from 79 workover of Cerro Prieto wells, through 1988 to 1994, Table 1, shows the results, these pointed out the best steam flow rate recovered by sidetrack and deepening techniques with 70 and 68 % (similar values), the less steam flow rate recovered correspond to clean out workover with 48 % [4].

An analysis of 17 workover realized in Cerro Prieto wells during 1995 to 1997, showed reduced steam flow rate recovers in all wells cleaned in theirs casing productions. Besides, almost all wells were producing from zones deeper than average traditional feeding zone (after repaired) recovered steam flow rate greater than 100 of the original steam flow rate. Table 2, shows some characteristics recorded from the wells that were deepened. The average depth of deepening realized in these wells during workover was 404 m and the steam flow rate average recovered was 95.5 % respect to the original steam flow rate produce [11].

6. WORKOVER WELLS CASES IN CERRO PRIETO FIELD

Figures 3 and 4 show the wells 609 and 625 completion including the silica profile estimated from caliper logs after these decline theirs steam flow rate until stop to flowing, both wells were repaired eliminating the silica scaling (cleanout) and deepening, The steam flow rate of these two wells was reduced as a consequence of silica scale, well 625 were repaired only two and half years after start its production stage. Figures 5 and 6 show the steam flow rate trends of both wells.

The workover cost of sidetrack can be about three or four times the deepening cost, The workover technique selected depend of several factors, such as steam flow rate recovery, workover cost, inversion return, etc.

7. CONCLUSIONS

The decline production in the Cerro Prieto geothermal field is caused mainly by two mechanisms: a drop in reservoir pressure as well as by flow restriction created by silica deposition in both reservoir and casing production.

Was analyzed the data obtained from workover realized in Cerro Prieto geothermal field through 31 production years, the most common workover techniques used have been mechanical clean of production casing (remove of scale), deepening, side track, and under reamed.

The statistical data from all these workover reveal the deepening and side track technique as the best steam flow rate recover alternatives, and cleanout as the wore alternative. Many wells had recorded steam flow rate recover high than 100 % respect to the original production after workover.

8. REFERENCES

Ocampo, D.J., Moya, S.L., De Leon, J., (2003). Lost Production As Consequence of Silica Scaling in Cerro Prieto Geothermal Wells, Mexico,. *Proceedings, Twenty-Fifth Workshop on Geothermal Reservoir Engineering*, Stanford University, Stanford, California.

Ocampo, J., Pelayo, A., De Leon, J., Goyal, K., Box, T., (1998). Reservoir Characteristics Obtained From steam Decline Trends in The Cerro Prieto Geothermal Field. *Proceedings, Twenty-Third Workshop on Geothermal Reservoir Engineering*, Stanford University, Stanford, California, p. 27-32.

Ocampo, D.J., Pelayo, L.A., Box, T., (2000). Scaling Plug Problems Observed in Some Cerro Reservoir Prieto Geothermal Production Wells. *PROCEEDINGS, Twenty-Fifth Workshop on Geothermal Reservoir Engineering*, Stanford University, Stanford, California.

Gutierrez, P., Gutierrez, P., Mendoza, M.A., (1995). Techniques for Rehabilitation of Wells in Cerro Prieto, *Geothermal Resources Council Transactions*, Vol. 19, p. 401-407.

De Leon, J., Ocampo, J., Pelayo, A., (2001). New Tolls for Reservoir Engineering in Cerro Prieto Geothermal Field, *Geothermal Resources Council Transactions*, Vol. 25, pp. 625-630.

Ocampo, J., Pelayo, A., De Leon, J., Keshav, G., Box, T., (1999). Improvement in Steam Production Through Orifice Plate Cleanout in The Cerro Prieto Geothermal Field, *Proceedings, Twenty-Fourth Workshop on Geothermal Reservoir Engineering* Stanford University, Stanford, California, pp. 102-107.

Halfman, S.E., Lippmann, M.J., Boadvardson G.S, (1986). Quantitative Model of Cerro Prieto Field. *LBL-20523*.

Lippman, M.J., Truesdell, A.H., Manon, A., and Halfman, S.E., (1989).The Hydrogeologic-Geochemical Model of Cerro Prieto Revisited. *LBL-26819*.

Elders, W.A., Hoagland J.R., McDowell, S.D., and Cobo J.M., (1978). Hydrothermal Mineral Zones in the Geothermal Reservoir of Cerro Prieto. Baja California, Mexico. *First Symposium on the Cerro Prieto Geothermal Field*. San Diego, CA. Comision Federal de Electricidad, pp. 68-75.

Cobo, R. J. M., (1979), Geología y Mineralogía del Campo Geotérmico de Cerro Prieto. Baja California, México. *Actas Segundo Simposium sobre el campo Geotérmico de Cerro Prieto*. Mexicali B.C. pp. 103-114.

Ocampo, J., Pelayo, A., De Leon, J., Box, T., Goyal, K., (1997). Recent Results of Deepening Wells Below Cerro Prieto II and III Traditional Exploitation Zones. *Geothermal Resources Council Transactions*, Vol. 21, pp. 585-590.

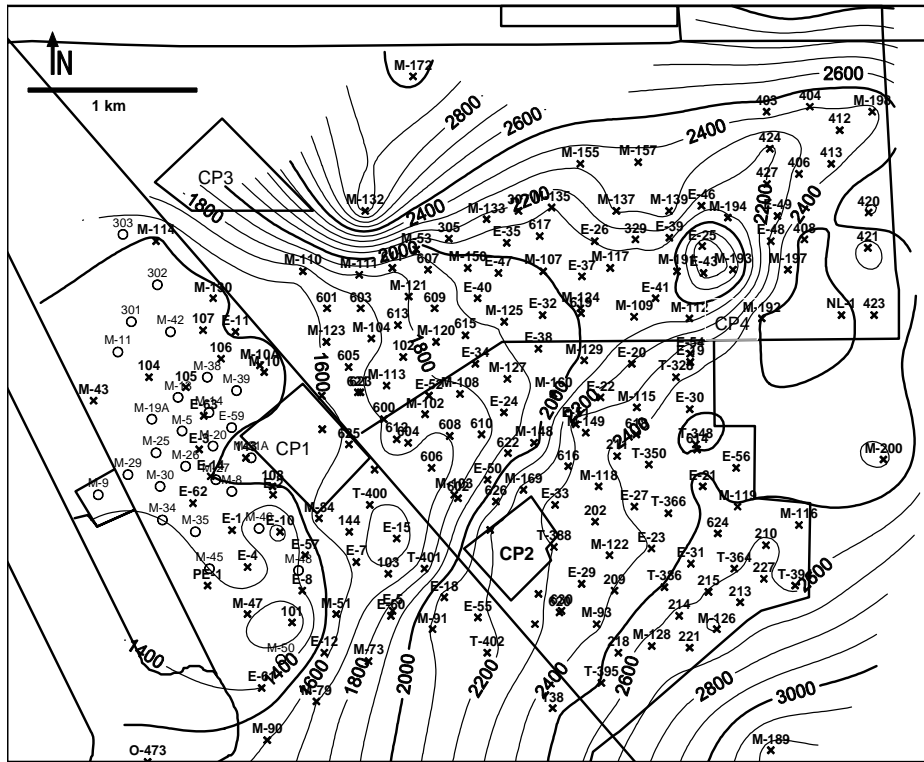


Figure 1 Cerro Prieto geothermal field locations

ANNUAL WORKOVER WELLS STATISTICAL

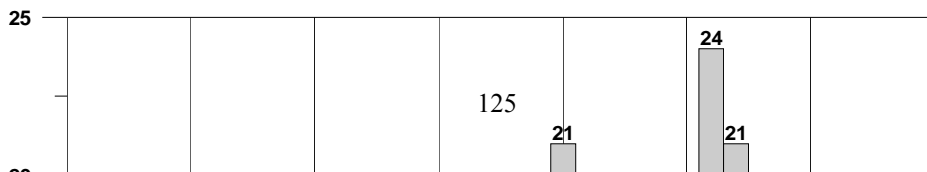


Figure 2 Annual Repaired Wells in Cerro Prieto Field

Figure 2 Workover annual statistical in Cerro Prieto geothermal field

Figure 2 Cerro Prieto field workover statistical for 1973 -2004

Workover Type	Workover Wells	Initial Average Flow rate	Average by Workover Well	% of initial Flow Rate
Side Tracking	29	69	49	70 %
Deepening	30	76	52	68 %
Cleanout	20	79	38	48 %

Table 1 Workover Type Statistical for 1988-1994 of Cerro Prieto field

Well	Deepening (m)	Thickness (m)	Workover Type	Steam recovery (% of Original)
603	1801-2312	511	Under reamed	95.0
605	1854-2190	336	Sidetrack	132.4
611	2135-2524	389	Deepening vertical	125.3
613	2028-2587	559	Deepening vertical	113.1
607	2075-2289	223	Deepening vertical	71.5
609	2158-2600	442	Deepening vertical	91.2
615	2154-2605	451	Deepening vertical	100.0
617	2310-2783	473	Deepening vertical	131.9
619	2545-3011	466	Deepening vertical	83.7
600	2025-2450	425	Sidetrack	69.2
604	2242-2648	406	Sidetrack	94.5
612	2026-2284	258	directional	92.5
606	2193-2560	367	Deepening Vertical and & 7" Ø blind liner installed	71.5
608	2041-2460	419	Deepening vertical	97.8
602	2025-2483	450	Deepening vertical	85.8
616	2705-2953	248	Sidetrack and 7" Ø slotted blind liner	86.3
618	2885-3335	450	Deepening vertical	81.2

Table 2 1988-1994 Cerro Prieto Deepened Wells Statistics

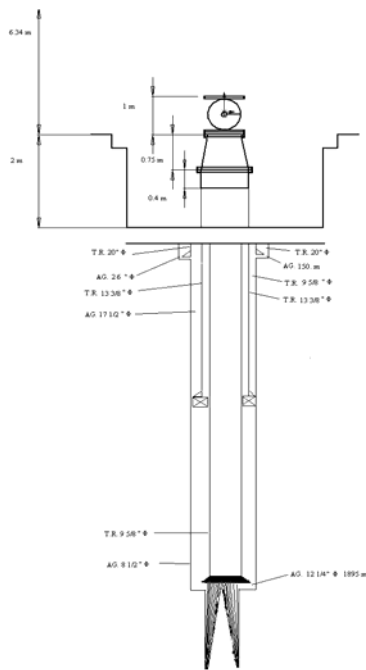


Figure 3 Completion of well 609 with silica scaling

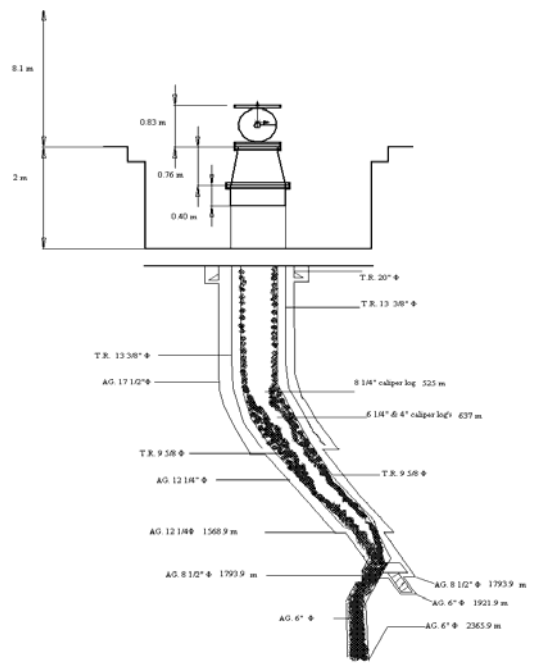


Figure 4 Completion of well 625 with silica scaling

Steam Production Behaviour Well 609

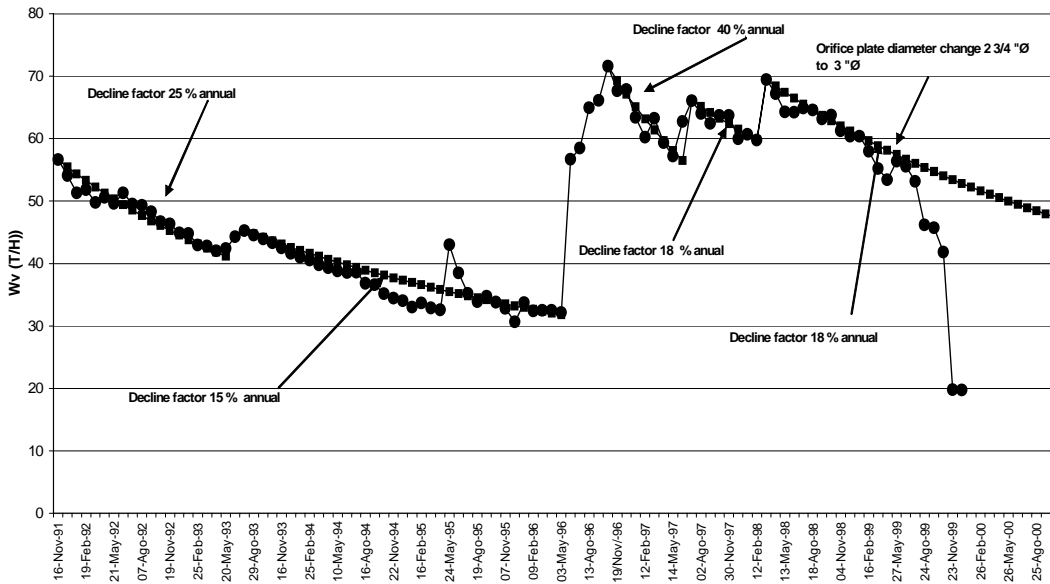


Figure 5 Steam flow rate trends of well 609

Steam flow rate behaviour Well 625

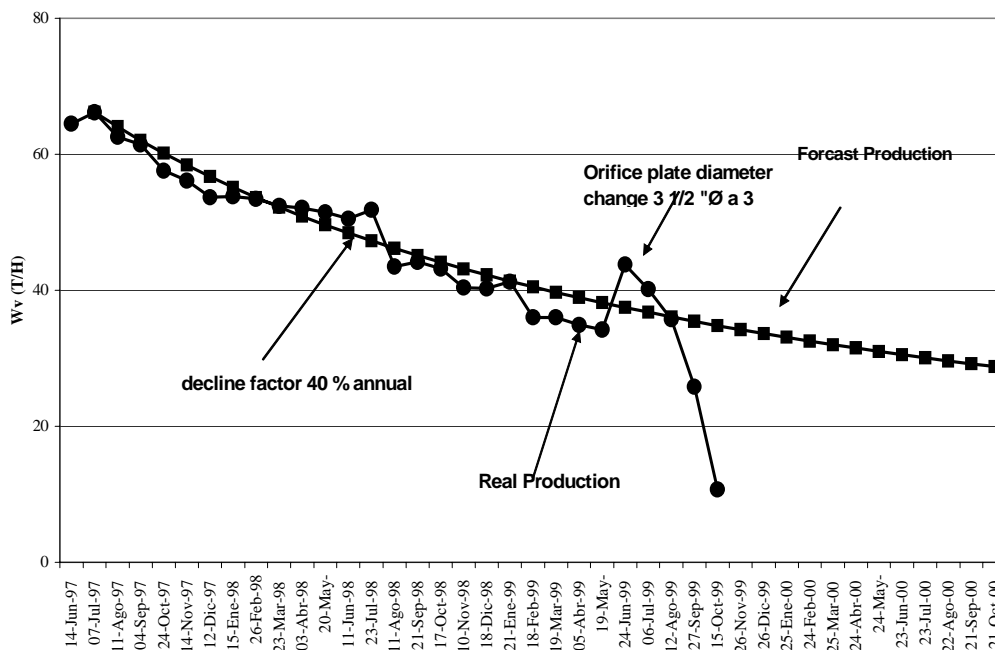


Figure 6 Steam flow rate trends of well 625

LESSONS LEARNED IN DRILLING DB-1 AND DB-2 BLUE MOUNTAIN, NEVADA

Susan Petty¹, Brian Fairbank², Stephen Bauer³

(1) Black Mountain Technology, Seattle, Washington, USA, e-mail: blackmountaintech@earthlink.net (2) Noramex, Vancouver, B.C., Canada, e-mail: fairbank@intergate.ca (3) Sandia National Laboratory, Albuquerque, NM, USA, e-mail: sjbauer@sandia.gov

ABSTRACT

The second stratigraphic test well, DB-2, drilled at the Blue Mountain Geothermal Project 30 kilometers (20 miles) west of Winnemucca, Nevada, was successfully completed on April 29, 2004. The hole was drilled under a cost sharing agreement between Noramex Corp. and the US DOE under the GRED II program to explore the geothermal resource to the west of Blue Mountain in an area previously explored for gold.

Noramex drilled DB-1, the first deep stratigraphic test well, to 672.1 meters (2205 feet) in 2002. DB-1 intersected economic temperatures of 145°C (292.5°F) at a depth of 645 m (2115 ft). DB-1 had lost circulation and indications from the temperature survey of high permeability in the almost 366 m (1200 ft) of hole with high temperatures.

DB-2 encountered higher temperatures, 167°C (333°F) at 585.2 m (1920 ft), also with good indication of permeability from lost circulation and from the temperature surveys from 201.17 m (660 ft) to bottom.

Both wells were drilled with close cooperation and assistance from Sandia National Laboratories. The first well tested the resource along a major north-south trending fault. DB-1 was planned with 7" casing cemented to a depth of 120 m (400 ft) and 4 ½" casing cemented to a nominal depth of 250 m (820 ft). The hole was drilled using a Universal Drill Rig 1500, capable of drilling both the rotary and core sections. The upper part of the hole in the cased intervals was planned for rotary drilling and cementing by the displacement method.

Massive zones of lost drilling circulation required constant remedial work and attention in the upper part of DB-1. The loss zones caused difficulty in cementing both the 7" and the 4 ½" casing strings. Shallow, hot fluid was later found to be migrating down behind the 4 ½" casing from a zone near the bottom of the 7" casing indicating that a complete

cement bond was not achieved. Drilling of DB-1 took 43 days from spud to completion.

The second well, DB-2, tested faults to the north of DB-1 in a second area of high temperature anomaly closer to the range front. DB-2 was planned to use flooded reverse circulation technique for the single string of 4 ½" casing to be cemented to 200 m. (650 ft.) using the tremmie pipe method. This method would allow the hole to advance despite lost circulation. Although cementing with tremmie pipe requires an oversize hole, it allows cementing to surface despite the presence of severe loss zone. Below the cemented casing, the hole was to be HQ cored to total depth of 1000 m (3281 ft) using a different rig set up for wireline coring. Noramex relied on information gained from Sandia's research into the use of these techniques to combat the problems of lost circulation, to help make the decision to change the drilling strategy for DB-2.

This plan was very successful and smooth progress allowed DB-2 to be drilled to a depth of 1128 m (3700 ft) or 11% deeper than originally planned in a total of 33 days from spud to completion. Circulation problems in the open hole below the cemented casing, but above the temperature target for the well were controlled using lost circulation materials. A cement plug was finally set after coring through this zone to reduce the potential for down-flow of cool water.

INTRODUCTION

The geothermal resource at Blue Mountain Nevada was first discovered during drilling for precious metals on mineral claims in the early 1980's. Hot water with temperatures up to 190°F was encountered in holes drilled for gold exploration. Noramex acquired the geothermal rights to two sections of private land and five sections of BLM land in 1993 and 1994. Noramex then remapped the area, examined aerial photos, ran an SP survey and drilled 11 new coreholes as part of a geothermal exploration and evaluation effort.

Structural mapping identified three primary fault sets related to Basin and Range tectonics: The oldest faults trend nearly northwest and are steeply dipping. Next in age, north-south trending faults such as the Central, West and Graben Faults, dip west and offset earlier gold mineralization. (Map 1) The youngest faults trend to the northeast and dip steeply west, also offsetting the gold mineralized zone. An SP survey conducted as part of the exploration program indicated a zone of geothermal fluid upwelling.

DRILLING OF DB-1

In 2000, Noramex proposed a 2300 ft (700 m) deep hole to test the geothermal potential at Blue Mountain and secured a cost-sharing agreement with the US Department of Energy under the GRED program, DOE contract No. DE-FC04-00AL66972. The contract was administered through Sandia National Laboratory and technical assistance was provided by Sandia as well.

In April of 2002, Noramex began drilling of DB-1. The well was sited to intersect the north-south trending West and Central faults in a thermal anomaly found with shallow gradient holes. DB-1 was planned with 7" casing cemented to a depth of 120 m (400 ft) and 4 1/2" casing cemented to a nominal depth of 250 m (820 ft). The hole was drilled using a Universal Drill Rig 1500, capable of drilling both the rotary and core sections. The upper part of the hole in the cased intervals was planned for rotary drilling and cementing by the displacement method.

A hung liner of used drill rod with a diameter of about 2 3/8" was planned to keep the hole open for testing and logging.

A permeable zone at 49 m. (163 ft) produced artesian hot water. Circulation was first lost at a depth of 84 m. (276 ft.) in highly altered, fractured rock. The loss was controlled with cottonseed hulls and sodium bentonite granular plugging material and a cement plug. At 99 m (325 ft), circulation was again lost, but could not be controlled. After setting 6 cement plugs and pumping significant amounts of loss control material, the hole had only advanced to 105 m (345 ft.) by drilling with no returns. In order to be able to drill ahead, the 7" casing was set, but hung up in the fractured zone and was finally set at 98 m. (321 ft.) in highly altered fractured rock, probably the West Fault.

Attempts to drill ahead with rotary drilling were unsuccessful due to continued loss of circulation. Finally, the hole was advanced by switching to coring with PQ size tools at 112 m. (367 ft.) The hole was drilled without returns to 176 m. (579 ft.) No further attempt was made to control losses. The 4 1/2" casing

was set at 175 m. (573 ft.) in metasedimentary argillite with significant quartz veining and brecciation with open spaces.

The hole was completed by coring with HQ sized tools to a depth of 672 m. (2205 ft.) without regaining circulation. An unstable zone in fractured and highly altered felsic dike material was encountered at around 225 m. (737 ft.). This zone made it difficult to run the liner tubing to bottom and may have caused later problems with running temperature surveys. The well completion with loss zones marked is show in Figure 1.

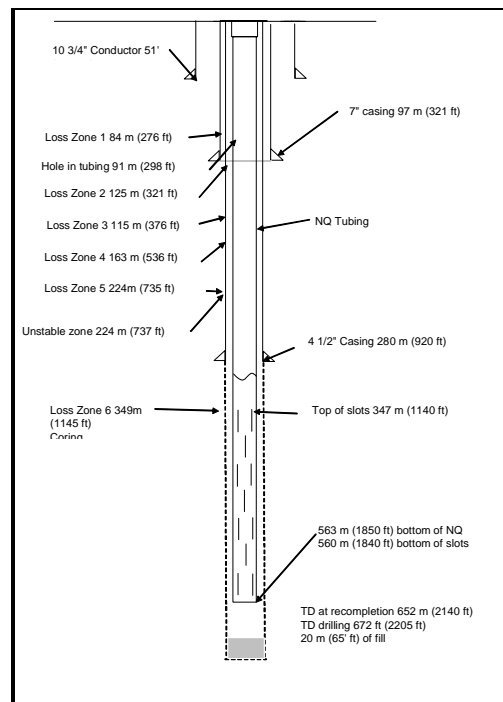


Figure 1. DB-1 permanent wellhead and well profile

Cementing of the DB-1 casing was complicated by the severe loss zone at the casing shoe for the 7" casing, and by the small annular space and lost circulation in fractured rock behind the 4 1/2" casing. During logging for well testing, it was discovered that shallow, hot fluid is migrating down behind the 4 1/2" casing from a zone near the bottom of the 7" casing indicating that a complete cement bond was not achieved. (Figure 2).

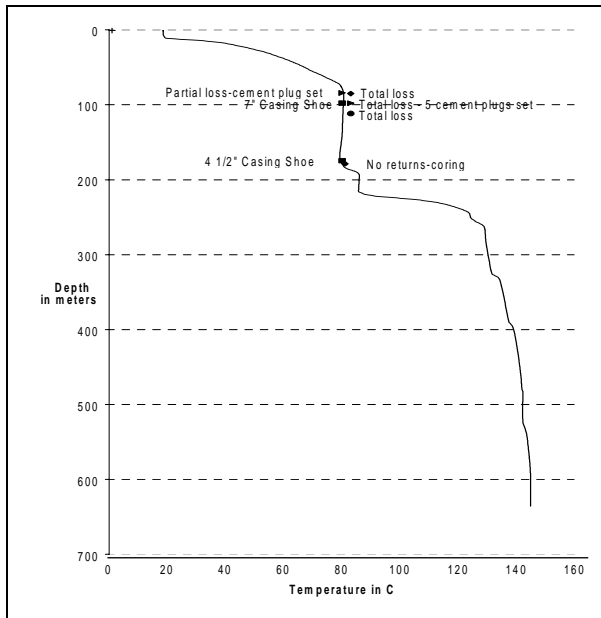


Figure 2. Temperature profile of DB-1 showing loss zones.

The drilling cost of DB-1 exceeded the original cost estimate and the GRED grant had to be extended to complete the hole. The total drilling time was 43 days with 47 days from spud to rig release. A plot of drilled depth with time is shown in Figure 3. Note that the loss zones correspond with periods where no progress is made.

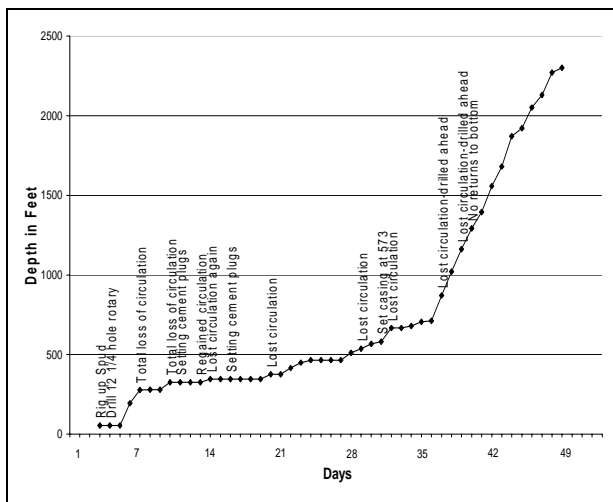


Figure 3. DB-1 drilling history.

DRILLING OF DB-2

The experience with the drilling of DB-1 lead Noramex to review the drilling program when planning for DB-2. With further cost shared funding from the DOE GRED program, the hole was planned from the start to deal with expected large-scale circulation losses. Sandia National Laboratory again provided administrative oversight and technical

assistance in planning and drilling of the hole. Since one of Sandia's primary research objectives is finding methods to deal with extremes of lost circulation during drilling of geothermal holes, data and information was available to help Noramex succeed in drilling this second hole within their budget.

During cost estimating for DB-2, a drilling contractor experienced in geothermal drilling proposed the use of flooded reverse circulation drilling. This method, frequently used in water well drilling, circulates drilling fluid down through the annulus of a dual walled drill string. Cuttings with drilling fluid then return through the inner string. This reduces the loss of drilling fluid and the risk of differential sticking and high torque by maintaining fluid around the bit and bottom hole assembly. Although the drilling contractor on DB-1 had done everything feasible to control lost circulation (see Figure 7) showing a comparison of drilled depth vs. time, shows that the losses brought drilling virtually to a standstill until the switch was made to coring.

Sandia had an ongoing research program studying the use of flooded reverse circulation drilling to deal with lost circulation in geothermal drilling. (Rickard, 2001) They provided information on the method that reassured Noramex that the technique would be beneficial in controlling costs and should work well in Basin and Range drilling at Blue Mountain.

The hole was planned to use flooded reverse circulation drilling in the cased part of the hole to control losses. Coring would then be used after the casing was set.

After discussion with Sandia, the hole was planned for cementing through the annulus from the bottom up with tremmie pipe. (Rickard, 2001) This requires a larger annulus, so the intermediate 7" casing string was eliminated. A 9 5/8" hole was planned for the 4 1/2" casing to accommodate the tremmie pipe cementing. Since Sandia is also studying tremmie pipe cementing and other cementing methods to deal with loss zones behind casing, they were able to provide data to support the feasibility of tremmie pipe cementing long intervals in a geothermal setting.

The hole site was also selected to intersect any faults at a deeper depth than DB-1. This would keep the loss of fluid to the smaller diameter hole and thus reduce the cost of the loss, while also making the faults potential production zones.

The 10 3/4" casing was set at 56 ft in silicified meta-sediments and the hole was drilled out with a 9 7/8" bit for the 4 1/2" casing. The first loss zones in DB-2 were encountered at 85 m (280 ft) and drilling was switched to flooded reverse circulation. Circulation was eventually regained after drilling ahead with

some loss additives. Two more loss zones were encountered, but could be drilled through with reverse circulation and loss control additives.

The 4 1/2" casing was set and cemented in place with no trouble. Tremmie pipe was used to stage in the cement, with time between each batch for the cement to set. Cement was successfully pumped to surface despite the loss zones in the cemented interval.

The remainder of the hole was cored with HQ sized tools. A significant loss zone was encountered at 203 m (665 ft). The loss was cured with loss additives of shredded paper, and Magma Fiber, an extrusion-spun mineral fiber as well as Drispac, a long-fiber cellulose polymer. Several more loss zones to a depth of 240 m (788 ft) were cured with LCM, but the zone was finally cemented from 240 m (788 ft) to the casing shoe at 201 m (660 ft) after temperature measurements showed that it was probably below the temperature of the main reservoir. Cool water zones can down flow into hotter zones below, making it difficult to test the well and obtain unmixed reservoir fluid samples. However, this zone later heated up to reservoir temperature, and the cementing of the zone was found to have caused some formation damage. Figure 4 shows the completion of DB-2 with the loss zones marked.

Although, for the most part, coring in DB-2 allowed drilling ahead, in deeper zones once target temperatures had been reached and mud additives had been reduced, high torque became a problem. Torque reduction additives helped reduce torque, but near the bottom of the hole the pipe stuck despite torque additives. The stuck pipe was quickly fished and drilling progressed to TD without further problems.

Figure 5 shows the temperature profile of DB-2 immediately after drilling. The temperature at the loss zones below the casing shoe to a depth of about 584 m (1925 ft) are lower than the maximum temperature. The loss at 238 m (775 ft) was cemented to prevent flow of cool fluids down the wellbore where they could cool off the deeper zones and mix with hotter fluids.

Figure 6 shows drilled depth vs. drilling time for DB-2. It is clear from this plot that the only period where no progress was made was the time needed to change out the rigs to switch from reverse circulation drilling to coring.

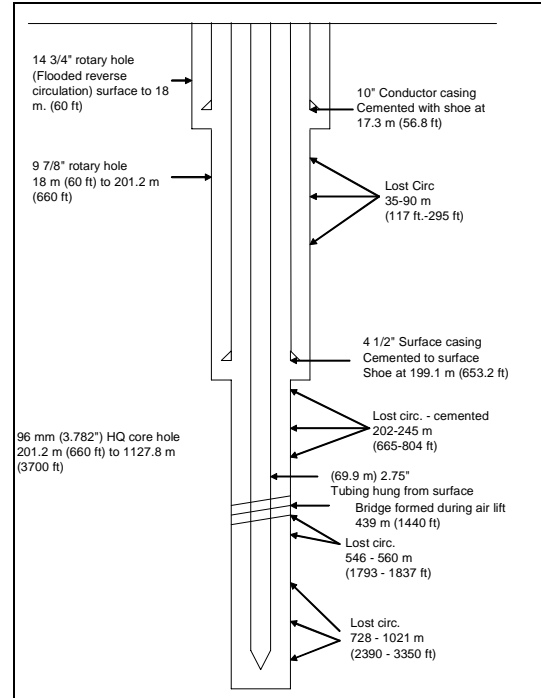


Figure 4. DB-2 well profile with loss zones

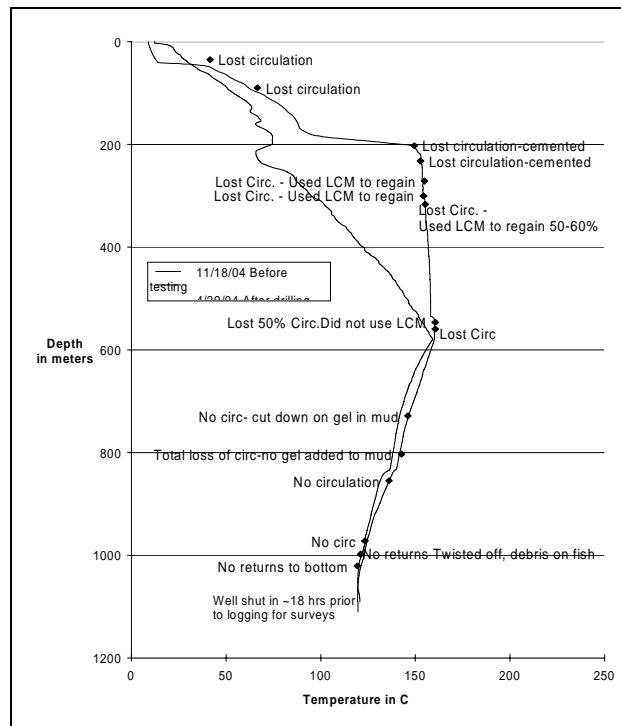


Figure 5. DB-2 temperature profile immediately after drilling.

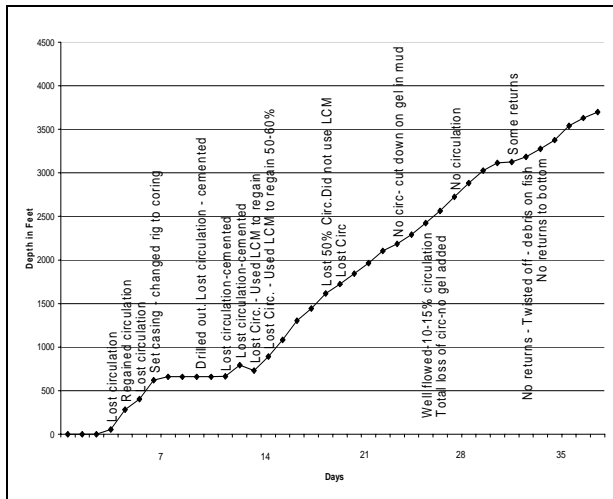


Figure 6. DB-2 drilling history.

COMPARISON OF DRILLING EXPERIENCE-DB-1 & DB-2

Several factors besides the drilling methods differed between DB-1 and DB-2:

- DB-1 was sited close to the surface expression of the steeply dipping Central Fault, in the hope of intersecting it or the West Fault at depth.
- DB-1 intersected the Central fault much shallower than anticipated, with much more problematic lost circulation than if the fault had been intersected deeper.
- Lost circulation was much more severe over a longer, shallower interval in DB-1 than in DB-2.
- Severe hydrothermal alteration in DB-1 caused hole instability. Alteration was also severe in DB-2, but it was encountered at greater depth.
- In DB-1, lost circulation was encountered first at about 84 m (276 ft) with the most severe losses ended by 115 m (376 ft). In DB-2, the first loss was encountered at a similar depth, 85 m (280 ft), but it didn't become severe until just below the 4 1/2" casing shoe at 203 m (665 ft). The severe losses continued until 317 m (1040 ft) when LCM sweeps regained partial returns.

It is difficult to separate the less severe lost circulation problems in DB-2 from the improvement in drilling technology, but an overall comparison of the two holes can be made and then allowance for the different drilling conditions can perhaps be overlain afterward.

Figure 7 shows a comparison of drilled depth with days of operation for both wells. The slow progress in the severe loss zone in DB-1 from day 8 at 84 m (276 ft) to day 32 at 176 ft (579 ft) after the casing was set and the cement drilled out is clear from the graph. Even after switching to coring on day 20 at 105 m (345 ft), progress is still slow through these loss zones. Core from this area shows that the drilled rock was broken and altered with open fractures. By comparison, DB-2 does not have similarly highly fractured and broken rock until about 216 m (710 ft). However, DB-2 was not cored in the interval where the large losses occurred in DB-1.

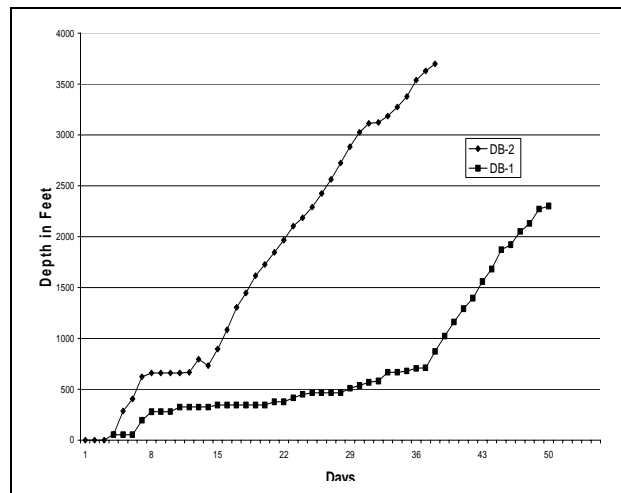


Figure 7. Comparison of DB-1 and DB-2 drilling days with depth.

In order to better understand the difference between the two wells, rate of penetration, ROP, was compared (Figure 8). ROP was calculated by dividing the total footage drilled during each shift by the hours that the bit was rotated. This eliminates time spent pumping LCM sweeps and tripping. It is obvious from this plot that DB-2, with the use of flooded reverse circulation, had much higher ROP through the shallow interval than did DB-1. ROP after both wells were cored is similar.

Drilling fluids used in the two wells were similar. Both were bentonite based. However, lost circulation material chosen for DB-2 included the use of long fiber cellulose polymer Drispac along with the cotton seed hulls used in DB-1. For particularly difficult sections, a spun mineral fiber was added in DB-2 along with a diatomaceous earth based loss control material. It isn't clear how much difference this made, but it is possible that these additives helped recover circulation during coring.

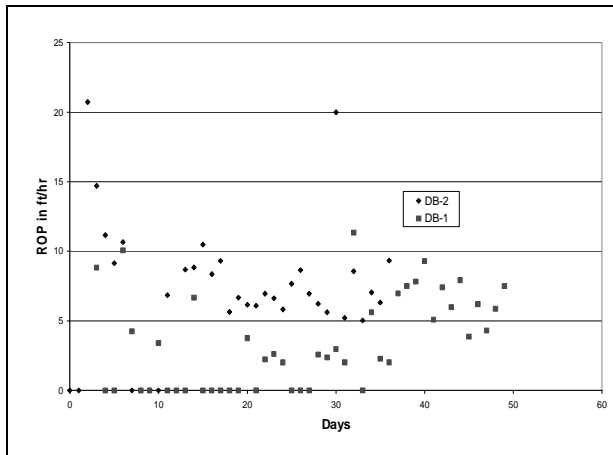


Figure 8. DB-1 and DB-2 rates of penetration

The dual tube reverse circulation allows drilling to continue even when losses occur as long as the bit and drilling assembly have fluid around them. The method not only saves the time spent attempting to recover circulation, it also reduces torque and the risk of twisting off, and can extend bit life and reduce the amount of tripping, thus saving rig time and improving drilling economics. Figure 9 shows a comparison of bit life for DB-1 and DB-2. Bit life for DB-2 is significantly higher throughout the depth of both wells, even through the cored sections. Based on core photos, rocks in both wells appear to have similar drilling characteristics. In some sections they are highly silicified, which could make rocks harder, decreasing bit life.

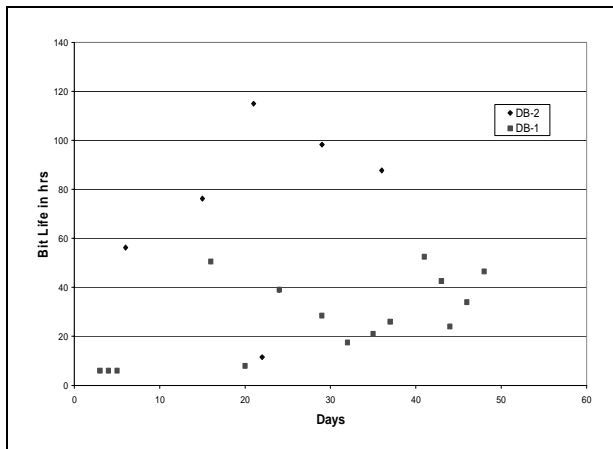


Figure 9. DB-1 and DB-2 bit life comparison.

The highly fractured sections can also decrease bit life due to uneven loading. However, the softer altered zones found in DB-1 should have improved bit life. The most likely conclusion to be drawn from this data is that the bits used in DB-2 wore better in these rocks than those used in DB-1. This emphasizes the importance of proper bit selection in keeping hole cost under control.

Another factor in extending bit life is reducing wear on the gauge cutting surfaces on the sides of the bit. High torque and uneven loading caused by highly fractured and hard rocks can decrease bit life rapidly. Drilling fluids used in DB-1 and DB-2 included additives to reduce torque and lubricate the bit through sections with fluid loss when the bit might not have had as much fluid cooling it and torque might have increased wear. It is clear from noted torque measurements in the drilling records that these additives worked to reduce the torque when it built up except in DB-2 where pipe stuck near the bottom of the hole..

Another factor in improving the outcome of DB-2 compared to DB-1 was the use of tremmie pipe cementing in stages. This allowed a good cement sheath in sections where losses had occurred and not been cured. Cementing with tremmie pipe took slightly longer than conventional cementing by displacement through the bottom of the annulus used in DB-1. With tremmie pipe, an extra half day was needed for setting the small diameter pipe before running the casing. However, this would be worth the extra time to ensure a good cement job, particularly in a highly fractured zone with corrosive fluids such as wet CO₂ or H₂S rich steam. It is clear from the temperature profile in DB-1 that fluid is flowing down behind the casing in DB-1 due to a poor cement job in the area with severe fluid losses.

One of the recommendations from Sandia for improving loss control with cement is the pumping of sodium silicate into the loss zone ahead of the cement. This causes the cement to harden at the leading edge as it is injected into the formation, slowing the advancing cement front. This was suggested to help cure the loss zone in the section just below the 4 1/2" casing shoe in DB-2, but from the drilling record it does not seem to have been tried, although commercial additive names don't always reveal the content of the additives. It might have been helpful in DB-1 when multiple cement plugs were set to try to control losses around 98 m (320 ft).

LESSONS LEARNED

Despite the differences in drilling conditions, some important lessons can be gleaned from the shortened time and cost for drilling DB-2 compared to DB-1:

- Open fractures, particularly at shallow depths can result in extreme losses of circulation. If it is at all possible, wells in areas of steeply dipping faults should be sited down dip from the surface expression of the fault to avoid intersecting these open fractures at shallow depths.
- Use of flooded reverse circulation can reduce drilling time and improve overall ROP in areas

with lost circulation. Bit life in loss zones can also be improved using this drilling method.

- Although coring can allow holes to be drilled despite circulation loss, with extreme losses and highly fractured rock, coring is not a panacea since high torque and stuck pipe can still occur.
- Selection of LCM is important. If cement is used for loss control, additives or use of improved techniques may improve success.
- If loss zones can not be sealed or, due to the drilling method chosen, are not attempted to be sealed, use of an alternative cementing method, such as tremmie pipe or reverse circulation cementing down the annulus may allow for a good cement job.
- When coring ahead without returns, use of lubricant mud additives can improve bit life and ROP, and thus overall drilling performance.

These wells are typical of drilling conditions to be expected in the Basin and Range and so should allow us to apply the lessons to planning future drilling. The next step is to apply these methods to larger, production diameter wells.

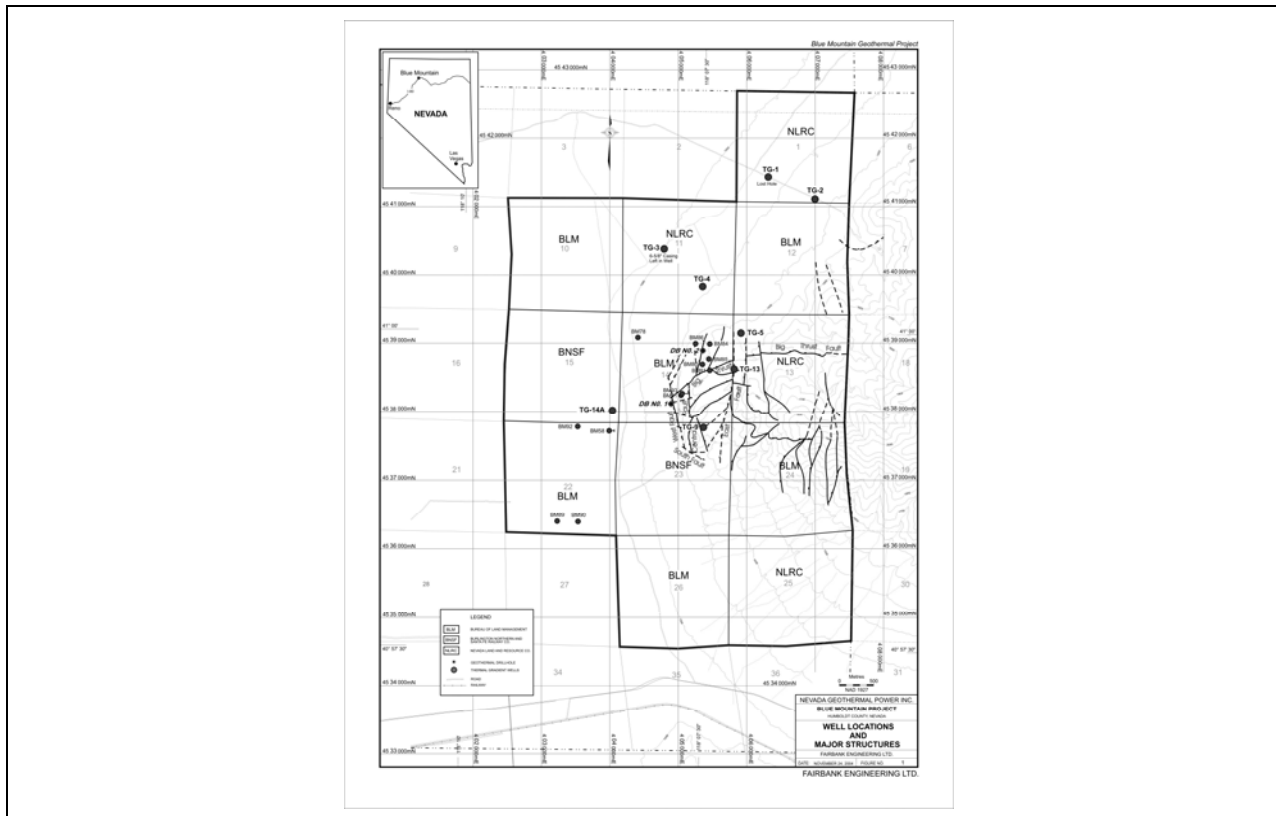
REFERENCES

Finger, J. T., and Livesay, B.J., August 2002, "Alternative Wellbore Lining Methods: Problems and Possibilities," Sandia National Laboratories, Albuquerque NM, SAND2002-2798.

Johnson, L., Murphy, P., and Arsanious, K., June 2002, "Improvements in Lost-Circulation Control During Drilling Using Sehar-Sensitive Fluids," Proceedings of the Canadian International Petroleum Conference: Technology 2000, Calgary, AB Canada.

Mansure, A.J., Westmoreland, J.J., Staller, G.E., Jacobson, R.D., Leberigood, H., Smith, E., Galbreath, D., Ricard, W.M., October 2001, "Plugging Polyurethane Grouting of Rye Patch Lost Circulation Zone," Geothermal Resources Council Transactions, Vol. 25.

Rickard, W.M., Johnson, B., Mansure, A.J., and Jacobson, R.D., August 2001, "Application of Dual Tube Flooded Reverse Circulation Drilling to Rye Patch Lost Circulation Zone," Geothermal Resources Council Transactions, Vol 25.



Map 1. Structure and well locations at Blue Mountain, Nevada.

A PRELIMINARY EVALUATION OF THE CONVECTIVE ENERGY ESCAPING FROM SUBMARINE HYDROTHERMAL CHIMNEYS

Mario César Suárez-Arriaga¹ and Fernando Samaniego V.²

¹ Faculty of Sciences, Michoacan University - UMSNH

² Faculty of Engineering, National University of Mexico- UNAM

Edificio "B", Ciudad Universitaria

Morelia, Mich., 58090 México

e-mail: msuarez@zeus.umich.mx

ABSTRACT

Hydrothermal submarine reservoirs contain an infinite energy potential. This deep submarine energy is related to the existence of hydrothermal vents emerging in many places along the oceanic spreading centers between tectonic plates. These systems have a total length of about 65,000 km in the Earth's oceanic crust and are located at more than 2000 m below sea level. Shallow submarine geothermal heat is related to faults and fractures in the sea bottom close to some coasts. Shallow resources are found near to continental platforms between 1 and 50 m depth. Both types of resources exist, for example, in the Gulf of California, Mexico. The specific chemical characteristics of the submarine hydrothermal waters indicate that water-oceanic rock interactions occur at high temperature-pressure conditions. In this paper we present a description and preliminary estimation of the amount of geothermal energy contained in some submarine systems that is escaping through fissures in the oceanic floor. Hydrothermal fluid at 350- 400°C exits the seafloor at velocities of about 70 to 236 cm/s and mixes with seawater at 2°C. Thermal fluxes measured at some chimneys range from 1 to 93 MW_T, with an average value for a single orifice of about 8 MW_T. Some heat fluxes of about 1000 MW_T have been estimated.

INTRODUCTION

Hydrothermal circulation at the deep ridges of the sea is a fundamental complex process controlling mass and energy transfer from the interior of the Earth through the oceanic lithosphere, to the hydrosphere and to the atmosphere. The properties and behavior of such a complex system cannot be thoroughly explained by the isolated understanding of each one of its single components. These systems act as a whole and is not possible to understand their operation without considering the interactions among all their parts.

Submarine hydrothermal interactions influence the composition of the oceanic crust and the oceans' chemistry. The fluid circulating in seafloor hydrothermal systems is chemically altered due to processes occurring during its passage through the oceanic crust at elevated temperatures and pressures. This mechanism produces hydrothermal vent fields which support diverse biological communities starting from microbial populations that link the transfer of the chemical energy of dissolved chemical species to the production of organic carbon, (Humphris *et al*,1995). The eventual transfer of some gases input by hydrothermal activity from the ocean to the atmosphere, extend the influence of hydrothermal activity far beyond the oceans themselves. The understanding of this mass and energy flows among those complex geological, chemical, geophysical and biological subsystems requires the development of integrated models that include the interactions between them. There are two kinds of submarine hydrothermal systems: deep resources, located at certain places along the rifts between tectonic plates of the oceanic crust at more than 2000 m below sea level, and shallow resources near to continental platforms between 1 m and 50 meters depth. This condensed work has two purposes: to trace the outline of the fundamental characteristics of submarine hydrothermal chimneys and to present a preliminary evaluation of the convective energy escaping from them.

SUBMARINE GEOTHERMAL DISCHARGES, CHIMNEYS AND PLUMES

Geothermal Discharges, Plumes and Venting

Hot springs and geysers are vents and plumes located on the continental land. Most of the known vents in the ocean are at the mid-ocean ridge systems (MORS) in the deep sea (Damm 1995). The crest of the MORS is the place where new lithosphere is

created through igneous activity. Such magmatic processes provide the energy to drive hydrothermal circulation of seawater through the oceanic crust, originating rock-seawater interaction at temperatures between 200°C and 400°C, (Grijalva, 1986; Mercado, 1990; Damm 1995). The resulting mechanism gives rise to venting at seafloor deepness, ranging between 840 and 3600 meters depth and contributing considerably to the global balance of the total Earth's heat (Fornari and Embley, 1995). This venting is associated to fissures located directly above magma injection zones. The observed vent fields are typically tens of meters in diameter ranging in areas between 4 m² to 800 m², (Hessler and Kaharl, 1995). The heat input from those systems affects the mid-depth circulation of the oceans.

Hot rocks of the marine bottom cause chemical reactions, altering the natural chemical composition of sea water. Analysis performed by Mercado (1993) in the Gulf of California, described processes involving water-rock interaction and mixing with magmatic fluids that cause variations of salts dissolved in seawater. Lead, manganese and iron dissolved in the hydrothermal fluid, have higher concentrations than the same elements found in normal seawater by factors of about 8000, 50,000 and 59,000 times respectively. Seyfried and Ding (1995) reported results of mineral solubility experiments and theoretical phase relations for the CaO-Na₂O-Al₂O₃-SiO₂-FeO-Fe₂O₃-CuO-H₂S-H₂O-HCl system, which indicate that temperatures and pressures of approximately 375°C and 400 bars respectively are required to account for the chemistry of hot spring fluids at mid-ocean ridges. Other higher pressure and temperature are possible, but these conditions “*best represent conditions of last equilibration between hydrothermal fluid and altered oceanic crust, prior to ascent of the fluid to the seafloor*”, (ibid.).

The two principal factors affecting the development of these hydrothermal systems are heat from a magmatic source and the permeability structure of the oceanic crust. The vents in the deep sea are markedly short-lived and ever changing. The depth and size of the heat source and the type of permeability, for example related to faults and fractures acting as recharge conduits, will determine the longevity of a vent area (Fornari and Embley, 1995).

Hydrothermal Plumes and Mega-Plumes

The plumes hold many clues to the characteristics of hydrothermal venting and its effect on the ocean. Hydrothermal plumes are created by the thermal and chemical fluid input from submarine hot spring systems into the deep sea (Figures 1 and 2). The rising plumes entrain deeper and saltier water, carrying it up in the water column affecting the thermoaline circulation of the oceans (Damm, 1995).



Figure 1. The bird of a plume at the top of a submarine chimney located 3000 m depth in the Pacific Ocean (BBC, 2004).

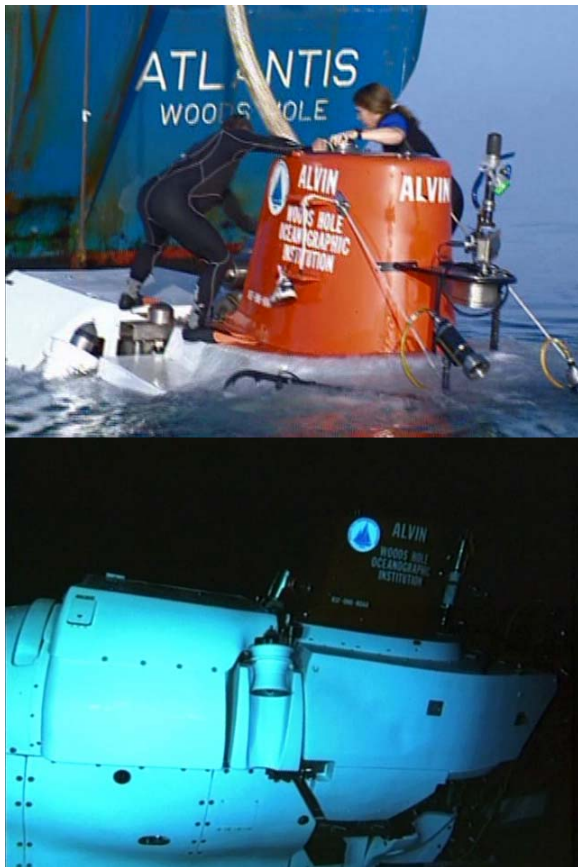
The plumes' active discharge orifices cover only a minuscule percentage of the seafloor. But there is an enormous range of temporal and spatial scales involved in these events. Baker *et al.* (1995) found that the hydrothermal fluids discharged from vents form plumes that are rapidly diluted in the seawater and the mixture rises hundreds of meters and spreads laterally from tens to thousands of kilometers. Those plumes formed by mixing of seafloor vent fluids and ambient seawater are easily detectable by physical and chemical tracers. That is why the careful study of plumes is a useful tool for hydrothermal exploration.



Figure 2. Plume with vortices emerging from a black smoker at 342°C. (Lupton, 1995).

In 1986 a Mega-plume was discovered in the region of the Juan de Fuca ridge in the Pacific Ocean (JFR) having an extension of about 20 Km, 600 m thick and included 10¹¹ MJ of excess heat. Bemis, *et al.* (1993) achieved an experiment using the submersible Alvin

from the Woods Hole Oceanographic Institution (Figs. 3a, b) to collect data while the vessel was stationed at different locations close to a vent source on the JFR. They were able to calculate the vertical heat flow in a buoyant plume. Many other measurements have been done subsequently to that year. The dynamics of buoyant plumes ascent in a stably stratified seawater is shown in figures 4, 7, 8 and 9.



Figures 3a, 3b. The special submarine Alvin, made of titanium and able to submerge 5000 m depth into the sea (BBC, 2004).

Black and White Smoker Chimneys

Divergent plate movements in the deep sea produce fissures, allowing vertical transfer of magmatic heat toward the ocean floor. As cold seawater enters those fissures, it becomes hot and is chemically changed during its contact with the rock. In this way the oceanic crust is cooled significantly by convection. The recharge areas where seawater enters the crust are diffuse and widespread (Alt, 1995). At seafloor hydrothermal vent sites, hot, acidic hydrothermal fluids are injected into cold, alkaline seawater, resulting in precipitation of vent deposits and particle-rich plumes (Mercado, 1990; Kingston, 1995). These deposits and plumes are the surface

expression of large hydrothermal systems that transfer significant heat and mass from the mantle and crust to the hydrosphere. Many vent fields have vertical structures forming chimneys built of materials which precipitate from the heated vent fluid as it mixes with seawater (Figs. 1, 2 and 4). Black smoker chimney walls are initially emplaced as hydrothermal fluid mixes turbulently with seawater (Fig. 4). This occurs because it “is the subsequent dominance of horizontal transport across the wall, mineral dissolution and precipitation within pore spaces of the wall, and deposition of Cu-Fe sulfide along the inside of the flow conduit”, (ibid).

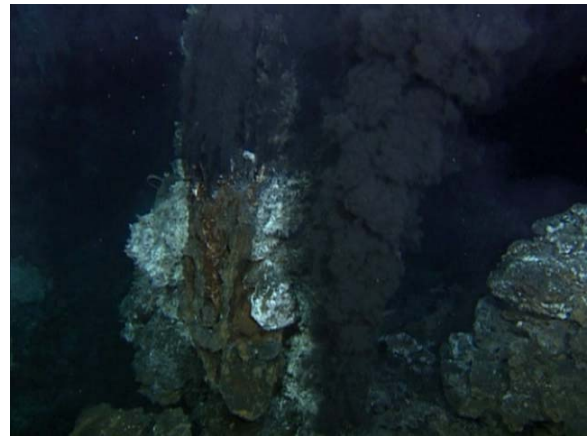


Figure 4. Submarine hydrothermal discharges forming a chimney (BBC, 2004).

In the 1980s oceanographic studies were made in the pull-apart basins of the Gulf of California, including thirteen dives in the submarine Alvin. This cruise was organized by the Scripps and Woods Hole Oceanographic Institutions, in a region located between 21°N and 109°W, at 200 km south of Cape San Lucas (Fig. 5), covering an area of 50 km radius.

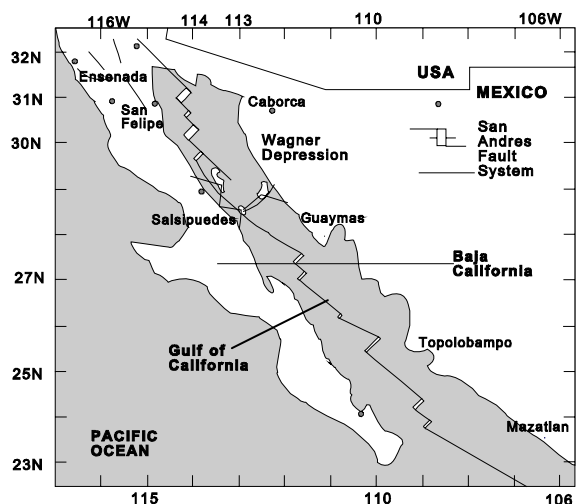


Figure 5. The Gulf of California or Sea of Cortes.

During the dives with the Alvin, diverse hydrothermal manifestations were observed. The so called "Hanging Gardens" were discovered 2600 m depth (Fig. 6). Similar impressive natural chimneys up to 6 meters high, approximately at the same depth, were also observed (Figs. 7 and 8). Those almost metallic natural chimneys are formed in part by iron and copper sulfides, (Mercado, 1990 & 1993) and discharge spouts of water at 350°C. Mercado (1990) reported sampling of sea water containing anomalies of methane, helium and hydrogen associated with geothermal fluids were measured. The flow of hot water expelled by white and black chimneys, has an approximate speed of 2.5 m/s flowing through diameters between 10 and 20 cm (*ibid*).



Figure 6. A strange "flower" or tube-worm opening in a submarine garden, (BBC, 2004).



Figure 7. Two natural chimneys in the Pacific Ocean, discharging fluids at temperatures of about 350°C (BBC, 2004).

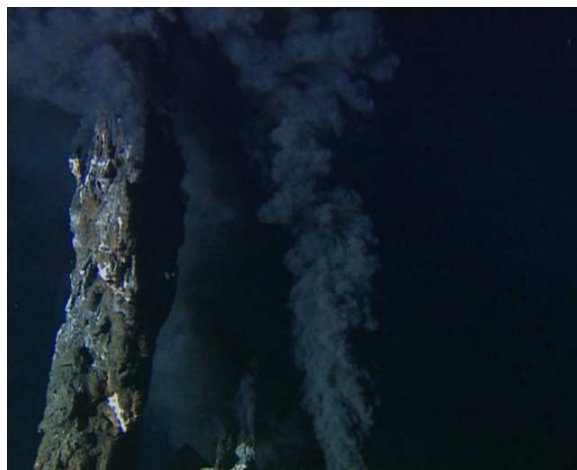


Figure 8. Another perspective of a double chimney system in the Pacific Ocean (BBC, 2004).



Figure 9. Illustration of the upper portion of a black smoker chimney (BBC, 2004).

The effluent emanating from these constructions may be as hot as 403°C (Grijalva, 1986; Mercado, 1990; Hannington *et al.*, 1995). The metal zonation within black smoker chimneys and hydrothermal mounds is a consequence of the precipitation of sulfide minerals, in open spaces or as replacements of preexisting minerals (*ibid*). Kingston (1995) mentioned that initial models describing formation of black smoker chimneys were based on petrologic studies of samples recovered from deposits venting 350°C fluid at 21°N on the East Pacific Rise. These growth models separate the formation of chimneys into stages. The first stage is precipitation of porous anhydrite walls that contains fine inclusions of sulfide (Fig. 10).



Figure 10. Illustration of the first step in the formation of a chimney (BBC, 2004).

This stage occurs when hydrothermal fluid at 350°C exits the seafloor at velocities of about 100 cm/s and mixes with seawater at 2°C. Velocities measured in the hydrothermal plumes 3 to 5 cm above the orifices of chimneys at 21°N EPR varied from 70 to 236 cm/s (Kingston, 1995). Also, in the Mid-Atlantic Ridge, small white smoker chimneys with measured temperature between 250°C and 300°C have been observed (Fig. 11).

All the images in figures 7, 8, 9 and 11 show only some meters of plume ascent because the optical depth of seawater is very limited. They correspond to portions of plumes from black smokers with a heat flux of about 60 MW_T (thermal mega-Watts), venting into an ocean with a constant density gradient given by the following equation (Lupton, 1995):

$$N^2 = -\frac{g}{\rho_0} \frac{d\rho}{dz} = 1.5 \times 10^{-6} \text{ s}^{-2} \quad (1)$$

Where g is the gravity acceleration, ρ_0 is the average local density and $d\rho/dz$ is the vertical density gradient, $\rightarrow d\rho/dz \approx 1.53 \times 10^{-4} \text{ kg/m}^4$. N is called the Brunt-Väisälä buoyancy frequency. Turner (1973) established another useful equation to estimate the maximum height Z_M of rise of a plume as a function of the buoyancy flux F_0 and the frequency N :

$$Z_M = 5 \left(\frac{F_0}{\pi} \right)^{\frac{1}{4}} N^{-\frac{3}{4}} \quad (2)$$

From measured data reported by Lupton (1995), we obtain $F_0 = 0.17 \text{ m}^4 \text{ s}^{-3}$; using the frequency N , it is possible to estimate a maximum height for the plume: $Z_M \approx 370 \text{ m}$ above seafloor. After these models, a plume of 750 m height will correspond to a heat flux of about 1000 MW_T.



Figure 11. A white smoker chimney, 1 m high, at 3660 m, 26°8'N in the Mid-Atlantic Ridge. Humphris et al., 1995. (Reprinted with permission of the American Geophysical Union – WHOI).

Other thermal fluxes measured at black smokers range from 1 to 93 MW_T, with an accepted average value for a single orifice of about 8 MW_T, (Lupton, 1995; Bemis, et al., 1993). The weak dependence of Z_M on the effective heat flux indicates that the mega plume observed in the region of the Juan de Fuca ridge in 1986, was able to affect the water column up to 1000 m above the seafloor. Such megaplume could be the impressive result of an instantaneous and huge release of heat flux at the corresponding source. The fact that other megaplumes have been observed, leads to the conclusion that the total convective heat outflowing from the ocean is discharged in the form of both, continuous steady state venting and mega plumes.

Alt (1995) estimated that submarine hydrothermal discharges remove about 30% of the heat lost from oceanic crust. The average heat flow in the Mexican Volcanic Belt is about 0.10 W_T/m² (García, 2000). The submarine heat flow measured in some places of the Gulf of California was of the order of 0.34 W_T/m² at an average temperature of 330°C (Mercado, 1990).

Using two models, Stein et al. (1995) predicted an average hydrothermal heat loss for the oceanic crust of about 1.5 W_T/m². The same parameter predicted for the ridges is between 2 and 100 MW_T/Km (per unit ridge length). The first value is for a slow ridge and the last value corresponds to a plume with a heat content of 1000 MW_T. Thus, the plumes remove more heat than the steady state surface flux for the cooling lithosphere.

EXPLORA1: A SIMPLE MATHEMATICAL MODEL TO EVALUATE THE GEOTHERMAL POTENTIAL OF CHIMNEYS' DISCHARGES

With the available information extracted from different sources, it is possible to make a preliminary estimation of the global convective energy escaping from submarine hydrothermal chimneys and its geothermal potential. We used a simple mathematical model for submarine reservoirs developed by Suárez (2000). For the application of the model we considered, in all cases, a density average of volcanic rock of 2500 kg/m³, a porosity of 10% , a specific heat C_R of 1000 J/kg/°C and a fixed rock volume of one cubic kilometer (1.0×10⁹ m³). This operation is necessary because the volume of porous hot rock is the main unknown in this type of systems.

We have in the following equations the traditional parameters: φ is porosity, ρ is density, S is saturation, e and h are specific energy and enthalpy, subscripts α (L, V) and R hold for liquid or vapor and rock respectively, T is temperature in °C and V is the rock volume in m³. We have for the fluid Energy Density:

$$E_{fluid} = \frac{\text{Internal energy}}{\text{fluid volume}} = \sum_{\alpha} \varphi S_{\alpha} \rho_{\alpha} e_{\alpha} \left(\frac{kJ}{m^3} \right) \quad (3)$$

For the Rock Energy Density:

$$E_{rock} = \frac{\text{rock energy}}{\text{solid volume}} = (1 - \varphi) \rho_R C_R T_R \left(\frac{kJ}{m^3} \right) \quad (4)$$

The Total initial Energy in the submarine reservoir is:

$$E_0 = (E_{fluid} + E_{rock}) \cdot V_{rock} \quad (kJ) \quad (5)$$

The final energy corresponds to the Thermodynamic State calculated for an abandonment pressure of 5 bar and other data collected in the zone of Punta Banda, close to the port of Ensenada in Baja California, Mexico (Fig. 5). The algebraic differences between both states are considered equal to the available energy and is given by the following formulas.

For the Rock:

$$\Delta E_{rock} \Big|_{initial}^{final} \approx (1 - \varphi) \rho_R C_R (T_{initial} - T_{final}) \quad (6)$$

For the Fluid:

$$\Delta E_{fluid} \Big|_{initial}^{final} \approx (\varphi \rho_F h_F) \Big|_{liquid}^{initial} - (\varphi \rho_F h_F) \Big|_{2-phase}^{final} \quad (7)$$

The Total Energy available in the submarine reservoir is:

$$\Delta E_{Total} = \Delta E_{rock} + \Delta E_{fluid} \quad (8)$$

The transformation coefficient for the available energy (Suárez, 2000) that can be used directly in the form of heat (MW_T) is given by:

$$C_E = \frac{1.0 \times 10^{-6}}{31,557,600 t_A} \quad (9)$$

Where t_A is the payoff time of the investment realized for the hypothetical submarine project. To calculate the recoverable electric power from the reservoir it is necessary to multiply the available energy given by equation (8), by the coefficient C_E given by equation (9) and by the coefficient f_E of recoverable electric energy:

$$G_E = f_E \cdot C_E \Delta E_{Total} \quad (MW_e) \quad (10)$$

These calculations are restricted to the submarine areas close to the coast of the Pacific Ocean and to the region defined by the following coordinates: latitudes between 32°N and 23°N; longitudes between 117°W and 106°W (Figure 5). With the available data the following values shown in Table 1 were obtained.

Table 1.- Potential Energy of Two Submarine Geothermal Systems in Baja California, Mexico.

Zone	P (bar)	T (°C)	Energy Density MJ/m ³	Available Energy (10 ¹⁵ J)	Geothermal Potential (MW _T /km ³)
Punta Banda	51	220	574	232	245
Gulf of California	220	360	906	832	880

The thermodynamic properties of Punta Banda were estimated with a linear model (z is the sea depth in meters). For the pressure:

$$p(z) = 1.0 + 0.1 z \quad (bar) \quad (11)$$

For the temperature:

$$T(z) = 97.082 + 0.246 z \quad (°C) \quad (12)$$

The last column of Table 1 is the geothermal potential per km³ of oceanic rock in the vicinity of the hydrothermal vents. Considering that only 1% of the thermal submarine energy could be transformed into electricity (f_E = 0.01), during t_A = 30 years, and using the data of different references available (Suárez, 2004), the minimum electric capacity of these mexican submarine resources is about 26,100 MW_e.

CONCLUSIONS

- Deep submarine geothermal resources contain practically an infinite energy potential. Volcanic and tectonic processes control hydrothermal activity at mid-ocean ridge spreading centers, influencing all aspects of Oceanography. It includes both, general ocean circulation and the chemistry of the oceans and atmosphere.

- The deep submarine energy is related to the existence of hydrothermal vents emerging in many places along the oceanic spreading centers between tectonic plates. These systems have a total length of about 65,000 km in the Earth's oceanic crust and are located at more than 2000 m below sea level. Shallow submarine geothermal heat is related to faults and fractures in the sea bottom close to some coasts. Shallow resources are found near to continental platforms between 1 and 50 m depth.

- Spreading centers activity occurring throughout the oceans is confirmed by the presence of chemical traces from hydrothermal plumes and mega plumes. There may be a direct relationship between the size and type of plumes and the spreading rate activity. Stable isotope geochemistry has been applied to studies of mid-ocean ridge hydrothermal systems. The fractionation of stable isotopes between co-existing phases provides a powerful tool for understanding interactions among chemical, physical and biological processes. The high temperature hydrothermal vents provide unique deep seawater biological communities of organisms associated with seafloor hydrothermal activity. At hydrothermal vents, the food source is rich and life is abundant.

- This hydrothermal fluid differs significantly in composition from seawater, because of its continuous interaction with the oceanic crust. The seawater-rock reactions in the recharge and discharge zones determine the nature of the oceanic lithosphere and the chemistry of hydrothermal fluids flowing out the seafloor. Seawater experiences progressive reaction as it penetrates the crust and is heated. The heat removed from the crust raises the temperature of the deep sea and gives rise to the precipitation of mineral deposits on the seafloor building chimneys. These natural chimneys discharge spouts of water at temperatures of about 350°C at 2600-3000 m depth in many places located in both main oceans.

- Using available data from different sources, we performed a preliminary estimation of the amount of convective geothermal energy contained in submarine systems escaping through fissures in the oceanic floor: Hydrothermal fluids at temperatures between 350°C and 400°C exits the chimneys on the seafloor at velocities of about 70 cm/s to 236 cm/s

and mixes with deep seawater at 2°C. Thermal fluxes measured at some chimneys range from 1 to 93 MW_T, with an average value for a single orifice of about 8 MW_T. Using some practical formulas it is possible to estimate maximum heights for the plumes formed at the chimneys: 370 m above seafloor for heat fluxes of about 60 MW_T; a Mega-plume of 750-1000 m height will correspond to a heat flux of about 1000 MW_T.

- The observed megaplumes are the spectacular result of an instantaneous and huge release of heat flux at a focal submarine source. The total convective heat outflowing from the ocean is discharged in the form of both, continuous steady state venting and mega plumes. As a comparison, the average conductive heat flow in the Mexican Volcanic Belt is about 0.10 W_T/m². The same submarine heat flow measured in the Gulf of California is 0.34 W_T/m² at an average temperature of 330°C. Other researchers predicted an average hydrothermal heat loss for the oceanic crust of about 1.5 W_T/m². The same parameter predicted for the ridges is between 2 and 100 MW_T/Km (per unit ridge length). It is estimated that submarine hydrothermal discharges remove about 30% of the total heat lost from oceanic crust.

- The energy of the interior of the Earth is a planetary resource, virtually infinite and equitable distributed all around the world, more than any other source of energy. Due in fact to its nature, geothermal energy is inextricably bound to the origin, evolution and destiny of this planet. As primary energy source, the geothermal submarine systems are an immense hope for the future.

REFERENCES

- Alt, J. (1995), Subseafloor Processes in Mid - Ocean Ridge Hydrothermal Systems. *Geophysical Monograph* **91**, American Geophysical Union, 85-114.
- Baker, E., German, C. and Elderfield, H. (1995), Hydrothermal Plumes over Spreading-Center Axes: Global Distributions and Geological Inferences. *Geophysical Monograph* **91**, American Geophysical Union, 47-71.
- Bemis, K., Von Herzen, R. and Mottl, M. (1993), Geothermal Heat Flux from Hydrothermal Plumes on the Juan de Fuca Ridge. *Journal of Geophysical Research*, **98**, 6351-6365.
- Damm, K. (1995), Controls on the Chemistry and Temporal Variability of Seafloor Hydrothermal Fluids. *Geophysical Monograph* **91**, American Geophysical Union, 222-247.

- Fornari, D. and Embley, R. (1995), Tectonic and Volcanic Controls on Hydrothermal Processes at the Mid-Ocean Ridge: An Overview Based on Near-Bottom and Submersible Studies. *Geophysical Monograph* **91**, American Geophysical Union, 1- 46.
- García, G. H. (2000), Modelo del Estado Térmico Inicial del Campo Geotérmico de Los Azufres, Michoacán, México. *Tesis de Doctorado*, Instituto de Geofísica, UNAM, pp.184. México, D.F.
- Grijalva, N. (1986), *Investigación de la Energía Geotérmica en la Depresión de Wagner en el Golfo de California. Latitud 31° 00' al 31° 15' y Longitud 113° 50' al 114° 10'*. (Unpublished reports prepared for the Comisión Federal de Electricidad under Contract No. CCP-CLS-002/86, Cerro Prieto, B.C, Mexico. Date of 1st Report: 10/1/86, 22 pp. Date of 2nd Report: 11/22/86, 38 pp.).
- Hannington, M., Jonasson, I., Herzig, P. and Petersen, S. (1995), Physical and Chemical Processes of Seafloor Mineralization at Mid-Ocean Ridges. *Geophysical Monograph* **91**, American Geophysical Union, 115-157.
- Hessler, R. and Kaharl, V. (1995), The Deep-Sea Hydrothermal Vent Community: An Overview. *Geophysical Monograph* **91**, American Geophysical Union, 72-84.
- Humphris, S.E., Zierenberg, R.A., Mullineaux, L. S. and Thomson, R.E., Editors. (1995), Seafloor Hydrothermal Systems. Physical, Chemical, Biological and Geological Interactions. *Geophysical Mono.* **91**, American Geophysical Union, ISBN 0-87590-048-8, 466 pp.
- Kingston, M. (1995), Modeling Chimney Growth and Associated Fluid Flow at Seafloor Hydrothermal Vent Sites. *Geophysical Monograph* **91**, American Geophysical Union, 158-177.
- Lupton, J. (1995), Hydrothermal Plumes: Near and Far Field. *Geophysical Monograph* **91**, American Geophysical Union, 317-346.
- Mercado, S. (1990), Manifestaciones Hidrotermales Marinas de Alta Temperatura (350 °C) Localizadas a 21°N, a 2600 m de Profundidad en la Elevación Este del Pacífico. *GEOTERMIA, Revista Mexicana de Geoenergía*, **6**, No. 3, 225-263.
- Mercado, S. (1993), Geotermoquímica de Manifestaciones Hidrotermales Marinas de Alta Temperatura, *Revista Mexicana de Geoenergía*, **9**, No. 2, 155-164.
- Seyfried, W. and Ding, K. (1995), Phase Equilibria in Subseafloor Hydrothermal Systems: A Review of the Role of Redox, Temperature, pH and Dissolved Cl on the Chemistry of Hot Spring Fluids at Mid-Ocean Ridges. *Geophysical Monograph* **91**, American Geophysical Union, 248-272.
- Stein, C., Stein, S. and Pelayo, A. (1995), Heat Flow and Hydrothermal Circulation. *Geophysical Monograph* **91**, American Geophysical Union, 425-445.
- Suárez, M. C. (2000), Modelo Volumétrico para la Evaluación de Reservorios Geotérmicos con Información Incipiente. Informe Técnico No. DEX-013/2000, Dpto. de Exploración – CFE, México.
- Suárez, M.C. (2004), Evaluación del Potencial, Biogénesis y Características esenciales de los Sistemas Geotérmicos Submarinos en Mexico: Norte de la Costa Mexicana del Océano Pacífico y Golfo de California. *GEOTERMIA, Revista Mexicana de Geoenergía*, **17**, No. 1, 31-43.
- Turner, J. S. (1973), Buoyancy Effects in Fluids, Cambridge University Press, 368 pp.
- Video of the BBC (2004), Blue Planet: A Natural History of the Oceans. The Abyss. DVD No. 1. Eds. Folio and Tycoon Entertainment Group.

Tracers

- Alcohol Tracer Testing at the Matsukawa Vapor-Dominated Geothermal Field, Northeast Japan** [145](#)
D. Fukuda, M. Asanuma, Y. Hishi, K. Kotanaka
- Double Porosity Model with Transient Interporosity Flow for the Response of Tracers in Naturally Fractured Reservoirs, Considering Constant Mass Flux Injection** [153](#)
Héctor Pulido, Fernando Samaniego V., Jesús Rivera, Rodolfo Camacho and Jetzabeth Ramírez S.
- A Systematic Method for Tracer Test Analysis: An Example Using Beowawe Tracer Data** [166](#)
G. Michael Shook
- Tracer Testing at Mori Geothermal Field, Japan, Using Aromatic Compounds** [172](#)
Masato Watanabe, Fumiaki Arai, Daisuke Fukuda, Mikihiro Asanuma, Yasuyuki Hishi and Jiro Tsutsumi
- A Method of Analyzing Tracer Data to Calculate Swept Pore Volume and Thermal Breakthrough in Fractured Geothermal Reservoirs Under Two-Phase Flow Conditions** [178](#)
Xingru Wu, Gary A. Pope, G. Michael Shook, and Sanjay Srinivasan

ALCOHOL TRACER TESTING AT THE MATSUKAWA VAPOR-DOMINATED GEOTHERMAL FIELD, NORTHEAST JAPAN

Daisuke Fukuda¹, Mikihiro Asanuma¹, Yasuyuki Hishi¹, and Koichi Kotanaka²

¹JMC Geothermal Engineering Co., Ltd. (Geo-E)
101-1 Hosoyachi, Ukai
Takizawa, Iwate, 020-0172, Japan
e-mail: fukuda@geothermal.co.jp

²Tohoku Hydropower & Geothermal Energy Co., Inc.
1-7-25 Chuo-dori
Morioka, Iwate, 020-0021, Japan

ABSTRACT

A series of water injection was practiced in the Matsukawa vapor-dominated geothermal field, northeast Japan, and the necessity of a tracer test emerged to evaluate the returns of injected water. Because production wells produced superheated or saturated steam, vapor-phase tracers (sulfur hexafluoride and hydrofluorocarbons) and two-phase tracers (alcohols) were examined in terms of their practical use. We selected the alcohols because (1) they were significantly soluble in water and thus handled simply during injection, sampling and analysis, and (2) they were expected to boil and flow as with injected water in the reservoir.

Five tracer tests were conducted on the four production wells from 2000 to 2003, and the returns of tracers were successively detected for each test. The results of the tests using mixed solutions of ethanol and i-propanol showed variation in the ethanol/i-propanol ratios and different peak times between the alcohols, which may depended on the difference in volatility and the mechanism of two-phase flow in the vapor-dominated reservoir. The tracer test using mixed alcohol may have potential to give some information about the boiling process of injectate and properties of two-phase flow in the reservoir.

INTRODUCTION

The Matsukawa Geothermal Field

The Matsukawa Geothermal Power Station is located in the Hachimantai volcanic area, Iwate prefecture, northeast Japan (Figure 1). The station started power generation in October 1966 with 9.5 MWe as the first commercial geothermal power station in Japan. The

capacity has been increased gradually up to 23.5 MWe by June 1993.



Figure 1. The location of the Matsukawa field.

The geothermal field is in a valley and the production wells are distributed along a stream (Figure 2). The productive fractures are found in a Miocene formation composed mainly of dacitic lapilli tuff and sandy tuff, and around the southeastern boundary of a dioritic body intruding into the Miocene. The cap rock of the reservoir is composed of andesitic lava and welded tuff covering the productive formation.

The field has contained over 10 production wells and one re-injection well (Figure 2). Although almost all of the production wells had been producing superheated steam, a couple of them started production of saturated steam following water injection. Therefore, monitoring of the returns of

injected water became important for the reservoir management.

Injection History

One re-injection well (MR-1) and three production wells (M-6, M-13 and M-14) were used for water injection and tracer tests. The re-injection well was used for long-term injection and the three production wells were used for short-term injection tests. Steam condensate, stream water, brine and their mixture were injected. Long-term injection has been carried out at well MR-1 for 15 years (from March 1988 to July 2003). The range of injection rates were from 10 t/h to 130 t/h. Short-term (less than nine months) injection were conducted on wells M-6 and M-13. Fluid was injected at the average rates of 20 t/h for well M-6 (from February to October 2000), and 40 t/h for well M-13 (from October to November 2002). The test at well M-6 was terminated when increased brine production was observed in well M-8. At well M-14, injection was conducted only during drilling and tracer was injected at the end of the drilling before the start of production.

Monitoring of Injected Water

Chemical and physical monitoring clearly detected the returns of injected waters in some cases of the short-term tests: e.g. (1) changes in chemical composition of steam, (2) decrease in steam temperature and (3) beginning of brine production. The monitoring for the long-term injection lacked noticeable signs of returns except during the primary period of injection. It was especially difficult to detect the injection flow toward the relatively new wells which started production after the beginning of the injection, because the reservoir conditions around the wells could have been changed by the long-term injection.

For more accurate and more sensitive tracing of injectate in the vapor-dominated reservoir, two-phase and vapor-phase tracer tests were considered as the best method. Accordingly, we selected alcohols as the two-phase tracers. This paper presents the basic results of five tracer tests conducted from 2000 to 2003 in the Matsukawa field.

SELECTION OF TRACERS

Sulfur hexafluoride (SF_6), hydrofluorocarbons (HFCs, e.g. R-23 and R-134a) and hydrochlorofluorocarbons (HCFCs, e.g. R-12 and R-13) have been used extensively as vapor-phase tracers at The Geysers, California, U.S.A. (Adams et al., 1991a, b and 2001; Adams, 1995; Beall et al., 1994, 1998; Voge et al., 1994) and Wairakei, N.Z. (Glover and Kim, 1993). The potential of alcohols as two-phase tracers were reported by Adams (1995) and Adams et al. (2000), although their practical use

in the field had not been tested sufficiently. Lovelock (2001) showed the usefulness of alcohols in tracer flow testing, where i-propanol was used at temperatures up to 225 °C.

Based on these previous studies, we examined the use of SF_6 and HFCs as vapor-phase tracers, and alcohols (e.g. methanol, ethanol, i-propanol and n-propanol) as two-phase tracers. Alcohols were selected because of the properties discussed below. HCFCs were excluded since they are ozone depleting substances.

Thermal Stabilities and Detection Limits of SF_6 , HFCs and Alcohols

Adams et al. (2000) reported that SF_6 and methanol showed high stability (< 5% decay) at temperatures up to about 300 °C, pHs of 3 to 7 and for durations of up to two weeks. Ethanol and n-propanol showed decay of 10-20%. R-134a, one of HFCs, showed 10 - 50% decay at temperatures up to 290 °C and durations up to 19 days (Adams et al., 2001).

Sulfur hexafluoride and HFCs are detectable in the order of ppb to ppt using a gas chromatograph (GC); in contrast, our detection limits of alcohols are 0.03 to 0.1 ppm using a GC. Therefore, SF_6 is superior to alcohols in terms of thermal stability and detection limit.

Physical Properties of SF_6 , HFCs and Alcohols Related to Injection, Sampling and Analysis

Despite their theoretical advantages, SF_6 and HFCs have some disadvantages for injection and sampling. It is difficult to inject the all of the gas into formations from the surface. For example, in order to optimize the injection of SF_6 gas tracer, Glover and Kim (1993) employed a downhole injection method in which a glass ampoule containing SF_6 was broken at the desired depth during water injection. Furthermore, vapor-phase tracers do not always follow the same path as the injected water, which takes time to boil in the reservoir (Adams, 1995).

Also, SF_6 and HFCs are collected into specially sealed and evacuated flasks containing an alkali solution, as used for general steam sampling. This is not suitable for frequent sampling, e.g.: once an hour to several times a day for more than 10 wells. In contrast, alcohols have advantages as two-phase tracers:

- 1) The vapor pressures are similar to that of water;
- 2) Alcohols are miscible or significantly soluble in water;
- 3) Several alcohols with different saturated vapor pressures are available: e.g. methanol, ethanol, n-propanol and i-propanol.

Being liquid at atmospheric temperature and pressure, alcohols are injected easily using a simple

pump as is the case with liquid-phase tracers. Since alcohols are miscible or significantly soluble in water and their vapor pressures are similar to that of water, it is expected that alcohols boil and flow in the vapor-dominated reservoir as the injected water. Being condensed at atmospheric temperatures, alcohols are collected quite easily into screw-cap bottles as steam condensate. Furthermore, it is possible to use different alcohols at the same time for the different wells, or mix them to take advantage of their different vapor pressures for investigating the boiling process of the injected water.

In addition to the advantages mentioned above, we have developed a direct-injection method for alcohol analysis by modifying an existing gas chromatograph. This technique shows greater sensitivity than the head-space gas chromatographic method used in tracer flow testing (Lovelock, 2001). For these reasons, alcohols were employed as tracers at the Matsukawa field, even though SF₆ and HFCs are more thermally stable and detectable as shown by the results of previous studies. We also thought that alcohols would not decay significantly at the temperatures found in the Matsukawa field (< 260 °C), unlike the result of the experiments at the high temperature up to 300 °C by Adams et al., (2000).

METHOD

Tracer Injection

For a well with negative wellhead pressures, tracers were injected directly from metal barrels at the wellhead. For wells with positive wellhead pressures, a pump was used. The injection took less than 25 minutes for a negative wellhead pressure and 20 to 45 minutes for the positive ones. Methanol, ethanol, i-propanol, n-propanol and mixtures of these were used. These solutions were diluted to 60% because of the inflammability of alcohols. In order to make detection easier, about 100 kg to 3,000 kg of alcohols were used per test (Table 1). Water injection continued during tracer tests at the rates ranging from 10 t/h to 40 t/h.

Sampling

Cooling coils were connected to the steam lines and 100 ml of condensates were collected into screw-cap bottles. Samples were treated with 0.1 ml of 5% zinc acetate solution to precipitate H₂S to protect the GC column. Sampling for a well was done within 10 minutes. Sampling continued for one to more than six months. About 10 production wells were sampled

approximately once an hour at the beginning of tests, twice a day after three days, once a day after a weeks, and once several days after a few weeks.

Analysis

The analyses were performed on a Shimadzu GC-14B gas chromatograph equipped with a flame ionization detector. Separation was achieved with a 3 m x 3 mm column containing 80/120 mesh Carboxpack, and the carrier gas of nitrogen. Samples and calibrators (1-5 µl) were injected into the GC directly by an auto injector. Alcohol concentrations were calculated by comparing peak area values of samples and calibrators. The detection limits were 0.03 ppm for ethanol, i-propanol and n-propanol, and 0.1 ppm for methanol in the steam condensates.

RESULTS AND DISCUSSION

Five tracer tests were conducted on the four wells from 2000 to 2003. The basic results are summarized in Table 1. The returns of tracer were detected for each test, and then injector-producer pairs were determined (Figure 2). To compare quantitatively the returns of various tracer materials injected in various amount, the normalized tracer-production rates were used for drawing return curves. The normalized tracer-production rates were calculated by dividing the tracer-production rate (g/h) by the number of kilograms of tracer material injected. Since an area under a return curve shows the recovery of a tracer, the degree of connectivity between an injectors and a producer can be inferred by the normalized return curves. Results from the individual tests are presented below.

Tracer test on well MR-1

Water injection into well MR-1 has continued for 15 years (1988 to 2003) at injection rates ranging from 10 t/h to 130 t/h. On 6 August 2000, the first two-phase tracer test was conducted to determine the flow paths from well MR-1. The mixed solution of 770 kg ethanol and 130 kg i-propanol was injected directly from metal barrels to the wellhead in eight minutes under negative pressure. Tracer returns were found in production wells M-1, M-5 and M-12 (Figure 3). The tracer first arrived at well M-1 in 30 hours, and then at wells M-5 and M-12 in 120-150 hours after tracer injection (Table 1). The highest recovery in well M-12 indicated the strongest return from well MR-1. The returns lasted for more than two months, which indicates that the alcohols were stable long enough for evaluation of tracer returns in the field.

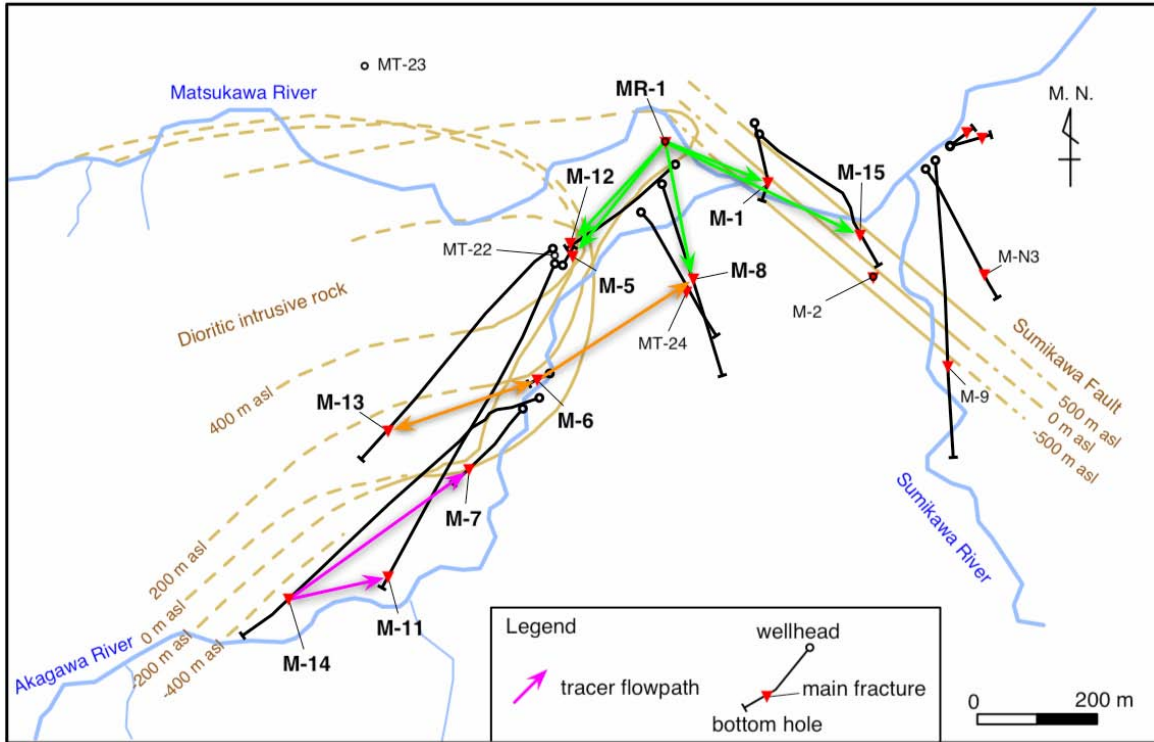


Figure 2. Well locations and flow paths of tracers. Well MR-1 is the only re-injection well in the field.

Injection well	Injection date / tracer	Production well	Recovery (%)	Initial detection time (h)	Tracer velocity (m/h)
MR-1	6-Aug-00 ethanol: 770 kg + i-propanol: 130 kg	M-1	ethanol 1.5 i-propanol 2.5	30	7
		M-5	ethanol 5.1 i-propanol 3.3	145	3
		M-12	ethanol 24 i-propanol 17	121	3
MR-1	13-May-03 i-propanol: 3,200 kg + toluenesulfonate: 100 kg	M-5	i-propanol -	192	3
		M-8	i-propanol -	1,510	0.2
		M-12	i-propanol > 6.8 toluenesulfonate > 6.2	96 171	3 1.6
		M-15	i-propanol -	1,850	0.2
M-6	12-Sep-00 n-propanol: 1,530 kg	M-8	n-propanol 73	10	39
		M-13	n-propanol 9.1	49	5
M-13	24-Oct-02 methanol: 710 kg + ethanol: 680 kg	M-6	methanol 18 ethanol 9.8	- 45	- 6
		M-7	i-propanol 0.08	17	32
M-14	18-May-01 ethanol: 650 kg + i-propanol: 1,290 kg	M-11	ethanol 0.30 i-propanol 0.24	4	61

Table 1. Results from tracer tests at the Matsukawa geothermal field.

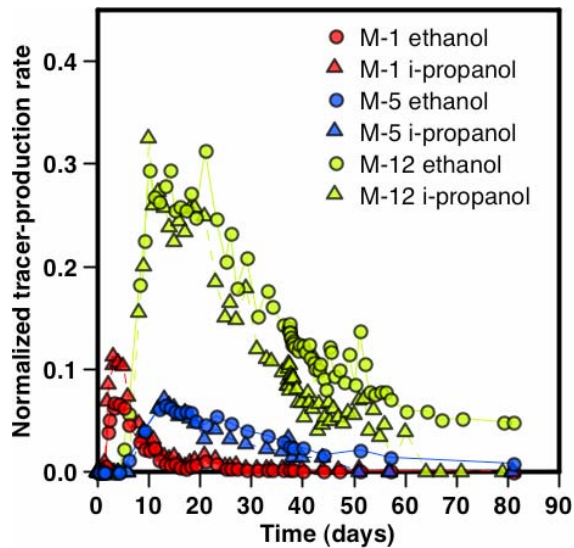


Figure 3. Normalized tracer-return curves from the first MR-1 tracer test in 2000

In contrast to the case of the test on well M-14 as described later, the peak concentrations of ethanol and i-propanol were detected simultaneously in each production well, although the alcohols had different vapor pressures. Furthermore, because well M-1 and M-12 had been producing water, a large part of tracer may have moved as a liquid and then boiled finally near or in the wells.

As Figure 4 shows, the ethanol/i-propanol ratios of samples taken from well M-1 was smaller than that of the tracer, although the ratios of samples from wells M-5 and M-12 were equal to that of the tracer. Since ethanol is more volatile than i-propanol, steam enriched in ethanol may have been generated and then escaped to a fracture disconnected to well M-1. In consequence, the residual tracer flowing into well M-1 may have become depleted in ethanol.

The second test on well MR-1 was conducted on 13 May 2003 with more two-phase tracer (3,200 kg of i-propanol) and a liquid-phase tracer (100 kg of toluenesulfonate) injected almost simultaneously. The returns of i-propanol were observed in wells M-5, M-8, M-12 and M-15 (well M-1 was shut in at this time). The additional detection of i-propanol in wells M-5 and M-8 can be attributed to the more mass of i-propanol and the change of injection depth observed by well logging before the test.

The only toluenesulfonate return was only seen in well M-12, although wells M-8 and M-15 had been producing brines during the test. This observation indicates that the two-phase tracer spread more widely than the liquid-phase tracer did. As shown in Figure 5, the return curves of i-propanol and toluenesulfonate are close together and thus indicate the tracer recoveries are similar (M-12 was shut in 30

days after tracer injection due to a periodic inspection). This observation suggests that a large part of the i-propanol moved together with toluenesulfonate as liquid phase to well M-12.

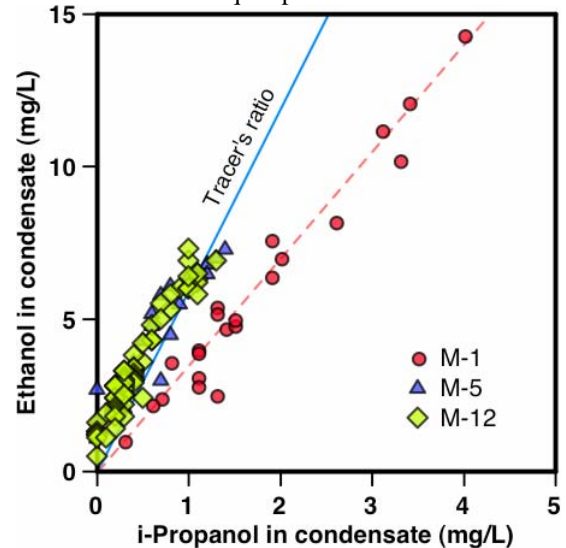


Figure 4. Relationship between ethanol and i-propanol concentrations in samples taken from well M-1, M-5 and M-12. The correlation line for well M-1 (broken line) differs from the line indicating the ethanol/i-propanol ratio of the tracer (solid line).

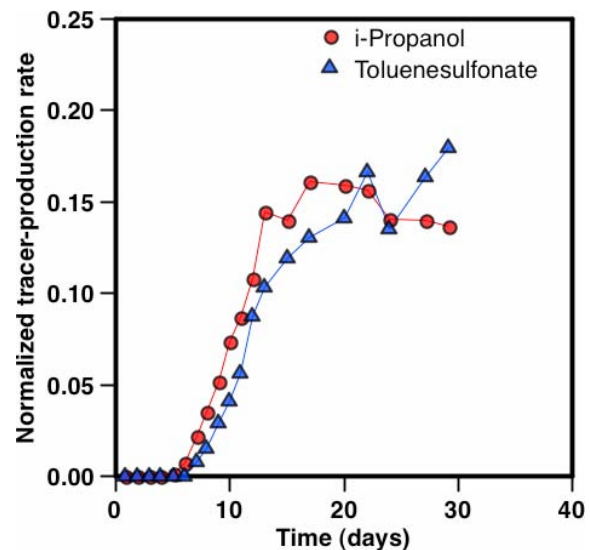


Figure 5 Normalized i-propanol and toluenesulfonate returns from well MR-1 to well M-12 during the second MR-1 test in 2003. Well M-12 was shut in 30 days after due to a periodic inspection.

Tracer tests on wells M-6 and M-13

Short-term injection including tracer tests was conducted on well M-6 for nine months in 2000. Four to six months after the injection, well M-8 showed decreases in NCG concentration and

wellhead temperature, an increase in steam flowrate, and the beginning of water production (Figure 6). These chemical and physical changes indicate the obvious breakthrough from well M-6 to well M-8. In contrast, well M-13 had been producing superheated steam during the injection, and the only decrease in NCG concentration was seen. These observations revealed the strong connectivity between wells M-6 and M-8.

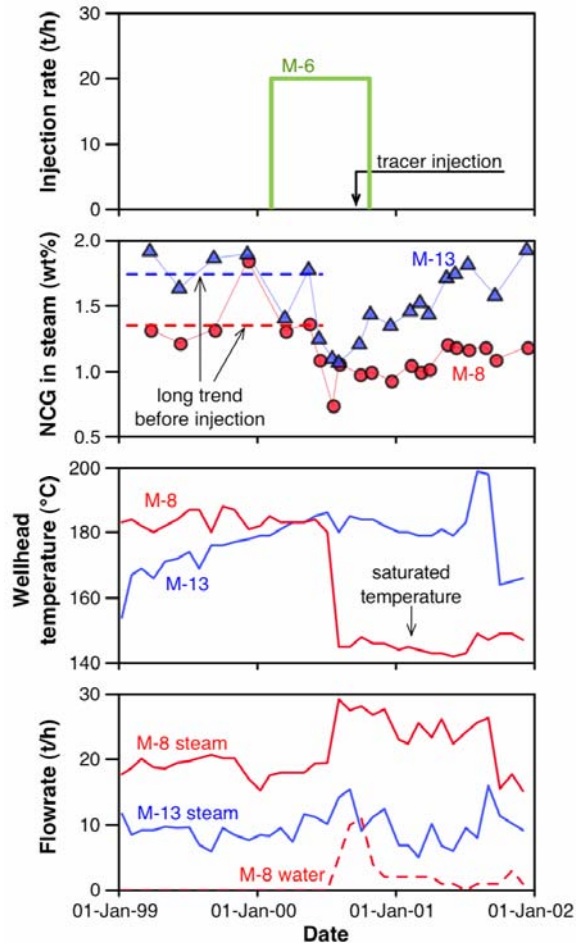


Figure 6. Chemical and physical changes in wells M-8 and M-13, showing decrease in steam temperature and NCG concentration and increase in steam flowrate, and the beginning of water production in well M-8 after injection. In contrast, M-13 showed only the decrease in NCG concentration.

On 12 September 2000, 1,560 kg of n-propanol was injected over a period of 20 minutes into well M-6, and then the returns of the tracer were detected in wells M-8 and M-13 (Table 1, Figures 2 and 7). The tracer return at well M-8 showed the short period for the first arrival (10 hours) and the extremely high recovery (73%) of the mass injected. As with the chemical and physical changes, the tracer test

suggested the strong connectivity between wells M-6 and M-8.

Short-term injection including a tracer tests was conducted on well M-13 for a months in 2002. On 24 October 2002, a mixture of 710 kg methanol and 680 kg ethanol was injected over a period of 45 minutes into well M-13. The returns of the alcohols were observed only in well M-6; the tracer may have flowed in a same path indicated by the return from well M-6 to well M-13 in the previous test on well M-6.

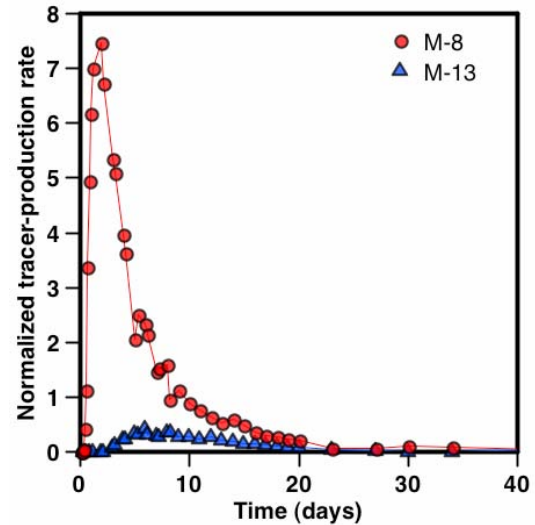


Figure 7. Normalized n-propanol returns from well M-6 to wells M-8 and M-13.

Tracer test on well M-14

The water and tracer injection into well M-14 was conducted during its drilling, using a drilling pipe set close to the main fracture. Well M-14 has been a production well and the aim of the test was to evaluate interference with the surrounding wells before start of production. Being located in the highest-temperature upflow zone, well M-14 and the two neighboring wells, M-7 and M-11, have been producing superheated steam.

On 18 May 2001, a mixed tracer of 650 kg ethanol and 1,290 kg i-propanol was injected into well M-14 with a pump in five minutes. The returns were found in wells M-7 and M-11 (Table 1, Figures 2, and 8). The tracer first arrived at well M-11 in four hours and then at well M-7 in 17 hours. The returns lasted for only two days and the recoveries were quite small (< 0.5%), which means the more than 99% of tracer was missing. It is possible that most of the tracer and injected water flowed downwards in the vapor-dominated region because of the difference in density between steam and water.

As Figure 8 shows, the peak concentration of ethanol was detected earlier than that of i-propanol in well M-11. This time difference of peak concentrations was reflected in the ethanol/i-propanol ratios of M-11 samples. Figure 9 shows that the samples collected from well M-11 contained ethanol excessively compared to the tracer at the beginning of return. The ratio of samples approached and then became equal to that of the tracer 14 hours after tracer injection.

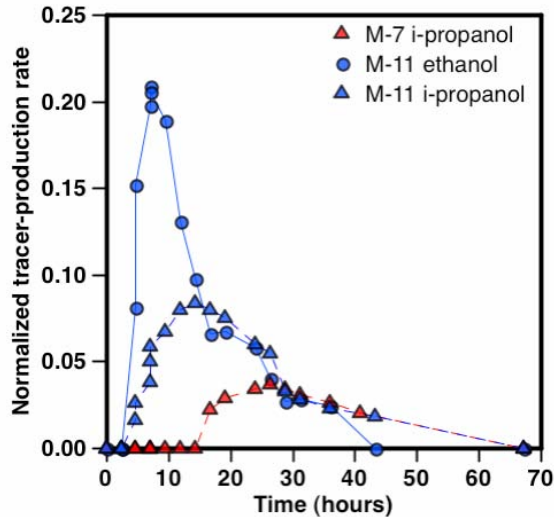


Figure 8. Normalized ethanol and i-propanol returns from well M-14 to wells M-7 and M-11. Well M-11 shows the difference in peak time between the alcohols.

The time difference of peak concentrations and the change in the ethanol/i-propanol ratios can be explained as follows:

- 1) The injected fluid containing tracer moved slowly when it was liquid under the vapor-dominated condition.
- 2) The fluid was heated and more ethanol vaporized faster than i-propanol because ethanol is more volatile than i-propanol. As a consequence, ethanol-rich steam was generated.
- 3) Since steam moves faster than water in a vapor-dominated region, the ethanol-rich steam flowed ahead of the residual fluid.
- 4) Then the fluid was kept heated and more i-propanol began to vaporize. As a result, the ethanol/i-propanol ratio approached that of the tracer. Finally whole fluid flowing to M-11 evaporated, and the ethanol/i-propanol ratio became equal to that of the tracer.

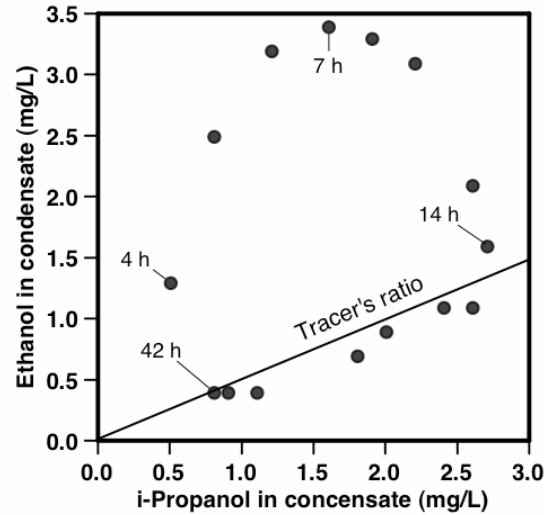


Figure 9. Relationship between ethanol and i-propanol concentrations of samples taken from well M-11. The ethanol/i-propanol ratio of the tracer injected was shown as solid line. Samples contained excess ethanol compared to the tracer's ratio at the beginning of return. The ratio of samples approached and then became equal to that of tracer 14 hours after tracer injection.

CONCLUSIONS

A series of water injection was practiced in the Matsukawa vapor-dominated geothermal field, and the tracer test using vapor-phase or two-phase tracers was requested for evaluation of injectate returns. We selected alcohols as the two-phase tracer because they were expected to boil and flow as injected water in the reservoir. Five tracer tests were conducted on the four wells, and the returns were successfully observed for each tests.

Results from the first test on well MR-1, in which a mixed tracer of ethanol and i-propanol was used, showed that the ethanol/i-propanol ratios of samples taken from well M-1 were lower than that of the tracer and samples from wells M-5 and M-12. Since ethanol is more volatile than i-propanol, ethanol-rich steam may have been generated and escaped to a fracture disconnected to well M-1. A liquid-phase tracer (toluenesulfonate) was used together with i-propanol for the second test on well MR-1. The observation indicated that i-propanol spread more widely than the liquid-phase tracer did. The results from the test on well M-6 showed the high recovery in well M-8 that is consistent with the chemical and physical changes after water injection.

The tracer test using a mixed tracer of ethanol and i-propanol were conducted on well M-14. The returns showed that the peak concentration of ethanol was

detected earlier than that of i-propanol in well M-11, and the samples collected from well M-11 contained excess ethanol compared to the tracer at the beginning of return. The observations indicates that ethanol-rich steam was generated soon after tracer injection, and then the steam arrived first at well M-11.

ACKNOWLEDGMENTS

The authors wish to thank Tohoku Hydropower & Geothermal Energy Co., Inc. for allowing us to publish this paper.

REFERENCES

Adams, M. C. (1995), "Vapor, Liquid, and Two-phase Tracers for Geothermal Systems", *Proc. World Geothermal Congress*, 1875-1880.

Adams, M. C., Yamada, Y., Yagi, M., Kondo, T., and Wada, T. (2000), "Solubility of Methanol, Propanol, and SF₆ as High-temperature Tracers", *Proc. World Geothermal Congress*, 3015-3019.

Adams, M. C., Beall, J. J., Eneedy, S. L., and Hirtz, P. (1991a), "The Application of Halogenated Alkanes as Vapor-phase Tracers: a Field Test in the Southeast Geysers", *Transactions, Geothermal Resources Council*, **15**, 457-463.

Adams, M. C., Moore, J. N., and Hirtz, P. (1991b), "Preliminary Assessment of Halogenated Alkanes as Vapor-phase Tracers", *Proceedings, 16th Workshop*

on Geothermal Reservoir Engineering, Stanford University, 23-25.

Adams, M. C., Beall, J. J., Eneedy, S. L., Hirtz, P. N., Kilbourn, P., Koenig, B. A., Kunzman, R., and Smith, J. L. B. (2001), "Hydrofluorocarbons as Geothermal Vapor-phase Tracers", *Geothermics*, **30**, 747-775.

Beall, J. J., Adams, M. C., and Hirtz, P. N. (1994), "R-13 Tracing of Injection in The Geysers", *Transactions, Geothermal Resources Council*, **18**, 151-159.

Beall, J. J., Adams, M. C., and Hirtz, P. N. (1998), "Evaluation of R-134A as an Injection Water Tracer in the Southeast Geysers", *Transactions, Geothermal Resources Council*, **22**, 20-23.

Voge, E., Koenig, B., Smith, J. L. B., and Eneedy, S. (1994), "Initial Findings of The Geysers Unit 18 Cooperative Injection Project", *Transactions, Geothermal Resources Council*, **18**, 353-357.

Glover, R. B. and Kim, J. P. (1993) "SF₆ - A New Nonradioactive Geothermal Tracer", *Proc. 15th New Zealand Geothermal Workshop*, **15**, 125-132.

Lovelock, B. G. (2001) "Steam Flow Measurement Using Alcohol Tracers", *Geothermics*, **30**, 641-654.

Lovelock, B. G. and Stowell, A. (2000), "Mass Flow Measurement by Alcohol Tracer Dilution", *Proc. World Geothermal Congress*, 2701-2706.

DOUBLE POROSITY MODEL WITH TRANSIENT INTERPOROSITY FLOW FOR THE RESPONSE OF TRACERS IN NATURALLY FRACTURED RESERVOIRS, CONSIDERING CONSTANT MASS FLUX INJECTION

Héctor Pulido 1, Fernando Samaniego V. 2, Jesús Rivera 2, Rodolfo Camacho 1, 2, and Jetzabeth Ramírez S. 2, 3

1. Pemex, 2. National University of Mexico, 3. IMP.

Facultad de Ingeniería
México, D. F, 04510, México
ance@servidor.unam.mx

ABSTRACT

In tracer test interpretation, fissured reservoirs are commonly referred to as double porosity systems. Different approaches have been proposed for analyzing their well tracer concentration responses. This work presents a double porosity model with *transient* fracture-matrix transfer, considering constant mass flux at the injection well, for the interpretation of the observed tracer response in the producing wells for continuous injection of a tracer. A new parameter is presented which represent the gradient of mass flow that governs the fracture-matrix transfer and it is used to characterize the porous media. The solution for the proposed mathematical model was obtained in Laplace space.

The numerical inversion was carried out with Stehfest's algorithm. In addition, approximate analytical solution for short and long dimensionless time are obtained, and are compared with the solution obtained by numerical inversion, providing satisfactory results. The values of the numerical inversion were used to generate the "type curve", presented in terms of the dimensionless groups obtained from the approximate analytical solution.

INTRODUCTION

Radioactive tracers are substances that are added to the injected fluid and they are used to study the trajectory of the fluids inside a reservoir, as they advance toward the producing wells. A tracer should meet certain characteristics, among others: not interfere with the fluid flow, require a small concentrations and easy detection. Another purpose of introducing a tracer in the injected fluid is to detect the fractures preferential orientation or discontinuities in the reservoir. In any project of fluid injection, the channels of high permeability in the reservoir can quickly establish "short-circuits" for the injected fluid, reducing the efficiency of the process drastically, and in some cases can cause the failure of

the project. The field tests with well to well tracer injection and the data analysis with the correct model, provide the possibility for the improvement of the reservoir characterization.

The information that is possible to obtain from well to well tracer tests is the following: sweeping efficiency, identification of high permeability zones, inadequate injectors wells, preferential flow tendencies, location of barriers, relative velocity of the injected fluids, and in general the trajectories of the fluids injected into the reservoir toward the producing wells. Radioactive tracers that have been successfully used in the industry are: tritiated methane, ammonium nitrate, isopropilic alcohol, thorium, tritium, deuterium, krypton 85, iodide and strontium. These tracers have fulfilled the national and international norms of security.

Radioactive tracers such as tritium and krypton 85 emit beta radiation, and can be detected using a highly sensitive proportional counter, in concentrations as low as of one picocurie/liter. Tritium in water is detected using a Geiger counter coupled with wireline. With respect to chemical tracers, these must be used in high concentrations, are relatively most expensive and easily detectable. The perfluorinated molecules are of great interest as gas tracers. SF₆ has been used with success for many years. The focus has been put on perfluorinated cyclic molecules, like perfluorodimethylcyclobutane (PDMCB) and, perfluoromethylcyclopentane; these are commonly named PFTs. The PFTs are non toxic products, low-cost and with an exceptionally low detection limit with Geiger counters. The first field injection of PFTs was carried out in the Ekofisk field in the North Sea in 1987, on a trial-and error basis. The mass of radioactive tracer injected depends among other factors on the travel distance half life, degree of adsorption in the rock, high permeability channels, (short circuits), formation temperature, magnitude of the inaccessible pore volume, etc.

The injection of a tracer in a naturally fractured reservoirs allows through a solution of the mathematical models that describe these flow problems, the interpretation of the response in producers wells, as a result we can estimate parameters of practical interest.

The purpose of this study is to present a new model with transient fracture-matrix transfer, for the tracer response in the producing wells, considering the continuous injection of a tracer. The main contributions of this work consist in taking into account radioactive decay, the inaccessible matrix pore volume, the definition of a dimensionless radius similar to that previously used in well test analysis (instead of the traditional one that is referred to as the mixing coefficient [dispersivity]), the approximate analytical solutions for short and long dimensionless times, and a type curve that allows the estimation of the radial dispersion coefficient (D_r). Models previously presented for Tracer Flow Study of the tracer dispersion in naturally fractured reservoirs is of growing interest for the characterization of a geothermal reservoir, mainly due to the current importance of fluid injection projects to improved the recovery of energy. The dispersion effect controls the success of a tracer injection process. In the past, several papers have discussed the theory related to the flow of tracers in porous media. A complete revision was presented by Perkins and Johnston (1963), as well as Pozzi and Blackwell (1963); Raimondi et al. (1959), presented an approximate solution for the chemical tracer flow under radial flow conditions. Bentsen and Nielsen (1965) presented laboratory data for radial systems, and showed that the tracer dispersion behavior can be appropriately described by means of the solution of Raimondi et al., when the mobility relationship is favorable. Brigham and Smith⁸ applied the solution of Raimondi et al. to predict the behavior of a chemical tracer in a five spot pattern. Yuen, Brigham and Cinco (1979), presented a methodology to predict the radial flow behavior of a chemical tracer in a stratified reservoir, where the response showed peaks depending on strata characteristics. Later, Abbaszadeh and Brigham (1984) continued this work to determine stratified characteristics. Moench and Ogata (1981), presented a solution in Laplace space for chemical tracer radial flow, and obtained the numerical inversion with the algorithm of Stehfest (1970), and through a finite difference solution. Tang and Babu (1979) presented a solution for the radial dispersion problem and confirmed the results of Moench and Ogata. Hsieh (1986) presented the solution to the problem of Moench and Ogata, expressed in terms of an integral in the complex plane.

Ramírez S. et al.(1991) obtained a solution in Laplace space for the radial flow of tracers in

naturally fractured reservoirs, and carried out the inversion of their Laplace space solution with Crump's algorithm, coupled with Epsilon's algorithm for acceleration. They considered slabs and cubic models for the matrix-fracture geometry.

PROPOSED MATHEMATICAL MODEL

With the purpose of allowing a mathematical analysis of the tracer flow problem, it is necessary to model the real system, irregular and complex, composed of matrix and fractures by matrix blocks that have the same size and form (**Fig. 1**). High percent of the connected pore volume in naturally fractured reservoirs is not accessible to injection; thus changes are required to include inaccessible pore volume in the mathematical models, because it affects tracer propagation significantly.

The double porosity model proposed in this work considers the following assumptions:

1. The matrix and fractures are homogeneous and compressible systems.
2. Fluid is injected across the fractures and then flows from the fractures to matrix.
3. There is not resistance to flow between the fracture and matrix.
4. The matrix-fracture geometries considered are slabs and cubic blocks (**Fig. 1**).
5. Injected flow rate is constant and uniformly distributed over the interval.
6. Fracture width is small compared with that of the matrix block.
7. The effective diffusivity coefficient in the fractures is constant, and in the matrix the longitudinal dispersion coefficient is proportional to the radial velocity.
8. Diffusion in the fractures and in the matrix obeys Fick's law.
9. A uniform vertical gradient concentration exists in the fractures in z direction.
10. The porous media are of infinite extent.

Under the previous assumptions, the equation for the radial flow of tracers in naturally fractured reservoirs can be expressed:

$$\frac{1}{r} \frac{\partial}{\partial r} \left(r D_r \frac{\partial C_f(r,t)}{\partial r} \right) - v_r \frac{\partial C_f(r,t)}{\partial r} - \lambda [C_f(r,t) - C_i] - \frac{J^*(h_f,t)}{\phi_{fb} \sigma} = \frac{\partial C_f(r,t)}{\partial t} \quad (1)$$

The longitudinal dispersion and radial velocity are expressed by Eqs. (2) and (3):

$$D_r = \alpha v_r \quad (2)$$

$$v_r = \frac{q}{2\pi r h} = \frac{a}{r} \quad (3)$$

Combining Eqs. (2) and (3):

$$rD_r = \alpha a \quad (4)$$

Substituting Eqs. (3) and 4 in Eq. (1), the equation for the radial flow of tracers in naturally fractured reservoirs is obtained:

$$\frac{\alpha a}{r} \frac{\partial^2 C_f(r,t)}{\partial r^2} - \frac{a}{r} \frac{\partial C_f(r,t)}{\partial r} - \lambda [C_f(r,t) - C_i] - \frac{J^*(h_f,t)}{\phi_{fb}\sigma} = \frac{\partial C_f(r,t)}{\partial t} \quad (5)$$

Where the tracer mass transfer by rock volume unit $J^*(h_f,t)$ is given by Eq. (6):

$$J^*(h_f,t) = \frac{D_m}{V_b} \frac{\partial C_m(h,t)}{\partial z} \quad (6)$$

Substituting Eq. (6) in Eq. (5), the equation for the radial flow of tracers in naturally fractured reservoirs can be expressed as follows:

$$\frac{\alpha a}{r} \frac{\partial^2 C_f(r,t)}{\partial r^2} - \frac{a}{r} \frac{\partial C_f(r,t)}{\partial r} - \lambda [C_f(r,t) - C_i] + \frac{D_m}{\phi_{fb}\sigma V_b} \frac{\partial C_m(h_f,t)}{\partial z} = \frac{\partial C_f(r,t)}{\partial t} \quad (7)$$

It is important to notice that in the left-hand side of Eq. (7) the first term refers to the tracer transfer by *dispersion*, the second to the concentration change of tracer due to the *convection*, the third to the *radioactive decay*, and the fourth term refers to *fracture-matrix transfer*, where the new interporosity flow coefficient governs the tracer flow to the matrix, and therefore controls the time period of the transition between the early tracer flow only through the fractures to the composite by fractures and matrix tracer flow. The right-hand side member of Eq. (7) considers the concentration change with time that represents the cumulative effect.

Equation for linear flow in the matrix taking into account the inaccessible pore volume:

$$D_m \frac{\partial^2 C_m(z,t)}{\partial z^2} - \lambda [C_m(z,t) - C_i] - [1-f] \frac{\partial C_{sm}(z,t)}{\partial t} = f \frac{\partial C_m(z,t)}{\partial t} \quad (8)$$

In Eq. (8) the first term on the left-hand side refers to the tracer transfer by *diffusion*, the second to the *radioactive decay*, and the third term represents the loss of tracer to the inaccessible pore volume; the right member of Eq. (8) considers the concentration change with the time, that represents the cumulative effect.

Transfer between two zones in the matrix by inaccessible pore volume:

$$\frac{\partial C_{sm}(z,t)}{\partial t} = \frac{M_m}{1-f} [C_m(z,t) - C_{sm}(z,t)] \quad (9)$$

The dimensionless model for the radial flow of a tracer in a fractured system, is given by Eqs. (10) to (19).

Tracer flow equation:

$$\frac{\alpha_D}{r_D} \frac{\partial^2 C_{fD}(r_D,t_D)}{\partial r_D^2} - \frac{1}{r_D} \frac{\partial C_{fD}(r_D,t_D)}{\partial r_D} - \lambda_D C_{fD}(r_D,t_D) + \frac{1}{\sigma_D} \frac{\partial C_{mD}(z_{Df},t_D)}{\partial t_D} = \frac{\partial C_{fD}(r_D,t_D)}{\partial t_D} \quad (10)$$

Initial condition:

$$C_{fD}(r_D, 0) = 0 \quad (11)$$

Internal boundary condition: constant mass flux at injection well.

$$\frac{\partial C_{fD}(1,t_D)}{\partial t_D} = -1 \quad (12)$$

External boundary condition: infinite medium:

$$\lim_{r_D \rightarrow \infty} C_{fD}(r_D,t_D) = 0 \quad (13)$$

Dimensionless equation for linear flow in the matrix, taking into account the inaccessible pore volume:

$$D_{mD} \frac{\partial^2 C_{mD}(z_D, t_D)}{\partial z_D^2} - \lambda_D C_{mD}(z_D, t_D) - [1-f] \frac{\partial C_{smD}(z_D, t_D)}{\partial t_D} = f \frac{\partial C_{mD}(z_D, t_D)}{\partial t_D} \quad (14)$$

Initial condition:

$$C_{mD}(z_D, 0) = 0 \quad (15)$$

Internal boundary condition: free interaction between fracture and matrix:

$$C_{mD}(z_{fD}, t_D) = C_{fD}(r_D, t_D) \quad (16)$$

External boundary condition: closed system:

$$\frac{\partial C_{mD}(z_{HD}, t_D)}{\partial z_D} = 0 \quad (17)$$

Transfer between two zones in the matrix by adsorption:

$$\frac{\partial C_{smD}(z_D, t_D)}{\partial t_D} = \frac{M_{mD}}{1-f} [C_{mD}(z_D, t_D) - C_{smD}(z_D, t_D)] \quad (18)$$

Initial condition:

$$C_{smD}(z_D, 0) = 0 \quad (19)$$

Dimensionless variables:

Dimensionless radius:

$$r_D = \frac{r}{r_w} \quad (20)$$

Dimensionless time:

$$t_D = \frac{\alpha_D a_f t}{r_w^2} \quad (21)$$

Dimensionless length in the matrix:

$$z_D = \frac{z}{r_w} \quad (22)$$

Dimensionless fracture half width:

$$z_{fD} = \frac{h_f}{r_w} \quad (23)$$

Dimensionless (symmetrical) maximum distance for tracer flow in the matrix:

$$z_{HD} = \frac{H + h_f}{r_w} \quad (24)$$

Dimensionless tracer concentration in the fractures:

$$C_{fD}(r_D, t_D) = \frac{D_m 2\pi h}{\dot{m}_w} [C_i - C_f(r, t)] \quad (25)$$

where \dot{m}_w is defined by Eq. (A-1).

Dimensionless tracer concentration in the matrix:

$$C_{mD}(z_D, t_D) = \frac{D_m 2\pi h}{\dot{m}_w} [C_i - C_m(z, t)] \quad (26)$$

Dimensionless tracer concentration in the matrix inaccessible pore volume:

$$C_{smD}(z_D, t_D) = \frac{D_m 2\pi h}{\dot{m}_w} [C_i - C_{sm}(z, t)] \quad (27)$$

Dimensionless mixing coefficient:

$$\alpha_D = \frac{\alpha}{r_w} \quad (28)$$

Dimensionless interporosity coefficient:

$$\sigma_D = \frac{\phi_{fb} V_b a \sigma}{r_w D_m} \quad (29)$$

Dimensionless effective diffusivity in the matrix:

$$D_{mD} = \frac{D_m}{\alpha_D a} \quad (30)$$

Dimensionless adsorption coefficient for the inaccessible pore volume:

$$M_{mD} = \frac{r_w^2 M_m}{\alpha_D a} \quad (31)$$

Dimensionless radioactive decay constant:

$$\lambda_D = \frac{r_w^2 \lambda}{\alpha_D a} \quad (32)$$

The wellbore concentration in Laplace space for the problem considered is (see Appendix A):

$$\bar{C}_{wD}(s) = \frac{-1}{s \left[0.5\alpha_D + (\beta(s))^{1/3} Ai'(Y_0)/Ai(Y_0) \right]} \quad (33)$$

where:

$$Y_0 = \frac{\beta(s) + 1/4\alpha_D^2}{(\beta(s))^{2/3}} \quad (34)$$

$$m(s) = \frac{1}{D_{mD}} \left[\frac{[1-f]M_{mD}}{M_{mD} + s[1-f]} + f + \frac{\lambda_D}{s} \right] \quad (35)$$

For slabs matrix:

$$\beta(s) = \frac{\sqrt{sm(s)}}{\alpha_D \sigma_D} \left[\frac{h(z_{HD} \sqrt{sm(s)})}{1 - h(z_{HD} \sqrt{sm(s)})} - \frac{h(z_{fD} \sqrt{sm(s)})}{h(z_{fD} \sqrt{sm(s)})} \right] + \frac{\lambda_D}{\alpha_D} + \frac{s}{\alpha_D} \quad (36)$$

For cubic matrix:

$$\beta(s) = \frac{1}{\alpha_D \sigma_D} \left[\sqrt{sm(s)} \frac{h(\sqrt{sm(s)} z_{Df})}{z_{Df}} - \frac{1}{z_{Df}} \right] + \frac{\lambda_D}{\alpha_D} + \frac{s}{\alpha_D} \quad (36-b)$$

Approximate analytical solution for short times

During the early injection phase when a small pore volume has been injected, the fracture-matrix mass

transfer is negligible, and the naturally fractured formation behaves as a “homogeneous in fractures media”. Thus for short dimensionless times, it is possible to invert Eq. (33) (see Appendix C):

$$C_{wD}(t_D) = \frac{t_D^{1/3}}{0.2968\Gamma(4/3)} \quad (37)$$

Approximate analytical solution for long times

For long dimensionless times the solution for the radial flow of a radioactive tracer in naturally fractured reservoirs, Eqs. (10) and (33) (see Appendix C), can be expressed as follows:

$$C_{wD}(t_D) = \frac{t_D^{1/4}}{0.6619 \Gamma(5/4)} \quad (38)$$

These solutions given by Eqs. (37) and (38) were used in the present work to test the validity of the numerical inversion results.

Derivation of the dimensionless groups

If the analytical solution for short times for the continuous radial flow of a radioactive tracer given by Eq. (38), is derived with respect to time t_D and multiplied by t_D , a useful way to present the results of this problem is obtained in terms of:

$$t_D \frac{dC_{wD}(t_D)}{dt_D} \text{ vs. } t_D \quad (39)$$

Numerical inversion

The comparison between the numerical inversion with Stehfest's algorithm and the approximate analytical solutions for short and long dimensionless times indicates that the numerical solution is correct. (Figs. 2 and 3) were generated through numerical inversion using the algorithm of Stehfest (1970). Fig. 3 shows in addition to the tracer response a graph of its logarithmic derivative.

Numerical inversion has the advantage that the calculation time is smaller than the time simulation using finite differences. In addition, it has been concluded that the numerical inversion is efficient for any boundary condition.

CONCLUSIONS

The main aim of this work has been to develop an improved model and its solution for the flow of tracers in naturally fractured reservoirs, that considers injection under constant mass flux. This model assumes transient fracture matrix tracer transfer.

From the result of this work, the following conclusions can be established:

1. A solution for the tracer response has been derived.
2. Approximate analytical solutions were presented for short and long dimensionless times, which can be used to interpret the response of the radioactive tracer, and to obtain a representative value of the "in situ" mixing coefficient.
3. A dimensionless "type curve" was developed for the interpretation of the continuous constant mass flux injection of a radioactive tracer.
4. The combination of the interpretation techniques through the "type curve" and of the analytical solutions, allows the improvement of reservoir characterization obtained by the interpretation of a tracer injection test.

NOMENCLATURE

a_f	= injection constant, Eqs. 2 and 3 = $q/2\pi h$, L^2/T .
C_o	= initial tracer concentration, M/L^3 .
$C_{sm}(z, t)$	= tracer concentration absorbed in the matrix, M/L^3 .
$C_m(z, t)$	= tracer concentration in the matrix, M/L^3 .
$C_f(r, t)$	= tracer concentration in the fractures, M/L^3 .
D_r	= longitudinal dispersion coefficient, L^2/T .
D_m	= effective diffusivity coefficient, L^2/T .
f	= ratio between accessible and inaccessible porosity
$G(r, t)$	= mass as a function of the radial distance and time.
h	= thickness of the porous media, L .
h_f	= fracture half width, L .
H	= half of the average matrix block size, L .
J	= mass flux density, M/L^2T .

J^*	= rock volume unit, mass transfer $(M/L^3)/(L^2T)$.
M	= amount solute mass injected
q_i	= injection flow rate in the porous media, L^3/T .
r	= radial distance, L .
t	= time
U	= macroscopic velocity, L/T .
v	= microscopic velocity, L/T .
V_u	= fluid volume in the fracture, transfer area of the matrix block multiply by half of the width fracture, L^3 .
$Ai(z)$ and $Bi(z)$	= Airy functions.
$\beta(s)$	= transfer function in the Laplace space, Eq. 10.
$\delta(t)$	= Dirac's δ -function.

Greek symbols

α	= fracture mixing coefficient α (dispersivity), L .
ϕ	= effective porosity, dimensionless.
λ	= radioactive decay constant, $1/T$.
κ	= mass flow gradient, $1/T$.
σ	= interporosity shape factor, $1/L^2$.

Subscripts

b	= bulk.
D	= dimensionless.
f	= fracture.
m	= matrix.
sm	= inaccessible matrix pore volume.
w	= well.

REFERENCES

- Abbaszadeh, M. and Brigham, W. E., 1984: *Analysis of Well to Well Tracer Flow to Determine Reservoir Heterogeneity*, JPT (Oct.), 1753-1760.
- Abramowitz, M., 1964: *Handbook of Mathematical Functions with graphs and mathematical tables*, U.S. Department of Commerce, National Bureau of Standards, Applied Mathematical Series 55, Washington D. C.
- Bender, C. M. and Orszag, S. A., 1978: *Advanced Mathematical Methods for Scientists and Engineers*, McGrawHill Book Company, USA page 100.
- Bentsen, R. G. and Nielsen, R. F., 1965: *A Study of Radial Miscible Displacement in a Consolidated Porous Medium*, SPEJ (March) 1-5.
- Crump, K. S., 1976: *Numerical Inversion of Laplace Transforms Using Fourier Series Approximation*. J. of the Association of Computing Machinery, Vol. 23, No. 1 (January), 89-96.
- Chen, C-S., 1987: *Analytical Solutions for Radial Dispersion with Cauchy Boundary at Injection Well*,

Water Resources Research, Vol. 23, No. 7 (July) 1217-1224.

Moench, A. F. and Ogata, A., 1981: *A Numerical Inversion of the Laplace Transform Solution to Radial Dispersion in Porous Media*, Water Resources Research, Vol. 17, No. 1 (February), 250-252.

Perkins, T. K. and Johnston, O. C., 1963: A Review of Diffusion and Dispersion in Porous Media, SPE (March) 70-84.

Pozzi, A. L. and Blackwell, R. J., 1963: *Design of Laboratory Models for Study of Miscible Displacement*, SPEJ (March).

Raimondi, P., Gardner, H. F. and Patrick, C. B., 1959: *Effect of Pore Structure and Molecular Diffusion on the Mixing of Miscible Liquid Flow in Porous Media*, paper No. 43 presented in the AIChE-SPE Joint Symposium on Fundamental Concepts of Miscible Displacement, Part II, San Francisco, Calif. (Dec. 6-9).

Ramírez, S. J., Samaniego, V. F., Rivera, R. J. and Rodríguez, F., 1991. *An Investigation of the Radial Tracer Flow in Naturally Fractured Reservoirs*. Proceedings of the Sixteenth Workshop on Geothermal Reservoir Engineering", Stanford U., Stanford, Ca., January 23-25.

Stehfest, H., 1970. *Algorithm 368, Numerical Inversion of Laplace Transforms*, Communication of the ACM, 47 (Jan.) 13.

Tang, D. H. and Babu, D. K. 1979: *Analytical Solution of a Velocity Dependent Dispersion Problem*, Water Resources Research, Vol. 15, No. 6. (December).

Yuen, D. L., Brigham, W. E. and Cinco Ley H., 1979: *Analysis of Five Spot Tracer Tests to Determine Reservoir Layering*, DOE Report SAW 1265-8 (Feb.), Washington, D. C.

APPENDIX A. INTERNAL BOUNDARY CONDITION USING FICK'S LAW.

The mass flux is generated due to a gradient concentration across a perpendicular area, and it is proportional to the molecular diffusion constant:

$$\dot{m}(r,t) = \frac{\partial G(r,t)}{\partial t} = D_m A \frac{\partial C_f(r,t)}{\partial r} \quad (\text{A-1})$$

The mass flux per unit area (mass flux density) can be obtained from the previous Eq. A-1:

$$\frac{\dot{m}(r,t)}{A} = J_f(r,t) = D_m \frac{\partial C_f(r,t)}{\partial r} \quad (\text{A-2})$$

Solving for the derivative:

$$\frac{\partial C_f(r,t)}{\partial r} = \frac{J_f(r,t)}{D_m} \quad (\text{A-3})$$

For the conditions at the well:

$$\frac{\partial C_f(r_w,t)}{\partial r} = \frac{J_f(r_w,t)}{D_m} \quad (\text{A-4})$$

Defining mass flux at the well:

$$\dot{m}(r_w,t) = \dot{m}_w \quad (\text{A-5})$$

Substituting Eq. (A-5) in Eq. (A-4), the internal boundary condition for a continuous constant mass flux tracer injection is obtained:

$$\frac{\partial C_f(r_w,t)}{\partial r} = \frac{\dot{m}_w}{D_m 2\pi r_w h} \quad (\text{A-6})$$

The internal boundary for conditions of a constant mass flux pike injection:

$$\frac{\partial C_f(r_w,t)}{\partial r} = \frac{M\delta(t)}{D_m 2\pi r_w h} \quad (\text{A-7})$$

Initial condition: uniform distribution.

$$C_f(r,0) = C_i \quad (\text{A-8})$$

$$C_{fD}\left(\frac{r}{r_w}, \frac{\alpha_D a[0]}{r_w^2}\right) = \frac{D_m 2\pi h}{\dot{m}_w} [C_i - C_f(r,0)] = \frac{D_m 2\pi h}{\dot{m}_w} [C_i - C_i] = 0$$

$$C_{fD}(r_D, 0) = 0 \quad (\text{A-9})$$

Internal boundary condition: *constant mass flux*:

$$\frac{\partial C_f(r_w,t)}{\partial r} = \frac{\dot{m}_w}{D_m 2\pi r_w h} \quad (\text{A-10})$$

$$\frac{-\dot{m}_w}{D_m 2\pi r_w h} \frac{\partial C_{fD}(1, t_D)}{\partial r_D} = \frac{\dot{m}_w}{D_m 2\pi r_w h} \frac{\partial C_{fD}(1, t_D)}{\partial r_D} = -1 \quad (\text{A-11})$$

Internal boundary condition: *pulse mass flux*:

$$\frac{\partial C_f(r_w,t)}{\partial r} = \frac{M\delta(t)}{D_m 2\pi r_w h} \quad (\text{A-12})$$

$$\frac{-\dot{m}_w}{D_m 2\pi r_w h} \frac{\partial C_{fD}(1, t_D)}{\partial r_D} = \frac{M\delta(t)_D}{D_m 2\pi r_w h}$$

$$\frac{\partial C_{fD}(1, t_D)}{\partial r_D} = -T_0 \delta(t)_D \quad (\text{A-13})$$

where T_0 is given by Eq. (A-14).

$$T_0 = \frac{M}{\dot{m}_w} \quad (\text{A-14})$$

External boundary condition: infinite reservoir:

$$\lim_{r \rightarrow \infty} C_f(r, t) = C_i \quad (\text{A-15})$$

$$\lim_{\substack{r \rightarrow \infty \\ r_m}} C_{fD} \left(\frac{[r]}{r_w}, \frac{\alpha_D a[t]}{r_w^2} \right) = \frac{D_m 2\pi h}{\dot{m}_w} [C_i - \lim_{r \rightarrow \infty} C(r, t)]$$

$$\lim_{r_D \rightarrow \infty} C_{fD}(r_D, t_D) = 0 \quad (\text{A-16})$$

APPENDIX B. SOLUTION IN LAPLACE SPACE FOR THE FLOW OF TRACERS IN NATURALLY FRACTURED RESERVOIRS.

Flow in the matrix taking into account the inaccessible pore volume:

$$D_{mD} \frac{\partial^2 C_{mD}(z_D, t_D)}{\partial z_D^2} - \lambda_D C_{mD}(z_D, t_D) - [1-f] \frac{\partial C_{smD}(z_D, t_D)}{\partial t_D}$$

$$= f \frac{\partial C_{mD}(z_D, t_D)}{\partial t_D} \quad (\text{B-1})$$

Initial condition:

$$C_{mD}(z_D, 0) = 0 \quad (\text{B-2})$$

Internal boundary condition: free fracture matrix interaction:

$$C_{mD}(z_{Df}, t_D) = C_{fD}(r_D, t_D) \quad (\text{B-3})$$

External boundary condition for the matrix block:

$$\frac{\partial C_{mD}(z_{DH}, t_D)}{\partial z_D} = 0 \quad (\text{B-4})$$

Transfer in the matrix between the effective and non-effective (inaccessible) pore volume:

$$\frac{\partial C_{smD}(z_D, t_D)}{\partial t_D} = \frac{M_{mD}}{1-f} [C_{mD}(z_D, t_D) - C_{smD}(z_D, t_D)] \quad (\text{B-5})$$

Initial condition:

$$C_{smD}(z_D, 0) = 0 \quad (\text{B-6})$$

Applying the Laplace transform to equation (B-5), substituting the initial condition given by Eq. (B-6) and solving for the tracer concentration in the inaccessible matrix volume pore:

$$\bar{C}_{smD}(z_D, s) = \left[\frac{M_{mD}}{(1-f)s + M_{mD}} \right] \bar{C}_{mD}(z_D, s) \quad (\text{B-7})$$

Applying the Laplace transform to the Eq. (B-1) and substituting the initial conditions (B-2) and (B-6):

$$D_{mD} \frac{d^2 \bar{C}_{mD}(z_D, s)}{dz_D^2} - \lambda_D \bar{C}_{mD}(z_D, s) - (1-f)s \bar{C}_{smD}(z_D, s)$$

$$= f s \bar{C}_{mD}(z_D, s) \quad (\text{B-8})$$

Substituting Eq. (B-7) in Eq. (B-8):

$$\frac{d^2 \bar{C}_{mD}(z_D, s)}{dz_D^2} - \frac{1}{D_{mD}} \left[\frac{\lambda_D}{s} + f + \frac{M_{mD}(1-f)}{(1-f)s + M_{mD}} \right] s \bar{C}_{mD}(z_D, s) = 0 \quad (\text{B-9})$$

The general solution for flow in the matrix can be obtained solving Eq. (B-9):

$$\bar{C}_{mD}(z_D, s) = A \cosh(z_D \sqrt{sm(s)}) + B \sinh(z_D \sqrt{sm(s)}) \quad (\text{B-10})$$

where:

$$m(s) = \frac{1}{D_{mD}} \left[\frac{(1-f)M_{mD}}{M_{mD} + s(1-f)} + f + \frac{\lambda_D}{s} \right] \quad (\text{B-11})$$

Applying the Laplace transform to Eqs. (B-3) and Eq. (B-4):

$$\bar{C}_{mD}(z_{Df}, s) = \bar{C}_{fD}(r_D, s) \quad (\text{B-12})$$

$$\frac{d\bar{C}_{mD}(z_{DH}, s)}{dz_D} = 0 \quad (\text{B-13})$$

Applying the condition Eq. (B-13) to the general solution for matrix:

$$B = -A \tanh(z_{DH} \sqrt{sm(s)}) \quad (\text{B-14})$$

Substituting Eq. (B-14) in Eq. (B-10):

$$\bar{C}_{mD}(z_D, s) = A \left[\cosh(z_D \sqrt{sm(s)}) - \tanh(z_{DH} \sqrt{sm(s)}) \sinh(z_D \sqrt{sm(s)}) \right] \quad (\text{B-15})$$

Evaluating Eq. (B-15) in the fracture-matrix interface, and using (B-12):

$$A = \frac{\bar{C}_{fD}(r_D, s)}{\cosh(z_{Df} \sqrt{sm(s)}) - \tanh(z_{DH} \sqrt{sm(s)}) \sinh(z_{Df} \sqrt{sm(s)})} \quad (\text{B-16})$$

Substituting Eq. (B-16) in Eq. (B-15), obtaining the equation that represents the tracer matrix concentration in function of the fracture concentration:

$$\bar{C}_{mD}(z_D, s) = \left[\frac{(z_D \sqrt{sm(s)}) - (z_{DH} \sqrt{sm(s)})}{(z_{Df} \sqrt{sm(s)}) - (z_{DH} \sqrt{sm(s)})} \frac{(z_D \sqrt{sm(s)})}{(z_{Df} \sqrt{sm(s)})} \right] \bar{C}_{fD}(r_D, s) \quad (\text{B-17})$$

The gradient concentration in the matrix block is obtained deriving Eq. (B-17), and the resulting expression at the fracture-matrix interface is:

$$\frac{d\bar{C}_{mD}(z_{Df}, s)}{dz_D} = \sqrt{sm(s)} \left[\frac{(z_{Df} \sqrt{sm(s)}) - (z_{DH} \sqrt{sm(s)})}{(z_{Df} \sqrt{sm(s)}) - (z_{DH} \sqrt{sm(s)})} \frac{(z_{Df} \sqrt{sm(s)})}{(z_{Df} \sqrt{sm(s)})} \right] \bar{C}_{fD}(r_D, s) \quad (\text{B-18})$$

Radial tracer flow in the fractures, source term including the that considers the fracture matrix interaction:

$$\frac{\alpha_D}{r_D} \frac{\partial^2 C_{fD}(r_D, t_D)}{\partial r_D^2} - \frac{1}{r_D} \frac{\partial C_{fD}(r_D, t_D)}{\partial r_D} - \lambda_D C_{fD}(r_D, t_D) + \frac{1}{\sigma_D} \frac{\partial C_{mD}(z_{Df}, t_D)}{\partial t_D} = \frac{\partial C_{fD}(r_D, t_D)}{\partial t_D} \quad (\text{B-19})$$

Initial condition: uniform distribution:

$$C_{fD}(r_D, 0) = 0 \quad (\text{B-20})$$

Internal boundary: constant mass flux:

$$\frac{\partial C_{fD}(1, t_D)}{\partial t_D} = -1 \quad (\text{B-21})$$

External boundary: infinite reservoir:

$$\lim_{r_D \rightarrow \infty} C_{fD}(r_D, t_D) = 0 \quad (\text{B-22})$$

Applying the Laplace Transform to Eq. (B-20) and substituting the initial condition given by (B-20):

$$\frac{\alpha_D}{r_D} \frac{d^2 \bar{C}_{fD}(r_D, s)}{dr_D^2} - \frac{1}{r_D} \frac{d\bar{C}_{fD}(r_D, s)}{dr_D} - \lambda_D \bar{C}_{fD}(r_D, s) + \frac{1}{\sigma_D} \frac{d\bar{C}_{mD}(z_{Df}, s)}{dz_D} = s \bar{C}_{fD}(r_D, s) \quad (\text{B-23})$$

Substituting the Eq. (B-18) in Eq. (B-23):

$$\frac{\alpha_D}{r_D} \frac{\partial^2 C_{fD}(r_D, t_D)}{\partial r_D^2} - \frac{1}{r_D} \frac{\partial C_{fD}(r_D, t_D)}{\partial r_D} - \lambda_D C_{fD}(r_D, t_D) + \frac{\sqrt{sm(s)}}{\sigma_D} \left[\frac{(z_{Df} \sqrt{sm(s)}) - (z_{DH} \sqrt{sm(s)})}{(z_{Df} \sqrt{sm(s)}) - (z_{DH} \sqrt{sm(s)})} \frac{(z_{Df} \sqrt{sm(s)})}{(z_{Df} \sqrt{sm(s)})} \right] \bar{C}_{fD}(r_D, s) = s \bar{C}_{fD}(r_D, s)$$

This may be written:

$$\frac{d^2 \bar{C}_{fD}(r_D, s)}{dr_D^2} - \frac{1}{\alpha_D} \frac{d\bar{C}_{fD}(r_D, s)}{dr_D} - \beta(s) r_D \bar{C}_{fD}(r_D, s) = 0 \quad (\text{B-24})$$

where:

$$\beta(s) = \frac{\sqrt{sm(s)}}{\alpha_D \sigma_D} \left[\frac{(z_{Df} \sqrt{sm(s)}) - (z_{DH} \sqrt{sm(s)})}{(z_{Df} \sqrt{sm(s)}) - (z_{DH} \sqrt{sm(s)})} \frac{(z_{Df} \sqrt{sm(s)})}{(z_{Df} \sqrt{sm(s)})} \right] + \frac{\lambda_D}{\alpha_D} + \frac{s}{\alpha_D} \quad (\text{B-25})$$

The general solution of the ordinary variables coefficients differential equation is given for Eq. (B-26):

$$\begin{aligned} \bar{C}_{fD}(r_D, s) = e^{\frac{r_D}{2\alpha_D}} & \left[B_1 Ai \left(\frac{r_D \beta(s) + \frac{1}{4\alpha_D^2}}{(\beta(s))^{2/3}} \right) \right. \\ & \left. + B_2 Bi \left(\frac{r_D \beta(s) + \frac{1}{4\alpha_D^2}}{(\beta(s))^{2/3}} \right) \right] \end{aligned} \quad (\text{B-26})$$

Applying the Laplace transform to the boundary conditions given by Eq. (B-21) and (B-22):

$$\frac{d\bar{C}_D(1, s)}{dr_D} = -\frac{1}{s} \quad (\text{B-27})$$

$$\lim_{r_D \rightarrow \infty} \bar{C}_D(r_D, s) = 0 \quad (\text{B-28})$$

Applying the external boundary condition and considering that the Airy function $Ai(x)$ for big arguments tend to zero, $B_2 = 0$ in Eq. (B-26).

Substituting the constant B_1 in Eq. (B-26):

$$\bar{C}_D(r_D, s) = e^{\frac{r_D}{2\alpha_D}} B_1 Ai \left(\frac{r_D \beta(s) + 1/4\alpha_D^2}{\beta(s)^{2/3}} \right) \quad (\text{B-29})$$

Applying the internal boundary condition:

$$\begin{aligned} \frac{d\bar{C}_{fD}(1, s)}{dr_D} &= \frac{1}{2\alpha_D} e^{\frac{1}{2\alpha_D}} B_1 Ai \left(\frac{1\beta(s) + 1/4\alpha_D^2}{(\beta(s))^{2/3}} \right) \\ &+ e^{\frac{1}{2\alpha_D}} (\beta(s))^{1/3} B_1 Ai \left(\frac{1\beta(s) + 1/4\alpha_D^2}{(\beta(s))^{2/3}} \right) = -\frac{1}{s} \end{aligned}$$

From this equation, B_1 can be expressed:

$$B_1 = \frac{-1}{s} \frac{e^{-\frac{1}{2\alpha_D}}}{\left[Ai(Y_0)/2\alpha_D + (\beta(s))^{1/3} Ai(Y_0) \right]} \quad (\text{B-30})$$

Substituting this constant in the general solution given by Eq. (B-26):

$$\bar{C}_{fD}(r_D, s) = \frac{-e^{\frac{r_D-1}{2\alpha_D}}}{s} \left[\frac{Ai \left(\frac{r_D \beta(s) + 1/4\alpha_D^2}{\beta(s)^{2/3}} \right)}{Ai \left(\frac{\beta(s) + 1/4\alpha_D^2}{\beta(s)^{2/3}} \right)^{1/2\alpha_D} + (\beta(s))^{1/3} Ai \left(\frac{\beta(s) + 1/4\alpha_D^2}{\beta(s)^{2/3}} \right)} \right] \quad (\text{B-31})$$

The wellbore concentration:

$$\bar{C}_{wD}(s) = \bar{C}_{fD}(1, s) \quad (\text{B-32})$$

The wellbore concentration:

$$\bar{C}_D(1, s) = \frac{-1}{s \left[1/2\alpha_D + (\beta(s))^{1/3} \right] Ai(Y_0)/Ai(Y_0)} \quad (\text{B-33})$$

where:

$$Y_0 = \frac{\beta(s) + 1/4\alpha_D^2}{\beta(s)^{2/3}} \quad (\text{B-34})$$

Using the Bender and Orszag method (Bender and Orszag, 1978) we proposed a **new** original approximation for Airy Function (**Fig. 2**).

$$Ai(Y_0) = 0.355 e^{-0.729Y_0 - 0.18Y_0^2}$$

The **original analysis** for the relationship between the Airy function and derivative (**Fig. 3**):

$$\begin{aligned} \frac{Ai(Y_0)}{Ai'(Y_0)} &= \frac{0.355 [-0.729 - 0.36Y_0] e^{-0.729Y_0 - 0.18Y_0^2}}{0.355 e^{-0.729Y_0 - 0.18Y_0^2}} \\ &= -0.729 - 0.36Y_0 \end{aligned} \quad (\text{B-35})$$

Using the ratio between the Airy function and its derivate, we get for $r = r_w$:

$$\bar{C}_{wD}(s) = \frac{1}{s \left[-1/2\alpha_D + (\beta(s))^{1/3} [0.36Y_0 + 0.729] \right]} \quad (\text{B-36})$$

where:

$$\beta(s) = \frac{\sqrt{sm(s)}}{\alpha_D \sigma_D} \left[\frac{(z_{DH} \sqrt{sm(s)}) - (z_{DF} \sqrt{sm(s)})}{1 - (z_{DH} \sqrt{sm(s)}) (z_{DF} \sqrt{sm(s)})} \right] + \frac{\lambda_D + s}{\alpha_D \alpha_D} \quad (\text{B-37})$$

$$m(s) = \frac{1}{D_{mD}} \left[\frac{(1-f)M_{mD}}{M_{mD} + s(1-f)} + f + \frac{\lambda_D}{s} \right] \quad (\text{B-38})$$

Appendix D discusses the solution of or a constant mass flux pulse injection.

APPENDIX C. APPROXIMATE ANALYTICAL SOLUTIONS

For large s values $\rightarrow \infty$:

$$Y_0 \approx (\beta(s))^{1/3} \quad (\text{C-1})$$

When substituting practical values of **Table 1** in Eq. (B-39), the function $m(s)$ presents an almost constant value (**Fig. 4**):

$$m(s) \approx 2500 \quad (\text{C-2})$$

Then:

$$\sqrt{sm(s)} \approx 50\sqrt{s} \quad (\text{C-3})$$

Then, when $m(s)$ is substituted in $\beta(s)$ given in Eq. (B-38), we obtain the behaviour for this function also shown in (**Fig 4**):

$$\beta(s) \approx 0.75\sqrt{s} \quad (\text{C-4})$$

Then:

$$Y_0 \approx (0.75\sqrt{s})^{1/3} \approx 0.908s^{1/6} \quad (\text{C-5})$$

Using the ratio of the Airy function given by Eq. (35):

$$Ai(Y_0)/Ai(Y_0) = -0.36[0.908s^{1/6}] - 0.729 \quad (\text{C-6})$$

Substituting (C-5) and (C-6) in the second term of the denominator of Eq. (B-33):

$$\begin{aligned} (\beta(s))^{1/3} Ai(Y_0)/Ai(Y_0) &= -0.908s^{1/6} \left[0.36[0.908s^{1/6}] + 0.729 \right] \\ &= -0.2968s^{1/3} - 0.6619s^{1/6} \end{aligned} \quad (\text{C-7})$$

Substituting Eq. (C-7) in Eq. (B-33):

$$\bar{C}_{wD}(s) = \frac{1}{s \left[-0.5/\alpha_D - \left[0.2968s^{1/3} + 0.6619s^{1/6} \right] \right]} \quad (\text{C-8})$$

For large arguments ($s \rightarrow \infty$), this expression can be written as,

$$\bar{C}_{wD}(s) = \frac{-1}{0.2968s \left[s^{1/3} + 0.5/0.2968\alpha_D \right]} \quad (\text{C-9})$$

The analytical inversion for **short times** of Eq. (C-9) is given by Eq. (C-10):

$$C_{wD}(t_D) = \frac{t_D^{1/3}}{0.2968 \Gamma(4/3)} \quad (\text{C-10})$$

For large times (short arguments, \rightarrow),

$$\sqrt{sm(s)} \approx 50\sqrt{s} \quad (\text{C-11})$$

Substituting this value in Eq. (B-37), (**Fig 5**):

$$\beta(s) \approx 0.75s^{3/4} \quad (\text{C-12})$$

Then, from Eq. (C-1):

$$Y_0 \approx (0.75s^{3/4})^{1/3} \approx 0.908s^{1/4} \quad (\text{C-13})$$

Using Eq. (C-13), the second term of the denominator of Eq. (B-33) can be expressed:

$$Ai(Y_0)/Ai(Y_0) = -0.36[0.908s^{1/4}] - 0.729 \quad (\text{C-14})$$

Similarly to the short times previous solution, substituting Eqs. (C-13) and (C-14) in the second term of the denominator of Eq. (B-33).

$$\begin{aligned} (\beta(s))^{1/3} Ai(Y_0)/Ai(Y_0) &= -0.908s^{1/4} \left[0.36[0.908s^{1/4}] + 0.729 \right] \\ &= -0.2968s^{1/2} - 0.6619s^{1/4} \end{aligned} \quad (\text{C-15})$$

Substituting Eq. (C-15) in Eq. (B-33):

$$\bar{C}_{wD}(s) = \frac{1}{s \left[-0.5/\alpha_D - \left[0.2968s^{1/2} + 0.6619s^{1/4} \right] \right]} \quad (\text{C-16})$$

For large times arguments ($s \rightarrow 0$),

$$\bar{C}_{wD}(s) = \frac{-1}{0.6619 s \left[s^{1/4} + 0.5/0.6619 \alpha_D \right]} \quad (C-17)$$

The analytical inversion for **large times** is expressed as follows:

$$C_{wD}(t_D) = \frac{t_D^{1/4}}{0.6619 \Gamma(5/4)} \quad (C-18)$$

APPENDIX D. A SOLUTION FOR CONSTANT MASS FLUX PULSE INJECTION.

Applying the Laplace transform to the inner boundary condition for a pulse mass flux given by Eq. (A-13):

$$\frac{d\bar{C}_{fD}(1, s)}{dr_D} = -T_0 \quad (D-1)$$

The solution for a constant mass flux pulse:

$$\bar{C}_{fD}(r_D, s)_{pulse} = -T_0 e^{\frac{r_D-1}{2}} \left[\frac{Ai(Y_w)}{Ai(Y_0)/2\alpha_D + (\beta(s))^{1/3} Ai(Y_0)} \right] \quad (D-2)$$

where:

$$Y_w = \frac{r_D \beta(s) + 1/4\alpha_D^2}{\beta(s)^{2/3}} \quad (D-3)$$

and Y_0 is given by Eq. (B-34).

The wellbore concentration for a constant mass flux pulse:

$$\bar{C}_{wD}(s)_{pulse} = T_0 \left[\frac{1}{-1/2\alpha_D - (\beta(s))^{1/3} Ai(Y_0)/Ai(Y_0)} \right] \quad (D-4)$$

Considering only one pulse:

$$T_0 = 1 \quad (D-5)$$

Comparing Eq. (D-5) with Eq. (B-31):

$$\bar{C}_{wD}(s)_{pulse} = s\bar{C}_{wD}(s) \quad (D-6)$$

The analytical inversion of Eq. (D-6):

$$C_{wD}(t_D)_{pulse} = \frac{dC_{wD}(t_D)}{dt_D} \quad (D-7)$$

From this expression we observe the known fact that the derivative of the continuous tracer injection solution yields the pulse injection solution (Chen, 1887).

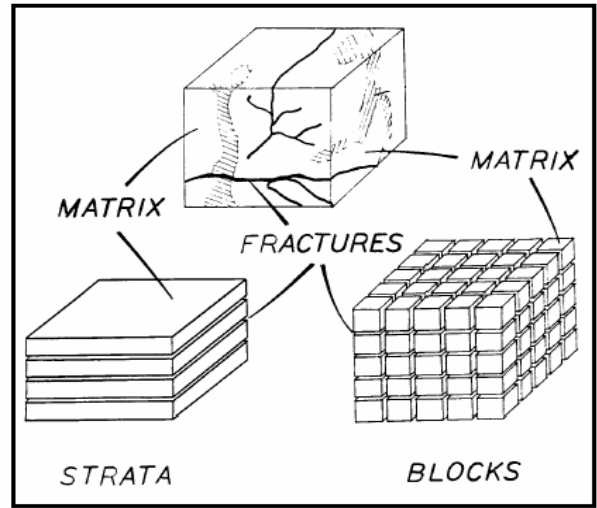


Fig. 1. Representation of a naturally fractured reservoir.

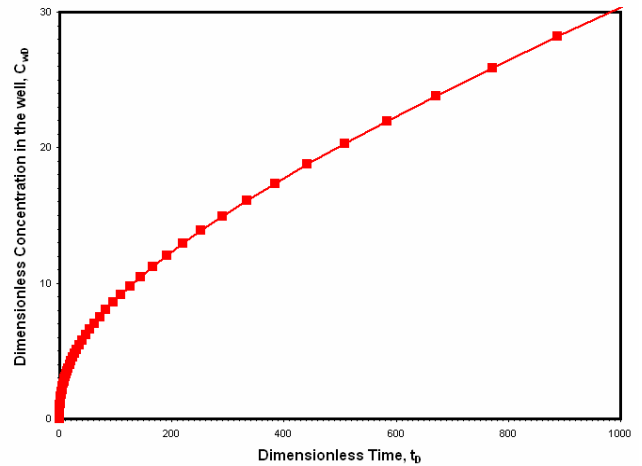


Fig. 2. Solutions for homogeneous continuous constant mass flux tracer injection, for radial flow in a slabs naturally fractured reservoir.

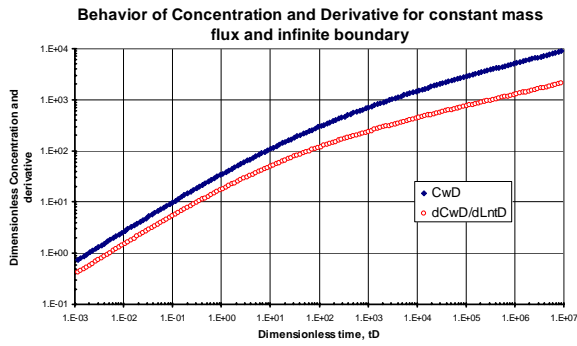


Fig. 3. Solutions for homogeneous continuous constant mass flux tracer injection, for radial flow in a slabs naturally reservoir with transient fracture-matrix transfer.

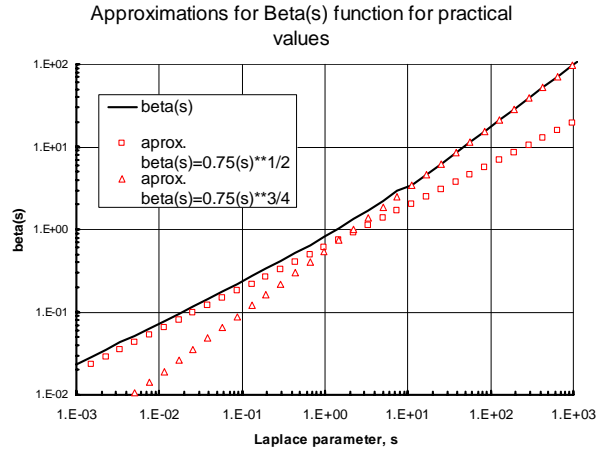


Fig. 6. Approximations for the Beta(s) function using the practical values of Table 1.

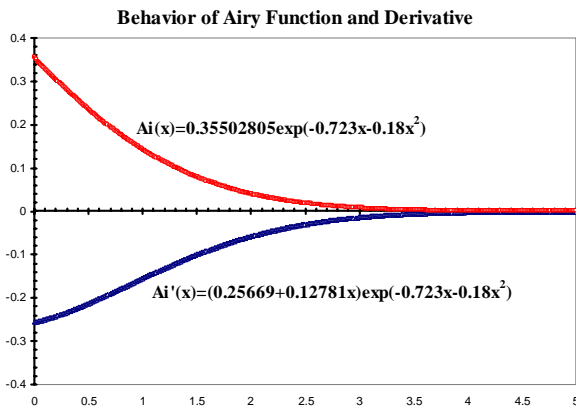


Fig. 4. Airy function and its derivative compared with data of Abramowitz and Stegun

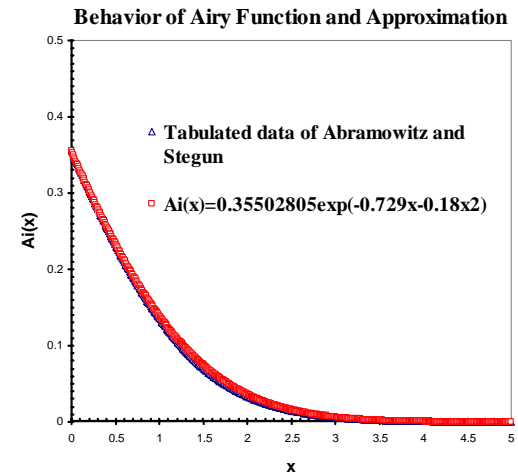


Fig. 7. New approximation for the Airy function.

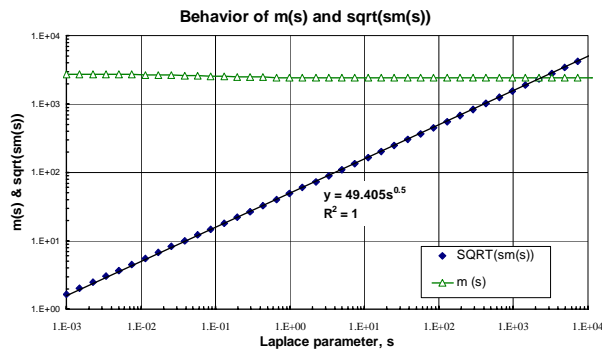


Fig. 5. The $m(s)$ function is constant for several set of practical values; it only changes when the inaccessible pore volume is higher than 50%.

Table 1. Practical values used in the evaluation of $m(s)$ function.

Q	h	a	α	M_m	D_m	λ	σ
$m3/D$	m	$M2/H$	m	1/s	$m2/s$	1/s	adim
2	200	0.04	0.5	0.500	1.E-04	1.E-06	0.032

ϕ_t	ϕ_{fb}	ϕ_{mb}	H	h_f	v_b	ϕ_{sm}	$f = (\phi_{mb} - \phi_{sm}) / \phi_{mb}$
fraction	fraction	fraction	m	m	M3	adim	adim
0.130	0.0169	0.1131	1.5	0.0085	3.43	0.01	0.89

A SYSTEMATIC METHOD FOR TRACER TEST ANALYSIS: AN EXAMPLE USING BEOWAWE TRACER DATA

G. Michael Shook

Idaho National Engineering and Environmental Laboratory
PO Box 1625
Idaho Falls, ID 83415-2107 USA
ook@inel.gov

ABSTRACT

Quantitative analysis of tracer data using moment analysis requires a strict adherence to a set of rules which include data normalization, correction for thermal decay, deconvolution, extrapolation, and integration. If done correctly, the method yields specific information on swept pore volume, flow geometry and fluid velocity, and an understanding of the nature of reservoir boundaries. All calculations required for the interpretation can be done in a spreadsheet.

The steps required for moment analysis are reviewed in this paper. Data taken from the literature is used in an example calculation.

INTRODUCTION

Tracer testing remains a crucial tool for characterizing geothermal resources, with more than 100 geothermal tracer tests conducted worldwide in the last 40 years (M. Adams, 2003, personal communication). A vast majority of these tests were interpreted qualitatively, ignoring the temporal evolution of the tracer breakthrough curve and resulting in gross test interpretation (e.g., size of the arrow indicative of relative tracer flow). Others have used tracer tests to constrain numerical models, using the data to estimate heat transfer parameters (Robinson and Tester, 1984; Axelsson et al., 2001), or to constrain reservoir-scale numerical models (e.g., Gunderson et al., 2002; Bloomfield and Moore, 2003).

There are a host of tracer test analysis methods that consider the temporal behavior of tracers. The methods were originally developed for closed reactor vessels (Danckwerts, 1958; Levenspiel, 1972), but have been applied to more general conditions of open boundaries (Pope et al., 1994; Sinha et al., 2004), characterization of fractured media under continuous tracer reinjection (Robinson and Tester, 1984), and estimates of flow geometry (Shook, 2003). These

methods have a rigorous mathematical basis and offer additional information on the subsurface. The analysis is useful independently, but also can be used to constrain numerical models by defining interwell volume and flow geometry.

The methods and applications mentioned above are all based on analysis of tracer residence times. The mean residence time, or first temporal moment, is the most useful single property derived from a tracer test, although other properties have been used as well. Levenspiel (1972) shows the total pore volume swept by a tracer can be determined from its mean residence time. There are certain restrictions inherent in the calculation; for example, steady state conditions and conservative tracer behavior. Nevertheless, the method has a rigorous mathematical basis, and has been extensively validated analytically and experimentally.

The purpose of this paper is to describe the individual steps necessary to apply moment analysis to tracer test interpretation. For the purposes of illustration, the Beowawe tracer dataset described by Rose et al. (2004) is used in an example interpretation. No attempt to verify the dataset was made, and some assumptions regarding injection were made, so this might be better called a Beowawe-like tracer test. The dataset serves a useful purpose in that it is actual field data and has been analyzed and published. A discussion of assumptions and limitations of the method follow the example interpretation.

The discussions below make several assumptions regarding the tracer (fluorescein in this case). First, we assume it is conservative; that is, it does not adsorb or volatilize. We also assume that, at the concentrations injected, it is an ideal tracer; it does not affect the flow properties of the liquid phase (density, viscosity, etc.). The latter assumption is almost certainly true, as the injected concentration is approximately 0.4 wt%. The former assumption, however, is of potential concern. Fluorescein has shown sorptive behavior under certain conditions (Sabatini and Austin, 1991), and adsorption was

suspected under geothermal conditions (Gunderson et al., 2002). Axelsson et al. (2001) show that fluorescein was non-sorptive under conditions at the Laugaland geothermal field. However, adsorption results from rock-water interactions and is site-specific.

Nevertheless, for the purposes of this discussion, fluorescein is assumed conservative. On July 13, 1994 ($t=0$), 91 kg of fluorescein was mixed with 23 m³ of water, and injected as an aqueous slug. Injection and production mass rates are both assumed constant, and equal to 7.88×10^5 T/hr (18.9×10^6 kg/d). This information was extracted from the discussion by Rose et al. (2004). Data was collected over the course of the following 9 years. Individual production rates from the three production wells were not available; rather, an averaged tracer history was reported. The raw concentration history for the Beowawe tracer test was given to the present author by P. Rose. The raw data is plotted in Figure 1.

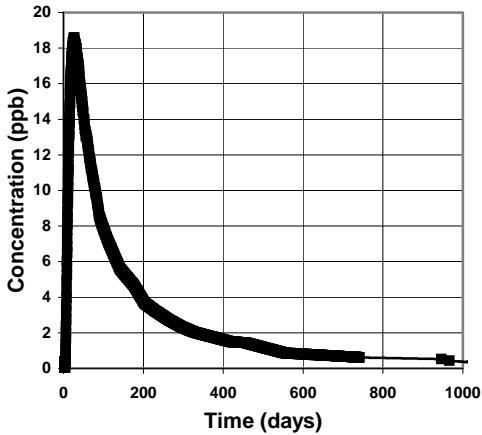


Figure 1. Tracer history from Beowawe test, as reported by Rose et al. (2004). Symbols are individual observations.

NORMALIZING THE TRACER HISTORY

The method of moments is based on age distribution functions as originally described by Danckwerts (1958). To avoid ambiguity in terminology, however, we will use the nomenclature of Levenspiel (1972). The age distribution function is referred to as $E(t)$, and has units of $(1/t)$. We will refer to the tracer concentration history in Figure 1 as $C(t)$, whose units in the present case are (ppb). In order to convert $C(t)$ to $E(t)$, we multiply by the mass flow rate pq and divide by the total mass of tracer injected, M :

$$E(t) = \frac{C(t)pq}{10^9 M} \quad (1)$$

Normalizing $E(t)$ in such a fashion has distinct advantages. First, normalization of the output signal accommodates treating the input signal as a Dirac delta function (e.g., a pulse injection). The properties of the Dirac delta function are required to deconvolve the tracer history as discussed in a following section. The area under the curve $E(t)$ vs. t is unity in a closed system (100% tracer recovery), so the normalized curve offers a quick means of evaluating the flow system. The normalization also puts all tracer response curves on an equal footing, making direct comparison easier. It is conventional to normalize time as well, so E is independent of formation size, flow rates, etc. However, time is usually normalized by the mean residence time (Levenspiel, 1972), the determination of which is one purpose of this paper.

Normally a tracer history must first be corrected for thermal degradation using the Arrhenius equation (Levenspiel, 1972). However, Rose et al. (2004) indicate that fluorescein is not expected to degrade at the temperatures encountered in the tracer test, so no correction was applied to the example tracer data.

DECONVOLVING THE TRACER HISTORY

When tracer is reinjected, the observed tracer history is a combined response to the initial slug tracer injection and the continuous recycling of the produced tracer. Moment analysis is based on the response to slug tracer injection, so we must first remove the effect of tracer recycling before calculating residence times and swept volumes. The convolution integral is used to deconvolve the tracer response (Levenspiel, 1972):

$$E_{app}(t) = \int_0^t E_{in}(t - \tau)E(\tau)d\tau \quad (2)$$

Equation (2) states the observed (apparent) residence time distribution, $E_{app}(t)$, is a result of injection E_{in} and the true residence time distribution, $E(t)$. Following arguments presented by Robinson and Tester (1984):

$$E_{app}(t) = \frac{C(t)pq}{M} \quad (3a)$$

$$E_{in} = \delta(t) + \frac{1}{1 - f_{loss}} \cdot \frac{C(t)pq}{M} \quad (3b)$$

Substituting Equations 3 in Equation 2 gives

$$E_{app}(t) = \int_0^t \left\{ \delta(t - \tau) + \frac{1}{1 - f_{loss}} \cdot E(t - \tau) \right\} E(\tau)d\tau \quad (4)$$

Using the definition of the delta function and rearranging Equation 4 gives the correction needed to remove the effects of reinjection:

$$E(t) = E_{app}(t) - \frac{1}{1 - f_{loss}} \int_0^t E(t - \tau)E(\tau)d\tau \quad (5)$$

The integral in Equation 5 must be calculated anew at each time using the current tracer concentration, $C(t)$, the previous injection history, $C(t-\tau)$, and residence time ages, $E(\tau)$. At the upper limit of the integration, the argument is zero, so the current residence time age, $E(t)$, can be calculated explicitly at each time step.

The raw $E_{app}(t)$ data and the deconvolved $E(t)$ data for the example are given in Figure 2 below. We have assumed that f_{loss} is zero in this example. That is, the concentration that is produced is the same as that subsequently injected. This would be the case even if water were lost in cooling towers, for example, if makeup water were used to maintain a constant injection rate. Note that the deconvolved signal is always a subset of the raw data.

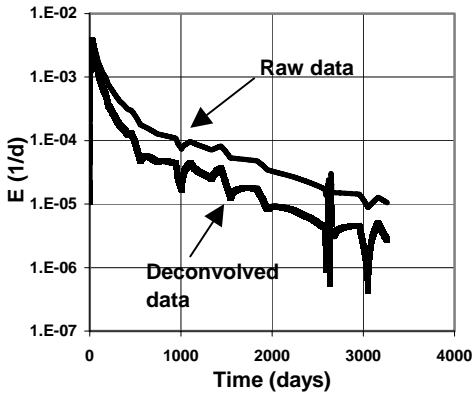


Figure 2. Raw vs. Deconvolved Age Distribution Functions, $E(t)$. Note the deconvolved signal is always a subset of the raw data.

CALCULATING MEAN RESIDENCE TIMES

The mean residence time, or first temporal moment, of a tracer is determined directly from the deconvolved, thermally-corrected age distribution function, $E(t)$ by the following equation:

$$t^* = \frac{\int_0^{\infty} E(t)tdt}{\int_0^{\infty} E(t)dt} - \frac{t_s}{2} \quad (6)$$

If the data is known only at discrete times, t_i , the integral can be approximated as:

$$t^* = \frac{\sum_{i=1}^N E_i t_i \Delta t_i}{\sum_{i=1}^N E_i \Delta t_i} - \frac{t_s}{2}$$

If the data itself is sufficiently smooth, a function may be fit to the tracer history, and Equation 6 may be calculated analytically. Usually, however, the data is integrated numerically in a spreadsheet. The trapezoid rule can be used to determine t^* accurately.

EXTRAPOLATING THE HISTORY TO LONG TIMES

Sampling for tracer is frequently terminated long before the tracer concentration is zero. Because the first moment is a time-weighted average, failure to include late time data leads to underprediction of mean residence time, and consequently, in pore volume calculations. This is fixed by breaking the integrals in Equation 6 in two:

$$t^* = \frac{\int_0^{t_b} E(t)tdt + \int_{t_b}^{\infty} E(t)tdt}{\int_0^{t_b} E(t)dt + \int_{t_b}^{\infty} E(t)dt} - \frac{t_s}{2} \quad (7)$$

If a curve is fit through the late time tracer data, the second integral in numerator and denominator can be evaluated in closed form. For example, if the plot of $\log(E)$ vs. time is linear for $t > t_b$, the decline is exponential and the tracer data can be represented as:

$$E(t) = be^{-at} \quad \text{for } t > t_b \quad (8)$$

Exponential decline is probably the most common tracer decline observed. Other curves may be used, but only with caution. Table 1 below shows the potential dangers of other types of curves used to extrapolate the example data. Both linear and power law extrapolation give non-physical results for this example, and therefore should not be used.

DETERMINING PORE VOLUME

Pore volume estimates follow directly from the mean residence time (Levenspiel, 1972). For open boundaries, multiple production wells, and/or incomplete recovery of injected tracer, the pore volume swept by the tracer is given as (Pope et al., 1994)

$$V_p = \frac{m}{M} q_{inj} t^* \quad (9)$$

The fractional recovery of tracer at any given well, m/M , is the integral of $E(t)$ for that well; again, a simple spreadsheet calculation.

Table 1. Summary of models used for extrapolating tracer data.

Form	Equation	Comments
Linear (Rose et al. 2004)	$E = 1.42 \times 10^{-4} - 4.74 \times 10^{-8} t$ Predicts C < 0 for t > 2900 days	Non-physical
Exponential	$E = 2.17 \times 10^{-4} e^{-0.0015t}$ $R^2 = 0.914$	
Power law	$E = 11407t^{-1.74}$ $R^2 = 0.878$ Too slow a decline; E > 0 at 30 years.	Not feasible

CALCULATING FLOW GEOMETRY

Shook (2003) showed that the flow and pore volume geometry of a formation (fractured or otherwise) could be estimated directly from a tracer test. Individual flow paths are imagined as streamlines, independent of the exact formation properties. The flow capacity, f_i , of the individual streamline is its specific velocity, relative to the bulk velocity. The storage capacity, c_i , is the pore volume associated with that streamline. We can approximate the true streamline geometries, F and C , from the $E(t)$ curve as

$$C(t) \equiv \frac{\int_0^t E(\tau) \tau d\tau}{\int_0^{\infty} E(t) dt} \quad (10a)$$

$$F(t) \equiv \frac{\int_0^t E(\tau) d\tau}{\int_0^{\infty} E(t) dt} \quad (10b)$$

From the equations given above, it is clear that $C(t)$ and $F(t)$ are incremental summations of streamline geometries. A value F_n , for example, is the fraction of streamlines with velocity equal to or greater than streamline n . C_n is the fraction of the total pore volume comprising those streamlines. Flow, F , and storage, C , capacity are most often plotted on a F - C plot. The shape of the F - C curve is useful as a diagnostic tool; for example, indicating what fraction

of the pore volume contributes what fraction of the fluid flow. The slope of the F - C curve is the instantaneous fluid velocity (Lake, 1989, p 195), which can be useful in predicting thermal velocities arising from injection. This application remains a goal of the INEEL tracer test interpretation program.

EXAMPLE MOMENT ANALYSIS

The methods discussed above were applied to the "Beowawe-like" tracer test data. The data were first normalized and deconvolved as discussed above. The corrected curve in Figure 2 is that used in these example calculations. Late time data was fit with exponential curve. The data from $t > 1630$ days shows good correlation between the data and the curve. The exponential equation is given in Table 1.

The first moment is calculated thusly. First, the trapazoid rule can be applied to the corrected $E(t)$ data to calculate the integrals in Equation 7 from $0 < t < 1630$ days. Symbolic integration of the exponential decline equation shows

$$\int_{t_b}^{\infty} E(t) dt = \frac{b}{a^2} e^{-at_b} (1 + at_b) \quad (11)$$

and

$$\int_{t_b}^{\infty} E(t) t dt = \frac{b}{a} e^{-at_b} \quad (12)$$

Using the values of a and b from Table 1, numerator and denominator for the moment calculation can be determined. Results of the calculation are given in Table 2. The mean residence time, t^* is 268.8 days. Pore volume swept by the tracer is calculated as

$$V_p = qt^* \frac{m}{M} = (19000 \frac{m^3}{d})(268.8d)(0.396) = 2.04 \times 10^6 m^3.$$

Table 2. Summary of piecewise integration of example tracer data.

Numerator	Denominator	t^*
$\sum_{i=2}^{1630} \frac{(E_i t_i + E_{i-1} t_{i-1})}{2} \Delta t_i$	$\sum_{i=2}^{1630} \frac{(E_i + E_{i-1})}{2} \Delta t_i$	
$+ \int_{1630}^{\infty} C t dt$	$+ \int_{1630}^{\infty} C dt$	
= 77.81 + 28.7	= 0.384 + 0.0125	268.8
= 106.55	= 0.3965	days

As an aside, consider the effect of not extrapolating the tracer data to infinite time. By ignoring all data for $t > 1500$ days, the apparent mean residence time can be calculated as 195.3 days. Thus, failure to include late time data results in an error

(underprediction) in residence time and pore volume estimates of 40%.

The F-C data is also calculated readily from the integrated E(t) data. The F-C curve is shown in Figure 3 for the example data. The F-C curve is useful for conceptualizing the nature of the flow paths. For example, it appears that about 60% of the flow is coming from some 12% of the total pore volume. This indicates a few high permeability streaks (fractures) are dominating the interwell flow.

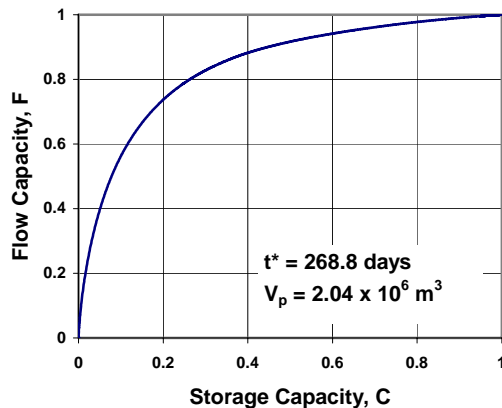


Figure 3. F-C Diagram for Example

Other information is available from a review of the tracer data. The tracer history continues to decline, despite continued tracer reinjection. This clearly suggests the Beowawe reservoir is open. That is supported by tracer recovery data as well; only 40% of the tracer injected was recovered. The implication of low recovery is that *for existing flow conditions* (e.g., direction) there is net discharge from the reservoir between points of injection and extraction. It would be interesting to reverse the flow field (exchange injection for production) and see what difference that would have on tracer recovery. There may be a means of optimizing injection/production locations such that net outflow is minimized.

LIMITATIONS OF THE METHOD

Moment analysis suffers from very few assumptions and limitations. The flow field is required to be in steady state, otherwise the streamlines (and therefore swept volumes) are changing with time. Small excursions from steady state flow can be mitigated in the following manner. Time is replaced as the independent variable with “volumes injected” (qt) in the definitions for E(t) etc. above. Variations in flow up to 15% over time have been treated successfully in this manner. Minor disruptions in flow (e.g., temporary suspension of injection or extraction) can usually be ignored.

Moment analysis is also based on the behavior of the tracer itself. The tracer is just a proxy for the reservoir fluids, so the tracer must behave like the reservoir fluids. Strictly speaking, that implies the tracer be conservative and ideal. The first requirement means the tracer strongly partitions into a single phase, the volume of which we are interrogating. The second requirement implies the tracer does not change the flow field itself. Unfortunately, failure to confirm the tracer requirements above does not preclude a test analysis. The problem is that, in the absence of site-specific verification, we cannot know if the analysis is correct.

A final observation on moment analysis is that it provides information on the pore volume swept by injectate. This is hardly a surprise, since pore volume not contacted by injectate cannot be interrogated via tracers – or any other injection-derived test. There is not, to this author’s knowledge, any method that estimates total (swept and unswept) volumes in an open system. All methods proposed suffer from one or more weaknesses, including physical inconsistencies and issues of non-uniqueness.

SUMMARY

Moment analysis offers a mathematically rigorous means of analyzing the temporal behavior of fluid flow to derive reservoir properties. Developed originally in the late 1950’s for closed systems, the methods have been enhanced, and new estimation methods have been developed. The formula for applying moment analysis is straightforward: convert raw data to age distribution functions, correct for thermal degradation, deconvolve the data, extrapolate the tracer tail, and numerically integrate the results. Swept pore volume, degree of outflow, and flow geometry are readily extracted from the analysis. All the calculations can be done in a spreadsheet. The spreadsheet used in the current example can be made available to interested parties.

ACKNOWLEDGEMENTS

This work was supported by the U.S. Department of Energy, Assistant Secretary for Energy Efficiency and Renewable Energy, under COE Idaho Operations Contract DE-AC07-99ID1377, whose support is gratefully acknowledged. The author also wishes to thank Joel Renner, Gopi Nalla, and Gary Pope for a careful review of the manuscript, and Pete Rose for providing the example tracer data.

NOMENCLATURE

- a exponent in the exponential decline equation
[=] day⁻¹

b	coefficient in the exponential decline equation [=] day ⁻¹
C(t)	produced tracer concentration [=] parts per billion (ppb)
E(t)	age distribution function of a tracer [=] day ⁻¹
E _{in}	age distribution function injectate [=] day ⁻¹
E _{app}	apparent age distribution function of a tracer – equal to true E(t) if no recycling of tracer occurs [=] day ⁻¹
f _{loss}	fluid loss between extraction and injection that leads to increased injection concentrations. Required in deconvolution calculations.
m	mass of tracer recovered [=] kg
M	mass of tracer injected [=] kg
t	time [=] day
t _b	time at which tracer begins exponential decline [=] day
t _s	tracer slug injection duration [=] day
t*	first temporal moment, or mean residence time [=] day
V _p	pore volume swept by tracer [=] m ³
q _{inj}	volumetric injection rate [=] m ³ /day
δ	Dirac delta function
ρ	fluid density [=] kg/m ³

REFERENCES

- Axelsson, G. O.G. Flovenz, S. Hauksdottir, A. Hjartarson, and J. Liu, 2001, "Analysis of tracer test data, and injection-induced cooling, in the Laugaland geothermal field, N-Iceland," *Geothermics*, **30**, pp 697-725.
- Bloomfield, K. K., Moore, J. N., 2003, "Modeling hydrofluorocarbon compounds as geothermal tracers," *Geothermics* **32**, pp 203-218.
- Danckwerts, P.V., 1958, "Continuous Flow Systems, Distribution of Residence Times," *Chemical Engineering Science*, **2**(1), pp 1-18.
- Gunderson, R., M. Parini, and L. Sirad-Azwar, 2002, "Fluorescein and Naphthalene Sulfonate Liquid Tracer Results at the Awibengkok Geothermal Field, West Java, Indonesia," *Proceedings, 27th Workshop on Geothermal Reservoir Engineering, Stanford, Cal, Jan 28-30, pp 53-58.*
- Lake, L.W., 1989, *Enhanced Oil Recovery*, Prentice Hall, Englewood Cliffs, New Jersey, 550 p.
- Levenspiel, O., 1972, *Chemical Reaction Engineering*, 2nd Edition, John Wiley and Sons, New York, NY, Ch. 9.
- Pope, G.A., M. Jin, V. Dwarakanath, B. Rouse, K. Sepehrnoori, 1994, "Partitioning Tracer Tests to Characterize Organic Contaminants," *Proceedings of the Second Tracer Workshop, Center for Petroleum and Geosystems Engineering, The U. Texas at Austin*, Nov. 14–15, pp 65-71.
- Robinson, B.A., and J.W. Tester, 1984, "Dispersed Fluid Flow in Fractured Reservoirs: An Analysis of Tracer-Determined Resedence Time Distributions," *J. Geophy Res.*, Vol. 89, No. B12, pp 10374-10384.
- Rose, P.E., M. Mella, C. Kasteler, and S.D. Johnson, 2004, "The Estimation of Reservoir Pore Volume from Tracer Data," *Proceedings, 29th Workshop on Geothermal Reservoir Engineering, Stanford, Cal, Jan 26-28, pp 330-338.*
- Sabatini, D.A. and T.A. Austin, 1991, "Characteristics of Rhodamine WT and Fluorescein as Adsorbing Ground-water Tracers," *Ground Water*, **29**, p. 341.
- Sinha, R., K. Asakawa, G.A. Pope and K. Sepehrnoori, "Simulation of Natural and Partitioning Interwell Tracers To Calculate Saturation and Swept Volumes in Oil Reservoirs," **SPE 89458**, *Proceedings of the SPE/DOE Fourteenth Symposium on Improved Oil Recovery, Tulsa, OK, 17-21 April 2004.*
- Shook, G.M., 2003, "A Simple, Fast Method of Estimating Fractured Reservoir Geometry from Tracer Tests," **Trans.**, *Geothermal Resources Council*, Vol. 27, pp 407-411.

TRACER TESTING AT MORI GEOTHERMAL FIELD, JAPAN, USING AROMATIC COMPOUNDS

Masato Watanabe¹, Fumiaki Arai¹, Daisuke Fukuda¹, Mikihiro Asanuma¹, Yasuyuki Hishi¹ and Jiro Tsutsumi²

¹JMC Geothermal Engineering Co., Ltd.,
101-1 Hosoyachi, Ukai,
Takizawa, Iwate, Japan
e-mail: watanabe@geothermal.co.jp

²Hokkaido Power Engineering Co., Ltd.,
108-5 Nigorikawa, Mori,
Hokkaido, Japan

ABSTRACT

The three tracers were simultaneously injected into the three different re-injection wells: toluenesulfonate (methylbenzenesulfonate), 1-naphthalene sulfonate and 1,5-naphthalene disulfonate. Toluenesulfonate was injected into NF-6 having injection points in the southwest part of caldera wall, then detected in the three wells having their feed points below injection point of NF-6. 1-Naphthalene sulfonate and 1,5-naphthalene disulfonate were injected into NF-2 and NF-8, respectively, and then detected in all the production wells in the field. The injection points of NF-2 and NF-8 are in the southeast part of caldera wall, and very close each other. Although we had expected that tracer flow patterns of 1-naphthalene sulfonate and 1,5-naphthalene disulfonate would be similar, the pattern of 1-naphthalene sulfonate returns was different from that of 1,5-naphthalene disulfonate. To illustrate the each tracer flow comprehensively, we tried to visualize them three-dimensionally in the view of mass transfer. The contour plots showed that most of the 1,5-naphthalene disulfonate flowed downward to the depth of the reservoir along the southeast part of caldera wall in a short period of time, and the 1-naphthalene sulfonate spread not only to the depth also horizontally to the intermediate depth and shallow region.

INTRODUCTION

The Mori liquid-dominated geothermal field is located in the Nigorikawa Caldera in southwest Hokkaido, Japan (Figure 1). The Mori geothermal power station started power generation of 50 MWe with six production wells and seven re-injection wells in 1982. Ten production wells and nine injection wells are presently used.

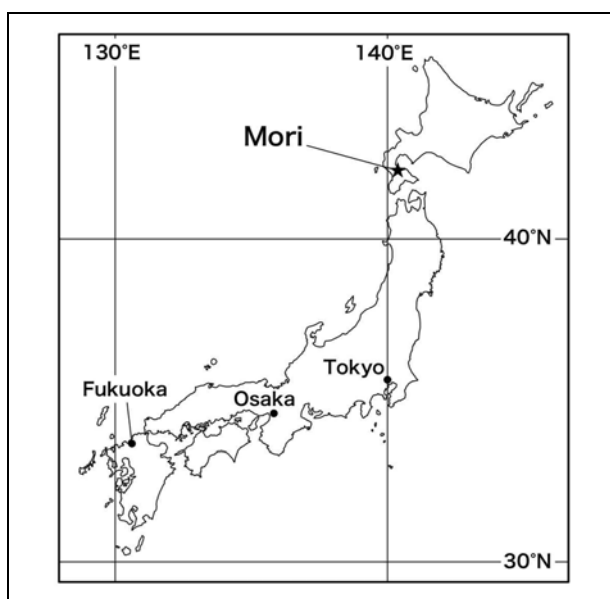


Figure 1. Location of the Mori geothermal field.

The Nigorikawa Caldera was formed about 12,000 years ago (e.g. Yanai et al., 1992). The caldera is shaped like a funnel, about 3 km in diameter at the surface (Figure 2). Below about -2,000 masl, the caldera has a vertical vent, about 300 to 500 m in diameter, infilled with post-caldera intrusion (Kurozumi and Doi, 2003). The outside of the caldera is comprised of Tertiary and pre-Tertiary formations covered with Quaternary sediments.

The production wells in the reservoir are divided into three groups as follows:

- (1) Deep production wells: having feed points in the deep part of the caldera wall (ND-7, ND-11, NF-1, NF-10, NF-11 and NF-12, 2,100-2,900 m depth).
- (2) Shallow production wells: having feed points in the pre-Tertiary formation outside of the caldera at

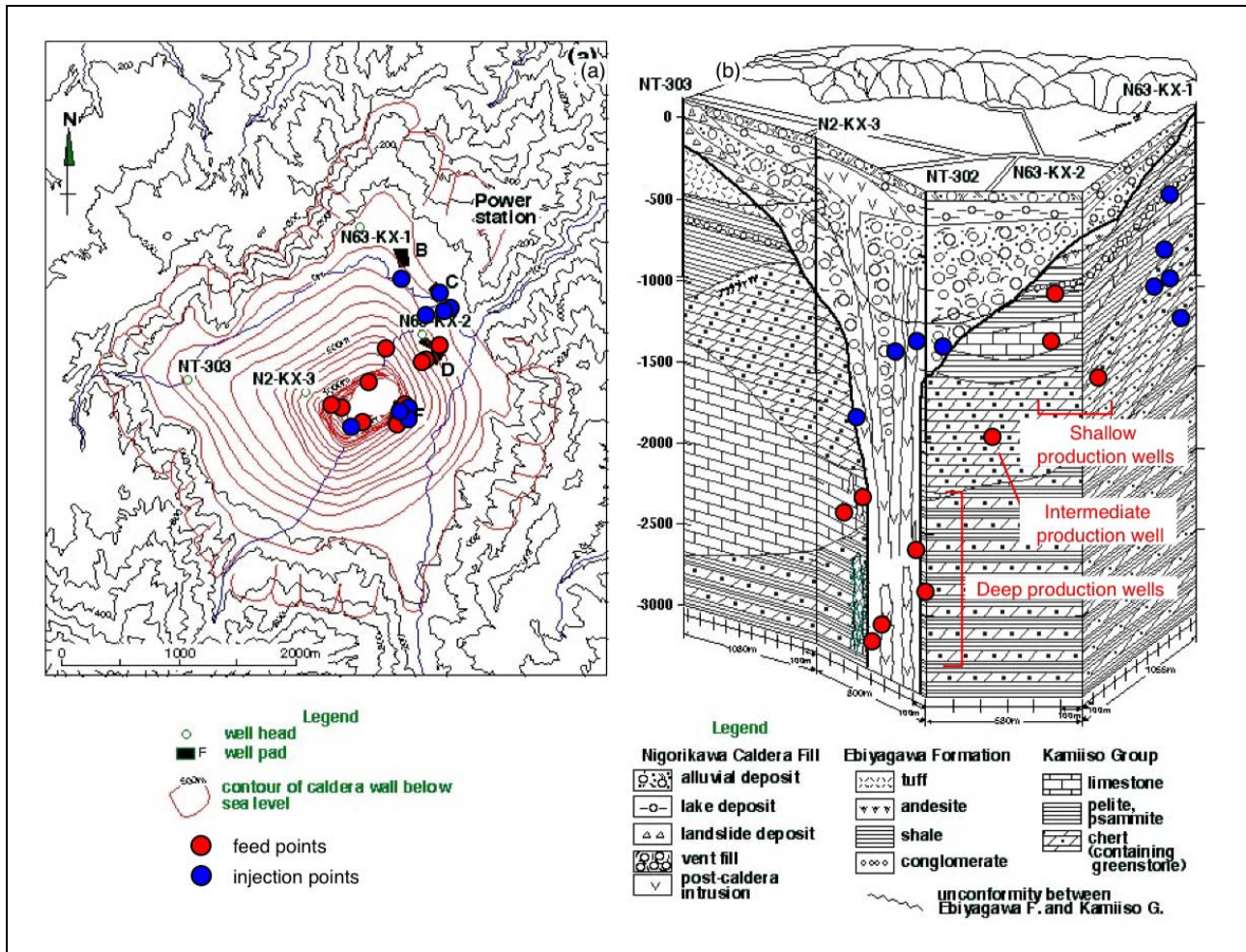


Figure 2. (a) Isocontour map of the caldera wall (after Kurozumi and Doi, 1994). (b) Schematic cross section of the Nigorikawa caldera (after Kurozumi and Doi, 1993).

shallow depth (ND-5, ND-8 and ND-9, 500-1,000 m depth).

(3) Intermediate-depth production well: having feed point in north part of the caldera wall at intermediate depth (ND-1, 1300 m depth).

Additionally, the injection points are divided roughly inside and outside of the caldera.

Most of fluids are produced from a fracture network in the caldera and more than a half of total injection fluid are returned back to the same fracture network. Therefore, it is important to evaluate quantitatively the returns of injected water for the reservoir management.

Tracer test has been one of the most important methods to evaluate the injection returns conducted periodically in the field. The potassium iodine (KI) and potassium bromine (KBr) were used before May 2000. However, the sensitive detection of KI and KBr became difficult because of the accumulation of them by a number of injections. To trace the injection sensitively, we started to use aromatic

compounds in October 2000 (Hishi et al., 2001). The compounds are more detectable than KI and KBr, and thus give more practical information to us.

This paper presents the results from the tracer tests in which three aromatic compounds were injected almost simultaneously into the three different wells in 2004.

METHOD

The three tracers were injected into the three different re-injection wells: toluenesulfonate (methylbenzenesulfonate), 1-naphthalene sulfonate and 1,5-naphthalene disulfonate. The three tracers were injected in series within six hours on 26 August 2004: 473 kg of toluenesulfonate was injected into well NF-6, 300 kg of 1-naphthalene sulfonate was injected into well NF-2, and 285 kg of 1,5-naphthalene disulfonate was injected into well NF-8. The each tracer was dissolved with about 2.5 kl of brine (re-injection water) in a mixer tank equipped with a pump (Figure 3). The each tracer was injected using the pump in 20-30 minutes.



Figure 3. Photograph of the tracer mixer tank used in the Mori geothermal field. The tank is 3 kl in volume and equipped with a pump for mixing and injecting the tracer solution.

All of the production wells in the field were subsequently monitored for the three tracers over the subsequent three months. The wells were sampled once per day for one week after injection, and then in low frequency as time passed. We collected 25 samples (flushed brine) in 100ml polyethylene bottles for each production wells during the monitoring period.

The samples were analyzed by High Performance Liquid Chromatograph (HPLC) equipped with an ultraviolet (UV) detector (Shimadzu, SPD-6A), fluorescence detector (Shimadzu, RF-10A_{XL}) and C-18 column (Shimadzu, VP-ODS). Toluenesulfonate and naphthalenes were analyzed with the UV detector and the fluorescence detector, respectively. Excitation and emission wavelength of the fluorescence detector were set 290 nm and 340 nm, respectively. The mobile phase was consisted of 35 wt% methanol solution buffered 25 mmol KH₂PO₄.

RESULTS AND DISCUSSION

The return curves for toluenesulfonate, 1-naphthalene sulfonate and 1,5-naphthalene disulfonate are shown in Figure 4. To compare the return mass of the tracers, we use tracer production rate (g/h) instead of concentration in samples.

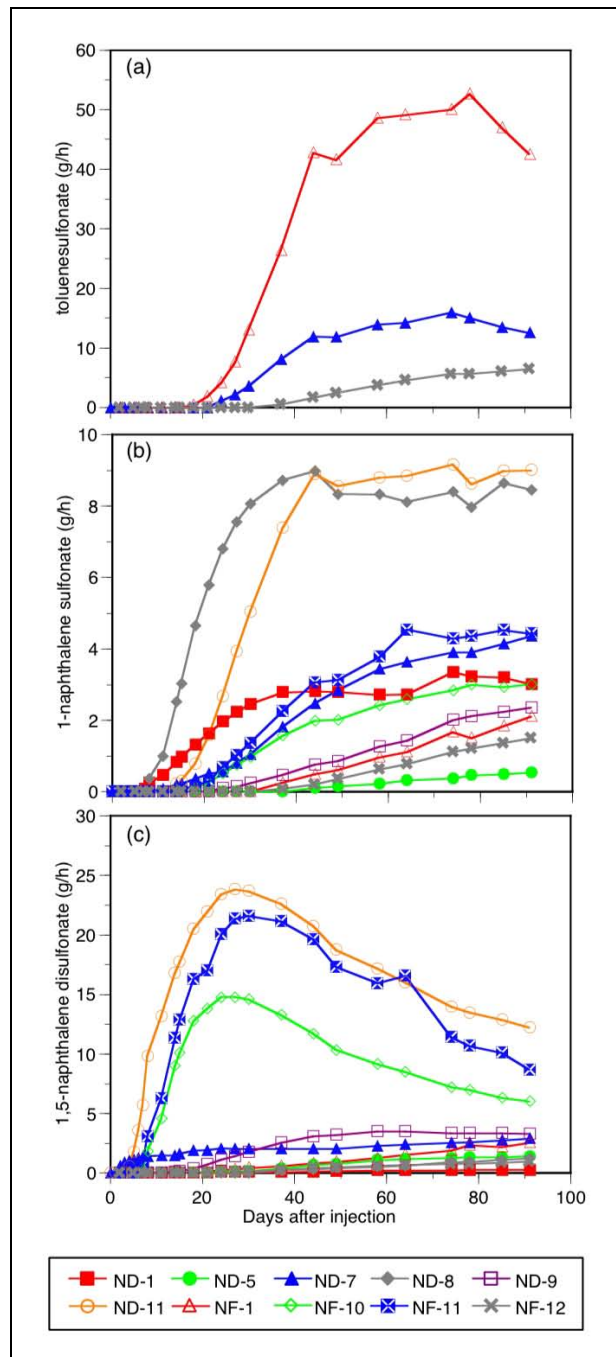


Figure 4. Tracer return curves; (a) toluenesulfonate (injected into NF-6), (b) 1-naphthalene sulfonate (injected into NF-2) and (c) 1,5-naphthalene disulfonate (injected into NF-8).

Breakthrough from a re-injection well to all the production wells were observed in the tests for NF-2 and NF-8. Breakthrough had been observed from a half of production wells in the previous tests for NF-2 and NF-8 using KI and KBr. Because KI and KBr were contained originally in the geothermal water, the background concentrations of them were rather high. In contrast, aromatic compounds were not

contained originally in the geothermal fluid. Furthermore, the detection limits of aromatic compounds are significantly lower than that of KI and KBr. Therefore, the tracer tests using aromatic compounds revealed the previously undetected breakthroughs.

Test on NF-6

Toluenesulfonate was injected into NF-6, and detected in ND-7, NF-1 and NF-12. As Figure 4 (a) shows, the arrivals of the tracer were seen first in NF-1, secondly in ND-7 and finally in NF-12. The highest and second highest tracer production rates were observed in NF-1 and ND-7, respectively. NF-12 showed the lowest tracer production rate. The above results consist with the distance between the injection point and feed points of the three production wells; the shorter the distance is, the faster the tracer arrived and the higher the production rate was.

The injection point and feed points distribute in the southwest part of the caldera wall. Additionally, because the injection point was shallower than the feed points, the tracer obviously moved downward in the southwest part of the caldera wall.

Test on NF-2

1-Naphthalene sulfonate, injected into NF-2, was returned from all production wells. As Figure 4 (b) shows, the strongest returns were observed in wells ND-8 and ND-11. The tracer production rates of ND-8 and ND-11 increased more rapidly than the other wells. The flow paths from NF-2 to ND-8 and ND-11 are quite different in direction. The injection point of NF-2 and feed point of ND-11 are located in the southeast part of caldera wall, and the injection point is shallower than the feed point. As with the case of NF-6 test, a part of the tracer moved downward along caldera wall. On the other hand, the feed point of ND-8 is in a pre-Tertiary formation outside of the caldera. Furthermore, because the injection point and the feed point are at the similar depth, another horizontal path exists in the pre-Tertiary formation.

Test on NF-8

As with the test of NF-2, 1,5-naphthalene disulfonate injected into NF-8 was returned from the all production wells. As Figure 4 (c) shows, the returns were stronger to ND-11, NF-10 and NF-11 than to the other production wells. The return curves of the three wells showed their peaks of tracer production rates in 27-30 days after injection. The feed points of ND-11 and NF-11 are located in the southeast part of caldera wall, and that of NF-10 is located in the north

part of the caldera wall. These feed points are at the deep part of the caldera wall. The injection point of NF-8 is located in the southeast of caldera wall, and is shallower than these feed points. This indicates that the tracer moved downward along the southeast part of the caldera,

As mentioned above, the results from the tests on NF-2 and NF-8 showed the strong tracer flows toward the deep feed points around the caldera wall, and the moderate flows in the pre-Tertiary formation. The results also showed a variety of return-curve patterns (Figure 4 (b) and (c)), although the injection points of NF-2 and NF-8 are very close each other; they are in the southeast part of caldera wall at about 900 m depth. On the other hand, as Figure 2 shows, the locations of feed points are of wide distribution. To understand the tracer flows spreading widely, we tried to visualize them three-dimensionally in the view of mass transfer.

Contour plots of 1-naphthalene sulfonate and 1,5-naphthalene disulfonate production rates

To follow the mass transfer of 1,5-naphthalene disulfonate (the tracer of NF-8) and 1-naphthalene sulfonate (the tracer of NF-2), we tried to draw the contour plots of the tracer production rates. The contour plots of each tracer were drawn at 5, 14, 30, 58 and 91 days after tracer injection. We aligned these five contour plots with time in Figure 5 and 6.

In order to make the contour plots, we created a rectangular grid model including all feed points with a software (Tecplot 10). Then we set the tracer production rates on the feed points in the model. The colored contour plots were drawn base on the ordered data interpolated by Kriging.

Figure 5 and 6 show the contour plots of the production rates of 1,5-naphthalene and 1-naphthalene sulfonate, respectively. Note that the scales of the plots are different; maximum scales are 25 g/h and 10 g/h for 1,5-naphthalene disulfonate and 1-naphthalene sulfonate, respectively.

Figure 5 shows that the higher tracer production area is along the southeast part of caldera wall. The highest value (>20 g/h) was seen in deep part of the caldera wall in 30 days after tracer injection. Therefore, most of the tracer flowed downward and was produced from the deep wells. In contrast, the tracer production rates in the pre-Tertiary formation are much lower than those in the deep part of caldera. This indicates the higher permeability between NF-8 and deep feed points in the southeast part of caldera wall.

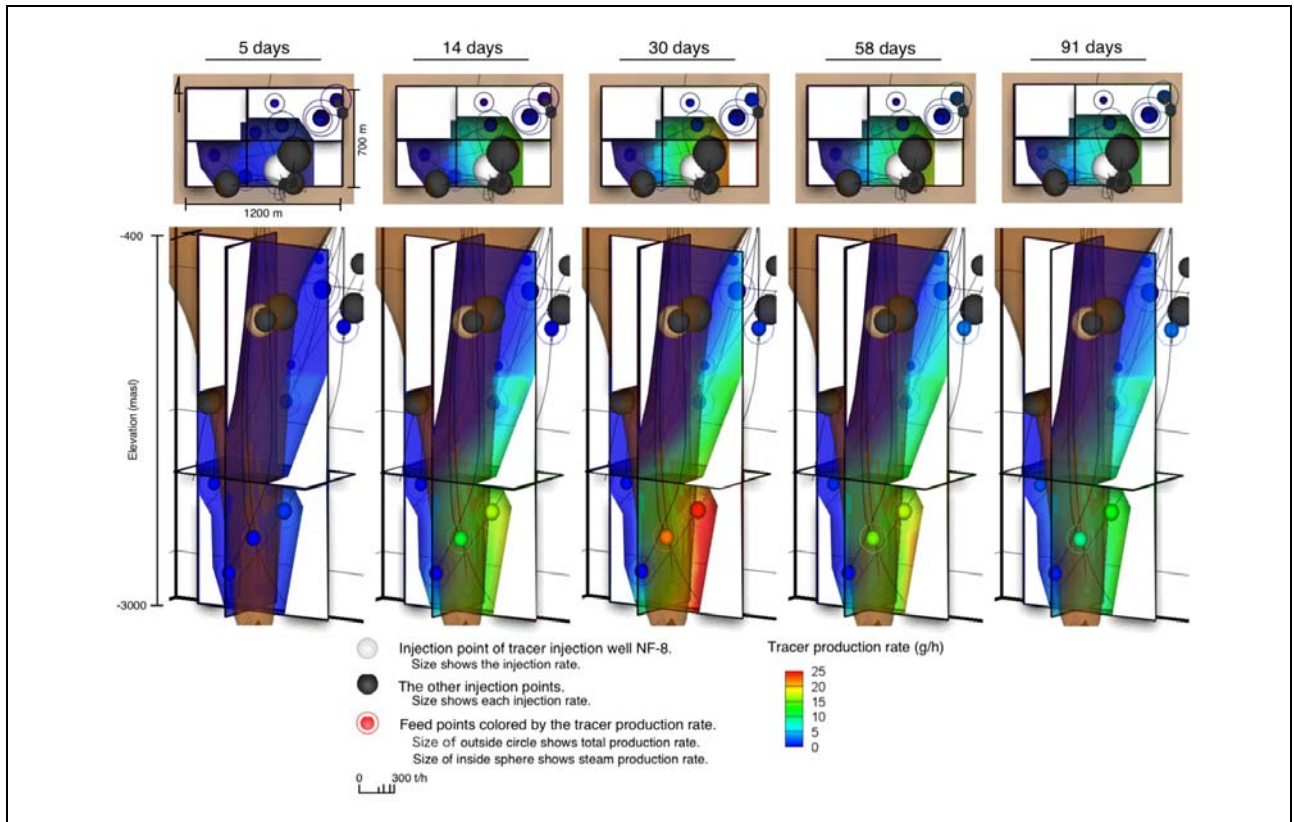


Figure 5. Contour plots of 1,5-naphthalene disulfonate production rate in order of time (5, 14, 30, 58 and 91 days after tracer injection). The upper contour plots are planes at the depth of 2,000 m.

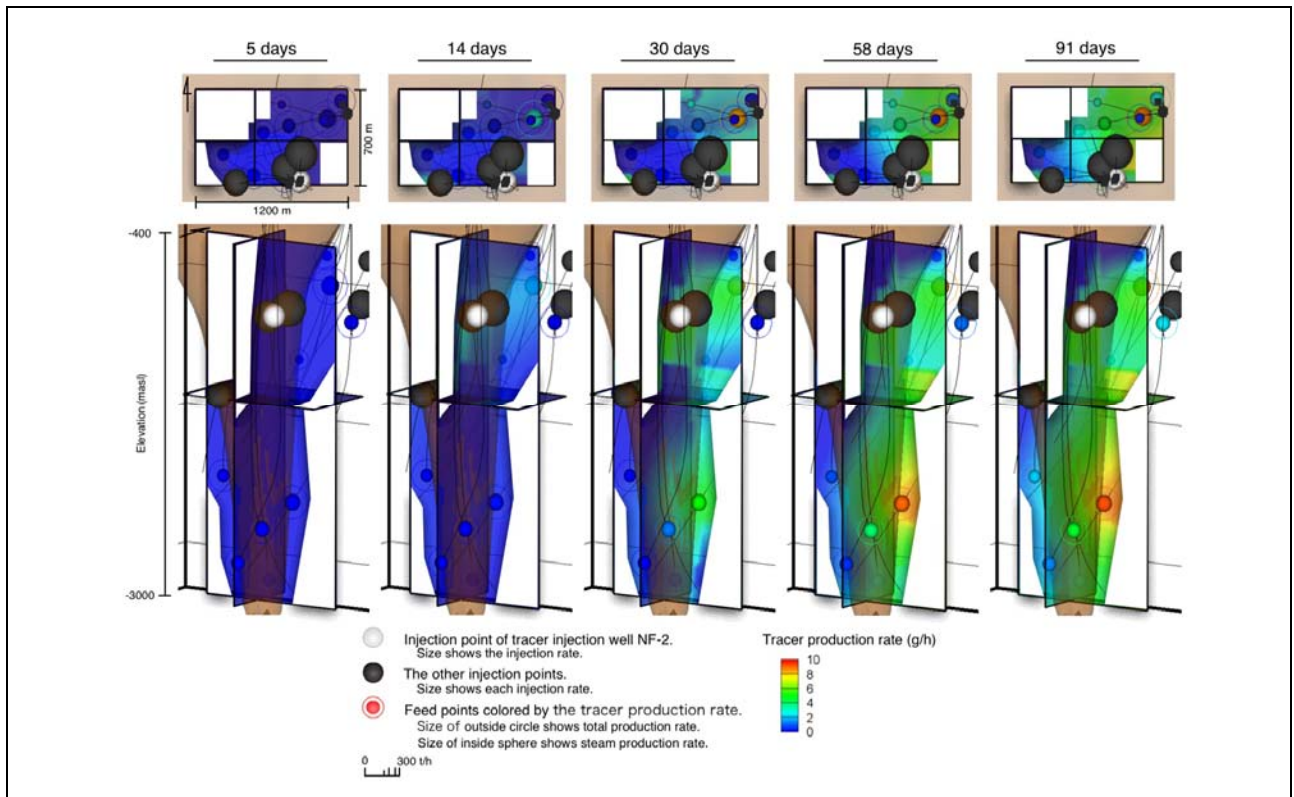


Figure 6. Contour plots of 1-naphthalene sulfonate production rate in order of time (5, 14, 30, 58 and 91 days after tracer injection). The upper contour plots are planes at the depth of 1,500 m

Figure 6 showed that the higher tracer production rate was found not only in deep region close to caldera wall also in the shallow pre-Tertiary formation. The highest value (ca. 8 g/h) was seen in the shallow and deep region in 58 days after tracer injection. Furthermore, an appreciable change is not seen between the contour plots of 58 days and 91 days. Additionally, the intermediate value (ca. 5 g/h) is seen widely. These results indicated that the 1-naphthalene sulfonate spread widely and slowly not only to deep region also to intermediate depth and shallow region.

The injection points of NF-2 and NF-8 were very close each other, and almost same weight of tracers was injected into them. However, the tracer flow pattern of 1-naphthalene sulfonate was different from that of 1,5-naphthalene disulfonate as found in the contour plots of tracer production rate. These observations may be caused by injection into NF-5. NF-5 has injection point close to those of NF-2 and NF-8, and the largest amount of brine was injected into NF-5 (ca. 300 t/h) in the field. Therefore, the tracer flows may have been affected by the injection of NF-5. Because a tracer test on NF-5 is untried for several years, we believe that it is important to conduct a tracer test targeting NF-5 and understand the interference among NF-2, NF-8 and NF-5.

CONCLUSION

On 26 August 2004, the three tracer tests targeting three injection wells were conducted simultaneously using toluenesulfonate, 1-naphthalene sulfonate and 1,5-naphthalene disulfonate. As results from the tests, breakthroughs undiscovered in the past tracer tests using KI and KBr were found. Toluenesulfonate injected into NF-6 having injection points in the southwest part of caldera wall was produced from the three wells having their feed points below the injection points of NF-6. Therefore, the tracer moved downward in the southwest part of the caldera wall. 1-Naphthalene sulfonate and 1,5-naphthalene disulfonate were injected into NF-2 and NF-8, respectively. The injection points of NF-2 and NF-8 are in the southeast part of caldera wall, and very close each other. The both tracers were detected in all the production wells in the field, but the patterns of the each tracer return were different. To illustrate the tracer flows comprehensively, we visualized them three-dimensionally in the view of mass transfer. The contour plot of tracer production rate indicated the characteristics of tracer returns as follows:

(1) The most of 1,5-naphthalene disulfonate flow downward to the depth of the reservoir along the southeast part of caldera wall in a short period of time.

(2) The 1-naphthalene sulfonate spread not only to the depth also horizontally to the intermediate depth and shallow region.

The geochemical temperatures of produced fluids have been almost constant under the current condition of injection. Therefore, current injection rates are acceptable. However, the returns of largest injection into NF-5 have not been evaluated recently, so that it is important to conduct tracer test targeting NF-5 next time.

ACKNOWLEDGMENTS

Hokkaido Power Engineering Co. Ltd. and Hokkaido Electric Power Co. Inc. allowed us to use the results of the tracer tests and much of their various information. The authors thank very much persons for their supports and advices.

REFERENCES

- Hishi, Y., Fukuda, D., Asanuma, M., Kobayashi, K. and Kasai, K. (2001), "Tracer testing at the liquid dominated reservoirs, using aromatic compounds (in Japanese)." *Abstract, 2001, Meeting of the Geothermal Soc. Japan*, P32.
- Kurozumi, H. and Doi, N. (1993), "Inner Structure of the Nigorikawa Caldera." *Abstract, 1993, No.2 Meeting of the Vol. Soc. Japan*, A14
- Kurozumi, H. and Doi, N. (1994), "Inner Structure of the Nigorikawa Caldera (Part 2)." *Abstract, 1994, No.2 Meeting of the Vol. Soc. Japan*, G14
- Kurozumi, H. and Doi, N. (2003), "Inner Structure of the Nigorikawa Caldera, Hokkaido, Japan." *Bull. Volcano. Soc. Japan, Vol.48 (3), 259-274.* (in Japanese with English abstract)
- Yanai, S., Ganzawa, Y. and Komori, Y. (1992), "The Stratigraphy and Distribution of the Nigorikawa Tephra, Latest Glacial Age Time-marker in Southwest Hokkaido." *Jour. Geol. Soc. Japan, Vol.98, No. 2, 125-136*

A METHOD OF ANALYZING TRACER DATA TO CALCULATE SWEEPED PORE VOLUME AND THERMAL BREAKTHROUGH IN FRACTURED GEOTHERMAL RESERVOIRS UNDER TWO-PHASE FLOW CONDITIONS

Xingru Wu¹, Gary A. Pope¹, G. Michael Shook², and Sanjay Srinivasan¹

1. The University of Texas at Austin, Austin, TX, 78712, USA, Xingru_Wu@mail.utexas.edu

2. Idaho National Engineering and Environmental Laboratory, P.O. Box, 1625, Idaho Falls, ID, 83415, USA,
OOK@inel.gov

ABSTRACT

One of the goals of using tracers in geothermal reservoirs is to predict the thermal breakthrough as early as possible. Shook (2001) has shown how this can be accomplished for the case of single-phase flow. In this paper, we show how the thermal breakthrough can be calculated from tracer data for the case of two-phase flow of steam and liquid water in a fractured reservoir without matrix permeability. In particular, we present a method to estimate the swept pore volume of the fracture in a hot, dry geothermal reservoir using partitioning tracers of high volatility. When a tracer with a high partition coefficient (concentration in the vapor divided by the concentration in the liquid) is injected in water, it will partition into the vapor phase and subsequently transport in the vapor phase (steam) toward the production wells. The method uses the first temporal moment of the tracer concentration distribution recorded at the producer to calculate the pore volume contacted by the injected tracer (the swept pore volume). This method has a rigorous theoretical basis and has been widely used in both groundwater and oil field applications. It can be used in the absence of detailed reservoir characterization data or flow and transport models since only a very simple, fast and easy integration of the production data is needed to yield the mean residence time of the tracer. Once the pore volume of the fracture is known, then the thermal breakthrough can be calculated using a retardation factor that takes into account the latent heat of the water.

INTRODUCTION

Reinjection of spent water into a geothermal reservoir is a standard reservoir management practice to maintain the pressure, replenish reservoir fluids, enhance energy extraction efficiency, and dispose of condensed water for environmental reasons. However, reinjection is not risk-free. For example, short-circuiting of injected water can lead to premature thermal breakthrough if injectors are

placed too close to the producers. On the other hand, if the injection wells are located too far away, the injected water does not provide sufficient pressure support for production.

Tracer testing is a powerful tool for reservoir characterization and management. Appropriately designed tracer tests yield information such as heat transfer area, reservoir volume, fluid velocities and thermal sweep efficiency (Kumagai et al, 2004; Pruess et al, 2005; Shook, 2001a). Tracers are usually injected in finite slugs and monitored in the surrounding producers to get the tracer return curve. Tracer breakthrough is more rapid than thermal breakthrough (Bodvarsson, 1972; Shook, 2001b), which implies that thermal breakthrough and consequently energy extraction efficiency can be predicted using the tracer return data. However, although 100+ tracer tests have been conducted in the past decade, most of tracer analysis is still qualitative (Shook, 2003).

Fractures are one of the most common characteristics in geothermal reservoirs. In naturally fractured geothermal reservoirs, the rock matrix stores most of energy, while the fracture network serves as flow conduits. The matrix often has very low permeability, typically of the order of 1 micro-darcy or less (Finsterle and Persoff, 1997). The permeability contrast between fracture and matrix is also very high. In a vapor-dominated reservoir, when a tracer with a high partition coefficient (concentration in the vapor divided by the concentration in the liquid) is injected together with spent water, it will partition into the vapor phase and subsequently transport in the vapor phase (steam) toward the production wells. Suitable tracers are available that will partition almost entirely into the vapor, so even though they are injected in the liquid water phase, they will transport almost entirely in the vapor phase. By analyzing the tracer data from the vapor phase, the swept pore volume of the fractures can be calculated in a very simple way as shown in this paper.

A synthetic case study is set up to demonstrate the methodology. A geothermal reservoir simulator is used to calculate synthetic tracer concentration data. The produced tracer concentration data are then integrated to yield the mean residence time and swept pore volume and this pore volume is compared with the known pore volume of the fractures in the part of the reservoir contacted by tracer. Results indicate that accurate calculations of swept pore volume are possible for reservoirs with a high permeability contrast between the fracture and the matrix. After the calculation of swept pore volume, thermal breakthrough is calculated by applying a thermal retardation factor. The whole procedure is very easy to perform and the estimated thermal breakthrough time is close to the time given by the simulator. Although a more complete investigation is needed, these preliminary results indicate that this remarkably simple and robust method of treating geothermal tracer data shows good potential for yielding useful early information to predict energy production from geothermal reservoirs under the special conditions tested described in this paper.

THEORETICAL APPROACH

Shook demonstrated that the reservoir pore volume and geometry could be estimated from conservative tracer tests corresponding to single phase flow (Shook, 1998, 2003). The analysis uses the first temporal moment of the tracer concentration distribution recorded at the producer to calculate the pore volume contacted by the injected tracer (the swept pore volume). This method has a rigorous theoretical basis and has been widely used in both groundwater and oil field applications (Dwarakanath et al, 1999; Sinha et al, 2004). It can be used in the absence of detailed reservoir characterization data or flow and transport models, since only a very simple, fast and easy integration of the production data is needed to yield the mean residence time, which can be done with a spreadsheet. A classical derivation of method of moments theory is available in the work by Himmelblau and Bischoff (1968) with application to packed bed reactors and was later generalized to three-dimensional flow fields (see Sinha et al., 2004, for a recent application to oil reservoirs).

The mean residence volume can be calculated for a finite tracer slug using the following expression.

$$\bar{V} = \frac{\int_0^{\infty} VC(t)dV}{\int_0^{\infty} C(t)dV} - \frac{V_s}{2} \quad (1)$$

V is the volume of vapor produced at the well. If the concentration values are only known at discrete

times, then the mean residence volume can be calculated as:

$$\bar{V} \cong \frac{\sum V_i C(t_i) \Delta V_i}{\sum C_i \Delta V_i} - \frac{V_s}{2} \quad (2)$$

In the above equation, V_i is the total vapor production volume over time interval i and $C(t_i)$ is the concentration of the tracer at time t_i . V_s is the vapor production volume during the period of tracer injection, and the $V_s/2$ term accounts for the finite size of the tracer slug.

TETRAD (Vinsome and Shook, 1993) was used to perform the numerical simulations. Tracers with K values of 1 and 4500 were used. The K value is defined as:

$$K_i = \frac{y_i}{x_i} \quad (3)$$

For a specific component, the K value is a function of temperature and pressure. In TETRAD, the K value is calculated from the following equation:

$$K_i = \left(\frac{A}{P} + B + CP \right) e^{-\frac{D}{T-E}} \quad (4)$$

Where A, B, C, D and E are component-dependent constants. The parameters in equation (4) can be calculated using standard thermodynamic data from sources such as Sander (1999). In particular, A and D can be calculated from Henry's law constant (k_H^\ominus) and the enthalpy of solution (ΔH) as follows:

$$A = \frac{\rho_a^\ominus}{k_H^\ominus} e^{\frac{D}{T^\ominus}} \quad \text{and} \quad D = \frac{-\Delta H}{R} \quad (5)$$

The values of B, C and E were taken as zero in this study. For specific tracer candidates, their K values can be estimated using equation (4) and (5). For example, the K values of tritiated water and 1,1,1,2-tetrafluoroethane (R134a) are about 1 and 4500 under the reservoir conditions of 240°C and 3380 kPa. Tracers with high K values (more volatile tracers) give early information concerning thermal breakthrough as shown in Figure 1. In this paper, R134a is used in the simulations since it can be used to obtain earlier information about reservoir conditions than low K value tracers.

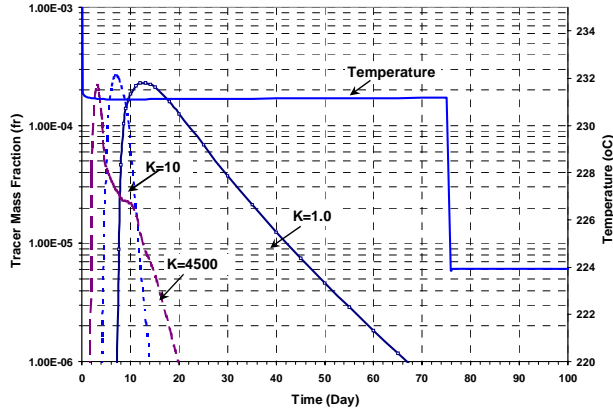


Figure 1: Tracer breakthrough time and K value relationship for a reservoir with initial water saturation of 0.3.

MODEL DESCRIPTION

Geothermal reservoirs are usually very complex with features as fractures, heterogeneity, multiple fluid phases and phase transitions, chemical reactions, and thermal effects. A conceptual model of a vertical fracture network in a geothermal reservoir is shown in Figure 2. In this diagram, a producer or injector penetrates a series of parallel, equally spaced, vertical fractures uniformly separated by isotropic and homogeneous matrix blocks. Usually the producer is located in the upper part of the reservoir and the injector is located in the lower part of the reservoir to prevent instability caused by gravity.

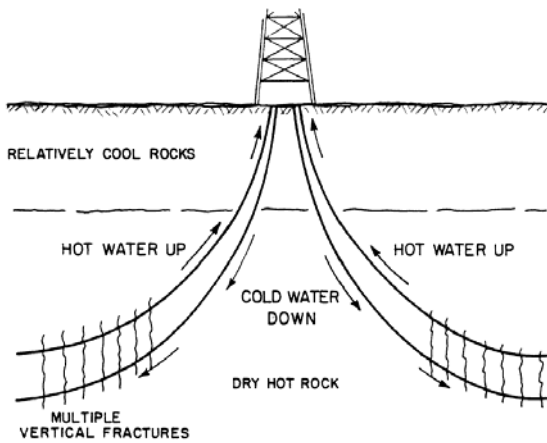


Figure 2: Schematic diagram of vertical fractures in geothermal reservoirs (after Gringarten and Witherspoon, 1975)

Initially, a single fracture was explicitly modeled so the transient process of the heat and mass transfer could be easily visualized. In addition, the single vertical fracture model is sufficient to capture the essential features of tracer transportation and phase transition. Besides, the symmetry of the problem

permits the proposed single fracture model. Since the matrix blocks are equally spaced and symmetric in the x direction, only a half plane of the fracture and matrix block was modeled as shown in Figure 3.

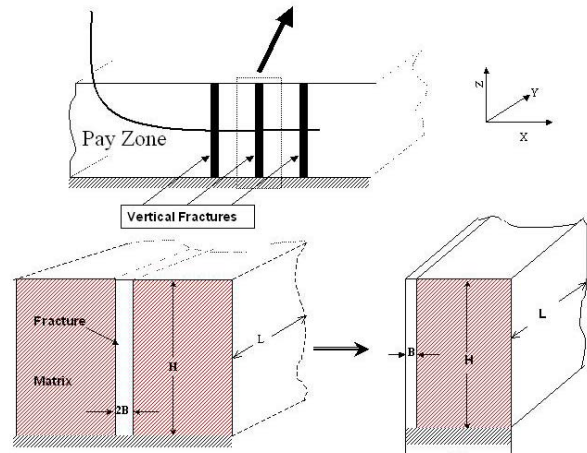


Figure 3: Diagram of the simplified model of Single Vertical Fractured

The half plane domain is discretized as shown in Figure 4. The main characteristic of this grid is that it is logarithmically spaced in the horizontal direction, which is considered to be the most accurate grid for diffusive-type problems (Bodvarsson and Tsang, 1982). In the vertical direction, 100 grid blocks of uniform size were used.

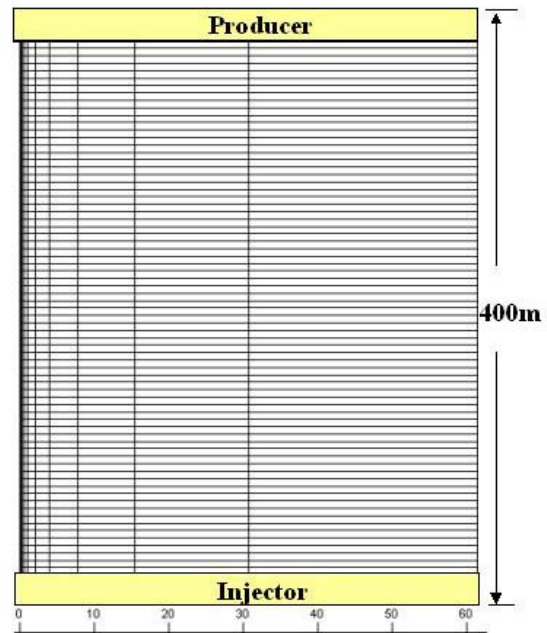


Figure 4: Grid used for the single fracture model

Table 1 is a summary of the key simulation parameters. A tracer with a K value of 4500 under reservoir conditions was injected for 0.5 days. The following relative permeability models were used:

Fracture:

$$k_{rwf} = \left(\frac{S_w - S_{wrf}}{1 - S_{wrf}} \right)^{1.5} \quad (6)$$

$$k_{rgf} = \left(\frac{S_g - S_{grf}}{1 - S_{grf}} \right)^{1.25} \quad (7)$$

Matrix:

$$k_{rwm} = \left(\frac{S_w - S_{wrm}}{1 - S_{wrm}} \right)^4 \quad (8)$$

$$k_{rgm} = \left(\frac{S_g - S_{grm}}{1 - S_{grm}} \right)^{2.5} \quad (9)$$

<i>Input Parameters</i>	<i>Value</i>
Length, m	100
Width, m	61.48
Thickness, m	400
Grid	12×1×100
Temperature, °C	240
Initial Pressure, kPa	3380
Rock density (kg/m ³)	2650
Fracture Permeability (md)	500
Fracture Porosity(fr.)	0.4
Fracture aperture (m)	0.05
Matrix Permeability (md)	0.0
Matrix Porosity(fr.)	0.03
Initial Water Saturation (fr.)	0.00001
Residual Water Saturation in Matrix(fr.)	0.3
Residual Water Saturation in Fracture (fr.)	0.1
Injection Rate (kg/d)	2880
Producer BHP (kPa)	2500
Injection Temperature (°C)	35

Table 1: Input summary for the base case

SIMULATION RESULTS

The produced tracer concentration data are integrated to yield the mean residence time or volume and swept pore volume, and this pore volume is compared with the known pore volume of the fractures in the part of the reservoir contacted by the injected tracer.

In this case, all injected fluid would flow through only the fracture since the matrix blocks are impermeable. Figure 5 shows the produced mass fraction in vapor phase of tracer R134a. Tracer breaks through at 9 days after injection, and liquid breakthrough occurs at 272 days. By the liquid breakthrough, more than 99% of injected tracer R134a has been produced.

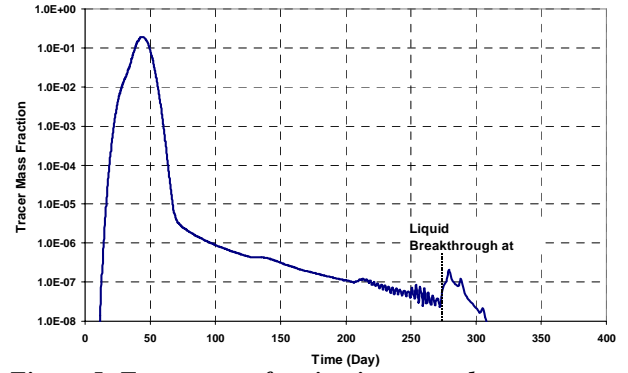


Figure 5: Tracer mass fraction in vapor phase

The volume of vapor production in the first 0.5 days is about 30.27 m³, and the cumulative vapor volume produced at the time of liquid breakthrough is 8218 m³. The calculated swept pore volume by applying equation (2) is 813.2 m³. The actual fracture pore volume is 800 m³. The relative error is less than 1.7%.

Multiple Vertical Fractures

Figure 6 shows a diagram in which both producer and injector penetrate two identical vertical fractures. This model uses the same initial condition and rock properties as the base case.

The calculated swept pore volume from the tracer data in the vapor phase is 1638 m³. This result is very close to the actual fracture pore volume of 1600 m³. This indicates that for a matrix with zero permeability, the method works for multiple fractures as well as for a single fracture.

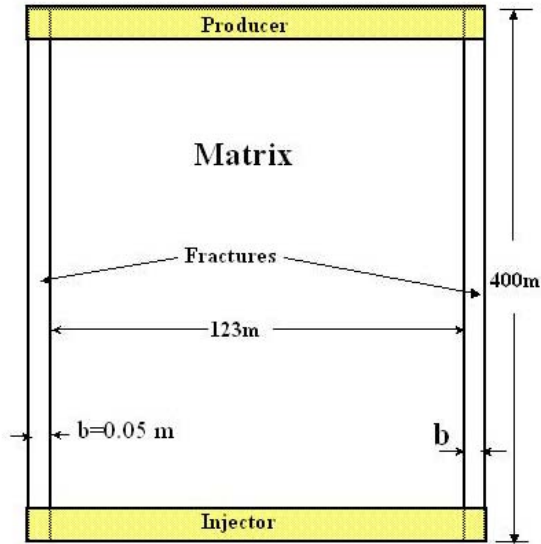


Figure 6: Diagram of model with two parallel vertical fractures

ESTIMATE OF THERMAL BREAKTHROUGH TIME FROM TRACER

For one-dimensional flow, the relationship between liquid water velocity and thermal velocity is as follows (Shook, 2001c):

$$v_{Ti} = \frac{v_w}{1 + D_{Ti}} \quad (8)$$

$$D_{Ti} = \frac{(1 - \phi) \rho_R C_{pR} (T_i - T_i)}{\phi \rho_w L_v} \quad (9)$$

In above equations, T_i is the initial reservoir temperature; T_i is the interface temperature, $T_i = T_{sat}(P_{wf})$; v_w is the liquid water velocity, and v_{Ti} is the thermal front velocity. The transfer of heat from the rock to the fluid results in a slow down of the thermal front and this is expressed by the retardation factor in equation (9).

Although equations (8) and (9) were derived for flow in a one-dimensional porous media, they can be applied to fractured reservoirs with zero matrix permeability. First of all, the thermal breakthrough time is short in the life of a typical geothermal reservoir, and heat transferred from the matrix is limited in such a short time. Secondly, the temperature gradient between the matrix and the fracture in the vapor zone is low so that the heat flux is minimal at early times.

Since the swept pore volume can be estimated from the tracer data, we can estimate the thermal breakthrough time by performing following steps.

- Calculate the swept pore volume from tracer data, V_p
- Calculate thermal retardation factor from equation (9)
- Calculate thermal breakthrough time

$$T_{BT} = \frac{V_p}{q_{inj}} (1 + D_{Ti})$$

where q_{inj} is the volumetric injection rate

The case with zero matrix permeability and 500 md fracture permeability was calculated to estimate the thermal breakthrough time. The calculated breakthrough time is 292 days, while the TETRAD simulation result is 272 days.

In general, the length of the fractures is complicated with tortuous fracture patterns, and the porosity of fracture may vary, so the thermal velocity may vary greatly in space. From equation (9), the retardation factor is inversely proportional to the porosity. For example, for a porosity of 0.4, the retardation factor D_{Ti} is only 0.042. This indicates that a superheated initial condition does not retard the thermal velocity very much. In this case, the thermal velocity is approximately equal to the liquid velocity.

ANALYSIS OF ERROR SOURCES

When spent water is injected into superheated geothermal reservoir, it is subject to vigorous vaporization up to 10-100 kg/s regardless of the injection rates (Pruess, 1997). During the phase transition process, properties of tracer and fluid would change dramatically. The complexity of the process gives rise to some uncertainty in applying the method of moments to this problem. Some of the main sources of uncertainty are thought to be as follows:

- Unsteady-state production rate caused by the boiling of the water causes uncertainty in the calculation of the mean residence time.
- A permeable matrix would result in a large overestimation of the pore volume of the fracture.

The case of a permeable matrix is currently under investigation. In addition to the more complicated physics, issues such as the numerical accuracy of the simulation needed to compare with the simple analytical method must be carefully considered.

SUMMARY AND CONCLUSIONS

Thermal breakthrough can be calculated from tracer data for the case of two-phase flow of steam and liquid water in a fractured geothermal reservoir without matrix permeability. The first temporal moment of the tracer data is used to calculate the swept pore volume of the fracture and then a

retardation factor is applied to calculate the thermal breakthrough time. A tracer with a high partition coefficient is injected in the liquid water but quickly vaporizes and transports in the vapor phase to the production well where its concentration is measured as a function of time. The concentration data and vapor production rate are all that is needed to calculate the swept pore volume of the fracture. So far this method has been applied only to the case of zero matrix permeability and one or two ideal fractures. Extending the proposed method to multiple fractures with variable properties should not be a problem in principle. Extending the method to cases with significant flow in the matrix will be more complicated.

NOMENCLATURE

\bar{V}	mean residence volume (m^3)
V	cumulative production volume of vapor phase (m^3)
V_s	cumulative production volume of vapor phase during the time of tracer injection (m^3)
C	tracer concentration (ppm)
K	thermodynamic equilibrium ratio
T	temperature ($^{\circ}C$)
P	pressure (kPa)
R	gas constant (J/mol.K)
S	saturation (fr)
k	relative permeability (md)
C_p	specific heat capacity (kJ/kg.K)
k_H	Henry's law constant ($mol/m^3 \cdot atm$)
x_i	mole fraction of species i in aqueous phase
y_i	mole fraction of species i in vapor phase
ρ	density (kg/m^3)
ϕ	porosity of the reservoir (fr).

Superscript

ϑ	standard condition, $T=298.15K$
-------------	---------------------------------

Subscripts

R	rock
I	Initial condition
a	aqueous phase
f	fracture property
g	vapor phase water
i	component i
r	residual phase saturation
m	matrix property
w	liquid phase water

REFERENCES

Bodvarsson, G.S. and Tsang C.F., 1982, "Injection and Thermal Breakthrough in Fractured Reservoirs,"

Journal of Geophysical Research, **87**, No. B2, 1031-1048.

Bodvarsson, G., 1972, "Thermal Problems in Siting of Reinjection Wells," *Geothermics* **1(2)**, 63-66.

Dwarakanath, V., Deeds, N. and Pope, G.A. (1999), "Analysis of Partitioning Interwell Tracer Tests," *Environ. Sci. Technol.*, **33**, 3829-2836.

Finsterle, S. and Persoff, P. (1997), "Determining Permeability of Tight Rock Samples Using Inverse Modeling," *Water Resour. Res.*, **33(8)**, 1803-1812.

Gringarten, A.C., Witherspoon, P.A. and Ohnishi, Y. (1975), "Theory of Heat Extraction from Fractured Hot Dry Rock," *Journal of Geophysical Research*, Vol. 80, **No. 8**, 1120-1124.

Himmelblau, D.M. and K.B. Bischoff (1968), "Process Analysis and Simulation: Deterministic Systems," John Wiley & Sons, Inc. New York.

Kumagai, N., Tanaka, T., and Kitao, K. (2004), "Characterization of Geothermal Fluid Flows at Sumikawa Geothermal Area, Japan, Using Two Types of Tracers and An Improved Multi-path Model," *Geothermics*, **33**, 257-275

Pruess, K. (1997), "On Vaporizing Water Flow in Hot Sub-vertical Rock Fractures," *Transport in Porous Media*, **28**, 335-372.

Pruess, K., van Heel, T., and Shan, C. (2005) "Tracer Testing for Estimating Heat Transfer Area in Fractured Reservoirs," Proceedings World Geothermal Congress, Antalya, Turkey, 24-29 April.

Sander, R. (1999), "Compilation of Henry's Law Constants for Inorganic and Organic Species of Potential Importance in Environmental Chemistry (version3)," <http://www.mpch-mainz.mpg.de/~sander/res/henry.html>

Shook, G.M. (1998), "Prediction of Reservoir Pore Volume from Conservative Tracer Tests," *Geothermal Resources Council Transactions*, **22**, September 20-23.

Shook, G.M. (2001a), "Predicting Thermal Velocities in Fractured Media from Tracer Tests," *Geothermal Resources Council Transactions*, **Vol. 25**, 465-468.

Shook, G.M. (2001b), "Predicting Thermal Breakthrough in Heterogeneous Media From Tracer Tests," *Geothermics*, **30**, 573-589.

Shook, G.M. (2001c), "Thermal Velocities Arising from Injection in 2-phase And Superheated reservoirs," Proceedings, Twenty-Sixth Workshop on Geothermal Reservoir Engineering, Stanford University, California, January 29-31, 2001.

Shook, G.M. (2003), "A Simple, Fast Method of Estimating Fractured Geometry from Tracer Tests," *Geothermal Resources Council Transactions*, **27**, October 12-15.

Sinha,R., Asakawa,K., Pope, G.A. and Sepehrnoori, K. (2004), "Simulation of Natural and Partitioning Interwell Tracers to Calculate Saturation and Swept Volumes in Oil Reservoirs," SPE 89458, Proceedings of the 2004 SPE/DOE Fourteenth Symposium on Improved Oil Recovery held in Tulsa, Oklahoma, U.S.A., April 17–21.

Visome, P.K.W. and Shook, G.M.(1993), "Multipurpose simulation," *J. Petroleum and Engineering*, **9**, 29-38.

Modeling

- Improving a Numerical Tool and Evaluating Impact of Density Changes of Injected Fluids in the Hydraulic Behaviour of HDR Reservoir** [186](#)
C. Baujard and D. Bruel
- Coupling the HOLA Wellbore Simulator with TOUGH2** [194](#)
Ashish Bhat, Daniel Swenson, Shekhar Goshavi
- Modeling the Viability of Underground Coal Fires as a Heat Source for Electrical Power Generation** [200](#)
Andrew Chiasson and Cenk Yavuzturk
- Crack Propagation Under Thermal Influence of a Well-Bore** [207](#)
A. Dobroskok, A. Ghassemi, A. Linkov
- Lattice-Boltzmann Simulation of Fluid Flow in Synthetic Fractures** [212](#)
Erdinc Eker and Serhat Akin
- Architecture for a Coupled Code for Multiphase Fluid Flow, Heat Transfer, and Deformation in Porous Rock** [222](#)
Shekhar Gosavi, Daniel Swenson
- Modeling of the Fault Type Geothermal Reservoir (Dachny Site, Mutnovsky Geothermal Field)** [229](#)
Kiryukhin A.V., Vereina O.B.
- Numerical Simulation of Liquid and Two-Phase Tracers in a Part of the Kakkonda Geothermal Field, Japan** [237](#)
Kei Sato, Yukihiro Sakagawa and Takemi Omiya

IMPROVING A NUMERICAL TOOL AND EVALUATING IMPACT OF DENSITY CHANGES OF INJECTED FLUIDS IN THE HYDRAULIC BEHAVIOUR OF HDR RESERVOIR

Clement BAUJARD and Dominique BRUEL

Ecole des Mines de Paris, CIG
35, rue Saint Honoré
F-77305 Fontainebleau Cedex
e-mail: clement.baujard@ensmp.fr, dominique.brue@ensmp.fr

ABSTRACT

During the last five years, the European Hot Dry Rock Project at Soultz-sous-Forets (France) has known major advances. Three deep wells were drilled into the crystalline basement at 5000 m depth. Stimulation of the wells by high rate fluid injections gave much information thanks to the microseismic events recorded on site. In order to better understand the development of the reservoir, a numerical model based on a Discrete Fracture Network approach was written to interpret and predict the pressure distribution in the reservoir and the hydraulic behavior of such a system. The hydraulic part of this finite volume code is strongly coupled with the mechanical behavior of the fractures.

The last years experiments showed that the density difference between autochthonous fluid (density 1060 kg/m³) and injected fluid (heavy brine or fresh water) might play a significant role during the stimulation phases of the wells. It was then decided to enhance the numerical code, under the assumption of immiscibility of the two fluids. A new variable was introduced in the code, saturation; flow equations are now solved with an IMPES scheme.

These recent improvements allow us to evaluate the impact of fluid density on the pressure distribution in the reservoir during stimulation or circulation tests. Therefore we provide better estimates of both extension and shape of the stimulated areas and we are able to define new stimulation strategies. The new version is also proven fruitful in predicting the evolution of flow distributions in fractures intersecting the bore holes as well as in giving breakthrough estimates for tracers (chlorure contend) migration in between injection and production bore holes.

INTRODUCTION

The general background of this study is the European Hot Dry Rock Research Program located in Soultz-sous-Forets, France. The purpose of this program is to generate electrical power from a deep enhanced geothermal system. The idea consists in injecting cold water into a hole while producing hot water in adjacent ones. The first step of this geothermal exploitation of the subsurface is the development of the reservoir, released by very high pressure injections in the system. The role of these injections is to enhance the permeability of the fractures by increasing the water pressure until shear can develop along the fractures. The injected fluid is essentially cold, fresh water that will be in contact in the reservoir with hot rocks and heavy hot brines.

The model presented here has been written in order to simulate potential density driven flows during stimulation of the reservoir, occurring between brine and fresh water. It is based on the Discrete Fracture Network approach; flows in rock matrix are neglected. Fractures are considered as discs: their distribution in space, orientation and thickness respond to stochastic laws inferred from the available statistics. The continuity equation is written at the center of each fracture. Each center of a fracture is a node of the mesh, and the controlled volume of each node is the fracture volume.

This paper describes the mathematical model, the spatial discretisation used, the resolution of the nonlinear system, a validation of the model, with the Buckley-Leverett problem and applications of this code, first at the scale of one well, and then with a more complex multi-well system.

The equations are the continuity equation of each phase, commonly used (Huyakorn and Pinder 1983; Slough et Al. 1999). The spatial discretisation is done using a finite volume scheme, and the evaluation of fluxes between two connected nodes considers the geometry of intersection of the two fractures (Cacas

1989; Jeong 2000). The system is solved with an IMPES scheme for Implicit Pressure - Explicit Saturation (Coats 2000; Forsyth 1999). It consists in resolving implicitly a single pressure equation, and explicitly a saturation equation, using the computed pressure values.

The Buckley-Leverett test case, commonly used in the petroleum industry is used as a numerical benchmark. Briefly, it simulates the advancement of a saturation front in a porous media. Computed results can be compared with results of the analytical solution written by Buckley and Leverett (1946).

The first application presents works that are done in order to understand mechanisms of the stimulation of the last well (GPK4) and to determine what is the role of the density of the injected fluid. The second application presents a more global model of the Soultz-sous-Forets fracture network and the results obtained.

FORMULATION

Governing equations

The equations describing a two-phase flow are obtained by combining Darcy's law with the individual phase conservation. They may be written in the following form (Huyakorn et Al.1994):

$$\nabla \cdot (k \tau_l \nabla (P_l + \rho_l g z)) = \frac{\partial}{\partial t} (\rho_l \Phi S_l) - M_l$$

where subscript l denotes the phase; k is the intrinsic permeability; τ_l is the mobility of the phase l ($\tau_l = k_r^l \rho_l / \mu_l$, in which k_r^l is the relative permeability, ρ_l is the fluid density and μ_l is the fluid dynamic viscosity); t is time; P_l is the pressure of the phase l ; g is the gravitational acceleration; z is the elevation above the datum plane; Φ is the porosity; S_l is the saturation of the phase l ; M_l is the rate of mass injection or withdrawal of fluid phase l per unit volume of the medium.

In addition to these flow equations, the following constitutive relations have to be considered, with P the average pressure of the two fluids:

$$\begin{aligned} S_l + S_l &= 1 \\ k_r^l &= k_r^l(S_l) \\ k &= k(P) \end{aligned}$$

Major assumptions

The Boussinesq assumption

This is quite a common assumption in reservoir modeling; it consists in neglecting variations of the fluid densities in the conservation equation, except in the buoyancy term ($P_l + \rho_l g z$). This equation now becomes:

$$\nabla \cdot (k \frac{k_r^l}{\mu_l} \nabla (P_l + \rho_l g z)) = \frac{\partial}{\partial t} (\Phi S_l) - Q_l$$

where Q_l is the volumic rate of injection of fluid phase l per unit volume of the medium.

The zero capillary pressure assumption

The capillary pressure is often neglected in reservoir modelling because it is usually very small compared to pressure variations in subsurface flows (Helmig 1997).

Practically, this leads to:

$$P_{l1} = P_{l2} = P$$

NUMERICAL TREATMENT

The numerical method used is very classical; it consists in a finite volume discretisation, associated with an IMPES resolution scheme.

Finite volume spatial discretisation

The finite volume method is a well-established method that is used in porous media. Our purpose is to adapt this method to a discrete network of fractures. This can be done thanks to the physical aspect of the finite volume formulation.

This formulation is obtained by integrating the conservation equation over the volume V_{frac} of one fracture:

$$\int_{V_{frac}} \nabla \cdot (k \frac{k_r^l}{\mu_l} \nabla (P + \rho_l g z)) dV = \int_{V_{frac}} (\frac{\partial}{\partial t} (\Phi S_l) - Q_l) dV$$

At that point it should be underlined that Φ no longer is the porosity of an equivalent porous media but it is the porosity of the considered fracture.

Applying the divergence theorem to the last equation, and making the assumption that saturation and porosity are constant in a single fracture, one obtains:

$$\int_{S_{int}} \nabla \cdot (k \frac{k_r^l}{\mu_l} \nabla (P + \rho_l g z)) \underline{n} dS = V_{frac} \frac{\partial}{\partial t} (\Phi S_l) - q_l$$

where q_l is the rate of injection of fluid phase l , S_{int} is the surface of the intersection between two fractures and \underline{n} is a unit vector, normal to the surface of intersection of the two fractures and pointing outside of the considered fracture.

Physically, the left term of the last equation is the flow going out of the considered fracture through an adjacent one. In our code this term is computed using an "integrated intrinsic permeability", k_{ij}^{int} , for the link between fractures i and j , calculated as follows:

$$k_{ij}^{int} = \frac{k_i k_j}{k_i + k_j} \cdot S_{int}(fracture_i, fracture_j)$$

Then, making the assumption that pressure is constant over one fracture and developing the gradient term to the first order, the conservation equation, written for the fracture i becomes:

$$\sum_j k_{ij}^{int} \frac{k^l(S_{ij}^l)}{\mu} \left(\frac{(P_i + \rho^l g z_i) - (P_j + \rho^l g z_j)}{\Delta x_{ij}} \right) = V_i \frac{\partial}{\partial t} (\Phi_i S_i^l) - q_i^l$$

using an upstream weighting scheme for the calculation of relative permeabilities:

$$S_{ij}^l = \alpha S_i + (1 - \alpha) S_j$$

with $\alpha=1$ if $P_i + \rho^l g z_i > P_j + \rho^l g z_j$ and $\alpha=0$ if not.

The IMPES scheme

Only the main ideas of this method are exposed here as many authors describe it in details.

Solving such a system of equations is not easy; as underlined by Peaceman (1977) the problem is parabolic in pressure and hyperbolic in saturation. An important point is that using a finite volume formulation provides numerical stability to the computation method. The IMPES method consists in solving implicitly the pressure equation and in solving explicitly the saturation equation, with the computed pressure values. The basic idea is to obtain a single pressure equation by summing the flow equations for each fluid phase (Settari and Aziz 1990).

The transient term of the conservation equation is written using Euler's implicit temporal discretisation scheme, and the final equation is solved using Newton-Raphson's algorithm because of the strong non linearity of $k_{ij}^{int}(P_i, P_j)$. The saturation is obtained explicitly by replacing the newly computed pressure value in one of the flow equation, assuming that porosity is constant during one time step.

TEST CASE: THE BUCKELEY-LEVERETT PROBLEM

This test problem is a very classical numerical benchmark for simulation codes in reservoir modeling. More precisely, it is a one dimensional flow problem, that was first solved by Buckley and Leverett (1946), since then it has been used by many scientists in order to evaluate the behavior of their codes (Settari and Aziz 1990; Huyakorn and Pinder 1978).

Physical parameters

The Buckley-Leverett problem consists in injecting a fluid at one side of a one-dimensional porous media while extracting the initial fluid at the other side of it (Figure 1). The geologic media and both fluids are assumed to be incompressible, and capillary pressure is neglected. A moving saturation front between the two fluids is observed; its shape and its migration rate are a severe test for numerical models. As pointed out by Buckley and Leverett (1946), the shape of the front strongly depends on the relative permeabilities. The analytical solution, obtained by the characteristics method, won't be given here. Please refer to Dahle et al. (1990) for further information.

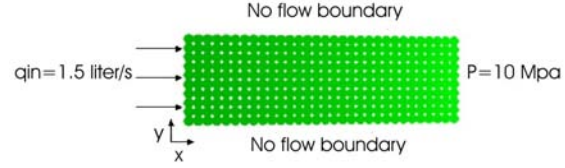


Figure 1. Geometry for the Buckley-Leverett Problem.

The difficulty is to adapt this example from a porous media to a discrete fracture network. Two ways to proceed are possible: build a stochastic network and deduce its equivalent permeabilities and porosity, or work on a deterministic network, like a plane, built by juxtaposition of fractures. This method appeared to be easier to perform. Nodes of the mesh are at the center of the fractures, every 10 meters. In order to fit to a finite difference scheme, the radius of the fractures is set to 5.64m. Using this value, the area of one fracture is equal to the area of one cell, which means that the porosity of the network is equal to the porosity of a single fracture. This fracture network is equivalent to a porous media of a cross section of 10^{-1} m^2 .

The table presented in figure 2 shows the physical parameters used to compute the Buckley-Leverett solution. As it can be seen on this table, the equivalent area of cross section of our model is 10^{-1} m^2 ; implying a Darcy velocity of $1,5 \cdot 10^{-2} \text{ m/s}$. It means that the simulation duration of 1296s is equivalent to an elapsed time of 1500 days following the values used by Thorenz (2001).

Parameter	Used value	Thorenz Value
Length	300m	302m
Width	100m	1m
Height	-	10m
Frac. thickness	10^{-3} m	-
Sim. Time	1296s	1500d
Porosity	0.2	0.2
Permeability	$1 \cdot 10^{-8} \text{ m/s}$	No influence
Viscosity	1000Pa.s	1000Pa.s
Inject. Rate	$1 \cdot 10^{-3} \text{ m}^3/\text{s}$	$1.5 \cdot 10^{-6} \text{ m}^3/\text{s}$
Init. Sat.	0.2	0.2
Sat. injected	0.8	0.8

Figure 2. Parameters used by Thorenz in the Buckley-Leverett example.

In both examples the relative permeability is computed by:

$$k^l = \left(\frac{S_l - 0.2}{0.6} \right)^2$$

Results

The figure 3 is a cross section of the model along the x axis and shows the advancement and the shape of

the saturation front at a time of 1296s. The time step of this simulation is set to 20s, and the mesh size is set to 5m. The theoretical front was established with the characteristic method. The mass balance is good, as the areas delimited by the two curves are equal.

The shape of the computed front is acceptable as the shock wave is not damaged too much by numerical diffusion. One can observe (fig. 3) a small difference between the two profiles. It is due to the inability of the finite volume method to capture sharp fronts. As underlined by Faust (1985), this kind of difficulties is very usual in reservoir simulation. Thorenz (2001) proposed numerical methods in order to skip this problem (*mass lumping* and *Gaussian point upwinding*), but none of them could be applied to a finite-volume numerical scheme.

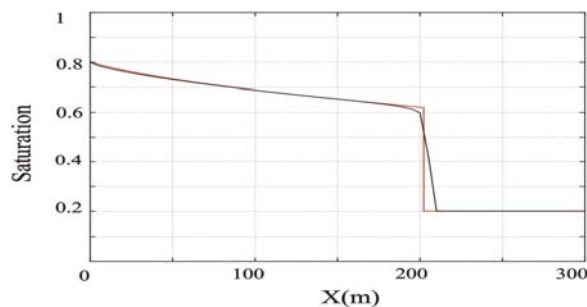


Figure 3. Results for the Buckley-Leverett problem

Various other tests have been performed with our code to characterize its accuracy. In order to see which results could be obtained with a stochastic network, we successfully simulated a salt water intrusion in a fracture network representing a coastal aquifer (Bruel and Baujard 2004).

INTEREST OF A MULTIPHASE APPROACH OF SOULTZ-SOUS-FORETS HDR SITE

One must keep in mind that during the injection tests at Soultz-sous-Forets, an important contrast exists between densities of autochthonous fluid ($d=1060 \text{ kg/m}^3$) and injected fluid ($d=1200 \text{ kg/m}^3$ or $d=1000 \text{ kg/m}^3$). The question is to understand the importance of this difference on the fluid circulation and the fracture stimulation.

An other aspect of our code is its ability to take into account the fracture shear failure, thanks to a hydro mechanical coupling. The mechanical aspect appears through a Mohr Coulomb failure criterion, calculated in all the fractures at every time step; if the resulting calculated shear stress for a considered fracture is greater than the value given by the Mohr Coulomb criterion, the failure of the fracture leads to an opening of the considered fracture and to a new permeability calculation law. This change is supposed to be irreversible during a simulation.

Concerning the parameters used to allow this hydro mechanical coupling, we have to define values and orientations of principal field stress components and

a friction angle and cohesion for the Mohr Coulomb criterion. Many authors have published stress evaluation of the Soultz-sous-forets rock masses (Rummel and Baumgartner 1990; Heinemann and Kappelmeyer 1994). In our recent works, we used the stress distribution proposed by Cornet et al. (2004) which allows much better results in term of stability of the fractures in field conditions before injection. The friction angle used in our simulations is 40° , and the cohesion is taken in a range from 2 to 4 Mpa (Cornet et al. 2004).

The case of GPK4

In October 2004 began the stimulation campaign of GPK4. We simulated the injections performed during that period with different densities of the injected fluid, in order to characterize the influence of this parameter on the stimulated area.

Pressure results

Density doesn't have a great influence on the downhole pressure of the well during the simulation (figure 4). With the same model, changing only the injected fluid density doesn't give drastically different pressure response at the well.

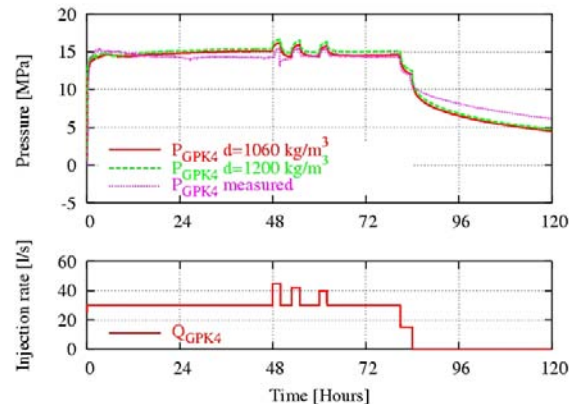


Figure 4. Results for the GPK4 stimulation campaign, modeling the influence of density of injected fluid.

It doesn't clearly appear on that particular model, but the main differences between the two simulations are observed during the shut in periods of the well; we think that this effect could be due to density driven flows that would during the shut in phase of the well take the advantage on injected flow.

Stimulation results

As we could expect, injecting heavy brine instead of water in the well implies major differences on the location of calculated shear events (see figure 5). It can clearly be observed on this image that shear events calculated while injecting a heavy fluid in the fracture network are more numerous and more at the bottom of the reservoir than those calculated while

injecting fresh water. With this particular model, we obtain 919 shear events in the case of injecting fresh water and 1044 in the case of injecting heavy brine, what makes an increase of approximately 14% of the number of shear events only thanks to the influence of fluid density.

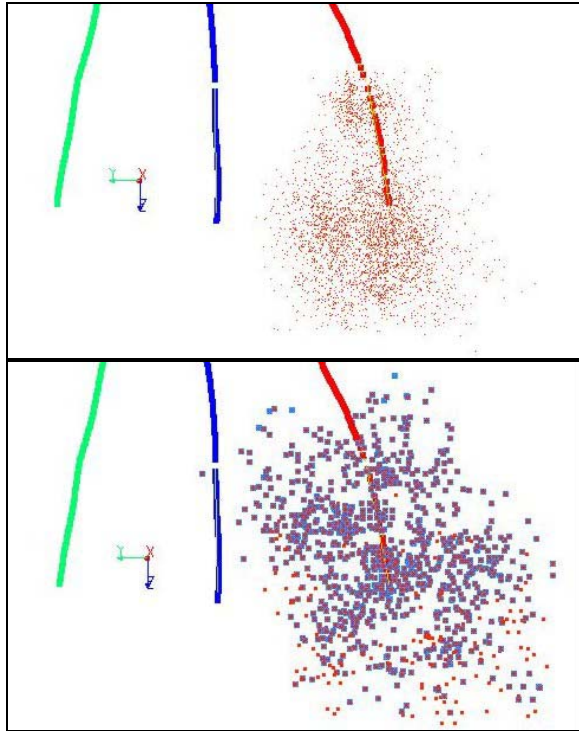


Figure 5. Location (view from west) of recorded seismic events (on top) and of calculated shear events (on bottom) for GPK4 stimulation (blue bold points: injecting at $d=1000 \text{ kg/m}^3$; red small points: injecting at $d=1200 \text{ kg/m}^3$).

More precisely, we tried to understand the mechanisms of this difference between the two injections with calculated flowlogs; fractures that intersect boreholes in our model are deterministic ones, which means that their orientations and thickness are the ones given by the UBI and flowlogs interpretation on site. Their extensions are assumed. The purpose of this strategy is first to reduce the variability of the hydraulic response of the fracture network due to its stochastic aspect and secondly to simulate a flowlog as close to the observations as possible. This technique has the advantage of presenting fractures that will in our model shear at the same pressure that on site fractures. Figure 6 shows the calculated flowlogs obtained with the GPK4 stimulation campaign, at a time $t=48$ hours. The injection rate is equal to 45 l/s. We clearly observe on that image a difference due to the density of the injected fluid. The injection rate in the deepest

fracture (depth 4975 m) is 21.46 l/s for an injection of fresh water, and 21.86 l/s for an injection of heavy brine, which makes an increase of nearly 2% of injected flowrate for this fracture. It is not a huge difference, but if we consider all the stimulation campaign, it means an increase of about 170 m^3 of injected fluid going into the deepest fracture, in the case of injecting heavy brine. This difference could explain the greater deepness of calculated shear events in this scenario.

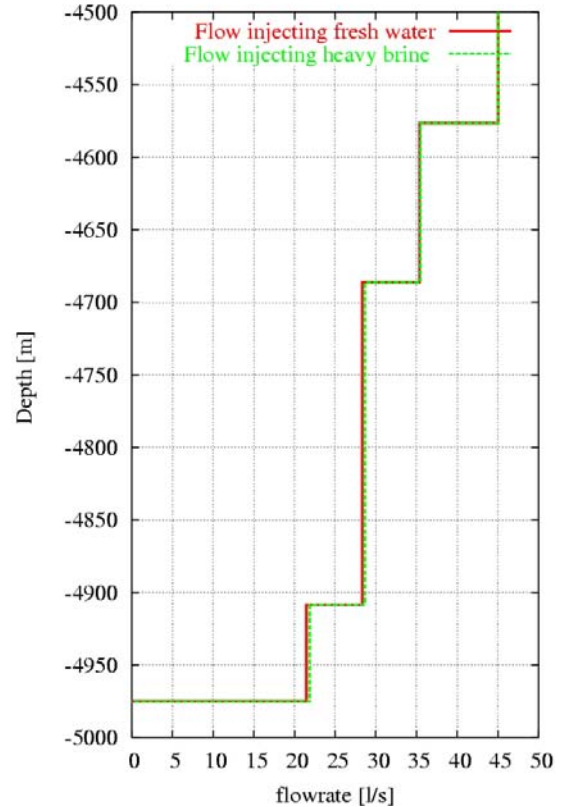


Figure 6. Calculated flowlogs during GPK4 stimulation campaign.

Conclusion on the influence of the density of the injected fluid on stimulation

If the influence of the fluid density during all the stimulation can be clearly established, the problem is that injecting heavy brine during more than three days supposes to have a tank of more than 9000 m^3 of this brine. So the question is to know what could be the influence on stimulation of injecting heavy brine only during the 6 first hours of injection, as it was the case during the stimulation of GPK4 on site. This case shows an increase of more than 50 shear events during the entire stimulation. But these events are not located in the lowest part of the reservoir, as it is the case with the injection of brine during all the stimulation campaign. The distribution in space of

these events is very homogeneous. So far, our simulations showed that the shear events that take place at the bottom of the reservoir with the heavy brine begin during the third day of injection, during the first pulse at 45 l/s. In order to try other scenarios of injection, we simulated the stimulation campaign with the injection of brine during this pulse. Results obtained show a less good efficiency of this case, compared to the injection of brine at the beginning of the stimulation. Finally, from all the stimulation strategies defined, the best results were definitely obtained with the injection of brine at the beginning of the stimulation.

APPLICATION TO THE DEVELOPMENT OF THE RESERVOIR

The model

Since 1989, many stimulation campaigns have been performed in Soultz-sous-forets. We will only focus here on the stimulation of the wells GPK2, GPK3 and GPK4 in the 5km depth reservoir. The idea is to try different stochastic models of fracture distribution and to see which one gives the best results in term of pressure response of the wells, saturation distribution in the reservoir and breakthrough estimates, extension and shape of the calculated shear events compared to the seismic cloud recorded on site. As we use the same model for the three wells, we can save the stimulated fractures from the first stimulation campaign (GPK2), and keep them for the GPK3 stimulation campaign, and do the same for GPK4. We can thereby simulate the development of the 5km depth reservoir since 2000, date of the stimulation of GPK2. We must specify here that the multiphase version of our code doesn't take in account the temperature variations of the fluids; their densities are thereby constant during the simulation, which doesn't allow us to predict eventual convection movements of the injected fluid in the reservoir.

The last model we built is constituted of fractures concentrated along great subvertical structures of orientation N160 and N20 (figure 7).

The extension of the model is 2km along the x-axis (eastern), 3km along the y-axis (northern) and 2km depth. The boundary of this model are closed ($q=0$) except for the subvertical structures. This means that these structures behave as conductive areas that are the only ones capable of taking water in the far field. This solution is the one that gives best results for the shut in of the wells. This model contains 45000 fractures of average radius 31m and 1mm aperture.

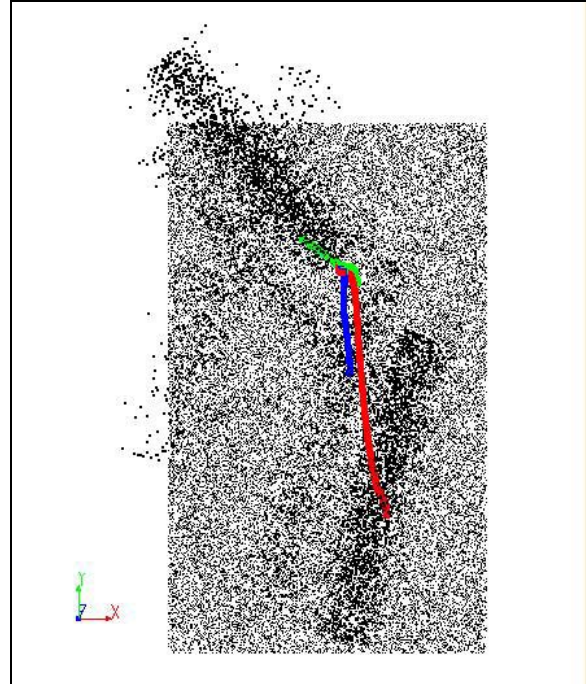


Figure 7. Location of the center of the fractures in our model (top view). Well bores are from north to south GPK2, GPK3 and GPK4.

Pressure Results

One simulation has been run for every stimulation campaign on one single well. This model gives acceptable results (in terms of pressure response) for all the wells. As an example, the figure 8 shows the pressure response of the wells during the GPK3 stimulation campaign. All the tests consist in injecting fresh water (density $1000 \text{ m}^3/\text{s}$) in the autochthonous brine (density $1060 \text{ m}^3/\text{s}$).

As one can observe, the pressure response calculated with this model corresponds with the pressure recorded on site, except during the shut in phase of the wells. Concerning the saturation, the calculated breakthrough is estimated to 3 days for GPK4 and a bit less for GPK3, which is also acceptable. The same kinds of results were observed with the stimulation of the other wells (The simulated GPK4 stimulation campaign results were shown above, and the GPK2 response during the 2000 stimulation campaign is also correct).

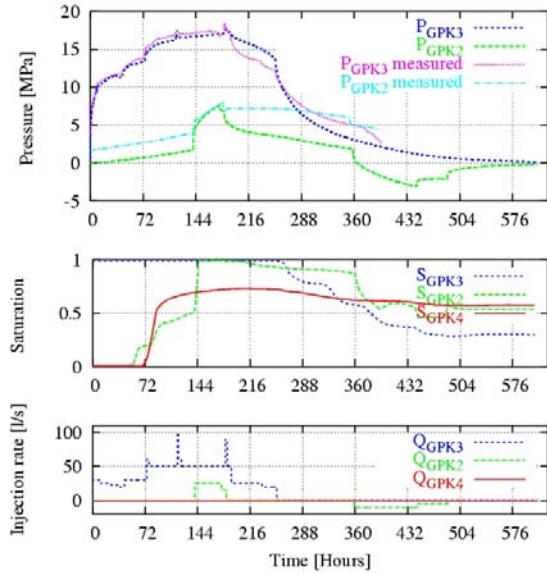


Figure 8. Hydraulic response of the model for the GPK3 stimulation.

Extension of the stimulated area

Figure 9 shows the correspondence between calculated shear events and recorded seismic events.

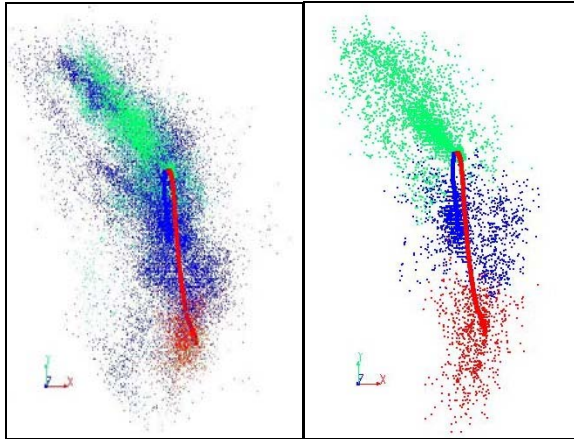


Figure 9. Recorded seismic events (on the left) and calculated shear events during the stimulation campaigns (top view). Green light points: recorded during GPK2 stimulation; blue points: recorded during GPK3 stimulation; red points: recorded during GPK4 stimulation.

We can observe on these images that the location of calculated shear events globally corresponds to the recorded seismic events, even if localized uncertainties still remain. The main problem of this model concerns the extension of the GPK3 stimulation area that is really underestimated in our model. This may come from a too active stimulation

of GPK2 and of a too bad connectivity of the fractures intersecting GPK3 in our model.

CONCLUSION

The recent improvements made on the code to allow a multiphase resolution of the problem seem to give interesting results; the first application example explained in this paper clearly shows that the density of the injected fluid plays an important role in the hydraulic fracturing process. It also allows us to better fit the shut in curves, even if these results are the most difficult to reproduce with our model; its stochastic aspect leads to a great variability at that point. Acceptable results are also obtained in the estimations of shape and extension of the shear events cloud. This would let us think that the assumption of a globally closed system, with a few drainage structures connected to the far field is quite close from reality.

On the other hand, this model needs important geometrical assumptions, concerning the orientation of the fractures, their localization, thickness and extension... Nevertheless results can be obtained with this kind of modeling, like prediction of shearing events localization.

The next step of modeling may concern temperature changes in both fluids and rock matrix, in order to introduce a variable density of the fluids and to see what impact heating of the injected has on the reservoir development, or on circulation. Another direction would be to simulate a circulation test with the three wells in order to try to predict what ratio of the injected fluid could be recovered to the other wells.

ACKNOWLEDGEMENTS

We warmly thank Mr. F. Cornet for his useful advices, BRGM (France) for the data sharing of the flowlogs interpretation, EEIG Heat Mining for providing the data from the European HDR site at Soultz-sous-Forets, which is supported mainly by the European Commission, BMBF (Germany), and ADEME (France).

REFERENCES

- Bruel, D. and Baujard, C. (2004), "A multiphase flow model in a discrete fracture network: formulation and simulation examples", *18th Salt Water Intrusion Meeting proceeding*.
- Buckeley, S. E. and Leverett, M. C. (1946), "Mechanism of fluid displacement in sands", *Trans. AIME*, **146**, 107-116
- Cacas, M. C. (1989), "Développement d'un modèle tridimensionnel stochastique discret pour la simulation de l'écoulement et des transferts de masse

et de chaleur en milieu fracturé”, *Ph. D. Thesis, Ecole Nationale Supérieure de Mines de Paris*.

Coats, K. H. (2000), “ A note on IMPES and IMPES-based simulation models”, *Society of Petroleum Engineers*, **September**, 245-251.

Cornet, F. H., Berard, TH. And Bourouis, S. (2004), “How close to failure is a natural rock mass at 5km depth ?”, submitted for publication in *Int. J. of Rock Mech. Min. Sc.* , sept 2004.

Dahle, H., Espedal, M., Ewing, R. And Saevareid, O. (1990), “Characteristics adaptative subdomain methods for reservoir flow problems”, *Numerical Methods for Partial Differential Equations*, **6**, 279-309.

Faust, C. R. (1985), “Transport of immiscible fluids within and below the unsaturated zone: A numerical model”, *Water Resources Research*, **21(4)**, 587-596

Forsyth, P., Unger, A. and Sudicky, E. (1997), “Nonlinear methods for nonequilibrium multiphase subsurface flow”, *Advances in Water Resources*, **21**, 433-489.

Helmig, R. (1997), “Multiphase flow and transport processes in the subsurface”, *Springer Verlag*.

Huyakorn, P., Panday, S. and Yu, Y. (1994), “A three dimensional multiphase flow model for assessing NAPL contaminant in porous and fractured media, 1. Formulation”, *Journal of contaminant hydrology*, **16(2)**, 109-130.

Huyakorn, P. and Pinder, G. F. (1978), “A new finite element technique for the solution of two phase flow through porous media and fractured media”, *Advances in Water Resources*, **1(16)**, 285-298.

Jeong, W. (2000), “Modélisation de l’influence d’une zone de faille sur l’hydrogéologie d’un milieu fracturé: application au domaine du stockage des déchets nucléaires”, *Ph. D. Thesis, Ecole nationale Supérieure de Mines de Paris*.

Heinemann, B. and Kappelmayer, O. (1994), “Results of scientific investigation of HDR test-site Soultz-sous-Forets, Alsace”, *SOCOMINE report*.

Rummel, F. and Baumgartner, J. (1991), “Hydraulic Fracturing stress measurements in the GPK-1 borehole, Soultz-sous-Forets”, *Geothermal Sc. And Tech.*, **3**, 119-148.

Settari, A. and Aziz, K. (1990), “Petroleum reservoir simulation”, *Elsevier applied science*.

Slough, K., Sudicky, E. and Forsyth, T. (1999), “Numerical simulation of multiphase flow and phase partitioning in discretely fractured media”, *Journal of Contaminant Hydrology*, **40**, 107-136.

Thorenz, C. (2001) “Model adaptative simulation of multiphase and density driven flow in fractured and porous media”, *Ph. D. Thesis, Universität Hannover*.

COUPLING THE HOLA WELLBORE SIMULATOR WITH TOUGH2

Ashish Bhat
Daniel Swenson
Shekhar Gosavi

Kansas State University
Mechanical and Nuclear Engineering Department
Manhattan, KS-66506, USA.
e-mail: ashish@ksu.edu

ABSTRACT

This paper describes a coupled model between the reservoir simulator TOUGH2 and wellbore simulator HOLA. The goal is to provide increased capability in TOUGH2 to better model flow in geothermal systems containing inclined wells with multiple feedzones. The model accounts for varying flowing bottomhole pressure and flow entering the wellbore from multiple feedzones at different depths, with the fluid in different thermodynamic states.

This approach facilitates a more accurate simulation of behavior of the geothermal reservoir being exploited. The standard TOUGH2 input data is extended to support the new capability. Some sample problems are solved using coupled simulator and compared with the results obtained from the current deliverability model in TOUGH2.

MOTIVATION

An Enhanced Geothermal System (EGS) is being exploited at the East Flank area of Coso Geothermal field, California. It is an ideal testing site with high rock temperatures at depths less than 10,000 ft and a high degree of fracturing and tectonic stresses. However, some of the wells within this portion of the reservoir are relatively impermeable and exhibit a significant drawdown. Characterization of the flow near the wellbore, becomes even more important in such settings.

Field data for the Coso wells also reveals the presence of two-phase flow and multiple feedzones. This leaves the standard coupled wellbore flow option in TOUGH2 unusable, since it is limited to wells with a single feedzone.

Previous authors have developed coupled well and reservoir models. Murray and Gunn (1993) presented coupling between the TETRAD reservoir simulator

and WELLSIM wellbore simulator. They generate a series of *wellbore tables* using WELLSIM, which are then used for interpolation by TETRAD.

Hadgu et al., (1995) describe a coupling of TOUGH2 and WFSA. The WFSA simulator is one of the three parts of the WELLSIM simulator package (Gunn and Freeston, 1991). However, discussion with the author indicated that development of this coupled package had stopped and that the software was not readily available.

This paper describes coupling of TOUGH2 specifically with the HOLA simulator. We plan to extend this to the GWELL, GWNACL and HOLA family of wellbore simulation models, to form a complete package. All source code is available publicly for use by others.

HOLA WELLBORE SIMULATOR

HOLA is a multi-feedzone geothermal wellbore simulator for pure water (modified after Bjornsson, 1987). It can handle both single phase and two phase flows in a well, with variable grid spacing and wellbore radii. GWELL(Aunzo,1990) and GWNACL are modified versions of HOLA, that can handle H₂O-CO₂ and H₂O-NaCl systems respectively. They were developed using FORTRAN language.

HOLA reproduces the measured pressure and temperature profile in a flowing well and determines thermodynamic properties of water, relative flow rates at each feedzone for a given discharge condition at the wellhead. It has two approaches (Option 1 and Option 2) for wellbore flow simulation. Option 1 needs known discharge condition at the wellhead (pressure, temperature and enthalpy), in addition to flow rates and enthalpies of all but the last feedzone. The simulator proceeds from wellhead-to-bottomhole to calculate the flowing temperature and pressure profile along the well. In Option 2, the user specifies the required flowing wellhead pressure and

bottomhole pressure and for each feedzone, the productivity indices and thermodynamic properties of reservoir fluid. The simulator then proceeds bottomhole-to-wellhead to calculate the expected wellhead output (wellhead enthalpy, flowrate, temperature and phase composition) for the required wellhead pressure.

Governing equations are represented by two sets of equations. Namely, *Between the feedzone* and *At the feedzone*. The important equations are given below.

Flow between feedzones

Between the feedzones the flow is represented by one-dimensional steady-state momentum, energy and mass flux balances.

Mass Balance

$$\frac{d\dot{m}}{dL} = 0 \quad (1)$$

Where \dot{m} = mass flow rate, L = length of pipe

Momentum Balance

The total pressure gradient is the sum of the friction gradient, acceleration gradient and potential gradient.

$$\frac{dP}{dL} - \left[\frac{dP}{dL} \right]_{fri} - \left[\frac{dP}{dL} \right]_{acc} - \left[\frac{dP}{dL} \right]_{pot} = 0 \quad (2)$$

Where,

$$\left[\frac{dP}{dL} \right]_{fri} = \phi_{Flow}^2 \left[\frac{dP}{dL} \right]_{LO} \quad (3)$$

$$\left[\frac{dP}{dL} \right]_{acc} = \frac{d(Gu_m)}{dL} \quad (4)$$

$$\left[\frac{dP}{dL} \right]_{pot} = p g \sin \theta \quad (5)$$

$\left[\frac{dP}{dL} \right]_{LO}$ is the pressure drop for a flowing single-

phase liquid and ϕ_{Flow}^2 is the two-phase multiplier.

G is the mass flux, u_m is average fluid velocity, θ is well deviation angle from horizontal.

Energy Balance

$$\frac{dE_t}{dL} \pm Q_t = 0 \quad (6)$$

The total energy flux gradient, $\frac{dE_t}{dL}$ is the sum of discharges in the heat content of the fluid, kinetic and potential energy. It is expressed as,

$$\frac{dE_t}{dL} = \dot{m} \frac{d}{dL} \left[h_m + 0.5u_m^2 + g(L - D) \right] \quad (7)$$

Where h_m is enthalpy of mixture, D is measured depth till the current grid-node.

An approximate solution for Q_t when we have the term, $\frac{\tau t}{r_w^2} \gg 1$ (Carslaw and Jaeger, 1959) is given as,

$$Q_t \approx 4\tau\pi(T_w - T_r) \left[\ln \left\{ \frac{4\tau t}{r_w^2} - 2\eta \right\} \right]^{-1} \quad (8)$$

Where, η is the Euler's constant ($= 0.577216\dots$), τ is rock thermal conductivity, t is time, τ is rock thermal diffusivity, T_w and T_r are temperatures in the well and reservoir respectively. Above equation does not take into account, transient changes in temperature and additional heat losses due to convection, when the well is flowing. However the heat loss term in equation (6) is very small compared to total energy flux term.

At the feedzone

At the feedzone, the mass and energy of inflow (or outflow) are given, and then mass and energy balance are performed, to continue further along the well. Here assumptions made are, instantaneous mixing occurs and it occurs at the wellbore pressure.

Mass Balance

$$\dot{m}_m = \dot{m}_w - \dot{m}_f \quad (9)$$

Subscripts m , w , f represent mixture, well, feedzone respectively.

Flow from the feedzone for Option 2 is calculated using Darcy's law as follows,

$$q = kA \left[\frac{k_{rl}\rho_l}{\mu_l} + \frac{k_{rv}\rho_v}{\mu_v} \right] \left[\frac{dP}{dr} \right] \quad (10)$$

where k is intrinsic permeability, k_{rl} and k_{rv} is relative permeability for water and vapor. μ is the viscosity.

Energy Balance

$$\dot{m}_m H_m = \dot{m}_w H_w - \dot{m}_f H_f \quad (11)$$

Where H is fluid enthalpy. Positive flowrate at the wellhead or a feedzone indicates production, while negative flowrate indicates injection. The mass flow in the well can have two possible directions, upward (producing) and downward (injecting). Also the flow for feedzone can be towards the well(producing) or towards reservoir (injecting). HOLA takes all such six combinations into consideration. It can be noted here that simulator WFSA assumes the fluid that enters the well from a feedzone, flows upward only.

Formulae for two-phase flow calculations are taken after Chisholm (1983). Gas and liquid phase velocities are needed in the evaluation of momentum flux and energy equations. They can only be obtained by empirical correlations. Two choices are provided to user, to calculate these velocities, namely Armand(1946) correlation and Orkiszewski(1983) correlation. Reader is referred to Aunzo et al. (1991) for further details on input-output format of HOLA and various correlations.

TOUGH2 SIMULATOR

TOUGH2 is a numerical simulator for non-isothermal flow of multi-component, multiphase fluids in one, two or three dimensional porous and fractured media (Pruess et al., 1999). It is a member of MULCOM family of codes, written in standard FORTRAN77 language and widely used in geothermal applications. Hence just a brief description of it is being given here with emphasis on sink/source feature.

Darcy's law is used to describe the single phase and two-phase flow. For the EOS1 water module, primary thermodynamic variables are pressure and temperature for a single phase flow, while pressure, temperature and phase saturation for two-phase flow. Various relative permeability functions and capillary pressure function, as a function of phase saturation are provided. TOUGH2 solves fluid motion by space discretization using the "Integral Finite Difference" Method (Edwards, 1972; Narasimhan and Witherspoon, 1976). Time is also discretized in a fully implicit manner as a first order backward finite difference. As a result, a set of strongly coupled non-linear algebraic equations are formed, which are rearranged in a residual form. These equations are then solved iteratively by Newton-Raphson method, with time-dependent primary thermodynamic variables of all grid blocks as unknowns to be determined by bringing residual within a specified error limit.

A well is represented as a sink/source. Sink/Source is specified directly as a grid block that acts as a region where injection or production of fluid mass and/or heat from the reservoir occurs. Various options are available for specifying the injection/production. One

of them is also a deliverability model for production wells to evaluate well-output based on a fixed specified bottomhole pressure and productivity index. The mass production rate with this option for phase β from a grid block with phase pressure $P_\beta > P_{wb}$ is,

$$q_\beta = \frac{k_{r\beta}}{\mu_\beta} \rho_\beta \cdot PI \cdot (P_\beta - P_{wb}) \quad (12)$$

Thus the total rate of production for mass component κ is,

$$\hat{q}^\kappa = \sum_\beta X_\beta^\kappa q_\beta \quad (13)$$

X_β^κ is the mass fraction of phase β of component κ . As opposed to HOLA, a negative flow rate in TOUGH2 indicates production and a positive flow means injection.

COUPLING OF HOLA WITH TOUGH2

Typically geothermal wells operate at almost a constant wellhead pressure. The well-output (flow rate and enthalpy at wellhead) varies with time, which means well bore pressure gradient and/or bottomhole pressure change with time. Thus it is more accurate to simulate a flowing wellbore against a variable bottomhole pressure. This exact approach is followed in our work, summarized as follows,

- i) A separate input file for each well in the reservoir is read in TOUGH2.
- ii) Unlike the current coupled wellbore flow option in TOUGH2 with 'F----' type of wells (in which interpolation into predetermined well-tables is performed), an explicit call is made to HOLA, at the start of each new timestep. It can be noted that HOLA has been converted into a subroutine in the coupled code.
- iii) Required reservoir parameters are supplied to HOLA as input. Choice of initial guess value for bottomhole pressure and pressure step for iteration is left to the user through the input file.
- iv) HOLA then iterates using 'option 2' to calculate flow rates and enthalpies at various feedzones and at the wellhead.
- v) A positive (negative) flow rate calculated at a feedzone in HOLA is supplied as a constant production(injection) rate to the corresponding source/sink element in TOUGH2, during regular timestep calculations of TOUGH2.
- vi) Enthalpies for the producing element are calculated inside TOUGH2. For injection, enthalpy is taken from by HOLA. This approach is comparable to the two basic options in TOUGH2 for specifying the source/sink, namely 'MASS' option and 'COM' option. 'MASS' option specifies constant mass production rate with enthalpies to be determined from conditions in producing block. While option 'COM'

represents mass injection at a constant rate with specified enthalpy.

- vii) Procedure from step (ii) to (vi) is then repeated for the next time-step with updated values of reservoir parameters. Now the initial guess for the bottomhole pressure is the converged value at the previous timestep.

Some of the features of the coupled code are,

- There is no change in the TOUGH2 input file. A coupled simulation with HOLA, is indicated in the GENER block of TOUGH2 input file. User specifies up to a five character long string name that starts with either 'H' or 'h', for each well. e.g. if a TYPE and ITAB record were specified as 'H349' and 'a', the program expects an input file with the name, 'H349a' present in the folder.
- Input file for each well, is in similar spirit of the standard HOLA input file for option 2.
- The user can also specify the wellhead pressure as time dependent data. Triple linear interpolation is then performed on this data and an average of wellhead pressure at the starting and ending time of current time-step is used for the calculation.
- User may not want to keep a well flowing through the complete time-span of a reservoir run. Hence shut-in and flowing option is provided to the user.
- With a proper choice pressure-step for iterations and a reasonable error limit on wellhead pressure, HOLA computes very fast, Hence comparatively there is not much compromise on computational time.

The coupling procedure was aimed to make minimal changes in TOUGH2 and HOLA. The TOUGH2 subroutines in which the changes were made are, INPUT, RFILE, CYCIT, QU and OUT. Mostly new code blocks were added rather than a change in the original code. The input file for HOLA is read in RFILE and care is taken to properly preserve the sink/source indices and total number of generation grid blocks. The call to HOLA is made in CYCIT before the iterations for TOUGH2 begin. One more case was added to sink/source subroutine, QU to handle the coupled simulation with HOLA. Appropriate terms for Newton-Raphson iterations are calculated here. A small block of code was added to OUT, to get a printed output of well flow-rates, enthalpies and bottomhole pressure.

The "Main" program of the original HOLA code is abandoned and a new subroutine HOLA() is written. Its purpose is same as the original main program, but there is no user interactive feature involved. Also some other new routines and functions are written. Here is their brief description,

- i) SUBROUTINE PrepHOLA(): gets the required reservoir parameter values from TOUGH2 and supplies them to HOLA.
- ii) SUBROUTINE TabPwh(): finds current wellhead pressure from time-dependent table data.
- iii) SUBROUTINE FindTime(): locates the current time in a tabular time data.
- iv) SUBROUTINE PwhInter(): calculates wellhead pressure at given time, by doing triple linear interpolation between the values for starting time and end time.

The hard-coded simulation parameters in HOLA were all brought at one place, so that they are accessible to user and could be changed as per problem size. Choice of a pressure step for bottomhole pressure iteration is left to the user's discretion. More study is required to improve the performance of HOLA (Hadgu and Bodvarsson, 1992). Some issues in HOLA that have been addressed are,

- i) In subroutine VINNA2, while calculating the mass flow rate for the last feedzone, an average of reservoir fluid parameters and wellbore fluid parameters such as density, saturation, viscosity was being taken. A scenario in which one fluid could be single phase and other two-phase was not handled, leading to erroneous results. As an alternative to that we followed a simpler approach of using only reservoir parameters when fluid is entering the well and for the case of injection we use only wellbore fluid parameters.
- ii) Some instances of un-initialized variables have been corrected.
- iii) For relative permeability calculations, HOLA follows a simple approach. They are assumed to vary linearly between 0 to 1 and are equal to the phase saturation. We extended the various relative permeability calculation options available in TOUGH2 to HOLA also. And then HOLA uses the same choice of calculation as chosen by user in TOUGH2 input file.
- iv) We encountered a case in which the reservoir pressure was same as iterative value of bottomhole pressure. It lead to a division by zero calculation putting the program into an infinite loop. This was taken care of.
- v) We are correcting a minor error regarding the way inclined wells are currently handled in HOLA.

SAMPLE PROBLEM

Sample problem number 5 from the TOUGH2 user's guide is chosen as an example. This problem was originally taken after Hadgu et al., 1995. In this example, a coupled simulation model is compared with the deliverability option in TOUGH2.

A well of inside diameter 0.2 m produces from a 500 m thick two-phase reservoir containing water at initial conditions of $P = 60$ bars, $T = T_{\text{sat}}(P) = 275.5$ °C, $S_g = 0.1$. Wellhead pressure is 7 bars and the feedzone depth is 1000 m. A 1-D radial grid was created by means of MESHMAKER input file provided in the TOUGH2 user's guide. The wellblock radius is 100 m and the grid extends to 10,000 m. The well productivity index is $4.64e-11$ m³. Simulation starts with a time-step of $1.e5$ seconds and ends at a time of $1.e9$ seconds (approx. 31.7 years)

First a run with coupled simulation is performed. Then 'H----' type in GENER block is replaced by DELV type so as to run the problem on deliverability model, with a fixed bottomhole pressure of 57.12 bar. This was the bottomhole pressure at the end of first timestep in the coupled simulation.

Results obtained are plotted as shown in Figure 1. In the figure, Q is flow rate and h is the flowing enthalpy. Both Q and h are plotted for the coupled simulation (HOLA) and the deliverability model (DELV). Pwb (HOLA) is the varying bottomhole pressure for coupled simulation.

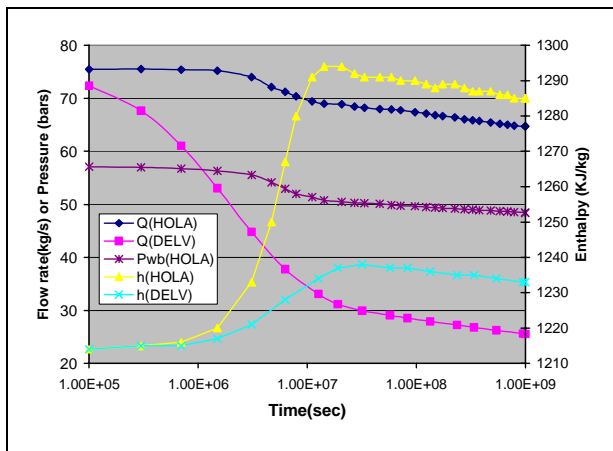


Figure 1 :Flow rate, enthalpy and bottomhole pressure plotted against a logarithmic time scale.

These trends match the results given in the TOUGH2 users manual. The deliverability model shows a rapidly declining production rate while the coupled reservoir-wellbore system shows a long term production at a much higher rate than a deliverability model. This certainly emphasizes the necessity of a coupled-reservoir model.

CONCLUSION

With the results obtained we believe that we should be able to predict more accurately the production at the Coso EGS site. Future plans involve a careful review of the HOLA source code and coupling of

GWELL and GWNACL simulators to form a complete package of coupled code.

ACKNOWLEDGEMENT

The authors appreciate discussions with Teklu Hadgu at Sandia National Laboratories and Karsten Pruess at LBNL. This work is supported by the U.S. Department of Energy, Assistant Secretary for Energy Efficiency and Renewable Energy, under DOE Financial Assistance Award DE-FC07-01ID14186.

REFERENCES

Au, A., "TETRAD User Manual", ADA International Consulting Inc., Calgary, Alberta, Canada, 1995.

Aunzo, Z. P., "GWELL: A Multi-Component Multi-Feedzone Geothermal Wellbore Simulator.", M.S. Thesis, University of California at Berkley, Berkley, CA, USA, May, 1990.

Aunzo, Z.P., Bjornsson, G., and Bodvarsson., G.S. , "Wellbore Models GWELL, GWNACL, and HOLA", Lawrence Berkeley National Laboratory Report LBL-31428, Berkeley, CA, October 1991.

Bjornsson, G., "A Multi-Feedzone, Geothermal Wellbore Simulator.", Earth Sciences Division, Lawrence Berkeley Laboratory Report LBL-23546, Berkeley, USA, 1987.

Carslaw, H. S., and Jaeger, J. C., "Conduction of Heat in Solids", 2nd ed., Oxford Univ. Press, London, 1959.

Edwards, A.L., "TRUMP: A Computer Program for Transient and Steady State Temperature Distributions in Multidimensional Systems", National Technical Information Service, National Bureau of Standards, Springfield, VA, 1972.

Gunn, C., and Freeston, D., "Applicability of Geothermal Inflow Performance and Quadratic Drawdown Relationships to Wellbore Output Curve Prediction", Geothermal Resources Council Transactions, Vol. 15, pp. 471-475, 1991.

Hadgu, T., Bodvarsson, G.S., "Supplement to wellbore models GWELL, GWNACL, and HOLA User's Guide," LBL report LBL-32907, 1992.

Hadgu, T., Zimmerman, R.W. , and Bodvarsson., G. S., "Coupled Reservoir-Wellbore Simulation of Geothermal Reservoir Behavior," *Geothermics*, 24(2), 145—166. LBL-36141, 1995.

Murray, L., and Gunn, C., "Toward Integrating Geothermal Reservoir and Wellbore Simulation:

TETRAD and WELLSIM”, Proceedings of the 15th New Zealand Geothermal Workshop, Geothermal Institute, The University of Auckland, Auckland, New Zealand, 1993.

Narasimhan, T.N., and Witherspoon, P.A., “An Integrated Finite Difference Method for Analyzing Fluid Flow in Porous Media”, *Water Resources Research*, Vol. 12(1), pp. 57-64, 1976.

Orkiszewski, J., “Predicting Two-Phase Pressure Drops in Vertical Pipe”, *J. Pet. Tech.*, pp. 829-838, 1967.

Pruess, K., Oldenburg, C., and Moridis, G., “TOUGH2 User's Guide, Version 2.0”, Lawrence Berkeley National Laboratory Report LBNL-43134, Berkeley, CA, November 1999.

MODELING THE VIABILITY OF UNDERGROUND COAL FIRES AS A HEAT SOURCE FOR ELECTRICAL POWER GENERATION

Andrew D. Chiasson¹ and Cenk Yavuzturk²

1. Geo-Heat Center, Oregon Institute of Technology, Klamath Falls, OR, 97601 USA
chiassoa@oit.edu

2. Dept. Civil & Architectural Engineering, University of Wyoming, Laramie, WY, 82071 USA
cyturk@uwyo.edu

ABSTRACT

The objective of this study is to examine the viability of extracting thermal energy produced from underground coal mine fires for electrical power generation. Underground coal mine fires present a high temperature heat source available at relatively shallow depths as compared to conventional geothermal resources. Several hundreds of burning underground coal mines are believed to exist worldwide. They may extend in plan area up to tens of square kilometers and are estimated to burn for up to tens of decades.

The performance of a closed-loop thermal energy extraction system, consisting of an array of vertical boreholes, is modeled using computer simulation. At various underground temperatures, a two-variable optimization scheme is used to determine minimum borehole depth and mass flow rate required to yield a fluid temperature of 100°C entering a theoretical binary-cycle power plant. Geologic and thermal data for the model are taken from field studies of an actual underground coal mine fire in Wyoming, USA. Life-cycle cost analyses are conducted to assess the feasibility of production of 100 kW_e to 1000 kW_e. Simulation results show that, under certain conditions, the concept is economically comparable to other alternative power generation technologies.

1. INTRODUCTION

This paper presents a concept for potentially extracting thermal energy from underground coal mine fires for electrical power generation. The concept originated from observations made at an underground coal mine fire near Sheridan, WY, USA (Figure 1), where a 25-m to 30-m deep coal seam was mined using the room-and-pillar method from the early 1900s to 1943. Subsequent subsidence pits and cracks are believed to have triggered combustion of the un-mined coal (Dunrud and Osterwald, 1980). Exploratory drilling and surface temperature

measurements revealed underground temperatures exceeding 500°C.

Underground coal fires in abandoned mines ignite primarily by spontaneous combustion when oxygen and water are introduced through subsidence cracks and unsealed shafts. Two of the more important factors causing heating and ignition appear to be coal rank and changes in moisture content (Dunrud and Osterwald, 1980). Most underground coal fires exhibit smoldering combustion and may only involve relatively small amounts of coal capable of burning in the presence of as little as 2% oxygen. Heat transfer to the surrounding rock occurs primarily by conduction and by convection within the collapsed zones.



Figure 1. Surface effects (steam and smoke) of an underground coal mine fire near Sheridan, Wyoming (Dunrud and Osterwald, 1980). Note tire tracks for scale.

There are currently about 600 underground coal mine fires throughout the United States (Drakon Energy, 2002). With poor success in extinguishing them, most fires are left to burn themselves out with a predicted combustion time of up to 80 years for some locations. Fires at shallow depths (to <150 m) may have

potential for thermal energy extraction for a variety of applications, particularly electricity production. A review of the literature yielded no publications reporting on electricity production from underground coal mine fires.

The objective of this research work has been to evaluate the concept of extracting thermal energy from underground coal mine fires for electrical power generation. This evaluation is made by means of a system simulation approach using TRNSYS (SEL, 2000). Life-cycle cost analyses are presented to assess the economic viability of electrical power production with a binary-cycle power plant.

2. METHODOLOGY

2.1. The Physical Model

A conceptual diagram of the physical system is shown in Figure 2. The physical parameters relevant to the modeling study were characterized as geologic, thermal, and system parameters.

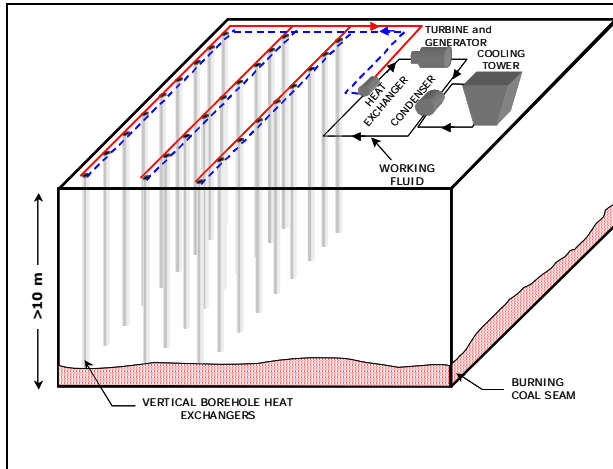


Figure 2. Conceptual diagram of the underground thermal energy extraction system and binary power plant.

The geologic parameters include soil and rock types and depth to the coal seam. The thermal parameters consist of thermal conductivity, volumetric heat capacity, and average temperature of the geologic materials. The system parameters consider the number, spacing, and depth of boreholes; heat transfer fluid properties and flow rate; and the borehole heat exchanger geometry (Figure 3). The system parameters must also account for the overall efficiency of the binary power plant in order to determine the electric power output.

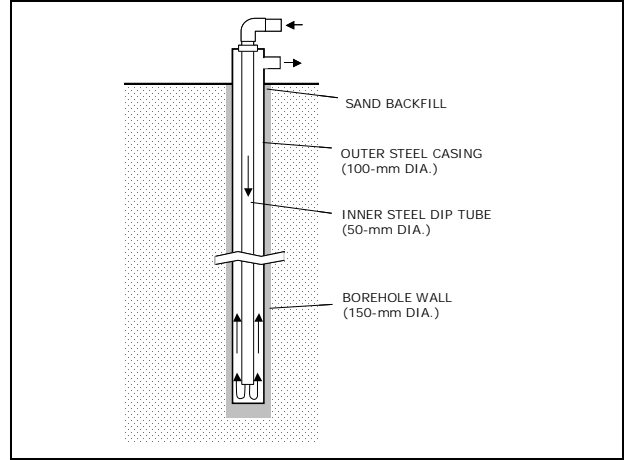


Figure 3. Conceptual diagram of a concentric-type borehole heat exchanger.

2.2. The Mathematical Model

The basis of the mathematical model for this study was the work of Yavuzturk and Spitler (1999), which is an extension of Eskilson (1987). A series of dimensionless, time-dependent temperature response factors known as g -functions have been developed from a transient finite difference model that approximates the time-dependent solution to the heat diffusion equation in and around the heat extraction borehole. The g -functions are fixed for prescribed borehole field geometry and borehole spacing/depth ratio. The g -function allows the calculation of the temperature change at the borehole wall in response to a step heat extraction pulse, which can be determined by summing the responses of the previous step functions:

$$T_{borehole} = T_{\infty} + \sum_{i=1}^n \frac{(q_i - q_{i-1})}{2\pi k} g\left(\frac{t_n - t_{i-1}}{t_s}, \frac{r_b}{H}\right) \quad (1)$$

where t is the time (s), t_s is a time scale (s) ($H^2/9\alpha$, where α is the thermal diffusivity of the rock (m^2/s)), r_b is the borehole radius (m), H is the borehole depth (m), k is the thermal conductivity (W/m-K), $T_{borehole}$ is the temperature at the borehole wall ($^{\circ}C$), T_{∞} is the average underground temperature, q is the step heat extraction pulse per length of bore (W/m), i denotes the time step, and g is the temperature response factor (g -function). The temperature of the heat transfer fluid exiting the borehole is calculated iteratively by an overall energy balance.

2.3. The Computer Model

The mathematical model has been implemented for use in TRNSYS (SEL, 2000), a component-based, transient system simulation environment. The

purpose was to allow the underground heat extraction model the versatility to be coupled to other component models such that larger system simulations could be conducted, such as a complex power plant with associated equipment.

The thermal performance of each TRNSYS component model is described by a FORTRAN subroutine. By a script language, components are linked together in a manner similar to piping and wiring in a physical system. Each component model is formulated on the concept of inputs, parameters, and outputs. Inputs are received by the model and may change with time. Parameters are fixed in the model and do not change with time. Outputs are calculated by the model and also change with time. The configuration of the underground heat extraction model is shown graphically in Figure 4.

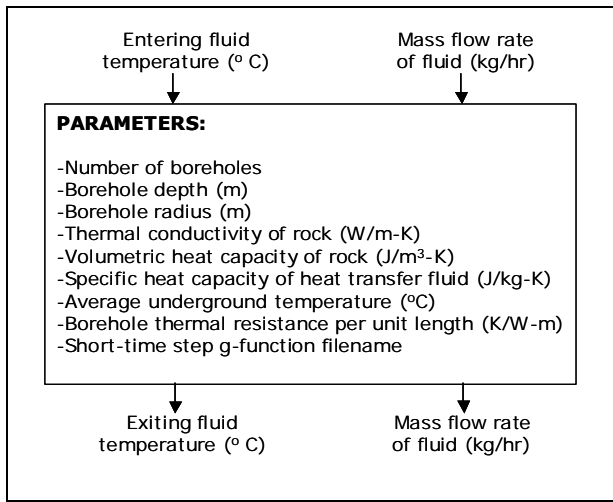


Figure 4. Underground heat extraction component model configuration for TRNSYS.

2.4. The Overall Modeling Approach

In a closed-loop system, many factors are interdependent, and it was therefore necessary to make some simplifying assumptions. The overall modeling approach consisted of optimizing borehole depth and mass flow rate through the borehole heat exchanger network to meet a fixed acceptable minimum entering fluid temperature to the power plant. This approach assumed a constant thermal extraction rate from the borehole network. One major simplifying assumption was that the average underground temperature remains constant throughout the simulated life.

GenOpt (LBNL, 2004), a generic optimization software package was coupled to TRNSYS to optimize the borehole depth and mass flow rate. The optimization scheme used was the simplex method of

Nelder and Mead (1965) with updates by O'Neill (1971). The minimization function was defined as:

$$|T_{\min} - T_{\text{desired}}| \times H^2 \times \dot{m} \quad (2)$$

where T_{\min} is the minimum temperature of the fluid exiting the boreholes (°C), T_{desired} is the desired minimum temperature exiting the boreholes (°C), H is the borehole depth (m), and \dot{m} is the total mass flow rate (kg/hr). Squaring the borehole depth gives a heavier weighting to this parameter. The desired minimum acceptable fluid temperature exiting the borehole network (i.e. the fluid temperature entering the power plant) was fixed at 100°C.

System simulations were conducted for various heat extraction rates ranging from 100 kW_t to 1000 kW_t. The simulated life cycle was 20 years. Based on field observations at the underground coal mine fire near Sheridan, WY, model parameters were as follows:

- borehole radius: 76 mm
- rock thermal conductivity: 2.1 W/(m-K)
- rock volumetric heat capacity: 2000 kJ/(K-m³)
- heat transfer fluid: water
- average underground temperature range: 160°C to 360°C

To estimate the actual electrical power output, it was necessary to estimate the net plant thermal conversion efficiency. The ideal theoretical efficiency (η_{ideal}) is given by:

$$\eta_{\text{ideal}} = 1 - \frac{T_L}{T_H} \quad (3)$$

where T_L is the absolute temperature of the condenser (K), T_H is the temperature of the fluid exiting the underground borehole heat exchanger network (K). The net efficiency of the binary power plant was taken as 50% of the ideal efficiency based on the work of Nichols (1986) and Entingh et al. (1994). The condenser temperature was assumed to be 30°C.

The foregoing system simulations assumed no borehole-to-borehole thermal interference. In order to investigate thermal interference between boreholes, the heat extraction model was used to simulate a 10 x 10 borehole matrix. The boreholes were assumed to be equally spaced in a square pattern. Model parameters were those described above with an average underground temperature of 260°C. The borehole spacing was successively increased, and an optimum borehole spacing was assumed to be approached when the incremental heat extraction rate became negligible.

2.5. Economic Analysis

A simple economic analysis was conducted by determining the levelized cost of electricity production for various plant capacities and underground temperatures. To examine the sensitivity to drilling costs, levelized costs were computed at drilling rates of \$50/m and \$75/m. Factors included in the simple economic model were capital costs, operating and maintenance costs, and plant capacity factor.

Capital and operating and maintenance (O&M) cost models were determined from curve-fits to data presented in DiPippo (1998). Capital cost (in U.S. dollars) of binary plants up to 1000 kW_e capacity is given by:

$$\text{Capital Cost} = 0.44x^2 + 2390x \quad (4)$$

and annual O&M costs are given by:

$$\text{Annual O \& M Cost} = 26.3x + 17717 \quad (5)$$

where x refers to the binary plant capacity in kW_e. The plant capacity factor is taken as 0.8 and an annual discount rate of 6% is assumed over the 20-year life cycle. The drilling costs are expressed in \$ per meter of vertical bore and include all materials and labor to install all vertical and horizontal transfer piping.

3. RESULTS AND DISCUSSION

3.1 System Simulations

The optimized borehole depths and mass flow rates at various average underground Earth temperatures are shown in Figure 5 that produced a minimum exiting fluid temperature of 100°C over a 20-year life-cycle. The borehole length is expressed in m per kW of thermal energy extracted. An example temperature profile versus time is shown in Figure 6 for an average underground temperature of 260°C. An example of the optimization results from GenOpt are shown for this same case in Figure 7. Note that for these results, borehole-to-borehole thermal interference was not considered.

A review of the data presented in Figure 6 reveals that the borehole length begins to increase exponentially below average underground temperatures of about 300°C. A review of Figures 6 and 7 shows that the optimization scheme proved to be quite reliable. The underground exiting fluid temperature does not approach the target of 100°C until about year 17, typical of a conduction heat transfer profile. At that temperature, the approximate

net binary plant efficiency is 10%, which is in agreement of values reported by Nichols (1986) and Entingh et al. (1994).

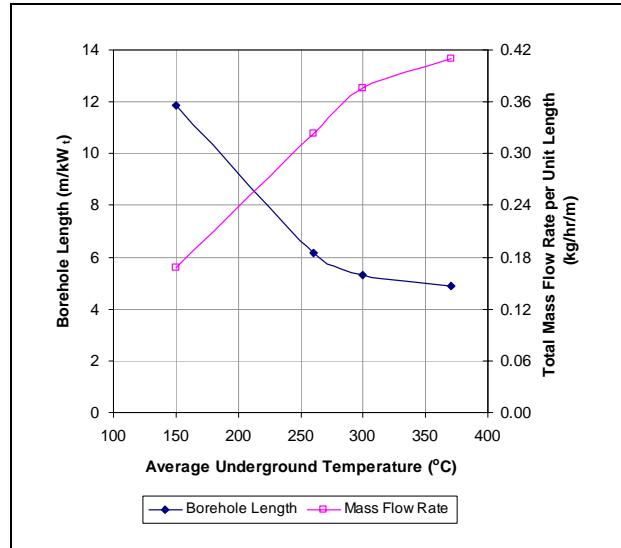


Figure 5. Optimized borehole lengths (per kW heat extracted) and mass flow rates at various average underground temperatures.

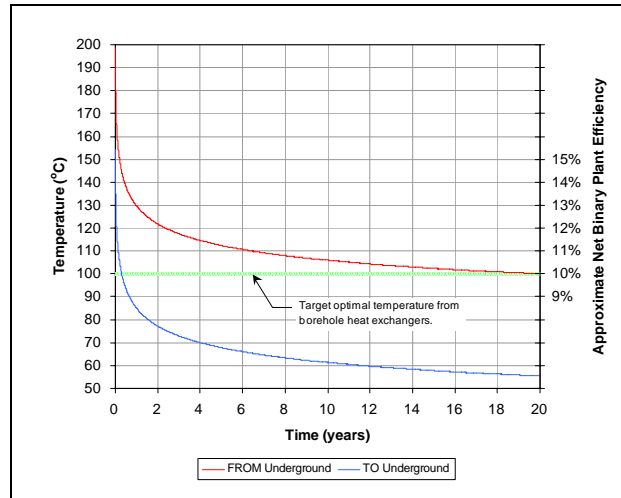


Figure 6. Example temperature profile of fluid exiting the underground thermal energy extraction system with an average underground temperature of 260°C.

Considering the net conversion efficiency of the binary plant, the number of boreholes of arbitrary depth can be determined to provide a desired electrical power output. Figure 8 shows the number of 100 m deep boreholes required to provide various quantities of electrical power at various underground temperatures.

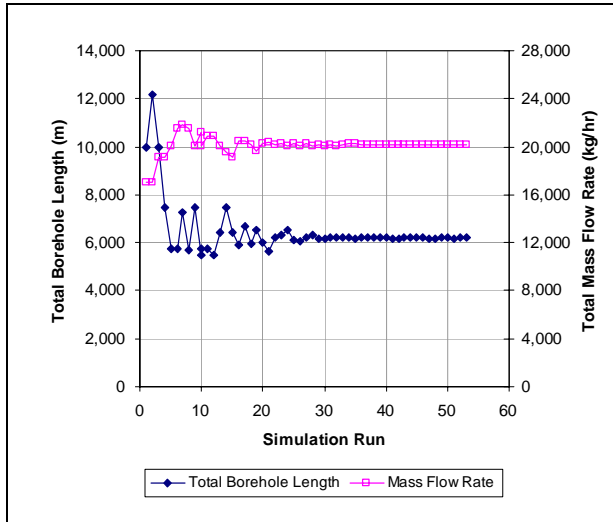


Figure 7. Optimization results for the case with a heat extraction rate of 1000 kW at an average underground temperature of 260°C.

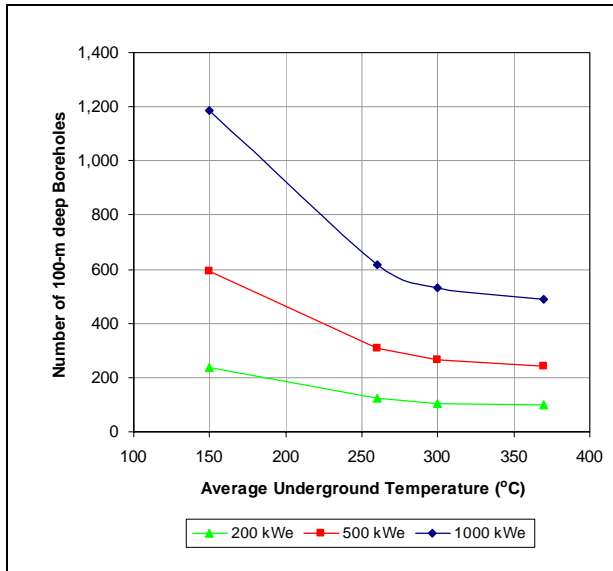


Figure 8. Number of 100-m deep boreholes required to produce various electrical power outputs at various average underground temperatures.

Results of the borehole interference simulations are shown in Figure 9. A review of Figure 9 shows that optimum borehole spacing is approached at about 50 m. These results indicate that a borehole spacing of progressively less than 50 m would result in increasing thermal interaction between boreholes, and therefore a progressively less than optimum quantity of thermal energy extraction. On the

contrary, borehole spacings larger than 75 m would result in less than optimum use of land.

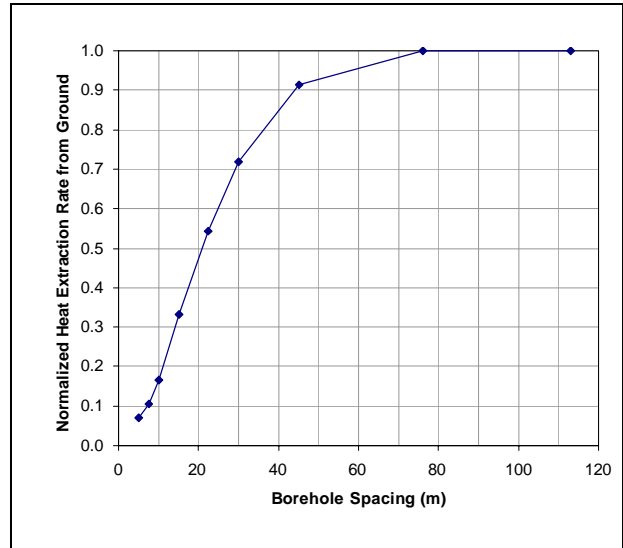


Figure 9. Normalized heat extraction rate versus borehole spacing.

Combining the results presented in Figures 8 and 9, the required land area for an underground thermal energy extraction system can be determined. Assuming a borehole spacing of 50 m, required land areas are shown in Figure 10. A review of this figure reveals that quite large expanses of land would be required to produce 1 MW of electrical power, particularly at average underground temperatures less than 300°C.

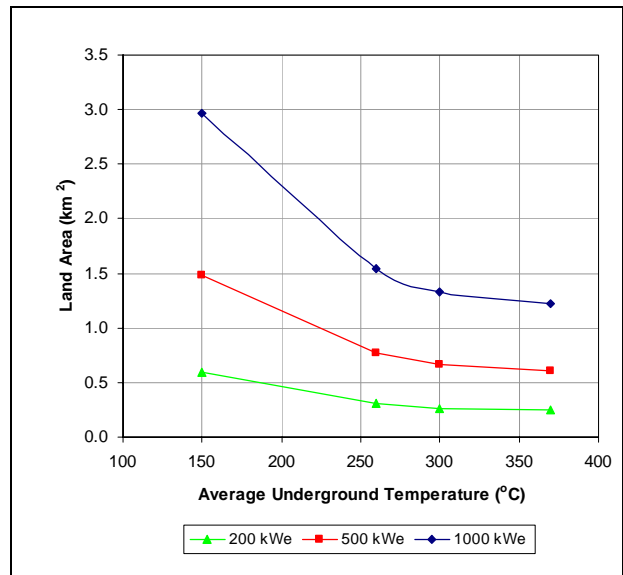


Figure 10. Land area (with 100-m deep boreholes) required to produce various electrical power outputs at various average underground temperatures.

3.2. Economic Analysis

The levelized cost of electricity production for various plant capacities and underground temperatures is shown in Figure 11. For comparison purposes, levelized costs of electricity production with other technologies are shown in Figure 12.

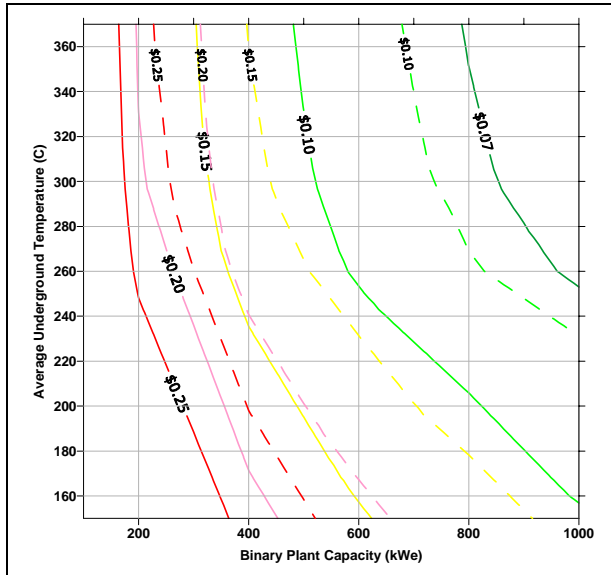


Figure 11. Levelized costs of electricity production at various binary plant capacities and average underground temperatures. Solid lines represent \$50/m and dashed lines represent \$75/m drilling cost.

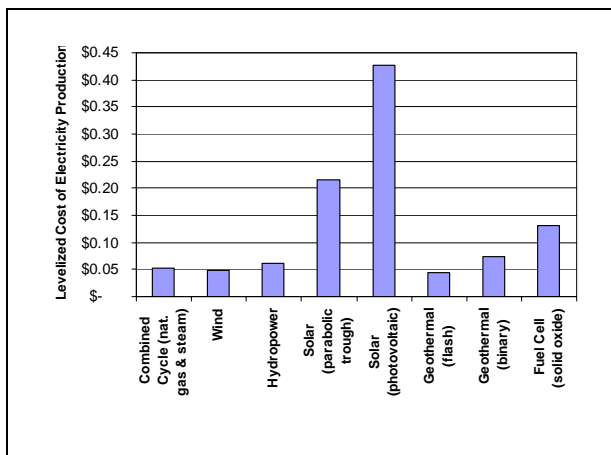


Figure 12. Levelized costs of electricity production for various alternative technologies (California Energy Commission, 2003).

A review of Figures 11 and 12 shows that the concept of extracting thermal energy from underground coal fires for electricity generation is comparable to other

alternative power generation technologies only under certain conditions. As with other geothermal technologies, the levelized cost of electricity generation is strongly dependent on the average underground temperature, drilling cost, and plant capacity. Economies of scale for larger capacity binary plants can be seen in Figure 11.

At relatively low underground temperatures (i.e. 160°C), larger-capacity plants appear more favorable, assuming adequate availability of land area for the underground extraction system. Drilling costs would need to be kept below \$50/m for this technology to be economically competitive at low underground temperatures. With increasing underground temperature, slightly smaller capacity plants appear favorable depending on the drilling rate.

4. CONCLUSIONS

This paper has presented a concept for potentially extracting thermal energy from underground coal mine fires for electrical power generation. The system consists of a closed-loop array of vertical boreholes with electricity being produced by a binary power plant. A system simulation approach was used to evaluate the viability of the concept.

Simulation results showed that in order to produce a minimum entering fluid temperature of 100°C to a binary power plant over a 20-year life cycle, required borehole depths per kW of electrical power output would need to range from 50 m/kW_e (at 360°C underground temperature) to 120 m/kW_e (at 150°C underground temperature). At 100°C entering water temperature, the binary plants considered in this study are about 10% net efficient. For minimum thermal interference between boreholes, the required spacing was found to exceed 50 m.

An economic analysis revealed the levelized cost of electricity to be strongly dependent on the average underground temperature, drilling cost, and plant capacity. Currently, the concept can be competitive to other alternative electric power generation technologies if drilling rates are kept below \$50/m and/or the average underground temperature is relatively high.

This study represents a first step in evaluating the concept of electricity generation from underground coal fires, and further work is necessary to fully evaluate its viability. In particular, assumptions were made regarding the spatial and temporal uniformity of the underground temperature. In reality, this would not be the case, and little work has been done to date to estimate the life-cycle of a coal fire and its evolution with time. Further, it would be desirable to develop remote-sensing and other field techniques to explore and track these fires.

ACKNOWLEDGEMENTS

The authors would like to acknowledge funding for this project from National Science Foundation (NSF) as well as contributions from Drakon Energy and Peter Kiewit and Son's Co.

REFERENCES

California Energy Commission (2003). “*Comparative Cost of California Central Station Electricity Generation Technologies*”, Publication # 100-03-001.

DiPippo, R. (1998). “Geothermal Power Systems”, In *Standard Handbook of Power Plant Engineering*, 2nd Ed., pp. 8.27-8.60, McGraw-Hill, Inc., New York.

Drakon Energy (2002). Personal communication.

Dunrud, C.R. and Osterwald, F.W. (1980). *Effects of Coal Mine Subsidence in the Sheridan, Wyoming, Area*. Geological Survey Professional Paper 1164, United States Department of the Interior, U.S. Government Printing Office, Washington, D.C.

Entingh, D.J., Easwaran, E., and McLarty, L. (1994). “Small Geothermal Electric Systems for Remote Power”, *Geothermal Resources Council Bulletin*, Vol. 23, No. 10. pp. 331-338.

Eskilson, P. (1987). *Thermal Analysis of Heat Extraction Boreholes*. Doctoral Thesis, University of Lund, Department of Mathematical Physics, Lund, Sweden.

Lawrence Berkeley National Laboratory (LBNL) (2004). *GenOpt 2.0, Generic Optimization Program, Version 2.0*. Simulation Research Group, Building Technologies Department, Environmental Energy Technologies Division, Lawrence Berkeley National Laboratory.

Nelder, J.A. and Mead, R. (1965). “A Simplex Method for Function Minimization”, *Computer Journal*, Vol. 7, No. 4, pp. 308-313.

Nichols, K.E. (1986). “Wellhead Power Plants an Operating Experience at Wendel Hot Springs”, *Geothermal Resources Council Transactions*, Vol. 10, pp. 341-346.

O'Neill, R. (1971). “Function Minimization Using a Simplex Algorithm”, *Journal of Applied Statistics*, Vol. 20, No. 3, pp. 338-345.

SEL, (2000). *TRNSYS Reference Manual, a Transient Simulation Program*, Version 15, Solar Engineering Laboratory, University of Wisconsin-Madison.

Yavuzturk, C. and Spitler, J.D. (1999). “A Short-Time Step Response Factor Model for Vertical Ground Loop Heat Exchangers”, *ASHRAE Transactions*, Vol. 105(2), pp. 475-485.

CRACK PROPAGATION UNDER THERMAL INFLUENCE OF A WELLBORE

A. Dobroskok and A. Ghassemi

University of North Dakota
P.O. Box 8358
Grand Forks, NS, 58203, USA
e-mail: ahmadghassemi@mail.und.nodak.edu

ABSTRACT

The paper presents a numerical investigation of processes of fracture propagation and accumulation of shear displacements on joint surfaces in the vicinity of a wellbore under a thermoelastic load. Results indicate that under suitable in-situ stress regimes, thermal stimulation can lead to significant fracture propagation. Investigation of the behavior of a pre-existing natural fracture indicates that thermal influence of a wellbore is sufficient to cause fracture instability for fractures in a critical state.

INTRODUCTION

In-situ stress, pore pressure and temperature variations as well as dissolution/precipitation reactions are some of the major factors responsible for the behavior of discontinuities in the reservoir. The influences of coupled thermal and poroelastic (e.g., McTigue, 1990; Li et al., 1998) processes on fracture opening has been addressed previously (Ghassemi and Zhang, 2004a; Hayashi and Okitsuka, 2004). It has been shown that poroelastic and thermally induced stresses can contribute to fracture width change and permeability variation. These effects are of particular implication and interest in geothermal systems. Classical stress analysis indicates that large thermally-induced thermal stresses occur around a cooled geothermal well giving rise to tensile cracking and fracture initiation (Ghassemi and Zhang, 2004b). It has also been shown that cooling of a rock due to injection of a fluid strongly influences in-situ stress state in the vicinity of the injection zone and around the wellbore and can affect stability of discontinuities by fracture propagation or fault slip. As a result, thermal stimulation has been suggested as a means of enhancing reservoir permeability. The plausibility and the conditions for success of such approach are numerically investigated by considering the influence of cooling of the wellbore on fracture propagation with particular reference to the reservoir rock and temperature conditions of the Coso geothermal field.

Both tensile and shear fracture propagation is considered.

METHOD OF ANALYSIS

In order to study the behavior of a discontinuity (e.g. fracture, fault) in the vicinity of a cooled wellbore it is suggested that stress field is represented by a superposition of elastic component influenced by the wellbore and its pressure plus the far field stress, and the thermal component induced by the transient process of rock cooling. Then, the combination of a complex variable boundary integral equation (CV BIE) of elasticity theory (Linkov, 2002) and analytical solution for an infinite medium with a cooled circular opening are employed. In such a combination, thermally induced normal σ_n^{therm} and tangential σ_τ^{therm} components of traction vectors on cracks surfaces and opening wall are given by the analytical solution. These tractions should be accounted for while formulating boundary value problem of elasticity

$$\sigma_n = \sigma_n^p - \sigma_n^{therm}, \quad \sigma_\tau = \sigma_\tau^p - \sigma_\tau^{therm},$$

where σ_n^p , σ_τ^p are prescribed values on surfaces (e.g. zero tractions for a traction free contact) and σ_n^p , σ_τ^p are the values used as BC for elasticity BIE solved by CV boundary element method (BEM).

The superposition of the mechanical and thermal load must be taken into account within the solid rock, on cracks surfaces, and on a borehole wall. It is supposed then, that existence of cracks does not perturb the temperature field (e.g. cracks are small enough, closed, or filled by fluid with the same temperature; or that the temperature front does not reach the cracks). Also, it is assumed that the cool fluid does not enter the crack. For cracks emanating from a wellbore this may correspond to the case of fast pressurization rate or the presence of a filter-cake at the wellbore wall. If the fluid enters the crack surfaces, then it would be necessary to account for cooling of the crack and the fluid pressure. These

cases should be treated by employing more advanced BEM techniques. However, the results of the suggested analysis may be quite representative for the considered problems.

NUMERICAL RESULTS

First, consider the isothermal problem of a wellbore with multiple micro-cracks emanating from it (the crack length is equal to $0.1R$). The crack inclination angles are randomly distributed. The rock is subjected to in-situ stresses and a wellbore pressure. The following values of elastic constants and stresses were used: $E = 65\text{GPa}$, $\nu = 0.185$, $S_H = 46.1\text{MPa}$, $S_h = 36.9\text{MPa}$, well pressure $P_w = 23.2\text{MPa}$. An example of the considered initial configuration is shown in Figure 1. Assuming symmetry, a quarter of the problem domain is modeled. Our calculations show that under the chosen conditions very few cracks will propagate into the rock mass. Cracks with angles $\varphi < -60^\circ$ and $\varphi > 60^\circ$ tend to coalesce with the borehole wall. This implies that such cracks are unlikely to propagate. It can be suggested that these cracks may lead to the separation of thin shells (chips) from the borehole wall. Cracks with $\theta > 60^\circ$ show the tendency to propagate in shear towards the y -axis. The cracks located at angles $60^\circ < \theta < 75^\circ$ often make one or two propagation increments in the tensile mode before changing to shear propagation towards the y -axis. This behavior may be interpreted as a part of the process of *breakout formation*.

The cracks not included in the above categories ($\theta < 60^\circ$, $-60^\circ < \varphi < 60^\circ$) tend to coalesce with the neighboring cracks, stabilize, or deviate in tensile mode along the borehole wall (an example of cracks propagation is shown in Figure 2). These cracks never tend to propagate far from the wellbore. It may be proposed that natural fractures in the rock mass, neglected in the numerical model, may strongly influence propagation of the micro-cracks by increasing the crack propagation driving force or by shielding.

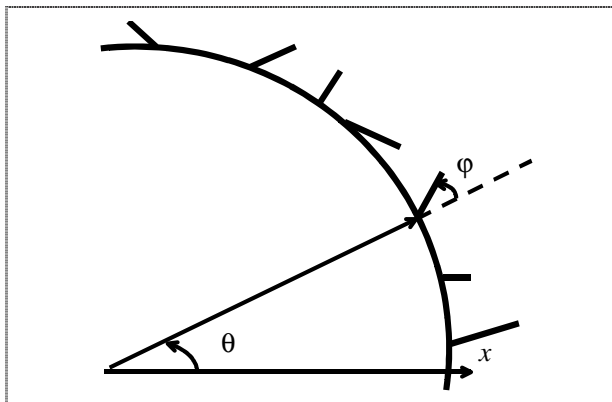


Figure 1. An example of initial configuration of drilling induced cracks

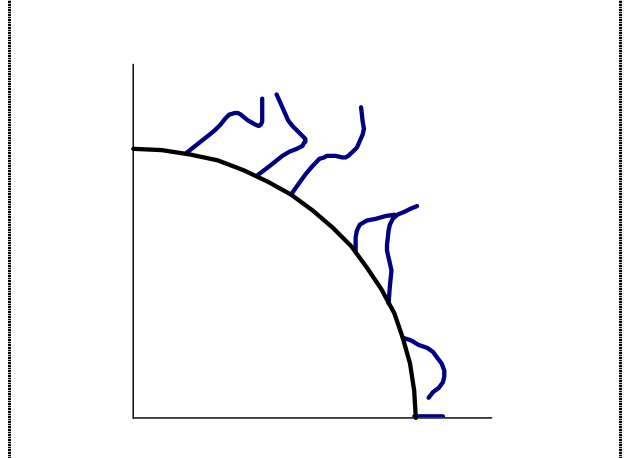


Figure 2. An example of propagation of drilling induced cracks obtained numerically

Special attention was given to a crack aligned with the maximum principal stress ($\theta = \varphi = 0^\circ$). In most experiments for the chosen loading, the crack did not propagate at all. In some experiments, it deviated in shear towards the neighboring cracks or advanced one increment in tensile mode along the x -axis and then stabilized.

For natural fractures in a solid rock, simulations show that fractures with the inclination in the range of $0 - 75$ degrees with the maximum principal stress tend to propagate in the tensile mode in the direction of maximum compression. Thus, fractures in the following experiments were modeled using straight cracks aligned with maximum compressive stress.

THE INFLUENCE OF TEMPERATURE

The next step in the investigation consists of taking into account the influence of a transient temperature and well pressure. In doing so, we focus on the influence of cooling of the wellbore and assume that all cracks are without fluid penetration.

Let us consider a crack in the vicinity of a wellbore shown by the solid line in Figure 3. The following values of parameters were used in the study: Young's modulus $E = 65\text{GPa}$, Poisson ratio $\nu = 0.185$, thermal expansion coefficient $\alpha = 2.4 \cdot 10^{-6} K^{-1}$, thermal diffusivity $c = 5.1 \cdot 10^{-6} m^2/sec$, fracture toughness

$$K_{Ic} = 1\text{MPa}/\sqrt{m}, S_H = 46.05\text{MPa}, \text{well}$$

$$\text{pressure } P_w = 23.2\text{MPa}, R = 10\text{cm}, L/R = 3, l/R = 1, \Delta T = 200\text{K}.$$

In our numerical experiments, cooling of a well caused only tensile propagation. Calculations show that for considered configuration cooling causes crack propagation only in cases of sufficiently small minimum in-situ stress. The diagram presented in Figure 4 illustrates the influence of the minimum in-

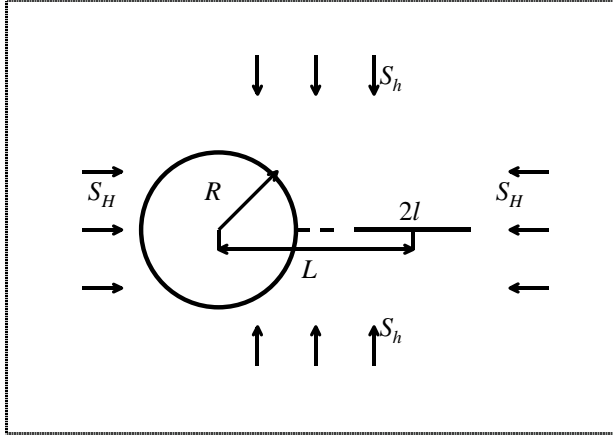


Figure 3. Crack aligned with the maximum compression in the vicinity of a well bore

situ stress on crack growth in time. Triangles show times of cooling at which crack starts to propagate for different ratios S_h/S_H . The higher the lateral pressure the longer time is needed to initiate propagation from initial tip of the crack. It can be seen that for $S_h/S_H > 0.32$, cooling only the wellbore does not contribute to crack propagation. Even after temperature reaches a steady-state, cracks do not propagate. For values of $S_h/S_H < 0.17$, propagation of cracks involves a stage of unstable growth. Time at which crack stabilizes is shown by circles. Calculations reveal that if propagation involves period of unstable growth cracks are capable of increasing their lengths up to tens of times; while for $S_h/S_H > 0.23$ they propagate only a few increments. Time of cooling at which propagation stops also varies for different ratios S_h/S_H . Squares in Figure 4 illustrate the corresponding dependence.

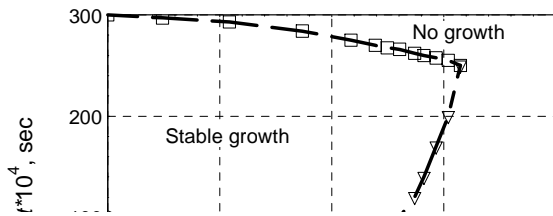


Figure 4. Influence of time and ration of lateral to axial compression on crack propagation.

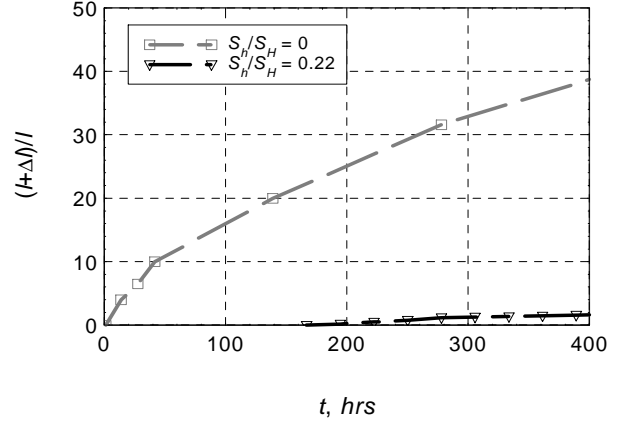


Figure 5. Crack growth in time for $S_h/S_H = 0$ (squares) and $S_h/S_H = 0.22$ (diamonds)

It should be noted that the crack shown by a solid line in Figure 3 propagates from both tips, and for sufficiently small lateral pressure S_h , crack growth involves coalescence with the borehole wall. In this case, the governing process influencing crack propagation can change to fluid pressure, currently neglected in the model. Figure 5 illustrates crack propagation in time for two values of $S_h/S_H = 0$ (squares) and $S_h/S_H = 0.239$ (diamonds). Calculations for a drilling induced crack aligned with the maximum compressive stress (dashed line in Figure 3) show that such cracks propagate even for hydrostatic far field load $S_h/S_H = 1$ (under an applied ΔT of 200). This is in contrast to the behavior of cracks within the solid rock, and could be explained by the strong influence of cooling-induced tensile stress on the borehole wall. However, under hydrostatic pressure and cooling the crack does not propagate for a long distance and tends to deviate

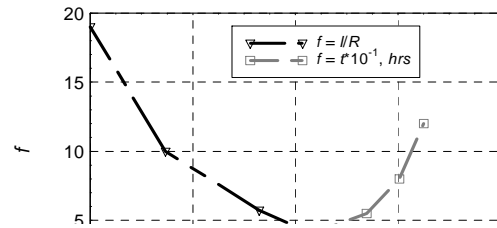


Figure 6. Dependence of the final crack length (diamonds) and starting time of propagation upon the ratio of the least to maximum horizontal stress S_h/S_H .

from its original straight trajectory. When the external load is not hydrostatic, crack propagates along the maximum principal stress.

Diagram in Figure 6 shows the dependence of the final length of a pre-existing or drilling-induced crack (triangles) and the cooling time required to initiate propagation (squares) for various ratios of the least to maximum horizontal stress S_h/S_H . It can be seen that the greater the ratio, the longer the wellbore cooling time needed to initiate fracture propagation.

THE INFLUENCE OF COOLING OF THE WELL ON FRACTURE SLIP

Special numerical procedure (Dobroskok et. al., 2001) was used to trace the accumulation of deformation on the contact of a fracture intersecting a wellbore. It was supposed that irreversible deformation starts when the elastic potential (that is negative for elastic deformation) defined as:

$$\varphi = \text{sign } \sigma_\tau \cdot \sigma_\tau - \text{tg } \rho_c \cdot (-\sigma_n) - c_c = 0$$

becomes equal to zero. Herein φ is the elastic potential, σ_n , σ_τ are the normal and tangential components of traction, ρ_c is the friction angle and c_c is the cohesion. When the potential reaches zero the law of interaction on the contact changes from elastic

$$\mathbf{B}^c = \begin{pmatrix} 1/E_n & 0 \\ 0 & 1/E_\tau \end{pmatrix},$$

to inelastic one:

$$\mathbf{B}^c = \begin{pmatrix} 1/E_n & 0 \\ 0 & 1/E_\tau \end{pmatrix} + \frac{1}{H_c} \begin{pmatrix} \text{tg}^2 \rho_c & \text{sign } \sigma_\tau \text{tg } \rho \\ \text{sign } \sigma_\tau \text{tg } \rho & 1 \end{pmatrix},$$

where \mathbf{B}^c is the matrix of contact compliance; E_n , E_τ are normal and shear rigidity of the contact; and H_c is the parameter characterizing softening.

The geometry used in study of influence of cooling on slip on pre-existing closed fracture is shown in Figure 7. The properties of the rock are taken the same as in the previous example, the applied load is $S_H = 46.1\text{MPa}$, $S_h = 36.9\text{MPa}$, and well the pressure is $P_w = 23.2\text{MPa}$. The properties of the contact are as follows: normal and shear rigidities are $E_n = 0.1\text{MPa}$ and $E_\tau = 0.05\text{MPa}$, coefficient characterizing softening is $H_c = -0.01\text{MPa}$, cohesion is $c_c = 0$, and friction coefficient is $\mu = 0.7$ (corresponding to a joint friction angle of

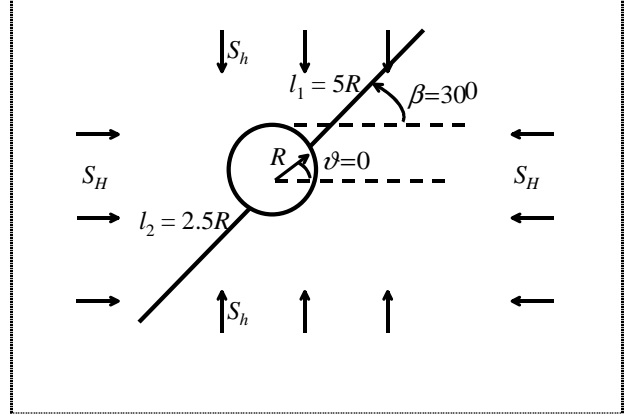


Figure 7. A wellbore and a pre-existing fracture

$\rho = 35$ degrees). Irreversible deformations were traced using incremental procedure with time step equal to 100 sec.

The graph in the Figure 8 illustrates the changes in the total shear DD on the fracture contact due to transient cooling of the wellbore. Herein squares illustrate the slip without the influence of temperature, while triangles show slip after 60 sec of cooling. Although, the difference is not significant (about 4%) in magnitude, in the considered case it is sufficient to start the process of irreversible deformations on the contact. Once softening has started, deformation on the contact increases with decreasing external load.

With time, the cooling front spreads and a zone of unloading forms along the fracture in the vicinity of the wellbore, while the remaining part of the fracture continues to accumulate irreversible deformations. The edge of unloading zone remains behind cooling front. Evidently, the joint deformation decreases in the zone of unloading. The zone of unloading grows in time, and at about $t = 27$ hours the entire fracture starts to unload. At that time ($t = 27$ hours) the maximum slip under external load and cooling on the

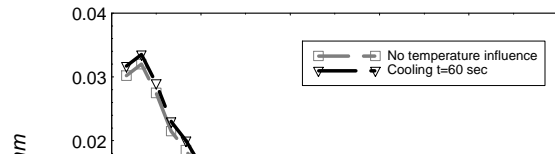


Figure 8. Slip along a fracture influenced by cooling of a wellbore

fracture reaches about 0.015 mm and unloading leads to a maximum decrease of shear displacements of 0.004mm.

For a longer (about 10 meters) joint in a critical state calculations showed the similar dependencies. The total amount of cooling induced slip is of the same order as for a joint discussed above.

It should be noted that a decrease in the normal stress and slip entails opening of a part of the fracture in the vicinity of a wellbore making fracture accessible to fluid. Then, at least a part of the fracture becomes lubricated which allows a larger slip and consequently greater opening. This implies that the initial weak influence of cooling can entail sufficient changes in the state of the fracture and its permeability. To study corresponding process more complicated numerical model will be used.

CONCLUSIONS

Summarizing the results of the current investigation, it can be concluded that:

- Cooling of a borehole alone causes changes in geometry of preexisting fractures only for relatively low ratios of in-situ stress, $S_h/S_H < 0.32$
- For ratios of $S_h/S_H < 0.17$, crack propagation involve a stage of unstable growth. Then, crack may increase its length up to tens of times
- Cooling of a borehole can lead to propagation of a crack emanating from a wellbore (e.g., a drilling induced crack) even for a hydrostatic far field load. The higher the S_h/S_H ratio, the longer the time necessary to initiate fracture propagation from a drilling induced crack aligned with the maximum principal stress
- Cooling of the wellbore influences the amount of slip on a preexisting fracture intersecting the well. For a softening fracture in the critical state of stress, cooling induces initial slip which leads to accumulation of irreversible deformation on the fracture. Finally decrease in normal stress and fracture entails opening of the fracture in the vicinity of a wellbore making it accessible to fluid

ACKNOWLEDGEMENTS

The financial support of the U.S. DOD (N-68936-02-C-0214) is gratefully acknowledged. The original model was developed with financial support from DOE (DE-FG07-99ID13855).

REFERENCES

- Dobroskok, A. A., Linkov, A. M., Myer, L., Roegiers, J-C. (2001). On a new approach in micromechanics of solids and rocks. *Mechanics in the National Interest. Proc. of the 38th US Rock Mechanics Symposium*. eds. Tinucci & Heasley, Swets & Zeitlinger Lisse. 1185-1190.
- Ghassemi, A. and Zhang, Q. (2004a), A transient fictitious stress boundary element method for porothermoelastic media. *Eng. Analysis with Boundary Elements*, **28**, 11, 1363-1373.
- Ghassemi, A. and Zhang, Q. (2004b). Porothermoelastic Mechanisms in Wellbore Stability & Reservoir Stimulation. *29th Stanford Geothermal Workshop*, Stanford, 2004.
- Hayashi, K., Okitsuka, R.. (2004), Hydraulic characterization of the fractured heat exchange region in the subsurface system for extracting energy directly from magma. *Geothermal Resources Council Transactions*, **28**, 289-293.
- Li, X., Cui, L, Roegiers, J-C. (1998), Thermoporoelastic modeling of wellbore stability in non-hydrostatic stress field. *Int. J. of Rock Mech. & Min. Sci.*, **35** (4/5): Paper No. 063.
- Linkov, A.M. (2002). *Boundary Integral Equations in Elasticity Theory*. Dordrecht-Boston-London, Kluwer Academic Publishers.
- McTigue, D.F. (1990), Flow to a heated borehole in porous, thermoelastic rock: analysis, *Water Resour Res.*, **26**, 8, 1763–1774.

LATTICE BOLTZMANN SIMULATION OF FLUID FLOW IN SYNTHETIC FRACTURES

Erdinc Eker and Serhat Akin

Middle East Technical University
Department of Petroleum and Natural Gas Engineering
Ankara, 06531 TURKEY
e-mail:serhat@metu.edu.tr

ABSTRACT

Fractures play an important role in geothermal reservoir engineering as they dominate the fluid flow in the reservoir. Because of this reason determination of fracture permeability is very important to predict the performance of the geothermal reservoir. A fracture is usually assumed as a set of smooth parallel plates separated by a constant width. The absolute permeability of a smooth-walled fracture is related to the fracture aperture using the cubic law. However, the flow characteristics of an actual fracture surface would be quite different, affected by tortuosity and surface roughness. Though several researchers have discussed the effect of friction on flow, a unified methodology for studying flow on a rough fracture surface has not emerged. As experimental methods are expensive and time consuming most of the time numerical methods are used. In this work, we present results of the numerical computations for single phase flow simulations through two-dimensional synthetically created fracture apertures. These synthetic rock fractures are created using different fractal dimensions, anisotropy factors, and mismatch lengths that are obtained from the producing geothermal reservoirs in South Western Turkey. Lattice Boltzmann Method, which is a new computational approach suitable to simulate fluid flow especially in complex geometries, was then used to determine the permeability for different fractures. Regions of high velocity and low velocity flow were identified. The resulting permeability values were less than the ones obtained with the cubic law estimates. It has been found that as the mean aperture-fractal dimension ratio increased permeability increased. Moreover as the anisotropy factor increased permeability decreased with a second order polynomial relationship.

1 INTRODUCTION

The problem of modeling and simulating fluid flow in porous media always remained as the major research subject in reservoir engineering. Petrophysical properties of the reservoir rocks must be realistic and accurate for reservoir simulation works. One of the most important properties of the reservoir rock is the permeability, which is defined as the measure of the capacity of the medium to transmit fluids (Amyx, *et al*, 1960). The ability of a fracture to conduct a fluid when the saturation of that fluid is 100 percent of the space is known as the absolute permeability of that fracture to that fluid. The effective permeability of the fracture to the fluid is the permeability when the fluid has a saturation of less than a 100 percent. Researchers beginning with Lomize (1951), Snow (1965), Louis (1969), Bear (1972), Witherspoon *et al* (1980) and Golf-Racht (1982) studied the permeability of single-phase flow in fractures extensively. They have all shown that for steady state, isothermal, laminar flow between parallel glass plates the absolute permeability is a function of fracture spacing, b , and is given by the following equation:

$$k_{abs} = \frac{b^2}{12} \quad (1)$$

But as this equation does not represent the surface roughness of the real fractures a modification should be performed to consider the effect of surface roughness to the fracture permeability (Witherspoon *et al*, 1980):

$$k_{abs} = \frac{b^2}{(12f)} \quad (2)$$

Where f is defined as the surface roughness factor.

Accurate representation of fracture permeability is still a challenging research topic in reservoir engineering. In order to tackle this problem the use of lattice Boltzmann method is proposed (McNamara and Zanetti, 1988). In this work, by using the lattice Boltzmann method two dimensional fluid flows in synthetically created realistic fractures were simulated. Fracture fractal dimensions of some geothermal fields located in Turkey were used to create synthetic fractures using a fractal approach. The results were compared with the aforementioned empirical equations. The paper is organized as follows: in Section 2 the theory of synthetic fracture generation and lattice Boltzmann method is introduced. In Section 3 the process of synthetic fracture generation and the usage of these fractures in lattice Boltzmann simulation are described. Section 4 presents the results of the lattice Boltzmann simulation and comparison with other techniques. Finally, in Section 5 the main conclusions of this study are outlined.

2 BACKGROUND

In this section, theory of the lattice Boltzmann method is presented and compared with other numerical simulation techniques. Then, the concept of synthetic fractures and their reliability for defining the real fractures are described.

2.1 Lattice Boltzmann Method

Before giving the details of the method Cellular Automata theory will be given as it is the basis for lattice Boltzmann method.

Cellular automata theory

Cellular Automata (CA) are discrete dynamical systems whose behavior is completely specified in terms of local relations. They are mathematical models for complex natural systems containing large numbers of simple identical components with local interactions (Wolfram, 1984). Cellular Automata can be characterized as follows (Wolf-Gladrow, 2000):

- CA is regular arrangements of single cells of the same kind.
- Each cell holds a finite number of discrete states.
- The states are updated simultaneously at discrete time levels.
- The update rules are deterministic and uniform in space and time.
- The rules for the evolution of a cell depend only on a local neighborhood of cells around it.

CA is valuable because of its capability to display complex behavior by using the simple update rules. This property makes CA a strong candidate for the simulation tool for the physical phenomena like fluid flow. As it is stated in Ilachinski (2001) the most successful practical application of CA as *computing* devices is in the field of fluid mechanics. Despite still being in their infancy, CA models of fluid dynamics have already demonstrated that they can reproduce many of the essential features of thermodynamical and hydrodynamical behavior. This capability of CA is proved by Frisch *et al* (1986). They stated that a simple CA obeying nothing but conservation laws at microscopic level was able to reproduce the complexity of real fluid flows and named it as “Lattice Gas Automata (LGA)”.

Lattice gas automata belong to a special class of CA designed to study various physical systems. Lattice Boltzmann method (LBM), which is used in our work, was developed by McNamara and Zanetti (1988) in response to the drawbacks of the lattice gas automata method. The main difference between two methods is that LBM describes the particle density as a continuous function instead of a Boolean variable. Moreover, LBM reduces the statistical noise produced by the Boolean arithmetic of the lattice gas automata.

Principles of the Lattice Boltzmann method

LBM as all other CA based methods that simulate natural phenomena like fluid flow uses an approach that is different from the conventional methods. This approach is named as “*bottom-up*” approach and is totally different from the techniques such as the “finite-element” and “finite-difference” methods. Figure 1 (Wolf-Gladrow, 2000) shows the difference between two methods.

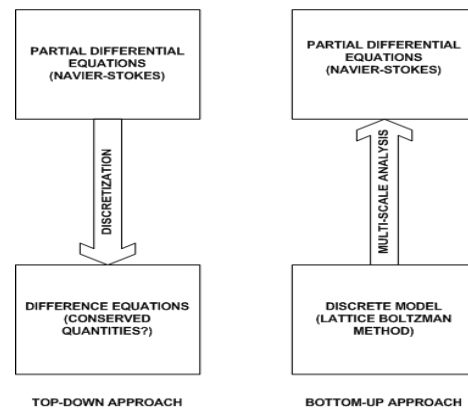


Figure 1. Difference between top-down and bottom-up approach (After Wolf-Gladrow, 2000).

In traditional methods (top-down approach) normally partial differential equations (PDEs) are used to

simulate fluid flow. These PDEs are discretized by finite differences, finite volumes or finite elements. The resulting algebraic equations or systems of ordinary differential equations are solved by standard numerical methods. As for numerical simulations, conventional highly nonlinear Navier-Stokes equations are solved for both porous and fractured media. Numerical simulations have serious drawbacks like long computation times, poor convergence and numerical instabilities.

LBM is developed as another computational method that is more efficient and it uses simple rules to represent the fluid flow rather than partial differential equations. LBM is a discrete computational method based upon the Boltzmann equation. It considers a typical volume element of fluid to be composed of a collection of particles that are represented by a particle velocity distribution function at each grid point. In discrete time steps the fluid particles can collide with each other as they move. The rules that govern the collisions of the particles are designed such that the time averaged motion of the particles is consistent with the Navier-Stokes equation. One of the most important advantages of the LBM is its capability for handling fluid flow especially in complex geometries (Succi *et al*, 1989). The complex geometric details in the porous media and fractures can be handled in terms of simple bounce-back rules. Moreover, LBM could be applied to both two and three dimensional flows.

2D Lattice Boltzmann BGK model

In our work two-dimensional Bhatnagar-Gross-Krook (BGK) Lattice Boltzmann method is used. This model uses a D2Q9 lattice with nine discrete velocities. The velocity vectors are illustrated in Figure 2.

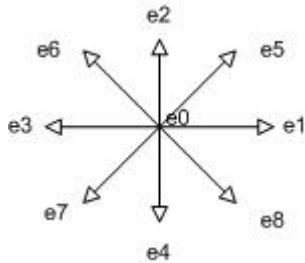


Figure 2. The nine-speed square lattice used in the lattice Boltzmann simulations. (After Guo *et al*, 2000)

The velocity directions of the D2Q9 Lattice Boltzmann BGK model are defined as (Guo *et al*, 2000).

$$e_i = \begin{cases} (0,0) & i=0 \\ (\cos[(i-1)\pi/2], \sin[(i-1)\pi/2]) & i=1,2,3,4 \\ \sqrt{2}(\cos[(i-5)\pi/2+\pi/4], \sin[(i-5)\pi/2+\pi/4]) & i=5,6,7,8 \end{cases} \quad (3)$$

Let $f_k(x,t)$ be a non-negative real number describing the distribution function of the fluid density at site x and time t moving with velocity e_k towards the neighboring lattice site located at $x+e_k$, where the subscript k refer to the velocity direction ($k=1,\dots,9$). The distribution functions evolve according to the Boltzmann equation that is discrete in both time and space.

$$f_k(x+e_k, t+1) = f_k(x,t) + \Omega_k(x,t) \quad (4)$$

Where $\Omega_k(x,t)$ is the collision operator representing the rate of change of the particle distributions due to collisions (Kumar *et al*, 1999). Collection of particles of unit mass and unit momentum moves on the lattice. Mass and momentum of the particles are locally conserved after collision of the particles.

The fluid density ρ and velocity u are obtained from the density distribution function $f_k(x,t)$:

$$\rho = \sum_k f_k \quad (5)$$

$$\rho u = \sum_k f_k e_k \quad (6)$$

As it is stated in (Wolf-Gladrow, 2000) at macroscopic scale the behavior of these particles is the same as that is predicted by the incompressible Navier-Stokes equations.

Boundary Conditions

A boundary condition with a constant pressure difference is used at inlet and outlet of the fracture aperture, where all fluid densities are propagated from non-occupied nodes along the lattice-connection lines to their next neighbors. The physical boundary condition at solid-fluid interfaces is the no-slip boundary condition, which in LBM is usually realized as bounce-back rule. This is physically appropriate whenever the solid wall has a sufficient rugosity to prevent any net fluid motion at the wall (Succi, 2001). The complete bounce-back scheme is used to simulate the no-slip boundary condition, which requires that when a particle distribution streams to a solid boundary node, it scatters back to the node it came from. The velocity vector of all fluid densities is inverted, so all the fluid densities will be sent back to the node where they were located before

the last propagation step, but with opposite velocity vector.

Algorithm

There are many different algorithms available for implementing LBM. The following pseudo code shows how LBM was implemented in Matlab V 7.0 in this study (Keehm, 2003).

```
Start Program
Read in Obstacle Location File
Set initial density distribution
Loop for T time Steps
{
    Redistribute along first lattice column
    Propagate fluid particles
    Check for obstacle (bounce-back)
    Calculate density and velocity from Eqn 5 & 6
    Calculate permeability
    If((new perm-old perm) < tolerance_value))
exit loop
}
Write velocity data to file
End
```

2.2 Synthetic Fractures

It is very important to understand the fluid flow through natural fractures in rocks. The geometry of the fracture surfaces affects the hydraulic properties of the fractured rock. Roughness at the surface of the fractures could be described efficiently by using the fractal geometry concepts (Feder, 1988). Since studying rough, anisotropic fractures in the laboratory is difficult synthetic fractures could be used. Synthetic fracture is the term used to describe fractures that are created numerically in such a way that they share the same mean geometrical characteristics as specific natural fractures measured by profiling and then tuning (Glover, *et al*, 1998). For example numerical synthetic fractures can be created from unmatched fractal surfaces (Amedei *et al*, 1994). Geostatistical techniques like conventional kriging and conditional simulation (Deutsch and Journel, 1992) could also be used to create synthetic fractures. In this work numerical modeling is used to simulate fluid flow in synthetic rock fractures that share the same physical properties with the natural fractures. In our work SynFrac software is used to create synthetic fractures (Glover *et al*, 1998). This software uses modified methods for producing synthetic rough surfaces whose geometric properties are tuned to mimic natural fractal surfaces in rocks in order to create synthetic fractures that are statistically identical to those found in rocks.

3 FRACTURE GENERATION AND FLOW SIMULATION

In this section methodologies used both for synthetic fracture generation and the simulation of the fluid flow in these fractures will be defined.

3.1 Synthetic Fracture Generation

SynFrac software originally generates three-dimensional fractures. The resolution of the fracture can be altered with in the range from 64x64 to 1024x1024. In addition to resolution, parameters like fractal dimension or anisotropy factor could be altered to generate fractures that have the same resolution but different physical properties. Fractal dimension for each surface is a value between 2 and 3; this value determines the roughness of the fracture surface. Another parameter that is altered is the anisotropy factor, which is used to generate anisotropic synthetic fractures. As the anisotropy factor deviates from unity all the scales in one direction along the fracture surface will be greater than the scales in other direction. A sample fracture surface created by SynFrac is given in Fig 3 (Glover *et al*, 1998).

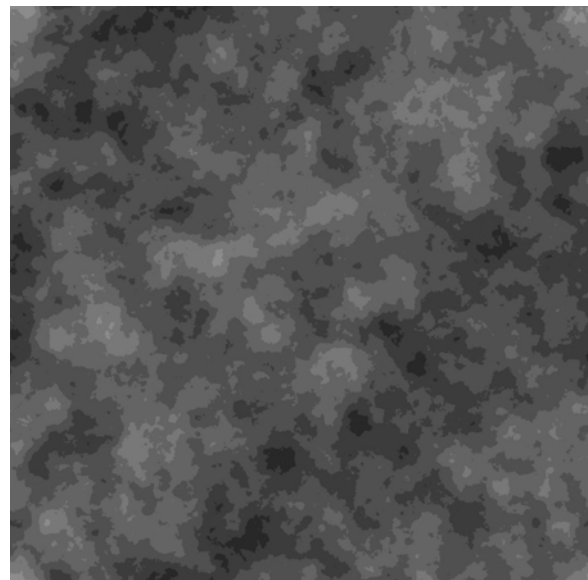


Figure 3. Fracture aperture distribution created by SynFrac. Blacks are low aperture areas.

As the lattice Boltzmann simulation is performed at two-dimensions, 2D slices are obtained from the 3D fracture apertures. Figure 4 shows a 2D fracture aperture obtained by slicing the three-dimensional fracture for a given plane.

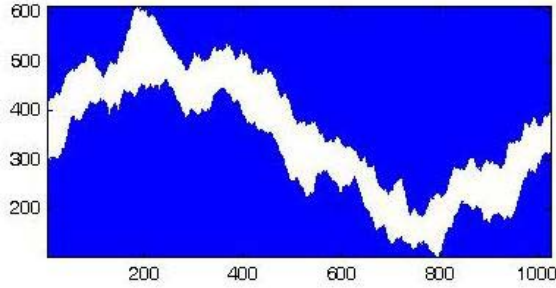


Figure 4. Two dimensional fracture aperture obtained by slicing.

This sliced two-dimensional fracture forms the basis for our lattice Boltzmann simulation. SynFrac software outputs the heights of the top and bottom surfaces of the created fracture, an instance of the output data is shown in Table 1. This data is then converted into binary format (1's and 0's) in order to be used with lattice Boltzmann algorithm. This process is illustrated in Fig 5, where 1's represent grains and 0's represent pore space. In order to increase accuracy of the simulation synthetic fractures are created at maximum resolution (1024). Resolution of the fracture is, 1024 in x-direction and a value which is determined according to the min-max value of the bottom and top in y-direction changes between 500 and 700.

Table 1. Sample 2D fracture data.

X-Loc	Y-Loc	Top (mm)	Bottom (mm)	Aperture (mm)
1	103	4.879	4.140	0.738
1	104	4.852	4.151	0.701
1	105	4.848	4.165	0.683
1	106	4.856	4.165	0.691
1	107	4.828	4.193	0.636
1	108	4.812	4.216	0.596

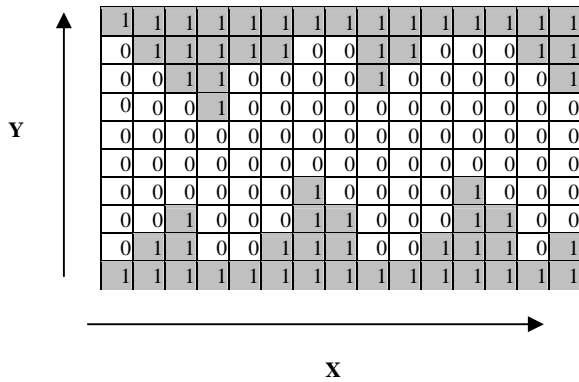


Figure 5. Binary representation of two-dimensional fracture aperture.

3.2 Lattice Boltzmann Simulation of Fluid Flow in Fractured Geothermal Reservoirs

Fractal dimensions of the fracture patterns of some geothermal reservoirs (Kizildere and Germencik) located in south western Turkey was used to generate synthetic fractures (Babadagli, 2001; Babadagli, 2002). Fractal dimensions obtained by applying methods like box counting from aerial photographs, outcrops and thin sections ranged from 2.21 to 2.50 (Table 2).

Table 2. Results of the lattice Boltzmann simulations for different fractal dimensions.

Fractal Dimension	Mean Aperture (mm)	LB-Perm (md)
2.21	1.3443	1.59E+06
2.25	1.4550	1.68E+06
2.30	1.6051	1.81E+06
2.32	1.6691	1.86E+06
2.35	1.7693	1.94E+06
2.38	1.8746	2.02E+06
2.40	1.9478	2.05E+06
2.45	2.1411	2.18E+06
2.47	2.2224	2.23E+06
2.50	2.3486	2.29E+06

Simulations (Table 3) were performed in order to understand the effects of the parameters during the fracture generation phase to the absolute permeability of the fractures. At each step synthesized fracture with its fractal dimension or anisotropy factor was changed, converted into binary format and used as an input for the lattice Boltzmann simulation. Velocity vectors on each grid point were calculated by the lattice Boltzmann method (Fig 6). Absolute permeability k of the fracture could then be obtained by calculating the mean flux from the velocity vectors and with the Darcy's law.

$$\langle q_x \rangle = \frac{k}{\mu} \frac{dP}{dx} \quad (7)$$

Where μ is the dynamic viscosity of the fluid and $\langle q_x \rangle$ is the volumetric average of fluid flux.

Table 3. Parameters used in the LBM simulations for different fractal dimensions, anisotropy factors and mismatch lengths.

Resolution	1024
Physical size (mm)	100.00
Transition length (mm)	10.00
Standard deviation (mm)	1.00
Max matching fraction	1.00
Min matching fraction	0.00

Permeability values obtained by LBM are compared by the empirical results that are calculated by using Eqn 1 without or with roughness. Moreover, permeability is estimated from the following equation (Zhang *et al*, 1996):

$$k \approx \delta^\beta \quad (8)$$

Where δ is mean fracture aperture and β is an exponent.

4 RESULTS OF THE LATTICE BOLTZMANN SIMULATION

The method was first verified for pipe flow using Hagen-Poiseuille law. It was observed that the difference between the results were less than %0.09. Then several runs were conducted to identify flow velocity patterns. Synthetic 2D fractures were selected from the same location in 3D. That's why the fracture geometry was similar but the rugosity was somewhat different for each case (Fig 6). Thus, the fracture sloped upwards first following a downhill that ended with increasing slope. It was observed that for a constant pressure gradient the highest velocity was observed near the inlet of the fracture corresponding to locations where the aperture was significantly lower than the rest of the fracture. Then the high velocity flow dissipated near the end of the fracture for all cases. For constant anisotropy factor, as the fractal dimension increased (from 2.21 to 2.5 corresponding to %13 increase) the magnitude of the highest velocity observed increased (approximately %30). On the other hand, as the anisotropy factor increased from 1 to 3, the location of highest velocities along the fracture changed. Moreover, the magnitude of the highest velocity decreased. As the mismatch length increased mean fracture aperture increased and thus the permeability increased (Fig. 7). The magnitude of the highest velocity observed along the fracture couldn't be correlated.

Simulations were then conducted to understand the effect of fractal dimension and anisotropy factor to fracture permeability. While creating synthetic fractures each of these parameters was altered and other parameters were held constant. Table 2 shows the result of the LBM permeability calculations for different fractal dimension values. Figure 8 shows permeability values that are calculated by LBM vs. mean aperture – fractal dimension ratio. The fracture permeability increases linearly with a high correlation coefficient as the mean aperture fractal dimension ratio increases. LBM fracture permeabilities were two orders of magnitude lower than the permeabilities obtained from the cubic law (Eqn 2). This suggests that for a rough self-affine fracture one may have a fractal dimension dependent exponent that is larger than 2. Our simulations suggest an exponent range from 4.27 to 5.66 that are in accord with the range (2 to 6) provided by Zhang

et al (1996). Moreover, for anisotropy equal to 1, there is a linear relationship between the fractal dimension D and the exponent given by the following equation: $\beta = 4.8065D - 6.4154$ (9)

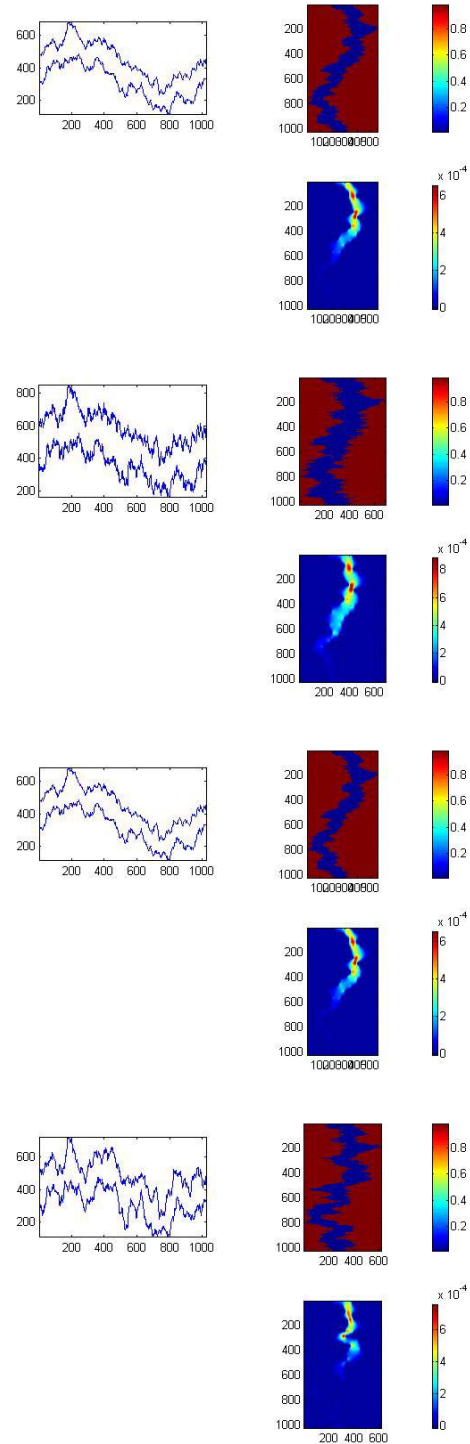


Figure 6. Generated fracture aperture and velocity distribution for fractal dimension and anisotropy factor values top to bottom (2.21 and 1.0), (2.5 and 1.0), (2.25 and 1.0), (2.25 and 3.0).

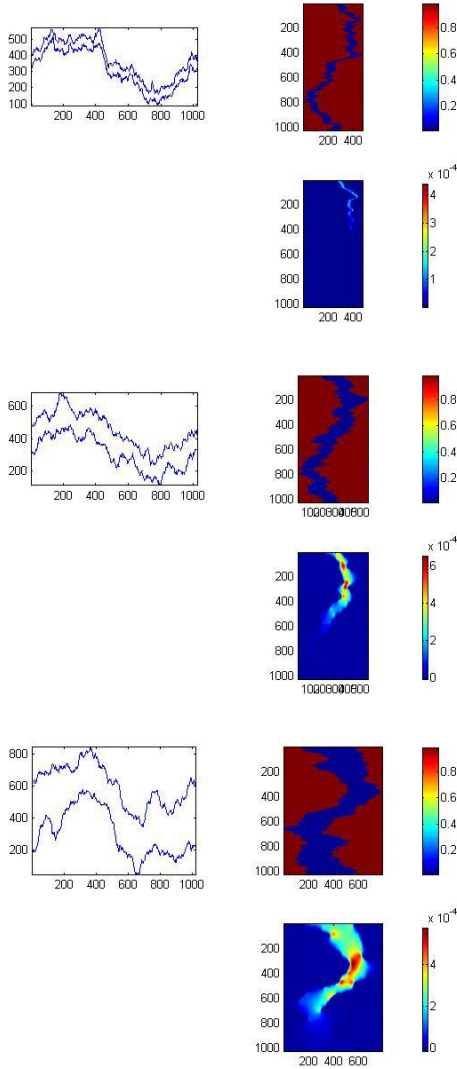


Figure 7. Generated fracture aperture and velocity distribution for mismatch length of 5, 15 and 25 mm.

Another set of simulations was performed to understand the effect of the changes in anisotropy factor to the fracture permeability. Anisotropy factor is a ratio of the wavelengths in each direction. If anisotropy factor is less than 1 anisotropy is transverse to x direction; however, if anisotropy factor is more than 1 anisotropy is transverse to y direction (Glover *et al*, 1998). As the anisotropy factor increased from 1 to 3, permeability decreased (Table 3). Similar results are reported in the literature for self-affine fractures (Madadi and Sahimi, 2003). When permeability values are plotted against anisotropy factors a second-order polynomial relationship was observed (Fig 9). It was observed that for a given fractal dimension, anisotropy and exponent relationship is linear. For example for D

equals to 2.25 the following relationship was observed.

$$\beta = 0.5063 * A + 3.8642 \quad (10)$$

Where A is anisotropy factor.

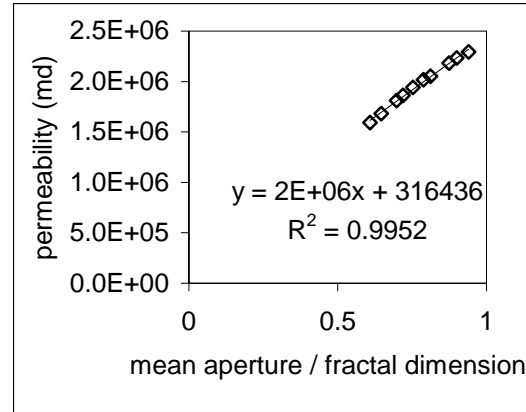


Figure 8. Relationship between LBM permeability and mean aperture-fractal dimension ratio.

Table 3. Permeability values of the fractures for different anisotropy factors.

Anisotropy Factor	LB-Permeability (md)
1,00	1,68E+06
1,20	1,60E+06
1,30	1,56E+06
1,35	1,53E+06
1,40	1,51E+06
1,50	1,46E+06
1,60	1,42E+06
1,80	1,33E+06
2,50	1,21E+06
3,00	1,15E+06

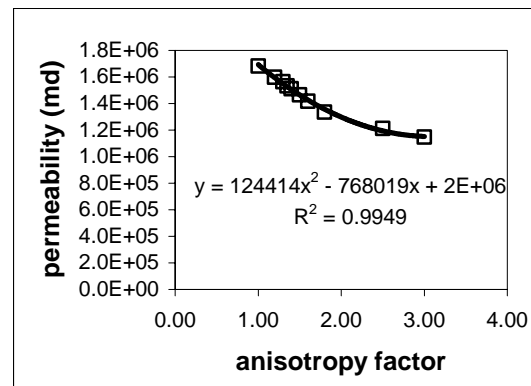


Figure 9. Relationship between LBM permeability and anisotropy factor.

The final parameter that affects fracture permeability is mismatch length. It was shown previously that natural fractures are correlated to some degree at long

wavelengths but at short wavelengths the surfaces are not identical (Brown, 1995). These two different behaviors are modeled by a critical wavelength called the mismatch length. Above this length the fracture surfaces are correlated but below it the fractures behave independently. In our simulations, as the mismatch length increased the fracture surfaces became correlated and smoother for a given fractal dimension. The mean aperture also increased. This results in an increase in permeability. A linear relationship was observed with mismatch length and the LBM permeability (Fig 10).

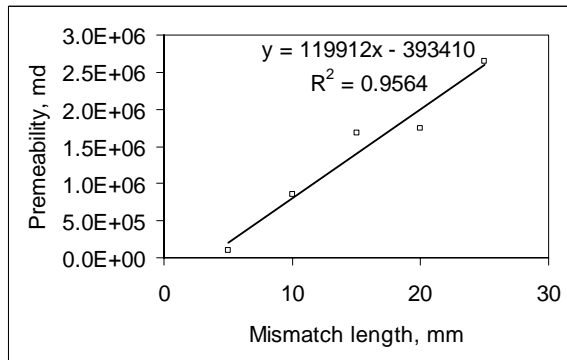


Figure 10. Relationship between LBM permeability and mismatch length.

In order to generalize the findings, simulations that cover a wide range of fractal dimensions, anisotropy factors, mean fracture apertures and mismatch lengths need to be conducted. However, it is not possible to cover all parameters within a reasonable time frame. In order to tackle this problem artificial neural network (ANN) technology was used (Fig 11). Back propagation technique (Rumelhart *et al*, 1986) and 71 different LBM simulations were used to train different artificial neural networks and the best performing network was selected (Table 4). ANN input parameters consisted of fractal dimensions, anisotropy factors, average mean apertures and fracture porosities and LBM permeability is selected as ANN output. Approximately %10 of the input data was held for validation purposes. Since there were several orders of magnitude difference between the input data the LBM permeability was scaled to values between 0 and 1 by dividing the LBM permeabilities to maximum calculated permeability (2.29×10^6 md). It was observed that the mean square errors were less than %0.71 for the validation data set (Fig 12). Using the trained ANN several runs were conducted to check the aforementioned results.

Table 4. ANN model properties.

Input nodes	4
Output nodes	1
Hidden layer 1	20
Hidden layer 2	8
Momentum factor	0.1

Learning parameter 0.2

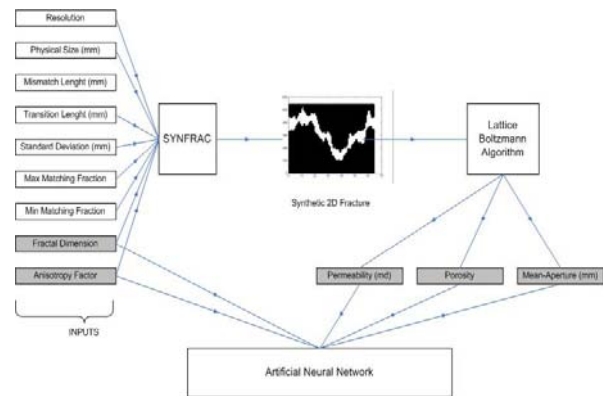


Figure 11. Architecture for LBM simulation and artificial neural network training.

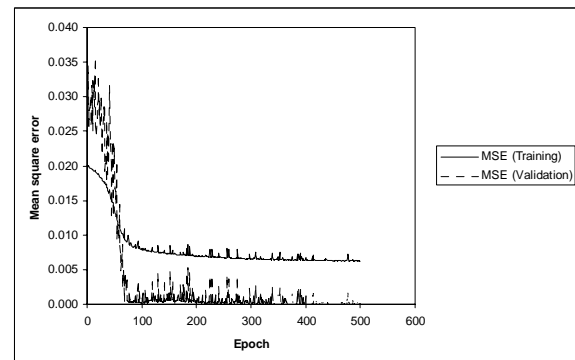


Figure 12. Mean square errors observed for artificial neural network training and validation data sets.

The ANN results confirmed the aforementioned findings (Fig 13). For example the second order relationship observed between the anisotropy factor and LBM permeability was obtained for all fractal dimensions. One of the advantages of using the ANN technology is that one can establish the importance of parameters that influence a process. For a given average fracture aperture it was observed that the as anisotropy factor increased from 1 to 3 the permeability decreased %62 and %75 for low and high fractal dimensions respectively. On the other hand, for a given mean fracture aperture, the fractal dimension change from 2.25 to 2.35 resulted in approximately %1.8 to %5.2 change in permeability. It was also observed that as the anisotropy factor increased from 1 to 3 the change in permeability decreased as the fractal dimension or mean fracture aperture increased. Thus it could be concluded that as the fracture rugosity increases mean fracture aperture and fractal dimension do not dominate the permeability change anymore.

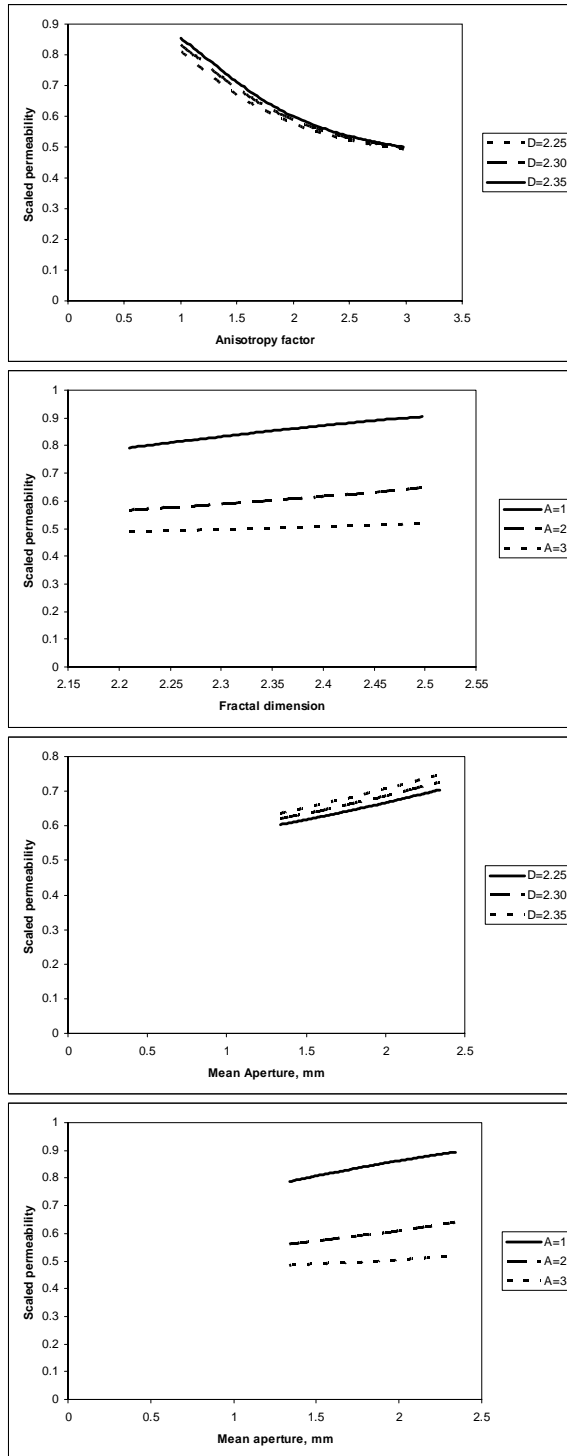


Figure 13. ANN results. Permeability anisotropy factor, mean fracture aperture and fractal dimension relationships.

5 CONCLUSIONS

Lattice Boltzmann Method was used to obtain fracture permeabilities of synthetic fractures created using a fractal technique. For the fractal geothermal reservoirs located in South West Turkey it was

observed that velocity increased at locations where the fracture aperture decreased along the fracture. There is a linear relationship between permeability and mean aperture – fractal dimension ratio as well as the mismatch length. However, the relationship is second order for anisotropy factor. A neural network trained using the LBM simulations showed that anisotropy of the fracture has more influence on the fracture permeability than the fractal dimension and the mean fracture aperture. Thus the fracture geometry is important.

REFERENCES

- Amedei, B., Illangsekare, T., “A Mathematical Model for Flow and Transport in Non-Homogeneous Rock Fractures”, *Int. J. Rock Mech. Min. Sci. Geomech. Abstr.*, 31, 719-731, (1994).
- Amyx, J., Bass, D., Whiting, R., “Petroleum Reservoir Engineering”, (1960).
- Bear, J. “Dynamics of Fluids in Porous Media”, American Elsevier Publishing Co., New York: 764 pp., (1972).
- Babadagli T “Fractal analysis of 2-D fracture networks of geothermal reservoirs in south-western Turkey” *J VOLCANOL GEOTH RES* 112 (1-4): 83-103 DEC (2001).
- Babadagli T “Scanline method to determine the fractal nature of 2-D fracture networks” *MATH GEOL* 34 (6): 647-670 AUG (2002).
- Brown, S.R. “Simple mathematical model of a rough fracture” *J. Geophys. Res.* 100, 5941-5952, 1995.
- Deutsch C. V. Journel, A. G. “GSLIB: Geostatistical Software Library and User's Guide”, Oxford University Press, New York, (1992), 61-116.
- Feder, J., “Fractals”, Plenum Press, NY, 283 pp, (1988).
- Frisch, U., Hasslacher, B., Pomeau, Y., “Lattice Gas Automata for the Navier-Stokes Equations”, *Phys. Rev. Lett.* 56, 1505, (1986).
- Glover, P. W. J., Matsuki, K., Hikima, R., Hayashi, K., “Synthetic Rough Fractures in Rocks”, *Journal of Geophysical Research* 103, B5, 9609-9620, (1998).
- Golf-Racht, Van, T. D, “Fundamentals of Fractured Reservoir Engineering”, Elsevier Publishing Company, 710 pp (1982).
- Guo, Z., Shi, B., Wang, N., “Lattice BGK Model for Incompressible Navier-Stokes Equation”, *Journal of Computational Physics* 165, 288-306, (2000).

Ilachinski A., "Cellular Automata, a Discrete Universe", World Scientific Publishing Company; 1st edition, 840 pp, (2001).

Keehm, Y., "Computational Rock Physics: Transport Properties in Porous Media and Applications", Phd Thesis, Stanford University Department of Geophysics, (2003).

Kumar, R., Sriram, S., Nivarthi, H., Davis, T., Kroll, D. M., Maier, R. S., "Application of the Lattice-Boltzmann Method to Study Flow and Dispersion in Channels with and without Expansion and Contraction Geometry", Int. J. Numer. Meth. Fluids 31: 801-819, (1999).

Lomize, G.M. "Flow in fractured rocks" (In Russian), Gosenergoizdat, Moscow: 127 pp, (1951).

Louis, C.A. "A study of groundwater flow in jointed rock and its influence on the stability of rock masses", Rock Mech. Res. Rep. 10, Imperial College, London: 90 pp., (1969).

Madadi, M., Sahimi, M. "Lattice Boltzmann simulation of fluid flow in fracture networks with rough, self-affine fractures", Physical Review E, 67, 026309, (2003).

McNamara, G., Zanetti, G., "Use of the Boltzmann Equation to Simulate Lattice-Gas Automata", Phys. Rev. Lett. 61, 2332-2335, (1988).

Rumelhart, D. E., Hinton, G. E., and Williams, R. J., 1986. Learning representations by back-propagating errors. Nature, 323, 533-536.

Snow, D.T. "Anisotropic permeability of fractured media", Water Resources Research, 5 (6): 1273-1289, (1965).

Succi, S., Foti, E., Higuera, F., "Three-dimensional flows in complex geometries with lattice Boltzmann method", Europhysics Letters, 10(5): 433-438, (1989).

Succi, S., "The Lattice Boltzmann Equation for Fluid Dynamics and Beyond", Oxford University Press, 368 pp (2001).

Witherspoon, P. A., Wang, J. S. Y., Iwai K., Gale, J. E., "Validity of the cubic law for fluid flow in a deformable rock fracture", Water Resources Research, 16, 6, 1016 (1980).

Wolfram, S., "Universality and Complexity in Cellular Automata", Physica D, 10, 1-35, (1984).

Wolf-Gladrow, D., "Lattice-Gas Cellular Automata and Lattice Boltzmann Models", Springer-Verlag Telos, 308 pp, (2000).

Zhang, X., Knackstedt, M.A., Sahimi, M. "Fluid flow across mass fractals and self-affine surfaces", Physica A, 233, 835, (1996).

ARCHITECTURE FOR A COUPLED CODE FOR MULTIPHASE FLUID FLOW, HEAT TRANSFER AND DEFORMATION IN POROUS ROCK

Shekhar Gosavi
Daniel Swenson

Kansas State University
Mechanical and Nuclear Engineering Department
Manhattan, KS, 66506, USA
e-mail: shekharg@ksu.edu, swenson@ksu.edu

ABSTRACT

This paper presents the architecture and implementation in which two computer codes-TOUGH2 and GeoCrack3D are linked. A fully coupled thermal-hydrologic-mechanical (THM) analysis of multiphase fluid flow, heat transfer, and deformation in a porous rock can be carried out. The codes are simultaneously executed to run as one module T2STR.

The forward coupling is achieved by using the thermal, hydrostatic and poroelastic effects in the effective stress calculations. The backward coupling includes the effect of strain on the fluid flow and also includes the corrections in porosity, permeability, and capillary pressure as function of mean effective stress.

BACKGROUND

TOUGH2 is a program for calculation of multiphase, multi-component, non-isothermal flow in porous media (Pruess et.al., 1999). It uses a modified dual-permeability approach (MINC) to represent flow in fractured media. Some of the strengths of the code include:

- Use of the integral finite difference approach, which can accommodate general geometry (with the constraint that the mesh be Voronoi).
- Implementation of several equation-of-state modules to represent different fluid mixtures.
- Continual development to add new capability such as multiple volatile organic compounds (TMVOC) and chemical reactions (TOUGHREACT).

One physical phenomenon that is not included in TOUGH2 is deformation and stress. For some problems, stress coupling can be important (Swenson et.al., 2004). It is a logical extension of TOUGH2 to consider how to add stress coupling.

CONSERVATION EQUATIONS

The balance equations for the mass, momentum and energy used in the formulation are as follows.

Conservation of Mass

The mass balance for the solid phase of the porous medium in Eulerian form can be written as follows

$$\frac{\partial((1-\phi)\rho_s)}{\partial t} + \nabla \cdot ((1-\phi)\rho_s \mathbf{v}_s) = 0$$

Using the following relation between the solid velocity and volumetric strain (Bear and Bachmat, 1991)

$$\nabla \cdot \mathbf{v}_s \approx \frac{\partial \epsilon_v}{\partial t}$$

and assuming the solid density to be function of pressure, temperature and effective stress, we can write (Lewis and Schrefler, 1998)

$$\frac{1}{\rho_s} \frac{\partial \rho_s}{\partial t} = \frac{1}{(1-\phi)} \left[\frac{(\alpha-\phi)}{K_s} \frac{\partial p_s}{\partial t} - (\alpha-\phi)\alpha_T \frac{\partial T}{\partial t} - (1-\alpha) \frac{\partial \epsilon_v}{\partial t} \right]$$

where, α is the Biot-Willis factor, α_T is the thermal expansion coefficient, and the solid phase pressure, p_s , is given as

$$p_s = p_l S_l + p_g S_g = \sum_{\psi} p_{\psi} S_{\psi}$$

The macroscopic mass balance for the fluid flow can be written as

$$\frac{\partial}{\partial t} (M_{\psi}^{\kappa}) + \nabla \cdot \mathbf{I}_{\psi}^{\kappa} + \nabla \cdot \mathbf{J}_{\psi}^{\kappa} - Q_{\psi}^{\kappa} = 0$$

where M_{ψ}^{κ} , $\mathbf{I}_{\psi}^{\kappa}$, and $\mathbf{J}_{\psi}^{\kappa}$ denote, the mass per unit volume of the porous medium and the advective and the diffusive/dispersive mass flux respectively, of a component κ in a phase ψ . Q_{ψ}^{κ} is the rate of production of component κ per unit volume.

The advective mass flux \mathbf{I}_ψ^κ can be written as the sum of the advective mass flux of the solid, $\mathbf{I}_{S\psi}^\kappa$, and the advective flux with respect to the moving solid particles, $\mathbf{I}_{r\psi}^\kappa$, as follows

$$\mathbf{I}_\psi^\kappa = \mathbf{I}_{r\psi}^\kappa + \mathbf{I}_{S\psi}^\kappa$$

where

$$\mathbf{I}_{r\psi}^\kappa = \phi S_\psi \rho_\psi^\kappa \mathbf{v}_{r\psi} \quad \text{and} \quad \mathbf{I}_{S\psi}^\kappa = \phi S_\psi \rho_\psi^\kappa \mathbf{v}_{S\psi}$$

Combining the diffusive/dispersive and advective flux with respect to the moving solids, we can write the total mass flux of each component κ in a phase ψ as

$$\mathbf{q}_{r\psi}^\kappa = \mathbf{I}_{r\psi}^\kappa + \mathbf{J}_\psi^\kappa$$

while the total flux can be written as

$$\begin{aligned} \mathbf{q}_\psi^\kappa &= \mathbf{I}_{r\psi}^\kappa + \mathbf{I}_{S\psi}^\kappa + \mathbf{J}_\psi^\kappa \\ &= \mathbf{q}_{r\psi}^\kappa + \mathbf{I}_{S\psi}^\kappa \end{aligned}$$

Now, the mass balance of the fluid component becomes (Rutqvist et.al., 2001)

$$\left[\frac{\partial(\phi S_\psi \rho_\psi^\kappa)}{\partial t} + \nabla \cdot \mathbf{q}_{r\psi}^\kappa + Q_\psi^{\kappa e} \right] + [\nabla \cdot (\phi S_\psi \rho_\psi^\kappa \mathbf{v}_S)] = 0$$

The solid velocity terms will be neglected owing to small strain assumption. Using the solid density relation and combining all the phases of a component we get

$$\begin{aligned} &\frac{\partial \left(\phi \sum_\psi S_\psi \rho_\psi^\kappa X_\psi^\kappa \right)}{\partial t} + \nabla \cdot \mathbf{q}_{r\psi}^\kappa - Q^\kappa + \\ &\sum_\psi S_\psi \rho_\psi^\kappa X_\psi^\kappa \left(\frac{(\alpha - \phi)}{K_s} \frac{\partial (\sum_\psi S_\psi p_\psi)}{\partial t} - (\alpha - \phi) \alpha_T \frac{\partial T}{\partial t} \right. \\ &\quad \left. + \alpha \frac{\partial \varepsilon_v}{\partial t} - \frac{\partial \phi}{\partial t} \right) = 0 \end{aligned}$$

where we have re-inserted the source term in the equation. The fourth term represents the additional terms required to the existing TOUGH2 equation.

Conservation of Energy

The combined energy balance equation for three phases, neglecting the terms related to the conversion of kinetic energy to internal energy, is (Faust and Mercer, 1979, Bear and Bachmat, 1991)

$$\begin{aligned} \frac{\partial (\phi \sum_\psi S_\psi \rho_\psi^\kappa u_\psi^E + (1 - \phi) \rho_s u_s^E)}{\partial t} &= -\nabla \cdot (\sum_\psi \mathbf{q}_{r\psi}^\kappa h_\psi) \\ &\quad - \nabla \cdot \mathbf{J}_C^H \end{aligned}$$

Conservation of Momentum

Neglecting the inertial terms and the forces due to the interaction between the non-wetting and wetting fluid, the momentum equation becomes a static equilibrium equation as follows (Bear and Bachmat, 1991)

$$\nabla \cdot \boldsymbol{\sigma} = \rho \mathbf{F}$$

CONSTITUTIVE EQUATIONS

The required set of constitutive equations follow.

Hydraulic

The advective mass flux of the component κ of a fluid phase ψ is given by the generalized Darcy law as follows (Pruess et.al., 1990)

$$\mathbf{I}_{r\psi}^\kappa = -\rho_\psi^\kappa \frac{\mathbf{k} k_{r\psi}}{\mu_\psi} (\nabla p_\psi - \rho_\psi \mathbf{g})$$

where the $\mathbf{k} = \mathbf{k}(\phi)$ is the hydraulic permeability tensor which is a function of porosity and is a property of the solid, while $k_{r\psi}$ is the relative permeability function of the fluid phases.

The diffusive flux can be computed using the Fick's law,

$$\mathbf{J}_\psi = -\rho_\psi D_v \mathbf{m} \nabla X_\psi^\kappa$$

where D_v is the effective molecular diffusion coefficient in a porous media.

Thermal

Heat conduction is governed by Fourier's law and is given by

$$\mathbf{J}_C^H = -\lambda_m \mathbf{m} \nabla T$$

where λ_m is the thermal conductivity over all phases and vector \mathbf{m} is $[1 \ 1 \ 1 \ 0 \ 0 \ 0]^T$.

Mechanical

The total strain tensor, $\boldsymbol{\varepsilon}$, and the volumetric strain, ε_v , assuming the small strain condition, are defined as,

$$\boldsymbol{\varepsilon} = \frac{1}{2} (\nabla \mathbf{u} + (\nabla \mathbf{u})^T)$$

and

$$\varepsilon_v = \nabla \cdot \mathbf{u}$$

where \mathbf{u} is the displacement vector.

The thermal strain is given by

$$\Delta \boldsymbol{\varepsilon}_T = \mathbf{m} \alpha_T \Delta T$$

where α_T is the linear thermal expansion coefficient.

The strain due to the poroelastic effect, $\Delta \varepsilon_p$, caused by the uniform compression of the particles by the pore pressure is given by (Lewis and Schrefler, 1998)

$$\Delta \varepsilon_p = \left(\frac{-1}{3K_s} \right) \mathbf{m} \Delta p$$

where K_s represents the bulk modulus of solid phase and Δp represents the change in pore pressure.

The modified effective stress law for a partially saturated medium gives the total stress as (Lewis and Schrefler, 1998)

$$\boldsymbol{\sigma} = \boldsymbol{\sigma}'' - \alpha \mathbf{m} p$$

where $\boldsymbol{\sigma}''$ represents the modified effective stress and α is the Biot-Willis coefficient (Wang, 2000). The modified effective stress causes all the relevant deformation of the solid skeleton and the solid grain compression. The constitutive equation relating the effective stress to strain, in incremental form, is

$$\boldsymbol{\sigma}'' = \mathbf{D}(\Delta \boldsymbol{\varepsilon} - \Delta \boldsymbol{\varepsilon}_T) + \boldsymbol{\sigma}''_0$$

\mathbf{D} is the elastic material matrix and $\boldsymbol{\sigma}''_0$ is the initial effective stress. Substituting for $p = p_0 + \Delta p$, we can write the total stress as

$$\boldsymbol{\sigma} = \mathbf{D} \Delta \boldsymbol{\varepsilon} - 3K \alpha_T \mathbf{m} \Delta T + \boldsymbol{\sigma}''_0 - \alpha \mathbf{m} \Delta p - \alpha \mathbf{m} p_0$$

CHANGES IN HYDRAULIC PROPERTIES

The relationship between porosity and mean effective stress is (Davies and Davies, 1999),

$$\phi = \phi_r + (\phi_0 - \phi_r) \exp(a \sigma'_M)$$

where, ϕ_0 is porosity at zero stress, ϕ_r is the residual porosity at high stress, a is the constant to be determined experimentally (a material property), and σ'_M is the mean effective stress.

The permeability and porosity are related as follows (Rutqvist et. al., 2002)

$$k = k_0 \exp \left(c \left(\frac{\phi}{\phi_0} - 1 \right) \right)$$

where k_0 is the permeability at zero stress and the exponent c should be determined experimentally.

The capillary pressure is modified with permeability and porosity according to the Leverett function (Rutqvist et.al., 2002)

$$p_c = p_{c0} \frac{\sqrt{k_0/\phi_0}}{\sqrt{k/\phi}}$$

DISCRETIZATION METHOD

The equations of conservation of mass and energy are solved in TOUGH2 code using the Integrated Finite Difference Method (IFDM) (Narasimhan and Witherspoon, 1976). The aspect of deformable porous media is added through additional terms in flow equations and through the addition of equation of conservation of momentum for the solid phase. The momentum equation is discretized using the finite element method (FEM). These coupled set of equations will be combined using the dual mesh concept.

Space Discretization

Integrated Finite Difference Method

Using the appropriate volume averages for volume-normalized extensive quantities and approximating the surface integral as a discrete sum of averages over surface segments A_{nm} (between the volume elements V_n and V_m), the balance equations, can be converted to a set of first-order ordinary differential equations in time. The nomenclature is shown in the Figure 1.

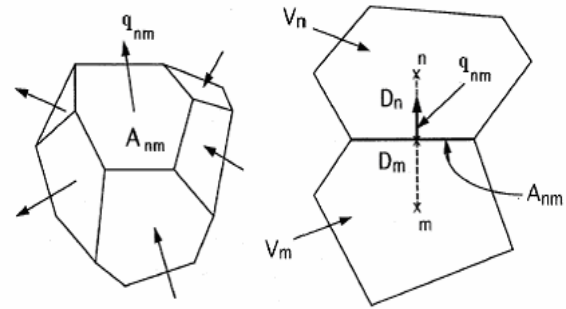


Figure 1 Space discretization and geometry data in IFDM (Pruess et. al., 1999)

The discretized mass conservation equation becomes

$$\begin{aligned} & \left[\frac{d(M_n^k)}{dt} \right] + \theta_n^k \left(\frac{(\alpha - \phi_n)}{K_s} \frac{d(\sum S_n^v p_n^v)}{dt} \right) \\ & - \theta_n^k \left((\alpha - \phi_n) \alpha_r \frac{dT_n}{dt} + \frac{d\phi_n}{dt} \right) + \theta_n^k \frac{\alpha}{V_n} \frac{d(\sum_m A_{nm} u_{nm})}{dt} \\ & = \frac{1}{V_n} \sum_m A_{nm} q_{nm}^k - Q_{nm}^k + Q_{nm}^{sk} \end{aligned}$$

where

$$M_n^\kappa = \phi_n \sum_\psi S_\psi \rho_\psi^\kappa X_\psi^\kappa$$

$$\theta_n^\kappa = \sum_\psi S_\psi \rho_\psi^\kappa X_\psi^\kappa$$

$$q_{nm}^\kappa = \sum_\psi X_\psi^\kappa q_{\psi,nm}$$

The basic Darcy flow for each phase ψ is given as

$$q_{\psi,nm} = -k_{nm} \left[\frac{k_{r\psi} \rho_\psi}{\mu_\psi} \right]_{nm} \left[\frac{P_{\psi,n} - P_{\psi,m}}{D_{nm}} - \rho_{\psi,nm} g_{nm} \right]$$

The IFDM representation of the energy balance is

$$\frac{dM_n^\kappa}{dt} = \frac{1}{V_n} \sum_m A_{nm} q_{nm}^\kappa + Q_{nm}^\kappa$$

where

$$M_n^\kappa = (1 - \phi_n) \rho_s C_s T + \phi_n \sum_\psi S_\psi \rho_\psi u_\psi^E$$

$$q_{nm}^\kappa = -\lambda \left(\frac{T_n - T_m}{D_{nm}} \right) + \sum_\psi h_\psi q_{\psi,nm}$$

and the Darcy flow equation is same as before.

Finite Element Method

Based on the principal of virtual work, the weak formulation of equation of conservation of momentum is given as (Bathe, 1997)

$$\int_V \delta \boldsymbol{\varepsilon}^T \boldsymbol{\sigma} dV - \int_V \delta \mathbf{u}^T \mathbf{b} dV - \int_S \delta \mathbf{u}^T \mathbf{t} dS = 0$$

We will use the standard finite element interpolations

$$\delta \mathbf{u} = \mathbf{N} \delta \mathbf{u}_a$$

and

$$\delta \boldsymbol{\varepsilon} = \mathbf{B} \delta \mathbf{u}_a$$

where \mathbf{N} denote the shape functions and \mathbf{B} the derivatives of shape functions.

Then using the modified effective stress law and interpolating the displacements using the shape functions we get

$$\begin{aligned} \left(\int_V \mathbf{B}^T \mathbf{D} \mathbf{B} dV \right) \Delta \mathbf{u}_a &= \int_V \mathbf{N}^T \mathbf{b} dV + \int_S \mathbf{N}^T \mathbf{t} dS \\ &- \left(\int_V \mathbf{B}^T \mathbf{D} \mathbf{B}_u dV \right) \Delta \mathbf{u}_u \\ &- \left((3K\alpha_T) \int_V \mathbf{B}^T \mathbf{m} \mathbf{N} \Delta T dV \right) \\ &- \int_V \mathbf{B}^T \boldsymbol{\sigma}''_0 dV + \int_V \mathbf{B}^T \boldsymbol{\alpha} \mathbf{m} \mathbf{N} p_0 dV \\ &+ \left(\int_V \mathbf{B}^T \boldsymbol{\alpha} \mathbf{m} \mathbf{N} \Delta p dV \right) \end{aligned}$$

where \mathbf{u}_u denotes the known displacements.

Time Discretization

Time is discretized as a first-order finite difference, and a fully implicit scheme is adopted (Pruess et. al., 1999) where the fluxes are expressed in the terms of the unknown thermodynamic parameters at time level $t^{k+1} = t^k + \Delta t$.

DUAL MESHES

Dual meshes are alternate representations of the same geometry. The dual mesh approach is natural for combining the IFDM and FEM discretization methods (Swenson et. al., 2004) and is used in our implementation. The Voronoï mesh (integrated finite difference mesh) is used for the flow analysis in TOUGH2, and its dual, the Delaunay mesh (finite element mesh) is used for the calculation of stress using FEM. Currently only the Cartesian duals, shown in Figure 2, are used in the implementation.

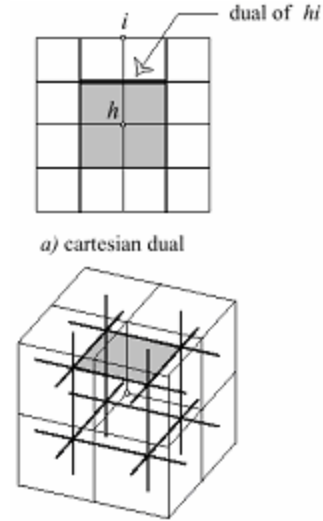


Figure 2: Duals for Cartesian meshes (Figure from Tonti, 2002)

Mesh Generation

In order to minimize the task of performing a stress analysis, the coordinates of the TOUGH2 cells (the Cartesian mesh) are read and used to create the finite element mesh (the Cartesian dual) automatically. This is done in a small translation program. At the present time, the TOUGH2 mesh must be a Cartesian (rectangular) grid. This simplifies the generation of the corresponding finite element mesh. In addition, the program that performs the mesh translation also is used to select the type of finite element (Brick 8 or Brick 20) used, to define the material properties, and to select the boundary conditions for the finite element stress model.

RESIDUAL FORM

The Newton-Raphson technique requires the residual formulation, which is shown below.

Mass Balance

$$R_n^{\kappa,i+1} = M_n^{\kappa,i+1} - M_n^{\kappa,i} - \frac{\Delta t}{V_n} \left[\sum_m A_{nm} q_{nm}^{\kappa,i+1} - V_n Q_{nm}^{\kappa} \right] + \theta_n^{\kappa,i+1} \left[\begin{array}{l} \left(\frac{\alpha - \phi_n^{i+1}}{K_S} \right) \left(\sum_{\psi} S_n^{\psi} \{ p_n^{\psi,i+1} - p_n^{\psi,i} \} \right) \\ - (\alpha - \phi_n^{i+1}) \alpha_T (T_n^{i+1} - T_n^i) \\ - (\phi_n^{i+1} - \phi_n^i) + \frac{\alpha}{V_n} \left(\sum_m A_{nm} \{ u_{nm}^{i+1} - u_{nm}^i \} \right) \end{array} \right]$$

Energy Balance

$$R_n^{\kappa,i+1} = M_n^{\kappa,i+1} - M_n^{\kappa,i} - \frac{\Delta t}{V_n} \left\{ \sum_m A_{nm} q_{nm}^{\kappa,i+1} + V_n Q_{nm}^{\kappa,i+1} \right\}$$

Momentum Balance

$$\mathbf{R} = \left[\int_V \mathbf{N}^T \mathbf{b} dV + \int_S \mathbf{N}^T \mathbf{t} dS \right] - \left[\int_V \mathbf{B}^T \boldsymbol{\sigma} dV - \left(\int_V \mathbf{B}^T \boldsymbol{\alpha} \mathbf{m} \mathbf{N} \mathbf{p} dV \right) \right]$$

SOLUTION TECHNIQUE

The discretized equations can be solved by the Newton-Raphson technique already implemented in TOUGH2. Expanding the residuals at $p+1^{\text{th}}$ iteration step in a Taylor series and retaining only the first order terms and setting the expansion equal to zero, we obtain (Pruess et al., 1999)

$$-\sum_N \frac{\partial R_n^{\kappa,i+1}}{\partial x_N} \Big|_p (x_{N,p+1} - x_{N,p}) = R_n^{\kappa,i+1}(x_{N,p})$$

The solution is achieved when the residual R becomes smaller than a predefined allowable error.

The term $-\sum_N \frac{\partial R_n^{\kappa,i+1}}{\partial x_N} \Big|_p$ is called as the Jacobian. It

can be represented as:

$$\begin{bmatrix} J_{FF} & J_{FS} \\ J_{SF} & J_{SS} \end{bmatrix} \begin{Bmatrix} p_F \\ u_S \end{Bmatrix} = \begin{Bmatrix} R_F \\ R_S \end{Bmatrix}$$

where the unknowns have been divided into the primary variables for the flow solution p_F and the displacements for the stress solution u_S .

To evaluate the Jacobian terms, we will denote the term in the equations of conservation of mass and energy using I and represented as

$$I(\phi, k, p, T, S_g, u) = f_1(\phi, k) f_2(p) f_3(T, S_g) f_4(u) C$$

where $f(\)$ represents functions independent of other variables.

Fluid Flow Equations J_{FF}

These represent the partial derivatives of the mass and energy balance residuals with respect to the TOUGH2 primary variables. These are evaluated numerically in TOUGH2 (Pruess, 1997). Due to the variable porosity and permeability there is addition to these terms as follows.

$$\frac{\partial I}{\partial X_i} = f_2 f_3 f_4 C \left(\frac{\partial f_1}{\partial \phi} \frac{\partial \phi}{\partial X_i} + \frac{\partial f_1}{\partial k} \frac{\partial k}{\partial X_i} \right) + \mathbf{T2} - \text{term}$$

where X_i is one of the TOUGH2 primary variables.

The addition to these terms can be evaluated as

$$J_{FF}^* = f_2 f_3 f_4 C \left(\frac{\partial f_1}{\partial \phi} \frac{\partial \phi}{\partial \sigma'_m} \frac{\partial \sigma'_m}{\partial X_i} + \frac{\partial f_1}{\partial k} \frac{\partial k}{\partial \phi} \frac{\partial \phi}{\partial \sigma'_m} \frac{\partial \sigma'_m}{\partial X_i} \right) = f_2 f_3 f_4 C \left(\frac{\partial f_1}{\partial \phi} + \frac{\partial f_1}{\partial k} \frac{\partial k}{\partial \phi} \right) \frac{\partial \phi}{\partial \sigma'_m} \frac{\partial \sigma'_m}{\partial X_i}$$

Also, there are additional terms in the conservation of mass equation which can be evaluated numerically. The partials with respect to the TOUGH2 primary variables represent the effects of changes in fluid pressure or fluid mass on the strain in the solids. Hence the poroelastic constants used while finding these partials are evaluated at constant stress condition.

Stress Equilibrium Equation J_{SS}

The Newton-Raphson formulation for the stress equilibrium equations is given as (Bathe, 1997)

$${}^{t+\Delta t} \mathbf{K}^{(i-1)} (\delta(\Delta u_a))^{(i)} = \left(\int_V \mathbf{N}^T \mathbf{b} dV + \int_S \mathbf{N}^T \mathbf{t} dS \right) - \left(\int_V \mathbf{B}^T \boldsymbol{\sigma} dV \right)^{(i-1)}$$

It can be seen that the stiffness matrix \mathbf{K} represents the Jacobian terms J_{SS} .

Solid to fluid coupling J_{FS}

These are the partial derivatives of terms in the flow equations with respect to displacements. The partials will be of the form

$$\frac{\partial I}{\partial u_n} = f_2 f_3 f_4 C \left(\frac{\partial f_1}{\partial \phi} + \frac{\partial f_1}{\partial k} \frac{\partial k}{\partial \phi} \right) \frac{\partial \phi}{\partial \sigma'_m} \frac{\partial \sigma'_m}{\partial u_n} + f_1 f_2 f_3 \frac{\partial f_4}{\partial u_n}$$

Since there are no displacement terms in the energy equation the second term on the right hand side will not exist in the residuals of it.

These terms represent the solid to fluid coupling. These are the partial derivatives with respect to the displacement while the pore pressure remains constant. Hence, the poroelastic constants used in the calculation of these are evaluated at drained condition which guarantees no change in pore pressure. For example, in the following partial we will use the drained bulk modulus K

$$\frac{\partial \sigma'_m}{\partial u_n} = \frac{\partial \sigma'_m}{\partial \varepsilon_v} \frac{\partial \varepsilon_v}{\partial u_n} = K \frac{\partial \varepsilon_v}{\partial u_n}$$

The terms in the conservation equations are expressed in terms of volumetric strain ε_v . To evaluate the partial of volumetric strain with respect to the displacement, assuming only Cartesian mesh, we express the volumetric strain using the IFDM concept as summation of the displacements of the confining areas, i.e.,

$$\varepsilon_v = \sum_m A_{nm} \{u_n - u_m\}$$

i.e. the volumetric strain is represented as the summation of displacements of individual areas confining the volume. Then, we can also write

$$\frac{\partial \varepsilon_v}{\partial u_n} = \sum_m A_{nm}$$

Hence we can represent the complete partial derivative as

$$\frac{\partial \sigma'_m}{\partial u_n} = K \sum_m A_{nm}$$

Fluid to solid coupling J_{SF}

The fluid to solid coupling is expressed through the change in the stresses due to the variation in the pore pressure. It is represented in the partials of the stress equilibrium equation with respect to the TOUGH2 primary variables. To evaluate these we represent the residual for the momentum equation as

$$\mathbf{R} = {}^{t+\Delta t} \mathbf{F}_{\text{ext}} - {}^{t+\Delta t} \mathbf{F}_{\text{int}}^{(i-1)}$$

The external forces will not vary with variation in the TOUGH2 primary variables hence we can write

$$\frac{\partial \mathbf{R}}{\partial X_i} = \frac{\partial}{\partial X_i} ({}^{t+\Delta t} \mathbf{F}_{\text{int}}^{(i-1)})$$

Each row in the Jacobian represents an equation for individual degree of freedom of a single node. The

corresponding internal forces can be calculated from stresses. The thermal and poroelastic stresses generated due to pore pressure and temperature changes in the cell affect only the normal stresses and do not vary the shear stresses, hence the residuals for internal forces due to shear stresses will be zero. We will limit the following discussion to the Cartesian meshes. The normal internal forces at each node can then be obtained, with an approximation, from the normal stress calculated at the node and the interface area between that TOUGH2 cell and the adjacent cell in that normal direction i.e.

$$F_{\text{int}}^l = -\sigma_{ll} A_l$$

where l denotes the normal direction. Then, using the expression for stress we can evaluate the residual with respect to the TOUGH2 primary variables easily.

CONCLUDING REMARKS

The general governing equations and related constitutive equations for a fully coupled THM process in porous media have been stated. IFDM representation of the coupled flow equation and FEM representation of coupled stress equilibrium equations is discussed. The ground work for integrating two discretization methods, IFDM and FEM used in TOUGH2 and Geocrack3D respectively, is presented. The dual mesh technique is used to achieve the integration of the meshes. The cross coupling is effectively achieved, restricting to Cartesian meshes, through parallel representation of volumetric strain and internal forces in both the codes. The variable porosity and permeability models are integrated into the derivations to complete the coupled formulation.

REFERENCES

- Bathe, Klaus-Jurgen, "Finite Element Procedures", Prentice Hall, ISBN 81-203-1075-6, 1997.
- Bear, J., and Bachmat, Y., "Introduction to modeling of transport phenomena in porous media", Netherlands: Kluwer Academic Publisher, 1991.
- Cosmi, F. and F. Di Marino, "A New Approach to Sintered Alloys Mechanical Behaviour Modelling", Dipartimento di Energetica, Università di Trieste, 34127 Trieste, Italy, 2002, manuscript obtained from the web, publication volume unknown, 2002.
- Davies, J.P., Davies, D.K., "Stress-Dependent Permeability: Characterization and Modeling", Society of Petroleum Engineers, SPE 56813, 1999
- Faust, C.R., Mercer, J.W., "Geothermal Reservoir Simulation 1. Mathematical Models for Liquid- and

Vapor-Dominated Hydrothermal Systems”, *Water Resources Research*, Vol. 15(1), pp. 23-30, 1979.

George, Paul-Louis, and Borouchaki, Housman, “Delaunay Triangulation and Meshing: Application to Finite Elements”, Hermes, Paris, ISBN 2-86601-692-0, 1998.

Hardeman, Brian, Sarang Kulkarni, Daniel Swenson, and Mark James, “Design of an Object-Oriented Finite Element Framework for Multi-Physics Problems”, 5th U.S. National Congress on Computation Mechanics, August 4-6, 1999.

Lewis, R.W., and Schrefler, B.A., “The Finite Element Method in the Deformation and Consolidation of Porous Media”, John Wiley & Sons, ISBN 0-471-92809-7, 1998.

Pruess, K., Oldenburg, C., and Moridis, G., “TOUGH2 User's Guide, Version 2.0”, Lawrence Berkeley National Laboratory Report LBNL-43134, Berkeley, CA, November 1999.

Rutqvist, J., and Tsang, Chin-Fu, “TOUGH-FLAC: A Numerical Simulator for Analysis of Coupled Thermal-Hydrologic-Mechanical Processes in Fractured and Porous Geological Media under Multi-Phase Flow Conditions,” Proceedings, TOUGH Symposium, 2003, Lawrence Berkeley National Laboratory, Berkeley, California, May 12-14, 2003.

Rutqvist, J., Borgesson, L., Chijimatsu, M., Nguyen, TS., Jing, L., Noorishad, J., Tsang, C-F, “Thermohydromechanics of partially saturated geological media: governing equations and formulation of four finite element models”, *I.J. of Rock Mechanics and Mining Sciences*, Vol. 38, pp. 105-127, 2001.

Rutqvist, J., Wu, Y-S. , Tsang C-F. , and Bodvarsson, G., “A modeling approach for analysis of coupled multiphase fluid flow, heat transfer, and deformation in fractured porous rock”, *I.J. of Rock Mechanics and Mining Sciences*, Vol. 39, pp. 429-442, 2002.

Swenson, D., Gosavi., S. Hardman, B., “Integration of Poroelasticity into TOUGH2” Proceedings, Twenty-Ninth Workshop on Geothermal Reservoir Engineering (Stanford University, Stanford, California), 2004.

Tonti, E., “A Direct Discrete Formulation of Field Laws: The Cell Method”, *Computer Modeling in Engineering & Sciences*, Vol. 2(2), 2001.

Wang, Herbert, “Theory of Linear Poroelasticity with Applications to Geomechanics and Hydrogeology”, Princeton University Press, ISBN 0-691-03746-9, 2000.

MODELING OF THE FAULT TYPE GEOTHERMAL RESERVOIR (DACHNY SITE, MUTNOVSKY GEOTHERMAL FIELD)

A.V. Kiryukhin¹, O.B. Vereina²

¹-Institute of Volcanology and Seismology FEB RAS
Piip- 9, Petropavlovsk-Kamchatsky, 683006
e-mail: *avk2@kcs.iks.ru*

²- Geological Institute RAS
Pyzhevsky per. 7, Moscow, 119017
e-mail: *vega-iris@mail.ru*

ABSTRACT

Fault-type geothermal fields are common in recent volcanism areas. The recent model of the Dachny site, Mutnovsky geothermal field (Kamchatka, Russia) represented a single fault production zone with the heat exchange to ambient rocks expressed in terms of “confining beds TOUGH2 option” (Kiryukhin, Stanford Workshop 2004) was improved by add of the 5-layer external grid connected to the production zone. Model calibration against 2002-2004 exploitation data and modeling of the possible future scenarios to maintain sustainability of the 50 MWe PP (Dachny) discussed.

INTRODUCTION

The history of numerical models applications to Mutnovsky geothermal field started from large-scale 3D rectangular models (Kiryukhin, 1992, 1996) which were designed to understand heat and mass transfer processes in geothermal reservoir as a whole, and to forecast possible exploitation scenarios. This model (1996) consist of 500 elements 500 x 500 x 500 m³ each with total volume of 5 x 5 x 2.5 km³ used to forecast 20 year period of exploitation based on existing wells and it shown 44 MWe as a minimum yield of the field. Later this model was used by WestJec (Japan) company to do feasibility study of the Mutnovsky PP (1997).

Since the fault geometry of specific production zones distribution reveals (Kiryukhin et al, 1998), and central part of the Dachny Site proved to be a single-fault type geothermal field (the Main Production Zone in Dachny site strikes north-north-east and dip east-east-south at the angle 60°), next development of numerical modeling applications to this field was targeted to description of specific geometry of the Main Production Zone (Kiryukhin et al, 2003, 2004, 2005).

Reservoir modeling also used as an instrument for optimal design of the exploitation load of the Dachny Site in Mutnovsky geothermal field, where SC “Geotherm” having put 50 MWe PP into operation in October 2002.

MODEL SETUP

Grid generation

Geothermal reservoir is represented as association of the Main Production Zone (MPZ) reservoir and Host Rocks (HR) reservoir (Fig.1). Both reservoirs grids coincide with the Basic Grid (grid related to existing wells) in horizontal projection (Fig.2).

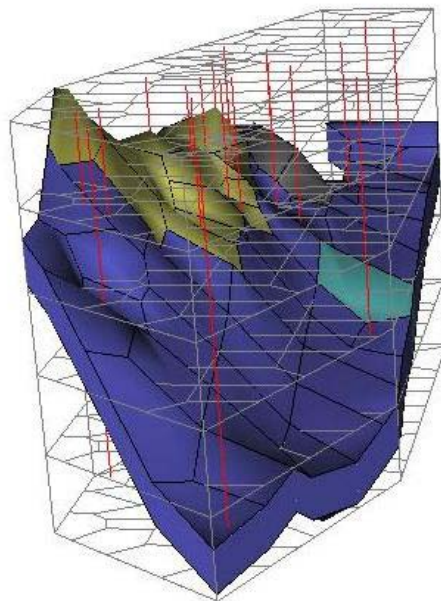


Figure. 1. Geometry of the 3-D numerical model of the Main Production Zone of the Dachny Site Mutnovsky geothermal field.

Basic Grid created on AMESH preprocessor (1999), which generated TOUGH2 mesh file in terms of horizontal connections parameters d_1 , d_2 , AREA.

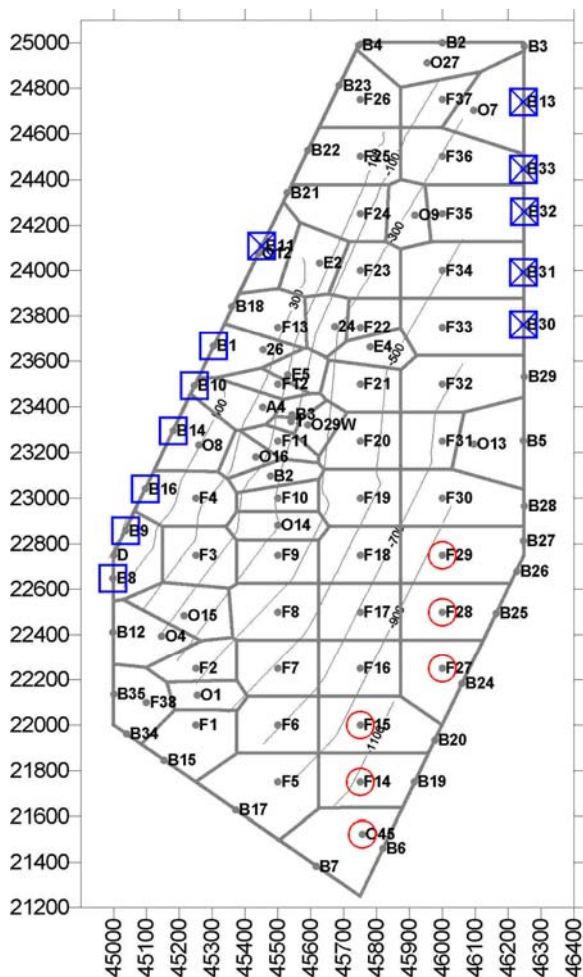


Figure. 2. Basic Grid of the reservoir. Counters elevations (m.a.s.l.) correspond to the top of the Main Production Zone. Open circles - sources assigned in the model, squares – inactive boundary elements valid for natural state stage (steam discharge), crossed squares- inactive boundary elements valid for natural state and exploitation (liquid discharge).

Main Production Zone subdivided on two reservoirs: A-reservoir and B-reservoir. A-reservoir corresponds to the Main Production Zone itself with averaged vertical thickness 240 m (actual thickness 120 m), each element of which is located at the specified elevation corresponding to the roof of the Main Production Zone (Figs.1 and 2). B-reservoir correspond to diorite intrusion contact permeability zones, adjacent to Main production zone. Additional correction procedure was applied to mesh file to specify vertical component of grid connection, including more accurate BETAX presentation

(format F20.14 instead of F10.4) to avoid “parasitic circulation” in the model (according to K. Pruess, pers. com., 1998) (Fig.3).

Host Rocks (HR) grid generated as a 5-layer system (at elevations +750, +250, -250, -750, -1250 m), each element of which connected to the Main Production Zone (MPZ) element, if such MPZ element center occur inside of HR element volume.

Basic Grid include 24 existing wells, 39 additional interior elements (F-elements and D-element) and 12 boundary (inactive) elements (B-elements). Total number of the elements of the model is 378 (Fig.1).

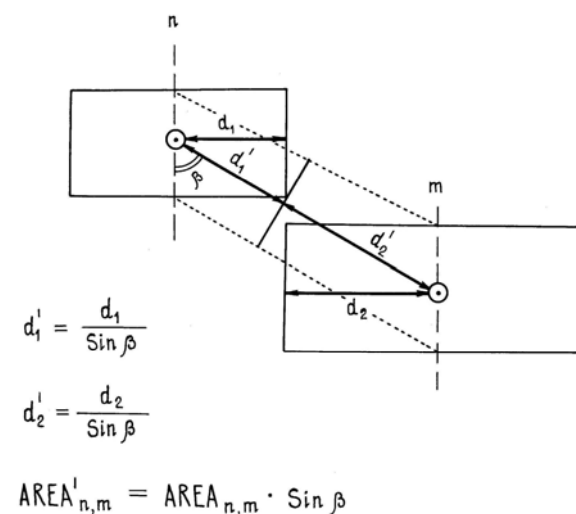


Figure. 3. Mesh parameters (d_1 , d_2 , AREA) corrections applied to A-MESH output.

Sinks/Sources, Permeability Distribution and Boundary Conditions

Figs. 2 and 4 demonstrates grid and permeability distributions assigned to the Main Production Zone reservoir of the model. «Sources» in the model are O45, F27, F28, F14, F15, F29 (9 kg/s, 1390 kJ/kg), permeability and rock properties assign based on the previous natural state modeling results (1996-2005).

Boundary conditions assign in B-elements (Fig.2). Liquid discharge elements assigned as $P=\text{const}$ and $T=\text{const}$ and are valid anytime in the model. These elements simulate liquid discharge from hydrothermal system to Verkhne-Zhirovsky natural discharge area and into ambient aquifers. Steam discharge elements assigned as $P=\text{const}$ and $S=\text{const}$, and valid only for natural state modeling. Those elements correspond to unsaturated zone (Dachny steam discharge area), so they switch to “no flow”

found no satisfactory match in key calibration elements (modeling pressures lowering), if Host Rock permeability increases above 10^{-16} m² (that mean permeable production volume of the central part of the Dachny Site is basically limited to the Main Production Zone space).

MODELING OF THE EXPLOITATION (MAIN PRODUCTION ZONE OF THE DACHNY SITE)

Data for Model Calibration

Exploitation model calibration is based mainly on the data received from initial production tests of wells 016, 26, 029W, 4E and 5E (used for PI estimations, Table 1), operating wellhead pressure of the exploitation wells (Fig.5) and data of the total steam and total separate production from Mutnovsky PP separator (wells 016, 26, 029W, 4E, 5E, A2, O37 and 24) (Fig.6). There is no reliable data for individual exploitation wells production history. Pressure monitoring in well O12 (0.75 bar drop per year) rather characterized Host Rocks reservoir conditions, than production zone.

While production took place, individual wells wellhead pressures (Fig.5) and PP separator pressures (Fig. 6) gradually decline. From 5.4 bars to 5.0 bars (ati) at PP separator during 1.5-year exploitation period) (Fig.6).

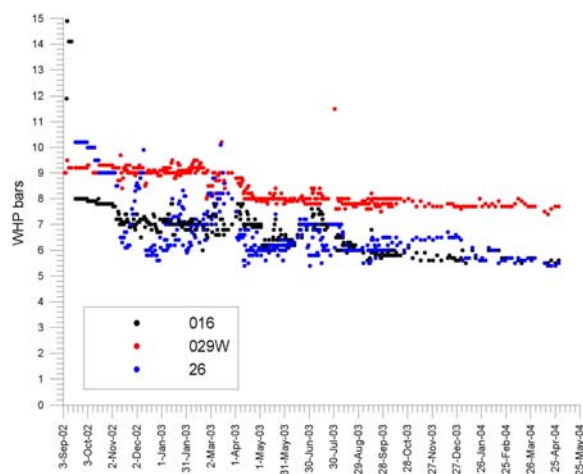


Figure. 5. Well Head Pressure (WHP, bars (ati)) variations in exploitation wells of the Dachny site Mutnovsky geothermal field (SC “Geotherm”, 2004).

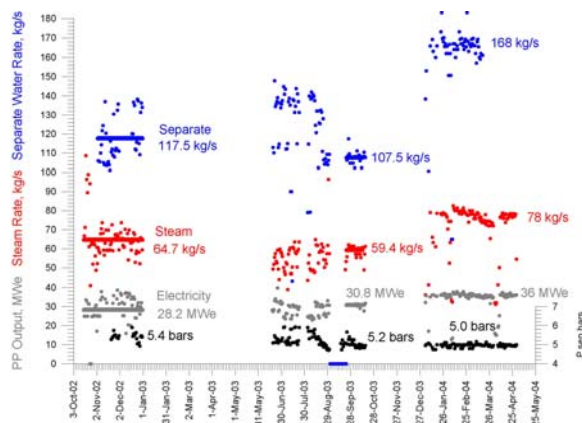


Figure. 6. Mutnovsky PP electricity output, total steam and separate water production, and separator pressure (bars, ati) (SC “Geotherm”, 2004).

Total steam production varies from 64.9 kg/s (2002) to 59.4 kg/s (2003) and to 78 kg/s (2004), the total separate production varies from 117.5 kg/s (2002) to 107.5 kg/s (2003) and to 168 kg/s (2004). Wells A2, 24 (Dachny) and O37 (Verkhne-Mutnovsky) contribution (steam – 3.5 kg/s (2003), 18.3 kg/s (2004), separate - 15 kg/s (2003), 77.7 kg/s (2004)). Hence, the total production of wells (wells 016, 26, 029W, 4E and 5E) estimated as 64.9 kg/s (2002), 55.9 kg/s (2003), and 59.7 kg/s (2004) (steam at PP separator at 5.0 – 5.4 bars (ati)), and 117.5 kg/s (2002), 104.0 kg/s (2003) and 90.3 kg/s (2004) (separate at PP).

Exploitation Model Calibration

Compressibility coefficient assign $5.0 \cdot 10^{-7}$ Pa⁻¹ in the Main Production Zone reservoir and $2.0 \cdot 10^{-8}$ Pa⁻¹ in the Host Rock reservoir. Well 027 (North Reinjection Site) assign as reinjection with 150 kg/s rate and enthalpy of 700 kJ/kg. The switch to “no flow” boundary conditions during exploitation implemented in B1, B10, B14, B16, B9, B8 boundary elements of the model. Production wells specified at wellhead pressure conditions corresponding to the PI_0 data from Table 1. Two-phase wells were switched off, if mass flowrate dropped less than 5 kg/s, steam wells were switched off, if mass flowrate dropped below 2 kg/s.

Model calibration targeted to match total steam (referenced to 5.2 separation pressure) and total separate production data against modeling (wells 016, 26, 029W, 4E and 5E) data. Actual production data estimated as 64.9 kg/s (2002), 55.9 kg/s (2003), and 59.7 kg/s (2004) (steam at PP separator at 5.0 – 5.4 bars (ati)), and 117.5 kg/s (2002), 104.0 kg/s (2003) and 90.3 kg/s (2004) (separate at PP).

Initial model scenario #1 show good steam production match (56.0 kg/s vs 59.7 kg/s), and not satisfactory separate production match by the end of 1.5-year exploitation period (Fig. 7). Separate production decline more rapidly (30 kg/s), compare to actual data with additional wells correction (90.3 kg/s) (Fig.7).

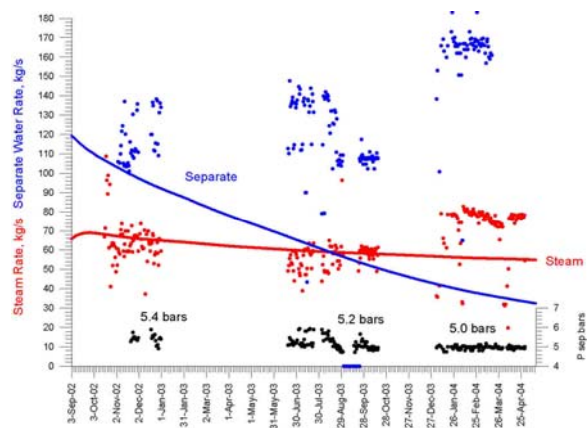


Figure. 7. Model match (Initial scenario #1): modeling steam and separate production from wells 016, 26, E4, 029W, E5 (referenced to 5.2 separation pressure, ati) against total PP production during exploitation of the Dachny site. Dots – PP exploitation data (Fig.6), solid line – modeling results.

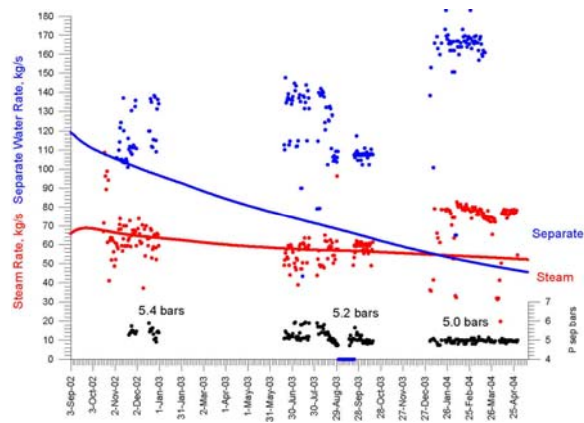


Figure. 8. Model match (scenario #2): modeling steam and separate production from wells 016, 26, E4, 029W, E5 (referenced to 5.2 separation pressure, ati) against total PP production during exploitation of the Dachny site. Dots – PP exploitation data (Fig.6), solid line – modeling results.

Scenario #2 assume possibility of the lateral cold water recharge to the Main Production Zone reservoir from Host Rock reservoir by assuming elimination

production zone boundaries under exploitation conditions (Host Rock permeability assign $2 \cdot 10^{-15} \text{ m}^2$). The explanation of the physical meaning of such boundary conditions switch under exploitation conditions explained in Geothermics Vol.25 #1 p.85 (Kiryukhin, 1996), when possibilities of different exploitation scenarios of the Mutnovsky field were discussed.

In case of such “lateral cold water recharge” (scenario #2) good steam production match (54.0 kg/s vs 59.7 kg/s), and more satisfactory separate production match (52 kg/s vs 90.3 kg/s) by the end of 1.5-year exploitation period obtained (Fig. 8).

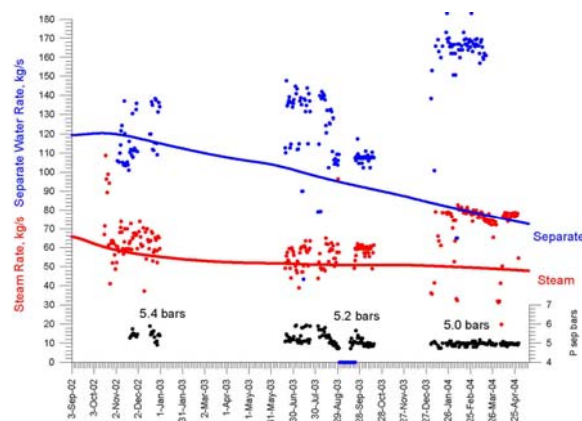


Figure. 9. Model matches (scenario #3): modeling steam and separate production from wells 016, 26, E4, 029W, E5 (referenced to 5.2 separation pressure, ati) against total PP production during exploitation of the Dachny site. Dots – PP exploitation data (Fig.6), solid line – modeling results.

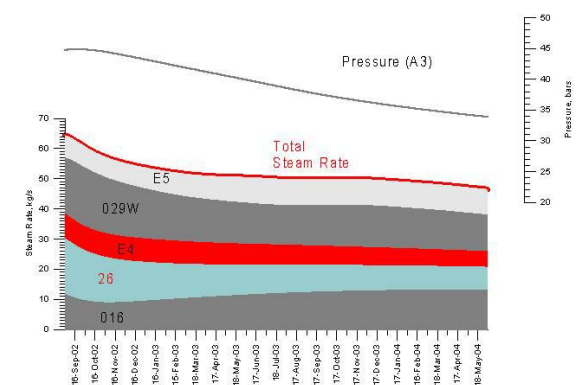


Figure. 10. Scenario #3: modeling of the steam production at 7 bars (wells 016, 26, E4, 029W, E5) and reservoir pressure (A3 model element) response in the Dachny site.

Scenario #3 assume possibility of vertical downflow of the cold water recharge to the Main Production Zone reservoir directly from abandoned wells of the Dachny Site Mutnovsky geothermal field. Those wells are basically characterized by poor casing cementing. Downflows from local cold groundwater aquifers with water levels near surface into geothermal reservoir with levels –600 m through abandoned wells casings is possible and really observed in some wells (O11, O42, etc). High possibility of such scenario un-directly confirmed by high fractions of meteoric gases observed in production wells during exploitation (Kiryukhin et al, 2005). To model such possibility additional cold water sources were assigned in the elements E4, E5, O29, O16, B2, where abandoned wells and significant pressure drop co-exist. Sources parameters assign: rates 12.0 kg/s (total downflow rate 60 kg/s), enthalpies 420 kJ/kg.

In case of “abandoned wells recharge” scenario #3 relatively good steam production match (50.0 kg/s vs 59.7 kg/s), and relatively satisfactory separate production match (82 kg/s vs 90.3 kg/s) by the end of 1.5-year exploitation period obtained (Figs. 9 and 10). Note some increase of actual production rates by 2004 may caused by wellhead pressures decline of production wells (Fig.5), which not accounted in the model.

F-wells Exploitation Scenarios

Mutnovsky 50 MWe PP needs 95 kg/s of 7 bars steam in stable terms during exploitation period. Previously obtained modeling results show existing wells (O16, 26, O29W, E4 и E5) are not able to maintain steam supply for PP needs. So, additional production wells needed to maintain sustainable PP operations.

Study of the possibility of sustainable steam production (from model elements F16, F17, F18, F19, F20, F29 and F30) was performed. Corresponding F-wells locations and constructions are shown in Fig.11 and Table 2. F-wells targeted to the high temperature upflow zone in the south-eastern part of the Main Production Zone. All F-wells suggested deviated wells, drilled from positions of existing wells O13 and O10 correspondingly (Fig. 11). Wellbore diameter assumed to be 0.246 m until depth 900 m, and then 0.168 m. Time-schedule of the F-wells putting into operation is the following: F20 (immediately), F19 (1 year), F18 (2 years), F30 (3 years), F29 (4 years), F17 (6 years), F16 (8 years).

Modeling of the steam production from additional F-wells confirm possibility of the 97.8 kg/s steam production in average terms during 10-year exploitation period, which is sufficient for 50 MWe

Power Plant production (Fig. 12) for scenario #1. In case of cold water recharge inflows scenarios #2 and #3 – 96.3 kg/s and 86.7 kg/s steam production available in average terms during 10-year exploitation period.

Although scenario #3 (“abandoned wells recharge”) seems as the most probable of discussed above, there is possibility to switch to scenario #1, in case of isolation of the Main Production Zone reservoir from the leakage above by proper cementing of all abandoned wells.

Modeling of various reinjection regimes (based on scenario #1) show there is no important where reinjection took place (North or South Reinjection Sites) and whether reinject or not to reinject during first 10-years exploitation period (Fig.13). The situation is changes significantly by 10-year of exploitation. At this time reservoir boiling may induce significant pressure drop, with magnitude depending of reinjection regime. The optimal strategy was found in the model is - to reinject no less then 75 kg/s in the South Reinjection Site which maintain sustainable conditions for 50 MWe PP during 20-year exploitation period (Fig. 13).

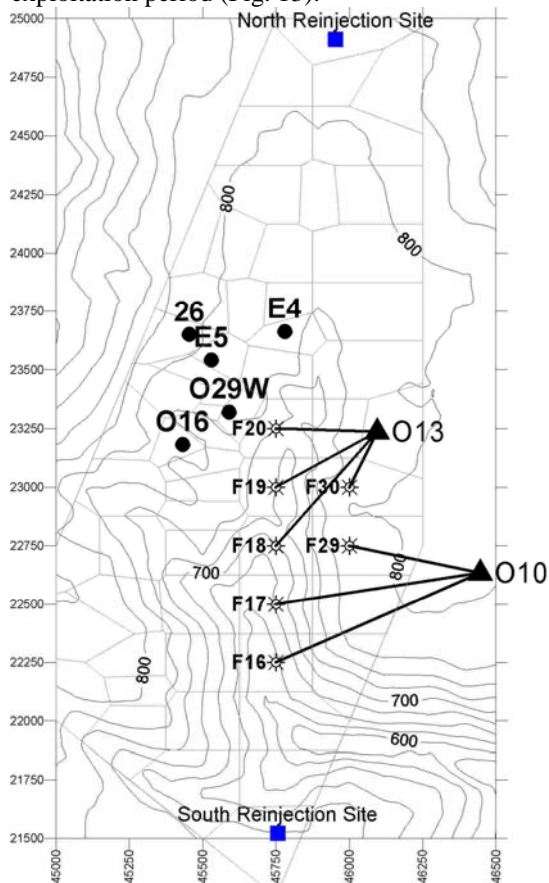


Figure. 11. Existing operating wells: solid circles. Additional F-wells: drilling targets (stars) and drilling rig positions (triangles). Reinjection Sites – squares.

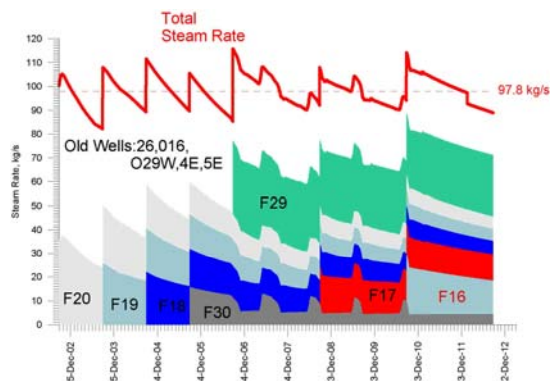


Figure. 12. Scenario #1. Modeling of the steam production (old wells: 016, 26, E4, 029W, E5 and additional F-wells) in the Main production fault zone Dachny Site. ReInjection 150 kg/s (South polygon) assign.

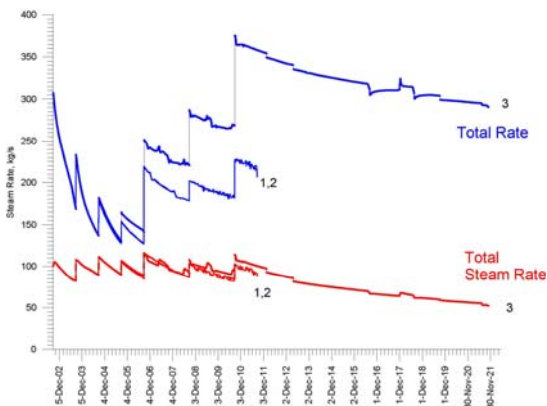


Figure. 13. Influence of reinjection on steam production sustainability of the Main Production Zone of the Dachny Site (based on model scenario #1): 1 - no reinjection, 2 - reinjection 150 kg/s in well O27 (North Reinjection Site), 3- reinjection 150 kg/s (South Reinjection Site). Upper graphs - total production rates, lower graphs - steam production at 7 bars.

CONCLUSIONS

1. The previous model of the fault type Main Production Zone of the Dachny Site Mutnovsky geothermal field (Kirjukhin, 2004) was up-dated based on TOUGH2V2.0 coupled wellbore flow option; and by introducing the Host Rocks as a 5-layers array, with the elements directly connected to corresponding elements of the Main Production Zone (which occurs along 60° dip fault zone).

2. Model calibration based on 1.5-year exploitation data reveals the most probable conditions during exploitation is downflow recharge (60 kg/s, 420

kJ/kg) into the Main Production Zone reservoir. This scenario explained change of the total steam and separate production from group of the wells (016, 26, E4, 029W, E5).

3. Modeling of the additional F-wells (wells to drill in the south-east portion of the MPZ) exploitation scenario confirmed possibility of the 97.8 kg/s steam production in average terms during 10-year exploitation period (which is sufficient for 50 MWe Power Plant production), if cold water inflows to production zone will be neutralized.

4. In terms of long-term exploitation (more than 10 years) the importance of reinjection strategy increase. Modeling shows that North Site reinjection has no effect on production characteristics of the field, and by 10-year of exploitation reservoir boiling may induce significant pressure drop, which quenches some of production wells. In opposite to this, reinjection into the South Site of the field (at least 75 kg/s, 700 kJ/kg) show positive influence on the total steam productivity, which may extend sustainable production for at least 20-year exploitation period.

5. In terms of stable conditions of steam supply to 50 MWe Mutnovsky Power Plant and future extension of PP's capacity - the possibility of use Verkhne-Mutnovsky site located 1.5-2.5 km north-east from Dachny site should be analyzed (Fig.13). This study is on-going.

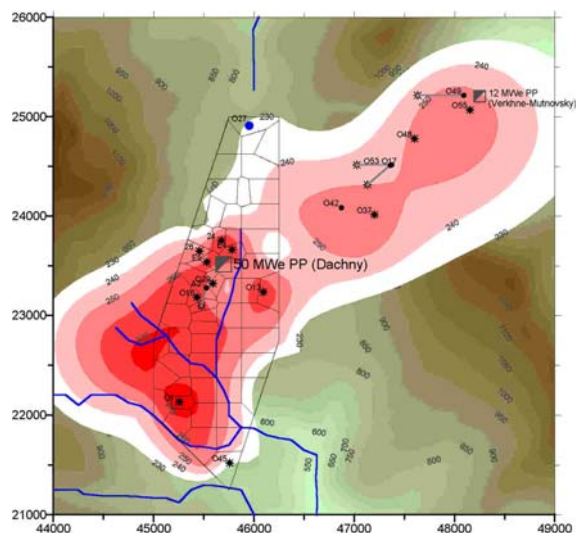


Figure. 14. Mutnovsky geothermal field in the limits of the model-1996, grid corresponding to Main Production Zone reservoir, topo counters, temperature distributions at -250 m.a.s.l., and Power Plants positions are shown too. Production wells – filled circles, feed zones projections – stars.

ACKNOWLEDGEMENTS

The authors express gratitude to SC "Geoterm" staff: General Director V.E. Luzin, Chief Manager V.M. Morgun, hydrogeologists I.I. Chernev and L.K. Moskalev for helpful discussion and data support; Kamchatka EMSD GS RAS scientist D.V. Droznin for computer graphics support. This work has been supported by Russian Basic Sciences Foundation grant 03-05-65373, and Russia Ministry of Education Grant 02.01.023.

REFERENCES

- Z.P. Aunzo, G. Bjornson, G.S. Bodvarsson (1991), Wellbore models GWELL, GWNACL, and HOLA. Users Guide // Draft, 81 p.
- S.G. Assaulov, N.P. Assaulova (1996) Mutnovsky geothermal field, DATABASE 1996 (Copy presented to WestJEC for implementation of the Kamchatka Feasibility Study).
- Feasibility Study of the Integrated Power and Heating Plant System Sustained by the Mutnovsky Geothermal Field in Kamchatka (1997) // West JEC, Report for EBRD.
- Geothermal and Geochemical Studies of High-Temperature Hydrothermal (Using the Pattern of the Mutnovsky Geothermal Field). Moscow, Science, 1986, p. 305.
- K. Goko (2000) Structure and hydrology of the Ogiri field, West Kirishima geothermal area, Kyushu, Japan. Geothermics 29 (2), 127-149.
- C. Haukwa (1999) AMESH A mesh creating program for the Integral Finite Difference Method // LBNL Users Manual, 54 p.
- A.V. Kiryukhin (1992) Progress Report on Modeling Studies.... LBL-32729, p. 21.
- A.V. Kiryukhin (1996) Modeling Studies: Dachny Geothermal Reservoir, Kamchatka, Russia // Geothermics, v.26, No.1, 1996, pp.63-90.
- A.V. Kiryukhin, M. Takahashi, A. Polyakov, M. Lesnykh and O. Bataeva (1998) Studies of the Mutnovsky Geothermal Field Water Recharge Conditions with the Use of Data on Oxygen (O^{18}) and Hydrogen (D) Isotopy // Volcanology and Seismology, № 4-5, pp.54-62.
- A.V. Kiryukhin (2003) Modeling of the Exploitation of the Mutnovsky Geothermal Field in Relation to 50 MWe PP steam supply // International Geothermal Workshop, Russia, Sochi, 6-10 Oct. 2003, 91 p.
- A.V. Kiryukhin (2004) Modeling of the Exploitation of the Mutnovsky Geothermal Field in Connection to 50 MWe PP steam supply // PROCEEDINGS, Twenty-Ninth Workshop on Geothermal Reservoir Engineering Stanford University, Stanford, California, January 26-28, 8p.
- A.V. Kiryukhin (2004) MODELING OF THE MUTNOVSKY GEOTHERMAL FIELD (DACHNY) IN APPLICATION TO OPTIMAL EXPLOITATION LOAD DESIGN // Geothermal Resources Council, Palm Springs, CA, p.595-597.
- A.V. Kiryukhin, V.L. Leonov, I.B. Slovtsov, I.F. Delemen, M.Y. Puzankov, A.Y. Polyakov, G.O. Ivanysko, O.P. Bataeva, M.E. Zelensky (2005) Modeling of the exploitation of the Dachny geothermal field in relation to steam supply to Mutnovsky PP// Volcanology and Seismology Journal, 50 p. (in Russian)
- A.V. Kiryukhin (2005) Modeling of the Dachny Site Mutnovsky Geothermal Field (Kamchatka, Russia) in Connection with the Problem of Steam Supply for 50 MWe Power Plant // Proceedings World Geothermal Congress 2005, 12 p.
- A.V. Kiryukhin, M.Y. Puzankov, I.B. Slovtsov, S.B. Bortnikova, M.E. Zelensky, A.Y. Polyakov (2005) THC-Modeling of the Secondary Mineral Deposition in Production Zones of Geothermal Fields // Volcanology and Seismology Journal, 30 p. (in Russian)
- V.L. Leonov (1989) Structural Conditions of Localization of high temperature hydrotherms, Moscow, Nauka publ., 104 p. (in Russian).
- K. Pruess (1991) TOUGH2 - a general purpose numerical simulator for multiphase fluid and heat flow, Lawrence Berkeley Lab. Report, LBL-29400, Berkeley, California, 102 p.
- K. Pruess (1999) TOUGH2 Users Guide, Version 2.0 // LBL-43134.
- G.A. Rosly (2003) Main Results of Exploitation Drilling // Report on AO Geoterm Workshop, Petropavlovsk-Kamchatsky, 35 p.
- O.B. Vereina (2003) Natural State Modeling of the Mutnovsky Geothermal Field, Kamchatka, Russia // UNU Geothermal Training Program Report #21, 22 p.

NUMERICAL SIMULATION OF LIQUID AND TWO-PHASE TRACERS IN A PART OF THE KAKKONDA GEOTHERMAL FIELD, JAPAN

Kei Sato^{*1}, Yukihiro Sakagawa^{*1} and Takemi Omiya^{*2}

^{*1} JMC Geothermal Engineering Co., Ltd., 101-1 Hosoyachi, Ukai, Takizawa, Iwate, Japan.

^{*2} Tohoku Hydropower & Geothermal Energy Co., Inc., 1-7-25, Chuo-dori, Morioka, Iwate, Japan
e-mail: ksato@geothermal.co.jp

ABSTRACT

We simulated the injectate flow based on the results from a tracer test to optimize an appropriate reinjection rate and deduce the physical condition of the Kakkonda geothermal reservoir. Two-phase tracers (methanol and ethanol) and liquid-phase tracer (toluenesulfonate, xylenesulfonate and KI) were injected in the test, and the different return curves were observed for each tracer. The simulator TOUGH2-EOS7R was used for the modeling of tracer flow in the reservoir. The numerical model was focused on a part of the reservoir which included an injection well and three production wells. Calculated tracer return curves, which were similar to observed ones, were obtained by adjusting the volume fraction of fracture and gas saturation; the small volume fraction of fracture (<1%) was required for short tracer arrival time, and the distribution of water saturation (less than 0.7) was required to reproduce the difference in peak time of the return curves between two-phase and liquid-phase tracers. After completing the matching of the tracer return curves, the prediction of the reservoir response to various reinjection rate was calculated. The results provided useful information for optimizing the reinjection rate for effective heat extraction.

INTRODUCTION

Tracer test has been a standard tool for tracing fluid flow within geothermal reservoirs (e.g. Grant et al., 1982). The analysis of tracer test provides not only reservoir characteristics, but also practical information for optimizing reinjection strategies. Furthermore, the future reservoir performances can be calculated by using numerical simulation with tracer flow. Pruess (2002), and Trew et al. (2001) reported mathematical representation and thermodynamics properties of tracers. Shook (2001) presented a method of predicting thermal breakthrough from numerical tracer test analysis, and Axelsson et al. (2001) predicted temperature decline for some cases of long-term reinjection.



Figure 1. location of the Kakkonda geothermal Field.

The Kakkonda geothermal field is located in northeastern Honshu, Japan. Tohoku Hydropower and Geothermal Energy Co., Ltd currently provides steam to power stations unit 1 (50MWe) and to unit 2 (30MWe). The Kakkonda hydrothermal system consists of a shallow and a deep reservoir, which are hydraulically connected but otherwise with different characteristics (Hanano, 1998). The shallow part is permeable reservoir of 230-260 °C. The deep part is less permeable reservoir of 330-350 °C. Tracer tests have been conducted to several reinjection wells in this field. The analysis of the tracer test has been used in the design and management of production and reinjection operations. In 2001, two-phase tracers (methanol and ethanol) and liquid phase tracers (toluenesulfonate, xylenesulfonate and KI) were injected into a well having an injection point in the deep reservoir (2,700m depth) (Hishi et al., 2001). Tracers were returned from four production wells near the injection well. As Shown in Table 1, tracers returned at 4-5 hours to the nearest production well P-1. Two-phase tracers returned faster than liquid-phase tracers at the production well P-2.

Table. 1. Results of tracer test at the Kakkonda geothermal field

Injection Well	Tracers	Production Well	Recovery (%)		Initial detection Time(h)
I-1	methanol 270kg + ethanol 270kg + toluenesulfonate 100kg + xylenesulfonate 100kg + KI 460kg	P-1	methanol	26	4
			ethanol	19	4
			toluenesulfonate	7.5	5
			xylenesulfonate	6.9	5
			KI	34	5
		P-2	methanol	5.9	36
			ethanol	3.4	30
			toluenesulfonate	1.4	77
			xylenesulfonate	1.4	77
		P-3	KI	4.4	78
			methanol	-	-
			ethanol	-	-
			toluenesulfonate	1.1	72
		P-4	xylenesulfonate	-	-
			KI	1.8	73
			methanol	-	-
ethanol	-		-		
toluenesulfonate	-		-		
			xylenesulfonate	-	-
			KI	0.2	21

In this paper, the numerical reservoir simulation of tracer flow in the Kakkonda field is presented. Firstly, we describe the expression of phase partitioning behavior of alcohols for application to the geothermal reservoir simulator TOUGH2 (Pruess et al., 1999). Secondly, the future reservoir performance was simulated with various reinjection rates after the matching of tracer return curves.

THE NUMERICAL MODEL

Description of the Model

Injectate flow within a part of the reservoir was simulated by using the data from the tracer test with the PC version of TOUGH2. To simplify the calculation, we limited a simulated region to a part of the reservoir including one reinjection well (I-1), and three production wells (P-1, P-2 and P-3) where tracers were detected. Although a tracer was detected in production well(P-4), the well was excluded from the model because only the tracer KI was detected and its recovery ratio was very low(<0.2%). We employed a three-dimensional model because of the distribution of the wells. The model specification and the grid geometry are shown in Table 2 and Figure 2, respectively.

Other tracer tests and changes in chloride concentrations indicate that the deep reservoir including simulated region is connected to the shallow reservoir. Observed enthalpies of all production wells in the simulated region had decreased gradually because of the low-enthalpy fluid flow from the shallow reservoir. To create the

same condition in the simulation, mass sources of the low-enthalpy were added to the upper region of the numerical model.

Table 2. Specifications of the model

Reservoir Properties	
Fracture permeability	$10 \times 10^{-15} \text{ m}^2$
Matrix permeability	$1 \times 10^{-18} \text{ m}^2$
Fracture porosity	1%
Matrix porosity	1%
Fracture spacing	50m
Relative permeability	
Corey's curve(1954)	$S_{gr}=0.05, S_{Ir}=0.3$
Initial condition	
Pressure	20MPa
Temperature	340 °C
Boundary condition -Dirichlet conditions	
Top Pressure	15.5MPa
Temperature	340 °C
Bottom Pressure	23.2MPa
Temperature	340 °C
Reinjection rate during tracer test	20t/h
Injection rates of tracers	
Methanol	270kg/3min.
Toluenesulfonate	100kg/3min.
Mol diffusivity in the gas phase	
Methanol	$1.52 \times 10^{-5} \text{ m}^2/\text{s}$ (at 15 °C, Ohe,2002)
Mol diffusivities in the aqueous phase	
Methanol	$1.28 \times 10^{-9} \text{ m}^2/\text{s}$ (at 15 °C and 1atm, Ohe,2002)
Toluenesulfonate	$1.0 \times 10^{-9} \text{ m}^2/\text{s}$ (general mol diffusivity of solvents in water)

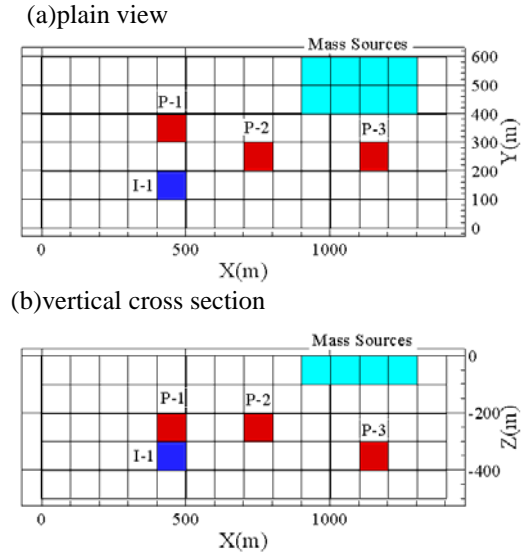


Figure 2. Geometry of 3D model in a part of the Kakkonda geothermal field. Red Blocks and Blue Blocks indicate feed points and injection points, respectively.

Because initial detection time of tracers were very fast (the fastest detection time was 4 hours for methanol at the nearest producer P-1), fractured-porous media double-porosity (Warren and Root, 1963) was used in the simulation.

Deliverability model, i.e., production occurs against specified wellhead pressure, was used in the simulation. Tabular data of various flowing bottomhole pressures vs. flow rates and flowing enthalpies were calculated in advance by the geothermal wellbore simulator WELLSIM (GENZL, 1997). Same tabular data was used for the three production wells because these production wells have almost the same feed zone depths and casing programs. Productivity index was adjusted to match calculated production rates with measured production rates.

Figure 3 shows production and reinjection rates used in the numerical simulation. ReInjection was continued over periods of one month before the tracer injection and 10 days after that. We chose methanol as a two-phase tracer because of its relatively high recovery compared to ethanol, and toluenesulfonate as a liquid-phase tracer because of its relatively clear return curves compared to that of KI. 270kg of methanol and 100kg of toluenesulfonate were injected simultaneously within 3 minutes.

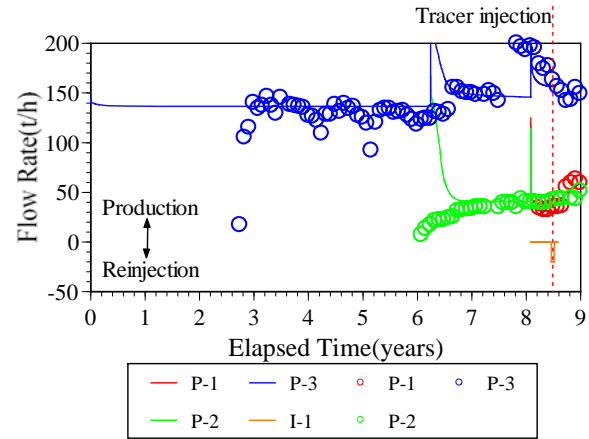


Figure 3. Production and reinjection rates in the numerical simulation. open circles: field data, solid lines: flow rates in the numerical simulation.

The simulator TOUGH2-EOS7R was used in the reservoir simulation. EOS7R includes physical properties of water, brine, radionuclide 1, radionuclide 2 and air. Methanol and toluenesulfonate were treated as Radionuclide 1 and 2, respectively. The Henry's law constant of methanol and toluenesulfonate were assumed to be 50MPa, as described later, and 10^{-5} Pa, respectively. Toluenesulfonate was assumed to be partitioned only in liquid phase.

The model was calibrated in two stages; at first, by matching the flowing enthalpy and then by matching the tracer return curves.

Modeling of the Phase Partitioning Behaviors of Methanol

TOUGH2 contains the various Equation-of-State (EOS) modules. Its tracer modeling is designed with EOS7R in which water, brine, radionuclide 1 and radionuclide 2 and air are treated. In this module, two radionuclides can be considered to be water soluble as well as volatile. The partial pressure of the gas P_{Rn} is calculated according to Henry's law with given the mol fraction of dissolved Radionuclide in the aqueous phase x_{aq}^{Rn} and the Henry's law constant

$$K_h : \quad P_{Rn} = K_h x_{aq}^{Rn} \quad (1)$$

Henry's law can be used for the gases less soluble in water at low partial pressure similar to the ideal gas, such as O_2 , H_2 , CO_2 and CH_4 . Henry's law cannot be used for methanol due to its polar character. In case of methanol, an activity coefficient γ_i must be used to describe the partial pressure P_i in the gas phase (Ohe, 2002):

$$P_i = \gamma_i P_i^* x_i \quad (2)$$

where P_i^* is saturated vapor pressure and x_i is the mol fraction of dissolved methanol in the aqueous phase. Using (1) and (2) together, we expressed the Henry's law constant as a product of an activity coefficient and saturated vapor pressure.

$$K_h = \gamma_i P_i^* \quad (3)$$

The Wilson expressions for the activity coefficients of a binary mixture are:

$$\ln \gamma_l = -\ln(x_l + \Lambda_{lw} x_w) + x_w \left[\frac{\Lambda_{lw}}{x_l + \Lambda_{lw} x_w} - \frac{\Lambda_{wl}}{\Lambda_{wl} x_l + x_w} \right] \quad (4)$$

$$\ln \gamma_w = -\ln(x_w + \Lambda_{wl} x_l) - x_l \left[\frac{\Lambda_{lw}}{x_l + \Lambda_{lw} x_w} - \frac{\Lambda_{wl}}{\Lambda_{wl} x_l + x_w} \right] \quad (5)$$

where Λ_{lw} and Λ_{wl} are binary interaction parameters.

The binary interaction parameters are determined for every combination of the two components based on experimental data. Parameters of the binary interaction for a methanol-water mixture are $\Lambda_{lw}=0.4180$, $\Lambda_{wl}=0.9699$ (Ohe, 2002). Saturated pressure P_i^* is calculated by Antoine's expression:

$$\log P_i^* = A - \frac{B}{t + C} \quad (6)$$

Parameters of the Antoine's expression for a methanol are $A=7.87863$, $B=1473.11$ and $C=230.00$ (Ohe, 2002). The reservoir temperature of simulated area is estimated to be 330-340 °C. Using (1)-(5) relations, the Henry's constant is calculated for the temperatures 310-340 °C (Figure 4). Because of the very low concentration of methanol in produced fluid, the mole fraction of methanol in the aqueous phase is calculated to be less than 10^{-4} . Henry's law coefficient is about 50MPa when the mol fraction is less than 10^{-4} .

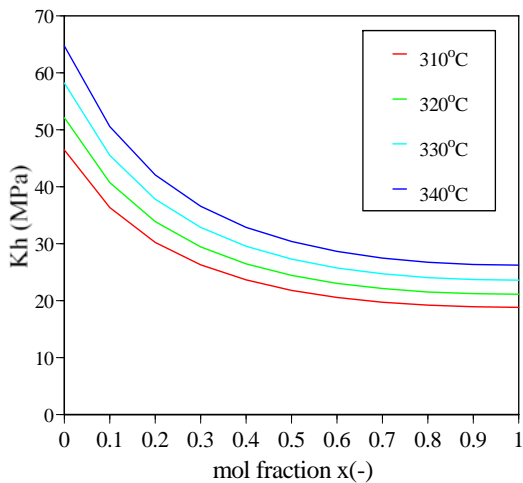


Figure 4. Henry's law coefficient for dissolved methanol in water

RESULTS

Production History Matching

Figure 5 compares the observed flowing enthalpies with calculated enthalpies. The trends of observed enthalpies of three production wells declined because this region had been affected by the reinjection flow from shallow reservoir. Achieving a good matching of the calculated enthalpies to the measured ones was difficult. The calculated enthalpies of the producer P-3 is much lower than the observed ones until 7.5 years. We consider the model too simple for two-phase simulation. However, The calculated enthalpies of the producer P-3 is relatively in agreement with the observed enthalpies after 7.5 years. The trends of calculated enthalpies of producers P-1 and P-2 are also similar to those of observation.

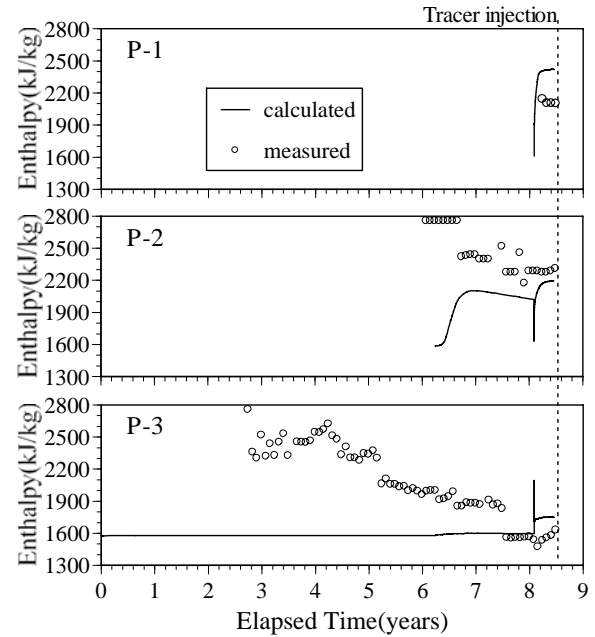


Figure 5. Measured vs. calculated flowing enthalpies. open circles: measured flowing enthalpies, solid lines: calculated flowing enthalpies

The Matching of Tracer Return Curves

For the matching of tracer return curves, adjustments was made to porosity, the volume fraction of fracture and matrix continuum, and liquid saturation distribution. The results of matching suggest that the volume fraction of fracture continuum or fracture porosities are very small ($< 1\%$), indicating fluid flows through narrow paths. This estimation is consistent with the other numerical model applied for the whole reservoir (NEDO, 2000). Regarding the water saturation distribution, the difference in peak time peak requests the spatial variation of water

saturation(Figure 6). For example, less than 0.7 of water saturation is estimated to show the peak-time difference in well P-2.

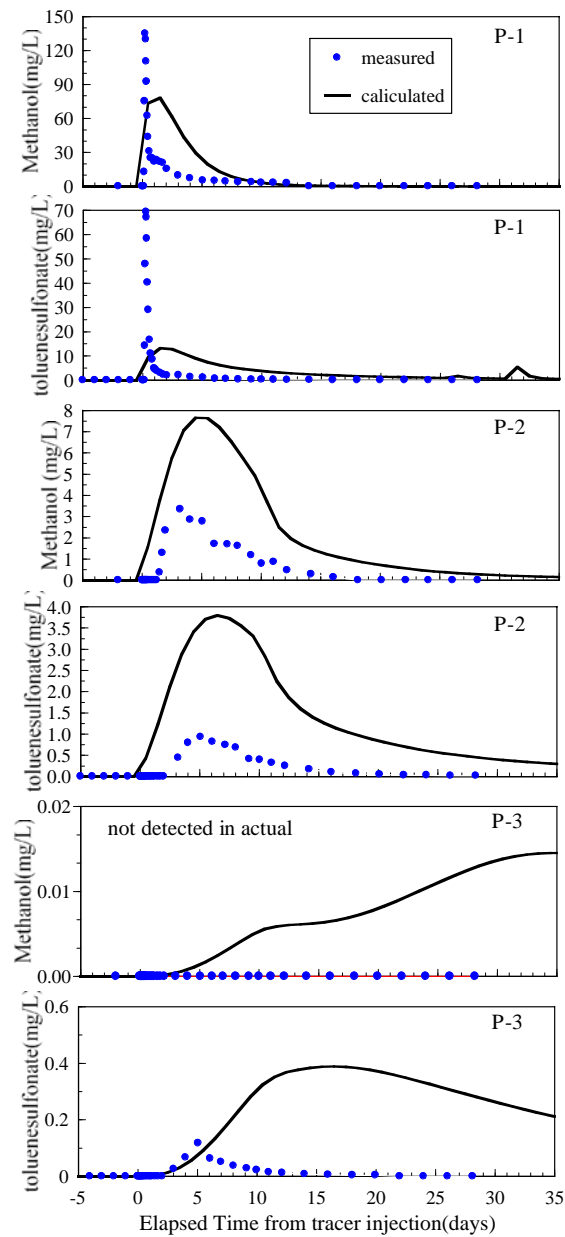


Figure 6. measured vs. calculated tracer return curves of methanol and toluenesulfonate

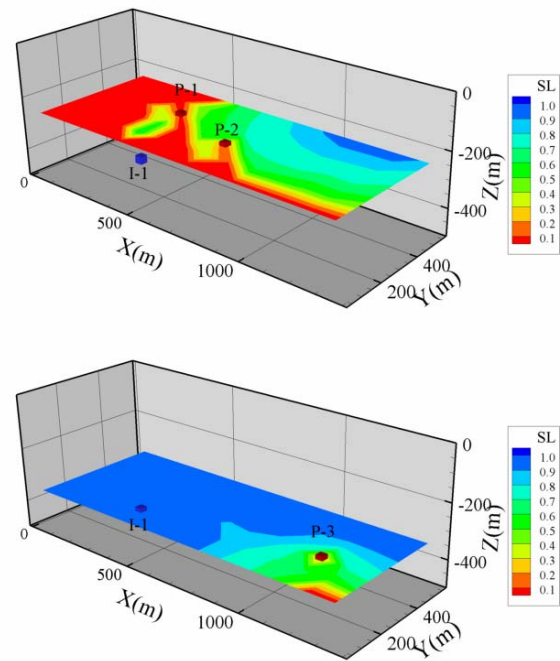


Figure 7. Water saturation contours during the tracer test. (upper) slice at injection point upper I-1 and two production points P-1 and P-2; (lower) slice at lower I-1 and P-3.

The Prediction of Production for Various Reinjection Rate

After the matching of tracer return curves, the future reservoir performance were predicted with reinjection rates ranging from 0t/h to 160t/h. The each prediction run covers a period of 5 years after the beginning of reinjection.

Figure 8 and 9 show the trends of pressures at feed points and flowing enthalpies under various reinjection conditions. The results indicate that only the trend of pressure for 160t/h of reinjection rate uprises at well P-3, though the reinjection causes the increase of the pressures in the entire reservoir. In contrast, the flowing enthalpies decrease immediately after reinjection.

Figure 10 shows the trends of production rates of steam and water under various condition. The results show that the higher reinjection rates result in higher production rates of steam, and the degree of the increase is consistent with tracer recovery. However, in case of 160t/h of reinjection, the flow rates becomes decreasing after downward in 0.5 years at producer P-1 and in 4 years at producer P-2. Therefore the 80t/h of reinjection is considered appropriate from this simulation.

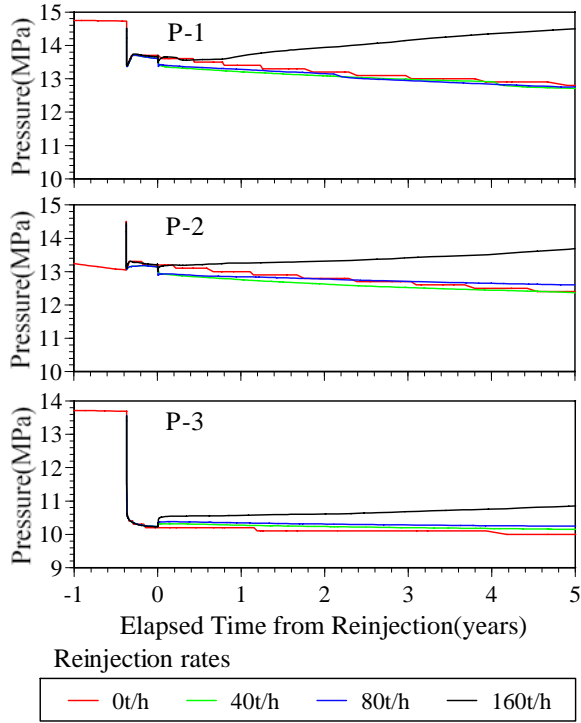


Figure 8. Predicted feed point pressure under various reinjection conditions.

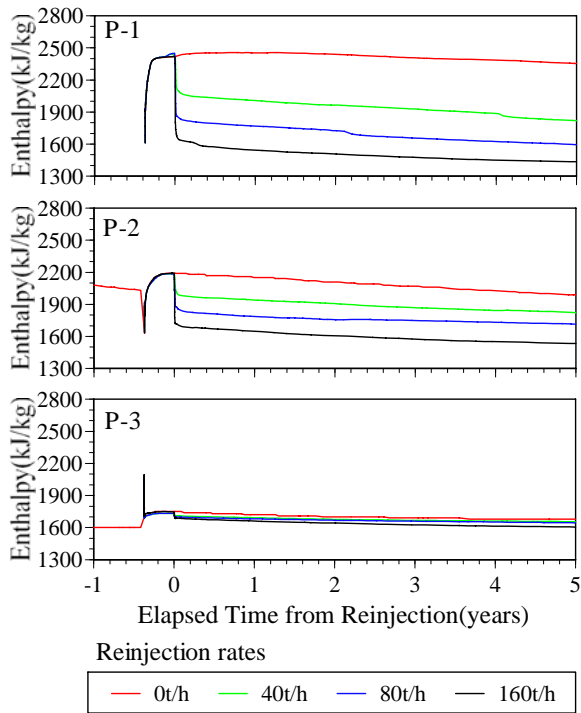


Figure 9. Predicted flowing enthalpies under various reinjection conditions.

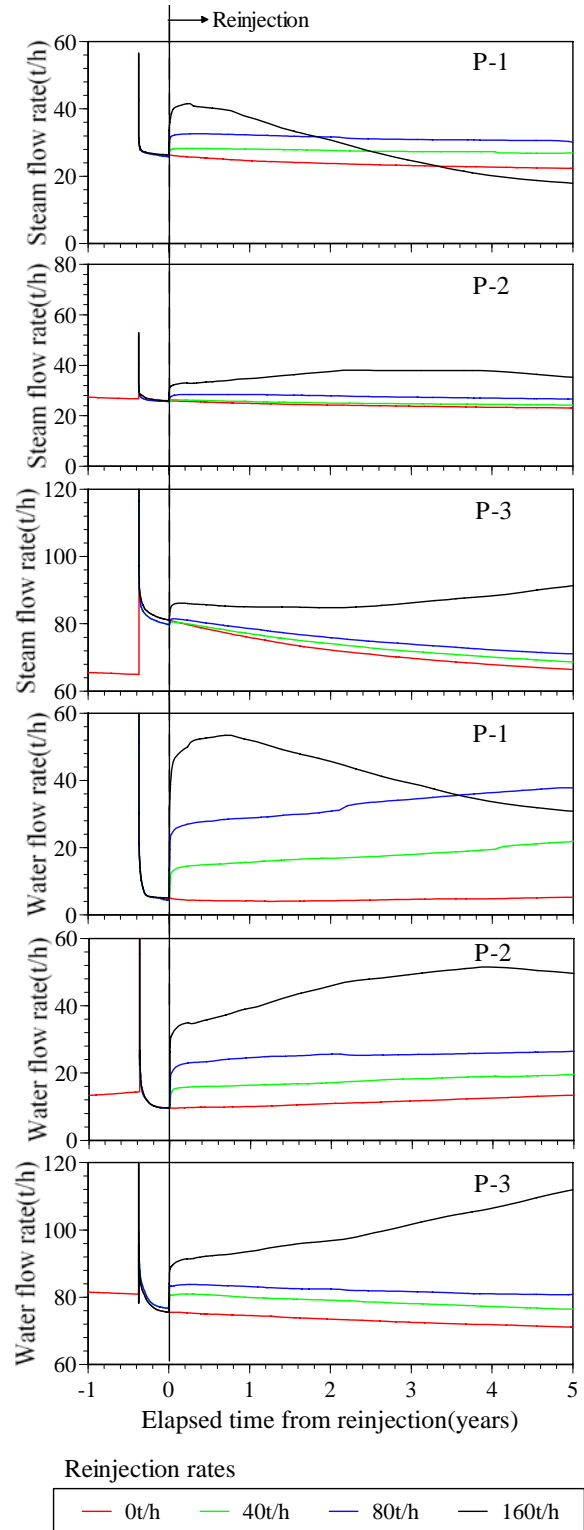


Figure 10. Predicted production rates of steam and water under various reinjection conditions.

CONCLUSIONS

This paper presented a simplified estimation of phase partitioning behavior of two phase tracers aimed at estimating the physical condition of the reservoir and forecasting the future reservoir performance under various reinjection rates.

The simulator TOUGH2-EOS7R was used for the modeling of tracer flow in the reservoir. To apply methanol in the model, we expressed the Henry's law constant as a product of an activity coefficient and saturated vapor pressure.

The observed fast returns of methanol were achieved in the model by setting porosities low and volume fraction of fracture continuums low, which indicate fluid flows through narrow paths. The observed peak-time difference between methanol and toluenesulfonate was achieved by adjusting the distribution of water saturation.

The results of prediction runs showed that the higher reinjection rates resulted in higher production rates of steam and water. The degree of the increase was consistent with tracer recovery. The reinjection rate of 80t/h was estimated to be appropriate in the simulation.

ACKNOWLEDGEMENTS

The authors are grateful to Tohoku Hydropower & Geothermal Energy Co., Inc. for their permission to publish this paper. The authors also thank Dr. Mineyuki Hanano and Mr. Daisuke Fukuda for critically reviewing this paper.

REFERENCES

Axelsson, G., Flovenz, O. G., Hauksdottir, S., Hjartarson, A. and Liu, J. (2001), "Analysis of tracer test data, and injection-induced cooling, in the Laugaland geothermal field, N-Iceland", *Geothermics* 30, 697-725.

Corey, A.T., (1954) The interrelation between gas and oil relative permeabilities. *Producers Monthly*, November pp. 38-41.

GENZL/ Auckland Uniservices Ltd. (1997), *WELLSIM Geothermal Wellbore Simulation. Ver.4.*

Grant, M. A., Donaldson, I. G., and Bixley, P. F. (1982) *Geothermal Reservoir Engineering*, Academic Press.

Hanano, M. (1998), "A simple model of a two-layered high-temperature liquid-dominated geothermal reservoir as a part of large-scale hydrothermal convection system", *Transport in*

Porous Media 33, Kluwer academic Publishers, Neitherlands: pp. 3-27.

Hishi, Y., Fukuda, D., Asanuma, M., Kobayashi, K. and Kasai, K. (2001), "Tracer testing at the liquid dominated reservoirs, using aromatic compounds (in Japanese)", 2001 Annual Meeting Geothermal Society of Japan, Abstracts with Programs, P32.

New Energy and Industrial Development Organization (NEDO) (2000), "Deep-seated geothermal resources survey(in Japanese)".

Ohe, S. (2002), "Prediction Methods of Physical Properties(in Japanese)", Data Book Publishing Inc., Tokyo.

Pruess, K., Oldenburg, C., Moridis, G. (1999), *TOUGH2 User's Guide, Version 2.0*, Lawrence Berkeley National Laboratory Report LBNL-43134, Berkeley, CA, November.

Pruess, K. (2002), "Numerical simulation of 'multiphase tracer transport in fractured geothermal reservoirs", *Geothermics* 31, pp. 475-499.

Shook, G., M., (2001) "Predicting thermal breakthrough in heterogeneous media from tracer tests", *Geothermics* 30, pp. 573-589.

Trew, M., O'Sullivan, M., J. and Yasuda, Y. (2001), "Modeling the phase partitioning behavior of gas tracers under geothermal reservoir conditions, *Geothermics* 30, pp. 655-695.

Warren, J. E. and P. J. Root (1963), "The behavior of naturally fractured reservoirs", *Soc. Pet. Eng. J., Transactions, AIME*, 228, 245-255, September.

Production Engineering

- Two-Phase Flow Behavior and Spinner Data Analysis in Geothermal Wells** [245](#)
Jorge A. Acuna and Brian Arcedera
- Calcite Precipitation in Low Temperature Geothermal Systems: An Experimental Approach** [253](#)
Omer Izgec, Birol Demiral, Henri Bertin and Serhat Akin
- Non-Condensable Gases at the Miravalles Geothermal Field** [259](#)
Paul Moya and Eddy Sánchez
- Cerro Prieto IV, the Newest Power Plant in Cerro Prieto Geothermal Field** [270](#)
Juan De Dios Ocampo Díaz

TWO-PHASE FLOW BEHAVIOR AND SPINNER DATA ANALYSIS IN GEOTHERMAL WELLS

Jorge A. Acuña^a and Brian A. Arcedera^b

(a) Unocal Geothermal Technology and Services, 1160 N Dutton Ave Suite 200, Santa Rosa, California, 95401

(b) Philippine Geothermal, Inc., 12th Floor, Citibank Tower, 8741 Citibank Plaza, Paseo de Roxas, Makati City, Philippines 1226

jacuna@unocal.com, barcedera@unocal.com

ABSTRACT

A method has been developed for interpretation of Pressure-Temperature-Spinner (PTS) surveys. Drift-flux and homogenous flow models are evaluated for application in two-phase flow in geothermal wells. It was found high fluid velocity makes possible simple assumptions regarding holdup and friction losses. The analysis method provides sufficient resolution to determine mass contribution and enthalpy of individual feed zones in geothermal wells. Technique is described and a field example provided.

INTRODUCTION

Pressure-temperature-spinner (PTS) surveys are a valuable surveillance tool for diagnosing performance problems with geothermal wells and evaluating changes in reservoir conditions.

Interpretation of PTS surveys typically relied heavily on wellbore simulation. To match a model to observations a trial and error procedure must be followed to determine location and individual feed zone contribution both in terms of mass and enthalpy in the two-phase part of the well. The contribution of individual feed zones is usually seen as increases in fluid velocity. An estimation of the feed zone enthalpy must be made in order to convert velocity changes to mass contributions. If a well has a particularly cold shallow feed zone or a thief zone, there is a decrease or no change in spinner velocity. In those circumstances the interpretation becomes difficult.

In the past we have used pressure gradient of the well to estimate minimum flowing enthalpy. As long as the friction losses are small and can be neglected this method provides an estimate of flowing enthalpy that agrees reasonably well with measured wellhead enthalpy. The assumption of small friction losses, however is only valid in the deeper part of the well where fluid velocity is small.

We set out to develop a simple method to estimate the mass and energy distribution in the wellbore so that we could calculate the location and contribution of the individual feed zones.

THEORETICAL BACKGROUND

In wellbore simulation for every section of the well there are two main unknowns: the liquid holdup and the friction loss. The liquid holdup is the ratio of the area of the pipe occupied by liquid to the total area. This ratio depends on the velocity of the individual phases. Steam is expected to flow faster than liquid. The difference between the two velocities is called slip velocity. Instead of liquid holdup (f_l), volumetric gas fraction (f_g) can be used, the two are related by equation (1).

$$f_g + f_l = 1 \quad (1)$$

Modern treatment of two-phase flow in vertical wells describes four different flow regimes: bubbly, slug, churn and annular. Some other regimes are also mentioned such as dispersed bubbly (Hasan and Kabir, 2002) and wispy annular (Collier and Thome, 1996). For each of those flow regimes holdup and friction loss expressions are available in Hasan and Kabir (2002).

For each section of the well the flow regime must be determined first in order to apply the corresponding equations of liquid holdup and friction loss. This requires knowing mass flow and enthalpy. For geothermal wells these variables are measured only at the surface, therefore the analysis must start by defining the feed zone locations and contributions that determine the mass flow and enthalpy variation along the well.

The homogenous and drift flux models

To determine liquid holdup two models are available: homogenous flow and separated flow. The homogeneous flow model provides a simple treatment of two-phase flow. It assumes that both

phases can be treated as a single fluid moving at the same velocity with no slip velocity. Appropriate expressions for density and viscosity are used. The mixture density of the two-phase fluid is related to volumetric gas fraction (f_g) as

$$\rho_m = (f_g)\rho_g + (1 - f_g)\rho_l \quad (2)$$

where ρ is density and the subscripts m , l and g refer to mixture, liquid and gas. The same expression using viscosity instead of density can be applied to calculate average viscosity and corresponds to the Dukler formulation described in Hasan and Kabir, (2002). Under non-slip conditions, characteristic of homogeneous flow, the flowing fluid density or mixture density is equal to the static density or mass averaged density.

Contrary to the homogeneous flow model, separated flow models treat each phase separately. These models account for different velocity of the phases or slip velocity. One of the most common models used to describe two-phase flow is the drift flux model as described by Hasan and Kabir (2002). This model can be used without reference to any particular flow regime for high pressure steam-water mixtures according to Collier and Thome (1996).

The flowing gas volumetric fraction (f_g) according to the drift flux model can be expressed as follows.

$$f_g = \frac{v_{sg}}{C_o v_m + v_\infty (1 - f_g)^n} \quad (3)$$

where v_{sg} , v_m , C_o , v_∞ are gas superficial velocity (volumetric gas rate divided by total pipe area), total superficial velocity (total volumetric rate divided by pipe area), flow parameter and terminal-rise velocity respectively. The exponent n can range from 0 to 3 depending on flow regime (Kleinstreuer, 2003). Ansari et al. (1994) found that a value of 0.5 provided the best fit to their data.

The flow parameter C_o , also called “concentration factor” is an empirical factor that accounts for the fact that the velocity profile and the void or “bubble concentration” profile across the pipe may vary independently of each other. If the void fraction profile is uniform across the pipe then the flow parameter C_o is equal to 1 (Kleinstreuer, 2003). The recommended value of this parameter, however, is 1.2 based on experiments in 1- to 2-in diameter pipes. For steam-water flow at elevated pressures a value of 1.13 is recommended (Collier and Thome, 1996).

The terminal-rise velocity is the velocity of a single bubble rising in an infinite liquid medium. An expression for this velocity as recommended for high

pressure steam-water mixtures (Collier and Thome, 1996) is the following.

$$v_\infty = 1.41 \left[\frac{\sigma g (\rho_f - \rho_g)}{\rho_f^2} \right]^{0.25} \quad (4)$$

In this equation σ , g , ρ are surface tension, gravity constant and density respectively. The subscripts f and g refer to liquid and steam respectively. In two-phase flow gas and liquid density as well as surface tension are functions of pressure or temperature as they are related by saturation conditions. The terminal-rise velocity varies very little with pressure, it changes between 0.21 and 0.19 m/s for pressures between 6 and 30 bar.

According to Collier and Thome (1996), for the drift flux model to be applicable, the terminal-rise velocity must be significant with respect to the volumetric velocity ($v_\infty > 0.05 v_m$). This is not the case for many geothermal wells.

Flow in a typical well occurs mostly in the high velocity flow regimes: churn and annular. Churn flow is sometimes also referred to as semi-annular, annular-slug or froth flow. It is characterized by the liquid phase being mainly displaced to the pipe wall with the vapor flowing in a chaotic manner through the liquid. Annular flow is characterized by the vapor phase flowing in the core of the pipe while the liquid phase is dragged along the pipe walls forming an annulus. A fraction of the liquid, sometimes most of it, flows as droplets entrained in the gas core (Hasan and Kabir, 2002).

A volumetric steam fraction of 0.52 is the criteria for transition from slug to churn flow (Hasan and Kabir, 2002). Figure 1 shows the pressure below which the volumetric steam fraction is larger than 0.52 as a function of enthalpy. Figure 1 also shows the flashing pressure for liquid at that enthalpy.

As can be seen in Figure 1 at low enthalpies there is very little difference between flashing pressure and the pressure required to reach churn flow. It can be shown that a volumetric gas fraction greater than 0.52 is reached less than 200 m above the flashing level for fluid enthalpy below 1100 kJ/kg. The criteria for transition from churn to annular flow is when the gas fraction is greater than 0.52 and the gas velocity exceeds that given by equation (5).

$$v_{gs} = 3.1 \left[\frac{\sigma g (\rho_f - \rho_g)}{\rho_g^2} \right]^{0.25} \quad (5)$$

where the symbols have the same meaning of equation (4). As the flow gets dryer the terminal-rise velocity term disappears from equation (3) as f_g gets

closer to 1. The flow parameter C_0 can be set to 1 in annular flow according to Kleinstreuer (2003). The assumption of homogeneous flow is made for the equivalent of annular flow, called “mist” flow, in the Duns and Ros two-phase flow correlation (Hasan and Kabir, 2002).

Depending on pressure and flow rate a well can transition directly from slug to annular flow without going through churn flow.

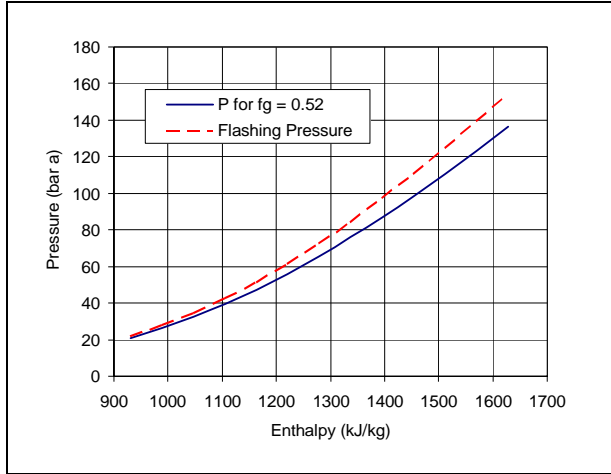


Figure 1: Pressure below which volumetric steam fraction is larger than 0.52 and flashing pressure for liquid at that enthalpy.

The gas velocity given by equation (5) is called “terminal velocity” in oil and gas literature. It has been described as the minimum velocity required by gas to carry liquid droplets in suspension (Coleman et al. 1991). In gas wells when the gas velocity is below the “terminal velocity” the well starts to “load up” or accumulate liquid in the wellbore and flow eventually stops. This usually leads operators to replace the production tubing with a smaller diameter in order to extend the well life.

Experimental results have shown that at high fluid velocity flow behavior evolves towards homogeneous flow. This is known as the “mass velocity” effect. Mass velocity is actually a velocity per unit area and it is defined as mass flow divided by pipe area. Experimental evidence suggests that at mass velocities larger than 1000 kg/m²s fluid behavior approaches homogeneous flow and results match predictions of homogeneous flow at mass velocities of 2000 kg/m²s (Collier and Thome, 1996).

Experimental results for large diameter pipes such as those used in geothermal wells, however, are not available. We expect that the transition should occur at lower mass velocities in large pipes. The reason is that the wall shear effect that creates the bubble concentration profile will affect a smaller fraction of

the pipe area in a large diameter than in a small diameter pipe.

The working hypothesis for this paper is that flow velocity is large enough so that there is no slip velocity and the flow is homogenous. Our experience in matching PTS surveys shows that this assumption should be reasonable for volumetric gas fraction greater than 0.52 and fluid velocities greater than 3 m/s.

Friction factor considerations

The equation that describes the total pressure gradient in a well is composed by three terms: gravity term, friction losses and acceleration term as shown in equation (6)

$$\frac{dP}{dz} = \rho_m \frac{g}{g_c} \cos \theta + \rho_m \frac{fv_m^2}{2g_c D} + \rho_m \frac{v_m}{g_c} \frac{dv_m}{dz} \quad (6)$$

where z , dP/dz , ρ_m , g , D , f , v_m , θ are measured depth, total pressure gradient, mixture density, gravity constant, pipe diameter, Moody friction factor, mixture velocity and angle with respect to vertical. g_c is a conversion factor equal to 1 for metric units and 32.17 for English units.

We can write equation (6) as follows

$$\rho_m = \frac{\frac{dP}{dz}}{\frac{g}{g_c} \cos \theta + \frac{fv_m^2}{2g_c D} + \frac{v_m}{g_c} \frac{dv_m}{dz}} \quad (7)$$

In a PTS survey the total pressure gradient (dP/dz) is known as well as all other variables in the right hand side of equation (7) with the exception of the Moody friction factor f .

For the estimation of the Moody friction factor we will take advantage of our assumption of large fluid velocity. In this condition Reynolds numbers are large. For large Reynolds number ($Re > 10^6$) the friction factor depends only on relative pipe rugosity. For example, in a 0.25 m diameter steel pipe with gas volumetric fraction of 0.52 the Moody friction factor will become dependent mostly on pipe relative rugosity when fluid velocity is greater than 1.1 m/s for pressure between 6 and 30 bar.

Relative rugosity changes along the well with diameter and absolute rugosity. To account for these variations the following approximate relationship

derived from the Coolebrook-White equation can be applied.

$$f_1 \left[\log\left(\frac{\varepsilon_1}{D_1}\right) \right]^2 = f_2 \left[\log\left(\frac{\varepsilon_2}{D_2}\right) \right]^2 \quad (8)$$

In this equation f , ε and D are Moody friction factor, absolute pipe rugosity and pipe diameter. Subscripts 1 and 2 refer to two different pipe sections. Obviously it cannot be used for smooth pipe sections. At lower fluid velocities the Reynolds number may not be large enough for the friction factor to be independent of fluid velocity. In this case, however friction losses may not be too important and errors in the friction factor will not affect too much the estimate of density.

Fluid velocity, mass flow and energy

For fluid velocity we use the spinner calculated fluid velocity. The spinner fluid velocity has been proven to be proportional to mass average velocity and not to mixture velocity (Gang et al., 1990). Both definitions of velocity in two phase flow, however, are equivalent for homogeneous flow.

By solving equation (7) for every section of the pipe we will end up with a profile of calculated fluid density as a function of measured depth. Since fluid velocity and pipe cross section are also known, a graph of mass flow versus depth can be constructed. Gas mass fraction or flash x can be calculated once density is known using the following relationship

$$x = \frac{V_m - V_f}{V_g - V_f} \quad (9)$$

where V is the specific volume or inverse of density. Subscripts m , f and g refer to mixture, liquid and gas respectively. Liquid and gas specific volume are calculated at corresponding pressure of pipe section. Once flash is known enthalpy can be calculated using standard thermodynamic relationships.

Internal energy per unit mass for a section of the pipe with no feed zones is calculated by adding fluid enthalpy, heat losses, kinematic and potential energy components. The internal energy for a given point in the pipe is given by equation (10)

$$U = h + q + \frac{v_m^2}{2g_c} + \frac{g}{g_c} H \quad (10)$$

where U , h , q , v_m , g and H are internal energy, enthalpy, heat loss, fluid velocity, gravity constant

and elevation. g_c is set to 1 in metric units and 32.17 in English units. The units of the three terms must be consistent. The wellhead is a good reference point to set the elevation term to zero. The kinematic and elevation energy terms are small compared to enthalpy. The kinematic term for a fluid velocity of 50 m/s is only 1.25 kJ/kg. The elevation term is -9.81 kJ/kg 1000 m below wellhead elevation. Both terms decrease with well depth therefore the enthalpy increases slightly with depth.

Using this method, graphs of mass and internal energy versus depth can be constructed. The selection of the friction factor will change the shape of the curves. Ideally the mass flow rate and internal energy graphs should look like a sequence of straight lines with step changes at the feed zones. The size of the change in each curve makes it possible to calculate the mass and enthalpy of the feed zones.

Measured wellhead mass flow and enthalpy can also be used to constraint the friction factor even more. The wellhead values are used to calculate a curve of fluid velocity versus depth in the cased part of the well. This helps in constraining the spinner derived fluid velocity.

The calculated mass and internal energy curves are normalized by dividing them by the wellhead mass and internal energy. This produces two curves that when the correct friction factor is selected form two straight lines in the cased part of the well that coincide at the value of one.

This method in which homogenous flow is assumed and friction factor calculated to match observed total pressure gradient has been used before. It is called, not surprisingly, the "friction factor" model (Collier and Thome, 1996). The main difference with our application is that it will be applied to interpretation of PTS surveys and the shape of the mass and energy curves versus depth is used to determine the correct friction factor. A good matching friction factor should represent the proper balance between gravity and friction effects in the total pressure gradient.

APPLICATION OF THE METHOD

We will apply this method to well A in the Bulalo geothermal field in the Philippines. Well A is a directional well cased to 975 m measured depth with a 0.273 m (10 3/4") tie back. The slotted liner diameter is also 0.273 m down to 2195 m and 0.219 m (8 5/8") down to total depth at 2746 m.

Fluid velocity

We have to correct the fluid velocity obtained from the spinner to reflect a consistent set for the entire well. We have observed that in the vertical section of

the well the spinner measures higher velocity than in the non-vertical section of the well. This is clearly seen at the directional kick-off of the well and we call it “kick-off” effect. It is believed that this is due to the spinner traveling close to the center of the pipe in vertical parts of the well where fluid velocity is larger. In non-vertical parts of the well the spinner travels close to the pipe wall and fluid velocity is smaller. Figure 2 shows the well angle in degrees as well as the uncorrected and angle effect corrected fluid velocities.

The upper part of the well is cased-off therefore the estimation of fluid velocity using wellhead pressure, enthalpy and mass flow should be reliable. The calculated fluid velocity in the upper part of the well is also plotted and it serves as a guide to make the angle correction. This velocity is shown as calculated in Figure 2. The lower velocity observed below 830 m is due to completion effects.

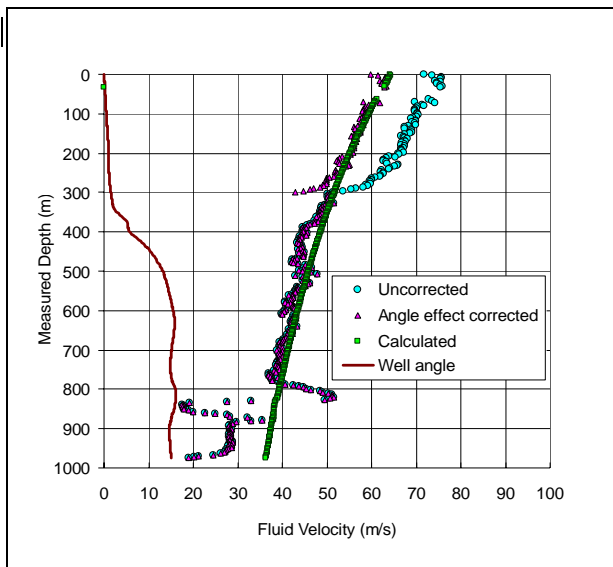


Figure 2: Comparison of fluid velocity from PTS survey uncorrected, corrected by angle effect and calculated using wellhead measured mass flow and enthalpy and survey pressure. Well angle is degrees also shown.

The angle correction is made by dividing the fluid velocity in the vertical part of the well by a factor (1.2 in this case). We have found that segments where the well angle is less than 1.5 degrees can be approximated as vertical. The angle effect shows clearly that PTS derived fluid velocities depend on the location of the tool with respect to the well center. It is expected that by doing the angle correction we will end up with a consistent set of velocities for the entire well. Matching calculated fluid velocities in the cased part of the well we expect the PTS velocity to reflect the average fluid velocity for the entire well.

Fluid density

The next step in the calculation is to apply equation (7) to calculate fluid density. Then calculate mass flow rate and internal energy as given by equation (10). The wellhead measured pressure for this wells is 18.7 bar a, mass flow is 52.9 kg/s. Wellhead enthalpy is 1839 kJ/kg and internal energy is 1840 kJ/kg. Calculated mass flow and internal energy are then normalized by dividing them by the wellhead values.

For this case we neglected heat losses. We also neglected the kinematic term in equation (7). This term was calculated after the solution was reached and it was confirmed that it represents only a small fraction of the total pressure gradient.

The process of estimating the friction factor by trial an error is illustrated in Figure 3. This figure shows the normalized curves that result from selecting too low a friction factor (0.005) and too high a friction factor (0.02).

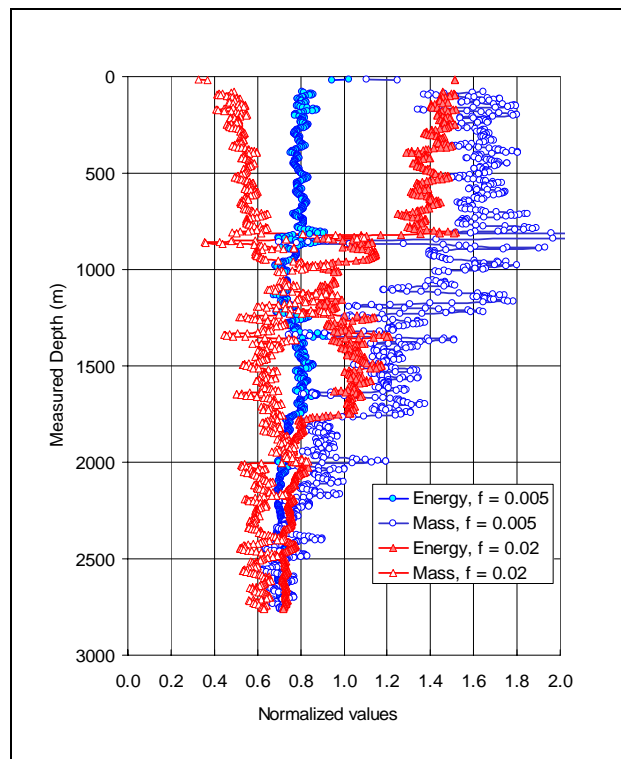


Figure 3: Normalized mass and energy curves for two selections of the Moody friction factor: 0.005 (circles) too low a value and 0.02 (triangles) too high a value.

Figure 3 shows how the selection of friction factor does not affect significantly the deepest part of the well. The reason is that fluid velocity is low enough for friction to be a small component of the total

pressure gradient although fluid velocity at the deepest part of the well is still more than 6 m/s. The mass and energy curves move in opposite direction with variations of the Moody friction factor f . This makes selection of the correct friction factor easier. Another important feature is that curves are not straight when the friction value is not correct. This may be sometimes difficult to assess due to the noise characteristic of PTS surveys.

Figure 4 show the normalized curves for a friction factor on 0.0097. This selection of the Moody friction factor produces two curves that are composed of straight segments. The mass curve should increase in steps from bottom to top of the well unless there is a “thief” zone, with the steps corresponding to feed zone locations. The enthalpy may increase, decrease or remain the same depending on the enthalpies of the feed zones. The upper cased part of the well should show two straight lines coinciding at the value of 1. This means that the wellhead measured values are being honored. The possibility of errors in the wellhead measurements should always be kept in mind when a match is difficult to achieve.

For the calculation of the slotted liner part of the well it was assumed that the well diameter is the diameter of the slotted liner and the pipe rugosity equals that of the normal steel pipe (0.046 mm) used in the cased part of the well. We justify this selection by noting that the absolute pipe rugosity (ϵ) should be higher than that of the non-slotted pipe but the diameter should also be larger than the one used. Therefore relative pipe rugosity (ϵ/D) should not change too much. This assumption may not work as well for mass flow calculations. Those depend on using actual pipe area with fluid velocity and density to obtain mass flow. This aspect of the calculation can cause discontinuities at the contact between casing and slotted liner as well as at different diameter contacts and it is being revised at this time.

Once the friction factor is selected some additional interpretation must be done. Feed zones must be located and their contribution in terms of mass and enthalpy must be determined to match the flowing profiles.

Table 1 shows our interpretation of the location and contribution of each feed zone for well A. A feed zone at the top of the 10 3/4” liner at 831 m was added to improve the match. To corroborate the thief zone at 1116 m, the flowing wellbore pressure was compared to reservoir pressure and it was found that wellbore pressure is indeed larger than reservoir pressure at this elevation.

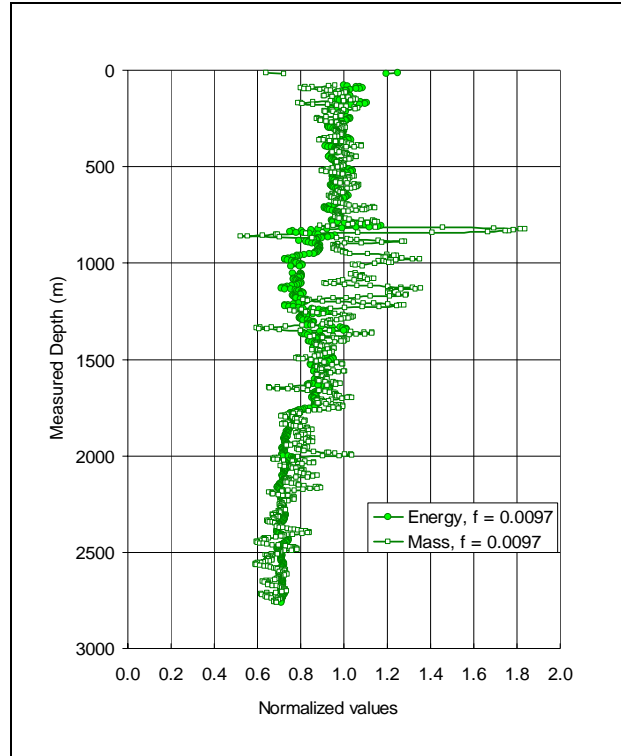


Figure 4: Normalized mass and energy graphs for correct selection of Moody friction factor: 0.0097.

Depth (m)	Flow (kg/s)	Enthalpy (kJ/kg)
831	5	2791
975	9	2791
1116	-28	N/A
1250	19	977
1768	8	2791
2134	5	1861
2775	38	1326

Table 1. Depth and contribution of feed zones in well A

Figure 5 shows the final calculated mass flow and enthalpy variation with depth compared to the expected variation assuming the mass and enthalpy contributions of the feed zones described in Table 1.

This figure shows that assuming constant enthalpy between feed zones is a good approximation. The entire well can be matched reasonably well.

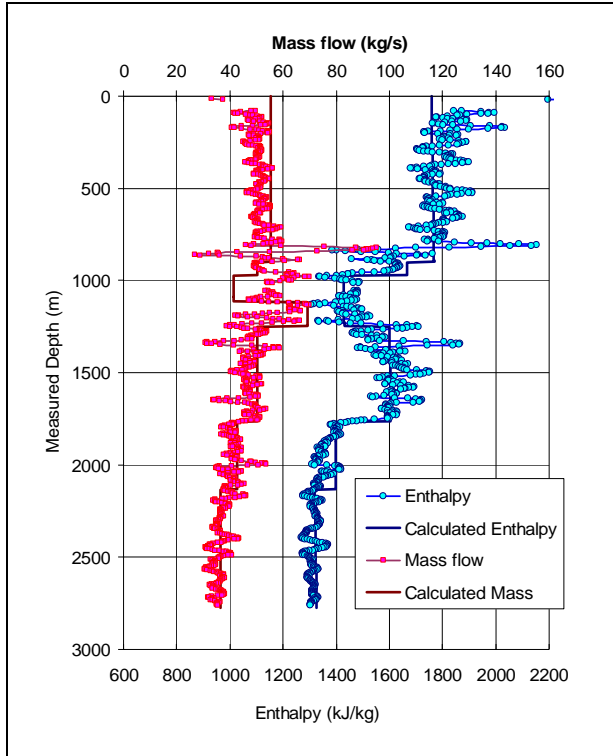


Figure 5: Interpretation of variation of mass flow and enthalpy with depth. Feed zone depths and contributions are shown in Table 1.

Consistency of results

A very valid question is how consistent is the obtained friction factor with respect to more conventional ways of calculating it. Figure 6 shows the comparison of the friction factor calculated using Blasius smooth pipe friction factor formula, Colebrook-White equation for rough pipe and the assumed value obtained with this method. Interestingly enough the results fall in between the two values. The absolute rugosity required by the Colebrook-White equation to match the observed results is 0.0064 mm.

In order to check independently the consistency of the results with a different method, the feed zone contributions shown in Table 1 were simulated in our wellbore simulator using the Duns and Ros correlation (Hasan and Kabir, 2002) and also the Orkiszewski correlation (Brill and Beggs, 1991). Both correlations use the same formulation (Duns and Ros) for the “mist” flow regime. The measured and calculated temperature pressure and mixture velocity are shown in Figure 7.

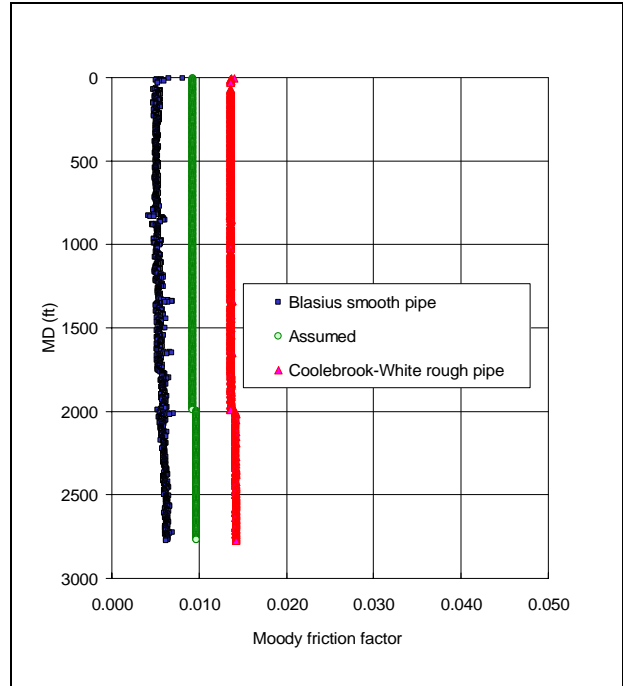


Figure 6: Comparison of assumed Moody friction factor obtained from this analysis with values for smooth pipe (Blasius) and rough pipe (Coolebrook-White).

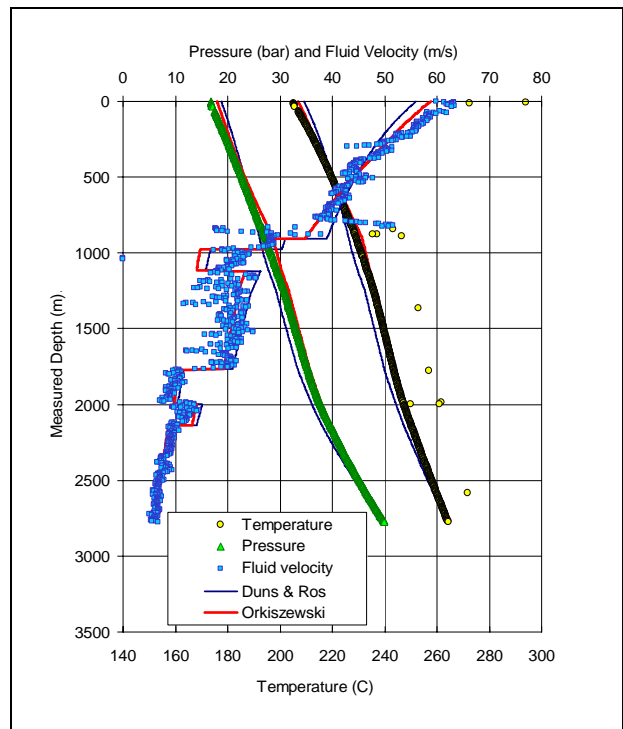


Figure 7: Wellbore simulator match of pressure, temperature and mixture velocity using Duns & Ros (blue) and Orkiszewski (red) correlations.

As expected the results are different because the holdup and friction loss treatment in the correlations may be different from the one used here. The Orkiszewski correlation shows a better agreement than Duns and Ros.

CONCLUSIONS

The method for PTS survey interpretation presented in this work has been applied to more than 10 wells in Unocal. In most cases it has shown results that are consistent with our previous interpretations. Sometimes, however it shows unexpected results that offer alternative and interesting interpretations.

Contrary to normal methods of solution in two-phase flow in which the holdup is calculated separately from friction losses, this method offers the possibility of balancing the gravity and friction components of the total pressure gradient by selecting the friction factor that makes the profiles of mass and internal energy consistent.

Including reliable wellhead measurements of mass and enthalpy improves the precision of the method. These measurements, however are not strictly required. It is possible to determine a friction factor that provides the correct shape of mass and energy curves with depth without wellhead measured values.

The main limitation of the method is that assumptions made for its derivation require fluid velocity to be large enough so homogeneous flow can be assumed. We have found that as long as the fluid velocity is larger than 3 m/s the method works well. In lower enthalpy high diameter wells we found some inconsistencies possibly related to low flow velocity.

This method has provided an alternative way to check consistency of feed zone location, enthalpy and mass flow rate contributions found with our conventional trial and error wellbore simulator based method. It has also provided an unprecedented level of resolution in the interpretation of two-phase sections in flowing geothermal wells.

ACKNOWLEDGEMENTS

We thank Unocal, Philippine Geothermal, Inc. (PGI) and National Power Corporation (NPC) for supporting this project and granting permission to publish this paper.

REFERENCES

- Ansari, A.M., Sylvester, N.D., Sarica, C. and Shoham, O.: A Comprehensive Mechanistic Model for Upward Two-Phase Flow in Wellbores. SPE paper 20630, (1994).
- Brill, J.P and Beggs, H.D.: Two-Phase Flow in Pipes. University of Tulsa, (1991).
- Coleman, S.B., Hartley, B.C., McCurdy, D.G., Norris H.L.: A New Look at Predicting Gas-Well Load-Up, SPE paper 20280, (1991).
- Collier, J.G and Thome, J.R.: Convective Boiling and Condensation, Clarendon Press, Oxford (1996).
- Gang, X.Z., Golan, M and Sveen, J.: Determining Downhole Flow Rates of Oil and Gas in Oil Wells Using Pressure Drop and Spinner Response Measurements. SPE paper 20893, (1990).
- Hasan, A.R., and Kabir, C.S.: Fluid Flow and Heat Transfer in Wellbores, SPE, Richardson, Texas (2002).
- Kleinstreuer, C.: Two-Phase Flow Theory and Applications, Taylor and Francis, New York, (2003).

CALCITE PRECIPITATION IN LOW TEMPERATURE GEOTHERMAL SYSTEMS: AN EXPERIMENTAL APPROACH

Omer Izgec¹, Birol Demiral¹, Henri Bertin², Serhat Akin¹

1 Petroleum and Natural Gas Engineering Department, Middle East Technical University, Inonu Bulvari 06531
Ankara – Turkey

2 Laboratoire TREFLE, site de l'ENSAM, UMR CNRS 8508, 33405 Talence Cedex France
e-mail: serhat@metu.edu.tr

ABSTRACT

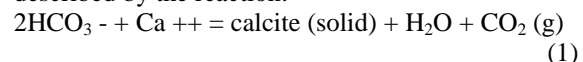
One of the most common production problems in geothermal fields is calcite (calcium carbonate) scale deposition. Calcite formed in the wellbore and in near wellbore region significantly decreases the output of a production well. Calcite scaling is experienced in almost all the geothermal fields around the world. Calcite may form from hydrolysis, boiling and heating of cooler peripheral fluids. Although there are plenty of mathematical modeling studies that try to explain the rock-fluid-carbon dioxide reaction kinetics, experimental studies are limited in number. This study presents results of computerized tomography (CT) monitored laboratory experiments where CO₂ was injected in carbonate cores at three different temperatures. Porosity changes along the core plugs and the corresponding permeability changes were reported for differing temperatures. CT monitored experiments were designed to model fast near well bore flow and slow reservoir flows. It was observed that permeability initially increased and then decreased for slow injection cases. As the salt concentration decreased, the porosity and thus the permeability decrease was less pronounced. Furthermore, rock-fluid-carbon dioxide interactions were seen to be affected by the orientation of the core plugs used in experiments. In vertical experiments, it is observed that permeability increased at the beginning, and then decreased for later times. On the other hand, for horizontal core plugs, permeability change was observed to be completely in reverse order. Because of the preferential paths, sometimes permeability alteration trend did not match with the porosity alteration trend. Experiments showed that solubility of CO₂ is larger compared to mineral trapping and temperature have great influence on chemical kinetics, thus on permeability change.

INTRODUCTION

One of the most common production problems in geothermal fields is calcite (calcium carbonate) scale deposition. Calcite blockages formed in near wellbore region or in the wellbore decrease significantly the output of the production well.

Calcite scaling is experienced in almost all the geothermal fields around the world, i.e. in the Dixie Valley geothermal field, Nevada (Benoit, 1989), in Ohaaki geothermal field, New Zealand (Clotworthy et al., 1995 and Nogara, 1999), in Seltjarnarnes geothermal field, Iceland (Kristmansdottir et al., 1995) and in Coso geothermal area in California (Evanoff et al., 1995). In extreme cases, most of the production wells and surface facilities may get blocked by calcite scale and serious generation losses could be encountered, i.e. Kizildere geothermal field in Turkey (Durak et al., 1993). In some cases calcite deposition, together with anhydrite (calcium sulphate) in the wellbores were also reported, i.e. Oguni geothermal field in Kyushu, Japan (Todaka et al., 1995). Likewise in Sumikawa field, Akita, Japan, for example, CO₂-rich groundwaters are thought to have reacted with reservoir rocks to form a carbonate and kaolinite alteration assemblage (Ueda et al., 2001).

Calcite may form from hydrolysis (involving replacement of calcium aluminosilicates), boiling of geothermal fluids (from fluids having high dissolved carbon dioxide concentrations and in the absence of mineral pH buffer) and heating of cooler peripheral geothermal fluids (Simmons and Christenson, 1993). In a boiling environment, platy calcite precipitates in open spaces upon loss of carbon dioxide with the carbonate species mostly controlling the pH and is described by the reaction:



While most of the carbon dioxide is evolved at the first flash (probably due to a large gas distribution coefficient), the reaction does not always proceed to completion to the right (Todaka et al., 1995). Thus, there are always components available for deposition as the fluid travels from the wellbore to the surface.

Although there are many studies related to the calcite scaling in the wellbore and in the surface lines, studies related to calcite scaling in near wellbore region is limited (Satman et al, 1999) and most of them tried to explain the rock-fluid-carbon dioxide reaction kinetics. There are only a few experimental studies. This study presents results of computerized tomography (CT) monitored laboratory experiments

where CO₂ was injected in carbonate cores at three different temperatures. Porosity changes along the core plugs and the corresponding permeability changes were reported for 21°C, 35°C and 50°C. CT monitored experiments modeled fast near well bore flow and slow reservoir flows.

EXPERIMENTAL APPARATUS AND PROCEDURE

The experimental apparatus consisted of, X-ray CT scanner (3rd generation Philips Tomoscan TX60), injection system, core holder, and data recording system (Figure 1). The injection system was made up of a constant displacement pump, CO₂ bottle, gas flow meter controller, and a pressure transducer. For horizontally aligned experiments a Hassler type X-ray transparent aluminum core holder wrapped with Fiberfrax insulation and carbon fiber materials to minimize x-ray scanning artifacts is used (Akin and Kovscek, 2003). For vertically oriented experiments a core holder placed in a water jacket that enabled fast adjustment of the system temperature at a constant level was used. Carbonate core plugs drilled from Midyat formation located in Diyarbakir, South East Turkey, were used in all experiments. Midyat rock is mainly a heterogeneous carbonate with vugs and fractures. The core plugs contained mainly calcite with 5% alteration. For vertically aligned experiments epoxy coated core plugs of 10.7 cm long and 4.72 cm in diameter as opposed to 7 cm long and 3.81 cm ones in horizontal experiments were used. Table 1 gives physical properties of the core plugs used in the experiments. The system confining pressure was kept at 500 psi using a manually operated hydraulic pump. The temperature of the system was kept at the desired temperature using an electronic temperature controller with an accuracy of 0.1°C and a heating rod. In all experiments prior to start CO₂ was injected into the core plug in order to remove possible air stuck in pores. Core plug was then saturated with NaBr brine. NaBr brine as opposed to NaCl brine allowed an accurate determination of the porosity. Breakthrough time and pore volume of the core plug were determined at this stage. Pressure readings obtained from a pressure transducer (accuracy %0.1) were recorded when the brine flow reached steady conditions using a data logger. Prior to each experiment reference dry CT scans (Table 2) of 8 equally separated volume elements (slices) were acquired and after each CO₂ injection period (approximately 10 pore volumes) permeability and porosity of the core plugs were measured. At the end of each CO₂ injection period the core plugs were re-saturated with brine and reference wet CT scans were shot at the same locations. Porosity of each slice was then obtained by averaging porosities obtained in a circular region of interest that is slightly smaller than the diameter of

the core plug. The porosity for a slice was obtained using the following equation (Akin and Kovscek, 2003).

$$\phi = \frac{CT_{wr} - CT_{ar}}{CT_w - CT_a} \quad (2)$$

In this equation subscripts w and a represent brine and CO₂ CT numbers, whereas wr and ar refer to brine-saturated and CO₂-saturated rock, respectively. The distribution of porosities and raw CT images (Fig. 2) showed the heterogeneous nature of the core plugs. Experiments were conducted at differing injection rates (3, 6 and 60 cc/min), temperatures (20, 35 and 50°C) and brine salinities (0, 2.5, 5 and 10 weight percent).

Table 1. Physical properties of the core plugs used in the experiments

Plug	D cm	L cm	Initial ϕ %	Initial md	K
1	4.72	10.7	2.4	44	
2	4.72	10.7	11	23.4	
3	3.81	7	22.3	451.9	
4	4.72	10.7	-	19.9	
5	4.72	10.7	26.8	58.7	
6	4.72	10.7	24.4	38.6	
7	3.81	7	10.3	2.9	
8	3.81	7	-	79.0	

Table 2. CT scan parameters used in the experiments

Scan time	3 seconds
Field of view	16 cm
Current	250 mA
Voltage	130 kV
Slice thickness	10mm
Positioning accuracy	±1 mm

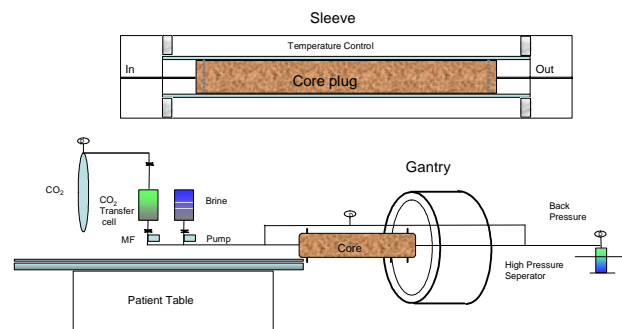


Figure 1. Experimental setup.

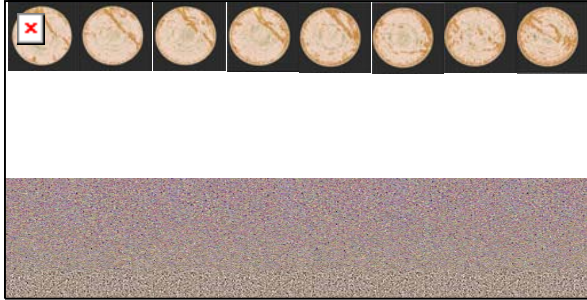


Figure 2. Locations of CT slices and sample CT images taken along the core plug (injection is from left to right).

RESULTS AND DISCUSSIONS

Figures 3 through 6 presents the results of experiments conducted with varying temperatures (Fig 3), brine salinities (Fig 4), core orientations (Fig 5) and injection rates (Fig 6).

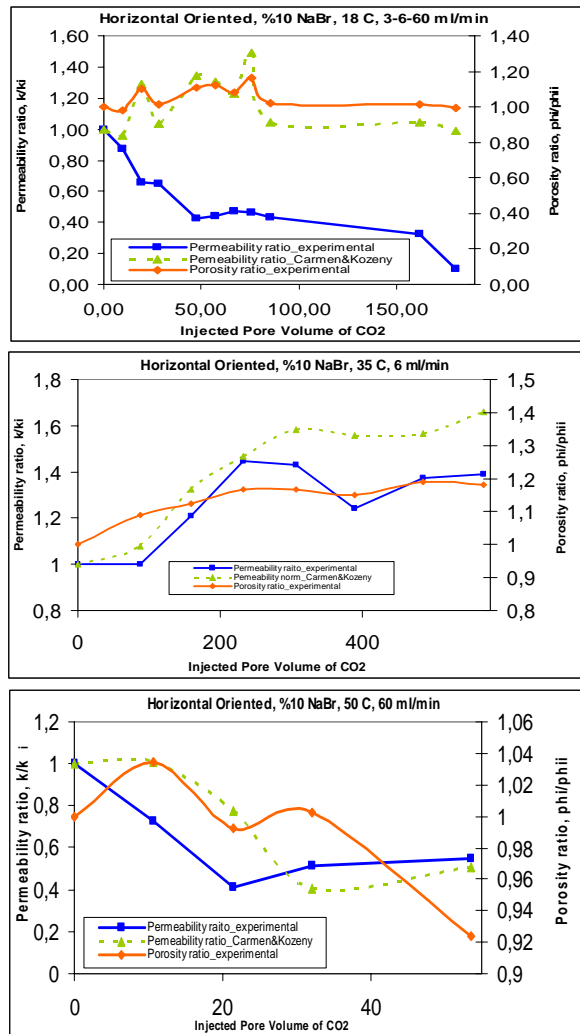


Figure 3. Effect of temperature on permeability and porosity change.

In general for vertically oriented core plug experiments, it was observed that the permeability increased and then decreased after a certain pore volume regardless of the salinity and injection rate (Fig. 5). On the other hand, for horizontally oriented core plugs the permeability initially decreased and then after a certain injection stabilized. Porosity observations however did not one to one match the permeability behavior but showed similar trends. In horizontally aligned cases the porosity stayed above the original level for a long time. Results of these experiments suggest that orientation of cores have a strong impact on permeability and porosity alteration trends. In vertically oriented core plugs due to gravitational forces CO₂ easily moves to the top of the core. This in turn increases the contact area of the CO₂ in pores near the inlet and increases chemical reaction frequency leading to the formation of carbonic acid. As the injection continues some of the dissolved calcite blocks the smaller pores along the flow path and thus results in a decrease in permeability later during the experiment. On the other hand, for horizontally aligned core plug experiments injected carbon dioxide does not move easily to the end of the core plug and forms carbonic acid near the inlet. This results in an increase in porosity near the inlet only. Calcite particles then deposit along the flow path especially near the exit which results in a decrease in permeability. CT derived porosity values support this theory as shown in Fig 7. Later in the experiment permeability keeps on decreasing until an equilibrium state where no longer alteration in permeability and porosity is observed.

The effect of temperature on calcite scaling was analyzed using three experiments conducted at 18°C, 35°C and 50°C. The latter is a typical temperature observed in shallow geothermal reservoirs in Turkey. The CO₂ injection rates covered a wide range (3 to 60 ml/min) corresponding to slow reservoir flows to fast near wellbore flows. In horizontally oriented core plugs the permeability decreased to 40% of the initial permeability after CO₂ injection then stabilized around this value for a while (Fig 3). Then it started to decrease again. This behavior was observed for two experiments with different temperatures (18° and 50°C). For the 35°C experiment, permeability stayed constant for a while and then increased. The porosity trends for these experiments followed the permeability trends. The permeability calculated from porosity using a Cozeny type equation (CMG, 2004) given below did not exactly match the observed permeability but the trend was similar.

$$K_f = K_0 \left(\frac{\phi}{\phi_0} \right)^c \left(\frac{1-\phi_0}{1-\phi} \right)^2 \quad (3)$$

In this equation, K_0 and ϕ_0 are the original or initial permeability and porosity, and c is a user defined power that is adjusted to have a match with the experimental data. Note that permeability calculated from porosity using the above equation assumes that tortuosity is constant. In practice; however, as carbonic acid dissolves calcite and the calcite particles deposit, the tortuosity should change continuously. For the experiments where the Cozeny type model represents the permeability change it could be speculated that the tortuosity does not change or stays nearly constant.

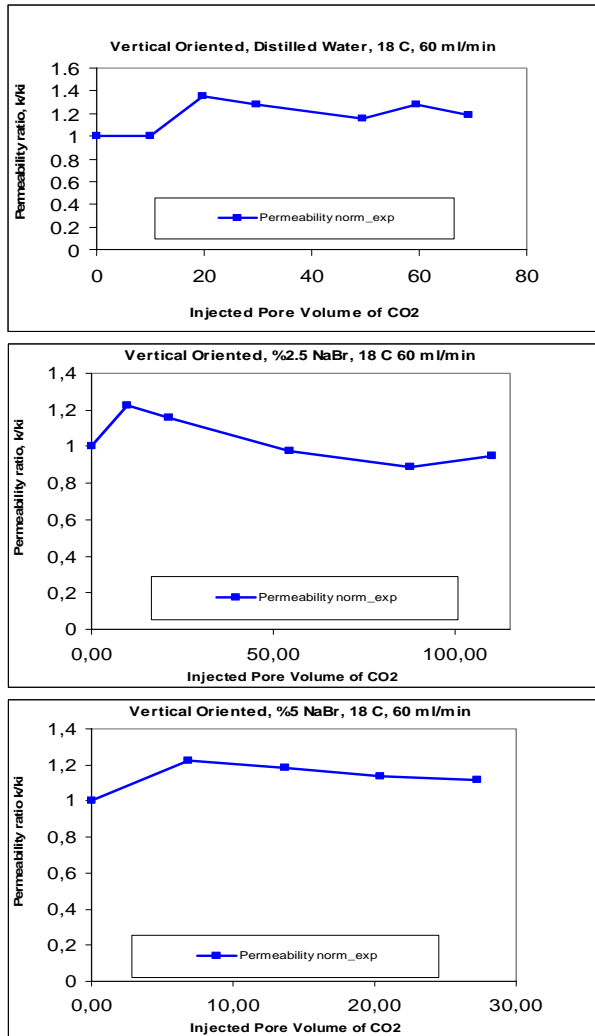


Figure 4. Effect of salinity on permeability and porosity change.

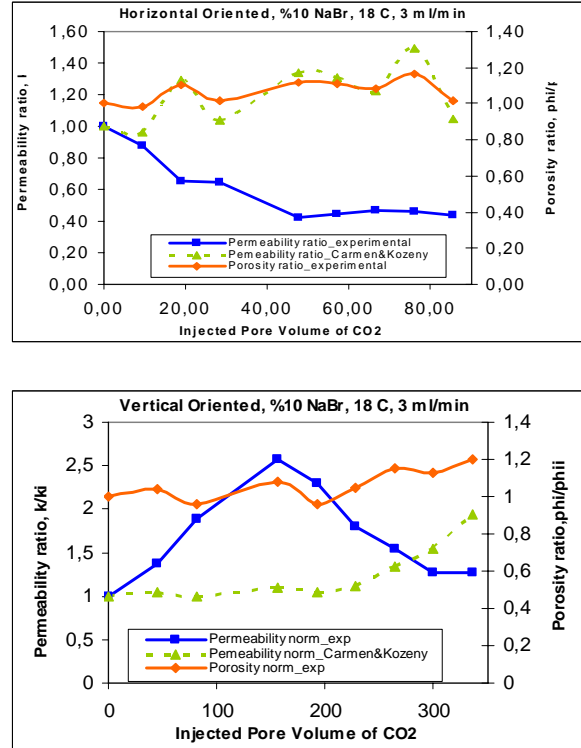


Figure 5. Effect of orientation on permeability and porosity change.

It was observed that salinity (Fig 4) and injection rate (Fig 5) of CO_2 has no drastic effect on changes in rock properties as the salinity was increased from 0 to 5% by weight and injection rate of CO_2 was increased from 3 ml/min to 60 ml/min. It was observed that when distilled water was used the permeability increase was 40% more compared to saline cases, 20%. As the salt content of the brine increased permeability drop was pronounced more. The length of CO_2 – rock contact time and the amount of area contacted by CO_2 seems to have a more pronounced effect compared to rate effect.

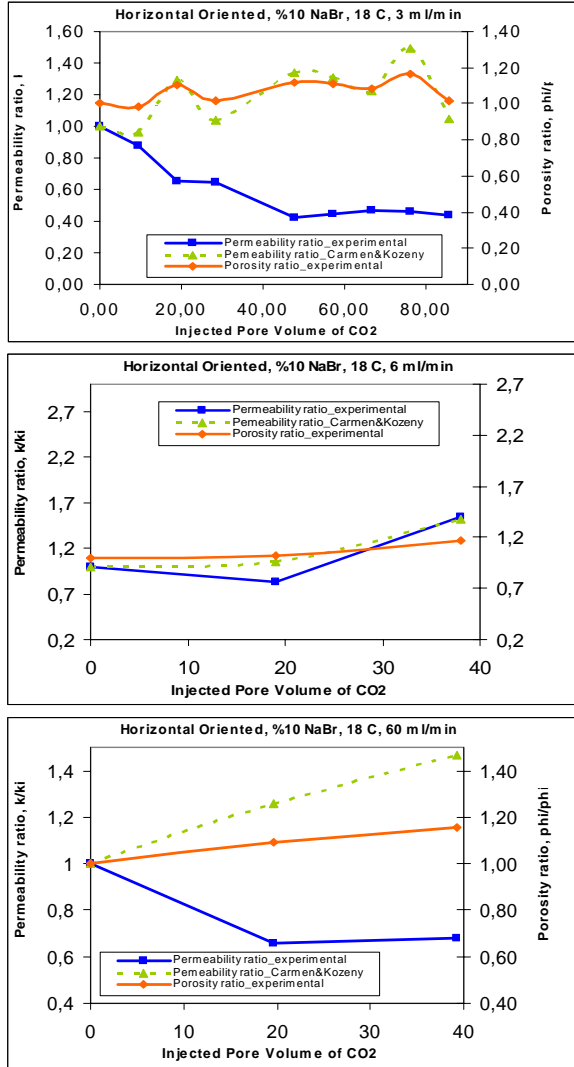


Figure 6. Effect of flow rate on permeability and porosity change.

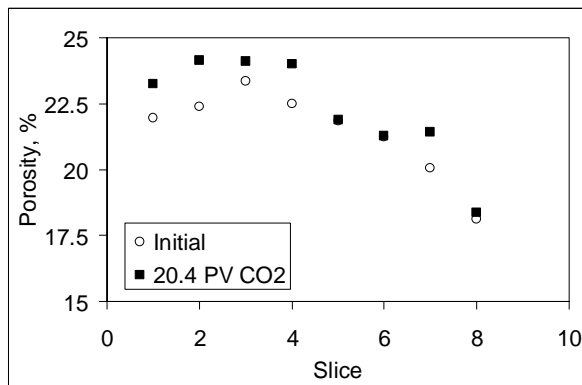


Figure 7. Porosity change observed during a horizontal experiment (10% NaBr, 18°C, 3ml/min).

The change in pH of the aqueous phase was also studied (Fig. 8). It was observed that pH of the effluent was basic as opposed to acidic in many

instances. In essence the pH of the effluent closely followed the porosity change. Thus these results are in accord with the aforementioned observation, i.e., for horizontal experiments injected carbon dioxide does not move freely to the end of the core plug and forms carbonic acid near the inlet. This results in an increase in porosity near the inlet only. Calcite particles then deposit along the flow path especially near the exit which results in a decrease in permeability and an increase in pH.

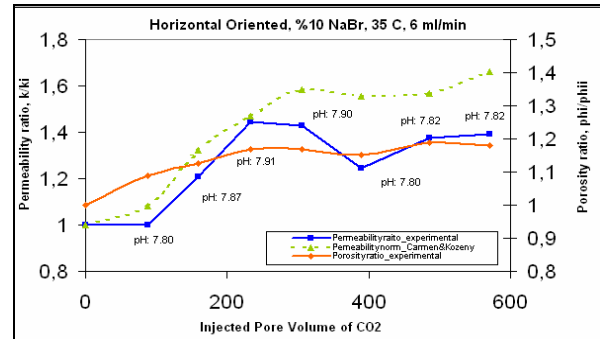


Figure 7. Porosity change observed during experiment 3.

CONCLUSIONS

Results of CT monitored CO₂ injection experiments showed that:

1. Calcite scaling is mainly influenced by orientation and horizontal flow resulted in larger calcite deposition compared to vertical flow.
2. The duration of CO₂ – rock contact and the amount of area contacted by CO₂ seems to have a more pronounced effect compared to rate effect.
3. For the temperature range studied (18°C – 50°C) permeability and porosity alteration trends were similar.
4. Once the porosity is known the permeability behavior could be predicted by a Cozeny type equation.

ACKNOWLEDGEMENTS

We are grateful to TUBITAK (Turkey) and CNRS (France) for kindly providing this work with financial support through project No. 102Y154. We also wish to thank to Middle East Technical University Petroleum Research Center (PAL) management for enabling us to use the CT scanner.

REFERENCES

- Akin, S. and A. R. Kovscek (2003). "Computerised Tomography in Petroleum Engineering Research," in Applications of Computerized X-ray Tomography in Geology and Related Domains, Jacobs, P., Mees, F., Swennen, R, Van Geet, M. (eds), Special Publication, Geological Society, London.
- Akin, S., Yeltekin K. and Parlaktuna M., (2003). "Numerical Modeling of Kizildere Geothermal Field, Turkey" European Geothermal Conference - 25-30 May, Szeged, Hungary
- Benoit, W. R. (1989). Carbonate scaling characteristics in Dixie Valley, Nevada geothermal wellbores. *Geothermics*, vol. 18, pp. 41-48.
- Clotworthy, A. Lovelock, B and Carey, B. (1995). Operational history of the Ohaaki geothermal field, New Zealand. Proc. World Geothermal Congress, 1995, pp. 1797-1802.
- Durak, S., Erkan, B. and Aksoy, N. (1993). Calcite removal from wellbores at Kizildere geothermal field, Turkey. Proc. 15th New Zealand Workshop, pp. 11-15.
- Evanoff, J., Yeager, V., and Spielman, P. (1995). Stimulation and damage removal of calcium carbonate scaling in geothermal wells: A case study. Proc. World Geothermal Congress, 1995, pp. 2481-2486.
- Kristmannsdottir, H. Arnornonsson, H., Axelson, G., Olafsson, M., Hakanarson, S., Thorhallson, S. (1995). Monitoring of Iceland geothermal field during production. Proc. World Geothermal Congress, 1995, pp 1813-1817.
- Nogara, J.B. (1999). Calcium carbonate scaling in geothermal wells at Ohaaki. Proc. 20th Annual PNOG-EDC Geothermal Conference, pp. 91-98.
- Satman, A., Ugur, Z., Onur, M.: "The Effect of Calcite Deposition on Geothermal Well Inflow Performance", *Geothermics*, June 1999, 4(1), 425-444.
- Simmons, S. F. and Christenson, B. W. (1993). Towards a Unified Theory on Calcite Formation in Boiling Geothermal Systems. Proc.15th New Zealand Geothermal Workshop, pp. 145-148.
- Todaka, N., Kawano, Y., Ishii, H. and Iwai, N. (1995). Prediction of Calcite Scaling at the Oguni Geothermal Field, Japan: Chemical Modeling Approach. Proc. World Geothermal Congress, 1995, pp. 2475-2480.
- Ueda, A., Ajima, S., and Yamamoto, M.: Isotopic study of carbonate minerals from the Sumikawa geothermal area and its application to water movement, *J. Geotherm. Res. Soc. Japan*, 23, 181-196, 2001.

NON-CONDESABLE GASES AT THE MIRAVALLS GEOTHERMAL FIELD

Paul Moya and Eddy Sánchez

Instituto Costarricense de Electricidad, UEN Proyectos y Servicios Asociados
C. S. Recursos Geotérmicos, Apartado Postal 10032-1000
San José, Costa Rica, Centro América
e-mail: pmoya@ice.go.cr , esanchezr@ice.go.cr

ABSTRACT

The Miravalles Geothermal Field has been producing electric energy since March 1994. It has provided steam for Unit 1 (55 MWe) since 1994, a Wellhead Unit (5 MWe) installed in 1995, Unit 2 (55 MWe) in 1998, Unit 3 (29 MWe) in 2000 and Unit 5 (19 MWe, a binary plant) in year 2004. The total installed capacity (163 MWe) has been increasing since 1994, and so have the non-condensable gases in the steam. With these increases, the compressors at the generating units have reached their maximum gas capacity without ejectors, and therefore options to decrease the non-condensable gases have been analyzed. Field management strategies have been implemented in order to minimize the total amount of non-condensable gases that are sent to the generating units.

INTRODUCTION

The Miravalles geothermal field is located on the southwestern slope of the Miravalles volcano. The extent of the geothermal field already identified is greater than 21 km², of which about 16 km² are dedicated to production and 5 km² to injection. There are 53 geothermal wells (Figure 1), including observation, production and injection wells, whose depths range from 900 to 3,000 meters. The production wells produce between 3 and 12 MW each, and the injection wells each accept between 70 and 450 kg/s. The reservoir has a temperature of about 240 °C and is water-dominated (Moya, 2003).

The Miravalles geothermal field has been producing since 1994. Normally, two or three production wells supply two-phase fluid to each separation station. Seven separation stations now supply the steam needed for Unit 1, Unit 2, Unit 3 and one active Wellhead Unit. At present there is a need to supply enough steam to produce 55 MWe (Unit 1), 5 MWe (Wellhead Unit), 55 MWe (Unit 2) and 29 MWe (Unit 3), for a total of 144 MWe. This capacity was increased to 163 MWe when a bottoming-cycle

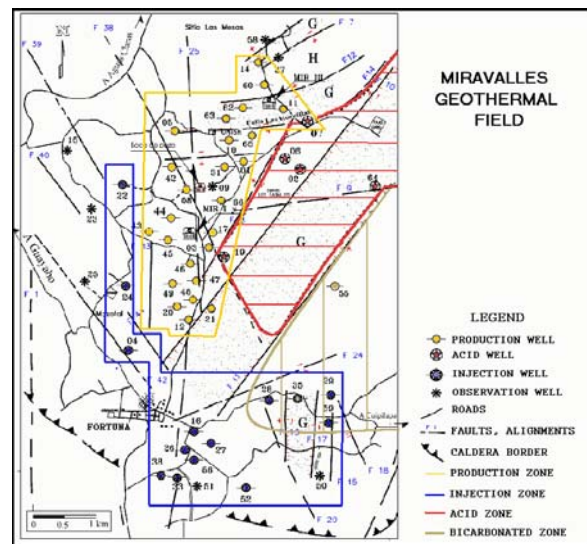


Figure 1. Miravalles Geothermal Field.

binary plant came online in January of 2004. As indicated in Table 1, two wellhead units from the Comisión Federal de Electricidad (Mexico) were in operation while Unit 2 was being built, but these have been decommissioned.

Plant Name	Power (MW)	Belongs to	Start-up Date	Final Date
Unit 1	55	ICE	3/1994	
WHU-1	5	ICE	1/1995	
WHU-2	5	CFE	9/1996	4/1999
WHU-3	5	CFE	2/1997	4/1998
Unit 2	55	ICE	8/1998	
Unit 3	29	ICE (BOT)	3/2000	
Unit 5	19	ICE	1/2004	

Table 1: Units at the Miravalles geothermal field.

In Table 1, the abbreviations stand for: ICE - Instituto Costarricense de Electricidad; CFE - Comisión Federal de Electricidad (México); WHU - Wellhead Unit; and BOT – build-operate-transfer.

NON-CONDENSABLE GAS EVOLUTION

Data from the first wells drilled at the Miravalles geothermal field showed that there was a wide range of concentrations of non-condensable gases in the steam. As new wells were drilled, it was determined that, under natural conditions, the field's non-

condensable gas content ranged from 0.4 to 1.2 % w/w. Figure 2b shows the natural distribution of non-condensable gas contents. In Figure 2a the values are disturbed by air-drilling, which had begun in 1992.

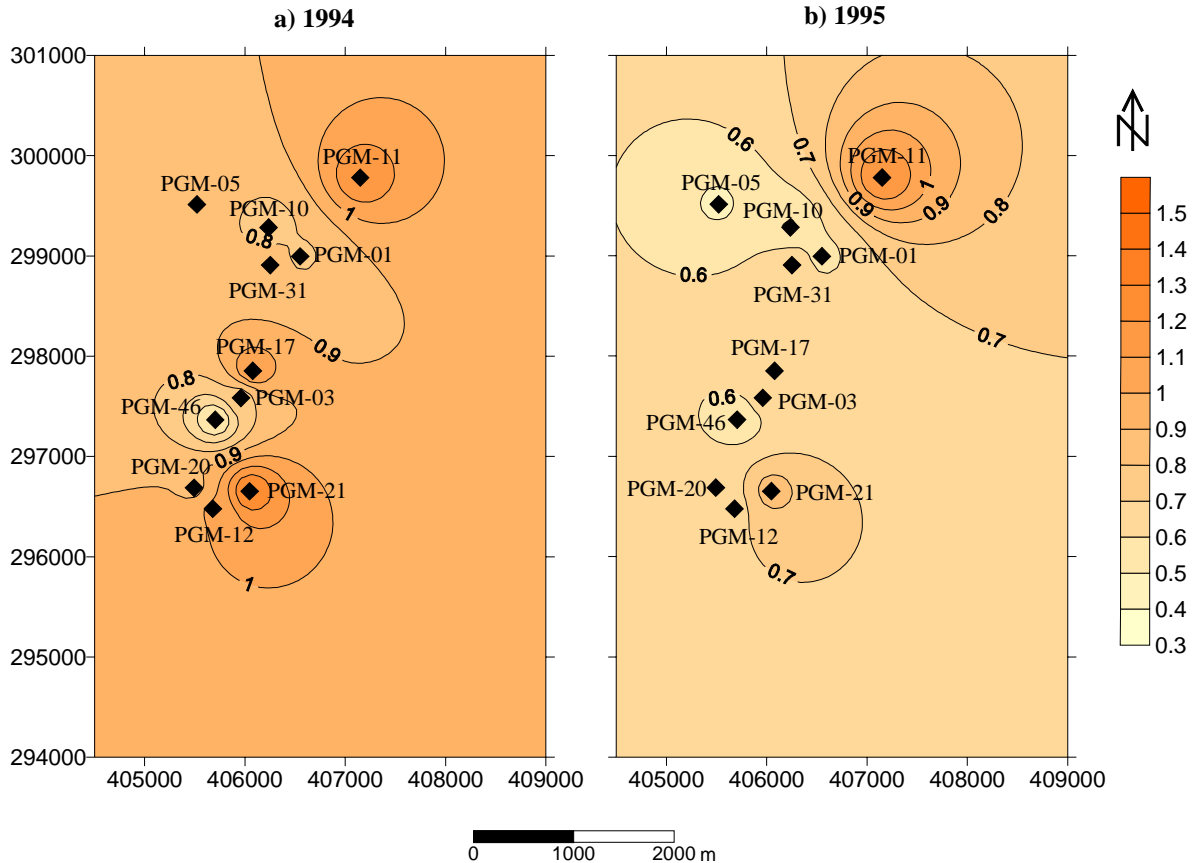


Figure 2. Distribution of non-condensable gases in 1994 and 1995 (% w/w in steam separated at 7 bar a)

All values of non-condensable gas concentration presented here are in weight percent (weight/weight). In Figure 2b, it can be seen that in 1995 the non-condensable gases in the northern part of the field (at wells PGM-11 and PGM-10) were 1.21 % and 0.48% respectively, in the central part (at PGM-46) they were 0.52 %, and in the southern zone (at well PGM-21) they were 0.86 %. Almost every well fell within the range mentioned above (Sánchez, 2004a). Non-condensable gas contents have been affected during commercial operation by the following factors:

1. The “bubble effect”, which takes place when drilling with aerated fluids (to protect open fractures) causes the upper layers of the reservoir to become richer in non-condensable gases, due to the carbon

dioxide (CO₂) present in the reservoir as well as the nitrogen (N₂) provided by air injection when drilling. Figure 3 shows the non-condensable gas content behavior in well PGM-21 from 1994 to 2004. The gas content was close to 1.3 % initially and decreased a year later to around 0.8 % (Figure 3, yellow box).

A similar behavior of the non-condensable gases is shown in Figures 4 and 5, in which the wells PGM-10 (northern zone) and PGM-20 (southern zone), respectively, experienced an increase followed by a decrease within a year.

2. Changes in the hydrogeology of the system due to continuous exploitation cause fluids which may have high or low gas contents to move from one sector of the field to another.

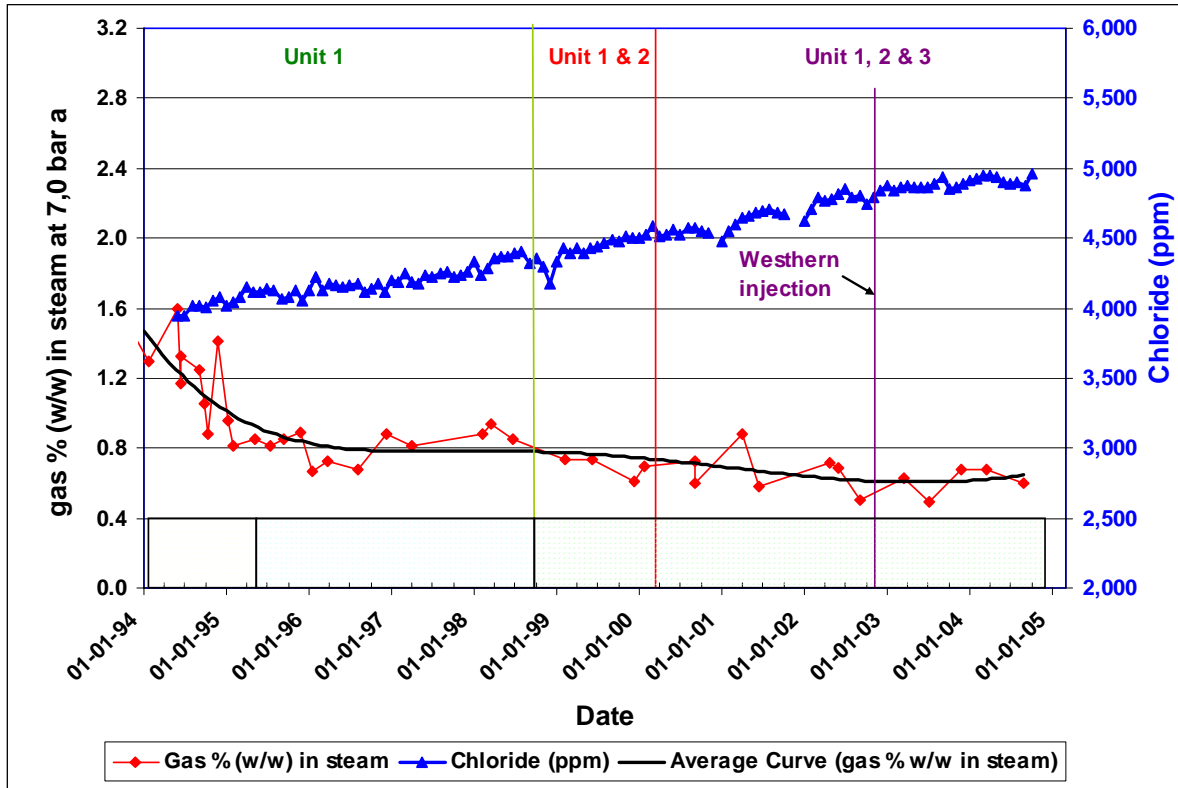


Figure 3. History of non-condensable gases in well PGM-21 (% w/w in steam separated at 7 bar a)

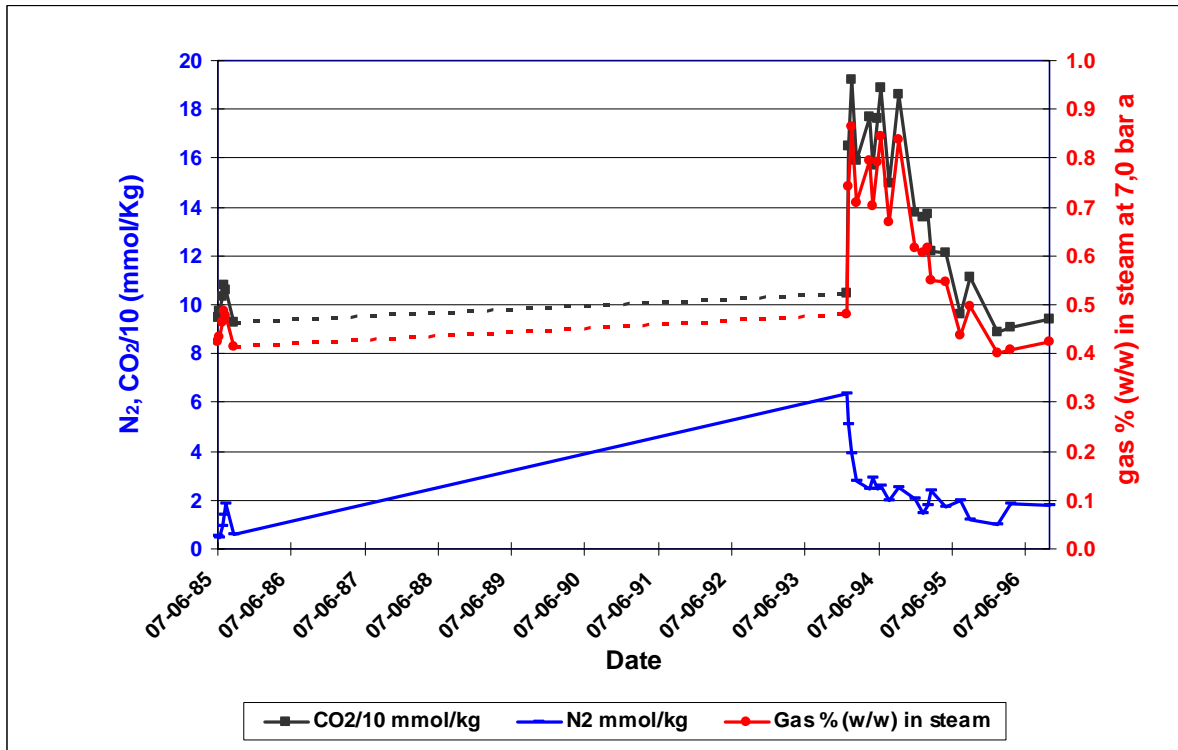


Figure 4. History of non-condensable gases in well PGM-10 (% w/w in steam separated at 7 bar a)

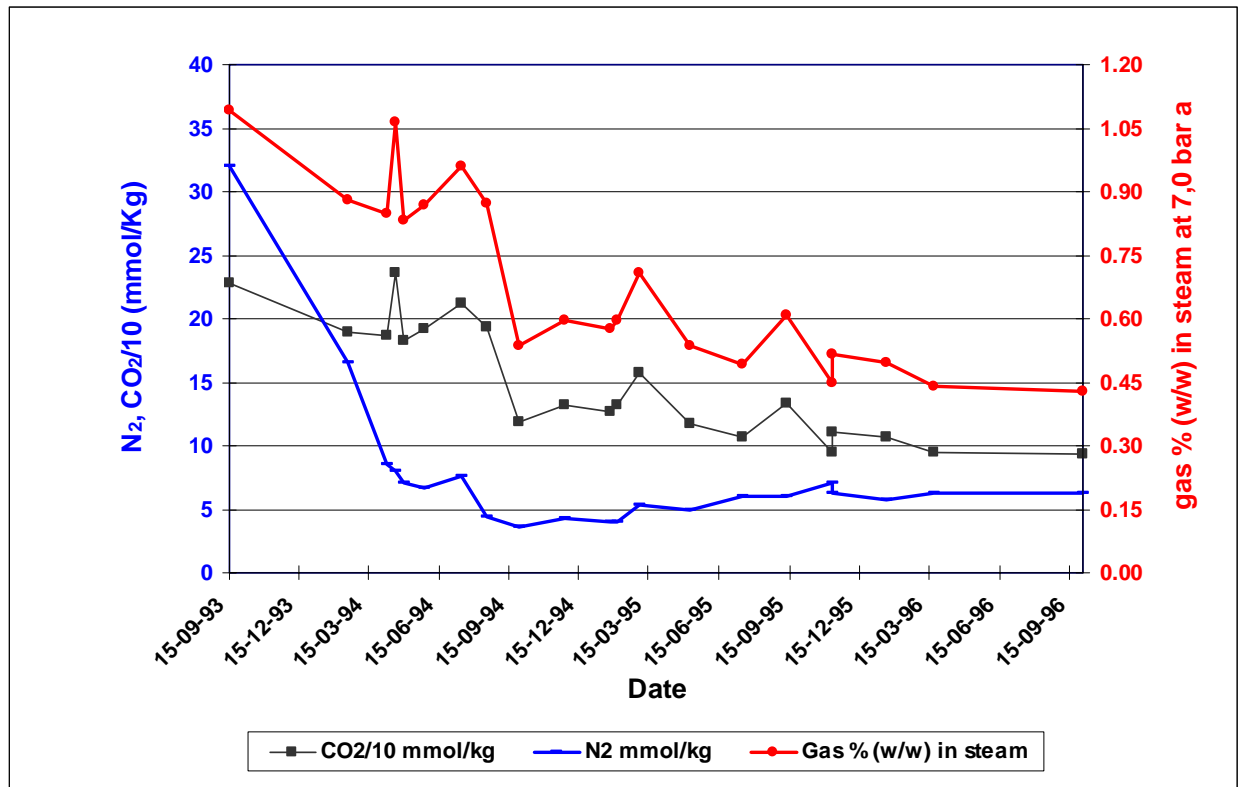


Figure 5. History of non-condensable gases in well PGM-20 (% w/w in steam separated at 7 bar a)

3. Injected fluids, which are degassed, travel back to some production sectors, causing a decrease in the non-condensable gases in those particular zones. In Figure 3 (green box) it can be seen that the non-condensable gases decreased from the end of the year 1999 to the end of 2004. The decrease coincided with an increase in the chloride content, also shown in Figure 3 (green box), which indicates that injected water was reaching that sector of the production zone 4. Sustained production due to continuous exploitation generates a pressure drawdown in the reservoir and an increase in the steam fraction. This increases the steam fraction, but at the same time increases the non-condensable gases in the steam. Figure 6 shows the behavior of the non-condensable gases in well PGM-10. The well was drilled during 1984, but air-drilling in the surrounding wells (PGM-09 and PGM-31) increased the non-condensable gases to a value close to 0.8% in early 1994. The gases then began to decrease (until the end of 1997) and finally increased from the end of 1997 to the end of 2004. The increment in the non-condensable gases coincided with an increase in enthalpy values for the same period (1997 to 2004). In well PGM-10, the pressure drop (close to 2 bar/year from 1998 to 2003) caused the wellhead pressure to decrease, impeding

PGM-10 from supplying its two-phase flow to the gathering system, which finally caused the well to stop producing.

The bubble effect was transitory; that is, it increased the non-condensable gases up to 100% in some cases, but it disappeared within the following year, leaving non-condensable gas content of the particular zone at its natural level. The other three effects (hydrogeology, injected fluids and pressure drop) have been present since production started and have influenced the increase in non-condensable gases one way or another. Figures 7 and 8 show that, in several production wells and reservoir sectors (respectively), the non-condensable gases have been increasing from 1994 to 2004. It can be seen from these two figures that the non-condensable gas increase in the reservoir has taken place since the three major units (Units 1, 2 and 3) began been producing continuously.

The bubble effect due to air-drilling, as well as the hydrogeologic effects and pressure decline caused by the continuous exploitation of the reservoir, have produced a strong increase in the non-condensable gases at the Miravalles geothermal field. Only the effect of injected fluids has tended to decrease the non-condensable gas content.

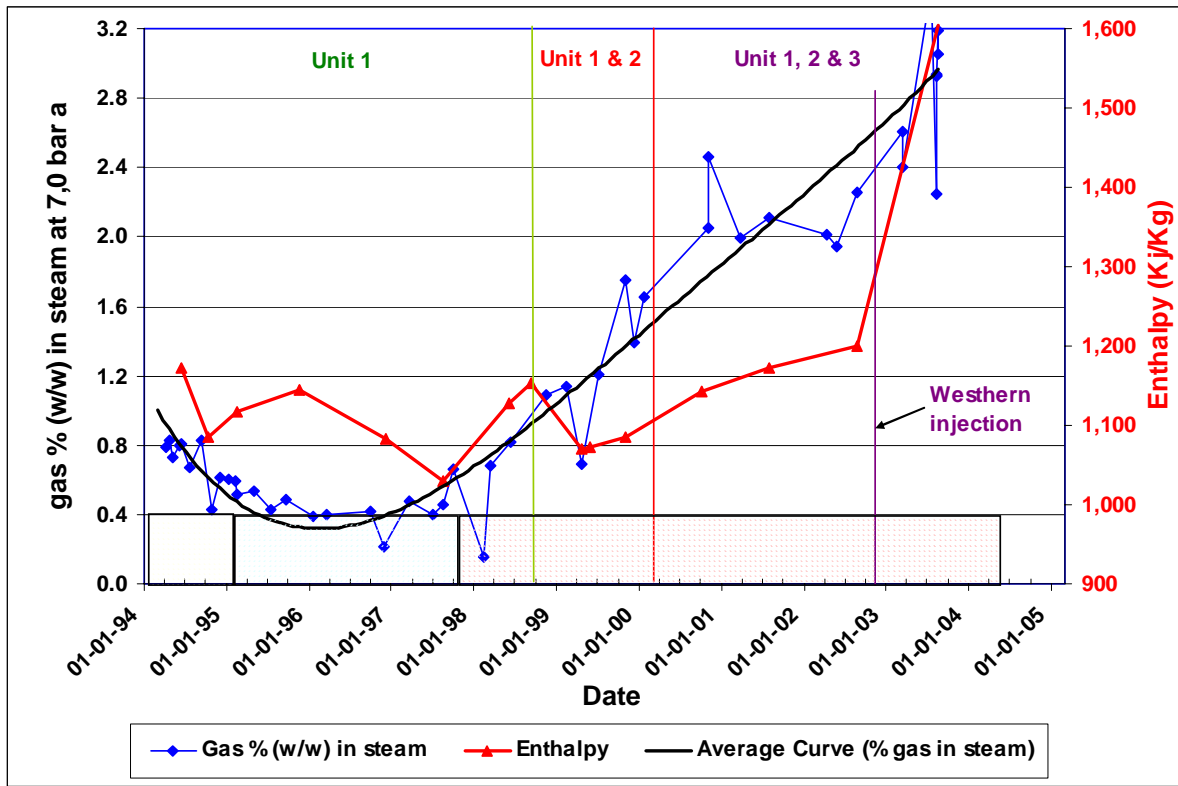


Figure 6. History of non-condensable gases in well PGM-10 (% w/w in steam separated at 7 bar a)

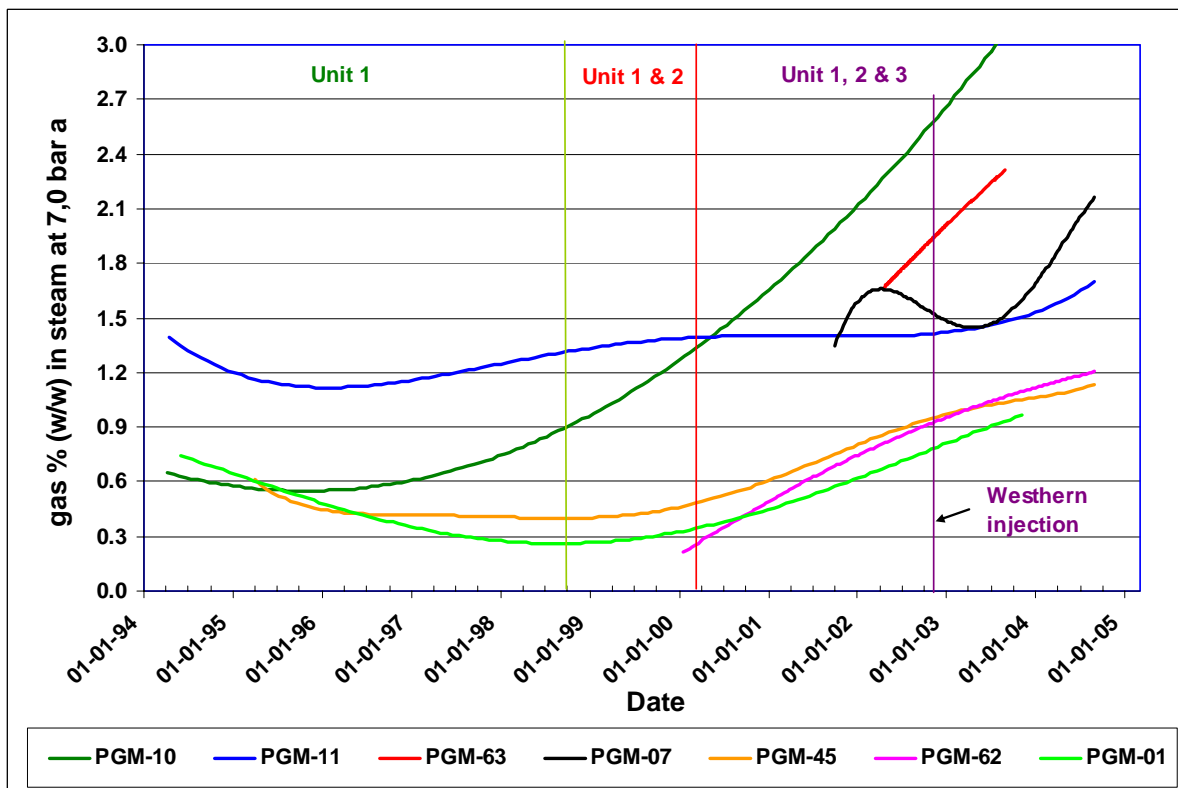


Figure 7. History of non-condensable gases from 1994 to 2004 (% w/w in steam separated at 7 bar a)

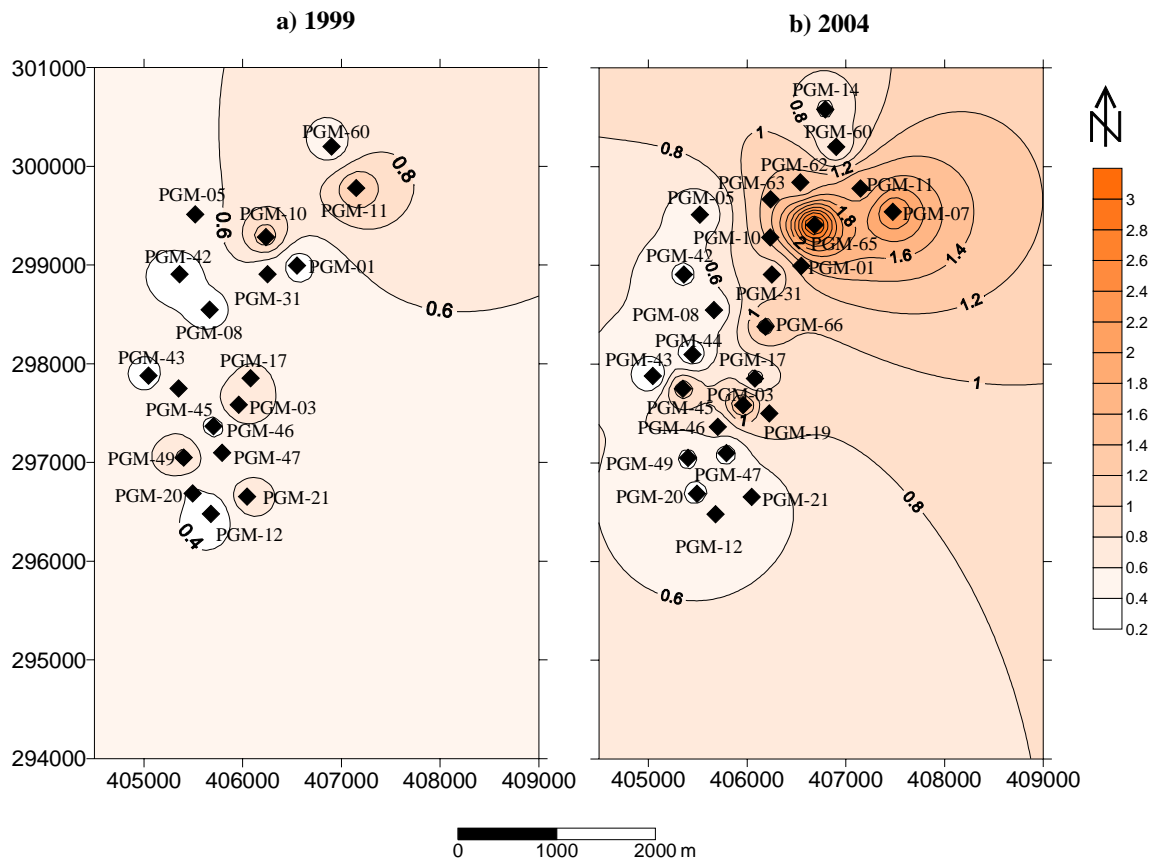


Figure. 8. Distribution of non-condensable gases from 1999 to 2004 (% w/w in steam separated at 7 bar a)

FIELD STRATEGIES

The continuous exploitation of the reservoir has tended to increase the non-condensable gases in the reservoir, which in turn has provoked the establishment of a program of detailed monitoring of the non-condensable gases at each well in order to determine the principal causes of the increase, and also the implementation of injection and production strategies to improve the current operating conditions.

The studies that have been carried out have indicated that the principal cause of the increase in non-condensable gases is the pressure decline of the reservoir. In order to minimize this tendency, three different strategies have been or will be implemented. First, by increasing the volume of fluids injected in the western sector (wells PGM-22 and PGM-24), it was possible to decrease the non-condensable gases in the vicinity of well PGM-45 and also in all of the wells located in the western sector. Figure 9 shows that well PGM-45 had a trend of increasing non-condensable gases from early 1999 to late 2003.

Diverting more fluid to the western sector caused an immediate decrease in the non-condensable gases reported in this well (a positive effect). Also, the enthalpy began to decrease as a consequence of the arrival of injected fluids in the reservoir near well PGM-45.

Since positive results have been obtained by injecting hot fluids in the western and southern parts of the production zone, in the near future it is planned to inject more hot fluids into PGM-63, which could contribute to stopping the current pressure drop as well as decreasing the non-condensable gases in the northern zone. Wells such as PGM-01, PGM-10 and also PGM-63 were initially production wells (in 1994), but due to the pressure drop in the northern zone they have had to be taken out of production.

Second, the studies carried out have indicated that the non-condensable gases were increasing rapidly in the northern part of the production zone, that is, near wells PGM-11, PGM-60 and PGM-62. It has been necessary to produce these wells at a minimum flow rate in order to reduce the pressure drop and consequently the non-condensable gas contents. The resulting deficit in steam supply for Unit 3 (located in

the northern sector) is compensated for by steam from the central part of the field. This strategy has at least allowed the non-condensable gas content in that particular area to be kept constant. Third, two existing acidic wells (PGM-02 and PGM-06) are planned to be placed online to extract fluids from the “acidic zone” instead of the main production zone.

The production from the acidic zone will add to the steam supply in the northern zone (Unit 3), and will stabilize or slow down the pressure decline and consequently moderate the increase in non-condensable gas content in that sector of the reservoir.

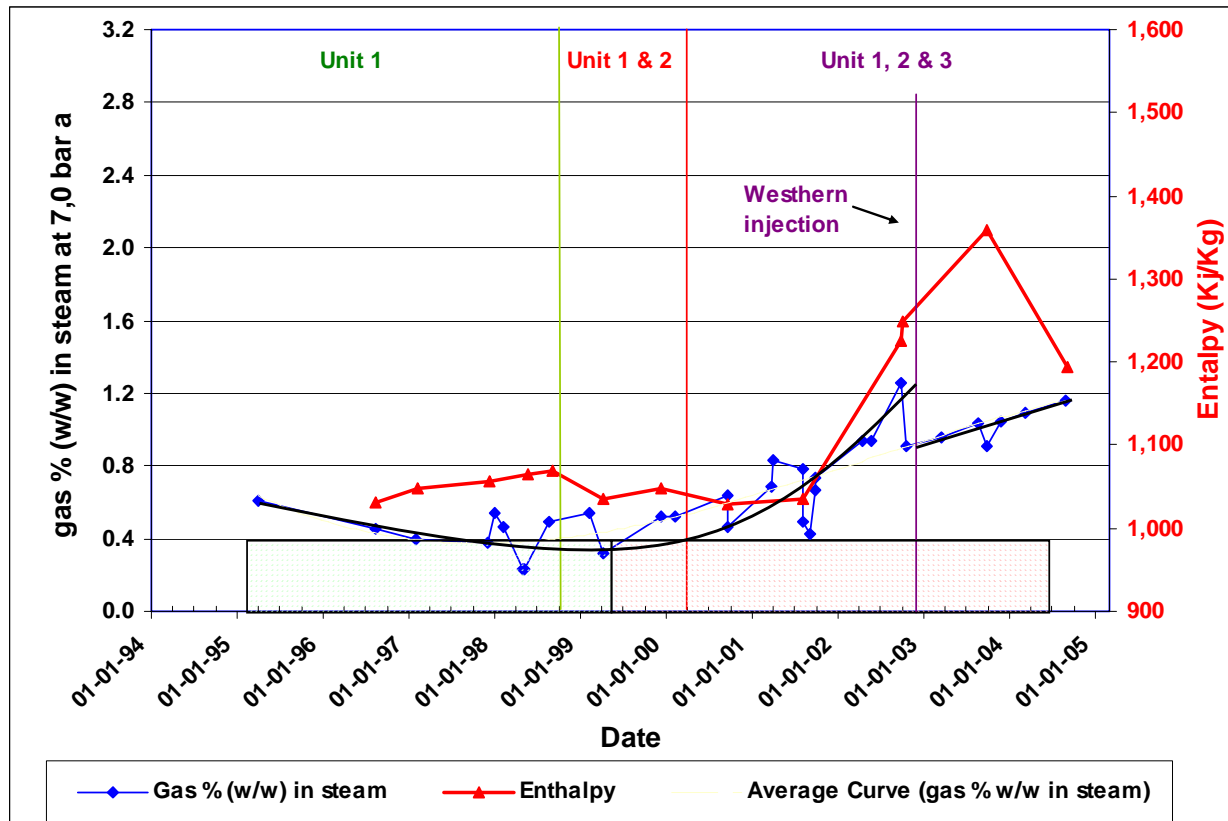


Figure. 9. History of non-condensable gases in well PGM-45 (% w/w in steam separated at 7 bar a)

IMPROVEMENTS

The strategies described in the above section have allowed optimization of the available steam supply for the generating plants. A new strategy has been established for managing the steam supply from the field. Initially (in 1994) there was no particular strategy for supplying steam to the various units, but now it is important to manage the supply based on non-condensable gas contents, in order to maximize the final power output.

The compressor capacities for the main units are 0.66% (Unit 1), 0.88% (Unit 2) and 1.5 % (Unit 3). If the non-condensable gas content is higher than the compressor capacity, then the ejectors provide the extra capacity needed to process the steam. Unfortunately, the ejectors require some of the

supplied steam to operate, decreasing the efficiency of the energy generation.

Higher compressor capacities were specified for the new units coming online, but nevertheless those capacities are becoming too small to process the current levels of non-condensable gases being sent to the units.

Initially, separation stations 1, 2 and 3 supplied their steam to Unit 1, while separation stations 4, 5 y 6 supplied their steam to Unit 2. Separation station 7 supplies steam to Unit 3, but this unit can also receive steam from a pipeline coming from separation station 1.

Figure 10 indicates that, by the end of 2003, the compressor capacity of Unit 1 (0.66%) was insufficient for the non-condensable gases coming from separation stations 1 (1.66%), 2 (1.0%) and 3 (0.46%), with a weighted average of 0.94%. On the other hand, the compressor capacity of Unit 2

(0.88%) was much higher than the capacity required for the steam from separation stations 4 (0.37%), 5 (0.75%) and 6 (0.44%), with an average of 0.58%. After studying the case and looking for the best option, it was decided to interchange separation stations 1 and 4. Beginning in early 2004 the steam

coming from separation station 1 was sent to Unit 2 and vice versa, that is, the steam from separation station 4 was sent to Unit 1. The interchange resulted in a better distribution of the non-condensable gases among the compressors (Figure 11).

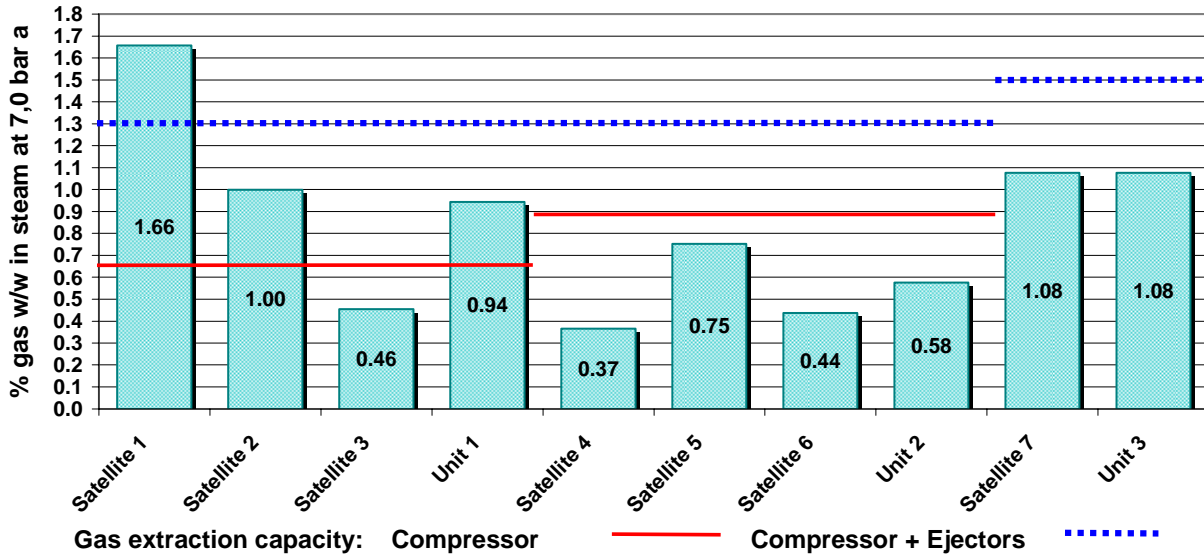


Figure. 10. Non-condensable gases per satellite in 2003 (% w/w in steam separated at 7 bar a)

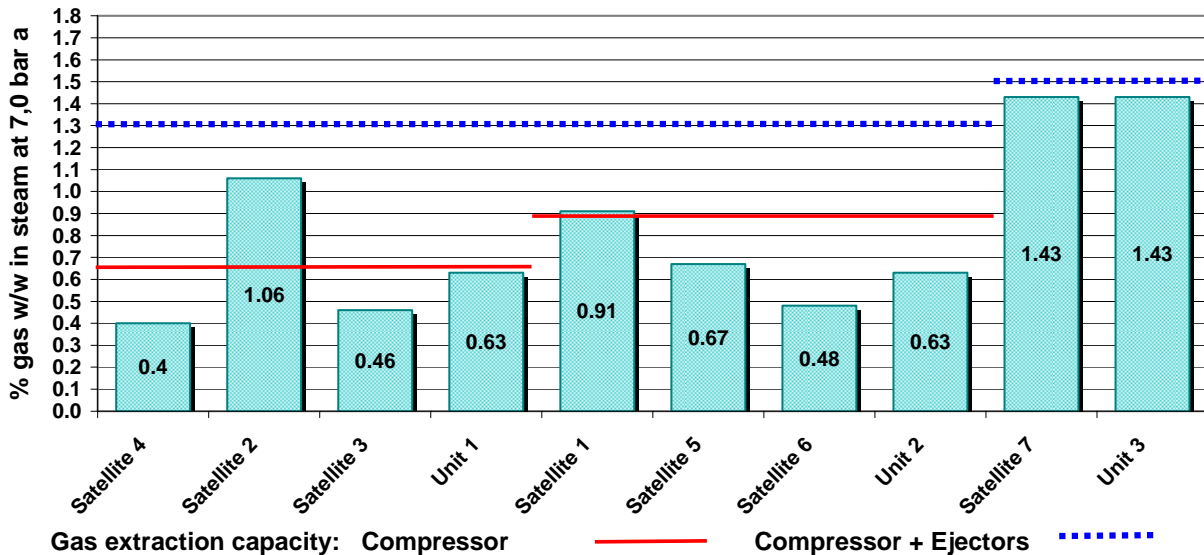


Figure. 11. Non-condensable gases per satellite in 2004 (%w/w in steam separated at 7 bar a)

The effect of the switch can be observed in Figures 12 and 13. Figure 12 shows the measured non-condensable gas data, the average curve for the

measured data and the maximum compressor capacity at Unit 1. Once the interchange was made, a decrease in the total non-condensable gas content was

observed (Figure 12). In contrast, Figure 13 shows an inverse effect, that is, an increase occurred after switching the non-condensable gases from the separation stations 1 and 4. Since the non-condensable gas content in the reservoir keeps increasing, due to continuous exploitation, the gas content at the three units has consequently increased (Figures 12, 13 and 14).

Even though interchanging the separation stations had a positive effect, at present the non-condensable gas contents are getting close to the maximum compressor capacities at Units 1, 2 and 3 (Figures 12, 13 and 14).

In order to fully utilize the compressor capacities at Units 1 and 2, there is the option of installing a set of

valves (upstream of the steam collectors of these Units) that would allow the steam from separation stations 1 and 4 to be variably distributed to Units 1 and 2. This would permit the non-condensable gas levels to be matched as closely as possible to the available compressor capacities.

The second and most expensive option would be to increase the non-condensable extraction capacity of the main units. This can be done by: a) increasing the current capacity of the compressor (improving it), b) adding a vacuum pump to the system, c) increasing the existing ejectors (increasing the amount of steam required per ejector), or d) buying a new compressor with the required capacity.

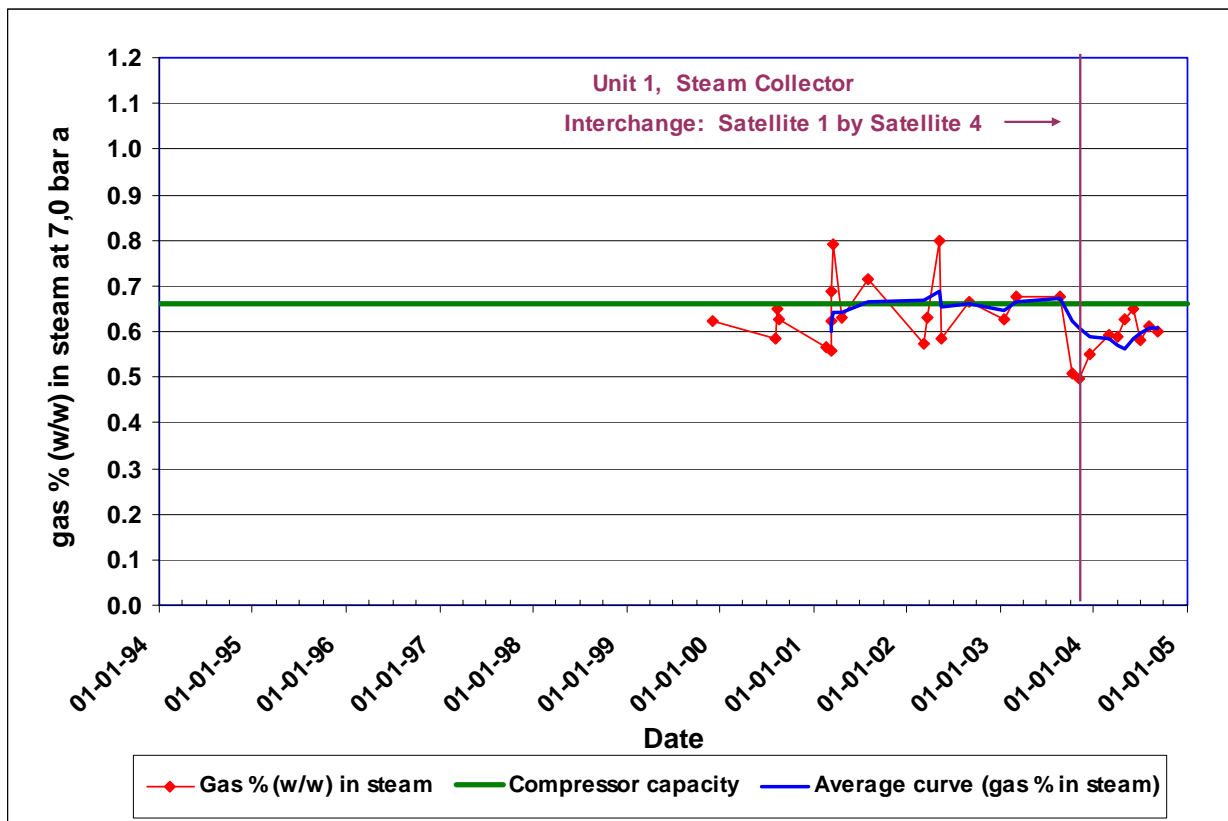


Figure. 12. History of non-condensable gases at Unit 1 (% w/w in steam separated at 7 bar a)

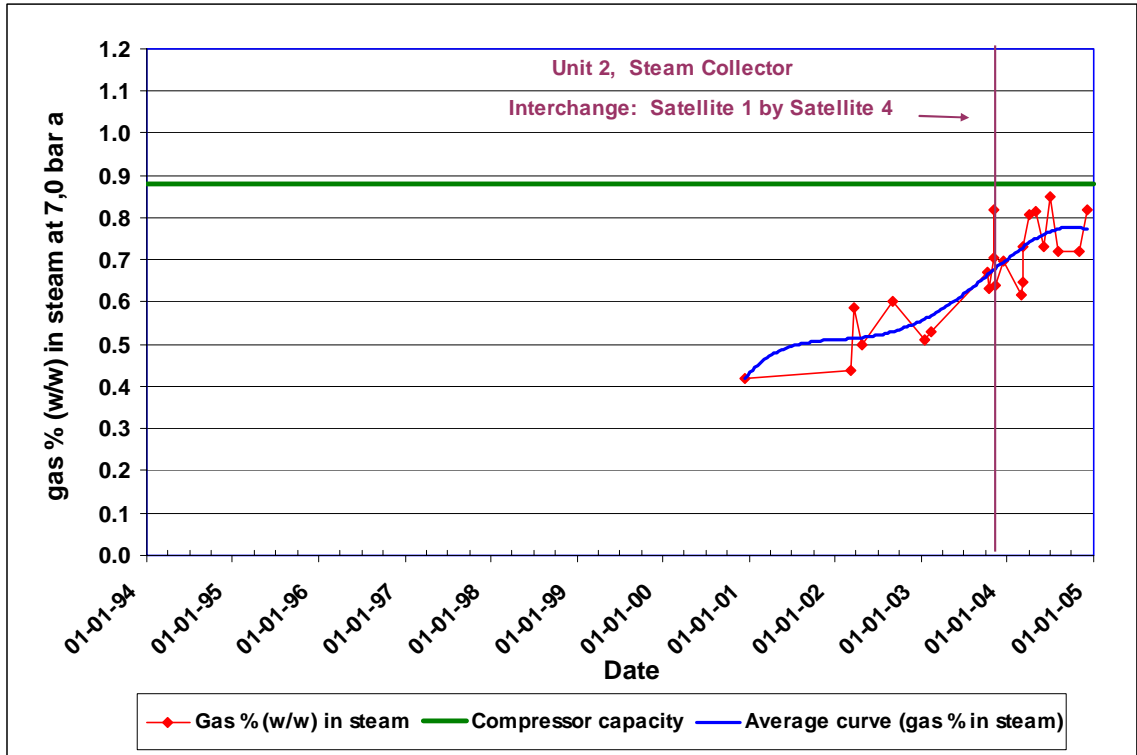


Figure. 13. History of non-condensable gases at Unit 2 (% w/w in steam separated at 7 bar a)

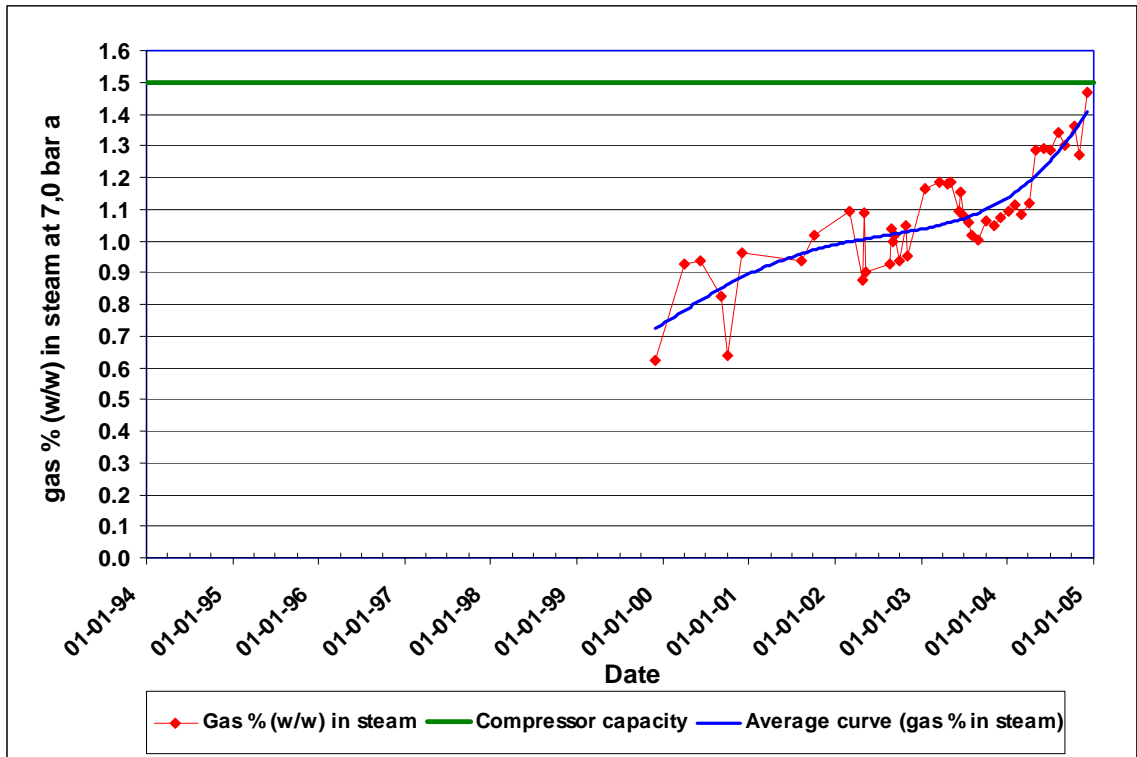


Figure. 14. History of non-condensable gases at Unit 3 (% w/w in steam separated at 7 bar a) (Sánchez, 2004b).

FINAL REMARKS

Air-drilling caused a temporary increase in non-condensable gases in the Miravalles reservoir that lasted for about a year.

The arrival of the injected fluids to some production sectors has contributed to a decrease of the non-condensable gases in those sectors. So far, most of the production wells in the western and southern sectors have been benefited from hot injection.

Hot fluid injection into PGM-63 should contribute to stopping the current pressure drop as well as decreasing the non-condensable gases in the northern zone.

Minimum flow production from the wells located in the northern sector has at least allowed the non-condensable gas content in that particular area to be kept constant.

Wells PGM-02 and PGM-06 are planned to be placed online to extract fluids from the "acidic zone" instead of the northern sector. This will allow a reduction of both, the pressure drop and the non-condensable gases in this part of the reservoir.

The pressure drop in the reservoir, due to continuous exploitation, is the principal cause of the increase in the non-condensable gas content of the system.

Interchanging the fluids from separation stations 1 and 4 contributed to obtaining a better distribution of the non-condensable gases at Units 1 and 2.

At the present non-condensable gas levels, the compressors of the main units are very close to their maximum capacities. The trend of increasing non-condensable gases suggests that in the near future the current compressor capacities will be exceeded.

A set of valves installed upstream of the steam collectors of Units 1 and 2 will allow diversion of part of the non-condensable gases to the compressor that is not operating at its maximum capacity, thus optimizing the current compressor capacities.

Under normal exploitation of the reservoir, it is expected that the trend of increasing non-condensable gas contents is going to persist. Investments in higher extraction capacities are foreseen at the generating units.

ACKNOWLEDGEMENTS

The authors thank Roger Henneberger (GeothermEx, Inc.) for editing and improving the manuscript.

REFERENCES

Moya, P., (2003), "The Costa Rican Geothermal Energy Development," *The IERE Central America Forum Transnational Electrical Interconnections and Sustainability in Central America*, Session 2, November 24-25, 2003. San José, Costa Rica.

Sánchez, E. (2004a), "Evaluación y tendencias del contenido de gases en el vapor entregado a las unidades 1 y 2 de Miravalles, periodo 2000-2004," *ICE Internal Report*, Equipo de Geoquímica, Area de Geociencias, 18 de setiembre de 2004.

Sánchez, E. (2004b), "Evaluación del contenido de gas en el vapor entregado a la Unidad 3 de Miravalles y pozos del Satélite 7, causas y consecuencias," *ICE Internal Report*, Equipo de Geoquímica, Area de Geociencias, 31 de octubre de 2004.

CERRO PRIETO IV, THE NEWEST POWER PLANT IN CERRO PRIETO GEOTHERMAL FIELD

Juan De Dios Ocampo-Díaz
 Universidad Autónoma de Baja California, Carrera de Ingeniería Mecánica,
 Blv. Benito Juárez, s/n, C.P. 21900, Mexicali, B. C., México
 Email: juandios@uabc.mx

Capacity installed

ABSTRACT

The Cerro Prieto IV power plant is the newest power plant in Cerro Prieto geothermal field, it started the production commercial generating in 2000, at present the entire installed capacity of generation in the geothermal field of Cerro Prieto is 720 MWE, the plant CP IV has a capacity of 100MW distributed in four units of 25 MW each one, all these units are feeding by the steam produced by twenty wells approximately. The total accumulate gross electricity generated through four years by this power plant is about 2'796,580 MWH.

The Cerro Prieto IV power plant is the newest plant in Cerro Prieto field and was constructed between April 1998 and July 2000, under a BLT (Build, Lease and Transfer) contract won by Mitsubishi Corporation responding to international bid issued by the Comision Federal de Electricidad, Quijano, et al. (2001).

INTRODUCTION

Cerro Prieto, Located in the State of Baja California, northwestern Mexico, close to border with USA, is the largest known water-dominated geothermal field in the world and one of the more thoroughly studied, Heard et al. (1986). The generation of electrical power from geothermal fluids on a commercial scale was begun by Comision Federal de Electricidad on April 4, 1973 with the Cerro Prieto Plant I, originally equipped with two turbogenerators of 37.5 MW each one, Dominguez (1981). Since that date, annual power generation has gradually increased. Its installed capacity is 720 MW, which at present, there are 13 units in operation include the Cerro Prieto IV (100 MW). Cerro Prieto IV is the first new geothermal plant built in Mexico, since 1994. At present, there are 13 units in operation housed in four power plants, see Ta. 1.

STEAM PRODUCTION OF CERRO PRIETO FIELD

In Cerro Prieto geothermal field, the steam flow rate is supplied from large diameter wells (0.24 m) drilled to depths which vary between 2000 m and 3500 m depth. About 150 wells distributed over an area of 15 km² (Fig. 1) are required to satisfy the needs of the four power plants.

Cerro Prieto	# Units	Capacity MW
I	4	37.5
II	1	30
III	2	110
IV	2	110

Table 1. Cerro Prieto Power Plant

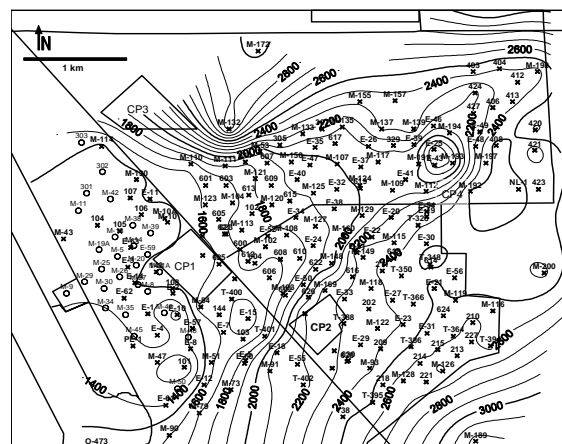


Figure 2. Cerro Prieto wells locations associated to reservoir top depth

The maximum temperature at the bottom of some of these wells reaches 350 °C and the maximum measure wellhead discharge pressure in one of this was about 120 bars. The initial mixture flow rate of

some wells exceeded 500 tonnes/h, Mercado, et al. (1987). Present day the steam produce by wells allocated in each Cerro Prieto production area is shown in Tab. 2.

Production area	High pressure steam flow rate (tonns/h)	Low pressure steam flow rate (tonns/h)	Producer wells number
CP I	347.86	-----	20
CP II	1974.52	284.11	57
CP III	1653.08	113.17	52
CP IV	969.79	79.83	18
Total			

Table 2. Cerro Prieto Steam flow rate by production area

CERRO PRIETO IV POWER PLANT

The power plant houses four 25-MW condensing units. Each of them requires 183 t/h of steam at 182 °C and 10.5 bar absolute, under standard operating conditions, the specific consumption for these units is about 7.3 tons of steam per MWh. Fig. 2 and Tab. 3 show the gross generation data for Cerro Prieto IV power plant from July 2000 to March 2004

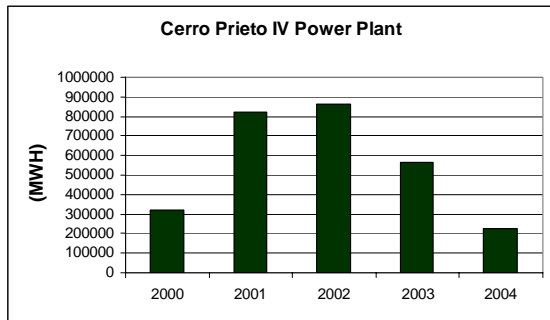


Figure 2. Cerro Prieto IV Power Plant Gross Generation

Year	Total Gross Generation (MWH)
2000	321,295
2001	823,477
2002	862,615
2003	563,269
2004	225,924
Total	2'796,580

Table 3. Cerro Prieto IV Power Plant Annual Gross Generation

Figure 3 shows a basic diagram of Cerro Prieto IV central power station.

CONCLUSION

The commercial exploitation of liquid dominate geothermal reservoir has been clearly demonstrate wit the installations and operation of the four power plants CP I CP II, CP III and CP IV. After 32 years of commercial operation the thermodynamics efficiency of the plants is good within the limitations of the cycle used and the variations in the supply wells.

Present the total power capacity installed in Cerro Prieto geothermal field is 720 MWe. Cerro Prieto IV is the newest power plant builds in Mexico since 1994, with a capacity of 100 MW, The power plant houses four 25-MW condensing units. Each of them requires 183 t/h of steam at 182 °C and 10.5 bar absolute, under standard operating conditions, the specific consumption for these units is about 7.3 tons of steam per MWh. The accumulated gross generation for Cerro Prieto IV power plant from July 2000 to March 2004 was about 2'796,580 MWH.

REFERENCES

Dominguez, B., (1981), Brief Commentaries of The Generation in the Main Plant in Cerro Prieto, *Geothermal Resources Council TRANSACTION*, Vol. 5, pp. 9-14.

Heard, C.L., Siqueros, J., Jiménez, J., Ortega L., (1986), Developments in Geothermal Energy in Mexico – part seven: thermodynamic analysis of the operation of geothermal electrical power generation facilities, *J. Heat Recovery Systems* 6, pp. 345-354.

Mercado, S., Bermejo, F., (1987), Mecanismo de Producción del Pozo M-147 de Cerro Prieto II y posible zona de vapor en la profundidad, *Boletín IIE*. Vol. 1, #4, pp. 162-167.

Mercado, S., Bermejo, F., Heard, C., Fernandez, H., Angulo, R., (1990), Cerro Prieto II (220 MW) and III (220 MW) Geothermoelectric Plants, *Geothermal Resources Council TRANSACTIONS*, Vol. 14, Part II, pp. 1043-1048.

Quijano, J.L., Gutierrez, N., L., (2001), Geothermal Production in Mexico in the Year 2000, *Geothermal Resources Council TRANSACTIONS*, Vol. 25, pp. 593-596.

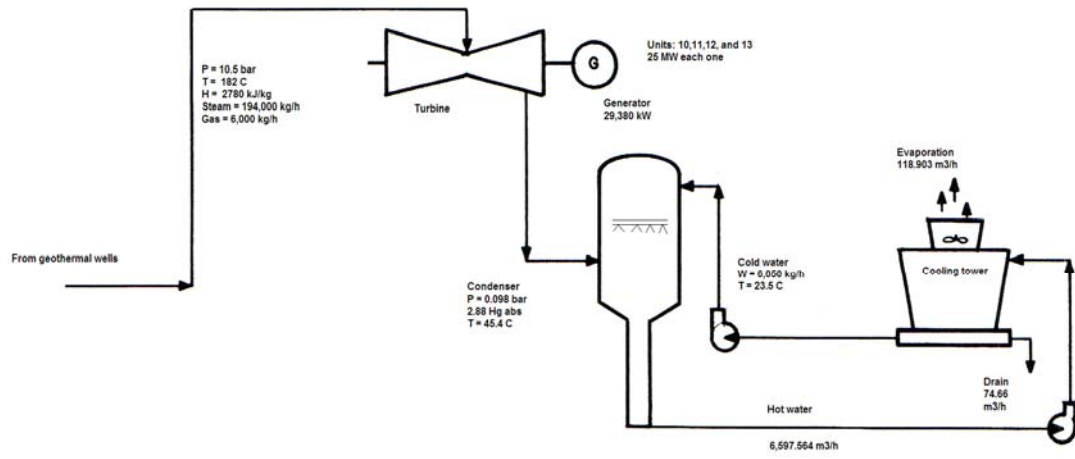


Figure 3. Cerro Prieto IV Central Power Plant Station

Injection

Reinjection Problems in Overpressured Geothermal Reservoirs

Umran Serpen

[274](#)

REINJECTION PROBLEMS IN OVERPRESSURED GEOTHERMAL RESERVOIRS

Umran Serpen* and Niyazi Aksoy⁺

*Dept. of Petroleum and Natural Gas Engineering of Istanbul Technical University
Maslak, Istanbul, 34469 Turkey
e-mail: serpen@itu.edu.tr

⁺Torbali Technical Institute of Nine September University
Dokuz Eylul University, 35210 Alsancak, Izmir, Turkey
e-mail: niyazi.aksoy@deu.edu.tr

ABSTRACT

In this study, high injection pressure problems in geothermal reservoirs with pressure gradients higher than hydrostatic are examined. For this reason, mechanisms controlling injection pressures are identified and investigated. Two geothermal field cases (Kizildere and Salavatli) with overpressured reservoirs from Turkey are presented. The reasons for high injection pressures in those geothermal fields are presented, solutions to overcome those problems are investigated and the results are reported.

INTRODUCTION

Reinjection of waste hot water has always been the most challenging issue for the exploitation of geothermal fields since early 70's. Most of the experimental work and research on this subject have been directed to cooling effect of relatively cold disposal water on the geothermal reservoir (Horne, 1982), which has been a real concern from the power production point of view. Horne, (1985) investigated reinjection effects on production in fractured geothermal fields, and concluded that it carries the danger of production damage due to premature thermal breakthrough. He also stated that locating reinjection wells to a safe distance is desirable, but underground flow paths are complex and a safe distance above ground is not necessarily a safe distance below ground.

Another concern was the injectivity changes during the exploitation of the fields. In some cases injectivity of individual wells declined as stated by Bixley and Grant, (1979) and Itoi et al., (1989), while it increased in other cases (Bixley and Grant, 1979 and Dobbie and Menzies, 1979). Declining injectivity has usually been attributed to silica deposition. While some of declining cases were identified as silica deposition by well testing and well documented (Bixley and Grant, 1979), some others are presumed. In some cases, silica deposition within the reservoir

was alleviated either by separating at higher pressures (Hibara et al., 1989) or preventing air exposure, or injecting the water as quickly as possible (Horne, 1985).

In most of the cases, injectivity has been reportedly found to increase with time (Bixley and Grant, 1979, Horne et al., 1982 and Horne, 1985). The cause has been attributed to either inflation of fractures under injection pressure, or thermal contraction of rock causing opening of fissures (Horne, 1985). Sometimes the disposal water is injected into two phase zone causing condensation with resulting pressure decline.

Geothermal fields are located in highly fractured areas of the earth crust and formation pressures encountered in those areas are generally abnormally low due to pressure gradients below hydrostatic. Sometimes, pressure gradients change within the same field depending on the location of well is found whether in upflow or peripheral zone. Sometimes topography creates favorable position from the reinjection point of view since water table remains below the wellhead. In those cases, reinjection is said to be carried out by gravity. Reinjection of disposal waters into geothermal reservoirs with below hydrostatic gradient is not problematic, provided that no cooling effect and silica deposition occurs. Water levels are sometimes well below the surface, and therefore, reinjection operation is conducted by taking advantage of adding water column head to the existing hydrostatic head in the wellbore. In fact, this creates an extra hydraulic head just like pumping without using power in the surface. Sometimes, separation pressure is also used to help to overcome small wellhead pressures built. Downhole pressure surveys taken in AH-5 during the reinjection test conducted (Einarsson et al., 1974) indicated such an extra head around 17.5 bars. Much bigger hydraulic heads are created in some other fields.

Above hydrostatic gradients are originally found in some unexploited geothermal fields, such as

Wairakei (Donaldson et al., 1983) and Kizildere (Serpen, 2000). Table 1 lists the excess pressure gradients observed in some geothermal fields around the world. Reinjection tests conducted roughly 30 years after the exploitation began in Wairakei. At that point, reservoir pressures must have been substantially declined; therefore, no problem related high wellhead pressures are reported. Partial reinjection operation in Kizildere started after roughly 20 years of exploitation due to pressure decline (more than 10 bars) occurred and has been proceeding smoothly in the last 2 years.

Table 1. Excess Gradients Observed in Some Geothermal Fields (Donaldson, et al., 1983, Serpen, 2000)

Fields	Excess Gradient, %
Kizildere	18
Wairakei	7
Broadlands	15
Broadlands	9
Baca	4
Tongonan	6
Ngawha	2
Kawerau	7
Yellowstone	10-40

Some overpressured geothermal fields have been discovered in Turkey. Difficulties of reinjection have been initially observed in this type of the geothermal fields due to high wellhead pressures required. These might create serious operational, economic and environmental problems to solve. Therefore, in this study, reinjection problems related to overpressures encountered in some geothermal fields will be investigated.

MECHANISMS CONTROLLING INJECTION PRESSURE

The following mechanisms are identified to change the injection pressure in a reinjection system:

- Injection Well Performance into a Liquid Filled Reservoir

In the injection system design of injection field cases, the most important issue is the estimation of the injection well performance. Darcy's law for steady state flow of single-phase fluids in a well centered in a circular reservoir is used:

$$q = \frac{k_w h (p_{wf} - p_e)}{18.665 B_w \mu_w [Ln(r_e/r_w) + s]} \quad (1)$$

where, “ r_e ” is the radius extending from wellbore to the front of the cool water bank, i.e., the interface of injected cool water and the hot reservoir water, p_e is the reservoir pressure at this front, and “ p_{wf} ” is the bottom hole injection pressure.

As can be observed from Eq. 1, increasing r_e value with rising injection volume will reduce injection rate (q) with time, provided that the other parameters are not changed. Although a negative skin factor value will initially increase injection rate, as will be seen later the same declining injection rate trend will follow.

Numerical study conducted by Ahmed et al., (1979) indicated similar results, that is, increasing wellhead pressures if the same injection rate is maintained. Reinjection tests in Bulalo geothermal field indicated the same declining trend of the injection rate in some wells (Messer, 1979).

- Mobility Ratio

Mobility ratio, M in geothermal reinjection involves mobilities of cold injection bank and hot water reservoir. Assuming that the permeability is the same in both banks, mobility ratio will be reduced to the ratio of viscosities of both banks.

Assuming a line drive reinjection scheme, for a piston like flow, injection rate can be expressed as follows:

$$q = \frac{\pi \lambda_h h (p_{wi} - p_{wp})}{\left(\frac{1}{M} - 1\right) \ln \left(\sqrt{\frac{r_f}{r_w}}\right) + \ln \frac{a}{r_w} + 1.571 \frac{d}{a} - 1.927} \quad (2)$$

Considering hot and cold bank viscosities, mobility ratio for geothermal injection will be less than 1, which will in turn reduce injection rate in Eq. 2. This will increase the injection pressure for the same rate. Ariki and Akabayashi, (2001) obtained similar results in their numerical study, in which injection pressures increase for horizontal flow during the injection with low temperatures. They also indicated that if injection fluid temperature is the same as the reservoir fluid temperature, pressures do not change in neither downward vertical nor horizontal flow.

On the other hand, Willhite, (1969) cautions that the effects of mobility ratio on injection rates can be observed in early injection. Thus, injection rates based on short pilot tests or early injection performance can be misleading when projected to entire injection operation. In fact, Kun, (2003) observed wellhead pressure increases during a short run pilot reinjection test, but reinjection reportedly proceeded smoothly without any pumping effort during the exploitation period.

- Skin Effect due to Partial Penetration

In case of limited entry or partial penetration, the well communicates with only a fraction of producing

zone thickness. Partial penetration corresponds to a reduction of the surface of contact between the well and the reservoir. In fractured wells, skin due to partial penetration is not normally expected since fractures increase this contact. But, in geothermal wells where horizontal flow dominates with no vertical fractures around, partial penetration might occur if the whole production zone is not exposed. Partial penetration has been observed in some geothermal wells (Serpen, 2001).

Bourdet, (2002) studied several scenarios for partial penetration well, and concluded that even with a small penetration ratio, geometrical skin is seldom larger than 30 or 50. On the other hand, he stated that on limited entry wells wellbore damage is amplified and total skin can reach values of several hundreds. This could be a real concern for geothermal wells drilled with mud, and increasing skin will cause pressure increase and injection rate decline.

- Non-darcy Flow

Non-darcy flow effects have been observed during production tests in some geothermal wells (Satman et al., 2001 and Onur, 2004). High rate injections in this sort of wells might cause non-darcy flow in the bottomhole of the wells that will in turn increase the injection pressures.

- Gravity Effects

The effect of gravity in vertical flow can be expressed based on the following equation:

$$m = -\frac{\rho k}{\mu}(\Delta p + \rho g) \quad (3)$$

where: m is mass-flux.

It is evident from the Eq. 3 that injection capacity of a geothermal reservoir with vertically oriented fractures is enhanced with increasing gravity term $\rho^2 g k / \mu$. Ariki and Akabayashi, (2001) concluded that the injection capacity drastically improves when the low temperature water is injected into shallow part of a geothermal reservoir with vertically oriented fractures.

- Permeability Enhancement

Permeability improvement due to cold water injection into geothermal fields has been observed in several geothermal fields (Horne, 1985, Bixley and Grant, 1979 and Dobbie and Menzies, 1979). It is believed that permeability is enhanced due to hot rock contraction, creating new fractures around the cooled zones, increasing fracture aperture and increasing storativity that cause pressure decline. It is clear that permeability improvement in Eq. 1 will increase the injection rate. Ariki and Akabayashi,

(2001) in their study also found permeability enhancement of especially vertically oriented fractures with downward injection fluid flow.

- Constrains in Well Flowing Diameter

The 9^{5/8}" dia. casing is regularly used in either production or reinjection wells. Sometimes larger diameter casings are used in some reinjection wells to alleviate frictional pressure drops. The frictional pressure drop through 700 m long 9^{5/8}" casing at moderate injection rates (250 t/h) is negligible, but it is becoming substantial (approx. 5 bars) when the injection rates rise to 500 t/h. If disposal water collected from several production wells is desired to inject in one well, then constrain on casing diameter becomes important. In that case, wells with larger diameters should be planned for reinjection purpose.

REINJECTION TESTING EXPERIMENTS IN OVERPRESSURED RESERVOIRS

In this section, two reinjection testing experiments conducted in Kizildere and Salavatli geothermal fields are examined.

Kizildere Geothermal Field

This field originally was an overpressured reservoir as seen in Fig. 1. The pressure gradients over hydrostatic encountered in geothermal fields of Turkey are generally caused by partial pressure of CO₂, which makes 60%-75% of total reservoir pressures in deep thermal and hot water reservoirs of Kizildere geothermal system, respectively.

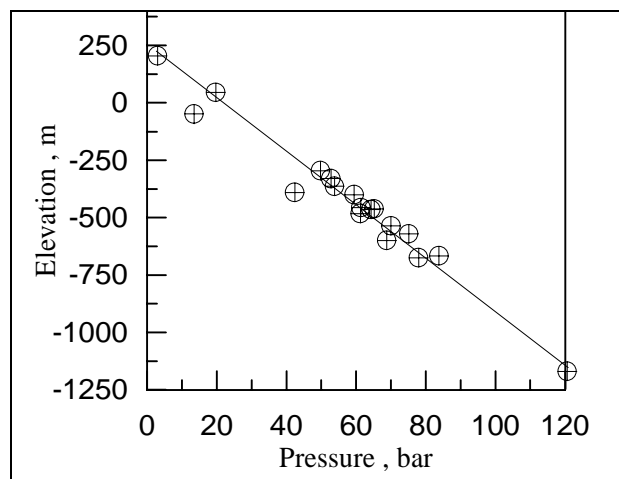


Fig. 1. Reservoir pressures of Kizildere geothermal field.

The first reinjection test in Kizildere was conducted in 20/9/1971. In well KD-1, a maximum reinjection rate of 125 t/h and a minimum reinjection rate of 27.5 t/h were obtained at wellhead pressures of 13.8 bars and 4.7 bars, respectively (Serpen, 2000). Similar

trend (increasing wellhead pressures with rising injection flow) was obtained in another well, KD-9.

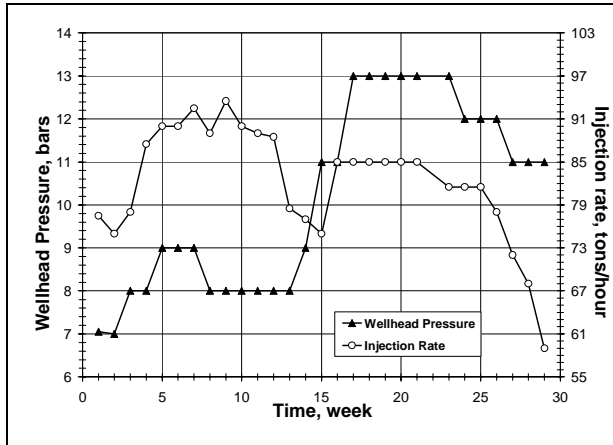


Fig. 2. Variation of wellhead pressure and injection rate with time for the injection well KD-1A.

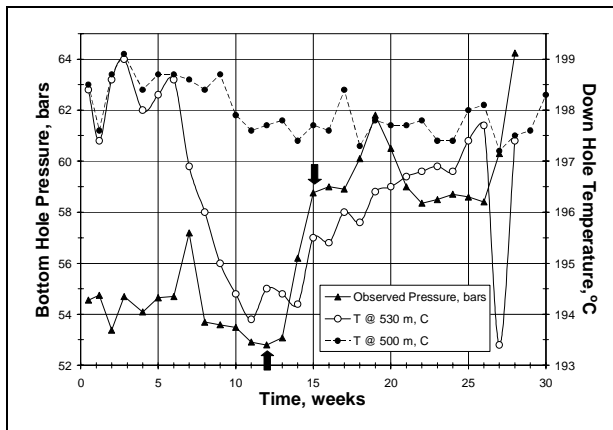


Fig. 3. Down-hole temperatures, at the depths of 500 and 530 meters, and bottom-hole pressures monitored at the observation well KD-1.

In 1975-1976, a long term reinjection test was carried out in a nearby well KD-1A, which took 29 weeks (Kasap, 1976). During the 29-week long injection operation the average injection rate was approximately 83 tons per hour, and the injection water temperature varied between 30°C and 42°C. The results of the test are illustrated in the Fig. 2 and Fig. 3. The behavior of wellhead pressure and injection rates, recorded at well KD-1A can be seen in Fig. 2. The well KD-1, 68 meters away from the injector, was the observation well and its down-hole temperatures, at the depths of 500 and 530 meters, and bottom-hole pressures were monitored as seen in Fig. 3. For the first 5 weeks, the injection rate increases from 75 t/h to 90 t/h, and the wellhead pressure follows a similar trend by increasing from 7 bars to 9 bars. In the following two weeks the pressure remains constant, although injection rate increases slightly. As seen in Fig. 3, in the mean time, both the temperature and the bottomhole

pressure in the observation well KD-1 remain constant with some minor fluctuations.

From 7th to 12th weeks, the injector wellhead pressure drops down to 8 bars, while the injection rate fluctuates around 90 tons/hr. In the observation well, however, both the pressure and temperature at the depth of 530 m drop 2 bars and 5°C, respectively. The cooling effect is felt at the observer 6 weeks after the start of injection.

It is known that two long term production tests of hot water reservoir conducted earlier caused a small reservoir pressure decline and the subsequent formation of a free gas phase, consisting of essentially carbon dioxide and some water vapor, into the hot water reservoir in Kizildere geothermal system (Serpen, 2000). After the arrival of injected water at the observation well, on the 6th week of operation, it is more likely that the further injection is filling up the reservoir while compressing the free gas phase. The sharp increase in bottom-hole pressure, shown in between the solid arrows in Fig. 3, may be attributed to the dispersion of free gas phase in liquid water upon compression. Simultaneously the decline in injection rate is lessened (Fig. 2) as the volume of dispersed gas phase is replaced by slowly increasing volume of water (Mihcakan et al., 2005).

After the 12th week, the injection rate drops to 75 tons/hr, until the 15th week. In the mean time, the wellhead pressure increases to 11 bars. As expected, the pressure at the observer follows the same trend and increases to 59 bars, indicating a good hydraulic communication in between the two wells. The temperature at KD-1 increases about 2°C due to conductive heating of the rock, since the delivery of cooler water toward the observation well is mitigated with the rapidly decreasing injection rate. Based on these facts, the actual reason for the rapid drop in injection rate is thought to be the filling up of the reservoir with the cumulative water injected by that time. Thus, the attempt of forcing more water into the already filled up reservoir back pressured the reinjection well (Satman et al., 2000).

As seen in Fig. 2, the injection rate suddenly increases and reaches 85 t/h level, as the wellhead pressure remains constant, between the 15th and 16th weeks. Such behavior is likely to be the initiation of hydraulic fracturing of the rock of a pressured up formation. It is well known fact that once the formation is broken down, it does not take much pressure to progress the fracture. Thus, the injection pressure in Fig. 2 starts increasing up to 13 bars until the 17th week, and then remains constant for six weeks. Injection rate also remains constant for six weeks. Another evidence for the probable fracture enhancement may be deduced from the pressure behavior at the observation well in Fig. 3. The

observation well begins to sense the slow progressing fracturing action at the 17th week. The pressure at the observer begins to a sharp drop at 19th week (255000 tons of water is injected) and the fracture progress is completed. Steady increase of the temperature at the depth of 530 m in the observation well indicates that the fracture was not enhanced at that direction and depth.

Kizildere field is situated in a graben, and near vertical fractures are very characteristic of such structures. Fracture enhancement in the above test after 15 weeks, during which horizontal flow dominated, probably occurred through vertically oriented fractures downward as Ariki and Akabayashi, 2001 study indicated.

On the other hand, a deep well, R-1 (2300 m) was completed in 1997 for reinjection purpose, and struck a hotter horizon at depth. Injection attempts to this well ended with negative results. But, well R-1 with permeability thickness of 6.5-7.5 d-m and higher temperatures (205°C vs. 240°C) resulted in a good producer. Though permeability thickness of this well can be considered as reasonable, injection into this well was not possible because of excessive wellhead pressures.

Ongur, (2005) states that near vertical fractures in graben structures tend to close to horizontal at depth. Horizontal flow might be dominating at deeper levels due to the scarcity or lack of vertically oriented fractures, and for that reason, injection pressures may be increasing as Ariki and Akabayashi, (2001) study explained.

Salavatli Geothermal Field

Salavatli is a newly developing big geothermal field with relatively moderate temperatures of 170°C and relatively high static wellhead pressures of 7 to 12 bar (Serpen and Tufekcioglu, 2003). The field is also situated on the same graben structure (B. Menderes) as Kizildere, and is evidently overpressured as pressure measurements indicate due to also relatively high CO₂ content. Three wells have been drilled so far, 2 for production and 1 for the reinjection. A forth well is being drilled for reinjection. The first 2 wells (AS-1 and AS-2) were drilled 20 years ago, and they are now being considered for production. They are producing at flow rates varying between 250 t/h and 300 t/h from the depths of 800 m-900 m. The injection capacities of these wells are limited to their production level at wellhead pressures of approx. 20 bars. The first reinjection well ASR-1, drilled to 1420 m approx. 1.5 km away and at a lower elevation resulted to be a good producer with a flow rate of 550 t/h. The permeability thickness of this well is estimated as 17 d-m by both build-up and injection tests.

Injectivity indexes of the wells AS-1, AS-2 and ASR-1 are 2.45 lt/s-bar, 4 lt/s-bar and 1.55 lt/s-bar, respectively (Table 2). On the other hand, productivity index of the well ASR-1 is 22 lt/s-bar, which is substantially higher than the injectivity index. This seems to be characteristic of the geothermal fields with pressure gradients over hydrostatic. The production rate of ASR-1 is as much as the sum of the other wells (AS-1 and AS-2), although the injectivity indexes of the wells AS-1 and AS-2 are higher than the injectivity index of ASR-1. As expected the deeper the wells get, the difficulties in injection increases. This could also be due to normal permeability decline with depth. As seen in Kizildere case beforehand, there is also difficulty for reinjection in Salavatli field. High wellhead pressures are needed to inject the disposal fluids.

Table 2. Injectivity and Productivity Indexes of Salavatli Wells.

Wells	Well Depths, (m)	Injectivity Index, (t/h-bar)	Productivity Index, (t/h-bar)
AS-1	1500	2.5	36
AS-2	900	4	26.5
ASR-1	1430	1.5	22

In our opinion, injection tests conducted in Salavatli geothermal field are very short and inconclusive. Injectivity index of ASR-1 well has improved in three consecutive injection tests. Remembering Willhite, (1969) warning against short run pilot tests, long term injection performance of the well ASR-1 was studied using infinite reservoir model. To obtain injection rates and volume, the following Eq. 4 and Eq. 5 are utilized coupled with reservoir parameters obtained through the wells tests conducted in well ASR-1.

$$q = \frac{1}{18.66} \frac{kh}{\mu} \frac{\Delta p}{\ln\left(\frac{\sqrt{V_w}}{\sqrt{(\pi\phi hr_w^2)}}\right)} \quad (4)$$

$$t = \frac{18.66V_w\mu_w}{kh\Delta p} \left[\ln\left(\frac{1}{r_w} \sqrt{V_w / (\pi\phi h)} - \frac{1}{2}\right) \right] \quad (5)$$

where: V_w is injected volume and $\Delta p = p_{wf} - p_e$

Fig. 4 and Fig. 5 illustrate reinjection performance results. Fig. 4 shows injection rate change with the injected volume, with and without skin factor. Actually, ASR-1 well has a negative skin factor of 6. As can be observed in Fig. 4, although initial injection rates are higher, decline in those injection rates with increased injection volume are much

pronounced with respect to no skin. Fig. 5 shows the change of the injection time with injection volume; and it can be noted that the elapsed time between the cases with or without skin widens as injection volume increases and pressure differential decreases.

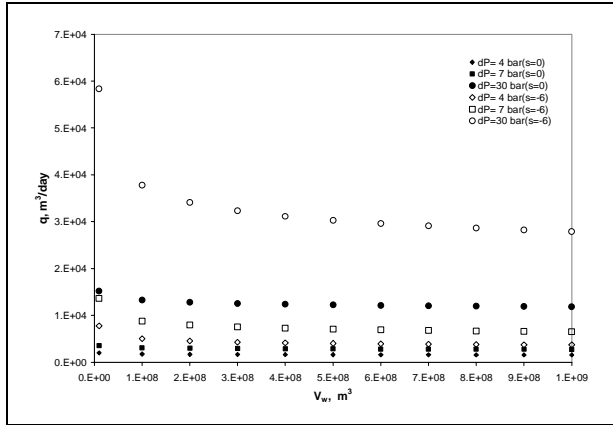


Fig. 4. Injection rates vs injection volume for Salavatli field.

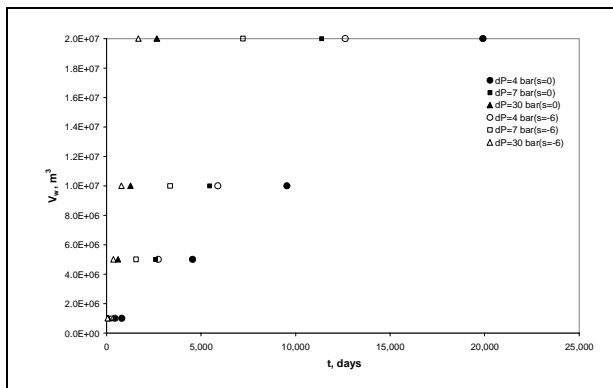


Fig. 5. Injection time vs injected volume for Salavatli field.

Salavatli geothermal field is situated in the northern flank of B. Menderes graben, which is a big 200 km long, important structure. Several small scale grabens and horsts are formed through stepwise faulting within the B. Menderes graben where Salavatli field is sited. Four belts of alternating production and reinjection wells are planned to locate along these faulting zones, expecting that more permeable structures are developed along these faults. Conductivity between the production and reinjection belts is thought to be weaker, since there no direct contact was unearthed so far. Therefore, injection is not expected to influence the production wells in short run, which are approx. 650 m away. This sequence of production and reinjection wells resembles a line-drive system used in oil field waterflooding operations.

A long term injection performance study for the Salavatli field was conducted using line drive

solution (Eq. 2), and the results are shown in Fig. 6. As seen from the Fig. 6, there is a sharp initial injection rate drop, as predicted by Willhite, (1969), and afterwards, injection rate decline is gradual.

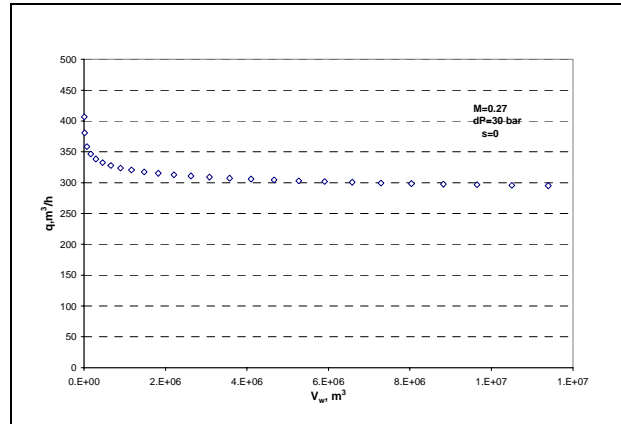


Fig. 6. Injection rate vs injected volume for line-drive solution.

ALTERNATIVE SOLUTIONS

Since there were reinjection problems because of overpressured reservoir when the Kizildere geothermal power plant started power production in 1984, a laboratory study (Tolun et al., 1985) was conducted with the aim of eliminating boron from Kizildere waste water using boron selective resin Amberlite IRA 743. Single and double stage regenerations of resin were found feasible. A preliminary economic evaluation resulted in extra cost of 1 cent/kWh for boron removal (Recepoglu and Beker, 1991). Although this extra cost could be affordable, for 1500 t/h geothermal water production rate, the process would have yearly produced 125000 m³ of alkaline, 100000 m³ of acidic solutions and 400000 m³ of contaminated washing water to dispose (5% of total disposal water). Salavatli geothermal water has boron content twice that of Kizildere. Therefore, more by-product disposal water might be produced.

Tolun et al., (1985) also proposed the reverse osmosis process as an alternative for boron removal, which could eliminate all TDS in the waste water, producing also substantial amount of fresh water to be used elsewhere. The first Salavatli geothermal power plant is being manufactured with air cooling system, which loses roughly 1 MW_e of power with respect to the water cooling. In the next enlargement of power production, this fresh water could be also used for cooling purpose. They stated that according to their information, the cost of such process would be around 1 cent/kwh. Twenty years after this estimation, it is expected that new technologies could provide more economical solutions. Even if the above solutions were implemented, depletion of the reservoir should be controlled. After

some pressure drop in the reservoir, reinjection operation should certainly be initiated. Since dissolved CO₂ provide driving energy for the geothermal reservoir just like a depletion drive oil reservoir, it would be advisable to keep reservoir pressure over bubble point pressure. The natural recharge of the Salavatli field is not known yet. The planned production rate of the first binary power plant could be partly or fully met by the natural recharge, thus no pressure decline could be also observed with the planned production rate. Therefore, a comprehensive reservoir engineering study is needed as the numbers of wells are increasing and the testing data are accumulated.

On the other hand, our economic evaluations indicate that reinjection operation would roughly cost 0.5 cent/kWh, and it is still cheaper and more attractive than the above alternative solutions. Though modeling studies show otherwise, permeability enhancement during injection could occur as happened elsewhere. In that case, the injection rate would increase in long run.

SUMMARY

The following subjects are investigated in this study:

- Mechanisms controlling injection pressures are investigated.
- Injection experiments in two overpressured reservoirs of Turkey are examined and the behavior of those fields under injection is explained.
- Possible alternative solutions are presented.

ACKNOWLEDGEMENTS

We extend our gratitude to Ege Energy for supporting this work. We appreciate Prof. Dr. Mustafa Onur for his valuable help.

REFERENCES

Ahmed, U., Wolgemuth, K.M., Abou-Sayed, A.S.; Jones, A.H. (1979), "Injection Capability at the Raft River Geothermal Site", *Proc. of 5th Geothermal Workshop Stanford*, 29-39.

Ariki, K. and Akibayashi S. (2001), "Effects of Injection Temperature on Injection Capacity of Geothermal Wells-Numerical Study," *GRC Transactions*, Vol. **25**, 445-454.

Bourdet, D. (2002), "Well Test Analysis: The Use of Advanced Interpretation Models," Elsevier, 69-74.

Bixley, P.F., Grant, M.A. (1979), "Reinjection Testing at Broadlands", *Proc. of 5th Geothermal Workshop Stanford*, 41-47.

Dobbie, T.P. and Menzies, A.J. (1979), "Geothermal Wastewater Reinjection Trials, Mahia Reservoir, Republic of Philippines," *GRC Transactions* Vol. **3**, 169-172.

Donaldson, I.G., Grant, M.A., Bixley, P.F. (1983), "Nonstatic Reservoirs: The Natural State of the Geothermal Reservoir," *Journal of Petroleum Technology*, 189-194.

Einarsson, S.S., Vides, A., Cuellar, G. (1974), "Disposal of Geothermal Waste Water by Reinjection," a Report to UNDP, Managua.

Hibara.Y., Tahara, M. and Sakanashi, H. (1989), "Operating Results and Reinjection of Milos Field in Greece," *Geothermics*, Vol. **18**, No. ½, 129-135.

Horne, R.N. (1982), "Geothermal Reinjection Experience in Japan," *JPT*, March, 495-503.

Horne, R.N., Grant, M.A. and McCabe, W.J. (1982), "Geothermal Reinjection Experience in New Zealand," *SPE* 12712.

Horne, R.N., (1985). "Reservoir Engineering Aspects of Reinjection," *Geothermics*, Vol. **14**, No.2/3, 449-457.

Itoi, R., Fukuda, M., Jinno, K., Hirowatari, K., Shinohara, N. and Tomita, T. (1989), "Long Term Experiments of Waste Water Injection in the Otake Geothermal Field," *Geothermics*, Vol. **18**, No. ½, 153-159.

Kasap, I. (1976), "Re-injection Test in Kizildere Geothermal Field," unpublished MTA Report (in Turkish), Ankara, Turkey.

Kun, W. (2003), "Studies of the Reinjection Tests in Basement Geothermal Reservoir, Tianjin, China," *GRC Transactions*, Vol. **27**, 393-396.

Messer, P.H. (1979), "Injection Performance in the Bulalo Geothermal Field Makiling-Banahao Area, Philippines," *Proc. of 5th Geothermal Workshop Stanford*, 275-289.

Mihcakan, M., Altinay, E., Kasap, I. (2005), "Injection Test The Hall Plot Analysis of a Water Affected by Geothermal Reservoir Response," submitted and accepted for *WGC 2005*.

Ongur, T. (2005), Personal Communication, Geosan, Istanbul.

Onur, M. (2004), "Personal Communication", ITU, Istanbul.

Recepoglu, O. and Beker, U. "A Preliminary Study on Boron Removal from Kizildere/Turkey Geothermal Waste Water," *Geothermics*, Vol. **20**, No. ½, 83-89.

Satman, A., Serpen, U., Mihcakan, I.M. (2000), "Assessment of Reinjection Trials in Kizildere Geothermal Field," *Proceedings*, World Geothermal Congress, Kyushu – Tohoku, Japan, 1695-1700.

Satman, A., Serpen, U., Onur, M. (2001), "Reservoir Performance Analysis of Balcova-Narlidere Geothermal System," Report to Balcova Geothermal Ltd.

Serpen, U., Satman, A., Kasap, . (1998), "Well Testing in Kizildere Geothermal Field," *GRC Transactions*, Vol. **22**,

Serpen, U. (2000), "Technical and Economical Evaluation of Kizildere Geothermal Reservoir". PhD Dissertation, Istanbul Technical University, Istanbul.

Serpen, U. (2001), "Reinjection Strategies for Kizildere Geothermal Field", 27th Annual Workshop Geothermal Reservoir Engineering, Jan. 28-30,, Stanford, Cal. USA.

Tolun, R., Recepoglu, O. and Bulutcu, N. (1985), "Boron Removal from the Waste Water of Kizildere Geothermal Field," Tubitak Project Report No. MAG-614, Istanbul.

Willhite, G.P. (1986), "Waterflooding", *SPE Textbook Series* Vol. 3, 195-198.

Serpen, U., Tufekcioglu, H. (2003), "Developments in Salavatlı Geothermal Field of Turkey," *GRC Transactions*, Vol. 27,

HDR/EGS

- Simulated Evolution of Reservoir Properties for the Enhanced Geothermal System at Soultz-Sous-Forêts: The Role of Hot Brine-Rock Interactions** [283](#)
Laurent André, François.-D. Vuataz
- A 5000 m Deep Reservoir Development at the European HDR Site at Soultz** [291](#)
R. Baria, S. Michelet, J. Baumgaertner, B. Dyer, J. Nicholls, D. Teza, T. Hettkamp, N. Soma, H. Asanuma and L. Kueperkoch
- Using the Migration of Induced Micro-Seismicity as a Constraint for HDR Reservoir Modelling** [299](#)
Dominique Bruel
- The Genesys-Project: Extraction of Geothermal Heat from Tight Sediments** [306](#)
R. Jung, J. Orzol, T. Tischner, R. Jatho, P. Kehrer
- Stimulation Techniques Used in Enhanced Geothermal Systems: Perspectives from Geomechanics and Rock Physics** [312](#)
Stephen L. Karner
- Coupled Hydro-Mechanical Modelling of the GPK3 Reservoir Stimulation at the European EGS Site Soultz-sous-Forêts** [320](#)
T. Kohl and T. Mégel
- Models of Subsurface Rock-Water Processes Affecting Fluid Flow** [328](#)
Nancy Moller and John H. Weare
- A Hybrid Semi-Analytical and Numerical Method for Modeling Wellbore Heat Transmission** [335](#)
Karsten Pruess and Yingqi Zhang
- An EGS Stimulation Experiment under Low Wellhead Pressures** [340](#)
Peter Rose, Jess McCulloch, Cliff Buck, Mike Adams, and Mike Mella
- Sorbing Tracers - A Potential Tool for Determining Effective Heat Transfer Area in Hot Fractured Rock Systems** [346](#)
Chao Shan and Karsten Pruess
- Use of TOUGHREACT to Simulate Effects of Fluid Chemistry on Injectivity in Fractured Geothermal Reservoirs with High Ionic Strength Fluids** [352](#)
Tianfu Xu, Guoxiang Zhang, and Karsten Pruess

SIMULATED EVOLUTION OF RESERVOIR PROPERTIES FOR THE ENHANCED GEOHERMAL SYSTEM AT SOULTZ-SOUS-FORÊTS: THE ROLE OF HOT BRINE-ROCK INTERACTIONS

Laurent André^(1,2) and François-D. Vuataz⁽²⁾

⁽¹⁾ Centre of Hydrogeology – University of Neuchâtel, E.-Argand, 11, CH-2007 Neuchâtel, Switzerland

⁽²⁾ Centre of Geothermal Research – CHYN, University of Neuchâtel, E.-Argand, 11, CH-2007 Neuchâtel, Switzerland

laurent.andre@unine.ch; francois.vuataz@unine.ch

ABSTRACT

Rock porosity and permeability do not remain constant with time. In particular, the fluid circulation within the fractured reservoir involves chemical reactions between the brine and the altered granite, which modify porosity and permeability. The FRACHEM code, a Thermo-Hydraulic-Chemical coupled code, has been developed especially to forecast the evolution of the Soultz system. For the time being, this code can simulate fluid-rock interactions and determine the dissolution/precipitation reactions of eight minerals (carbonates, pyrite, silicated minerals). The last simulations demonstrate an important dissolution of carbonates close to the injection well, whereas small amounts of silicates precipitation are inferred.

INTRODUCTION

The geothermal research program for the extraction of energy from Hot Fractured Rock at the Soultz-sous-Forêts site began in 1987 (Hettkamp et al., 2004). The project aims to convert heat to electricity from a deep fractured and granitic reservoir. This site has been selected because of its temperature gradient in the sedimentary cover ($100^{\circ}\text{C.km}^{-1}$) and its high heat flow reaching locally 0.15 W.m^{-2} (Kohl and Rybach, 2001).

To extract the heat from the reservoir, three deviated wells have been installed at a depth of 5000 m and their bottoms are separated by 650 m. The reservoir encountered at this depth presents a temperature of 200°C . One well (GPK3) is dedicated to the injection of cold water in the granitic reservoir whereas the two others (GPK2 and GPK4), located on both sides of injector, are used to pump hot water. At Soultz, the injection-production system is a closed loop and the fluid used is the formation brine existing in the fractured granite.

This accelerated circulation of hydrothermal brine takes place within the fractured reservoir, but chemical and thermodynamic equilibria will be

disturbed, involving chemical processes which can affect the properties of this reservoir.

The aim of this study is to predict the long-term behavior of this system under continuous production. To reach this objective, many aspects as heat, hydraulics, fluid transport and geochemical processes have to be taken into account, and their impact on porosity and permeability evolution has to be evaluated. We have examined in details the water-rock interactions on fluid flow, as well as the variations of reservoir properties with production time.

Considering the high mineralization of brine and the temperature of the reservoir, a new Thermo-Hydraulic and Chemical coupled code, called "FRACHEM", has been built for the Soultz reservoir conditions. It results from the combination of two existing codes, FRACTure and CHEMTOUGH 2. FRACHEM code determines the thermal and hydraulic processes and simulates the reactive transport. The Pitzer formalism has also been implemented in FRACHEM code to calculate the activity coefficients of selected chemical species; then, the precipitation/dissolution reactions of some minerals, i.e carbonates, quartz, amorphous silica, pyrite and some aluminosilicates can be estimated. At last, a supplementary module allows the determination of porosity and permeability variations linked to chemical processes occurring in the reservoir.

GEOLOGICAL SETTING

The Soultz-sous-Forêts Enhanced Geothermal System (EGS) is established in the Rhine Graben (Figure 1), 50 km in the North of Strasbourg (France). This graben runs along 300 km from south to north and is bordered by the Vosges to the West and the Black Forest to the East and it is affected by many faults and structures principally oriented N-S.

The granite basement is covered by 1400 m of Triassic, Jurassic and Oligocene sediments which permeability is weak. But the most interesting feature of this site is the temperature anomaly

observed within the sedimentary cover. The zone of Soultz presents a geothermal gradient which reaches $100\text{ }^{\circ}\text{C.km}^{-1}$ down to a depth of 1000 m. Below this zone, the gradient decreases to values in the range $15\text{-}30\text{ }^{\circ}\text{C.km}^{-1}$, which allows a rock temperature close to 200°C at 5000 m deep (Schellschmidt and Pribnow, 2001).

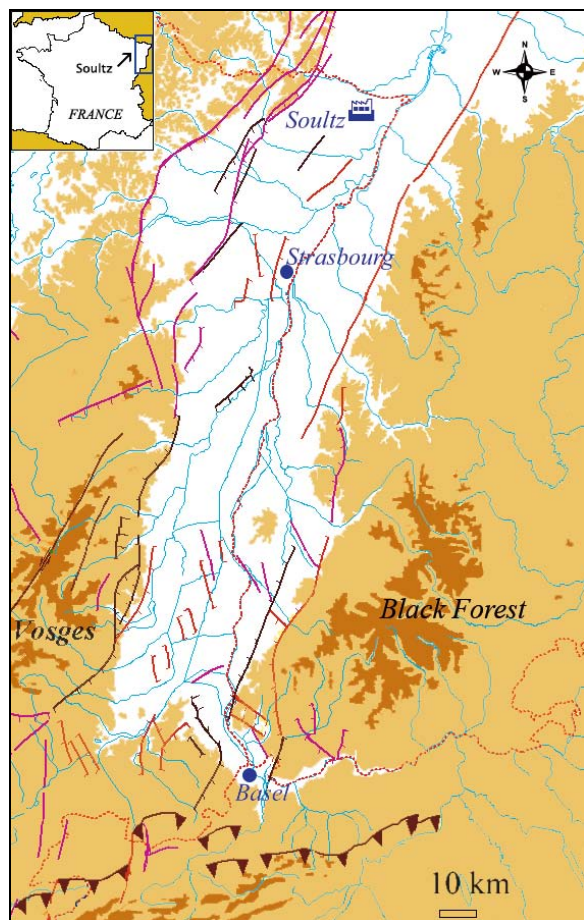


Figure 1. Location of Soultz site in the Rhine Graben.

MINERALOGICAL ASSEMBLAGE

The geothermal reservoir at Soultz is composed of three types of granite (Jacquot, 2000). The first one is a healthy granite (Table 1), characterized by the predominance of feldspars, plagioclases and quartz. This granite is not altered and contains no water. The second facies is a fractured hydrothermalised granite. Its composition revealed the following alteration: quartz is the major mineral, the amount of feldspars decreases and some secondary minerals appear like galena, pyrite, smectite or illite. This rock facies is more porous than the first one. The last facies corresponds to the vein of alteration, characterized by minerals such as illite, smectite and quartz. This facies is the most altered one but precipitation of these secondary minerals in the fractures network involves a decrease of porosity and permeability. As

a result, the porosity of the second facies is the only one assuming fluid circulation in the granitic rock.

Table 1. Mean composition (in percent) of the different types of granite in the Soultz reservoir (Jacquot, 2000).

	Healthy granite	Hydrothermalised granite	Vein of alteration
Quartz	24.2	40.9	43.9
K-Feldspar	23.6	13.9	
Plagioclases	42.5		
Illite		24.6	40.2
Smectite		9.7	9.6
Micas	9.3		
Calcite	0.3	3.3	4.3
Dolomite		0.8	0.7
Pyrite		0.7	1.0
Galena		1.3	0.3
Chlorite		4.8	

FLUID COMPOSITION

The fluid circulating in the fractures network is the formation fluid, a sodium-chloride brine with total dissolved solids close to 100 g.L^{-1} . pH value reaches 4.9 and its temperature is equilibrated with the rock at this depth i.e. $200\text{ }^{\circ}\text{C}$. The brine composition, obtained from the fluid extracted during the production test in 1999, is given in Table 2.

Table 2. Mean composition of fluid coming from reservoir at a depth of 5 km.

Species	Concentration [mmol/kg]
Na^+	1079
K^+	68.5
Ca^{2+}	157
Mg^{2+}	3
Cl^-	1452
S	1.6
C	19
Fe^{2+}	2.4
SiO_2	5.7

NUMERICAL MODELLING

To predict the long-term evolution of the Enhanced Geothermal System, several Thermo-Hydraulic and Chemical (THC) coupled codes are available. They model the behavior of hot diluted fluids or cold brines, but not of hot hypersaline brines. Consequently, a new THC code had to be built for the Soultz reservoir conditions. Instead of creating a totally new modelling programme, two existing codes, FRACTure and CHEMTOUGH 2, have been combined in a new code called "FRACHEM" (Durst,

2002; Bächler, 2003; Rabemanana et al., 2003). FRACTure is a 3-D finite elements code and it determines thermal and hydraulic processes in fractured and porous rocks (Kohl and Hopkirk, 1995). CHEMTOUGH 2 is a 3-D finite volumes code (White, 1995); it simulates the reactive transport and allows the variation of permeability according to chemical reactions occurring between the fluid and the rock of the reservoir. This last code has been modified because of the high fluid salinity of the Soultz reservoir by several implementations: thermodynamic model and computation of the activity coefficients of selected species in solution; kinetic model for dissolution and precipitation of minerals as well as the relationship between porosity and permeability.

The thermodynamic model

The thermodynamic model has to determine the state of the fluid in regard to mineral phases present in granite i.e. the under- or over-saturation of the fluid towards these minerals. To reach this goal, the ionic activity product (Q) must be compared to the equilibrium constant of the reaction (K). If $Q < K$, the solution is undersaturated and the mineral has a tendency to dissolve. If $Q = K$, the system is at equilibrium, but if $Q > K$, the solution is oversaturated and the mineral precipitates.

In order to calculate these factors, the activity coefficients of each species in solution must be determined. In CHEMTOUGH2, the Debye-Huckel model is used to calculate these coefficients but this model can only be considered with dilute solutions.

Knowing the high salinity of the brine of the Soultz system, this model has been substituted by Pitzer formalism. The Pitzer equations have the advantage to take into account more types of ionic interactions than Debye-Huckel model.

To simplify the system, some assumptions have been made concerning the fluid, such as no boiling, no degassing, no condensing and no mixing with a different fluid.

Assuming these hypotheses, the activity coefficients of ionic species can be defined and only depend on two parameters, temperature and pressure.

$$\gamma_i(T, P) = (B_0 + B_1T + B_2T^2 + B_3T^3 + B_4T^4) \cdot f(P)$$

Where B_i are coefficients calculated for each mineral and $f(P)$ is a factor depending on pressure.

Then, the activity of the species i is expressed in function of the molality m_i as:

$$a_i = \gamma_i(T, P) \cdot m_i$$

The kinetic model

The thermodynamic model allowed determining the equilibrium or non equilibrium state of the fluid in regard to the rock. But a thermodynamic

disequilibrium involves chemical reactions with kinetics varying according to minerals.

A general kinetic model has been adopted to explain the dissolution/precipitation reactions of minerals. Its overall form is expressed as:

$$v = k_m \cdot s_m \cdot \left(1 - \left(\frac{Q_m}{K_m} \right)^\mu \right)^n$$

Where v is the reaction rate ($\text{mol} \cdot \text{s}^{-1}$), k_m is the rate constant ($\text{mol} \cdot \text{s}^{-1} \cdot \text{m}^{-2}$), s_m is the surface of mineral in contact with fluid (m^2), μ and n are positive empirical parameters. Positive values of v correspond to dissolution rates, whereas negative values refer to precipitation rates.

This equation is adapted to each mineral and the determination of parameters k_m , μ and n are deduced from published experiments, conducted at high temperature in NaCl brines.

For the present time, the behavior of eight minerals (calcite, dolomite, pyrite, quartz, amorphous silica, K-feldspars, albite and illite) is investigated. Detailed information on the determination of the reaction laws can be found in Durst (2002).

The porosity/permeability relationship

As seen before, many chemical processes can have an influence on porosity and permeability of the system. To assume this, the porosity variations are calculated and a combination of a fracture model and a grain model is used to determine the evolution of permeability. This double model has been validated considering the structural characteristics of the altered granite crossed by the fluid.

The fracture model is based on the work of Norton and Knapp (1977) and modified by Steefel and Lasaga (1994), whose consider the case of three sets of mutually orthogonal fractures, which produce an isotropic permeability and where all the fractures have the same spacing and fracture apertures. The permeability k_F (in m^2), in this case, is:

$$k_F = \frac{\Phi_F^3}{324 \cdot n_F^2}$$

Where Φ_F represents the fracture porosity and n_F the fracture frequency in m^{-1} .

The grain model is based on the model of Kozeny-Carman which has been modified by Bolton et al. (1996). The expression of the permeability k_G is:

$$k_G = \frac{R_0^2}{45} \cdot \frac{\Phi_G^3}{(1 - \Phi_G)^2}$$

Where Φ_G and R_0 represent the grain porosity and the initial radius of closed pack spherical grains, respectively.

APPLICATION OF FRACHEM TO THE SOULTZ SYSTEM

Model set up

The present application of FRACHEM is the modelling of a 2-D simplified model with a geometry close to the Soultz system. The injection and the production wells are linked by fractured zones and surrounded by the granite matrix. The model is composed of 1250 fractured zones. Each fractured zone has an aperture of 0.1 m, a depth of 10 m, a porosity of 10%, and contains 200 fractures. Initially the temperature was set to the reservoir temperature of 200°C. One of these fractured zones is modelled with the assumption that the fluid exchange with the surrounding low permeability matrix is insignificant. Due to the symmetrical shape of the model, only the upper part of the fractured zone is considered in the simulation. The area is discretized into 222 2D elements (Figure 2).

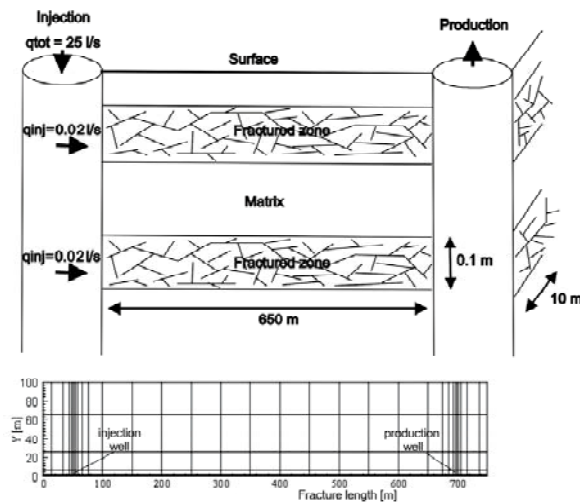


Figure 2. Simplified model and spatial discretization.

The size of the elements ranges from a minimum of 0.5 m x 0.05 m near the injection and the production wells to a maximum of 50 m x 35 m. Considering a production rate of 25 l s⁻¹, the fluid was re-injected in each of the fractured zones at a rate of 2×10^{-2} l s⁻¹ and at a constant temperature of 65°C. During this simulation a constant overpressure of 8 MPa was assumed at the injection well and a hydrostatic pressure at the production well. Dirichlet boundary conditions were applied to the upper, left and right side of the model. Due to the sensitivity of the sequential non iterative approach (SNIA) method on the time discretization, the time step used for this simulation is limited to 10² s, meaning that several years of simulations take several days of computer time. The values of thermo-hydraulic parameters considered in the simulation are listed in Table 3.

Table 3. Thermo-hydraulic model parameters.

Parameters	Fracture	Matrix	Fluid
Hydraulic conductivity [m ² /Pa]	$7.4 \cdot 10^{-8}$	10^{-15}	-
Thermal conductivity [W/m.K]	2.9	3	0.6
Density [kg/m ³]	-	2650	1000
Heat capacity [J/kg.K]	-	1000	4200
Porosity [%]	10	0	-

Results

Reservoir temperature

Before fluid circulation in the fractured zone, all the system (rock and brine) is chemically and thermally at equilibrium. The brine is in chemical equilibrium with the granite and these two components are at a constant temperature of 200°C. But, during the injection of cold fluid at 65°C in the reservoir, the system is disturbed and the rock progressively cools down (Figure 3).

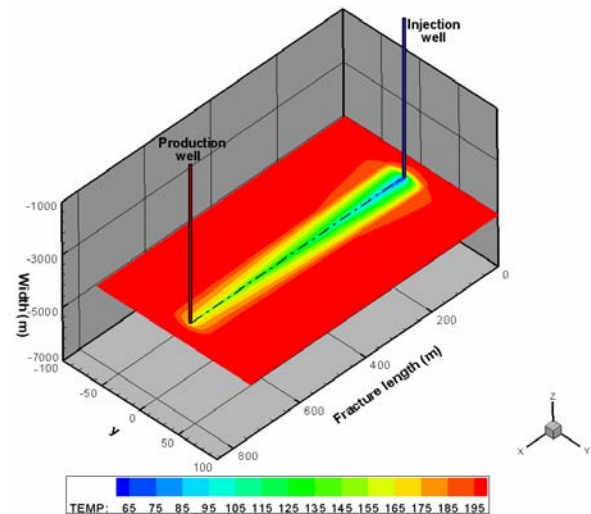
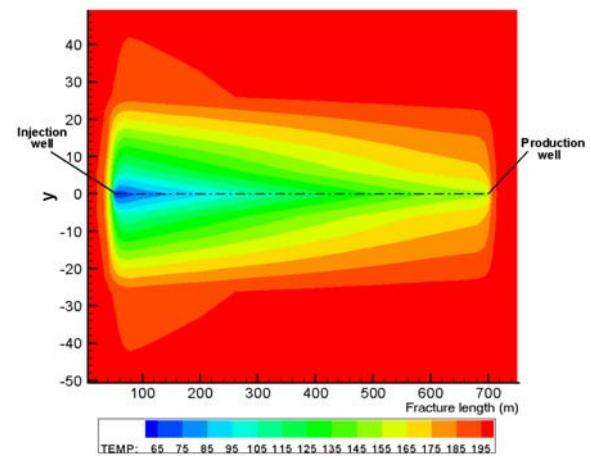


Figure 3. Temperature of rock around the fractured zone after 1500 days of fluid circulation.

The fracture is represented between the injection and the production wells, in a plane at -5000 m from surface. All along the fractured zone, we observe a global decrease of temperature, more important close to the injection well, due to the temperature of the re-injected fluid. After 1500 days of fluid circulation, the temperature in the vicinity of production well is close to 160°C. The development of this thermal front due to the thermal diffusion from rock to fluid affects a zone of 30 to 40 meters around the fractured zone (Figure 3). This temperature decrease of the produced fluid is particularly important but this value of 160°C is very dependent of the geometric model. In that case, we consider a direct circulation, in right line, between the injection and the production wells, without taking in consideration parallel paths. As a consequence, the cooling effect modelled here is probably more pronounced than in a real reservoir.

Minerals-brine interactions

The circulation of cold fluid in the fracture disturbs the chemical equilibrium of the rock-brine system involving chemical reactions such as minerals precipitation and dissolution. In this paragraph, the investigations only concern the behavior of five minerals: calcite, dolomite, quartz, amorphous silica and pyrite. For the aluminosilicates, their results will be presented later.

The calcite is a secondary mineral, crystallized in granite fractures in relative weak proportions, but it represents the most reactive mineral. As shown in figure 4, for every time period, the calcite reacts in the entire fracture. Positive values of the reaction rate indicate a dissolution and the negative ones, a precipitation process.

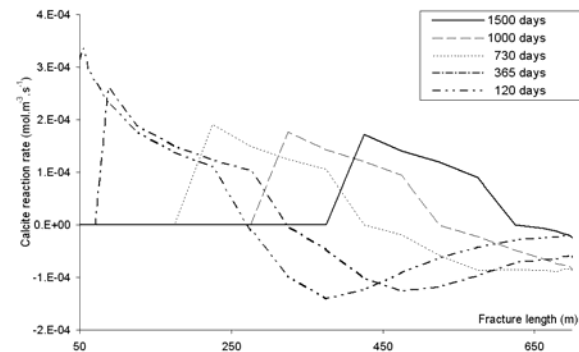


Figure 4. Calcite reaction rate along the fracture.

In the vicinity of the injection well, the calcite dissolves whereas it precipitates close to the production well. This is due to the solubility of calcite which decreases when temperature increases. At the beginning of the fluid circulation in the reservoir, the dissolution of calcite occurs mainly in the first 300 meters of fracture and a maximum of dissolution rate is reached after 120 days. This dissolution involves an enrichment of calcium Ca^{2+} in

solution and later the temperature increase along the fracture causes the precipitation of calcite in the last 300 meters of fracture. The dissolution of calcite goes on until all the mineral has been consumed. Figure 5 demonstrates that in the vicinity of the injection well, about 300 days are needed to dissolve all the calcite present in the fractured granite.

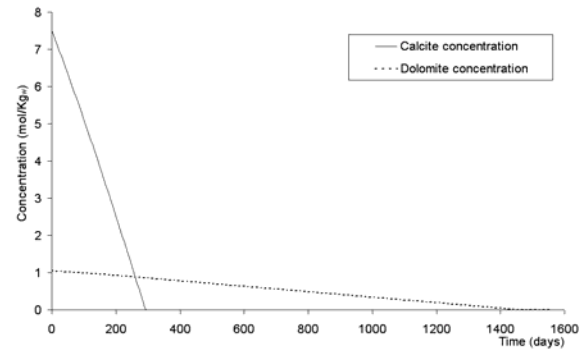


Figure 5. Evolution of dolomite and calcite concentration in the granite, close to the injection point.

With increasing simulation time, and with the decrease of the rock temperature, the dissolution zone of calcite extends towards the production well.

Another carbonate has also been investigated. The dolomite, present in granite, is less reactive than calcite. Figure 6 shows that dolomite dissolves everywhere in the fracture, but the reaction rate is one order of magnitude less than for calcite. Similarly to calcite, dolomite dissolution is stopped by the lack of mineral but, around the injection well, more than 1400 days are needed to the total disappearance of this mineral (Figure 5).

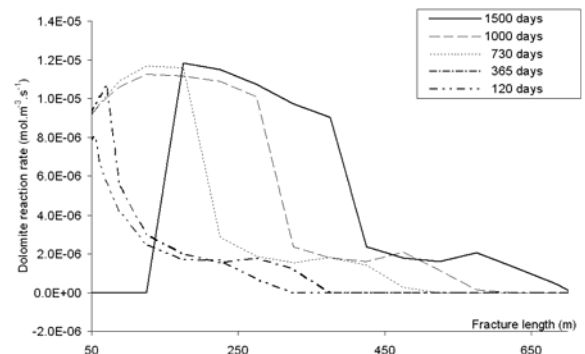


Figure 6. Dolomite reaction rate along the fracture.

Concerning the silicates, the most reactive one is amorphous silica. Quartz, which is a major mineral in granite, has a reaction rate three order of magnitude smaller than the one of amorphous silica. Contrary to calcite, the solubility of amorphous silica augments with temperature increase. As a consequence, this property involves the precipitation of this mineral near the injection well (Figure 7). With increasing the circulation time, the precipitation

zone of this mineral extends towards the production well and concerns, after 1500 days, the first half of the fracture. But, the reaction rate stays one to two orders of magnitude smaller than the one of calcite.

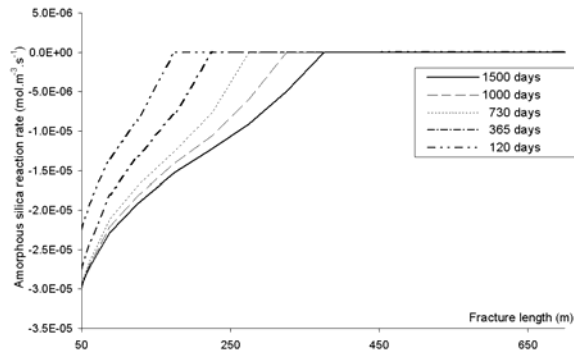


Figure 7. Amorphous silica reaction rate along the fracture.

Concerning pyrite, this mineral precipitates all along the fracture but, like in the case of quartz, the reaction rate stays negligible in comparison with calcite.

Amounts of precipitated and dissolved minerals

Knowing the reaction rate, the amount of each mineral, precipitated or dissolved, can be estimated at each time and in each fracture element of the model. Table 4 presents the total amount of precipitated and dissolved mineral after 1500 days of fluid circulation.

Table 4. Amounts of precipitated and dissolved minerals within the entire fractured zone, after 1500 days of fluid circulation.

Minerals	Total precipitation (kg)	Total dissolution (kg)
Calcite	-534	1737
Dolomite	-	328
Quartz	-0.4	-
Amorphous silica	-153	0.05
Pyrite	-0.02	-

As calculated above by the reaction rates, calcite is the most reactive mineral. Including dolomite, more or less 2 tons of carbonates are dissolved in the fracture within 1500 days, whereas only 500 kg precipitate. We can also observe that the amounts of other reactive minerals stay far below the ones of carbonates. The only significant amount concerns the amorphous silica with about 150 kg, which precipitate close to the injection well.

Influence on porosity and permeability

The amounts of dissolved and precipitated minerals have a direct consequence on the reservoir properties, mainly porosity and permeability.

As Figure 8 shows it, calcite dissolution, close to the injection well, involves an increase of the porosity until all the carbonates have disappeared.

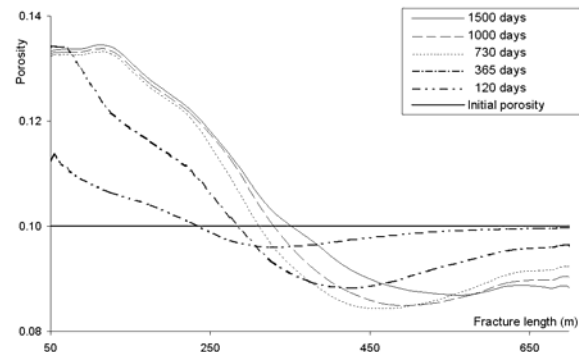


Figure 8. Evolution of porosity within the fracture according to time of circulation.

When calcite and dolomite have been dissolved, the reservoir porosity stabilizes at about 0.135; this value indicates an increase of 30-35 % compared to the initial porosity. The precipitation of amorphous silica within this zone has a limited influence on the porosity. After 1500 days of circulation, this increase of 30 % concerns only the first 100 m of fractured zone but, with an increase of circulation time, we can suppose that the porosity of all the fracture will reach this value.

Close to the production well, calcite precipitation causes a decrease of the fracture porosity of about 15 % after 1500 days of fluid circulation.

Considering the relationship between porosity and permeability used in this model, the same tendency is observed for reservoir permeability.

The case of aluminosilicates

As yet mentioned in the mineralogical description of the granite, aluminosilicates constitute an important part of the mineral assemblage.

However, taking into consideration their reactions in the model presents some difficulties. Some assumptions had to be done: the dissolution reactions are considered as congruent; aluminium in solution is under the form of Al^{3+} . Considering the temperature and the hydrostatic pressure in the reservoir, $Al(OH)_3^0$ and $Al(OH)_4^-$ species must be used (Pokrovskii and Lasaga, 1995). Nevertheless, the determination of activity coefficients of these species in the Soultz conditions presents some uncertainty and with the brine pH close to 4.8-4.9, the species Al^{3+} has been chosen. The calculation of the activity coefficient of this ion has been carried out with the EQ3nr programme (Wolery, 1992) and by the method presented by Barrett and Anderson (1988). The aluminium concentration in solution is fixed to 0.1 ppm.

From the hypothesis defined above, K-feldspars and illite seem to be more reactive than albite (Figure 9).

These two minerals precipitate close to the injection point and this process decreases when temperature increases.

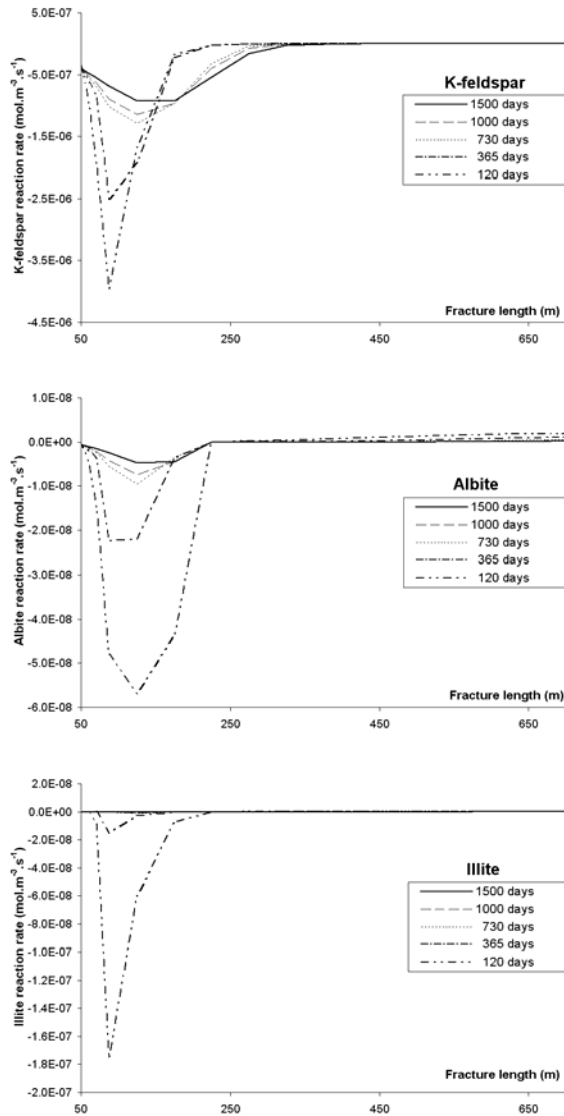


Figure 9. Aluminosilicates reaction rate along the fracture.

Above 110°C, the reaction rates of all the aluminosilicates could be considered as negligible. We can also note that the main precipitation of aluminosilicates occur at the beginning of the fluid circulation and that the reaction rates decrease with increasing circulation time, particularly in the case of illite.

After 1500 days of circulation, the precipitated amounts of K-feldspar and illite are relatively low and are negligible for albite (Table 5). Addition of aluminosilicates in the code involves small modifications of the reactive amounts of the other minerals which has some effects on the reservoir properties (Figure 10).

Table 5. Amounts of precipitated and dissolved minerals including the aluminosilicates within the entire fractured zone, after 1500 days of fluid circulation.

Minerals	Total precipitation (kg)	Total dissolution (kg)
Calcite	-453	1939
Dolomite	/	407
Quartz	-0.44	/
Amorphous silica	197	0.05
Pyrite	-0.078	-
K-feldspar	-48	-
Albite	-0.53	0.02
Illite	-0.95	0.003

Porosity of the reservoir increases until the complete dissolution of calcite and dolomite, reaching a maximum of 0.135 close to the injection zone. Following this step, the precipitation of amorphous silica and mainly K-feldspar involves a porosity decrease to a value of 0.125 after 1500 days of circulation.

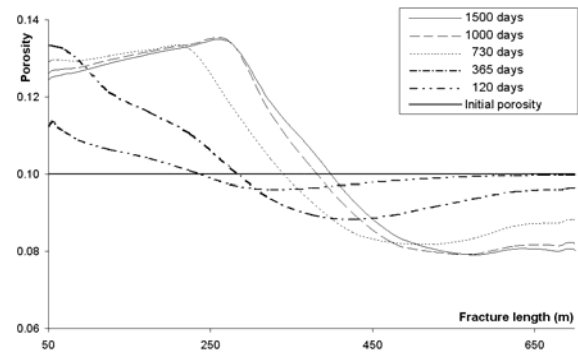


Figure 10. Influence of the reactions of aluminosilicates on the fracture porosity.

CONCLUSION

The circulation of injected cold brine in the Soutz reservoir is modelled using a Thermo-Hydraulic and Chemical coupled code. The fluid flow within the granitic reservoir modifies the chemical and thermal equilibrium of the system involving dissolution and precipitation of some minerals. Calcite is the most reactive of them with more than 1500 Kg of mineral dissolved in the first half of the fractured zone and 500 Kg precipitated close to the production well. Silicates and aluminosilicates tend to precipitate near the injection well but in small quantities. A consequence of these reactions is the impact on porosity and permeability of the reservoir. In the vicinity of the injection well, the porosity increases of about 30 %, mainly due to calcite dissolution, while it decreases of about 15% close to the production well. Carbonates reactions seem to control the porosity of the reservoir, at least during the first 1500 days of

circulation. Silicates and aluminosilicates however play a secondary role.

These porosity variations have an impact on injectivity and productivity of the EGS system with an increase of the first one and at the same time a decrease of the latter.

ACKNOWLEDGEMENTS

The authors thank the Swiss Federal Office for Education and Science for funding this project (OFES-N° 03.04.60).

REFERENCES

Bächler, D. (2003), "Coupled Thermal-Hydraulic-Chemical Modelling at the Soultz-sous-Forêts HDR reservoir (France)", PhD Thesis, ETH-Zürich, Switzerland, 150 p.

Barrett, T.J. and Anderson, G.M. (1988), "The solubility of sphalerite and galena in 1-5 m NaCl solutions to 300°C". *Geochimica et Cosmochimica Acta*, **52**(4): 813-820.

Bolton, E.W., Lasaga, A.C. and Rye, D.M. (1996). "A model for the kinetic control of quartz dissolution and precipitation in porous media flow with spatially variable permeability; formulation and examples of thermal convection", *Journal of Geophysical Research, B, Solid Earth and Planets*, **101**(10), 22157-22187.

Durst, P. (2002), "Geochemical modelling of the Soultz-sous-Forêts Hot dry Rock test site: Coupling fluid-rock interactions to heat and fluid transport", PhD thesis, University of Neuchâtel, Switzerland, 127 p.

Hettkamp, T., Baumgärtner, J., Baria, R., Gérard, A. Gandy, T., Michelet, S. and Teza, D. (2004), "Electricity production from hot rocks". *Proceedings, 29th Workshop on Geothermal Reservoir Engineering*, Stanford University, Stanford, California, January 26-28, 2004, 184-193.

Jacquot, E. (2000), "Modélisation thermodynamique et cinétique des réactions géochimiques entre fluides de bassin et socle cristallin: application au site expérimental du programme européen de recherche en géothermie profonde (Soultz-sous-Forêts, Bas-Rhin, France)", PhD thesis, Université Louis Pasteur-Strasbourg I, France.

Kohl, T. and Hopkirk, R. J. (1995), "'FRACTURE' – A simulation code for forced fluid flow and transport in fractured, porous rock", *Geothermics*, **24**, 333-343.

Kohl, T., and Rybach, L. (2001), "Assessment of HDR reservoir geometry by inverse modelling of non-laminar hydraulic flow", *Proceedings, 26th Workshop on Geothermal Reservoir Engineering*, Stanford University, Stanford, California, January 29-31, 2001, 259-265.

Norton, D. and Knapp, R. (1977), "Transport phenomena in hydrothermal systems; the nature of porosity", *American Journal of Science*, **277**, 913-936.

Pokrovskii, V.A. and Helgeson, H.C. (1995), "Thermodynamic properties of aqueous species and the solubilities of minerals at high pressures and temperatures: the system $\text{Al}_2\text{O}_3\text{-H}_2\text{O-NaCl}$ ", *American Journal of Science*, **295**, 1255-1342.

Rabemanana, V., Durst, P., Bächler, D., Vuataz, F.-D., and Kohl, T. (2003), "Geochemical modelling of the Soultz-sous-Forêts Hot Fractured Rock system: comparison of two reservoirs at 3.8 and 5 km depth", *Geothermics*, **32**(4-6), 645-653.

Schellschmidt, R. and Pribnow, D. (2001). "GGA Temperature Logs from the HDR site in Soutz-sous-Forêts". In: Baria, R., Baumgärtner, J., Gérard, A., Weidler, R. and Hopkirk, R. (Editors). *European Hot Dry Rock Geothermal Research Programme 1998-2001*. European Commission Final Report, contract no. JOR3-CT98-0313, Annex 7, 15p.

Steefel, C.I. and Lasaga, A.C. (1994), "A coupled model for transport of multiple chemical species and kinetic precipitation/dissolution reactions with application to reactive flow in single phase hydrothermal system", *American Journal of Science*, **294**, 529-592.

White, S.P. (1995), "Multiphase nonisothermal transport of systems of reacting chemicals", *Water Resources Research*, **31**, 1761-1772.

Wolery, T.J. (1992), "A computer program for geochemical aqueous speciation solubility calculations: theoretical manual user's guide, and related documentation (Version 7.0)", Lawrence Livermore Nat. Lab. Report, UCRL-MA-110662 PT III. 246 pp.

A 5000 M DEEP RESERVOIR DEVELOPMENT AT THE EUROPEAN HDR SITE AT SOULTZ

R.Baria¹, S.Michelet¹, J.Baumgaertner^{1,2}, B.Dyer³, J.Nicholls,
T.Hettkamp^{1,3}, D.Teza⁴, N.Soma⁵, H.Asanuma⁶, J. Garnish, T.Megel⁷, T.Kohl⁷ & L.Kueperkoch

¹EEIG "Heat Mining", Kutzenhausen, France.

²BESTEC GmbH, Kandel, Germany.

³Semore Seismic, Falmouth, UK.

⁴BGR, Hanover, Germany.

⁵National Institute of Advanced Industrial Science and Technology (AIST) Tsukuba, Japan.

⁶Tohoku University, Sendai Japan., ⁷GEOWATT AG, Dohlenweg 28, CH-8050, Zurich

ABSTRACT

During the present phase of the development of the European HDR program (2001 to 2005), two additional 5000 m deep wells have drilled in to a crystalline basement to form a three well HDR module. These two wells are named GPK3 and GPK4. The existing well GPK2 and one of the new well GPK4 will be producers. The second central new well GPK3 will be the injector. The first well GPK2 was drilled in 1999 and stimulated in 2000.

Microseismic monitoring was carried out during this stimulation. A second well GPK3 (injector) was targeted using microseismic and other data and drilled in 2003. The bottom hole temperature was 200°C and separation between the two wells (GPK2 & GPK3) at the bottom was around 650 m. This well was then subsequently stimulated to enhance the permeability between the wells (Baria et al., 2004).

Based on the microseismic data the trajectory of GPK4 was planned whereby the bottom of GPK4 was around 1200 m away from the top of the well forming a deviated and complex targeting exercise. Before the main stimulation of the highly deviated well GPK4, a small scale injection tests were carried out in GPK3 to evaluate it's properties as an injector, which indicated that the injectivity of GPK3 was approximately 0.4 l/s/Bar and the data indicate that it was in a closed system. A short production test was carried out using buoyancy effect and under a backpressure of 12 Bars from GPK3. The productivity of GPK3 under these conditions was found to be was 1.3 l/s/Bar.

A test was also carried out to measure the undisturbed in-situ injectivity of GPK4 which was found to be <0.015 l/s/Bar. This test was followed by the injection of saturated brine initially and subsequently by fresh water. A high-resolution seismic network was used to monitor the stimulation of GPK4. The results show that the use of saturated brine to enhanced the downward

of seismicity to allow the predominant stimulation to take place at the bottom of the well, as planned, had been fulfilled. This was supported by the flow log carried out during injection, which showed that over 60% of the injected flow left at the bottom of GPK4. The stimulation had to be stopped prematurely due to the collapse of the upper part of the borehole casing. Hydraulic and seismic data indicate that an acceptable hydraulic connection between GPK3 and GPK4 was not achieved and further stimulation is necessary.

INTRODUCTION

The European HDR site is located near Soultz-sous-Forêt around 50 km north of Strasbourg in France (Fig. 1). The background to the establishment of the European program at Soultz and the progress to date has been given by Baria et al (1993), Garnish et al (1994), Baria et al (1995), Baumgaertner et al (1995), & Baumgaertner et al (1998), Baria et al (2004,) and others. The present phase consists the development of a deep underground reservoir at 5000 m depth with a bottom hole temperature ~200 °C.

The present phase started in April 2001 and will last until March 2005. It is called a Scientific Pilot Plant (Phase 1). The brief is to drill two additional deviated 5000 m deep wells to form a three-well system and to create an enhanced permeability fractured rock reservoir by hydraulic stimulations. It also includes use of various diagnostic techniques to understand and quantify various properties of the stimulated reservoir. The program also includes the establishment of a database of the potential HDR resource in the Western Europe.

BASIC CHARACTERISTICS OF THE SITE

GEOLOGY

The European HDR test site is in the Northern flank of the Rhine Graben, which is part of the

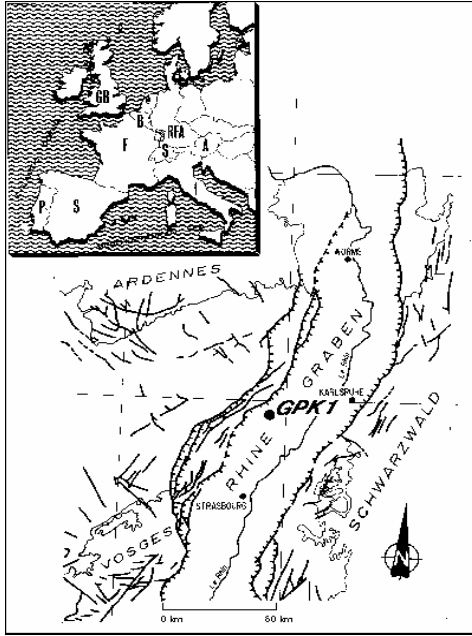


Figure 1: The location of the European HDR site at Soultz-sous-Forêts

Western European rift system (Villemin, 1986). The rift extends approximately N-S for 300 km from Mainz (central Germany) to Basel (Switzerland). The Soultz granite is part of the same structural rocks that form the crystalline basement in the Northern Vosges, and intrudes into Devonian - Early Carboniferous rocks.

The geology of the Soultz site and its tectonic setting have been described by Cautru (1987). The pre-Oligocene rocks that form the graben have slipped down a few hundred meters during the formation phase of the graben. The Soultz granitic horst (above which the site is located) has subsided less than the graben. The graben is about 320 million years old (Köhler, 1989) and is covered by sedimentary layers about 1400 m thick at the Soultz site.

Boreholes

The eight boreholes available at the site are shown in Fig. 2. They range in depth from 1400 m to 5000 m. The five boreholes #4601, #4550, #4616 and EPS-1 are old oil wells that have been extended to 1600 m, 1500 m, 1420 m and 2850 m respectively in order to deploy seismic sondes in the basement rock. Additionally, the well OPS4 was drilled in 2000 to a depth of 1800 m.

The first purpose-drilled well (GPK1) was extended from 2000 m to 3590 m in 1993 (Baumgärtner et al., 1995) and has a 6-1/4" open hole of about 780 m. GPK1 was used for large-scale hydraulic injection and production tests in 1993, 1994 and 1997 but presently it is used as a deep seismic observation well. GPK2 is about

450 m south of GPK1 and was drilled in late 1994 to a depth of 3890 m and subsequently deepened to 5000 m in 1999. GPK3 is a 5000m deviated well with the bottom hole located about 600 m south of GPK2. After the completion of GPK3, a large stimulation was carried out in GPK3 to connect GPK3 to GPK2 and also to provide information to target the third deep well GPK4 (Baria et al 2004).

The trajectory of GPK4 was defined after the stimulation of GPK3 using the microseismic data to target GPK4. The drilling of GPK4 took 2.5 months longer than planned. This was caused by a number of unforeseen problems, the drilling of the highly deviated well in granite was difficult and slow, there was also an incident with a faulty manufactured casing string, whose connectors broke during deployment and fell to the bottom. The faulty casing had to be fished out and replaced. There were also problems with downhole motors for directional drilling and being able to hold the trajectory to finish it in the targeted zone. This was found to be the most difficult trajectory to hold as the well was 5000 m deep with the bottom being something like 1200 m to the south of the wellhead. The drilling of GPK4 started in august 2003 and was completed in April 2004. The layout of the boreholes is shown in Fig 2.

During the drilling of GPK4 scientific activities such cutting analysis, drilling fluid analysis, bit monitoring and geophysical measurement while drilling etc. were also carried out.

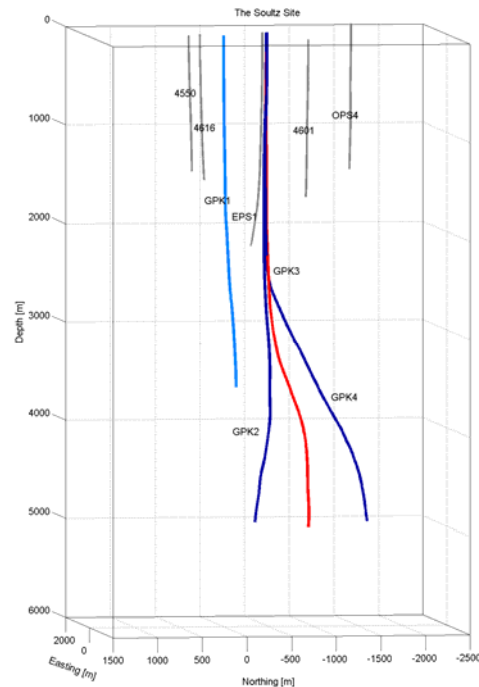


Figure 2: layout of the boreholes

Temperature gradient

In the Soultz area the temperature trend has been determined using numerous measurements in the boreholes. The variation in temperature gradient can be roughly described as 10.5°C/100 m for the first 900 m, reducing to 1.5°C/100 m down to 2350 m (Schellschmidt & Schultz, 1991) then increasing to 3°C/100 m from around 3500 m to the maximum depth measured (5000 m).

This irregular gradient suggests that there is a zone of enhanced circulation between the granite basement and the sedimentary cover. The reduction in the temperature gradient and its subsequent increase suggests that there are convective cells present, which may extend to greater depth. Thermal modeling and the available data (geochemical and hydraulics) both support this view.

Joint network

Information on the joint network at the Soultz site has been obtained from continuous cores in EPS1 and borehole imaging logs in GPK1 (Genter and Traineau (1992a) and (1992b)). The observations suggest that there are two principal joint sets striking N10E and N170E and dipping 65°W and 70°E respectively (Genter and Dezayes, 1993). The granite is pervasively fractured with a mean joint spacing of about 3.2 joints/m but with considerable variations in joint density.

Stress regime

At the Soultz site, the stress regime was obtained using the hydrofracture stress measurement method (Klee and Rummel, 1993). The stress magnitude at Soultz as a function of depth (for 1458-3506 m depth) can be summarized as:

(Min. horizontal stress) $S_H = 15.8 + 0.0149 \cdot (Z - 1458)$

(Max. horizontal stress) $S_H = 23.7 + 0.0336 \cdot (Z - 1458)$

(Overburden) $S_V = 33.8 + 0.0255 \cdot (Z - 1377)$

S_H, S_H, S_V in MPa and Z = depth (m)

Note that this implies a cross-over between S_V and S_H around 3000 – 4000 m depth, with a consequent transition in failure mode from normal faulting to strike-slip.

Microseismic network & real time reservoir monitoring

A microseismic network has been installed at the site for detecting microseismic events during fluid injections and locating their origins (Fig. 2). The equipment consists of three 4-axis accelerometer sondes and 3-axis geophone sondes (Calidus Electronics), linked to a fast seismic data acquisition (Perseids, IFP) and processing system (DIVINE, Semore Seismic). The sondes were deployed at the bottoms of wells #4550, #4601,

#4616, EPS1, OPS4 and GPK1. Additionally, the teams from Tohoku University and AIST, Japan, carried out continuous digital recording.

In addition, a surface network consisting of around 35 stations was installed by EOSt in order to be able to characterize larger events and event magnitudes.

The seismic activity generated during the stimulation was monitored continuously using a dedicated system based on subsurface sensors. The seismic data from the monitoring wells were continuously transmitted to the acquisition room by a combination of landline and radio telemetry. During the stimulation of GPK4, the acquisition system detected in excess of 16 000 potential seismic events. The event rate was typically around 100 events/hour. The peak rate was just in excess of 250 events/hour, one event every fifteen seconds. Larger events were below 2.0 ML.

The seismic trace data were transferred continuously to an automatic timing and event location package, (Divine, Semore Seismic), to obtain real time event locations. The network at the site is *sparse* and around 4 000 events were located in this way using auto-picked P and S timing. The event locations could be viewed in the hydraulic control room and other sites remote from the acquisition room over the network. This was the second time that seismic data have been available in real time at the site.

HYDRAULIC CHARACTERISATION OF GPK3 AND GPK4

During the stimulation of GPK3 in 2003, there were constraints on certain aspects of hydraulic investigation because of the concern that a sudden shut-in might cause the initiation of larger seismic events. This meant that the hydraulic tests performed during the stimulation of GPK3 did not have an adequate shut-in. Therefore the pseudo-shut-in became somewhat more difficult to analyze. As the hydraulic set up in 2004 was so flexible, this provided an opportunity to quantify some of the characteristics of GPK3 prior the stimulation of GPK4. The investigation consisted of determining the post-stimulation injectivity and productivity of GPK3. 7000 m³ of fresh water was injected in GPK3 at 12, 18 and 24 l/s as shown in Fig 3. During this period GPK2 was active (pressurised) and GPK4 was killed. The injectivity of GPK3 was calculated to be #0.4(l/s)/Bar, although the target value for high flow rates is #1.0 (l/s)/Bar. This indicates that it behaves like a relatively closed system. There was also clear pressure response in GPK4 to the injection test in GPK3..A production test was also carried out in GPK3 to evaluate its productivity and to clean the near well bore region. Around 2710 m³ of fluid was produced from GPK3 while keeping a backpressure of #12 bars and observe the behavior of the flow. Fig 4 shows the data obtained.

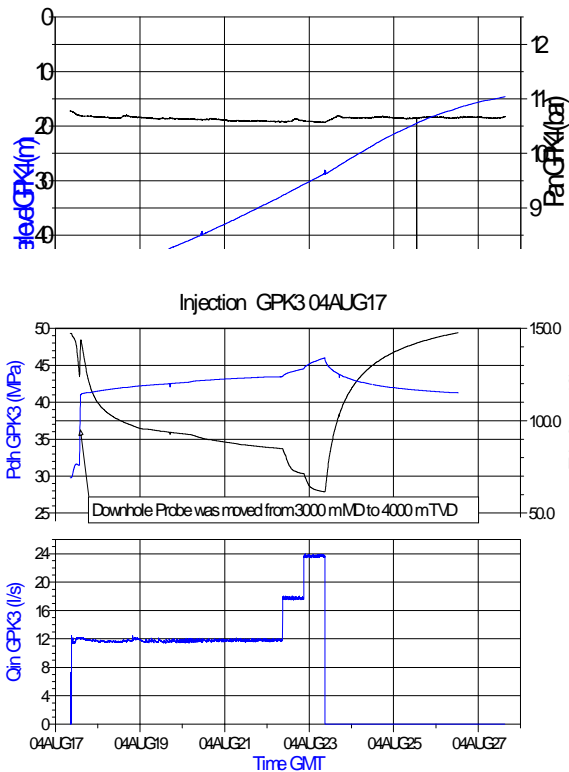


Figure 3. Hydraulic data from the injectivity test in GPK3

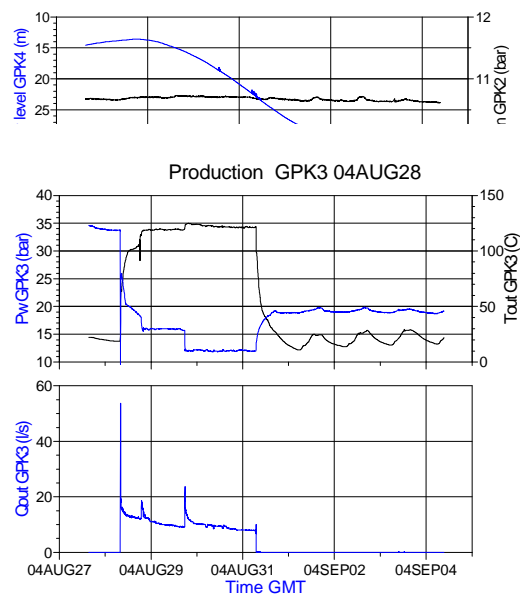


Figure 4. Hydraulic data from the production test in GPK3

The productivity of GPK3 was calculated to be 1.3 (l/s)/bar assisted by buoyancy effect. This had improved by a factor three, although there is a clear indication that the production flow was decreasing as a function of time.

Following the injection test in GPK3, a low flow rate injection test was carried out in the new well GPK4 to assess the undisturbed injectivity of GPK4. The well was filled with brine of 1.19 g/cm³ prior to the stimulation. Around 250 m³ of saturated brine was injected in GPK4 at a flow rate of 0.8 l/s over 4 days. GPK2 and GPK3 were made active by pressuring the wells.

The results indicate that the injectivity of GPK4 was <0.015 (l/s)/bar, very low and comparable to that of GPK2 in 2000. No pressure communication to either GPK3 or GPK4 was observed.

STIMULATION OF GPK4

The above test was followed by the main stimulation of GPK4, which consisted of injecting ~9134 m³ of fresh water at predominant injection flow rate of 30 l/s over 3.5 days, although three unsuccessful attempts were made to increase the flow rate to 45 l/s, without success because of the breakdown of an injection pump due to overheating of a bearing. The injection pressure required to pump 30 l/s was around 17 MPa, which is very close to the limit of the pump. The data obtained is shown in Fig 5.

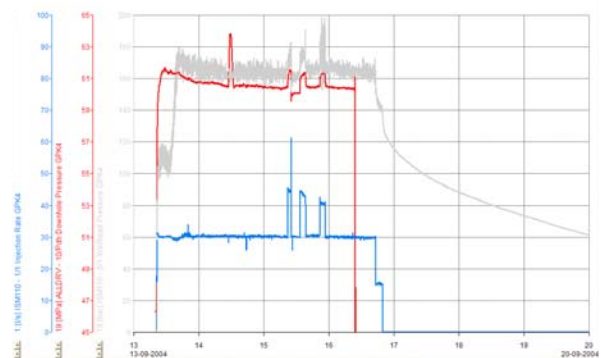


Figure 5. Hydraulic data from the stimulation test in GPK4

During the injection in GPK4 at 30 l/s, the wellhead pressures of GPK3 and GPK2 were also monitored. The pressure response of GPK2 and GPK3 is shown in Fig 6. A flowlog was also carried out to identify flowing zones and flow exits in the open-hole section of GPK4 while injecting, which is shown in Fig 7. The flow log shows that the majority of the flow left the well GPK4 at the bottom (~ 60%) and the other two identifiable exits at around 4775 m and 8225 m MD took ~15% each.

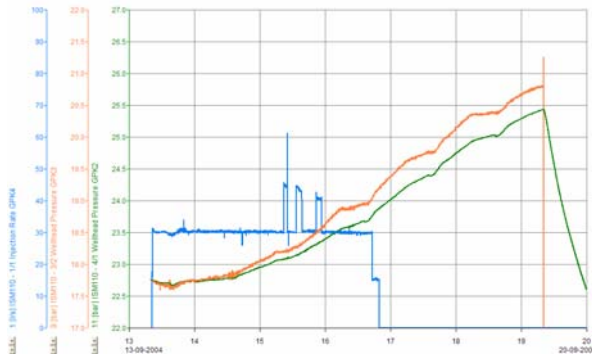


Figure 6. Pressure response in GPK2 and GPK3 during the stimulation of GPK4

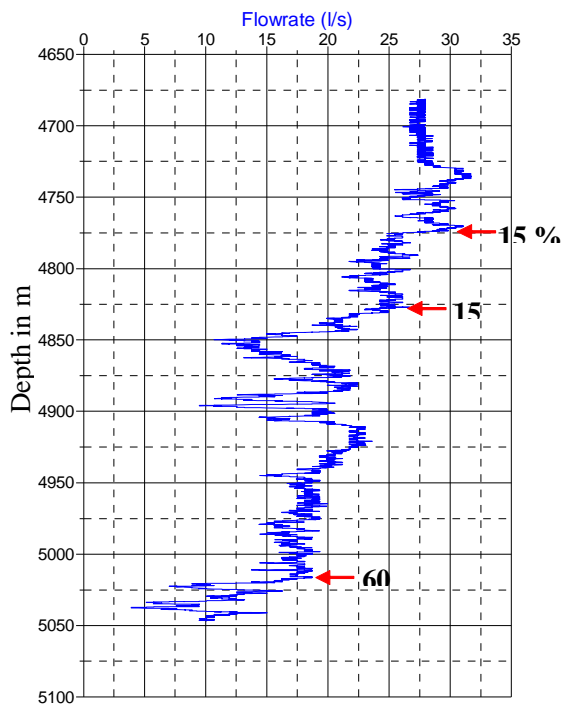


Figure 7. Flow log in GPK4 during the injection of fresh water at 30 l/s

Microseismic monitoring was carried out during the stimulation of GPK4 and the data obtained are shown in Fig 8. These were located in real time during the stimulation of GPK4. These six views of the locations represent locations after 6 hours (heavy brine period), 12 hours (fresh water injection), 1 day, 2 days, 3 days and 6 days.

The economic argument suggests that production from a zone as deep as possible from the open-well will deliver fluid with higher temperature and therefore give better return on the investment. In order to achieve this, saturated brine was inject earlier on before the main stimulation. The stress field at Soultz is such that the horizontal minimum

stress is very close to the hydrostatic and therefore by using heavier brine, the hydrostatic force is made even close to the value of the minimum stress, thus encouraging the joints near the bottom of the well to open/shear earlier than those above. The evidence of this can be clearly seen in the grown of earlier seismicity below the well as shown in Figure 8a.

After the initial injection of brine, fresh water was used to continue the stimulation of GPK4. The effect of fresh water in this specific stress setting can be seen as few seismic events begin to occur around 300 m above the bottom of the well ie 4700 tvd. This can be seen in Figure 8b. Subsequent figures (Figures 8c to 8e) show the continuous development of the deeper and shallower structure. These flow exits associated with the development of microseismicity can also be seen on the flow log (Fig. 7) and although there are three discreet exits, it would be difficult to separate the affect of the two upper exits as they are so close to each other. The flow log therefore supports the data from microseismic locations.

Three days into the stimulation of GPK4, the PTF sonde stopped working and it was decided to withdraw it from the well to repair it. While withdrawing the sonde, it was observed that the sonde could not be pulled into the riser. In view of the difficult situation, the stimulation of GPK4 was stopped, the reservoir was killed in order to investigate and rectify the cause inaccessibility of getting the PTF tool into the riser.

The microseismic and the hydraulic data indicated that although a good progress was being made towards creating and establishing a hydraulic link between GPK4 and GPK3, a satisfactory link was not established yet. Further analysis of the seismic data was made by comparing with the density map of the seismic events created during the stimulation of GPK3. Figure 9 shows the plan and vertical view of the microseismic density map created during stimulation of GPK3 in 2003 and GPK4 in 2004. The high density of microseismic activity associated with the stimulation of GPK4 (marked by dotted circle) has not broken through into the previous high density microseismic activity associated with the stimulation of GPK3 There is a clear indication that the connection has not been fully established yet and that further stimulation will be necessary to improve the link.

The results of the hydraulic data show that high pressures were required to stimulate GPK4 (at 30 l/s, ~17 MPa) than before. It was difficult to inject 45 l/s because of the high pressure encountered. Further stimulation will be necessary to reduce the flow impedance to GPK3 and the shut in curve indicated that it is a relatively tight system and may be classified as a so-called “closed” system.

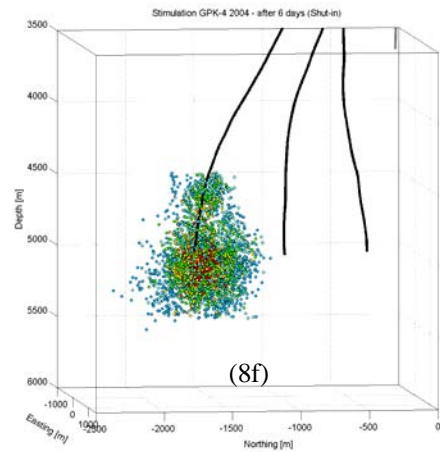
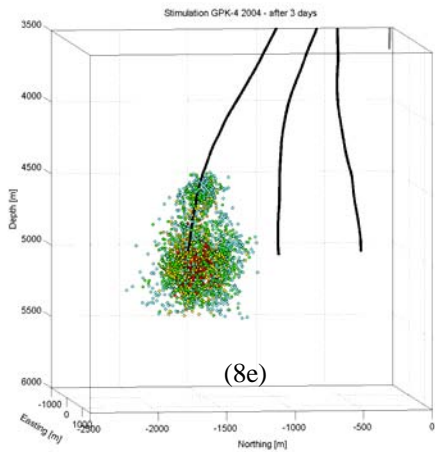
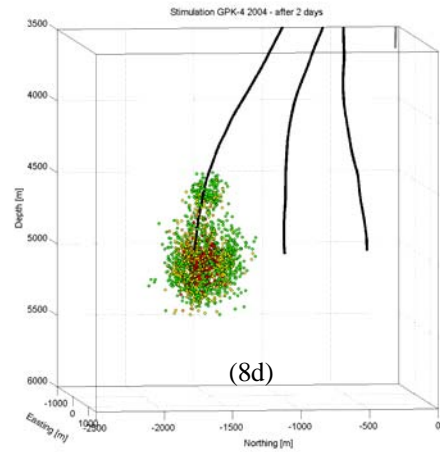
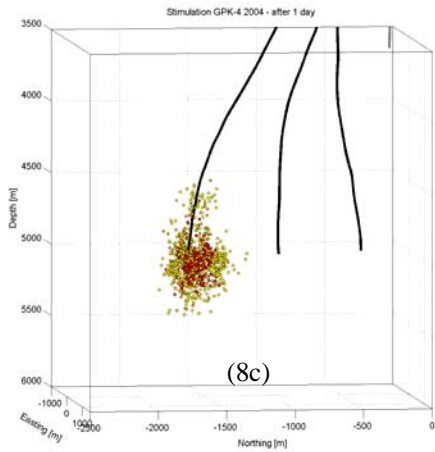
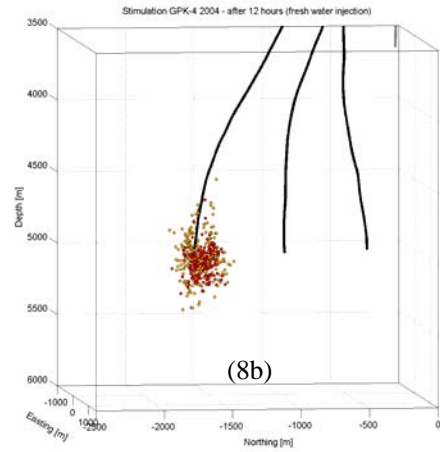
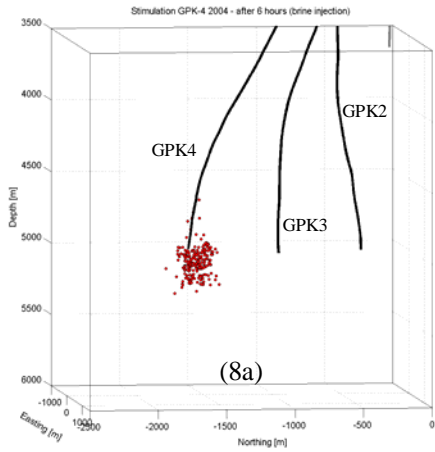


Figure 8. Microseismic locations during the stimulation of GPK4

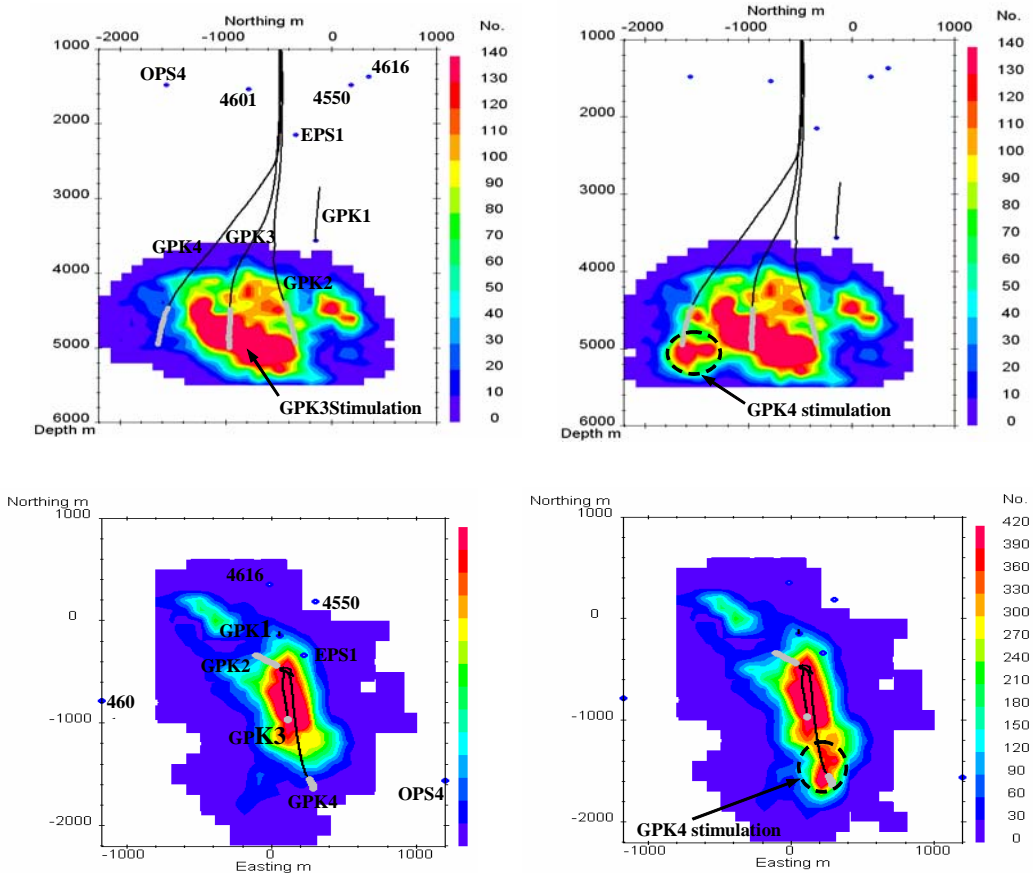


Figure. 9. Vertical and plan view of the microseismicity intensity map during the stimulation of GPK3 and GPK4

On dismantling the wellhead assembly of GPK4, it was noticed that the upper part of the 9^{5/8}" casing had collapsed (Fig 10), reducing the accessible diameter of the casing and therefore making it impossible to withdraw the PTF sonde. The collapsed part of the casing was cut off and the logging tool and the wireline cable were recovered. Further investigation showed that cuttings created during the drilling of GPK4 and the lubricating oil had somehow got behind the 9 5/8" casing and formed a seal just below the landing ring on the casing. This seal in conjunction with the packer assembly, which allows the casing to expand, had trapped water between the two, which could not escape. When the casing shrunk during the injection, as the trapped water could leak away, the casing came under enormous pressure and collapsed locally.

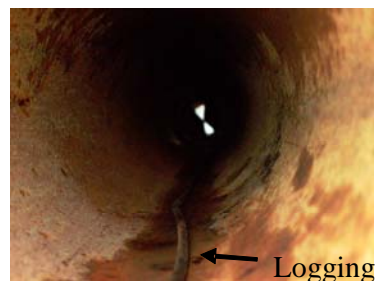


Figure. 10. Collapsed casing, looking from underneath

PRELIMINARY OBSERVATIONS & CONCLUSIONS

1. There appears to be good correlation between the spatial growths of microseismic events and the distribution of flow exits in the well as indicated by flow logs.
2. The injectivity and productivity of GPK3 after stimulation is #0.4(l/s)/Bar and 1.3 (l/s)/bar respectively. The productivity was declining.
3. The undisturbed injectivity of GPK4 is ~ 0.015 (l/s)/bar i.e. very poor
4. In excess of 17 MPa overpressure was required to inject 45 l/s.

5. The above and other hydraulic data indicate that the system at 5000 m depth behaves like a relativity-closed system.
6. Microseismic data is a good indicator of what was happening during the stimulation and supports the view that a satisfactory hydraulic breakthrough between GPK4 and GPK3 was not established.
7. The strategy of using smaller volume for stimulation to reduce the generation of larger microseismic events appears to be promising.
8. The permeability between the wells GPK3 and GPK4 has not been enhanced to a required degree and a further stimulation with higher flow rate will be necessary.

FUNDING

Work at Soultz is funded and supported by the European Commission Directorate-General Research, the French Ministère délégué à la Recherche et aux Nouvelles Technologies, the French Agence de l'Environnement et de la Maîtrise de l'Energie, the German Bundesministerium für Umwelt, Naturschutz und Reaktorsicherheit within the frame of the "Zukunftsinvestitionsprogramm", the Projektträger of the Forschungszentrum Jülich in Germany and by the Members of the EEIG "Exploitation Minière de la Chaleur".

ACKNOWLEDGEMENTS

The authors would like to thank all who contributed to the success of the project at Soultz. Special thanks go to all participants and contractors who were actively involved during hydraulic program (T. Gandy (GI), MeSy, GTC, IPG (Strasbourg), W. Reich (BGR), J-P Fath, J-L Riff & V. Can.

REFERENCES

Baria R, Baumgärtner J and Gérard A, 1993; Heat mining in the Rhinegraben; Socomine Internal project report.

Baria R, Garnish J, Baumgartner J, Gerard A, Jung R, 1995. Recent development in the European HDR research program at Soultz-Sous-Forets (France). Proceeding of the World Geothermal Congress, Florence, Italy, International Geothermal Association, Vol. 4, 2631-2637, ISBN 0-473-03123-X.

R.Baria, S.Michelet, J.Baumgaertner, B.Dyer, A.Gerard, J.Nicholls, T.Hettkamp, D.Teza, N.Soma, H.Asanuma, J. Garnish, T.Megel, 2004. Microseismic monitoring of the world's largest potential HDR reservoir. Twenty-ninth Workshop on geothermal reservoir engineering, Stanford University, Stanford, California, January 26-28, 2004

Baumgärtner J, Moore P and Gérard A, 1995. Drilling of hot and fractured granite at Soultz -

Proceeding of the World Geothermal Congress, Florence, Italy, International Geothermal Association, Vol. 4, 2657-26663, ISBN 0-473-03123-X.

Baumgärtner, J., Gérard, A., Baria, R., Jung, R., Tran-Viet, T., Gandy, T., Aquilina, L., Garnish, J., 1998. Circulating the HDR reservoir at Soultz: maintaining production and injection flow in complete balance. Proceedings of the 23rd Workshop on Geothermal Reservoir Engineering, Stanford University, California

Cautru JP, 1987; Coupe géologique passant par le forage GPK1 calée sur la sismique réflexion; BRGM/IMRG document.

Garnish J, Baria R, Baumgärtner J, and Gérard A, 1994. The European Hot Dry Rock Programme 1994-1995, GRC Trans.

Genter A, and Dezayes C, 1993; Fracture evaluation in GPK1 borehole by using FMI data; field report, BRGM Orléans.

Genter A, and Traineau H, 1992a; Hydrothermally altered and fractured granite in an HDR reservoir in the EPS1 borehole, Alsace, France, 17th Workshop on geothermal reservoir engineering, Stanford Univ., Jan. 29-31, 1992; preprint.

Genter A, and Traineau H, 1992b; Borehole EPS1, Alsace, France; Preliminary geological results from granite core analyses for Hot Dry Rock research; Scientific drilling 3; pp 205-214.

Klee G, and Rummel F, 1993; Hydraulic data from the European HDR Research Project test site, Soultz sous Forets. Int. J. Rock Mech. Min Sci & Geomech. Abstr., Vol 30, No 7, 973-976, 1993..

Köhler H, 1989; Geochronology on the granite core material from GPK1, Soultz-sous-Forêts; Ruhr Universität Bochum report 70844.

Schellschmidt R, and Schulz R, 1991; Hydrothermic studies in the Hot Dry Rock Project at Soultz-sous-Forêts; Geothermal Science and Technology, vol. 3(1-4), Bresee (Ed), Gordon and Breach Science Publishers, pp. 217-238.

Villemin T, 1986; Tectonique en extension, fracturation et subsidence: le Fossé Rhénan et le Bassin de Sarre-Nahe; Thèse de doctorat de l'univ. Pierre et Marie Curie, Paris VI.

USING THE MIGRATION OF INDUCED MICRO-SEISMICITY AS A CONSTRAINT FOR HDR RESERVOIR MODELLING

Dominique Bruel

Ecole des Mines de Paris
35 rue St Honoré
773005, Fontainebleau, France
dominique.brue@ensmp.fr

ABSTRACT

The challenge of the Hot Dry Rock technology is to develop a heat exchanger in deep-hot-rock masses and to circulate a fluid in order recover and to exploit the energy at the ground surface. The present day strategy at the European project is to take advantage of natural fractures that pre-exist at these depths and to improve their hydraulic properties. The extension of the area with enhanced properties must then be evaluated so that the best locations for further boreholes can be proposed. By now, this development procedure is based on fluid injections at high rates, forcing hydrau-mechanical interactions to take place along pressurized fractures. These pore pressure driven mechanisms are accompanied by some seismic activity. Some authors have developed a theory to derive the virgin hydraulic diffusivity of the reservoir from the analysis of the spatio-temporal growth of the induced seismicity. Our work is partly aimed at verifying this approach using a numerical code to solve for hydrau-mechanical interactions. It assumes that the seismic activity is controlled by a shear criterion and we show how the interpretation of spreading rate of the modelled shear activity coincide with the hydraulic diffusivity of the same fracture network, computed from an independent numerical procedure. This is important for further quantitative analysis of any reservoir open to the far field, as the overall mass balance will be linked to the – in general poorly known- hydraulic properties of the neighbouring non-stimulated areas.

INTRODUCTION

Regarding scientific and pre-industrial objectives, valuable results have been obtained at Soultz sous Forêts, in the Rhine Graben, at a depth of around 3.5 km (Baumgartner *et al.*, 1998). After this significant success at a this moderated depth, the European project has evolved toward a three well system at a

depth of 5 km, and a temperature close to 200 C. Hydraulic tests obtained in the recent wells GPK2 and GPK3 during the 2000 - 2003 field campaign, and again during the development of the most recent well, GPK4, in late 2004, have shown from their micro-seismic signature, that fractures in the new targeted reservoir are still easy to re-activate (Baria *et al.*; 2004), with over-pressure at the wells in the range of 14 to 18 MPa.. The discussion now focuses on the possibility of deriving some additional hydraulic knowledge from the shear failure mechanism, considered as the source of the acoustic emissions. A pre-rupture quantification of the hydraulic diffusivity of the fracture network is already under discussion and will be recalled in the next section. We will also show how post rupture hydraulic properties can be accounted for at this stage of global understanding by simple mechanical rules.

This work forms part of the basis required for the evaluation of the overall impedance of a circulated HDR system at flow rates compatible with an economic exploitation scheme. New hydraulic tests are planned at the European site in between pair of wells for this purpose.

FORWARD MODELLING OF THE SHEARING PROCESS AND DERIVATION OF THE VIRGIN HYDRAULIC DIFFUSIVITY

Background

It is well established, in this particular field of engineered geothermal reservoirs (Pine *et al.*, 1984, Fehler, M.C., 1989), that any increase of the pore pressure in a pre-existing fracture can induce a shear rupture with a microseismic signature, as soon as a strength criterion for failure is met. Many work has been done for a quantitative interpretation of the spatial structure of the seismic cloud, for mapping fault zones and for discussing stress perturbation along sheared areas (Cornet and Scotti, 1993). Such efforts to delineate and identify internal structures

give geometrical constraints in reservoir models (Bruehl, 2002). Microseismic studies also provide at distance from observation wells a good insight on principal stress orientation from the inversion of focal mechanisms (Yin and Cornet, 1994). Reservoir survey based on passive monitoring is being widely used in the field of petroleum engineering. Among all the possible applications, we mention two particular field cases that refer to couplings at a scale similar to the investigated geothermal problem: fault slip analysis during storage or depletion in an underground gas storage facility (Nagelhout *et al.*, 1997), and forecasting gas leakage through the poorly fractured cap rock. (Deflandre *et al.*, 1995) during the reservoir exploitation.

The Seismic Based reservoir Characterization approach

The growth of the seismic cloud during an injection phase remains however a matter of debate. Shapiro *et al.* (1999) uses a spatio-temporal analysis of the induced microseismicity to derive an *in-situ* estimate of the hydraulic diffusivity tensor of the virgin rock mass. It is also shown in Shapiro *et al.* (2002) that this tensor is directly proportional to the permeability tensor. The main assumption of the so called SBRC approach (Seismicity Based Reservoir Characterization) is that the triggering front of the hydraulic-induced events propagates like the process of pressure relaxation in a isotropic poro-elastic saturated medium. According to these authors, the spatial position of the triggering front at time t with a scalar diffusivity D is given by $r = \sqrt{4\pi Dt}$.

On the other hand it can be argued that the rupturing process along discontinuities, is mostly controlled by the stress tensor, (Cornet, 2000), and therefore that the growth of the seismic cloud reflects these couplings between mechanic and hydraulic at the local scale.

The present paper is a numerical contribution to the above debate. We suggest to analyze the hydraulic behavior of a set of fracture networks under various hydrau-mechanical conditions in a such a way that its permeability, its hydraulic diffusivity and the diffusivity of the shearing migration can be separately obtained. This method offers the opportunity of comparing the magnitudes of both diffusion processes. It will reinforce the attempt of running an inversion for hydraulic properties of rocks, performed by Shapiro *et al.* (2002) that was based on a pore-pressure relaxation model in a 2D homogeneous isotropic background with randomly distributed critical zones, but did not integrate a real fluid flow model in a discrete system of fractures.

Overview of the numerical tool used for the verification of the SBRC approach

A description of rationales and concepts of the Discrete Fracture Network model, FRACAS, used in the present paper to model fluid migration in 3D random networks of fractures can be found in Rejeb and Bruehl (2001) and Bruehl (2002) and presented in a companion paper (Baujard and Bruehl, 2005, this issue). The approach assumes that fluid flow in deep hard rocks occurs in disc shaped fractures, that assemble into a 3D network, and that the contribution of blocs to the overall flow is negligible in comparison.

The numerical package accounts for some hydro-mechanical interactions and shear slip along unstable fractures is allowed. The next sub-section recalls the numerical implementation of the rupturing process.

Implementation of a failure criterion

At any given fracture center of known depth and orientation, the normal stress and shear stress components are derived, assuming a homogeneous stress state, linearly variable with depth. The algorithm translating excess of shear forces into slip and dilation is derived from Willis-Richard *et al.* (1996). The shear stability of each fracture is assessed according to the Coulomb criterion, in which the shear forces on the fracture are resisted by cohesive and frictional forces. Shear slip along fracture surfaces is accompanied by an increase in fracture hydraulic aperture. This behavior is modeled in FRACAS by increasing the fracture hydraulic aperture in proportion to the relative shear displacement of the fracture surfaces; using a constant dilation angle.

The failure criterion, namely the friction coefficient and the cohesion coefficient, are chosen so that the stability of all fractures, prior to any fluid injection is insured. They also allow a proportion of the fractures to be very close to failure, which is a requirement of the SBRC approach...

We will not discuss the sensibility of the SBRC analysis to these parameters, even when they obviously control the spreading of the triggering front.

Simplification of the fluid flow model

Time-dependant analysis requires assumptions to be made concerning the form of fluid flow within the fracture network. The general form of fluid flow assumed in each fracture is based on an analytical solution, known as the "cubic law", for fluid flow between approximately parallel surfaces. A Bandis closure law relating the fracture hydraulic aperture to effective normal stress is usually used to reflect the fracture compliance with a change in normal stress.

Here after we will not consider stress dependency for the hydraulic parameters but simply use hydraulic transmissivity distributions.

Dealing with the fracture storativity S , a constant value S_0 is used instead of the standard stress dependant value given by the following formulation:

$$S = \rho g (1/k_{ni} + 2L/E + \beta e_i)$$

E being the Young's modulus of the surrounding rock layer, with thickness $2L$, β the fluid compressibility, ρ the fluid density, g the gravity, k_{ni} and e_i the Bandis parameters at a given normal effective stress.

The hydro-mechanical coupling is thus only introduced when shear can develop. When the failure criterion is met, the increment of hydraulic aperture resulting from the dilation of the sheared fracture is turned into an additional contribution to the local transmissivity of that fracture. This additional transmissivity is however calculated according to the cubic law. As a consequence, we can model with time the spatial spreading of a sub-network of highly conductive fractures within an initial network made of poorly conductive elements.

Fracture networks used in the present evaluation of the SBRC analysis

Geometry

The fracture networks considered here after are built to reflect hydraulic processes developing at the scale of the in-situ measurements in HDR reservoirs. Blocks of kilometre in size are generated, filled with fractures whose parameters can be compared with those of the Soutz sous Forêts data base. The size of a block is 2500 m times 2500 m in the horizontal directions, 200 m in vertical directions. The choice of such an aspect ratio of the rock volume is later justified for hydraulic modelling reasons. Principal directions are aligned with West-East axis, and South-North axis (respectively x and y). Fractures belong to 3 sub-vertical directional sets, with mean direction respectively pointing toward North-170, North-20 and North-110. The spatial distribution of fracture centres within the rock volume is Poissonian, as no in situ data are available to discuss fracture clustering or fractal distributions. The distribution of the radius of the fractures follows a power law, with exponent 2.75 and a threshold value set at 15 m. Densities, and other local hydraulic parameters are tabulated here below:

	SET 1	SET 2	SET 3
Strike direction/North	170	20	110
Density [m^{-3}]	$6 \cdot 10^{-6}$	$4 \cdot 10^{-6}$	$5 \cdot 10^{-6}$
transmissivity [m^2/s]	$1 \cdot 10^{-5}$	$5 \cdot 10^{-6}$	$5 \cdot 10^{-6}$
storativity [-]	$2 \cdot 10^{-6}$	$2 \cdot 10^{-6}$	$2 \cdot 10^{-6}$

Stress distribution and mechanical parameters

Stresses acting on the fractures populating the volume of rock are not depth dependant. Numerical values are extracted from a pre-existing work (Bruehl, 2002) and reflect a real reservoir operated at an averaged depth set to 3500 m. Minimum and maximum principal stress components are fixed to 47 MPa and 87 MPa respectively. The maximum horizontal component is pointing toward North 170. The failure criterion is governed by a friction coefficient of 0.80 and a cohesion coefficient of 0.5 MPa (see next section). The dilation angle is set at 3 degrees.

Results

Evaluation of the block transmissivity

Ten equivalent alternatives in a statistical sense are considered. For each of these ten different networks, a square block 1 km in size located at the centre of the rock volume is isolated and a head gradient applied in between pair of opposite boundaries (respectively North – South and East -West). This parallel flow global condition allows us to calculate a flux in both directions successively. Figure 1 shows the traces of the fractures intersected by a horizontal plane, median to the rock volume. The green lines denote the contour where prescribed boundaries are applied.

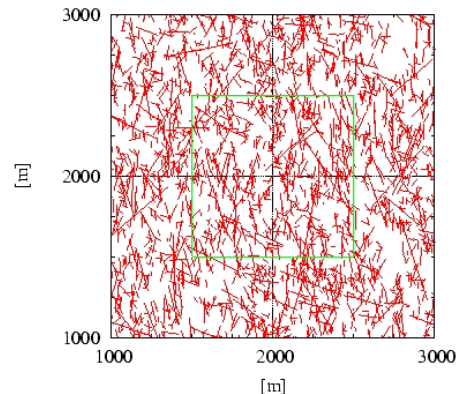


Figure 1. Over view of the hydraulic boundaries for deriving the bloc scale permeability in x and y directions respectively.

The hydraulic head prescribed on the opposite boundaries are +0.5 MPa and -0.5 MPa, which result in a head gradient of 0.001 Mpa/m. Because of the transient nature of the flow, the calculations are performed until a balance is established inbetween inflow and outflow. Figure 2 shows that durations as long as one month are required..

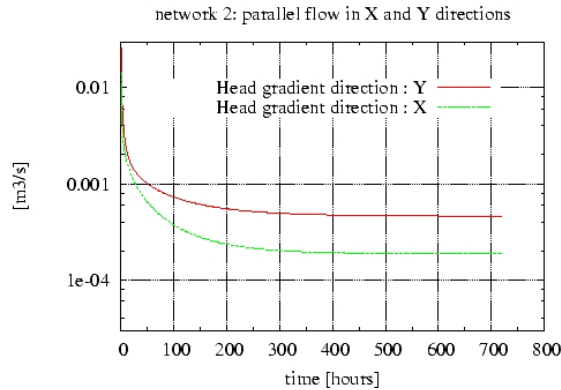


Figure 2. Derivation of an asymptotic flux values for network 2, in directions x (east-west) and y (south-north)

The average flux in y direction is $0.4 \cdot 10^{-3} \text{ m}^3/\text{s}$, with minimum and maximum values of $0.25 \cdot 10^{-3} \text{ m}^3/\text{s}$ and $0.72 \cdot 10^{-3} \text{ m}^3/\text{s}$. Given the size of the block and the applied head gradient, we derive an average transmissivity in Y direction of $T_Y = 0.4 \cdot 10^{-5} \text{ m}^2/\text{s}$. Similarly we obtain along X an average flux of is $0.12 \cdot 10^{-3} \text{ m}^3/\text{s}$, leading to a transmissivity in X direction close to $T_X = 0.12 \cdot 10^{-5} \text{ m}^2/\text{s}$. The geometric mean T of these two values is taken as an estimate of the transmissivity of the fracture network at a scale of 1 km. We obtain $T = 0.23 \cdot 10^{-5} \text{ m}^2/\text{s}$.

Evaluation of the block storativity and the equivalent hydraulic diffusivity of the fracture network

To derive an up scaled storativity, we suggest to simulate and interpret a pumping test, rather than to upscale this parameter from fracture spacing statistics and assigned local storativity values. We do not approximate this coefficient using an equivalent poro-elastic modulus for low-porosity crystalline rocks as suggested in Shapiro et al. (1999) because porosity has to be speculated as well as bulk moduli for dry frame and grain material within the fractures. Thus, a vertical borehole is added at the centre of each of the ten fracture networks and a long term pumping test at low constant rate is simulated. The extracted rate is set constant and equal to $0.001 \text{ m}^3/\text{s}$. Drawdown is observed at 8 locations along vertical wells, at a radial distance of 250 m from the source (Figure 3). The number of fractures intersected by these wells varies from 0 to about 6. Networks have been selected so that the injection into the central well is possible.

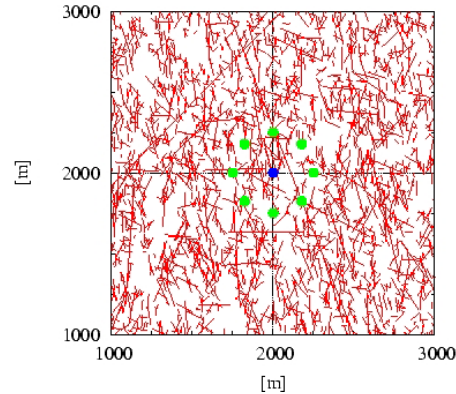


Figure 3. Plan view of the intersection of a network by a horizontal plane, showing the location of the source and monitoring zones for the simulation of a pumping test.

Calculated drawdowns are varying among the various locations mostly because the connectivity at the local scale close to bore holes remains highly variable. This is shown in figure 4, which is related to the network alternative 3 and where variations of no more than one order in magnitude are found from one piezometer to another.

When averaging all the available responses, mixing all the sets of piezometer of each network alternative, we are able to produce an equivalent drawdown at the distance 250 m from the source, which can be treated as if the medium was equivalent to a continuous porous medium. Although this may appear not justified, the Theis approach is used, taking advantage of the already known transmissivity to calibrate the storativity. Figure 5 shows that the calibration is possible and therefore we are able to produce an equivalent storativity coefficient for these fracture networks. The calibrated value of S_{eq} is about $4.25 \cdot 10^{-5}$. As a conclusion, we state that the set of considered fracture networks have a hydraulic diffusivity D_h equal to $0.055 \text{ m}^2/\text{s}$.

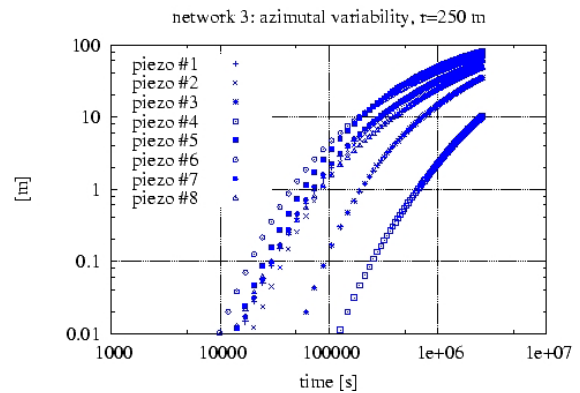


Figure 4. Calculated drawdown expressed in m, at the various monitoring wells, at a radial distance of 250 m from the source (network alternative 3)

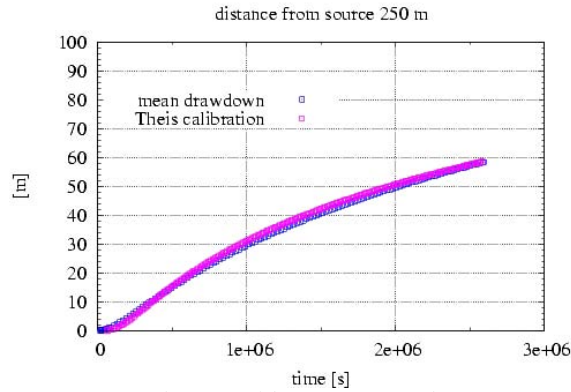


Figure 5. Theis calibration of the averaged calculated drawdown, using the transmissivity obtained from parallel flow calculations.

Evaluation of the shear diffusivity from the numerical simulation of a stimulation under high pressure - high flow rate conditions

This second step of the verification procedure is aimed at evaluating the validity of the SBRC approach. We simulate in the same set of networks, an injection along the central well at a high constant rate. This flow rate has been set to $0.015 \text{ m}^3/\text{s}$ to reflect hydraulic tests performed at Soultz site, and the injection is 4 days long. Outer boundaries, namely the four lateral edges of the blocks are open to flow, with a hydrostatic prescribed hydraulic head. It is expected that the corresponding injection pressure increase will generate hydrau-mechanical interactions. To fulfill the Shapiro's requirement of pre-existing fractures in a near-failure regime under hydrostatic conditions, we have to calibrate the Mohr failure criterion. Given the stress tensor, the depth and orientation of all the fractures in the network, this statement can be achieved using a friction coefficient of 0.8 and a cohesion of 0.5 MPa.

At each time step, a pressure field is then calculated and we check at any fracture in the network if the failure criterion is met. In case it is, we save the location of the fracture and the time at which the event occurred. By the end of the 4 days of injection, the area where shear has developed is identified (e.g. figure 6) and we built a diagram reporting for all shearing events, the distance to the source versus the time of occurrence, that is the diagram used by Shapiro et al.(1999) to derive their diffusivity coefficient. Such a diagram is displayed in figure 7 for the injection test in the network. number 2. A parabolic envelope can be fitted that describes the rate of migration of the moving front of the shearing mechanism. From the fitted parameterisation of the parabolic envelope, we derive a diffusive coefficient.

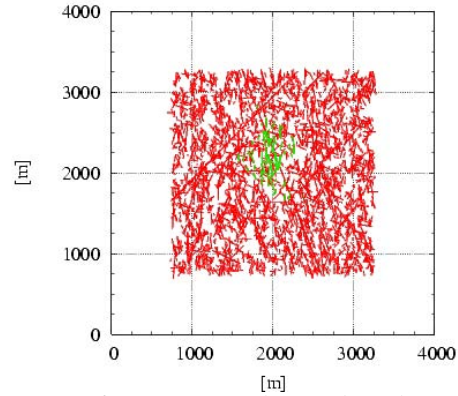


Figure 6. Traces in the median horizontal plane through the rock volume of the sheared fractures (green) superimposed to the traces (red) of the global network of fractures in that plane

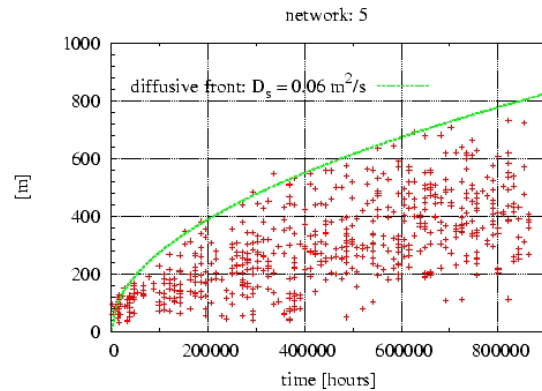


Figure 7. Distance in between the centre of the injection zone and the centre of the sheared elements as a function of time. The envelope has a parabolic shape denoting a diffusive process with a diffusivity coefficient of about $0.06 \text{ m}^2/\text{s}$

Ten different values for this diffusivity coefficient of shear are obtained, ranging in $0.045 \text{ m}^2/\text{s}$ for network 4 toward $0.12 \text{ m}^2/\text{s}$ with network 2.

Looking at the mean value, we obtain by this numerical procedure a diffusivity of $0.065 \text{ m}^2/\text{s}$. Thus the modeled shearing mechanism is migrating through the rock at a rate that compare to the rate of diffusion of a pressure wave. The hydraulic diffusivity was independently characterized in the previous section. and estimated to $D_h = 0.055 \text{ m}^2/\text{s}$.

DISCUSSION AND CONCLUSIONS

This paper presents a direct verification of the validity Shapiro et al. (1999) approach to estimate the hydraulic diffusivity of a fractured system before any hydrau-mechanical perturbation takes place. It is based on a 3D approach for flow in fractured systems

with realistic geometrical characteristics that can be directly translated to those of a real reservoir.

Although the seismic measurements are obtained during a somehow destructive experiment and do not help to characterize the new permeability field within the stimulated zone, the success of the proposed numerical verification is an important step forward for HDR activities. Indeed, it allows us to obtain a quantification of large scale parameters of the area that can be extended to the surrounding zones of the developed reservoirs, without running numerous local, short -and expensive- measurements at low regime and at many places in boreholes, with the remaining problem of averaging or up scaling of the results.

Strong assumptions have been made all along the numerical derivation of the equivalent hydraulic parameters. More detailed analysis including anisotropy or heterogeneity has been undertaken for the understanding of the growth of a seismic cloud. Similarly various options are already available to consider for instance fracture clustering in discrete fracture networks model or correlation in between fracture size and initial fracture transmissivity. Much work is therefore needed to improve the global understanding of the hydraulic significance of a series of microseismic events in such contexts..

A significant progress is however proposed for modeling purposes, since the diffusivity directly obtained from the spatio-temporal analysis of the induced seismicity can be considered as a measure of the hydraulic diffusivity of the rock mass before the pressure perturbation propagates through it. An important observation must be raised. In some cases, the seismicity is recorded only after a given pressure threshold is obtained. Therefore the parameters controlling the failure criterion, i.e. the friction coefficient and the cohesion, must be fitted separately to agree with this observation. Then it is possible to match the shearing migration rate in a synthetic fracture network, by updating (lowering) the permeability distribution assigned to the fracture elements, starting from the precedent case where a proportion of these elements were close to failure. Post failure parameters, like the dilation angle, can be lately calibrated using the change in impedance in the vicinity of stimulated wells.

AKNOWLEDGEMENTS

The research described in this paper was supported by the European Commission DG XII, in the framework of the Non Nuclear Program, and ADEME (French agency for Environment). The author would like to thank Heat Mining GEIE for sharing data and making fruitful suggestions for this study.

REFERENCES

- Baujard, C. and Bruel, D. (2005) Improving a numerical tool and evaluating impact of density changes of injected fluids in the hydraulic behavior of HDR reservoirs. *Proc. Of Stanford Geothermal Workshop*, Stanford, California, January 31-February 2, 2005
- Baumgartner, J., Gérard, A., Baria, R., Jung, R., Tran-Viet, T., Gandy, T., Aquilina, L. and Garnish, J. (1998) Circulating the HDR reservoir at Soultz: maintaining production and injection flow in complete balance. *Proc. of Twenty-third Workshop on Geothermal Reservoir Engineering*, Stanford University, Stanford, California, Jan. 26-28.
- Bruel, D. (2002), Impact of induced thermal stress during circulation tests in an engineered fractured geothermal reservoir. *Oil & Gas Science and Technology - Rev. IFP*, **57**, no. 5, 459-470
- Cornet, F.H., (2000) Comment on 'large scale in situ permeability tensor of rocks from induced microseismicity' by S.A. Shapiro, P. Audigane and J.J. Royer. *Geophysical Journal International*, **140**, 465-469
- Cornet, F.H. and Scotti, O. (1993) Analysis of induced seismicity for fault zone identification. *Int. J. Rock. Mech. Min. Sci. & Abstr.* **30**, n°7, 789-795
- Deflandre, J.P., Laurent, J., Michon, D. and Blondin, E. (1995) Microseismic surveying and repeated VSPs for monitoring an underground gas storage reservoir using permanent geophones. *First Break*, **13**, n°4, 129-138.
- Nagelhout, A.C.G. and Roest, J.P.A. (1997) Investigating fault slip in a model of an underground gas storage facility. *Int. J. Rock. Mech. & Min. Sci.*, **34:3-4**, paper 212.
- Rothert, E., Shapiro, S.A., (2002) Microseismic monitoring of borehole fluid injections: Data modeling and inversion for hydraulic properties of rocks. *Geophysics*, manuscript GEO-2002-024
- Shapiro, S.A., Royer, J. and Audigane, P. (1999), Large scale in situ permeability tensor of rocks from induced microseismicity. *Geophysical Journal International*, **137**, 207-213.
- Shapiro, S.A., Robert, E., Rath, V., Rindschwentner, J., (2002) Characterization of fluid properties of reservoirs using microseismicity. *Geophysics*, **67**, 212-220.

Rejeb, A. and Bruel, D. (2001) Hydromechanical effects of shaft sinking at Sellafield site. *Int. J. Rock of Mech and Min. Sci. & Geom. Abstr*, **38**, 17-29.

Yin, J.M. and Cornet, F.H. (1994) Integrated stress determination by joint inversion o hydraulic tests and focal mechanisms. *Geophysical Research Letter*, **21**, n°24, 2645-2648

Willis-Richards, J., Wanatabe, K. and Takahashi H. (1996) Progress toward a stochastic rock mechanics model of engineered geothermal systems. *J. of Geoph. Research*, **101**, B8, 17481-17496.

THE GENESYS-PROJECT: EXTRACTION OF GEOTHERMAL HEAT FROM TIGHT SEDIMENTS

Reinhard Jung⁽¹⁾, Jens Orzol⁽¹⁾, Reiner Jatho⁽²⁾, Peter Kehrer⁽²⁾, Torsten Tischner⁽²⁾

⁽¹⁾ Leibniz Institute for Applied Geosciences (GGA-Institute), Stilleweg 2, 30655 Hannover, Germany

⁽²⁾ Federal Institute for Geosciences and Natural Resources (BGR), Stilleweg 2, 30655 Hannover, Germany

e-mail: r.jung@gga-hannover.de

ABSTRACT

Massive waterfrac tests have been performed at great depth in the Northern German Basin in order to investigate the possibility of accessing geothermal energy from tight sedimentary rock formations.

The results of these tests and of post-frac hydraulic experiments showed, that a very large tensile fracture was created by injecting about 20,000 m³ of water at flow rates up to 50 l/s. The fracture initiated in a thin sandstone layer clearly propagated upward and downward through the adjacent clay stone layers and reached a total height of at least 150 m. The high storage capacitance of the fracture is indicative of a fracture area up to 5·10⁵ m². The fracture retained a high hydraulic conductivity after pressure relief even though no proppants were used to keep the fractures open.

Micro-seismicity was very low during the tests and did not allow to monitor fracture propagation.

Despite of the large fracture surface area the long term production flow was too low for geothermal application. A cyclic injection-production scheme however showed promising results.

INTRODUCTION

The tight deep seated sedimentary rocks of the Northern German Basin are a huge geothermal resource that could contribute a significant portion of the energy consumption in the northern states of Germany. These sediments are to a major part formed by alternating layers of fine grained sandstones, siltstones and clay stones. Their porosity and permeability is generally low. Accessing heat from these rock formations therefore requires techniques and concepts similar to the techniques and concepts developed for the crystalline basement (Hot-Dry-Rock). Key technology of most of the concepts proposed so far is the waterfrac technique. This technique has been successfully applied in crystalline rock in vari-

ous Hot-Dry-Rock projects worldwide. It has been proofed in these projects that fracture surfaces in the order of several square kilometres can be created or stimulated by massive water injections. Due to a self propping effect these fractures are kept open after pressure relief. The residual hydraulic conductivity of these fractures exceeds the transmissivity of propped fractures created with the “conventional” hydraulic fracturing technique. Production flow rates in the order of 10 – 20 l/s were achieved from single fractures in the Hot-Dry-Rock-Project Soultz at a depth of about 3000 m.

Within the project GeneSys (Generated Geothermal Systems) the GEOZENTRUM Hanover is studying whether the waterfrac technique can also be applied in tight sedimentary rock formations for geothermal energy production. For this purpose several massive waterfrac tests have been performed in an abandoned gas well at about 4000 m depth. Various post-frac experiments were then performed in order to develop and to test concepts for geothermal energy production from a single well. The tests performed during the winter 2003 and in 2004 addressed the following questions:

- Will the fractures, initiated in the sandstone layers be able to propagate through the adjacent clay stone horizons?
- Will self-propping keep the fractures open after pressure release and, will the residual fracture width and transmissivity suffice to provide relevant production rates?
- Will the fractures connect the well to water bearing discontinuities?

TEST SITE AND WELL HORSTBERG Z1

Location and Geology

The well Horstberg Z1 is located some 80 km North-East of Hanover in the centre of the Northern German Basin. It has been drilled into a 15 km long sub vertical fault (Fig. 1), striking NEE-SWW and bounded at each end by a salt dome. The stratigraphy is typical for the Northern German Basin (Fig. 1 and 2). The Middle Bunter (3636 m – 3926 m) including the sub formations Volpriehausen-, Detfurth- and Solling Sandstone was selected as test horizon. The thickness of these sandstone layers ranges from approx. 6 m to 20 m. Their porosity varies from 3% to 11%. Their permeability is unknown but is most likely in the Millidarcy or Submillidarcy range. The only aquifer in the whole sequence of rock formations is the “Kalkarenit” (depth 1150 m to 1250 m). This karstic carbonate cretaceous layer was used for re-injecting the highly saline fluids produced during the post fracturing experiments.

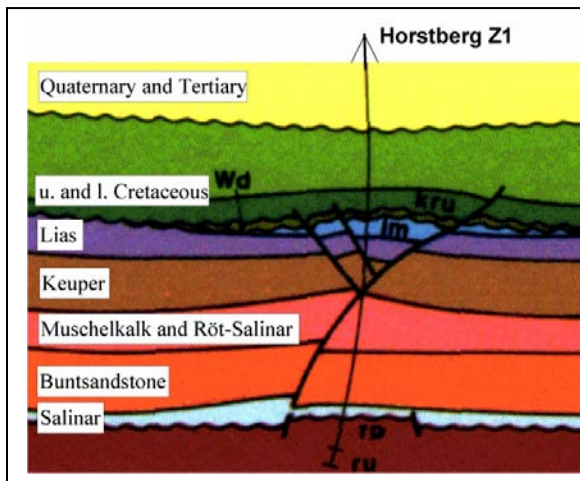


Figure 1. N-S cross-section at the borehole Horstberg Z1. (from Baldschuhn et al., 1991). Buntsandstone: Bunter

Stress Field

For the specific location no definite information on stress directions or magnitudes is known. For the Permian layers an extended data set on stress directions and magnitudes has been established from the activities of the oil and gas industry. Hardly any data are available to constrain the stress field for the Early Triassic formations, which contain the formations of interest. A uniform N-S striking direction of the maximum horizontal stress direction can be assumed for the Permian formation (Röckel & Lempp, 2003).

In the post Permian formations the stress field is influenced by the numerous salt domes and is therefore very variable in magnitude and direction. Generally the minor horizontal principal stress component is often enhanced compared to the Permian formations.

Subsurface Temperatures

Prior to hydraulic testing an undisturbed temperature-depth profile was recorded using the wire line logging equipment of the GGA-Institute. For the final depth, a maximum temperature of 158°C was measured (Fig. 2). This temperature is approximately 30°C above the average temperature for that depth in Germany.

Completion of the well

The completion of the well is typical for a deep gas exploration well in the Northern German basin (Fig. 2). The well is equipped with a 7” casing cemented in from final depth to 2035 m. The high internal yield strength of the casing of 750 bar allows injection operations at high pressures and flow rates. The “Kalkarenit” is accessible via the 9 5/8”– 13 3/8” annulus. Prior to the tests the Permian gas deposits at around 4900 m depth were sealed-off by plugging the borehole back from final depth of 4918 m to 4120 m.

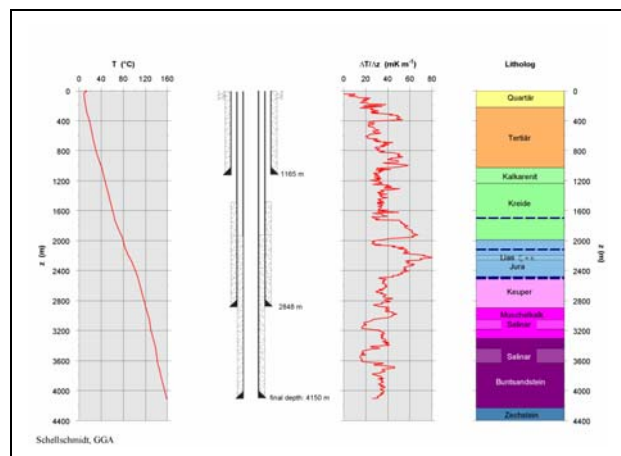


Figure 2. Depth profile of temperature, temperature gradient, stratigraphy and scheme of the well completion of the Horstberg Z1 well.

Test Site

The fully developed well site offered optimal conditions for the hydraulic experiments. A 400 kVA electrical power supply, drinking water supply and telephone line were available. Supply of the huge volumes of fresh water required for the waterfrac tests was secured by the use of shallow irrigation wells. For the waterfrac tests 10 high pressure pumps with

an overall drive power of 4000 kW had been installed at the site (maximum flow rate realized 180 m³/h at 350 bar). For the acquisition of hydraulic data and temperatures, two autonomous systems were operated.

TEST PROGRAM

In 2003 and 2004 an extensive hydraulic test program was performed in several intervals of the borehole (Orzol et al., 2005). In the following text only the tests in the Detfurth Sandstone are described.

Waterfrac tests in the Detfurth Sandstone

Four waterfrac tests were performed in a 6 m thick sandstone layer of this formation after perforating a 4 m long interval in the center of this layer. During the waterfrac-tests a total volume of about 20,000 m³ of water without any additives or proppants were injected at a maximum flowrate of 50 l/s. The records of the first three waterfrac tests are shown in Fig. 3.

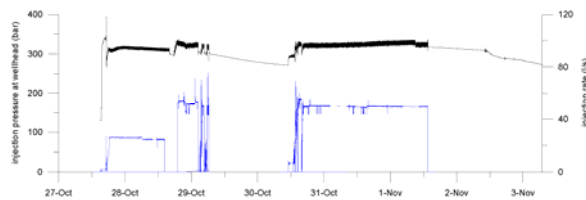


Figure 3: Injection pressure at wellhead (black curve) and injection rate (blue curve) recorded during the first two waterfrac-tests in the Detfurth Sandstone formation.

Fracture initiation in the Detfurth-Sandstone formation occurred unintentionally after perforating due to the shut-in pressure resulting from the preceding waterfrac test in the Volpriehausen-Sandstone (see pressure maximum of 340 bars in Fig. 4). The Pressure dropped rapidly after the start of injection and increased afterwards for about 1 hour as long as the saltwater column in the borehole was replaced by freshwater. The moderate decrease of the wellhead pressure towards the end of the first test is possibly due to the density effect resulting from temperature changes in the borehole. Despite these disturbances one can see that the fracture propagation pressure is almost constant during the first two waterfrac tests. The higher pressure level during the second test compared to the first is possibly caused by the higher friction losses resulting from the increased flow rate. During the third test and the fourth test (not in Fig. 3) a significant increase of the fracture propagation pressure is observed. The same applies to the instantaneous shut-in pressures observed immediately after the stop of injection. The instantaneous shut-in pressure of the four tests increased from 300 bar after

waterfrac test 1 to 303 bar after test 2, to 318 bar after test 3 and to 325 bar after test 4. This remarkable increase of the instantaneous shut-in pressure during the last two tests is possibly caused by the fact that the fracture tip is now migrating into the clay stone layers adjacent to the frac-horizon.

After test 3 and 4 a sharp instantaneous pressure drop was observed followed by very slow pressure decline. This indicates that toward the end of injection the friction pressure losses are restricted to the borehole and its immediate vicinity (perforation or fracture inlet). These friction losses are only about 10 bar for a flow rate of 50 l/s thus indicating that the fracture is well connected to the perforation. The instantaneous pressure drop is followed by a long period with a very slow almost linear pressure decline. During this period the pressure can be regarded as the average fluid pressure within the fracture since the friction losses within the fracture are negligible. The slope of the linear pressure decline which was 0.35 bar/h after the fourth test is therefore a direct measure of the storage capacitance of the fracture if assumptions about the fluid losses from the fracture into the surrounding rock are made. An upper limit for the storage capacitance of the fracture can be determined by assuming that the fluid loss rate at the end of test 4 was equal to the injection flow rate of 50 l/s. With this assumption the storage capacitance of the fracture is determined to $5 \cdot 10^{-5}$ m³/Pa. For a penny shape crack and a Young's Modulus of 40 GPa this corresponds to a fracture surface area of $5 \cdot 10^5$ m².

Postfrac hydraulic tests

Venting test

In order to investigate the transport- and storage properties of the fracture created in the Detfurth sandstone as a function of pressure, an intermittent venting test was performed at the end of the shut-in period of the fourth waterfrac test. During this test the borehole was periodically vented and shut in for 12 hours at a time. This procedure was repeated daily for more than two weeks. In doing so, a total volume of 7,000 m³ of brine was produced from the frac in the Detfurth Sandstone formation and re-injected into the Kalkarenit formation. The test yields the following results:

- Despite a pressure release of more than 100 bar, the frac retains a high hydraulic conductivity (transmissivity). A self-propping mechanism similar to the one assumed for crystalline rock seems to provide an enduring fracture width (Jung & Weidler, 2000).
- Temperatures of the produced fluid exceeded 90°C at the well head a few days after beginning of the test and reached more than 100 °C toward the end of the test.

These observations are important for the further development of extraction of geothermal energy from tight sediments.

Cycle Tests

The positive results from the intermittent production tests drew the attention to another concept that may be practicable for providing geothermal energy. It consists of a cyclic injection of cool water into the frac and production of the water from the frac after a period of heating-up in the fracture. To test the feasibility of the concept, respective tests with daily and weekly cycles were performed in January and February 2004. Planning and accomplishment of the tests, i.e. length of injection, shut-in and production period, fluid volumes injected and produced, obeyed the necessities of a practical operation. For the daily cycle about 400 m³ of water was injected in the hours before midnight and the well was then shut-in for the rest of the night, followed by a 14 h production period during the day.

For the weekly cycle, approximately 2,500 m³ of water were injected at the beginning of the weekend and the well was then shut-in until early Monday morning (Fig. 4). On the following five weekdays, water was produced from the frac for 15 hours per day in the daytime and was re-injected in the Kal-karenit without cooling.

In contrast to the realistic scenario, where water of about 60 °C will be injected in the fracture water with a temperature of 10°C was used. Despite these unfavourable conditions, produced temperatures amounted to 80°C for the daily cycle and more than 90 °C for the weekly cycle. A memory sonde recorded temperatures of approx. 110°C downhole (depth: 3770 m) in the vicinity of the production zone. The average thermal power for the weekly cycle is estimated to approximately 1 MW_{th}.

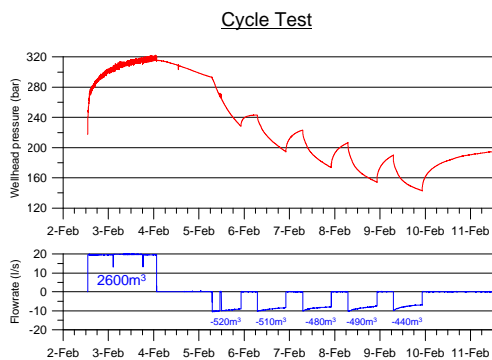


Figure 4. Wellhead pressure (top) and flow rate (bottom) records of the Cyclic Test. Negative flow rate means venting.

The pressure records showed an almost perfect square root of time behaviour during the 4 last shut-in periods of the test. This was interpreted as formation linear flow. Our model assumes that only the stripe of the fracture within the Detfurth Sandstone layer is open and that the fracture in the adjacent clay stone layers is closed at this pressure level. For higher fluid pressure also the part of the fracture in the claystone layer is open (indicated by a linear fluid decline during the first shut-in period). Since the radial flow period was not reached during shut-in, one can only determine the product:

$$A \cdot (s \cdot k / \mu)^{1/2}$$

from the slope of the square-root of time plot (Fig. 5).

With

$\mu = 3 \cdot 10^{-4}$ Pa · s for the viscosity of the fluid
 $k = 10^{-15}$ m² for the permeability of the sandstone
 $s = 10^{-11}$ Pa⁻¹ for the storage coefficient of the sandstone layer

we can determine the fracture area A of the stripe of the fracture in the Detfurth sandstone layer to:

$$A = 2 \cdot 10^4 \text{ m}^2.$$

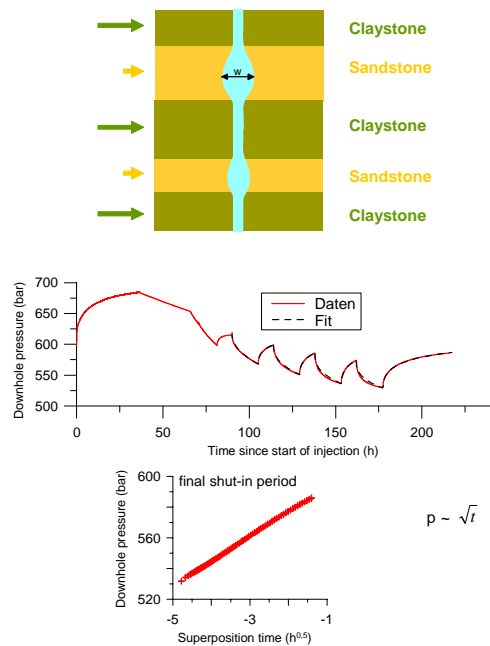


Figure 5. Record and fit of the downhole pressure of the Cycle Test (middle), downhole pressure data of the final shut-in period of this test versus superposition time (bottom) and model scheme (top).

Geophysical Fracture mapping

Several geophysical methods were applied in order to investigate the geometry, size and orientation of the fracture.

Temperature logging

The height of the fracture can be derived from the temperature log shown in Fig. 6. This log was recorded about 9 months after the waterfrac test and still shows a significant impact of the massive injection of cold water. The log indicates that the fracture induced in the 6 m thick Detfurth Sandstone layer propagated almost symmetrical upward and downward. Its vertical extension is at least 150 m. It may be higher at greater distances from the borehole since it is likely that the fracture plane deviates from the borehole axis, which has an inclination of about 11° at this depth. The question why the temperature minimum has been preserved over such a long time period is still open.

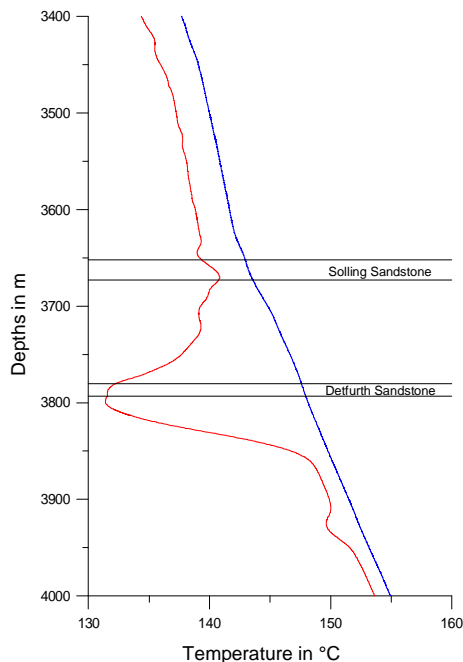


Figure 6. Temperature logs performed before (right) and 9 months after (left) the massive waterfrac tests in the Detfurth Sandstone.

Monitoring of Microseismicity

To monitor microseismicity induced during stimulations (Phillips et al., 2002), a seismic network was installed. It consists of eight stations installed on two circles with a radius of 800 m and 1600 m respectively, centred on the well position at depth and a

surface array of 60 geophones (Buness and Druivenga, 2004). At each of the stations, an about 100 m deep well was drilled and 3-component 4.5 Hz geophones were installed at the bottom of these wells. Additionally a 3-component 1 Hz seismometer was placed at each station. Data acquisition was secured by EDL and PDAS systems operating at 500 Hz and 200 Hz sampling rate respectively. A velocity model for the region around the well was calibrated using the seismic signals that evolved from the ignition of the perforator guns.

Using the energy of the explosives and assuming a seismic efficiency between 0.01 and 0.001 the detection level M_L of the seismic network was estimated to about $-0.5 < M_L < 0$ (M_L : Magnitude).

In contrast to water frac tests in crystalline rock, where several thousands or tens of thousands microseismic events were detected and located with geophones of comparable sensitivity (e.g. Audigane et al., 2002) only 11 events were detected. A reliable source location could not be inferred for any of these events.

The lower level of micro seismicity in the sediments compared to granite may be explained by the fact that the sandstones and clay stones are less brittle than granite or by the fact that the principal stress components at our site are very similar so that the shear stresses and accordingly the stress drop resulting from rupture are very low.

Monitoring of Self-Potential

Before, during and after the stimulation tests the electric self potential was continuously monitored in order to investigate whether the fluid injection has an effect on the self potential measured at the surface. A correlation between fluid injection in a deep well and changes of the self potential has been observed by Marquis et al. (2002) for stimulation operations at the European HDR test site Soultz-sous-Forêts, France.

In the vicinity of the Horstberg site, 49 copper-copper-sulphate sondes were installed on two perpendicular profiles with a spacing of 100 m.

There was no obvious impact of the water injections in any of the records of the self potential. Nevertheless a more detailed analysis of the data is underway (Grinat et al., 2004).

Monitoring of Surface-Deformation

For the monitoring of deformations caused by frac operations tiltmeters are routinely used by the oil and gas-industry (Poe and Economides, 2000). An array of wells in the vicinity of the treated well is required to install the tiltmeters, however.

As an alternative, the use of high sensitive tiltmeters installed near the surface has been investigated as a method to monitor deformation induced by the fracture propagation (Wood, 1979). At the Horstberg test site four tilt meters were installed near the surface (3 m depth) on a profile, perpendicular to the expected

direction of fracture propagation. There was no obvious impact of the massive waterfrac tests in the Detfurth Sandstone. Only during a series of smaller waterfrac tests in the deeper Volpriehausen Sandstone the tiltmeter records show some correlation to the water injection periods.

CONCLUSION AND OUTLOOK

The results of the experiments in the borehole Horstberg Z1 have proved that a very large tensile fracture (up to $5 \cdot 10^5 \text{ m}^2$) could be created in tight sedimentary rock by massive water injections. The fracture migrated upward and downward through thick clay stone layers adjacent to the sandstone horizon where the fracture was initiated. Although no proppants were used the fracture retained a high hydraulic conductivity after pressure relief at least within that sandstone layer. Despite of the large fracture plane the long term fluid production of the well was too low for geothermal application. A cyclic injection-production scheme however showed positive results and is a promising option for accessing heat from tight sediments.

REFERENCES

- Audigane, P., Royer J. J. & Kaieda, H.: Permeability characterization of the Soultz and Ogachi large-scale reservoir using induced seismicity, in Seismic signatures of fluid transport, *Geophysics*, 67,1, p. 204-211, Society of Exploration Geophysicists, 2002
- Baldschuhn, R. Binot, F., Fleig, S., Kockel, F., Best, G., Brückner-Röhling, S., Deneke, E., Frisch, U., Hoffmann, N., Jürgens, U., Tectonic atlas of Northwest Germany and the German North Sea Sector: Structures, Structural Development and Paleogeography, *Geologisches Jahrbuch*, Reihe A, 153, pp. 3-95, 2001
- Buness, H. & Druivenga, G.: Aufbau eines Messnetzes zur Beobachtung induzierter mikroseismischer Ereignisse, 64. Jahrestagung der Deutschen Geophysikalischen Gesellschaft, Berlin, SOP37, pp. 544-545, 2004
- Grinat, M., Sauer, J. & Stüdekum, W.: Ein Eigenpotential-Experiment zum Nachweis von Fluid-Injektion im Rahmen des GeneSys-Projektes, 64. Jahrestagung der Deutschen Geophysikalischen Gesellschaft, Berlin, GE05, pp. 264-265, 2004
- Jung, R. & Weidler, R.: A conceptual model for the stimulation process of the HDR-system at Soultz, *Geothermal Council Transactions*, Vol. 24, September, pp. 143-147, 2000
- Marquis, G., Darnet, M., Sailhac, P. & Singh, A. K.: Surface electric variations induced by deep hydraulic stimulation: An example from the Soultz HDR site, *Geophysical Research Letters*, Vol.29, 2002
- Marquis, G., Darnet, M., Sailhac, P. & Singh, A. K.: Surface electric variations induced by deep hydraulic stimulation: An example from the Soultz HDR site, *Geophysical Research Letters*, Vol.29, 2002
- Orzol, J., Jung, R., Jatho, R., Tischner, T., Kehrer, P.: The GeneSys-Project: Extraction of Geothermal Heat From Tight Sediments.- Proc. WGC, Antalia Turkey, in press, 2005
- Phillips, W. S., Rutledge, J. T., House, L. S. & Fehler, M. C.: Induced Microearthquake Patterns in Hydrocarbon and Geothermal Reservoirs: Six Case Studies.- *Pure & App. Geoph.*, Vol. 159, no. 1-3, 345-369, Birkhäuser Verlag, Basel, 2002
- Poe, B. D. & Economides, M. E.: Post-Treatment Evaluation and Fractured Well Performance, in Economides, M.E. und Nolte, K.G.(ed.), Reservoir Stimulation, John Wiley and Sons, 2000
- Röckel, Th. & Lempp, Chr.: *Erdöl, Erdgas, Kohle*, 119(2), 73-80, 2003
- Wood, M. D.: Monitoring massive fracture growth at 2-km depths using surface tiltmeter arrays, *Tectonophysics*, Vol. 52, Iss. 1-4, p. 643, 1979

STIMULATION TECHNIQUES USED IN ENHANCED GEOTHERMAL SYSTEMS: PERSPECTIVES FROM GEOMECHANICS AND ROCK PHYSICS

Stephen L. Karner

Idaho National Laboratory
PO Box 1625, Mailstop 2107
Idaho Falls, ID, 83415
e-mail: karnsl@inel.gov

ABSTRACT

Understanding the processes that enhance fluid flow in crustal rocks is a key step towards extracting sustainable thermal energy from the Earth. To achieve this, geoscientists need to identify the fundamental parameters that govern how rocks respond to stimulation techniques, as well as the factors that control the evolution of permeability networks. These parameters must be assessed over a variety of spatial scales: from microscopic rock properties (such as petrologic, mechanical, and diagenetic characteristics) to macroscopic crustal behavior (such as tectonic and hydro-dynamic properties). Furthermore, these factors must be suitably monitored and/or characterized over a range of temporal scales before the evolutionary behavior of geothermal fields can be properly assessed. I am reviewing the procedures currently employed for reservoir stimulation of geothermal fields. The techniques are analyzed in the context of the petrophysical characteristics of reservoir lithologies, studies of wellbore data, and research on regional crustal properties. I determine common features of geothermal fields that can be correlated to spatio-temporal evolution of reservoirs, with particular attention to geomechanics and petrophysical properties. The study of these correlations can then help guide procedures employed when targeting new prospective geothermal resources.

INTRODUCTION

For thousands of years humans have utilized the naturally heated waters of the Earth. While ancient civilizations recognized the therapeutic value of thermal spas, our modern society has realized the potential of these geothermal fluids as a source of energy. To date, research and development activities for geothermal energy have concentrated on geologic terrains having high heat flow (typically associated with a shallow heat source) and fluid-saturated reservoirs having adequate storage capacity and permeability. At issue here is the observation that such conditions are not universally available, thereby

restricting the growth of geothermal energy as a commodity. With the advance of technologies and an increased reliance on electrical power, geothermal activities will inevitably seek energy from a range of geologic terrains where heat sources may be cooler, reservoirs are tapped at deeper subsurface levels, or where percolating fluids are absent. To this end, the techniques and concepts employed for enhanced geothermal systems (EGS) are designed to increase the amount of thermal energy extracted from the Earth. The knowledge gained from EGS work may be useful for prospecting new geothermal resources.

I am reviewing results from various EGS sites to assess the universality and relative success of geothermal reservoir stimulation procedures. I then consider the commonalities of current EGS activities and highlight those geomechanical and petrophysical aspects that have relevance to enhanced stimulation of geothermal systems.

SUMMARY OF EGS SITES

In Table 1 I summarize details for a number of geothermal fields for which EGS activities have been tested. For each field, the summary indicates the approximate location, tectonic and/or structural aspects, thermal characteristics, reservoir lithology, and type of EGS research activity.

The chief objective of EGS procedures is to extract thermal energy from existing fields that contain areas of low productivity, or from new geothermal fields that have low capacity for energy production. While this description may include areas of comparatively low geothermal gradient, current research is primarily directed at prospects displaying high temperatures in relatively impermeable rocks (note the lithologies described in Table 1). In such cases it is necessary to improve or create a permeability network with a fluid-rock surface area large enough to efficiently extract the thermal energy. To date, this has largely been achieved by using hydraulic fracturing techniques to stimulate the thermal reservoir (note the stimulation techniques in Table 1).

Geothermal field	Location	Approx. Latitude / Longitude	Thermal reservoir (lithology)	Tectonics & structural elements	Depth to thermal reservoir	Temperature of thermal reservoir	Potential power output	EGS activity	Ref.
Cooper Basin (Habanero)	Approximately 8km SSE of Innamincka, South Australia	27.85 S 140.72 E	Carboniferous granitic intrusives	Permo-triassic basin; intra-cratonic region with evidence for Carboniferous compression	3700 to 4900m	In excess of 240 °C	37 wells to produce an estimated 275 MWe	Hydraulic stimulation of sub-horizontal joints and fractures	1, 2
Coso Geothermal Field	California, USA (Naval Weapons Air Station near China Lake, CA); ~161 km N of Los Angeles, CA	36.00 N 117.75W	Complex, interfingering sequence of Mesozoic diorite, granodiorite, and granite	Situated in major volcanic area with 38 rhyolite domes and abundant basalts; transition between regions of strike-slip and extension.	less than 3000 m	In excess of 300 °C at depths less than 3000 m	240 MWe	Hydraulic fracturing of existing reservoir	3, 4, 5
Desert Peak	Nevada, USA; ENE of Reno, NV	39.76 N 118.92 W	Fault dissected, tertiary volcanics & sedimentary rocks that overlie Mesozoic metamorphics	Humboldt Structural zone (extensional normal faults, strike-slip transfer faults)	762 to 1280 m	~200 °C	9.9 MWe (year 2000)	Hydraulic stimulation	6, 7
Geysers Geothermal Field	California, USA (south of Clear Lake, CA); ~193 km N of San Francisco, CA	38.8 N, 122.8 W	Steam reservoir rocks are typically massive greywacke turbidites of the Mesozoic Franciscan Fm. Underlain by a 2.4-0.9 Ma silicic batholith (felsite).	Fault-bounded, quasi-extensional region; fractures in greywacke are randomly oriented & sub-horizontal, while in the felsite are oriented NW and are near vertical.	60 to ~3000 m	~40 °C at shallow depths to greater than 240 °C in the deepest wells	2043 MWe cumulative installed gross capacity in 1989	Recharge reservoir at depths between 2134-3048 meters.	8,9,10
Hijiori, Japan	south edge of the inner Hijiori caldera, Okura Village in Yamagata Prefecture	38.60N 140.18E	Granodiorite	Max. compressive stress direction is E-W; tectonic regimes are strike-slip and normal faulting	upper reservoir at 1800m; lower at 2200m	~250-270 °C		Hydraulic fracturing and stimulation	11, 12
Larderello, Italy	A few km W of Larderello, Tuscany, Italy	43.25N 10.87E	Upper reservoir has anhydrites and dolomitic limestones; quartzites and phyllites in lower reservoir	Structural high; series of nappes with predominant ENE vergence.	~4 km	>400 °C	547 MWe in 1999	Recharge of reservoir by reinjection	13
Rosemanowes Quarry, UK	near Penryn, Cornwall, UK	50.15N 5.1W	Late Carboniferous to early Permian Carnmenellis Granite	No major faults outcrop at Earth surface; sub-horizontal joints near Earth surface; two main sub-vertical joint sets at depth (NE-SW, NW-SE)	Initial borehole depths to 300m; subsequent depths to 2000m	80 °C at 2000m (average geothermal gradient of 35 °C/km)	Not established for power generation	Hydraulic stimulation; explosive stimulation	14, 15
Soultz-sous-Forêts, France	~ 50 km north of Strasbourg, Alsace	48.93N 7.88W	Granites	Local horst structure within the extensional tectonics of the Rhine Graben	3500 to 5000 m	150 °C to more than 200 °C	6 MWe (year 2005)	Hydraulic fracturing and stimulation	16, 17

Table 1. Summary details for geothermal fields identified as EGS sites. Cited sources are as follows (full details are in the reference section): 1 - Chopra & Wyborn (2003); 2 - Asanuma et al. (2004); 3 - Kovac et al. (2004); 4 - Wannamaker et al. (2004); 5 - Adams et al. (2000); 6 - Faulds et al. (2002); 7 - Tiangco et al. (2004); 8 - Koenig (1992); 9 - Walters & Combs (1992); 10 - Thompson & Gunderson (1992); 11 - Yamaguchi et al. (2000); 12 - Oikawa & Yamaguchi (2000); 13 - Cappetti et al. (1995); 14 - Tenzer (2001); 15 - Parker (1999); 16 - Genter et al. (2000); 17 - Durst & Vuataz (2000)

With the exception of EGS sites at The Geysers and Larderello, the reservoir lithologies currently exploited are mainly crystalline, igneous rocks that inherit little porosity or permeability during their formation. Whatever porosity and/or permeability these rocks do have typically stems from post-emplacement deformation (perhaps by contraction during cooling or via tectonic forces). I also note that a majority of EGS sites are located in areas that have experienced at least one episode of tectonism. The

imprint of such regional deformation takes the form of fractures and metamorphic features – and it is these fabrics that are exploited by EGS stimulation.

Thus, a clear pattern emerges from the analysis of current EGS research inasmuch as the activities are restricted to hydraulic stimulation of low permeability rocks in areas that are, or once were, tectonically active. To properly assess the efficiency of stimulation procedures it is necessary to consider

petrophysical properties of the reservoir, the influence of the present-day regional stress field, the interaction with pre-existing rock fabric, and the spatio-temporal evolution of the permeability network. While I am presently analyzing these details for several EGS sites, I review here some key geomechanical and petrophysical aspects that can be applied to the many of the existing EGS fields.

MECHANICAL CONSIDERATIONS

A fundamental observation from early EGS projects such as Fenton Hill (e.g. Brown, 1995) was that the formation of hydraulically induced fracture networks can be influenced by the regional and/or local stress field, pre-existing fabric (e.g. fractures, foliation), and rock properties. While the geometry of the induced fracture network can be adequately monitored via seismic techniques (e.g. Asanuma et al., 2004), proper modeling of the fracture network generation requires that these various mechanical factors be considered.

Regional Tectonics

Intuitively, the character of the regional stress field can determine the orientation of newly generated fractures. If we assume an Andersonian stress state (with one principal compression stress axis normal to Earth's surface) then compressive, strike-slip, and extensional tectonic regimes develop when the vertical stress (σ_v) is the least (σ_3), intermediate (σ_2), and greatest (σ_1) principal stress, respectively (Jaeger and Cook, 1979; Sibson, 1983). For rock failure via tensional strain mechanisms, simple models indicate that newly generated opening type fractures (Mode I) form approximately perpendicular to the minimum compressive stress, σ_3 (Jaeger and Cook, 1979). Thus, hydraulically induced cracks would be sub-horizontal (i.e. normal to the σ_v) in compressive regions and they would be near vertical (i.e. normal to the minimum horizontal stress, σ_h) in either extensional or strike-slip tectonic regions.

In addition to lateral variations of tectonic stresses, studies of seismic focal mechanisms indicate that stress conditions can vary systematically with depth (e.g. Vetter and Ryall, 1983; Iio, 1996; Bokelman and Beroza, 2000). Such observations can be conceptualized by simple models that incorporate Andersonian mechanics (e.g. Figure 1) by assuming that vertical stress varies linearly with burial depth and that the region is subjected to a uniform horizontal stress field (with maximum, σ_H , and minimum, σ_h , horizontal stresses unequal). This simplified model illustrates that vertical stress can act as either the minimum, intermediate, or greatest compressive stress as depth varies (Figure 1). These systematic variations in tectonic style as a function of depth would be reflected by the various deformation

indicators (e.g. seismic focal mechanisms, borehole breakouts) – as can be noted by the transition from reverse to strike-slip to normal faulting in Figure 1). Furthermore, the orientations of hydraulically created fractures would also vary with depth because these cracks are typically generated normal to the least compressive stress direction (i.e. the seismic T-axis). For the conditions shown in Figure 1, fracture orientations would transition from sub-horizontal at shallow depths to near vertical at deeper levels.

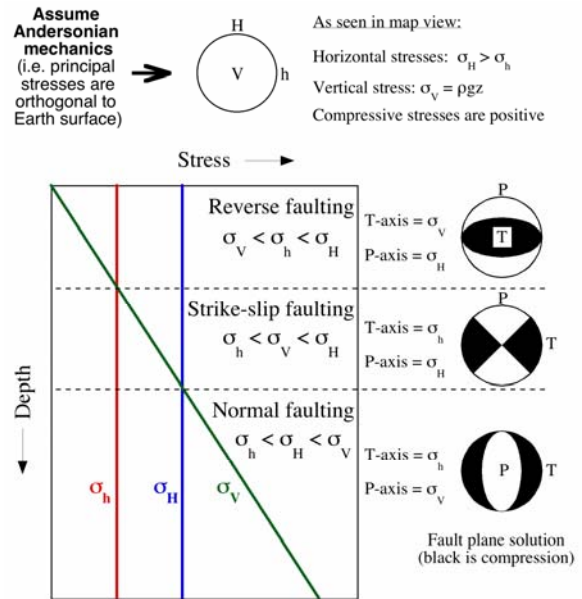


Figure 1. Conceptual model showing the variation of deformation style with burial depth, assuming an Andersonian stress field where only the vertical stress varies with depth. Faulting style transitions from being reverse near the surface, to strike-slip at intermediate depths, and normal faulting at deeper levels. These transitions would be observable from seismic focal mechanisms (with the tensile, T, and compressive, P, axes as shown).

It is important to note that estimates of horizontal stress from geologic data (e.g. Zoback and Zoback, 1980), borehole observations (e.g. Abou-Sayed et al., 1978; Zoback and Zoback, 1980; Zoback et al., 1980; Warpinski et al., 1985; Klee and Rummel, 1993) and seismic data (e.g. Zoback and Zoback, 1980; Sbar, 1982; Vetter and Ryall, 1983; Iio, 1996; Hardebeck and Michael, 2004) exhibit lateral and vertical variations that are more complex than simple models predict (e.g. Figure 1). Thus, studies of 3-D regional stress fields will have strong site-specific aspects. The differences between localities may be attributed to tectonic and burial forces. However, it is important to recall that other factors can significantly alter the stress field – such as crustal thickness, geothermal gradient, style and abundance of damage features, and rock properties (to name a few).

Pre-existing rock fabric

When coupled with Mohr-Coulomb theory, the Andersonian view of brittle deformation in the crust can describe many geologic problems. Yet, several observations indicate the limitations of this simplified view – such as the roles of pore fluids (e.g. Hubbert and Rubey, 1959), stress rotation (e.g. Scholz, 1992), and pre-existing fractures (e.g. Angellier, 1984).

The influence of pore fluid pressure and pre-existing fractures can be understood using a schematic representation of Mohr-Coulomb fracture mechanics (Figure 2). The key to the analysis lies in the fact that while fluids can support compressional forces they cannot support shear tractions. An increase in fluid pressure lowers effective normal stress and does not change shear stress (note the lateral shift in the Mohr circle in Figure 2). The resulting stress state may exceed the material strength and induce failure (e.g. Terzaghi, 1925) and it is this principle that is exploited during hydraulic fracturing of rocks.

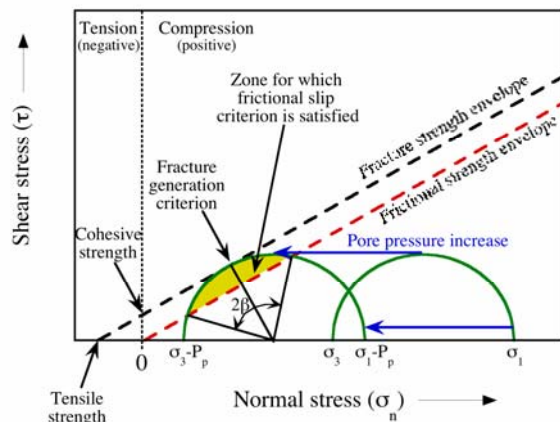


Figure 2. Schematic of Mohr-Coulomb behavior illustrating the role of pore fluid pressure together with a comparison of fracture and frictional strength. Pore fluid pressure acts to reduce effective normal stress. Cracks oriented within the angular range indicated by 2β will fail in preference to creation of a new fracture.

Another important aspect relating to material strength is that of pre-existing fractures (Figure 2). The key here is that cracks exhibit lower frictional strengths than the fracture strength that originally created them. With larger pore pressure, the Mohr circle translates towards the failure envelopes. If a fracture is ideally oriented for failure, then deformation occurs when the stress state satisfies the frictional failure criterion. As Figure 2 shows, the fracture criterion can only be satisfied when pre-existing cracks have orientations that are not optimal for frictional slip to occur.

Intuitively, the frictional and fracture envelopes shown in Figure 2 reflect distinctly different strength

characteristics. Therefore, cracks in a rock mass may be responsible for anisotropy of material strength. It is important to note here that strength anisotropy can be induced by other factors, such as lithologic variations, sedimentary bedding, foliation, diagenesis (to name a few). Hence, in using the Mohr-Coulomb analysis of rock failure (Figure 2) we should also consider the influence of pre-existing rock fabric.

Rock properties

Results from laboratory deformation experiments show large variations in rock strength depending on the conditions studied. It can generally be concluded that the strength of a rock will change systematically as certain parameters are varied. For example, the compressive strength of a given rock typically increases with the applied confining pressure (e.g. Griggs, 1936; also shown schematically in Figure 2), typically decreases with the presence of water (e.g. Raleigh and Paterson, 1965; Griggs, 1967), and typically increases with increasing strain rate (e.g. Paterson, 1978). However, it is important to recognize that these generalizations are not universal and that other parameters do not systematically influence rock strength (e.g. compositional variations, diagenetic reactions). Yet, the systematics that are observed from laboratory tests can be readily applied to the study of geothermal systems.

Extensional strain tests on necked rock samples have particular relevance to stress orientations estimated from hydraulically-induced fractures. Ramsey and Chester (2004) performed room temperature, room humidity extension experiments on necked (dogbone) samples of Carrara Marble. They explored failure characteristics for a range of confining pressures and observed a systematic change in fracture style and material strength (Figure 3). At low confining pressures, samples failed under extensional stress conditions with tensile strengths compatible with those of previous studies. The through-going fractures associated with sample failure display orientations that are nearly normal to the direction of the minimum stress. At high confining pressures, samples failed with compressive minimum stresses and the extensional fractures form at low angles ($<20^\circ$) to the minimum stress direction. Further, the high confining pressure fractures have displacements and surface morphologies consistent with opening mode shear fractures. Similar results have been reported for Berea Sandstone (Bobich et al., 2004), indicating that these trends may be observed for a variety of rock types. Measurements of rock properties at a variety of conditions are fundamental for applied research and modeling of geothermal systems. Observations such as those of Ramsey and Chester (2004) and Bobich et al (2004) are particularly relevant for exploration of geothermal resources situated at large depths.

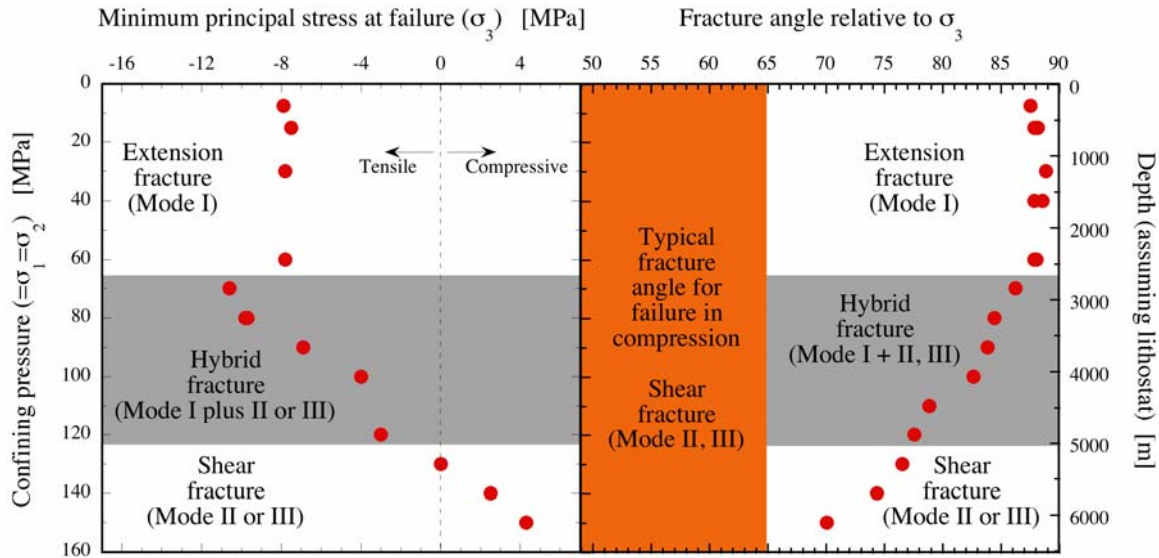


Figure 3. Results from failure experiments on necked (dog-bone) samples of Cararra Marble (modified from Ramsey and Chester, 2004). For all experiments, samples were subjected to tensile strain leading to failure. The minimum compressive stress at failure transitions from tensile to compressive as a function of increasing confining pressure (or depth - assuming a lithostatic gradient of ~ 24.5 MPa/km). The observed fracture orientation relative to σ_3 systematically decreases with increasing confining pressure. Similar results have been reported from identical tests on Berea Sandstone (Bobich et al., 2004).

Their results also highlight the hazards of applying the common assumption that rock properties are single-valued and static constants. Thus, we must also consider that these properties could vary with a number of factors – such as physical conditions, chemical environment, and time.

TEMPORAL EVOLUTION OF FRACTURES

Concern over fractures in geothermal systems does not end with the successful generation of an interconnected network. When hydraulic stimulation involves pre-existing fractures, an anisotropic stress field, or certain rock properties, the stimulated fractures may experience some portion of the total deformation in the form of shear displacement. The shearing may be contemporaneous with the stimulation process itself, but will likely include a protracted stage of creep following stimulation. Also, as the stimulation and/or production fluids are transmitted through the fracture network they may enter into chemical reactions with the fracture walls. The reaction kinetics and fluid solubilities will control temporal evolution of diagenetic reactions. Such time-dependent deformation and/or diagenetic reactions can influence the temporal evolution of strength and permeability of the fracture network.

Mechanical evolution

Let us consider the mechanical evolution of a hydraulically-induced fracture after it has been generated. Initially, the fracture is held open by the force of the pressurized fluid. With even a small

drop of fluid pressure, the stresses within the Earth will act to close the fracture aperture. If closure does not result in perfect mating of opposite sides of the fracture, any rough asperities on the fracture walls will impinge on each other and support part of the normal load. From a mechanical perspective, the material that comprises these asperities will deform over time thereby increasing the real area of contact between the fracture walls. The closure of the fracture and subsequent increase in contact area will not only lower porosity and permeability, but will also increase the cohesive strength of the fracture.

The time-dependent strengthening (or aging) of a fracture is exemplified by results from frictional slide-hold-slide experiments on shear zones that may or may not contain wear material (Figure 4; for a review see Marone, 1998). In these tests, shear zones are deformed at a constant sliding rate (slide) with episodic intervals for which the imposed loading rate is set to zero (hold). During the hold interval, the shear zone supports a residual shear stress that decays exponentially with time due to frictional creep (Figure 4a). On reloading after a hold (slide), the frictional resistance increases to a peak value and subsequently approaches the steady-state sliding value. As the reloading peak is considered to be a measure of static friction levels, then the difference between the peak friction and the steady-state sliding friction level provides a measure of restrengthening. Laboratory slide-hold-slide tests consistently show that frictional strength increases logarithmically with stationary hold time (Figure 4b). For bare sliding

surfaces (with no wear material, or gouge), the time-dependent restrengthening is associated with growth of asperity contacts and an increase in adhesion (e.g. Bowden & Tabor, 1954, 1964). When sand layers are sheared (simulating gouge), the restrengthening is associated with compaction (or densification) of the layer (Figure 4c, consistent with the notion that frictional restrengthening is due to time-dependent increase in real area of contact (e.g. Dieterich, 1972).

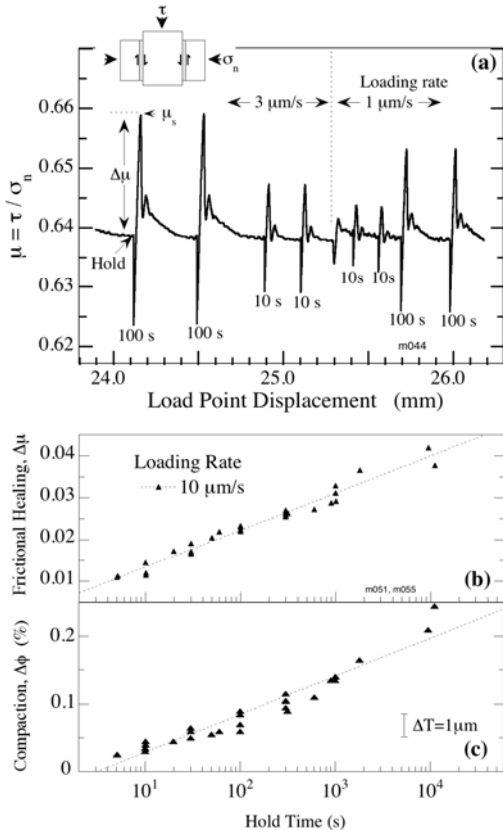


Figure 4. Results from slide-hold-slide shear tests in quartz sand (modified from Karner and Marone, 1998). Holds start when loading rate is to zero. In holds, stress-relaxation occurs (Figure 4a) with compaction of the layer (Figure 4c). Friction restrengthening occurs on reloading ($\Delta\mu$; Figure 4a) and this scales with the logarithm of hold time (Figure 4b).

Geochemical evolution

While fractures can obtain greater adhesion (hence, strength) via mechanical deformation of contacting asperities, fracture strength can also be influenced by pressure solution of contacting asperities or by diagenetic precipitation of cements bonding fracture walls (e.g. Karner et al., 1997; Tenthorey et al., 2003). Further, the permeability of porous media has been observed to vary as hydrothermal diagenesis proceeds (e.g. Karner and Schreiber, 1993, Tenthorey et al., 2003). This is because geochemical reactions are inherently rate-dependent.

At low temperatures (less than $\sim 400^\circ\text{C}$), the strength of aqueous silicate-bearing shear zones (i.e. quartz, feldspar) generally increases with longer reaction time (e.g. Karner et al., 1997) while the permeability typically decreases (e.g. Tenthorey et al., 2003). At high temperatures (greater than $\sim 400^\circ\text{C}$), silicate shear zones may show little to no time evolution in strength (e.g. Karner et al., 1997) and permeability reduction may be enhanced. However, it is important to note that these generalizations may not be universal. For example, common by-products from low temperature diagenesis are clays – which have been shown to dramatically reduce frictional strength of shear zones (e.g. Marone, 1998). Thus, the temporal evolution of strength, porosity, and permeability of fractures in geothermal systems will likely be determined by a variety of site-specific properties (e.g. physico-chemical environment, lithology and/or mineralogy, fluid composition).

CONCLUSIONS

I have researched several existing EGS sites to analyze reservoir stimulation procedures. To date, stimulation activities have primarily focused on hydraulically creating or enhancing a permeable network of fractures in low porosity/permeability reservoir rocks (typically crystalline) – many of which are imprinted by past episodes of tectonic deformation. With this in mind, I have described various mechanical and geochemical issues that must be considered when establishing geothermal fields. A better understanding of the generation and temporal evolution of geothermal reservoirs can be achieved when these aspects are coupled with results from remote sensing techniques (e.g. monitoring micro-seismicity, electrical conductivity, fluid geochemistry). With such knowledge in hand, the success of hydraulic fracturing can be adequately evaluated compared to predicted successes of alternate stimulation practices (e.g. explosives, high-energy gas gun, acid-treatment).

ACKNOWLEDGEMENTS

This work was supported by the U.S. Department of Energy, Assistant Secretary for Energy Efficiency and Renewable Energy, Office of Geothermal Technology, under DOE Idaho Operations Office Contract DE-AC07-99ID13727, whose support is gratefully acknowledged. I thank Joel Renner, Mike Shook, Kit Bloomfield, Gopi Nalla and Jen Bobich for their discussions and input for this paper.

REFERENCES

Abou-Sayed, A.S., C.E. Brechtel, and R.J. Clifton (1978), “In-situ stress determination by hydrofracturing: A fracture mechanics approach”, *Journal of Geophysical Research*, **83**, 2851-2862.

- Adams, M.C., J.N. Moore, S. Bjornstad, and D.I. Norman (2000), "Geologic history of the Coso geothermal system", *Proceedings World Geothermal Congress*, Kyushu-Tohoku, Japan, 2463-2469.
- Angelier, J. (1984), "Tectonic analysis of fault slip data sets", *Journal of Geophysical Research*, **89**, 5835-5848.
- Asanuma, H., Y. Kumano, T. Izumi, N. Soma, H. Kaieda, Y. Aoyagi, K. Tezuka, D. Wyborn, and H. Niitsuma (2004), "Microseismic monitoring of a stimulation of HDR reservoir at Cooper Basin, Australia by the Japanese team", *Transactions Geothermal Resources Council*, **28**, 191-195.
- Bobich, J.K., F.M. Chester, and J.S. Chester (2004), "Experimental Analysis of Hybrid Fracture in Berea Sands", *Eos Transactions AGU*, **85** (47), Fall Meeting Supplement, Abstract T41F-1297.
- Bokelmann, G. H. R., and G. C. Beroza (2000), "Depth-dependent earthquake focal mechanism orientation evidence for a weak zone in the lower crust", *Journal of Geophysical Research*, **105**, 21683-21695.
- Bowden, F. P., and D. Tabor (1954, 1964), "The Friction and Lubrication of Solids", Parts I, II. Oxford University Press, London.
- Brown, D. (1995), "The US Hot Dry Rock Program - 20 Years of Experience in Reservoir Testing", *Proceedings World Geothermal Congress, Florence, Italy*, **4**, 2607-2611.
- Capetti, G., L. Parisi, A. Ridolfi, and G. Stefani (1995), Fifteen years of reinjection in the Larderello-Valle Secolo area: Analysis of the production data", *Proceedings World Geothermal Congress, Florence Italy*, **3**, 1997-2000.
- Chopra, P. and D. Wyborn (2003), "Australia's first hot dry rock geothermal energy extraction project is up and running in granite beneath the Cooper Basin, NE South Australia", IN: P. Blevin, M. Jones & B. Chappell editors, *Magma to Mineralisation: The Ishihara Symposium, Geoscience Australia*, Record 2003/14, 43-45.
- Dieterich, J.H. (1972), "Time-dependent friction in rocks", *Journal of Geophysical Research*, **77**, 3691-3697.
- Durst, P. and F-D. Vuataz (2000), "Fluid-rock interactions in hot dry rock reservoirs: A review of the HDR sites and detailed investigations of the Soultz-sous-Forêts system", *Proceedings World Geothermal Congress, Kyushu-Tohoku, Japan*: 3677-3682.
- Faulds, J., L. Garside, G. Johnson, J. Muehlberg, and G. Oppliger (2002), "Geologic Setting and Preliminary Analysis of the Desert Peak-Brady Geothermal Field, Western Nevada", *Transactions Geothermal Resources Council*, **26**, 491-494.
- Genter, A., H. Traineau, B. Ledésert, B. Bourguine, and S. Gentier (2000), "Over 10 years of geological investigations within the HDR Soultz project, France", *Proceedings World Geothermal Congress, Kyushu-Tohoku, Japan*: 3707-3712.
- Griggs, D.T. (1936), "Deformation of rocks under high confining pressures", *Journal of Geology*, **44**, 541-577.
- Griggs, D.T. (1967), "Hydrolytic weakening of quartz and other silicates", *Geophysical Journal of the Royal Astronomical Society*, **14**, 19-31.
- Hardebeck, J.L. and A.J. Michael (2004), "Stress orientations at intermediate angles to the San Andreas Fault, California", *Journal of Geophysical Research*, **109**, Art. No. B11303.
- Hubbert, M.K. and W.W. Rubey (1959), "Role of fluid pressure in mechanics of overthrust faulting: 1. Mechanics of fluid-filled porous solids and its application to overthrust faulting", *Geological Society of America Bulletin*, **70**, 115-166.
- Iio, Y. (1996), "Depth-dependent change in the focal mechanism of shallow earthquakes: Implications for brittle-plastic transition in a seismogenic region", *Journal of Geophysical Research*, **101**, 11209-11216.
- Jaeger, J.C., & Cook, N.G.W. (1979), *Fundamentals of Rock Mechanics*, Publ. Chapman and Hall, London.
- Karner, S.L., C. Marone, and B. Evans (1997), "Laboratory study of fault healing and lithification in simulated fault gouge under hydrothermal conditions", *Tectonophysics*, **277**, 41-55.
- Karner, S.L. and C. Marone (1998), "The effect of shear load on frictional healing in simulated fault gouge", *Geophysical Research Letters*, **25**, 4561-4564.
- Karner, S.L. and B.C. Schreiber (1993), "Experimental simulation of plagioclase diagenesis at P-T conditions of 3.5km burial depth", *Pure and Applied Geophysics*, **141**, 221-247.
- Klee, G. and F. Rummel (1993), "Hydrofrac stress data for the European HDR research project test site at Soultz-sous-Forêts", *International Journal of Rock*

Koenig, J.B. (1992), "History of development at the Geysers Geothermal Field, California", IN: *Geothermal Resources Council, Monograph on the Geysers Geothermal Field*, Special Report Number 17, 7-18.

Kovac, K.M., J. Moore, J. McCulloch, D. Ekart (2004), "Geology and mineral paragenesis within the Coso-EGS project", *Proceedings, 29th Workshop on Geothermal Reservoir Engineering*, Stanford University, Stanford, CA, 262-267.

Marone, C. (1998), "Laboratory-derived friction laws and their application to seismic faulting", *Annual Review Earth and Planetary Sciences*, **26**, 643-696.

Oikawa, Y. and T. Yamaguchi (2000), Stress measurement using rock core in an HDR field", *Proceedings World Geothermal Congress*, Kyushu-Tohoku, Japan, 3819-3822.

Parker, R. (1999), "The Rosemanowes HDR project 1983-1991", *Geothermics*, **28**, 603-615.

Paterson, M.S. (1978), "Experimental Rock Deformation - The Brittle Field", Publ. Springer-Verlag, New York, 254 pp.

Raleigh, C.B. and M.S. Paterson (1965), "Experimental deformation of serpentinite and its tectonic implications", *Journal of Geophysical Research*, **70**, 3965-3985.

Ramsey, J.M. and F.M. Chester (2004), "Hybrid fracture and the transition from extension fracture to shear fracture", *Nature*, **428 (6978)**, 63-66.

Sbar, M.L. (1982), "Delineation and interpretation of seismotectonic domains in western North America", *Journal of Geophysical Research*, **87**, 3919-3928.

Scholz, C.H. (1992), "The Mechanics of Earthquakes and Faulting", Cambridge University Press New York, 439 pp.

Sibson, R.H. (1983), "Continental fault structure and the shallow earthquake source", *Journal of the Geological Society of London*, **140**, 741-767.

Tenthorey, E., S.F. Cox, and H.F. Todd (2003), Evolution of strength recovery and permeability during fluid-rock reaction in experimental fault zones", *Earth and Planetary Science Letters*, **206**, 161-172.

Tenzer, H. (2001), "Development of hot dry rock technology", *Geo-Heat Center Bulletin*, **22**, 14-22.

Terzaghi, C. (1925), "Principles of soil mechanics: II - Compressive strength of clay", *Engin. News-Record*, **95**, 796-800.

Thompson, R.C. and R.P. Gunderson (1992), "The orientation of steam-bearing fractures at the Geysers Geothermal Field", IN: *Geothermal Resources Council, Monograph on the Geysers Geothermal Field*, Special Report Number 17, 65-68.

Tiangco, V., Simons, G., Kukulka, R., Masri, M., and Therkelsen, R.L. (2004), "New Geothermal Site Identification And Qualification", (*California*) *Public Interest Energy Research Program - Final Project Report prepared by Geothermex, Inc.:* California Energy Commission, Energy Technology Development Division Publication 500-04-051.

Vetter, U.R. and A.S. Ryall (1983), "Systematic change of focal mechanism with depth in the Western Great Basin", *Journal of Geophysical Research*, **88**, 8237-8250.

Walters, M.A. and J. Combs (1992), "Heat flow in the Geysers-Clear Lake geothermal area of northern California, USA", IN: *Geothermal Resources Council, Monograph on the Geysers Geothermal Field*, Special Report Number 17, 43-53.

Wannamaker, P.E., P.E. Rose, W.M. Doerner, B.C. Berard, J. McCulloch, and K. Nurse (2004), "Magnetotelluric surveying and monitoring at the Coso Geothermal Area, California, in support of the Enhanced Geothermal Systems concept: Survey parameters and initial results", *Proceedings, 29th Workshop on Geothermal Reservoir Engineering*, Stanford University, Stanford, CA, 287-294.

Warpinski, N.R., P. Brannagan, R. Wilmer (1985), "In-situ stress measurements at U.S. DOE's multiwell experiment site, Mesaverde Group, Rifle, Colorado", *Journal of Petroleum Technology*, **37**, 527-536.

Yamaguchi, S., A. Akibayashi, A. Rokugawa, Y. Fujinaga, N. Tenma, and Y. Sato (2000), "The numerical modeling study of the Hijiori HDR test site", *Proceedings World Geothermal Congress*, Kyushu-Tohoku, Japan, 3978-3980.

Zoback, M.D., H. Tsukahara, S. Hickman (1980), "Stress measurements at depth in the vicinity of the San Andreas Fault: Implications for the magnitude of shear stress at depth", *Journal of Geophysical Research*, **85**, 6157-6173.

Zoback, M.L. and M. Zoback (1980), "State of stress in the conterminous United States", *Journal of Geophysical Research*, **85**, 6113-6156.

COUPLED HYDRO-MECHANICAL MODELLING OF THE GPK3 RESERVOIR STIMULATION AT THE EUROPEAN EGS SITE SOULTZ-SOUS-FORÊTS

T. Kohl and T. Mégel

GEOWATT AG
Dohlenweg 28
CH-8050 Zürich; Switzerland
e-mail: kohl@geowatt.ch

ABSTRACT

In 2004 the European EGS project got into its decisive state when reaching the targeted reservoir depth. Currently, three boreholes, (GPK2, GPK3 and GPK4) have been drilled to 5 km. Improvement of the reservoir conditions by stimulation and minimizing the seismic risk represents now a primary challenge to enable economic operation and future extension. In this context, the new HEX-S code has been developed to simulate the transient hydro-mechanical response of the rock matrix to massive hydraulic injections. The present paper describes the modeling results of the GPK3 stimulation starting at May 27, 2003. Maximum flow rates of >60 l/s have been used, triggering >30'000 microseismic events. The transient numerical simulation intends to obtain a match of both, the microseismic and the hydraulic behavior. Different model calculations demonstrate the capabilities of our new approach. It is noteworthy that the modeling became possible only due to the excellent data quality at the Soultz project. The results demonstrate that simulations based on solid physical ground can reveal the complex reservoir behavior during hydraulic stimulation. The use of HEX-S also provides perspectives for future developments such as design calculations that enable optimizing cost-intensive hydraulic stimulations before hand.

INTRODUCTION

In 2004, the final borehole of the current pilot phase at the European EGS site Soultz-sous-Forêts (France) has been drilled. Details of the project are described by e.g. Baria et al. (2000). The planned triplet consists of the two boreholes GPK2 and GPK4 as producers and a central borehole, GPK3 as injector. The boreholes are aligned in roughly N-S direction, reflecting the normal/strike-slip stress regime at the Rhine-Graben location. Recently, the 5 km reservoir

has been stimulated by three major injections at each borehole during 2002 – 2004. Details of the current measurement program is described in Gérard (2004)

Since the fracture at GPK2 could only be roughly estimated (see later), the present paper is concentrating on the GPK3 injection test from May 27th to June 06th, 2003. Flow rate has been varied at several steps up to > 60 l/s at short term and more than 30'000 microseismic events have been recorded. Fig.1 illustrates the seismic response to the change in flow rate: clearly, each flow step change is accompanied by a variation of seismicity, with increasing seismicity at increasing hydraulic flow rate.

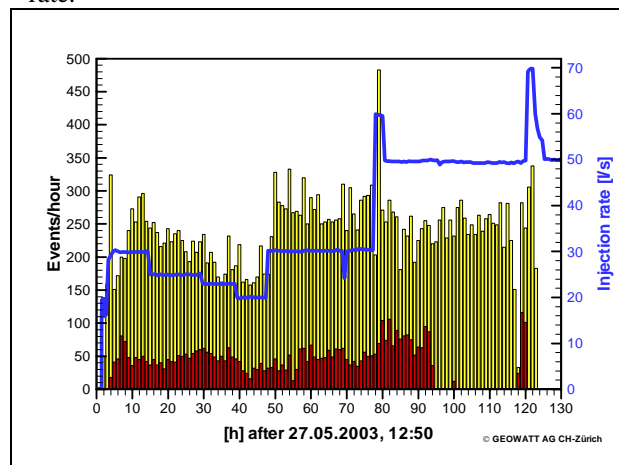


Fig. 1. Flow rate (right axis) and induced seismicity (left axis) during the 2003 stimulation of GPK3. The located seismic events – normalized on 1 hr intervals - represent only a fraction of the total number and are illustrated by a darker colour.

The connection between hydraulic and brittle elastic processes is obvious and has also been observed at various other circumstances and locations. This evidence led us to the development of the new code HEX-S. It was envisaged to model the hydraulic and

seismic processes in a way that the complex non-linear processes are characterized on solid physical ground. Especially, the code should reproduce the observed transient 3-D evolution of shear events in the rock matrix in space and time, as well as the downhole pressure observed in the boreholes.

STIMULATION OF GPK3

The hydro-mechanical code HEX-S

The hydro-mechanical code HEX-S has been developed to calculate the stimulation processes in a fractured reservoir during a massive injection into a borehole. The code takes into account the aperture change of each fracture in the model due to the corresponding overpressure resulting from the injection. The propagation of the overpressure in the reservoir as well as the development of the highly anisotropic reservoir permeability as a result of the fracture apertures is calculated as a time-dependent process.

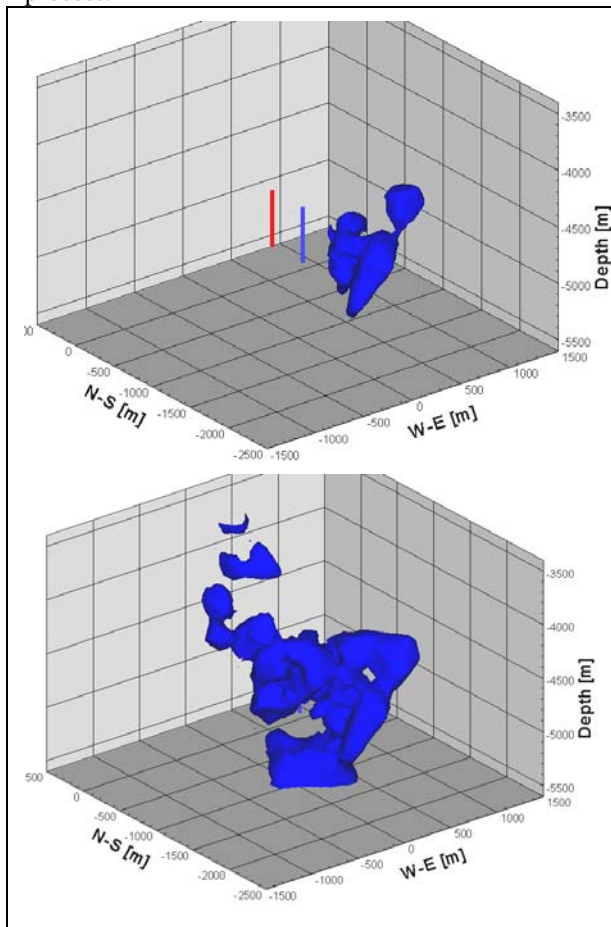


Fig. 2.: Calculated iso-surface of the 0.1 mm fracture aperture after 5 hours (top) and 20 hours (bottom) of injection into GPK4 for the 5 km deep reservoir domain at Soutz-sous-Forêts

Hence the reaction of the reservoir permeability due to an arbitrary injection rate history can be calculated. Fig. 2 illustrates the typical transient development of a 0.1 mm aperture change in a fractured reservoir due to hydraulic injection..

Generation of the fracture network

The permeability distribution in a HEX-S model depends essentially on the location, orientation and aperture of the incorporated fractures. HEX-S allows defining an arbitrary number of both, stochastic and deterministic, fracture sets. Experience from various EGS test sites demonstrates that microseismic events often follow planar structures (i.e. Asanuma 2004, Evans et al. 2005; Cuenot et al. 2005). Since we assume that in most cases an induced microseismic event represents the shear failure of a along an area of a fracture ("slip patch"), the locations of the calculated shearing events can be compared with the microseismic clouds. In contrary, possible mode I events (normal stress variations) remain unidentified. In HEX-S every fracture or fracture zone is represented by a number of circular slip patches with small, predefined radii, generated by subdivision of a planar, and so far circular fracture zone. The aperture of each specific slip patch contributes to the final permeability distribution in the model. Starting from an initial value (see below), the aperture change of a fracture depends on the orientation, the local effective stress field and its defined mechanical parameters.

Each fracture zone in HEX-S can be generated from deterministic or stochastic data, with the following detailed properties:

1. Deterministic fracture zones of defined radii, orientations and classes of mechanical behaviour for their slip patches: The corresponding data is generally derived from borehole logs (e.g. FMS, UBI) but may also include post-experimental interpretation of individual, microseismically active planar structures (Fig. 3).
2. Stochastic generation of fracture zones with random location and orientation: The statistical distribution of the orientation of fracture zones seen in borehole logs is used as the input parameter for the stochastic generation. Each random seed number generates a new distribution of fracture zones in the model (Fig. 4). Each stochastically generated model, independent from the random seed number, has the same distribution of orientations of fracture zones. Stochastically generated fracture zones are generally reasonably used at locations with little information (i.e. at greater distance from the boreholes). The herewith-defined model domain is filled-up until a predefined fracture (or slip

patch) density is reached. Generally, sets of >20'000 slip patches are generated in this way.

The initial aperture of each slip patch is proportional to its radius and adjusted with an overall factor in such a way that the whole reservoir model has a predefined average permeability.

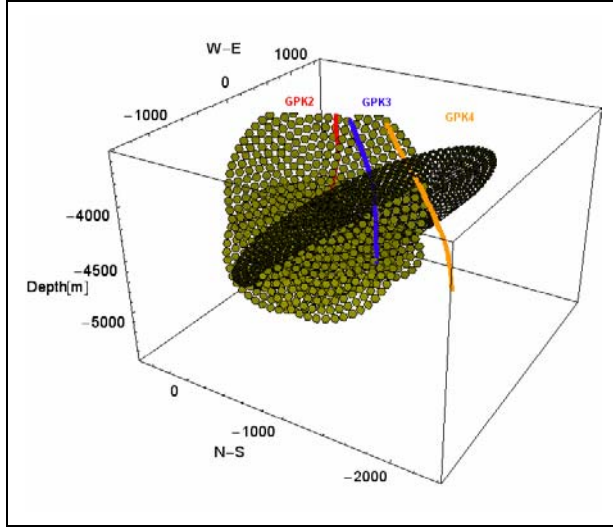


Fig. 3: Example of a model with deterministic fracture zones subdivided into slip patches for the 5 km deep reservoir domain at Soutz-sous-Forêts. Also indicated are the boreholes GPK2, GPK and GPK4

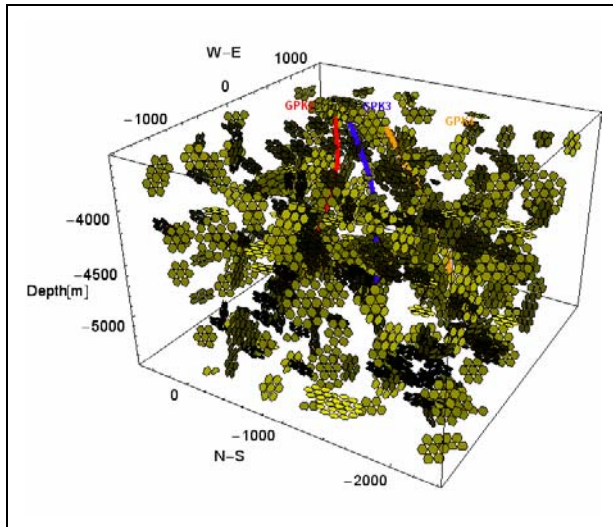


Fig. 4: Example of stochastically generated fracture zones for the 5 km deep reservoir domain at Soutz-sous-Forêts. Also indicated are the boreholes GPK2, GPK and GPK4

Implemented fracture aperture laws

The implemented aperture laws for the fractures or slip patches are basically of analytical kind (Willis-

Richards et al., 1996, Jing et al., 1998, Bächler et al., 2001). The aperture of a fracture depends on three sets of parameters:

1. The mechanical properties of the fracture
2. The fluid pressure in the fracture space
3. The normal and the shear stress on the fracture plane

The effective normal stress $\sigma_{n,eff}$ and the effective shear stress τ_{eff} on the plane of a fracture are derived from the three regional principal stress components and the fluid pressure P at the fracture location. Depending on the pore and fracture fluid pressure P , the fracture aperture at a given location is assumed to react:

- a) By compliance only
- b) By compliance and shearing
- c) By jacking and shearing

a. Compliance only

Under the condition of low effective shear stress, τ_{eff} , only a compliant reaction of the fracture walls to fluid pressure will affect the aperture. The conditions for this behaviour are

$$\sigma_{n,eff} > 0$$

$$\Delta\tau = \tau_{eff} - \sigma_{n,eff} \cdot \tan(\Phi) < 0$$

(Mohr-Coulomb criterion)

As convention, stress is positive for compression. The friction angle Φ of the fracture walls is implemented as a function of $\sigma_{n,eff}$. The aperture increase is treated as reversible and vanishes as soon the pressure declines after the end of injection.

b. Compliance and shearing

If the effective shear stress τ_{eff} at the fracture walls exceeds the friction resistance, i.e. $\Delta\tau > 0$, and the effective normal stress $\sigma_{n,eff}$ still is positive, the fracture fails. The additional "shear" aperture change, a_s , due to the shear offset, U , is

$$a_s = U \cdot \tan(\Phi_{dil})$$

The shear dilation angle of the fracture wall, Φ_{dil} , is also implemented as function of $\sigma_{n,eff}$. The shear offset is defined from fracture shear stiffness, K_s , as:

$$U = \Delta\tau / K_s$$

This portion of the aperture increase is considered to be irreversible when injection test has stopped and the pressure field in the reservoir has reached its ambient value.

c. Jacking and shearing

In the case the effective normal stress, $\sigma_{n,eff}$, becomes negative, the fracture walls separate and the friction forces acting on them disappear. In addition to the shear aperture change, a contribution from jacking conditions, a_j , arises. Clearly, a_j is considered to be fully reversible.

Although the shear induced, mode II, aperture change of a fracture is the only permanent effect after an injection test has ended, the contributions from jacking and compliance are also of major importance for the propagation of the pressure front during the stimulation process.

Hydraulic processes

The time-dependent pressure calculation in HEX-S is performed with a new finite element (FE) algorithm which is a further development of the FRACTure code (Kohl & Hopkirk, 1995). The main advantages of the FE algorithm are in efficient and flexible formulations:

- Local mesh refinement at specified locations in the reservoir domain such as boreholes,
- Utilization of an implicit time-step procedure for the transient calculation
- Easy extension to further physical processes or constitutive laws

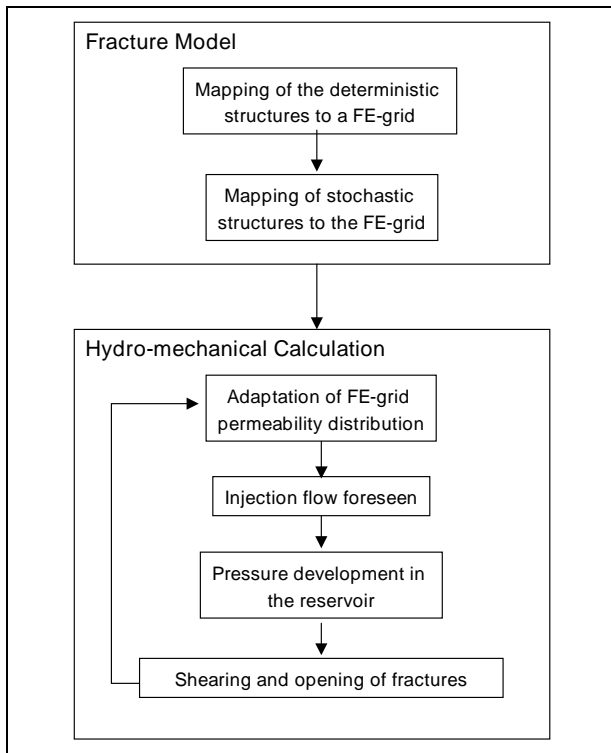


Fig. 5: Principle flow chart of HEX-S

The hydraulic conductivity for each element is derived from the apertures of the intersecting slip patches by a specific mapping procedure. The intersection of the discrete fractures with the continuous FE grid is calculated using a "Rock-to-Fracture volumetric index", RFVI. The mapping results in individual FE volumes of strongly anisotropic properties. Thereby, the hydraulic properties of the FE grid are modified after each time-step. HEX-S calculates the pressure in the model and determines the new apertures of the slip patches. When the hydraulic conductivities of the elements have been updated from the corresponding slip patch apertures, a next time-step is carried out (Fig. 5).

Model of GPK2/GPK3

The numerical model used for the simulation of the hydraulically induced shearing events consists of ~450'000 nodes, covering a surface area of 12x10 km² and a total depth range of 3000-6000 m. As general Soultz convention, the origin of the model (coordinates 0/0/0) is set to the head of the 3.5 km deep GPK1 borehole. The model is strongly refined towards its center, along the stimulated open-hole sections of GPK2, GPK3 and GPK4 between 4500-5000m depth. Fig. 6 illustrates this refinement in vertical and horizontal direction. Towards the boreholes, hexahedrons with partly less than 25x25x25m³ have been applied. The hydraulic behavior along the open-hole sections of the boreholes is simulated using vertical 1D elements. The hydraulic boundary conditions account for the large vertical fault zones in the Rhine Graben area. Hence, Dirichlet boundary conditions ($\Delta P=0$) best describe such drainage systems along the lateral borders. The injected flow is simulated as Neuman boundary condition at the top of the open-hole section (i.e. at the topmost part of the 1-D borehole element). GPK2 was shut-in during the first stimulation phase. The variation of flow rate is controlled in the model by load-time functions that allow specifying the transient change of boundary conditions at arbitrary time intervals.

In a preliminary compilation of R. Maurer (2004), a total of 17 deterministic fractures for GPK2 and GPK3 were implemented into the stimulation model. Location of the GPK2 hydraulically active fractures, which permit the fluid circulation between the reservoir and the borehole, had to be determined by the BRGM (French Geological Survey) based on the analysis of flow logs. As UBI (Ultrasonic Borehole Imager) logs were not carried out in the open hole section of the GPK2 well, the orientation of the flowing fractures have been best-estimated by BRGM based on past experience of the deep-seated structures of the Soultz granite and on hydraulic data.

In the GPK3 well, UBI imaging along the entire granite section was performed. Relevant fracture parameters (depth, orientation, apparent aperture) have been also interpreted by BRGM. Along the open-hole sections, only the large and open fractures have been taken into account in the model. A

preliminary data set of these fractures, listed in the following table, was established from apparently relevant fracture thickness with clear response on the transit time at UBI images.

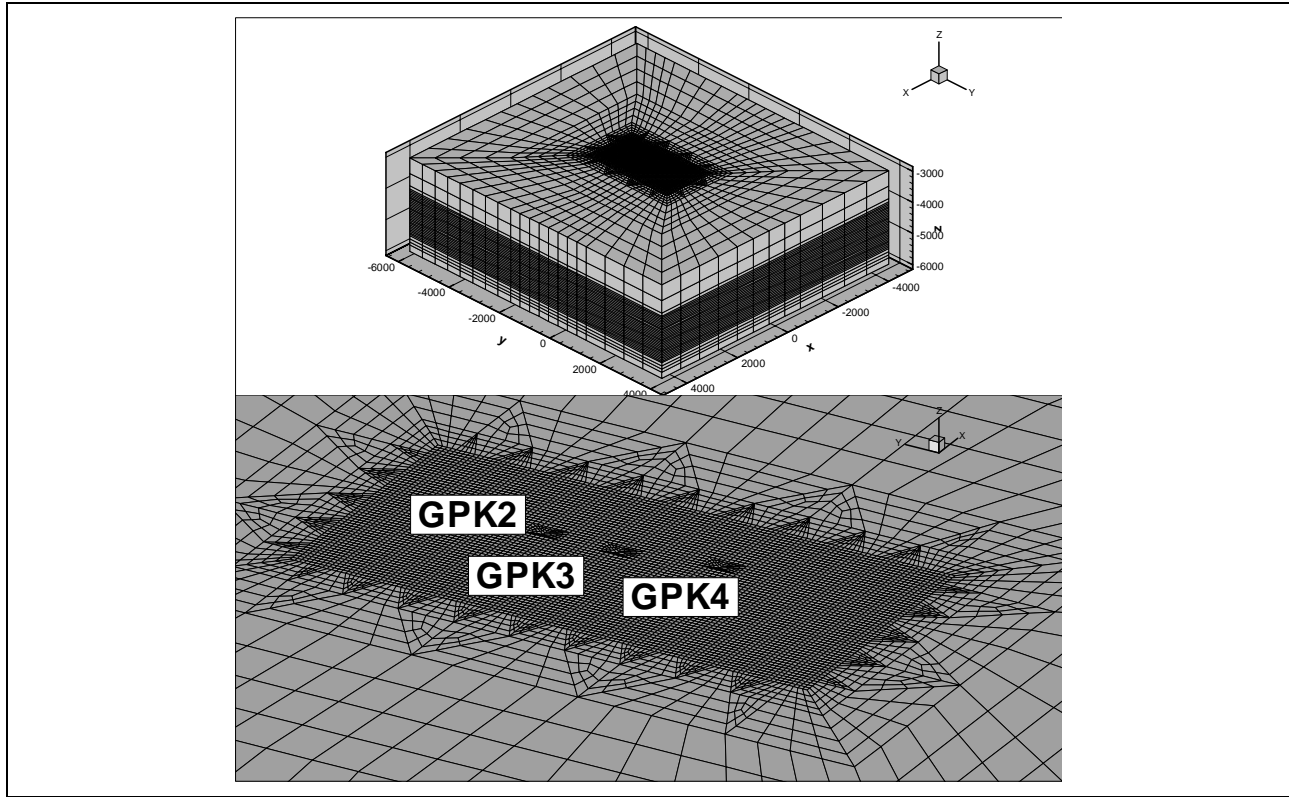


Fig. 6: FE model for the reservoir domain in Soultz-sous-Forêts with the 5 km boreholes GPK 2/3/4, used for the hydraulic calculations in HEX-S. Consisting of ~400'000 elements. North direction is aligned along the y-axis.

Table 1: Preliminary fracture data from GPK2 and GPK3

Bore-hole	x	y	z	azimuth dip angle
GPK2	33.5	-438.7	-4394.8	250/70
GPK2	11.8	-419.5	-4458.5	70/70
GPK2	-6.4	-408.4	-4525.1	70/70
GPK2	-53.7	-376.6	-4716.8	250/65
GPK2	-79	-355.9	-4816.5	250/65
GPK2	-108.5	-337.8	-4936.6	250/70
GPK3	111.5	-956.8	-4517.4	122/66
GPK3	111.5	-956.8	-4517.7	124/61
GPK3	111.5	-957.1	-4542.3	330/54
GPK3	111.5	-957.1	-4542.6	320/54
GPK3	111.4	-957.3	-4569.1	307/60
GPK3	111.7	-960.4	-4660.0	266/52
GPK3	112.2	-962.3	-4685.9	065/68
GPK3	112.3	-962.7	-4691.7	247/67
GPK3	112.3	-968.2	-4992.8	249/40
GPK3	111.8	-966.7	-4943.0	292/58
GPK3	111.2	-966.7	-4971.3	356/48

In future calculations, a meanwhile slightly revised selection of the GPK3 fracture dataset has to be accounted for. Apart from the deterministic fractures intersecting the boreholes, deterministic fault zones at larger distance - derived from the location of microseismic events - and a stochastic fracture distribution in the intermediate rock matrix - calculated from the fracture distribution statistics - will be included in the model.

MODEL RESULTS

Hydraulic stimulation at GPK3 started on May 27th, 2003 at 12:50. This time represents the time "zero" for all our considerations. Although the total injection period extended to June 7th, the treated time span only covers 530'000 s (>6 days). Flow rate was varied in numerous steps, starting with 30 l/s at the first day. In a first phase, flow was stepwise reduced to 20 l/s until 170'000 s, then reestablished at 30 l/s until 280'000s and finally set to 50 l/s, with a short-time (~3 hr) high injection rate of 70 l/s. Due to misplaced pressure sensors, the downhole pressure

records had to be corrected using the borehole simulator HEX-B (Mégel 2005). Pressure response was less pronounced with a first pressure level at $\Delta P = 10$ MPa that nearly continuously increased until $\Delta P = 16$ MPa at $t = 530'000$ s, irrespective of decreasing flow rate at early stage. The complete flow rate and (corrected) pressure record can be recognized on Fig. 7.

The hydraulic simulation results do not fully reflect the described smooth ΔP -behavior. However, the base level and short-term pressure variation are generally well reproduced. Especially, if positive flow steps are well represented (note pressure variation at $t \approx 60'000$ s, $170'000$ s; and $290'000$ s). However, the effect of decreasing flow at the first stage is overestimated. A possible explanation is that the shearing aperture has been treated as irreversible and that the real transmissivity drops stronger at decreasing flow than anticipated by the model. Another impact might arise from the choice of the boundary condition. Very probably, the boundaries are less permeable than assumed – this effect could be strongly responsible for the continuous increase in

pressure. However, the strong non-linear behavior is especially well described. The flow regime is clearly non-linear, the increase of flow rate by 70% (29 to 50 l/s) only results in a 30% pressure increase, an effect that is very well explained by the data simulation. Another most important effect is the over-all little increase of reservoir transmissivity (or injectivity). Normalizing the pressure/flow record at an arbitrary 100% level at the end of the first flow step at injection, our model predicts a variation of relative injectivity that finally reaches 125% at $t \approx 530'000$ s. Although, the data indicated only 101% at the same time, the agreement is amazing, accounting for the strong cubic law between aperture change and permeability. Easily, the simulation could result in completely different orders of magnitude! Noteworthy is the effect of anisotropic flow elucidated by further sensitivity investigations. Flow seems to spread first in radial direction around the borehole, aligns however quickly in the direction of the flow field. This could cause a strong lateral pressure variation in the matrix, an effect that is also well known from the analysis of seismic locations.

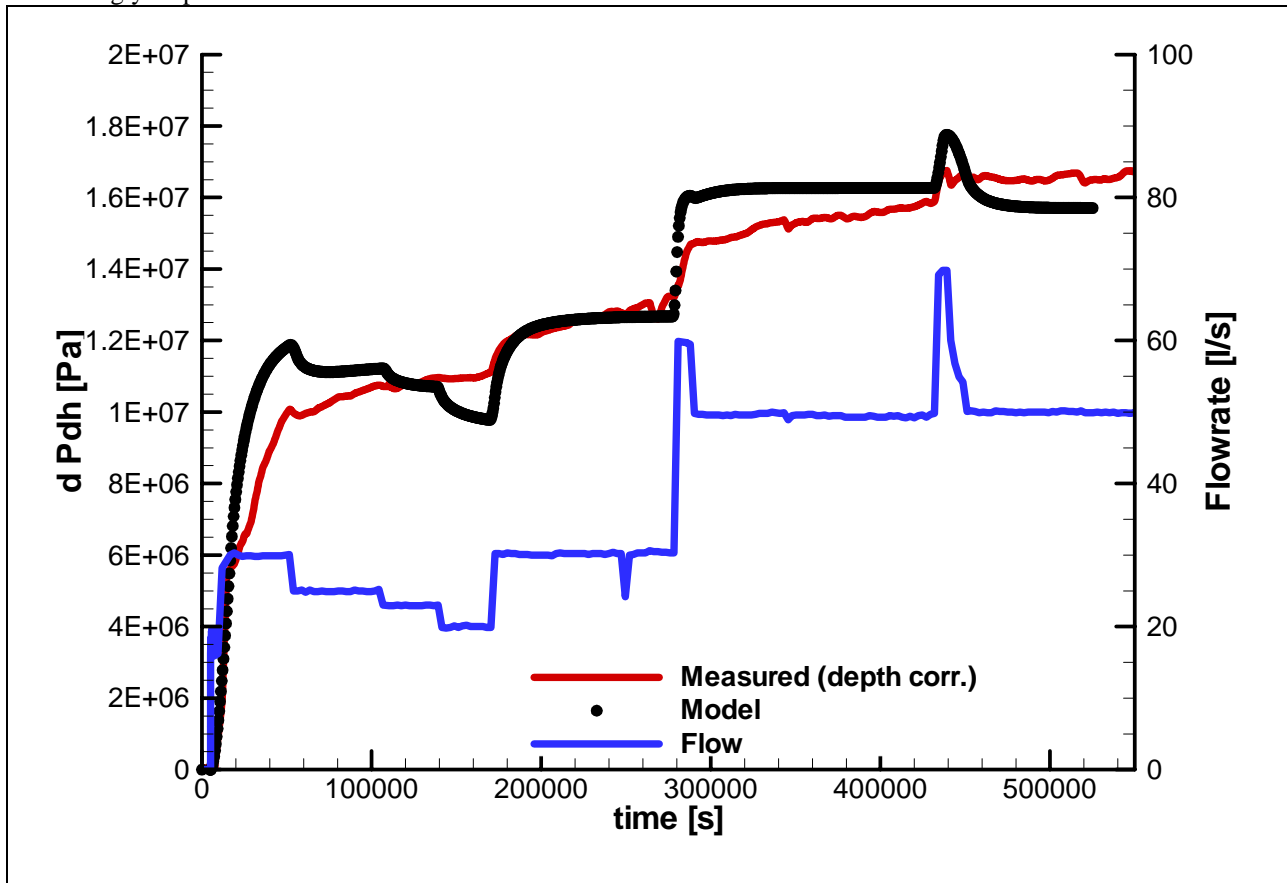


Fig. 7: Hydraulic data from stimulation of GPK3 starting 27. May 2003, 12:50. Pressure data are provided as differential pressure (compared to ambient situation) by a red line, quantified by the left axis; flow rate (blue line) is given at the right axis. Also provided are the modelled differential pressure data (frequent black dots).

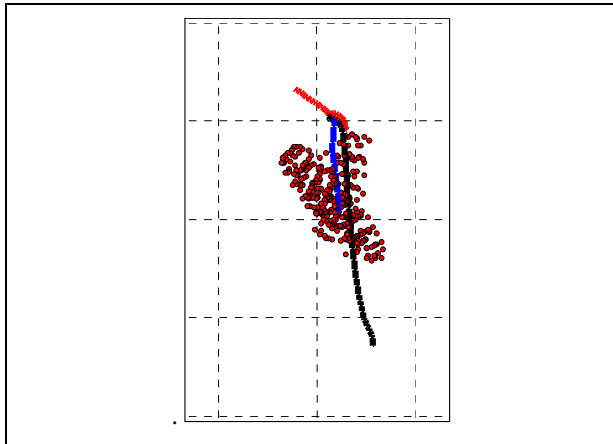


Fig. 8: Simulated shear failure (right). The plane view also illustrates the trajectories of the three boreholes (Red GPK2, blue GPK3 and black GPK4). The seismic cloud is spreading next to the injection at GPK3. The underlying grid has 500 m spacing.

Seismicity was strongly evolving starting next to GPK3. Already after the 1 day, the seismic cloud was spreading to distance of >500 m from open-hole (see also Asanuma 2004 for details). The general pattern of seismicity is directed in ~N-S direction, in agreement with the direction of the maximum horizontal stress direction, σ_{max} . As contribution to the determination of the stress field, it can be stated that our model clearly favour a pure normal stress field, a transfer into a strike-slip regime would cause unstable fracture system, right from the beginning of the simulation. The induced shearing events as simulated by HEX-S (under pure normal stress regime), also tends to spread in N-S direction. Since HEX-S simulates shear slippages when the shear stiffness is exceeded by the shear stress during a time step at optimum oriented fractures, also minimum slip displacement are simulated that certainly don't have any seismic significance (under the M -1 threshold). For a minimum slippage displacement of 0.5 cm, the simulated area is well in agreement with the located events. A different slippage threshold would not produce a strongly different pattern. Hence, it can be stated that HEX-S is well able to reproduce spatial constants of shear events that are identical to the extension of microseismic cloud. This, again, is a clear indication that the simulated pressure field in the rock matrix is well understood.

CONCLUSION

The new hydromechanical reservoir model HEX-S has been successfully tested on data from the European EGS site Soultz-sous-Forêts (France). The

model allows an insight in the complex reservoir behavior under the conditions of massive flow injections that are required for reservoir stimulation. HEX-S supplies a physical reservoir model by jointly interpreting the hydraulic field and the hydraulic-induced shearing events. A further important aspect is that the simulation of the dynamic reservoir behavior is strongly based on a combined data analysis integrating lithological, hydraulic, thermal and stress evaluation, such as evaluated in an excellent way at the Soultz project.

This also provides perspectives for future developments such as design calculations that enable optimizing cost-intensive hydraulic stimulations before hand under financial or logistical restrictions. Therewith it is also possible design optimum reservoir creation strategies or to quantify effects like dual-injections as proposed by Baria et al. (2004) under the conditions of Soultz-sous-Forêts, together with the seismic impact. Clearly, the prognosis of microseismicity is certainly a key factor for actual projects in Europe that are partly located in strongly populated areas.

REFERENCES

- Asanuma, H., T. Izumi, Y. Kumano, N. Soma, H. Niitsuma, R. Baria, and S. Michelet, 2003, Data Acquisition and Analysis of Microseismicity from the Stimulation at Soultz in 2003 by Tohoku University and AIST, Japan., *Geothermal Resource Council, 2004*, Palm Spring Sep. 2004
- Baria, R., Baumgärtner, J., Gérard, A., Garnish, J., 2000, The European HDR programme: main targets and results of the deepening of the well GPK2 to 5000 m. *In: Proc. World Geothermal Congress 2000*, p. 3643-3652.
- Baria R., Michelet S., J.Baumgaertner, B.Dyer, A.Gerard, J.Nicholls, T.Hettkamp, D.Teza, N.Soma, H.Asanuma, J. Garnish, T.Megel, 2004, Microseismic monitoring of the world's largest potential HDR reservoir, *Proc. Twenty-Ninth Workshop on Geothermal Reservoir Engineering Stanford University, Stanford, California, January 26-28, 2004*
- Bächler D., Evans K., Hopkirk R., Kohl T., Mégel T., Rybach L., Data Analysis and controls towards understanding reservoir behaviour and the creation of a conceptual model, Final Report to the Bundesamt für Bildung und Wissenschaft, Projekt 98.0008-1 - EU Project No. JOR3-CT98-0313, Bern, Switzerland
- Cuenot N., Dorbath C., Dorbath, L., 2005, Analysis of the microseismicity induced by fluid injections at the Hot Dry Rock site of Soultz-sous-Forêts (Alsace,

France): implications for the characterization of the geothermal reservoir properties, *Pure and Applied Geophysics*, submitted

Gérard A., 2004, Stimulation hydraulique du puit GPK3 et tests de circulation entre les puits GPK3 et GPK2 - Note de synthèse, *Rapport ADEME / GEIE "Exploitation Minière de la Chaleur No. 01.05.030"*

Kohl, T. and Hopkirk, R.J., 1995. "FRACTure" a simulation code for forced fluid flow and transport in fractured porous rock. *Geothermics*, 24(3): 345-359.

Evans K.F., Moriya H., Niitsuma H., Jones R. H., Phillips W. S., Genter A., Sausse J., Jung R., Baria R., 2005, Microseismicity and permeability enhancement of hydrogeologic structures during massive fluid injections into granite at 3 km depth at the Soultz HDR site, *Geophys. J. Int.*, 160: 388-412.

Jing, Z., Watanabe, K., Willis-Richards, J. and Hashida, T., 2002. A 3-D water/rock chemical interaction model for prediction of HDR/HWR geothermal reservoir performance. *Geothermics*, 31: 1-28.

Maurer R., 2004, Erstellung von Kluftmodellen und vergleichende hydraulische Modelle des geothermischen Reservoirs von Soultz-sous-Forêts, *Diploma Thesis Univ. Freiburg (D)*, 95 p

Mégel, T., Kohl, T., Gérard, A., Rybach, L., Hopkirk, R., 2005, Downhole pressures derived from wellhead measurements during hydraulic experiments, *Proceedings World Geothermal Congress 2005, Antalya, Turkey*

Willis-Richards, J., Watanabe, K. and Takahashi, H., 1996. Progress toward a stochastic rock mechanics model of engineered geothermal systems. *Journal of Geophysical Research*, 101(B8): 17,481-17,496.

ACKNOWLEDGEMENTS

The authors are very grateful to the Swiss Federal Office of Education and Science and to the Swiss Federal Office for Energy which support (under the contract number 03.0460) this research, under the EU contract (SES6-CT-2003-502706). Also the support from EEIG staff in Soultz-sous-Forêts, their subcontractors and especially Dimitra Teza is thankfully acknowledged.

The authors want to acknowledge especially R. Maurer's involvement, providing geological data and performing HEX-S sensitivity analyses during his diploma thesis. Especially, the authors express their appreciation to C. Dezayes and A. Genter from the BRGM (French Geological Survey) who deliberately provided their data.

MODELS OF SUBSURFACE ROCK-WATER PROCESSES AFFECTING FLUID FLOW

Nancy Moller, Christomir Christov and John Weare

University of California San Diego
La Jolla, California, 92093
e-mail: nweare@ucsd.edu; jweare@ucsd.edu

ABSTRACT

The TEQUIL rock-water interaction models (MOLLER et al., 1998) developed at UCSD include most of the solution species necessary to describe the saturation status of hydrothermal fluids for the temperature, pressure, and concentration (TPX) conditions encountered in natural and enhanced geothermal systems (EGS). Important solutes not incorporated are the various hydrolysis products of the Al^{3+} ion. These are needed to predict the chemical behavior of hydrothermal fluids in contact with aluminosilicate minerals, which are found throughout the earth's surface and crust.

The aqueous chemistry of aluminum is extremely complicated. The species in solution include mononuclear (e.g., $Al(OH)_n^{(3-n)+}$, $n = 0 - 4$) and polynuclear (e.g., $Al_{13}O_4(OH)_{24}^{7+}$) aluminum ions and neutral species. Recently, great progress has been made measuring the thermodynamic properties of the mononuclear species in the aluminum-water system. However, the data base for modeling the polynuclear species is far from complete. In this article, using an approximate model, we show that polynuclear aluminum species are not expected to be present in high concentration in hydrothermal fluids that are in near chemical equilibrium with the mineral phases commonly present in reservoir formations. This finding is important for interpreting the data used in the model parameterization. It also indicates that we can develop a highly accurate hydrothermal fluid model containing only mononuclear aluminum solution species for rock-water applications. Our initial efforts to model the aluminum-water system up to 125°C are reported. Results show that the modeling phenomenology we have developed can predict the complicated chemical behavior of this system with accuracies near that of the experimental data.

INTRODUCTION

The successful enhancement of fluid flow in high temperature, low permeability reservoirs (EGS) would significantly advance geothermal energy as an economically competitive contributor to the nation's energy supply. However, progress in this approach is limited by insufficient knowledge about the

subsurface rock-water chemical processes controlling fluid flow in high temperature formations. The purpose of our research is to provide new modeling technologies that accurately characterize the reservoir rock-water chemistry of EGS systems. An initial objective is to construct an accurate variable temperature (0-250°C) model of the H-Na-K-Al-OH-Cl-H₂O system to add to our TEQUIL models that include the aqueous chemistry of silica. This model will adapt the Pitzer (PITZER, 1987) liquid density free energy representation to the complicated chemistry of the aluminum system. When completed, it will be the first model that can accurately calculate the activities of aluminum species in hydrothermal fluids to high concentration and temperature. Our suite of solution models will then include the components necessary to describe the interaction of many hydrothermal minerals (e.g., those compiled in the report of Browne (BROWNE, 1978)) with formation fluids. This model will provide an important tool for understanding the behavior of hydrothermal systems and EGS applications. It will be made available to many users via our web site, geotherm.ucsd.edu.

METHODOLOGY

The temperatures addressed in the model discussed here are below the critical temperature of aqueous natural fluid mixtures. The pressures considered are along the aqueous mixture saturation line. Although pressure can also affect equilibria under these TPX conditions, the largest variation of the solution free energy comes from changes in X and T (e.g., changes in pH, mineral/solution and solution/gas solubilities, etc.). In order to provide the highest accuracy, we have tailored our selection of equations of state to reflect the important properties of each phase in this TPX range. The aqueous phase activities are based on the solution free energy equations introduced by Pitzer (PITZER, 1987). An ideal mixture or mixing equation of state is used for the vapor phase.

The equilibrium compositions of all the phases in the system can be found by minimizing the free energy of the total system for constant T and P subject to the conditions of conservation of mass and charge balance for each solution phase (HARVIE et al.,

1984). The chemical potential (activity) of each species in a solution phase is given by,

$$\mu_i = \mu_i^o + RT \ln \gamma_i m_i, \quad (1)$$

where μ_i^o is the standard chemical potential of species i , usually referred to infinite dilution. γ_i is the activity coefficient for species i , and m_i is the molal concentration. The Gibbs free energy may be written in terms of the chemical potentials as,

$$G = \sum_{\text{species}} \mu_i n_i. \quad (2)$$

n_i is the number of moles of species i and the sum is over all species (HARVIE et al., 1984).

Theoretical results can provide general guidance as to the form of the expression used for μ^o and γ as a function of TPX (e.g., the equation of state, EOS). However, to achieve the accuracy needed in geochemical applications it is necessary to adjust parameters in the EOS to obtain agreement with experimental data.

The range and variation in solution composition encountered in possible EGS applications is very large. Formation waters with ionic strengths up to ≈ 10 m have been reported (SHVARTSEV and BUKATY, 1995; WHITE et al., 1963). Values of pH can vary from 0.4 (WHITE et al., 1963) to 10.0 (HENLEY and ELLIS, 1983; WHITE et al., 1963). The ability to provide accurate chemical predictions for such large composition variation is a requirement of the phenomenology that we are developing.

Aqueous solutions models usually begin with a Debye-Huckel ionic strength dependent contribution, ($\ln \gamma_{DH} = -A_\gamma |z_+ z_-| I^{.5} / (1 + I^{.5})$), which provides reasonable predictions for very low ionic strength solutions ($I \approx .01$ m). To treat higher ionic strengths, it is necessary to account for specific ion interactions.

In the model we are developing, our (HARVIE and WEARE, 1980; HARVIE et al., 1984; WEARE, 1987) implementation of the Pitzer activity expressions for the aqueous solution phase is used. Because this formalism is based on the excess free energy, all the activity expressions are consistent, allowing different kinds of data (e.g., osmotic, e.m.f., and solubility measurements) to be used in the parameter evaluations. These equations have been given in many publications. Here, we give only the activity coefficient expression for the interaction of cation, M , with the other solute species.

$$\begin{aligned} \ln \gamma_M = & z_M^2 F + \sum_a m_a (2B_{Ma} + ZC_{Ma}) + \\ & \sum_c m_c (2\Phi_{Mc} + \sum_a m_a \psi_{Mca}) + \\ & \sum_a \sum_{a' < a} m_a m_{a'} \psi_{Maa'} + |z_M| \sum_c \sum_a m_c m_a C_{ca} \\ & + \sum_n m_n (2\lambda_{nM}) + \sum_n \sum_a m_n m_a \zeta_{naM} \end{aligned} \quad (3)$$

$$\begin{aligned} F = & -A^\phi \{ I^{.5} / (1 + 1.2I^{.5}) + \\ & (2/1.2) \ln(1 + 1.2I^{.5}) \} \\ & + \sum_c \sum_a m_c m_a B'_{ca} + \sum_c \sum_{c' < c} m_c m_{c'} \Phi'_{cc'} \\ & + \sum_a \sum_{a' < a} m_a m_{a'} \Phi'_{a,a'} \end{aligned} \quad (4)$$

$$\begin{aligned} B_{ma} = & \beta_{Ma}^0 + \beta_{Ma}^1 g(\alpha, I^{.5}) + \beta_{Ma}^2 g(12I^{.5}), \\ g(x) = & 2(1 - (1+x)e^{-x}) / x^2, \quad (5) \\ \Phi_{ij} = & \Theta_{ij} + {}^E \Theta_{ij}(I), Z = \sum_i |z_i| m_i \end{aligned}$$

This expression is symmetric for an anion. The B coefficients describe the ionic strength dependence of binary solutions. When either the cation or anion for an electrolyte is univalent, we set α equal to 2.0 and omit the $\beta^{(2)}$ term. For 2-2 or higher valence pairs, $\alpha = 1.4$. In addition the $\beta^{(2)}$ term accounts for the increased tendency of these higher charged species to associate in solution. When strong ion association is present (e.g., HCO_3^-) the ion pair species must be added to the species list (HARVIE et al., 1984). The ionic strength dependence of the ternary mixing coefficients is found in the Φ terms, which account for mixing between two ions of like charges. In Φ_{ij} , Θ_{ij} is the only adjustable parameter. The ionic strength dependent ${}^E \Theta_{ij}(I)$ term accounts for electrostatic unsymmetric mixing effects that depend only on the charges of ions i and j and the total ionic strength. The terms with λ and ζ account for neutral species interactions with anions and cations (FELMY and WEARE, 1986). In this model the third virial coefficients, C , and the ψ terms, are independent of ionic strength. All these parameters are adjusted to fit the available data in binary and ternary systems using a non-linear least squares method (HARVIE et al., 1987). We note that only binary and ternary data are required to evaluate all the parameters in the Pitzer equations described here no matter how many components are in the solution. This formalism, Eqs. 3-5, therefore, provides a means to extrapolate data from ternary and lower systems to systems of higher order. We (CHRISTOV and MOLLER, 2004; HARVIE et al., 1984) have shown that these equations can provide solubility predictions for a range of ionic strengths that include most of the compositions found

in nature. Temperature dependence (MOLLER, 1988; MOLLER and GREENBERG, 1989; CHRISTOV and MOLLER, 2004) of the solution parameters is built into the model by adjusting selected constants in the following equation,

$$\text{parameter}(T) = a_1 + a_2T + a_3(T^2) + a_4(T^3) + a_5/T + a_6 \ln T + a_7(1/(T-263)) + a_8(1/(680-T)). \quad (6)$$

This equation is consistent with the temperature dependence reported by other workers both for heat properties and free energy properties.

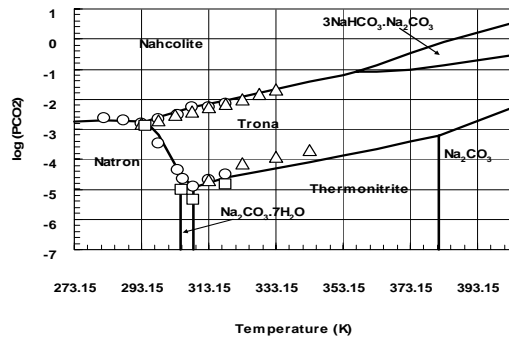


Figure 1

Fig. 1 above and Fig. 2 below illustrate that our modeling strategy has the capability of calculating the solubilities (Fig. 1: solubility of carbonate minerals as a function of CO_2 and T) and weak acid/base properties (Fig. 2) in hydrothermal fluids (solid lines are model predictions; symbols are experimental data).

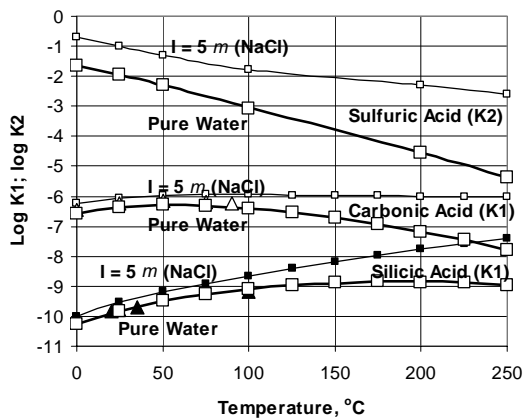


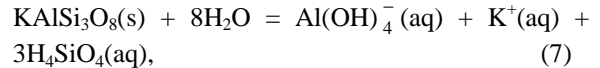
Figure 2

DEVELOPMENT OF THERMODYNAMIC MODEL FOR ALUMINUM

Aluminosilicate minerals are found throughout the earth's surface and crust (commonly as feldspars; e.g., alkali feldspar, $\text{Na/KAlSi}_3\text{O}_8$) in metamorphic and igneous rock (DEER et al., 1966), as clays in well-weathered soils (DRISCOLL and SCHECHER, 1989) and as authigenic constituents of evaporites

(KASTNER, 1971)). The ability to correctly model the solubility of these minerals as a function of fluid composition and temperature is critical to understanding the formation and evolution of rock- and soil-forming minerals and flow properties such as reservoir permeability in hydrothermal systems.

The condition determining equilibrium between a mineral phase and a solution phase can be written in terms of a free energy balance equation. For example, for the dissolution of K-feldspar ($\text{KAlSi}_3\text{O}_8(\text{s})$) via the reaction,



this free energy condition leads to the equation,

$$\Delta G_f(T, P)(K - \text{spar}) = \mu_{\text{Al}(\text{OH})_4^-} + \mu_{\text{K}^+} + 3\mu_{\text{H}_4\text{SiO}_4} - 8\mu_{\text{H}_2\text{O}}. \quad (8)$$

$\Delta G_f(T, P)$ is the free energy of formation of K-spar. In order to use this expression to determine the solubility status of the K-spar mineral, we need models for the chemical potentials or activity coefficients of the species in solution. In our prior work we have developed TPX dependent model parameterizations for all the species (see, for example, Fig. 1) in Eq. (8) except $\text{Al}(\text{OH})_4^-(\text{aq})$. The activity of this species is a function of TP and all the composition variables in the solution.

The aqueous chemistry of aluminum is highly complicated. Thermodynamic and spectroscopic evidence for several mononuclear (MN) hydrolysis products (e.g., $\text{Al}(\text{OH})_2^+$, $\text{Al}(\text{OH})_3$, and $\text{Al}(\text{OH})_4^-$) has been reported. Less well defined polynuclear (PN) hydrolysis species (e.g. $\text{Al}_2(\text{OH})_2^{4+}$, $\text{Al}_3(\text{OH})_4^{5+}$, $\text{Al}_{13}\text{O}_4(\text{OH})_{24}^{7+}$ or $\text{Al}_{13}\text{O}_4(\text{OH})_{24}(\text{H}_2\text{O})_{12}^{7+}$) have been proposed to explain data in concentrated aluminum solutions in certain pH ranges (BAES and MESMER, 1986). Experimental data available for parameterization in the high and low pH region include osmotic, potentiometric and solubility measurements. In the near neutral pH region, most commonly encountered in hydrothermal systems, the low solubility and complex solution chemistry of aluminum have made the determination of activity and formation constants of the various aluminum solutes difficult. However, recent advances in potentiometric titration methods and in determining effective formation constants for aluminum speciation reactions via solubility studies of aluminum (oxy)hydroxide minerals are now providing the data needed to characterize the thermodynamics of Al^{3+} and its mononuclear hydrolysis products. The data base available defining the activities of the polynuclear hydrolysis products on the other hand is still very incomplete.

The role of polynuclear aluminum species

Since the data required to define a high accuracy model including PN species is not available, a first step in the development of a model for natural water applications is to determine the composition ranges where these species do not play an important role. Obviously, the model we develop using only the well determined MN species will produce highly accurate predictions only for hydrothermal solutions with these compositions.

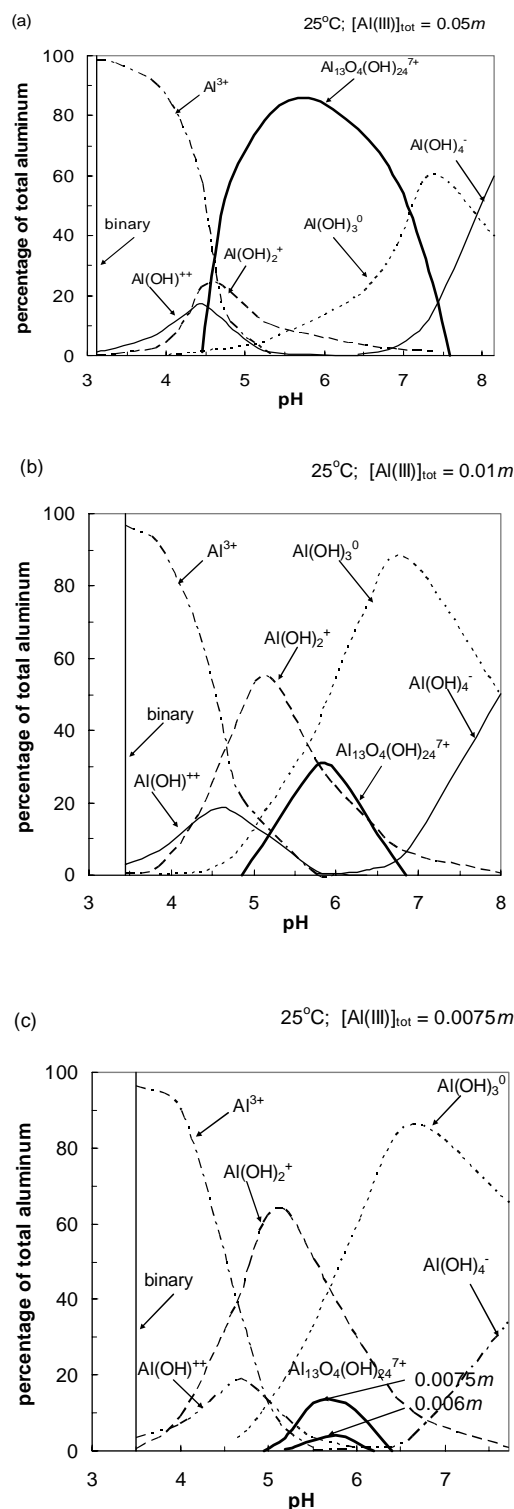
For our modeling effort there is an additional problem. The stoichiometry of the PN species suggests that they will be more important at high aluminum concentrations and high OH⁻ concentrations. In the high and low pH region we rely heavily on high aluminum concentration data to evaluate parameters in our model. If PN species are important in these solutions, it would be necessary to take them into account in the data analyses. With the present understanding of the aluminum system this would be difficult to do.

Because of the possible nonlinear hydrolysis effects at high aluminum and OH⁻ concentrations and the competition of the various solution species for Al³⁺ and OH⁻, it is difficult to estimate aluminum speciation in solution without a computational model. Fortunately, enough data has been reported to allow the development of an *approximate* model including both the MN and PN species.

To test the impact of neglecting PN species in our high accuracy model and data analyses, we constructed an approximate model at 25° and 100°C using the concentration products for Al³⁺ hydrolysis and polymerization reactions (Al₂(OH)₂⁴⁺, Al₃(OH)₄⁵⁺, Al₁₃O₄(OH)₂₄⁷⁺ or Al₁₃O₄(OH)₂₄(H₂O)₁₂⁷⁺) taken from Baes and Mesmer (BAES and MESMER, 1986) and Furrer et al. (FURRER et al., 1992). Examples of the predictions of this model for 25°C (where the approximate model is better determined) are given in Fig's. 3a-c below. In these figures, the pH of a binary AlCl₃-H₂O solution has the pH indicated by the line marked binary. The graphs are made by titrating these solutions with base to obtain the speciation for higher pH solutions predicted by the model.

There are several important observations to make about the results illustrated in Fig's. 3a-c. First, the Al₁₃O₄(OH)₂₄⁷⁺ species, which is the only PN species that appears in significant concentrations, can play a dominant role in the pH range from 4.5 to 7.5, at total aluminum concentrations above about 0.01 m. (see Fig's. 3ab). Since most natural waters have pHs in the intermediate pH range (4-8), this would suggest

that it is necessary to include this species in a model for hydrothermal applications. However, we note from Fig. 3c that as the amount of total aluminum in solution decreases the model predicts that the concentration of this PN is quite low (e.g., PN < 9%; see the solid line in the 5 to 6 pH range).



Figures 3 a-c

For applications in which the formation water is in near chemical equilibrium with formation minerals, the neglect of polynuclear species is justified because the solubility of the hydroxide minerals, such as gibbsite and kaolinite, common to most hydrothermal reservoir keeps the total concentration of aluminum very low ($<10^{-5} m$) (NORDSTROM, 1982). For these solutions, the PN concentration is negligible.

For acid mine and volcanic waters, which can have low pH values (BIRD et al., 1989; ROCHELLE et al., 1989; WHITE et al., 1963), and carbonate rich waters, which can have high pH values (WHITE et al., 1963), the concentration of aluminum can become quite high (WHITE et al., 1963). The stoichiometry of the species, $Al_{13}O_4(OH)_{24}^{7+}$ is also high in OH. Therefore, at low pH, the low OH concentration destabilizes this species as illustrated in the low pH region of Fig's. 3a-c. At high pH, the dominant species is the MN species $Al(OH)_4^-$ for which we have data.

These results at 25°C suggest that an accurate model of aluminum speciation using only MN species can be developed and has wide application to formation water problems. In Fig. 4 the results of a similar (but less well defined) model at 100°C are reported. For this temperature, the aluminum concentration at which the PN species become important is higher than for 25°C, supporting the use of a model containing only MN species for high temperatures.

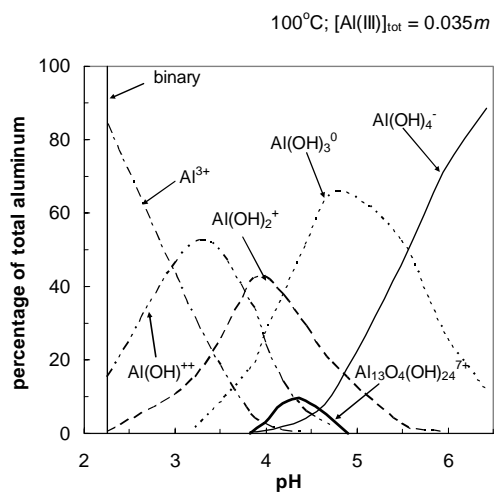


Figure 4

Development of a high accuracy aluminum speciation model (MN only):

Our development of a high accuracy model begins with aluminum speciation in low pH aqueous sodium chloride solutions. For these solutions we assume the only solutes are H, Na, Al and Cl, as justified by Fig's. 3a-c and 4. We used e.m.f., osmotic and solubility data in the literature and unpublished e.m.f.

data (Andrew Dickson) to establish temperature functions for the binary interaction parameters β^0_{AlCl} , β^1_{AlCl} , and C^0_{AlCl} and the ternary mixing parameters θ_{AlNa} , θ_{AlH} , ψ_{AlHCl} and ψ_{AlNaCl} . An example of this model's agreement with solubility data for solid $AlCl_3 \cdot 6H_2O$ in the low pH region is given in Fig. 5. Having established these parameters in the low pH regions, they are used for all compositions in the model.

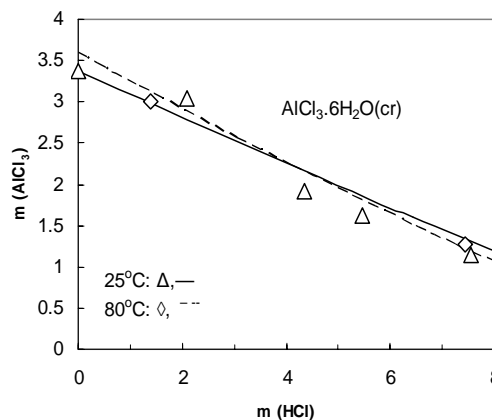


Figure 5

The complex aqueous chemistry of aluminum and its low solubility in the near neutral region common to natural systems have made model development difficult. However, recent advances in determining molal equilibrium quotients as a function of composition for aluminum speciation reactions via solubility studies of aluminum (oxy)hydroxide minerals (e.g., gibbsite $Al(OH)_3(cr)$; boehmite $AlOOH(cr)$) and potentiometric titration are now providing the data needed to characterize the activities of Al^{3+} and its MN hydrolysis products in this difficult region (BENEZETH et al., 1997; BENEZETH et al., 2001; BOURCIER et al., 1993; CASTET et al., 1993; PALMER et al., 2001; PALMER and WESOLOWSKI, 1992; PALMER and WESOLOWSKI, 1993; WESOLOWSKI, 1992; WESOLOWSKI and PALMER, 1994).

Using these data and the acid-side parameterization described above, we constructed a Pitzer ion interaction model of aluminum speciation (Al^{3+} , $Al(OH)^{2+}$, $Al(OH)_2^+$, $Al(OH)_3^0$ and $Al(OH)_4^-$) in H-Na-Al-OH-Cl- H_2O solutions ($NaCl \approx 0-5m$) as a function of pH and temperature from 0° to 125°C. In Fig. 6 the agreement of the model with the observed aluminum hydrolysis quotients (WESOLOWSKI and PALMER, 1994) as a function of NaCl concentration and temperature is reported. In Fig's. 7ab, the predicted distribution of aqueous aluminum species as a function of pH in $10^{-7}m$ $AlCl_3$ solutions at 25° and 90°C is shown. Note the movement of the hydrolysis reactions to lower pH with temperature. With small exceptions, the model predictions are in

good agreement with the hydrolysis curves estimated from experimental data (e.g., Castet et al., 1993).

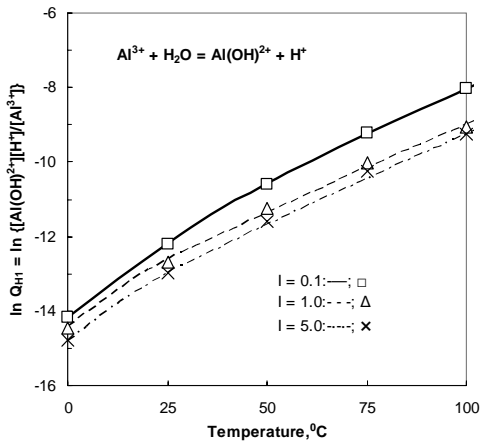
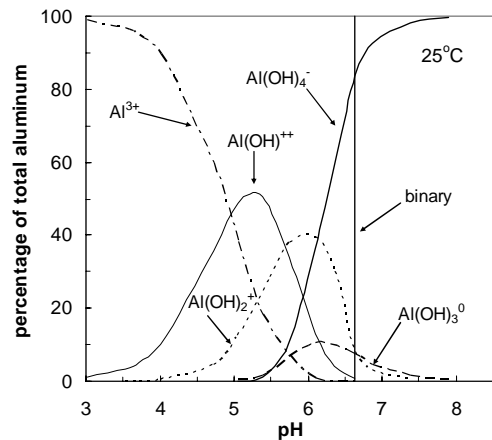
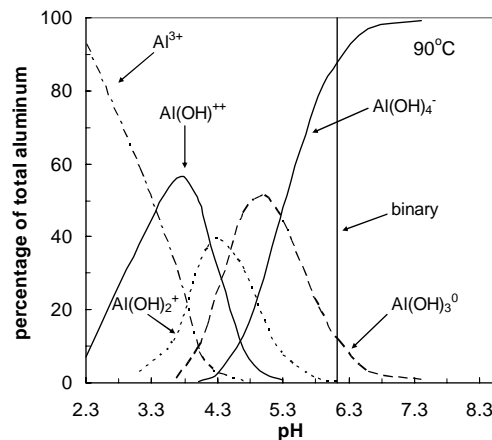


Figure 6

(a)



(b)



Figures 7ab

SUMMARY

Using an approximate model based on “best possible” estimates in the literature of equilibrium constants for polynuclear and mononuclear aluminum hydrolysis species, we demonstrate that for applications to hydrothermal fluids near chemical equilibrium with reservoir rocks a chemical model based only on mononuclear species should provide a very accurate description of the reservoir chemistry. Based on this assessment, a Pitzer type model has been constructed using only mononuclear species. This model accurately reproduces the data for aluminum speciation in high concentration aqueous NaCl solutions to high temperature. This is the first model to summarize these data. The results reported in Fig. 6 demonstrate that our modeling strategy is capable of very accurately representing existing data. The theoretical structure of the model, Eq’s. 3-4, and our experience with other systems suggest that use of this parameterization in much more compositionally complicated hydrothermal fluids will produce a highly accurate model of the solubility status of hydrothermal minerals for EGS applications.

ACKNOWLEDGEMENTS

This work is supported by the U.S. Department of Energy, Assistant Secretary Energy Efficiency and Renewable Energy under DOE Golden Operations Financial Assistance Award DOE DE-FG36-04GO14300 and grants from the National Science Foundation, NSF ERA0126331.

REFERENCES

- Baes C. F. J. and Mesmer R. E. (1986) *The Hydrolysis of Cations*. Robert E. Krieger Publishing Company.
- Benezeth P., Palmer D. A., and Wesolowski D. J. (1997) The aqueous chemistry of Aluminum - a new approach to high-temperature solubility measurements. *Geothermics* **26**(4), 465-481.
- Benezeth P., Palmer D. A., and Wesolowski D. J. (2001) Aqueous high-temperature solubility studies. II. The solubility of boehmite at 0.03 m ionic strength as a function of temperature and pH as determined by in situ measurements. *Geochim. Cosmochim. Acta* **65**(13), 2097-2111.
- Bird M. I., Andrew A. S., Chivas A. R., and Lock D. E. (1989) An isotopic study of surficial alunite in Australia: I. Hydrogen and sulphur isotopes. *Geochim. Cosmochim. Acta* **53**, 3223-3237.
- Bourcier W. L., Knauss K. G., and Jackson K. J. (1993) Aluminum hydrolysis constants to 259°C from boehmite solubility measurements. *Geochim. Cosmochim. Acta* **57**, 747-762.
- Browne P. R. L. (1978) Hydrothermal alteration in active geothermal fields. *Annual Review of Earth and Planetary Science* **6**, 229-250.

- Castet S., Dansurand J.-L., Schott J., and Gout R. (1993) Boehmite solubility and aqueous aluminum speciation in hydrothermal solutions (90-350°C): Experimental study and modeling. *Geochim. Cosmochim. Acta* **57**, 4869-4884.
- Christov C. and Moller N. (2004) Chemical equilibrium model of solution behavior and solubility in the H-Na-K-OH-Cl-HSO₄-SO₄-H₂O system to high concentration and temperature. *Geochim. Cosmochim. Acta* **68**(6), 1309-1331.
- Deer W. A., Howe R. A., and Zussman J. (1966) *An Introduction to the Rock-Forming Minerals*. Longman.
- Driscoll C. T. and Schecher W. D. (1989) Aqueous Chemistry of Aluminum. In *Aluminum and Health: A Critical Review* (ed. H. J. Gitelman), pp. 27-65. Marcel Dekker, Inc.
- Felmy A. R. and Weare J. H. (1986) The prediction of borate mineral equilibria in natural waters: Application to Searles Lake, California. *Geochim. Cosmochim. Acta* **50**, 2771-2783.
- Furrer G., Trusch B., and Müller C. (1992) The formation of polynuclear Al₁₃ under simulated natural conditions. *Geochim. Cosmochim. Acta* **56**, 3831-3838.
- Greenberg J. P. and Moller N. (1989) The prediction of mineral solubilities in natural waters: a chemical model for the Na-K-Ca-Cl-SO₄-H₂O system to high concentration from 0 to 250°C. *Geochim. Cosmochim. Acta* **53**, 2503-2518.
- Harvie C., Greenberg J. P., and Weare J. H. (1987) A chemical equilibrium algorithm for highly non-ideal multiphase systems: Free energy minimization. *Geochim. Cosmochim. Acta* **51**, 1045-1057.
- Harvie C., Moller N., and Weare J. (1984) The prediction of mineral solubilities in natural waters: The Na-K-Mg-Ca-H-Cl-SO₄-OH-HCO₃-CO₃-CO₂-H₂O system from zero to high concentration at 25 C. *Geochim. Cosmochim. Acta* **48**, 723-751.
- Harvie C. E. and Weare J. H. (1980) The prediction of mineral solubilities in natural waters: The Na-K-Mg-Ca-Cl-SO₄-H₂O systems from zero to high concentration at 25°C. *Geochim. Cosmochim. Acta* **44**, 981-997.
- Henley R. W. and Ellis A. J. (1983) Geothermal systems ancient and modern: A geochemical review. *Earth-Sciences Reviews* **19**, 1-50.
- Kastner M. (1971) Authigenic feldspars in sedimentary rocks. *Amer. Mineralogist* **56**, 1403-1442.
- Moller N. (1988) The prediction of mineral solubilities in natural waters: a chemical model for the Na-Ca-Cl-SO₄-H₂O system, to high temperature and concentration. *Geochim. Cosmochim. Acta* **52**, 821-837.
- Moller N., Greenberg, J. P., and Weare, J. (1998) Computer modeling for geothermal systems: predicting carbonate and silica scale formation, CO₂ breakout and H₂S exchange. *Transport in Porous Media* **33**, 173-204.
- Nordstrom D. (1982) The effect of sulfate on aluminum concentrations in natural waters: Some stability revelations in the system Al₂O₃-SO₃-H₂O at 298 K. *Geochim. Cosmochim. Acta* **46**, 681-692.
- Palmer D. A., Benezeth P., and Wesolowski D. J. (2001) Aqueous high-temperature solubility studies. I. The solubility of boehmite as functions of ionic strength (to 5 molal, NaCl), temperature (100-290 degrees C), and pH as determined by in situ measurements. *Geochim. Cosmochim. Acta* **65**(13), 2081-2095.
- Palmer D. A. and Wesolowski D. J. (1992) Aluminum speciation and equilibria in aqueous solutions: II. The solubility of gibbsite in acidic chloride solutions from 30 to 70°C. *Geochim. Cosmochim. Acta* **56**, 1093-1111.
- Palmer D. A. and Wesolowski D. J. (1993) Aluminum speciation and equilibria in aqueous solutions: III. Potentiometric determination of the first hydrolysis constant of aluminum (III) in sodium chloride to 125°C. *Geochim. Cosmochim. Acta* **57**, 2929-2938.
- Pitzer K. S. (1987) Thermodynamic model for aqueous solutions of liquid-like densities. In *Reviews in Mineralogy--Thermodynamic Modeling of Geological Materials: Minerals Fluids and Melts*, Vol. 17 (ed. I. S. E. Carmichael and H. P. Eugster), pp. 499. Mineralogical Society of America.
- Rochelle C. A., Milodowski A. E., Savage D., and Corella M. (1989) Secondary mineral growth in fractures in the Miravalles geothermal system, Costa Rica. *Geothermics* **18**, 279-286.
- Shvartsev S. L. and Bukaty M. B. (1995) Evolution of CaCl₂ brine of Tungusky Basin (Siberian Platform): The role of water-rock interaction. *Proceedings: 8th International Symposium Water-Rock Interaction*, 477-481.
- Weare J. H. (1987) Models of mineral solubility in concentrated brines with application to field observations. In *Thermodynamic modeling of geological materials: minerals, fluids and melts*, Vol. 17 (ed. I. S. E. Carmichael and H. P. Eugster), pp. 143-174. Mineralogical Society of America.
- Wesolowski D. J. (1992) Aluminum speciation and equilibria in aqueous solutions: I. The solubility of gibbsite in the system Na-K-Cl-OH-Al(OH)₃ from 0-100°C. *Geochim. Cosmochim. Acta* **56**, 1065-1091.
- Wesolowski D. J. and Palmer D. A. (1994) Aluminum speciation and equilibria in aqueous solution: V. Gibbsite solubility at 50°C and pH 3-9 in 0.1 molal NaCl solution (a general model for aluminum speciation; analytic methods). *Geochim. Cosmochim. Acta* **58**, 2947-2969.
- White D. E., Hem J. D., and Waring G. A. (1963) Chemical Composition of Subsurface Waters. In *Data of Geochemistry*, Vol. Chapter F (ed. M. Fleischer), pp. 1-67.

A HYBRID SEMI-ANALYTICAL AND NUMERICAL METHOD FOR MODELING WELLBORE HEAT TRANSMISSION

Karsten Pruess and Yingqi Zhang

Earth Sciences Division, Lawrence Berkeley National Laboratory
One Cyclotron Road
Berkeley, CA 94720
e-mail: K_Pruess@lbl.gov

ABSTRACT

Fluid flow in geothermal production and injection wells can be strongly affected by heat transfer effects with the formations surrounding the wellbore. Various techniques and approximations to model wellbore heat transmission have been presented in the literature. The objective of the present work is to develop a treatment of conductive heat transfer in the formations surrounding a wellbore that is simple, yet provides good accuracy for transient effects at early time. This is accomplished by adapting the well-known semi-analytical heat transfer method of Vinsome and Westerveld (1980) to the problem of heat transfer to and from a flowing well. The Vinsome-Westerveld method treats heat exchange between a reservoir and adjacent cap and base rocks by means of a hybrid numerical-analytical method, in which temperature distributions in the conductive domain are approximated by simple trial functions, whose parameters are obtained concurrently with the numerical solution for the flow domain. This method can give a very accurate representation of conductive heat transfer even for non-monotonic temperature variations over a broad range of time scales. The only enhancement needed for applying the method to wellbore heat transmission is taking account of the cylindrical geometry around a flowing well, as opposed to the linear flow geometry in cap and base rocks. We describe the generalization of trial functions needed for cylindrical geometry, and present our implementation into the TOUGH2 reservoir simulator. The accuracy of the method is evaluated through application to non-isothermal flow through a pipe.

INTRODUCTION

The components of a hot dry rock (HDR) geothermal reservoir include injection and production wells, and a network of fractures at a depth where sufficiently high temperatures are encountered, nominally around 200 °C or more, to permit electricity generation from the produced fluids at a "reasonable" level of thermodynamic efficiency. The wells not only convey fluid

to and from the deep, hot fracture system, but due to their large surface area form an important part of the total heat exchange system. For an 8" well ($r \approx 0.1$ m), surface area is 628.3 m² per km depth, so that for a 4 km deep production-injection system, total surface area is more than 5,000 m², a number that approaches heat transfer areas of major fractures.

The migration of fluids through a permeable domain coupled with heat transfer to or from adjacent rocks of low permeability is a common problem in reservoir engineering. In addition to heat transmission between a wellbore and surrounding formations (Ramey, 1962; Wu and Pruess, 1990), examples include non-isothermal fluid injection into a permeable layer sandwiched between impermeable formations (Lauwerier, 1955), and non-isothermal injection into fractured reservoirs (Pruess and Bodvarsson, 1984; Pruess and Wu, 1993). In many cases rock permeability may be negligibly small for the time scales considered, and the problem can be reduced to solving a heat conduction equation in the low-permeability domain. This can be easily accomplished by means of finite differences or other space-discretized techniques, but at considerable computational expense. Analytical and semi-analytical treatments have been presented in the literature that use various simplifying assumptions. The classical treatment of Ramey (1962) provides a good approximation for the longer-term quasi-steady heat exchange between wellbore fluids and surrounding formations. Wu and Pruess (1990) obtained an analytical solution in Laplace space that accurately represents transient heat transfer effects in layered formations. The goal of the work presented here is to develop a simple treatment for the heat conduction problem around a pipe of cylindrical cross section that can accurately represent transient effects at early times, and is readily interfaced with a numerical solution approach for the permeable domain.

THE METHOD OF VINSOME AND WESTERVELD

Vinsome and Westerveld (1980) developed a semi-analytical approach for the problem of non-isothermal fluid injection into a permeable layer that is sandwiched between impermeable base and cap rocks. Their method greatly simplifies the heat conduction problem, while providing satisfactory accuracy. Vinsome and Westerveld considered that heat conduction perpendicular to the conductive boundary will be more important than parallel to the boundary. Noting that heat conduction will tend to wipe out sharp temperature differences, they suggested that the temperature profile in the conductive domain may be approximated by means of a simple trial function that contains a few adjustable parameters. More specifically, they proposed that the temperature profile in the cap or base rock may be represented by a low-order polynomial with an exponential tail, as follows.

$$T_{\text{lin}}(x, t) - T_i = (T_f - T_i + px + qx^2)\exp(-x/d) \quad (1)$$

Here, $T_{\text{lin}}(x, t)$ is the temperature at time t and distance x from the conductive boundary, T_i is the initial temperature in the conductive domain (assumed uniform in the direction perpendicular to the boundary), T_f is the time-varying temperature at the conductive boundary, p and q are time-varying fit parameters, and d is the penetration depth for heat conduction, given by

$$d = \sqrt{\Theta t}/2 \quad (2)$$

where $\Theta = \lambda/\rho C$ is the thermal diffusivity, λ the thermal conductivity, ρ the density of the medium, and C the specific heat.

In the context of a finite-difference simulation of nonisothermal flow, each grid block at the conductive boundary will have an associated temperature profile in the adjacent impermeable rock given by Equation (1). The parameters p and q are different for different grid blocks and are determined concurrently with the flow simulation from the following physical constraints: (1) temperatures throughout the conductive domain must satisfy a heat conduction (diffusion) equation, and (2) cumulative heat flow across the boundary must equal the change of thermal energy in the conductive domain. Numerous test calculations have shown the Vinsome-Westerveld technique to provide excellent accuracy for conductive heat exchange, even under conditions of non-monotonic temperature variations in the fluid flow domain (Vinsome and Westerveld, 1980; Pruess and Wu, 1993).

EXTENSION TO HEAT CONDUCTION AROUND A WELL

Here we propose to adapt the Vinsome-Westerveld method for the problem of conductive heat transfer in the region surrounding a wellbore. The general concept involves representing the wellbore itself as a 1-D feature that is discretized into grid blocks in the direction of flow, while heat transfer perpendicular to the wellbore is treated by a semi-analytical technique. Depending on depth and prevailing geothermal gradients, each wellbore grid block would have a different initial temperature T_i associated with it. The main difference in comparison to the system investigated by Vinsome and Westerveld is in the geometry for heat transfer, which is linear for their base and cap rock problem, while it is cylindrical in the region surrounding the wellbore. Total rate of heat flow at distance x from the conductive boundary is given by

$$G(x) = -A(x)\lambda \nabla T \quad (3)$$

where the cross-sectional area for heat transfer is $A(x) = A_0 = \text{const.}$ for the linear case, while it is $A(x) = 2\pi r h$ in the case of a wellbore segment of length h . Here, $r = r_0 + x$ is the radial distance from the center of the wellbore and r_0 is the wellbore radius. For small x , the leading term in the temperature gradient derived from Eq. (1) involves an exponential tail multiplied by a constant. This will provide a leading term for conductive heat flow, Eq. (3), that in the linear case also involves an exponential tail with a constant coefficient. In the cylindrical case, however, the leading term will involve an exponential tail multiplied by radial distance r , which means that total heat flow would increase with distance from the boundary, which is unphysical. To better account for heat transfer in the radial flow geometry around a wellbore, we therefore propose to use a modified temperature trial function T_{rad} that is defined as follows,

$$T_{\text{rad}}(x, t) - T_i = \frac{r_0}{r} (T_{\text{lin}}(x, t) - T_i) \quad (4)$$

where $x = r - r_0$ measures the distance from the conductive boundary. This form maintains proper limiting behavior $T_{\text{rad}} \implies T_f$ for $r \implies r_0$ and $T_{\text{rad}} \implies T_i$ for $r \implies \infty$, and will provide a leading term proportional to $1/r$ in ∇T , which will cancel the r -coefficient in the cross-sectional area. For modeling conductive heat exchange around a cylindrical pipe, we have incorporated Eq. (4) in our TOUGH2 code (Pruess et al., 1999). The coefficients p and q in Eq. (4) are determined concurrently with the flow simulation as in the linear case by requiring that (a) temperatures at the conductive boundary satisfy a heat conduction equation,

$$\frac{\partial T_f}{\partial t} = \Theta \left. \frac{\partial^2 T_{\text{rad}}}{\partial x^2} \right|_{x=0} + \Theta \left. \frac{\partial T_{\text{rad}}}{\partial x} \frac{\partial \ln A}{\partial x} \right|_{x=0} \quad (5)$$

and (b) the rate of change of thermal energy in the conductive domain is equal to the rate of conductive heat loss at the boundary,

$$\frac{d}{dt} \int_{r_0}^{\infty} \rho C T_{\text{rad}} dV = -2\pi r_0 h \lambda \left. \frac{\partial T_{\text{rad}}}{\partial r} \right|_{r=r_0} \quad (6)$$

EXAMPLE

As a demonstration and test of the method, we consider non-isothermal flow along a 1 km long pipe of $r = 0.1$ m radius. To better focus on the heat transfer problem, we leave out initial temperature and pressure gradients, i.e., we assume that the pipe is horizontal. The impermeable medium surrounding the pipe is assumed at a uniform initial temperature of $T = 200$ °C, and the following typical values are chosen for thermal parameters: conductivity $\lambda = 2.1$ W/m °C, density $\rho = 2650$ kg/m³, and specific heat $C = 1000$ J/kg °C. These parameters result in a thermal diffusivity of $\Theta = \lambda/\rho C = 0.80 \times 10^{-6}$ m²/s. The pipe is discretized into 50 segments of 20 m length. Fluid at a temperature of 30 °C is injected at one end at a constant rate of 5 kg/s; at the other end of the pipe pressures are maintained constant at the initial value of 100 bar. For comparison, the same problem is run with a fully numerical approach, using a radial grid of 48 blocks around each of the pipe segments, for a total of 2,450 blocks. Radial discretization is very fine near the pipe, starting with $\Delta r = 4$ mm, becomes coarser at increasing radial distance, and extends to a large outer radius of $r = 100$ m so the system will be infinite-acting for the time periods considered. The numerical solution is considered highly accurate and serves as a benchmark against which the accuracy of the semi-analytical method can be ascertained. All simulations were done with the TOUGH2 code (Pruess et al., 1999). Results are presented in Figs. 1 and 2 as temperature profiles along the pipe at different times and as time-varying temperatures at specific locations.

The semi-analytical temperature profiles are seen to be very accurate at earlier times, but accuracy is deteriorating over time. Temperatures at late time are systematically underpredicted by the semi-analytical solution. The same pattern is evident in the temperature breakthrough curves. Near the pipe inlet, where breakthrough is rapid, the semi-analytical and numerical solutions virtually coincide at all times. Near the center and towards the outlet of the pipe, temperatures agree closely to 10^5 s. Subsequently the semi-analytical temperatures trend lower than the numerical solution. From these comparisons it appears that at later time the semi-analytical solution

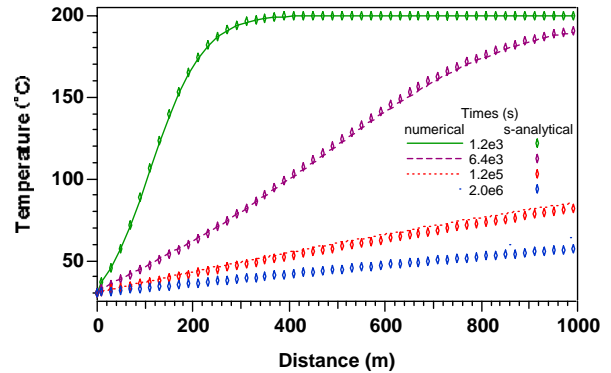


Figure 1. Temperature profiles along the pipe at different times.

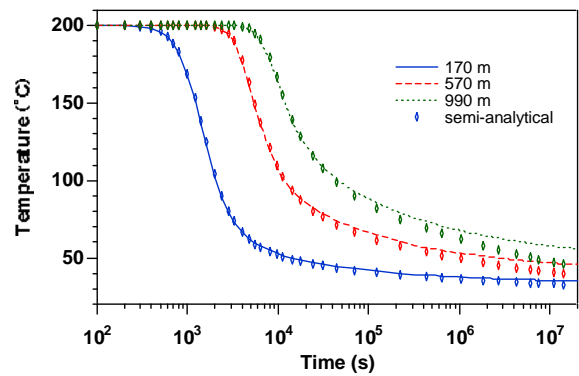


Figure 2. Thermal breakthrough curves at different distances from the pipe inlet.

underestimates the conductive heat supply to the cooling pipe.

In order to better pinpoint the limitations in the semi-analytical solution, we examine the temperature profiles in the conductive domain. Fig. 3 shows temperature profiles in the conductive domain that is attached to the first pipe segment (inlet). The numerical solutions are shown as data points at the radial distances corresponding to the nodal points in the finite difference solution; the semi-analytical profiles were calculated from Eqs. (4) and (1), using the values for the parameters p , q , and d obtained in the simulation.

From Fig. 3 it can be seen that the semi-analytical solution tends to underpredict temperatures near the pipe while overpredicting them at greater distance, with discrepancies increasing as time goes on. The semi-analytical solution systematically underpredicts temperature gradients, hence conductive heat supply, near the pipe, which explains why the semi-analytical temperatures trended too low in Figs. 1 and 2. In effect, the semi-analytical solution is taking too much heat out of the region near the pipe, and not enough from larger distance. We conclude that the trial

function proposed in Eqs. (4, 1) is adequate for early times, but for larger time scales does not allow the temperature perturbation at the conductive boundary to adequately penetrate into the interior of the conductive domain, and does not permit an adequate heat supply from larger distances.

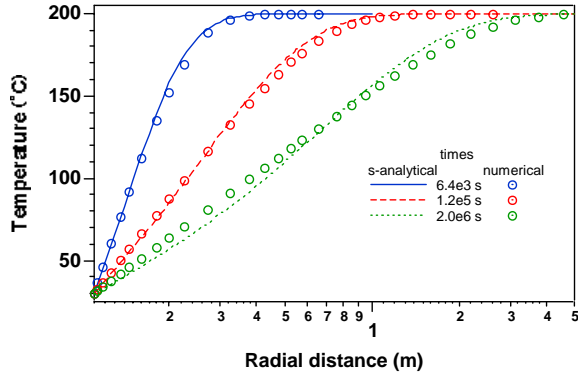


Figure 3. Simulated temperature profiles in the conductive domain surrounding the pipe inlet.

A BETTER TRIAL FUNCTION

How can the trial function be improved to deliver a more accurate description of the conductive profile for longer time? The analysis presented above suggests that a larger depth of penetration (parameter d in Eq. 1) may help to better tap into heat reserves at greater radial distance. However, calculations with a larger penetration depth, such as $d = \sqrt{\theta t}$, yielded even lower temperatures at small radial distance, while shifting the region of overpredicted temperatures to larger distance.

Fig. 4 shows numerically simulated conductive profiles at the pipe inlet at different times. It is seen that temperatures near the conductive boundary fall on a straight line in a semi-log plot, suggesting that the conduction solution for "small" r should have the form (Wu and Pruess, 2000)

$$T_{\text{rad}} = T_f + c \cdot \ln(r/r_0) \quad (7)$$

In other words, the polynomial in Eq. (1) should not be written in terms of $x = (r - r_0)$, but in terms of $(\ln r - \ln r_0)$. The physical interpretation is straightforward: differentiating Eq. (7) with respect to r delivers a temperature gradient and heat flux proportional to $1/r$, which in turn produces a constant rate of heat flow when multiplied by the flow area $A = 2\pi r h$. Heat flow rate would be expected to be essentially constant in the quasi-steady heat transfer regime at "small" r , out to a distance of approximately $\sqrt{\theta t}$ beyond the boundary (pipe surface at $r_0 = 0.10$ m). For the four times shown in Fig. 4, this amounts to distances of $r = 0.17, 0.41, 1.36,$ and 4.10 m

(measured from the center of the pipe at $r = 0$). Comparison with Fig. 4 shows that the conductive profiles at the different times indeed match straight line behavior out to those distances.

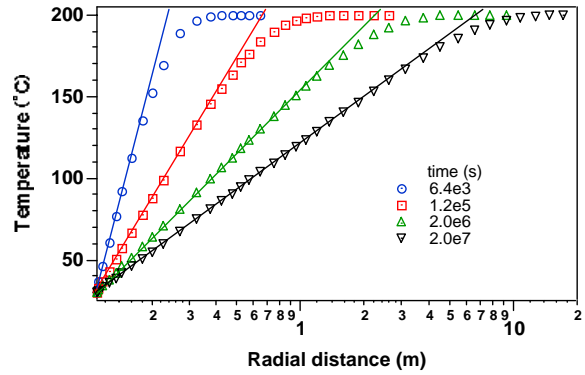


Figure 4. Numerically simulated conductive temperature profiles at different times. The straight lines are drawn to guide the eye.

Implementation of a trial function with a logarithmic expansion in terms of $(\ln r - \ln r_0)$ is currently underway. One difficulty is that for a logarithmic temperature profile it is no longer possible to evaluate the integral in the energy balance, Eq. 6, in closed analytical form.

CONCLUDING REMARKS

This paper has presented an adaptation of the semi-analytical technique of Vinsome and Westerveld (1980) to the problem of conductive heat transfer around a cylindrical pipe, such as an injection or production well. A slight generalization of the temperature trial function to account for the radial geometry, as opposed to the linear geometry considered by Vinsome and Westerveld, is sufficient to obtain an accurate treatment of conductive heat transfer for time periods of order one week. At later time the accuracy of the method deteriorates, which could be traced to the inability of the trial function to represent the quasi-steady heat transfer regime around the well that over time extends to increasing distance. Our analysis provided guidance for selecting a better trial function, computational implementation of which is currently underway.

A semi-analytical approximation for conductive heat transfer around a cylindrical pipe can find applications not only for wellbore flow, but also for non-isothermal flow in fractured media. Indeed, it is well established experimentally and theoretically that flow in heterogeneous fractures is not an area-filling phenomenon, but instead tends to proceed primarily along localized preferential pathways, or "channels" (Tsang and Tsang, 1987; Tsang and Neretnieks, 1998). The model of a cylindrical pipe may provide a

better representation of heat transfer to these pathways than the idealization of sheet flow in a homogeneous fracture.

ACKNOWLEDGEMENT

Thanks are due to Yu-Shu Wu for a review of the manuscript and the suggestion of improvements. This work was supported by the Assistant Secretary for Energy Efficiency and Renewable Energy, Office of Geothermal Technologies, of the U.S. Department of Energy under Contract No. DE-AC03-76SF00098.

REFERENCES

- Lauwerier, H.A. The Transport of Heat in an Oil Layer Caused by the Injection of Hot Fluid, *Appl. Sci. Res.*, 5, Section A (2-3), 145-150, 1955.
- Pruess, K. and G.S. Bodvarsson. Thermal Effects of Reinjection in Geothermal Reservoirs with Major Vertical Fractures, *J. Pet. Tech.*, 36 (10), 1567-1578, 1984.
- Pruess, K. and Y. S. Wu. A New Semianalytical Method for Numerical Simulation of Fluid and Heat Flow in Fractured Reservoirs, *SPE Advanced Technology Series*, Vol. 1, No. 2, pp. 63-72, 1993.
- Pruess, K., C. Oldenburg and G. Moridis. TOUGH2 User's Guide, Version 2.0, Lawrence Berkeley National Laboratory Report LBNL-43134, Berkeley, CA, November 1999.
- Ramey, H.J., Jr. Wellbore Heat Transmission, *J. Petrol. Tech.*, April 1962, pp. 427-435; *Trans.*, AIME, Vol. 225, 1962.
- Tsang, C.F. and I. Neretnieks. Flow Channeling in Heterogeneous Fractured Rocks, *Reviews of Geophysics*, Vol. 36, No. 2, pp. 275-298, May 1998.
- Tsang, Y.W. and C. F. Tsang. Channel Model of Flow Through Fractured Media, *Water Resour. Res.*, Vol. 23, No. 3, pp. 467-479, March 1987.
- Vinsome, P.K.W. and J. Westerveld. A Simple Method for Predicting Cap and Base Rock Heat Losses in Thermal Reservoir Simulators, *J. Canadian Pet. Tech.*, 19 (3), 87-90, July-September 1980.
- Wu, Y. S., K. Pruess. An Analytical Solution for Wellbore Heat Transmission in Layered Formations, *SPE Reservoir Engineering*, pp. 531-538, November 1990.
- Wu, Y.S. and K. Pruess. Integral Solutions for Transient Fluid Flow Through a Porous Medium with Pressure-Dependent Permeability, *J. Rock Mechanics and Mining Sci.*, Vol. 37. No. 1-2, pp. 51 - 61, 2000.

AN EGS STIMULATION EXPERIMENT UNDER LOW WELLHEAD PRESSURES

Peter Rose, Jess McCulloch, Mike Adams, and Mike Mella

Energy and Geoscience Institute at the University of Utah
423 Wakara Way suite 300
Salt Lake City, Utah, 84108, USA
e-mail: prose@egi.utah.edu

ABSTRACT

A stimulation experiment was conducted involving Coso injection well 34A-9 as part of the DOE-funded Coso/EGS project. When the well was first drilled, its measured temperatures were among the highest ever recorded within the Coso field, but its permeability was poor. Steam condensate was then injected into the well, resulting in significant and immediate injectivity improvements. 34A-9 was subsequently used for several years as a steam condensate injector, but was shut in due to leaks in the shallow casing. Upon repairing the liner, a second stimulation test was conducted in August 2004, again resulting in injectivity improvements. Significant microseismicity was measured in the vicinity of the well during the early stages of injection. Tracer testing was conducted during a subsequent circulation test, revealing excellent communication with a neighboring production well. The potential for mineral scaling in the reservoir adjacent to 34A-9 was simulated for injection fluids of various compositions. The maximum dissolution of silica and calcite was calculated based upon injection-fluid chemistry and injection flow rate into 34A-9 between 1999 and 2003.

INTRODUCTION

During the past three decades, a number of research efforts around the globe have been directed towards developing EGS technologies under the various titles of Hot Dry Rock, Hot Wet Rock, Deep Heat Mining, Enhanced Geothermal Systems, and Engineered Geothermal Systems. The first of these projects was conducted in the United States, followed by others in the United Kingdom, Germany, France, Japan, Sweden, Australia and Switzerland. Vuataz (2001) reviewed the EGS papers presented at the 2000 World Geothermal Congress. More recently, an extensive EGS reference database has been compiled (Vuataz and Cattin, 2004).

The east flank of the Coso geothermal field is an excellent setting for testing Enhanced Geothermal

System (EGS) concepts (see Figure 1). Fluid temperatures exceeding 300°C have been measured at depths of less than 10,000 ft, and the granitic reservoir is both highly fractured and tectonically stressed. However, some of the wells within this portion of the reservoir are relatively impermeable. High rock temperatures, a high degree of fracturing, high tectonic stresses and low permeability are the qualities that define an ideal candidate-EGS reservoir. With a grant from DOE, a team of scientists and engineers from Coso Operating Company, Geomechanics International (GMI), the Navy Geothermal Program Office, the USGS, Kansas State University, the Energy and Geoscience Institute and Q-con was formed for the purpose of developing and evaluating an approach for the creation of an EGS within the Coso east flank reservoir.

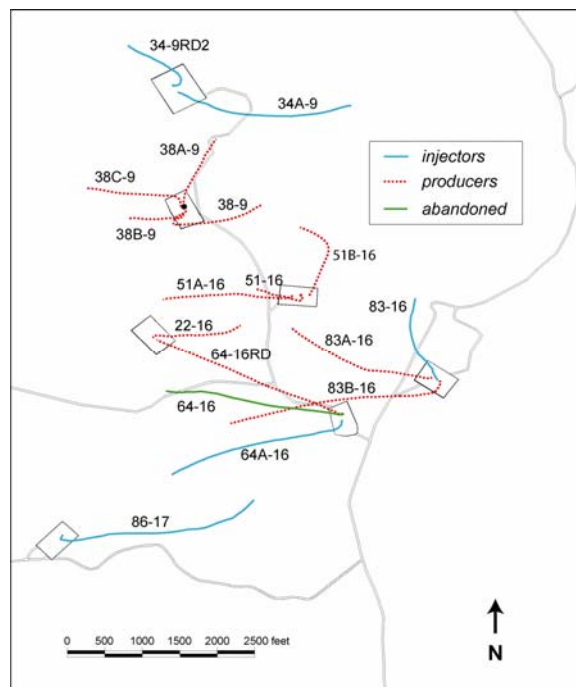


Figure 1. Locations and trajectories of wells within the east flank EGS study area of the Coso geothermal field.

PROGRAM OBJECTIVES AND APPROACH

The objective of the EGS project at Coso is to stimulate one or more low permeability injection wells through a combination of hydraulic, thermal and chemical methods and to hydraulically connect the well(s) to at least one production well. Thus, the objective is not only to design and demonstrate an EGS on the periphery of an existing geothermal reservoir, but to understand the processes that control permeability enhancement. The primary analytical tools used include borehole logs for imaging fractures and determining regional stresses, petrographic and petrologic analyses of borehole cuttings, petrophysical measurements of core samples, geophysical methods including microseismology and magnetotelluric (MT) studies, structural analysis, fluid-flow modeling, and geochemical modeling. Lessons learned at Coso will make it possible to design and create an EGS wherever appropriate tectonic, thermal and hydraulic conditions exist, thereby allowing geothermal operators to greatly extend their developmental reach beyond the relatively few naturally occurring hydrothermal resources.

This project is currently in the fourth of five years. The first year consisted of an analysis of existing data with an emphasis on characterizing the stress state of the Coso east flank and identifying candidate injection wells for hydraulic and thermal stimulation. Subsequent efforts focused on preparations for the creation of an EGS doublet between injection well 34-9RD2 and a newly drilled production well, 38C-9 (see Figure 2).

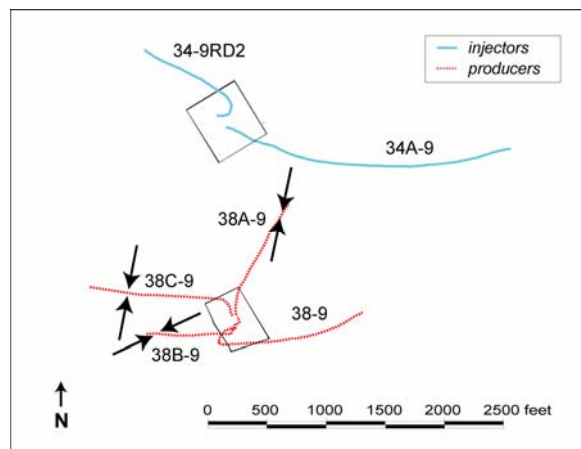


Figure 2. Plan view of the northern section of the EGS study area showing the wellhead locations and trajectories of wells 34-9 and 38-9. Also shown are the average SH_{max} azimuths for the three production wells 38A-9, 38B-9, and 38C-9 as determined from drilling induced tensile fractures imaged within the wellbores.

The injection well 34-9RD2 will be redrilled and hydraulically stimulated in 2005 (year 4) with the objective of creating permeability between it and production well 38C-9.

STIMULATION OF COSO WELL 34A-9

A stimulation experiment was conducted on Coso well 34A-9 in order to test the effects of injecting cold separated brine under high-flow, low-pressure conditions and to test many of the tools that have been developed in preparation for the hydraulic stimulation of other Coso wells.

Petrography and Petrology of Well 34A-9

Petrographic and petrologic studies of drill cuttings from Coso wells indicate that the reservoir has had a long and complex thermal history. Propagation and stimulation of fractures, particularly those that have been active during recent episodes of geothermal activity, can be expected to play a critical role in reservoir development. Thus an understanding of mineral parageneses and lithologic controls on fracturing is needed for understanding the effects of hydraulic stimulation in hot tight wells.

Analyses of thin sections and fluid inclusion measurements indicate that faults that were recently conductive can be distinguished from older, sealed faults. These studies have documented an early widespread episode of quartz, epidote and chlorite mineralization related to regional metamorphism of dioritic basement rocks that was followed by the intrusion of granitic rocks that are relatively unaltered and only weakly fractured. Younger veins related to recent geothermal activity and recharge by meteoric waters are dominated by minor quartz and later blocky calcite and hematite. It is possible that the calcite-filled fractures will preferentially fail in shear and become hydraulically conductive during stimulation experiments. However, shear failure itself does not guarantee subsequent increased permeability, since some faults may reseal upon failing in shear.

Careful petrographic and petrologic analyses were conducted on cuttings obtained during the drilling of well 34A-9. Shown in Figure 3 is a summary of rock type and vein mineralogy as a function of depth for injection this well. The rock in the deeper, more relevant portion of the well (between about 6,000 and 9,000 ft) consists mostly of biotite-granodiorite and hornblende-biotite-quartz-diorite, interspersed with minor sequences of metasediments and granite.

Injection History of Coso Well 34A-9

34A-9 was drilled to a depth of approximately 9,000 ft in 1993 with the trajectory shown in Figure 2.

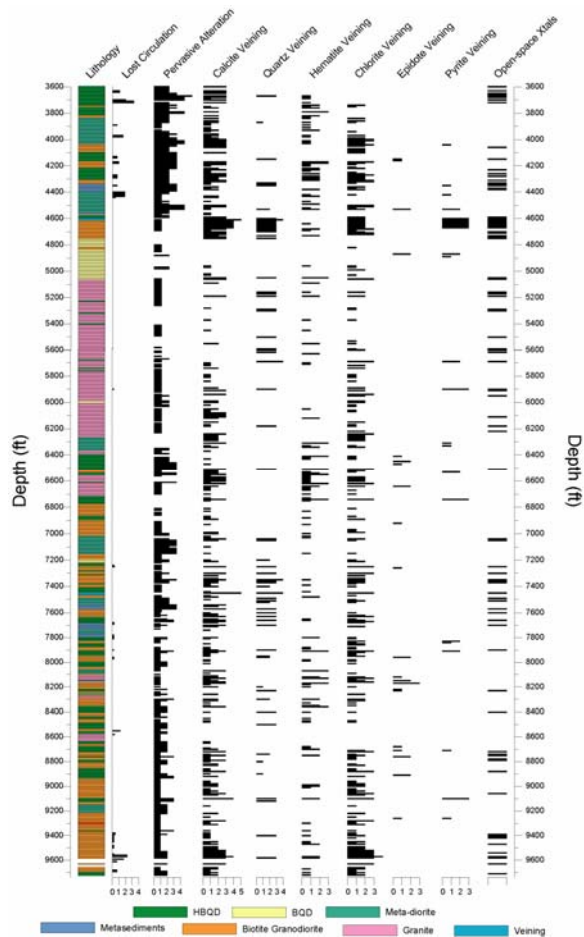


Figure 3. Summary of rock type and vein mineralogy as functions of depth for injection well 34A-9.

The well was drilled into the hottest portion of the East Flank but had low productivity due to low permeability. Coso Operating Company then conducted a series of low pressure stimulation experiments with the intent of increasing the productivity of the well. They injected cold condensate intermittently over a period of approximately two weeks. At the beginning of the two-week period, the well could accept only 40 gpm with a wellhead pressure of 100 psi. At the end of the period, the well was accepting 800 gpm with a vacuum at the wellhead. Significant microseismicity was observed during the periods of injection.

34A-9 was then allowed to flow and its output was determined to be approximately 3 MWe. Whereas this represents a very significant and successful EGS result, the study was never documented and reported in the open literature. Likewise, the operators did not record and correlate much of the associated hydraulic, petrologic, geophysical and geomechanical data.

Repair and Low-Wellhead-Pressure Stimulation of 34A-9

34A-9 was used as an injection well for several years, but was shut-in due to a leak that developed at the top of the 9 5/8" casing. As a result of the leak, most of the injected fluid entered the reservoir at shallow depths rather than at greater depths where it was needed to provide reservoir-pressure support. It was therefore necessary to cement a 7-in casing 'tie-back' across the top of the 9 5/8" liner. The well would then be subjected to a series of tests to determine if injection of cold brine under low wellhead pressures could produce sufficient permeability to allow 34A-9 to be returned to service as an injection well. The well would be considered successfully stimulated if it could sustain an injection flow rate of at least 750 gpm with a wellhead pressure of 100 psi or less.

A stimulation experiment was conducted in 34A-9 in August, 2004 for the purpose of evaluating the effect of low-pressure injection on changes in permeability. Since the fluid level in 34A-9 was drawn down before the initiation of the experiment by approximately 3,000 ft, simply filling the wellbore would result in downhole pressure increasing by approximately 1300 psi. If some of the fractures intersected by the 34A-9 wellbore were optimally oriented and critically stressed, then such an increase in downhole pressure would result in shear failure with concomitant increases in permeability.

Prior to the initiation of the test, a helium-filled capillary tube was inserted into the wellbore to a depth of 3500 ft for the purpose of measuring downhole pressure. Pressure was also monitored at the wellhead and within the pipeline supplying the wellhead. Separated brine at a temperature of 260°F was injected into the wellbore for one week at a rate of approximately 2,000 gpm. Brine having a temperature of 160°F was subsequently injected at a rate decreasing from about 1600 to about 800 gpm over approximately five weeks. Significant microseismicity accompanied the injection experiment (Julian et al., 2005).

These data show that significant permeability improvements can be realized in wells stimulated under mild conditions. The stated objective of achieving 750 gpm at less than 100 psi wellhead pressure was achieved by a large margin. It must be noted, however, that the stimulation experiment summarized in this section was preceded by long periods of injection of steam condensate between 1994, when the well was first stimulated, and August of 2004, when the second stimulation experiment was conducted.

Tracer Testing of the Newly Stimulated 34A-9

In order to determine the fate of fluids injected into the newly stimulated 34A-9, a tracer test was initiated on 1 September, 2004. In this test, 100 kg of the tracer 1,3,6-naphthalene trisulfonate was injected as a pulse. The neighboring liquid-producing east flank wells were subsequently sampled and analyzed for the tracer. Figure 4 shows a plot of 1,3,6-naphthalene trisulfonate returns to the sampled wells. The return curve confirms that the stimulation of 34A-9 resulted in a very strong hydraulic connection to the neighboring well 38-9, with a slower but significant and building return to 38A-9.

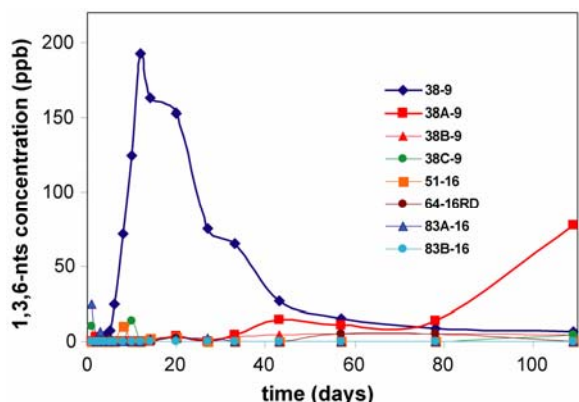


Figure 4. Tracer returns from tagged injection well 34A-9 to several Coso east-flank production wells.

Precipitation and/or Dissolution upon Injection

The scaling potential of various water compositions injected into 34A-9 was evaluated. A scenario was modeled in which each of four different waters—groundwater, acidified brine, a brine-condensate mixture, and steam condensate—was mixed with reservoir water. The heating of the mixtures to reservoir temperatures was simulated using the reaction path modeling program REACT (Bethke, 1994). Reservoir water was titrated into the injectate while the temperature was raised from 100° to 275°C. The final ratio of injected to reservoir water was 1:1. More details of these simulations are given in Adams et al. (2005).

Figure 5 shows the maximum amount of scale that would form from acidified brine (Fig. 5b) if quartz precipitated at temperatures below 200°C. However, quartz is slow to precipitate at these temperatures (Rimstidt and Barnes, 1980). Amorphous silica is more likely, but the practice of acidifying injectate at Coso is designed to delay precipitation of this mineral until temperatures are reached at which the fluid is less saturated in amorphous silica. This applies to brine-condensate mixtures and pure condensate as well (Figs. 5c and 5d, respectively).

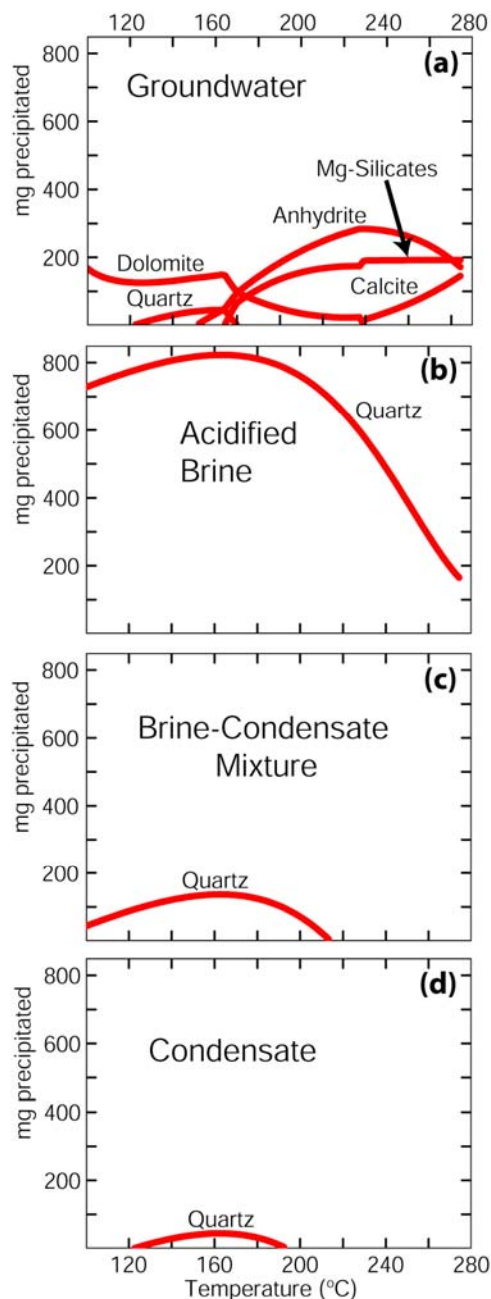


Figure 5. Chemical simulation in which different injectate compositions are mixed with reservoir water while being heated. Quartz precipitation is shown for comparison, although its actual precipitation is chemically inhibited.

Groundwater would clearly produce the most scale because of its relatively high concentrations of Ca, Mg, and SO_4 (Fig. 5a). Precipitation from groundwater injected into the Coso field is discussed further in Adams et al. (2005).

These simulations do not consider reaction of injectate with reservoir vein minerals. Dissolution of minerals along fractures was examined using a very simple model in which the maximum solubilities of calcite and quartz were calculated using REACT. The amount of mineral that could be dissolved was then calculated from the difference between the maximum-solubility concentrations and the measured calcium and silica concentrations in the injectate. The resulting concentrations were combined with flow rate data and integrated over the range of available data, which span the years 1999-2003 (Figure 6).

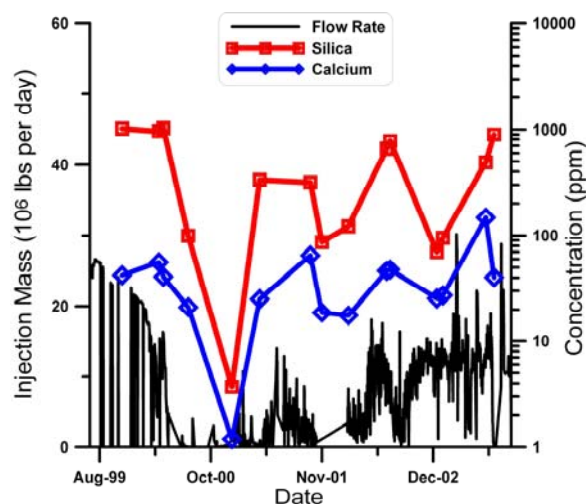


Figure 6. Injection data for well 34A-9 between 1999 and 2003. The black line shows the injectate flow rate, whereas the red and blue curves indicate the concentrations of silica and calcium in the injectate, respectively.

These calculations indicate that the waters may have dissolved as much 170 m^3 of quartz and 60 to 190 m^3 of calcite during the four years. The quantity of quartz dissolved is almost certain, since it does not depend on pH or the temperature gradient near the injection well. Calcite dissolution, in contrast, is very dependent on the temperature gradient near the well bore and the amount of mixing with reservoir water. It will dissolve near the well bore because of its retrograde solubility and then deposit away from the wellbore as temperature increases (Durst and Vuataz, 2001). Quartz, in contrast, will dissolve continuously as the water heats, but the amount will be greatest at the higher temperatures because of the logarithmic dependence of the solubility on temperature. Thus, dissolution of calcite may have the greater effect on increasing injectivity because of its proximity to the well bore, even though a greater volume of quartz is dissolved.

SUMMARY AND CONCLUSIONS

A stimulation experiment was conducted on Coso injection well 34A-9 as part of the DOE-funded Coso/EGS project. Significant improvements in injectivity resulted from this stimulation, which was achieved under low wellhead pressure. Microseismicity was measured in the vicinity of the well during the early stages of injection, with many of the earthquakes occurring between the 34A-9 and an adjacent well 38-9. A tracer test was conducted during a subsequent circulation test, revealing that excellent hydraulic communication had been established between these two wells. A petrographic and petrologic study was conducted on 34A-9 for the purpose of identifying rock types and alteration mineralogy.

The potential for mineral scaling in the reservoir adjacent to 34A-9 was simulated for injection fluids of various compositions. Groundwater would clearly produce the most scale because of its relatively high concentrations of Ca, Mg, and SO_4 . The maximum dissolution of silica and calcite in the reservoir adjacent to 34A-9 was modeled based upon injection-fluid chemistry and injection flow rate into 34A-9 between 1999 and 2003. These calculations indicate that the waters may have dissolved as much 170 m^3 of quartz and between 60 to 190 m^3 of calcite during the four years.

ACKNOWLEDGEMENTS

This project was supported by the U.S. Department of Energy Office of Energy Efficiency and Renewable Energy under Cooperative Agreement DE-FC07-01ID14186. This support does not constitute an endorsement by the U.S. Department of Energy of the views expressed in this publication.

REFERENCES

- Adams, M.C., Moore, J.N., Bjornstad, S., McCulloch, J. and Buck, C., 2005. Fluid-mineral equilibria and injection in EGS - effect of injecting groundwater, Thirtieth Workshop on Geothermal Reservoir Engineering, Stanford University, Stanford, California.
- Bethke, C., 1994. *GWB reaction modeling guide: a user's guide to react and gplot*. Hydrogeology Program, University of Illinois.
- Durst, P. and Vuataz, F.-D., 2001. Fluid-rock interactions and geochemical modelling of the formation brine in the fissured reservoir of Soultz-sous-Forêts HDR test site. N° UE JOR3-CT98-0313, Centre of Hydrogeology, University of Neuchatel, Neuchatel, Switzerland.
- Julian, B.R., Foulger, G.R., and Richards-Dinger, K., 2005. Monitoring microearthquake activity and structure changes at the Coso geothermal area,

PROCEEDINGS, Thirtieth Workshop on Geothermal Reservoir Engineering, Stanford University, Stanford, California, January 31-February 2, 2005.

Rimstidt, J.D. and Barnes, H.I., 1980. The kinetics of silica-water reactions. *Geochemica et Cosmochimica Acta*, 44: 1683-1699.

Vuataz, F.D. 2001. Review of the papers on HDR and Enhanced Geothermal Systems presented at the World Geothermal Congress 2000 in Japan: <http://www.dhm.ch/dhm-downloads.html>

Vuataz, F.D. and Cattin, S. 2004. The EGS_REF.enl EGS database on EndNote6: <http://www.dhm.ch/dhm-downloads.html>

SORBING TRACERS - A POTENTIAL TOOL FOR DETERMINING EFFECTIVE HEAT TRANSFER AREA IN HOT FRACTURED ROCK SYSTEMS

Chao Shan and Karsten Pruess

Earth Sciences Division, Lawrence Berkeley National Laboratory
Berkeley, CA 94706, U.S.A.
e-mail: c_shan@lbl.gov

ABSTRACT

A key parameter controlling the performance and lifetime of a Hot Fractured Rock (HFR) reservoir is the effective heat transfer area between the fracture network and the matrix rock. In a vapor-dominated system, this area can be estimated by conducting a tracer test of non-adsorptive chemical, based on the unique signature of a long tail in a typical tracer breakthrough curve (BTC) due to diffusion of tracers between fractures and matrix rocks. The tailing strength increases systematically with the fracture-matrix interface area. In a water-dominated system, however, aqueous phase diffusivities are too small to generate a meaningful tail in the BTC of an inert solute tracer. Recent numerical studies have shown that reversible tracer sorption on matrix rocks will enhance tailing in BTCs for aqueous solutes in fracture-matrix systems. In this paper we develop an analytical solution to theoretically explore such a useful phenomenon. In deriving the solution, we used a boundary condition of a finite-length tracer slug, and neglected the diffusion along fractures. The solution shows that in a water saturated fractured rock system, increase of the retardation factor (that is practically manageable) should have the same effect on BTCs as increase of the diffusion coefficient (that is practically restricted). The strong enhancement in the BTC tails of sorbing tracers provides adequate sensitivity for determining the heat transfer area. The solution is useful for understanding transport mechanisms, verifying numerical codes, and for identifying chemicals with appropriate sorption properties as tracers for the characterization of a fractured reservoir.

INTRODUCTION

Fluid flow and chemical transport in fractured porous media has been a research topic for decades. The topic is important because many geologic formations are fractured to some extent. The topic is also difficult because fracture networks can have quite different geometry (such as the direction, aperture, and density of fracture sets, and the number of

fracture sets), which has significant impact on flow and transport processes. Thus, it is crucial to obtain a clear geometric picture of a fractured reservoir before developing it for energy extraction. For example, in the design and operation of hot fractured rock (HFR) reservoirs, it is very important to estimate the heat transfer area between the fracture network and the matrix rock. An effective way to obtain this geometric information is to conduct an appropriate tracer test. Extensive studies on tracer transport in fractured porous media have been conducted in the context of nuclear and chemical waste disposal (e.g., Moreno, et al., 1996; Polak, et al., 2003). Based on these studies, mathematical models have been developed for analyzing tracer test data. Since a naturally fractured reservoir is usually very complex, an appropriate numerical code is usually needed.

However, numerical codes must be verified against analytical solutions before application to practical problems. Analytical solutions for contaminant transport in fractured porous media were available as early as the early 1980s (Tang et al., 1981; Sudicky and Frind, 1982). The former paper is for a single fracture where the matrix is assumed to extend to infinity away from the fracture. The later paper is for the case of a set of parallel fractures with uniform fracture spacing and identical concentration at the entrance of the fractures. In both solutions the authors assumed a constant concentration at the fracture entrance. In a tracer test, however, this assumption is usually invalid. Instead, we may assume a slug-like flux boundary condition at the fracture entrance. More recently, Moridis (2002) developed semianalytical solutions for radioactive or reactive solute transport in variably fractured layered media. Here we develop a solution for a slug tracer test in a fractured rock under single-phase flow conditions, using some simplifying assumptions.

THEORY

To simplify the problem, we assume that the system has a single set of plane, parallel fractures with a uniform fracture spacing, $2B$ [L], and a uniform

fracture aperture, $2b$ [L]. We also assume that the tracer injection is uniformly distributed at each fracture entrance. Tracer concentration applied at the fracture entrance is denoted by C_0 [M/L³]. Taking advantage of the symmetry, we can restrict the solution to an elementary part of the system (one-half of a fracture and one-half of its adjacent matrix block) as shown in Figure 1. The z -axis is in the direction of the fracture, while the x -axis is perpendicular to the interface, pointing away from the fracture (Figure 1). The fracture is thus in the domain $-b \leq x \leq 0$ and $0 \leq z < \infty$; and the matrix is in the domain $0 \leq x \leq B$ and $0 \leq z < \infty$. The solid lines in Figure 1 represent zero-mass-flux boundaries.

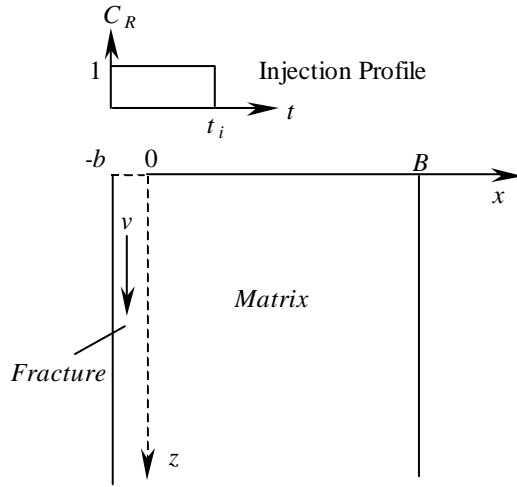


Figure 1. Schematic section of an elementary part of the parallel-fracture matrix system.

The aperture is assumed much smaller than the length of the fracture, and transport in the fracture is assumed one-dimensional along the fracture. The diffusive mass flux across the fracture-matrix interface is treated as a sink term in the mass conservation equation for the fracture. We neglect any advective flow across the interface. By this assumption, there is no advection in the matrix; and mass transport in the matrix is only through diffusion perpendicular to the fracture-matrix interface. We ignore diffusion and adsorption inside the fracture, as well as any tracer decay. Reversible sorption in the matrix is accounted for by a retardation factor. Based on these assumptions, we use the following governing equations simplified from Sudicky and Frind (1982):

$$\frac{\partial C_R}{\partial t} + v \frac{\partial C_R}{\partial z} + \frac{q}{b\phi C_0} = 0 \quad (z \geq 0) \quad (1a)$$

$$\frac{\partial C_R'}{\partial t} - \frac{D'}{R'} \cdot \frac{\partial^2 C_R'}{\partial x^2} = 0 \quad (0 \leq x \leq B) \quad (1b)$$

where C_R and C_R' (both dimensionless) are the relative solute concentrations in the fracture and the matrix, respectively, which are defined by:

$$C_R = C / C_0; \quad C_R' = C' / C_0 \quad (1c)$$

Here C [M/L³] and C' [M/L³] represent the chemical concentrations in the fracture and matrix, respectively.

In (1a) and (1b), t [T] is time, v [L/T] the groundwater velocity in fracture, q [M/L²/T] the diffusive mass flux across the fracture-matrix interface, ϕ the intrinsic porosity of the fracture, D' [L²/T] and R' the diffusion coefficient and retardation factor of the matrix, respectively. Both C_R and q are functions of z and t , i.e. $C_R(z, t)$ and $q(z, t)$. The relative concentration in the matrix, C_R' , depends on the migration distance in the fracture, z , as a parameter through the interface boundary conditions; in (1b) it is an explicit function of x and t only.

The following formulae are provided for estimating some parameters:

$$D' = \tau D^* \quad (2a)$$

$$R' = 1 + K_m \rho_b / \phi' \quad (2b)$$

where τ is the tortuosity of the matrix; D^* [L²/T] is the chemical molecular diffusion coefficient in water, typically of order 10^{-9} m²/s; and K_m [L³/M] is the matrix distribution coefficient (Freeze and Cherry, 1979). In (2b) ρ_b [M/L³] and ϕ' are the bulk mass density and the porosity of the matrix, respectively.

We assume an initially solute-free condition, i.e., the chemical concentrations in the fracture and matrix are both zero at the beginning:

$$C_R(z, 0) = C_R'(x, 0) = 0 \quad (3)$$

Setting $t = 0$ at the start time of tracer injection, and assuming an injection period t_i [T], the boundary conditions for the fracture are:

$$C_R(0, t) = 1 \quad (0 < t < t_i); \quad C_R(0, t) = 0 \quad (t > t_i) \quad (4a)$$

$$C_R(\infty, t) = 0 \quad (4b)$$

One boundary condition for the matrix is:

$$\left(\frac{\partial C_R'}{\partial x} \right)_{x=B} = 0 \quad (5)$$

At the fracture-matrix interface, we must have:

$$C_R(z, t) = C_R'(0, t) \quad (6a)$$

$$q = -\phi' D' C_0 \left(\frac{\partial C_R'}{\partial x} \right)_{x=0} \quad (6b)$$

Sudicky and Frind (1982) gave a general solution for the above problem under a constant boundary concentration that is different from (4a). We obtained an analytical solution for tracer concentration in the fracture for the case of a finite slug injection as (Shan and Pruess, to be published):

$$C_R = \begin{cases} 0 & (t \leq t_T) \\ \frac{2}{\pi} \int_0^\infty \frac{e^{\varepsilon_R} \varepsilon_A}{\varepsilon} d\varepsilon & (t > t_T) \end{cases} \quad (7)$$

where ε [$T^{-1/2}$] is the integration variable, ε_R and ε_A are given by:

$$\varepsilon_R = -\frac{t_T \varepsilon}{2\sqrt{t_F}} g_2(\sqrt{t_M} \varepsilon) \quad (8a)$$

$$\varepsilon_A = \sin \left[\frac{\varepsilon^2}{2} (t_s - t + t_T) + \frac{t_T \varepsilon}{2\sqrt{t_F}} \cdot g_1(\sqrt{t_M} \varepsilon) \right] + \sin \left[\frac{\varepsilon^2}{2} (t - t_T) - \frac{t_T \varepsilon}{2\sqrt{t_F}} \cdot g_1(\sqrt{t_M} \varepsilon) \right] \quad (8b)$$

The four time parameters, t_T , t_F , t_M , and t_s are defined by:

$$t_T = z/v \quad (9a)$$

$$t_F = \frac{\phi^2 b^2}{\phi'^2 D' R'} \quad (9b)$$

$$t_M = B^2 R' / D' \quad (9c)$$

$$t_s = \begin{cases} t - t_T & (t < t_i + t_T) \\ t_i & (t \geq t_i + t_T) \end{cases} \quad (9d)$$

The two functions, g_1 and g_2 , are defined by:

$$g_1(u) = \frac{\sinh(u) + \sin(u)}{\cosh(u) + \cos(u)} \quad (9e)$$

$$g_2(u) = \frac{\sinh(u) - \sin(u)}{\cosh(u) + \cos(u)} \quad (9f)$$

RESULTS

There are four characteristic times that determine the relative concentration, C_R . Among them, the injection period, t_i is a known parameter; t_T , t_F , and t_M are three parameters representing the properties of the fractured formation. According to (9a), t_T is the tracer transit (or travel) time to the observation point. Therefore, (7) indicates that the tracer concentration

at a specified calculation point will remain at its initial value (zero) before the transit time has elapsed. This is because, by assumption, tracer transport in the fracture is through advection only. At a given point, the shape of the BTC is thus affected by two other characteristic times, t_F and t_M . According to (9b) and (9c), t_F and t_M can be thought of as two characteristic times for crossing the interface and the matrix block, respectively.

The Role of t_M

By definition (9c), t_M is the product of B squared and the ratio R'/D' , both factors originating from (1b), the governing equation for the matrix. Thus t_M affects the tracer concentration distribution in the matrix, but does not affect the tracer concentrations in the fracture in most practical applications. Physically, t_M represents a time to reach the interior no-flow boundary of the matrix through diffusion; the longer the time, the later the boundary effect will come into play. Mathematically, t_M affects the concentration in the fracture only through the two functions, $g_1(u)$ and $g_2(u)$ that are essentially a constant of unity for $u > 6$ (see Figure 2).

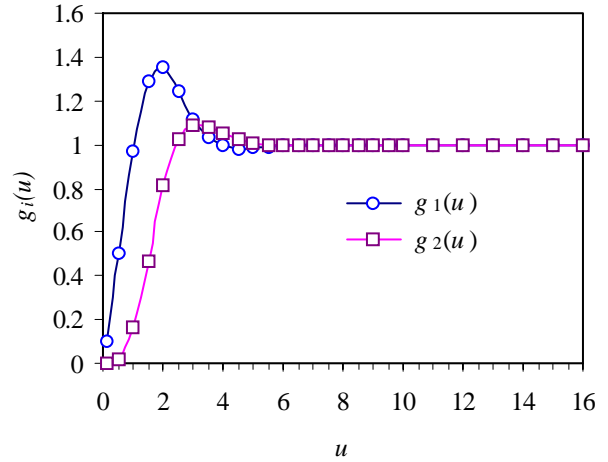


Figure 2. The functions, $g_1(u)$ and $g_2(u)$.

In other words, t_M affects the solution only in the interval $0 < \varepsilon < \varepsilon_0$ where

$$\varepsilon_0 = 6/\sqrt{t_M} = \frac{6}{B} \sqrt{\frac{D'}{R'}} \quad (10)$$

For a matrix block size of meters or larger, since $R' \geq 1$ and D' is usually less than 10^{-9} m²/s, the resulting value of ε_0 is usually on the order of or less than 10^{-4} s^{-1/2}. The integral in (7) usually has negligible contribution in the interval 0 to 10^{-4} . We used the input parameters in Table 1 to calculate the BTCs at two different locations (two different values of t_T).

Table 1. Base parameters used in Figures 3a, 3b and 4.

b (m)	t_i (s)	v (m/s)	D' (m^2/s)	ϕ	ϕ'	R'
0.005	28800	0.001	10^{-10}	1.0	0.05	1.0

At each location, we calculate the BTCs for three different values of fracture spacing ($2B$), keeping all other parameters fixed. Figures 3a and 3b show the comparisons of the calculated BTCs at a near location ($t_T = 0.5 t_i$) and a far location ($t_T = 10 t_i$), respectively. Both figures indicate that the effect of B (or t_M) is insignificant. At the near location ($t_T = 0.5 t_i$, Figure 3a), a smaller B does cause a slight increase in concentration due to the boundary effect. However, the transit time for a practical observation point is usually much larger than the injection period, t_i , which will not show such a difference.

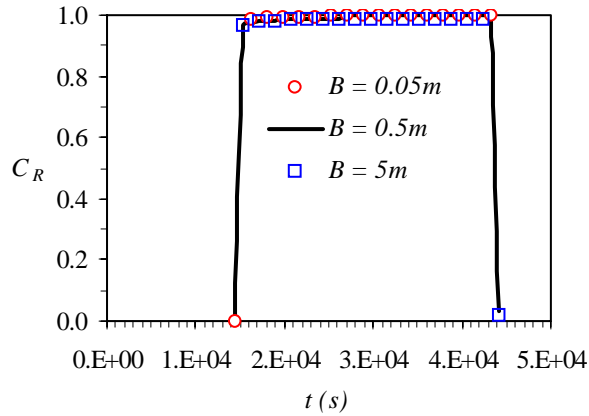


Figure 3a. Breakthrough curves for three different B values at $t_T = 0.5 t_i$.

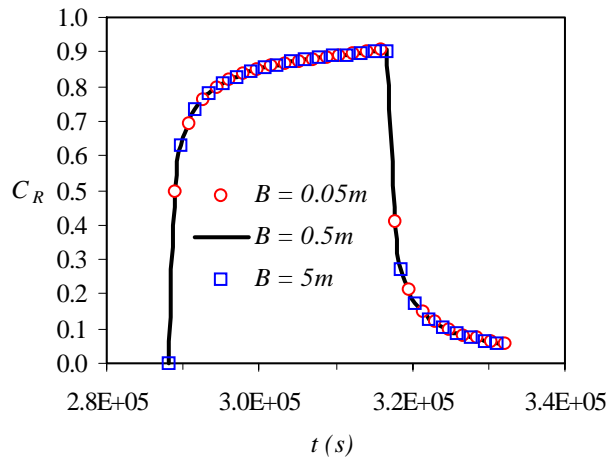


Figure 3b. Breakthrough curves for three different B values at $t_T = 10 t_i$.

In Figures 3a and 3b, the smallest B value is 5 cm. Although further decrease of B can cause larger differences in the BTC, very small B values are not of interest in practical applications. We should also remember the assumption of $B \gg b$ in deriving the solution.

The Role of t_F

In practice, the only parameter, apart from the tracer transit time t_T , which affects a fracture BTC is t_F . According to (9b), t_F depends on the matrix diffusion coefficient (D') and the retardation factor (R') only through the product $D'R'$. Therefore the impact of matrix retardation on tracer concentrations in the fracture is the same as that of an increased matrix diffusion coefficient. This equivalence of matrix retardation factor to diffusion coefficient is demonstrated in Figure 4, where the BTCs at $t_T = 50 t_i$ are calculated using three different pairs of D' and R' with a constant product ($10^{-10} m^2/s$).

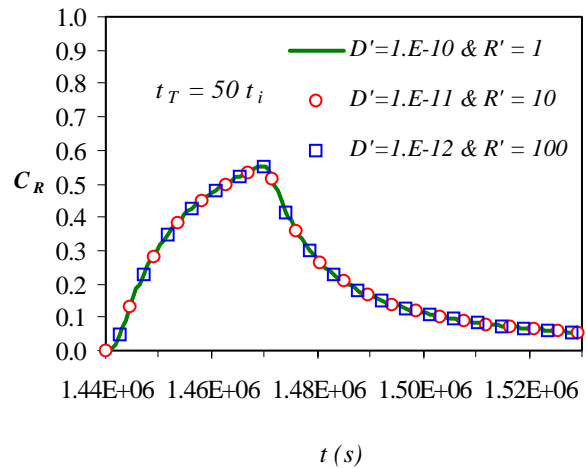


Figure 4. Breakthrough curves for three different combinations of D' (m^2/s) and R' .

The three calculated BTC curves in Figure 4 are identical because we maintained t_F a constant (10^8 s). Any reduction of t_F value implies a faster passage for tracer to enter the matrix, and thus causes a decrease of tracer concentration in the fracture during tracer injection but an increase of tracer concentration in the fracture after tracer injection.

In Figure 5, we used constant values for t_i (10^4 s), t_T (10^6 s), and t_M (10^9 s) but varied t_F (10^9 s, 10^8 s, and 10^7 s). The decrease of peak and the increase of tail of the BTC curve are both significant. For relatively large t_F (e.g., 10^9 s, or even 10^8 s), the BTC peak appears approximately at the time $t = t_T + t_i$. However, as t_F is further decreased to 10^7 s, the BTC peak appears at a time that is significantly larger than $t_T + t_i$ (Figure 5).

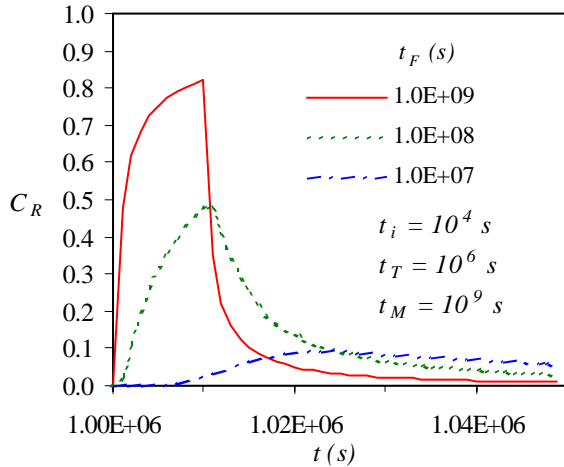


Figure 5. The effect of t_F on breakthrough curves.

Verification

TOUGH2 (Pruess, et al., 1999) is a numerical code for multiphase, multi-component flow, transport, and heat transfer problems. This code has been verified against many analytical solutions. Here we demonstrate the verification of TOUGH2 against the analytical solution (7). By using the same set of input parameters, we calculated the BTC curve at the same point in the fracture using TOUGH2 and (7). We compare the results in Figure 6.

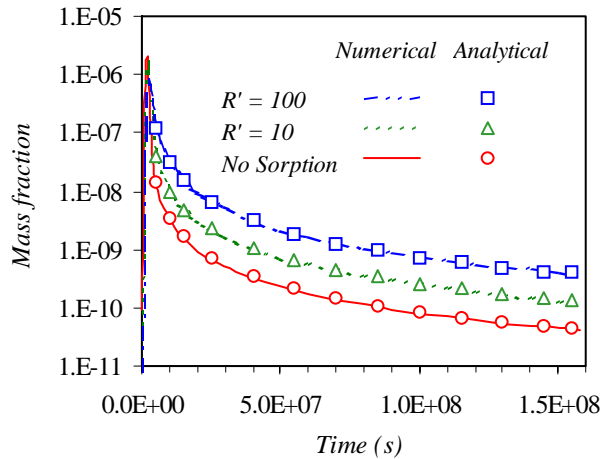


Figure 6. Comparison of the analytical solution with the numerical (TOUGH2) solution.

For three different retardation factors, the corresponding numerical and analytical solutions agree very well. Note that TOUGH2 uses “mass fraction” instead of relative concentration. The results of the analytical solution were converted to mass fraction for the comparison.

Application

Although analytical solutions are usually too idealized for actual field cases, here we offer some guidelines for the potential application to a simplified field condition, such as a one-dimensional tracer test in a horizontal fractured formation. The main purpose of application is to inversely estimate the average fracture spacing, $2B$, and from that the fracture-matrix interfacial (heat transfer) area per unit volume.

The injection period, t_i , is known; and the breakthrough time (the tracer transit time), t_T , is observed in the tracer test. A BTC can be calculated by applying the known t_i and t_T , and an assumed t_F and t_M (e.g., 10^9 s) to (7). Varying t_F , we obtain a set of BTCs. We then estimate t_F by fitting the observation data to the calculated BTCs. After t_F is estimated, we can calculate B by rewriting the definition formula, (9b) into:

$$t_F = \frac{\phi_f^2 B^2}{\phi'^2 D' R'} \quad (11)$$

where ϕ_f is the continuum (average) fracture porosity defined by:

$$\phi_f = \frac{\phi b}{B + b} \approx \frac{\phi b}{B} \quad (12)$$

For a given fracture porosity, variation of fracture spacing results in different BTC tails. Figure 7 shows the effect of fracture spacing by using $\phi'/\phi_f = 10$, $D' R' = 10^{-9}$ m²/s, and fixed values for t_i , t_T , and t_M . We see that smaller fracture spacing causes larger tracer concentration in the BTC tail.

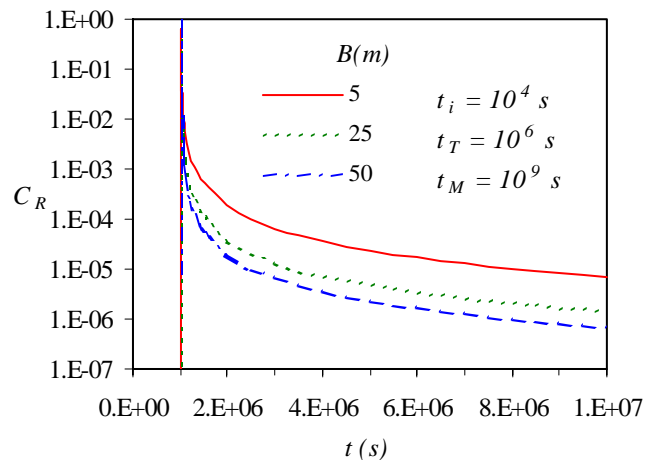


Figure 7. The effect of fracture spacing on BTC.

The fracture porosity ϕ_f can be estimated by means of the injection flux rate (q_i) and the pore velocity, v , by:

$$\phi_f = q_i / v = q_i \cdot t_T / z \quad (13)$$

The matrix porosity, ϕ' , can be estimated by laboratory tests on rock samples. The matrix tortuosity τ can be determined by laboratory tests or estimated using the Millington (1959) model:

$$\tau = (\phi')^{1/3} \quad (14)$$

Substituting this tortuosity and the known tracer molecular diffusion coefficient D^* into (2a) we obtain D' , the diffusion coefficient in the matrix. The bulk mass density, ρ_b , can be estimated by:

$$\rho_b = \rho_s (1 - \phi') \quad (15)$$

where ρ_s is the rock grain density (approximately 2650 kg/m³). The distribution coefficient of tracer in the matrix (K_m) can be determined by laboratory tests. Therefore, we can calculate the retardation factor, R' , using (2b). Finally we use (11) and obtain:

$$B = \frac{\phi'}{\phi_f} \sqrt{t_F D' R'} \quad (16)$$

The fracture-matrix interface area available for heat transfer per unit volume of the flow system is then $A/V = 1/(B + b) \cong 1/B$.

CONCLUSION

A simplified analytical solution for solute tracer migration in fractured porous media reveals some important facts. In most practical cases, the tracer concentration in the fracture is dependent on three characteristic times: the injection period t_i , the tracer transit time t_T , and the crossing-interface time t_F . The independence of the solution on another characteristic time t_M and the definition of t_F theoretically validate a new finding, namely, the retardation factor and the diffusion coefficient of the matrix have the same effect on tracer concentrations in the fracture. This equivalence provides the basis for using reversibly sorbing chemicals as tracers to test a fractured formation. The verification of a numerical code, TOUGH2, against the analytical solution demonstrates excellent agreement. The analytical solution can also be useful in selecting solutes with appropriate sorption properties, and analyzing field data under simplified conditions. Such analysis can inversely estimate the two important parameters: the average fracture porosity and fracture spacing, from which effective heat transfer area per unit reservoir volume may be obtained.

ACKNOWLEDGEMENTS

This work was supported by the Assistant Secretary for Energy Efficiency and Renewable Energy, Office of Geothermal Technologies, of the U.S. Department of Energy under Contract No. DE-AC03-76SF00098. The authors would like to thank Drs. G. Moridis, and G. Zhang for reviewing the manuscript and making constructive suggestions.

REFERENCES

- Freeze, R. A., and J. A. Cherry (1959), *Groundwater*, Prentice-Hall, Englewood Cliffs, New Jersey.
- Millington, R. J. (1959), "Gas diffusion in porous media," *Science*, 130: 100-102.
- Moreno, L., B. Gylling, and I. Neretnieks (1997), "Solute transport in fractured media – the important mechanisms for performance assessment," *J Contam. Hydrol.*, 25: 283-298.
- Moridis, G. (2002), "Semianalytical solutions of radioactive or reactive solute transport in variably fractured layered media," *Water Resour. Res.*, 38(12): 1310-1633.
- Polak, A., A. S. Grader, R. Wallach, and R. Nativ (2003), "Tracer diffusion from a horizontal fracture into the surrounding matrix: measurement by computed tomography," *J Contam. Hydrol.*, 67: 95-112.
- Pruess, K., C. Oldenburg, and G. Moridis (1999), *TOUGH2 User's Guide, Version 2.0*, Lawrence Berkeley National Laboratory Report, LBNL-43134, Berkeley, CA, November, 1999.
- Sudicky, E. A., and E. O. Find (1982), "Contaminant transport in fractured porous media: Analytical solutions for a system of parallel fractures," *Water Resour. Res.*, 18(6): 1634-1642.
- Tang, D. H., E. O. Find, and E. A. Sudicky (1981), "Contaminant transport in fractured porous media: Analytical solution for a single fracture," *Water Resour. Res.*, 17(3): 555-564.

USE OF TOUGHREACT TO SIMULATE EFFECTS OF FLUID CHEMISTRY ON INJECTIVITY IN FRACTURED GEOTHERMAL RESERVOIRS WITH HIGH IONIC STRENGTH FLUIDS

Tianfu Xu, Guoxiang Zhang, and Karsten Pruess

Earth Sciences Division, Lawrence Berkeley National Laboratory
University of California, Berkeley, CA 94720
e-mail: Tianfu_Xu@lbl.gov

ABSTRACT

Recent studies suggest that mineral dissolution/precipitation and clay swelling effects could have a major impact on the performance of hot dry rock (HDR) and hot fractured rock (HFR) reservoirs. A major concern is achieving and maintaining adequate injectivity, while avoiding the development of preferential short-circuiting flow paths. A Pitzer ionic interaction model has been introduced into the publicly available TOUGHREACT code for solving non-isothermal multi-phase reactive geochemical transport problems under conditions of high ionic strength, expected in typical HDR and HFR systems. To explore chemically-induced effects of fluid circulation in these systems, we examine ways in which the chemical composition of reinjected waters can be modified to improve reservoir performance. We performed a number of coupled thermo-hydrologic-chemical simulations in which the fractured medium was represented by a one-dimensional MINC model (multiple interacting continua). Results obtained with the Pitzer activity coefficient model were compared with those using an extended Debye-Hückel equation. Our simulations show that non-ideal activity effects can be significant even at modest ionic strength, and can have major impacts on permeability evolution in injection-production systems. Alteration of injection water chemistry, for example by dilution with fresh water, can greatly alter precipitation and dissolution effects, and can offer a powerful tool for operating hot dry rock and hot fractured rock reservoirs in a sustainable manner.

1. INTRODUCTION

A major concern in the development of hot dry rock (HDR) and hot fractured rock (HFR) reservoirs is achieving and maintaining adequate injectivity, while avoiding the development of preferential short-circuiting flow paths such as those caused by thermally-induced stress cracking. Past analyses of HDR and HFR reservoirs have tended to focus

primarily on the coupling between hydrology (flow), heat transfer, and rock mechanics. Recent chemistry studies suggest that rock-fluid interactions and associated mineral dissolution and precipitation effects could have a major impact on the performance of HFR reservoirs (Jacquot, 2000; Durst, 2002; Bächler, 2003).

High ionic strength brines are expected in typical HDR and HFR systems, for which Pitzer's ionic interaction theory (Pitzer and Mayorga, 1973; Pitzer, 1991) can be used to study ionic activity in electrolytes. Ionic strength I is defined as

$$I = \frac{1}{2} \sum_i c_i z_i^2 \quad (1)$$

where the summation is over all aqueous species, and c_i and z_i are concentration (mol/kg H_2O) and electrical charge of species i , respectively.

In this study, a Pitzer ionic interaction model was introduced into the publicly available reactive transport simulator TOUGHREACT. We explored chemically-induced effects of fluid circulation in HFR systems. We examine ways in which the chemical composition of reinjected waters can be modified to improve reservoir performance by maintaining or even enhancing injectivity. We performed coupled thermo-hydrologic-chemical simulations in which the fractured medium was represented by a one-dimensional MINC model (multiple interacting continua; Pruess and Narasimhan, 1985).

2. NUMERICAL MODELING APPROACH

2.1. Computer Code

A Pitzer ionic interaction model was introduced into the reactive geochemical transport simulator TOUGHREACT (after its release to the public through the US Department of Energy's Energy Science and Technology Software Center (<http://www.osti.gov/estsc/>). Information on

TOUGHREACT is available on the web at <http://www-esd.lbl.gov/TOUGHREACT>. Physical and chemical process capabilities and solution techniques of TOUGHREACT have been discussed by Xu and Pruess (2001) and Xu et al. (2004b). The simulator can be applied to one-, two-, or three-dimensional porous and fractured media with physical and chemical heterogeneity, and can accommodate any number of chemical species present in liquid, gas and solid phases. A general form of rate law for kinetic mineral dissolution and precipitation is used. Temporal changes in porosity and permeability due to mineral dissolution and precipitation and clay swelling can modify fluid flow path characteristics. This feedback between flow and chemistry is considered in our model. The released version of TOUGHREACT uses an extended Debye-Hückel equation after Helgeson et al. (1981) for calculating activity coefficients of aqueous species, and details are given in Xu et al. (2004b). The Pitzer ionic interaction model is described below.

2.2. The Pitzer activity model

Pitzer's ionic interaction theory (Pitzer and Mayorga, 1973; Pitzer, 1991) is often used to represent ionic activity in electrolytes. The ionic activity in electrolytes is determined by the excess free energy, mostly arising from the ionic interactions of binary ionic pairs and ternary ionic combinations in the solution. Virial equations are used to quantify the excess free energy, and then the ionic activity. Harvie and Weare (1980) and Harvie et al. (1984) developed an ion-interaction equilibrium model (HMW model) for the seawater system (Na-K-Mg-Ca-Cl-SO₄-H₂O) based on Pitzer's ionic interaction theoretical model. This model is equivalent to Pitzer's original model (Pitzer and Mayorga, 1973), but different in definition of interaction coefficients and mathematical expressions (Rard and Wijesinghe, 2003). The HMW model is practically convenient for numerical implementation. The HMW model was implemented in several computer codes: PHRQPITZ (Plummer et al., 1988), UNSATCHEM-2D (Simunek and Suarez, 1994), GMIN (Felmy, 1995), and BIO-CORE^{2D}® (Zhang et al., 2005). Pitzer's original model was implemented in EQ3/6 (Wolery and Daveler, 1992; Wolery et al., 2004), but from input HMW model parameters (through internal conversion).

The model implemented in TOUGHREACT is the standard HMW model (Harvie et al., 1984) using the database of Wolery et al. (2004), with user-options for simplifications dealing with solutions at different level of ionic strength. The most simplified version is the Debye-Hückel model that does not account for any ionic interaction terms and generally is only applicable to solutions with ionic strength less than 1 M. It has already been used in the released version of

TOUGHREACT (Xu and Pruess, 2001; Xu et al., 2004b).

The Pitzer activity model in TOUGHREACT accounts for interaction terms of cation-anion, cation-neutral, anion-neutral, cation-anion-anion, cation-cation-anion, neutral-cation-anion, neutral-cation-cation and neutral-anion-anion interaction terms. When dealing with reactive transport problems for a given solution with a pre-estimated ionic strength range, simplifications may be made for a significant saving of computational time without losing accuracy. It has been shown that with only binary (cation-anion, cation-neutral, anion-neutral) terms, the HMW model is applicable to solutions with ionic strength lower than 7 M (Zhang et al., 2005). All equations in the HMW model (Harvie et al., 1984) related to water activity, osmotic coefficient, activity coefficients of cations, anions, and neutral species are summarized in Zhang et al. (2005).

3. PROBLEM SETUP

3.1. Mineralogical Condition

We consider three different mineral assemblages (Table 1). The first represents strongly altered minerals from a highly fractured vein, and includes minerals from the original granite (mainly quartz) that are fully cemented by clays, carbonates, and secondary quartz veins. The second assemblage is composed of altered granite blocks partly cemented by alteration products that consist essentially of clay minerals and carbonates. The third is the unaltered granite in which the fracture density is close to zero. Mineral dissolution and precipitation are considered under kinetic constraints. A general kinetic rate expression is used in TOUGHREACT (Xu et al., 2004b). Kinetic parameters are taken from Xu and Pruess (2004).

Table 1. Initial mineralogical composition of the three zones used in the simulations. Data were taken from Jacquot (2000), Durst (2002), and Bächler (2003).

Mineral	Volume percentage of solid rock		
	Fractured vein Alteration	Altered granite	Unaltered granite
Quartz	43.9	4.09	24.2
K-feldspar		13.9	23.6
Plagioclase			42.5
Biotite			4.2
Hornblende			3.1
Chlorite		4.8	2
Calcite	4.3	3.3	0.3
Dolomite	0.7	0.8	
Illite	40.2	24.6	
Na-smectite	7.392	7.469	
Ca-smectite	2.208	2.231	
Pyrite	1	0.7	
Galena	0.3	1.3	
Non- reactive		36.81	0.1

3.2. Fluid flow conditions

A one-dimensional MINC (multiple interacting continua) model was used to represent the fractured rock (Figure 1). Subgrid 1 represents the fracture vein alteration, while subgrids 2 and 3 represent the altered and unaltered granite, respectively. The MINC method can resolve “global” flow and diffusion of chemicals in the fractured rock and its interaction with “local” exchange between fractures and matrix. Details on the MINC method for reactive geochemical transport are described by Xu and Pruess (2001).

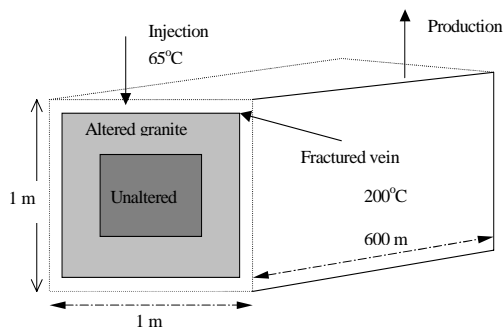


Figure 1. Subgridding of a matrix in the “multiple interacting continua” (MINC) method. The figure represents a view of a rock matrix column that is bounded by fractures.

We used an idealized fractured porous medium with two perpendicular sets of planar, parallel fractures of equal aperture and spacing. Because of the assumed symmetry only one column of matrix blocks needs to

be modeled. Our conceptual model considers a one-dimensional flow tube between injection and production well, which should be considered as a small sub-volume of a much more extensive 3-D reservoir. From the injection side to the production side, the model consists of 72 grid blocks representing 600 m distance. The block size gradually increases from 0.1 m at the injection side to 20 m at the production side.

Hydrological parameters used in the present simulations are listed in Table 2. Notice that some are different from those of Durst (2002) and Bächler (2003). For example, previous investigators used a permeability of $1 \times 10^{-11} \text{ m}^2$ and a porosity of 0.1 for the fractured vein. The objective of the present study is to explore methods for minimizing mineral scaling and clay swelling, mitigating injection water chemistry, and preserving or enhancing injectivity.

Even though we took some data from the European HDR site as a starting point, we attempted to use thermophysical conditions and parameters that could represent general geothermal reservoirs. Initial reservoir temperature and pressure were 200°C and 50 MPa, respectively. An over-pressure of 2 MPa was applied at the injection (left) side, and was held constant over time. Injected water temperature was taken as 65°C. Conductive heat exchange with the surrounding low-permeability rock is an important process, and is treated with a semi-analytical technique developed by Vinsome and Westerveld (1980). In the present simulations, chemical interactions in the unaltered granite zone were not considered. This does not significantly affect chemical changes in the fractured vein because of the extremely low permeability of the granite.

Table 2. Hydrogeologic and thermal parameters used for the three mineralogical zones (a density of 2650 kg.m^{-3} , a heat capacity of $1000 \text{ J.kg}^{-1} \text{ K}^{-1}$, and an diffusivity of $1 \times 10^{-9} \text{ m}^2 \cdot \text{s}^{-1}$ were used for all three zones).

Parameters	Fractured vein	Altered granite	Unaltered granite
Volume	10%	60%	30%
Permeability (m^2)	2×10^{-12}	2×10^{-15}	2×10^{-18}
Porosity	0.2	0.1	0.02
Thermal conductivity ($\text{W.m}^{-1} \text{ K}^{-1}$)	2.9	3	3
Tortuosity	0.3	0.1	0.05

3.3. Water chemistry

We started with a 165°C water sample taken from Soultz Well GPK1 at 3500 m depth (Table 3). Initial water chemical compositions for the fractured vein

and altered granite zones were obtained by equilibrating the sample water with their corresponding mineral compositions (Table 1) at a temperature of 200°C.

Two types of injection waters with different chemical compositions were considered in the present simulations, and were held constant over time. The first type corresponded to the native water in the fractured vein zone but with a lower temperature of 65°C, which should be close to the produced reservoir water without surface treatment (base case). The second injection water was obtained by diluting the native water by a factor of 2 (i.e., one unit of reservoir water was mixed with one unit of fresh water; mixing case).

Table 3. List of water chemical concentration (mol/l) of Soutz Well GPK1 sample (Durst, 2002). No measurements for Fe, Al, and Pb concentrations in the sample were reported, and small values were assumed for consistency because of the presence of minerals with these components.

Chemical components	Soutz Well GPK1 at 3500 m depth (165°C)
Ca	1.820×10^{-1}
Mg	4.610×10^{-3}
Na	1.213
K	7.180×10^{-2}
Fe	1.491×10^{-6}
Cl	1.72
SiO ₂ (aq)	3.500×10^{-3}
HCO ₃	7.500×10^{-3}
SO ₄	2.020×10^{-3}
Al	5.656×10^{-9}
Pb	1.000×10^{-12}
pH	5.03
I (ionic strength)	1.8834

3.4. Simulation setup

A total of four simulations were performed using the two different types of injection waters mentioned above (base and mixing cases) for each activity model, Pitzer and Debye-Hückel (DH). The native reservoir water has an ionic strength (I) equal to 1.8834, the mixing case injection water has an I of 0.9417. The minimum ionic strength I_{\min} (Eq. A.2 in Appendix A) to maintain clay density is dependent on the type of clays, type of salts dissolved in water, and temperature and pressure conditions. In the present simulations, we simply selected $I_{\min} = 1.5$, which is slightly below the I of the native reservoir water. The maximum density reduction factor f_{\max} is

also a predetermined parameter. Experiments on compacted bentonite showed that density could be reduced due to swelling by 26% (JNC, 2003). Studies conducted by Newman (1987) and de Siqueira et al. (1999) indicated that the layer spacing in dry clays is about 9.8 Å. If one assumes that the diameter of a water molecule is 2.7 Å, clay hydrates containing one, two, and three molecular layers of water will have a spacing of around 12.5, 15.2 and 17.9 Å. In the reservoir, the clay may not be well contacted by the injected water and conditions could be different from the lab. We used a maximum density reduction factor $f_{\max} = 5\%$.

The Verma and Pruess porosity-permeability relationship (Appendix B) used requires two parameters, one is the “critical” porosity ϕ_c , and the other is n, a power law exponent. In the present simulations, we used a ϕ_c of 0.16 (80% of initial porosity of 0.2 for the fractured vein), and an n of 2. A ϕ_c of 80% initial porosity is quite reasonable and may be conservative. Precipitation and dissolution of all minerals were modeled as kinetic processes.

4. RESULTS AND DISCUSSION

4.1. Base case

The 65°C injection water is under-saturated with respect to calcite because this water was in equilibrium with reservoir rock at 200°C. Significant calcite dissolves close to the injection side because calcite solubility decreases with temperature (Figure 2). As temperatures increase away from the injection point, calcite becomes over-saturated and precipitation occurs. Areas of calcite dissolution and precipitation move gradually away from the injection point due to changes in temperature along the flow path. A maximum of about 4% volume of calcite has been precipitated after three years. Dolomite also dissolves close to the injection side but later precipitates, and quartz precipitation occurs (no amorphous silica precipitation is observed for this range of temperatures). The amounts of dolomite and quartz precipitation are about one order of magnitude smaller than calcite. Some pyrite and galena precipitation, and very slight illite and smectite precipitation occur near the injection point. Notice that amounts of precipitation and the distribution depend on their precipitation kinetics.

Changes in porosity due to mineral dissolution and precipitation (mainly calcite) are presented in Figure 3. Porosity increases indicate that mineral dissolution is dominant, while porosity decreases when precipitation dominates. The dissolved ions from calcite dissolution close to the well are transported along the flow path, and then induce precipitation at further distance from the well. If we used a 1-D radial

model, calcite precipitation would spread over a much larger area than in the 1-D column model.

Figure 4 shows the time dependence of injection (flow) rate. The way in which flow gets reduced from precipitation reduces porosity towards the critical value (Appendix B). As flow rate decline, temperatures increase, causing additional calcite precipitation and further injectivity decrease. This is because calcite has retrograde solubility (is less soluble at higher temperatures), which makes this mineral prone to precipitation from reinjected waters as they are being heated in the reservoir.

Results obtained from the Pitzer and Debye-Hückel activity coefficient models are different, which can be clearly seen in Figures 2-4. In the Pitzer model, a minimum porosity due to calcite precipitation develops at 30 m from the well after three year of injection. The injection rate is close to zero (Figure 4). In actual field operation, the injection would stop before that.

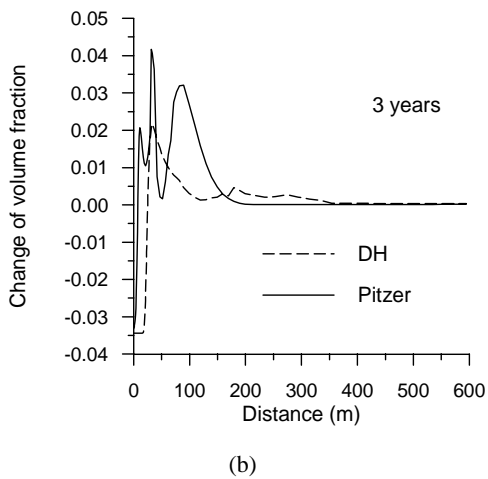
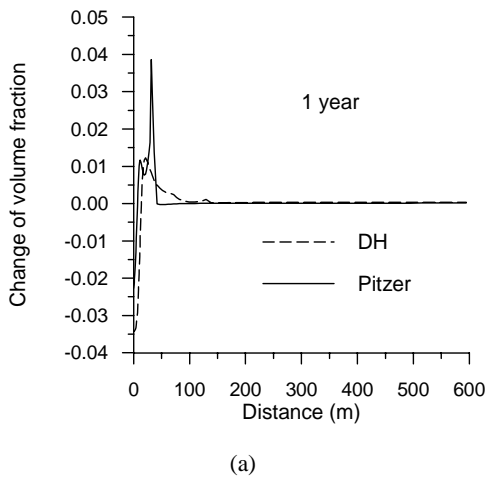


Figure 2. Changes of calcite abundance (given in reservoir volume fractions) obtained from the base case.

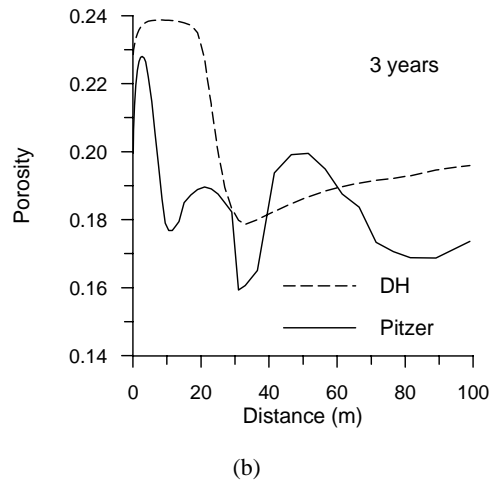
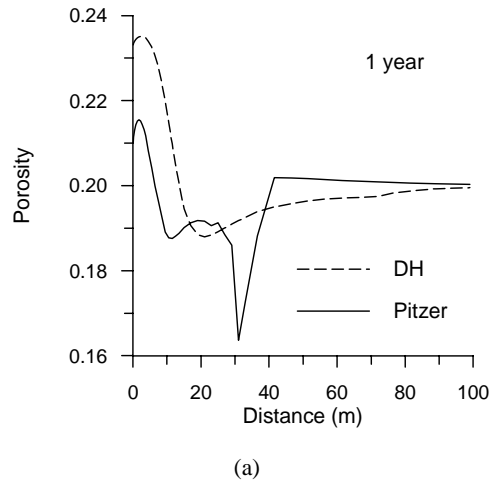


Figure 3. Distribution of porosity obtained from the base.

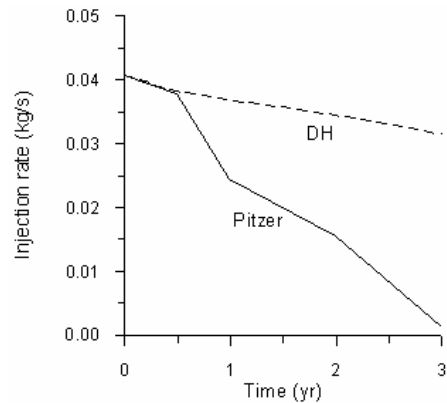
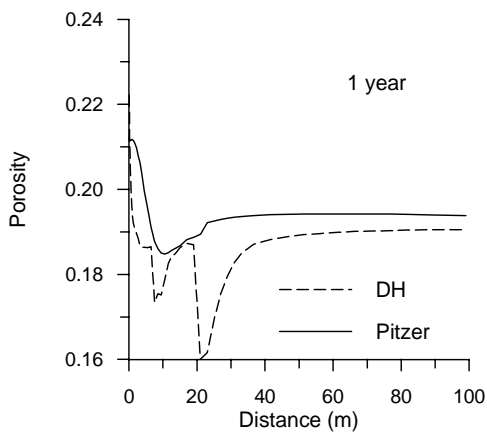


Figure 4. Injection rate (kg/s) over time of the fracture-matrix column with an area of 1 m^2 obtained from different simulations.

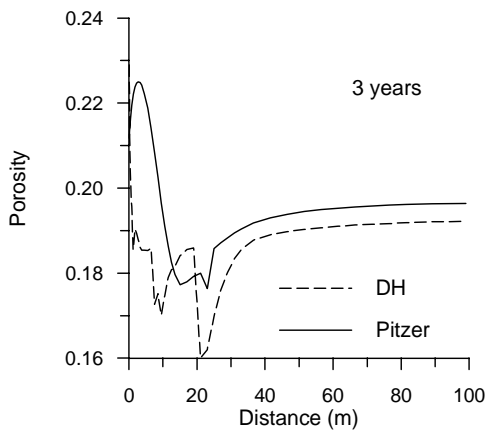
4.2. Mixing case

The mixing case injection water (with an $I = 0.93315$) causes the clay swelling that contributes a porosity decrease of about 0.01 along the entire flow path. Note that the extent of porosity decrease depends upon the minimum ionic strength I_{\min} and the maximum density reduction factor f_{\max} (Eq. A.2 in Appendix A).

For the Pitzer model, the mixing injection water is favorable for porosity development and maintaining injectivity. In contrast to the base case, the Debye-Hückel model results in a minimum porosity due to calcite precipitation at 20 m from the well after three years, and then an injection rate close to zero. Once again, we should note that if a 1-D radial model was used, calcite precipitates would spread over a larger area than in the 1-D column model, resulting in less porosity decreases.



(a)



(b)

Figure 5. Distribution of porosity obtained from the mixing case.

4.3. Discussion

For the base case with an ionic strength (I) of 1.8834, the result of the Debye-Hückel model is quite different from that of the Pitzer model. As mentioned before the Debye-Hückel model does not account for any ionic interaction terms and generally is only applicable to solutions with I less than 1 M. Figure 6 shows the measured and calculated mean activity coefficients of $NaCl$. The mean coefficient γ_{NaCl} is calculated as $\ln\gamma_{NaCl} = (\ln\gamma_{Na} + \ln\gamma_{Cl})/2$, where γ_{Na} and γ_{Cl} activity coefficients of Na^+ and Cl^- , respectively. For $I > 1$ M, the extended Debye-Hückel models deviates from the Pitzer model.

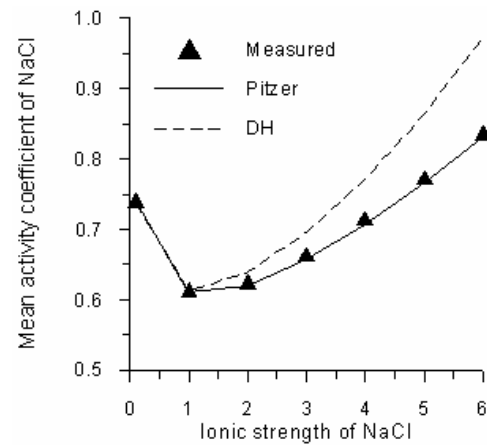


Figure 6. Mean activity coefficient of $NaCl$ vs. ionic strength of $NaCl$ solution. Measured data were taken from Colin et al. (1985)

Calcite solubility ($CaCO_3 + H^+ = Ca^{+2} + HCO_3^-$) depends on ion activities according to

$$K = \gamma_{Ca^{+2}} C_{Ca^{+2}} \gamma_{HCO_3^-} C_{HCO_3^-} / \gamma_{H^+} C_{H^+} \quad (2)$$

where K is the solubility (equilibrium) constant, C is concentration of aqueous species (mol/kg H_2O). At high ionic strength and high temperature, activity coefficients of Ca^{+2} calculated from the Pitzer model are much larger than from the Debye-Hückel. This means a lower Ca^{+2} concentration is needed to maintain calcite equilibrium or calcite is less soluble. The effect of increased Ca^{+2} activity coefficients on calcite solubility in this case is similar to the “salting out” effects for dissolution of non-condensable gases such as CO_2 .

5. SUMMARY AND CONCLUSIONS

A total of four simulations have been performed using the produced reservoir and the mixing waters for each activity model, Pitzer and Debye-Hückel. For the case of directly using the produced reservoir water, the Pitzer model predicted more calcite precipitation and a precipitation peak is developed at

30 m from the well. The mixing water causes a porosity decrease close to 0.01 due to clay swelling along the entire flow path for both models. However, the Pitzer model results in less calcite precipitation than the Debye-Hückel, indicating that calcite is more soluble at one half of the ionic strength of the reservoir water. Overall, the effect of less calcite precipitation (over clay swelling) is dominant. The Pitzer model suggests that the mixing injection water is favorable for porosity development and maintaining injectivity. We should note that if a 1-D radial model was used, calcite precipitation would spread over a much larger area than for the 1-D column model, resulting in less porosity decreases.

The Debye-Hückel model deviates increasingly from the Pitzer one at elevated temperatures and at high ionic strength greater than 1 M. Because high temperature and high ionic strength water are encountered in geothermal reservoirs, the Pitzer model should be used.

Calcite has retrograde solubility (is less soluble at higher temperatures), which makes this mineral prone to precipitation from reinjected waters as they are being heated in the reservoir. Such precipitation will reduce porosity and may have major detrimental impacts on permeability. Most minerals are more soluble at higher temperatures, tending to dissolve as injected waters are being heated. Precipitation and dissolution effects depend sensitively on concentrations and activities of participating ionic species. Our simulations show that non-ideal activity effects can be significant even at modest ionic strength, and can have major impacts on permeability evolution in injection-production systems. Alteration of injection water chemistry, for example by dilution with fresh water, can greatly alter precipitation and dissolution effects, and can offer a powerful tool for operating hot dry rock and hot fractured rock reservoirs in a sustainable manner.

The reaction kinetics of mineral alteration and the relationship between porosity and permeability changes are uncertain. Sensitivity studies should be performed in the future. The well configuration and data for mineralogical composition in this study were taken from the European HDR research site, but the results and conclusions should be useful for other HFR reservoirs, because calcite is commonly present in geothermal systems.

ACKNOWLEDGEMENTS

We are grateful to Nicolas Spycher and Chao Shan for suggestions for improvement of this manuscript. This work was supported by the Assistant Secretary for Energy Efficiency and Renewable Energy, Office of Geothermal Technologies, of the U.S. Department

of Energy, under Contract No. DE-AC03-76SF00098.

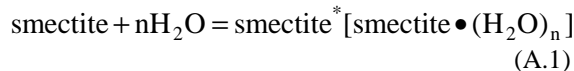
REFERENCES

- Bächler, D., 2003. Coupled thermal-hydraulic-chemical modeling at the Soultz-sous-Forêts HDR reservoir (France). PhD dissertation, Swiss Federal Institute of Technology, Zurich, Switzerland.
- Colin, E., W. Clarke, and D. N. Glew, 1985, Evaluation of the thermodynamic functions for aqueous sodium chloride from equilibrium and calorimetric measurements below 154°C, *J. Phys. Chem. Ref. Data*, Vol.14, No.2, 489-541.
- de Siqueira, A.V., Lobban, C., Skipper, N.T., Williams, G.D., Soper, A.K., Done, R., Dreyer, J.W., Humphreys, R.J., and Bones, J.A.R., 1999. The structure of pore fluids in swelling clays at elevated pressures and temperatures. *J. Phys.: Condens. Matter* 11, 9179-9188.
- Durst, D., 2002. *Geochemical modeling of the Soultz-sous-Forêts Hot Dry Rock test site: Coupled fluid-rock interaction to heat and fluid transport*. PhD dissertation, Université de Neuchâtel, France.
- Felmy, A. R., 1995, GMIN, A computerized chemical equilibrium program using a constrained minimization of the Gibbs free energy: Summary report, Soil Science Society of America, Special publication, 42, 377-407.
- Harvie, C. E., and J. H. Weare, 1980, The prediction of mineral solubilities in natural waters: The Na-K-Mg-Ca-Cl-SO₄-H₂O system from zero to high concentration at 25 °C, *Geochim. Cosmochim. Acta*, 44(7), 981-997.
- Harvie, C. E., N. Moller, and J. H. Weare, 1984. The prediction of mineral solubilities in natural waters: The Na-K-Mg-Ca-H-Cl-SO₄-OH-HCO₃-CO₃-H₂O-system to high ionic strengths at 25 °C. *Geochim. Cosmochim. Acta*, 48(4), 723-751.
- Helgeson, H.C., D.H. Kirkham, and D.C. Flowers, Theoretical prediction of the thermodynamic behavior of aqueous electrolytes at high pressures and temperatures: IV. Calculation of activity coefficients, osmotic coefficients, and apparent molal and standard and relative partial molal properties to 600 C and 5 kb. *Am. J. Sci.*, v. 281, p. 1249-1516, 1981.
- Jacquot, E., 2000. *Modélisation thermodynamique et cinétique des réactions géochimiques entre fluides de bassin et socle cristalline. Application au site expérimental du programme européen de recherché en géothermie profonde (Soultz-sous-Forêts, Bas Rhin, France)*. PhD dissertation, Univ. Louis Pasteur, Strasbourg, France.
- JNC (Japan Nuclear Cycle Development Institute), 2003. Repository Design and Engineering Technology. Technical Report.
- Malmstrom M., S. Banwart, J. Lewenhagen, L. Duro, and J. Bruno, 1996. The dissolution of biotite and

- chlorite at 25°C in the near-neutral pH region. *Contaminant Hydrology*, 21, 201-213.
- Newman, A.C.D., 1987. *Chemistry of Clays and Clay Minerals* (London: Mineralogical Society).
- Pitzer, K.S., and G. Mayorga, 1973. Thermodynamics of electrolytes. II. Activity and osmotic coefficients for strong electrolytes with one or both ions univalent. *J. Phy. Chem.*, 77, 2300-2307.
- Pitzer, K.S., 1991. Ion interaction approach: Theory and data correlation. In: *Activity Coefficients in Electrolyte Solutions*, edited by K. S. Pitzer, 2nd ed., CRC Press, 75-155.
- Plummer, L. N., D. L. Parkhurst, G. W. Fleming, and S. A. Dunkle, 1988, *A Computer Program Incorporating Pitzer's Equations for Calculation of Geochemical Reactions in Brines*, USGS Water Resources Investigation Report 88-4153, 1-310.
- Pruess, K., and T.N. Narasimhan, A practical method for modeling fluid and heat flow in fractured porous media: *Society of Petroleum Engineers Journal*, 25, 14-26, 1985.
- Rard J.A., Wijesinghe, A.M., 2003. Conversion of parameters between different variants of Pitzer's ion-interaction model, both with and without ionic strength dependent higher-order terms. *J. Chem. Thermodynamics*, 35, 439-473.
- Simunek, J., and L. Suarez, 1994, Two-dimensional transport model for variably saturated porous media with major ion chemistry, *Water Resour. Res.*, 30(4), 1115-1131.
- Verma, A., and K. Pruess, 1988. Thermohydrological conditions and silica redistribution near high-level nuclear wastes emplaced in saturated geological formations. *J. Geophys. Res.*, 93, 1159-1173.
- Vinsome, P. K. W., and J. Westerveld, 1980. A simple method for predicting cap and base rock heat losses in thermal reservoir simulators. *J. Canadian Pet. Tech.*, 19 (3), 87-90.
- Wolery T. J., and S. A. Daveler, 1992, *EQ6, A Computer program for Reaction Path Modeling of Aqueous Geochemical System: Theoretical Manual, User's Guide, and Related Documentation (version 7.0)*, Lawrence Livermore National Laboratory, UCRL-MA-110662 PT IV.
- Wolery T., Jove-Colon C., Rard, J., Wijesinghe, A., 2004. Pitzer Database Development: Description of the Pitzer Geochemical Thermodynamic Database data0.ypf. Appendix I in *In-Drift Precipitates/Salts Model (P. Mariner)* Report ANL-EBS-MD-000045 REV 02. Las Vegas, Nevada: Bechtel SAIC Company.
- Xu, T., and K. Pruess, 2001. Modeling multiphase non-isothermal fluid flow and reactive geochemical transport in variably saturated fractured rocks: 1. Methodology. *Am. J. Sci.*, 301, 16-33.
- Xu, T., and K. Pruess, Numerical simulation of injectivity effects of mineral scaling and clay swelling in a fractured geothermal reservoir, Proceedings of Geothermal Resources Council 2004 Annual Meeting (Vol 28 of *GRC Transactions*), Palm Springs, California, August 29-September 1, 2004.
- Xu, T., Y. Ontoy, P. Molling, N. Spycher, M. Parini, K. Pruess, 2004a. Reactive transport modeling of injection well scaling and acidizing at Tiwi Field, Philippines. *Geothermics*, 33(4), 477-491.
- Xu, T., E. Sonnenthal, N. Spycher, and K. Pruess, 2004b. *TOUGHREACT user's guide: A simulation program for non-isothermal multiphase reactive geochemical transport in variable saturated geologic media*, Lawrence Berkeley National Laboratory Report LBNL-55460, Berkeley, California, 192 pp.
- Zhang G. Z. Zheng, and J. Wan, 2005. Modeling Geochemical Reactive Transport of Concentrated Aqueous Solution, *Water Resour. Res.*, in press.

APPENDIX A. CLAY SWELLING

Swelling clays such as smectite and illite are layered minerals made up of negatively charged mica-like sheets, which are held together by charge-balancing interlayer cations such as Ca²⁺, Mg²⁺, or Na⁺ (de Siqueira et al., 1999). These cations adsorb water molecules, and water films form on clay surfaces. An increase of solution ionic strength causes a reduction of the thickness of the bonded water film (shrinking). When the clay is contacted by aqueous solutions of low ionic strength, the thickness will increase and clay will swell. Using smectite as an example, this process can be schematically formulated as



where smectite* is the swelled bulk clay with bonded water films. As water activity increases when diluting a solution of high ionic strength, the reaction (A.1) would be driven to the right. This will result in a decrease in bulk density of the clay, and consequently a reduction in porosity and permeability. The detailed mechanism of clay swelling (shrinking) is very complex. In the present study, we use a simple approach calculating the bulk clay density by

$$\rho = \rho_{\max} \left[1 - f_{\max} \frac{I_{\min} - I}{I_{\min}} \right] \quad I < I_{\min}$$

$$\rho = \rho_{\max} \quad I \geq I_{\min} \quad (\text{A.2})$$

where ρ_{\max} is the maximum clay density achieved when ionic strength I exceeds a certain minimum value I_{\min} , and f_{\max} is the maximum density reduction factor when $I = 0$.

APPENDIX B. CHANGES OF PERMEABILITY

Temporal changes in porosity and permeability due to mineral dissolution and precipitation and clay swelling can modify fluid flow path characteristics. This feedback between flow and chemistry is considered in our model. Changes in porosity are calculated from changes in mineral volume fractions. Four different porosity-permeability relationships were coded in TOUGHREACT, including the Kozeny-Carman grain model and the Verma and Pruess model (1988). In the present work, we used a relationship of Verma and Pruess (1988), with a more sensitive coupling of permeability to porosity than the Kozeny-Carman relationship

$$\frac{k}{k_0} = \left(\frac{\phi - \phi_c}{\phi_0 - \phi_c} \right)^n \quad (\text{B.1})$$

where ϕ_c is the “critical” porosity at which permeability goes to zero, and n is a power law exponent. Eq. (B.1) is derived from a pore-body-and-throat model in which permeability can be reduced to zero with a finite (“critical”) porosity remaining. Parameters ϕ_c and n are medium-dependent. The relationship of Verma and Pruess (1988) was found to better capture injectivity losses (Xu et al., 2004a).

Geochemistry

- Fluid-Mineral Equilibria and Injection in EGS— Effect of Injecting Groundwater** [362](#)
Michael C. Adams, Joe Moore, Steve Bjornstad, Jess McCulloch, and Cliff Buck
- Identifying Fractures and Fluid Types Using Fluid Inclusion Stratigraphy** [370](#)
Lorie M. Dilley, David I. Norman, and Jess McCulloch
- Near-Surface CO₂ Monitoring and Analysis to Detect Hidden Geothermal Systems** [377](#)
Jennifer L. Lewicki and Curtis M. Oldenburg
- Displaying and Interpreting Fluid Inclusion Stratigraphy Analyses on Mudlog Graphs** [385](#)
David I. Norman, Lorie M. Dilley, Jess McCulloch and Joseph N. Moore
- Verma Procedure for the Determination of Heat Capacity of Liquids** [394](#)
Mahendra P. Verma

FLUID-MINERAL EQUILIBRIA AND INJECTION IN EGS — EFFECT OF INJECTING GROUNDWATER

Michael C. Adams¹, Joe Moore¹, Steve Bjornstad², Jess McCulloch³, and Cliff Buck³

¹Energy & Geoscience Institute, 423 Wakara Way, Suite 300, Salt Lake City, UT 84108

²Geothermal Program Office, Code ESC 25, 429 E. Bowen Rd., China Lake, CA 93555

³Coso Operating Company, LLC, Coso Junction, CA

e-mail: madams@egi.utah.edu

ABSTRACT

Mineralization from groundwater injection augmentation in the Coso geothermal system was simulated to assess possible effects on the Coso-EGS injection well 34-9RD2. Anhydrite + dolomite or anhydrite + calcite dominate when the waters are conductively heated, while mixing produces these minerals plus a magnesium silicate. The quantities and relative proportions of the minerals are dependent on the relative rates of heating and mixing. The results of this study will be used in our ongoing petrographic and x-ray studies of injection-induced mineralization in existing wells.

INTRODUCTION

The Coso geothermal field is the site of a U.S. Dept. of Energy engineered geothermal system project (EGS; Rose et al., 2002). The goal of this project is to improve the connection between an injection and a production well on the eastern periphery of the field (Figure 1). An examination of any potential changes in permeability due to fluid-mineral interactions from the injection waters used at Coso has been undertaken in support of this program. Fluid-mineral reactions are an inevitable consequence of injecting cool water into a hot geothermal reservoir. The character of the interaction depends on the water that is injected and the difference in temperature between the injectate and the reservoir. Two compositionally distinct fluids have traditionally been used for injection, flashed reservoir fluid and condensate, although in EGS systems, low temperature groundwaters may represent an alternative source of fluid. Because the flashed reservoir fluid may contain high concentrations of silica, permeability degradation in the near well bore environment is possible. Two different approaches are commonly used to mitigate this effect. The fluid can be injected at temperatures above 150°C to avoid precipitation of amorphous silica in and around the wellbore. Alternatively the flashed fluid can be acidified with sulfuric acid to inhibit precipitation of silica. This

treatment is based on research originally performed at the Salton Sea geothermal field (Grens and Owen, 1977). Both methods are utilized at Coso. Although deposition of silica may still occur, it is more likely to be dispersed over a relatively large volume of the reservoir surrounding the well bore. Condensate, in contrast, has a very low salinity and therefore can be expected to dissolve minerals within the reservoir rock. It requires no treatment to be used as an injectate.

Outside sources of water have recently come into use as injectate. At The Geysers, CA, the injection of treated effluent from nearby population centers has been extremely successful (Goyal, 1999). Injection of groundwater from a low-temperature aquifer overlying the Dixie Valley geothermal system in Nevada has met with similar success (Benoit et al., 2000).

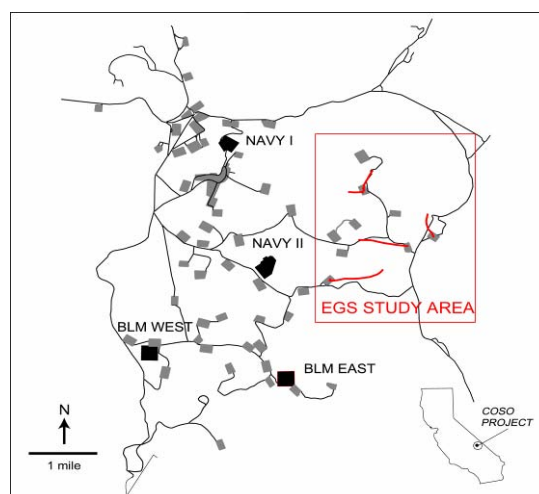


Figure 1. Location map of the Coso EGS study area.

Direct observations on the chemical reactions related to injection have been limited because reservoir rocks affected by injection are seldom sampled. Some research has been conducted on the treatment and behavior of injection waters from the Salton Sea, USA (e.g., Harrar et al., 1979), Cerro Prieto, Mexico

(Iglesias and Weres, 1981), Otake, Japan (Itoi et al., 1989) and high-temperature Icelandic geothermal systems (Gunnarsson and Arnorsson, 2003). Research specifically targeted at the injection of groundwater and low-temperature geothermal waters have been carried out by Bruton et al. (1997) and Kristmannsdottir et al. (1989).

At the Energy and Geoscience Institute, we have begun a three-pronged approach to the problem of investigating fluid-mineral interactions along the injection-production flow path. Moore and Norman are studying cuttings from a series of redrilled injection wells whose permeabilities had decreased after several years of use (unpublished proposal to DOE, 2004). Two sets of wells are from the Coso geothermal field. They expect to find and examine any evidence of mineralization or dissolution related to injection in these cuttings. Another study currently under way will examine the production fluids at Coso for evidence of changes in their chemical composition related to injection practices or treatment. The third approach uses batch reaction modeling to characterize the potential interactions of groundwater injected into the Coso geothermal reservoir. The effects of these interactions are discussed in this paper.

MODEL PARAMETERS

The initial-state composition of fluid from well 38B-9 was used as the reservoir fluid in the simulations. Water from this well was chosen because it is located on the East Flank, adjacent to the well that will be stimulated under the EGS project. The composition of the groundwater was taken from analyses of the water most likely to be used for augmentation. The compositions of these waters are listed in Table 1.

Data on aluminum concentrations in these waters were not available because specialized extraction and analysis techniques are required to measure monomeric aluminum concentrations in natural waters (Barnes, 1975). Aluminum was estimated for the simulations in this study by assuming equilibrium with reservoir minerals, in order to include aluminosilicate minerals which dominate the reservoir mineralogy. Magnesium was estimated for the reservoir water because it was below detection.

In this paper only the effects of injecting groundwater into the reservoir are considered. The effects of mixing injection fluids of different chemistries and dissolution of reservoir minerals will be considered in a future study.

The modeling program REACT, a code written by Bethke (1994) based on the speciation chemical model (Bethke, 1996) to examine the effects of injection. The default chemical database "Thermo.dat" was used, although the thermodynamic

data for quartz were modified to conform to those of Fournier and Potter (1982).

Table 1. Compositions of waters selected to simulate injection. Concentrations are in mg/kg of solution. NA=not analyzed. Nominal values of 0.1 mg/kg were used in the simulation for all species not analyzed but required for the mixing model. Concentrations are in mg/kg of solution. Compositions are given as the basis species input for the model, i.e., they are components, not actual chemical species. GROUNDWATER: the aluminum concentration was calculated assuming equilibrium with kaolinite. GEOTHERMAL WATER: the temperature was calculated from the NaKCa geothermometer of Fournier and Truesdell (1973). The aluminum and magnesium concentrations were calculated assuming equilibrium with albite, microcline, clinocllore, and muscovite. The measured calcium concentration was adjusted upward slightly by assuming equilibrium with calcite at the reservoir temperature to compensate for calcite deposition.

	Groundwater	38B-9
Temp. (°C)	20	274
pH	7.43	5.6
Al ⁺⁺⁺	0.003	0.0763
B(OH) ₃	NA	420
Ca ⁺⁺	97.5	30.3
Cl ⁻	67	2990
F ⁻	0.15	2.03
HCO ₃ ⁻	343	5400
HS ⁻	NA	42
K ⁺	8.66	333
Li ⁺	NA	11.3
Mg ⁺⁺	37.6	0.138
Na ⁺	136	1700
SO ₄ ⁻⁻	336	15
SiO ₂	5	612
CH ₄	NA	0.039

The composition of the water chosen to represent the reservoir fluid prior to injection was based on analyses of steam and liquid samples collected within minutes of each other shortly after initial well testing. Comparison of the total enthalpy of the well discharge with the adiabatic quartz geothermometer (Fournier and Potter, 1982) indicate that the well discharge contained no excess steam at the time of

sampling. Recombination of the steam and liquid into a reservoir fluid was accomplished by numerically reacting the gas sample with the liquid at their respective fractions, and then increasing the temperature to that of the NaKCa geothermometer (Fournier and Truesdell, 1973). As a quality check, the ion ratios of the restored reservoir fluid were examined on activity diagrams using the REACT thermodynamic database (Fig. 2). This comparison showed that the fluid plotted near the invariant point of albite, microcline, and muscovite; minerals that are present in the reservoir rocks. Another simulation was run in which the fluid was saturated with calcite, which moved the activity ratios nearly coincident with the invariant point (Fig. 2). At this point magnesium and aluminum concentrations were calculated on the assumption of equilibrium with the reservoir assemblage albite, microcline, muscovite, clinocllore (14A), calcite, and quartz. A similar procedure was followed for the groundwater sample. In all cases, the aluminum concentrations were close to those measured in Dixie Valley waters by Bruton et al. (1997) using the extraction technique of Trujillo et al. (1987).

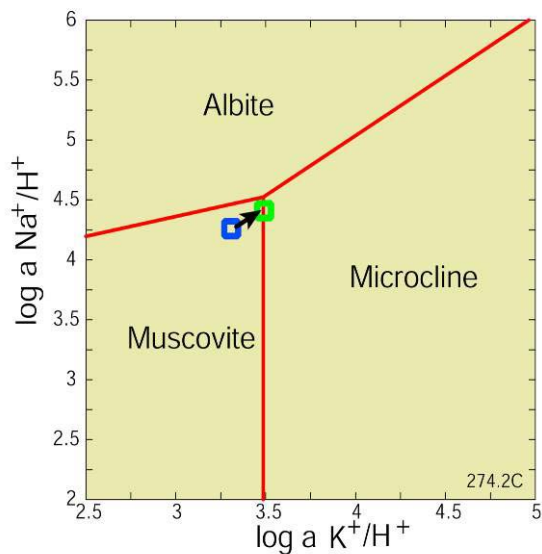


Figure 2. Activity diagram showing the reservoir composition of water from the East Flank of the Coso geothermal system. The square shows the position of recombined steam and liquid from well 34B-9 at a temperature of 274°C; the arrow and circle show the effect of saturating the fluid with calcite.

Precipitation can be handled in three different ways by the software. The first is to suppress all precipitation. This approach defines the saturation state of all of the minerals, irrespective of whether they are stable or metastable. Precipitation can be allowed with no back-reaction, which will calculate

the mineral assemblage without modifying the input fluid composition. This is a fictitious state since precipitation along the flow path would always modify the fluid composition, but it is a useful view because it compensates for the effect of delayed precipitation. For example, failure of quartz to precipitate early in the mixing process can allow magnesium silicates to form as mixing proceeds. This could occur due to kinetic inhibition or lack of nucleation.

Allowing back-reaction provides a more realistic but restricted view, in which the initial precipitation can determine the final assemblage by removing components from the fluid. Both views are shown in the following discussion to provide a wider view of possible mineral assemblages.

Temperature can be controlled in the simulations by assuming a closed system or an open system. Mixing was handled two ways in the simulations. For the case of the closed system, three kilograms of reservoir fluid were added to each kilogram of injected water. The temperature was controlled by the heat capacities of the waters. The open system only refers to conductive heat transfer, which was allowed in the open case. In this simulation one kilogram of reservoir water was added to each kilogram of injected water. The temperature and mixing fraction were a function of the final temperature, which was specified by the NaKCa geothermometer temperature of the reservoir water (274°C). The difference between the open and closed system models is illustrated in the mixing diagram in Figure 3.

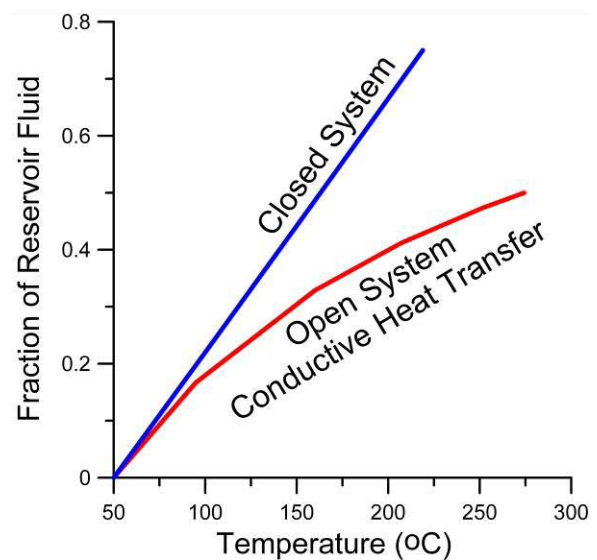


Figure 3. Temperature versus mixing fraction for the open and closed system scenarios used in the simulations. The temperatures shown apply only to a 50°C injectate temperature.

RESULTS

The output of the simulations are displayed in Figures 4 through 9 as temperature versus the saturation index, $\log(Q/K)$, or the mass (in mg) of mineral precipitated. The quotient Q/K is equal to the actual concentrations divided by those expected at equilibrium. All reference to saturation in the discussion below refers to $\log(Q/K)$. The mass of mineral precipitated is normalized to one kilogram of injectate, although minerals are in fact precipitated from a mass greater than one kilogram due to mixing.

DISCUSSION

Conductive Heating.

Waters injected into geothermal systems are heated in the reservoir to some extent prior to mixing. Simulations were run in which the waters were conductively heated to 300°C to examine this effect, although it is doubtful that this temperature would be attained without mixing in the reservoir. The simulations were run with all three precipitation options. The results clearly reflect the high magnesium and calcium of groundwater. Figures 4a and 4b show the saturation states of some magnesium and calcium minerals as the water is heated. The minerals shown are either those that are present in veins within the reservoir rocks (Adams et al., 2000; Echols, 1990; Kovac et al., 2004) or have been shown to precipitate from dilute, low-temperature, conductively-heated water (Kristmannsdottir et al., 1989). These minerals are primarily carbonates and magnesium silicates. Some aluminosilicates such as saponite are also shown in figures 4a and b, although their saturation state depends on the estimated, and extremely low, concentration of aluminum. Estimation of aluminosilicate mineral saturation states also suffers from the quality of thermodynamic data for clay minerals, which is poor.

Calcite and dolomite are saturated before they are even injected, as is expected for typical groundwaters. Most of the aluminosilicates and Mg-carbonates such as huntite and magnesite reach saturation relatively quickly, at temperatures between 50° and 75°C. Sulfate minerals such as anhydrite become saturated at temperatures of 100° to 150°C.

The predicted mineral assemblage changes with the fluid composition as minerals are allowed to precipitate. Figure 5a shows the mineral precipitation sequence that develops when back-reaction with previously precipitated minerals is allowed. Dolomite dominates up to 125°C, at which point anhydrite rapidly deposits until it nearly equals dolomite at 200°C. The same simulation with suppression of dolomite, which is generally considered to be kinetically inhibited, is shown in figure 5b. In this scenario anhydrite becomes more significant as a precipitate. In addition, magnesium precipitates

primarily as silicate minerals. This precipitation is relatively minor, but would be more significant if silica concentrations were higher due to dissolution of silica. The silica could come from reservoir quartz or injection-derived amorphous silica deposited from acidified brine.

Figure 6a illustrates precipitation for the case where there is no back-reaction. The sequence and quantities are not significantly different from the previous simulations. However, where dolomite is suppressed, the early precipitation of calcite robs the anhydrite of calcium, leading to significant calcite and minor anhydrite deposition, rather than to equal amounts of both (Fig. 6b). Thus, allowing back-reactions to occur can have a considerable effect on the shape of the mineralization curves because precipitated minerals are removed from the system as the temperature is increased along the flow path.

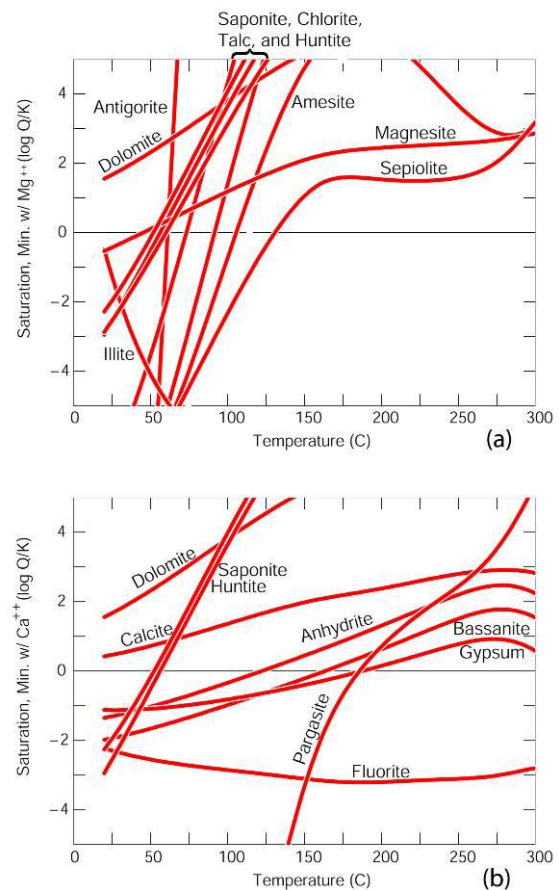


Figure 4. Coso groundwater conductively heating with precipitation suppressed to show possible (a) magnesium and (b) calcium phases.

Mixing

Mixing was simulated by incrementally combining reservoir water from 38B-9 with groundwater. A precipitation lag time, i.e., time for nucleation or conductive heating in the wellbore, was provided by

heating the injection waters to 20°, 50°, or 100°C prior to mixing. No precipitation was allowed to occur during this initial heating period. The simulations were run with all possible combinations in which back-reaction was allowed or disallowed, the system was open or closed to heat transfer, and initial heating varied from 20 to 100°C. Only a small number of the most relevant simulations are shown here due to space limitations.

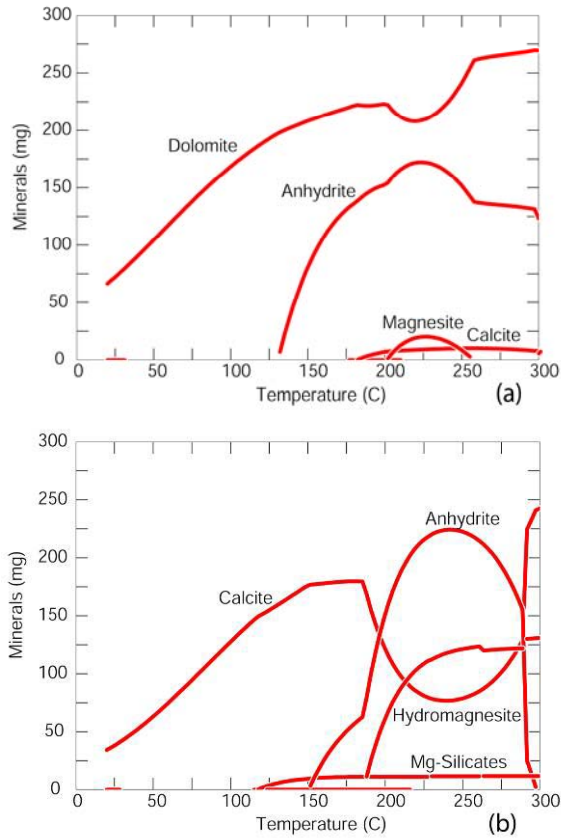


Figure 5. (a) Conductive heating of groundwater in which back-reaction with previously precipitated minerals is allowed and (b) an identical simulation in which precipitation of dolomite is suppressed.

The simulations demonstrate that the combined effects of temperature and mixing fraction are the dominant controls on the sequence of mineral precipitation. For example, consider the effect of changing the temperature of the groundwater. Although the minerals precipitated remain the same, their relative masses change considerably when the injection temperature is varied from 20° to 100°C (Fig. 7a-c). The minerals that precipitate upon mixing are mainly anhydrite, calcite, and/or dolomite. Silica as quartz is a major precipitate in the simulations. This occurs despite the fact that quartz is not oversaturated in either of the end-member waters.

However, because quartz oversaturation never exceeds 0.2, quartz may never actually precipitate.

The greatest quantity of precipitate is predicted under low permeability conditions (ignoring quartz). This condition was simulated by allowing conductive heat transfer and limiting the mixing to equal masses of injectate and reservoir water. Figure 8a shows the sequence of minerals precipitated under these conditions. The groundwater was first conductively heated to 100°C, at which point precipitation was allowed and dolomite precipitated.

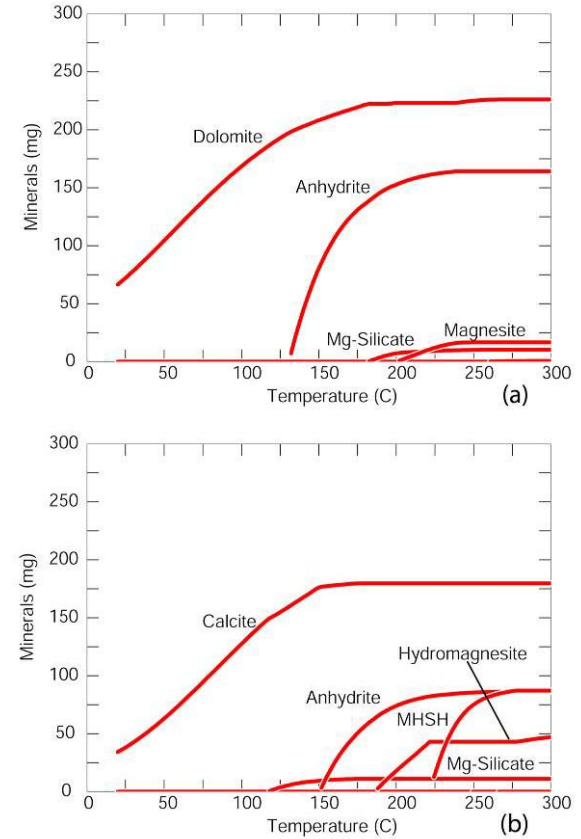


Figure 6. (a) Conductive heating of groundwater in which back-reaction with previously precipitated minerals is not allowed and (b) an identical simulation in which precipitation of dolomite is suppressed. Note that dissolution of a silica phase would prevent the formation of MSH, which is not known to form in geothermal systems.

As temperature rises and reservoir water mixes with groundwater, quartz becomes briefly saturated from 120° to 160°C. At 160°C a Mg-silicate (modeled thermodynamically as talc) replaces quartz as the stable silicate. Anhydrite also reaches saturation around 160°C and becomes the dominant precipitate by 230°C. At this temperature calcite becomes saturated and the quantity of calcite precipitated

progressively increases until it is equal to anhydrite at the reservoir temperature of 274°C. A similar sequence in which back-reaction was not allowed is shown in figure 8b. Because the dolomite and quartz that were initially precipitated do not redissolve, the amounts of anhydrite, calcite, and talc that are subsequently deposited are lower.

Simulating a high permeability environment yields the least precipitate, again assuming that silica precipitation as quartz is inhibited. This situation was simulated using a system that is closed to heat transfer and a 3:1 ratio of injectate to reservoir fluid, i.e., a higher water/rock ratio. Under these conditions, the simulations predict that dolomite will be the first mineral to precipitate, replaced by anhydrite and Mg-silicate (talc) from 160°C to 230°C (Fig. 9a). The final temperature is dictated by the temperatures of the mixing end-members. The simulation predicts that the amount of quartz deposited will be as much as three times the mass of other minerals, but as Log (Q/K) only reaches 0.2 it is problematic if quartz will actually precipitate. Altering the simulation so that back-reaction is not allowed yields similar results, except that the masses of quartz and dolomite increase and anhydrite and talc decrease (Fig. 9b).

SUMMARY AND CONCLUSIONS

The simulations in this study bring up issues that can be addressed by other techniques. For example, a petrographic and X-ray diffraction study of cuttings from a redrill of an injection well that was used for groundwater injection could reveal whether carbonates or silicates are dominant as magnesium precipitates. The identity of the magnesium minerals could also be ascertained as well. This would be of great value in showing whether dolomite, calcite, or some other carbonate dominates. Dolomite is known to be kinetically inhibited by the presence of sulfate ions at low temperatures. Since both magnesium and sulfate are present in low-temperature waters, high-magnesium calcite may form instead of dolomite.

As shown by comparing (a) and (b) in figures 5 and 6, the inhibition of dolomite will increase the amount of magnesium available for silicate deposition. Although not commonly thought of as a geothermal mineral, dolomite has been found in geothermal reservoirs in The Philippines at temperatures of up to 175°C. Ferroan dolomite has been found within shallow veins encountered in core hole TCH 74-18 (Echols, 1990). The high magnesium contents of the vein minerals and the presence of smectite in the wall rocks indicates that these veins were precipitated by low-temperature waters as they were heated. These petrologic studies of injection wells are currently underway at the Energy and Geoscience Institute by Moore and Norman.

Precipitation of silica is another issue brought up by the simulations. As we have noted, log (K/Q) never

exceeds 0.2. for the mixture of groundwater and reservoir water used in the simulations. If silica does not precipitate as a pure phase, more is available for the deposition of magnesium silicates. If silica does deposit as a pure phase, identification of the polymorph or polymorphs would help refine the simulations.

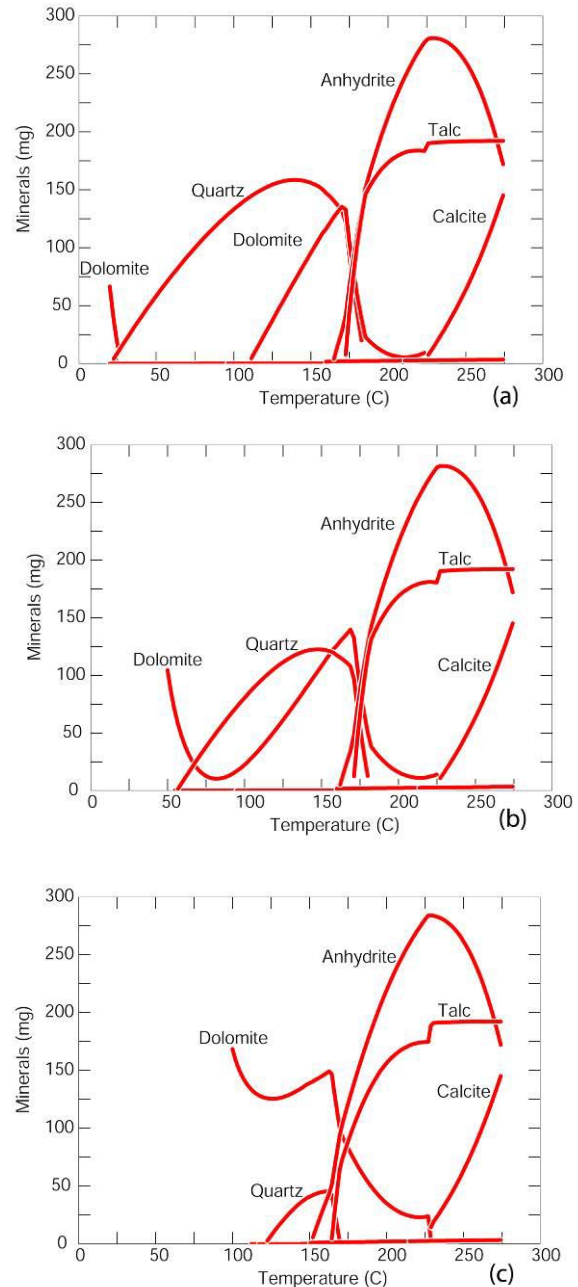


Figure 7. Variation in the temperature at which mixing starts after conductive heating (with no precipitation). (a) 20°C, (b) 50°C, and (c) 100°C.

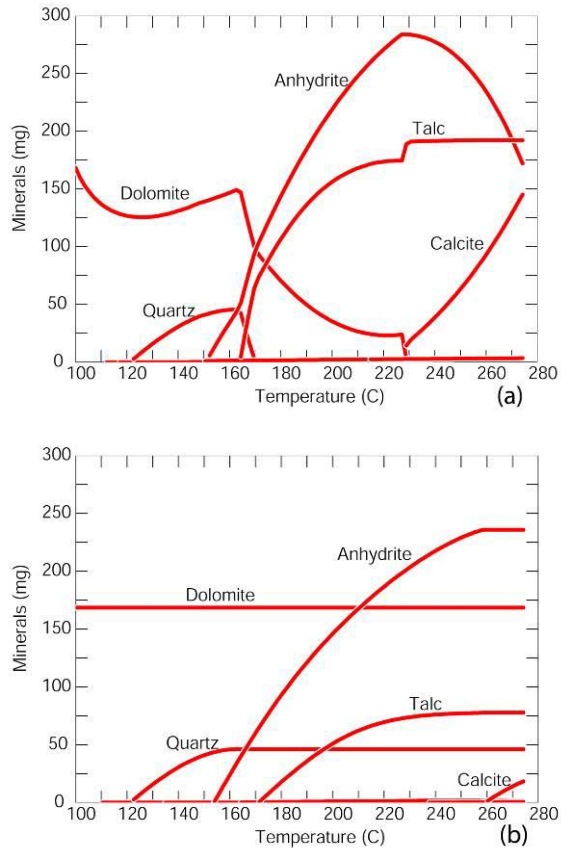


Figure 8. Simulation of injection into low permeability area. Simulation includes small amount of mixing (1:1) and conductive heat transfer (see fig. 3). (a) Back-reaction is allowed. (b) Back-reaction is disallowed.

The simulations also show the relevance of the previous history of the injection well. The length of time an injection well is in service will affect the temperature of the flow path, resulting in different amounts of heating before mixing. As previously discussed and shown in figures (6a-c), this can change the composition of the precipitated mineral assemblages and mineral ratios. The type of fluid that was previously injected can also have an effect on the behavior of injection induced mineralization. For example, if amorphous silica was deposited from injectate consisting of flashed brine, silica will be readily available for dissolution and reprecipitation as a magnesium silicate during subsequent injection and heating of silica deficient groundwater. The deposition of silica may be further confounded by acidification of the injectate. In addition to delaying the precipitation of amorphous silica by interfering with polymerization, acidification may progressively

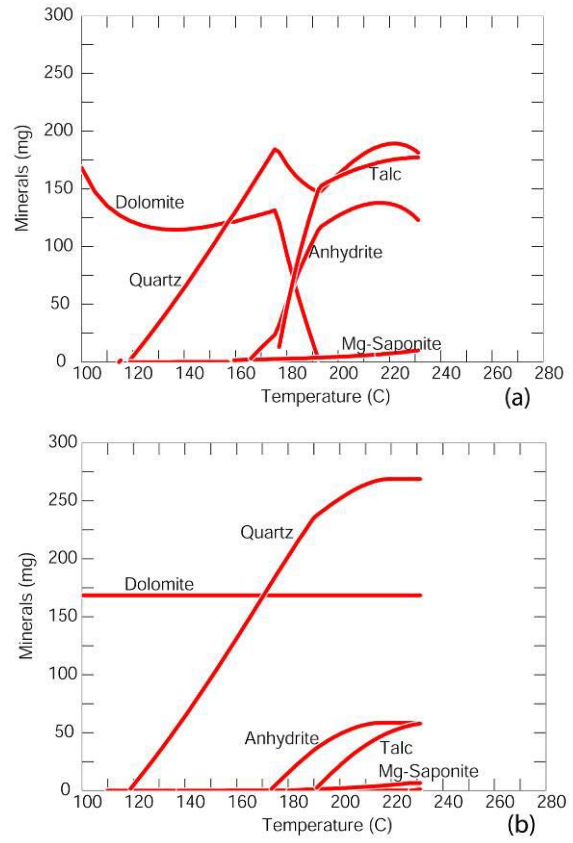


Figure 9. Simulation of injection into high permeability area. Simulation includes large amount of mixing (3:1, reservoir to injectate) and no conductive heat transfer (see fig. 3). (a) Back-reaction is allowed. (b) Back-reaction is not allowed.

lower the buffering capacity through reactions with vein carbonate minerals and the wall rocks. This may have the effect of maintaining the low pH and delaying silica precipitation, allowing the silica deposition to move further from the well bore.

Further simulations will be conducted for this study. One of the topics will be the benefits of alternating condensate, acid brine, and groundwater injection compositions in injection wells to minimize the persistence of scale.

ACKNOWLEDGEMENTS

Funding for these simulations was provided by the Department of Energy under contract No. DE-FC07-01ID14186. Such support does not constitute endorsement by the DOE of the opinions, findings, conclusions, or recommendations contained within this manuscript.

REFERENCES

- Adams, M.C., Moore, J.N., Bjornstad, S. and Norman, D.I., 2000. Geologic history of the Coso geothermal system, World Geothermal Congress, pp. 2463-2469.
- Barnes, R.B., 1975. The determination of specific forms of aluminum in natural water. *Chemical Geology*, 15: 177-191.
- Benoit, W.R., Johnson, S. and Kumataka, M., 2000. Development of an injection augmentation program at the Dixie Valley, Nevada geothermal field, Proceedings, World Geothermal Congress. International Geothermal Association, Kyushu-Tohoku, Japan, pp. 819-824.
- Bethke, C., 1994. *GWB reaction modeling guide: a user's guide to react and gplot*. Hydrogeology Program, University of Illinois.
- Bethke, C., 1996. *Geochemical Reaction Modeling*. Oxford University Press, New York, NY, 397 pp.
- Bruton, C.J. et al., 1997. Preliminary investigation of scale formation and fluid chemistry at the Dixie Valley geothermal field, Nevada, Transactions, Geothermal Resources Council, pp. 157-164.
- Echols, T.J., 1990. Petrology and paragenesis in core hole 74-18, Coso geothermal field, Inyo County, California. Masters Thesis, University of California at Riverside, Riverside, CA.
- Fournier, R.O. and Potter, R.W., II, 1982. A revised and expanded silica [quartz] geothermometer. *Geothermal Resources Council Bulletin*, 11(10): 3-12.
- Fournier, R.O. and Truesdell, A.H., 1973. An empirical Na-K-Ca geothermometer for natural waters. *Geochimica et Cosmochimica Acta*, 37: 1255-1275.
- Goyal, K.P., 1999. Injection experience in The Geysers, California -- A summary, Transactions, Geothermal Resources Council, pp. 541-547.
- Grens, J.Z. and Owen, L.B., 1977. Field evaluation of scale control methods: acidification, Transactions: Geothermal Resource Council, pp. 119-121.
- Gunnarsson, I. and Arnorsson, S., 2003. Silica scaling: the main obstacle in efficient use of high-temperature geothermal fluids, International Geothermal Conference, Reykjavik, Iceland, pp. 30-36.
- Harrar, J.E., Locke, F.E. and Lorensen, L.E., 1979. Studies of scale formation and scale inhibitors at the Salton Sea geothermal field. UCRL-83493, Lawrence Livermore National Laboratory.
- Iglesias, E.R. and Weres, O., 1981. Theoretical studies of Cerro Prieto brines' chemical equilibria. *Geothermics*, 3-4: 239-244.
- Itoi, R. et al., 1989. Long-term experiments of waste water injection in the Otake geothermal field, Japan. *Geothermics*, 18: 153-159.
- Kovac, K.M., Moore, J.N., McCulloch, J. and Ekart, D., 2004. Geology and mineral paragenesis study within the Coso-EGS project. Twenty-Ninth Workshop on Geothermal Reservoir Engineering. Kristmannsdottir, H., Olafsson, M. and Thorhallsson, S., 1989. Magnesium silicate scaling in district heating systems in Iceland. *Geothermics*, 18: 191-198.
- Rose, P.E. et al., 2002. Creation of an Enhanced Geothermal System through Hydraulic and Thermal Stimulation, Transactions, Geothermal Resources Council, pp. 245-250.
- Trujillo, P.E., Counce, D., Grigsby, C.O., Goff, F. and Shevenell, L., 1987. Chemical analysis and sampling techniques for the geothermal fluids and gases at the Fenton Hill laboratory. LA-11006-MS, Los Alamos National Laboratory, Los Alamos, New Mexico.

IDENTIFYING FRACTURES AND FLUID TYPES USING FLUID INCLUSION STRATIGRAPHY

Lorie M. Dilley¹, David I. Norman¹, and Jess McCulloch²

¹.Dept. of Earth and Environmental Sciences
New Mexico Tech
Socorro, New Mexico 87801, USA
E-mail: ldilley@hdlalaska.com, dnorman@nmt.edu

².Coso Operating Company
PO Box 1690
Inyokern, California 93527, USA
E-mail: jmcculloch@caithnessenergy.com

ABSTRACT

Fluid Inclusion Stratigraphy (FIS) is a method currently being developed for use in geothermal systems to identify fractures and fluid types. This paper is the third in a series of papers on the development of FIS. Fluid inclusion gas chemistry is analyzed and plotted on well log diagrams. The working hypothesis is that select gaseous species and species ratios indicate areas of groundwater and reservoir fluid flow and reservoir seals. Previously we showed that FIS analyses identify fluid types and fractures (Dilley et al, 2004). Here we look at the sampling interval and additional confirmation that FIS analyses identify fractures.

Sampling intervals of 20 ft and 10 ft. are evaluated to determine the optimal sampling interval and FIS are compared to fracture logs. Additionally, FIS samples were obtained from a core to evaluate the core interval is affected by a fracture fluid. The results show that generally a 20 ft sampling interval is sufficient, and that a vein affects the wall rock at distances of 5 to 10 feet beyond the fracture.

INTRODUCTION

Fluids trapped in inclusions are generally faithful indicators of pore fluid chemistry. Temperatures and composition of geothermal fluids are sensitive indicators of their origins, evolutions, and the processes that have affected them. Our working hypothesis is that samples of geothermal fluids are trapped in wall rock minerals within microfractures adjacent to veins. Mass spectrometer analyses of gases within these inclusions show fluid sources and processes within geothermal systems (Giggenbach 1997; Norman 1997; Blamey 2002).

Fluid Inclusion Stratigraphy (FIS) is currently being developed as a technique for use in geothermal system to assess reservoirs. The FIS method analyzes volatiles in fluid inclusions in drill cuttings, by mass spectrometry. The commercial process, developed in part by Fluid Inclusion Technology (FIT), is highly automated with thousands of analyses made in a day resulting in turnaround times in days and costs comparable to other logging methods. The procedure gives a downhole map of fluid distribution and chemistry plotted on borehole logs.

The purpose of this research, funded by the California Energy Commission, is to develop FIS technique for geothermal reservoir assessment. The assessment techniques seek to provide ways to: distinguish non-producing from producing wells; identify major fluid flow zones; and entrants of cold and steam-heated waters into the bore hole. This paper is the third in a series of papers on the development of FIS.

From the preliminary results, the question arose as to how accurately does this method reflect the location of fractures and what is the optimal sampling interval for the method. In order to address these questions we conducted studies on two sampling intervals to evaluate the optimal sampling spacing and we compare the gas analyses plotted on mud logs against a fracture density log. Additionally FIS samples were obtained from a COSO core to evaluate how far away from the fracture center there would be an indication of select chemical species and ratios we use in interpreting FIS analyses.

METHODS

Four wells from the Coso Geothermal Field were selected for the first round of analyses (Figure 1). Three of the wells are producers and one, Well # 3, a

non-producer. Of the three producing wells, Well # 4 has entrants of cold water. Splits of 10 to 20 grams were taken from drill cuttings at 20 foot intervals throughout each well. A total of 1,729 samples were submitted to FIT for analyses. Analyses were performed first by cleaning the samples, if necessary, then crushing a gram-size sample in a vacuum. The volatiles released are pumped through multiple quadrupole mass spectrometers where molecular compounds are ionized and separated according to the mass/charge ratio. The output data for each sample was the magnitude of mass peaks for masses 2 to 180. A volatile like CO₂ has a gram formula weight of 44 and will be measured by a peak at mass 44. FIT returned the raw data within three weeks.

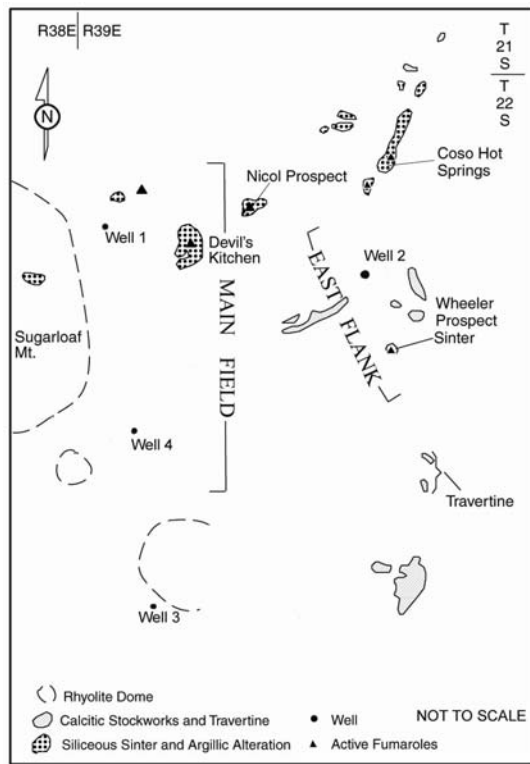


Figure 1. Location of wells used in the study and surface features of Coso. (After Lutz et al, 1999).

Select ratios and species were plotted next to each other and interpreted. Certain ratios were shown to indicate high temperature fluids, low temperature fluids and steam zones. See Dilley, Norman & Berard, 2004, for more on the interpretation and the FIS technique.

For this study, samples were collected at 10 foot intervals and plotted again to determine if the smaller sampling interval produced relevant results when compared to the 20 foot sampling interval. This was performed on portions of the three producing wells. Also samples were collected from a core to determine how far from a vein center, fluid inclusions would

extent. This was conducted for Well 64-16, which is located on the East Flank near Well 2. To determine if the peaks recorded by the various chemical species and ratios used in FIS are actually fractures in the borehole, select graphs were compared to a fracture density plot. The wide aperture fracture density plot was for Well 2 and was developed by Sheridan and Hickman (2004). This composite figure was compared to the temperature log for this well to determine how fracture density and the ratios developed would indicate high temperature fluids.

The chemical species and gas ratios selected for used in this study are H₂O, N₂/Ar (mass 28/40), CO₂/CH₄ (44/15), C₃H₈/C₃H₆ (mass 43/39, and (N₂/Ar + CO₂/CH₄) / (C₃H₈/C₃H₆). The ratios of N₂/Ar, CO₂/CH₄ and (N₂/Ar + CO₂/CH₄) / (C₃H₈/C₃H₆) are used to indicate reservoir fluids whereas the ratio of C₃H₈/C₃H₆ is an indicator of background or low temperature fluids (Norman et. al, 2004).

SAMPLING INTERVAL

Figure 2 is the temperature log for Well 2. The temperature logs for the well show entrants of hot fluids at depths of approximately 7,300 feet to 8,700 feet. This zone was targeted for the graphing of the various species and ratios.

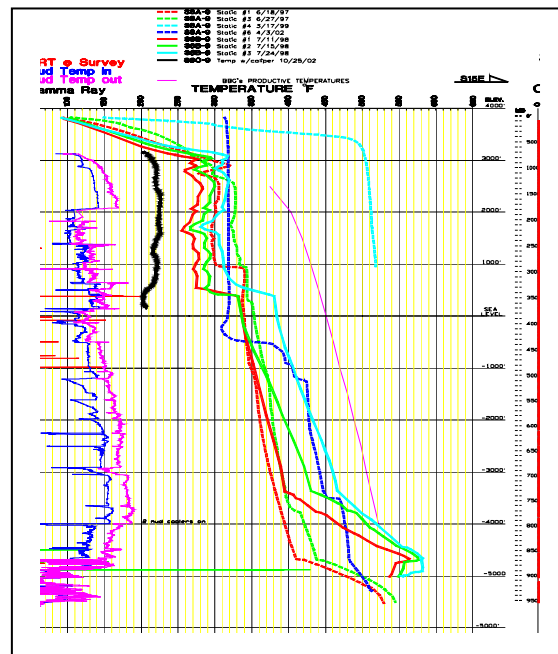
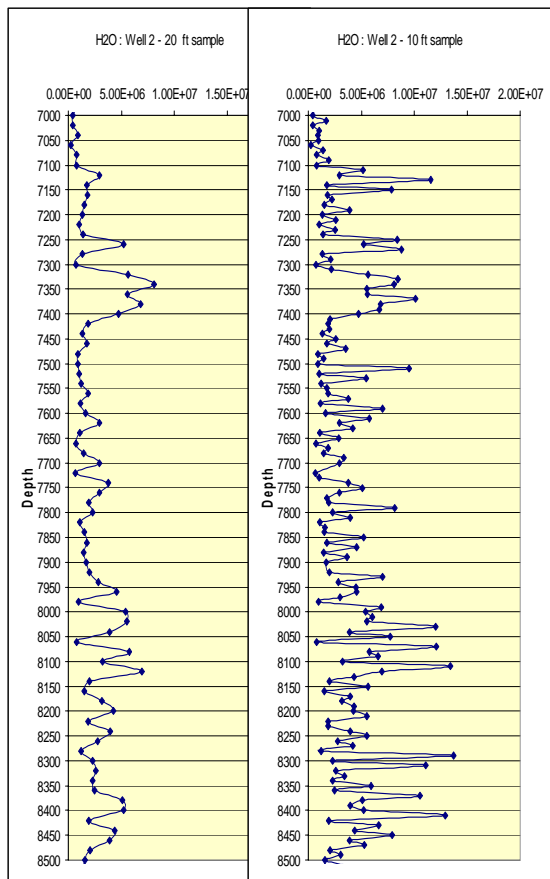


Figure 2. Temperature logs for Well 2.



Figures 3a and 3b: Graphs of H₂O for 20 ft and 10 ft sampling intervals. Note the 10 ft sampling interval indicates many more peaks and higher amounts sampling interval graph versus the 10 foot sampling interval graph.

Figure 3 shows the comparison of the select species and ratios for the two sampling intervals. The 10 ft. sampling in general provides more peak detail (Figures 3c and 3d). Mass peaks that are not evident in 20 ft. sampling are shown; see mass intervals (7,500, 7,690, 7,830 ft. Also from about 8,250 to 8,410 the broad peaks recorded by 20 ft sampling shows more detail by using a 10 ft. interval. The N₂/Ar peaks should be antithetic to propane/propene peaks. The former ratio indicates fluids with a magmatic contribution whereas high propane/propene indicates background or cool fluids. That relationship is much clearer in 10 ft sampling interval graphs.

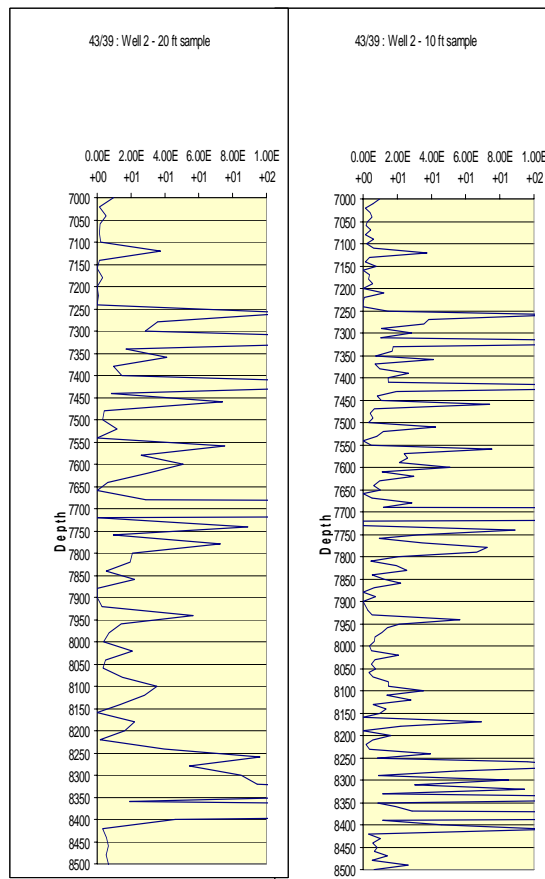
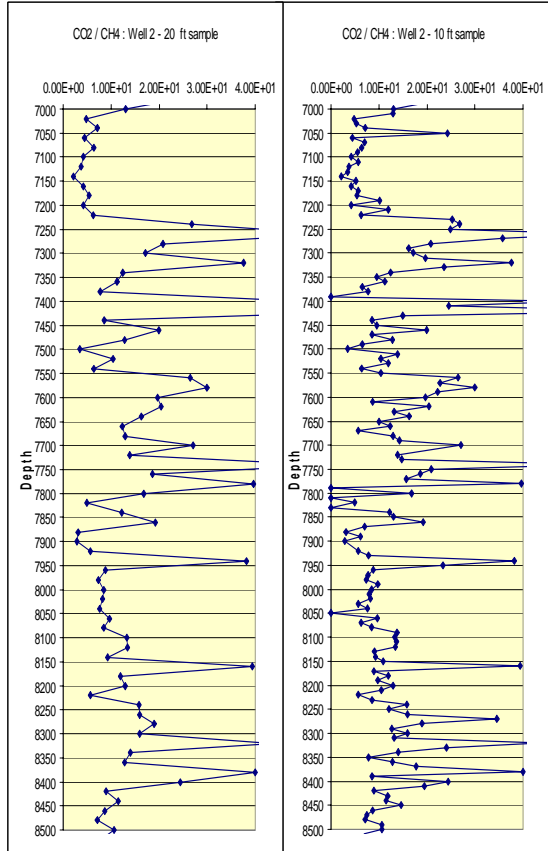


Figure 3c and 3d: Graphs for Mass 43/39 for 20 ft sampling interval and for 10 ft sampling interval. Note the number of peaks from 8250 to 8400 feet in the 10 ft sampling interval versus the 20 ft sampling interval.

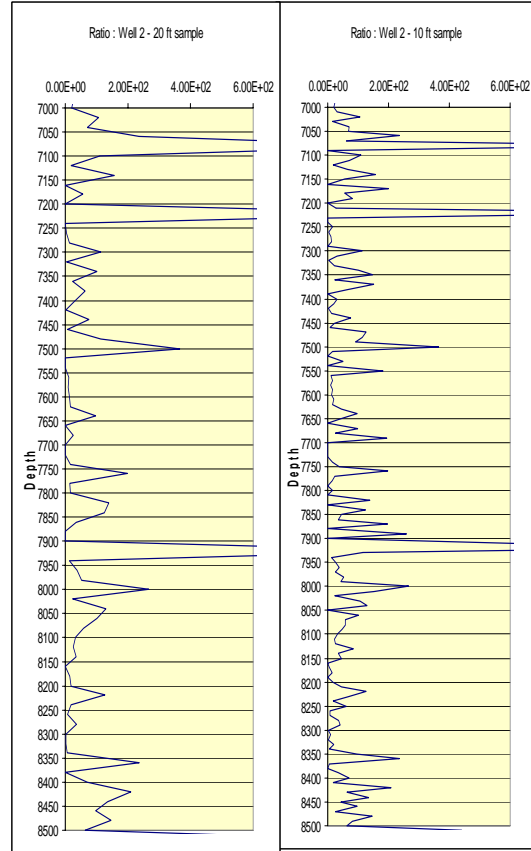
For the remaining ratios, the smaller sampling interval did not appear to make that much difference. For CO₂/CH₄ ratio (Figures 3e and 3f) one peak was missed at 7050 feet, but all of the other peaks were indicated when the sampling interval was 20 feet. For this ratio there were a few low points (7390, 7800, and 8050 feet) indicated in the shorter sampling interval than in the larger sampling interval.

For N₂/Ar ratio (Figures 3g and 3h) some of the minor peaks are missing or are subdued in the 20 ft sampling interval, but in general most of the peaks are similar in the 10 ft sampling interval as in the 20 ft sampling interval. The large ratio, (N₂/Ar + CO₂/CH₄) / (Mass 43/Mass 39), (Figures 3i and 3j) appeared to work equally well for both sampling intervals. These ratios have been used to identify high temperature fluid zones.



(3e)

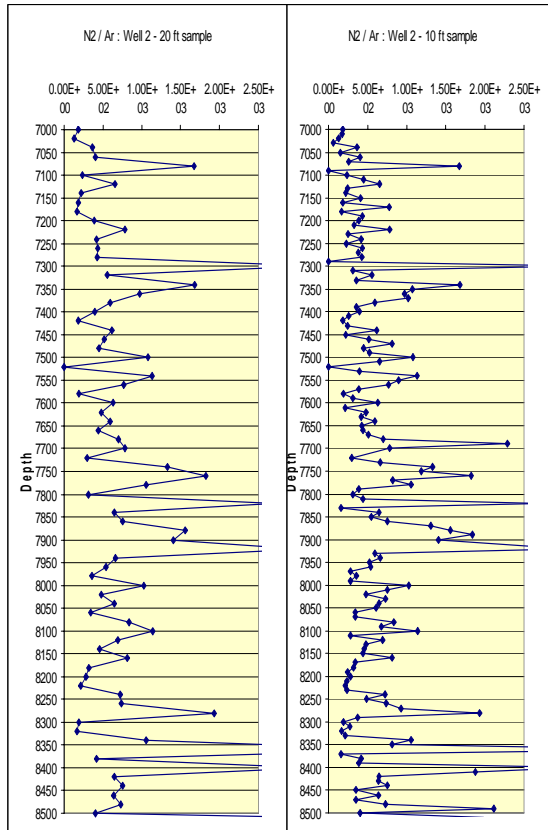
(3f)



(3i)

(3j)

Figures 3e through 3j are graphs for CO_2/CH_4 , N_2/Ar , and the ratio of $(N_2/Ar + CO_2/CH_4) / (Mass\ 43/Mass\ 39)$. Each of these ratios has been used to identify high temperature fluids using FIS. The smaller sampling interval (10 ft) does not indicate any additional high or low zones when compared to the larger sampling interval (20 ft).

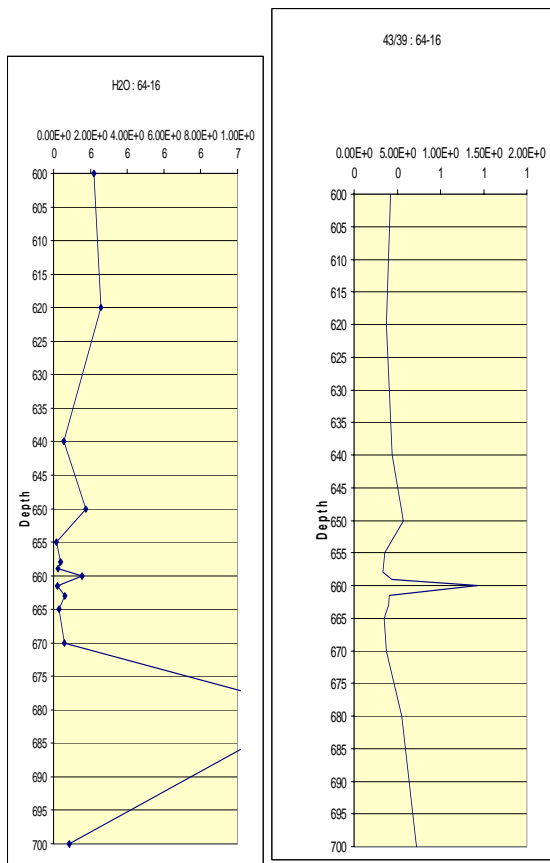


(3g)

(3h)

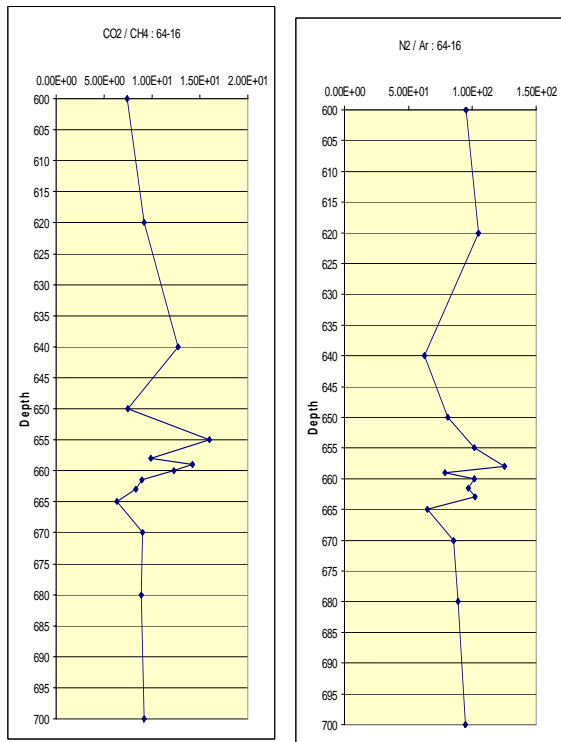
Rock samples were obtained from Coso Well 64-16 core. Sampling was conducted to determine how far from the vein the various ratio signature could be observed. The samples were crushed in a mechanical crusher and sieved in order to obtain fragments about the cutting size. The core sampled contained a noticeable calcite vein between 659 and 662 feet, with the vein center was at 660 feet. The sampling interval ranged from 20 ft at 600 feet to 1 ft at the vein center. The 660 ft sample is calcite, all other samples were green altered host rock. Figures 4a through 4d show the results of the sampling conducted.

It can be seen that for H_2O (Figure 4a) there is a small peak centered at 660 feet. There is a much larger peak centered at 683 feet. The small peak at 660 feet does not extend in depth more than about a foot on either side of the vein center.



(4a)

(4b)



(4c)

(4d)

Figures 4a through 4d are graphs of the various ratios for a calcite vein centered at 661 feet from Well 64-16. Note that the scales on the H₂O, N₂/Ar and CO₂/CH₄ graphs are expanded from graphs in Fig. 3 in order to show detail

For Mass 43/39 ratio (Figure 4b) at the vein center is a very sharp peak as well with no other peaks observed on the graph in this zone. A high ratio indicates cool waters were depositing this vein.

For CO₂/CH₄ (Figure 4c) and N₂/Ar (Figure 4d) the peaks are broader and the highest point of the peaks are above the center of the vein. For CO₂/CH₄ the width of the peak is about 15 feet, while for N₂/Ar the width of the peak is about 10 feet. The low CO₂/CH₄ ratio and high propane/propene ratio indicate low temperature fluids. The elevated N₂/Ar coupled with low CO₂/CH₄ is characteristic of steam heated water (Dilley et al., 2004).

FRACTURE PATTERN

Figure 5 is a composite of a fracture density log developed by Sheridan & Hickman in 2004 for Well 2 and the fluid inclusion gas analysis for the ratios of CO₂/CH₄ and N₂/Ar. The fracture density log is based on fractures with significant apparent apertures. There are several intervals where there is high fracture density and corresponding high ratios particularly from about 7,200 to about 7,900 feet. This zone is where the temperatures logs (Figure 2) show an increase in temperature. This composite figure ranges from 6000 feet to 9500 feet. When compared to the increase in temperature logs (Figure 2) the fracture density is high, and the ratios are high. This occurs from approximately 7,300 feet to about 8,600 feet. This is considered the production zone for this well.

Individual high fracture densities do not appear to always correspond to high peaks in the ratios however; this is most likely due to the lack of these compounds within these fractures. In general when there are peaks on either of the ratios this corresponds to the fracture density except in the production zone. For instance from approximately 6,700 to 7,100 feet there is a zone of low fracture density and the ratios are generally low with only a few high peaks. The highest fracture densities at 7,600, 7,700, 7,900 and 8,100 feet each have high CO₂/CH₄ and N₂/Ar ratios.

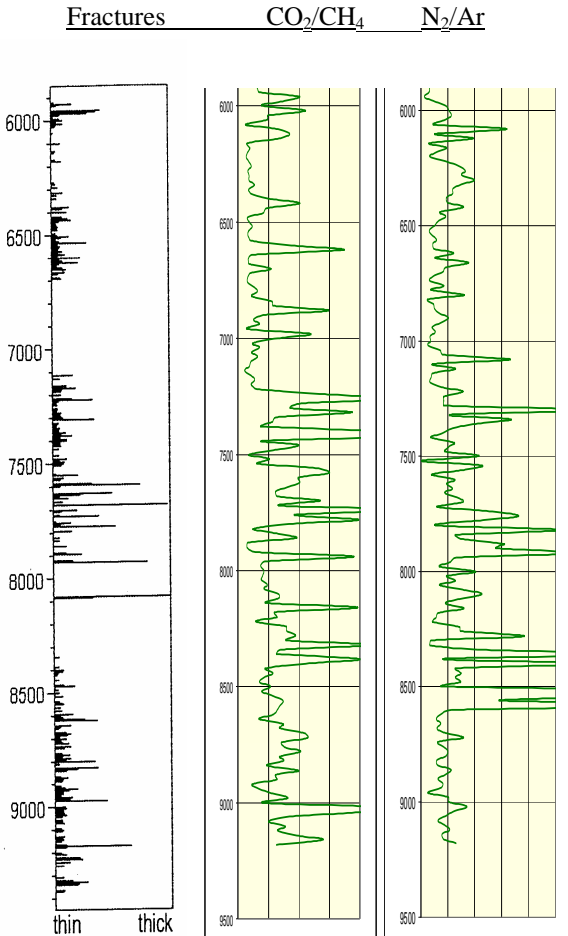


Figure 5: Fractures with significant apparent apertures, CO_2/CH_4 ratio and N_2/Ar ratio composite. Note that the where there is a high density of fractures, there appears to be corresponding peaks for the ratios. Note also the zone from 7,100 feet to about 7,900 feet with high fracture density and high CO_2/CH_4 and N_2/Ar ratios.

DISCUSSION

It is apparent from the core analyses that the analysis of calcite is little different than analyses of rock chips adjacent to the vein. The peaks across the vein are relatively low in comparison to the H_2O and ratio peaks in Well 2, and similar to analyses of the non-productive Well 3 (Dilley et al., 2004). The reason for this is not evident, but could be that the calcite vein is quite a bit older than veins in Well 2 that are in reservoir rocks where fluids are currently fluxing.

Analysis of Well 2 and for Well 64-16 both show H_2O and Mass 43/39 as sharp define peaks. Well 64-16 data for these species indicate they do not extend into the wall rock more than a few feet. For the gas ratios CO_2/CH_4 and N_2/Ar , there appears to be broad peaks and that the gases extend into the wall rock on

the order of 15 feet. This maybe due to an osmotic affects favoring of small molecular diameter gaseous species.

Based on the sampling interval analysis conducted it appears that a sampling interval of 20 feet would be sufficient for most of the well depth, however in areas of particular interest, a 10 foot sampling interval would provide more information. The more mobile gases of CO_2 and N_2 appear to pass into the wall rock and thus show a broader data for the core and well chips suggests an average anomaly for N_2/Ar and CO_2/CH_4 ratio peaks on the order of 15 feet in thickness.

The fracture analysis conducted would indicate that the peaks on the graphs from the fluid inclusion gas analysis do represent fractures either individual fractures or large densities of fractures. In the zone of increasing temperatures the density of large fractures was high, and the ratios of N_2/Ar and CO_2/CH_4 were also high indicating that the zone is near the reservoir fluids. In the production area, the fracture density was moderate however, the signatures for the ratios was low.

CONCLUSIONS

1. The gas chemistry of vein fluids in recorded in wall rock extending 5 to 10 feet from vein center.
2. A twenty-foot sample spacing will detect the most veins. However for better vein detail, and recording water and 43/39 ratio peaks a 10 ft. sampling interval is better.
3. Crushing wall rock adjacent to veins yields gas ratios similar to those in vein minerals.
4. The peaks developed from the ratios apparently indicate fractures, however not in all cases. Based on the core analysis conducted there is some diffusion of the gases into the wall rock.

REFERENCES

- Adams, M.C., Moore, J.N., Bjornstad, S., and Norman, D.I. (2000), Geologic history of the Coso geothermal system: *Proceedings: World Geothermal Congress, Kyushu-Tohoku, Japan, 2000*, 2463-2469.
- Blamey, N., Norman, David I. (2002). New Interpretations of Geothermal Fluid Inclusion Volatiles: Ar/He and N_2/Ar ratios - A Better Indicator of Magmatic Volatiles, and Equilibrium Gas Geothermometry: *Proceedings: Twenty-seventh Workshop on Geothermal Reservoir Engineering, Stanford University, Stanford, California*.
- Dilley, Lorie, Norman, David I., Berard, B. (2004). Fluid Inclusion Stratigraphy: New Method for

Geothermal Reservoir Assessment, Preliminary Results: *Proceedings: Twenty-ninth Workshop of Geothermal Reservoir Engineering, Stanford University, Stanford, California.*

Giggenbach, W. F. (1986). The use of gas chemistry in delineating the origin of fluid discharges over the Taupo Volcanic Zone: a review: *International Volcanological Congress, Hamilton, New Zealand Proceedings Seminar, 5: 47-50.*

Giggenbach, W. F. (1997). The origin and evolution of fluids in magmatic-hydrothermal systems. *Geochemistry of Hydrothermal Ore Deposits.* H. L. Barnes. New York, J. Wiley and Sons, Inc.: 737-796.

Hall, D. (2002). Fluid Inclusion Technologies, Inc. <http://www.fittulsa.com>.

Kovac, K.M., J. Moore, J. McCulloch, and D. Ekart (2004). Geology and Mineral Paragenesis Study within the COSO-EGS Project. *Proceedings: Twenty-ninth Workshop of Geothermal Reservoir Engineering, Stanford University, Stanford, California.*

Lutz, S.J., Moore, J.N., Adams, M.C., and Norman, D.I. (1999). Tracing fluid sources in the Coso geothermal system using fluid-inclusion gas chemistry: *Proceedings: Twenty-fourth Workshop of Geothermal Reservoir Engineering, Stanford University, Stanford, California.*

Lutz, S.J., Moore, J.N., and Benoit, D. (1998). Integrated alteration mineralogy and fluid-inclusion study at Dixie Valley geothermal field, Nevada: *Proceedings: Twenty-third Workshop of Geothermal Reservoir Engineering, Stanford University, Stanford, California.*

Moore, D.E., C.A. Morrow, et al. (1987). "Fluid-rock interaction and fracture development in "crystalline" rock types." Open-File Report - U. S. Geological Survey **Report No: OF 87-0279.**

Norman, D.I., Moore, J.N., Musgrave J. (1997). Gaseous species as tracers in geothermal systems: *Proceedings: Twenty-second Workshop of Geothermal Reservoir Engineering, Stanford University, Stanford, California.*

Norman, D. I., Moore, J.N., Yonaka, B., Musgrave, J. (1996). Gaseous species in fluid inclusions: A tracer of fluids and an indicator of fluid processes. *Proceedings: Twenty-first Workshop of Geothermal Reservoir Engineering, Stanford University, Stanford, California.*

Norman, D.I., Musgrave, J.A. (1995). N₂-Ar-He compositions in fluid inclusions: Indicators of fluid source. *Geochimica et Cosmochimica Acta* **58**: 1119-1131.

Norman, D. I., Nigel Blamey, Joseph N. Moore (2002). Interpreting Geothermal Processes and Fluid Sources from Fluid Inclusion Organic Compounds and CO₂/N₂ Ratios. *Proceedings: Twenty-seventh Workshop on Geothermal Reservoir Engineering Stanford University, Stanford, California.*

Sheridan, Judith M., and Stephen H. Hickman (2004). In Situ Stress, Fracture, and Fluid Flow

Analysis in Well 38C-9: An Enhanced Geothermal System in the Coso Geothermal Field. *Proceedings: Twenty-ninth Workshop of Geothermal Reservoir Engineering, Stanford University, Stanford, California.*

NEAR-SURFACE CO₂ MONITORING AND ANALYSIS TO DETECT HIDDEN GEOTHERMAL SYSTEMS

Jennifer L. Lewicki and Curtis M. Oldenburg

Lawrence Berkeley National Laboratory
Earth Sciences Division, 1 Cyclotron Rd.
Berkeley, CA, 94720, USA
e-mail: jllewicki@lbl.gov

ABSTRACT

“Hidden” geothermal systems are systems devoid of obvious surface hydrothermal manifestations. Emissions of moderate-to-low solubility gases may be one of the primary near-surface signals from these systems. We investigate the potential for CO₂ detection and monitoring below and above ground in the near-surface environment as an approach to exploration targeting hidden geothermal systems. We focus on CO₂ because it is the dominant noncondensable gas species in most geothermal systems and has moderate solubility in water. We carried out numerical simulations of a CO₂ migration scenario to calculate the magnitude of expected fluxes and concentrations. Our results show that CO₂ concentrations can reach high levels in the shallow subsurface even for relatively low geothermal source CO₂ fluxes. However, once CO₂ seeps out of the ground into the atmospheric surface layer, winds are effective at dispersing CO₂ seepage. In natural ecological systems in the absence of geothermal gas emissions, near-surface CO₂ fluxes and concentrations are predominantly controlled by CO₂ uptake by photosynthesis, production by root respiration, microbial decomposition of soil/subsoil organic matter, groundwater degassing, and exchange with the atmosphere. Available technologies for monitoring CO₂ in the near-surface environment include the infrared gas analyzer, the accumulation chamber method, the eddy covariance method, hyperspectral imaging, and light detection and ranging.

To meet the challenge of detecting potentially small-magnitude geothermal CO₂ emissions within the natural background variability of CO₂, we propose an approach that integrates available detection and monitoring techniques with statistical analysis and modeling strategies. The proposed monitoring plan initially focuses on rapid, economical, reliable measurements of CO₂ subsurface concentrations and surface fluxes and statistical analysis of the collected data. Based on this analysis, areas with a high

probability of containing geothermal CO₂ anomalies can be further sampled and analyzed using more expensive chemical and isotopic methods. Integrated analysis of all measurements will determine definitively if CO₂ derived from a deep geothermal source is present, and if so, the spatial extent of the anomaly. The suitability of further geophysical measurements, installation of deep wells, and geochemical analyses of deep fluids can then be determined based on the results of the near surface CO₂ monitoring program.

INTRODUCTION

Worldwide, most commercial geothermal projects have been developed in or near areas of surface manifestations (e.g., hot springs, geysers, fumaroles). Also, the majority of hydrothermal systems with obvious surface expressions in the U.S. have been explored to determine their development potential. Discovery of new geothermal systems will therefore require exploration of areas where the resources are either hidden or lie at greater depths than presently known reservoirs. As a result, research must be geared toward the development of novel exploration techniques to locate these less-obvious geothermal systems.

We define “hidden” geothermal systems as those with no apparent surface features. Emissions of moderate-to-low solubility gases (e.g., CO₂, He, CH₄) may be one of the primary near-surface signals from these systems. Therefore, the detection of anomalous gas emissions related to hidden geothermal systems may be an important tool to discover new resources (Klusman et al., 2000). We focus our study on the detection and monitoring of CO₂ in the near-surface environment as an approach to discover hidden geothermal systems because (1) CO₂ is the major noncondensable gas present in geothermal systems (e.g., Ellis and Mahon, 1977), (2) due to its moderate solubility in water, CO₂ from volcanic-hydrothermal

Table 1. Measured soil CO₂ fluxes and concentrations at selected locations.

Site	Maximum CO ₂ flux (g m ⁻² d ⁻¹)	Average CO ₂ flux (g m ⁻² d ⁻¹)	Maximum soil CO ₂ conc. (vol.%)	References
Solfatara crater, Italy	75,000	1520	na	Chiodini et al., 2001; Cardellini et al., 2003
Poggio dell'Ulivo cold degassing area, Italy	22,000	3911	na	Cardellini et al., 2003
Poas volcano, Costa Rica	140	na	16	Williams Jones et al., 2000
Arenal volcano, Costa Rica	291	na	7	Williams Jones et al., 2000
Masaya volcano, Nicaragua	50,000	na	na	Lewicki et al., 2003
Oldoinyo Lengai volcano, Tanzania	1350	166	90	Koepenick et al., 1996
Yellowstone volcanic system, USA	30,000	Travertine areas: 89 Acid sulfate areas: 1200	90	Werner et al., 2000
Dixie Valley Geothermal Field, USA	570	na	na	Bergfeld et al., 2001
Mammoth Mountain, USA	>10,000	1500-2100	90	Gerlach et al., 2001; Sorey et al., 1998
Miyakejima volcano, Japan	18,150	na	na	Hernandez et al., 2001

sources tends to migrate to the near-surface in the gaseous phase in equal or greater proportion than dissolved in groundwater (e.g., Cruz et al., 1999; Favara et al., 2001; Evans et al., 2002), and (3) a broad range of technologies are available to monitor CO₂ in the near-surface environment. Importantly, however, CO₂ is produced in the near surface by a variety of biological processes, and identifying CO₂ from hidden geothermal resources will involve monitoring a system with large variation in fluxes and concentrations arising from natural biologic and hydrologic processes. The detection of anomalous CO₂ will therefore require searching for potential geothermal anomalies, likely of small magnitude, over areas of tens of km² or more within the varying background CO₂ fluxes and concentrations. Here, we present integrated measurement, modeling, and analysis strategies to meet this challenge.

CO₂ IN KNOWN VOLCANIC AND HYDROTHERMAL SYSTEMS

Numerous diffuse CO₂ degassing studies have been conducted in known (i.e., "visible") volcanic and hydrothermal environments, many of which focused on characterizing the magnitude and spatial distribution of CO₂ emissions. Table 1 summarizes the maximum (and average, if applicable) surface CO₂ fluxes and soil CO₂ concentrations measured in selected known systems. As shown, the maximum CO₂ fluxes and concentrations measured varied widely, but could reach up to ~75,000 g m⁻² d⁻¹ and 90 vol.%, respectively. Both elevated CO₂ fluxes and concentrations were commonly associated with faults, fractures, eruptive fissures, and vents in the study areas. While surface CO₂ emission rates from hidden geothermal systems will likely be lower than

those measured in known volcanic and hydrothermal systems, the preferential pathways for CO₂ flow from depth to the near surface will probably be similar.

SIMULATIONS OF GEOTHERMAL CO₂ MIGRATION

We conducted numerical simulations to evaluate the magnitudes and spatial distribution of anomalous near-surface CO₂ concentrations and fluxes that might result when CO₂ leaks from a hidden geothermal system at depth. Based on this information, we can then design and evaluate potential monitoring and detection methods.

We use the numerical code T2CA (Oldenburg and Unger, 2004), a research module of TOUGH2 (Pruess et al., 1999). T2CA retains the fundamental porous media flow and transport capabilities of TOUGH2, and models five components (water, brine, CO₂, a gas tracer, and air) under isothermal or non-isothermal conditions. The main advance in T2CA is the implementation of a simple atmospheric transport and dispersion capability for dilute gases based on the variable-K theory (Arya, 1999). That is, a constant time-averaged logarithmic wind velocity profile is specified for advection, and atmospheric dispersion is modeled as a diffusion process with variable diffusivity as a function of height above the ground surface. In this way, T2CA models coupled subsurface and atmospheric surface layer gas flow and transport.

The geologic framework of the modelled hidden geothermal system is based loosely on an arid Basin and Range Province system like the Dixie Valley (Nevada) geothermal system, only without any surface manifestations. In particular, we consider a

two-dimensional system in which an alluvial fan covers a geothermal anomaly associated with deep range-bounding faults so that it is essentially invisible at the surface (Figure 1). Within this system, we model the upward migration of CO₂ from a small (15 m²) region that represents the top of a conductive fault, located near the water table, ~300 m in the horizontal direction from the left boundary. The CO₂ spreads in the heterogeneous system (i.e., the alluvial fan) as it migrates upward until it seeps out at the ground surface. We consider both a homogeneous permeability case, along with five realizations of heterogeneous permeability. The heterogeneous permeability cases are significant because gas migration will tend to follow high-permeability pathways. Here, permeability is characterized by a mean value of 10⁻¹² m², and varies by four orders of magnitude. There is a 45-m correlation length in the Y-direction (sub-horizontal), and no correlation in the vertical direction, thereby creating a layered structure intended to represent an alluvial fan. We simulated source strength CO₂ fluxes of 5.76, 57.6 and 576 g m⁻² d⁻¹. These fluxes were arbitrarily chosen to produce small CO₂ seepage fluxes, and are significantly lower than those measured in known/visible volcanic and hydrothermal systems (e.g., Table 1). We chose to model this low range of values to test the limits of available technologies for near-surface CO₂ detection. For reference, the largest source CO₂ flux we consider is similar to the highest surface CO₂ fluxes measured at Dixie Valley (Table 1). We present results for 200 years of simulation, at which point the gas seepage flux and concentrations are nearly steady.

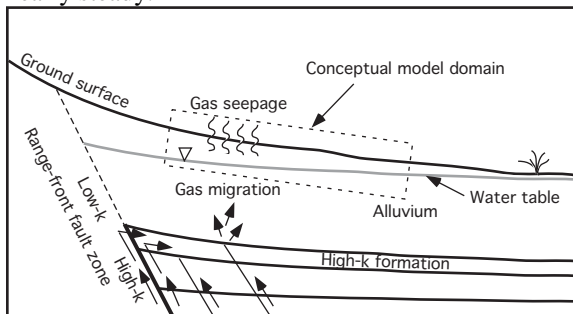


Figure 1. Conceptual model for gas migration from a deep hidden geothermal system. Also shown is the outline (dashed) of the two-dimensional model domain (see Figure 2).

To emphasize the key simulation results relevant to design of a near-surface CO₂ monitoring program, we present coupled CO₂ subsurface migration and surface-layer mixing for one of our five heterogeneous permeability realizations, high source CO₂ flux, and constant wind speeds of 1 and 3 m s⁻¹ (Figure 2). Figure 2 shows that the gas in the CO₂ plume is essentially pure CO₂ in the subsurface, even though the source CO₂ flux is quite small. Importantly, surface-layer winds are capable of

diluting CO₂ concentrations to very small values above the ground surface. For example, surface-layer CO₂ concentrations only reach maximum values of ~10⁻⁷ mole fraction (0.1 ppmv) for both wind speeds considered. Overall, the high simulated CO₂ concentrations observed at the ground surface and in the subsurface, relative to the atmospheric surface layer, suggest that monitoring of CO₂ in the subsurface or at the ground surface may have greater potential to detect anomalous CO₂ of geothermal origin than above-ground techniques.

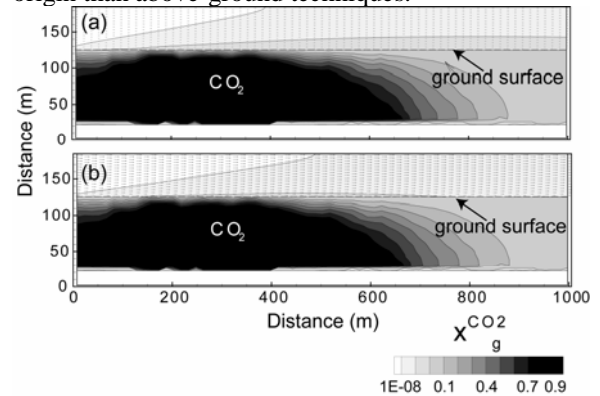


Figure 2. Coupled CO₂ subsurface migration and surface-layer mixing at $t = 200$ years for one heterogeneous permeability realization, high source CO₂ flux (576 g m⁻² d⁻¹), and constant wind speeds of (a) 1 m s⁻¹ and (b) 3 m s⁻¹. CO₂ concentration is in mole fraction.

Figure 3 shows horizontal profiles of CO₂ concentration at 3 m depth and surface CO₂ flux for the low, medium, and high source CO₂ flux and one heterogeneous permeability realization. These profiles all show a similar increase and then decrease in concentration and flux crossing the CO₂ plume. Maximum CO₂ concentrations for the low, medium, and high source strengths are about 2 × 10⁴, 2 × 10⁵ and 7 × 10⁵ ppmv, respectively, whereas maximum surface CO₂ fluxes are about 4 × 10⁻⁴, 0.52, and 100 g m⁻² d⁻¹, respectively. These profiles also show that the width of the CO₂ plume increases with increasing source strength. If the source area of CO₂ emission were increased (i.e., to simulate more diffuse, rather than focused CO₂ flow), the magnitude of the near-surface CO₂ concentration and flux signals would decrease, while the width of the anomaly would increase. Relative to the homogeneous permeability cases (not shown here), fluxes along the heterogeneous profiles are more spatially variable and maximum observed fluxes may be greater or lower, depending whether high or low permeability was assumed, respectively. Complete results for the five heterogeneous permeability realizations, homogeneous permeability, and three source CO₂ flux values can be found in Lewicki and Oldenburg (2004).

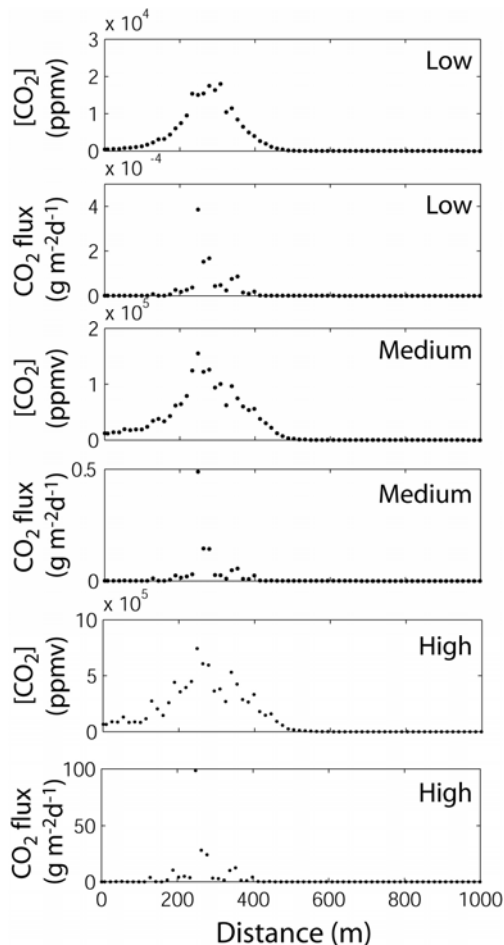


Figure 3. Horizontal profiles of shallow subsurface CO_2 concentration ($[CO_2]$, 3 m depth) and surface CO_2 flux for low, medium, and high (5.76 , 57.6 , and $576 \text{ g m}^{-2} \text{ d}^{-1}$, respectively) CO_2 source flux, one heterogeneous permeability realization, and $t = 200$ years.

BACKGROUND CO_2

We define “background” CO_2 as CO_2 derived mainly from the atmosphere and biologically mediated oxidation of organic carbon. Background soil CO_2 fluxes and concentrations are primarily dependent on CO_2 production in the soil by biological processes, flow of CO_2 from biologic/hydrologic sub-soil sources into the soil column, and exchange of CO_2 with the atmosphere by concentration and pressure-driven transport processes (diffusion and advection, respectively).

Biologically produced CO_2 in soils (i.e., soil respiration) is derived from root respiration and oxidative decay of organic matter. While many factors may regulate soil respiration rates, changes in atmospheric and soil temperature and soil moisture

have been shown to strongly influence these rates and related CO_2 concentrations and fluxes. CO_2 that enters soil from sub-soil sources can be derived from groundwater degassing of CO_2 derived from respiration, atmospheric, and carbonate mineral sources. Also, production of CO_2 at sub-soil depths can occur by oxidative decay of relatively young or ancient (peat, lignite, kerogen) organic matter in the vadose zone. Exchange of CO_2 from subsurface sources with the atmosphere can occur by diffusion and/or advection. Diffusive flow depends on the gas production rate and soil temperature, moisture, and properties such as porosity. Advective flow can be driven by changes in atmospheric temperature, pressure, wind, and rainfall.

The chemical and isotopic compositions of gases collected at soil and sub-soil depths provides information on CO_2 production and the source of this CO_2 (Table 2). CO_2 concentration profiles measured with depth in the vadose zone can yield information about CO_2 production. For example, an increase in CO_2 concentration with depth below the soil indicates CO_2 production at sub-soil depths. Production of CO_2 by oxidative decay of organic matter tends to consume O_2 at a similar rate. Also, atmospheric O_2 will diffuse down into the soil and sub-soil as sub-surface CO_2 diffuses to the atmosphere. A flux of geothermal CO_2 would produce elevated CO_2 concentration at depth, relative to the atmosphere, but would not be accompanied by O_2 consumption, although atmospheric O_2 would diffuse down into the soil. Based on these general processes, the CO_2 and O_2 concentration profiles should be different, depending on whether a geothermal flux is present. One might expect groundwater degassing of respiration and atmospheric-derived CO_2 to show similar chemical trends within the vadose zone to degassing of geothermal CO_2 . However, vadose zone CO_2 concentrations produced by groundwater degassing and biological respiration processes have generally been reported to be less than 13 vol.% CO_2 (e.g., Wood and Petraitis, 1984; Amundson and Davidson, 1990; Wood et al., 1993), whereas near-surface CO_2 concentrations associated with geothermal emissions could be much higher. For example, simulated geothermal source CO_2 fluxes of 57.6 to $576 \text{ g m}^{-2} \text{ d}^{-1}$ produce maximum near-surface CO_2 concentrations of ~ 20 – 70 vol.% (2×10^5 to 7×10^5 ppmv, Figure 2). Importantly, however, the maximum near-surface CO_2 concentration produced by a source CO_2 flux of $5.76 \text{ g m}^{-2} \text{ d}^{-1}$ is only predicted to be ~ 2 vol.% (2×10^4 ppmv, Figure 2), which could be problematic to distinguish from background CO_2 concentrations. Table 2 also shows that the ranges of typical carbon isotopic compositions of geothermal CO_2 are distinct from

Table 2. Chemical and isotopic signatures related to CO_2 derived from different sources.

CO ₂ source	$\delta^{13}\text{C}_{\text{CO}_2}$ (‰)	$\Delta^{14}\text{C}_{\text{CO}_2}$ (‰)	Near-surface CO ₂ conc.	CO ₂ conc. profile with depth	O ₂ conc. profile with depth
Atmosphere	-7	70	Low	na	na
Plant root respiration and oxidative decay of young soil organic matter	C ₃ : -24 to -38 C ₄ : -6 to -19	≥70	Low to moderate	Increasing through soil zone	Decreasing through soil zone
Oxidative decay of ancient organic matter	C ₃ : -24 to -38 Aquatic/C ₄ : -6 to -19	Highly depleted to absent, depending on age	Low	Potentially increasing through vadose zone	Potentially decreasing through vadose zone
Marine carbonate rocks	Also age dependent 0 ± 4	Absent	Low	Increasing through vadose zone	No effect
Geothermal	-2 to -6	Absent	Moderate to high	Increasing through vadose zone	No effect

Conc., C₃, and C₄, refer to concentration, C₃ plants, and C₄ plants, respectively. All near-surface concentrations given are general estimates; they are strongly dependent on the magnitude of the CO₂ flux.

those whose dominant sources are background biological CO₂. Therefore, analysis of the $\Delta^{14}\text{C}$ and $\delta^{13}\text{C}$ compositions of gases collected from the soil and, in particular, from the sub-soil where biologic CO₂ production rates are low can serve as a tool to distinguish CO₂ of geothermal from background origin.

INSTRUMENTATION FOR MONITORING CO₂

A broad range of technologies is available to measure near-surface CO₂ concentrations and fluxes to detect anomalous CO₂ of geothermal origin. These technologies include (1) the infrared gas analyzer (IRGA) for measurement of concentrations at point locations, (2) the accumulation chamber (AC) method for measuring soil CO₂ fluxes at point locations, (3) the eddy covariance (EC) method for measuring net CO₂ flux over a given area, (4) hyperspectral imaging of vegetative stress resulting from elevated CO₂ concentrations, and (5) light detection and ranging (LIDAR) that can measure CO₂ concentrations over an integrated path in the air column. These techniques differ from one another in terms of the spatial and temporal scale of the measurement, measurement sensitivity and error, and cost. Here, we focus on the relatively low-cost and reliable IRGA, AC, and EC methods for CO₂ concentration and flux measurements.

Infrared Gas Analyzer

The infrared gas analyzer (IRGA) is an instrument commonly used to measure CO₂ concentration in subsurface or atmospheric air. The measurement is based on CO₂ absorption of infrared radiation within a sample gas cell. Portable IRGAs are available for use in the field and can make single or continuous measurements over time, which may be made within

about one second to minutes, depending on the instrument. IRGAs are available to measure CO₂ concentration over a low range (e.g., 0-1000 ppmv) or over a high range (e.g., 0-100 vol.%). The precision and accuracy can be as good as ± 0.2 ppmv at 350 ppmv and ± 1%, respectively. The cost of equipment may range from \$500 to \$30,000.

Soil or subsoil gas CO₂ concentrations can be rapidly measured at many point locations within a large area using a probe and a portable IRGA. Using this method, a probe is driven down to the depth of interest, gas is pumped from the soil into the IRGA by an internal pump, and CO₂ concentration is measured.

Accumulation Chamber Method

IRGAs may be coupled with additional instrumentation to obtain surface CO₂ fluxes. For example, the accumulation chamber (AC) method (e.g., Chiodini et al., 1998) is used to measure soil CO₂ flux using an AC and an IRGA. An AC with an open bottom (cm² scale) is placed on the soil surface, the contained air is circulated through the AC and the IRGA, and the rate of change of CO₂ concentration in the AC is measured by the IRGA (Figure 4). The CO₂ flux is then calculated as proportional to the rate of change. The accuracy of the AC method was estimated to be -12.5 % due to alteration of gas flow by the AC (Evans et al., 2002); precision is ± 10 % (Chiodini et al., 1998). Each AC measurement is typically made within several minutes by one person, allowing for many measurements to be made over relatively short periods of time under variable terrain conditions. The cost of the portable AC instrumentation typically ranges from \$15,000 to \$25,000.

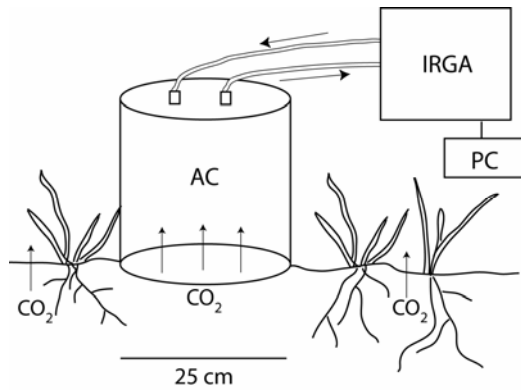


Figure 4. Schematic diagram of an accumulation chamber (AC) measurement system of soil CO₂ flux. The air contained in the AC is circulated through the AC and the infrared gas analyzer (IRGA) and the rate of change of CO₂ concentration in the AC is measured by the IRGA and recorded by the computer (PC).

Eddy Covariance

Eddy covariance (EC) (Baldocchi, 2003 and references therein) is a technique whereby high-frequency measurements of atmospheric CO₂ concentration at a fixed height above ground are made by an IRGA, along with micrometeorological variables such as wind velocity, temperature, and relative humidity (Figure 5). Integration of these measurements provides a gross conservation of energy and mass over an area of land (the EC footprint) from which the net CO₂ flux is derived. The method essentially involves time averaging the product of the time series of fluctuating CO₂ concentration and vertical wind velocity. Under steady-state conditions and for sufficiently long averaging time, this converges to the ensemble mean flux. The measured vertical CO₂ flux is an integral of the surface flux over the upwind footprint (typically m² to km²), the size of which scales with the measurement height, and is also dependent on meteorological conditions. One advantage of EC is that it provides a spatially and temporally averaged measurement, potentially providing more representative flux data and allowing for more efficient monitoring strategies than point measurements can provide. A limitation of the EC method is that it assumes a horizontal and homogeneous surface, and violations of this assumption can introduce significant error into the measurement. However, under acceptable terrain and meteorological conditions, estimates of daytime and nighttime error are generally less than 7 and 12%, respectively (e.g., Moore, 1986; Soegaard et al., 2000; Berger et al., 2001). The cost of EC equipment ranges from ~\$15,000 to \$40,000.

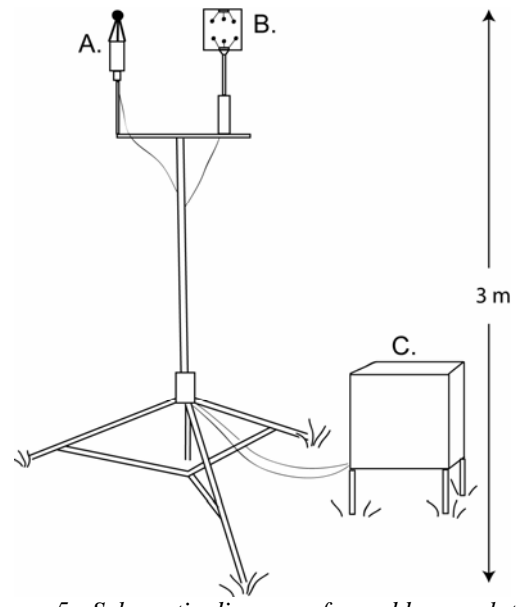


Figure 5. Schematic diagram of an eddy correlation (EC) instrumentation tower to measure surface CO₂ flux. An (A) open-path IRGA, (B) high frequency response sonic anemometer, and (C) box containing power source and datalogger/PC are shown.

STRATEGIES FOR DETECTION OF GEOTHERMAL CO₂

To meet the challenge of detecting potentially small-magnitude geothermal CO₂ emissions within the natural background variability of CO₂, we propose an approach that integrates available detection and monitoring techniques with statistical analysis and modeling strategies. Overall, we advocate a monitoring strategy that initially focuses on rapid, economical, reliable measurements of CO₂ concentrations in the soil and potentially in pre-existing wells/gradient holes within the study area, and surface CO₂ fluxes using the AC method ± EC. Our objective is to minimize the number of these measurements and then focus more time- and cost-intensive methods on “high-probability” anomalies of geothermal origin.

Even small geothermal source CO₂ fluxes are expected to produce high CO₂ concentrations within the vadose zone. As a result, if wells/gradient holes already exist within the area targeted for geothermal exploration, they should be sampled for CO₂ concentration (and additional chemical and isotopic analyses if CO₂ levels are high). Point measurements of soil CO₂ fluxes and concentrations should also be made along grids using the AC method and a portable IRGA, respectively. If the study area satisfies the terrain and vegetation distribution requirements of the EC technique, it should be used to measure net

surface fluxes. Particular attention should be paid to characterizing gas flow along high-permeability pathways, such as faults/fractures. Importantly, the spatial and temporal variability of soil CO₂ fluxes and concentrations should also be quantified within a background area with similar geologic, climatic, and ecosystem characteristics to the area targeted for geothermal exploration. Bayesian statistical analysis of CO₂ concentration and flux measurements in both the area targeted for geothermal exploration and the background study area should be used to identify the presence (or absence) of CO₂ anomalies with high statistical confidence, and estimate the number of measurements required to do this (e.g., Bayes, 1763; Lewicki and Oldenburg, 2004). Also, geostatistical methods should be used to map the spatial distribution of soil CO₂ concentrations and fluxes, and these parameters' autocorrelation and cross-correlation coefficients. These maps can be used to discern spatial patterns that may be indicative of geothermal CO₂ emissions and estimate total CO₂ emission rates from the study areas (e.g., Lewicki et al., in press).

Once CO₂ concentrations and fluxes have been determined with high confidence to be of geothermal origin, more expensive sampling of gas profiles with depth through the vadose zone, and chemical and isotopic analyses could be undertaken. In particular, an increase in CO₂ concentration with depth would indicate deep CO₂ emissions. Also, the carbon-13 and carbon-14 values of subsurface CO₂ should distinguish CO₂ of geothermal from background origin (Table 2). Integrated analysis of all measurements will determine definitively if CO₂ derived from a deep geothermal source is present, and if so, the spatial extent of the anomaly.

CONCLUSIONS

The properties of CO₂, methods for detection and monitoring of this gas, and the ranges of natural background CO₂ fluxes and concentrations are generally well known. We are able to gain some insight into near-surface CO₂ concentrations and fluxes resulting from CO₂ migration and seepage from hidden geothermal reservoirs using numerical simulation. Nevertheless, detecting small anomalous geothermal CO₂ fluxes and concentrations within natural background CO₂ variations poses a challenge. The exploration strategy that we propose to find geothermal CO₂ involves integrated measurement and statistical analysis to understand the natural background system. Once this understanding is achieved, integrated measurement, modeling, and sampling technologies can be applied toward the characterization of CO₂ within the study area targeted for exploration. If CO₂ concentrations and fluxes are suggestive of the presence of CO₂ derived from a geothermal source, the area should be investigated

further by more cost- and time-intensive vertical profile sampling and isotopic analyses. Integrated analysis of all measured data will determine definitively if CO₂ derived from a deep geothermal source is present, and if so, the spatial extent of the anomaly. The appropriateness of further geophysical measurements, installation of deep wells, and geochemical analyses of deep fluids can then be decided based on the results of the near surface CO₂ monitoring program.

REFERENCES

- Amundson, R.G. and E.A. Davidson (1990), "Carbon and nitrogenous gases in the soil atmosphere", *Journal of Geochemical Exploration*, **38**, 13-41.
- Arya, S.P. (1999), "Air Pollution Meteorology and Dispersion", Oxford University Press.
- Baldocchi, D., (2003), "Assessing the eddy covariance technique for evaluating carbon dioxide exchange rates of ecosystems: past present, and future", *Global Change Biology*, **9**, 479-492.
- Bayes, T. (1763), "An essay towards solving a problem in the doctrine of Chances", *Philosophical Transactions of the Royal Society of London*, **53**, 370-418.
- Berger, B.W., Davis, K.J., Yi, C., Bakwin, P.S., and Zhao, C., (2001). "Long-term carbon dioxide fluxes from a very tall tower in a northern forest: flux measurement methodology", *Journal of Atmosphere and Ocean Technology*, **18**, 529-542.
- Bergfeld, D., F. Goff, and C.J. Janik (2001), "Elevated carbon dioxide flux at the Dixie Valley geothermal field, Nevada; relations between surface phenomena and the geothermal reservoir", *Chemical Geology*, **177**, 43-66.
- Cardellini, C., G. Chiodini, F. Frondini, D. Granieri, J. Lewicki, and L. Peruzzi (2003) "Accumulation chamber measurements of methane fluxes: application to volcanic-geothermal areas and landfills", *Applied Geochemistry*, **18**, 45-54.
- Chiodini, G., C. Cardellini, F. Frondini, D. Granieri, L. Marini, and G. Ventura (2001), "CO₂ degassing and energy release at Solfatara volcano, Campi Flegrei, Italy", *Journal of Geophysical Research*, **106**, 16,213-16,221.
- Chiodini, G., G. R. Cioni, M. Guidi, B. Raco, and L. Marini (1998), "Soil CO₂ flux measurements in volcanic and geothermal areas", *Applied Geochemistry*, **13**, 543-552.
- Cruz, J.V., R.M. Couthinho, M.R. Carvalho, N. Oskarrson, and S.R. Gislason (1999), "Chemistry of waters from Furnas volcano, Sao Miguel, Azores: fluxes of volcanic carbon dioxide and leached materials", *Journal of Volcanology and Geothermal Research*, **92**, 151-167.

- Ellis, A.J. and W.A.J. Mahon (1977), *Chemistry and Geothermal Systems*, Academic Press, New York.
- Evans, W. C., M. L. Sorey, A. C. Cook, B. M. Kennedy, D. L. Shuster, E. M. Colvard, L. D. White, and M. L. Huebner (2002), "Tracing and quantifying magmatic carbon discharge in cold groundwaters: lessons learned from Mammoth Mountain, USA", *Journal of Volcanology and Geothermal Research*, **114**, 291–312.
- Evans, W.C., M.L. Sorey, B.M. Kennedy, D.A. Stonestrom, J.D. Rogie, and D.L. Shuster (2001), "High CO₂ emissions through porous media: Transport mechanisms and implications for flux measurement and fractionation", *Chemical Geology*, **177**, 15-29.
- Favara, R. S. Giammanco, S. Inguaggiatio, G. Pecoraino (2001), "Preliminary estimate of CO₂ output from Pantelleria Island volcano (Sicily, Italy): evidence of active mantle degassing", *Applied Geochemistry*, **16**, 883-894.
- Gerlach, T.M., M.P. Doukas, K.A. McGee, and R. Kessler (2001), "Soil efflux and total emission rates of magmatic CO₂ at the Horseshoe Lake tree kill, Mammoth Mountain, California", *Chemical Geology*, **177**, 101-116.
- Hernandez, P.A., J.M. Salazar, Y. Shimoike, T. Mori, K. Notsu, and N. Perez (2001), "Diffuse emission of CO₂ from Miyakejima volcano, Japan", *Chemical Geology*, **177**, 175-185.
- Klusman, R.W., J.N. Moore, and M.P. LeRoy (2000) "Potential for surface gas flux measurements in exploration and surface evaluation of geothermal resources", *Geothermics*, **29**, 637-670.
- Koepnick, K.W., S.L. Brantley, J.M. Thompson, G.L. Rowe, A.A. Nyblade, and C. Moshy (1996), "Volatile emissions from the crater and flank of Oldoinyo Lengai volcano, Tanzania", *Journal of Geophysical Research*, **101**, 13,819-13,830.
- Lewicki, J.L. and C.M. Oldenburg (2004), "Strategies for detecting hidden geothermal systems by near-surface gas monitoring", Lawrence Berkeley National Laboratory Report LBNL-56895.
- Lewicki, J.L. Bergfeld, D., Cardellini, C., Chiodini, G., Granieri, D., Varley, N., Werner, C. (in press), "Comparative soil CO₂ flux measurements and geostatistical estimation methods on Masaya volcano, Nicaragua", *Bull. Volcanol.*
- Lewicki, J.L., C. Connor, K. St-Amand (2003), J. Stix, and W. Spinner, "Self-potential, soil CO₂ flux, and temperature on Masaya volcano, Nicaragua", *Geophysical Research Letters*, **30**, 1817.
- Moore, C.J., (1986), "Frequency response corrections for eddy covariance systems", *Boundary Layer Meteorology*, **37**, 17-35.
- Oldenburg, C.M., and A.J.A. Unger (2004), "Coupled vadose zone and atmospheric surface-layer transport of CO₂ from geologic carbon sequestration seepage simulation", *Vadose Zone Journal*, **3**, 848–857.
- Pruess, K., C. Oldenburg, and G. Moridis (1999), "TOUGH2 User's Guide Version 2.0", Lawrence Berkeley National Laboratory Report LBNL-43134.
- Soegaard, H., Nordstroem, C., Friborg, T., Hansen, B.U., Christensen, T.R., and Bay, C., (2000), "Trace gas exchange in a high-arctic valley, 3. Integrating and scaling CO₂ fluxes from canopy to landscape using flux data, footprint modeling, and remote sensing", *Global Biogeochemical Cycles*, **14**, 725-744.
- Sorey, M.L., W.C. Evans, B.M. Kennedy, C.D. Farrar, L.J. Hainsworth, and B. Hausback (1998), "Carbon dioxide and helium emissions from a reservoir of magmatic gas beneath Mammoth Mountain, California", *Journal of Geophysical Research*, **103**, 15,303-15,323.
- Werner, C., S.L. Brantley, and K. Boomer (2000), "CO₂ emissions related to the Yellowstone volcanic system 2. Statistical sampling, total degassing, and transport mechanisms", *Journal of Geophysical Research*, **105**, 10,831-10,846.
- Williams-Jones, G., J. Stix, M. Heiligmann, A. Charland, B. Sherwood Lollar, N. Arner, G. Garzon, V.J. Barquero, and E. Fernandez (2000), "A model of diffuse degassing at three subduction-related volcanoes", *Bulletin of Volcanology*, **62**, 130-142.
- Wood, W.W. and M.J. Petraitis (1984), "Origin and distribution of carbon dioxide in the unsaturated zone of the southern high plains of Texas", *Water Resources Research*, **20**, 1193–1208.
- Wood, B.D., C.K. Keller, and D.L. Johnstone (1993), "In situ measurement of microbial activity and controls on microbial CO₂ production in the unsaturated zone", *Water Resources Research*, **29**, 647–659.

ACKNOWLEDGEMENTS

This work was supported by the Assistant Secretary for Energy Efficiency and Renewable Energy, Office of Geothermal Technologies, of the U.S. Department of Energy, and by the Office of Science, U.S. Department of Energy, under Contract No. DE-AC03-76SF00098. We thank C. Doughty (LBNL) and M. Lippmann (LBNL) for constructive review of this paper.

DISPLAYING AND INTERPRETING FLUID INCLUSION STRATIGRAPHY ANALYSES ON MUDLOG GRAPHS

David I. Norman¹, Lorie M. Dilley¹, and Jess McCulloch²

¹. Dept. of Earth and Environmental Sciences
New Mexico Tech
Socorro, New Mexico 87801, USA
E-mail: dnorman@nmt.edu, ldilley@hdalaska.com,

². Coso Operating Company
PO Box 1690
Inyokern, California 93527, USA
E-mail: jmcculloch@caithnessenergy.com

ABSTRACT

This is the fourth paper in a series on developing fluid inclusion stratigraphy (FIS) as a logging tool for geothermal bore holes. Here we address methods of displaying analyses and plotting gas ratios used for data interpretation on mudlog plots. The goal is to develop a rapid method of data display and interpretation for the up to 10,000 analyses returned by a geothermal well FIS analysis.

INTRODUCTION

Fluids trapped in inclusions are generally faithful indicators of pore fluid chemistry. Temperatures and composition of geothermal fluids are sensitive indicators of their origins, evolutions, and the processes that have affected them. Our working hypothesis is that samples of geothermal fluids are trapped in wall rock minerals within microfractures adjacent to veins. Mass spectrometer analyses of gases within these inclusions show fluid sources and processes within geothermal systems (Giggenbach 1997; Norman 1997; Blamey 2002, Dilley et al. 2004, Dilley and Norman, 2004, Norman et al., 2004).

California Energy Commission is funding us to develop Fluid Inclusion Stratigraphy (FIS) to use as a logging tool to assess geothermal bore holes. The assessment techniques seek to provide ways to: distinguish non-producing from producing wells; identify major fluid flow zones; and find entrants of cold and steam-heated waters into the bore hole. The FIS method analyzes volatiles in drill-cuttings fluid

inclusions by mass spectrometry. The commercial process, developed in part by Fluid Inclusion

Technology (FIT) for the hydrocarbon industry is highly automated. Thousands of analyses made in a day resulting in turnaround times in days and costs comparable to other logging methods. The procedure gives a downhole map of vein distribution and chemistry plotted on borehole logs. Fluid source is determined from gas chemistry.

This is the fourth paper on developing FIS for application to geothermal wells. Other papers show the gas analyses on simple depth versus gas line charts, e.g. see the paper by Dilley et al. 2005 elsewhere in this Proceedings. Our problem is that a FIS analyses covers the mass spectrum from 1 to 180. A typical FIS analysis yields about 10,000 analyses when performed at 20 ft intervals on a 10,000 ft well. It is difficult to visualize the analyses and see relationships between them for numerous species and gas ratios when presented on a series of charts. Here we address methods of data display and analysis that enable us to understand how fluid inclusion gas chemistry changes and fluid source varies with depth in geothermal bore holes.

We need to be able to clearly display downhole changes in gas chemistry and downhole changes in gas ratios and sums. In order for FIS to be a viable tool we must be able to routinely return analyses to a client with little added time or cost for data analysis. This requires that there be routine methods of plotting, analyzing and interpreting fluid inclusion gas analyses

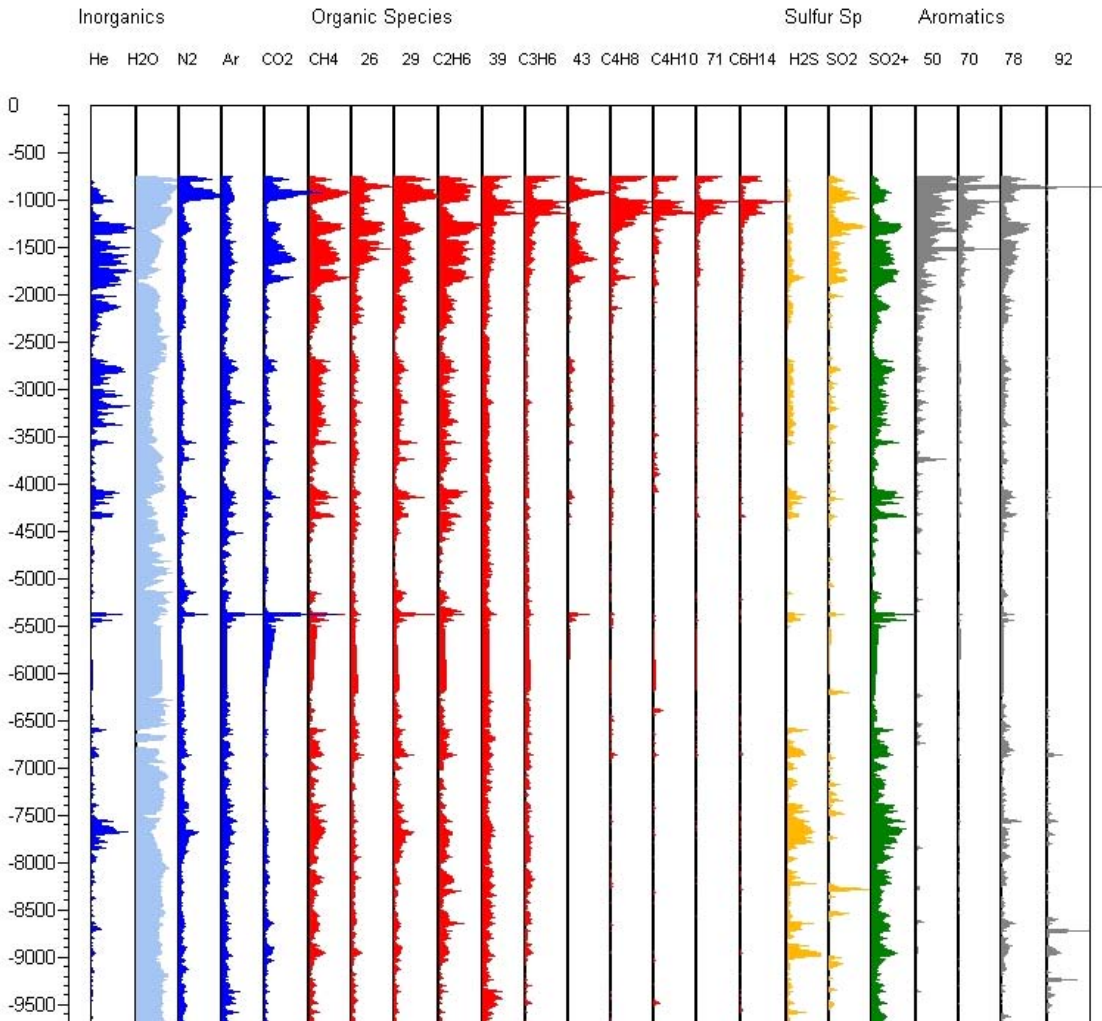


Figure 1. Well 1 species plotted versus depth. See text for details including species represented in columns headed by a number.

The volatile species of interest are the principal gaseous species in geothermal fluids and trace hydrocarbon species, which include H_2 , He, CH_4 , H_2O , N_2 , H_2S , Ar, CO_2 , C_2H_4 , C_2H_6 , C_3H_6 , C_3H_8 , C_4H_8 , C_4H_{10} , benzene, and toluene. Gas ratios and gas sums that we use, and their interpretations are as follows:

- Magmatic fluids are indicated by N_2/Ar , CO_2/CH_4 , $(N_2/Ar + CO_2/CH_4)/$ propane/propene that we term ratio 1, and $(N_2/Ar + CO_2/N_2)$ that we call ratio 2. Correctly magmatic fluids are indicated by $N_2/Ar > 105$; however FIT analyses are not calibrated. Instead we use the mass peak ratio of 28/40 to represent N_2/Ar . Duplicate analyses of Coso chip inclusions by FIT and
- Fractures are indicated by water and gas peaks.
- quantitative fluid inclusion gas analyses at New Mexico, indicate that the magmatic 28/40 ratios by FIT are values > 200 .
- Crustal fluids are indicated by 28/40 ratios < 200 , $44/15$ (CO_2/CH_4) < 40 , propane/propene (mass ratios 43/39) > 1 , and $1/ratio\ 1 > 0.5$
- Steam heated waters have elevated H_2S and H_2S/N_2 and sometimes elevated CO_2/N_2 . Elevated CO_2/N_2 is common in deep reservoir waters that can condense magmatic volatiles.
- Boiling and gascaps are indicated by high gas/water ratios and a gapcap by high total gas.

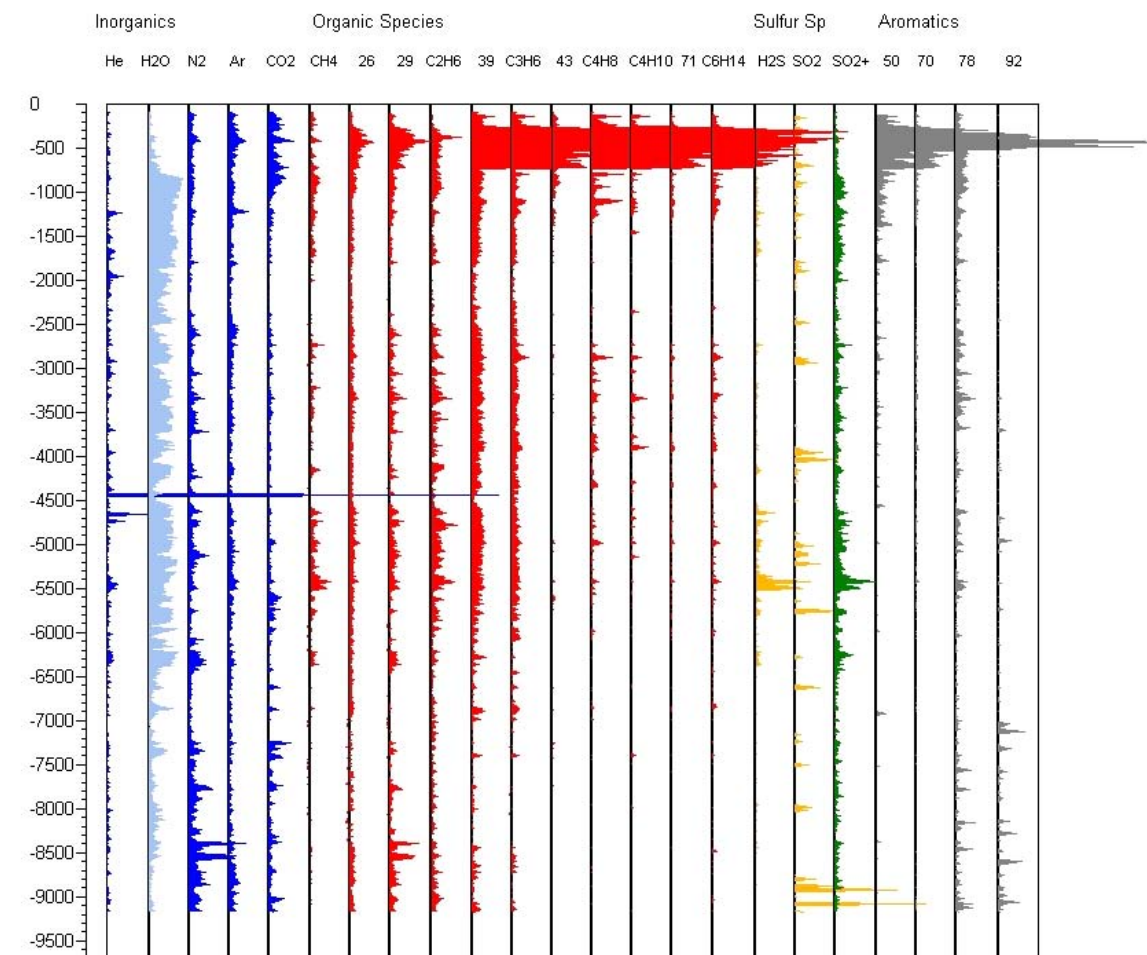


Figure 2. Well 2 species plotted versus depth. See text for details including species represented in columns headed by a number.

METHODS

Gas analyses for the four Coso wells previously reported on (Dilley et al., 2004) were plotted on the new diagrams. These are Well 1: BLM 33-7, Well 2: Navy 1 38C-9, Well 3: BLM 84-30, and Well 4: 58A-18. These wells were selected by COSO staff because Well 2 is an excellent producer, Well 1 is an average producer, Well 4 a problem producer, and Well 3 a nonproducer. For well locations see Fig. 1 in Dilley et al. 2005 in these Proceedings.

Analyses are plotted on two mudlog diagrams, one the displays inclusion gas chemistry, and the other gas ratios and species that are used for fluid source and fluid processes interpretation. We use the Rockware® program Logger to plot data in mudlog fashion. For each gas species we chose a major gas peak that has little interference from other species. For example, for He this is mass 4, and for methane this is mass 15. As explained in Dilley et al. (2004)

we check analyses to make certain that a mass peak like 28 represents nitrogen and the analyses interfere by a fragment of another species. To scale the species plots we calculated the mean and standard deviation for individual species. Generally the scale maximum is set at the mean plus 2σ . Analyses are plotted on a linear scale. We chose not to truncate the few analyses that exceed the scale maximum. Analyses are plotted using the Logger bar graph option.

On the species diagrams (Figs. 1, 2, 3, & 4) the species are grouped by chemical type, which are plotted in different colors. Inorganic species are plotted in blue with water distinguished by a lighter blue color. The C_2 - C_6 straight chain organic species are plotted in red; the sulfur species are plotted in orange and green; and organic aromatic peaks plotted in gray (Fig. 1 to 4). Sulfur species plotted are H_2S (mass 34), SO_2 (mass 48) and mass 64. Mass 64 is a major peak for SO_2 and CS_2 , and it a minor fragment

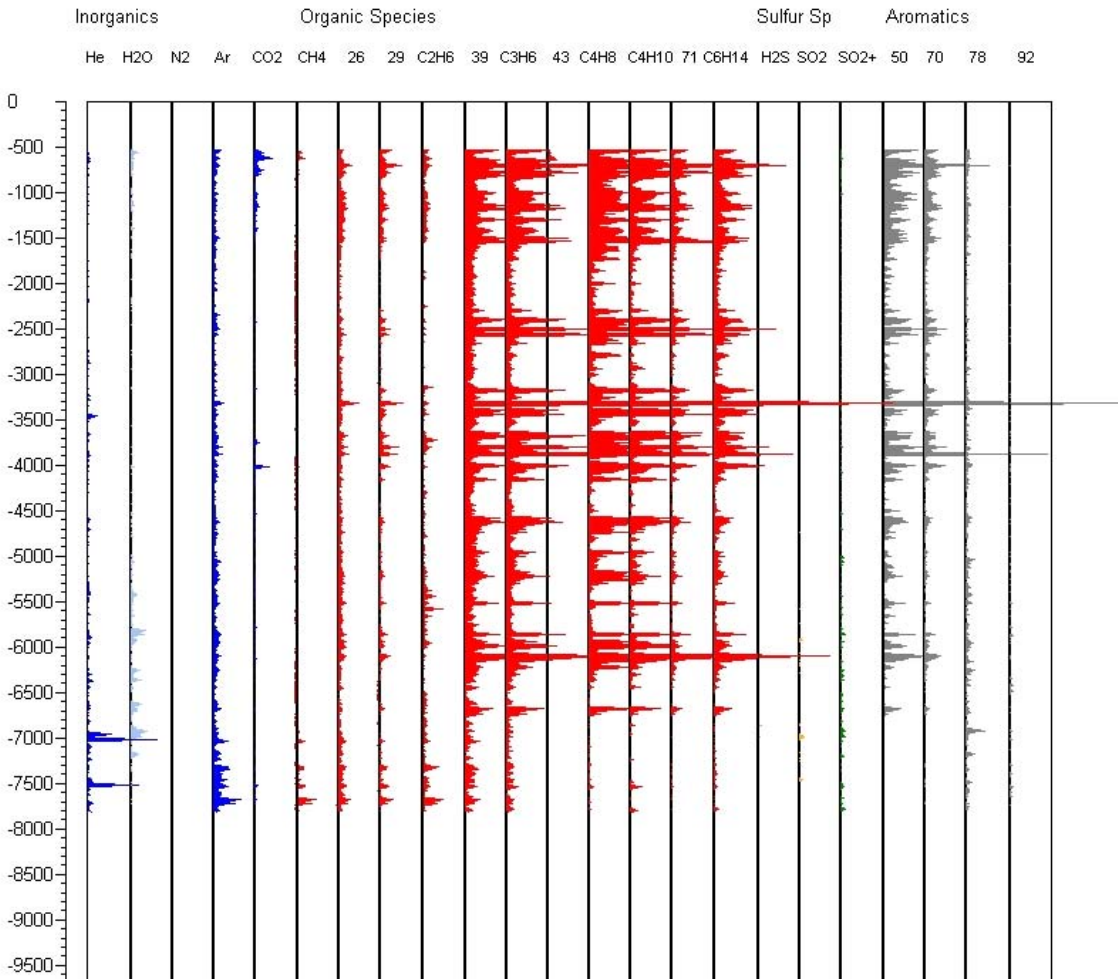


Figure 3. Well 3 species plotted versus depth. See text for details including species represented in columns headed by a number.

peak for some organic species. Hence mass 64 is distinguished by a different color than orange used for mass 34 and mass 48. Mass peaks 70, 78 and 92 are respectively the principal peaks for cyclopentane, benzene and toluene. Mass peak 50 is a common fragment peak for aromatic compounds. Quantitative analysis of fluid inclusion organic species shows that their concentrations are in the low ppm and ppb range (Norman et al., 2004). A quadrupole mass spectrometer can routinely measure species at concentrations of 1 part in 10^8 .

The second diagram (Figs 5, 6, 7 & 8) shows interpretive gas ratios, gas sums, and individual gaseous species. Gas ratios explained above are scaled identically to how they were scaled in Dilley et al. (2004), Dilley and Norman, 2004, and Norman et al. (2004). Two quantities not used before are

included. They are total gas, which is the sum of mass peaks from 2 to 180 minus mass 18 (water), and total gas/water. They are scaled in a similar fashion to the gaseous species. Water, total gas and gas/water ratio plotted in blue with water a lighter shade of blue. Deep hot reservoir fluid indicators are red; crustal fluid indicators in green; and condensate indicators are plotted in orange.

Interpretive gas ratios for N_2/Ar and CO_2/CH_4 ratios are plotted in both the magmatic and crustal columns. The N_2/Ar ratio is plotted on the magmatic column only if that ratio has a magmatic value or > 200 . Analyses with $N_2/Ar < 200$ are plotted in the crustal column. Scaling for the crustal fluid is 0 to 200; scaling for the magmatic column is as used in previous papers, which is from 0 to 1200. The CO_2/CH_4 ratios are plotted in a similar manner.

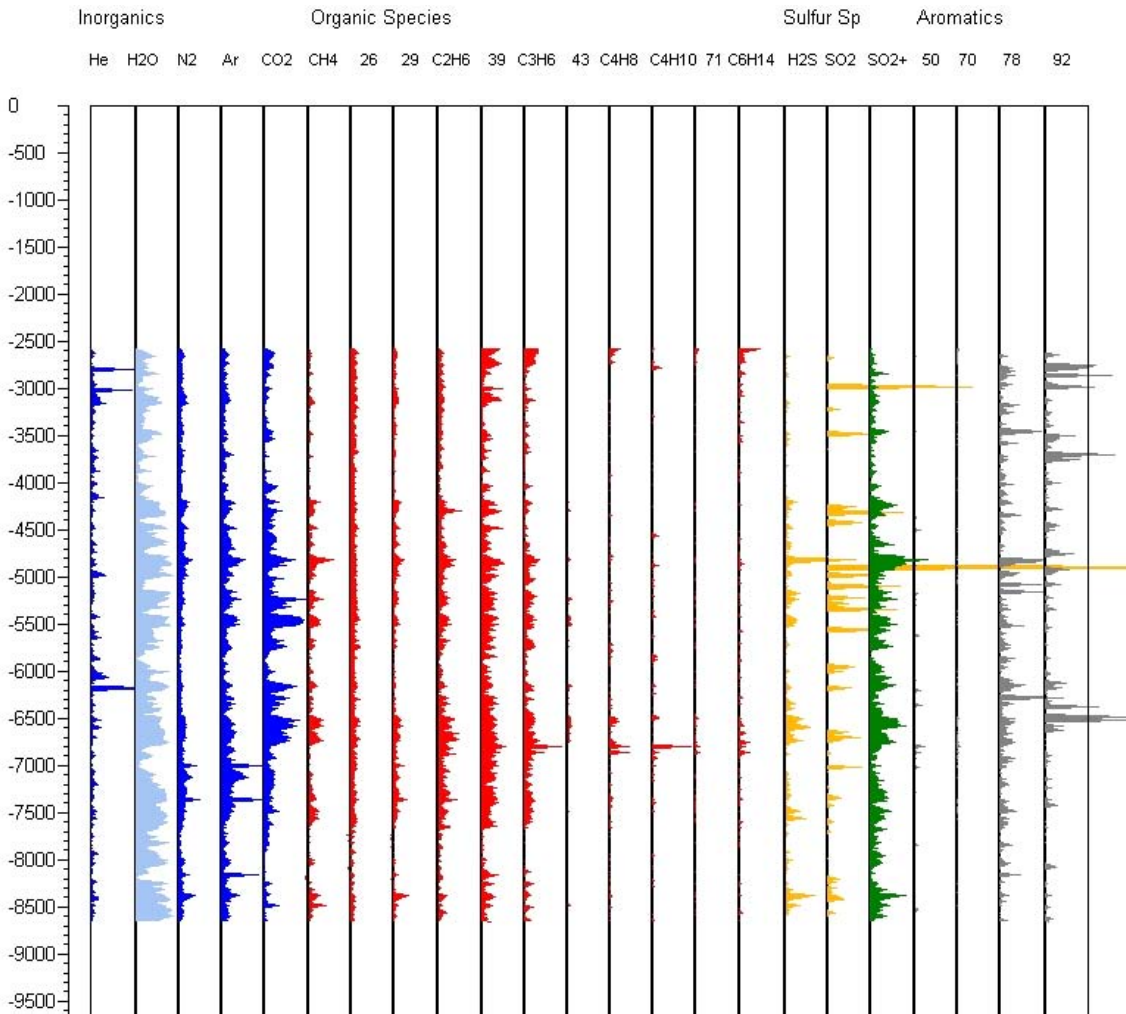


Figure 4. Well 4 species plotted versus depth. See text for details including species represented in columns headed by a number.

RESULTS

The gas analyses plotted in Figs 1 to 8 show clear differences between the wells. Analyses of the nonproducing well 3 differ remarkably from the analyses of the three producing wells. The species plot (Fig. 3) shows that Well 3 inclusions have significant amounts of the heavier hydrocarbon species and low concentrations of the lighter species. The producing wells (Figs. 1, 2, &4), except for the first few thousand feet show the opposite. Well 3 analyses differs from analyses of the producing wells in exhibiting little sulfur species gases and little water. The latter we interpret as indicating a low density of inclusions (Norman et al., 2004).

The Well 3 interpretive plot (Fig. 7) likewise shows clear differences between plots for the producing wells. The most remarkable difference is in the gas/water ratio, which is remarkably higher than the

ratios for production well analyses (Figs. 5, 6 & 8). Also, the Well 3 interpretive plot shows virtually no sulfur species gases and little indication of magmatic gases ratios.

There are distinct differences between the excellent producing well #2 and the two other producing wells (Fig. 5, 6 & 8). Principal production for Well 2 is from the interval 7,300 to 8,700 ft. The magmatic indicating ratios are higher than for the other two producing wells, and they are especially prominent in the producing interval. Below 6,000 ft. there is no indication of steam heated waters in H₂S and H₂S/N₂ plots; the fracture density indicated by water peaks is low; and fluid boiling indicated by elevated gas/water ratios is common, which is not true of the other two wells.

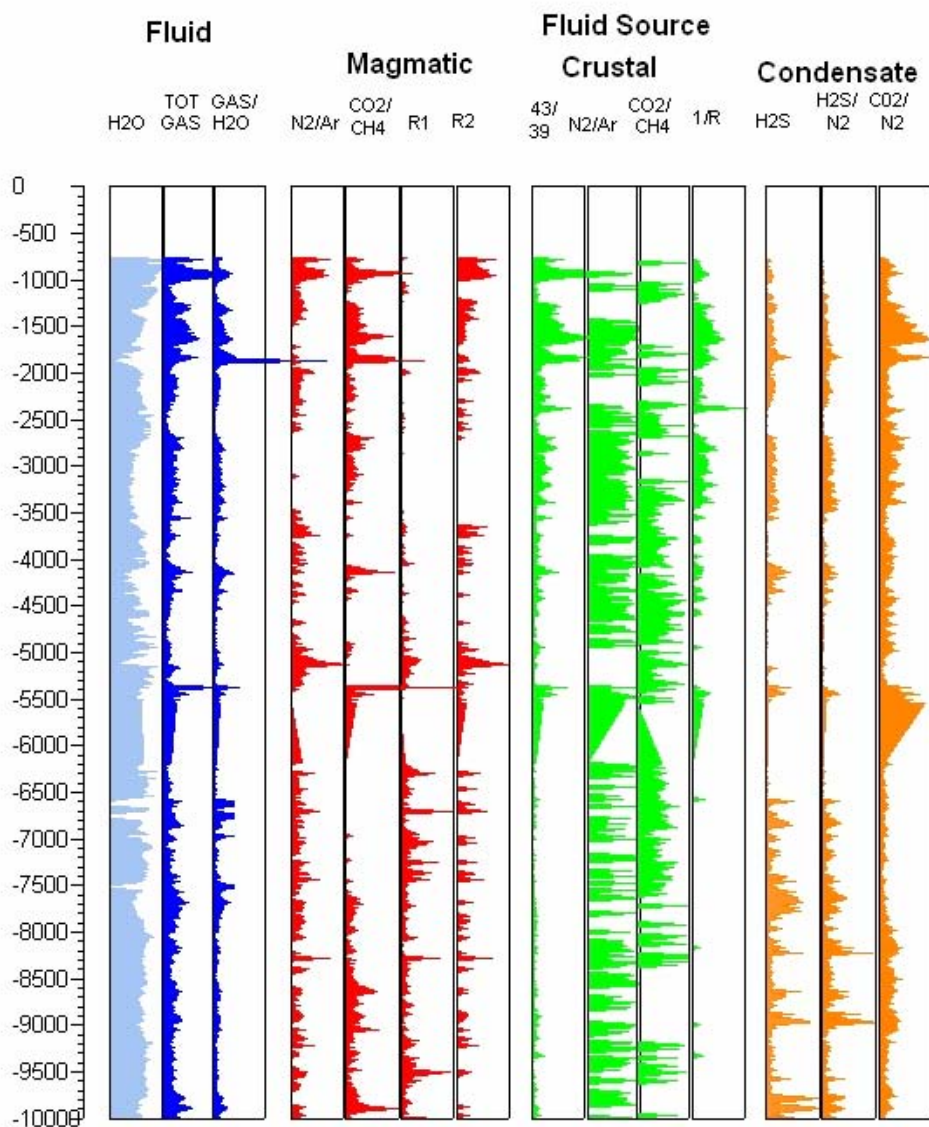


Figure 5. Well 1 interpretive mudlog plot. See text for details.

DISCUSSION

Plotting gas analyses on plots mud logs that show multiple species and multiple interpretations on a single diagram provides new insights into the analyses. The difference in the composition and concentration of organic species between producing wells and the nonproducer were not evident in past data analysis. The gas/water ratio shows inclusions with high gas contents, or assemblages of inclusions that include vapor-filled inclusions. The ubiquitous high gas water ratios in well 3 inclusions agree with a metamorphic origin for the inclusion fluids, because metamorphic fluid inclusions commonly have an order of magnitude or greater amounts of CO₂ and other volatiles than trapped geothermal fluids. It is to be expected that metamorphic inclusions should be

common in the countryrock that has been metamorphosed to amphibolite facies. The elevated gas/water ratios below 6,000 ft in well 2 (Fig. 6) suggest fluid boiling, which agrees with fluids having a major magmatic component. Extreme gas/water ratios and total gas exhibited in well 4 (Fig. 8) is what we expect for inclusions forming in a gas cap.

There are some unresolved problems with the methods of plotting gas analyses presented here. Scaling on the 1/ratio 1 plots in Figs. 5 to 8 needs to be addressed because using the current scheme this ratio provides little information. Attempts in using logarithmic values for 1/ratio 1 data were not helpful, and decreasing the scale resulted in peaks, like those for the gas/water ratio, that are extending beyond the plot. Not truncating peaks results in peaks that cover

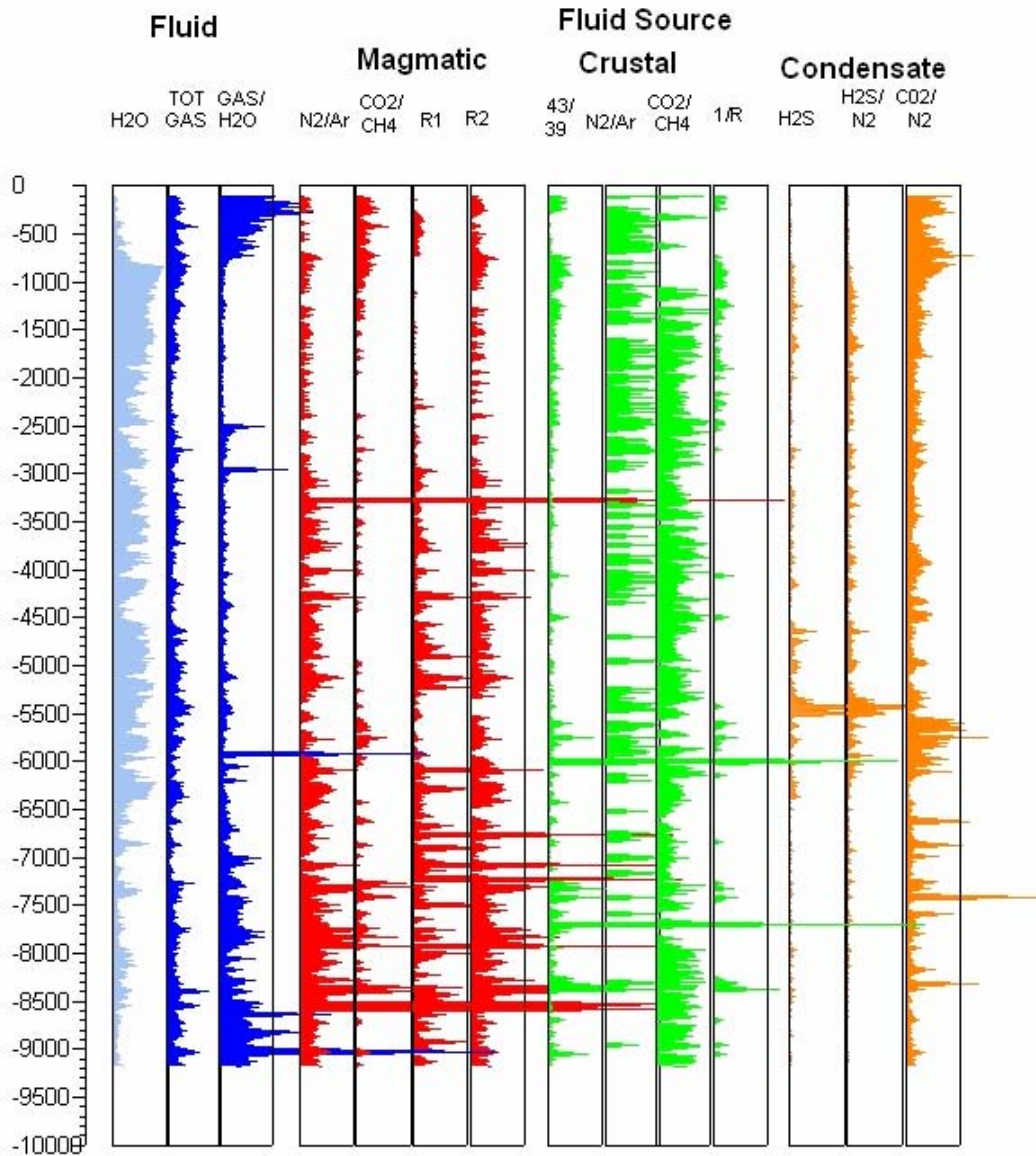


Figure 6. Well 2 interpretive mudlog plot. See text for details.

information in adjacent plots of the same color like the total gas column in Fig. 8. One way to correct this is to change the color for columns where information is obscured by not truncating. The mudlog diagrams were scaled for publication and presentation size. Using this scaling individual bars are hard to see. We plan to routinely scale graphs like those presented here to a 30" length rather than 10" length we used, and to print them in that size. Then individual analyses can be seen easily.

Graphs can be improved by automating data interpretation. At present we closely examine data downhole over small intervals and decide based on

the evidence if the analyses indicate reservoir fluids, mixed reservoir and recharging cool fluids, steam heated waters, shallow cool fluids, and background inclusions. This can be done on a spreadsheet using IF statements. The interpretation can be added to the mudlog graphs we present here. Spreadsheet generated interpretations of well analyzed will have to be checked to make certain the interpretations are reasonable. We expect that application of FIS analyses to another geothermal system will require some recalibration.

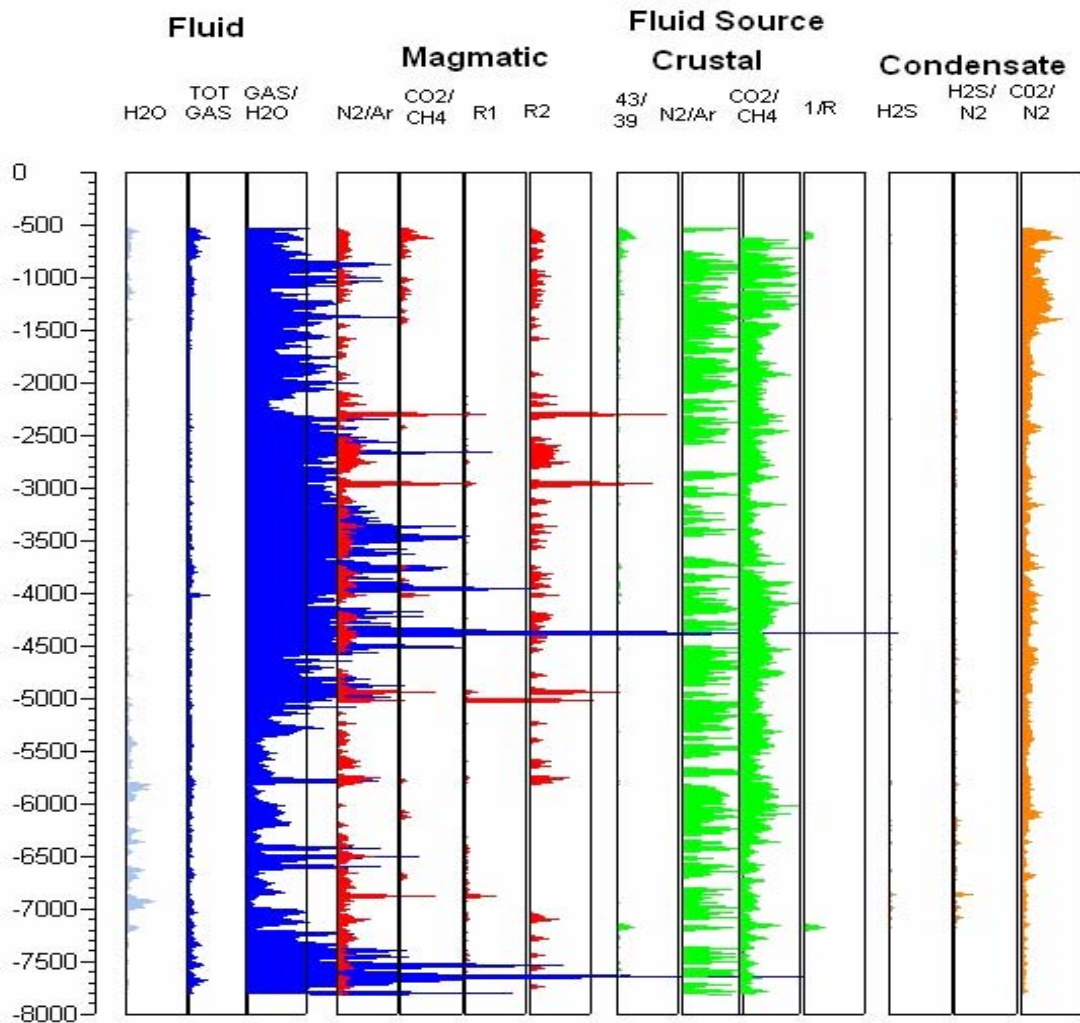


Figure 7. Well 3 interpretive mudlog plot. See text for details.

Data processing is required of FIT analyses. Analyses received from FIT are peak heights of mass peaks 1 to 180. For hydrocarbon companies FIT generates mudlog type graphs similar to Figs. 1 to 4 and provides a report with interpretations (Hall, 2002). Geothermal system FIS analyses are much more complicated to interpret in comparison to identifying a hydrocarbon reservoir. In order for FIS analyses to be economically applied to the geothermal industry the same approach to data analysis used by FIT has to be used. Preparation of diagrams for data interpretation has to be made quickly, and the interpretations have to be straightforward. The mudlogs here shown are rapidly prepared by use of spreadsheet template and macro to reduce analyses for plotting. The method of data plotting we show here is first step in simplifying geothermal-system FIS analysis data presentation and interpretation.

Mudlog graphs for a number of variables are more difficult to read that plotting analyses for individual

ratios or species versus depth. The advantages of Mudlog graphs are two fold. A significant number of variables can be easily compared. Analyses and gas ratios constructed for mudlog plots can be supplied in that form to the end users. They can then combine FIS data with other types of logs.

CONCLUSIONS

1. Mudlog type plots of FIT analyses provide an easy to comprehend way of presenting thousands of analyses.
2. Plotting multiple species and interpretive gas ratios on mudlogs has provided new insights into the four Coso borehole FIS analyses previously studied.
3. Analyses of the ten Coso boreholes planned for the near future as this study continues will be immediately plotted on mudlog diagrams.

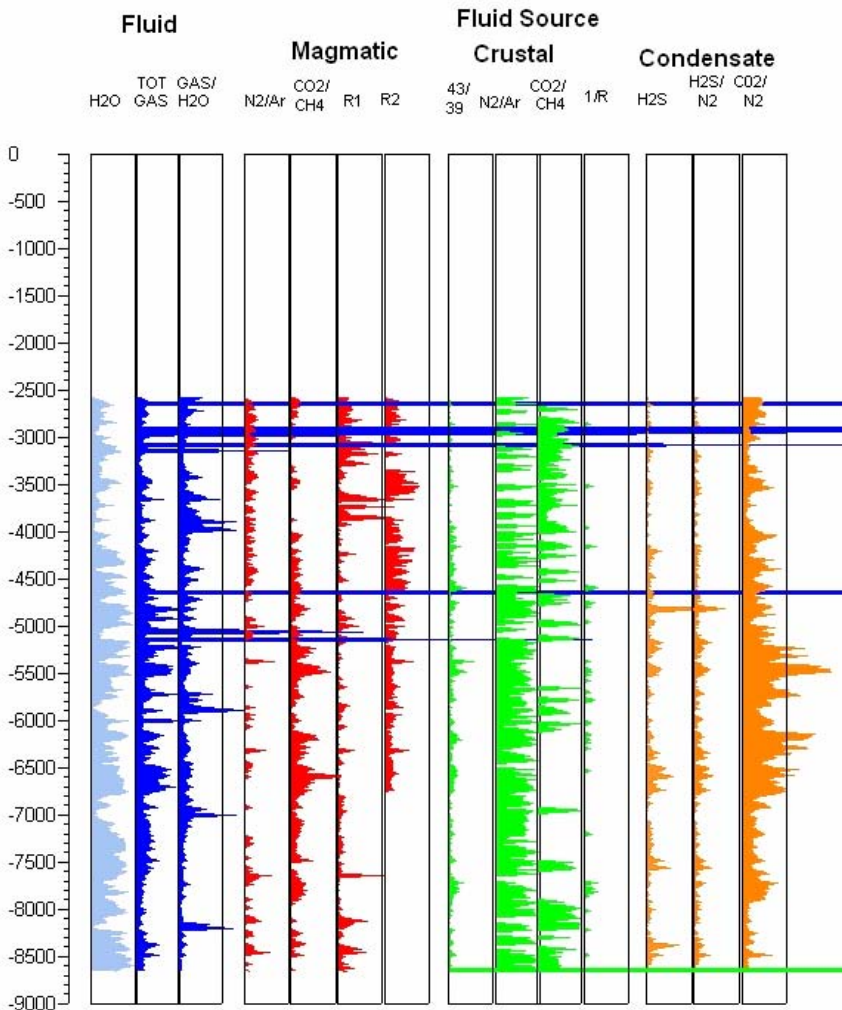


Figure 8. Well 4 interpretive mudlog plot. See text for details.

REFERENCES

Norman, D. I., Nigel Blamey, Joseph N. Moore (2002). Interpreting Geothermal Processes and Fluid Sources from Fluid Inclusion Organic Compounds and CO₂/N₂ Ratios. *PROCEEDINGS, Twenty-Seventh Workshop on Geothermal Reservoir Engineering Stanford University, Stanford, California*. p. 266-274

Dilley, Lorie M., David I. Norman & Brian Berard, (2004), Fluid Inclusion Stratigraphy: A New Method for Geothermal Reservoir Assessment – Preliminary Results; *Proceedings of the 29th Annual Stanford Geothermal Workshop*, p. 230-238.

Dilley, Lorie M. and David I. Norman (2004) Fluid Inclusion Stratigraphy: Determining Producing from Non-Producing Wells, *Geothermal Resources Council Transactions*, 18, p.387-391.

Giggenbach, W. F. (1997). The origin and evolution of fluids in magmatic-hydrothermal systems. *Geochemistry of Hydrothermal Ore Deposits*. H. L. Barnes. New York, J. Wiley and Sons, Inc.: 737-796.

Hall, D. (2002). Fluid Inclusion Technologies, Inc. <http://www.fittulsa.com>.

Norman, D.I., Moore, J.N., Musgrave J. (1997). Gaseous species as tracers in geothermal systems: *Proceedings: Twenty-second Workshop of Geothermal Reservoir Engineering, Stanford University, Stanford, California* pp.419-426.

Norman, DI and Joseph N. Moore, Lorie Dilley, and Brian Berard (2004), Geothermal Fluid Propene and Propane: Indicators of Fluid Source: *Twenty-Ninth Workshop on Geothermal Reservoir Engineering*

VERMA PROCEDURE FOR THE DETERMINATION OF HEAT CAPACITY OF LIQUIDS

Mahendra P. Verma

Geotermia, Instituto de Investigaciones Eléctricas
 Av. Reforma 113, Col. Palmira, Apdo. 1-475
 Cuernavaca, Morelos, 62490, México
 e-mail: mahendra@iie.org.mx

ABSTRACT

An ActiveX component, *SteamTablesIIE*, based on the IAPWS-95 formulation was written in Visual Basic 6.0 for calculating thermodynamic properties of pure water as a function of any two independent state variables from temperature (T), pressure (P), volume (V), internal energy (U), enthalpy (H), and Gibbs free energy (G). However, thermodynamic inconsistencies were found in the formulation.

The thermodynamic properties like U, H, G, and S are calculated from the experimental values of heat capacity at constant pressure (C_p) and/or at constant volume (C_v). The measurements of C_p of solids and C_v of gases are feasible; however, it is difficult to measure C_p or C_v for all the conditions of T and P required for calculating the thermodynamic properties of liquids.

The reported experimental values of C_p and C_v along the saturation curve increase drastically near to the critical point of water. Similarly, according to the IAPWS-95 formulation, the value of C_p or C_v at the critical point of water is $\sim 10^9$ kJ/kg K, which means that the critical point acts as a heat sink. Additionally, the calculated values of other thermodynamic properties from C_p or C_v are not in agreement with their values obtained from the formulation.

Heat capacity is not a state function. However, one can use the same trajectory for measuring the heat capacity and calculating the thermodynamic properties. Based on this criterion, a new Verma procedure is devised. Firstly, the heat capacity along the saturation curve, C_{Sat} is defined as the proportion of amount heat to the change in temperature. Similarly, the values of C_v can be measured precisely in the liquid and vapor phases. Then using the PVT characteristics, C_v and C_{Sat} , the thermodynamic properties of water are calculated. Accordingly, the internal energy for the compressed liquid and superheated steam are calculated as

$$U_{liq} = \int_{T_{ref}}^T C_{v,liq} dT + \int_{T_{ref}}^{T_{sat}} C_{sat,liq} dT - \int_{V_{f,p,liq}}^{V_1} PdV$$

$$U_{vap} = \int_{T_{ref}}^T C_{v,vap} dT + \int_{T_{ref}}^{T_{sat}} C_{sat,vap} dT - \int_{V_{f,p,vap}}^{V_2} PdV + L.H._{T_{ref},P_{ref}}$$

where the reference point is the triple point (T.P.) of water and L.H. is the latent heat at T.P.

INTRODUCTION

The geochemical modeling of aquatic systems like rain, rivers, lakes, groundwater aquifers, geothermal reservoirs, petroleum reservoirs, seas, oceans, etc. on our planet, Earth contemplates to understand the physical-chemical processes responsible for their origin and evaluation. The principle component of all these systems is water. Similarly, water is vital for the existence of life on the Earth. Additionally, water plays an important role in the geological processes like mass transportation, dissolution-precipitation, crust stratigraphy, etc.

In the electric industry, water is used to generate electricity. Water is heated to produce vapor by different sources of heat like carbon, oil, natural gas, nuclear fuel, geothermal heat, etc. and the vapor is used to move turbines.

Thus, to understand the above processes, the thermodynamic properties of water are of fundamental importance. The International Association for the Properties of Water and Steam (IAPWS) promotes scientific investigations for creating standard values for the thermodynamic properties of water. Wegner and Praß (2000) developed an empirical formulation, IAPWS-95 on the basis of least square fittings of experimental data for the properties of water. Using the formulation, Verma (2003) wrote an ActiveX component, *IAPWS95SteamTables* in Visual Basic 6.0 for calculating 23 properties of pure water as a function of temperature (190 to 2000 K) and pressure (3.23×10^{-8} to 10,000 MPa).

Since temperature (T), pressure (P), volume (V), internal energy (U), enthalpy (H), Gibbs free energy (G), etc. are state functions, Verma (2005) wrote a new ActiveX component, *SteamTablesIIE* in Visual Basic 6.0 to calculate the thermodynamic properties of pure water as a function of any two independent state variables from the state functions. However, some thermodynamic inconsistencies were found in the formulation, which were the limitations for the functionality of *SteamTablesIIE* for all the permissible ranges of the independent variables.

In this article we present the thermodynamic inconsistencies in the IAPWS-95 formulation. Similarly, a new Verma procedure for calculating thermodynamic properties of liquids is devised. An experimental setup for measuring the thermodynamic properties of water is presented.

STATE FUNCTION

Verma (2002) presented a method of interdependence of state variables in order to scrutinize the internal consistency among the thermodynamic datasets. Thermodynamic variables (e.g., T, P, V, G, U, H and S) including the equilibrium constant of a chemical reaction, solubility, viscosity, thermal conductivity, etc. are state functions. A state function does not depend on the past history of the substance or on the path it has followed in reaching a given state. It should be single valued and continuously differentiable unless there is a phase transition. On fixing the values of any two independent state functions (for example, T and P), the values of all the other state functions are uniquely defined.

Any three state variables X, Y and Z obey the following mathematical relation for exact functions

$$\left(\frac{\partial X}{\partial Y}\right)_Z \left(\frac{\partial Z}{\partial X}\right)_Y \left(\frac{\partial Y}{\partial Z}\right)_X = -1 \quad (1)$$

If Z is constant, we are looking for the dependence of X on Y and vice versa. Then

$$\left(\frac{\partial X}{\partial Y}\right) \left(\frac{\partial Y}{\partial X}\right) = 1 \quad (2)$$

If the same value of X exists for two values of Y (say Y_1 and Y_2) at constant Z, there should be at least one minimum or maximum in the behavior of X between Y_1 and Y_2 . At the minimum or maximum, one can write

$$\Delta Y = \pm ve, \quad \Delta X = 0, \quad \left(\frac{\partial X}{\partial Y}\right) = 0 \quad \text{and} \quad \left(\frac{\partial Y}{\partial X}\right) = \infty.$$

Thus,

$$\left(\frac{\partial X}{\partial Y}\right) \left(\frac{\partial Y}{\partial X}\right) = 0 \times \infty \Rightarrow \text{indeterminate, but not} = 1.$$

In summary, there cannot be any maximum or minimum in the behavior of a state function with an independent thermodynamic variable when the other independent variable is constant. In other words, a state function (or an exact function) cannot be a multi-valued function.

The mathematical concepts discussed above are explained through schematic diagrams in Figure 1. Let us consider a state function (say X) which is a function of independent thermodynamic variables P and T. Figure 1(a) shows two behaviors of X at a given value of P (i.e. at P_1 and P_2 , respectively). In case I there are two values of X at a given T, whereas in case II there are two values of T for a value of X. Thus $X(T)$ in case I and $T(X)$ in case II are not single valued functions.

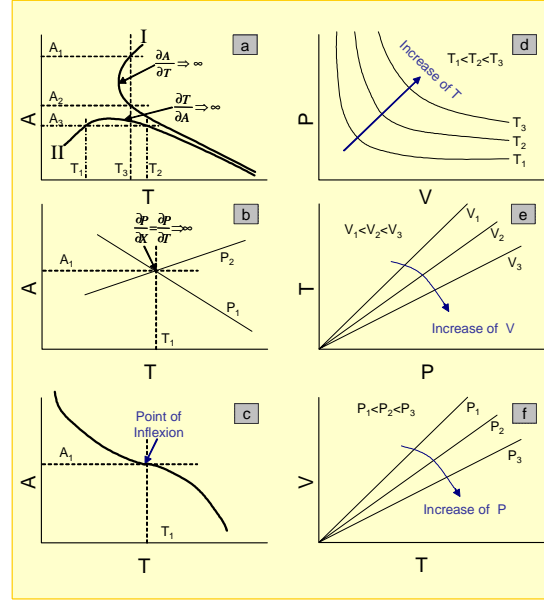


Figure 1. A schematic diagram to explain the behavior of a state function with independent thermodynamic variable (T and P). According to the definition, the behaviors in the Figs. 1(a, b, c) are impermissible for a state function. Similarly, the Figs. 1(d, e, f) represents the permissible behaviors of a state function, which were derived from the state equation of ideal gas ($PV=nRT$).

Similarly, $\frac{\partial T}{\partial X} = \infty$ in case I and $\frac{\partial X}{\partial T} = \infty$ in case II. It means that T or X are not continuously differentiable. In other words, neither T nor X is a thermodynamic state function in the respective cases.

Figure 1(b) presents the behaviors of X with T at two pressures P_1 and P_2 . The functions are crossing at temperature T_1 . Then at $T=T_1$, $\frac{\partial P}{\partial X} = \infty$ and

$\frac{\partial P}{\partial T} = \infty$. It means that P is not a state function.

Figure 1(c) shows a point of inflection in the variation of X with T at constant P. A point of inflection is not always singular. However, a rotation axes such that one of the axis is parallel to the tangent at the point of inflection, makes the point of inflection as singular in the new coordinate system (i.e. the gradient $\frac{\partial x'}{\partial T'}$ is positive or negative on both sides and 0 or infinite at the point of inflection). A linear transformation of state functions produces new state functions. So, there cannot be any point of inflection in the behavior of a state function.

In summary, the behaviors of a state function with an independent state variable when the other independent variable is constant, as shown in Figures 1 (a, b and c), are impermissible.

The ideal gas equation is $PV=nRT$. For an ideal gas system of constant mass, Figures 1(d, e and f) present

the behaviors of P with V at constant T, of T with P at constant V and of V with T at constant P, respectively. In the Figures 1(e and f) the behaviors converge to the origin (i.e., P or T is tending to zero); however, the classical thermodynamics is not valid when P or T is tending to zero. In these situations both dependent and independent variables are zero, which means the convergence point is indeterminate. Thus the behaviors presented in the Figures (d, e and f) are valid for a state function.

Additionally, thermodynamics does not impose any restriction on the behavior of a state function (say X) with respect to independent state variables (say T and P). However, if we know the behavior of T with P and behavior of X with T (or P) for a system, we can predict the behavior of X with P (or T). For an ideal gas system of constant mass and V, T increases with increasing P and vice versa. It means if V increases with T, it should decrease with P. On considering T and P as independent variables and V as constant, all the other state functions should be constant (i.e., uniquely defined) under the situation. Thus, the behavior of P and T should be similar for all the other state functions as that for V. For example, if H increases with T, it should decrease with P.

Let us rewrite the equation (1) in X, T and P as

$$\left(\frac{\partial X}{\partial P}\right)_T = -\left(\frac{\partial X}{\partial T}\right)_P \left(\frac{\partial T}{\partial P}\right)_X \quad (3)$$

If T increases with increasing P in a system, then $\left(\frac{\partial T}{\partial P}\right)_X = +ve$. If X increases with T, it should decrease with P in order to fulfill the equation (3).

Similarly, if we consider V and P as independent thermodynamics variables, V decreases generally with increasing P in a phase and vice versa.

$\left(\frac{\partial V}{\partial P}\right)_X = -ve$. If X increases (or decreases) with P, it should also increase (or decrease) with V.

In summary, the behavior of a state function with an independent state variable (say T) at the constant of another independent stable variable (say P) should be single valued and continuous differentiable in a phase. It is very similar to the behavior of electromagnetic fields, which never cross and are parallel for short displacements.

The scientific literature contains many experimental and theoretical determinations of a state function which are violating its definition. Here the basic aspects of a state function and its dependence with the independent thermodynamic variables will be used to scrutinize as an example the internal consistencies in the water steam tables.

STEAM TABLES OF PURE WATER

The IAPWS-95 formulation for the thermodynamic properties of pure water apparently provides more consistent values of the properties of water than the earlier formulations (Wegner and Praß, 2000). As mentioned earlier that any two state functions are

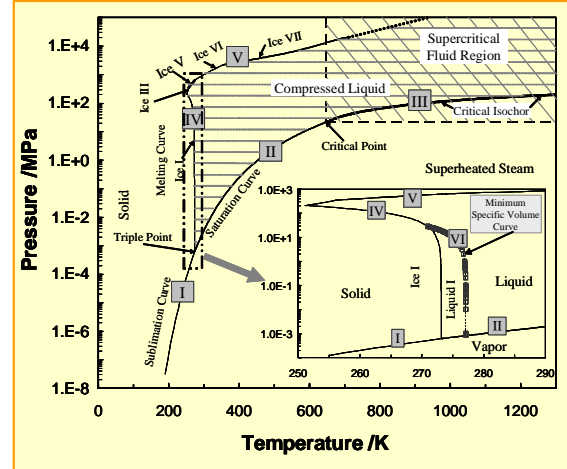


Figure 2. *PT-space of pure water according to the IAPWS-95 formulation, which is divided by six separation boundaries: (i) sublimation curve, (ii) saturation curve, (iii) critical isochor, (iv) ice I melting curve, (v) melting (Ice III to Ice VII) curve and (vi) minimum specific volume curve. The inserted figure depicts the location of liquid I and the minimum specific volume boundary.*

sufficient to define completely the values of all the other state functions in a phase for a pure system of constant mass. Using the interdependence among the state variables T, P, V, U, H, G and S on considering any two as independent variables, we will illustrate the thermodynamic inconsistencies in the IAPWS-95 formulation.

PVT Characteristics of Water

Verma (2003) demonstrated the PT relationship for pure water according to the IAPWS-95 formulation (Figure 2). He presented that the critical isochor (i.e., total specific volume $V = 0.003106 \text{ m}^3/\text{kg}$ or density = 322.0 kg/m^3) in the supercritical fluid region acts as a phase boundary between the liquid-like and vapor-like fluid. The saturation curve is the locus of T and P values where liquid and vapor coexist in equilibrium: it starts from the ice-liquid-vapor triple point and terminates at the critical point. Water has many solid forms, depending on the conditions of P and T. All the Ice curves (I, III, V, VI and VII) define the melting curve. The supercritical fluid region, existing at T and P higher than those of critical point, is shown by diagonal solid lines, which do not represent phase changes but depend on arbitrary definition of what constitutes the liquid and vapor phases. According to the IAPWS-95 formulation the supercritical fluid region also contains solid (ice) water. The region of vapor and liquid, bounded by the PT-space, will be drawn later in terms of different independent thermodynamic variables.

It is well known that the variation of specific volume of liquid water with T at P=0.1 MPa has a minimum volume at 277.127 K. We know that P, T and V are state functions. If we consider P and V as independent state variables, there are two values of T at a given value of P and V. But according to the definition of state function, it should be uniquely defined, if T is a state function. This cannot be explained thermodynamically if we consider the whole liquid water region as a single phase. It was called as an anomalous behavior since the development of thermodynamics. It is anomalous to the thermodynamic laws, if the whole liquid water is considered as single phase.

Recently, Sciortino et al. (2003) presented the physics of liquid-liquid transition. The editorial of the journal, Physical Review Letters (2003) summarized the work of Sciortino et al. as “A Tale of Two Liquids”. It says, “Any liquid which eventually expands as it cools must have a liquid-liquid critical point.” Thus there are two types of liquid water, which are represented by liquid and liquid I in Figure 2. Additionally, other works suggest that there is an effect of hydrogen bonding on the molecular structure of water at low temperatures (IAPWS, 2004). There are two types of structure: *one is associated with hydrogen bonding (below 4°C) and other is without hydrogen bonding.* According to the definition of “phase”, a change in the structure of water molecule will produce a different phase. Therefore, there is a phase transition along the minimum volume curve (Figure 2), but there are still many questions to be answered about the type of phase transition, etc. However, T is uniquely defined on fixing P and V in each liquid phase.

The inserted figure in Figure 2 shows that the minimum specific volume curve acts as a separation boundary between the liquid and liquid I phases of water. It is derived from the IAPWS-95 formulation, so its exactitude depends only on the formulation.

Figure 3a shows the VP-space for pure water. There is a triple line where liquid-vapor-solid (ice) coexists. The two phase region (liquid and/or liquid I and vapor) is bounded among the triple line, liquid saturation curve and vapor saturation curve. The vapor and liquid saturation curves meet at the critical point. The critical isochor, represented by a vertical line is the separation boundary between liquid and vapor. The liquid phase is up to the minimum specific volume curve. The liquid I phase will be bounded by the minimum specific volume curve, melting curve, and triple line. The solid (ice) will be on the higher volume side at the melting curve. A question comes in mind what type of water will be on the lower volume side at the minimum specific volume curve. The region is shown in the inserted figure with a question mark on phase. Probably, there may exist some solid phase. Here we are not interested in the thermodynamic properties of solid (ice) water; therefore, we will not discuss it further.

Figure 3b shows the VT-space. It is similar to VP-space and it also shows the location of Liquid I. Thus the behaviors of P, T and V in the IAPWS-95 formulation for the steam tables of pure water are thermodynamically consistent.

Behaviors of H, G and S of Water

Figure 4 shows (a) isobaric behavior of H with T and (b) isothermal behavior of H with P. In the pure water system of constant mass and V, P increases with increasing T and vice versa. It means if H increases with T, it should decrease with P. It can be observed in the Figure 4(a) that the behavior of H in the vapor phase is consistent with the definition of a state function. However, the behavior of H in the liquid phase is inconsistent. In the low temperature range H increases with both T and P and is overlapping with the two phase region, whereas it increases with T and decreases with P in the high temperature range. The tendencies are crossing in the middle temperature range. Thus the values of H in the low and middle temperature ranges are violating the definition of a state function.

Figure 4(b) shows the isothermal variation of H with P. There are two pressures for a given value of H in the compressed liquid region. For example, H=2000 kJ/kg for the 700 K isotherm is at P₁=63.458 MPa and P₂=456.356 MPa. If we consider T and H as independent variables, it is impossible to predict the right value of P. The meaning of two values of P is that P is not an exact solution. This way-thermodynamics is not an Exact Science. Everyone knows that thermodynamic is an exact science, therefore the two values of P in the above situation are incorrect.

Let us further exemplify the above situation. We have a container filled with water at T=700 K and P=63.485 MPa. Since there is same H (2000 kJ/kg) for P= 63.458 MPa and 456.356 MPa at T= 700 K (see Figure 4b), it means we can pressurize (from 63.458 to 465.356 MPa) the container without any work. In other words, we can increase the pressure in a system of constant V and T without doing any work. If it is possible, we can develop a Carnot cycle to solve the world energy problem with no expense. If we consider a change in volume in the above example (from V₁ to V₂), one has to do some work

$$W = \int_{V_1}^{V_2} PdV \quad (4)$$

W cannot be zero; however, $\Delta H = 0$ means that W should be zero. This is contradictory to the basic thermodynamics. Similar inconsistency was observed in the behavior of U. In summary there is a violation of fundamental laws of thermodynamics for H and U in the IAPWS-95 formulation.

Figure 5 shows (a) isobaric behavior of G with T and (b) isothermal behavior of G with P. The behavior of G is consistent with the definition of state function. It increases with P, but it decreases with T. It has a

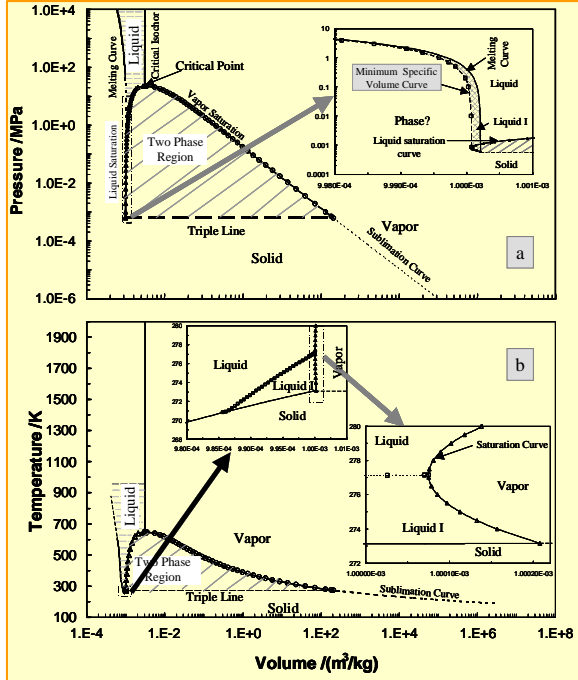


Figure 3. P-V and T-V spaces for pure water according to the IAPWS-95 formulation. The inserted figures illustrate the location of Liquid I phase.

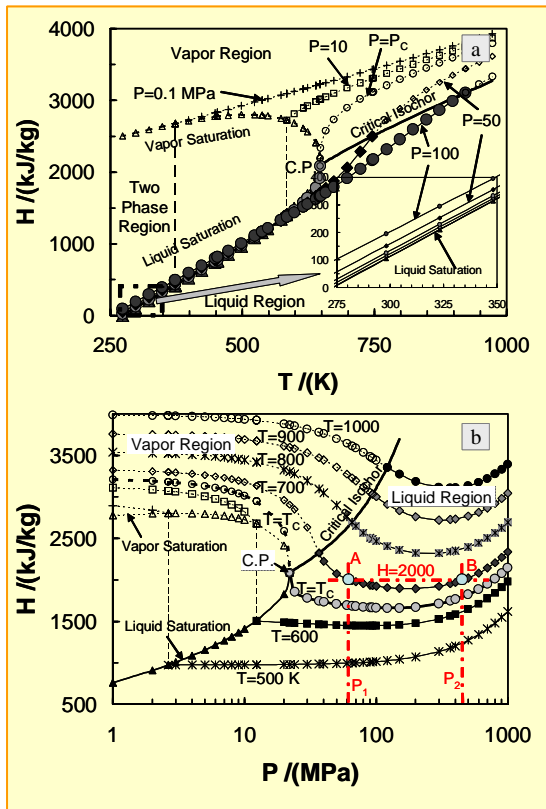


Figure 4. (a) Isobaric and (b) Isothermal variations of Enthalpy (H).

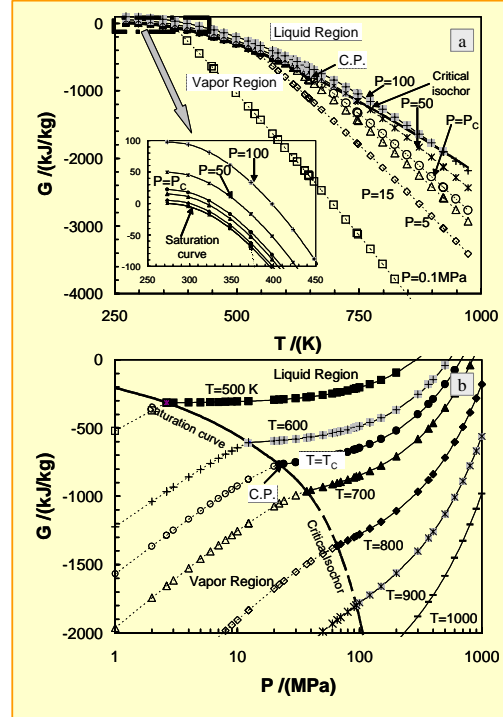


Figure 5. (a) Isobaric and (b) Isothermal variations of Gibbs free energy (G).

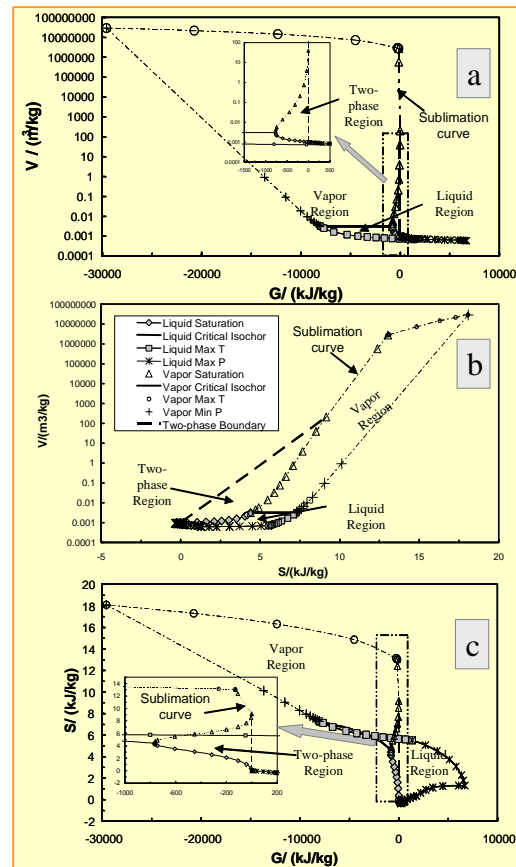


Figure 6. V-G, V-S and G-S spaces for pure water according to the IAPWS-95 formulation.

discontinuity along the saturation curve and a point of inflection along the critical isochor. It means that there is a first order liquid-vapor phase transition along the saturation curve, while a second order liquid-vapor phase transition exists along the critical isochor.

Figure 6 shows the V-G, V-S and S-G spaces for pure water according to the IAPWS-95 formulation. It covers the region corresponding to T (190 to 2000 K) and P (3.23×10^{-8} to 10000 MPa) for the liquid and vapor phases as shown in Figure 2. It can be observed that the V-G and V-S spaces do not overlap and are single valued, whereas the compressed liquid region is overlapping to the two phase and vapor regions in the case of S-G space. It means that G and S for the compressed liquid according to the IAPWS-95 formulation are multi-valued function and it is a violation of the definition of state function. Thus the values of U, H, G and S in the IAPWS-95 formulation are inconsistent thermodynamically. There is need to revise the procedure and the experimental values, used in the development of the IAPWS-95 formulation.

Behaviors of C_p and C_v of Water

The behaviors of P, V and T are consistent, while the behaviors of U, H, G and S are inconsistent thermodynamically in the IAPWS-95 formulation. To understand the thermodynamic inconsistencies we will analyze the experimental data for the heat capacity (C_p) at constant pressure.

Figure 7 shows the experimental values of C_p , used in the derivation of the IAPWS-95 formulation. The values for the liquid and vapor phases along the saturation curve are shown by solid and dashed curves, respectively. They are increasing with T for both the phases. The values of C_p are very high near to critical point (i.e., $\sim 10^9$ kJ/kg K). According to the behavior of C_p , the critical point acts as a heat sink, this cannot be explained with thermodynamics.

The values of C_p in the compressed liquid and superheated steam regions for the selected pressure ranges are also shown in Figure 7. The vertical lines are the positions of liquid-vapor separation boundary, obtained by the PVT characteristics of pure water. The blue vertical line is corresponding to the critical conditions. The red lines in the left of blue line are for the separation boundaries along the saturation curve, while the red lines in the right are the separation boundaries along the critical isochor.

The maximum in the behavior of C_p at a particular pressure is on the vertical lines or in the compressed liquid region. The heat capacity is not state function; however, C_p is defined along a specific path. So, it should have definite tendency, but it does not have. The multiple values in the compressed liquid region indicate that C_p increases first with T and then decreases. It cannot be explained with the basic laws of thermodynamics. Thus, the development of the

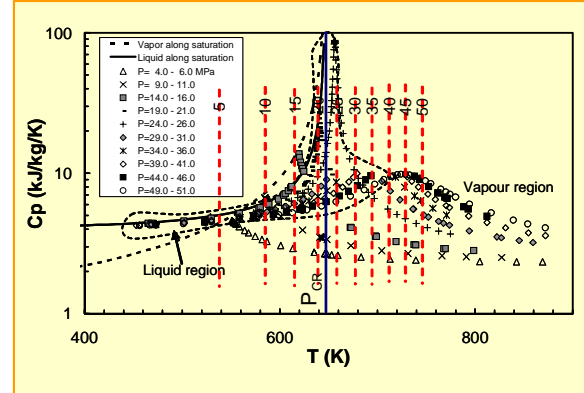


Figure 7. Experimental data of C_p for pure water used in the development of the IAPWS-95 formulation.

IAPWS-95 formulation is based on the thermodynamically inconsistent experimental data. The C_p and C_v of water have been measured along the saturation curve; however, their physical significance has never been explained. For example, there is need to know a relation between the increase in T and amount of heat given to a system at constant P in order to measure C_p . There will be a change in P on changing T along the saturation curve. It is not possible to keep constant P. Thus, the measurement of C_p or C_v along the saturation curve is not feasible.

VERMA PROCEDURE FOR MEASURING THERMODYNAMIC PROPERTIES OF LIQUID

Till now, the thermodynamic properties have been calculated from C_p and/or C_v . As it has been discussed above that it is not possible to measure C_p and C_v of liquids at all conditions of independent variables (say T and P), required for calculating the thermodynamic properties. Therefore, a new Verma procedure is devised.

The heat capacity along the saturation curve, C_{Sat} is defined as the proportion of amount heat to the change in temperature. Thus, C_{Sat} is a function of only one independent variable (say T).

Heat capacity is not a state function. Its value depends on the trajectory between two points. Therefore, one has to use the same trajectory (along the saturation curve and then the constant V path) for the calculation of the thermodynamic properties like U, H, G, S, etc.

The values of C_v in the compressed liquid region and superheated steam region can be measured quite precisely.

Actually, the liquid I region is based only on the experimental data of T and V at P=0.1 MPa. There are no other experimental data for T and V at constant P in this region. Therefore, we will not consider here the liquid I region and the triple point for liquid water is considered as the reference point.

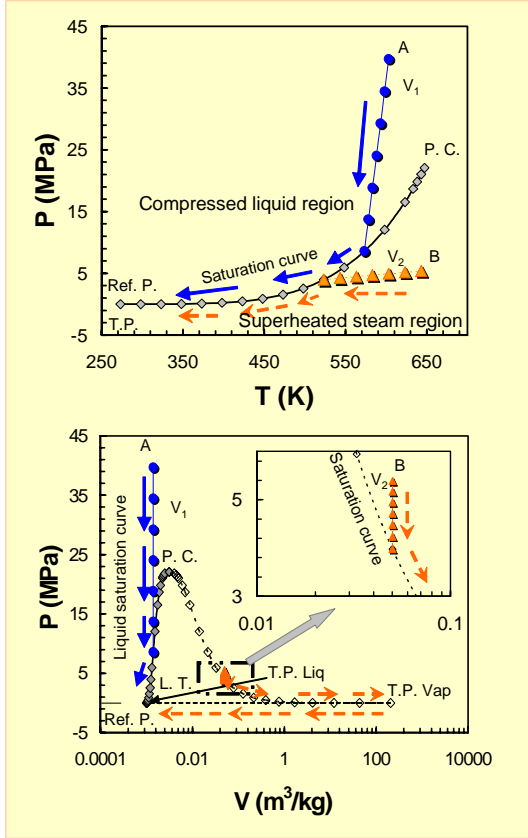


Figure 8. A schematic diagram to define trajectories for measuring the thermodynamic properties of pure water in the compressed liquid and superheated steam regions and along the saturation curve.

The thermodynamic properties of water are calculated using the PVT characteristics, C_V and C_{Sat} . Accordingly, the internal energy for the compressed liquid and superheated steam are expressed as (Figure 8)

$$\begin{aligned}
 U_{liq} &= \int_{T_{sat, para} V=V_1}^T C_{V, liq} dT + \int_{T_{ref}}^{T_{sat, para} V=V_1} C_{sat, liq} dT \\
 &\quad - \int_{V_{ref}}^{V_1} P dV \\
 U_{vap} &= \int_{T_{sat, para} V=V_2}^T C_{V, vap} dT + \int_{T_{ref}}^{T_{sat, para} V=V_2} C_{sat, vap} dT \\
 &\quad - \int_{V_{PT, vap}}^{V_2} P dV + L.H. \cdot T_{ref, P_{ref}}
 \end{aligned} \tag{5}$$

where reference point (ref.) is the triple point (T.P.) for liquid water and L.H. is the latent heat at T.P. We are working to create new experimental data of the steam tables for pure water using this approach.

Experimental Setup

Figure 9 shows a schematic diagram for an experimental setup to measure the heat capacity of

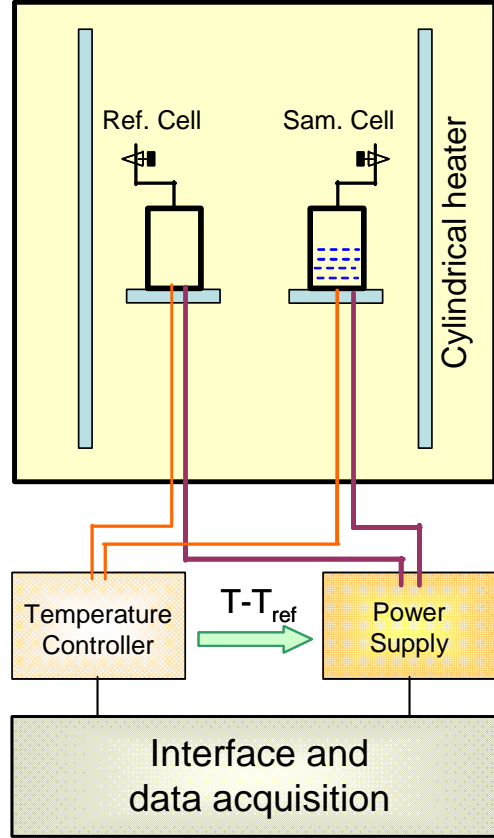


Figure 9. Experimental setup for measuring heat capacity in the compressed liquid ($C_{V,Liq}$) and superheated steam ($C_{V,vap}$) regions and along the saturation curve ($C_{Sat,Liq}$ and $C_{Sat,vap}$).

pure water along the saturation curve for liquid ($C_{Sat,Liq}$) and vapor ($C_{Sat,vap}$) and in the compressed liquid ($C_{V,Liq}$) and superheated steam ($C_{V,vap}$) regions. Basically, its principle of measurement is based on the Differential Scanning Calorimetry (DSC).

There are two identical cells which are placed on a pair of identically positioned platforms in a cylindrical furnace. There is sample (water) in one cell and other cell is empty. The platforms have heaters and thermocouples to measure temperature.

The cylindrical furnace is switched on to heat the cells at a specific rate. There will be same temperature in the cells, if both cells are empty. Since the cell 1 has sample, it will be heated with a lower heating rate. To get the same temperature at every instant, the cell 1 is heated by its platform heater. Let the heat flow rate of the heater be Q . The values of Q and T at every instant are stored in a computer.

Figure 10 shows a relation between Q and T for an experiment with total water mass m ($=m_{Liq}+m_{vap}$). For a temperature change (ΔT), some liquid will convert to vapor ($-\Delta m_{Liq} = \Delta m_{vap}$). We can write a mass and energy balance equation as

$$\begin{aligned}\frac{\Delta Q}{\Delta T} &= m_{\text{vap}} \frac{\Delta Q_{\text{vap}}}{\Delta T} + m_{\text{liq}} \frac{\Delta Q_{\text{liq}}}{\Delta T} + \Delta m_{\text{vap}} \cdot L.T.(T) \\ &= m_{\text{vap}} C_{\text{Sat.Vap}} + m_{\text{liq}} C_{\text{Sat.Liq}} + \Delta m_{\text{vap}} \cdot L.T.(T)\end{aligned}\quad (6)$$

In general there are three unknowns $C_{\text{Sat.Vap}}$, $C_{\text{Sat.Liq}}$ and $L.T.(T)$. So we run the same experiment three times with different total mass in order to solve the equation (6).

The fundamental problem in this approach is that there is relatively very small amount of vapor in the cell at low T (and P). Therefore, it may have high analytical uncertainty in the values of $C_{\text{Sat.Vap}}$. The alternative way to solve this problem is to measure the heat capacity of vapor according to the procedure used for pure gases. The vapor acts as a perfect gas at very low T and P . So, there is need to study the deviation in the behavior of $C_{\text{Sat.Vap}}$ from that of perfect gas near to the saturation curve and critical isochor.

CONCLUSIONS

An interrelation among thermodynamic properties (state functions) of a system is first step for creating the internal consistent thermodynamic dataset, which is fundamental to understand the physical-chemical processes in the laboratory and in nature. This work shows that the IAPWS-95 formulation for thermodynamic properties of pure water is incorrect. It is found that the experimental values of heat capacity at constant pressure (C_p) and at constant volume (C_v) along the saturation curve are measured by a physically incorrect concept. It is unfeasible to measure the values of C_p or C_v for all the conditions of temperature and pressure, required for calculating the thermodynamic properties of liquids. Therefore, the IAPWS-95 formulation is obtained by fitting the incorrect experimental dataset for the thermodynamic properties of pure water.

A new Verma procedure is devised. The heat capacity along the saturation curve, C_{Sat} is defined as the proportion of amount heat to the change in temperature. Additionally, it is shown that the values of C_v of liquid can be measured precisely in the liquid and vapor phases. Using the PVT characteristics, C_v and C_{Sat} , all thermodynamic properties of water can be calculated.

An experimental setup is presented to measure the heat capacity of liquid ($C_{\text{Sat.Liq}}$) and vapor ($C_{\text{Sat.Vap}}$) along the saturation curve. The same system can be used for measuring the heat capacity of compressed liquid ($C_{v,\text{Liq}}$) and superheated steam ($C_{v,\text{vap}}$) at constant volume.

We are working on the development of a laboratory to measure the heat capacity of liquids. Hope to present the new internal consistent thermodynamic data of pure water in the forthcoming Sanford Geothermal Symposium.

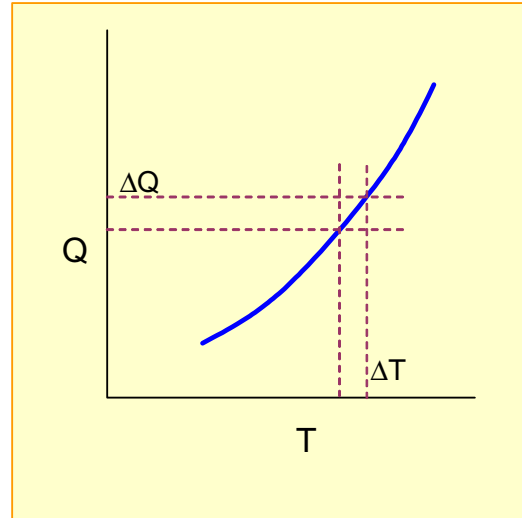


Figure 10. A schematic relation between heat flow rate (Q) and temperature (T) for a run with the total mass of water (m) in the cell.

ACKNOWLEDGEMENT

The author is grateful for the financial and technical support provided by his institute authority to conduct this project.

REFERENCES

- IAPWS (2004), "Release notes on the updated thermodynamic properties of liquid and vapor of water. International Association for the Properties of Water and Steam", Web page <http://www.iapws.org/>.
- Physical Review Letters (2003), "A tale of Two Liquids", Web page <http://focus.aps.org/story/v12/st11#author>.
- Sciortino F., La Nave E., Tartaglia P., "Physics of liquid-liquid critical point", *Physical Review Letters*, **91**, 155701-155704.
- Verma, M.P. (2002), "Geochemical techniques in geothermal development", In D. Chandrasekharam, and J. Bundschuh (eds.), *Geothermal Energy Resources for Developing Countries*. The Sweets & Zeitlinger Publishers, Netherlands, 225-251.
- Verma, M.P. (2003), "Steam Tables for pure water as an ActiveX component in Visual Basic 6.0", *Computers and Geosciences*, **29**, 1155-1163.
- Verma, M.P. (2005), "*SteamTablesIIE*: an approach of multiple variable sets for steam tables of pure water", *Computers and Geosciences*, In revision.
- Wegner, W. and Pruß, A. (2002), "The IAPWS formulation 1995 for the thermodynamic properties of ordinary water substance for general and scientific use", *Journal of Physical and Chemical Reference Data*, **31**, 387-535.

Geophysics

- Gravity Changes in the Leyte Geothermal Production Field, North Central Leyte, Philippines** [403](#)
Nilo A. Apuada and Rhoel Enrico R. Olivar
- Four Dimensional Velocity Structure of the Soultz-Sous-Forets Geothermal Reservoir During the 2000 and 2003 Stimulations** [412](#)
Jean Charléty, Nicolas Cuenot, Catherine Dorbath, Louis Dorbath
- Faulting Mechanisms and Stress Tensor at the European HDR Site of Soultz-Sous-Forets** [420](#)
Nicolas Cuenot, Jean Charléty, Louis Dorbath, Henri Haessler
- Determination of Shallow Groundwater Level Change Using Repeat Gravity Measurements at the Center Part of Unzen Volcano (Nagasaki Prefecture, Japan) from 1999 to 2004** [427](#)
H. Saibi, J. Nishijima, S. Ehara and Y. Fujimitsu
- Natural State Modeling, Structure, Preliminary Temperature and Chemical Synthesis of the Dixie Valley, Nevada Geothermal Field** [435](#)
J.R. McKenna; D.D Blackwell; M.R. Richards; D.S. Swenson
- 3D Magnetotelluric Characterization of the Coso Geothermal Field** [443](#)
G. A. Newman, G. M. Hoversten, Erika Gasperikova, and Phil Wannamaker
- Source Parameters of Microearthquakes from the 1.5 Km Deep Pyhäsalmi Ore Mine, Finland** [448](#)
Volker Oye and Michael Roth
- Imaging Geothermal Fractures by CSAMT Method at Takigami Area in Japan** [456](#)
Koichi Tagomori, Enjang Mustopa, Hisashi Jotaki, Hideki Mizunaga and Keisuke Ushijima
- Seismic Imaging of the Geothermal Field at Krafla, Iceland** [464](#)
C. Tang, J.A. Rial, J. Lees and E. Thompson
- Using Geodetic Data to Understand Hydrothermal Fluid Flow** [472](#)
D. W. Vasco
- Evaluating Heat Flow as a Tool for Assessing Geothermal Resources** [479](#)
Colin F. Williams

REPEAT MICROGRAVITY AND LEVELING SURVEYS AT LEYTE GEOTHERMAL PRODUCTION FIELD, NORTH CENTRAL LEYTE, PHILIPPINES

Nilo A. Apuada, Rhoel Enrico R. Olivar and Noel D. Salonga

PNOC Energy Development Corporation (PNOC-EDC)
Energy Center, Merritt Road, Fort Bonifacio
Taguig City, Philippines
e-mail: geophysics.edrm@energy.com.ph

ABSTRACT

Leyte Geothermal Production Field (LGPF) in North Central Leyte is the largest geothermal area in the Philippines. It is comprised of two independent hydrothermal systems: the Tongonan Geothermal Field (TGF) in the north and the Mahanagdong Geothermal Field (MGF) in the south.

The commissioning of additional power plants beginning 1996 to harness the full energy potential of the area led to a massive mass extraction from the field's reservoir, which to date has incurred a cumulative net mass loss of 291 Mt in TGF and 65 Mt in MGF. Microgravity measurements, in tandem with precise leveling survey were conducted over the area to determine the reservoir's response to exploitation by detecting the minute exploitation-induced changes in gravity over time. The most recent measurements were conducted in 2003.

Based on Gauss's Potential Theorem and mass balance equation, the negative gravity changes from 1997 to 2003 indicate that the system (LGPF) has incurred a net mass loss of about 244 Mt and a natural recharge of about 34 Mt or 12% of the total mass removed.

The measured decreases in gravity were associated with the mass loss from the reservoir. The data was also correlated with the pressure drawdown of about 4-4.5 MPa presently experienced over TGF and MGF.

INTRODUCTION

The Leyte Geothermal Production Field (LGPF) is the largest geothermal area in the Philippines located along the northwest trending structures of the Philippine Fault in north central Leyte (Fig. 1). LGPF comprises six geographic sectors, namely, Mahiao, Sambaloran, Malitbog, Mamban, Mahanagdong and

Bao valley. Two independent hydrothermal systems

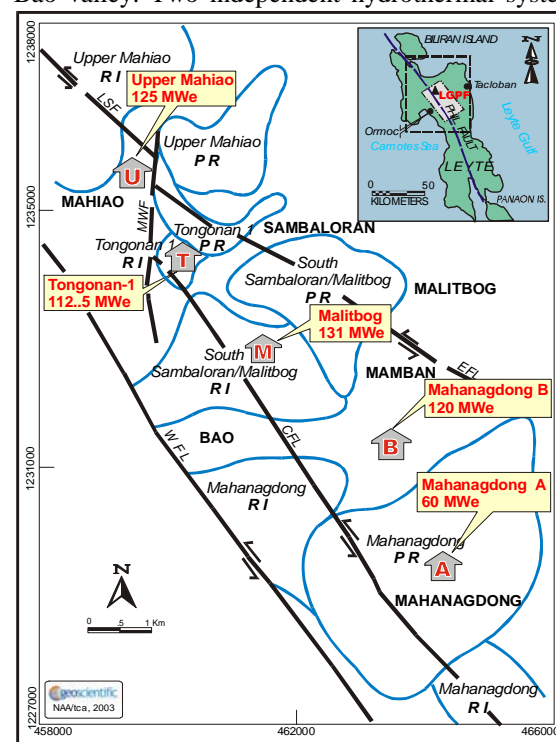


Figure 1. Generalized sectoral location of LGPF production (PR) and reinjection (RI) areas.

exist in LGPF: the Tongonan Geothermal Field (TGF) in the north and the Mahanagdong Geothermal Field (MGF) in the south.

TGF occupies approximately 15 km² of rolling to rugged topography and has three production sectors, namely, Upper Mahiao (UM), Tongonan-1 (TGN-1) and Malitbog-South Sambaloran (MB-SS) (Fig. 1). TGN-1 in turn encompasses the Mahiao-Sambaloran production sector that supplies the first 112.5 MWe power plant that began in 1983. Full exploitation of TGF started in 1996 with the commissioning of additional 125 MWe Upper Mahiao power plant (1996), the 231 MWe Malitbog power plant (1996-

1997) and the 50 MWe SLI or steamline interconnection (2000). The SLI pipes the excess steam of TGF to the neighboring Mahanagdong geothermal field.

Initial extraction rate started at 0.5 to 1.1 Mt per month from 1983 to 1989 (Fig. 2). Of the total amount, about 0.1 to 0.5 Mt were injected back into deep wells. With the commissioning of the additional power plants, the monthly extraction rate increased abruptly from 1.3 Mt in 1995 to 4.5 Mt in 1998 and further rose to around 5 Mt when SLI was put online. The cumulative net mass loss from 1983 to present is about 291 Mt.

On the other hand, MGF, located 8 km south of TGF, is divided into two sectors: Mahanagdong-A (MG-A) and Mahanagdong-B (MG-B). MG-A constitutes the 120 MWe main plant and 12 the MWe topping cycle plant, while MG-B supplies 60 MWe to the main power plant and 6 MWe to the topping cycle plant. Commercial operation of MGF commenced in 1997. Since the full exploitation of MGF, the cumulative extraction started at 9 Mt in 1997 and increased to 192 Mt in May 2003 (Fig. 3b). Of the total amount, 127 Mt were injected back into deep wells incurring a net mass loss of about 65 Mt.

To date, both TGF and MGF experienced pressure drawdown. For twenty years of continuous fluid extraction, TGF has experienced pressure drawdown of 4 to 4.5 MPa affecting the Upper Mahiao and South Sambaloran production fields (Fig. 4). Consequently, various physical and chemical changes occurred in the reservoir mainly in response to field utilization. Such changes include the rise in enthalpy, the lowering of the water level, which resulted in the lateral and vertical expansion of the steam zone and the decline of brine discharge (Dacillo and Siega, 2003).

As early as 1998, pressure drawdown was detected in MGF as evidenced by declining reservoir chloride concentration, silica geothermometer and well output, which decreased from 192 to 135 MWe. This pressure drawdown induced the inflow of cooler peripheral waters that has swamped the reservoir (Herras and Siega, 2003). Downhole pressure measurements recorded the highest drawdown of about 4.5 MPa in the vicinity of MG-28D, -30D and -31D (Fig. 4).

Repeat gravity measurements in other part of the world have become a standard geophysical method in monitoring the response of geothermal reservoir with exploitation. This technique in tandem with precise leveling survey could yield valuable information on the causes of gravity change between surveys.

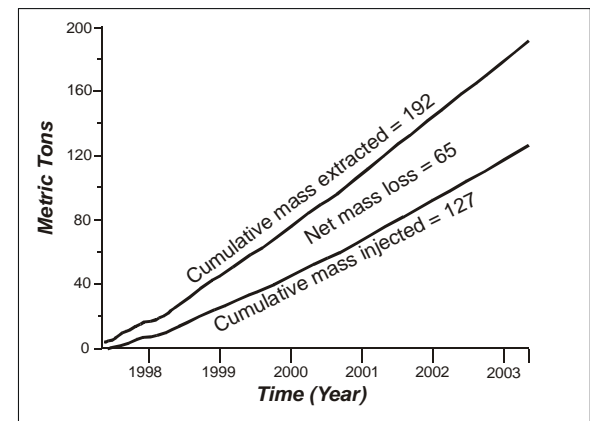
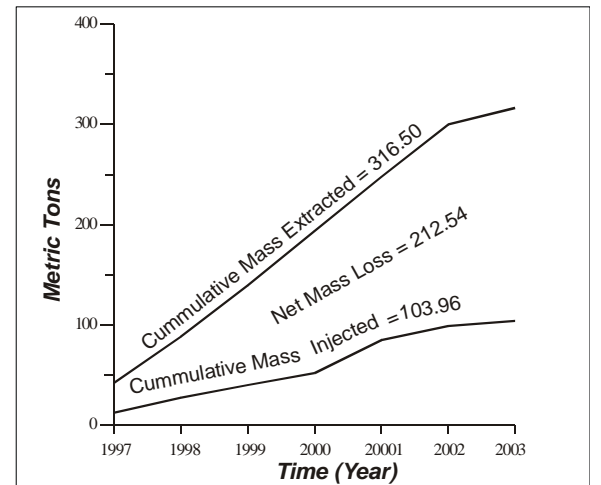
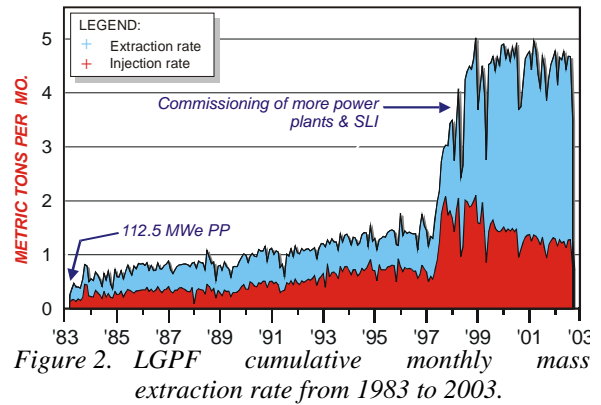


Figure 3. Cumulative mass extraction from 1997 to 2003; a) Tongonan Geothermal Field, b) Mahanagdong Geothermal Field.

The purpose of the survey is to demonstrate the importance of repeat gravity survey with regard to the field management of geothermal reservoirs.

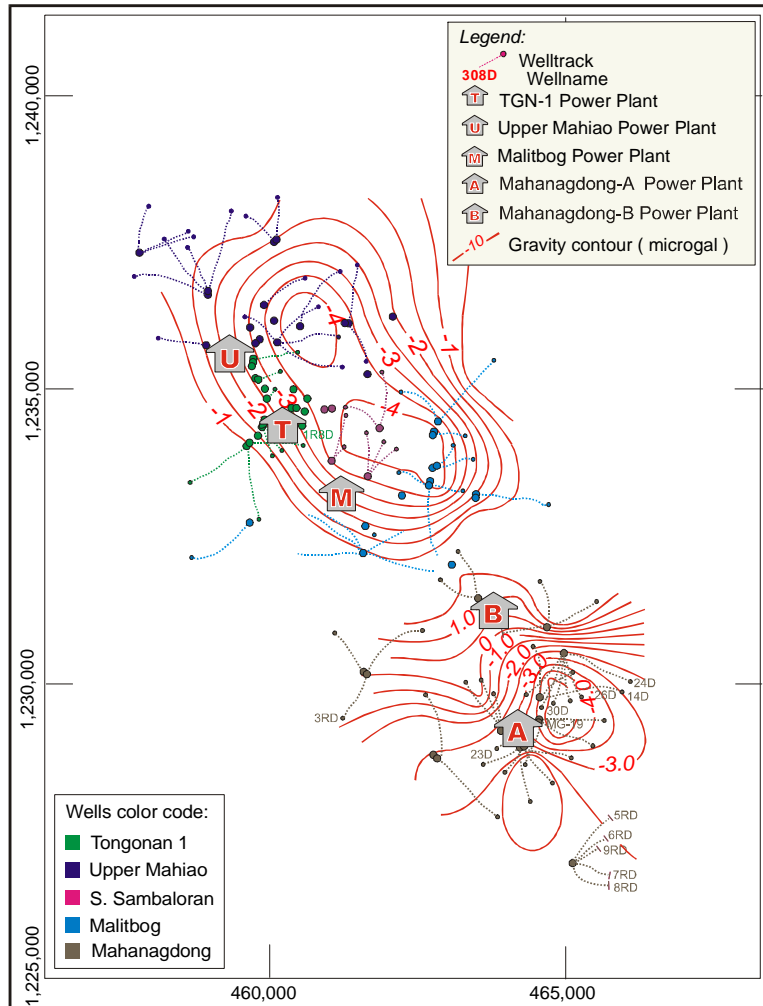


Figure 4. Pressure drawdown from 1996 to 2002.

GRAVITY DIFFERENCES

The main causes of gravity differences at the same point between surveys are vertical ground movements and net mass loss from the geothermal field (Hunt, 1977). Other factors that affect gravity differences are: changes in ground water level, changes in saturation (soil moisture content) in the aeration zone, local topographic changes, horizontal ground movement and changes in gravity at the base station. Except for the change in ground water level and the changes in gravity at the base station, all other factors affecting gravity differences are negligible. Gravity values may also vary with time (in million years) as a result of deep seated regional mass movements (active volcanism) but because geothermal fields generally occupy a relatively small area, and the difference in time between surveys is short, the gravity effects of such movements are usually small and can be neglected.

The gravity effects of mass movements in the geothermal reservoir, called gravity changes, are

obtained by correcting the measured gravity differences for the gravitational effects of vertical ground movements, changes in groundwater level and changes in base value.

For convention, a decrease in gravity is referred to as a negative change and an increase a positive change. Negative changes imply net mass loss and positive change imply net mass gain.

DISCUSSION OF RESULTS

The uncorrected gravity changes between 1997 and 2003 (Fig. 5) indicate that there was a decrease in the value of gravity with a maximum difference of $-160 \mu\text{gal}$ in the Upper Mahiao and TGN-1 sectors. The greatest decrease in gravity value occurred within the main TGF production field where it coincides with the location of the $\geq -100 \mu\text{gal}$ contours. Away from the production field, the gravity differences become smaller. Whilst in MGF, the production sector falls within the region where gravity generally decreased by about $-40 \mu\text{gals}$, which coherently centers on the

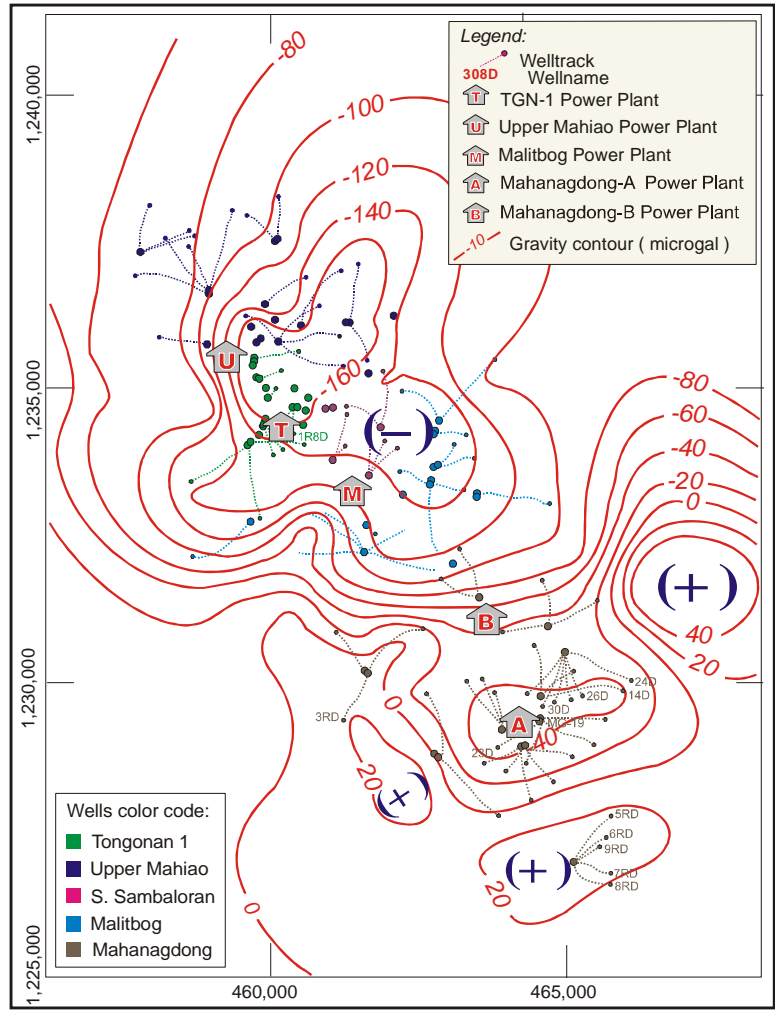


Figure 5. Uncorrected gravity changes from 1997 to 2003.

main production area, extending from MG-23D, -19, -30D, -28D, -26D, and -14D. A 20- μ gal increase in gravity can also be seen in the southern reinjection area near wells MG-5RD, -6RD, -7RD, -8RD, and -9RD. The production area itself does not lie directly over the zone with the largest change in gravity, but rather, along the gradient where the gravity changes from 0 to -40 μ gals. The centers of the largest gravity decrease form two separate “sinks”, one at the southeastern and the other at the western fringes of the production boundary.

The gravity changes between 1997 and 2003 corrected for elevation and base changes are depicted in Figure 6. The values used for vertical gravity gradient in elevation correction and base correction are -298 μ gal/m and 24 μ gal, respectively. They show no significant differences in pattern with that of the uncorrected gravity changes. However, the gravity values of about -100 μ gal are expectedly lower because they were corrected for elevation and base changes. From 1997 to 2003, TGF yielded a net

mass loss of 212 Mt of geothermal fluids (Fig. 3a). Pressure drawdown contours from 1996 to 2002 (Fig. 4) indicate that the highest drop in pressure are located in Upper Mahiaio and South Sambaloran (> 4.0 MPa) areas, which also coincide with the location of the highest negative gravity changes (≥ -100 μ gals). Similarly, the depressurized 1 bar PCO₂ area has extended from Upper Mahiaio to South Sambaloran sectors (Fig. 7), coinciding also with the -100 μ gal contour. This depressurized zone, likewise, corresponds to the areas where production wells are already discharging dry steam.

Beginning 1997 when Mahanagdong became online for geothermal power production until 2003, the sector has lost a net total of 65 Mt of mass from the reservoir as a consequence of exploitation (Fig. 3b). The production sector this time is roughly defined by a decrease in gravity of 20 to 40 μ gals (Fig. 6). Compared with the uncorrected data, the region where there is a decrease in gravity (negative values) is more extensive, and broadens out to include most

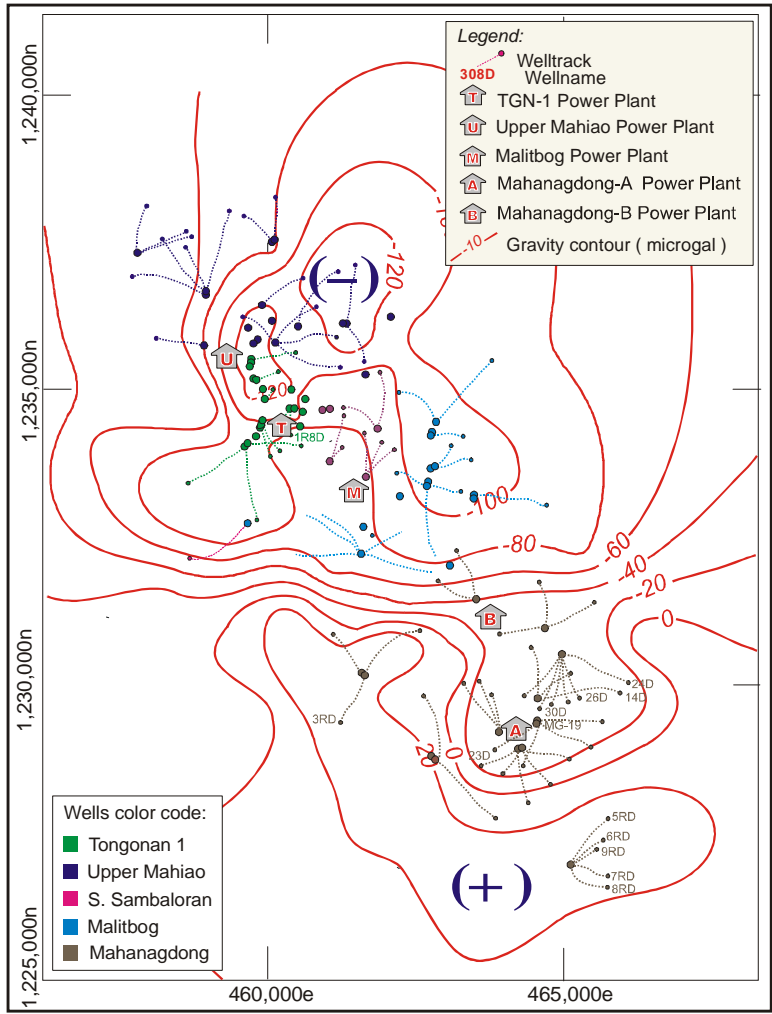


Figure 6. Corrected gravity changes from 1997 to 2003.

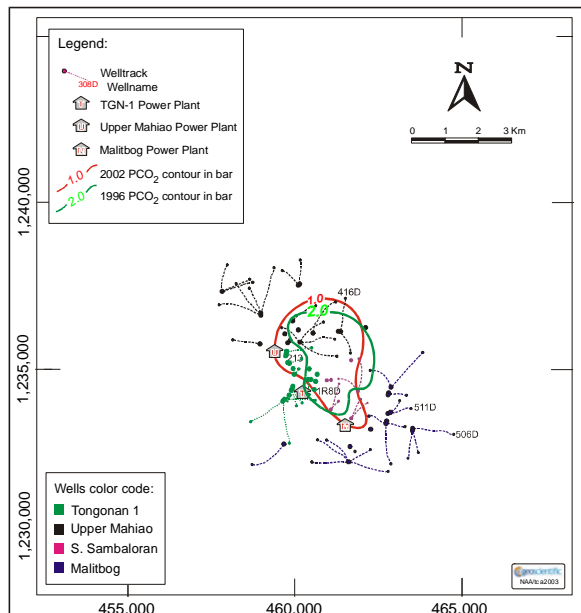


Figure 7. PCO₂ contour from 1996 to 2002.

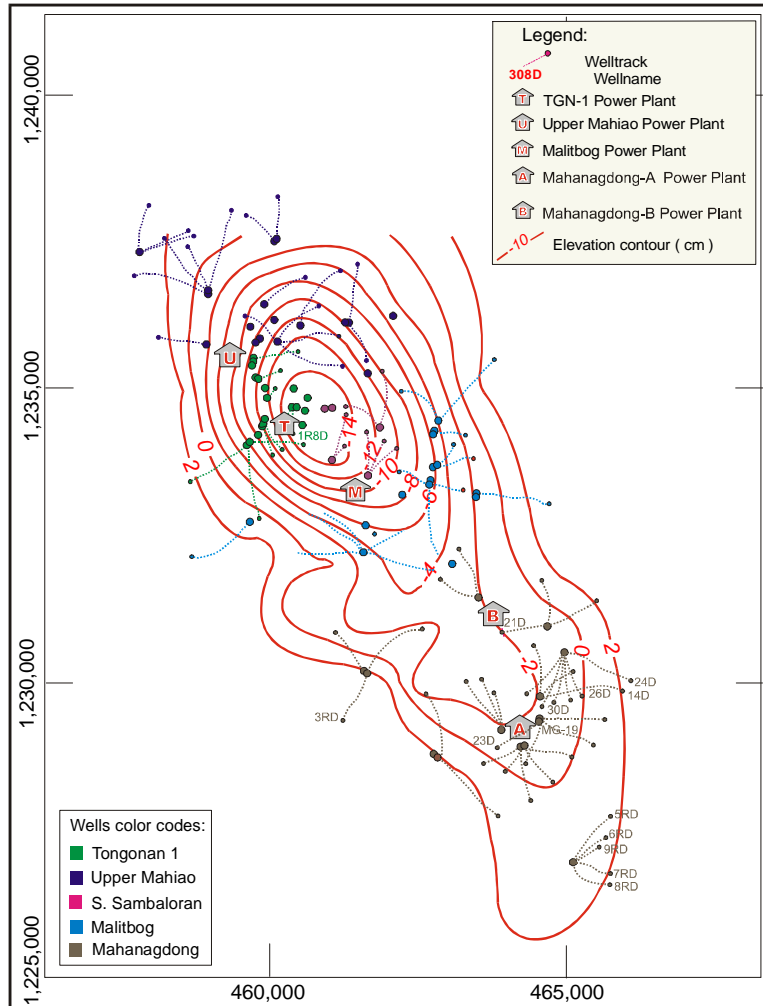


Figure 8. Elevation changes from 1997 to 2003.

of the eastern and the northeastern side of the production area. A well-defined 20- μ gal increase in gravity encloses the southern and western reinjection areas.

The ground vertical movements (elevation differences) observed on the network from 1997 to 2003 were mostly negative (Fig. 8). The highest recorded subsidence (180 mm) occurred at TGN-1 production sector 1 km north of well 1R8D.

Generally, the amount of subsidence is relatively small since full exploitation of TGF commenced only in 1998, hence, no significant physical evidence on the surface could be found. Furthermore, the very small variance in elevation between 1997 and 2003 may be attributed to the zero-waste disposal scheme of the company, which reinjects back a substantial amount of mass into the reservoir.

In MGF, an apparent subsidence occurred between 1997 and 2003. The subsided region has a general

northwest to southeast orientation and approximately follows the trace of the Philippine fault, which transects the area. The subsidence was minimal with only a maximum of about 20 mm and dips towards the northwest in the direction of TGF, where the magnitudes are relatively larger and are probably more significant.

INTERPRETATION

Significant gravity differences at LGPF occurred at TGF during the survey period 1997 to 2003. The large negative gravity difference was primarily caused by the net mass loss of 212 Mt of fluid and steam (Fig. 3) from the geothermal reservoir due to exploitation. At present, the effect of vertical ground movement is still minimal. However, the effect of changes in shallow groundwater level cannot be discounted.

The large negative gravity changes at TGF correlate well with the liquid pressure drawdown from 1996 to 2002 (Fig. 4) with corresponding lateral and vertical

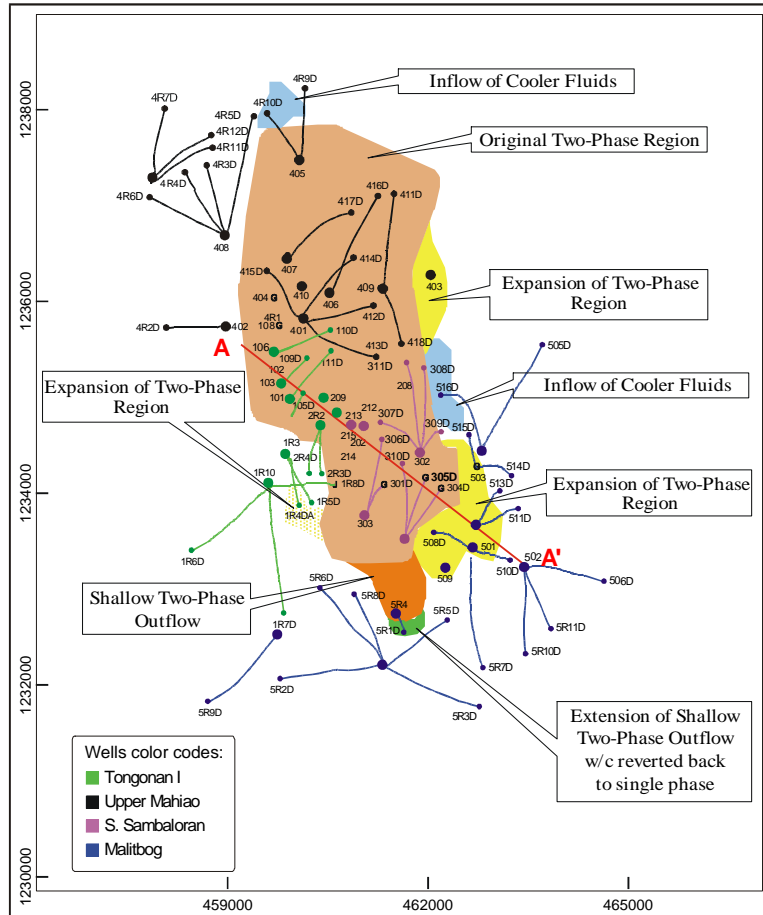


Figure 9. Lateral expansion of the 2-phase zone (after Sta. Ana, 2002).

expansion of the 2-phase zone (Figs. 9 and 10). Likewise, the depressurized 1 bar PCO₂ area where it extended from Upper Mahiao to South Sambaloran sector (Fig. 7) corresponding to the areas where production wells are discharging dry steam fall within the > -100 µgal contour. This also depicts the lateral expansion of the shallow steam cap towards South Sambaloran and the decline of the reservoir pressure (Dacillo and Siega, 2003).

The exploitation of MGF since 1997 has incurred pressure decline in the central part of the reservoir. This induced the inflow of cooler peripheral waters, particularly from the northwest and has presently swamped the reservoir thereby reducing the in-situ steam supply. Power output is now at about 135 MWe, which went from a high of 192 MWe in 1998 (Herras and Siega, 2003).

The pressure decline as a direct consequence of mass extraction is very apparent in the MGF. In the MG-DL area, for example, extensive drawdown since 1998 has resulted to a decline of almost 5 MPa in reservoir pressure in the central part of the production field. This decrease in subsurface mass is reflected in

the microgravity measurements by a corresponding decrease in gravity values. As shown in Figure 6, up to greater than 20-µgal decrease in gravity was observed occurring at the central portion of the production sector since 1997. The area includes well MG-23D in the southwest, wells MG-30D and MG-28D at the central part, and well MG-24D in the northeast. Comparing this figure with the plot of pressure drawdown contours (Fig. 4), it is plain that the maximum drawdown was experienced roughly over the same area, which also borders around wells MG-30D and MG-28D.

On the other hand, the positive gravity change experienced in the vicinity of wells MG-5RD, -6RD, -7RD, -8RD, and -9RD, which was as high as about 20 µgal could possibly be due to reinjected fluids, with the area being a reinjection sink.

According to Gauss's Potential Theorem (Hammer 1945; Hunt 1970),

$$\Delta M = \Sigma \Delta g \Delta s / 2\pi G$$

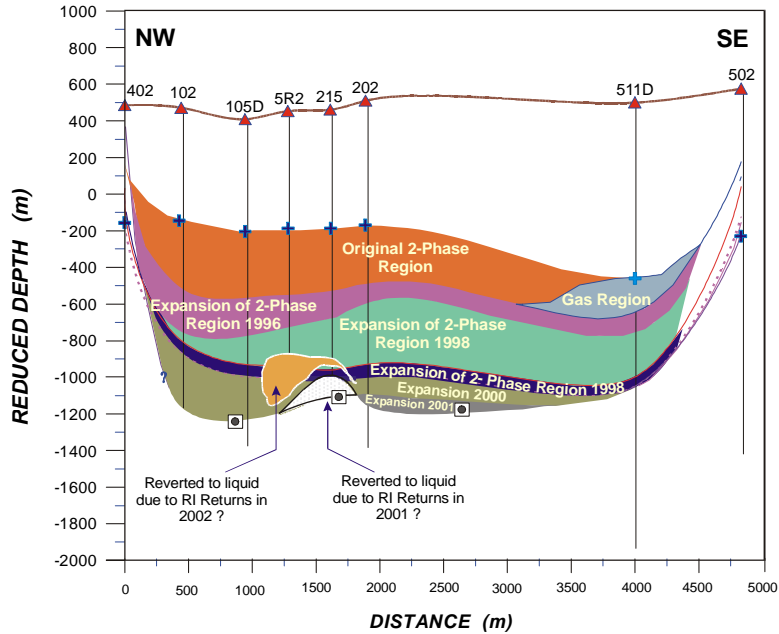


Figure 10. Yearly vertical expansion of the 2-phase zone zone along line A-A' (after Sta. Ana, 2002).

where: ΔM is the net mass loss from the system, Δg is the corrected gravity difference for area Δs , and G is the gravitational constant ($6.67 \times 10^{-11} \text{ N m}^2 \text{ kg}^{-2}$). The integrated sum of the corrected gravity difference ($\Sigma \Delta g \Delta s$) between 1997 and 2003 obtained from the contours in Fig. 6 is about $-10205 \mu\text{gal km}^2$, hence, the resulting net mass loss from the system (ΔM) is about 244 Mt. Using the mass balance equation,

$$(Mw + Ds) - (R + I) = \Delta M$$

where: Mw is the mass withdrawn from the wells, Ds is the surface discharge, R is the natural recharge, and I is the injected fluid. The natural recharge (R) is 34 Mt or 12 % of the total mass removed from the system.

Examination of the contour map of gravity changes (Fig. 6) shows that the gravity changes are generally negative, but the greatest is in TGF area. This is where the greatest degree of mass withdrawal compared with replacement is occurring, probably as a result of lateral and vertical expansion of the 2-phase zone (Figs 9 and 10). The negative gravity changes in the reinjection areas indicate that more fluid is still being withdrawn than being injected.

CONCLUSIONS

Based on Gauss's Potential Theorem and mass balance equation, the negative gravity changes from 1997 to 2003 indicate that the system (LGPF) has

incurred a net mass loss of about 244 Mt and a natural recharge of about 34 Mt or 12% of the total mass removed.

At TGF, the main causes of gravity changes resulting from mass changes in the reservoir are the liquid drawdown and the saturation changes in the 2-phase zone. This extraction, with a recharge deficit of about 212 Mt reflected a 4.5 MPa drawdown in reservoir pressure, which in turn induced the migration of cooler peripheral fluids towards the production reservoir, thereby lowering its steam capacity.

The pressure drawdown experienced in the MGF is a direct consequence of the massive mass withdrawal from the geothermal reservoir. Likewise, the field has lost a total of 65 Mt of water and steam to the atmosphere since its exploitation in 1997.

It was presented that the trends observed in the various reservoir monitoring methods were similarly attained using microgravity data. With several sets of microgravity data, trends can also be established that will allow tracking of the path taken by reinjected fluids within the reservoir. Reservoir properties, such as porosity and saturation can also be estimated using the method, and will be an invaluable aid in testing numerical models of the reservoir performance. Given the versatility, the microgravity method could be considered as an alternative if not a better method in monitoring reservoir processes.

REFERENCES

Allis, R.G. and Hunt, T.M. (1986). "Analysis of Exploitation-Induced Gravity Changes at Wairakei Geothermal Field." *Geophysics*, vol. 51, No. 8, 1647-1660.

Allis, R.G., Gettings, P. and Chapman, D.S. (2000). "Precise Gravimetry and Geothermal Reservoir Management." *Proceedings 25th Workshop on Geothermal Reservoir engineering (Stanford)*, 10pp.

Apuada, N.A. and Hunt, T.M. (1996). "Microgravity Measurements at Leyte Geothermal Power Project." *Proceedings 18th Annual PNOC-EDC Geothermal Conference (Makati)*, 12pp.

Atkinson, P.G. and Pedersen, J.R. (1998). "Using Precision Gravity Data in Geothermal Reservoir Engineering Modeling Studies." *Proceedings 13th Workshop on Geothermal Reservoir engineering (Stanford)*, 35-39.

Dacillo, D.B. and Siega, F.L. (2003). "Major Geochemical Changes in the Tongonan Geothermal Reservoir (Leyte, Philippines) during its Twenty Years of Operation." *Proceedings 24th Annual PNOC-EDC Geothermal Conference (Makati)*, 8pp.

Delfin, F.G., Maneja, F.C., Layugan, D.B. and Zaide-Delfin, M.C. (1995). "Stratigraphic and Geophysical Constraints on Injection Targets in the Greater

Tongonan Geothermal Field, Leyte, Philippines." *PNOC-EDC internal report*, 72pp.

Hammer, S. (1945). "Estimating ore masses in gravity prospecting." *Geophysics*, v. 10, no.1, 50-62.

Herras, E.B. and Siega, F.L. (2003). "The Perplexing Problem of Injected Fluids and Groundwater Inflow in Mahanagdong Geothermal Field, Leyte, Philippines." *Proceedings 24th Annual PNOC-EDC Geothermal Conference (Makati)*, 6 pp.

Hunt, T.M. (1970). "Gravity Changes at Wairakei Geothermal Field, New Zealand." *Geological Society of America Bulletin*, v. 81, 529-536.

Kasagi, J., Saito, H., Honda, H., Haruguchi, K. and Tsukamoto, S. (1996?). "Study on Reservoir Behavior From Gravity Changes and Density Modeling Analysis in the Hatchobaru Geothermal Field." *Proceedings 18th Annual PNOC-EDC Geothermal Conference (Makati)*, 7 pp.

Olivar, R.E.R. and Apuada, N.A. (1998). "Baseline Microgravity and Precise Leveling Survey Leyte Geothermal Production Field." *PNOC-EDC internal report*, 16 pp.

San Andres, R.B. and Pedersen, J.R. (1993). "Monitoring the Bulalo Geothermal Reservoir, Philippines, Using Precision Gravity Data." *Geothermics*, vol. 22, No. 5/6, 395-402.

FOUR DIMENSIONAL VELOCITY STRUCTURE OF THE SOULTZ-SOUS-FÔRETS GEOTHERMAL RESERVOIR DURING THE 2000 AND 2003 STIMULATIONS

J. Charléty¹, N. Cuenot¹, C. Dorbath^{1,2}, L. Dorbath^{1,2}

¹) EOST-ULP 5, rue René Descartes, Strasbourg, France

²) IRD, Toulouse, France

e-mail: jean.charlety@eost.u-strasbg.fr

ABSTRACT

The stimulation of 2000 and 2003 carried out on the HDR site of Soultz-sous-Forêts (Alsace, France) have generated a continuous, small magnitude seismic activity. For each experiment, a seismological network composed of about 25 stations were installed by the Ecole et Observatoire des Sciences de la Terre (EOST). More than 3500 seismic events has been pointed and located in both cases.

In order to estimate the variation of the physical properties of the reservoir due to the fluid circulation, we have performed a four dimensional tomography: the 3D velocity structure for different time windows. The whole data set has been apportioned into different temporal sets with a fixed number of events. We use the tomographic algorithm of Thurber (1983) for 2000 and a new, more accurate method for the set of 2003 based on a double difference tomography (Zhang & Thurber, 2003). The latter method gives a good resolution within the reservoir volume and allows a relatively good resolution in the vicinity of this volume. It enlightens the velocity structure variation in the reservoir all along the stimulation.

In this study, we propose a discussion based on the variation of the velocity in time during each stimulation and a comparison of the variation of the velocity in 2000 and 2003. This analysis allows us to appreciate the volume of influence of the hydraulic activity and points out the effect of the water circulation on the reservoir properties.

INTRODUCTION

In 2000 and 2003, massive hydraulic stimulations were carried out at the geothermal Hot Dry Rock site at Soultz-sous-Fôrets, France. These stimulations were performed in the 5000 m deep wells, in the crystalline basement. The objective was to create a dense network of enhanced permeability fractures, which would form the heat exchanger. The

deformation entailed by the injection of fluid caused a microseismic activity.

Network

In 2000, the seismic network comprises around 20 stations divided into a telemetered network with eight vertical sensors, a network composed by six autonomous three-component sensors, and three four-component sensors deployed in wells at around 1.5 km depth. The latter is owned by the EEIG "Heat mining". The network changed in 2003.

Since the beginning of 2003, a field-wide permanent seismic network has been in place and was run by a team at the Institut de Physique du Globe from Strasbourg (France). The network comprises 9 stations and covers the geothermal reservoir. The sampling rate is 6.66 ms. The frequency band of the acquisition is from 1 to 48 Hz. Three stations have three-component sensors and the others only vertical ones. Fourteen additional seismometers have supplemented the permanent network. Six stations have three-component sensors and the others only vertical ones. The three-components sensors have the same characteristics as the permanent network. The vertical seismometers have a sampling rate of 5.55 ms and the frequency band is from 1 to 60 Hz.

Hydraulic Stimulations

The aim of the stimulation of 2000 was to improve the hydraulic connexion between the well GPK2 and the endemic fracture system. It started the 30th of June and lasted almost seven days. The flow-rate followed a step-wise strategy. The first step lasted less than one day with a flow-rate of 30 l.s⁻¹; the second lasted more than one day with a flow-rate of 40 l.s⁻¹; the third part lasted around 4 days with a flow-rate of 50 l.s⁻¹ (figure 1 top).

The aims for the 2003 stimulation did not change but it concerned the well GPK3: improvement of its injectivity and the relatedness between the two wells. It started the 27th of May and lasted 11 days. The fluid injection strategy was more complex than in 2000.

The flow-rate has been up to 93 l.s^{-1} on a very short period (some hours) (figure 1 bottom).

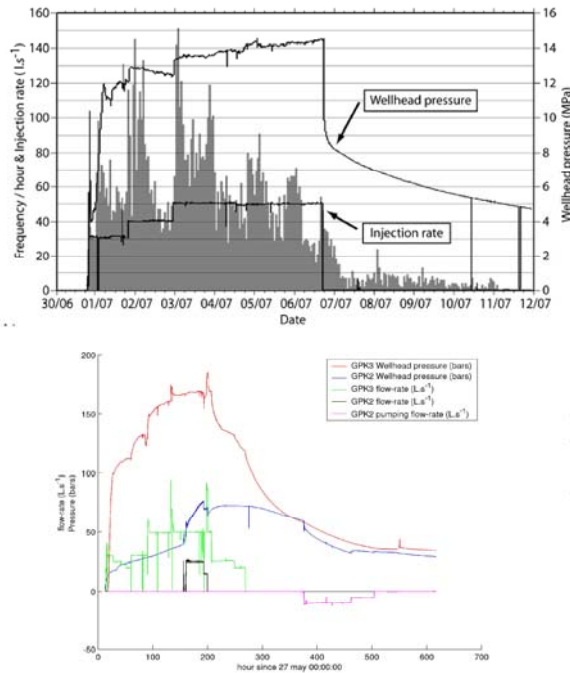


Figure 1 Injection strategy for 2000 (top) and 2003 (bottom). Top: are represented the wellhead pressure and the injection rate. In grey appears the number of seismic events per hour detected on the surface seismic network. Bottom: the wellhead pressure of GPK3 (red) and GPK2 (blue), and the flow-rate in GPK3 (green) and GPK2 (black and purple) are represented. The purple curve corresponds to the pumping strategy in GPK2.

METHOD

Data

The data from all the seismic sensors have been picked and used for the tomography. In 2000, more than 10 000 events has been recorded. More than 7000 events have been used to perform the tomography. The P and S arrival time have been manually picked (Cuenot et al., 2005). For 2003 an automatic detection algorithm has been used. The detection has been made for more than 6000 events. The data has been automatically picked by a AR-AIC algorithm (Leonard and Kennett, 1999). The tomography has been achieved with about 2250 events. Concerning the S wave arrival time picks, where shear wave birefringence was noted, the earliest S arrival was picked. S waves were picked only on horizontal components. A first location of the events was made by a hypoinverse-like algorithm

with a 8 tabular layer model. This model is based on the information derived from different log-data.

Tomography

The tomography used is based on the program simulps (Thurber, 1983). Simulps uses an iterative, damped least squares method to invert arrival times, simultaneously estimating earthquake locations and the three-dimensional V_p and V_p/V_s fields. The velocity structures are parameterized by values defined at the nodes of a three-dimensional grid, between which the V_p and V_p/V_s values are assumed to follow trilinear functions.

Zhang and Thurber (2003) have developed a new method that combines both absolute and relative arrival time data. The method determines a 3D velocity model jointly with absolute and relative event locations. They developed a double difference (DD) tomography code tomoDD based on the DD location code hypoDD (Waldhauser, 2001). In their simultaneous inversion for velocity structure and event locations, velocity anomalies are constrained by seeking a first-order smooth model. The same smoothing weight is applied to the horizontal and vertical regions. This smoothing regularization should provide a minimum-feature model that contains only as much as structure as can be resolved above the estimated level of noise in the data.

The two different types of data are combined into one system thanks to a hierarchical weighting scheme during the inversion. We start the inversion by applying greater weight to the absolute catalog data (1 for absolute data, 0.1 for differential catalog data) to establish the large scale result. The differential catalog data are weighted more to refine the event locations and the velocity structure near the source regions (1 for differential data, 0.1 for absolute catalog data). Then we finish the inversion by weighting equivalently both catalogs. For each step, two iterations are performed. The system is solved by a LSQR algorithm for the damped least-square problem.

The tomography method has changed between 2000 and 2003. In 2000, we used the simulps methodology while in 2003, tomoDD is used. As for both year the number of events is important, we decided to divide them into temporal sets so that the evolution of the velocity structure can be imaged. For 2000, a set of data is composed by 500 events (table 1). In 2003, as a differential catalog data is also used, the number of events per set is set to 250 (table2). In 2003 the number of events per set has been chosen in order to appreciate the effect of each injection stage: increase or decrease of the flow-rate, dual injection (injection in GPK2 and GPK3), shut-in.

Sample	Duration	Number of arrival times	
		P-wave	S-wave
1	30/06/00 @ 19h15 01/07/00 @ 08h16	5739	2263
2	01/07/00 @ 08h17 01/07/00 @ 19h46	5840	2140
3	01/07/00 @ 19h46 02/07/00 @ 03h18	5198	2305
4	02/07/00 @ 03h21 02/07/00 @ 12h12	5098	2488
5	02/07/00 @ 12h17 03/07/00 @ 04h26	5044	1707
6	03/07/00 @ 04h36 03/07/00 @ 13h58	5428	1875
7	03/07/00 @ 13h59 03/07/00 @ 20h22	5933	2523
8	03/07/00 @ 20h23 04/07/00 @ 04h23	5606	2373
9	04/07/00 @ 04h26 04/07/00 @ 17h09	4940	2111
10	04/07/00 @ 17h18 05/07/00 @ 02h55	5076	1965
11	05/07/00 @ 03h00 05/07/00 @ 15h41	5568	2290
12	05/07/00 @ 15h43 06/07/00 @ 01h04	6336	2757
13	06/07/00 @ 01h07 06/07/00 @ 16h30	6038	2955
14	06/07/00 @ 16h32 11/07/00 @ 05h58	6422	2989

Table 1: Detail of each set for the 2000 tomography with their duration and number of available P- and S-wave arrivals.

Sample	Duration	Number of arrival times	
		P-wave <i>dp data</i>	S-wave <i>ds data</i>
1	27/05/03 @ 18h37 30/05/03 @ 23h54	4246 42936	1773 19936
2	30/05/03 @ 23h54 01/06/03 @ 03h42	4118 40608	1759 19563
3	01/06/03 @ 03h42 02/06/03 @ 08h04	4202 42635	1796 19703
4	02/06/03 @ 08h04 03/06/03 @ 16h56	4514 44566	1795 19652
5	03/06/03 @ 16h56 04/06/03 @ 16h41	4559 43545	1983 20939
6	04/06/03 @ 16h41 05/06/03 @ 20h28	4474 42564	1982 20835
7	05/06/03 @ 20h28 07/06/03 @ 12h33	4473 41080	1938 19686
8	07/06/03 @ 12h33 09/06/03 @ 23h22	4435 40100	1927 18733
9	09/06/03 @ 23h22 19/06/03 @ 19h29	4699 42648	2002 19729

The grid covered all the area determined by the location of the seismic sensors. As the rays intercept each other in the volume of the reservoir the resolution of the tomography is good only at the depth of the injection. Thus the grid has been refined in this part.

Depth (km)	V_p ($km.s^{-1}$)	V_p/V_s
-15	1,5	2,14
0	1,85	2,14
0,8	2,87	2,14
1,6	5,8	1,75
2,6	5,82	1,75
3,6	5,85	1,75
4,6	5,87	1,75
5,6	5,9	1,75
6,6	5,92	1,75
15	5,95	1,75

Table 3: Initial velocity model for the tomography of 2000 and 2003. The depth is positive below sea level. The first and last layer are used as buffer.

The initial model for both tomography is the same for each set of data and tomography (table 3).

The tomDD code is similar to simulps if the relative catalog is not taking into account in the inversion (weight is put to 0). We have tested this approach on the first set in order to appreciate the difference between the methods. The difference in the results are quite small and it appears that the velocity values for the simulps inversion is almost always greater.

Other tests have been made. The 3D velocity model obtained is almost insensitive to starting model, event set and inversion strategy.

Table 2: Events samples for the 2003 tomography with their corresponding duration and number of available P- and S-wave arrivals for the absolute and relative catalog.

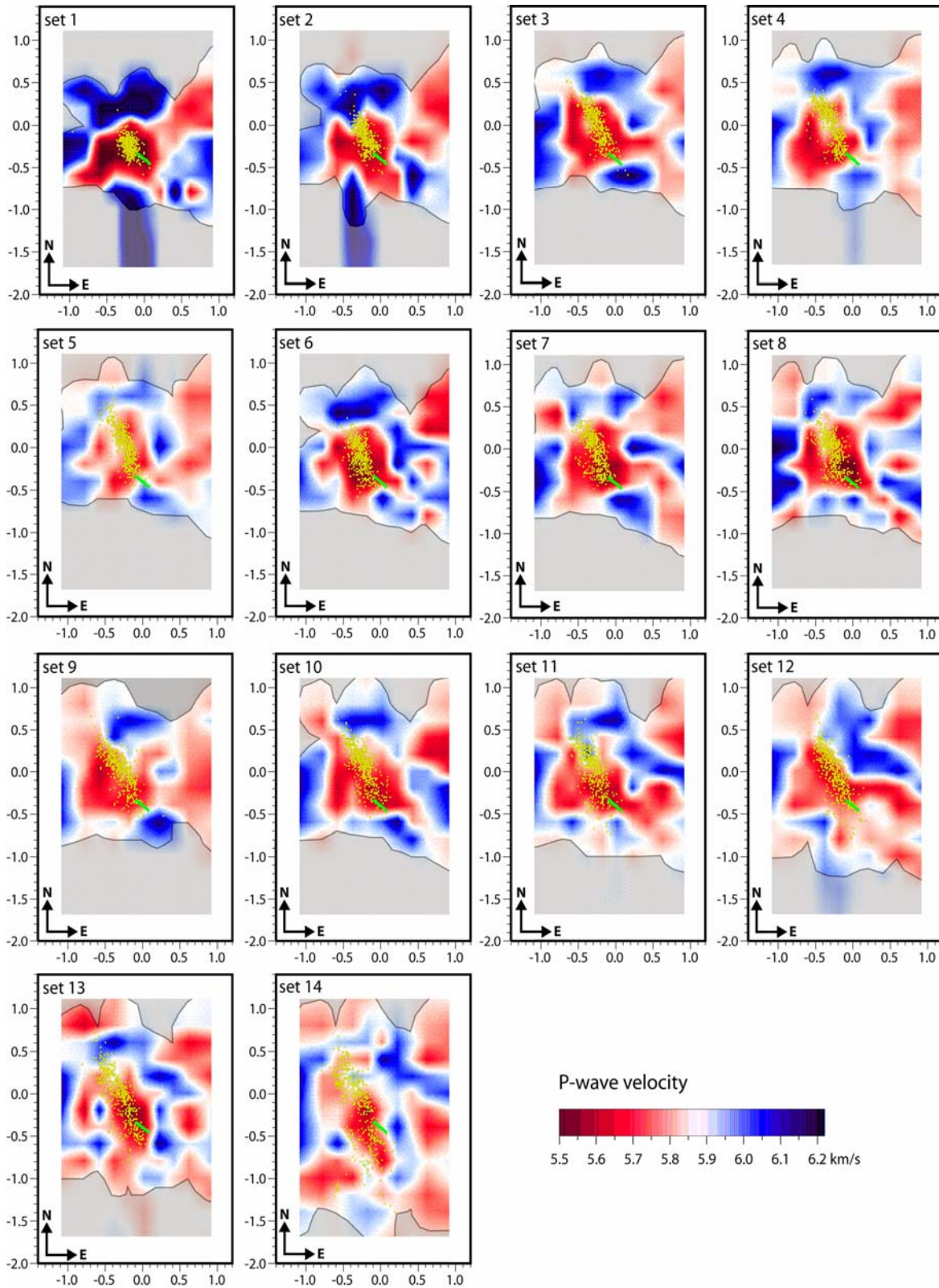


Figure 2: Evolution of the P-wave seismic velocity at 4.6 km depth during the 2000 stimulation test. Images are in chronological order from set 1 to set 14. Yellow dots represent the 500 events used in the computation for each subfigure. The green line corresponds to the open-hole section of the injection well GPK2. Grey areas do not have to be considered as they define zones of poor resolution.

RESULTS

The velocity structure of each tomography is corrupted by the lack of knowledge of the velocity model before the stimulation. The region is seismically quiet so that no natural seismicity has been locally recorded prior to the hydraulic experiments. It is also obvious that the seismicity is linked with the injection of fluid. This tomography could have given us essential information on the steady state in the reservoir. Nevertheless we described the global evolution of the velocity structure as in shape and value. We consider that as the treatment of each set is exactly the same the variation from one set to an other is meaningful.

Temporal evolution of the 2000 V_p velocity structure

A sequence of fourteen successive images was computed to observe the evolution of the V_p velocity in the geothermal reservoir (figure 2). On each plot are represented the corresponding 500 events used for the calculation to outline the shape and position of the microseismic cloud at that time. The trajectory of the open-hole section of the well GPK2 is also indicated. Hatchured zones do not have to be considered as they correspond to low-resolution areas.

Figure 2 presents the temporal evolution of the velocity structure at a depth of 4.6 km, corresponding to the location of the stimulated rock volume. Set 1 is calculated using the 500 first events of the stimulation. The dark red colour clearly denotes a significant low-velocity anomaly: the plotted microseismic cloud indicates that this anomaly corresponds to the geothermal reservoir. It is difficult to interpret this first result, as we cannot compare the present situation to that before the beginning of the injection: is the anomaly directly due to the start of the stimulation or does it actually exist before? Set 2 to set 5 show a slight increase of the velocity from 5.6 km.s^{-1} to about 5.8 km.s^{-1} . An interesting feature appears between set 5 and set 6: on the figure 2 one can notice the reappearance of the dark red colour at the place of the geothermal reservoir, indicating a sudden decrease of the P-velocity of about 0.2 km.s^{-1} . Then, until the end of the recording period, velocity slowly increases in the same way as at the beginning of the experiment. What does induce the quick decrease of the velocity? It appears from the injection curve that set 6 contains events occurred just after

the increase of the injection rate to 50 l.s^{-1} . We did not indeed observe such a variation between set 3 and set 4 although the injection rate was incremented from 30 l.s^{-1} to 40 l.s^{-1} between these periods. Nevertheless, we found some clear correlations between the increase of injection rate up to 50 l.s^{-1} and change in the hydrological parameters and seismic activity evolution that we cannot observe after the augmentation from 30 l.s^{-1} to 40 l.s^{-1} .

Temporal evolution of the 2003 V_p and V_s velocity structure

A sequence of nine successive images was computed to observe the evolution of the V_p velocity in the geothermal reservoir. On the figure 3, are represented for each set the seismicity in black dot and a white line demarcating the region where the number of rays per node is greater than or equal to 50. This number of rays commonly determine the part of the figure where the inversion resolution is good. The code tomoDD does not compute the resolution as the least square theory allows.

For the P wave velocity (figure 3), the views represent the evolution of the absolute velocity on horizontal plane at 4.6 km depth. On the first set, a large low wave velocity area dominates the first order spatial variation in V_p structure. This area is located around the well GPK3 near the coordinate (0;-1). This set is associated with the period where the flow-rate is not higher than 30 l.s^{-1} . Set 2 corresponds with an increase of the flow rate to 50 l.s^{-1} . We observe that the velocity decreases and that the region affected by this change grows. Then in the set 4 the velocity tends to slightly increase. The injection in both GPK2 (-0.2;-0.4) and GPK3 makes increase the velocity and grow the affected area on the northwestern part. Set 5 corresponds to the end of the dual injection. We note that the velocity increases around GPK3 and decreases around GPK2. Set 6 and 7 coincide with the end of the injection in GPK3. We can notice that the velocity remains nearly the same but the location of the maximum velocity region near GPK2 migrates to the northwestern part of the reservoir and that it appears a region southward of GPK3 where the velocity increases. In the set 8 and 9, the low velocity zone continues its migration toward the northwest and the south away from the injection point. The set 9 corresponds to a active period since, for accelerating the pressure decrease, a production strategy in GPK2 has been decided.

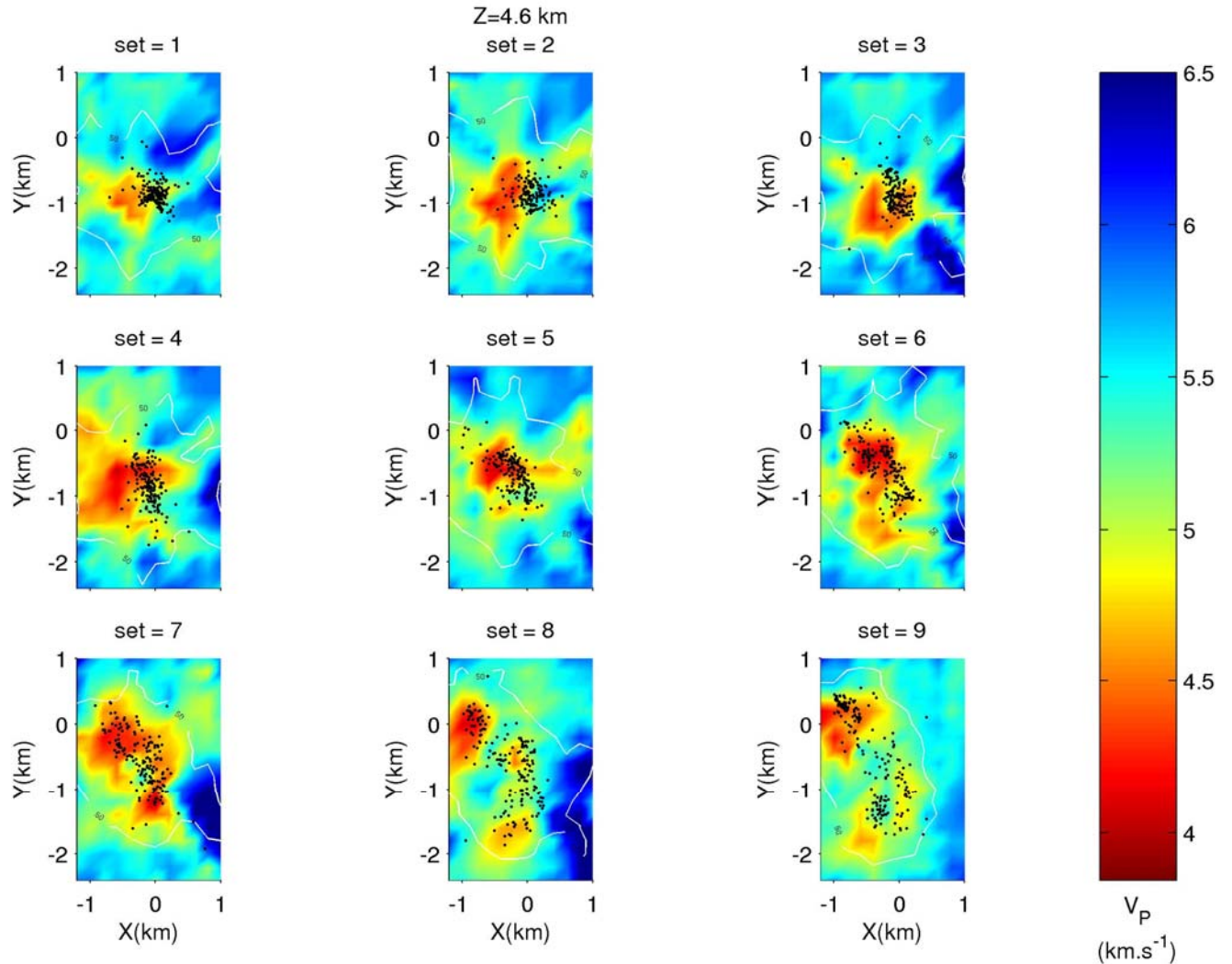


figure 3: Evolution of the P-wave seismic velocity at 4.6 km depth during the 2003 stimulation test. Images are in chronological order from set 1 to set 9. Black dots represent the 250 events used in the computation for each subfigure. The white line demarcates the zone in which the number of rays per node is greater than or equal to 50, supposed to be the good resolution area. North is directed toward positive Y while the East is toward positive X. GPK3 is around (0,-1) and GPK2 (-0.2,-0.5).

INTERPRETATION AND CONCLUSION

The relation between flow-rate change and the velocity variation is clear for both experiment. In 2000, a difference of behaviour from the geothermal reservoir appears between the flow-rate of $30\text{-}40 \text{ l.s}^{-1}$ and 50 l.s^{-1} . Actually, the decrease of the velocity is higher for the maximum flow-rate. This observation can also be made for 2003. Moreover for the last experiment the effect of the dual injection (injection in both well GPK2 and GPK3) appears clearly on the velocity of the P wave.

Factors that affect V_p include porosity (Wyllie *et al.*, 1956, 1958), pore pressure, partial saturation (Nur and Simmons, 1969), phase transition (Ito *et al.*, 1979) and temperature.

The correlation between the velocity decrease and the flow-rate means that a possible mechanism for the velocity variation is the increase of the pore pressure and/or the porosity, which both phenomenon entail a decrease of the velocity for P wave. The schematic model for this mechanism is an increase of the pressure near the well caused by the injection. This overpressure creates microcracks through which the fluid can migrate. The microcracking creates porosity and the fluid penetration in the rock mass increase the pore pressure. The effect of the pore pressure depends strongly on the saturation of the medium. Then the slow increase of the velocity afterwards can be due to the effects of the cooling of the medium due to the injected fresh fluid and the increase of the saturation of the medium. Both mechanisms make the velocity to increase. The direction of propagation northwest-

southeast corresponds to the direction of regional maximum horizontal stress. This direction has been determined (Tenzer *et al.*, 1991; Rummel and Baumgärtner, 1991; Klee and Rummel, 1993; Benderitter and Elsass, 1995; Helm, 1996) several times in the Upper Rhine Graben region.

In 2003 we note that the northwestern part of the reservoir has still a low velocity after the shut-in. In this region, the largest seismic events have occurred in 2000 and in 2003. The set 8 and 9 which correspond to the period after the shut-in show clearly this feature. The decrease of the velocity is due to either the porosity or the pore pressure. Therefore it could be guessed two scenarii. The first one considers that the fluid is led to this region for some reasons so that a large part of the injected fluid remains in this area. The mechanism to invoke is so the pore pressure. The second scenario considers that as the region is submitted to a seismic activity of large magnitude (up to 3 in duration magnitude), the porosity increased and thus the P wave velocity decrease.

The tomography of 2003 allows to observe that after the hydraulic activity, the medium returns to a kind of equilibrium state. It demonstrates that the medium is perturbed by the injection and permit to consider that the first image (set 1) is fully a consequence of the injections.

The tomography used either in 2000 or in 2003 relocate the seismic events in the 3D velocity model. This relocation refine the error in latitude, longitude and depth so that they are around 20 to 30 meters. In 2003 the relocation of the seismic event points out the relation that exists between the seismic activity and the natural endemic fractures. The figure 4 shows the relocation of the 250 first events corresponding to the first set. The fracture represented has been imaged by UBI and the characteristic of the plane has been determined by Dezayes *et al.* (2004). This fracture absorbed around 80 % of the fluid injected as determined by a flow-log. The weakening of the fracture by the fluid entails the occurrence of a large part of the seismicity.

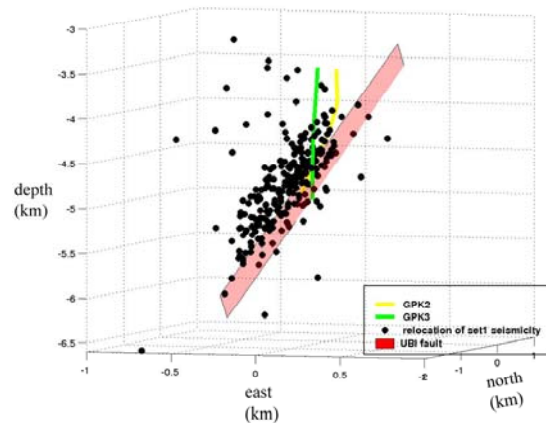


Figure 4 The seismicity relocated in the 3D model velocity determined by the tomography. This seismicity is located just above the fracture imaged by UBI (pink-red plane). The well GPK3 is in green and GPK2 in yellow.

Acknowledgment: this work is part of Jean Charléty Ph.D. thesis supported by ADEME.(Agence de l'Environnement et de la maitrise de l'énergie). We thank also the EEIG "Heat Mining" for having given us the hydraulic data. We also thank all the people who worked for maintaining the permanent network: Hervé Blumentritt, Michel Frogneux, Jacki Sahr.

REFERENCES

- Benderitter, Y., and Elsass, P. (1995), "Structural control of deep fluid circulation at the Soultz HDR site, France: a review", *Geotherm. Sci. Technol.*, vol 4, 227-237.
- Cuenot, N., Dorbath, C., Dorbath, L., (2005), "Analysis of the microseismicity induced by fluid injections at the Hot Dry Rock site of Soultz-sous-Forêts (Alsace, France): implications for the characterization of the geothermal reservoir properties.", *Pure and Applied Geophysics*, accepted
- Dezayes, Ch., Genter, A., Homeier, G., Degouy, M., Stein, G., (2003), "Geological study of GPK3 HFR borehole (Soultz-sous-Forêts, France)", *BRGM/RP-52311-FR*, 128 p.
- Helm, J.A. (1996), "The natural seismic hazard and induced seismicity of the European Hot Dry Rock geothermal energy project at Soultz-sous-Forêts (Bas-Rhin, France)", *Thèse de Doctorat, Ecole et Observatoire des Sciences de la Terre, Université Louis Pasteur (Strasbourg I)*, 197 p.
- Ito, H., De Vilbiss, J. and Nur, A., (1979), "Compressional and shear waves in saturated rock

during water-steam transition”, *Journal of Geophysical Research*, vol **84**, n° B9, 4731-4735.

Klee, G., and Rummel, F. (1993), “Hydrofrac stress data for the European HDR research project test site Soultz-sous-Forêts”, *Int. J. Rock Mech. Min. Sci. & Geomech. Abstr.*, vol **30**, 973-976.

Leonard, M., Kennett, B.L.N., (1999), “ Multi-component autoregressive techniques for the analysis of seismograms”, *Physics of the earth and Planetary Interiors*, vol. **113**, 247-263.

Nur, A., and Simmons, G. (1969a), “The effect of saturation on velocity in low porosity rocks”, *Earth Planet. Sci. Lett.* , vol **7.**, 183-193

Rummel, F., and Baumgärtner, J. (1991), “Hydraulic fracturing stress measurements in the GPK1 borehole, Soultz-sous-Forêts”, *Geotherm. Sci. Technol.*, vol **3**, 119-148.

Tenzer, H., Mastin, L., and Heinemann, B. (1991), “Determination of planar discontinuities and borehole geometry in the crystalline rock of borehole GPK1 at

Soultz-sous-Forêts”, *Geotherm. Sci. Technol.*, vol **3**, 31-67.

Thurber, C.H., (1983), “Earthquake locations and three-dimensional crustal structure in the Coyote Lake area, central California”, *Journal of Geophysical Research*, vol **88**, 8226-8236.

Waldhauser, F., (2001), “hypoDD: a computer program to compute double difference hypocenter locations”, *U.S. Geological Survey Open File Report 01-113*, 25 p.

Wyllie, M.R., Gregory, A.R., and Gardner, L.W. (1956), Elastic wave velocities in heterogeneous and porous media, *Geophysics*, vol **21**, 41-70.

Wyllie, M.R., Gregory, A.R., and Gardner, L.W. (1958), “An experimental investigation of factors affecting elastic wave velocities in porous media”, *Geophysics*, vol **23**, 459-493.

Zhang, H. and Thurber, C.H., (2003), “Double-difference tomography: The method and its application to the Hayward fault, California”, *Bulletin of the Seismological Society of America*, vol.**93**, n° 5, 1875-1889.

FAULTING MECHANISMS AND STRESS TENSOR AT THE EUROPEAN HDR SITE OF SOULTZ-SOUS-FORÊTS

N. Cuenot¹, J. Charléty¹, L. Dorbath^{1,2}, H. Haessler¹

¹IPGS-EOST Strasbourg, 5 rue René Descartes, 67084 Strasbourg Cedex, France

²IRD, LMTG Toulouse, 14 avenue Edouard Belin, 31400 Toulouse, France

e-mail: cuenot@eost.u-strasbg.fr

ABSTRACT

The state of stress and its implications for the shearing mechanisms on fault plane during hydraulic injection are crucial issues for the general functioning of HDR systems. It is especially true for hydraulic stimulation experiments, aimed at enhancing the permeability and connectivity of natural fracture network: they tend to induce the shearing of joints, which is controlled by the local stress tensor.

In this study we present some results about the shearing mechanisms of microseismic events occurred during the 2000 and 2003 stimulation tests at Soultz-sous-Forêts and their significance in terms of stress. About 7200 microearthquakes have been located in 2000 and 2250 in 2003, from a surface seismological network. In both cases, several hundreds of double-couple focal mechanisms have been automatically determined with the FPFIT program (Reasenber and Oppenheimer, 1985), using first-motion polarities. Results indicate a majority of normal-faulting movements with a more or less pronounced strike-slip component. Quasi-pure strike-slip events also occur, especially in the deeper part of the reservoir.

Although we find a double-couple solution for all events, we tried to observe and quantify the proportion of non-double-couple component in the seismic moment tensor for several microseisms from the 2003 data. The study shows that there is a higher proportion of tensional opening for the events in the vicinity of the injection well than in the far reservoir.

We used the method of Rivera and Cisternas (1990) to perform the inversion of the deviatoric part of the stress tensor from P-wave polarities. We applied this method to different sets of the 2000 data, taken from the shallower and deeper parts of the reservoir. Results shows a stable, horizontal, NE-SW-oriented trend of the minimum stress, but a rotation of the maximum stress from a subvertical direction (top of the reservoir) to a subhorizontal one (bottom of the

reservoir), which implies a change from a normal-faulting regime to a strike-slip regime with depth, in agreement with our fault-plane solutions. Finally we applied the stress tensor to the nodal planes of several events and we have been able to determine their fault plane and to obtain a 3D image of the fracture network, based on real data.

INTRODUCTION

In 1987, the European Hot Dry Rock project was founded at the site of Soultz-sous-Forêts (Alsace, France) by France, Germany and the European Commission (Kappelmeyer et al., 1991). Soultz-sous-Forêts is situated within the central upper Rhine Graben, about 50 km north of Strasbourg (Fig. 1). It is located within the former Pechelbronn oil field, in a zone of large temperature gradient anomaly, which was measured in the subsurface sedimentary layers (Schellschmidt and Schultz, 1991). These sediment deposits exhibit a thickness of about 1400 m and cover a large granitic rock massif, in which the geothermal reservoir is being developed: the purpose is to create an artificial, deep heat exchanger in the hot, fractured granite by stimulating the natural fracture network. Indeed the aim of stimulation experiments is to enhance the permeability and connectivity of the joint network and to connect it with the open-hole sections of boreholes. Hydraulic injections tend to induce shearing on fracture planes, which are favourably oriented for slip within the local stress field.

For almost 20 years, several phases of the project were completed, consisting mainly in the characterization of the granite massif down to 5 km depth and in the development of the technology needed to extract heat from rocks. Several wells have been drilled for this purpose. Five are observation boreholes, into which downhole seismic sensors are deployed and used to monitor the seismic activity associated with the hydraulic injections. 4 deep wells were also drilled during the course of development. GPK1, reaching 3590 m depth, has been stimulated in 1993 (Baria et al., 1995). In 1995, GPK2 has been

drilled down to 3876 m and stimulated twice in 1995 and 1996 (e.g. Baria et al., 1999; Gérard et al., 2002).

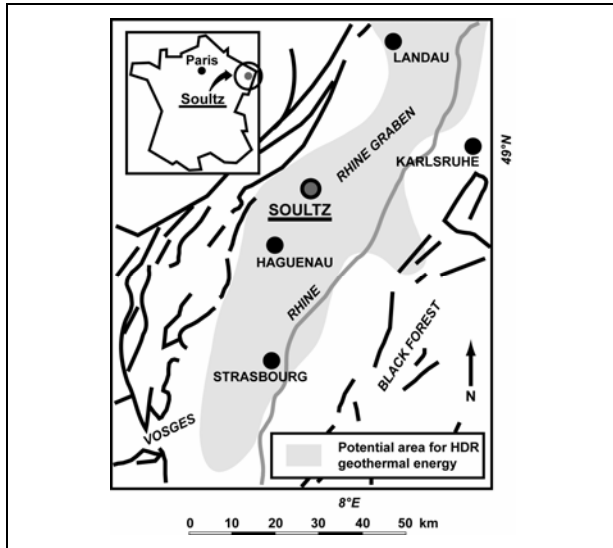


Figure 1: Location of the European HDR site at Soultz-sous-Forêts (from www.soultz.net).

In addition to several others hydraulic tests (injection and production) a successful 4-months circulation test has been performed between these 2 wells (Baumgärtner et al., 1998). In 1999 GPK2 was deepened to 5084 m, where a rock temperature of more than 200°C has been measured, and stimulated in 2000 (Weidler et al., 2002). In 2001 a new phase of the project began, during which a three-wells system is being developed as a scientific pilot plant: in addition to GPK2, GPK3 was drilled to 5091 m depth in 2002 and stimulated in 2003 (Baria et al., 2004). GPK4 was completed in 2004 down to 4981 m depth. Its stimulation began in late 2004 and will continue in early 2005.

In this study, we present some results on faulting mechanisms of induced microseismic events occurred during the 2000 and 2003 stimulation tests. The determination of several hundreds of focal mechanisms gives insights about the faulting regime in the geothermal reservoir. Furthermore, in order to better characterize the faulting mechanisms, we investigate the proportion of tensional opening in the seismic moment tensor for some 2003 events. Finally, we perform an inversion to calculate the deviatoric part of the stress tensor at Soultz. The results, combined with focal mechanisms, allows us to determine a 3D view of the fracture network.

THE 2000 AND 2003 STIMULATIONS

The 2000 and 2003 stimulation tests were performed using different injection strategies. In this paragraph we briefly describe the hydraulic parameters of both

stimulations, the seismic monitoring systems and general results on microseismic activity.

The 2000 stimulation

Hydraulic parameters

The injection scheme was rather simple in 2000. The injection lasted about 6 days (June, 30th – July, 6th) and were performed in 3 injection steps: 30 l.s⁻¹ during 24 h, 40 l.s⁻¹ during 27 h and 50 l.s⁻¹ during 90 h have been injected through the open-hole section of GPK2 (4400 m–5000 m). The measured overpressure in the reservoir instantaneously reached a peak of 12 MPa and then declines for the first 2 steps. On the contrary, the rate of 50 l.s⁻¹ induced an initial overpressure of 12 MPa, but the pressure continued to increase up to 13 MPa until the shut in (Weidler et al., 2002). After the shut in, an instantaneous pressure drop of about 5 MPa was observed, then the pressure decreased very slowly.

Seismic monitoring networks

In addition to the downhole seismic network, which consisted in three 4-components accelerometers and two hydrophones, several surface stations were installed by EOST, University of Strasbourg. The surface network was composed of eight vertical seismometers, six 3-components seismometers, one broad-band station and three permanent stations belonging to ReNaSS (French national seismic network). A plane view of the 2000 seismic monitoring system is given in Fig. 2.

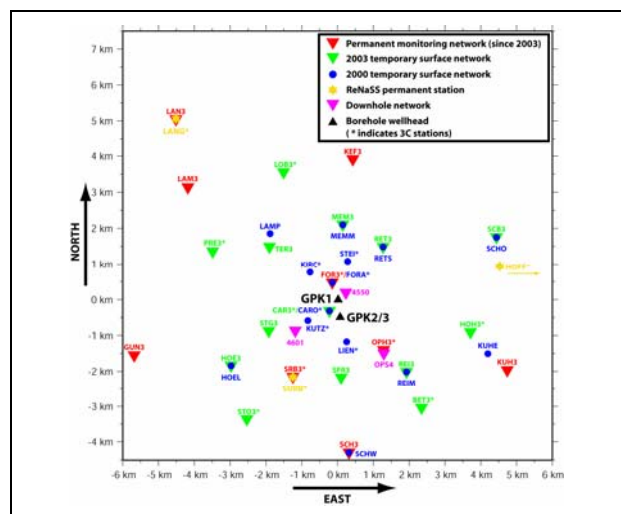


Figure 2: Downhole and surface seismological networks deployed for the 2000 and 2003 stimulation tests.

Microseismic activity

More than 10000 microseismic events have been recorded during the stimulation until the 11th of July

on the surface network. They range in magnitude between -0.9 and 2.6 . Among them, about 7200 have been precisely located with the method of Thurber, which is a simultaneous tomographic inversion of the velocity structure and location parameters (Thurber, 1983). They form a NNW-SSE oriented cloud of about 1.5 km long and 0.5 km wide. In depth the cloud ranges between 4 and 5.5 km (Cuenot et al.), (Fig. 3). The orientation of the microseismic cloud seems in agreement with the N-S to NNW-SSE trend of the majority of natural joints suggested by Genter and Traineau (1996).

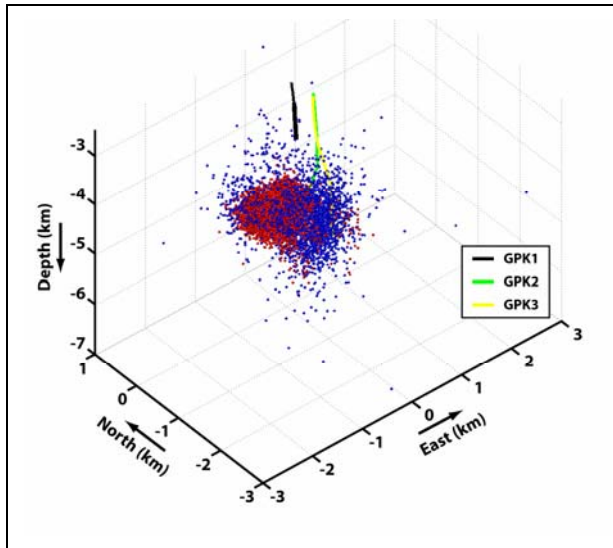


Figure 3: Plane view of the 2000 (red) and 2003 (blue) microseismic cloud.

The 2003 stimulation

Hydraulic parameters

The 2003 stimulation strategy of GPK3 was rather different from the 2000 stimulation of GPK2. Baria et al. (2004) described 4 phases during the 2003 stimulation. From May, 27th to June, 2nd injections began at 30 l.s^{-1} and were later increased to 50 l.s^{-1} , with two short periods at 60 and 90 l.s^{-1} . From June, 2nd to June 4th the concept of dual, focused injection was introduced: 50 l.s^{-1} were injected in GPK3 while 20 l.s^{-1} were pumped into GPK2. From June, 4th to June, 6th GPK2 was shut-in and, after a short increase to 90 l.s^{-1} , injection in GPK3 was decreased in 3 steps. Finally, because of a remaining microseismic activity after GPK3 shut-in, GPK2 was vented at 10 l.s^{-1} to reduce the pressure in the reservoir.

Seismic monitoring network

The 3 downhole 4-axis accelerometers were in the same configuration as 2000; 3-component geophones were also added. On surface, the main improvement consisted in the installation by EOST of a permanent

monitoring network (three 3-C sensors and six vertical sensors). In addition, a temporary surface network (six 3-C stations and eight vertical stations) has been deployed for the time of the stimulation test.

Microseismic activity

About 5000 microseismic events were recorded on the surface network in the magnitude range -0.9 to 2.9 . 2250 have been located using the TomoDD code (Zhang and Thurber, 2003). As in 2000, the cloud is oriented in the NNW-SSE direction. It is situated in a more southern position than the 2000 cloud. The cloud is about 2 km long and 1 km wide. It ranges between 3 and 7 km depth. On figure 3, the 2000 and 2003 seems to be imbricated. It would mean that at least a part of the seismic structures that had been stimulated in 2000, did not slip in 2003.

FOCAL MECHANISMS

We determine automatically several thousands of focal mechanisms using the program FPFIT (Reasenber and Oppenheimer, 1985): nodal planes are calculated from the first-motion polarities by a maximum likelihood procedure and manually checked afterwards. More than 14 polarities are available in average for the 2000 events and more than 16 for the 2003 seismicity. Results indicates a majority of normal-faulting movements, pure or with a more or less pronounced strike-slip component. But, on the deepest part of the reservoir, a strike-slip regime seems to dominate, with some quasi-pure strike-slip events. Some representative focal mechanisms examples for the 2000 and 2003 stimulation tests are given in Fig. 4 and Fig. 5.

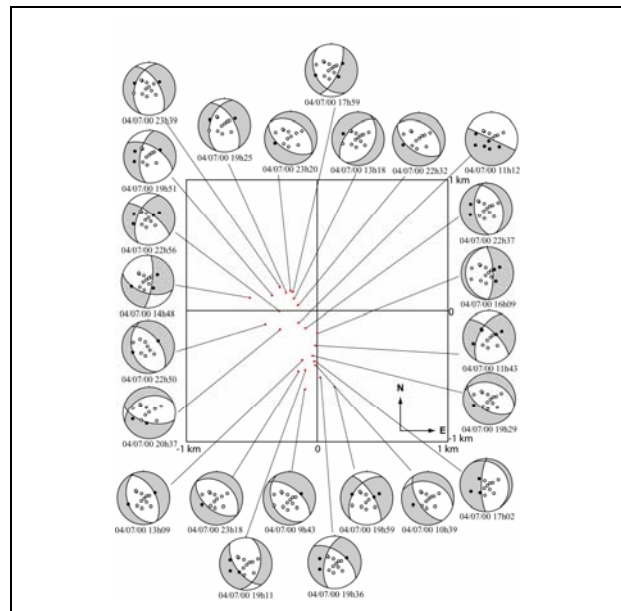


Figure 4: Representative focal mechanisms for the 2000 stimulation test.

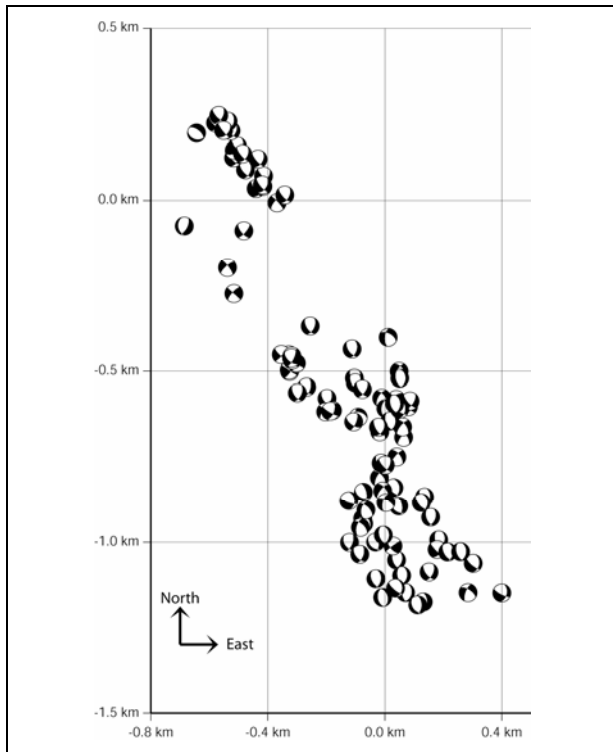


Figure 5: Representative focal mechanisms for the 2003 stimulation test.

NON DOUBLE COUPLE COMPONENT

From the full determination of the seismic moment tensor (1st order) we are able to describe the equivalent forces at the source, which can be correlated with the physical processes involved at the source. Moreover, the seismic moment tensor can be written as the sum of a double couple (DCC) component and a non double couple component (NDCC), which gives the proportion of tensional opening in the seismic rupture. This proportion is here expressed as a function of an index ϵ . ϵ ranges between -0.5 and 0.5 . A positive ϵ indicates tensional opening in addition to shearing, while a negative ϵ describes compressive movements in addition to shearing. If $0 \leq \epsilon \leq 0.25$, the DC component dominates. This the case in our study, as we have been able to find a DC solution for each seismic event. However, the variations of ϵ between 0 and 0.25 give the proportion of NDC component in the movement. On the Figure 6, several 2003 events are presented as coloured spheres. The colours correspond to the value of ϵ . As all events were similarly computed, the variations of ϵ between each others are significant. It is striking that events occurred at the direct vicinity of the injection well GPK3 show a high value of ϵ . However, events occurred far from the injection well do not show such

a high value of ϵ . Some of these latter events even have a zero ϵ value. It indicates that events in the vicinity of GPK3 have a non negligible NDC component, and the fractures that support the rupture may undergo tensional opening in addition to shearing. This result may be a consequence of a large overpressure increase near the well due to the massive injections, which can cause the joints to slightly open. On the contrary, as far as we depart from the injection well, the fracture tensional opening component seems to be in less proportion. It would mean that the overpressure is less effective, maybe because it quickly drops with the increasing distance from injection well.

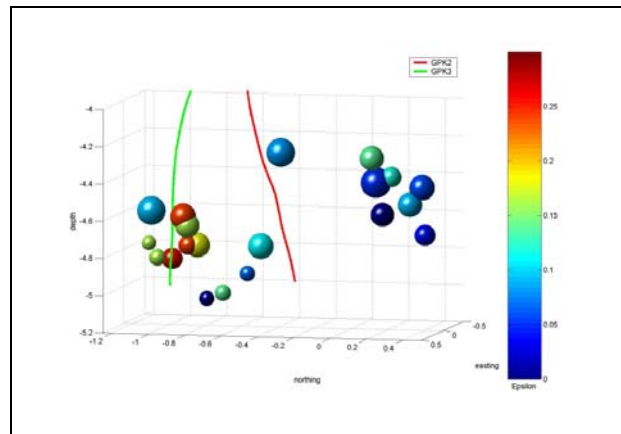


Figure 6: Non double couple component proportion for several 2003 events.

In conclusion, we determine a double couple solution for each microseismic event, which indicates that the dominant process of the faulting movements is shearing. This result seems quite common also at other HDR sites. But, by the analysis of the seismic moment tensor, we show that the rupture process involves a non double couple component. This indicates a proportion of tensional opening at the fracture planes. Moreover this NDC component is significantly higher for events in the vicinity of the injection well, probably because of greater pressure effects.

STRESS TENSOR INVERSION

Two observations suggested us to perform a stress tensor inversion. First our results on focal mechanisms show a higher proportion of strike slip events in the deepest part of the geothermal reservoir. Moreover Klee and Rummel (1993) determine a stress regime profile at Soultz-sous-Forêts using hydrofracturing stress measurements. Their results show a possible cross-over between the vertical stress S_V and the maximum horizontal stress S_H at around 3500-4000 m depth. This would imply a change in

the faulting regime with depth, from a normal-faulting regime to a strike-slip regime. In order to check the reliability of the assumption, we decided to perform the stress tensor inversion.

Method

We used the method of Rivera and Cisternas (1990), which involves the direct inversion of the deviatoric part of the stress tensor and of focal mechanisms from first-motion polarity data. The stress tensor is defined by three Euler angles and a shape factor, which indicates the faulting regime. From an initial trial solution (tensor and focal mechanisms), theoretical polarities are calculated and compared to the observed data at each iteration. Then the solution is modified in order to maximize a likelihood function. The quality of the solution is expressed in terms of likelihood and score (the score describes the fit between observed and theoretical polarities).

Data

We performed two inversions with two different data sets of events from the 2000 stimulation experiment. A first set contains microseisms occurred in the upper part of the reservoir (depth ≤ 4.5 km), the second is composed of events occurred in the bottom part of the reservoir (depth ≥ 5 km). For each set, about 60 microseismic events have been randomly selected among those which exhibit the largest number of available polarity data. Indeed, each selected event shows a number of polarities between 14 and 18. In order to check the reliability of the inversion, we performed several calculations with different sets containing different arrangements of events. Similar results have been obtained from the different calculations.

Results

The results of the inversion are shown in Figure 7 and Figure 8. In both figures, the picture at the top corresponds to the 100 best tensor solutions and the bottom picture gives the best estimate of the stress tensor. Figure 7 shows the inversion for the upper part of the reservoir while results of the inversion for the bottom part are displayed on Figure 8. Stresses are expressed in terms of σ_1 , σ_2 and σ_3 , where $\sigma_1 > \sigma_2 > \sigma_3$.

A first observation is the stability of the orientation of the minimum horizontal stress S_h , which trends in both cases NE-SW to NNE-SSW. This is in agreement with the general orientation of S_h at regional scale in the upper Rhine Graben. On both figures the maximum horizontal stress S_H is oriented NW-SE to NNW-SSE. This results is also consistent with regional estimates of S_H . However, at local scale, other studies show a more N-S orientation of the maximum horizontal stress (e. g. Bérard and

Cornet, 2003). The method of Rivera and Cisternas suppose that the stress tensor is homogenous over the studied region. In the case of Soultz-sous-Forêts, fluid injections may introduce strong local stress heterogeneities that we cannot see with our inversion method: our results may correspond to an “average” stress tensor, which could be more representative of the regional stress field. The relative scatter of the solutions may reflect these stress heterogeneities.

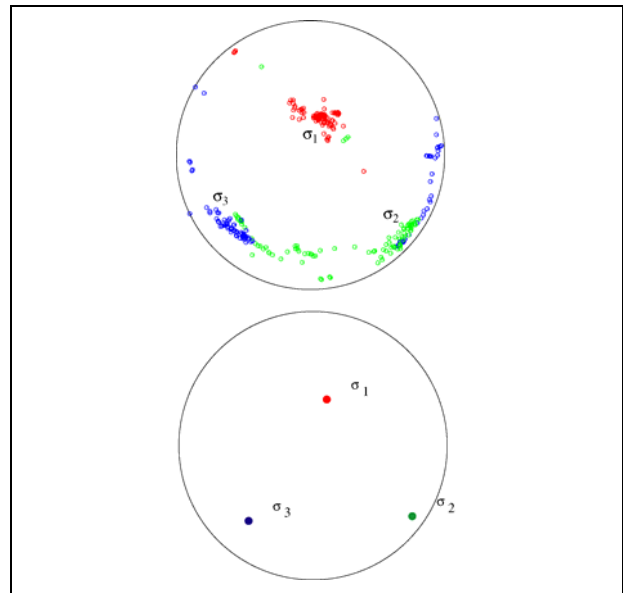


Figure 7: Results of the stress tensor inversion for the top of the reservoir. Top: 100 best tensor solutions; Bottom: best tensor solution.

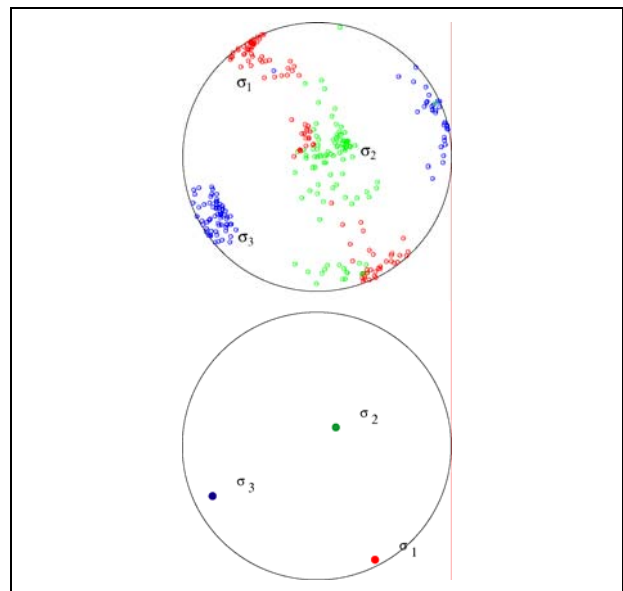


Figure 8: Results of the stress tensor inversion for the bottom of the reservoir. Top: 100 best tensor solutions; Bottom: best tensor solution.

But the most important result concerns the rotation of the maximum stress σ_1 from a subvertical orientation at the top of the reservoir (Fig. 7) to a horizontal direction (Fig. 8). We effectively observe this feature, which was predicted by other measurements. It means that the maximum horizontal stress S_H becomes the maximum stress at the bottom of the reservoir. Thus this implies a change in the failure mode. At the top of the reservoir, the dominant regime is normal-faulting whereas strike-slip is likely to occur in the deepest part of the reservoir. This result is in agreement with the results on focal mechanisms. Nevertheless, both figures 7 and 8 show a relative dispersion of the solutions. In particular on figure 8, some solutions still indicate a subvertical trend for σ_1 and a subhorizontal direction for σ_2 . This suggests that the faulting regime may have not completely changed at the bottom of the reservoir, that is, the stimulated volume is located within the region of stress rotation. And moreover, this confirms the fact that the magnitudes of S_V and S_H are very close, as suggested by Klee and Rummel (1993), facilitating the stress rotation.

3D imaging of the fracture network

We applied the stress tensor on the nodal planes that we determine for the 2000 stimulation in order to define the plane having sheared. Figure 9 shows the result in a 3D view.

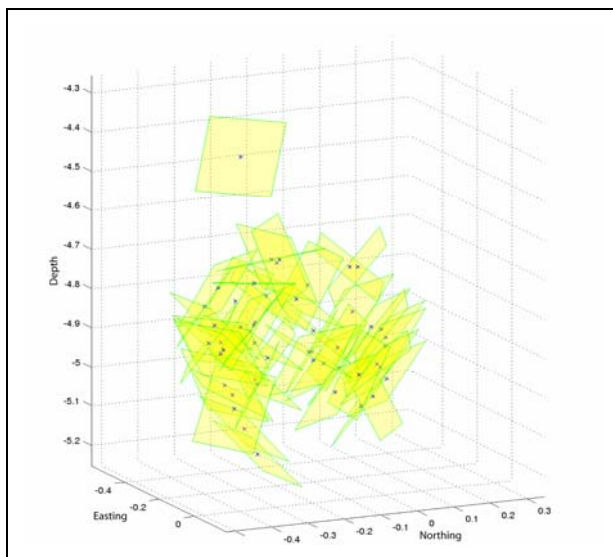


Figure 9: 3D representation of the fracture network.

The majority of fault planes are oriented NNW-SSE to NW-SE with a dip either to the West or to the East. We can also observe that most of the planes dipping to the West are subvertical, while those dipping to the East seems more subhorizontal. In addition, several fault planes exhibits an “en echelon” structure.

Nevertheless, the fracture system appears to be rather heterogeneous.

CONCLUSIONS

Our analysis of the faulting mechanisms suggests that the main involved process is shearing on the fault planes, which has already been highlighted at several other HDR site. Here at Soultz-sous-Forêts the faulting mechanisms are highly related to the extensional regime, which dominates in the Rhine Graben.

Thus from the determination of focal mechanisms, it appears that the failure mode is mainly normal-faulting, with a more or less marked strike-slip component. But in the deepest part of the reservoir, our observations suggest a strike-slip regime. The inversion of the deviatoric part of the stress tensor confirms this feature: the maximum stress rotates from a subvertical trend to a subhorizontal stress with depth, implying a change from a normal-faulting regime at the top of the reservoir to a strike-slip regime at the bottom of the reservoir. In reality the change is quite gradual and it is possible that the geothermal reservoir crosses the zone of stress rotation. Nevertheless, the stress conditions, as well as the pre-existing seismogenic structures seems to be suitable to ensure good stimulation results in terms of permeability and connectivity enhancement.

Furthermore, we have been able to determine a double couple solution for each event both in 2000 and 2003, indicating that shearing is the dominant process. But by calculating the seismic moment tensor of several 2003 events, we show that, at least a part of them have a non-negligible non-double-couple component. It is striking that they tend to occur in the vicinity of the injection well, whereas events located farther do not exhibit such high NDCC values, or do not exhibit NDCC at all. It means that events near the well show a part of tensional opening in addition to their main shearing process. This behaviour is highly correlated with the overpressure induced by the fluid injections. The pressure is highly effective close to the injection well and is able to slightly open the fracture. This leads to implications for the permeability creation in the vicinity of the injection well and for the connection between the well and the fracture network. However, the proportion of tensional opening is close to zero for events occurred far from the injection well: this indicates that the pressure effects on joints opening are limited to the vicinity of the injection well.

Finally, by applying the stress tensor to the nodal planes of events, we have been able to determine a 3D representation of the fracture system based on real data. As a next step, it would be interesting to

obtain a similar figure with fault lengths scaled to the magnitude of microseismic events.

ACKNOWLEDGMENTS

This work was funded by a grant from Ademe (French National Energy Agency) and Conseil Régional d'Alsace. We would like to thank the people of the EEIG "Heat Mining" for kindly providing us the hydrological data and the seismological downhole data. We also would like to thank Hervé Blumentritt, Michel Frogneux and Jacky Sahr for their active participation to the installation of the surface seismological networks.

REFERENCES

Baria, R., Garnish, J., Baumgärtner, J., Gérard, A. and Jung, R. (1995), "Recent developments in the European HDR research programme at Soultz-sous-Forêts (France)", In *Proceedings of the World Geothermal Congress*, Florence, Italy, International Geothermal Association, 1995, 2631-2637.

Baria, R., Baumgärtner, J., Gérard, A., Jung, R. and Garnish, J. (1999), "European HDR research programme at Soultz-sous-Forêts (France) 1987-1996", *Geothermics*, **28**, 655-669.

Baria, R., Michelet, S., Baumgärtner, J., Dyer, B., Gérard, A., Nicholls, J., Hettkamp, T., Teza, D., Soma, N., Asanuma, H., Garnish, J. and Megel, T. (2004), "Microseismic monitoring of the world's largest potential HDR reservoir", In *Proceedings of the 29th Workshop on Geothermal Reservoir Engineering*, Stanford University, USA, 2004.

Baumgärtner, J., Gérard, A., Baria, R., Jung, R., Tran-Viet, T., Gandy, T., Aquilina, L. and Garnish, J. (1998), "Circulating the HDR reservoir at Soultz: maintaining production and injection flow in complete balance -initial results of the 1997 circulation experiment-, In *Proceedings of the 23rd Workshop on Geothermal Reservoir Engineering*, Stanford University, USA, 1998.

Bérard, T. and Cornet, F. H. (2003), "Evidence of thermally induced borehole elongation; a case study at Soultz, France", *International Journal of Rock Mechanics and Mining Sciences*, **40**, 1121-1140.

Cuenot, N., Dorbath, C. and Dorbath, L., "Analysis of the microseismicity induced by fluid injections at the Hot Dry Rock site of Soultz-sous-Forêts (Alsace, France): implications for the characterization of the geothermal reservoir properties", *accepted for publication in Pure and Applied Geophysics*.

Genter, A. and Traineau, H. (1996), "Analysis of macroscopic fractures in granite in the HDR

geothermal well EPS-1, Soultz-sous-Forêts, France", *Journal of Volcanology and Geothermal Research*, **72**, 121-141.

Gérard, A., Baumgärtner, J., Baria, R., Jung, R., Gentier, S. and Genter, A. (2002), "Elements for a conceptual model of the underground heat exchanger at Soultz-sous-Forêts, France", In *4th International Hot Dry Rock Forum, Draft papers (1998)*, Geologisches Jahrbuch, Sonderhefte: Reihe E, Geophysik 1, 281-290.

Kappelmeyer, O., Gérard, A., Schloemer, W., Ferrandes, R., Rummel, F. and Benderitter, Y. (1991), "European HDR project at Soultz-sous-Forêts, General Presentation", *Geothermal Science and Technology*, **2**, 263-289.

Klee, G. and Rummel, F. (1993), "Hydrofrac stress data for the European HDR research project test site Soultz-sous-Forêts", *International Journal of Rock Mechanics and Mining Sciences & Geomechanics Abstracts*, **30**, 973-976.

Reasenber, P. A. and Oppenheimer, D. (1985), "FPFIT, FPLOT and FPPAGE: Fortran computer programs for calculating and displaying earthquake fault-plane solutions", *U. S. Geological Survey Open-File Report 85-739*, 25 pp.

Rivera, L. and Cisternas, A. (1990), "Stress tensor and fault-plane solutions for a population of earthquakes", *Bulletin of the Seismological Society of America*, **80**, 600-614.

Schellschmidt, R. and Schultz, R. (1991), "Hydrogeothermic studies in the Hot Dry Rock project at Soultz-sous-Forêts", *Geothermal Science and Technology*, **3**, 217-238.

Thurber, C. H. (1983), "Earthquake locations and three-dimensional crustal structure in the Coyote Lake area, Central California", *Journal of Geophysical Research*, **88**, 8226-8236.

Weidler, R., Gérard, A., Baria, R., Baumgärtner, J. and Jung, R. (2002), "Hydraulic and micro-seismic results of a massive stimulation test at 5 km depth at the European Hot Dry Rock test site Soultz, France", In *Proceedings of the 27th Workshop on Geothermal Reservoir Engineering*, Stanford University, USA, 2002.

Zhang, H. and Thurber, C. H. (2003), "Double-Difference Tomography; the method and its application to the Hayward Fault, California", *Bulletin of the Seismological Society of America*, **93**, 1875-1889.

DETERMINATION OF SHALLOW GROUNDWATER LEVEL CHANGE USING REPEAT GRAVITY MEASUREMENTS AT THE CENTRAL PART OF UNZEN VOLCANO (NAGASAKI PREFECTURE, JAPAN) FROM 1999 TO 2004

Hakim Saibi¹, Jun Nishijima², Sachio Ehara², Yasuhiro Fujimitsu² and Koichiro Fukuoka²

¹Dept. of Earth Resources Eng., Graduate School of Eng., ²Dept. of Earth Resources Eng., Faculty of Eng.
Kyushu University, 6-10-1 Hakozaki, Higashi-ku, Fukuoka, 812-8581, Japan
saibi-hakim@mine.kyushu-u.ac.jp

ABSTRACT

Unzen volcano is located in Shimabara Peninsula (Nagasaki prefecture), Kyushu Island, southwest of Japan, and one of the most active volcanoes in Japan. The most recent eruption occurred in 1990 to 1995. The possibility of existing or degenerating of a new hydrothermal system beneath Unzen volcano associated with the last eruption, was investigated by using repeat gravity monitoring since August 1999. The variations in observed gravity depend significantly on changes in shallow groundwater level changes. A good correlation of gravity with precipitation is observed with a phase lag about 3 months in some regions in the study area. The water level changes are studied by Unzen Scientific Drilling Project porosity data. The results show that the downflow of permeating rain water is dominant.

Keywords - Gravity, Groundwater, Unzen volcano, Hydrothermal system, Japan.

INTRODUCTION

Unzen volcano, located in Shimabara Peninsula of western Kyushu (Fig. 1), is a complex of many lava domes, thick lava flows and pyroclastics of andesite to dacite in composition (Watanabe et al., 1995). Phreatic eruptions occurred at Jigokuato crater, near the summit of Fugen-Dake on November 17, 1990, the eruption followed 198 years of dormancy. The purpose of this study is to determine changes in the level of ground water and investigate the possibility of a new hydrothermal system beneath the Unzen volcano associated with the 1990-1995 eruption events. In this study, we have carried out a repeat gravity measurement at the central part of Unzen volcano. Gravity network is composed of 15 stations (Fig. 2) performed with a Scintrex CG-3M gravimeter for assessing effects of local disturbances, which are caused essentially

by variations of groundwater level (Ehara, S. et al., 1995). The method of measurement is the two-way measurement method, which was used to evaluate the instrumental drifts and precision. The measurements were repeated at almost the same date, once a year from 1999 to 2004 (August 11th, August 11th, August 10th, August 9th, August 9th, and August 11th), respectively. The survey area lies west of the newly formed lava dome. This area was selected because of the trajectory of the volcanic conduit running from the west to the east below this area deduced from geophysical studies. Observation errors were calculated at 10 to 20 micro-gals. The main reasons of the gravimeter's errors are the environmental factors (wind, vibration, rain, etc.) during station occupations, elevation uncertainties, and operator errors.

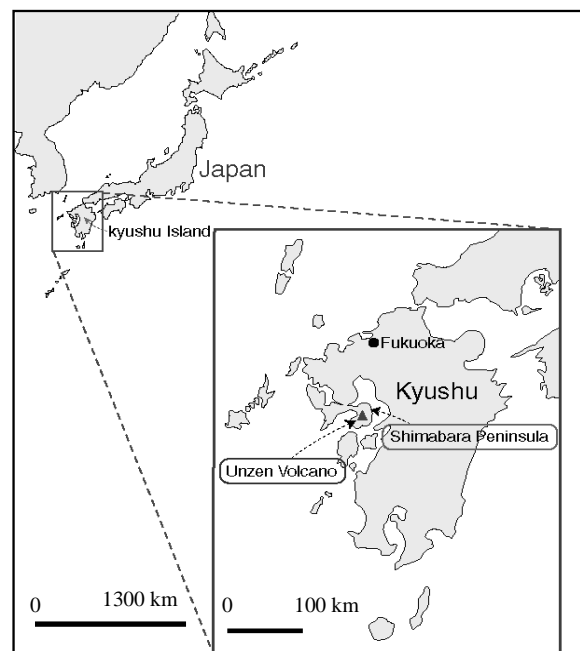


Figure 1: Location of Unzen volcano.

The data were reviewed carefully to make sure that only gravity changes due to the groundwater level changes are considered.

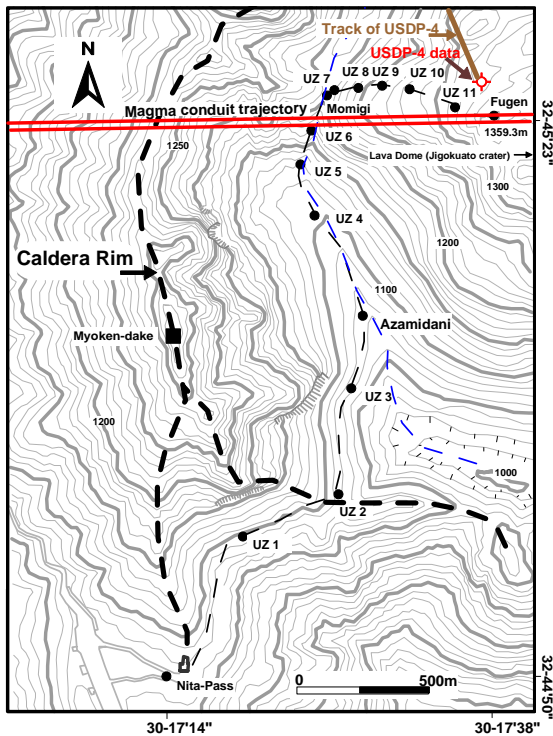


Figure 2: Location of stations (Nita to Fugen) for the repeat gravity measurement. The contour background represents the topography. Height is represented in meters.

The Unzen volcano area is not associated with artificial component like production and reinjection of groundwater. The natural effects are believed to control the gravity changes in Unzen volcano area. Seasonal changes in the shallow groundwater level can have a significant effect on the gravity. Depending on near-surface porosities and the magnitude of the changes in water level, the measured gravity may vary by tens or even hundreds of micro-gal (Allis and Hunt, 1986). Temporal variations of groundwater level causes direct gravitational effects (Torge, W., 1989). For this purpose correlations between hydrological data and gravimeter's readings have been computed in order to determine the relationship between hydrological processes and gravity changes. The hydrological data are presented by rainfall at Unzendake weather station, Japan Meteorological Agency (about 4 km SW of the lava dome). After recording gravity data, automated corrections were simultaneously done by the gravimeter for tide, instrument drift, temperature and data rejection. Then we have applied corrections for elevation (height correction) and drift (drift correction). The resulting gravity value was deduced

from the Nita station gravity value. In this paper, all gravity values represent the gravity difference referred to Nita station gravity in 2000.

METHODS AND RESULTS

Correlation between Gravity Changes and Precipitation

The gravity changes data were acquired from August 1999 to August 2004. The comparison between gravity and precipitation taken in the same period (1999-2004) reveals a certain correlation (Fig. 3). After examination, gravity changes at Unzen monitoring area from 1999 to 2004 shows three different patterns, those are the pattern (A) which includes UZ1, UZ2, UZ3, UZ4, Azamidani, UZ5, UZ6 and Momiji (Fig. 4), the pattern (B) which includes UZ7 and UZ8 (Fig. 5) and the pattern (C) which includes UZ9, UZ10, UZ12 and Fugen (Fig. 6). The three different patterns represent three regions: A, B and C. The gravity data have a good correlation with precipitation (>0.7 in (A) region, >0.77 in (B) region and >0.9 in (C) region), with a phase lag of about 3 months in (A) region, 4 months in (B) region and about 3 to 4 months in (C) region. The precise gravity data are shown in Table 1.

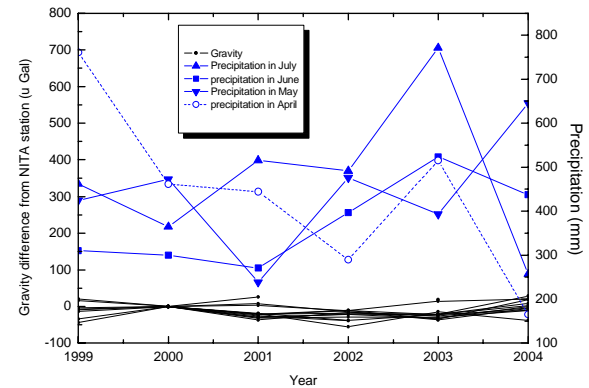


Figure 3: Comparison between gravity and precipitation at Unzendake Weather Station.

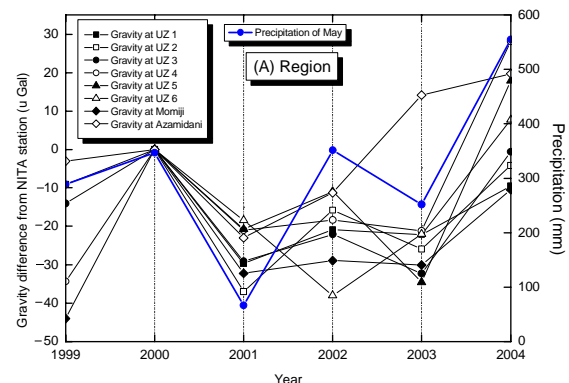


Figure 4: Correlation between gravity and precipitation in (A) region.

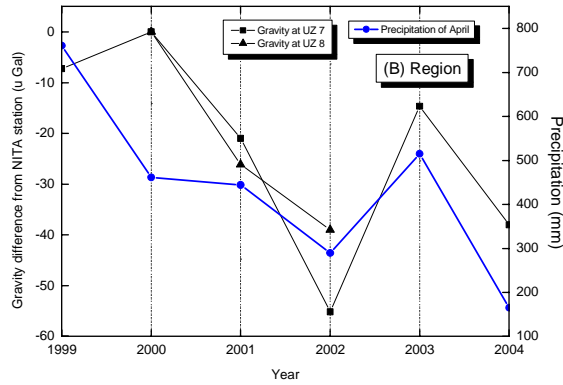


Figure 5: Correlation between gravity and precipitation in (B) region.

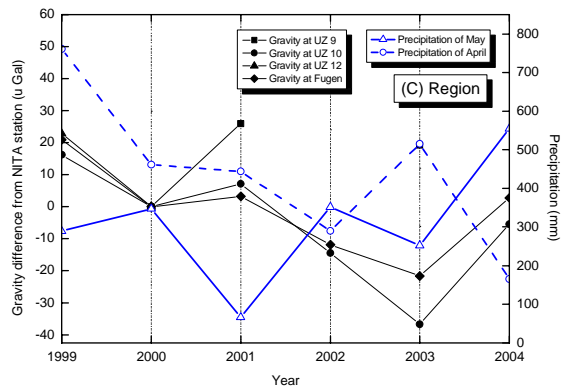


Figure 6: Correlation between gravity and precipitation in (C) region.

Calculation of Groundwater Level Change from Gravity Change

The gravity changes associated with a change in groundwater level is given by Allis and Hunt (1986):

$$\Delta g = 2 \pi G \phi \rho_w \Delta h \quad (1)$$

where Δg is the gravity change ($1\mu\text{Gal}=10^{-8} \text{ m/s}^2$), G is the universal gravity constant ($6.67 \times 10^{-11} \text{ m}^3 \text{ kg}^{-1} \text{ s}^{-2}$), ϕ is the porosity at the depth of water table, ρ_w is the density of groundwater ($\approx 1 \text{ kg.m}^{-3}$), Δh is the change in water level (m).

Using equation (1), the groundwater level change is calculated as follows:

$$\Delta h = \frac{\Delta g}{2 \pi G \phi \rho_w} \quad (2)$$

Porosity is the only unknown factor in the equation (2). To solve this problem, we will use porosity

measured by USDP-4 drilling log (JMC). The Unzen Volcano Scientific Drilling Project (USDP) has been conducted to target the magma conduit shortly after the 1990-1995 eruption. After two drillings of 752 m and 1463 m deep at the flank site, the conduit surveying well (USDP-4) was drilled to the depth of 1995.75 m in the mountainside to clarify the ascending and degassing mechanisms of magma. Many physical logging have been conducted to elucidate the structure and material properties in and around the conduit. One of the physical logging items is neutron porosity (Fig. 10). From the USDP-4 logging results the porosity value at the surrounding monitoring area is about 20 to 30 %. Using equation (2), the results of groundwater level changes are plotted with topographic elevation to deduce even relation with the flow pattern in shallow part of Unzen. The Figure 7 shows the changes of groundwater level with 20 % of porosity plotted with topographic elevation and the Figure 8 shows the changes of groundwater level with 30 % of porosity. The extremities of changing of groundwater level in the two cases ranges from -6.58m in UZ7 to +3.36m in UZ4 (20 % of porosity). We have large changes around the summit which is the recharge area of Unzen and in valley area (UZ3, Azamidani and UZ4) because the groundwater flows from the highlands to the lowlands. In general the results agree with the characteristics of groundwater flow system, the groundwater flow is downwards in the summit of Unzen; this region of the flow system is the recharge area. In Unzen the shallow zone around the magma vent should be highly fractured and hence, have especially large permeability, estimated as 60 Darcy (Hashimoto, 1997), also the summit region is characterized by many dykes related to the old volcanic conduit. The water table forms a subdued replica of the topography and its depth beneath the ground surface is greatest in the upper part of Unzen volcano and least in the lower part of Unzen volcano.

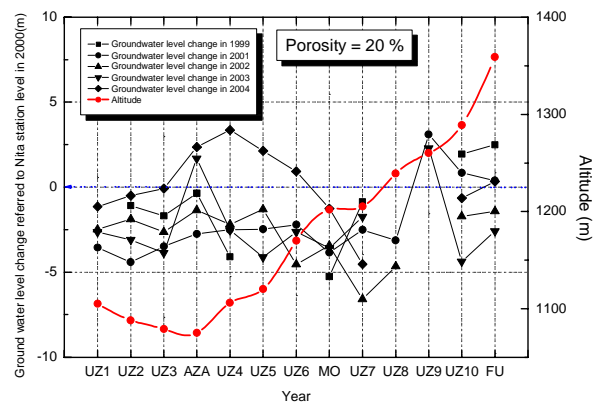


Figure 7: Change of groundwater level with 20 % of porosity and topographic elevation along the path crossing stations UZ1-Fugen in Fig. 2.

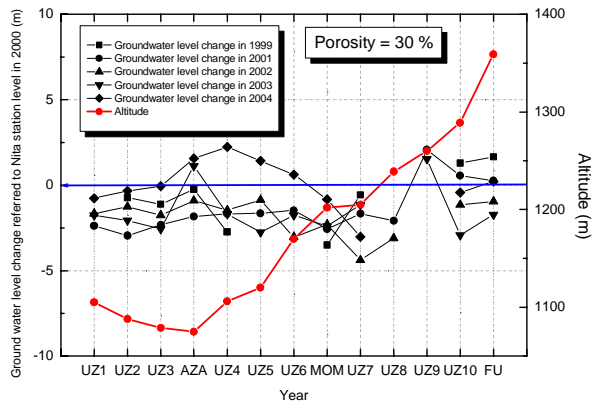


Figure 8: Change of groundwater level with 30 % of porosity and topographic elevation along the path crossing stations UZ1-Fugen in Fig. 2.

The observed gravity changes in Unzen depend significantly on changes in shallow ground water level change (Ehara, S. et al., 1995).

Gravity Change between 1999 and 2000

The gravity change from August 1999 to August 2000 is shown in Fig. 9. During this period, gravity changes from -44 to +23 μGal occurred at most of gravity stations. The largest positive gravity changes are detected in the zone occupied by station UZ12 (near the lava dome). This indicates a certain excess in mass balance. This could be explained by natural recharge by infiltration of water to the shallower aquifer. The gravity decrease coincides with the most fractured zone, around Momiji station.

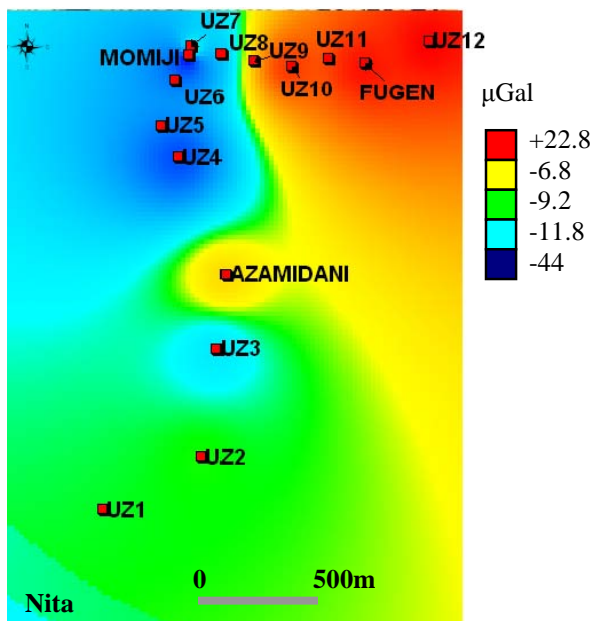


Figure 9: Contour map of the gravity changes at the central part of Unzen volcano from August 1999 to August 2000. Reference station is Nita.

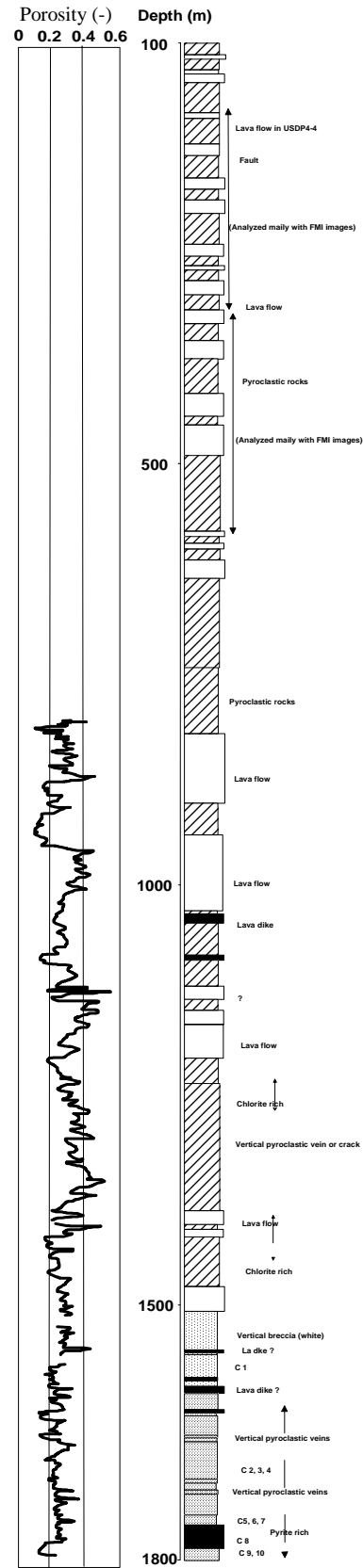


Figure 10: USDP - 4 drilling log with porosity results (JMC, 2004).

Gravity Change between 2000 and 2004

Gravity change for the period 2000 – 2004 is given in Fig. 11. There are differences (increases) of up +28 μGal in UZ4, the other of about +18 μGal in Azamidani, zone of low topography, therefore the groundwater flows to this region, as consequence increasing in gravity. On the other hand, gravity decreases around UZ7 about -38 μGal , near Momiji station. The increasing of gravity in low topography areas is explained by the good negative correlation between gravity changes and altitude (Fig. 12). The summit of Unzen volcano represents the recharge area where water moves downward through the high permeable rocks (pyroclastic flow deposits) and faults from a high topography area into the zone of saturation. In other words, the low topographic region (around Azamidani) replenishes groundwater, where groundwater moves towards this area.

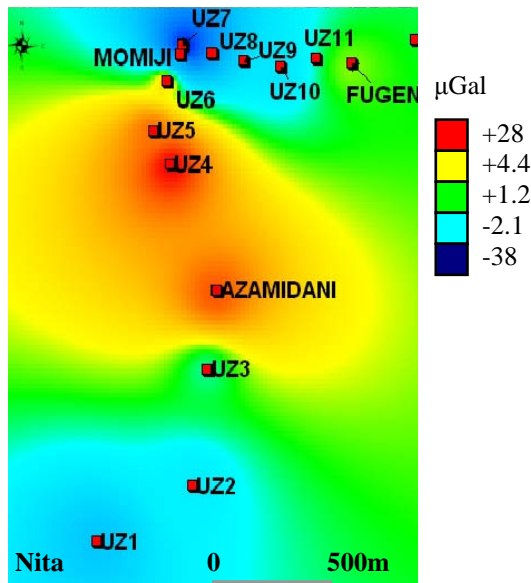


Figure 11: Contour map of the gravity changes at the central part of Unzen volcano from August 2000 to August 2004. Reference station is Nita.

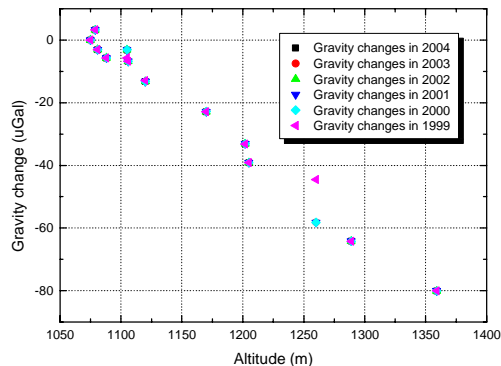


Figure 12: Comparison between gravity change and altitude.

Comparison between Gravity Changes and Ground Temperature Changes

In this section, we would like to check the relation between gravity changes and the 1-meter depth temperature changes. That for the case if up flowing of hot fluid is the cause of increasing in gravity.

In the same period of gravity monitoring (1999-2004), 17 temperatures recording (UT1 until UT17) at 1m depth were measured; each station is measured two times (go and back) referring to UT1 station (Fujimitsu, Y. et al., 2002). The raw temperature data were analyzed for original sensor error and daily change correction.

The measured temperature points are almost located on the same road of gravity monitoring. For convenience, we have chosen 6 points of temperature measurements, which are exactly on the same location of gravity stations, (UT2, UT4, UT5, UT8, UT9 and UT11 respectively Azamidani, UZ4, Momiji, UZ9, UZ11 and Fugen). The correlations are shown in Fig. 13. The results show a good correlation between gravity and temperature, except two different anomalies, one in Momiji and the other one in Azamidani. In Momiji, we observe decreasing of gravity with increasing of ground temperature; it is possible that this anomaly is caused by volcanic gas.

Note that high concentration anomalies of Hg and radon and thoron gases were also observed in this region (Unoki et al., 2003). In Azamidani, we observe increasing of ground temperature but with positive gravity. As cited in previous section, the gravity increases as fact of movement of ground water towards this area. The increasing of ground temperature particularly in the period (1999-2003) in Azamidani may suggest existing of magma pass beneath this area. Around Azamidani, the geochemical observations also revealed the existence of high soil air Hg (70 ng/m^3) and CO_2 (0.6%) (Unoki et al., 2003).

The observed high temperature changes are located essentially around UZ9 (+2°C) and UZ4 (+2°C). UZ9 and Momiji are above the plane image of the trajectory of the volcanic conduit estimated by geophysical methods (STA, 1999). Therefore the ground may be heated by a magma pass beneath those stations. For the case of UZ4, as it's near Azamidani (distant of 100m), the cause may be the same.

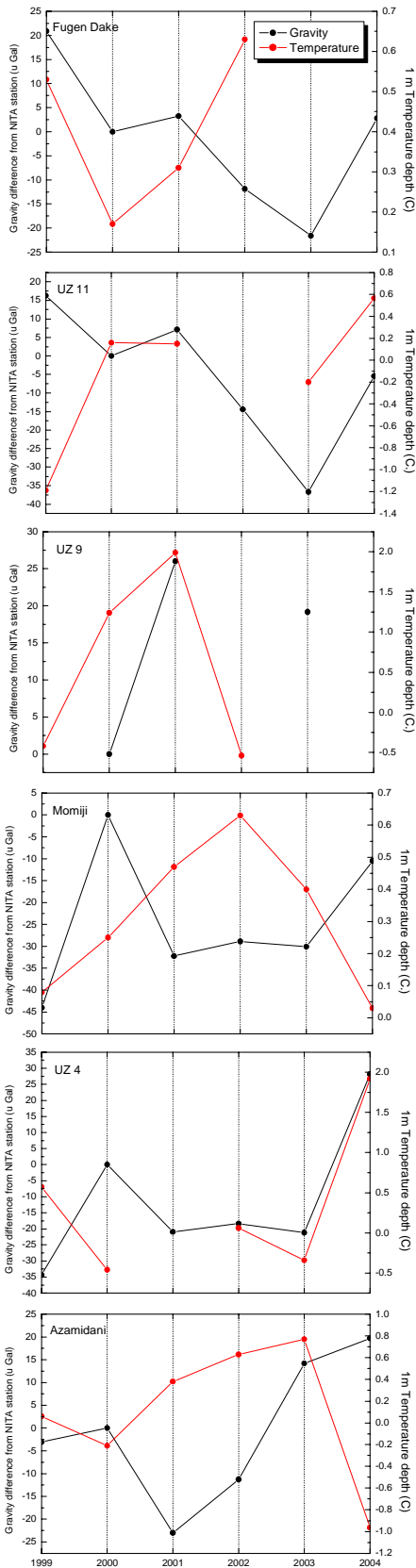


Figure 13: Correlations between gravity change (black) and 1-meter depth temperature change (red).

DISCUSSION AND CONCLUSION

We have carried out gravity measurements in the west area of the newly formed lava dome, Heiseishinzan at Unzen volcano, from 1999 to 2004. The results of the correlation between gravity changes and precipitation in Unzen area thought to be logical. To reach the shallower water table in the summit (region B and C), the infiltration takes time, while the low region (A). The water table forms a subdued replica of the topography and its depth beneath the ground surface. The changes of gravity are attributed to the changes of the shallower groundwater level. A shallower water layer was inferred by many geophysical works (JURG, 1992; Hashimoto, 1997, Kagiya, 1999, Fukuoka, 2003). As example: The Magneto-Telluric surveys conducted by Joint University Research Group have revealed that an aquifer exists widely below Shimabara peninsula at the depth between -1 km and 0.5 km above the sea level (JURG, 1992). The SP survey conducted by Hashimoto (1997) reveals existence of a shallower water-bearing layer in the summit area of Unzen volcano. It is noteworthy that the shallow ground temperature and gravity anomalies around Momiji and Azamidani areas match the geochemical observations. A magma pass beneath those regions is thought to be the cause of degassing. The flow pattern in shallower part of Unzen volcano is dominant down flow (Fig.14). Further studies are required to examine the proposed hydrothermal system beneath Unzen Volcano.

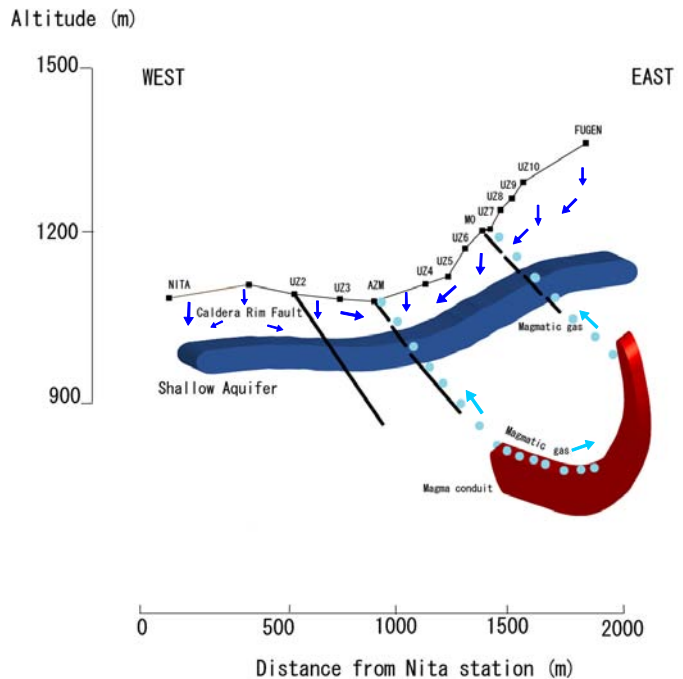


Figure 14: Conceptual hydrothermal model beneath Unzen Volcano deduced from geophysical and geochemical observations.

	1999/08/11		2000/08/11		2001/08/10		2002/08/09		2003/08/09		2004/08/11	
STATION	GRAVITY	ERROR										
AZAMIDANI	3.043	0.011	3.047	0.014	3.031	0.050	3.035	0.013	3.060	0.045	3.066	0.009
NITA	0.000	0.030	0.000	0.008	0.000	0.047	0.000	0.016	0.000	0.048	0.000	0.013
UZ1	-2.676	0.011	-0.066	0.005	-0.089	0.053	0.208	0.008	-0.090	0.012	-0.077	0.003
UZ2	-2.669	0.002	-2.659	0.009	-2.698	0.035	-2.676	0.026	-2.686	0.028	-2.664	0.021
UZ3	6.316	0.004	6.331	0.007	6.310	0.049	6.308	0.022	6.298	0.011	6.330	0.025
UZ4	-3.744	0.015	-3.709	0.024	-3.721	0.059	-3.728	0.008	-3.731	0.010	-3.682	0.032
UZ5	-9.866	0.010	-10.167	0.010	-10.185	0.045	-10.179	0.021	-10.203	0.021	-10.150	0.033
UZ6	-19.820	0.021	-19.801	0.013	-19.818	0.054	-19.841	0.022	-19.825	0.010	-19.795	0.002
MOMIJI	-29.086	0.037	-30.047	0.027	-30.110	0.007	-30.077	0.017	-30.078	0.005	-30.058	0.044
UZ7	-30.092	0.004	-36.094	0.008	-36.120	0.033	-36.141	0.002	-36.101	0.017	-36.124	0.019
UZ8	-36.093	0.001	-46.970	0.019	-47.009	0.056	-47.010	0.008	ND	ND	ND	ND
UZ9	-41.476	0.002	-55.156	0.007	-55.132	0.061	ND	ND	-54.664	0.020	ND	ND
UZ10	-47.006	0.006	-61.152	0.008	-61.166	0.079	-61.168	0.032	-60.868	0.033	-61.159	0.020
UZ11	-61.137	0.011	ND	ND								
FUGEN	-76.992	0.010	-77.012	0.012	-76.999	0.009	-77.025	0.013	-76.697	0.002	-77.010	0.011

Gravity: Gravity value referred to Nita station in μGal .

ND: Not Determined.

Table 1: Gravity Monitoring Data in Unzen Volcano From 1999 to 2004.

ACKNOWLEDGEMENTS

The first author gratefully acknowledges the financial support of the Ministry of Education, Culture, Sports, Science and Technology, Government of Japan in the form of scholarship.

REFERENCES

Allis, R.G. and Hunt, T.M. 1986: Analysis of exploitation induced gravity changes at Wairakei geothermal field. *Geophysics*, 51, 1647-1660.

Ehara, S. et al., 1995: Gravity monitoring of geothermal reservoirs-A case study of the production and reinjection test at the Takigami geothermal field, central Kyushu, Japan. *Proc. World Geothermal Congress 1995*, pp. 1955-1958.

Fujimitsu, Y. et al., 2002: Study on hydrothermal system development, Unzen volcano, Japan. A topic in phase 1 of the Unzen scientific drilling project. *Proceedings 24th NZ Geothermal Workshop 2002*, 283-287.

Fukuoka, K. et al., 2003: resistivity prospecting at Unzen volcano. Oral presentation.

Hashimoto T., 1997: Self-Potential changes and subsurface hydrothermal activity accompanying the 1990-1995 eruption of Unzen volcano. *J. Geomag. Geoelectr.* 49, 977-993.

Japan Metals and Chemicals (JMC) Co., Ltd, 2004: USDP-4 drilling results.

Joint University Research Group (Geophysical Party), 1992: Geophysical observations of the 1990 – 1992 eruption at Unzen volcano (part1), *Bull. Volcanol. Soc. Japan*, 37, 209-215 (in Japanese).

Kagiya, T. et al, 1999: Magma ascent beneath Unzen Volcano, SW Japan, deduced from the electrical resistivity structure. *Journal of Volcanology and Geothermal Research*, 89, 35-42.

STA, 1999: Unzen volcano – International Cooperative Research with Scientific Drilling for Magmatic Activity. *Brochure of Science and Technology Agency*, Japan.

Torge Wolfgang, 1989: Gravimetry. Edition: Walter de Gruyter. Berlin – New York.

Unoki, R. et al., 2003: Soil air gas and gamma-ray surveys at Unzen volcano, Japan. *Proceedings 25th NZ Geothermal Workshop 2003*. pp. 137-141.

Watanabe, K. et al., 1995: Geological map of Unzen volcano 1: 25.000, *Geological Survey of Japan*.

NATURAL STATE MODELING, STRUCTURE, PRELIMINARY TEMPERATURE AND CHEMICAL SYNTHESIS OF THE DIXIE VALLEY, NEVADA GEOTHERMAL FIELD

J.R. McKenna, D.D Blackwell, M.C. Richards

Southern Methodist University
Department of Geological Sciences
Dallas, Texas, 75275-0395, USA
e-mail: jmckenna@smu.edu; blackwel@smu.edu; mrichard@smu.edu

D.V. Swenson
Thunderhead Engineering Consultants, Inc.
1006 Poyntz Ave
Manhattan Kansas, 66502-5459, USA
e-mail: swenson@thunderheadeng.com

ABSTRACT

A number of geothermal systems in the Basin and Range Province, like the ones in Dixie Valley, Nevada have subsurface temperatures in excess of 200°C, and even 250°C by 2–3 km depth. These systems are typically associated with Quaternary normal faulting. Many of these systems are non-magmatic in origin, based on the helium isotope ratios in the hot water (Kennedy et al., 2000). A recent seismic, gravity, magnetic, and thermal synthesis of the Dixie Valley, Nevada geothermal system has shown that the fault system is much more complex and 3-dimensional than previously thought.

We have utilized this integrated geophysical image to provide structural control on a natural state regional fluid flow model for the valley-range systems to investigate several outstanding issues related to fluid recharge, and the thermal evolution of the high temperature reservoir.

INTRODUCTION

Dixie Valley, Nevada has been the subject of extensive geoscience studies ever since the large earthquake events of 1954. The presence of large-scale geothermal energy resources in the area has led to an intensification of these efforts. As a result, the structure of the contact (a large displacement normal fault zone, >5 km vertically over about 8 My) between the Stillwater Range and Dixie Valley is probably the best explored normal fault system in the world. The area of the valley/range contact has been penetrated by over 20 deep drill holes, several

thermal gradient surveys, numerous seismic reflection profiles, multiple gravity surveys, electrical sounding surveys, three levels of aeromagnetic surveys, and detailed geologic mapping (Blackwell et al., 2005). The situation differs from other extensively drilled and explored areas, such as Railroad Valley in eastern Nevada in that the target for geothermal activity is the fault zone itself.

Structural models of Basin and Range normal faults either predict high or low angle dipping structures, with the two end member cases both possessing strong support within the scientific community. The techniques utilized in geothermal exploration, particularly drilling, are critically dependent on the expected dip of structures related to the reservoir. So the uncertainty in the structure, based on the extremes of the generally accepted models, is a major factor in the drilling uncertainty, and ultimately the risk, involved in geothermal exploration and development. Structural models of the Dixie Valley system based on various interpretations in a wide variety of geological and geophysical data range from low angle (20° by 3 km) to high angle (>75° at 3 km) (see Blackwell et al., 2005).

Hence the Dixie Valley Producing Field (DVPP) and Dixie Valley Power Partners area (DVPP) examples are critical to our understanding of normal fault systems because in these two areas the geometry of the fault zone is now well understood from the numerous deep wells that have been drilled and consistent geophysical interpretations. The results of the synthesis of studies from these two areas are that:

1. A 20+ km strike length of the contact zone between the Stillwater Range and Dixie

Valley is presently the locus for fluid circulating at temperatures over 200°C (up to 285°C) at 2 - 3 km depth.

2. Areas along the zone have been intermittently to continuously active at time scales of ~100 ka.
3. The range/valley contact is a broad, complex zone with multiple fault strands both in the range and in the valley present in addition to the exposed range/valley bounding fault.
4. The dip of the individual fault strands is 60-75° or greater to a depth of at least 3 km.
5. As a consequence of point #4 *none* of the production wells in the field (located 2-3 km into the valley) produce from the exposed range/valley contact segment of the fault zone (the *Dixie Valley normal fault* as commonly defined), but from blind valley segments.
6. The surface expression of the fault zone (range-valley contact) does not reflect the subsurface structure in any simple way, so surface segmentation has limited relevance to locating the specific position of the geothermal resource or to earthquake hazard evaluation.
7. In general, the exposed fault along the topographic range front boundary *does not* accommodate the majority of the vertical displacement in areas of large vertical displacement.
8. Extensional strain in the Dixie Valley area is accommodated by the range bounding surface fault trace, and by the multitude of other range and valley structures present. Synclines in the valley fill delineate areas where buried extensional accommodation is focused.
9. Vertical as well as low angle structures can explain the complex surface shapes of the mapped scarps, but low angle faults cannot explain the thermal structure.
10. The Bend event (at 2 - 2.5 ka) probably affected the area of the power plant and the area to the north for several km, but the scarps were confined to the range and have either been erased by erosion or are not

recognized because they do not cut Quaternary materials. The thermal regime along the fault may have affected the style of faulting there.

Numerous lines of evidence support the interpretation that faulting within the Stillwater/Dixie Valley system is a complex zone of deformation, rather than a simple planar surface (see Figure 1). First, there are numerous Quaternary/Holocene faults in the valley whose scarps are quickly erased by erosion. The evidence for these faults comes from seismic reflection profiles, the high-resolution aeromagnetic surveys, and detailed air photo interpretation. These numerous basement faults propagate upwards through the basin fill sediments to the surface or stop at very shallow levels just below the surface. Small vertical displacements and subsequent rapid resurfacing of the valley floor by alluvial, playa, and eolian sedimentation removes or subdues the surface evidence of these faults. The best methods for mapping the distribution of these faults are detailed mapping of subtle surface features (small scarps, lineaments, spring alignments) on high resolution air photos (with field checking) and high-resolution aeromagnetic surveys.

Also present, but rarely recognized are numerous large displacement Quaternary/Holocene? normal faults within the Stillwater Range block. These were mapped in the vicinity of the DVPP and DVPF areas and in the area of Well 66-21, but their age is difficult to establish because they do not cut Quaternary deposits.

The presently producing geothermal reservoir lies along a piedmont/ramp fault segment. A steeply dipping, multiple fault system is required by the gravity, temperature distribution, drilling, surface mapping, and aeromagnetic survey observations, so at least the segments near the DVPP and DVPF are steeply dipping. This geometry means that only a few of the fault strands have been penetrated by wells. The reservoir is made up of an unknown number of these strands and their near vertical geometry means that some of them may not yet have been tapped unless they communicate with each other through fractures in the blocks bounding them. An additional complexity is that the present WNW-ESE direction of extension (since about 8 Ma) is superimposed on an earlier E-W episode of extension. A series of narrow grabens formed during the earlier episode. Some of the faults of that episode have been reactivated during the current extension resulting in additional structural complexity.

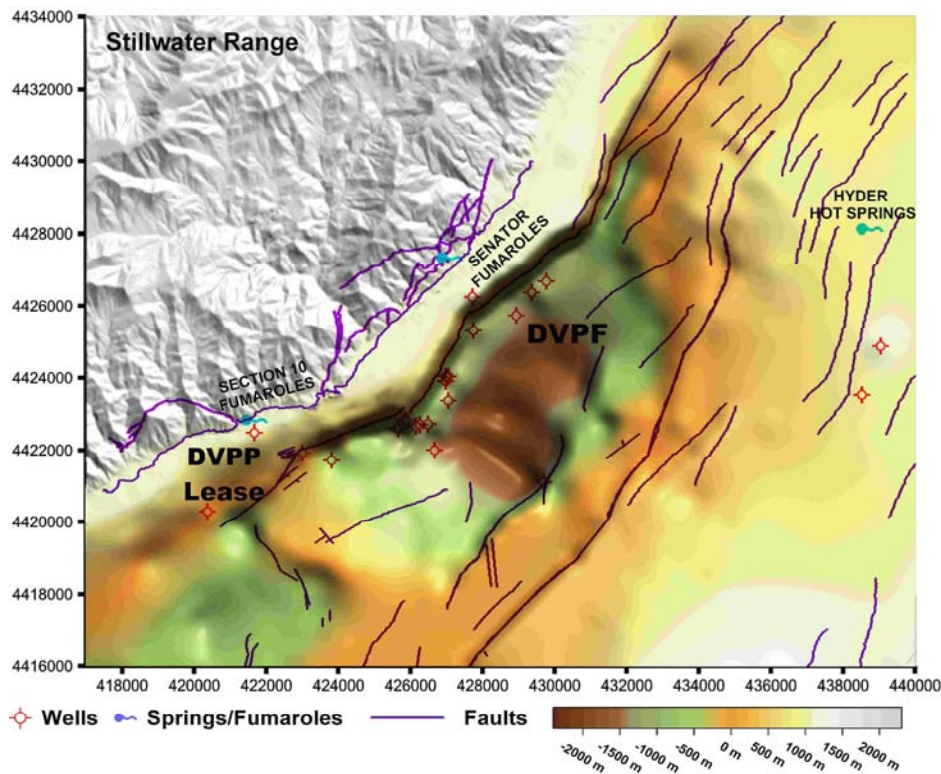


Figure 1. Dixie Valley mapped faults, well locations, and basin depth.

An area at least 5 km long and 2 km wide has temperatures of 225 to 245°C at depths near 2500 m and over 265°C below 3000 m. Fluid flow in this area has occurred over a sufficient time that the local thermal regime is nearly steady state in the upper 1-3 km depth range. However, there are major variations in the local hydrologic regime. Some paths are not connected or barely connected on the time scale of pressure and temperature measurements in the field (almost 20 years). The variable geochemistry of the fluids sampled at different places in the system must result from effects operating over a much shorter time frame than the thermal evolution (which is still short geologically).

The position of the highest reservoir temperatures is almost directly below the range front at a depth of about 3 km. Thus, there is little doubt the fractures feeding the geothermal field are steeper than 75° within the upper 4 km of the crust.

There is every reason to assume that the steep dip is typical of the western Basin and Range (and other rift areas where basement lithology dominates). Thus the fault structure described in here represents a practical model for exploration in the western Basin and Range. Hence, exploratory drilling in these systems will be more effective using inclined drilling, which will increase the opportunities to intersect steeply dipping structures. Using inclined wells rather than

vertical wells makes drilling more cost effective, which is an important impetus for utilizing Basin and Range geothermal systems (McKenna and Blackwell, 2004a).

TRUE-SCALE NATURAL STATE MODELS

The commonly-accepted conceptual model for fluid flow in a Basin and Range geothermal system is that upflow along a single range-bounding normal fault dipping at about 45-55° is responsible for most production, but this model ignores potential fluid flow associated with small displacement synthetic faults present in the valley and stratigraphically-bound aquifers in the valley fill, such as the Tertiary basalts present in Dixie Valley (see Benoit, 1999). So although the single fault model is conceptually attractive, it is not particularly useful as a working model. It is clear that the exposed range-bounding fault is only one of many fault components in the geothermal system from four aspects: (1) the pattern of breaks associated with historic earthquakes, (2) the extensive pattern of young faults mapped in Dixie Valley, (3) the surface mapping in the Stillwater Range, and (4) the low-level high-resolution aeromagnetic survey results. Thus it is more accurate to describe the deformation as *distributed across multiple zones* rather than a single plane.

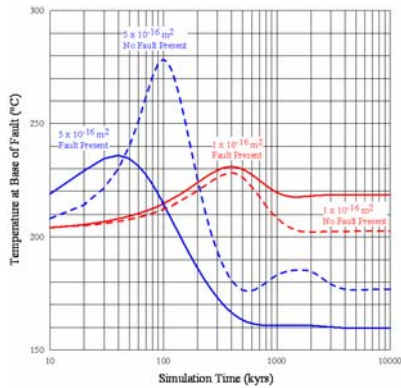


Figure 2. Temperature-time history of a cell at the base of the fault (3.85 km depth) for several bulk rock permeabilities utilizing a naturally convective media as the initial condition.

The fluid compositions in the Dixie Valley fluids are complicated and highly variable. It remains unclear how the fluid components interact and how the fluids have evolved with time and space. The chemistry (He and major elements in the fluids) suggests that several of the thermal manifestations in Dixie Valley have a common or similar source, even if they are not apparently directly connected. The natural state modeling requires a permeable basement ($> 1 \times 10^{-16} \text{ m}^2$) for deep flow to occur. The modeling also shows that the upflow can be confined to a limited portion of the system particularly if there is a short circuit present in the flow paths (i.e. a permeable fault), or it can be more wide spread if no high-permeability zones exist. Under some conditions, such as high-permeability in the basement rocks, or extremely heterogeneous permeability distributions, the flow could be more pervasive. The flow sometimes exists for some permeability distributions without a dominant (permeable) fault. In general, the upflow is composed of water that has sampled a large volume of the basement and thus possesses a complicated mixture of effects. The specific geothermal system in existence is tens to a few hundreds of thousands of years old based on the lack of evidence for temperature over-turns in the system, and the age dating of the sinters.

One implication of the structural model described is that much of the natural fluid loss in the geothermal system is apparently via leakage from the piedmont faults directly into the valley fill with minimal thermal indication. This extensive input of fluids of variable chemistry complicates the chemistry of the water in the valley fill and probably is at least partly responsible for the conflicting results observed in the natural spring geochemistry measurements in the valley.

Figure 2 shows the temperature-time histories for a cell located at the downdip edge of the fault,

approximately 3.85 km below and 2.15 km to the right of the fault/valley contact in the classes of models discussed by McKenna and Blackwell (2004b). This particular cell essentially records the maximum fault modeled temperature. For models utilizing bulk rock permeabilities of $1 \times 10^{-17} \text{ m}^2$ or less, the thermal regime is essentially conductive, and the temperature quickly reaches steady-state with only a few degrees of heating. For the higher bulk rock permeabilities, however, the temperature at the base of the fault varies strongly as a function of time. The maximum temperature for the cases where the starting regime is conductive is 255-275 °C. The temperature maximum does not occur at steady-state, but rather, within the first 100 ka for the $5 \times 10^{-16} \text{ m}^2$ bulk rock permeability model, and ~400 ka for the $1 \times 10^{-16} \text{ m}^2$ bulk rock permeability model. The transient behavior described above may help explain the lower than measured predicted temperatures (both bulk rock permeability models predict temperatures that are lower than the ~ 280 °C temperatures measured via precision temperature logs in Dixie Valley), and suggests that the relatively high reservoir temperatures observed in some extensional geothermal systems ($> 280 \text{ °C}$) must be a function of oscillating high/low fault permeability maintained by seismicity along the range-bounding fault.

Therefore the high temperatures observed in the Dixie Valley system are matched only for a geologically brief period of time on the order of 50,000 to 300,000 years, which is consistent with the sinter dating. However, the Dixie Valley fault zone system has been in existence (at least intermittently) for several million years. Exposed fault gouges have quartz with fluid inclusion temperatures of about 300°C (Parry et al., 1991) similar to the temperatures seen today at depths below 3 km. The water that is being produced is dated at about 10,000 as (Nimz et al., 1999), but it is water that has a traversed a wide variety of flow paths so that age is certainly a mixing age of some sort.

At Dixie Valley, the present producing area consists of only two small areas even though the thermal anomaly is over 20 km long. These two areas are hydrologically separated from each other in the upper 3 km, and from the rest of the system in the DVPP area, even though all three appear to be nearly thermally identical at depth. Thus the model that seems to fit the results best is not a single fault plane or set of fault planes, rather a complex interfingering system of fractures that host a variable flow system confined to the most open parts of the system at this moment. This type of model is similar to the model of vein structure associated with ore deposits. In fact gold mineralization has been found associated with the geothermal systems.

The models examined by McKenna and Blackwell (2004b) and Wisian and Blackwell (2004) were generic Basin and Range type of models. To examine the actual Dixie Valley setting a true scale model specifically tailored to that area was constructed. From west to east it includes the Carson Sink, the Stillwater Range, Dixie Valley, the Clan Alpine Range, and the Edwards Creek Valley. The model incorporates the actual topography present along the model transect between the Dixie Comstock Mine to the south and the producing geothermal field to the north. Structurally, the model is close to the synthesis discussed in the introduction. Each valley hosts a relatively permeable basin about 5 km deep. Near the Stillwater Range-Dixie Valley contact, a steeply dipping 5 km wide zone of highly permeable rocks is present that simulates the multistrand, multi-faulting geometry constrained by the geophysical synthesis.

Figure 3 shows the true scale-model of the Dixie Valley system. The modeling parameters utilized appear in Table 1, The model geometry was developed utilizing PetraSim by Thunderhead Engineering Consultants and solved numerically with TOUGH2 (Pruess et al., 1999). and are similar to other models of the Dixie Valley system (see McKenna and Blackwell, 2004b) with the exception of the grid geometry discussed above, and the host rock permeability which is an order of magnitude smaller than in similar models. This is to prevent unrealistically high recharge beneath the areally significant ranges (17-21 km wide, as opposed to 5 km in previously published models (e.g., McKenna and Blackwell 2004b) from depressing the regional thermal gradient, since inclusion of the asymmetric topography strongly impacts the resulting flow system. The temperature predicted by the model after 1 Ma is shown in Figure 3. The predicted temperature at the base of the steeply dipping range-bounding fault is somewhat lower than observed (200 °C as opposed to the ~280 °C measured *in situ*) because significant downflow is present in the model.

TRACER ANALYSIS

In Dixie Valley, the combination of groundwater isotope and minor-element chemistry with the mapped positions of Pleistocene Lake Dixie shorelines illustrates the importance of pluvial lakes in the recharge of Basin and Range geothermal systems. In addition to Dixie Valley production fluids, all the groundwater in the valley except for the shallowest unconfined aquifer near the Humboldt Salt Marsh, are Pleistocene waters that have remained isolated from meteoric recharge. On a regional scale, the distribution of known geothermal

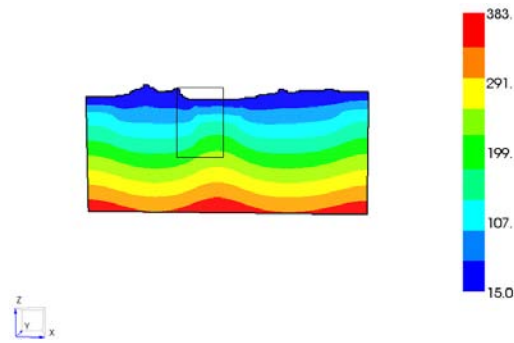


Figure 3. Modeled temperature in the Dixie Valley system at 1 Ma (V.E. is 3x). See Table 1 for model parameters and boundary conditions. The model domain consists of 23,435 elements, and is 65 km x 9 km (1km into the page). The rectangular area refers to the model domain in Figures 4-5.

Material	Wet Thermal Conductivity (Wm ⁻¹ K ⁻¹)	Horizontal Permeability (m ²)	Vertical Permeability (m ²)
Basement	2.50	1.0E-17	1.0E-17
Fault	2.50	1.0E-14	1.0E-14
Fault Seal	2.50	1.0E-18	1.0E-18
Range Seal	2.50	1.0E-18	1.0E-18
Fractured Basement	2.50	1.0E-16	1.0E-15
Valley Fill	1.25	1.0E-15	1.0E-16
Volcanics	1.25	1.0E-15	1.0E-16

Table 1. TOUGH2 modeling parameters. A constant density, heat capacity, and porosity of 2650 kgm⁻³, 1000 Jkg⁻¹K⁻¹, and 0.1, respectively, were utilized in the modeling. A basal heat flow of 90 mWm⁻², surface temperature of 20 °C, and surface pressure of 1.01 x 10⁵ Pa were specified as boundary conditions. The low-permeability domains flanking the fault zone and at the range-tops are utilized to represent probable fault-sealing, and prevent unrealistically high recharge rates, respectively.

systems corresponds closely to the distribution of late Pleistocene pluvial lakes as defined by their preserved high stand shorelines. This suggests that contemporary precipitation is not sufficient and/or infiltration is so slow that it is ineffective at recharging valley aquifers and deeper geothermal systems. Therefore, a major proposed consideration for the exploration of unstudied valleys is whether or not a Pleistocene pluvial lake was present near the exploration target.

Isotopic ages of 12 to 20 ka for Dixie Valley geothermal waters (Nimz et al., 1999; Janik et al., 2002) have been interpreted to provide strong support for recharge of the system during latest Pleistocene time and minimal infiltration of younger waters during Holocene time. The topographic position of

the high stand shows that the lake water would have had access directly into the range-bounding fault systems for much of their length, and through the sands and gravels that comprise the major portion of valley-fill sediments along the margins.

Isotopic and geochemical data show that shallow artesian aquifers have been augmented 15-25% by input from geothermal waters from depth. These aquifers (at depths of less than a hundred meters) feed the spring systems along intrabasin faults, which serve as conduits for the waters to rise to the surface. This water is also late Pleistocene in age (Nimz et al., 1999), and has remained very dilute during its residence time in the valley fill sediments. Although precipitation from the surrounding mountains is sufficient to recharge the shallow aquifers in the valley, very little of that water infiltrates these aquifers. Instead, it is removed by evapotranspiration in the mountains and valley floor, and moves by runoff into the Humboldt Salt Marsh area, where it leaves the system by evapotranspiration (Harrill and Hines, 1995).

In order to estimate the possible origin of produced fluids in the Dixie Valley geothermal system we modeled the length of time required for a non-reactive tracer to reach the production area given 2 end-member starting positions. The model results shown in Figure 3 are the initial conditions for the subsequent tracer models shown in Figures 4 and 5.

The results of simulations in which a 1 km x 300 m zone of tracer mass fraction = 1 are situated either at the top of the Stillwater Range, or base of the valley fill are shown in Figures 4 and 5, respectively. Each model shown is a 10 km x 7 km subset of the domain shown in Figure 3 and is comprised of about 6000 elements. Each simulation tracks the mass fraction of the tracer movement as it passes through the model domain. It is clear that the source of the fluids near the production area (i.e., within 1 km of the range/valley contact) is not meteoric recharge from the ranges, since it takes at least 2-5 Ma for these fluids to reach the production/valley area (see Figure 4). The tracer simulations also show that it takes fluids at least 10 ka to enter the valley fill from the underlying volcanics, and anywhere from 10-50 ka for 1 ppm of tracer to become entrained in the fault zone upflow (Figure 5). Hence the only possible source of production/valley fluids is the area below the valley fill. Lateral flow from the shallower levels of the valley fill may contribute, but because these fluids take significantly less time to appear in the production fluids than their isotopic age (i.e., 10 ka).

CONCLUSIONS

We discuss the geophysical, chemical, and seismic evidence for structural complexity in the Dixie

Valley system and present the first true-scale natural state flow model of the system. The thermal data are strong constraints in the characteristics of the system. The flow characteristics through the system have been examined and it is clear that there are inconsistencies between the chemical and thermal results that need to be further investigated.

ACKNOWLEDGEMENTS

This work was supported by the U.S. Department of Energy contract ID DE-FG07-02ID14414.

REFERENCES

- Benoit, Dick, 1999, Conceptual models of the Dixie Valley, Nevada Geothermal Field; *GRC Transactions*, 23, 505-511.
- Blackwell, D. D., Smith, M. Kennedy, R., F. Goff, et al., 2005, Synthesis of Geoscience Data for Dixie Valley. DOE Report.
- Harrill, J.R. and Hines, L.B., 1995, Estimated natural ground-water recharge, discharge, and budget for the Dixie Valley area, west-central Nevada, *U.S. Geological Survey, Water-Resources Investigations Report* 95-4052, 12p, plus 1 plate.
- Janik, Cathy, Nimz, G., and Goff, F., 2002, Origin, Age, and Geochemical Evolution of Dixie Valley Geothermal Fluid, Presentation to Dixie Valley Geothermal Workshop, June 12-13, 2002, Reno.
- Kennedy, B.M., Fischer, T.P., Shuster, D.L., 2000, Heat and helium in geothermal systems, *Proceedings 25th Workshop on Geothermal Reservoir Engineering*, Stanford Geothermal Program Report SGP-TR-165, 167-173.
- McKenna, J.R. and D.D. Blackwell, 2004a, Directed geothermal drilling using temperature: examples from numerical simulations, *GRC Transactions*, 28, 23-26.
- McKenna, J.R., and D.D. Blackwell, 2004b, Numerical modeling of transient Basin and Range extensional geothermal systems, *Geothermics*, 33, 457-476.
- Nimz, G., Janik, C., Goff, F., Dunlap, C. Huebner, M., Counce, D., and Johnson, S., 1999, Regional hydrology of the Dixie Valley geothermal field, Nevada: Preliminary interpretations of chemical and isotopic data, *Lawrence Livermore National Laboratory Publication*, UCRL-JC-135417, 9p.
- Parry, W.T., Hedderly-Smith, D., Bruhn, R.L., 1991, Fluid inclusions and hydrothermal alteration on the Dixie Valley fault, Nevada, *Journal of Geophysical Research*, 96, 19733-19748.
- Pruess, K., Oldenburg, C., Moridis, G., 1999, TOUGH2 User's Guide, Version 2.0. Report LBNL-43134, Lawrence Berkeley National Laboratory, Berkeley, CA, 197 pp.
- Wisian, K., and D.D. Blackwell, 2004, Numerical Modeling of Basin and Range geothermal systems, *Geothermics*, 33, 173-741.

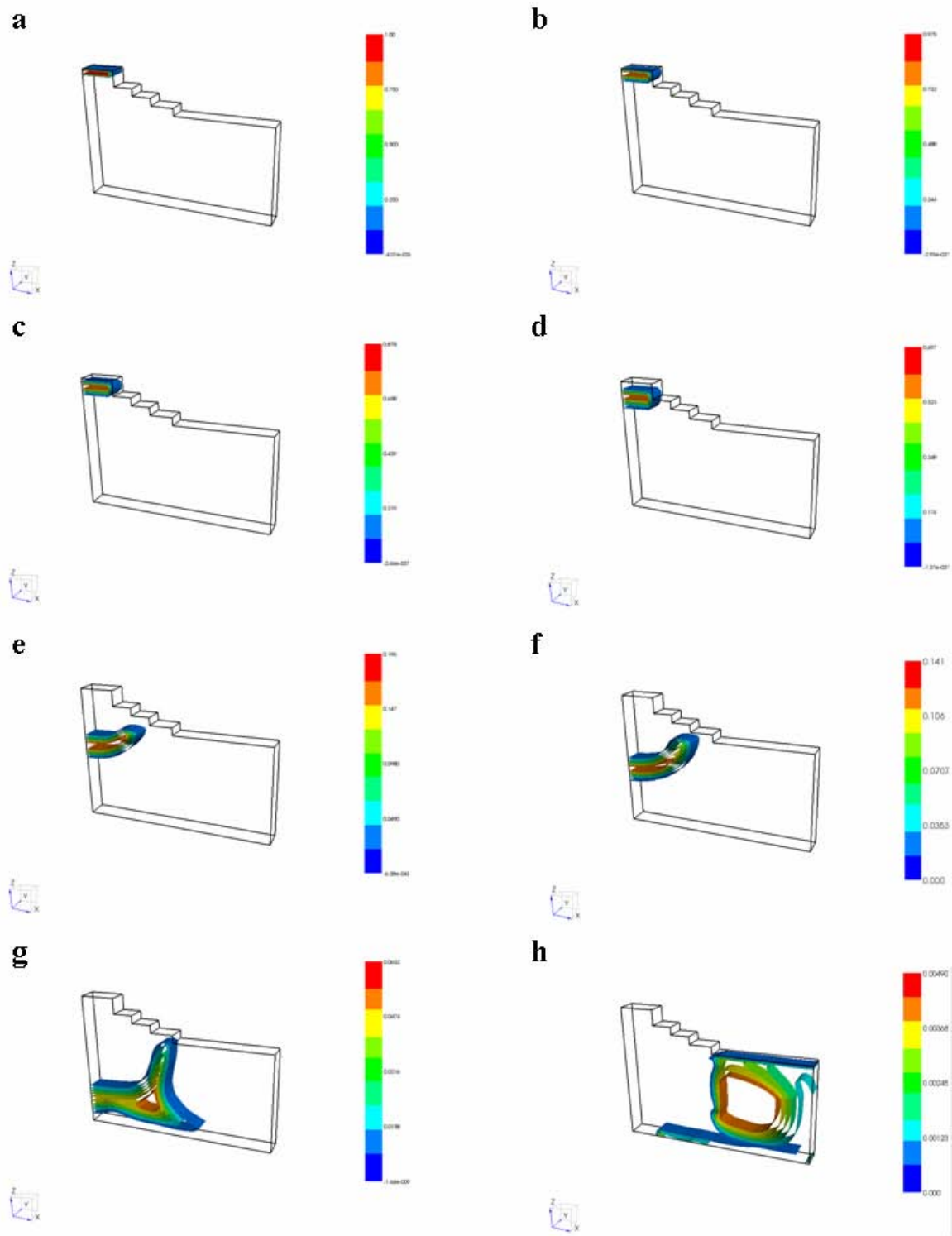


Figure 4. Results of tracer analysis with a 300 m thick, 1 km wide zone of tracer mass fraction = 1 situated the at the top of the Stillwater Range. Each model is a 10 km x 7 km subset of the domain shown in Figure 3 and represents about 6000 elements. The simulation times shown are (a) 0 ka, (b) 10 ka, (c) 50 ka, (d) 100 ka, (e) 500 ka, (f) 1000 ka, (g) 2700 ka, and (g) 10000 ka.

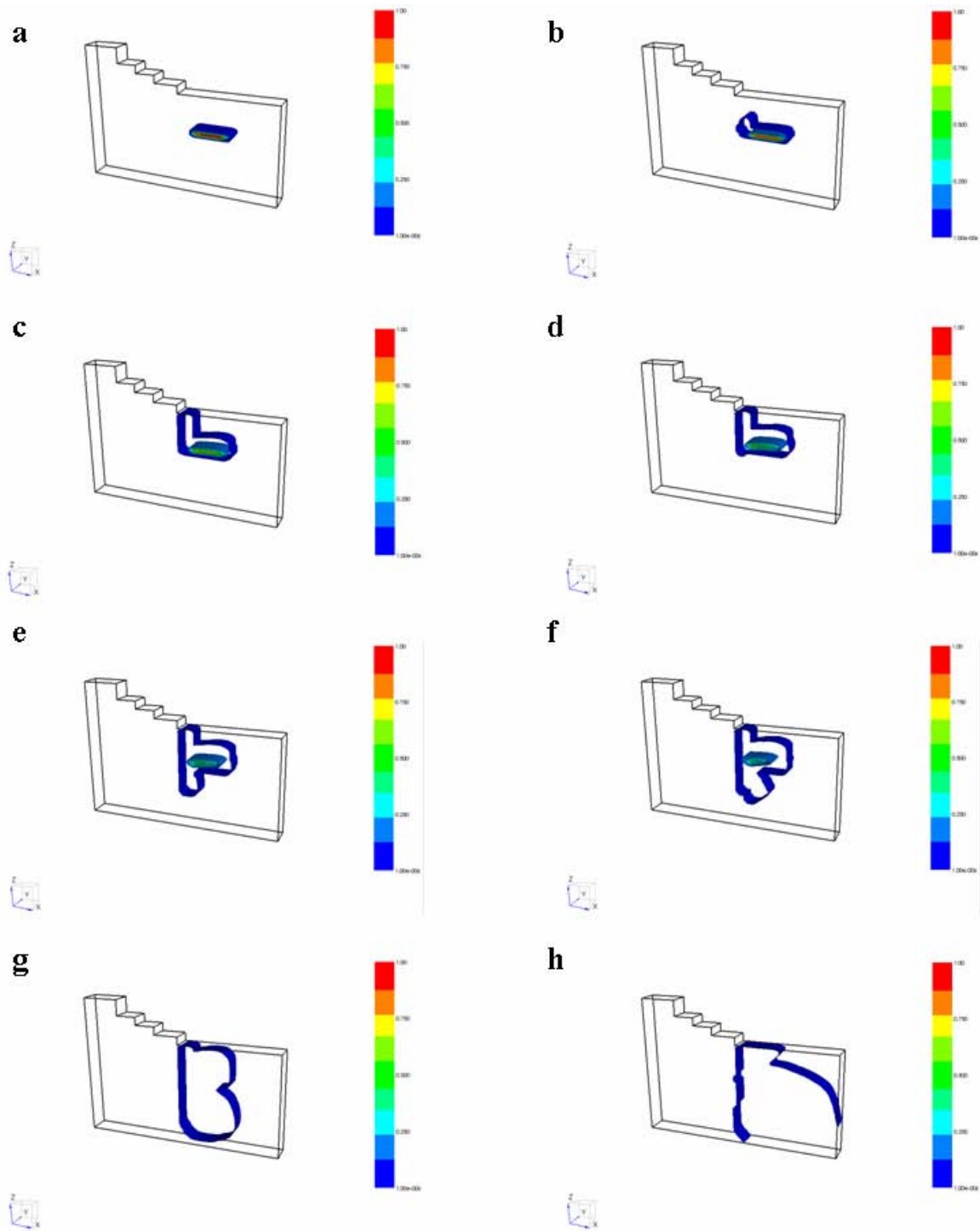


Figure 5. Results of tracer analysis with a 300 m thick, 1 km wide zone of tracer mass fraction = 1 situated the at top of the volcanics, and below the valley fill. Each model is a 10 km x 7 km subset of the domain shown in Figure 3 and represents about 6000 elements. The simulation times shown are (a) 0 ka, (b) 10 ka, (c) 50 ka, (d) 100 ka, (e) 160 ka, (f) 250 ka, (g) 500 ka, and (g) 1000 ka.

3D MAGNETOTELLURIC CHARACTERIZATION OF THE COSO GEOTHERMAL FIELD

Gregory A. Newman*, Michael Hoversten*, Erika Gasperikova* and Philip E. Wannamaker⁺

*Lawrence Berkeley National Laboratory, Earth Sciences Division
1 Cyclotron Road, Berkeley CA, 94720
e-mail:ganewman@lbl.gov

⁺University of Utah/Energy & Geosciences Institute
423 Wakara Way, Suite 300
Salt Lake City, UT 84108

ABSTRACT

Knowledge of the subsurface electrical resistivity/conductivity can contribute to a better understanding of complex hydrothermal systems, typified by Coso geothermal field, through mapping the geometry (bounds and controlling structures) over existing production.

Three-dimensional magnetotelluric (MT) inversion is now an emerging technology for characterizing the resistivity structures of complex geothermal systems. The method appears to hold great promise, but histories exploiting truly 3D inversion that demonstrate the advantages that can be gained by acquiring and analyzing MT data in three dimensions are still few in number. This project will address said issue, by applying 3D MT forward modeling and inversion to a MT data set acquired over the Coso geothermal field. The goal of the project is to provide the capability to image large geothermal reservoirs in a single self-consistent model. Initial analysis of the Coso MT data has been carried out using 2D MT imaging technology to construct an initial 3D resistivity model from a series of 2D resistivity images obtained using the inline electric field measurements (Z_{xy} impedance elements) along different measurement transects. This model will be subsequently refined through a 3D inversion process. The initial 3D resistivity model clearly shows the controlling geological structures possibly influencing well production at Coso. The field data however, also show clear three dimensionality below 1 Hz, demonstrating the limitations of 2D resistivity imaging. The 3D MT predicted data arising from this starting model show good correspondence in dominant components of the impedance tensor (Z_{xy} and Z_{yx}) above 1Hz. Below 1 Hz there is significant

differences between the field data and the 2D model data.

INTRODUCTION

A critical component in understanding the hydrothermal properties of complex geothermal reservoirs, typical of the Coso geothermal field, is technology to provide images of subsurface structures, which control geothermal fluid flow. Electrical resistivity/conductivity is a primary physical property of the Earth strongly influenced by hydrothermal processes present in geothermal reservoirs. If mapped, resistivity can be used to infer untapped fracture systems and regions of increased permeability and fluid content, as well as conductive alteration of minerals (clays, etc.) due to induced fracturing arising from hydraulic stimulation of the reservoir. Magnetotellurics (MT) has a long history in geothermal exploration. With the recent advent of distributed computing, 3D MT modeling and inversion has emerged as a promising technique to model and image geothermal reservoirs in a single self consistent manner at presumably optimal accuracy and resolution. This will be demonstrated on MT data acquired over the eastern portion of the Coso geothermal field (Figure 1). It is an opportunity to test whether three-dimensional imaging/inversion, can avoid artifacts inherent in 2D inversion of 3D data. Demonstrating this in the geothermal context will push geophysical characterization of geothermal systems beyond the current state and may provide a new quantitative tool for geothermal well location.

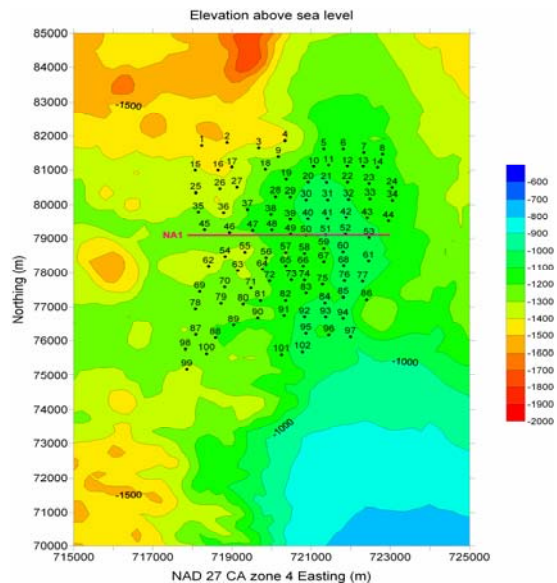


Figure 1. Coso MT Site and elevation map in meters. NA1 is contiguous bipole profile, Navy Array 1.

SUMMARY OF COSO MT MEASUREMENTS

MT exploits naturally occurring, broadband electromagnetic wave fields over the Earth's surface as sources to image underground resistivity structure. The EM fields arise from regional and worldwide thunderstorm activity and from interaction of the solar wind with the Earth's magnetosphere. Due to the remote nature of these EM sources and the high index of refraction of the Earth relative to the air, the waves are assumed to be planar and to propagate vertically into the Earth. The waves are arbitrarily polarized over a 3D Earth, which necessitates a tensor formulation, in other words a vector measurement of the EM fields, to completely represent the subsurface geoelectric structure. A simplified view of a five-channel MT detector as deployed over the Coso geothermal field appears in Figure 2. Bipoles and coils measured the electric (E) and magnetic (H) fields at 102 detector sites (Figure 1). The EM time series were decomposed to frequency spectra via Fourier transformation and band averaging. Also acquired was a profile of 52 contiguous E-field bipole MT measurements across presumed strike in the northern east flank of the field (Figure 1). This collection mode fully samples possibly discontinuous responses across strike, to enhance resolution and reduce bias (Torres-Verdin and Bostick, 1992; Wannamaker, 1999).

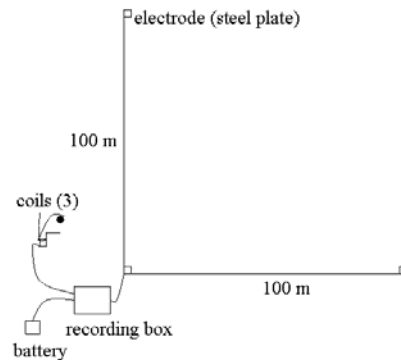


Figure 2. Simplified view of an MT station as deployed at the Coso geothermal field, after Wannamaker et al (2004).

The horizontal electromagnetic field spectra (E_x , E_y , H_x , H_y) are interrelated by

$$\mathbf{E} = [\mathbf{Z}]\mathbf{H} \quad (1)$$

where \mathbf{Z} is a 2×2 tensor, obtained for at each MT recording station as a function of frequency. By manipulating the elements of the impedance tensor off diagonal components, apparent resistivity and impedance phase quantities can be readily obtained, which are more intuitive to inspect and interpret (Vozoff, 1991). A 1×2 tensor relation between H_z and \mathbf{H} also is possible, but not considered here.

The 102 five-channel stations, including a contiguous measurement profile, were acquired utilizing 24-bit recording, narrow-band spectral scrubbing, and robust remote reference processing (Wannamaker et al., 2004). Substantial EM noise of a non plane-wave nature was nearly ubiquitous over the field, arising both from local power production activities and the nearby presence of a DC interstate power transmission system. This noise exhibited spatial correlations exceeding 100 km and required novel implementation of remote references over distances of 250-1000 km for its removal. In particular, efficacy of the Parkfield CA permanent MT observatory as a quiet remote reference was demonstrated. This site serves the western US for frequencies up to ~ 15 Hz (Wannamaker et al., 2004).

MAGNETOTELLURIC INVERSION

Our ultimate aim is to construct a 3D conductivity model of the Coso Geothermal system and use it to better understand the hydrothermal system. To accomplish this we will apply an inversion process, where the observed impedance data are fit in a least squares sense to model data. The model data are produced by solving Maxwell's equations for 3D conductivity variations and plane wave source excitation at a discrete set of frequencies. These frequencies correspond to those used to specify the impedance tensor in the field measurements. To stabilize the inversion process, additional constraints are added such as spatial smoothing of the conductivity model. Because the resources for 3D MT inversion and modeling are highly demanding, requiring significant computational resources and time (see Newman and Alumbaugh, 2000; Newman et al., 2003), it is logical to start to build the 3D conductivity model from 2D imaged sections of the reservoir. This starting model will be refined subsequently through the 3D inversion process.

2D DATA INTERPRETATION

The initial 2D inversion was performed on relatively sparse east-west profiles of 8-10 MT sites selected from the total survey data set of Figure 1, utilizing the 2D MT inversion algorithm of Rodi and Mackie (2001). The inversions were carried out using Z_{xy} impedance data and analyzed assuming the electric field is polarized perpendicular to a presumed N-S geological strike (y-axis); in actuality, polar diagrams show that geological strike varies with frequency and so is 3D, but at the lowest frequencies (<0.1 Hz), the polarization ellipses align in a north-northeast direction, which follows the trend of the Basin and Range fault-block geology. In spite of the obvious limitations in modeling and inverting the Coso data in 2D, it is a logical starting point for carrying out a full 3D analysis of the data. The transverse magnetic (TM) mode is used in the 2D inversion here because 3D modeling shows that it is usually more robust than the TE data to non-2D effects such as finite strike and static shifts (e.g., Wannamaker, 1999).

Shown in Figures 3 and 4 are 2D fits to Coso data (apparent resistivity and phase) along the profile containing MT station locations 45 through 53. Fits to the apparent resistivity data (red curves) agree closely with the field observations over the entire frequency

band. The phase data, however, are not fit as well, especially below 0.1 Hz, most likely indicating a three-dimensional characteristic of the data.

The resulting 2D resistivity image along this profile as well as those from other profiles are presented in Figure 5. Perhaps the most conspicuous feature of our ensemble of 2D inversion sections is a moderate resistivity zone dipping steeply west from the Coso east flank area. This zone terminates abruptly both to the south and the north. Several of the more productive wells on the east flank dip toward this structure suggesting some correlation with higher permeability and fluid content.

Wannamaker (2004) first identified this conspicuous feature using 2D TM mode analysis of the dense array line NA1 in Figure 1. The inversion model of this line (Figure 6) provides more detail than individual sections of Figure 5 due to the contiguous sampling over 52 bipoles, 100 m in length.

The array line inversion also shows the west dipping lower resistivity zone seen in the stitched sections of Figure 5. Producing well 34-RD2 grazes this zone along its east boundary. Shallow low resistivity material in the model represents thin alluvium and clay alteration over the east flank, plus deeper alluvium of Coso Wash toward the east part of the model section. Wannamaker (2004) also concluded that it was necessary to consider a 3D interpretational framework to fully explain the data.

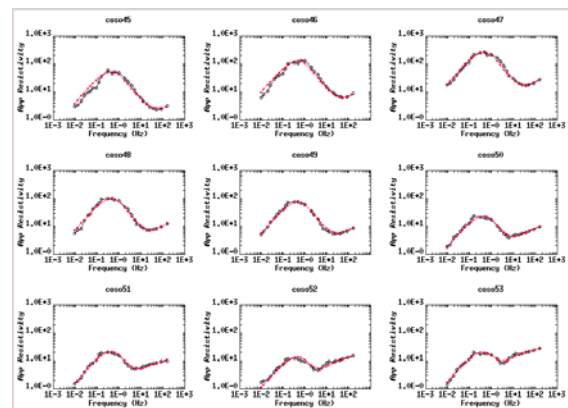


Figure 3. 2D TM fits to the Z_{xy} Coso data (apparent resistivity), where open circles represent the field data and red curves the model responses.

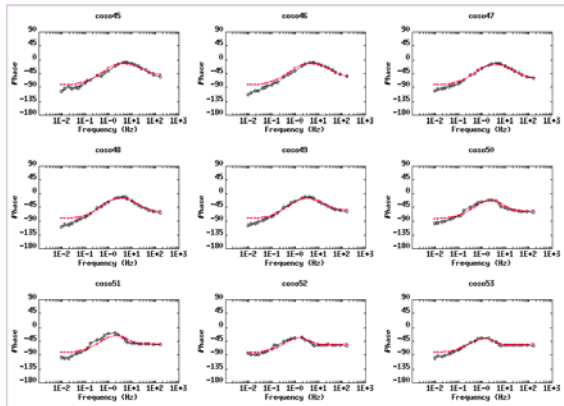


Figure 4. 2D TM fits to the Z_{xy} Coso data (impedance phase), where open circles represent field data and red curves are model responses.

INITIAL 3D MODEL OF THE COSO FIELD

In order to simulate the 3D MT fields from the resistivity model shown in Figure 5, we spatially interpolated the resistivity between the transects onto a finite difference grid with 120 nodes along each coordinate direction. This interpolated 3D resistivity model will serve as the starting model, which will be used to launch the full 3D inversion analysis of the data. The simulated fields (Z_{xy} and Z_{yx} apparent resistivity and phase) for this starting model are shown in Figures 7 and 8 and are compared with the corresponding field observations for sites 45 through 53.

For frequencies above 1 Hz, the 3D fields generally show good correspondence with the field data for both polarizations, even though there are some grid-induced statics arising from the interpolation process that affect primarily the predicted Z_{yx} apparent resistivity at a few sites. Significant differences, however, arise at all sites between the model and field curves in both apparent resistivity and phase at lower frequencies. When the field data were analyzed using 2D assumptions, such discrepancies appeared confined to the phase.

CONCLUSIONS AND PLANNED WORK

An initial 3D resistivity model of the Coso geothermal field has been constructed. The model shows geological structure that may correlate with a zone of higher permeability and fluid content, as

evidenced by the well locations at the field. Predicted Z_{xy} and Z_{yx} , apparent resistivity and phase data from the model show good correspondence to the field data above 1 Hz. Below 1 Hz, however, significant differences are evident.

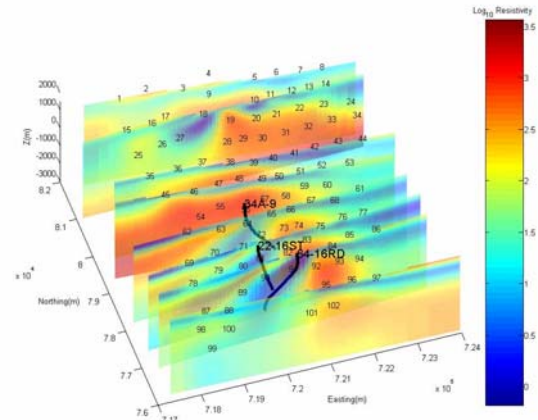


Figure 5. Resistivity model of the Coso geothermal site compiled from multiple 2D transects. Wells 64-16RD, 22-16ST and 34A-9 are also shown. The model view is from the southwest and includes site locations shown in Figure 1.

ACKNOWLEDGEMENTS

This work was carried out at Lawrence Berkeley National Laboratories with funding provided United States Navy and the Department of Energy, Geothermal Program Office. MT data at Coso were collected by Quantec Geoscience Inc. under subcontract to the Energy & Geoscience Institute (EGI). Wannamaker was supported under U.S. Dept of Energy contract DE-PS07-00ID1391 and U.S. Dept. of Navy contract N68936-03-P-0303. Digital elevation data at 30 m spacing were provided by Greg Nash of EGI.

REFERENCES

Newman, G. A. and Alumbaugh, D. L., 2000, Three-dimensional magnetotelluric inversion using non-linear conjugate gradients: *Geophysical Journal International*, **140**, 410-424.

Newman, G. A., Recher, S., Tezkan, B. and Neubauer, F. M., 2003, 3D inversion of a scalar radio magnetotelluric field data set: *Geophysics*, **68**, 782-790.

Rodi, W. and Mackie, R. L., 2001, Nonlinear conjugate gradients algorithm for 2-D magnetotelluric inversion: *Geophysics*, **66**, 174-187.

Vozoff, K, 1991, The magnetotelluric method, *in* *Electromagnetic methods in applied geophysics*, ed. by Nabighian, M. N., v. **2B**. Soc. Explor. Geophys., Tulsa, 641-711.

Wannamaker, P. E., 1999, Affordable magnetotellurics: interpretation in natural environments, *in* *Three-dimensional electromagnetics*, ed. by M. Oristaglio and B. Spies, *Geophys. Devel. Ser.*, no. 7, Soc. Explor. Geophys., Tulsa, 349-374.

Wannamaker, P. E., Rose, P. E., Doerner, W., Berard, B., McCulloch, J. and Nurse, K., 2004, Magnetotelluric surveying and monitoring at the Coso geothermal area, California, in support of the enhanced geothermal systems concept: survey parameters and initial results: *Proc. 29th Workshop on Geothermal Reservoir Engineering*, Stanford University, Stanford California, January 26-28, SGP-TR-175.

Wannamaker, P. E., 2004, Creation of an enhanced geothermal system through hydraulic and thermal stimulation – magnetotelluric surveying and monitoring: *Quarterly Project Information and Planning (PIP) Report*, July 1 – September 30, 2004, US Department of Wind and Geothermal Technologies, Enhanced Geothermal Systems Program.

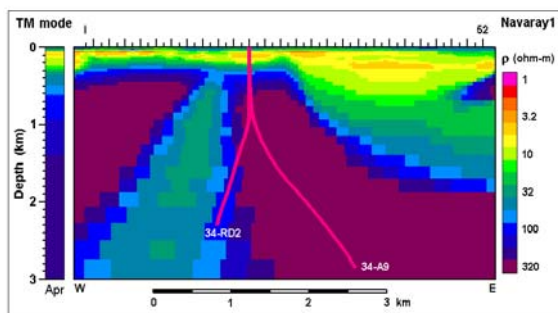


Figure 6. 2D inversion model using TM mode data of contiguous bipole profile NA1. Also plotted

are deep wells 34-RD2 and 34-A9 which project from about 500 m south of the profile. Inversion code used was developed by Wannamaker from the U. Utah finite element code and damps variations from an average 1D a-priori model (Apr). This plot adopts warm colors for low resistivity. View is toward the north.

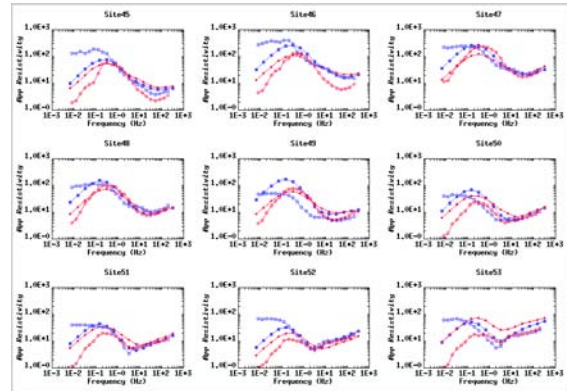


Figure 7. Plots of apparent resistivity for selected measurement sites, 45-53. The blue curves with solid and open squares denote predicted and observed Z_{xy} apparent resistivity. The red curves, solid and open circles, denote predicted and observed Z_{yx} apparent resistivity.

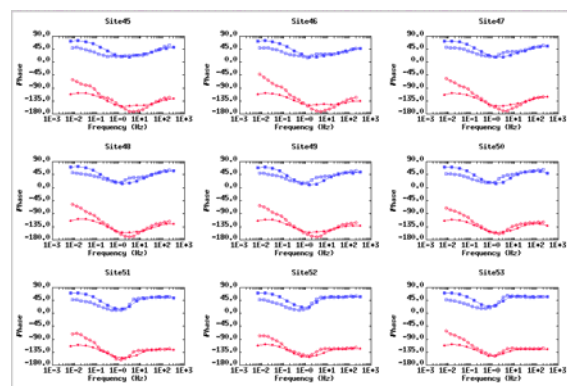


Figure 8. Plots of impedance phase for selected measurement sites, 45-53. The blue curves with solid and open squares denote predicted and observed Z_{xy} phase. The red curves, solid and open circles, denote predicted and observed Z_{yx} phase.

SOURCE PARAMETERS OF MICROEARTHQUAKES FROM THE 1.5 KM DEEP PYHÄSALMI ORE MINE, FINLAND

Volker Oye and Michael Roth

NORSAR
Instituttveien 25
2007 Kjeller, Norway
e-mail: volker.oye@norsar.no

ABSTRACT

The Pyhäsalmi ore mine in Finland is instrumented with 6 three-component and 12 one-component geophones in a depth between 1.2 and 1.4 km. The monitoring network (Integrated Seismic System International Ltd.) has been operational in a triggered mode since January 2003, and about 24,000 events were recorded until August 2004. About two third of the events are identified as production blasts from the mining operations, while the remaining 8000 seismic events are induced by stress changes that are related to the ongoing production.

We have developed a microseismic monitoring software that automatically determines microearthquake hypocenters and their source parameters. The recorded microseismic events occur throughout the mining area and they cluster in newly excavated tunnel systems. In moment magnitude (M_w), they vary from about -1.8 to 1.2 , while the bulk of events have M_w from -1.5 to -0.5 . We estimate the seismic moment and the corner frequency using a spectral integration method and alternatively we fit a theoretical Brune's shape spectra to the stacked spectra.

For two clusters of microseismic events we apply the multiple empirical Green's function method (MEGF), which allows us to determine source parameters without assuming path and site effects. We determined the ratio between the radiated seismic energy and the seismic moment and obtained a value of about $5 \cdot 10^{-7}$ for a magnitude range from $M_w -1.2$ to 0 . Compared to tectonic seismic events analyzed in other studies, our results for the energy-to-moment ratio are lower by about two orders of magnitude. This discrepancy may partly be explained by a more tensile fault mechanism of the mining events compared to earthquakes that are dominated by shear faulting.

INTRODUCTION

For more than 30 years seismic installations in mines have contributed to optimize the mining process and to improve hazard mitigation (McGarr and Simpson, 1997). Within the last decade the quality of in-mine instruments has significantly improved (Mendecki, 1997). Due to that fact, mining seismology can now contribute more reliably to the investigation of scaling relations (Aki, 1967; Abercrombie and Leary, 1993; Ide *et al.*, 2003). Only little data of earthquakes smaller than $M_w 2$ is available from conventional seismological databases. Therefore mining induced seismicity, which covers a magnitude range down to about $M_w -2$, plays a major role in the study of scaling relations, i.e.: is the rupture process of small earthquakes fundamentally different to the one of large earthquakes?

Mining induced seismicity is mainly related to the excavation and the associated stress changes in the rock formation, whereas microseismicity at geothermal energy sites is mainly related to the fluid pressure changes the associated stress changes (McGarr 1994; Richardson and Jordan, 2002; Michelet *et al.*, 2004). Nevertheless, there are many similarities between these two types of microseismic data. The majority of the microseismic events are in the same magnitude range, i.e. from about $M_w -2$ to 2 . The receivers are usually installed in boreholes in order to keep the source-to-receiver distances short and to avoid high attenuation in near surface rocks.

In the following we introduce the mining site and the concepts and applications of our data processing/analysis to the microseismic data recorded in the Pyhäsalmi ore mine.

THE PYHÄSALMI ORE MINE

Geology

The Pyhäsalmi ore mine with a depth of 1.5 km is located in central Finland and is the deepest of its

kind in Western Europe (Figure 1). The ore body of the Pyhäsalmi mine is located in the hinge of a large synform fold (Puustjärvi, 1999). The mine produces mainly zinc and copper, while most of the ore consists of uneconomic pyrite. The ore body is enclosed by quartz-rich felsic volcanics with amphibolite bands that vary in width from millimeters to some meters. Schistosity is clearly defined throughout the mining area and cracks are most prominent in the schistosity direction. Pegmatite veins are common near the ore contacts and they vary in size and orientation. Pegmatite veins might play an important role as they have been identified as fault planes. In the active mining area, however, there are no distinct faults that could be reactivated by mining.



Figure 1: The Pyhäsalmi ore mine is located in central Finland.

Stress measurements at a depth of 1225 m were carried out and revealed that the main stress is horizontal compression at N310°E, with maximum horizontal stress $\sigma_H=65$ MPa, minimum horizontal stress $\sigma_h=41$ MPa and vertical stress $\sigma_v=33$ MPa, (Ledger, 1999). This is largely in agreement with tectonic stress directions from the world stress map (Reinecker et al., 2004), even though secondary effects of mining might have disturbed the stress field as compared to intact rock conditions.

Microseismic monitoring system

The monitoring network in the Pyhäsalmi mine (Figure 2) is now instrumented with 6 three-component and 12 one-component geophones (in July 2004, two three-component stations were added). The monitoring network (Integrated Seismic System International Ltd.) samples with 3 kHz and runs in a triggered mode. All geophones are carefully cemented in 10 m long vertical boreholes that were drilled into the roof of the tunnels. Thereby coupling is well established and most of the infrastructure noise is avoided.

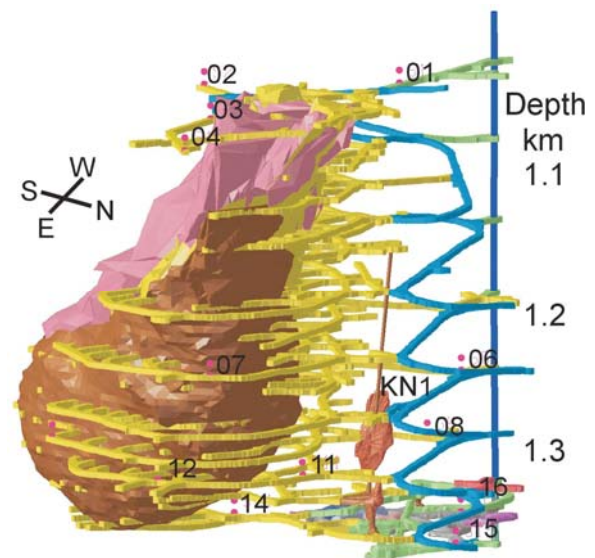


Figure 2: The Pyhäsalmi ore body consists mainly of copper- (brown) and zinc- (pink) pyrites. The mining infrastructure with its main tunnel system (blue) and the stopes (yellow) is shown together with the monitoring network. KN1 (brown) marks a pass where quarried ore is dropped down to the crusher level.

DATA PROCESSING

We used a microseismic software package (Oye and Roth, 2003) to process all triggered event files. The event files contained either single events or up to about 30 events in case of ripple-fired production blasts. The basic steps of the automatic processing are: event detection and event association, accurate P-wave onset picking, P-wave polarization analysis, S-wave onset picking and finally the event localization. Basic source parameters are also evaluated automatically, a more detailed analysis presented later, has been done interactively.

The event detection is based on the evaluation of the signal-to-noise ratio (SNR) for each geophone. The SNR in turn is computed from the short-time (STA) and long-time averages (LTA). A successful detection is assigned if the SNR exceeds a specified threshold at a minimum number of geophones within a common time window. In order to determine the P-wave onset times we first estimate the noise characteristics of each seismic trace within a time window prior to the detection time and conduct an error prediction filtering. Then we apply the Akaike Information Criterion (AIC) to the error prediction filtered seismic traces and find the P-wave onset times from the minimum of the AIC-function (Leonard and Kennett, 1999). In case of three-component geophones, we conduct a polarization

analysis of the P-wave signal and rotate the three channels into the ray coordinate system. Thereby we enhance the SNR for the S-wave signal on the two components perpendicular to the ray direction and then we pick the S-wave onset similar to the P-wave onset. A screenshot of the automatic P- and S-wave onset picking and P-wave polarization analysis is shown in Figure 3.

The hypocenters can be determined either for any 3D velocity model by using a directed grid search inversion, or for homogenous velocity models using a fast master-event location approach. In this study we used a homogenous velocity model, but we will also include the 3D velocity model at a later stage. Input parameters for the hypocenter inversion can include all or a selection of P- and S-wave onset times, S-P wave difference travel times, azimuth and incidence angles.

SOURCE PARAMETER DETERMINATION

The general form of the source displacement spectrum used in this study is

$$\Omega(f) = \frac{\Omega_0}{\left[1 + \left(\frac{f}{f_c}\right)^\gamma\right]^{\frac{1}{\gamma}}}, \quad \text{Eq. (1)}$$

Where Ω_0 is the low-frequency spectral level, f the frequency, f_c the corner frequency, n the high-frequency level fall-off rate and γ a constant. Our data was fitted best with the classical Brune spectrum, where $n=2$ and $\gamma=1$ (Brune, 1970; Brune,

1971). We determine the source parameters from the S-wave signal, since it is the most energetic part of the seismograms. In order to estimate the displacement spectrum we take a time window of 200 ms that starts at the S-wave onset and encloses most of the S-wave coda. Both ends of the time window are extended with cosine tapered time windows of 20 ms. The seismogram segments are then Fourier-transformed and compensated for geometrical spreading and intrinsic attenuation. There is no need to correct the spectra for the instrument response since it is flat for frequencies above 10 Hz and our signals are usually above the noise level from about 15-20 Hz up to the Nyquist frequency. We then stack the compensated spectra in order to cancel out effects of the radiation pattern.

Spectral integration technique

One method to determine source parameters, which is well suited for automatic processing, is to use integrals of spectra, because it is a quick and robust technique (Andrews, 1986; Snoke, 1987). The corrected and stacked amplitude spectra (D:displacement; V: velocity; A: acceleration) are squared and integrated from 15 Hz (f_1) up to 90% of the Nyquist frequency ($f_2=1350$ Hz):

$$S_{X2} = 2 \int_{f_1}^{f_2} X^2(f) df \quad \text{Eq. (2)}$$

with $X = (D, V, A)$.

The integration of the velocity spectrum provides a

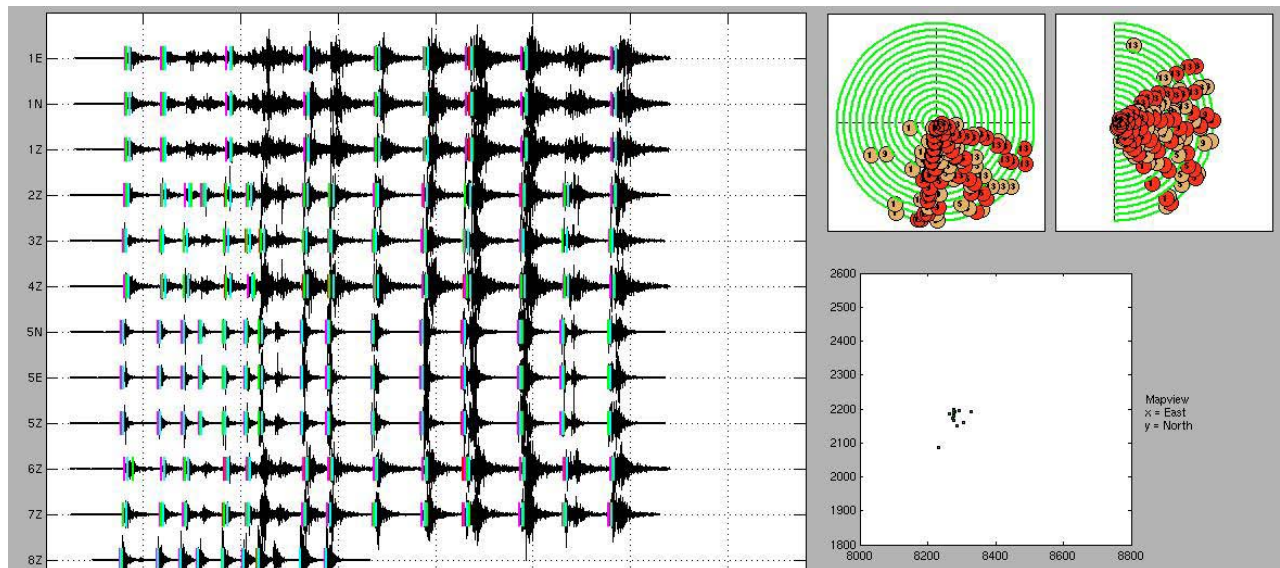


Figure 3: Automatic processing of an 8 second event file containing ripple-fired production blasts. Left: Seismic traces of one and three component geophones are shown with their automatic P- (red) and S-wave picks (green). Top right: Polarization angles azimuth and incidence for all events. Each green circle represents an event, the red filled circles show the angles for each three-component geophone. Lower right: Automatic locations of the 14 ripple-fired events.

measure of the radiated seismic energy E_{rad}

$$E_{rad} = 4\pi\rho\beta S_{V2} \quad \text{Eq. (3)}$$

where $\rho = 4000 \text{ kg/m}^3$ is the average density of the ore body. For a Brune type spectrum, only 20% of the radiated seismic energy is represented by frequencies smaller than the corner frequency. Since our data has high sampling rates, this is not a major concern, but for events with high corner frequencies (above about 200 Hz) this effect becomes significant. We therefore compensated for missing energy for frequencies above our upper integration limit by an extrapolation of the Brune shape model (Ide and Beroza, 2001).

The Brune spectrum in Eq. (1) is defined by the corner frequency

$$f_c = \frac{1}{2\pi} \sqrt{\frac{S_{V2}}{S_{D2}}} \quad \text{Eq. (4)}$$

and the low frequency spectral level (Andrews, 1986)

$$\Omega_0^2 = 4 \sqrt{\frac{S_{D2}^3}{S_{V2}}} \quad \text{Eq. (5)}$$

The seismic moment can be determined from Ω_0 by (e.g. Andrews, 1986)

$$M_0 = 4\pi\rho\beta^3 \Omega_0 / C \quad \text{Eq. (6)}$$

with $C = \sqrt{2/5}$ as the root mean square radiation pattern for S waves. The Brune stress drop as defined by Eshelby (1957) can also be expressed by integrals of spectra (e.g. Snoke, 1987)

$$\Delta\sigma_B = \frac{7}{16} \frac{M_0}{r^3} = \frac{2\rho}{2.34C} \sqrt[4]{\frac{S_{V2}^5}{S_{D2}^3}} \quad \text{Eq. (7)}$$

Fitting of source spectra

An alternative approach to determine source parameters is to fit a theoretical source spectrum to the stacked and corrected displacement spectra (e.g., Abercrombie, 1995; Prejean and Ellsworth, 2001). We hold the intrinsic attenuation Q constant and invert for Ω_0 and f_c using a Levenberg-Marquart algorithm. The best fit of the spectra was achieved with a constant Q of 350 and using the classical Brune spectrum. Figure 4 also shows results of other Q values and using different theoretical displacement spectra (Boatwright model: $n=2$, $\gamma=2$ and Haskell model $n=3$, $\gamma=2/3$).

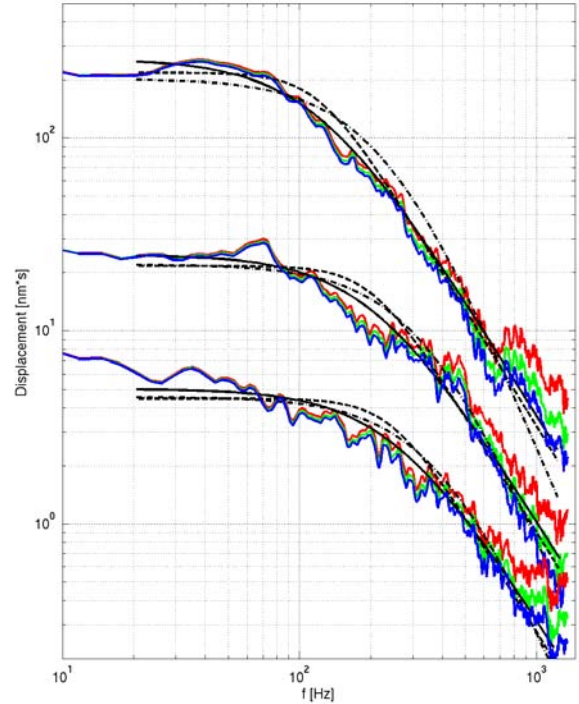


Figure 4: Stacked displacement spectra for three microearthquakes. Constant Q corrections are 200: red, 350: green, 800: blue. The theoretical spectra are in black with Brune: solid, Boatwright: dashed, Haskell: dash-dotted. The best fit is achieved with $Q=350$ and the classical Brune spectrum.

RESULTS

Automatically located hypocenters

The automatic monitoring of the Pyhäsalmi ore mine shows that the majority of events, whether they are mining blasts or induced seismic events, originate within the active mining area. The hypocenters of about 5000 events from the year 2003 with location errors smaller than 15m are displayed in Figure 5. One cluster of events is located to the north of the ore body and this seismic activity is related to an open ore pass (KN1 in Figure 2) that is used to dump the ore down to the crusher level. This particular pass has been expanding from 3 to about 30 m length. Most of the other events are directly related to mining. The largest events are usually mining blasts with magnitudes around M_w 1, while most of the smaller ones are rockbursts and microseismic events. In Figure 5, the origin time of the events is color-coded and shows that the main seismic activity moves with the most active mining activity.

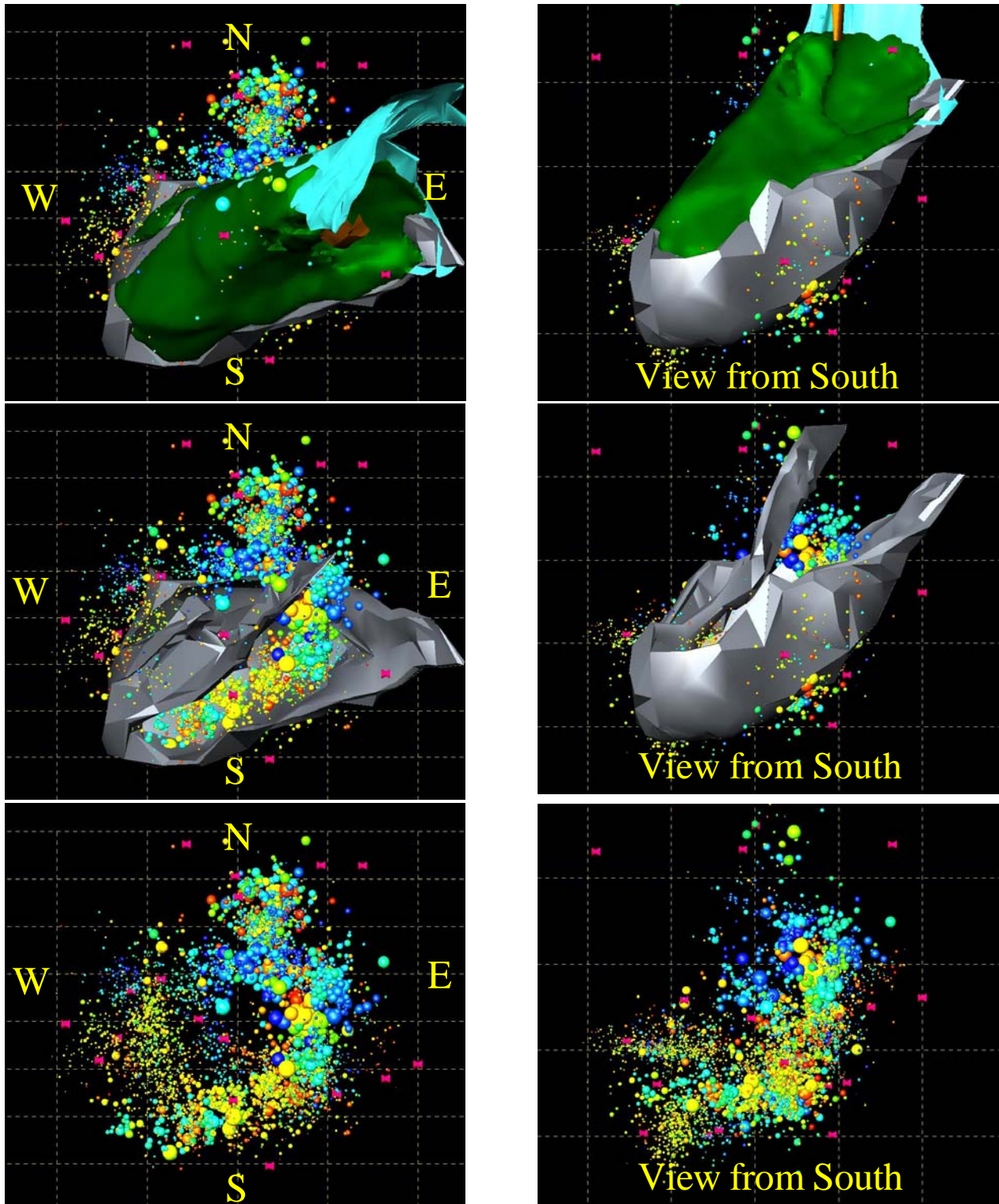


Figure 5: Map views and cross sections of the Pyhäsalmi ore body and hypocenter locations from the year 2003. The map views (left) and the cross sections (right) display an area of about 600x600m. The majority of the events occur within the ore body. The events plotted are identical on all sections, only the ore body is stripped away. The in-mine geophones are represented by the pink symbols, events are scaled to the source radius (size of the sphere) and color codes with the origin time (blue=Jan red=Dec).

Selected tectonic microearthquakes

In order to study scaling relations, we focus the analysis on tectonic microearthquakes. Further restrictions on the selection criteria as the SNR ratio (> 3), number of traces that report a detection (> 12), location error (< 10 m), rms time residual (< 5 ms) and a visual control of the onset quality lead to a much smaller data set of about 1500 events. Most interesting are the events around the ore pass (C1 in Figure 6). The mining company reported that the ore pass was expanding to the North. Our locations for events along ore pass agree with this observation as they first occur only in the South and then also occur further to the North.

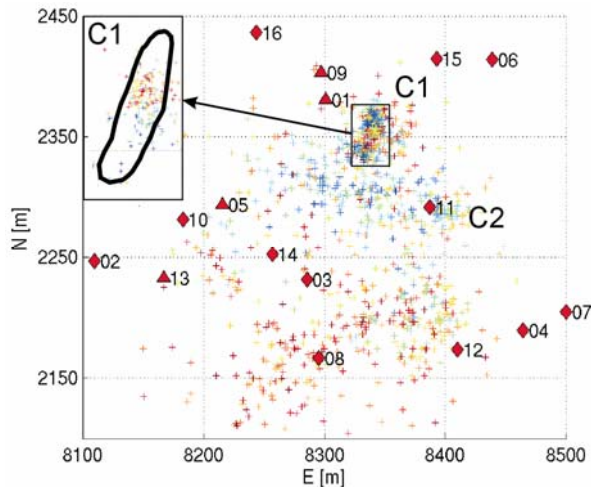


Figure 6: Map view of about 1500 visually inspected seismic events within the Pyhäsalmi ore mine. The installed geophones are indicated in red with numbers attached (three-component: triangles, vertical component: diamonds). The color scale in the main pictures represents the location error (blue: 5 m to red: 30 m). Most events occur in the cluster C1, close to the ore pass KN1, indicated as a black line in the inset. The color scale in the inset represents origin time (blue to red) indicating the extension of the pass to the north.

Using a constant Q of 350 and fitting the classical Brune shape model, our data in general supports the scaling relation between the seismic moment and the corner frequency $M_0 f_c^3 = \text{constant}$ (Figure 7). Also the bulk of the events have a Brune stress drop from about 0.01 to 1 MPa. However, there are variations from about 0.002 to 30 MPa in the Brune stress drop, which indicates that there are significant deviations from the constant stress drop model.

The radiated seismic energy E_{rad} is related to the velocity spectrum and the ratio of E_{rad}/M_0 is therefore

often used as a scaling parameter for the source dynamics. Our results for E_{rad}/M_0 varies between about $5 \cdot 10^{-8}$ to $5 \cdot 10^{-6}$, and seems to increase slightly with M_w . Equivalently, the apparent stress σ_{app} varies from about 0.0025 to 0.25 MPa.

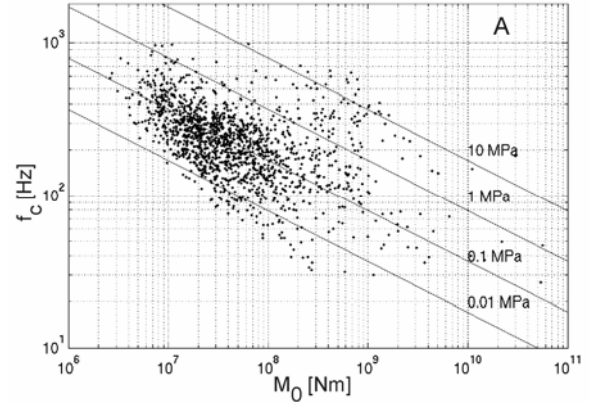


Figure 7: Corner frequency versus seismic moment for about 1500 tectonic events. Data points shown are determined using constant $Q=350$ and fitting a Brune shape spectrum. Lines of constant $M_0 f_c^3$ indicate constant stress drops.

DISCUSSION AND CONCLUSIONS

Source parameters are often determined using frequency independent Q and without accounting for site and path effects. In order to avoid these potential error sources we apply the multiple empirical Green's function method (MEGF) (Hough, 1997) to a selection of 38 events within the clusters C1 and C2 (Figure 6). These events cover a magnitude range from $M_w -1.2$ to 0. Within each cluster, we calculate theoretical spectral ratios between all events and fit them to the measured spectral ratios. We also calculated frequency dependent attenuation curves for each receiver and recalculated the radiated seismic energy (Oye et al., 2005). Then we determined the ratio E_{rad}/M_0 and obtained a value that is more or less constant at about $5 \cdot 10^{-7}$ over a magnitude range from $M_w -1.2$ to 0. Compared to the approach of a constant Q model, the results determined by the MEGF approach are much more reliable, since site and path effects as well as frequency dependent Q are eliminated. However, the amount of data available for this approach is limited, since the events must be close to each other and there must be significant differences in event size. Figure 8 shows our results in a composite picture with many other studies, mainly for larger earthquakes. Our results of E_{rad}/M_0 plot about two orders of magnitude below most others. However, following the trend of the data from Richardson and Jordan (2002), which are also mining induced earthquakes, a drop in the E_{rad}/M_0 ratio is obvious. This discrepancy to the results of most tectonic earthquakes may partly be explained by a more tensile fault mechanism of

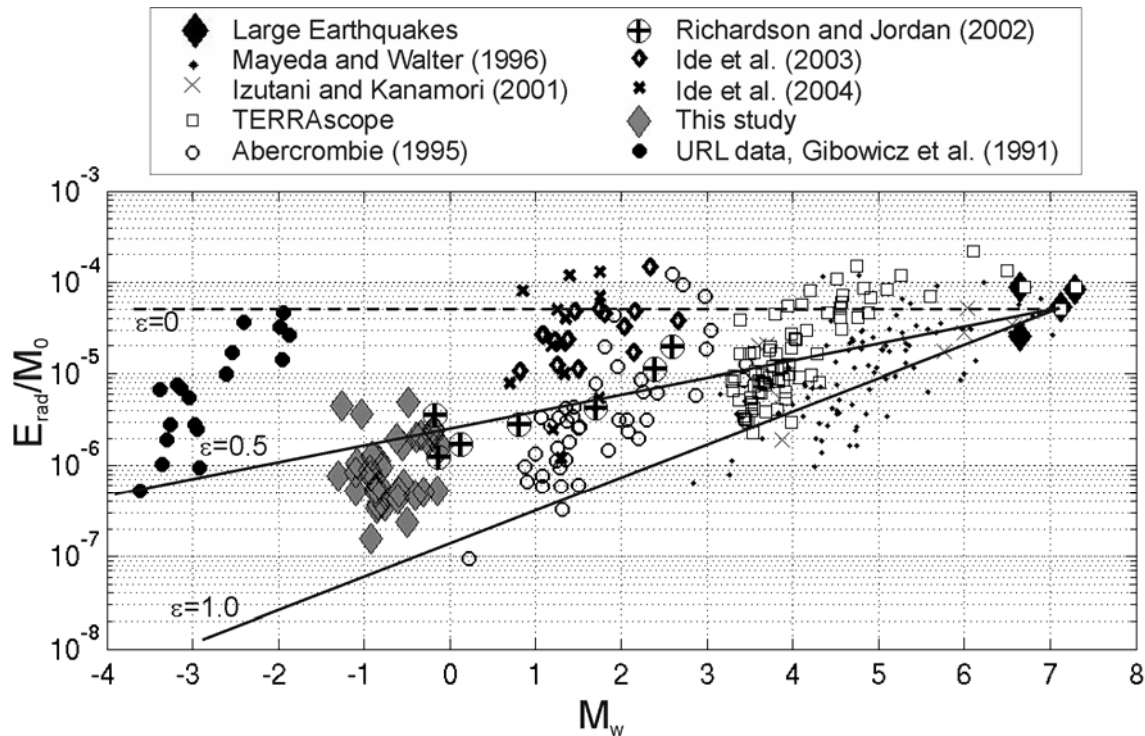


Figure 8: Energy-to-moment ratios vary with about 3 orders of magnitude over a range of 11 moment magnitudes. Our data comprises events from clusters C1 and C2 assuming $Q(f)$ using the MEGF method (gray diamonds). Black lines indicate trends for E_{rad}/M_0 for a modified scaling relation $M_0-f_c^{(3+\epsilon)}$ with $\epsilon=0, 0.5$ and 1 . Data from other studies are from deep South African gold mines (Richardson and Jordan, 2002), from the Long Valley Caldera, California (Ide et al., 2003), from the Hi-net, Japan (Ide et al., 2004), 18 events that are representative for the Underground Research Laboratory data (Gibowicz et al., 1991) and from events for shallow crustal earthquakes in California and Japan (compiled from Kanamori and Rivera (2004)).

mining induced events compared to earthquakes that are dominated by shear faulting.

We have automatically located microseismic events from the Pyhäsalmi ore mine and determined their source parameters. For events within two clusters we also applied the reliable MEGF approach to determine source parameters. Microseismicity in geothermal reservoirs could be investigated in exactly the same way.

ACKNOWLEDGMENTS

We thank Katja Sahala, Ilpo Mäkinen, and Timo Mäki, INMET Mining, and Errol de Kock, Integrated Seismic Systems (ISS), for access to the Pyhäsalmi mine data and for generous support and assistance in this connection. The first author has been supported by a grant from the Research Council of Norway and the work has also received support from US Department of Energy Award No. DE-FC03-02SF22636.

REFERENCES

- Abercrombie, R. (1995), "Earthquake source scaling relationships from -1 to 5 ML using seismograms recorded at 2.5 -km depth", *Journal of Geophysical Research* **100**, 24,015-24,036.
- Abercrombie, R., and Leary, P. (1993) "Source parameters of small earthquakes recorded at 2.5 km depth, Cajon Pass, Southern California: implications for earthquake scaling", *Geophysical Research Letters* **20**, 1511-1514.
- Aki, K. (1967), "Scaling law of seismic spectrum", *Journal of Geophysical Research* **72**, 1217-1231.
- Andrews, D.J. (1986), "Objective determination of source parameters and similarity of earthquakes of different size, in Earthquake source mechanics", S. Das, J. Boatwright, and C. H. Scholz (Editors), Vol. 6, American Geophysical Monograph 37, 259-267.
- Brune, J.N. (1970), "Tectonic Stress and the Spectra of Seismic Shear Waves from Earthquakes", *Journal of Geophysical Research* **75**, 4997-5009.

- Brune, J.N. (1971), Correction, *Journal of Geophysical Research* **76**, 5002.
- Eshelby, J. D. (1957), "The determination of the elastic field of an ellipsoidal inclusion and related problems", *Proceedings of the Royal Society of London* **241**, 376-396.
- Gibbowicz, S., Young, R., Talebi, S., and Rawlence, D. (1991), "Source parameters of seismic events at the Underground Research Laboratory in Manitoba, Canada: scaling relations for events with moment-magnitude smaller than -2 ", *Bulletin of the Seismological Society of America*, **81**, 1157-1182.
- Hough, S. E. (1997), "Empirical Green's function analysis: Taking the next step", *Journal of Geophysical Research*, **102**, 5369-5384.
- Ide, S, and Beroza, G. C. (2001), "Does apparent stress vary with earthquake size?", *Geophysical Research Letters*, **28**, 3349-3352.
- Ide, S., Beroza, G. C., Prejean, S. G., and Ellsworth, W. L. (2003), "Apparent break in earthquake scaling due to path and site effects on deep borehole recordings", *Journal of Geophysical Research*, **108**, 2271, doi:10.1029/2001JB001617.
- Ide, S, Matsubara, M., and Obara, K. (2004), "Exploitation of high-sampling Hi-net data to study seismic energy scaling: The aftershocks of the 2000 Western Tottori, Japan, earthquake", *Earth Planets Space*, **56**, 859-871.
- Kanamori, H., and Rivera, L. (2004), "Static and dynamic scaling relations for earthquakes and their implications for rupture speed and stress drop", *Bulletin of the Seismological Society of America*, **94**, 314-319.
- Ledger, A. (1999), "Stress measurement in the 1125 m level, Outokumpu Mining Pyhäsalmi Mine Oy, Rock Mechanics Technology Ltd. Pyhäsalmi Mine Oy", Internal report. 7 p.
- Leonard, M., and Kennett, B. L. N. (1999), "Multi-component autoregressive techniques for the analysis of seismograms", *Physics of the Earth and Planetary Interior*, **113**, 247-263.
- McGarr, A., and Simpson, D. (1997), "Keynote lecture: A broad look at induced and triggered seismicity", Rockbursts and Seismicity in Mines, Gibowicz, S., and Lasocki (Editors), Balkema, Rotterdam, 385-396.
- Mendecki, A. J. (Editor) (1997), "Seismic Monitoring in Mines", Chapman & Hall, London, 262 pp.
- Oye, V., Bungum, H., and Roth, M. (2005), "Source parameters and scaling relations for mining related seismicity within the Pyhäsalmi ore mine, Finland", submitted to *Bulletin of the Seismological Society of America*.
- Oye, V., and Roth, M. (2003), "Automated seismic event location for hydrocarbon reservoirs", *Computers and Geosciences*, **29**, 851-863.
- Prejean, S. G., and Ellsworth, W. L. (2001), "Observations of earthquake source parameters at 2 km depth in the Long Valley Caldera, Eastern California", *Bulletin of the Seismological Society of America*, **91**, 165-177.
- Puustjärvi, H., (1999), "Pyhäsalmi Modeling Project, Section B. Geology, Technical Report, Geological Survey of Finland, and Outokumpu Mining Oy", 66 pp.
- Reinecker, J., Heidbach, M. O., Tingay, M., Connolly, P., and Müller, B. (2004), "The 2004 release of the World Stress Map" (available online at www.world-stress-map.org).
- Richardson, E., and Jordan, T. H. (2002), "Seismicity in deep gold mines of South Africa: implications for tectonic earthquakes", *Bulletin of the Seismological Society of America*, **92**, 1766-1782.
- Snoke, J. A. (1987), "Stable determination of (Brune) stress drops", *Bulletin of the Seismological Society of America*, **77**, 530-538.

IMAGING GEOTHERMAL FRACTURES BY CSAMT METHOD AT TAKIGAMI AREA IN JAPAN

Koichi Tagomori*, Enjang Mustopa, Hisashi Jotaki, Hideki Mizunaga and Keisuke Ushijima

*West Japan Engineering Co. Watanabe-Dori 2-1-82, Fukuoka 810-0004, Japan

tagomori@wjec.co.jp

ABSTRACT

Controlled Source Audio-frequency Magneto-Telluric (CSAMT) survey was carried out in Takigami geothermal field. Stations were taken closely with regular grid spacing of 150 m. The purpose of the measurements is to delineate a detailed resistivity structure and location of electrical discontinuities that may reflect a possible faults and fractures correlated with a promising reservoir. Although the CSAMT measurements were conducted at a distance of 6 km away from a transmitter, the CSAMT data still contain some near field data when the frequency from transmitter signal is low range. Therefore, before applying two-dimensional (2-D) magnetotelluric (MT) inversion analysis of transverse magnetic (TM) mode, data corrections for a near field and transition zone were made. The interpretation results based on 2-D inversion show that there are some electrical discontinuities are found in the N-S and W-E directions, which correlate with the trend of some faults where the geothermal reservoir may exist. The electrical discontinuity F_d in N-S direction correlates with the Noine fault zone, which divides the subsurface into eastern and western parts according to the characteristics of electrical resistivity, permeability, temperature, and reservoir depth. The electrical discontinuity F_a in W-E direction corresponds to the Teradoko fault where the major production wells have been drilled in the area.

INTRODUCTION

Signal of magnetotelluric (MT) method is considered to be due to thunderstorms and solar winds in ionosphere for which the field strength and polarization vary with time of day and season. To improve the signal strength problem of the MT method, Goldstein and Strangway (1975) developed the audiofrequency MT technique with a grounded electric dipole as an artificial source called controlled-source audiofrequency magnetotelluric (CSAMT). Over the years, CSAMT has emerged as a powerful exploration tool and has found its application in a mineral exploration (Zonge, et al., 1986), geothermal investigation (Sandberg, 1982, Bartel 1987) and a potential radioactive waste disposal characterization (Unsworth, 2000). An excellent review of CSAMT and its application is given by Zonge and Hughes (1981). The advantages of this technique operated with MT method are that the polarization of the fields can be selected by the orientation of the transmitting antenna and the signal strengths do not depend on the time of day or season. However in the CSAMT method, the non-plane wave nature of the source limits the interpretation of the data. Recognizing this, the CSAMT measurement must be carried out at a distance greater than 3-5 skin depths from the transmitter site where the plane wave approximation is valid. Mustopa et al. (2001) have interpreted the MT data in the Takigami geothermal field to determine the subsurface resistivity structure correlated to the promising reservoir zone and distribution of fault systems and trends. However,

the stations of MT measurements are not in closely and regularly spaced. Accordingly, the MT data interpretation results do not sufficiently represent a full resistivity imaging reflected from the subsurface in the area. The CSAMT measurements, in the operating frequency range of 0.167 Hz to 1024 Hz, and one-dimensional (1-D) inversion of MT analysis have been carried out by West Japan Engineering Consultants under the project of Idemitsu Geothermal Co. in the Takigami geothermal field, central Kyushu, Japan (Fig.1). The CSAMT measurements were carried out in more closely and regular grid spacing station (150 m) than that in the MT measurements as shown in Fig.2. Since measurements were made using the electric field along the transverse, we assumed that the data correspond to the transverse magnetic (TM) mode (Sasaki, et al., 1992). Although the CSAMT measurements were carried out at the sites about 6 km away from the transmitter to maintain plane-wave assumption, the CSAMT data still contain some near field effect when the frequency from transmitter signal is low (deep survey). Therefore, it needs correction for a near-field effect before applying the MT interpretation technique.

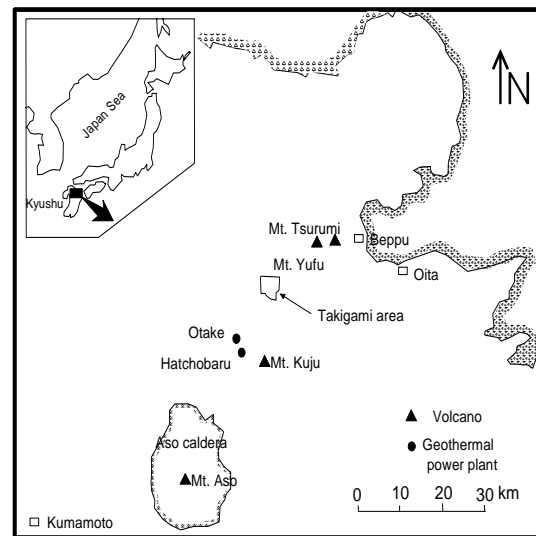


Figure 1: Northern Kyushu with location of Takigami area.

1-D inversion of MT data is good procedure when a regional structure is approximately horizontal, as in a sedimentary basin. However, when the structure is not approximately layered, the 1-D inversion technique is not valid. To overcome the problem, 2-D inversion procedure is an essential tool to interpret the MT data. In this paper we applied a 2-D inversion of MT data based on a non-linear conjugate gradient method (Rodi, et al., 2001) for the CSAMT data in Takigami geothermal field.

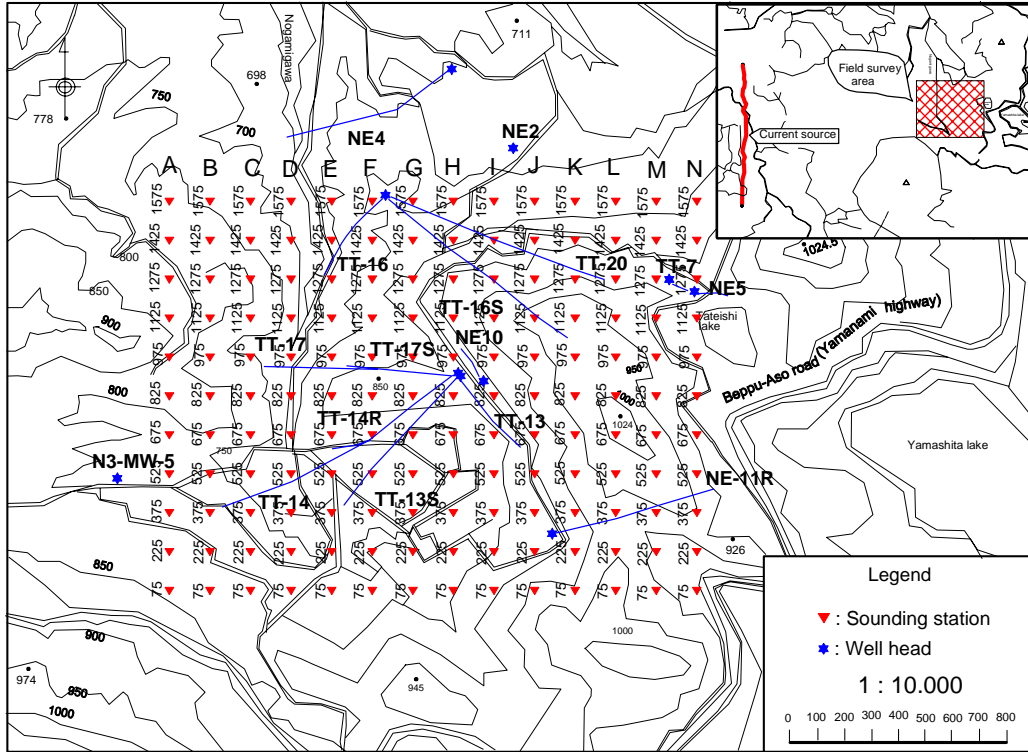


Figure 2: The location map of CSAMT measurements in Takigami area.

GEOLOGICAL SETTING

The Takigami area is located on the gentle western slope of Mt. Noine at the elevation of about 700 m and included to the Hohi geothermal region, which is one of the most active geothermal fields in Japan. The Hohi geothermal region has an outstanding level of geothermal resources, with many volcanoes and geothermal manifestation such as hot springs, fumaroles and hydrothermal alteration halos at the surface. Although Takigami area lies in the promising Hohi geothermal region, there are no surface geothermal manifestations in the immediate area. More than 20 exploration wells have been drilled in the field since 1981. As the results, the geothermal reservoir with high temperature was detected, which is covered with the thick impermeable layer. The maximum temperature of the reservoir is 252 °C (Takenaka, et al., 1991). The subsurface model of the area (Fig.3) is divided into three parts. The upper layer, which is composed of Quaternary Noine-dake volcanic rocks, Kusu and Ajibaru formation, shows low thermal gradients and low temperature below 50°C. The middle layer, which is composed of Tertiary dacitic and andesitic volcanics called Takigami formation, shows high thermal gradient. The lower layer, which is composed of Tertiary andesitic and dacitic rocks called Usa group, shows isothermal gradient and high temperature (160 –260 °C) where this layer is the geothermal reservoir of the field.

According to reservoir characteristics, the reservoir of Takigami geothermal field is divided regionally into two parts, that is, eastern and western (Furuya, et al., 2000). There are significant differences in terms of subsurface temperature distributions, depth of fractured reservoirs, and permeabilities. The boundary is probably the Noine fault zone. The eastern part of the reservoir system is shallow (700 – 1100 m depth), high permeability (30 – 100 darcy-m) and has the temperature ranges from 160 to 210 °C. On

the other hand, the western part of reservoir is deeper (1500 – 2000 m depth), low permeability (5 – 30 darcy-m) and high temperature (230 – 250 °C). This two-part reservoir accounts for the difference in chemical composition of the geothermal fluid, and the variation in the hydrology and thermal structure of the system. The present subsurface fluid flow pattern in the area has been analyzed by using distributions of geothermal indicators, such as lithium

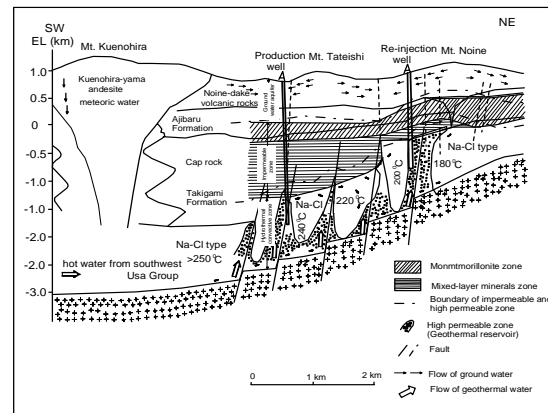


Figure 3. Schematic cross-section of geologic model of Takigami geothermal system.

concentration, chloride-lithium and sodium-potassium ratio. As the result the lithium concentration in the reservoir fluids decrease from southwest to the north, indicating that temperature decrease in the same direction. It means the fluids flow toward the north and northeast (shallower part) from the southwest (deeper part) where is no evidence for deep mixing with the cold surface ground water. Then the production and reinjection wells were drilled in the

southwestern and the northeastern part, respectively. The most adequate capacity (about 70 % of steam) of the production was estimated at 55 MW of power generation (Furuya, 1988).

CSAMT THEORY

Basic theoretical principle for CSAMT theory can be described in terms of Maxwell's equations. The general solutions of a tangential component of electric field (E_ϕ) and a radial component of magnetic field (H_r) are expressed in cylindrical coordinates (Kaufman and Keller, 1983) as

$$E_\phi = \frac{Idl \sin \phi}{2\pi\sigma r^3} \left[2 - e^{-kr} (1 + ikr) \right] \quad (1)$$

$$H_r = \frac{Idl \sin \phi}{2\pi r^2} \left\{ 3I_1 \left(\frac{ikr}{2} \right) K_1 \left(\frac{ikr}{2} \right) + \frac{ikr}{2} \left[I_1 \left(\frac{ikr}{2} \right) K_0 \left(\frac{ikr}{2} \right) - I_0 \left(\frac{ikr}{2} \right) K_1 \left(\frac{ikr}{2} \right) \right] \right\} \quad (2)$$

where dl is the dipole length, r is the source-sounding distance, and I_m and K_m are modified Bessel function of the m -th order.

From equations (1) and (2), it is evident that the relative strengths of these components are dependent upon r , media properties and frequencies. Media properties and frequency determine the skin depth δ . We can visualize the functional dependence of equations (1) and (2) as the ratio of r to δ , that is

$$|kr| = \frac{(r\sqrt{2})}{\delta} \approx \frac{r}{\delta} \quad (3)$$

where $|kr|$ is commonly referred to as the induction number.

According to the characterization of the induction number, there are three regions of propagating electromagnetic (EM) field in CSAMT method. The region near the transmitting dipole is electrically characterized by small induction ($|kr| \ll 1$) known as "near-field" zone. The region far from transmitting dipole is electrically characterized by large induction number ($|kr| \gg 1$) known as "far-field" or "plane-wave" zone. The region between these zones is called "transition" zone.

Near-field response ($|kr| \ll 1$)

The equations can be determined by using the appropriate approximations for the complex Bessel functions and exponentials. The results are:

$$E_\phi \approx \frac{Idl \sin \phi}{2\pi\sigma r^3} \quad (4)$$

$$H_r \approx \frac{Idl \sin \phi}{4\pi r^2} \quad (5)$$

From the equations (4) and (5), E is directly proportional to ground resistivity and independent of frequency. H is independent of both resistivity and frequency (saturated). The near-field apparent resistivity is a function of r , that is

$$\rho_a \approx \frac{r}{2} \left| \frac{E_\phi}{H_r} \right| \quad (6)$$

This shows that near-field measurement and depth penetration are controlled by array geometry, not by frequency.

Far-field response ($|kr| \gg 1$)

Far from dipole source, equations (1) and (2) approach the following limits, with quasi-static assumption,

$$E_\phi \approx \frac{Idl \sin \phi}{\pi\sigma r^3} \quad (7)$$

$$H_r \approx \frac{Idl \sin \phi}{\pi\sqrt{\mu\sigma\omega} r^3} e^{-\frac{r}{\delta}} \quad (8)$$

For a homogenous earth, the E -field is independent of frequency and directly proportional to resistivity. The horizontal H -field components are frequency-dependent and a function of the square root of ground resistivity. Hence H does not "saturate", and it is fully responsive to resistivity change and frequency.

As shown in equations (7) and (8) the horizontal fields in the far-field zone all decay as $1/r^3$, thus the far-field apparent resistivity can be determined by measuring the perpendicular E and H , that is

$$\rho_a = \frac{1}{\mu\omega} \left| \frac{E_\phi}{H_r} \right|^2 \quad (9)$$

which is commonly called the Cagniard resistivity (MT apparent resistivity).

Transition zone ($|kr| \approx 1$)

Between the near-field and far-field zones, the behavior E , H and impedance are described by the exact relation in equations (1) and (2). Data in this zone are smoothly transitional for the homogenous-earth case from near to far-field behavior. In non-homogenous environments, the transition zone become complex and dependent upon resistivity contrast. Therefore the CSAMT measurement must be carried out in the far-field zone that the plane-wave analysis technique can be applied.

Near-field correction

The problem in CSAMT method is the distortion of apparent resistivity and phase difference close to the transmitter caused by changing dependence of E and H on the source sounding separation r . In the far field zone, both E and H are proportional to $1/r^3$ (equations 7 and 9) and resistivity is thus independent of r . Close to the source, in near field zone, E decay as $1/r^3$ (equation 4) and H as $1/r^2$ (equation 5), making resistivity a function of geometry. At intermediate distance, in transition zone, E decay as $1/r^3$ (equation 1) and H decay as intermediate rate between $1/r^2$ and $1/r^3$ (equation 2). In this paper, the definition of far field zone is essentially free from nonplane-wave source effect less than 10 percent of the total response in the Cagniard resistivity parameter. The near field zone as the area where E and H are completely saturated and H decay as $1/r^2$. The area between them is the transition zone. The plane-wave aspects of the CSAMT technique have been examined in detail by previous authors (Goldstein and Strangway, 1975; Sabdberg and Hohmann, 1982). They have shown that under proper field (far field) conditions, the apparent resistivities calculated from CSAMT measurements using equation (9) are similar to the plane-wave apparent

resistivities. For E measured parallel to the direction of the transmitting bipole, the area of investigation should be at least three skin depths from the transmitter for broadside configuration (the electric field parallel to the transmitter bipole on its center line) as shown in Fig.4(a). The proper distance increases to five skin depths for collinear configuration (the electric field parallel to the transmitter bipole on its axis) as shown in Fig.4(b). Moreover, Zonge and Hughes (1991) described the acceptable zones of data acquisition for CSAMT measurements as presented in Fig.4(c) and (d).

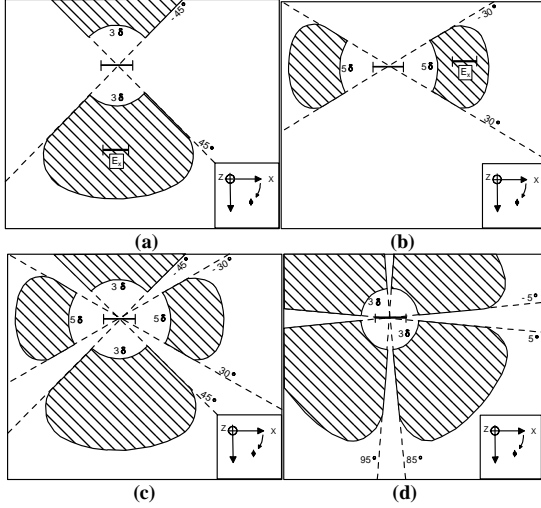


Figure 4: (a)Broad side configuration, (b)Collinear configuration, (c)Acceptable zone of CSAMT measurement (shaded-area) for E_x/H_y and (d)Acceptable zone of CSAMT measurement (shaded zone) for E_y/H_x .

Because of the need to minimize the transmitter-receiver separation for maximum signal, the far-field zone is restricted by this situation, therefore most CSAMT data sets will contain some near-field and transition zone data. To overcome the source effect problem, a correction technique to CSAMT data should be applied to obtain apparent resistivity value equivalent to the far field situation. In this paper, we used a simple technique to correct near-field CSAMT apparent resistivity proposed by Yamashita et al. (1985), that is, the plane wave apparent resistivity is apparent resistivity calculated by near field equation for the lower frequency and apparent resistivity calculated by Cagniard equation for the high frequency.

2-D inversion of MT

2-D inversion has been used to interpret MT data. This technique makes the interpretation more objective and less time-consuming than the trial-and-error approach but it does not yield a unique solution. Despite this, a common approach to fitting a 2-D MT data set is to construct a cross-section of the area based on prior geological knowledge and the model parameterization to solve for the conductivities by least-square inversion (Jupp and Vozoff, 1986). Recently, many useful 2-D MT inversion schemes have been developed. Among the many studies reported, the smoothness-constrained (“regularized” solution) least-squares method for 2-D MT inversion, which finds the smoothest change to the model and the residual error lies within a desired tolerance, was developed by Sasaki (1989), deGroot-Hedlin and Constable (1990) (Occam’s inversion), Smith and Booker (1991) (Rapid relaxation inversion), and

Uchida (1993) (Smoothing with Akaike’s Bayesian information criterion). All of the methods belong to the group with the most rigorous non-linear approach to calculate the 2-D Frechet derivative.

In this paper, we carried out 2-D inversion of MT data of transverse magnetic mode using the algorithm proposed by Rodi and Mackie (2001) that is a non-linear conjugate gradients (NLCG) algorithm. The NLCG scheme is to minimize an objective function containing data residuals and the second spatial derivatives of resistivity.

Tikhonov’s method defines a regularized solution of the inverse problem to the model m that minimize the object function (Rodi and Machie, 2001) is

$$\Psi(m) = (d - F(m))^T V^{-1} (d - F(m)) + \lambda \|L(m - m_o)\|^2 \quad (10)$$

where d is observed data vector, m is an unknown model vector, m_o is a priori model, F is a forward modeling operator, V is an error covariance matrix, L is a linear operator, and λ is a regularization parameter. Each datum d_i is log amplitude or phase of transverse electric (TE) or transverse magnetic (TM) mode of complex apparent resistivity at a particular station and frequency. The model vector is also log resistivity as a function of position ($m(x) = \log \rho(x)$). Laplacian operator can be written as follow

$$\|L(m - m_o)\|^2 = \int (\Delta(m(x) - m_o(x)))^2 dx \quad (11)$$

NLCG directly solves to minimize the objective function Ψ of equation (11). The model sequence is given by

$$\Psi(m_j + \alpha_j h_j) = \min_{\alpha} \Psi(m_j + \alpha h_j) \quad (12)$$

$$m_{j+1} = m_j + \alpha_j h_j \quad (13)$$

$$h_j = -C_j g_j + \beta_j h_{j-1} \quad (14)$$

where m_j is the step size, h_j is the search direction, C_j is the preconditioner, g_j is the gradient of objective function and β_j is the scalar calculated as

$$\beta_j = \frac{g_{j-1}^T C_{j-1} (g_j - g_{j-1})}{g_{j-1}^T C_{j-1} g_{j-1}} \quad (15)$$

In NLCG algorithm, the preconditioner has a big impact on efficiency. Two competing considerations in its choice are the computational cost of applying the preconditioner, and its effectiveness in “steering” the gradient vector into productive search direction.

CSAMT DATA INTERPRETATION

Two-dimensional inversion results

According to the results obtained through the 2-D inversion results of CSAMT data in TM mode, the 2-D resistivity section for each profile can be constructed (Figs.5 – 8). Generally, the Takigami area is composed mainly of three layers of resistivity structure. The surface layer (first layer) has a resistivity of 30 – 500 ohm-m and the thickness of 200 – 500 meters overlying an extremely low resistivity zone (second layer), which has a resistivity value of 3 – 15 ohm-m and a thickness of 500 – 800 meters. This second layer correlates with a strong hydrothermal alteration zone.

The bottom layer (third layer) has a resistivity value of 30 – 500 ohm-m that is more resistive than the second layer.

Fig.5 shows the 2-D resistivity sections in south to north direction of Line-A (Fig.5(a)) and B (Fig.5(b)) with survey lines as shown in Fig.2. There are two types of the electrical discontinuities found in those lines, that is Fa and Fb. The electrical discontinuity Fa clearly can be seen in the southwestern part of the survey area that is coincident with Teradoko fault. On the other hand, Fb is a remarkable electrical discontinuity in the area where the low resistivity is distributed broadly in the area in which the possible and close relation of a high geothermal activity may exist. The electrical discontinuities Fa and Fb extend from west to east up to Line-E and Line-H, respectively (Fig.7). In west to east direction, it is recognized also the electrical discontinuity Fc, which is located in the center of survey area from sites I-825 to N-825 (Fig.7). This area also has a high possibility of presence of geothermal reservoir.

2-D resistivity sections of Line-675 and Line-825 in west to east direction are also displayed in Fig.6. The figure

shows that there is electrical discontinuity Fd which is shown clearly below site K-675 (Fig.6(a)) and K-875 (Fig.6(b)). The Fd is also a remarkable electrical discontinuity because it is coincident with the position of Noine fault zone, extending from south to north (Fig.8). This fault divides the area into two parts, western and eastern part. It is clearly shown in the Figs.6(a) and (b) that the distribution of low resistivity is shallow and thin in the east and deepen and become thicker in the west. Accordingly, the underlain resistive layer correlated to the reservoir zone is shallower in the eastern part that that in the western part. This condition is similar with the interpretation of MT results for the survey line of SW-NE direction that the low resistivity in the second layer is shallow and thin in the northeast and become deeper and thicker in the southwest. The boundary of this condition is a Noine fault zone (Mustopa, et al., 2001). From these results, it may conclude that the geoelectrical structure of fractured type geothermal reservoir can be explained by the model as shown in the Fig.9.

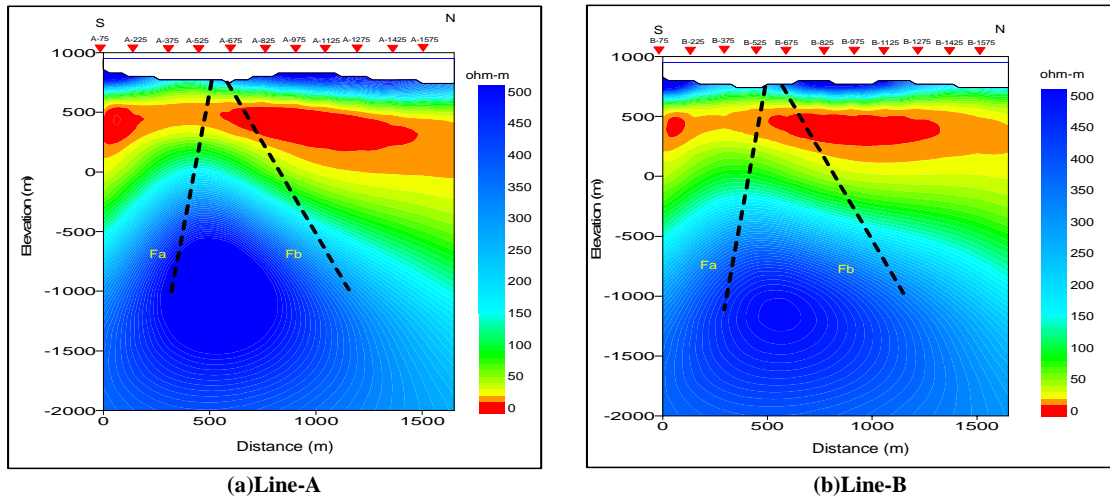


Figure 5: Resistivity profiles (S-N) direction based on 2-D inversion of CSAMT data with electrical discontinuities Fa and Fb.

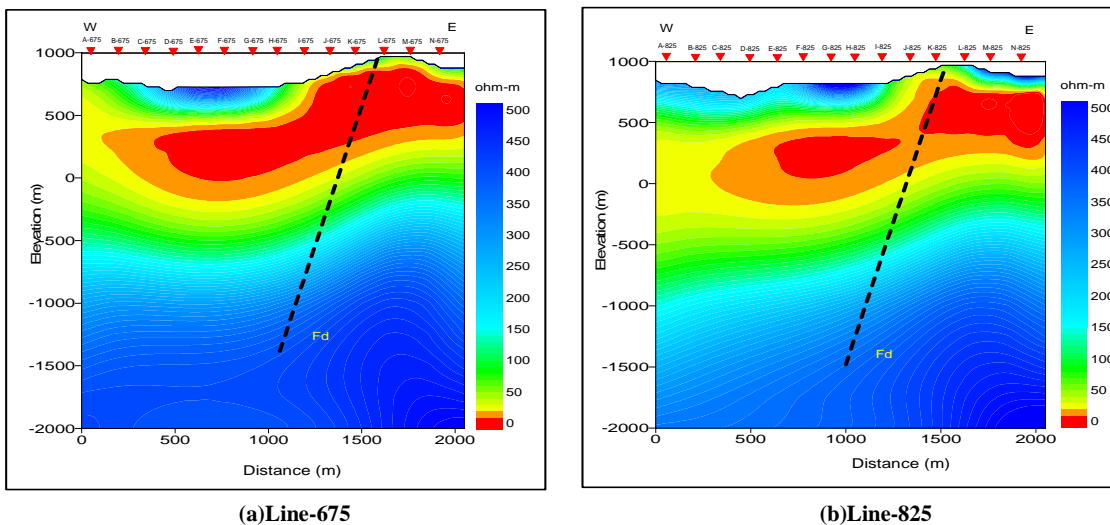


Figure 6: Resistivity profiles (W-E) direction based on 2-D inversion of CSAMT data with electrical discontinuities Fd.

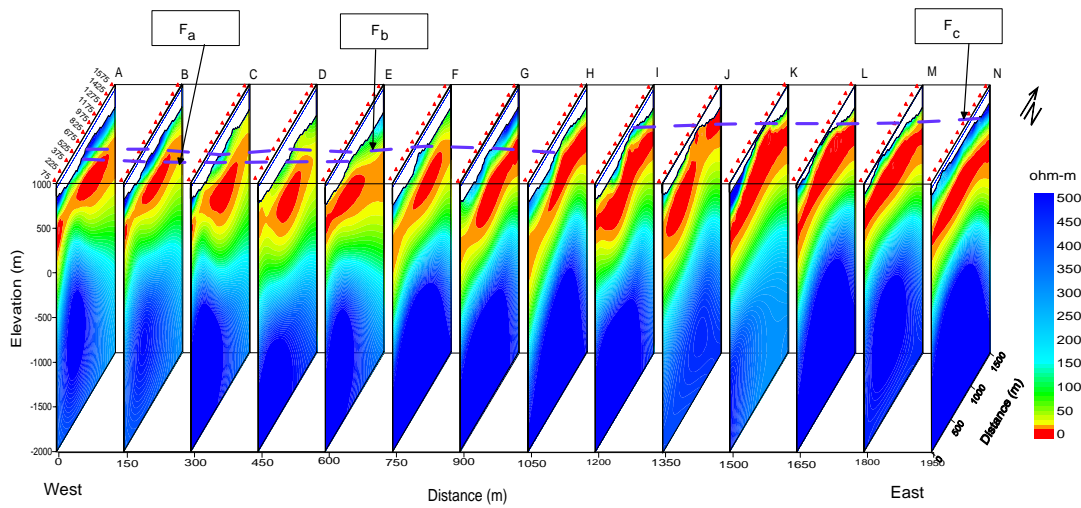


Figure 7: Resistivity sections of 2-D inversion results (W to E direction).

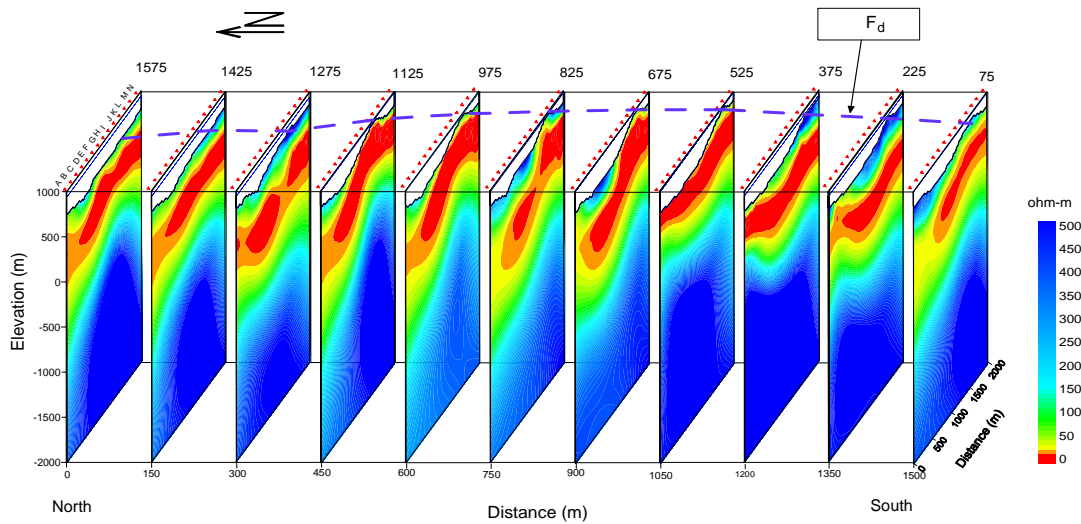


Figure 8: Resistivity sections of 2-D inversion results (N to S direction).

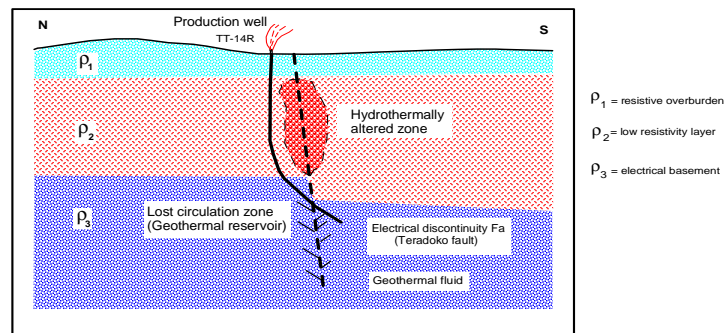


Figure 9: Geological model of fractured type geothermal reservoir.

The deep circulation of high temperature and pressure geothermal fluid along fracture zones will transfer heat to shallower level, and concentrating it into shallow reservoirs or discharging as hot springs. This process extends to lateral direction and forming the alteration zone.

The electric and electromagnetic exploration methods are more effective to detect a low resistivity zone on the vertical direction correlating with the existing alteration zone. If the low resistivity zone exist in the shallow depth and the electrical discontinuity is found around the low resistivity zone, the geothermal reservoir in the deep can be

predicted. Therefore, the geothermal reservoir in Takigami geothermal field may exist around the electrical discontinuities Fa, Fb, Fc and Fd. This condition is similar to a geothermal system in Hatchobaru area obtained from interpretation of resistivity data (Ushijima et al., 1984).

Comparison of 2-D inversion results with well log data

To confirm the 2-D CSAMT inversion results, resistivity well log and the temperature data from wells TT-13S, TT-14R, TT-16S and TT-20 are displayed in the Fig.10. The resistivity log data plotted with a semi log scale in ohm-m versus depth is put together in the same scale with the resistivity section. The lost circulation and temperature data are written on the sections. Figs.10(a) – (d) show the comparison of resistivity sections along wells with the temperature, lost circulation and resistivity log data obtained in the wells. The conductive features (3 –15 ohm-m) recorded up to 700 m below sea level (BSL) for each section can be attributed to the abundant presence of clay minerals due to hydrothermal alteration. The resistivity of formation increases, and reaches 200 – 300 ohm-m at the depth between 300 and 700 m BSL where the reservoir zone may exist in this formation (resistive layer). On the other hand, the resistivity well logs of the wells correspond to 2-D CSAMT inversion. The subsurface temperature distributions obtained from fluid inclusion measurement using rock samples from the wells (TT13S, TT-14R, TT-16S and TT-20) are displayed on the resistivity sections as shown in the Figs.10(a) – (d). At the conductive zone, the low temperature (100 °C) clay mineral such as

montmorillonite is dominated. The temperature increases rapidly from 100 to 200 °C at depth range of 0 to 400 m BSL that the temperature gradient is steep in this zone. Below 700 m BSL, the temperature distribution for each well becomes high with the temperature range from 230 °C (for TT-14R, TT-16S and TT-20) to 250 °C (for TT-13S). Therefore, this layer is expected as a reservoir zone. The temperature distributions from each well have a good correlation to the resistivity distribution for each section derived from 2-D inversion. The lost circulation of 18 ton per hour (t/h) was found in the depth of 500 m BSL for TT-13S (Fig.10(a)). For TT-14S, the lost circulation of 12 t/h occurred at the depth of 600 m BSL (Fig.10(b)). The lost circulation of 13.8 t/h was found at the depth of 200 m BSL for TT-16S and TT-20 (Figs.10(a) and (b)). The interesting point is found that the large lost circulation occurred at the depth of 1200 m BSL for the well TT-13S (114 t/h) and at the depth of 1300 m BSL for the well TT-14R (90 t/h) when the well crossed through the electrical discontinuity Fb in well TT-13S and TT-14R below the sounding site G-675 and G-825, respectively. Therefore, the electrical discontinuity Fb can be considered to indicate the presence of fault. On the other hand, the large lost circulation was found at the depth of 1000 m BSL for TT-16S and TT-20 with amount of 210 and 144 t/h mud, respectively, during the course of drilling. These high mud-water loss was encountered when the drilling well crossed through the electrical discontinuity Fc in the well TT-16S (Fig.10(c)) and TT-20 (Fig.10(d)) under CSAMT sites J-1125 and J-1425, respectively. Thus, the electrical discontinuity Fc also has a high possibility of promising fractures.

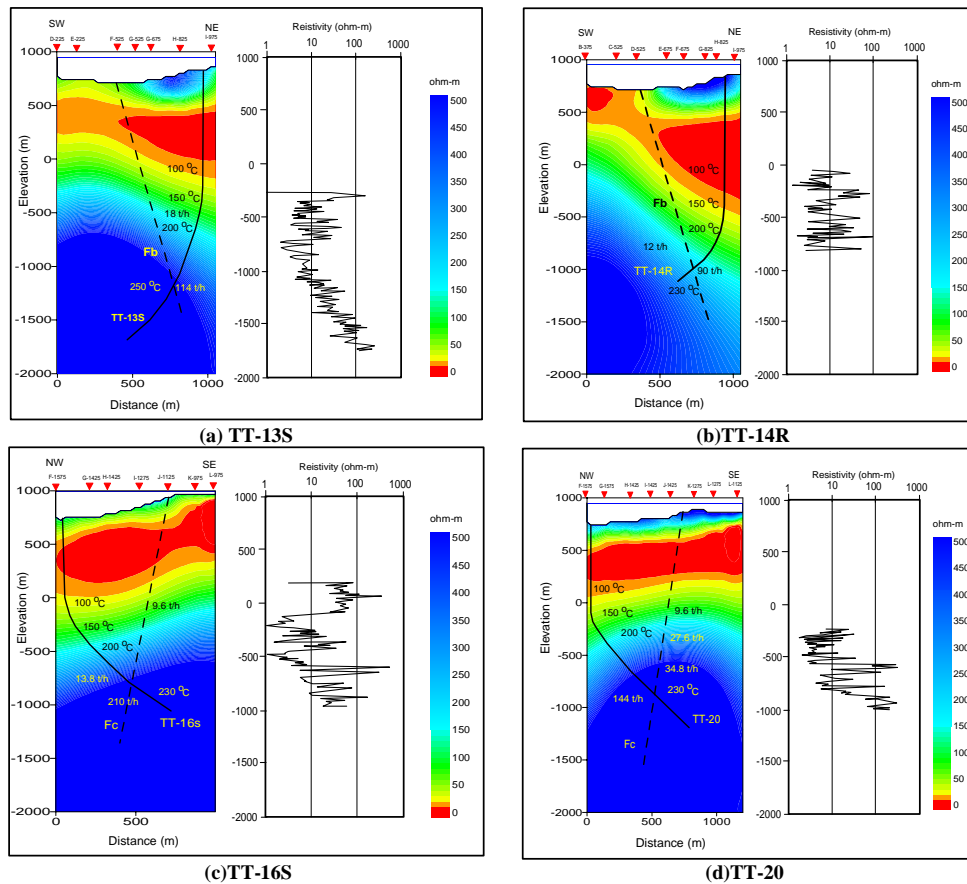


Figure 10: Comparison of 2-D inversion results with the temperature, lost circulation and electrical resistivity log.

CONCLUSIONS

Employing a 2-D inversion to CSAMT data, we have successfully obtained the reasonable resistivity structure. The results are compared to real geological condition confirmed by drilling and indicated four remarkable electrical discontinuities that may correlate with fractures in the area. Highly correlation has been found between 2-D inversion results and well log data (electrical resistivity log, temperature and lost circulation data). Especially, the electrical discontinuities obtained from 2-D resistivity section are coincided with the zones of good lost circulation, which can be considered to highly indication of potential fractures.

Generally, the subsurface resistivity structures in Takigami geothermal field are composed mainly by three types of resistivity feature, which are supported by both the 2-D inversion results of CSAMT data and resistivity logs (Figs.10(a) – (d)). The features of resistivity structure correlating with type of rocks and temperature distributions can be explained as follows; (1) The overburden (first layer) has a resistivity of 30 – 500 ohm-m and thickness of 300 to 500 m. This layer correlates with Noine-dake volcanic rock as non-altered zone and low temperature zone (50 °C) due to cold meteoric water circulation. (2) The intermediate (second) layer has an extremely low resistivity of 3 – 15 ohm-m that is 800 – 1000 m thick. The low resistivity layer as an anomalous feature can be considered as a hydrothermally altered zone (impermeable layer/cap rock). The second layer corresponds to Kusu, Ajibaru and Takigami formation composed of smectite and mixed clay minerals. The temperature distribution in the layer is characterized by a steep thermal gradient of about 20 °C/100 m. (3) The basement (third) layer is relatively more resistive than the second layer with resistivity of 30 - 500 ohm-m. This layer correlates with Mizuwake andesite rock, an illite-chlorite layer and high temperature zone (160 - 250 °C).

ACKNOWLEDGMENTS

We would like to express our gratitude to Idemitsu Oita Geothermal Co., Ltd. for provision of the CSAMT data and permission to release it in this paper.

REFERENCES

- Bartel, L. C., and Jacobson, R. D., 1987, Results of a controlled-source audio frequency magnetotelluric survey at the Puhimau thermal area, Kilauea Volcano, Hawaii: *Geophysics*, **52**, 665-677.
- deGroot-Hedlin, C., and Constable, S., 1990, Occam's inversion to generate smooth, two-dimensional models from magnetotelluric data: *Geophysics*, **55**, 1613–1624.
- Furuya, S., 1988, Geothermal resources of Takigami field, Japan, *Proceeding of Int. Geothermal Symp., Kumamoto and Beppu, Japan*, 119 - 120.
- Furuya, S., Aoki, M., Gotoh, H., and Takenaka, T., 2000, Takigami geothermal system, northeastern Kyushu, Japan: *Geothermics*, **29**, 191-211.
- Goldstein, M. A., and Strangway, D. W., 1975, Audio-frequency magnetotelluric with a grounded electric dipole source: *Geophysics*, **40**, 669-683.
- Jupp, D. L. B. and Vozoff, K., 1986, Two-dimensional magnetotelluric inversion, in Vozoff, K., ed. *Magnetotelluric Methods: Geophysics Reprint, Series no. 5, Soc. Expl. Geophys.*, 460-479.
- Kaufman, A. A., and Keller, G. V., 1983, *Frequency and transient sounding method: Elsevier Science Publ. Co. Inc.*
- Mustopa, E. J., Furuya, S., Jotaki, H., and Ushijima, K., 2001, Subsurface imaging of Takigami geothermal field derived from magnetotelluric data: Geothermal and Volcanological Research Report of Kyushu University, **10**, 77-96.
- Rodi, W., and Mackie, R.L., 2001, Nonlinear conjugate gradients algorithm for 2-D magnetotelluric inversion, *Geophysics*, **66**, 174-187.
- Sandberg, S. K., and Hohmann, G. W., 1982, Controlled-source audio-magnetotelluric in geothermal exploration: *Geophysics*, **47**, 100-116.
- Sasaki, Y., 1989, Two-dimensional joint inversion of magnetotelluric and dipole-dipole resistivity: *Geophysics*, **55**, 682-694.
- Sasaki, Y., Yoshihiro, Y., and Matsuo, K., 1992, Resistivity imaging of controlled-source audiofrequency magnetotelluric data: *Geophysics*, **57**, 952-955.
- Smith, J. T. and Booker, J. R., 1991, Rapid inversion of two- and three-dimensional magnetotelluric data: *J. Geophys. Res.*, **96**, 3905-3922.
- Takenaka, T., and Furuya, S., 1991, Geochemical model of the Takigami geothermal system, northeast Kyushu, Japan: *Geochemical Journal*, **25**, 267-281.
- Uchida, T., 1993, Smooth 2-D inversion for magnetotelluric data based on statistical criterion ABIC: *J. Geomag. Geoelectr.*, **45**, 841-858.
- Unsworth, M. J., Lu, X., and Watts, M. D., 2000, CSAMT exploration at Sellafeld: Characterization of a potential radioactive waste disposal site: *Geophysics*, **65**, 1070-1079.
- Ushijima, K., Yuhara, K., Tagomori, K., and Inoue, K., 1984, Anisotropic resistivity inversion of VES curve at Hatchobaru geothermal field, Japan: *Geothermal Resources Council Transactions, Vol. 8*, 517-522.
- Yamashita, M., Hallof, P. G., and Pelton, W. H., 1985, CSAMT case histories with a multichannel CSAMT system and near-field data correction: 55th SEG Annual Convention, 276-278.
- Zonge, K. L., and Hughes, L. J., 1991, Controlled source audio-frequency magnetotellurics, in Nabighian, M. N., Ed., *Electromagnetic methods in applied geophysics, 2: Soc. Expl. Geophys.*
- Zonge, K. L., Ostrander, A. G., and Emer, D. F., 1986, Controlled-source audiofrequency magnetotelluric measurements, in Vozoff, K., Ed., *Magnetotelluric methods: Soc. Expl. Geophys. Geophysics Reprint Series 5*, 749-763.

SEISMIC IMAGING OF THE GEOTHERMAL FIELD AT KRAFLA, ICELAND

Chuanhai Tang, Jose A. Rial, Jonathan Lees, and Eric Thompson

Department of Geological Sciences, University of North Carolina
Mitchell Hall, CB#3315
Chapel Hill, NC 27599, USA
e-mail: chhtang@email.unc.edu

ABSTRACT

During the summer of 2004 we recorded the seismicity at the Krafla geothermal field for forty days with an array of twenty PASSCAL L-28 4.5-Hz sensors. The Krafla field is located approximately 60 km East of Akureyri in northern Iceland. The array covered an area approximately 5 km N-S by 4 km E-W. The field area is located on Holocene lava flows on the Mid-Atlantic Ridge. The array recorded approximately 5 micro-earthquakes per day at a sampling rate of 500 Hz. This high sampling rate is required to exploit newly developed theories on the frequency-dependence of shear-wave splitting (SWS). During the experiment, the injection well was stopped for ten days to study the response of the subsurface crack system to changes in water pressure. SWS is an exploration method based on the analyses of polarizations and time delays of shear waves that have been distorted by the anisotropy of the medium through which the seismic waves have propagated. Epicenters roughly align along the E-W direction, while hypocenters are shallow around the injection well and appear to be related to the on-going injection. Observations of SWS at Krafla have provided evidence for at least two major crack systems oriented approximately N-S and E-W. This last, rather unexpected direction is consistent with results from a simultaneous MT (magneto-telluric) survey. Further SWS study will lead to a more detailed understanding of the fracture locations, sizes, and orientations in the geothermal field.

Keywords: shear-wave splitting, the Krafla geothermal field, seismic imaging, fractured reservoir

INTRODUCTION

The Krafla volcanic system is made up of the Krafla central volcano and an approximately 100 km long, transecting fissure swarms in northeastern Iceland. The central volcano is a major eruptive center which is less than 500, 000 years old. The Krafla central volcano is approximately 21 km long by 17 km wide

and encloses a 10 km by 7 km caldera that was formed 100,000 years ago during the last interglacial period. Two high-temperature geothermal areas occur within the Krafla volcanic system. One is located 5 km south of the Krafla caldera and the other, the NW-SE aligned Krafla-Leirhnukur geothermal field, is located inside the Krafla caldera. The eastern part of the Krafla-Leirhnukur geothermal field is utilized by the Krafla power plant which started operation in 1978. There is a shallow crustal magma reservoir with an upper boundary at a depth of approximately 3 km, near the center of inflation in the caldera (Einarsson, 1978). This magma chamber is smaller than the caldera, about 2-3 km in the N-S direction and 8-10 km in the E-W direction, with a thickness of 0.75-1.8 km (Brandsdottir et al., 1997). Geodetic measurements support the existence of a shallow magma chamber at a depth of 3 km within the caldera and have been used to argue for the existence of multiple magma reservoirs at depth (Tryggvason, 1986).

During the months of July and August 2004, a 20-station, 3-component seismic array was deployed around the Krafla geothermal field. The field area is located on Holocene lava flows on the Mid-Atlantic Ridge, and the array covered an area approximately 5 km in N-S by 4 km in E-W. Between July 5th and August 11th the array continuously recorded the seismic activity in the region surrounding the injection well K-26 located 1 km north of the power plant. The distribution of seismic stations, including both free-field and vault stations, is depicted in Figure 1. Vault stations (V) were deployed in cellars of abandoned wells. Each station in the seismic array consisted of a three-component short-period MARK4 L28 (4 Hz) seismic sensor, a data-logger or DAS (Data Acquisition System), a GPS antenna, and a 12V car battery. The data were collected continuously at a rate of 500 sps (samples per second) and recorded on 1- or 2-GB flash cards and microdisks. Stations recorded an average of 170 MB of data per day. Though the total number of functioning stations was never greater than 20, identification numbers run up to 23 because three stations had to be either moved to avoid excessive

seismic noise or entirely replaced, which required their old ID numbers to be changed.

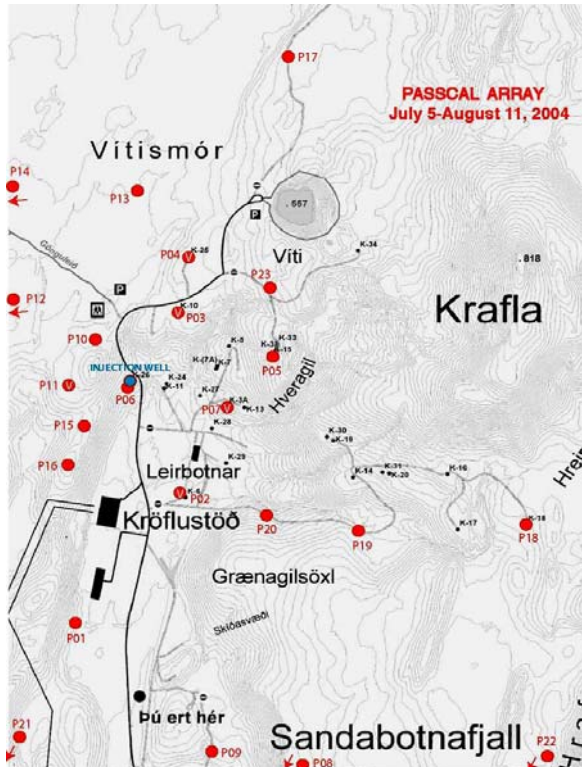


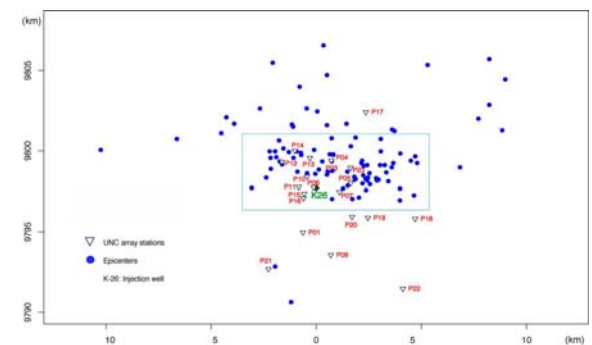
Figure 1. Distribution of the stations of PASSCAL seismic array in Krafla geothermal field, Iceland. The solid red dots represent free-field stations and the red dots with “V” are vault stations deployed in cellars of abandoned wells. The solid blue dot is where the injection well is located.

The seismic array is of the PASSCAL type, on loan from the Incorporation Research Institutions for Seismology (IRIS), which is underwritten by the US National Science Foundation. The main objective of this experiment is to use various seismic data processing techniques such as high precision earthquake location, shear-wave splitting (SWS), and tomographic inversion to detect the orientation, density and fluid content of the main subsurface fracture systems in Krafla. To further make use of the unique opportunity offered by Landsvirkjun to deploy the array, an experiment was conducted whereby injection in well K-26 was stopped on July 15th and subsequently resumed on July 26th. The response of the subsurface crack system to these transient changes in water pressure can be detected with seismic waves and will provide invaluable information on the preferred directions of fluid migration in the reservoir, permeability, effects of pore pressure on seismicity and crack activation, and three-dimensional stress variations throughout the reservoir.

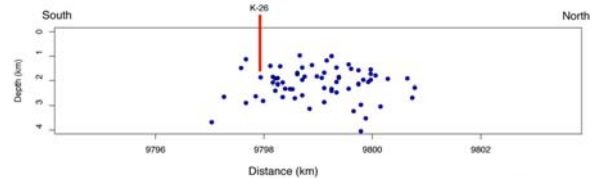
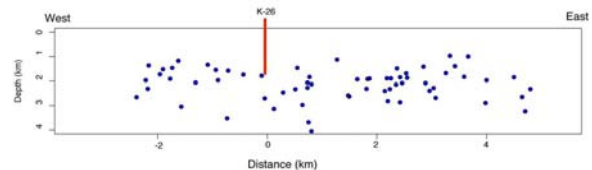
OBSERVATIONS AND MEASUREMENTS OF SWS

Seismicity

Figure 2a shows the epicenters of seismic events located from July 5th to August 11th and Figure 2b shows the depth distribution of some selected events along E-W and N-S cross-sections respectively. The velocity model used in the locating is from Brandsdottir et al. (1997). Although these are preliminary locations, it is apparent that epicenters roughly align along the E-W direction, while hypocenters are shallow around the injection well. Most focal depths are shallower than 4 km.



(a)



(b)

Figure 2. The seismicity recorded by UNC array from July 15th to August 11th is shown in (a). Totally 129 events are located and the depth distribution of the events located around the injection well K-26 (inside the rectangle) is shown in (b).

Seismicity at Krafla is not very high. Most events appear to be related to the on-going injection, while a few deep ones appear independent on injection. However, so far no clear relationship has emerged between injection changes and seismicity rates. During the 35 days of operations the array detected an average of 5 to 6 well-recorded events per day

(observed at 5 or more stations). These are very small earthquakes with magnitudes probably no greater than 2.

Recording seismicity at Krafla is complicated by the high level of seismic noise in the area, most of it resulting from vibrations of the steam pipes, routine plant operations, tourists, and local traffic, etc. To avoid strong sources of noise, several stations were relocated to quieter sites. Stations deployed in well cellars had a mixed performance, some noisy and some not. In spite of occasional and instrumental interruptions the UNC array performed excellently, recording over 300 GB of data in 35 days.

Shear-wave Splitting

Shear-wave splitting (SWS) is an exploration method of proven reliability and unique imaging power based on the analysis of polarizations and time delays of shear waves distorted by the anisotropic properties of the propagating medium, since no other imaging method detects both the direction and intensity of cracking. The method is based on the fact that a shear-wave propagating through rocks with stress-aligned micro-cracks (also known as *extensive dilatancy anisotropy* or EDA-cracks) will split into two waves, a fast one polarized parallel to the predominant crack direction, and a slow one, polarized perpendicular to it. The phenomenon is very similar to optical birefringence, whereby light transmitted through an anisotropic crystal undergoes analogous splitting and polarization parallel and perpendicular to the alignment of atoms in the crystal lattice. In the seismic case, the polarization direction of the fast split shear wave parallels the strike of the predominant cracks regardless of its initial polarization at the source (Crampin et al., 1986; Peacock et al., 1988). The differential time delay between the arrival of the fast and the slow shear waves (typically a few tens of milliseconds) is proportional to crack density, or number of cracks per unit volume within the rock body traversed by the seismic wave (Hudson, 1981; Crampin, 1987; Crampin and Lovell, 1991). In cracked reservoirs such as Krafla the anisotropy is likely caused by aligned systems of open, fluid-filled micro-fractures. Fortunately, the anisotropy effects on seismic waves induced by small, aligned open cracks in an otherwise isotropic rock are indistinguishable from those produced by an unfractured, but transversely isotropic medium.

Shear-wave splitting is clearly recorded in Krafla. In fact, we have recorded unusually well developed splitting that strongly points to the prevalence of at least two major crack systems oriented approximately N-S and E-W. SWS detects the predominant ~N-S fabric related to the rifting, but also provides strong evidence for an equally pervasive ~E-W lineament of

subsurface fractures roughly north and east of the injection well.

Measuring the Polarization and Time Delay

The polarization direction of the fast split shear-wave is parallel to the strike of the predominant cracks, regardless of its initial polarization at the source, and the time delay between the fast and the slow waves is proportional to the crack density. These split shear-wave properties (fast shear-wave polarization direction φ and differential time delay δt) thus constitute valuable data set to invert for the subsurface fracture geometry and to estimate the crack density and permeability anisotropy within fractured geothermal reservoirs, such as Krafla geothermal field. An important limitation to shear-wave splitting analysis is that seismic rays must be within the shear-wave window of the seismic stations. This window can be visualized as a right circular cone with vertex at the station and vertex angle $i_v = \sin^{-1}(\beta/\alpha)$, where α and β are the P- and S-wave surface velocities, respectively. For angles of incidence greater than i_v , shear waves interactive strongly with the free surface, distorting the incoming waveform (Booth and Crampin, 1985). For a half space with a typical Poisson's ratio of 0.25, the window's vertex angle, as measured from the vertical, is equal to 35°.

For the purpose of this study, we use φ and δt measurements from Krafla that correspond to high signal-to-noise ratio seismograms displaying linear horizontal particle motion and a clear well-defined shear-wave splitting event. Polarization diagrams (also known as particle motion plots) are used to accurately detect the marked switch in polarity of the two orthogonally polarized fast and slow shear-waves and to measure the split parameters (φ and δt). The polarity switch provides the clearest indication of splitting and thus of medium anisotropy. Time delays are measured after the seismogram is rotated to orient the fast and the slow waves along the instrument horizontal components. This operation cleanly decouples the two shear-wave arrivals allowing for direct and accurate measurement of the time delay. Time delays are normalized to the length of the raypath, presumed to be entirely fractured. This assumption is reasonable given that typical event depth does not exceed 4 km.

So far the data from five selected stations (P03, P04, P10, P13, and P23) have been investigated to measure the fast shear-wave polarization and time delay. These stations are selected because they either recorded the data of best quality (P13, P23) or have a relatively good coverage of raypaths coming from different azimuths (P03, P04, P10, P23). Station P13 had recorded the best data with highest signal-to-noise ratio of all the stations in the array but

unfortunately, its DAS (Data Acquisition System) was faulty and recorded no data from July 9 to 13 and was replaced with a new DAS on July 25. Station P23 was the previous P05 which was moved to the new location in order to avoid the high seismic noise there. Figure 3 shows the rose diagrams (polar histograms) of fast shear-wave polarization directions observed within the shear-wave window of the five stations. The bin size in the rose diagrams is 10° and the length of each bin is proportional to the number of polarizations within it. It can be seen from Figure 3 that the predominant polarization directions observed for stations P13 and P23 are close to E-W and those for stations P04 and P10 are close to N-S direction, while P03 shows a distinct subset of polarizations striking N-S in addition to and almost perpendicular to the main polarization set in E-W direction.

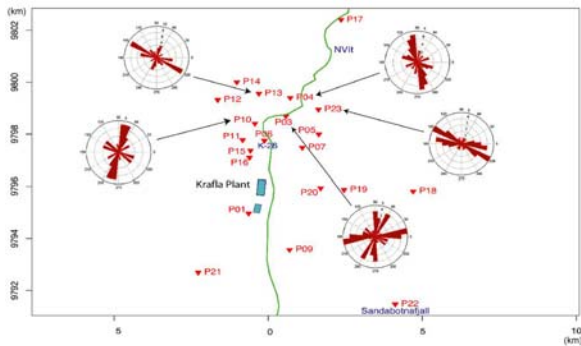


Figure 3. Rose diagrams of the fast shear-wave polarization directions observed at the five stations.

To inspect the azimuthal distribution of polarization angles, equal-area projection plot of the observed polarizations at station P13, as an example, is shown in Figure 4a. For all the five stations most shear-wave splitting events within the shear-wave window come from the NE and SE quadrants and fewest from the SW quadrant, which can be compared with the distribution of located epicenters in Figure 2a. Shown in Figure 4b is the equal-area projection plot of the observed time delays which are already normalized to the length of the corresponding raypath.

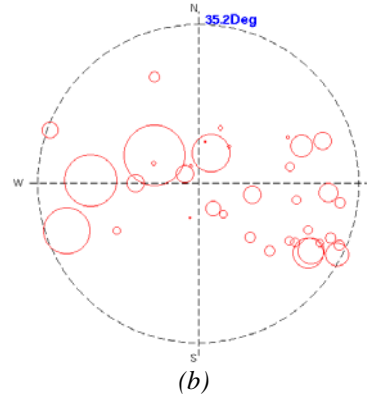
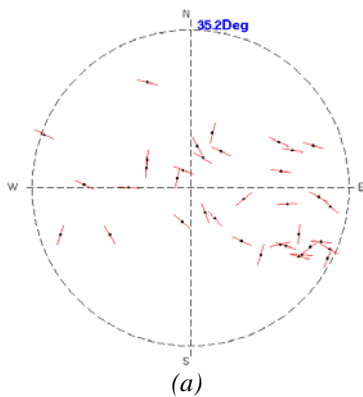


Figure 4. Observed fast shear-wave polarization angles (a) and differential time delays (b) at station P13 plotted in equal-area projection. The biggest circle corresponds to a time delay of 34 ms/km and the smallest to 1 ms/km. The shear-wave window is 35.2° .

INVERSION METHOD AND RESULTS

The pairs of anisotropy-related parameters, fast shear-wave polarization direction ϕ and differential time delay δt , read from many seismograms recorded at the five selected seismic stations at Krafla may provide a preliminary means of detecting the key subsurface fracture characteristics in the reservoir. Polarization orientations help delineate stress-aligned crack directions that represent potential conduits for subsurface fluid flow, while crack densities inferred from differential time delays may offer good prospects of depicting target-zones of increased cracking density and rock permeability within the reservoir rocks. To avoid potential ambiguity, it is worthwhile to mention that in an anisotropic medium, aligned fast shear-wave polarization orientations are independent of the initial polarization of the shear-wave at the source and are mainly caused by the medium's anisotropy (e.g. Crampin et al., 1986; Peacock et al., 1988; Crampin and Lovell, 1991).

Methodology

We use an inversion scheme employing both shear-wave splitting parameters ϕ and δt (Yang, 2003). As previously discussed, ϕ mainly depends on the angle between the crack normal and the seismic ray while δt is proportional to the crack density along the raypath. Station-by-station inversion for subsurface crack strike, dip and density is performed through successive trial-and-error comparisons of observed and theoretical fast shear-wave polarizations and associated time delays plotted in equal-area projections as functions of ray azimuth and angle of incidence. The trial-and-error process is guided, in the sense that the fit of a given crack model is interactively optimized by displaying the history of

all previous trial-and-error events, so that current results guide the next update trial until convergence to the best solution is achieved. Simultaneous minimization of both φ and δt residuals is accomplished by a non-linear least-squares algorithm whereby the goodness-of-fit of a given crack model is evaluated based on the root mean square (RMS) estimates given by

$$RMS(\varphi) = \left\{ \frac{1}{N-2} \sum_{n=1}^N ((\varphi_o)_n - (\varphi_t)_n)^2 \right\}^{1/2} \quad (1)$$

$$RMS(\delta t) = \left\{ \frac{1}{N-2} \sum_{n=1}^N ((\delta t_o)_n - (\delta t_t)_n)^2 \right\}^{1/2} \quad (2)$$

where φ_o and φ_t are observed and theoretical fast shear-wave polarization angles respectively, δt_o and δt_t are observed and theoretical differential time delays respectively, and N is the number of observations recorded at a given seismic station.

Essentially, inversion efforts are expected to identify regions of different crack densities in Krafla geothermal field and invert for 3-D fracture geometry in the subsurface. Based on seismic ray coverage and depending on the spatial patterns and azimuthal distributions of observed polarizations and time delays in the equal-area projection plots, crack-induced anisotropy is modeled by 1) a single system of vertical cracks, 2) a single system of non-vertically dipping cracks, or 3) two intersecting sets of vertically and/or non-vertically dipping cracks. Most of the stations we have analyzed so far showed just one chief polarization direction (Figure 3). The recording of a single prevalent polarization may in general be accounted for by anisotropic effects due to parallel vertical cracks. In this case, the chief polarization orientation is parallel to the strike of the main crack system in the neighborhood of the station. Station P03, however, showed two almost equally dominant polarization directions, which may provide important clues on the geometry of subsurface fractures and should not be regarded as scattering noise, especially if their distribution fits particular azimuthally dependent patterns.

In addition to the trial-and-error process described above, a more self-consistent algorithm was developed for inverting the measurements of polarizations and time delays of split shear waves. Such a multi-response (φ and δt) inversion problem as above can be reduced to two connected single-response processes due to the following three features of the shear-wave splitting data. 1) Either the polarization or the time delay dataset is mathematically adequate by itself to invert for fractures. 2) Polarization data are basically insensitive to the variations in crack density. 3) The measurement of time delays technically involves much more uncertainties than that of polarizations.

More specifically, crack strike and dip are mainly modeled from polarizations while crack density is modeled from delay times. In order to implement the inversion scheme, a 2-D model plane is defined in which the x -axis represents the crack strike and the y -axis the complement of the crack dip, both spanning the range from -90° to 90° . The root mean square of the residue functions (RMSRF) are computed at specific points in this plane (by default, these points lie on a $1^\circ \times 1^\circ$ resolution grid) and their distributions are visualized by contouring. According to the nonlinear least squares rule, the estimated crack model is inferred from the point where the absolute RMSRF minimum is located.

Preliminary Inversion Results

To model the effects of crack-related anisotropy (in terms of crack strike, dip and density) on shear-wave splitting behavior, the fractured medium is represented by an elastic continuum with anisotropic properties that reflect the crack's configuration. This representation applies to wavelengths that are significantly longer than individual crack dimensions. We use the elastic stiffness proposed by MacBeth (1999) for Transverse Isotropic (TI) conditions, which includes a first order perturbation to the isotropic elastic constants, to simulate the general 3-D mechanical properties of the fractured solid. By evaluating the eigenvalues and eigenvectors of the corresponding Christoffel matrix, which depend on the medium stiffness and direction of wave propagation, synthetic fast shear-wave polarizations, shear-wave phase velocities, and associated differential time delays can be calculated for prescribed transversely isotropic models (Babuska and Cara, 1991; Tsvankin, 2001).

The preliminary inversion results for crack strike, crack dip, and crack density using the measured fast shear-wave polarization directions and differential time delays from the five selected seismic stations in Krafla geothermal field are listed briefly in Table 1. Compared to the results of other stations, the shallow dip angle and high crack density inverted for P04 may indicate that the fracture model of a single set of vertical or non-vertically dipping cracks is probably not appropriate in this case. All the other inversion results are generally consistent with the assumption of the single set model in terms of their steep dip angles and relatively low crack densities. The crack strikes for stations P13 and P23 are close to E-W direction while at station P10 the strike is almost in N-S direction. These results again show that there may exist two different systems of fractures in Krafla, which is not very surprising. The fitting between the observed and theoretical fast shear-wave polarizations for station P13 is plotted in equal-area projection and shown in Figure 5. The fitting is generally good although there are still some cases in

which the observed and theoretical polarizations are nearly perpendicular to each other. These perpendicular cases may provide important clues to the possible relation between the subsurface crack systems and changes in water pressure as will be discussed in the following section.

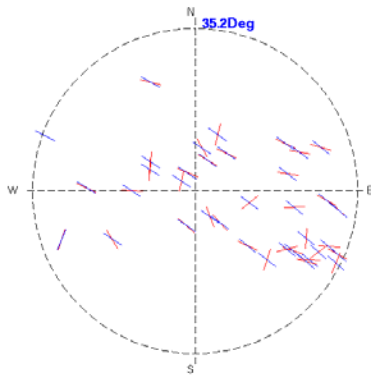


Figure 5. The fitting between the observed and theoretical fast shear-wave polarizations for station P13 plotted in equal-area projection. The red line segments are observed and blue ones are theoretical.

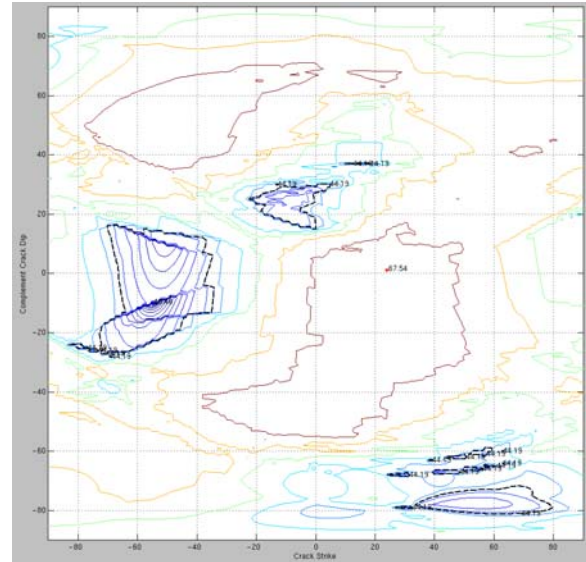
Shown in Figure 6 are the residual contours computed for stations P13 and P23 for the purpose of determining the crack strike, crack dip and crack density corresponding to the minimum of residuals in fast shear-wave polarizations and/or differential time delays. It is anticipated that the resulting pairs of crack strike and crack dip inferred from the global RMSRF minima in both residual contours are the same or very close to each other as the case for station P23 is, but actually the results from the two contours may be quite different from each other, probably because, as stated before, the measurement of time delays technically involves much more uncertainties than that of polarizations. For this reason we have listed in Table 1 only the results inverted for using the trial-and-error method for each analyzed station.

Table 1. Inversion results of crack parameters with trial-and-error method.

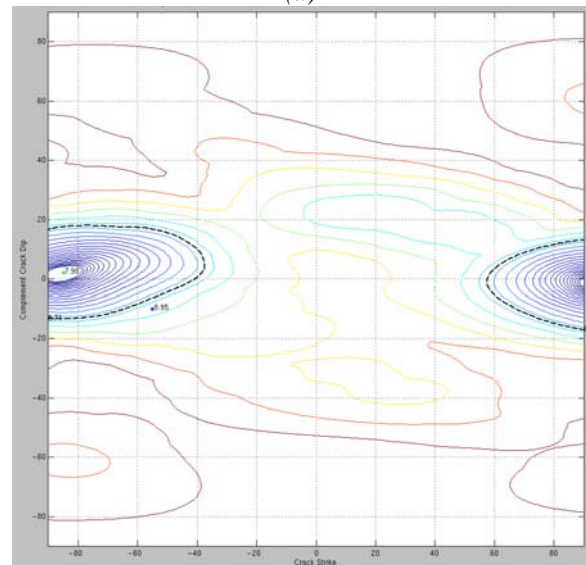
Station ID	Crack Strike (Degree)	Crack Dip (Degree)	Crack Density
P03	82	-55	0.065
P04	71	-16	0.072
P10	-1	73	0.027
P13	-55	80	0.024
P23	-73	-74	0.027

DISCUSSION AND CONCLUSION

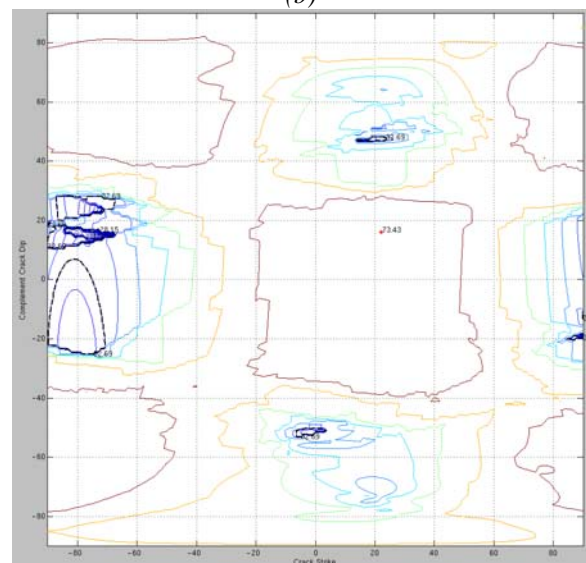
A 20-station, 3-component digital seismic array was deployed around the Krafla geothermal field in Iceland in July and August of 2004, and the seismic



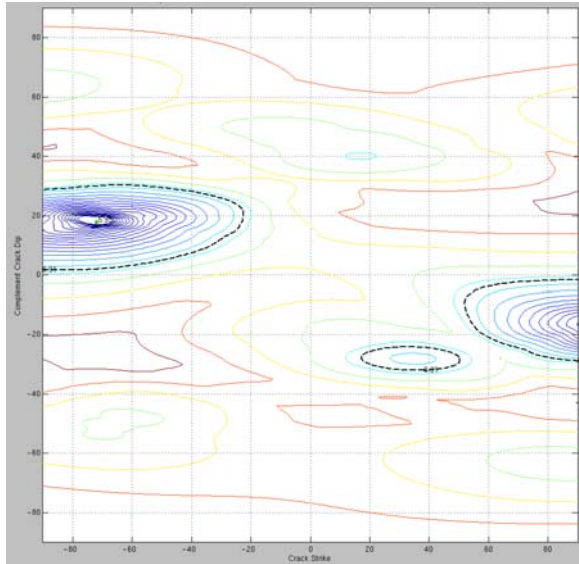
(a)



(b)



(c)



(d)

Figure 6. Residual contours computed for stations P13 and P23 to invert for the crack strike, dip and density. (a) The global minimum of polarization residual for P13 is located at strike=-55° and dip=80°. (b) The global minimum of time delay residual for P13 is located somewhere else. (c) The global minimum of polarization residual for P23 is located at strike=-73° and dip=-74°. (d) The global minimum of time delay residual for P23 is located at the same pair of strike and dip as in (c).

data set we have collected there is unique. We have also monitored the injection stoppage and resumption and collected data at a sampling rate of 500 sps which is high enough to allow detection of even the smallest variations in crack density and the possible flow of fluids through the crack system. The seismicity in the Krafla field is not very high (3-4 usable events per day), with most epicenters located along an E-W oriented belt north of the injection well and typical focal depths shallower than 4 km.

There is clear evidence of shear-wave splitting in the seismic data. In addition to the observed prevalence of a crack system oriented in approximately N-S direction which is consistent with the anticipated direction of major fractures in the area, fast shear-wave polarization directions along a general E-W direction are also persistent, more than along any other direction as shown in stations P13 and P23. The highest intensity of cracking detected so far occurs along N70-80E directions (stations P03 and P04), and most cracks have a relatively deep dipping angle.

In order to investigate the response of subsurface crack systems to changes in fluid pressure inside the medium, the injection in well K-26 was stopped for ten days before resumed on July 26. There is

preliminary evidence that the injection modifies the observed crack polarizations in some areas. In Figure 5 we can see that except for the prevalent nearly E-W polarizations, there are still a few cases whose polarizations are close to N-S. Two of these “irregular” events have been identified as shortly after the stoppage of injection and five as after the resumption. This may imply that changes in water pressure have to some extent changed the effects of the cracks on the polarization angles of the fast shear-wave propagating through them.

In hindsight it became clear that most of the 20 stations of the array had been placed in optimal locations to retrieve seismic information for fracture characterization. We expect that with a permanent array at these locations the field can be accurately monitored.

REFERENCES

- Babuska, V. and Cara, M. (1991), *Seismic Anisotropy in the Earth*, Modern Approaches in Geophysics, Vol. 10, pp. 217, Kluwer Academic Publishers, The Netherlands.
- Booth, D.C. and Crampin, S. (1985), “Shear-wave polarizations on a curved wavefront at an isotropic free-surface”, *Geophys. J. Roy. Astr. Soc.*, **83**, 31-45.
- Brandsdottir, B., Menke, W., Einarsson, P., White, R.S., and Staples, R.K. (1997), “Faroe-Iceland Ridge Experiment 2. Crustal structure of the Krafla central volcano”, *J. Geophys. Res.*, **102**, 7867-7886.
- Einarsson, P. (1978), “S-wave shadows in the Krafla caldera in NE-Iceland, evidence for a magma chamber in the crust”, *Bull. Volcanol.*, **41**, 1-9.
- Crampin, S. (1987), “Geological and industrial implications of extensive dilatancy anisotropy”, *Nature*, **328**, 491-496.
- Crampin, S., Booth, D.C., Krasnova, M.A., Chesnokov, E.M., Maximov, A.B., and Tarasov, N.T. (1986), “Shear-wave polarizations in the Peter the First range indicating crack-induced anisotropy in a thrust-fault regime”, *Geophys. J. Roy. Astr. Soc.*, **84**, 401-412.
- Crampin, S. and Lovell, J.H. (1991), “A decade of shear-wave splitting in the Earth’s crust: What does it mean? What use can we make of it? And what should we do next?” *Geophys. J. Int.*, **107**, 387-407.
- Hudson, J.A. (1981), “Wave speeds and attenuation of elastic waves in materials containing cracks”, *Geophys. J. Roy. Astr. Soc.*, **64**, 133-150.

Peacock, S., Crampin, S., Booth, D.C., and Fletcher, J.B. (1988), "Shear-wave splitting in the Anza seismic gap, southern California: temporal variations as possible precursors", *J. Geophys. Res.*, **193**, 3339-3356.

Tryggvason, E. (1986), "Multiple magma reservoirs in a rift zone volcano: Ground deformation and magma transport during the September 1984 eruption of Krafla, Iceland", *J. Volcanol. Geothermal Res.*, **28**, 1-44.

Tsvankin (2001), *Seismic Signature and Analysis of Reflection Data in Anisotropic Media, Handbook of Geophysical Exploration, Section I, Seismic Exploration*, 1st edn, Vol. 29, pp. 436, Pergamon, Amsterdam, New York.

Yang, M. (2003), *Inversion of shear-wave splitting data in geothermal reservoirs*, Master's thesis, University of North Carolina, Chapel Hill, NC.

USING GEODETIC DATA TO UNDERSTAND HYDROTHERMAL FLUID FLOW

D. W. Vasco

Berkeley Laboratory
University of California
Berkeley, CA 94720, USA
e-mail: dwvasco@lbl.gov

M. Battaglia

Department of Structural Geology and Geodynamics
University of Goettingen, Goldschmidtstr. 3
37077 Goettingen, Germany.
e-mail: mbattag@gwdg.de

ABSTRACT

Fluid flow in hydrothermal and magmatic systems frequently induces observable surface deformation. Such deformation can be used to better understand the factors controlling flow, for example, the role of faults as conduits or barriers to flow. In this paper we describe how surface deformation data can be used to obtain qualitative and quantitative information about subsurface flow associated with hydrothermal systems. Examples from hydrothermal/magmatic systems at Long Valley and Yellowstone are described. At Long Valley, GPS, levelling, and EDM data are used to determine the distribution of volume change in the subsurface. The source model contains two prominent features beneath the resurgent dome: one following the regional trend of north-south faults, and another parallel to a strike-slip fault that is the locus of most of the seismic activity in the calderas south moat. An inversion of Interferometric Synthetic Aperture Radar (InSAR) observations from the Yellowstone region indicated that two cross-cutting fault systems are interacting with an underlying magma body to produce rapid and complicated surface deformation.

INTRODUCTION

The flow of fluids associated with magmatic and geothermal systems is often poorly understood. Typically, fluid flow is constrained by sparsely distributed well data. The sampling provided by well

data is complicated, depending on the hydraulic connection between flow in the well and flow in the surrounding formation. Thus, well data do not provide a simple, detailed picture of subsurface flow and transport. Frequently, micro-seismic studies are used to better understand subsurface flow in geothermal areas. However, the relationship between micro-seismicity and pressure and temperature changes in the subsurface is complicated and strongly influenced by mechanical heterogeneity and regional and local stress fields. Time-lapse geophysical data could potentially provide high-resolution, three-dimensional images of changes in seismic velocity and electric conductivity that may be related to saturation and pressure changes at depth. Currently, primarily due to their expense, such surveys are not conducted at geothermal fields.

Geodetic data provide another source of information related to the movement of fluids at depth. Geodetic observations are of somewhat intermediate resolution. That is, they do not provide the high-resolution of active time-lapse geophysical surveys but they typically provide more constraints than well information. In addition, geodetic data are often directly related to volume change at depth which may be interpreted in terms of fluid movement and temperature changes. Thus, geodetic observations, such as Global Positioning System (GPS), leveling, EDM, and Interferometric Synthetic Aperture Radar (InSAR) measurements, can provide an important tool for understanding the factors controlling fluid movement in a hydrothermal system. In this paper we outline an approach for using surface deformation data. The potential of this approach is illustrated by

applications at the Long Valley Caldera in California and the Yellowstone Caldera in Wyoming.

METHODOLOGY

Inference of Subsurface Volume Change

Our goal is to image processes related to hydrothermal fluid flow. Fluid mass and temperature changes within the Earth give rise to effective volume changes. Such volume changes induce deformation which results in surface displacement. Specifically, volume change within an elastic or poroelastic Earth gives rise to the displacement of its surface (Mogi 1958, Segall 1985). The relationship between a distribution of volume change $\Psi(\mathbf{y})$ within the Earth and the i -th component of surface displacement, u_i , is given by the integral

$$u_i(\mathbf{x}) = \int_V g_i(\mathbf{x}, \mathbf{y}) \Psi(\mathbf{y}) d\mathbf{y}$$

where g_i is the Greens' function or point source response. For a homogeneous elastic half-space it is given by (Vasco et al. 1988)

$$g_i(\mathbf{x}, \mathbf{y}) = \frac{(V+1)}{3\pi} \frac{(x_i - y_i)}{S^3}$$

where V is the Poissons' ratio of the half-space and S is the distance between the observation point and the location of the point volume change. The integral expression for u_i provides a linear relationship between the i -th component of displacement and the volume change in the subsurface.

As described in Vasco et al. (2000) we may convert the above integral into a sum by representing the subsurface volume by a finite number of M non-overlapping cells. Each cell may undergo a distinct fractional volume change, denoted by ψ_j for the j -th cell or grid block. The contribution to the l -th component of displacement at \mathbf{x} due to the fractional volume change of the grid block, ρ_{lj} , is an integral over the volume of the j -th grid block V_j ,

$$\rho_{lj}(\mathbf{x}) = \psi_j \int_{V_j} g_l(\mathbf{x}, \mathbf{y}) d\mathbf{y}.$$

The total l -th component of displacement at an observation point \mathbf{x}_i is simply a sum over the complete set of M grid blocks

$$\rho_l(\mathbf{x}_i) = \sum_j L_{ijl} \psi_j$$

where L_{ijl} is the integral

$$L_{ijl} = \int_{V_j} g_l(\mathbf{x}_i, \mathbf{y}) d\mathbf{y}.$$

Given a number of displacement observations we may constrain the volume change in the subsurface. For a set of N observations there corresponds a linear system of N equations. Let us scale each equation by its standard error σ_i and consider the least squares minimization of the residuals. That is, the minimization of the sum

$$\Pi_d = \sum [d_{li} - \sum_j \Gamma_{ijl} \psi_j]^2$$

where

$$d_{li} = \frac{\rho_{li}}{\sigma_i}$$

and

$$\Gamma_{ijl} = \frac{L_{ijl}}{\sigma_i}$$

are the scaled data and matrix coefficients, respectively.

Sparse geodetic observations provide limited depth resolution and there are trade-offs between the shape of the volume change and the depth of the volume change (Dieterich and Decker 1975). Thus, the system of linear constraints on the volume change model is likely to be ill-conditioned and any solutions will be unstable with respect to perturbations in the observations and the coefficients. To address this instability, the constraints provided by the data are augmented by regularization terms that bias the model towards a smoothly varying solution (Menke 1984). The model roughness is measured by the magnitude of its spatial derivative vector

$$\Pi_r = \sum_j [D_j \psi_j]^2$$

where D_j is a finite difference approximation to the spatial derivative of the model. That is, an operator which differences the volume change in space, as discussed in Menke (1984). The penalized misfit is given by

$$P = \Pi_d + W_r \Pi_r$$

where W_r is the weight which controls the relative importance of fitting the observations and obtaining a smooth model.

APPLICATIONS

Long Valley Caldera

The Long Valley volcanic area (Fig. 1) has been active for the past 3 million years. A massive eruption 0.76 Ma ago resulted in the deposition of 600 cubic kilometers of Bishop Tuff and the

simultaneous subsidence of the magma chamber roof, creating the present 17-by-32 km oval depression of the Long Valley Caldera. The formation of the caldera was followed by resurgence and four major episodes of volcanic activity (Hildreth 2004).

Recent unrest began in May of 1980 with a strong earthquake swarm at the southern margin of the caldera (Bailey & Hill 1990). The seismic activity was accompanied by the uplift of the resurgent dome in the central portion of the caldera. Substantial deformation was also observed during the summer and fall of 1997. Following that the caldera has been relatively quiet, with no significant deformation since the spring of 1998 (Fig. 1; Langbein 2003).

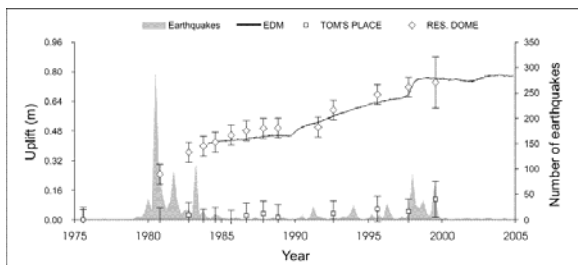


Figure.1. Long Valley caldera unrest. The plot shows the number of $M > 3.0$ earthquakes, the uplift at the resurgent dome (benchmark W911) and at Tom's Place (several km outside the caldera), and the extension of the CASA-KRAK baseline (EDM), a proxy of resurgent dome vertical deformation.

Several models have been developed to explain the deformation and seismicity within the caldera (Sorey et al. 2003). Two-color EDM and leveling surveys indicate that the intrusion of a magma body beneath the resurgent dome, and right lateral strike slip within the south moat of the caldera are the principle sources of deformation (Langbein et al. 1995; Langbein 2003). Radar interferometry (Thatcher & Massonet 1997; Fialko et al 2001), GPS surveys (Marshall et al. 1997) and gravity measurements (Battaglia et al. 2003b) confirm the intrusion beneath the resurgent dome. There is evidence that intrusion is also occurring beneath the south moat and Mammoth Mt (Sorey et al. 1993; Hill et al. 2003).

We can better constrain the source of inflation by combining various types of geodetic data. The United States Geological Survey (USGS) began an extensive geodetic monitoring program in Long Valley in 1980 (Bailey & Hill 1990). Data collected include levelling surveys from 1980 to 1997 (Savage et al. 1987; Langbein et al. 1995), and measurements of horizontal deformation using a two-color geodimeter (from 1985; Langbein et al. 1995) as well as GPS observations (from 1994; Marshall et al.

1997). The last complete leveling survey occurred in July and August of 1992.

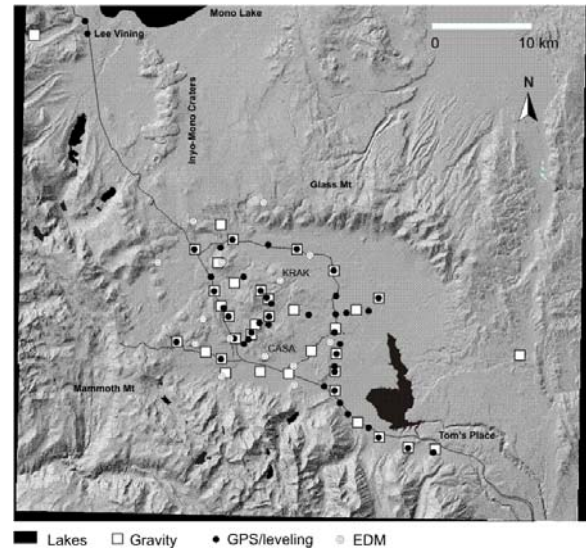


Figure.2. Map of Long Valley caldera. The map shows the leveling routes, the two-color EDM geodetic network, the leveling sites occupied with GPS, and the gravity network.

In an effort to update the vertical deformation measurements within the caldera, 44 of the existing leveling monuments in Long Valley were re-occupied in July 1999 (Fig. 2) using dual frequency GPS receivers (Battaglia et al 2003a).

The source model is constructed by first sub-dividing the volume beneath the caldera into a set of non-overlapping cells or grid-blocks, as described in Vasco et al. (1988) and Vasco et al. (2000). Each block in the grid may undergo a distinct fractional volume change. The displacement at any point on the surface is the integrated response to changes over the entire grid. For the most part, surface deformation observations cannot resolve detailed volume change variations with depth (Dieterich and Decker 1975). For this reason, we prescribe the depth boundaries of our model grid. Based upon earlier point source investigations and physical considerations, we adopt a three layer grid with depth boundaries: 5-7 km, 7-9 km, and 9-11 km. Each layer is further sub-divided into a 41 (east-west) by 41 (north-south) grid of cells. Because the observed surface deformation is linearly related to the fractional volume change of each grid block, each observation contributes a linear constraint on the volume change of the cells in the grid (Vasco et al. 1988).

Given an adequate distribution of data we may estimate the volume change distribution within the

grid. Specifically, using a regularized, linear least-squares procedure we can solve for the spatial distribution of volume change (Vasco et al. 2000). The resulting distribution of fractional volume change in the uppermost layer of the model is shown in Figure 3.

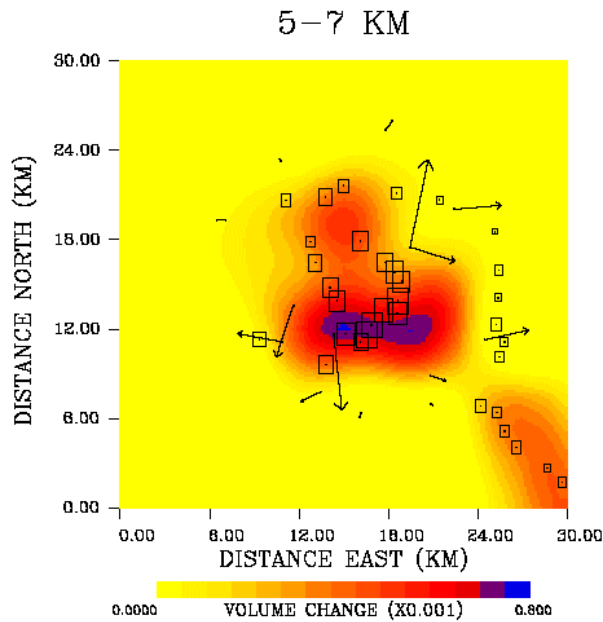


Figure 3. Volume change in the depth interval of 5 to 7 km.

Dark reds and blues in Figure 3 signify greater fractional volume change. The largest fractional volume change forms a dominantly east-west body. In addition, a north-south trending component of fractional volume change roughly parallels a system of north-northwest trending faults within the caldera. This component extends from the east-west anomaly to the northern edge of the caldera. The volume change in the deeper layers (7-9 km, 9-11 km) is much smaller in amplitude and similar in pattern to the overlying layer shown in Figure 3, most likely due to the poor depth resolution provided by the surface deformation data.

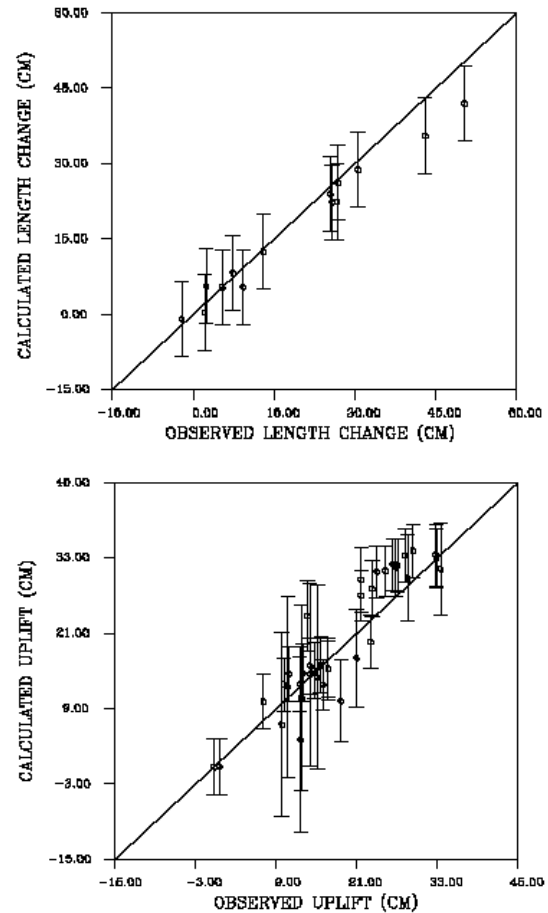


Figure 4. Fit to data. Comparison between the single source and distributed source models.

The fits to both the EDM and GPS data are shown in Figure 4. For the most part the model fits the geodetic observations within their associated errors.

Yellowstone Caldera

The Yellowstone volcanic system is a tectonically active region, shaped by three caldera-forming eruptions (Vasco et al. 1990). Current volcanic activity is thought to be driven by a body of hot, crystallizing magma located at least 8 km deep. Based upon Interferometric Synthetic Aperture Radar (InSAR), the ground surface over the caldera has been observed to be in an almost constant state of motion (Wicks et al. 1999). For example, between 1992 and 1995 much of the caldera was involved in approximately 2 cm of subsidence per year (Figure 5). The surface deformation provides some clues to the structures controlling fluid flow at depth. In order to better understand the factors influencing fluid movement in the subsurface we applied the

inversion methodology described above to the InSAR data shown in Figure 5.

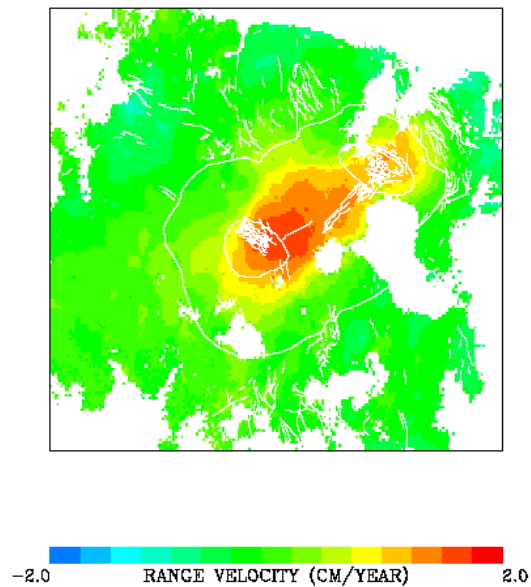


Figure 5. Range velocity between 1992 and 1995. The red colors signify motion away from the satellite due to the subsidence of the surface over the caldera.

Following the methodology outlined above we constructed a three-dimensional grid representing the possible volume change in the subsurface which is compatible with the observed surface deformation. The grid is composed of three layers 6-8, 8-10, and 10-12 km in depth. Each layer is sub-divided into a 41 by 41 grid of non-overlapping grid blocks. Using the least squares formulation outlined above we solve for the distribution of volume change in the grid which can explain the range change shown in Figure 5. The resulting model, shown in Figure 6, contains

several interesting features.

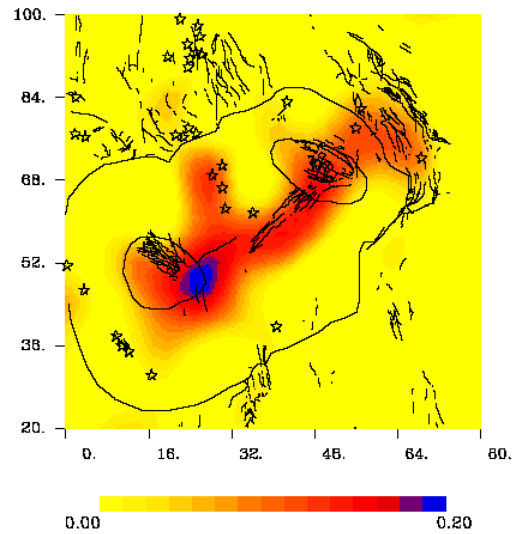


Figure 6. Fractional volume decrease produced by an inversion of the range change observations shown in Figure 5.

The primary volume decrease underlies a northeast trending fault zone, the Elephant Back Fault Zone (EBFZ), which lies along the long axis of the caldera. This fault zone is currently active and offsets recent sediments. The fault zone connects the two resurgent domes within the caldera, which are signified by the closed curves in Figure 6. In addition to volume decreases beneath the EBFZ we observe a linear trend of volume decrease extending almost due north. This feature underlies a string of volcanic vents which fed post-collapse lava flows (stars in Figure 6). The linear trend is heading in the direction of the Norris Geyser Basin which had been the site of renewed hydrothermal activity. Furthermore, more recent InSAR observations indicate significant uplift at the Norris Geyser Basin and in surrounding regions.

CONCLUSIONS

We have presented models of subsurface volume change which are compatible with observed surface deformation data. The distributed source models are very general and exploratory in nature. They offer insight into the dynamics of fluid movement at the Long Valley Caldera and at the Yellowstone Caldera.

At Long Valley the subsurface fractional volume change is suggestive in that it underlies existing north-trending faults. In addition, the east-west component of volume change parallels a hypothesized east-west fault in the south moat region. Furthermore, the east-west component of volume change connects two sets of north-south trending faults. The more easterly set extends from the central

caldera to the south, the other set cuts northward through the interior of the caldera (Figure 3).

The model helps shed light on the relation between deformation and seismicity. According to the existing interpretation (e.g., Sorey et al. 2003), dominant sources contributing to the deformation and seismicity within the caldera include (Fig. 3): (1) aseismic inflation of a source centred at approximately 6 km beneath the resurgent dome; (2) seismic inflation of a deeper one (10-20 km) beneath the South Moat Seismic Zone (SMSZ); and (3) right-lateral strike-slip motion on a series of west-northwest-striking faults in the 10-km-wide SMSZ (Langbein 2003).

At Yellowstone, the inversion of InSAR data suggest that volume change is concentrated beneath the Elephant Back Fault Zone (EBFZ) which cuts across the caldera. This fault zone connects the two resurgent domes within the Yellowstone Caldera. The fault zone has been the site of recent deformation. In addition, the pattern of subsurface volume change suggests that a north-south oriented fault or fracture zone is controlling fluid flow above the Yellowstone magma body. The deformation at Yellowstone appears to be due to the interaction of the EBFZ, the north trending fault/fracture zone, and an underlying magma body.

The association of subsurface volume change with mapped faults and earthquakes may be due to existing faults acting as conduits for fluid and gas movement beneath the caldera. That is, the faults represent high permeability zones. Alternatively, the faults may represent zones of weakness (or mechanical heterogeneity) which concentrate deformation. Or both processes may be operating in concert, and faults may concentrate fluid and gas flow as well as concentrating deformation.

ACKNOWLEDGEMENTS

This work was performed under the auspices of the U.S. Department of Energy by the Lawrence Berkeley National Laboratory. Support was provided by the Assistant Secretary for Energy Efficiency and Renewable Energy, Office of Geothermal Technologies of the U.S. Department of Energy under contract No. DE-AC03-76SF00098.

REFERENCES

Bailey, R.A. (1989), Geologic map of Long Valley Caldera, Mono-Inyo Craters volcanic chain, and vicinity, eastern California, Map **I-1933**, United States Geological Survey, Reston.
Bailey, R. A. & Hill, D.P. (1990), Magmatic unrest at Long Valley Caldera, California, 1980-1990, *Geoscience Canada* **17**, 175-179.

Battaglia M. & Segall, P. (2004), The Interpretation of gravity changes and crustal deformation in active volcanic areas. *Pure and Applied Geophys.*, **161**, 1453 – 1467, 2004.
Battaglia M., Segall, P., Murray, J., Cervelli, P. & Langbein, J. (2003a). The mechanics of unrest at Long Valley caldera, California: 1. Modeling the geometry of the source using GPS, leveling and 2-color EDM data, *J. Volcanol. Geotherm. Res.*, **127**, 195-217.
Battaglia M., P. Segall P. & Roberts, C. (2003b). The mechanics of unrest at Long Valley caldera, California: 2. Constraining the nature of the source using geodetic and micro-gravity data, *J. Volcanol. Geotherm. Res.*, **127**, 219-245.
van den Bogaard, P. & Schirnick, C. (1995). $^{40}\text{Ar}/^{39}\text{Ar}$ laser probe ages of Bishop Tuff quartz phenocrysts substantiate long-lived silicic magma chamber at Long Valley, United States. *Geology* **23**, 759-762.
Dieterich, J.H. & Decker, R.W. (1975). Finite element modeling of surface deformation associated with volcanism. *J. Geophys. Res.* **80**, 4094-4102.
Dixon, T., Mao, A., Bursik, M., Heflin, M., Langbein, J., Stein, R. & Webb, F. (1997). Continuous monitoring of surface deformation at Long Valley Caldera, California, with GPS. *J. Geophys. Res.*, **102**, 12,017-12,034.
Dvorak, J. & Dzurisin, D. (1997). Volcano geodesy: the search for magma reservoirs and the formation of eruptive vents. *Reviews of Geophysics*, **35**, 343-384.
Fialko, Y., Simons, M. & Khazan, Y. (2001). Finite source modelling of magmatic unrest in Socorro, New Mexico, and Long valley, California. *Geophys. J. Intern.* **146**, 191-200.
Hildreth, W., (2004). Volcanological perspectives on Long Valley, Mammoth Mountain, and Mono Craters: several contiguous but discrete systems. *Journal of Volcanology and Geothermal Research*, **136**, 169-198.
Hill D.P., Langbein J.O. & Prejean S. (2003). Relations between seismicity and deformation during unrest in Long Valley Caldera, California, from 1995 through 1999 *Journal of Volcanology and Geothermal Research*, **127**, 175-193.
Jachens, R. & Roberts, C. (1985). Temporal and areal gravity investigations at Long Valley Caldera, California, *J. Geophys. Res.*, **90**, 11,210-11,218.
Langbein, J. (2003). Deformation of the Long Valley Caldera, California: inferences from measurements from 1988 to 2001. *J. Volcanol. Geotherm. Res.*, **127**, 247-267.
Langbein, J., Dzurisin, D., Marshall, G., Stein, R. & Rundle, J. (1995). Shallow and peripheral volcanic sources of inflation revealed by modeling two-color geodimeter and leveling data

- from Long Valley Caldera, California, 1988-1992. *J. Geophys. Res.*, **100**, 12487-12,495.
- Marshall, G., Langbein, J., Stein, R.S., Lisowski, M. & Svarc, J. (1997). Inflation of Long Valley Caldera, California, basin and range strain, and possible Mono craters dike inflation from 1990-94 GPS surveys. *Geophys. Res. Lett.*, **24**, 1003-1006.
- Metz, J.M. & Mahood, G. (1985). Precursors to the Bishop Tuff eruption; Glass Mountain, Long Valley, California. *Journal of Geophysical Research*, **90**, 11,121-11,126.
- Prejean, S., Ellsworth, W., Zoback, M., & Waldhauser, F. (2002). Fault structure and kinematics of the Long Valley Caldera region, California, revealed by high-accuracy earthquake hypocenters and focal mechanism stress inversions, *J. Geophys. Res.*, **107**(B12), 2355, doi:10.1029/2001JB001168.
- Sackett, P.C., McConnell, V.S., Roach, A.L., Priest, S.S. & Sass, J.H. (1999). Long Valley coring Project, 1998—. Preliminary stratigraphy and images of recovered core. *U.S. Geol. Survey Open-File Report*, **99-158**.
- Savage, J.C., Cockerham, R., Estrem, J.E., & Moore, L.R. (1987). Deformation near the Long Valley Caldera, eastern California, 1982-1986. *J. Geophys. Res.*, **92**, 2721-2746.
- Sieh, K. & Bursik, M.I. (1986). Most recent eruption of the Mono Craters, eastern Central California. *J. Geophys. Res.*, **91**, 12,539-12,571.
- Sorey, M.L., McConnel, V.S., & Roeloffs, E. (2003). Summary of recent research in Long Valley Caldera, California. *J. Volcanol. Geotherm. Res.*, **127**, 165-173.
- Sorey, M.L., Kennedy, B.M, Evans, W.C., Farrar, C.D., & Suemnicht, G.A. (1993). Helium isotope and gas discharge variations associated with crustal unrest in Long Valley Caldera, California, 1989-1992. *J. Geophys. Res.*, **98**, 15,871-15,889.
- Thatcher, W. & Massonet, D. (1997). Crustal deformation of Long Valley Caldera, eastern California, 1992-1996, inferred from satellite radar interferometry. *Geophys. Res. Lett.*, **24**, 2519-2522.
- Vasco, D. W., Johnson, L. R., & Goldstein, N. E., (1988). Using surface displacement and strain observations to determine deformation at depth, with an application to Long Valley, caldera, California, *J. Geophys. Res.*, **93**, 3232-3242.
- Vasco, D. W., Smith, R. B., and Taylor, C. L., (1990). Inversion for sources of crustal deformation and gravity change at the Yellowstone caldera, *J. Geophys. Res.*, **95**, 19839-19856.
- Vasco, D. W., Karasaki, K., & Doughty, C., (2000). Using surface deformation to image reservoir dynamics, *Geophysics*, **65**, 132-147.
- Wicks, C., Thatcher, W., and Dzurisin, D., (1999). Migration of fluids beneath Yellowstone Caldera inferred from satellite radar interferometry, *Science*, **282**, 458-462.

EVALUATING HEAT FLOW AS A TOOL FOR ASSESSING GEOTHERMAL RESOURCES

Colin F. Williams

U.S. Geological Survey
345 Middlefield Road
Menlo Park, CA, 94025, USA
e-mail: colin@usgs.gov

ABSTRACT

Recent studies have highlighted an approximate proportionality between the rate of natural heat loss (both advective and conductive) and the electric power production capacity of geothermal reservoirs. This study investigates the possible reasons for these observations and addresses the question of whether heat flow measurements alone can be used to estimate the production potential of geothermal systems or at least provide a basis for assessing the magnitude of the resource. Results from a suite of numerical models for heat transport from reservoirs of varying shapes, sizes and depth extents support the hypothesis that the recoverable thermal energy of some reservoirs can vary over a wide range with little impact on the corresponding surface heat flux.

Transient effects due to cooling or warming over geologic time, as well as thermal anomalies arising from heat sources unrelated to fluid circulation, such as the shallow emplacement of magma, further complicate the relationship. For those geothermal reservoirs at or near a thermal steady state, near-surface heat flow measurements provide a direct measurement of the natural heat flux required to maintain the hydrothermal system and thus yield an approximate estimate of the potential renewable level of production. However, heat flow is best applied as a tool to estimate the thermal energy of a reservoir if the spatial distribution of the observed heat flow anomaly, or complementary geological, geochemical or geophysical data, can be used to constrain the reservoir's temperature and subsurface geometry.

INTRODUCTION AND BACKGROUND

Through the history of geothermal exploration and development a number of techniques have been applied to the problem of characterizing geothermal resources. Muffler and Cataldi (1978) identified four methods for assessing geothermal resources: surface heat flux, volume, planar fracture and magmatic heat budget. The volume method as developed by

Nathenson (1975), White and Williams (1975), Muffler and Cataldi (1978) and Muffler et al. (1979) was quickly established as the standard approach in resource assessments conducted by the USGS and other organizations (e.g., Lovekin, 2004). The volume method is a self-consistent and accurate approach to geothermal resource assessments, provided adequate data are available on the size, depth and thermal state of potential geothermal reservoirs. This need for detailed information on the nature of potential geothermal reservoirs is a significant limitation on the applicability of the volume method, particularly for those reservoirs only known through surface and near-surface observations.

Consequently, the observation by Wisian et al. (2001), that there is a rough proportionality between the rate of natural surface heat loss (both advective and conductive) and electric power production capacity of geothermal reservoirs (Figure 1), raises the question of whether the proportionality can be applied in a new heat flux approach to geothermal resource assessments (e.g., Sanyal, 2004).

ground surface temperature. This thermal energy can be related to electric power production through application of recovery and conversion factors, but given the significant variability of recovery factors among geothermal fields (e.g. Muffler, 1979; Sanyal, 2004; Williams, 2004), the analysis here is restricted to comparisons of reservoir thermal energy to natural heat loss. For comparison with heat loss measurements, this thermal energy can be converted to thermal “power”, P_R , as

$$P_R = H_R / t \quad (2)$$

with t representing a period of exploitation. In the comparisons below t is taken to be 30 years.

The natural heat flux from a geothermal system is the combination of both its advective (e.g., fluid discharge from natural hot springs) and conductive parts. As noted by Wisian et al. (2001), the conductive part usually predominates and is the focus of this study. Near-surface conductive heat flow, q , is measured as

$$q = k \frac{dT}{dz} \quad (3)$$

where k is the thermal conductivity of the rock and dT/dz is the vertical temperature gradient.

Recognizing that ρ , C , and k are approximately constant for any given geothermal reservoir, P_R/q should be relatively constant as long as variations in dimensions of reservoirs are reflected in the magnitude of the surface heat flux. If these variations are not reflected in surface heat flow, P_R/q will vary. In order to address this issue quantitatively, a series of two-dimensional, finite-element, conductive heat flow models were evaluated for reservoirs of varying shape, volume and depth.

Figure 1. Plot of installed geothermal reservoir production capacity versus surface heat loss from Wisian et al. (2001). Solid lines represent ratios of production equal to 10x and 1x surface heat loss.

Figure 1 reproduces the production capacity and surface heat loss data from Wisian et al. (2001). An important aspect of these observations is that the range of power production covers more than three orders of magnitude while the surface heat loss ranges over approximately two orders of magnitude, a result inconsistent with a strict proportionality. In some cases this may reflect incomplete development of a subset of producing geothermal fields or variations in the recovery factor, but consideration of the variables controlling both natural heat loss and reservoir thermal energy suggest this is not the sole explanation.

According to Muffler and Cataldi (1978), the electric power generation potential from an identified geothermal system depends on the thermal energy, H_R , present in the reservoir and the efficiency with which the reservoir thermal energy can be converted to electric power. (Both q and H have been used to represent reservoir thermal energy. In this paper H is used to avoid confusion with the common use of q for heat flow measurements.) This thermal energy is given by

$$H_R = \rho C V (T_R - T_{ref}) \quad (1)$$

where ρC is the volumetric specific heat of the reservoir rock, V is the volume of the reservoir, T_R is the characteristic reservoir temperature, and T_{ref} is a reference temperature, typically close to the average

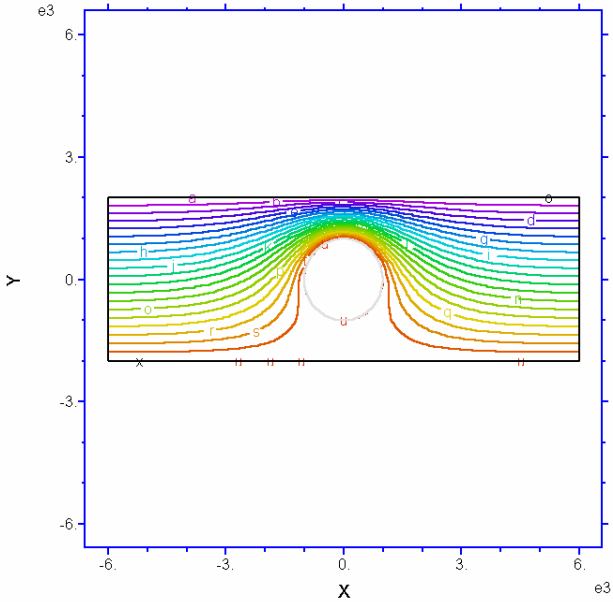


Figure 2. Temperature contours at 10 °C intervals for a 200 °C cylindrical reservoir of 1 km radius, with the top of the reservoir at 1 km depth. Lateral dimensions are in km.

CONSTANT TEMPERATURE RESERVOIRS

The models developed in this study determine subsurface temperatures and heat flow from constant temperature cylindrical and rectangular block reservoirs of varying size and depth. In each model the reservoir temperature was set at 200 °C, the surface temperature at 0 °C, and the thermal conductivity to 2.5 W m⁻¹ K⁻¹. The background geothermal gradient was set to 50 °C km⁻¹, and the depth to the top of each reservoir was varied from 1000 to 3000 meters. The lateral extent of the rectangular block reservoirs ranged from 250 meters to 6000 meters for a reservoir thickness of 1000 meters. Those models with lateral extent substantially greater than the reservoir thickness can be considered representative of relatively thin, laterally extensive reservoirs, such as might be found in the strata of sedimentary basins. Those with lateral extent substantially less than their thickness are considered representative of subvertical, fault-hosted reservoirs such as those found in the Great Basin of the western United States.

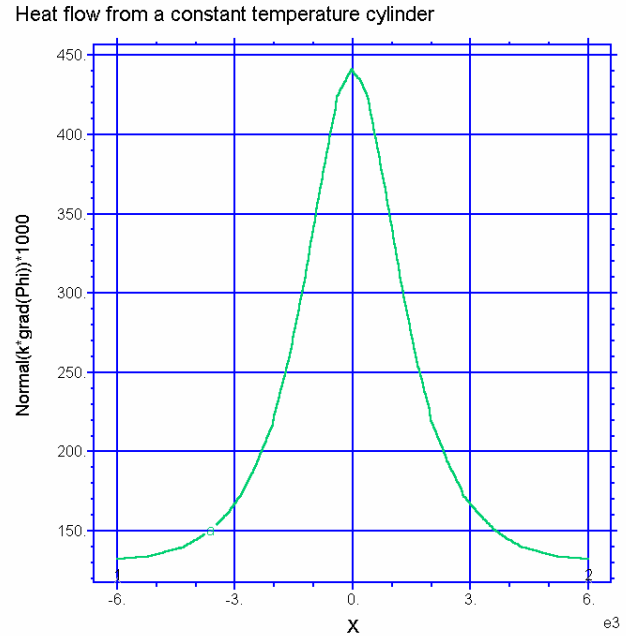


Figure 3. Surface heat flow for the cylindrical reservoir shown in Figure 2.

Figure 2 shows the temperature contours for a cylindrical reservoir with a top at a depth of 1 km and a radius of 1 km. The proximity of the model reservoir to the surface results in a substantial surface heat flow anomaly (Figure 3), with the total additional heat flux due to the geothermal reservoir equal to 1.1 MW for each meter of thickness out of the plane of the model. Figure 4 shows the temperature contours for a rectangular reservoir at 1 km depth with horizontal extent of 4 km and thickness of 1 km. The resulting heat flow anomaly (Figure 5) reflects the greater size and lateral extent of the reservoir.

Figure 6 is a summary of modeled thermal power versus heat loss for the two geometries where the top of the simulated reservoirs is varied from 1 to 3 km. Although the two-dimensional, constant temperature models represent an idealization, the correspondence with the data in Figure 1 is striking.

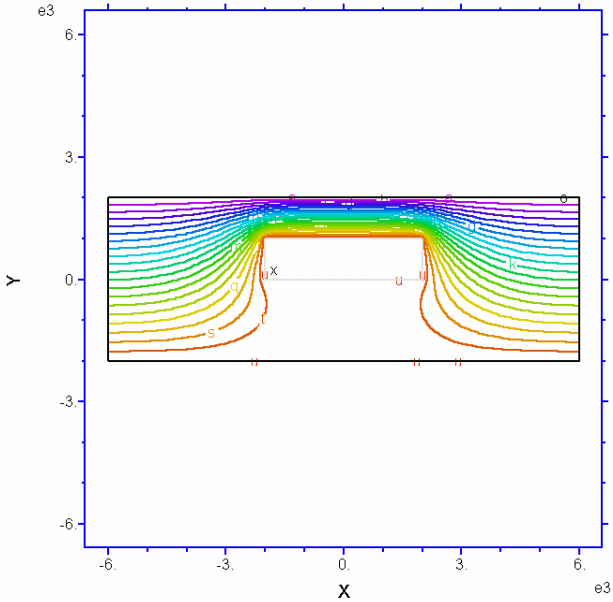


Figure 4. Temperature contours at 10 °C intervals for a 200 °C rectangular block reservoir of 4 km lateral extent, 1 km thickness, and the top of the reservoir at 1 km depth.

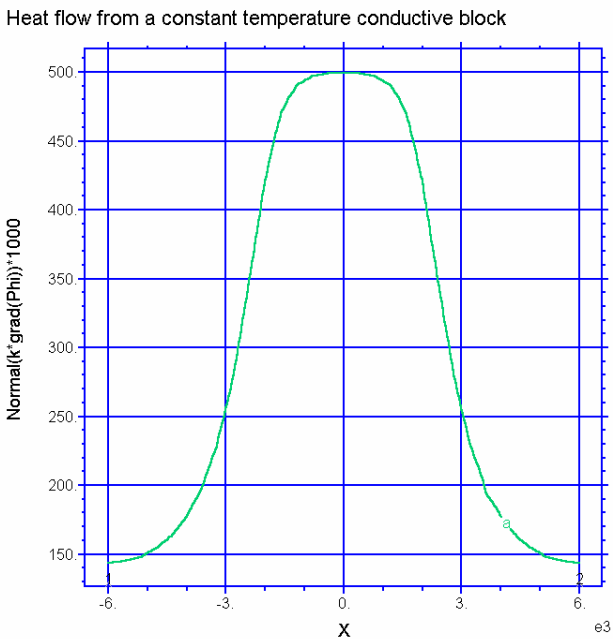


Figure 5. Surface heat flow for the rectangular block model shown in Figure 4.

For the cylindrical models, the heat loss from the varying reservoir sizes at a given depth is relatively insensitive to increasing reservoir volume. As a result, heat loss from the cylindrical reservoir increases by only a factor of 2.5 as the thermal power increases by more than two orders of magnitude. Also, increasing the depth to the top of the reservoir from 1 to 3 km (a typical range for producing

geothermal systems) reduces the heat loss by an order of magnitude for the same thermal power.

The narrow rectangular block models follow the same trend as the cylindrical models, but as the width of the block grows, the resulting heat flow anomaly approaches a one-dimensional geometry and the relationship between heat loss and power rolls over toward the proportional lines. These results are consistent with the concept of reservoir thermal power relating directly to heat loss as suggested by Wisian et al. (2001), with the primary variation in the proportionality arising from the varying depth of the reservoir.

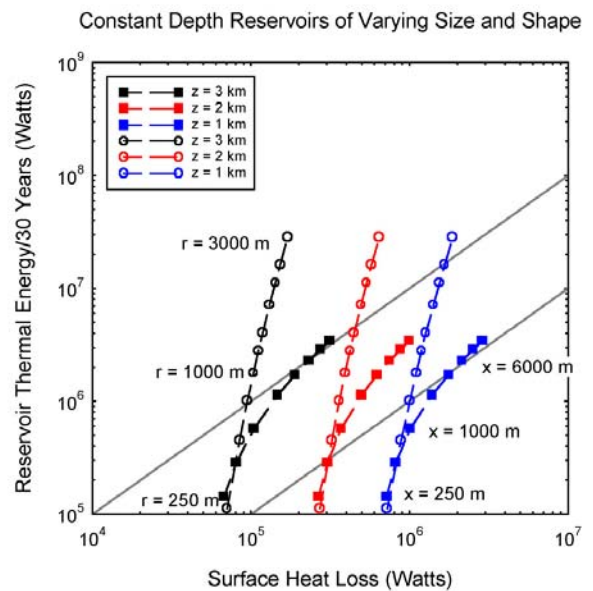


Figure 6. Plot of reservoir power versus surface heat loss for the 2-D models with top at z . Circles represent cylindrical models of radius r and squares block models with lateral extent x .

TRANSIENT MODELS

Other significant questions regarding heat flow and geothermal resources relate to the transient aspects of hydrothermal systems and heat transport through the crust. One question is whether near-surface heat flow measurements accurately represent deep thermal conditions. This is a relatively simple problem to investigate, and as noted by Urban et al. (1975), the critical parameter is the thermal time constant τ . This is defined as

$$\tau = \frac{z^2}{4\alpha} \quad (4)$$

where z is the depth to the reservoir and α is the thermal diffusivity. Surface heat flow will be close to equilibrium with the thermal state of a new reservoir at 1 km depth in approximately 8000 years. For a reservoir at 3 km, the equivalent time constant is approximately 70,000 years. For a reservoir at 5 km the time constant is approximately 200,000 years. This lag in surface heat flow is equally true for systems that have been active and then started to cool due to loss of permeability. The life spans of hydrothermal systems have been estimated to range from 10,000 years to nearly 1 My (Stein and Cathles, 1997), so heat flow measurements over a deep geothermal reservoir are less like to reflect thermal conditions in the reservoir.

On the other hand, given their lower anomalous heat flow, deeper geothermal reservoirs should be longer lived and perhaps more common than the more easily identified shallow reservoirs. The high heat flow from a shallow reservoir mines a large amount of heat very rapidly from the surrounding crust and shortens the duration of high reservoir temperatures (unless renewed by magmatic heat input). This is illustrated through application of a two-dimensional time-dependent model for heat transfer through a hydrothermal convection system. In this model, adapted from the one-dimensional convection model presented by Lachenbruch and Sass (1977), the rate of convective heat transport is given by a value of thermal conductivity in the reservoir many times that of the surrounding crust.

Figure 7 shows the mean reservoir temperature as a fraction of its initial value for a block reservoir 1 km wide and varying depth with convection extending to 5 km below the top of the reservoir. The results show strong depth dependence in the decline of the mean reservoir temperature after 1 My, with shallow reservoirs losing temperature much more rapidly than deeper reservoirs. This loss of temperature is a direct consequence of the higher heat loss to the surface required from a shallow reservoir.

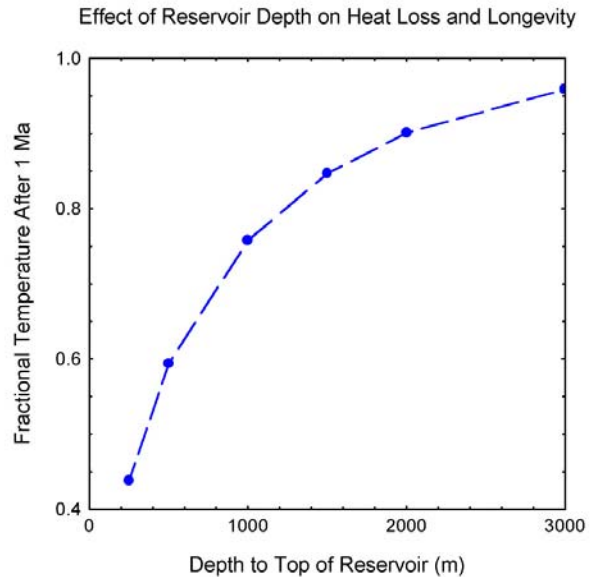


Figure 7. Plot of the ratio of reservoir temperature to initial temperature after 1 My of cooling for the rectangular block reservoir described in the text with varying depth to the top of the reservoir.

CONCLUSIONS

In summary, the simple conductive heat flow models described above indicate the following.

1. The observed relationship of thermal power and heat loss is consistent with the predictions of simple conductive reservoir models of varying geometry, size and depth.
2. Only laterally extensive reservoirs show a true proportionality between power and heat loss. For others heat flow is relatively insensitive to increasing reservoir size.
3. Existing observations are constrained by the limited exploitation depth of producing geothermal reservoirs. Deep reservoirs generate modest heat flow anomalies and are less likely to be in conductive equilibrium with the shallow crust.
4. Deep reservoirs require less additional heat to maintain high temperatures. They should be longer-lived, and if permeability conditions at depth are similar to those in the shallow crust, they should be more common. However, to the extent that production from a geothermal reservoir is in some way related to the permeability distribution that provides the "renewable" natural recharge, deep reservoirs may be poor candidates for development.
5. Heat flow is an important tool for characterizing shallow or relatively large geothermal reservoirs,

particularly in areas where magmatic heat input does not complicate interpretation of heat flow measurements. The measurement of heat loss from a geothermal reservoir provides critical information on the nature of the reservoir, and heat flow values should be derived from standard temperature gradient measurements whenever possible.

energy production for geothermal systems, Geothermal Resources Council, *Transactions*, v. 25, p.331-336.

REFERENCES

Lachenbruch, A. H., and J. H. Sass, 1977, Heat flow in the United States and the thermal regime of the crust, in *The Earth's Crust*, edited by J. H. Heacock, *Geophys. Monogr. Ser.*, 20, AGU, Washington, D.C., p. 625-675.

Lovekin, J., 2004, Geothermal inventory, *Bulletin Geothermal Resources Council*, v.33, n. 6, p. 242-244.

Muffler, L.P.J., (ed.), 1979, Assessment of Geothermal Resources of the United States – 1978, USGS Circular 790, 164p.

Muffler, L.P.J., and R. Cataldi, 1978, Methods for regional assessment of geothermal resources, *Geothermics*, v. 7, p. 53-89.

Nathenson, M., 1975, Physical factors determining the fraction of stored energy recoverable from hydrothermal convection systems and conduction-dominated areas, U.S. Geological Survey, Open-file Report 75-525, 50p.

Sanyal, 2004, Sustainability and renewability of geothermal power capacity, *Geothermal Resources Council Transactions*, v. 28, p. 617-625.

Stein, H.J., and L.M. Cathles, 1997, The timing and duration of hydrothermal events, *Economic Geology*, v. 92, n. 7/8.

Urban, T.C., W.H. Diment, J.H. Sass and I.M. Jamieson, 1975, Heat flow at The Geysers, California, USA, 2nd UN Symposium on Geothermal Energy, p. 1241-1245.

White, D.E., and D.L. Williams, 1975, Assessment of Geothermal Resources of the United States – 1975, USGS Circular 726, 155 p.

Williams, C.F., 2004, Development of revised techniques for assessing geothermal resources, Proceedings, 29th Workshop on Geotherm. Reserv. Engr., Stanford Univ., Stanford, Calif.

Wisian, K.W., D.D. Blackwell, and M. Richards, 2001, Correlation of surface heat loss and total

Geology

Geologic Framework of the East Flank, Coso Geothermal Field: Implications for EGS Development

[486](#)

K.M. Kovac, J.N. Moore, and S.J. Lutz

GEOLOGIC FRAMEWORK OF THE EAST FLANK, COSO GEOTHERMAL FIELD: IMPLICATIONS FOR EGS DEVELOPMENT

K.M. Kovac, J.N. Moore, and S.J. Lutz

Energy and Geoscience Institute
423 Wakara Way
Salt Lake City, UT, 84108, U.S.A.
e-mail: kkovac@egi.utah.edu

ABSTRACT

The Coso Geothermal Field is a large, high temperature system located in eastern California on the western edge of the Basin and Range province. The East Flank of this field is currently under study as a DOE-funded Enhanced Geothermal Systems (EGS) project. This paper summarizes petrologic and geologic investigations on two East Flank wells, 34A-9 and 34-9RD2 conducted as part of a continuing effort to better understand how the rocks will behave during hydraulic and thermal stimulation. Well 34A-9 is the hottest well at depth in the East Flank, reaching nearly 350°C.

The reservoir on the East Flank is dominated by diorite and granodiorite. Specifically, the diorites are several different quartz diorites and diorite. Thick intervals of granite, a minor rock type throughout most of the field, were encountered in 34A-9 and 34-9RD2. The granite tends to be much less altered, veined, and fractured than the other rock types, and thus probably a poor stimulation target.

Late stage vein minerals include calcite, quartz, chlorite, and hematite at shallow depths and rare epidote, chlorite, quartz, adularia, and wairakite in the deepest portions of East Flank wells. The distribution of mineral assemblages suggest well 34A-9 was drilled through the caprock and into the uppermost part of the reservoir rocks of a relict geothermal system.

The temperatures indicated by the clay minerals are much lower than would be predicted from the present day downhole temperatures, but are in good agreement with fluid inclusion temperatures. These relationships imply the system is currently being reheated.

Lost circulation zones tend to correlate with zones of relatively substantial calcite veining. Fluid inclusion measurements indicate some of the calcite was deposited by high salinity fluids not related to the current geothermal system. Other inclusions contain low salinity fluids that could be related to the current geothermal system. These fracture zones have been

episodically reactivated and modified by dissolution and reprecipitation of calcite.

INTRODUCTION

The Coso Geothermal Field is a large, high-temperature system located in California on the western edge of the Basin and Range province (Fig. 1). The system is related to young volcanic activity. The field produces 240 MWe. This study describes mineralogic and petrologic investigations undertaken as part of a DOE-funded Enhanced Geothermal Systems (EGS) project designed to improve permeabilities and injectivities of wells on the East Flank of the field. The objective of this work is to better understand the geologic setting of the East Flank, and in particular, its thermal and structural history. These studies and those of Adams et al. (2000) indicate that the system has undergone multiple thermal events and that the East Flank is currently reheating.

GEOLOGIC SETTING

The Coso geothermal field lies within a major volcanic center, which contains 38 rhyolite domes and almost as much basaltic material in its eastern portion. Two main periods of volcanism have occurred; the first was between 4.0-2.5 Ma, and the younger from 1.0 -0.4 Ma (Duffield et al., 1980). Both the rhyolite and the geothermal system are believed to be related to a partially molten body of magma located 5 to 20 km beneath the field (Duffield et al., 1980; Reasenberget al., 1980). Three periods of recent geothermal activity were documented by Adams et al (2000); the first occurred approximately 307,000 years ago and is associated with travertine deposits on the eastern side of the field. The second event produced a high- temperature geothermal system associated with sinter deposits that formed at ~238 ka on the East Flank. A major upflow center appears to have been located in the southwestern part of the field. The most recent activity has reheated rocks on the East Flank and reactivated the

southwestern upflow center. The present activity may have begun within the last several tens of thousands of years (Kurilovitch et al., 2003).

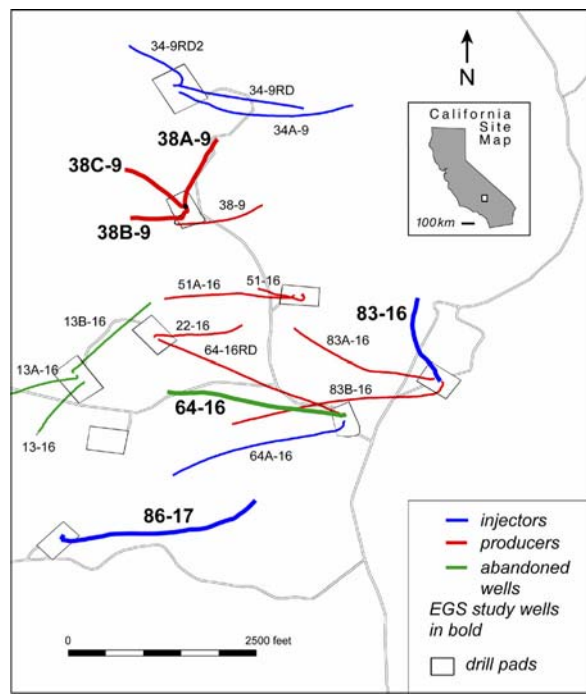


Figure 1. Area map of the East Flank.

PETROLOGY AND PETROGRAPHIC STUDY OF WELLS 34-9-RD2 AND 34A-9

Well 34-9RD2, the target of a DOE-funded EGS project, and well 34A-9, which is a proposed injector well on the same pad are located within the hottest part of the East Flank. Temperatures reaching close to 350°C have been encountered within well 34A-9. Cuttings samples from well 34-9RD2 were studied from 3600 feet to its total depth of 7310 ft and from well 34A-9 from 3600 feet to its total depth at 9735 ft. Observations taken on the chipboards and thin sections included: rock type, mineralogy and relative degree of pervasive alteration, veining types and relative amounts, and presence of euhedral crystal vein fillings. The summary log for well 34-9RD2 is shown in Figure 2.

The dominant rock types in the wells are quartz diorite, granodiorite, and granite. Petrologic and alteration studies by Kovac et al. (2004) indicate the quartz diorite is the oldest of the reservoir rocks. The granodiorite is intermediate in age. Granite is the youngest of the three rock types. The presence of extensive intervals of granite in these two wells is unusual because usually it is a minor rock type within the East Flank reservoir (Kovac et al., 2004). In both wells 34-9RD2 and 34A-9 granite occurs between approximately 5000 and 7000 ft. The granite is generally less altered and less veined than the other rock types and we infer from this observation that the

granite is less fractured. Low fracture permeabilities within the granite are supported by drilling results.

Many different vein minerals can be identified in the wells. As in other East Flank study wells, calcite and chlorite are the most abundant. However, quartz veins are more abundant in wells 34-9RD2 and 34A-9 than in other study wells.

HYDROTHERMAL ALTERATION AND MINERAL PARAGENESIS

Paragenetic relationships among the vein and alteration minerals were established to develop a conceptual model of the thermal history of the East Flank. Minerals were studied under a binocular microscope and in thin section. Select samples were also studied using X-ray diffraction techniques. The mineralogic relationships were corroborated by detailed studies of core samples from another East Flank well, well 64-16, which was cored to a depth of 2025 ft (Kovac, unpub. data). Figure 3 summarizes the paragenetic sequence of East Flank vein minerals based on these observations. The initial thermal event recorded by the reservoir rocks is represented by greenschist facies metamorphism of quartz diorites. This event is labeled Stage 0. This regional event produced chlorite, epidote, and sphene in the groundmass of the rocks. Locally the rocks are foliated and display poikilitic textures. The oldest recognized veins consist of massive pyrite, magnetite, epidote, and quartz followed by calcite. This event, referred to as stage 1 (Fig. 3) may have been related to the granite's emplacement. Stage 2 is represented by sealed veins of calcite + hematite + chlorite. Fluid inclusions in calcite from this stage often have higher salinities of up to a few weight percent NaCl equivalent than later stages of calcite. The next event, Stage 3, is divided into two substages. At shallow depths this stage (Stage 3A) is represented by hydrothermal breccias cemented by drusy quartz. Intergrown euhedral quartz crystals and calcite, which in places is bladed, formed during this stage. The presence of intergrown quartz and calcite are indicative of boiling. In the deepest part of well 34A-9 at 9710 ft, vein assemblages we interpret to be related to this thermal event consist of epidote (Fe-poor) + sericite + quartz +/- chlorite and adularia are present. This assemblage (Stage 3B) implies temperatures in excess of ~250°C (Browne, 1984; Henley and Ellis, 1983). The last major stage, Stage 4, is broken up into two substages. Calcite dominates the vein assemblages. The calcite exhibits several distinct morphologies. The earlier calcite (Stage 4.1) is represented by scalenohedral crystals. These crystals were encapsulated by later blocky calcite (Stage 4.2) which is often associated with hematite. Sometimes, several generations of calcite are present in the same sample, and the crosscutting relationships are evident. In the deepest parts of the

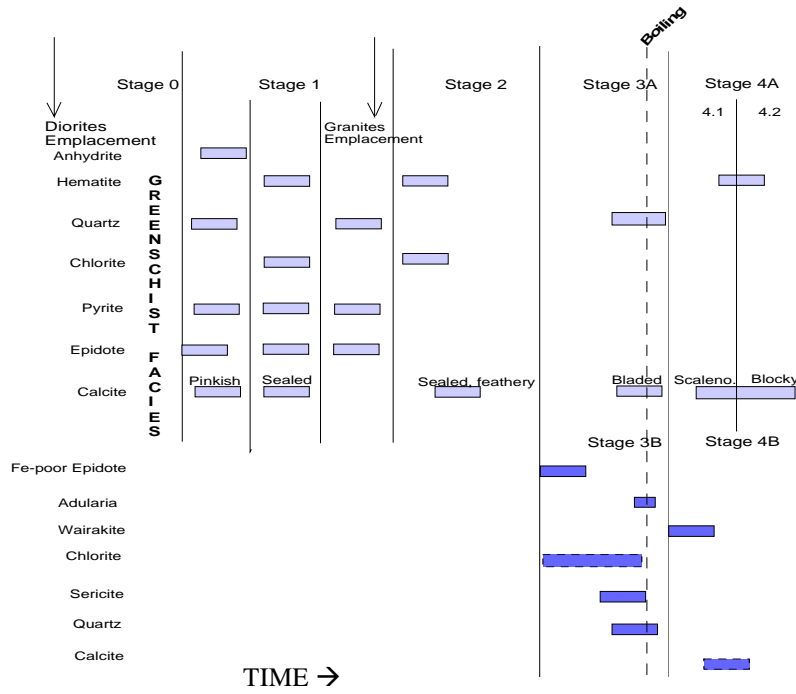


Figure 3. Generalized paragenetic sequence of East Flank vein minerals. The designations –A and –B refer to shallow and deep assemblages, respectively.

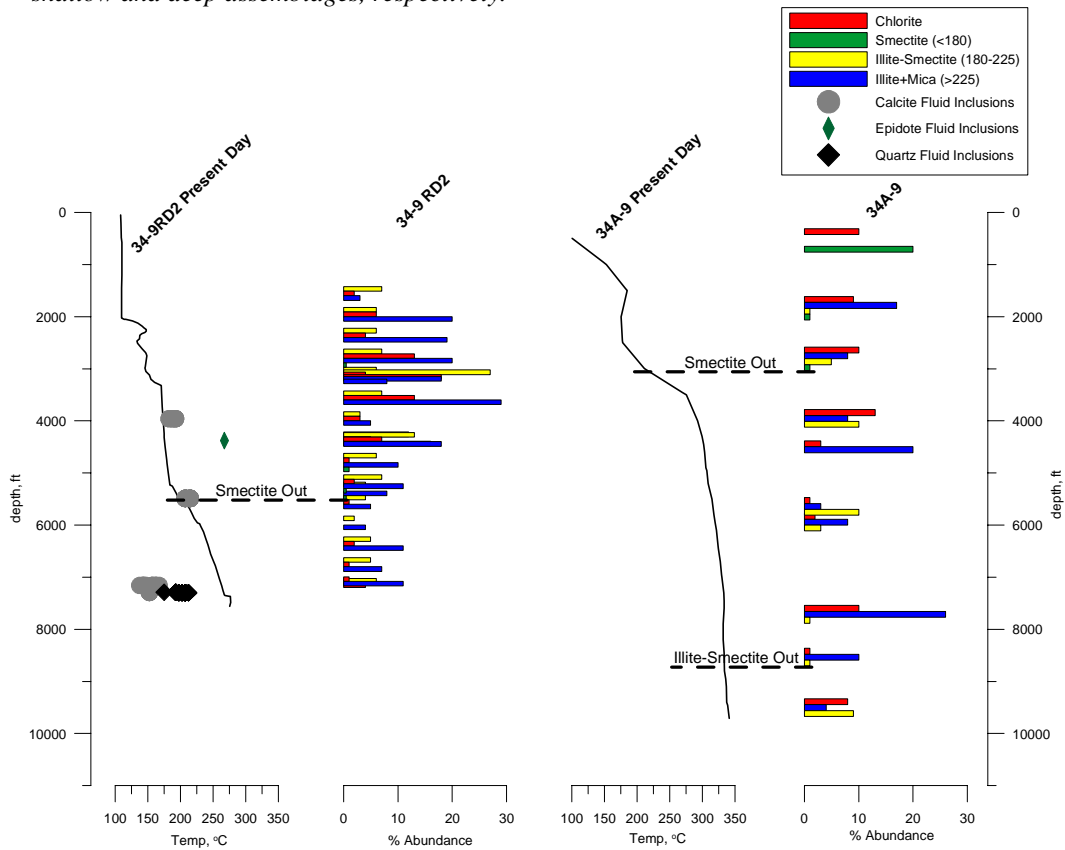


Figure 4. A summary of temperature, fluid inclusion, and clay mineral data for both wells. The dashed lines indicate the interpreted disappearance of smectite and illite-smectite.

reservoir, the silicate minerals were followed by wairakite (e.g. at 9710 ft in well 34A-9). In well 72-19, drilled within the upflow zone beneath the southwest portion of the field, wairakite postdates the assemblage quartz + epidote + calcite + pyrite + chlorite. Wairakite is a common late-stage mineral in geothermal systems, forming during the waning stages of activity (Moore et al., 2002). Additionally, calcite is still often found to be the last veining present even at great depth. Thus, Stage 4B, wairakite + calcite, is established. As noted below, calcite deposited during Stage 4 typically hosts fluid inclusions with the lowest homogenization temperatures and salinities. Simmons et al. (2000) assert that late, pure, massive calcite veins can be deposited from downward-moving, CO₂-rich, steam-heated waters.

The distribution of clay minerals can provide an independent estimate of temperature. Figure 4 shows the percentages of clay minerals, smectite, interlayered illite-smectite, illite and chlorite in the groundmass of the reservoir rocks encountered in wells 34-9RD2 and 34A-9. In general, smectite is stable up to temperatures of ~180°C, interlayered illite-smectite to ~225 °C and illite and chlorite at greater temperatures (Henley and Ellis, 1983; Browne, 1984).

Clay minerals are uncommon in the veins and thus they cannot be uniquely assigned to one of the paragenetic stages. However, the distribution of clay minerals shown in Figure 4 implies that at least several thermal events are represented. Despite the complexity of the clay distributions the abundances of both smectite and interlayered illite-smectite appear to vary with depth. The base of the smectite zone occurs at depths of ~5500 in 34-9RD2 and ~3000 in 34A-9. A temperature of ~180°C at about 5500 ft, implied by the disappearance of smectite, appears to be fairly consistent with both the measured downhole temperatures and with the homogenization temperatures of calcite fluid inclusions in well 34-9RD2. In contrast, interlayered illite-smectite persists in rocks where downhole measured temperatures exceed its typical stability range, suggesting this mineral formed during an earlier, lower temperature thermal event. These relationships suggest recent heating of the field, which has not yet been recorded by the rocks.

FLUID INCLUSION STUDIES

Samples of euhedral calcite and quartz crystals and one epidote crystal were chosen from the cuttings for fluid inclusion analysis. All of the inclusions found in these samples were two-phase (liquid and vapor) at room temperature. Homogenization temperatures and salinities of the inclusion fluids calculated as weight percent NaCl equivalent (Bodnar, 1993) were determined. Figure 6 summarizes relationships between depth, homogenization temperature, and

salinity for inclusions from well 34-9RD2. The measured downhole temperatures and boiling point to depth curve for a 0% salinity, gas-free fluid are also shown for comparison. Salinities are coded by symbol size. Inclusions in calcite had the lowest temperatures and salinities. Temperatures of homogenization in calcite varied between 150 and 215°C, and salinity varied between 0.9 to 2.7 weight % NaCl equivalent, which is generally the higher end of calcite salinities as measured in other wells. Quartz varied in homogenization temperatures between 175 and 213°C, and salinities varied between 1 and 4 wt. % NaCl equivalent. The primary inclusions in quartz had higher salinities than the secondary inclusions in quartz. The inclusions in epidote had by far the highest measured temperatures and salinities. Homogenization temperature was approximately 268°C while salinity was approximately 11 wt. % NaCl equivalent.

Histograms of salinities determined on calcite- and quartz- hosted inclusions suggest that several (three or more) distinct populations of fluids were trapped (Figures 6 and 7). Data from all studied East Flank wells were employed. More than half of the inclusions trapped in calcite recorded salinities between 0.5 and 1% NaCl equivalent; furthermore, over 70% of all calcite inclusions have salinities less than 1 weight percent equivalent. Salinities in quartz-hosted inclusions also define several populations with salinities tending to be higher than in the calcite. Less than 25% of the inclusions have salinities of 1 weight percent NaCl equivalent or less; in the calcite, the majority of inclusions had salinities less than 1 wt. percent. Significantly, almost 20% of the quartz inclusions had salinities of 5 wt. % NaCl equivalent and higher. Thus the fluid inclusion data provide a record of water-rock interactions that involved fluids with a wide range of compositions. The earliest fluids trapped in quartz and calcite deposited during Stage 1 had the highest salinities of about 8-10 weight percent NaCl equivalent. The youngest thermal event is represented by the lowest salinity fluids, which are usually equal to or less than 1 weight percent NaCl equivalent.

LOST CIRCULATION ZONES

Zones of lost circulation were encountered mainly between 3900-5500 ft in well 34-9RD2, and between 3600-4500 ft, 7600-8000 ft, and 9300-9700 ft in well 34A-9. Kovac et al. (2004) demonstrated that many of the lost circulation zones were associated with calcite veins, as indicated by the presence of euhedral calcite crystals. Fluid inclusions analyzed for these locations indicate however, that this veining is not necessarily related to the most recent fluids. Some of the inclusions have salinities of about 4 weight percent equivalent or more and temperatures in the mid 200's Celsius, which can be correlated with the oldest stages of the mineral paragenesis. In other

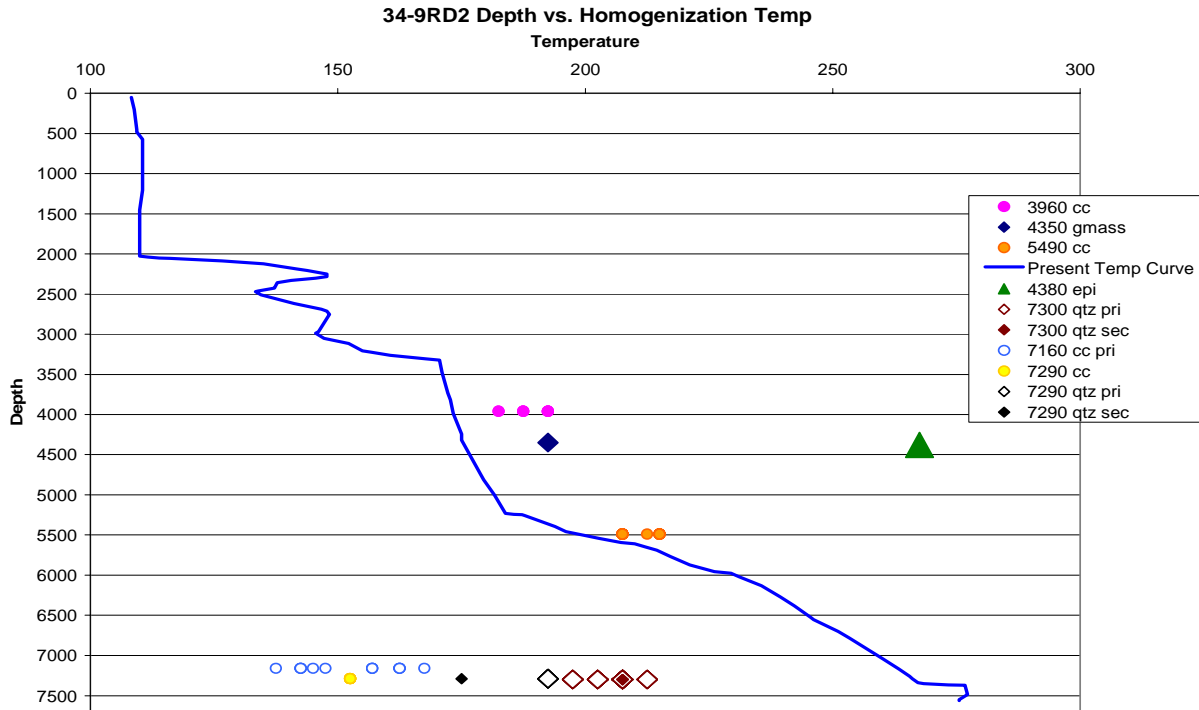


Figure 5. Depth vs. homogenization temperature for fluid inclusions from well 34-9RD2. Symbol size correlates positively with general salinity of the inclusion where the smallest are approximately 1 wt% NaCl equivalent and the largest are about 10 wt. % NaCl equivalent.

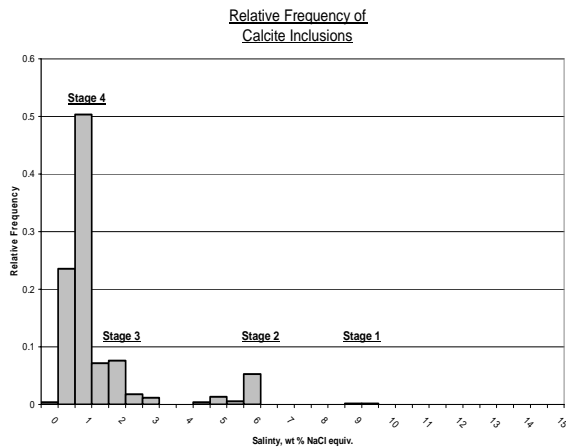


Figure 6. Relative Frequency of salinity in calcite hosted inclusions.

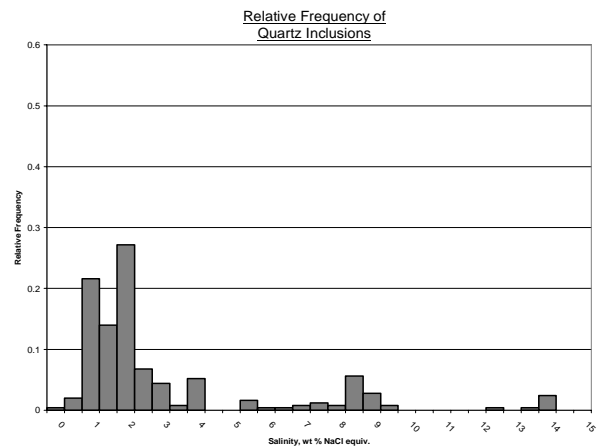


Figure 7. Relative frequency of salinity in quartz hosted inclusions.

cases, low salinities of about 1 weight percent equivalent or less suggest younger fluids were responsible for calcite deposition. Thus the data suggest that the fractures that are currently permeable may have formed at different times and during different hydrothermal events. Also, many of them have been reactivated by younger events over time. Therefore, these locations may be good stimulation targets.

CONCLUSIONS

- Diorites, granodiorites, and granites are the dominant rock types present in the East Flank wells.
- Generally, the granites are the slightest altered, and least veined and least fractured of the dominant rock types. These relationships suggest the granites generally have low permeabilities and have not been

strongly affected by geothermal events. They appear to be the poorest of the potential stimulation targets.

- Zones of lost circulation often correlate with zones of abundant veining. However, fluid inclusion and paragenetic studies show that this mineralization is not necessarily recent, and that some fractures developed during previous thermal events.

- Epidote and pyrite are the oldest vein minerals. At shallow depths, the recent veining assemblage is dominated by euhedral quartz and younger calcite. Furthermore, as indicated by the fluid inclusion studies, several generations of calcite and quartz are present.

- The clay minerals smectite and interlayered illite-smectite occur within the groundmass of the rocks. This assemblage is typical of the caprock sections of modern geothermal systems. In the deepest portions of the East Flank wells, the youngest vein assemblage consists of adularia, quartz, chlorite, Fe-poor epidote and younger wairakite. These minerals are typical of the reservoir sections of modern geothermal systems where temperatures exceed ~250°C.

- Fluid inclusion homogenization temperatures and the distribution of clay and silicate minerals indicate that the modern geothermal system is superimposed on rocks altered in an older, lower temperature thermal regime.

ACKNOWLEDGEMENTS

Financial support for this research was provided under DOE contract No. DE-FC07-01ID14186. We would like to thank Coso Operating Company for providing the samples.

REFERENCES

Adams, M.C., Moore, J.N., Bjornstad, S., and Norman, D.I. (2000), "Geologic History of the Coso Geothermal System," *Transactions, Geothermal Resources Council*, **24**, 205-209.

Bodnar, R.J. (1993), "Revised Equation and Table for Determining the Freezing Point Depression of H₂O-NaCl Solutions," *Geochimica et Cosmochimica Acta*, **57**, 683-684.

Browne, P. (1984), "Lectures on Geothermal Geology and Petrology," *UNU Geothermal Training Programme Report 1984-2*, 1-92.

Duffield, W.A., Bacon, C.R., and Dalrymple, G.B. (1980), "Late Cenozoic Volcanism, Geochronology, and the Structure of the Coso Range, Inyo County, California," *Journal of Geophysical Research*, **85**, 2381-2404.

Henley, R.W. and Ellis, A.J. (1983), "Geothermal Systems Ancient and Modern: A Geochemical Review," *Earth Science Reviews*, **19**, 1-50.

Kovac, K.M., Moore, J.N., McCulloch, J., & Ekart, D. (2004), "Geology and Mineral Paragenesis Study Within the Coso-EGS Project," *Proceedings, 29th Workshop on Geothermal Reservoir Engineering, Stanford, CA*, 262-267.

Kurilovitch, L., Norman, D., Heizler, M., Moore, J., and McCulloch, J. (2003), "⁴⁰Ar/³⁹Ar Thermal History of the Coso Geothermal Field," *Proceedings, 28th Workshop on Geothermal Reservoir Engineering, Stanford, CA*, 110-116.

Moore, J.N., Christenson, B.W., Browne, P.R.L., and Lutz, S.J. (2002), "The Mineralogic Consequences and Behavior of Descending Acid-Sulfate Waters: An Example From the Karaha-Telaga Bodas Geothermal System, Indonesia," *Proceedings, 27th Workshop on Geothermal Reservoir Engineering, Stanford, CA*, 257-265.

Reasenber, P.L., Ellsworth, W.L., and Walter, A.W. (1980), "Teleseismic Evidence For a Low-Velocity Body Under the Coso Geothermal Area," *Journal of Geophysical Research*, **85**, 2471-2483.

Simmons, S.F., Arehart, G., Simpson, M.P., and Mauk, J.L. (2000), "Origin of Massive Calcite Veins in the Golden Cross Low-Sulfidation, Epithermal Au-Ag Deposit, New Zealand," *Economic Geology*, **95**, 99-112.

Emerging Technology

- Physical and Chemical Characteristics of Hydrothermal Heat Carrier of Mutnovskoye Field** [494](#)
Gorbach V.A., Potapov V.V.
- A Reevaluation of Geopressured-Geothermal Aquifers as an Energy Source** [501](#)
Jeremy Griggs
- Experiments on Silica Precipitation from Hydrothermal Solution and Utilization of Precipitated Material (Kamchatka, Russia)** [510](#)
Potapov V.V., Kornilova T.I., Ratchina T.I.

PHYSICAL AND CHEMICAL CHARACTERISTICS OF HYDROTHERMAL HEAT CARRIER OF MUTNOVSKOYE FIELD

¹Gorbach V.A., ²Potapov V.V., ³Taskin V.V.

^{1,2,3}Research Geotechnological Center, Far East Branch of Russian Academy of Sciences (RGC FEB RAS),
Petropavlovsk-Kamchatsky, Kamchatka, 683002, Russia,
Severo-Vostochnoe shosse, 30, P.O. Box 56,
e-mail: nigtc@kcs.iks.ru

ABSTRACT

The experiments on researching of physical and chemical characteristics of hydrothermal heat carrier of Verhne-Mutnovsky geothermal electric power plant and wells 4E, 014 of Mutnovskoye field were carried out. The concentrations of cations and anions, pH, mineralization, ionic strength, conductivity of separate and vapor condensate solutions, concentration of gases in vapor phase of heat carrier were determined. Coefficients in linear dependence of ionic strength from solution mineralization for separate and condensate were established. The dependence of separate conductivity from solution temperature was investigated. The experimental data and theoretical values of conductivity were compared. The sizes and diffusion coefficients of colloidal silica particles were measured by the method of photon correlation spectroscopy. The results obtained in this work can be applied for development of technology of silica extraction and increasing of efficiency of hydrothermal heat carrier using.

INTRODUCTION

Chemical composition of hydrothermal heat carrier is depended on the interaction of water solution with minerals of aluminosilicate rocks of hydrothermal systems. This interaction occurs with increased temperature and pressure. Temperature in the deepest parts of the high-temperature systems similar to the system of Mutnovskoe field can reach 250-350°C. When heat carrier rises to the surface in productive wells of geothermal electric power stations part of heat carrier turns into vapour phase because of decrease in pressure. On the surface in separators of the geothermal electric power plant (GeoPP) vapour phase is separated and fed to the turbine for generation of electric power. Presence of vapour phase of hydrogen sulfide in gas composition leads to corrosion of heat equipment of geothermal electric power plant. Higher mineralization of liquid phase of heat carrier (separate) determines one more technical

problem – formation of solid deposits in wells, pipes and heat equipment of geothermal electric power plant. Solid deposits of silica make the largest difficulty. In this paper results of researching of the chemical composition and characteristics of heat carrier which are necessary for solving the technical problems of exploitation of geothermal electric power plant are given.

1. CHEMICAL COMPOSITION OF LIQUID AND VAPOUR PHASES OF HYDROTHERMAL HEAT CARRIER

Experiments on researching of physical and chemical characteristics were carried out using hydrothermal separate from productive wells of Verkhne-Mutnovsky geothermal electric power plant and, besides, from wells 014, 4E, 5E, A2 of Mutnovskoe field. pH value of samples of solution at 20°C was within 8.0-9.4, total mineralization – 1.0 – 2.5 g/kg, ionic strength of solution – 10 – 20 mmole/kg. Total content of silica in samples was 650 – 820 mg/kg, concentration of monomeric silica (monomeric orthosilicic acid) corresponded to solubility C_e at the temperature of the experiments. The most experiments were carried out with separate samples from the reinjection pipe-line of Verkhne-Mutnovsky geothermal electric power plant.

Productive wells 048, 049, 055 of Verkhne-Mutnovsky geothermal electric power plant(GeoPP) bring heat carrier to the surface as vapour-water mixture (VWM) with mass vapour content of 0.2-0.3. Mouth binding of productive wells is united in one common collector in which three flows of heat carrier mix. In separators of first and second line at pressure of 0.8 MPa and temperature 170.4°C vapour-water mixture is divided into vapour phase which is fed to the turbines and liquid phase (separate) with consumption of 50-55 kg/s. Separate comes to expander where pressure is about 0.4 MPa, and temperature – near 143.6°C. From expander separate with pressure of 0.4 bar is pumped through two reinjected wells back to the rocks of hydrothermal

field. Heat-exchanger was settled on the reinjection pipe-line of geothermal electric power plant.

Table 1a. Concentrations of anions and cations in hydrothermal separate from reinjection line of Verkhne-Mutnovsky geothermal electric power plant, $I_s = 14.218$ mmole/kg. n.d.- concentration was not determined, (-)- values were not calculated.

Component	mg/l	mg-equiv/l	
		mg-equiv/l	%mg-equiv/l
Na ⁺	239.4	10.413	88.044
K ⁺	42.0	1.074	9.080
Ca ²⁺	1.6	0.0798	0.6747
Mg ²⁺	0.72	0.0592	0.5005
Fe ^{2+,3+}	<0.1	<0.0053	0.0448
Al ³⁺	0.27	0.033	0.2790
NH ₄ ⁺	1.1	0.0609	0.5149
Li ⁺	0.71	0.102	0.8624
Sum of cations	285.9	11.827	100.0
Cl ⁻	198.5	5.591	47.664
HCO ₃ ⁻	81.0	1.327	11.312
CO ₃ ²⁻	19.9	0.663	5.652
SO ₄ ²⁻	192.1	3.9995	34.096
HS ⁻	4.95	0.15	
H ₂ S ⁰	5.92	-	-
F ⁻	n.d.	n.d.	-
Sum of anions	496.5	11.73	100.0
H ₃ BO ₃	106.9	-	-
(H ₄ SiO ₄) _t	1190	-	-
(H ₄ SiO ₄) _s	222	-	-
Mineralization M _b	1638.9	-	-
pH	9.35	-	-

Table 1b. Chemical composition of sample of steam condensate selected from vapour preparation plant of Verkhne-Mutnovsky geothermal electric power plant.

pH = 5.24, specific conductivity $\sigma = 0.0705$ mSm/cm.

Units	Cl ⁻	SO ₄ ²⁻	HCO ₃ ⁻	CO ₃ ²⁻	NO ₂ ⁻	NO ₃ ⁻	F ⁻	Sum
mg/l	2.385	6.00	10.07	0.00	<0.003	0.423	0.00	19.00
mg-equiv/l	0.067	0.125	0.165	0.000	0.000	0.007	0.000	0.364
mg-equiv %	18.00	34.00	46.00	0.00	0.001	2.00	0.00	100.00

Units	Na ⁺	K ⁺	Li ⁺	Ca ²⁺	Mg ²⁺	Fe ²⁺	Fe ³⁺	NH ₄ ⁺	Sum
mg/l	0.731	<1.00	<0.03	0.75	0.10	2.108	<0.05	9.00	13.036
Mg-eq/l	0.032	0.000	0.000	0.037	0.008	0.075	0.000	0.500	0.650
mg-eq %	5.00	0.00	0.00	6.00	1.00	11.00	0.00	76.00	100.00

Table 2a. Data on concentration of gases in composition of vapour phase of heat carrier of well 4E from Mutnovskoe field.

Date	CO ₂	H ₂ S	H ₂	CH ₄	N ₂	Ar	He	Volume gas content	Mouth pressure bar
5.11.98	82.2	10.0	0.62	0.13	6.9	0.16	0.0016	0.015	7.48
7.11.98	68.5	15.7	0.77	0.15	14.5	0.31	0.0018	0.009	8.79
9.11.98	81.7	9.3	0.85	0.22	7.7	0.22	0.0019	0.019	11.2
12.11.98	73.1	14.4	0.80	0.18	11.3	0.22	0.0021	0.014	11.83
13.11.98	67.0	11.4	1.27	0.29	19.7	0.36	0.0035	0.009	4.27
14.11.98	55.9	20.6	1.27	0.34	21.6	0.38	0.0045	0.015	6.31
average	71.4	13.6	0.93	0.22	13.6	0.27	0.0026	0.013	--

Table 2b. Results of chemical analysis of condensate and separate samples from well 4E, mg/kg.

condensate				
date	5.11.98	7.11.98	9.11.98	12.11.98
pH	4.93	5.1	5.3	4.78
NH ₄ ⁺	3.1	2.7	3.1	3.1
Na ⁺	0.02	0.21	0.02	0.03
K ⁺	0.07	0.2	0.11	0.07
Li ⁺	<0.01	<0.01	<0.01	<0.01
Ca ⁺	<0.4	<0.4	<0.4	<0.4
Mg ²⁺	<0.24	<0.24	<0.24	<0.24
Fe ^{2+ 3+}	<0.3	<0.3	<0.3	<0.3
Al ³⁺	<0.27	<0.27	<0.27	<0.27
Cl ⁻	<0.7	<0.7	<0.7	<0.7
SO ₄ ²⁻	3.3	4.8	3.3	6.7
HCO ₃ ⁻	6.1	4.88	7.3	3.7
CO ₃ ²⁻	0.04	0.03	0.03	0.02
F ⁻	0.04	0.03	0.03	0.02
H ₃ BO ₃	<0.7	<0.7	<0.7	<0.7
H ₄ SiO ₄ (p)	2.4	2.3	2.3	2.3
H ₄ SiO ₄ (κ)	3.3	3.3	3.3	3.3
As	0.04	0.06	0.074	0.046
G _s , kg/s	9.1	8.6	7	3.8
G _w , kg/s	17.6	17.6	15.2	7.1

Concentrations of basic components of hydrothermal separate solution selected from the reinjection pipe-line of GeoPP are given in table 1a. For comparison table 1B contains data on chemical composition of steam condensate. Table 2a presents data on concentration in vapour phase of heat carrier of well 4E obtained in the Mutnovskoye field (Potapov V.V., Alekseev V.I., 2001). Data shows, that CO₂, H₂S, N₂ prevail in gas composition of heat carrier. Tables 2b and 2c contains data on chemical composition of separate from well 4E.

Solution of separate from Mutnovskoye field is of chloride-sulphate-sodium-potassium type of hydrothermal solutions. Kurlov's formula of

chemical composition of water which reflects percentage of anions and cations in milligram-equivalents is the following: Cl47.66-SO₄34.09/Na88.04-K9.08.

Dependence of ionic strength I_s (mole/kg) of hydrothermal solution from wells of Mutnovskoe field on mineralization M_h (mg/kg) is expressed by the equation:

$$I_s = A_1 \cdot 10^{-6} \cdot M_h, \quad (1)$$

where A_1 – is coefficient which is (7.35 – 8.68) mole/mg for separate, and 17.34 mole/mg for vapour condensate.

Table 2c. Results of chemical analysis of condensate and separate samples from well 4E, mg/kg.

	separate			
date	5.11.98	7.11.98	9.11.98	12.11.98
pH	9.06	9.09	9.14	9.15
NH ₄ ⁺	0.3	0.3	0.3	0.55
Na ⁺	273	275	271	272
K ⁺	54	54.5	53.5	54.5
Li ⁺	1.42	1.43	1.43	1.42
Ca ⁺	3	3	3	3
Mg ²⁺	<0.24	<0.24	<0.24	<0.24
Fe ^{2+ 3+}	<0.3	<0.3	<0.3	<0.3
Al ³⁺	<0.27	<0.27	<0.27	<0.27
Cl ⁻	244.9	244.9	244.9	244.9
SO ₄ ²⁻	249.7	249.7	249.7	249.7
HCO ₃ ⁻	81.1	80.5	79.3	79.3
CO ₃ ²⁻	6.3	6.6	7.2	7.2
F ⁻	4.24	4.24	4.24	4.24
H ₃ BO ₃	110.8	109.5	110.8	109.5
H ₄ SiO ₄ (p)	187.3	200.3	186.6	197.7
H ₄ SiO ₄ (κ)	1048	1087	1160	1116
As	3.3	4.07	4.9	4.2
T Na/K, °C	275.1	275.4	274.8	277.1
T SiO ₂ , °C	254.1	259.7	265.8	258.7
T SiO ₂ (2), °C	278.8	282.5	289.3	285.3

2. CALCULATION OF HEAT CARRIER TEMPERATURE IN HYDROTHERMAL RESERVOIR BY GEOTHERMOMETERS

Data on concentration of silicic acid, cations of sodium Na⁺, potassium K⁺ and calcium Ca²⁺ in separate (Table 1a) were used to calculate temperature of liquid heat carrier in hydrothermal reservoir in productive zones of wells 048, 049 and 055. Calculations were done by equations for quartz (SiO₂)-geothermometer, and for sodium-potassium (Na-K) and sodium-potassium-calcium (Na-K-Ca)-geothermometers.

If temperature at which water-rock interaction occurs at a depth and type of rocks are known, then concentration of basic cations (Na⁺, K⁺) and anions

(Cl⁻, SO₄²⁻, HCO₃⁻, CO₃²⁻), ionic strength I_s , pH value at different temperature and pressure in heat equipment can be found from the condition of chemical equilibrium. Calculation of temperature by quartz SiO₂-geothermometer is based on the fact, that concentration of silica in water solution is determined by solubility of quartz at temperature of water-rock interaction (Fournier R.O., Rowe I.I. 1966). Thus, total content of silica is function of temperature. Different equations were suggested for approximation of this functional dependence which were obtained on the basis of mathematical processing of laboratory experimental data and data on measurements of temperature and silica concentrations in water solution of geothermal wells.

For SiO₂-geothermometer widely used are Fournier equation (Fournier R.O., Rowe I.I., 1966):

$$t_s = 1309 / (5.19 - \lg C_t) - 273, (0-250^\circ\text{C}) \quad (2)$$

and Rimstidt equation:

$$\lg(C_t / 60000) = 1.881 - 2.028 \cdot 0.001 \cdot (t_s + 273) - 1560 / (t_s + 273), \quad (3)$$

where C_t – is total content of silica in solution expressed according to SiO₂, mg/kg, t_s – temperature of solution expressed in Celsius degrees, °C.

Na-K-geothermometers are based on the fact, that ratio of concentrations of sodium Na⁺ and potassium K⁺ cations in water solution is a function of temperature at which interaction of water with alkaline aluminosilicate, for example, albite occurred. To calculate temperature by Na-K-geothermometers equation of White-Ellis is used (White D.E., 1965):

$$t_s = 855.6 / (\lg(C_{Na} / C_K) + 0.8573) - 273, (0-245^\circ\text{C}) \quad (4)$$

Determination of temperature by Na-K geothermometer is also carried out by equation of Arnorsson (Arnorsson S., Gunalaugsson E., Svavarsson H., 1983):

$$t_s = 933 / (\lg(C_{Na} / C_K) + 0.933) - 273, (25-250^\circ\text{C}) \quad (5)$$

In equations (4) and (5) C_{Na} , C_K – is concentration of sodium Na⁺, potassium K⁺ cations in solution, mg/l.

In some cases sodium-potassium-calcium (Na-K-Ca) geothermometer is used, which range of application is larger than that of sodium-potassium one. For this geothermometer additional ratio of concentrations of calcium Ca²⁺ cations and sodium Na⁺ cations in water solution is used. We calculated temperature by Na-K-Ca-geothermometer on the basis of Fournier-Truesdell equation (Fournier R.O., Truesdell A., 1973):

$$t_s = 1647 / (\lg(C_{Na} / C_K) + \beta_{CN} \cdot \lg((C_{Ca})^{0.5} / C_{Na}) + 2.24) - 273, (4 - 340^\circ\text{C}) \quad (6)$$

C_{Na} , C_K , C_{Ca} – are concentrations of sodium, potassium, calcium cations, correspondingly,

expressed in mole/l, β_{CN} – is coefficient which has the following values:

$$\beta_{CN}=1/3, \text{ if } (C_{Ca})^{0.5}/C_{Na}<1 \text{ и } t_s>100^{\circ}\text{C}, \quad (7-1)$$

$$\beta_{CN}=4/3, \text{ if } (C_{Ca})^{0.5}/C_{Na}>1 \text{ и } t_s<100^{\circ}\text{C} \quad (7-2)$$

Heat carrier of productive wells of Verkhne-Mutnovskaya geothermal electric power station has similar chemical composition, close vapour content and temperature. Therefore, temperature values calculated by named geothermometers should be considered as generalized characteristic of zone which is drained by wells.

Concentration of silica SiO_2 in separate sample (Table 1) was 643.8 mg/kg, concentration of cations Na^+ - 239.4 mg/l = $10.413 \cdot 10^{-3}$ mole/l, concentration of cations K^+ - 42.0 mg/l = $1.074 \cdot 10^{-3}$ mole/l, and concentration of cations Ca^{2+} - $0.0399 \cdot 10^{-3}$ mole/l. Substitution of these values into equations (2)-(7) gave the following results: temperature at the bottom hole according to Na-K-geothermometer (4) of White-Ellis - 269.3°C , temperature according to Na-K-geothermometer of Arnorsson (5) - 257.4°C , temperature according to Na-K-Ca-geothermometer of Fournier-Truesdell (6) - 249.1°C .

Temperature calculated by geothermometer of Fournier-Truesdell should be considered as the lowest temperature limit within area of hydrothermal reservoir drained by productive wells of Verkhne-Mutnovskaya geothermal electric power station - $246\text{-}249^{\circ}\text{C}$. Temperature calculated by geothermometer of Arnorsson should be considered as the highest limit of values of real temperature in draining zone by the moment of sampling - $279\text{-}284^{\circ}\text{C}$.

For separate sample which chemical composition is shown in Table 1a at maximum possible temperature at the bottom hole of wells 279.4°C concentration of silica SiO_2 before evaporation according to equation (3) was 519.1 mg/kg, and after evaporation - 643.8 mg/kg. Thus, minimal possible vapour content in heat carrier flow was $519.1/643.8 = 0.20$.

3. MEASUREMENT OF RADII OF COLLOIDAL SILICA PARTICLES IN SEPARATE SAMPLES

When heat carrier comes up through the productive wells of geothermal electric power plant, then because of decrease in temperature and transformation of a part of heat carrier in vapour phase solution oversaturated relatively to solubility of amorphous silica comes to the surface. This leads to the development of nucleation and polymerization of orthosilicic acid molecules, in form of which silicium is mainly present in solution before coming to the surface. Formation of colloidal silica particles is the

consequence of nucleation and polymerization. Flowing of separate through pipelines, heat equipment and reinjection wells is accompanied by the formation of complexes of silica particles on the walls of canals and growth of solid deposits layers.

The sizes and diffusion coefficients of colloidal silica particles which formed in hydrothermal solution during nucleation and polymerization were measured by the method of photon correlation spectroscopy (PCS). The experiments were done with photon correlation spectrometer of PhotoCor Complex class. Complete set of spectrometer includes optical block PhotoCor-Spec, correlator of PhotoCor-M class, laser and computer. He-Ne laser had capacity of 20 mW and wave length $\lambda_f = 633$ nm. Precision optical block of PhotoCor-Spec type contained precision goniometer which provided scattering angles $10^{\circ}\text{-}150^{\circ}$ and accuracy of turn up to 0.05° , thermostat, photon counting system PhotoCor-Count, power supply unit PhotoCor-PMT-PS, optical bench, focusing unit for laser, adapters of dishes. Aliquots of solution were placed in square dishes of 12×12 mm.

Photon counting system PhotoCor-Count has highly effective receiving optical system. Signal from the outlet of photoreceiving block is analyzed by the one-plate multichannel correlator which is put directly in one of the joints of mother board of personal computer. By computer control for the process of measurement and processing of measurement results are carried out. Computer IBM PC compatible with monitor and printer is equipped with a set of special programs for PhotoCor systems of PhotoCor Soft-WIN type. Software allows to machine signals which entered into photon counting system, accumulate measurements of correlation function in different points, construct plots of correlation function. On the basis of the mathematical apparatus of theory of quasi-elastic scattering of monochromatic light on separate centers program calculates according to the values of correlation function time of correlation, diffusion coefficient of particles with definite size which participate in light scattering, determines concentration of particles with sizes in definite interval and calculate their average size.

Table 3 presents results of measurement in one of the samples of hydrothermal solution as dependence of amplitude of monochromatic laser light scattering with wave length 633.0 nm S_{am} on radius of particles R. Amplitude of scattering is proportional to quantity of particles with radii in corresponding value range. Mathematical processing of data on light scattering was done for particles having radii from 1.0 to 10000 nm. Average radius for particles of mentioned solution sample was 11.09 ± 0.18 nm, diffusion coefficient – 1.923 ± 0.03 cm^2/s (Table 3).

Investigations carried out by the method of photon correlation spectroscopy in hydrothermal solution samples showed, that the main fraction of particles had dimensions from 1.0 to 50.0 nm. Average radius of particles has values from 7.0 to 25.0 nm. Quantity of particles with dimensions more than 100.0 – 200.0 nm is relatively small.

Table 3. Results of measurements by the method of photon correlation spectroscopy in sample of hydrothermal separate of Verkhne-Mutnovsky geothermal electric power plant.

R, nm	S _{am}	R, nm	S _{am}
1.0 - 1.44	0.0222322	83.17 - 120.22	0.0270527
1.44 - 2.089	0.0335038	120.226 - 173.78	0.0169228
2.0893 - 3.01995	0.0479776	173.78 - 251.189	0.00925547
3.019 - 4.365	0.0649203	251.189 - 363.078	0.00361224
4.365 - 6.309	0.0820874	363.078 - 524.807	0.0
6.309 - 9.12	0.0956918	524.807 - 758.578	0.0
9.12 - 13.18	0.101794	758.578 - 1096.48	0.0
13.18 - 19.05	0.0986029	1096.48 - 1584.89	0.0
19.05 - 27.54	0.0875023	1584.89 - 2290.87	0.0
27.54 - 39.81	0.0718849	2290.87 - 3311.3	0.0
39.81 - 57.54	0.0552209	3311.3 - 4786.3	0.0
57.544 - 83.176	0.0398972	4786.3 - 10000.0	0.0

4. DETERMINATION OF SPECIFIC CONDUCTIVITY OF HYDROTHERMAL SOLUTIONS

Specific conductivity σ is another important characteristic of hydrothermal solution:

$$\sigma = \frac{h_{el}}{R_{el} \cdot S_{el}} \quad (8)$$

h_{el} – is a distance between electrodes, S_{el} – area of electrode plates, R_{el} – ohmic resistance of volume of solution in space between electrodes. According to the value of specific conductivity σ hydrothermal solution from Mutnovskoe field is referred to diluted electrolytes, according to the type of dependence of σ on temperature – to ion conductors (Potapov V.V., 2000). To calculate power inputs for electric treatment by formula it is necessary to know resistance of the electrocoagulator which is determined by the construction of electrocoagulator, strength and density of current and temperature on which conductivity of solution depends. Specific conductivity σ of multicomponent solution is estimated theoretically on the basis of equivalent conductivity λ_s , which is connected with σ value (Gerasimov Ya.I. et al., 1973):

$$\lambda_s = \sigma/c, \quad (9)$$

where c – is volume concentration of ion, mg-equiv/l. According to Kohlrausch's law (Gerasimov Ya.I. et al., 1973) with infinite dilution of electrolyte solution equivalent conductivity is equal to the sum of

maximum ion mobilities u_i which are proportional to velocities of ion motion in electric field of E intensity and in approximation of Stock's regime flows of sphere of radius r_i are equal (Gerasimov Ya.I. et al., 1973):

$$u_i = \frac{z_i e}{6\pi r_i \mu} \cdot E \quad (10)$$

Using Kohlrausch's law we calculated theoretical value of specific conductivity σ for one of the samples of separate from well 014 of Mutnovskoe field. For 25°C theoretical value is equal $\sigma = 1.571 \cdot 10^{-3} \text{ Om}^{-1} \cdot \text{cm}^{-1}$, that shows qualitative correspondence with experimental value for $I = 1.5 \text{ A}$ at 20°C - $1.07 \cdot 10^{-3} \text{ Om}^{-1} \cdot \text{cm}^{-1}$. Na^+ , K^+ , Cl^- , HCO_3^- , SO_4^{2-} , CO_3^{2-} ions contribute to the largest extent to the value of specific conductivity of multicomponent solution. Total contribution of these ions to specific conductivity was 97.92%. Values of maximum ion mobility in water at temperature of 25°C, their concentrations and relative contribution to specific conductivity of hydrothermal solution are given in Table 4.

Table 4. Maximum ion mobilities in hydrothermal solution at 25 °C and relative contribution to specific conductivity of solution.

Ion	Maximum mobility, $\text{cm}^2/\text{Om} \cdot \text{g-equiv}$	Ion concentration, $\text{mg-equiv}/\text{dm}^3$	Relative contribution to specific conductivity, %
H_3O^{3+}	349.8	$10^{-5.9}$	0.00002
Li^+	38.6	0.1873	0.46
Na^+	50.1	10.43	33.24
K^+	73.5	1.46	6.82
NH_4^+	73.5	0.04	0.187
Mg^{2+}	53.0	0.0197	0.066
Ca^{2+}	59.5	0.2	0.757
Al^{3+}	63.0	0.0309	0.123
Fe^{2+}	53.5	0.0107	0.036
Fe^{3+}	68.0	0.0161	0.0697
OH^-	197.6	0.00606	0.083
F^-	55.4	0.08	0.281
Cl^-	76.4	8.20	39.85
HCO_3^-	44.5	0.72	2.039
SO_4^{2-}	80.0	2.60	13.23
CO_3^{2-}	69.3	0.62	2.73

Table 5a. Ohmic resistance of electrocoagulator and conductivity of solution depending on the temperature ($I = 1.5 \text{ A}$, $j = 112.7 \text{ A}/\text{m}^2$, $h_{el} = 10 \text{ mm}$).

$t_s, ^\circ\text{C}$	55.0	43.0	36.0	30.0	27.0	23.0	20.0
$\sigma \cdot 10^3, (\text{Om} \cdot \text{cm})^{-1}$	1.73	1.50	1.41	1.33	1.25	1.18	1.07

Table 5b. Specific conductivity of separate solution from Verkhne-Mutnovsky geothermal electric power plant depending on the temperature ($I = 1.0$ A, $j = 86.95$ A/m², $h_{el} = 10$ mm).

$t_s, ^\circ\text{C}$	$\sigma \cdot 10^3, (\text{Om}\cdot\text{cm})^{-1}$	$\sigma_{\text{theor}} \cdot 10^3, (\text{Om}\cdot\text{cm})^{-1}$	$\mu \cdot 10^3, \text{Pa}\cdot\text{s}$	$\alpha = \sigma / \sigma_{\text{theor}}$
130	3.85	6.200	0.211	0.620
128	3.64	6.113	0.214	0.595
123	3.50	5.866	0.223	0.596
117	3.32	5.543	0.236	0.598
109	3.05	5.150	0.254	0.592
99	2.92	4.655	0.281	0.627
89	2.78	4.166	0.314	0.667
76	2.38	3.545	0.369	0.671
63	2.01	2.959	0.442	0.679
50	1.76	2.404	0.544	0.732
36	1.45	1.858	0.704	0.780
20	1.28	1.307	1.001	0.979

To reveal dependence of resistance R_{el} upon temperature experiments were carried out on treatment of separate from well 014 at strength of current $I = 1.5$ A and current density $j = 112.7$ A/m² in a range $t_s = 20$ -60⁰C. Measurement results for specific conductivity of hydrothermal solution within temperature range 20-60⁰ C are given in Table 5a. Table 5b presents experimental data on measurement of σ value in separate solution from Verkhne-Mutnovsky geothermal electric power plant within a range of 20-130⁰ C.

According to the data from Table 5a, resistance of electrocoagulator with solution of hydrothermal separate decreased with increase in temperature: value R_{el} decreased 1.6 times with increase in temperature from 20 to 60⁰C. Specific conductivity σ increased 1.6 times with increase in temperature from 20 to 60⁰C. Growth in specific conductivity corresponded to the fact, that according to equation (10) with increase in temperature and decrease in viscosity of water μ mobilities of u_i ions of solution increase, that leads to the growth in equivalent λ_s and specific σ conductivities.

Equation (10) shows, that mobility of separate ions and, therefore, specific conductivity of solution, are inversely proportional to dynamic viscosity of solution. Table 5b gives values of viscosity at different temperature, calculated by equation (Vukalovich M.P., Rivkin S.L., Aleksandrov A.A., 1969):

$$\mu(t_s) = 0.0000001 \cdot 241.4 \cdot 10^{247.8/(t_s - 140)} \quad (11)$$

Taking into account dependence of viscosity upon temperature according to equation (10), theoretical values σ_{theor} of specific conductivity were calculated (see the last column in Table 5b). At 20⁰ C theoretical

value σ_{theor} slightly differs from the experimental one (Table 5b). At higher temperatures 50-130⁰ C this difference is more substantial: theoretical values are 1.4-1.69 times large than experimental ones. Thus, equations (9), (10) and (11) make it possible to estimate value σ at different ion concentrations, pH, temperature of solution by introducing the coefficient $\alpha = \sigma / \sigma_{\text{theor}}$ values of which are within 0.73-0.59 at higher temperature.

Table 6. Concentrations of anions and cations in hydrothermal separate of well 103 of Pausgetskoe field. $I_s = 52.401$ mmol/kg, $\sigma = 5.03 \cdot 10^{-3} (\text{Om}\cdot\text{cm})^{-1}$ (18.4⁰C), n.d.-concentration was not determined, (-) values were not calculated.

Com ponent	mg/l	mg-equiv/l		Relative contribution to specific conductivity, %
		mg-equiv/l	mg-equiv/l %	
Na ⁺	877.5	38.15	86.1	33.54
K ⁺	98.9	2.54	5.7	3.27
Ca ²⁺	54.08	2.7	6.1	2.819
Mg ²⁺	<1.2	-	-	-
Fe ²⁺	<0.1	-	-	-
Fe ³⁺	<0.3	-	-	-
Al ³⁺	n.d.	-	-	-
NH ₄ ⁺	1.0	0.06	0.1	0.077
Li ⁺	6.1	0.88	2.0	0.596
Sum of cations	1037.58	44.33	100.0	40.30
Cl ⁻	1418.4	40.0	91.1	53.639
HCO ₃ ⁻	44.82	0.73	1.7	0.57
CO ₃ ²⁻	0.45	0.02	0.0	0.024
SO ₄ ²⁻	134.48	2.8	6.4	3.931
H ₃ SiO ₄ ⁻	3.98	0.04	0.1	-
H ₂ BO ₃ ⁻	14.51	0.24	0.6	-
F ⁻	1.56	0.082	0.19	1.516
Sum of anions	1618.2	43.91	100.0	59.68
H ₃ BO ₃	207.02	-	-	-
(H ₄ SiO ₄) _t	512.0	-	-	-
Mineralization	3458	-	-	-
pH	8.03	-	-	-

In the table 6 data on the concentrations of cations and anions in hydrothermal separate of well 103 of Pausgetskoe field are presented. Experimental value of specific conductivity of separate at 18.4⁰C was $\sigma = 5.03 \cdot 10^{-3} (\text{Om}\cdot\text{cm})^{-1}$, theoretical value calculated from the equations (9), (10), (11) was $\sigma = 5.697 \cdot 10^{-3} (\text{Om}\cdot\text{cm})^{-1}$ at 25⁰C and $\sigma = 4.869 \cdot 10^{-3} (\text{Om}\cdot\text{cm})^{-1}$ at 18.4⁰C, so value $\alpha = \sigma / \sigma_{\text{theor}}$ at 18.4⁰C was 1.033. Thus, one can use these equations for prediction of

separate specific conductivity at different hydrothermal parameters of hydrothermal solution: temperature, ions concentrations, pH, ionic strength.

CONCLUSIONS

1. According to concentrations of silica, sodium and potassium in separate solution from wells of Mutnovskoe field temperature of heat carrier in drained zone of hydrothermal reservoir is within a range from 250 to 300°C. In solution of separate ions of sodium and potassium have the largest concentration among cations, chlorine-ion and sulphate-ion - among anions. Separate is referred to chloride-sulphate-sodium-potassium type of hydrothermal solutions.

2. Processes of nucleation and polymerization of orthosilicic acid in oversaturated solution of separate lead to the formation of colloidal silica particles average radii of which are within a range from 1.0 to 20.0 nm. The main fraction of particles has radii in a range from 1.0 to 50.0 nm.

3. Experimental values of specific conductivity of separate at different temperature are in quantitative correspondence with theoretical values calculated on the basis of Kohlrausch's law, of maximum values of ion mobility and viscosity of water. It makes it possible to forecast conductivity of hydrothermal solution at different temperature, ions concentrations, pH, ionic strength of solution and estimation of consumption of electric power for silica precipitation by electrocoagulation.

4. We revealed physical and chemical characteristics of hydrothermal separate which are important for solving the problem of solid deposits and for the development of silica precipitation technology: 1) total content C_t of silica in solution; 2) average radius, area of surface of colloid silica particles; 3) concentration of basic cations (Na^+ , K^+) and anions (Cl^- , SO_4^{2-}); 4) pH; 5) mineralization of solution M_h ; 6) ionic strength I_s ; 7) specific conductivity of solution σ .

REFERENCES

Arnorsson S., Gunalaugsson E., Svavarsson H. (1983), "The chemistry of geothermal waters in Iceland III. Chemical geothermometry in geothermal investigations", *Geochim. Cosmochim. Acta.*, v. 47., p. 567-577.

Fournier R.O., Rowe I.I. (1966), "Estimation of underground temperatures from the silica of water from hot springs and wet-steam wells", *Amer. J. Sci.*, v. 264, p. 685-697.

Fournier R.O., Truesdell A. (1973), "An empirical Na-K-Ca geothermometer for natural waters", *Geochim. Cosmochim. Acta*, v.37, p. 1543-1550.

Gerasimov Ya.I. et al. (1973), "Course of physical chemistry", v. II, Moscow: Chemistry, 624 p.

Potapov V.V. (2000), "Electrical and chemical processing of hydrothermal heat carrier before reinjection", *Teploenergetika*, №1, P. 33-38.

Potapov V.V., Kashpura V.N., Alekseev V.I. (2001), "Study of growth of solid deposits in geothermal heat power systems", *Teploenergetika*, № 5, p. 49-54.

Vukalovich M.P., Rivkin S.L., Aleksandrov A.A., (1969), "Tables of thermal and physical properties of water and water vapour", Moscow: Izdatelstvo "Standartov", 408 p.

White D.E. (1965), "Thermal waters of volcanic origin", Coll.: *Geochemistry of postvolcanic processes*, Moscow: Mir, p. 78-100.

A REEVALUATION OF GEOPRESSURED-GEOTHERMAL AQUIFERS AS AN ENERGY SOURCE

Jeremy Griggs

Unocal
14141 Southwest Freeway
Sugar Land, Texas, 77478
e-mail: jeremy.griggs@unocal.com

ABSTRACT

The search for more efficient and economical forms of energy is a continual process. Natural gas production and electricity generation from geopressured-geothermal aquifers is an unconventional hydrocarbon source that has long been unproductive due to its economic constraints and lack of technical certainty. Given current economic constraints and considering the application of modern potential technologies, geopressured-geothermal energy maintains a potential future as an alternative domestic energy source. This paper presents a range of conditions where the production of geopressured-geothermal aquifers offers an economically viable solution.

INTRODUCTION

During the energy crisis of the 1970's, the United States began to explore for potentially significant amounts of hydrocarbons stored in unconventional resources. Oil shales, oil sands, methane hydrates, coalbed-methane and geothermal-geopressured aquifers were given research priority due to large quantities of potentially recoverable energy. Industry and governmental financial support were given to projects that evaluated the economic viability and level of technological competency required to develop these unconventional sources of oil and natural gas. Due to government deregulation of the natural gas market and the ensuing price collapse, the economic incentive to commercially develop most unconventional sources of natural gas was not present. The commercial development of geothermal-geopressured aquifers was considered marginally economic in only special circumstances and considered a long-term alternative hydrocarbon source.

Once again, the United States is poised to enter an energy crisis. The oil and natural gas price crash of the 1980's, and the lack of energy value price parity between oil and natural gas, has motivated many power generation, industrial, residential and municipal users to transition to natural gas as a

primary energy and heating source during the past 15 years. The International Energy Administration (IEA) forecasts that this trend will continue and that world natural gas demand will increase by over 100% or 30 Tcf by the year 2030 (Oil & Gas Journal, December 1, 2003). This transition and the forecasted increase in demand places a greater burden on the ability of energy companies to meet the world market demand of natural gas. As supply tightens, natural gas imports to the U.S. have risen, and plans to reactivate or build liquefied natural gas (LNG) trains at several U.S. ports have been announced.

To meet the forecasted increase in domestic U.S. and world energy demand, the IEA stated that global spending on hydrocarbon exploration and production must exceed \$5.3 trillion dollars by 2030. Resources are again being dedicated to develop alternative domestic energy sources. Research currently focuses on economic methods to produce oil sands and oil shales, and the U.S. Department of Energy (DOE) has announced plans to fund a ten-year clean coal technology (coal gasification) pilot program (Department of Energy briefing, February 27, 2003).

Attention may return to geopressured-geothermal aquifers as an unconventional hydrocarbon resource. But, continued research should be justified by demonstrating that there is potential for sustainable, economic production of geopressured brines. The geopressured-geothermal resource base for the northern Gulf of Mexico could exceed 1,000 TCF of recoverable natural gas (Wrighton, 1981). This resource base is not insignificant; in 1995 the United State Geological Survey estimated that U.S. technically recoverable volumes of conventional and unconventional gas, excluding geopressured brines and clathrate structure-gas hydrates, was 1,073 Tcf (Petzet, 1995).

New technologies may allow more efficient extraction of methane and thermal energy from the geopressured brine. The use of binary-cycle power plants may improve thermal recovery efficiencies to

economically sustainable levels. The injection of paraffinic hydrocarbons into the produced fluid stream could improve methane recovery efficiencies while reducing the amount of surface equipment necessary for handling geopressured brines.

This paper presents a historical overview of research into geopressured-geothermal aquifers, discusses the range of reservoir properties encountered during experimental field developments, and discusses a range of economic and physical constraints that may enable the sustainable, economic development of geopressured-geothermal aquifers as an energy source.

BACKGROUND

Estimating the Geopressured Resource

Geopressured-geothermal aquifers are a subset of geopressured reservoirs. As a potential resource, energy contained in the geopressured-geothermal aquifer takes three forms: mechanical energy as excess pressure at the wellhead, thermal energy, and methane dissolved in the aquifer pore water. Geopressured aquifers are commonly defined to have a pore pressure in excess of 0.675psi/ft (13.0ppg) and a geothermal gradient of 1.8°F/100ft or higher. Total aquifer bulk volumes can be in excess of 3 cubic miles, but individual reservoirs may be smaller (Bassiouni, 1980). Fig. 1 presents the geographic range of the geopressured zone in the northern Gulf of Mexico (Bebout, 1981). Fig. 2 shows the major depocenters during the Upper Cretaceous and Tertiary along the northern Gulf of Mexico (Bebout, 1981).

Estimates of the amount of geopressured-geothermal energy available in the northern Gulf of Mexico vary widely. Papadopoulos et al (1975) estimated the resource total for onshore Texas and Louisiana to be 46,000EJ [1 EJ \cong 1.04 Tcf] of thermal energy, 25,000EJ of methane, and 2,300EJ of mechanical energy. Based on the occurrence of geopressured aquifers in the studied area, offshore and other onshore sediments not included in the study were estimated to be 1.5 to 2.5 times the amount estimated in the study. Papadopoulos also estimated absolute recovery efficiencies to be between 0.5% and 3.5% of the resource in place (Wallace, 1979). Jones (1976) estimated the total methane content to be 49,000Tcf, of which 17,000Tcf was offshore. He estimated that between 246 to 1,145Tcf of methane could be recovered. Brown (1976) went on to state that recovery efficiency “probably lies in the range of 4 to 50% of the methane within reservoirs which are eventually developed.” Hise (1976) estimated the total in place methane to be only 3000Tcf; and that perhaps 28Tcf of natural gas could be recovered

Bassiouni (1980) published a report that ranked the sixty-three most promising geopressured-geothermal prospects in the state of Louisiana according to estimates of the total recoverable energy available in each prospect. The report detailed reservoir properties of the six highest ranking prospects and the Tuscaloosa trend; recommending three of these prospects, Grand Lake, Lake Theriot and Bayou Hebert, as suitable test sites. The Table 1 presents a summary of aquifer properties for the six highest-ranking prospects.

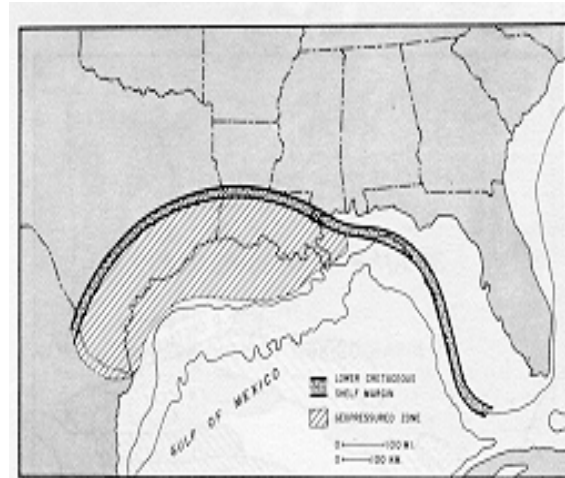


Fig. 1. Range of occurrence of geopressure in the Northern Gulf of Mexico Basin. (Bebout, 1981). (Note: not to scale).

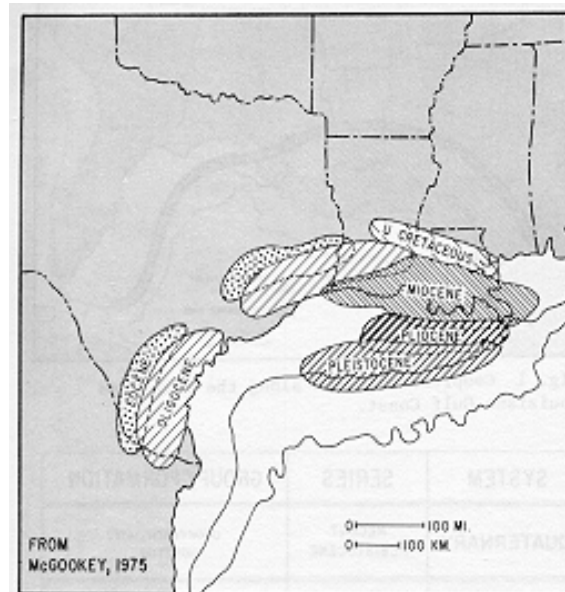


Fig. 2. Major depocenters during the Upper Cretaceous and Tertiary along the northern Gulf of Mexico. (Bebout, 1981). (Not: not to scale).

Prospect	Physio- graphy	Top of Geo- pressure (ft.)	Bulk Rock Volume (ft ³ x 10 ⁹)	k (md)	φ (%)	In-Place Water (bbl x 10 ⁹)	Avg. Pressure (psia)	Avg. Temp. (°F)	Avg. Water Salinity (ppm)	Gas Solub. (scf/bbl)	In-Place Dissolved Gas (Tcf)
Grand Lake	Marsh	13,600	657	21	18	21	12,600	240	100,000	28	0.6
Lake Theriot	Marsh	12,600	1,738	103	28	87	11,620	232	46,000	32	2.8
Bayou Hebert	Dry Land/ Marsh	13,000	543	45	16	15	11,600	230	87,000	26	0.4
Kaplan	Dry Land	12,000	312	273	23	13	12,770	259	57,000	37	0.5
South White Lake	Marsh	14,900	211	68	12	4	16,200	281	150,000	23	0.1
Solitude Point	Dry Land	19,000	1,914	5	9	30	15,000	328	60,000	58	1.7

Table 1. Louisiana geopressed aquifers. (Bassiouni, 1981).

Industry Experience with Geopressed Aquifers

In 1972 the National Science Foundation sponsored the Geothermal Resources Research Conference, which brought together scientists, engineers and environmentalists to discuss emerging geothermal technologies. In 1973, the conference report was published and geopressed water was recognized “as a significant and special type of geothermal energy, having in addition to thermal energy, natural gas and geohydraulic energy (Hickel, 1973; Hawkins).”

McMullan and Bassiouni (1981), recognizing that maximizing flowrate maximized NPV, presented an equation to predict brine flowrate given a constant tubing head pressure. Additionally, the results of the study showed that the location of the well in respect to the aquifer was relatively unimportant compared to the effect of tubing size, skin, and initial aquifer properties.

Isokari (1976) described a two-phase, two-dimensional reservoir simulation program for the modeling of a geopressed-geothermal aquifer. Knapp et al. (1977) included the effect of shale dewatering in the numerical simulation of geopressed aquifers. The results of the simulation’s sensitivity analysis found that water influx from underlying and inter-bedded shales would play a more important role in aquifer pressure maintenance than water influx from laterally adjacent shales. They also found the depletion of geothermal geopressed aquifers can be approximated as an isothermal process. Doscher et al. (1979) found critical gas saturation to be an important parameter controlling ultimate recovery from a geopressed aquifer.

Economic studies of geopressed aquifers focused on determining the sensitivity of wellhead gas price to differing reservoir and completion parameters. Randolph (1977) varied the tubing diameter, porosity, permeability, rock compressibility, flowrate and aerial extent and found that the “reservoir criteria

for natural gas production are much less stringent than for electricity generation from Gulf Coast geopressed aquifers.”

The “Wells of Opportunity” and “Design Well” Programs

In 1975, the United States Energy Research and Development Administration (now DOE) began funding studies of the geopressed-geothermal resource that performed geologic assessments of the Gulf Coast geopressed-geothermal potential. The scope of the program was later expanded to include projects that sought 1) to physically verify the reservoir fluid and near wellbore petrophysical properties of geopressed aquifers, and 2) test the long-term producibility of geopressed aquifers. Completion of the goals was chartered under the Wells of Opportunity (WOO) and the Design Well (DW) programs, respectively. The purpose of the programs were “to determine whether or not the resource has potential... as an economic, reliable and environmentally acceptable energy source (Westhusing, 1981).”

The WOO program was designed to provide large amounts of quickly available information from a diverse geographic and geologic area without great expense to the DOE. Short-term tests allowed for the data collection on aquifer fluid characteristics, near-wellbore petrophysical properties, fluid behavior under flow and well deliverabilities, the evaluation of completion techniques, and scale and corrosion potential.

There were limitations to the success of the WOO program. Wells selected for completion were not located in structurally favorable locations. Even though permeability barriers were encountered in all of the test wells, the short-term pressure transient tests did not provide information on complete reservoir limits. Due to the nature of the WOO

	Girouard No.1	Koelemay No.1	Saldana No.2	Prairie Canal No.1	Crown Zellerbach No.1	Fairfax Sutter No.2
Parish (County)	Lafayette, LA	Jefferson, TX	Zapata, TX	Calcasieu, LA	Livingston, LA	St.Mary, LA
Shut-in Surface Pressure (psia)	6695	4373	2443	6420	2736	-
Max Flow Rate (BWPD)	15,000	3,200	1,950	7,100	2,832	7,700
Max Gas Rate (Mcf/d)	600	1,017	105	390	93	-
Surface Flow Temp (F)	255	206	220	230	198	240
Produced Gas-Water Ratio (scf/bbl)	40	30-318*	47-54	43-55	33	22.5-30
Lab Gas-Water Ratio (scf/bbl)	44.5	35	41	43	-	22.8
Water Salinity-TDS (ppm)	23,500	15,000	12,800	42,600	32,000	190,000
Carbon Dioxide (Mole %)	6	7.2-2.7	26.4-16.4	9.6	22.6	7.8
Total Water Produced (bbls)	41,930	30,030	9,328	41,079	10,338	-
Formation	Frio - Marg. Tex No.1	Yegua - "Leger"	Upper Wilcox	Hackberry, Upper Frio	Tuscaloosa	-
Perforations (ft)	14,774-14,819	11,639-11,780	9,745-9,820	14,782-14,820	16,720-16,750	15,781-15,878
Gross Interval (ft)	107	139	90	25	36	-
Net Interval (ft)	91	77	79	14	35	58
Reservoir Pressure (psia)	13,203	9,450	6,627	12,942	10,075	12,203
Reservoir Temperature (F)	274	260	300	294	327	270
Porosity – Log (%)	26	20	16	28	17	19.3
Porosity – Core (%)	-	26	20	25	-	-
Permeability - Core (md)	-	85	20	-	-	-
Permeability - Test (md)	200-240	100-200	16.7	95	16.6	14.5
Radial Distance Explored (ft)	1,658	1,972	2,768	3,897	1,758	-

Table 2. Reservoir characteristics of selected Wells-of-Opportunity.

program, not all wells tested were in good condition: 11 wells were accepted to the WOO program, 8 wells were successfully re-completed in geopressed aquifers, and seven wells provided flow data (Swanson, 1986). Table 2 provides reservoir information for six of the WOO program wells (Kluzinski, 1981, McCoy, 1980).

In two wells, brine salinities were higher than expected and resulted in reduced methane solubilities. Carbon dioxide content of some wells was much higher than expected, resulting in reduced methane solubility in the brine. The Tuscaloosa sand test in Livingston Parish showed brine under-saturated with methane. The Lake Charles, LA and Laredo, TX wells produced gas at rates in excess of the methane solubility in brine. All other test wells showed methane content at or near saturation in the brine. Scaling and corrosion tendency depended on brine salinity and reservoir temperature. Bottom-hole

temperatures were between 7% and 16% higher than log derived data (Kluzinski, 1981).

The Design Well program focused on long duration tests to extensively study reservoir fluid composition, reservoir characteristics, and drive mechanisms. These wells were located at optimum reservoir locations and designed to produce geopressed brines at high rates for periods to 2 years. The location of design wells were chosen to allow testing of the most favorable fairways and to provide testing of sand complexes that had yet to be produced. Selection guidelines for design well sites were similar to the WOO. Table 3 describes the reservoir characteristics and flow properties of the Design Wells.

The Pleasant Bayou No.2 test well was the first well drilled and completed in the DOE Design Well program. Testing of the well lasted from 1979 until

	Pleasant Bayou No.2	Gladys-McCall No.1		Amoco Fee No.1		L.R. Sweezy No.1
Parish (County)	Brazoria, TX	Cameron, LA		Cameron, LA		Vermillion, LA
Formation	Lower Miocene Oligocene	Frio Oligocene		Miogypsinoides Sand Upper Oligocene		Upper Frio Oligocene
Tested Zone	-	Zone 3	Zone 5	Zone 8	Zone 9	-
Max Flow Rate (BWPD)	28,900	6,604	36,500	36,500	4,400	10,700
Sustained Flow Rate (BWPD)	18,900	-	15,700	33,300	-	8,500
Produced Gas-Water Ratio (scf/bbl)	23	20.2-24.1	23	27-29.8	32	20.2
Total Water Produced (bbls)	15.4E6	27E6		1.1E6		2E6
Water-in-Place (bbls)	5E9	7.8E9		1.8E9		106E6
Water Salinity-TDS (ppm)	131,320	168,650	165,000	97,800	96,500	99,700 +/-240
Carbon Dioxide (mol %)	11.28	-	-	9.92		-
Gross Interval (ft)	60	34	32	338	128	73
Net Interval (ft)	53	24	27	333	114	57
Res. Pres. (psia)	11,168	11,887	12,082	12,799	12,911	11,410
Res. Temp. (F)	305	293	298	291	294	237
Porosity	18	20	22	16	16	27
Permeability	192	42-140	12-162	160	67	126

Table 3. Reservoir characteristics and flow properties of Design Wells.

late August 1990 and approximately 15.4MMbbls water and 330MMscf natural gas was produced. Initial testing of the aquifer was conducted from 1979 through 1983, when wellbore failure occurred. In 1988 the well was re-completed and testing of an experimental Hybrid Power System (HPS) occurred until 1990. The Pleasant Bayou No.2 was the only Design Well to utilize the HPS for the generation of electricity (Chacko, 1998).

The Gladys-McCall No.1, drilled and completed in 1981, provided a successful field test of a moderately sized geopressured aquifer. The well produced over 27MMbbls of water and 675MMscf between its initial production date in 1983 and shut-in in 1987. Scale production was controlled through the use of continuous inhibitor injection into the production stream and through the periodic injection of an inhibitor pill into the formation (Tomsor, 1986). This enabled the well to produce brine at rates in excess of 30,000 BWPD. Short- and long-term pressure transient tests estimated the primary aquifer volume at between 270 and 408MMbbls. Long-term transient test estimated that an additional 7.5 billion barrels of water was partially connected to the primary volume.

The additional volume was hypothesized to come from either shale water influx, additional volume connected through a partially-sealing fault, or a combination of both (Lee, 2000; Rogers, 1991). Core analysis from the Gladys-McCall No.1 showed that both reservoir compaction and formation creep could greatly contribute to the reservoir drive mechanism (Chacko, 1998, Kelkar, 1983).

EXPERIMENTAL METHOD

Studies to determine the commercial potential of geopressured-geothermal aquifers typically focused either on reservoir performance or financial viability of field development (Quitau, 1981; Knapp, 1977). Unfortunately, no comprehensive studies to determine the commerciality of geopressured aquifers have been performed for almost twenty years. This study combines reservoir performance, facility efficiency and financial constraints to determine a range of potential outcomes for viable commercial development of geopressured-geothermal aquifers.

The reservoir performance model utilizes a commercial reservoir simulation program to predict the production rates from aquifers under constrained

surface pressure. Sensitivities consider single- well and multi-well developments. Reservoir model components are varied to determine a wide range of aquifer productivities. Varied parameters include bulk volume, depth, reservoir dip angle, porosity/permeability, initial pressure and temperature gradient, salinity, formation compressibility, maximum allowable flowrate, wellbore radius, formation dip angle, and initial gas saturation. If variations of reservoir input parameters are considered using full factorial design, over 470,000 simulation runs would be needed to provide the results of all combinations. By using a mixed-array (MA) the full range of solutions for all simulation parameters can be defined while reducing the number of required simulation runs to 36. Additional models were created to gauge the effect of shale-water influx and formation compaction.

The facility model uses reservoir temperature and flowrate from the reservoir performance model to estimate the net electric output of the thermal recovery system. The facility model assumes that a Kalina-cycle binary power plant is utilized. The financial model computes the discounted cash flow of geopressed aquifer developments. Input parameters for the financial model are flowrate from the reservoir model, discount rate, natural gas price, net electric output, electricity price, capital and operational costs, severance taxes and net revenue interest. Output parameters include discounted cash flow, payout time, profitability index and the internal rate of return. A range of input parameters that yield a positive life-cycle cash flow are delineated by combining the results of the reservoir, facility, and financial models. The ranges can be applied to

evaluate geopressed-geothermal resources and identify areas where additional research is warranted.

CONCLUSIONS

Economic viability can be broken into three performance groups: positive under all constraints, positive under a specific range of constraints (marginal), and never positive. For this study, negative performance is defined as having a negative ROR, marginal performance has a ROR below 30% and a positive NPV, and positive performance has a ROR above 30% and a positive NPV. Realized natural gas price, electricity price, capital cost, and operating expenses are the underlying constraints for this study. Table 4 and Fig. 3 rank the input parameters based on their effect on economic outcome.

Rank	
"Marginal or Economic"	"Economic"
V _b	D _w
S _{gi}	Phi/ k
Phi/ k	V _b
D _w	dP/dh
Salinity	Flowrate (q)
Aquifer height (h)	C _f
Flowrate (q)	Salinity
Depth	S _{gi}
dP/ dh	Dip Angle
C _f	Aquifer height (h)
Dip Angle	Depth
dT/ dh	dT/dh

Table 4. Rank of factors.

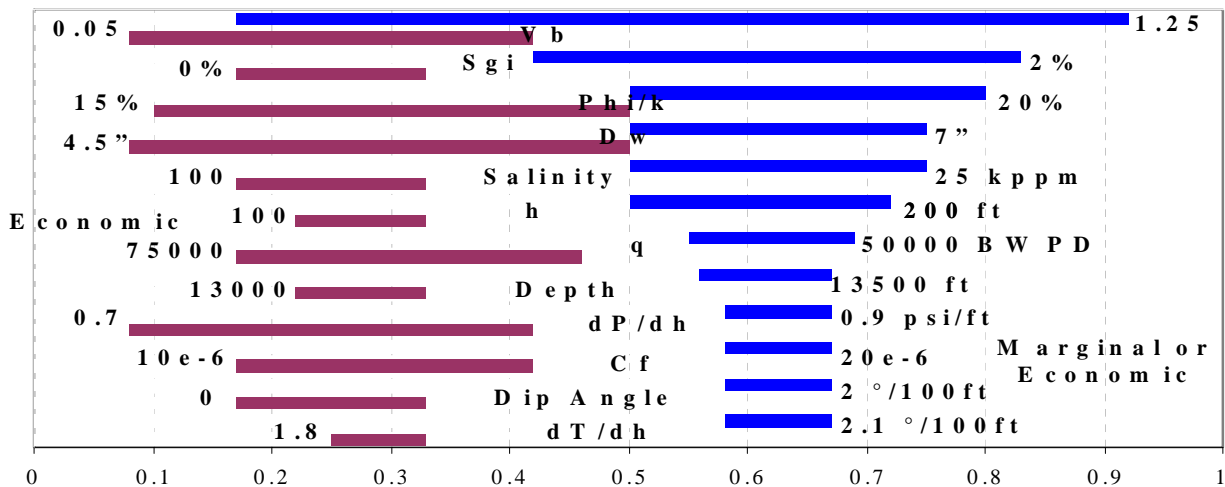


Fig. 3. Tornado diagram of results of sensitivity analysis for single-well developments with flowline length of 100 ft. Note that the x-axis represents the fraction of runs that exceed the requirement, not the probability that the requirement will be met.

Fig. 4 and Fig. 5 display the economic potential of a simulation case based on the interaction of two input variables. These “maps” were generated to determine the interaction of variables and the result on economic potential. Fig. 4 shows that low salinity/ large bulk volume aquifers have the largest potential for economic development. Salinity affects economic viability through methane solubility. Fig. 5 shows that greater economic potential exists for moderate flowrate/ large bulk volume systems than for high flowrate/ large bulk volume systems. This result can be explained through the incremental cost associated with transitioning from a moderate flowrate system to a high flowrate system.

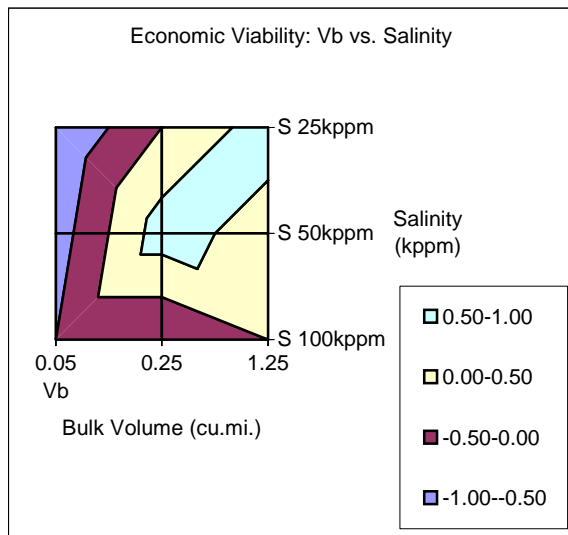


Fig. 4. Economic viability of a : V_b vs. pressure gradient.

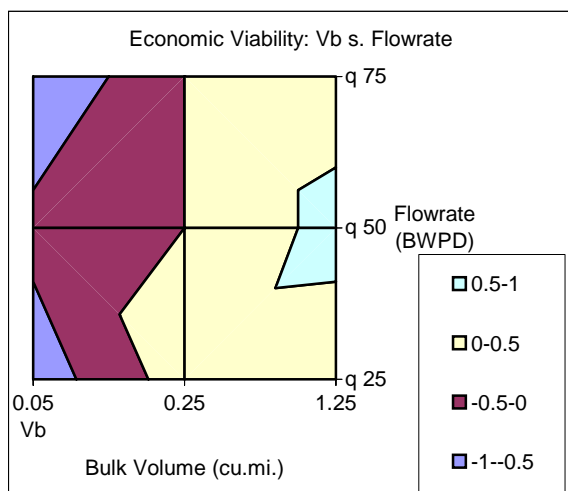


Fig. 5. Economic viability: V_b vs. flowrate (flowrate is divided as follows: $\leq 25,000$ BWPd, $\leq 50,000$ BWPd, and $\leq 75,000$ BWPd).

The inclusion of the binary-cycle power plant dilutes the economic incentive to develop geopressured-geothermal aquifers. Table 5 displays the effect removing the thermal recovery unit has on Rate of Return of a simulation case. However, the values for temperature gradient and depth used in this study represent a limited range of those expected in northern Gulf of Mexico environments. The temperature gradients used in this study ranged from 1.8°F/100ft to 2.1°F/100ft. Aquifers tested in the WOO and DW programs varied in depth from 9,500 ft to 15,500 ft and with geothermal gradients between 1.5 °F/100ft and 2.5 °F/100ft.

Sensitivity Run	ROR (%)	
	\$4.50 /Mscf \$0.03 /kW-hr	\$4.50 /Mscf No TRU
Case 09	31	32
Case 10	32	33
Case 11	5	6
Case 12	8	8
Case 21	27	31
Case 22	56	64
Case 23	11	23
Case 24	38	61
Case 33	27	29
Case 34	59	73
Case 35	35	36
Case 36	-	-

Table 5. Change in ROR for selected cases.

FUTURE WORK

The economic and technical constraints posed in this study determine a potential range of conditions where the development of geopressured aquifers may have commercial application. However, these factors also indicate that challenges remain before field development of geopressured aquifers can begin. Five groups emerge that warrant further investigation and could greatly enhance the value of the geopressured-geothermal resource:

1. Reservoir characterization and resource estimation. By refining estimates of rock compaction, shale-water influx, and diagenic history a more detailed analysis of aquifer drive mechanisms could be determined. The re-activation of the Wells of Opportunity

- program could refine estimates expected aquifer volumes and aid in quantitatively determining the effects of carbon dioxide and heavier hydrocarbons on methane solubility in brine.
2. Facility optimization and systems analysis. Detailed system analysis and facility optimization could decrease capital cost and operating expense while providing for more efficient extraction of methane. Accurate temperature, flowrate, and facility coupling could provide “fit-for-purpose” equipment and significantly reduce expense.
 3. High efficiency binary-cycle power plants. Further investigation of Kalina-cycle power plants could provide for a cheap, yet highly efficient, means of extracting thermal energy from geopressured brine. Detailed evaluation on the implementation of a Hybrid Power System could further enable geopressured aquifers to provide a “micro-scale” power grid.
 4. Detailed economic analysis. Accurate estimation of facility and power plant expense, along with more detailed estimates of drilling cost may provide a more economic opportunity. Commercial potential of geopressured aquifers could increase with the inclusion of dry-hole risk, well replacement cost, and the likely-hood of different development.
 5. Legal and political difficulties. The aerial extent of potentially commercial geopressured aquifers is likely to be in excess of 10 sq. mi. and small acreage landowners could derail the development of this energy source. Mineral law case history is vague concerning the ownership of sub-surface brine. The renewal of federal tax credits and the implementation of severance tax relief and federal loan guarantees could provide significant economic incentive to develop geopressured aquifers.

ADDENDUM

This paper presents a summary of text originally written as a Master’s thesis. The complete text of this study can be found at <http://etd.lsu.edu/docs/available/etd-07082004-102126/> and is available for unrestricted viewing.

REFERENCES

Bassiouni, Z.: “Evaluation of Potential Geopressure Geothermal Test Sites in Southern Louisiana”, Progress Report. DOE Contract No. DE-AS05-76ET28465. April 1980.

Bebout, D.G. and Gutierrez, D.R.: “Geopressured Geothermal Resource in Texas and Louisiana – Geological Constraints”, Proceedings of the 5th Geopressured-Geothermal Energy Conference held in Baton Rouge, La. October 1981. Edited by Bebout and Bachman.

Brown, W.M.: 100,000 Quads of Natural Gas?, Research Memorandum #31, Report HI-2415/2-P, Hudson Institute, Inc., Croton-on-Hudson, N.Y., July 1976.

Chacko, J.J., Maciasz, G, Harder, B.J.: “Gulf Coast Geopressured – Geothermal Program Summary Report Compilation”, Work performed under U.S. Department of Energy Contract No. DE-FG07-95ID13366. June 1998.

Doscher, T.M., et al.: “The Numerical Simulation of the Effect of Critical Gas Saturation and Other Parameters on the Productivity of Methane From Geopressured Aquifers”, paper SPE 8891 presented at the 1980 Annual California Regional Meeting of the Society of Petroleum Engineers of AIME held in Los Angeles, California. April 9-11.

Hawkins, M.F., and Parmigiano J.M.: “Geopressured Water as an Energy Source,” paper SPE 4725. Publication date unknown.

Hickel, W. J.: “Geothermal Energy-A National Proposal for Geothermal Resources Research”, Univ. of Alaska, 1973.

Hise, B.R.: “Natural Gas from Geopressured Aquifers,” pp.41-63 in Natural Gas from Unconventional Geologic Sources, National Academy of Sciences, Washington, D.C., 1976

Isokari, O.F.: “Natural Gas Production from Geothermal Geopressured Aquifers”, paper SPE 6037 presented at the 1976 Annual Fall Technical Conference and Exhibition held in New Orleans, Louisiana. October 3-6.

Jones, P.H.: “Natural Gas Resources of the Geopressured Zones in the Northern Gulf of Mexico Basin,” pp.17-23 in Natural Gas from Unconventional Geologic Sources, National Academy of Sciences, Washington, D.C., 1976.

Kelkar, S.M., Cooley, C.H., and Schatz, J.F.: “Mechanical Properties of Geopressure Core and Their Influence on Reservoir Performance: T-F&S/OE Gladys McCall No.1 Well”, paper SPE 12191 presented at the 1983 Annual Technical Conference and Exhibition held in San Francisco, CA. October 5-8.

Klauzinski, R.Z.: "Testing of Six 'Wells of Opportunity' During 1980 and 1981", Proceedings of the 5th Geopressured-Geothermal Energy Conference held in Baton Rouge, La. October 1981. Edited by Bebout and Bachman.

Knapp, R.M., et al.: "An Analysis of Production from Geopressured Geothermal Aquifers", paper SPE 6825 presented at the 1977 Annual Fall Technical Conference and Exhibition held in Denver, Colorado. October 9-12.

Lee, K.S.: "Analysis on the Depletion and Recovery Behavior of a Geopressured/Geothermal Reservoir", paper SPE 64516 presented at the 2000 SPE Asia Pacific Oil and Gas Conference and Exhibition held in Brisbane, Australia. October 16-18.

McCoy, R.L., Hartsock, J.H., and Dobson, R.J.: "Preliminary Results of the Wells-of-Opportunity Program Geopressured-Geothermal Testing Program", paper SPE 8958 presented at the 1980 SPE/DOE Symposium on Unconventional Gas Recovery held in Pittsburgh, PA. May 18-21.

McMullan, J.H., Bassiouni, Z.: "Prediction of Maximum Flow Rates From Geopressured Aquifers", paper SPE 10282 presented at the 1981 Annual Fall Technical Conference and Exhibition held in San Antonio, Texas. October 5-7.

Papadopoulos, S.S., et al.: "Assessment of Onshore Geopressured-Geothermal Resources in the Northern Gulf of Mexico Basin," pp.125-46 in Assessment of Geothermal Resources of the United States – 1975, D.E. White and D.L. Williams, eds., U.S. Geological Survey Circular 726, 1975.

Petzet, G. A.: "Partial U.S. Oil, Gas Resource Volumes Termed 'Astonishing'", Oil & Gas Journal. March 16, 1995.

Quitau, R., Bassiouni, Z.: "The Possible Impact of the Geopressure Resource on Conventional Oil and Gas Exploration", paper SPE 10281 presented at the 1981 Annual Fall Technical Conference and Exhibition in San Antonio, Texas. October 5-7.

Randolph, P.L.: "Natural Gas From Geopressured Aquifers?", presented at the 1977 Annual Fall Technical Conference and Exhibition held in Denver, Colorado. October 9-12.

Rogers, L.A., Randolph, P.L., Eaton, B.A. and Meahl, T.E.: "The DOE Gladys McCall Geopressure-

Geothermal Gas/Brine Well Test: Summary of Well Test Results", paper SPE 21485 presented at the 1991 SPE Gas Technology Symposium held in Houston, TX. January 23-25.

Swanson, R.K., Bernard, W.J., Osoba, J.S.: "A Summary of the Geothermal and Methane Production Potential of U.S. Gulf Coast Geopressured Zones From Test Well Data", Journal of Petroleum Technology. December 1986. pp. 1365-1370.

Tomsor, M.B, Rogers, L.A., Varughese, K., Prestwich, S.M, Waggett, G.G., Salimi, M.H.: "Use of Inhibitors for Scale Control in Brine-Producing Gas and Oil Wells", paper SPE 15457 presented at 1986 Annual Technical Conference and Exhibition held in New Orleans, LA. October 5-8.

Wallace, R.H., et al.: "Assessment of Geopressured-Geothermal Resources in the Northern Gulf of Mexico Basin," pp.132-55 in Assessment of Geothermal Resources of the United States – 1978, D.E. White and D.L. Williams, eds., U.S. Geological Survey Circular 790, 1979.

Westhusing, K.: "Department of Energy Geopressured Geothermal Program", Opening Comments. Proceedings of the 5th Geopressured-Geothermal Energy Conference held in Baton Rouge, La. October 1981. Edited by Bebout and Bachman.

Wrighton, F.: "An Economic Overview of Geopressured Solution Gas", in Proceedings of the 5th Geopressured Geothermal Energy Conference. Baton Rouge, LA 1981. Edited by Bebout and Bachman.

"FutureGen - Tomorrow's Pollution-Free Power Plant", Department of Energy briefing, February 27, 2003. <http://www.fossil.energy.gov/programs/powersystems/futuregen/>

"Rising oil, gas investment put at \$5.3 trillion to 2030", Oil & Gas Journal, December 1, 2003. http://ogj.pennnet.com/articles/article_display.cfm?Section=Archives&Article_Category=Gener&ARTICLE_ID=193330&KEYWORD=IEA

EXPERIMENTS ON SILICA PRECIPITATION FROM HYDROTHERMAL SOLUTION AND UTILIZATION OF PRECIPITATED MATERIAL (KAMCHATKA, RUSSIA)

¹Potapov V.V., ²Gorbach V.A., ³Taskin V.V., ⁴Smyvalov S.A., ⁵Kravchenko V.V.

^{1,2,3}Geotechnological Research Center, Far East Branch of Russian Academy of Science
Petrovavlovsk-Kamchatsky, Russia, 683002, Severo-Vostochnoe shosse, 30, P.O. BOX 56,
E-mail: vadim_p@inbox.ru

^{4,5}Kamchatka State Technical University, Petrovavlovsk-Kamchatsky, Russia

ABSTRACT

The experiments on researching of colloidal silica formation in hydrothermal solution, precipitation and utilization of precipitated material were done. Silica was precipitated by addition of coagulants, such as lime, salts of metal, sea water, by electrochemical coagulation, by filtration through membrane filters and by freezing of dispersed solution. Physical and chemical characteristics of precipitated material were determined: concentration of impurities, specific surface area, density of surface hydroxyl groups, reflectivity of light by the surface, oil absorption capacity. Methods of utilization of precipitated material in different industries were developed: 1) for addition to portland cement for increasing concrete strength; 2) for production of sorbent for purification of nature and industry waters from oil products; 3) for production of sorbent for gas chromatography; 4) for liquid glass production. On the base of obtained results technology of precipitation of silica with required properties was developed. Precipitation of silica will increase the efficiency of hydrothermal heat carrier using generating of additional electric and heat energy and by production of amorphous silica material which can be utilized in silicate, chemical and other industries.

INTRODUCTION

Colloidal silica formed in hydrothermal solution in several stages (Weres O., Yee A., Tsao L., 1980, 1981; Potapov V.V., 2003). Primarily silicium enters the solution as molecules of silicic acids as the result of chemical interaction of water with aluminosilicate minerals of hydrothermal field rocks at a depth of 1.0-3.5 km in zones of thermal anomalies at increased temperature (up to 250-350°C) and pressure (4.0-20 MPa). Hydrothermal solution is multicomponent: Na, K, Si, Ca, Mg, Al, Fe, Cl, S, C, B, Li, As, Cu, Zn, Ag, Au and other compounds are present in it in ionic and molecular form.

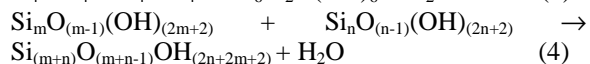
At the temperature of 250-350°C, when solution has a contact with rock minerals, total content of silicium C_t in water can be evaluated by α -quartz solubility 3. (Crerar D.A., Anderson G.M., 1971):

$$\lg(C_t/60) = -1.468 + 252.9/T - 3.217 \cdot 10^5/T^2, \quad (1)$$

At ascending filtration in the fissured-porous rocks or when moving in the productive wells of the geothermal electric- and heat electric power stations pressure and temperature of the solution decrease, and solution is divided into vapour and liquid phases. Total content of silica C_t in liquid phase can reach in this case 700-1500 mg/kg. Owing to this water solution becomes oversaturated with respect to the solubility of amorphous silica C_e . According to the experimental data, value C_e for pure water depends on absolute temperature T by the following way (Marshall W.L., 1980):

$$\lg(C_e/60) = -0.1185 - 1.126 \cdot 10^3/T + 2.3305 \cdot 10^5/T^2 - 3.6784 \cdot 10^7/T^3, \quad (2)$$

Such a state of monomeric silicic acid in water solution is unstable. Oversaturation of the solution S_m , equal to the difference ($C_s - C_e$) of silicic acids concentration (monomeric silica) C_s and solubility C_e , is the motive force for the processes of nucleation and silica acid molecules polymerization with condensation of silanol groups, formation of siloxane links and partial dehydration in the following reactions (Iler R., 1982):



There is a problem of studying the physical-chemical properties of the colloidal silica in hydrothermal solution. Results of the study are necessary for improvement of the model of hydrothermal system mineral formation, and also for working out technology of silica extraction and increasing the effectiveness of using hydrothermal heat-carrier of the geothermal heat electric power stations. The material extracted from the heat-carrier depending

upon its physical-chemical properties can be used in various spheres of industry for making paper, rubber, glue, glass, ceramics, brick, cement, concrete, sorbents, catalysts, and in chromatography and electronics also.

1. MODELING STUDY OF NUCLEATION OF SILICIC ACID MOLECULES

As follows from the model, worked out by Weres, Yee and Tsao (1980, 1981) on the basis of classical conceptions on nucleation, oversaturation $S_N(T)$, equal C_s/C_e , and pH are basic factors determining rate of silicic acid nucleation I_N in water solution:

$$I_N = Q_{LP} \cdot Z \cdot (R_{md} \cdot A_{cr} \cdot N_A \cdot M_{Si}^{-1}) \cdot \exp(-\Delta F_{cr}/k_B \cdot T) \quad (5)$$

where ΔF_{cr} – is a change in free energy, connected with the formation of critical radius nucleus R_{cr} , $R_{cr} = 2 \cdot \sigma_{sw} \cdot M_{Si} / (\rho \cdot N_A \cdot k_B \cdot T \cdot \ln S_N)$, A_{cr} – surface area of critical nucleus, $A_{cr} = 4 \cdot \pi \cdot R_{cr}^2$, $\Delta F_{cr} = \sigma_{sw} \cdot A_{cr} / 3 = (16 \cdot \pi / 3) \cdot \sigma_{sw}^3 \cdot (M_{Si} / \rho \cdot N_A \cdot k_B \cdot T \cdot \ln S_N)^2$, σ_{sw} – coefficient of surface tension at the boundary silica-water, R_{md} – rate of molecular deposition of SiO_2 on the solid surface, $\Gamma \cdot (\text{cm}^2 \cdot \text{min})^{-1}$, k_B – Boltzmann's constant, M_{Si} – molecular mass SiO_2 , N_A – Avogadro number, Q_{LP} – Loze-Paunde's factor, $Q_{LP} = 3.34 \cdot 10^{25} \text{ kg}^{-1}$, Z – Zeldovich's factor, $Z = [-(\partial^2 \Delta F_{cr} / \partial n_{cr}^2) / (2 \cdot \pi \cdot k \cdot T)]^{0.5} = (2/3) \cdot [3 \cdot M_{Si} / (4 \cdot \pi \cdot \rho \cdot N_A \cdot n_{cr}^2)]^{1/3} \cdot (\sigma_{sw} / k \cdot T)^{0.5}$, n_{cr} – quantity of molecules SiO_2 in nucleus of critical size, $n_{cr} = (4 \cdot \pi / 3) \cdot (\rho \cdot N_A / M_{Si}) \cdot R_{cr}^3$. Dependence of functions R_{md} and σ_{sw} upon temperature and pH of the solution in the model is expressed by the equations presented in work of Weres O., Yee A., Tsao L., 1980, 1981.

Equation (5) express maximum rate of nucleation I_N for particles having radius, which is somewhat higher than the critical one, and amount of molecules SiO_2 , equal $N = N_{CR} + 0.5/Z$. Time dependence $I_N(T)$ looks as follows (Weres O., Yee A., Tsao L., 1980, 1981):

$$I_N(t) = I_N \cdot (1 - e^{-t/\tau_{in}}), \quad (6)$$

where τ_{in} – time of the induction required for the growth and formation of the stable population of particles having sizes close to the critical one: $\tau_{in} = 1.08 \cdot 10^{-6} \cdot (6 \cdot R_{md})^{-1} \cdot (Q_{LP} \cdot Z \cdot R_{cr}^2 \cdot \exp(-\Delta F_{cr}/k_B \cdot T))^{-0.25}$

Calculations by equations (1), (5), (6) show that critical radius R_{cr} increases while the temperature rises because of lowering in oversaturation. As a result there is a tendency for decreasing the rate of nucleation I_N and increasing time of the induction τ_{in} . This leads to the decrease in concentration of the particles N_p and growth of the finite average radius of the particles R_f . Real time when hydrothermal solution is in wells and surface heat equipment of the geothermal electric power stations is not enough for the process of nucleation development at the

temperature of 120-150⁰ C . So, for solution having pH = 8.7, $pH_{nom} = 7.86$, $C_t = 700 \text{ mg/kg}$, at 20⁰C $S_N = 5.952$, $\sigma_{sw} = 24.46 \cdot 10^{-3} \text{ J/m}^2$, $R_{cr} = 0.30 \text{ nm}$, $\tau_{in} = 2.66 \text{ min}$, $I_N = 2.00 \cdot 10^{21} \text{ nuclei/kg} \cdot \text{s}$, $R_f = 0.44 \text{ nm}$, $N_p = 5.76 \cdot 10^{15} \text{ cm}^{-3}$; at 100⁰C - $S_N = 1.726$, $\sigma_{sw} = 13.84 \cdot 10^{-3} \text{ J/m}^2$, $R_{cr} = 0.44 \text{ nm}$, $\tau_{in} = 0.69 \text{ min}$, $I_N = 6.40 \cdot 10^{21} \text{ nuclei/kg} \cdot \text{s}$, $R_f = 0.65 \text{ nm}$, $N_p = 1.25 \cdot 10^{15} \text{ cm}^{-3}$; at 153⁰C - $S_N = 1.046$, $\sigma_{sw} = 6.91 \cdot 10^{-3} \text{ J/m}^2$, $R_{cr} = 2.34 \text{ nm}$, $\tau_{in} = 3966.8 \text{ min}$, $I_N = 6.72 \cdot 10^9 \text{ nuclei/kg} \cdot \text{s}$, $R_f = 7.00 \text{ nm}$, $N_p = 5.20 \cdot 10^9 \text{ cm}^{-3}$. Decrease of pH leads to the growth of surface tension and lowering of the deposits growth rate. Therefore, at low pH values critical radius significantly increases, rate of nucleation lowers and time of the induction becomes large: at 20⁰C and pH = 7.0 $\sigma_{sw} = 46.79 \cdot 10^{-3} \text{ J/m}^2$, $R_{cr} = 0.58 \text{ nm}$, $\tau_{in} = 368.3 \text{ min}$, $I_N = 3.99 \cdot 10^{14} \text{ nuclei/kg} \cdot \text{s}$, $R_f = 0.89 \text{ nm}$; at pH = 6.0 $\sigma_{sw} = 48.96 \cdot 10^{-3} \text{ J/m}^2$, $R_{cr} = 0.61 \text{ nm}$, $\tau_{in} = 3967.2 \text{ min}$, $I_N = 6.05 \cdot 10^{12} \text{ nuclei/kg} \cdot \text{s}$, $R_f = 1.20 \text{ nm}$; at pH = 5.0 $\sigma_{sw} = 49.27 \cdot 10^{-3} \text{ J/m}^2$, $R_{cr} = 0.61 \text{ nm}$, $\tau_{in} = 39162.0 \text{ min}$, $I_N = 4.67 \cdot 10^{11} \text{ nuclei/kg} \cdot \text{s}$, $R_f = 1.26 \text{ nm}$. In common case the rate of the processes of nucleation and particle growth, finite size of the particles and their concentration depend upon temperature, pH of the solution and sizes and quantity of nuclei which were present in solution prior to the initiation of nucleation.

2. KINETICS OF POLYMERIZATION OF SILICIC ACID

Kinetics of colloidal silica polymerization reaction was studied at 20⁰C and pH from 5.0 to 9.4. All the curves of oversaturation $S_m(t_p) = C_s - C_e$ obtained from the series of measurements at 20⁰C and natural pH from 8.0 to 9.4 had the same form with concavity and were characterized by close values of the derivative dS_m/dt_p .

The function S_m follows the differential equation (Fleming B.A.б 1986):

$$dS_m/dt_p = -k_p \cdot S_m^{np}, \quad (7)$$

where k_p – is a constant of polymerization reaction rate which depends upon temperature, pH, ionic strength of the solution, n_p – order of polymerization reaction. Dependence $\ln S_m(t_p)$ in the time period t_p from 0 to 6 h was close to linear, which pointed to exponential character of the function $S_m(t_p)$ at $n_p = 1$:

$$\ln S_m(t_p) = \ln S_0 - t_p/\tau_p, \quad (8)$$

$$S_m(t_p) = S_0 \cdot \exp(-t_p/\tau_p), \quad (9)$$

where τ_p – characteristic time of the polymerization reaction, $\tau_p = 1/k_p$.

Experimental dependence $\ln S_m(t_p)$ was approximated by equation (8), based on which constants τ_p и k_p were found. At 20⁰C and pH = 8.0-9.4 average value

of τ_p was 2.04 h, $k_p = 0.485 \text{ h}^{-1}$. According to Fleming's model polymerization reaction is the first order reaction regarding both the difference $(C_s - C_e)$, and surface concentration C_{SiO} of ionized hydroxyl groups SiO^- , that is the surface charge σ_s of colloid particles (Fleming B.A.6 1986):

$$dC_s/dt_p = -k_f A_s \cdot (C_s - C_e) \cdot C_{SiO}, \quad (10)$$

where A_s – is a specific surface area of the particles. Rate constant k_f depends upon the absolute temperature T and ionic strength of the solution I_s (Fleming B.A., 1986).

Calculations by equations (7)-(10) showed the following values of constants k_p and τ_p at increased temperatures: at 50°C - $\tau_p = 36.01 \text{ min}$; 75°C - $\tau_p = 20.91 \text{ min}$; 100°C - $k_p = 7.221 \text{ h}^{-1}$, $\tau_p = 0.138 \text{ h} = 8.3 \text{ min}$. At $\text{pH} = 7.0$ dependence $S_m(t_p)$ considerably changed, at t_p from 0 to 6 h curve $S_m(t_p)$ convex derivative dS_m/dt_p went noticeably lower than in the solution with $\text{pH} = 8.9-9.4$: silicic acid concentration started to reduce actively at $t_p = 3.0 \text{ h}$. At $\text{pH} = 5.0$ inhibition of polymerization reaction was observed, and considerable changes in concentration C_s occurred only in 5-7 days after reaction has started.

3. EXPERIMENTS ON COAGULATION AND PRECIPITATION OF COLLOIDAL SILICA

Experiments on colloidal silica particles precipitation were carried out with the probes of hydrothermal solution from the productive wells of Mutnovskoye hydrothermal field. Metal cations were introduced to solution with addition of lime CaO , calcium chloride CaCl_2 , magnesium sulphate $\text{MgSO}_4 \cdot 7\text{H}_2\text{O}$ and hydrolyzed salts: aluminium sulphate $\text{Al}_2(\text{SO}_4)_3 \cdot 18\text{H}_2\text{O}$, aluminium chloride $\text{AlCl}_3 \cdot 6\text{H}_2\text{O}$, ferric chloride $\text{FeCl}_3 \cdot 6\text{H}_2\text{O}$, copper $\text{CuSO}_4 \cdot 5\text{H}_2\text{O}$, cobalt $\text{CoSO}_4 \cdot 7\text{H}_2\text{O}$ and nickel $\text{NiSO}_4 \cdot 7\text{H}_2\text{O}$ sulphates, plumbous nitrate $\text{Pb}(\text{NO}_3)_2$. In the experiments residual concentrations of colloidal and monomeric silica, coagulating cations, pH value were determined, critical concentration of coagulants and coagulating cations was found. In precipitated material content of Ca, Mg, Al, Fe, Cu, Co and Pb was determined, and material was studied by methods of X-ray and thermochemical analyses, infra-red spectroscopy. The experiments with dispersed coagulants were carried out at 20°C and 96°C .

Concentrations of basic components in the solution before treatment had the following values (mg/kg): Na^+ - 239.4, K^+ - 42.0, NH_4^+ - 1.1, Ca^{2+} - 1.6, Mg^{2+} - 0.72, Li^+ - 0.71, Fe^{2+} - 0.1, Al^{3+} - 0.27, Cl^- - 198.5, SO_4^{2-} - 192.1, HS^- - 5.0, HCO_3^- - 81.0, CO_3^{2-} - 19.9, H_3BO_3 - 106.9, SiO_2 - 680.0, $\text{pH} = 9.2$, $M_h = 1638.9 \text{ mg/kg}$, $I_s = 14.22 \text{ mmol/kg}$.

Table 1 contains data on critical concentration of each coagulant and coagulating cation. It was established, that silica coagulation and precipitation occurred according to the following mechanism: 1) injection into the solution of a critical amount 50-120 mg/kg of Ca^{2+} , Mg^{2+} , Cu^{2+} , Co^{2+} , Pb^{2+} , Al^{3+} , Fe^{3+} cations (individual or in a combination); 2) sorption of a part of those cations (5-20 mg/kg) or their hydrated polycation complexes by the particle surface until the neutralization of the particles negative surface charge; 3) formation of bridge-bonds between the particle surfaces involving coagulant-cations, coagulation and precipitation of colloidal silica.

Table 1
Data on the mechanism of colloidal silica coagulation and precipitation in hydrothermal solution by metal cations, temperature 20°C .

Coagulant	Coagulating cation	Critical coagulant concentration, mg/kg	Critical cation concentration	
			mg/kg	mmol/kg
CaO	Ca^{2+}	80.0	57.1	1.424
CaCl_2	Ca^{2+}	500.0	180.18	4.495
$\text{CuSO}_4 \cdot 5\text{H}_2\text{O}$	Cu^{2+}	200.0	50.9	0.801
$\text{CoSO}_4 \cdot 5\text{H}_2\text{O}$	Co^{2+}	400.0	83.88	1.423
$\text{Pb}(\text{NO}_3)_2$	Pb^{2+}	150.0	93.6	0.451
$\text{NiSO}_4 \cdot 7\text{H}_2\text{O}$	Ni^{2+}	225.0	47.0	0.801
$\text{Al}_2(\text{SO}_4)_3 \cdot 18\text{H}_2\text{O}$	Al^{3+}	250.0	20.2	0.748
$\text{AlCl}_3 \cdot 6\text{H}_2\text{O}$	Al^{3+}	150.0	16.65	0.617
$\text{FeCl}_3 \cdot 6\text{H}_2\text{O}$	Fe^{3+}	250.0	55.66	0.996

Evaluation of density of the surface charge σ_s of colloidal silica particles was done according to the calcium concentration in the material precipitated with addition of CaO and CaCl_2 at the consumptions close to the critical one. In this case amount of sorbed cations Ca^{2+} was determined by the condition of neutralization of the surface charge as in the work of Iler R.K. (1975). The following values were obtained: $\text{pH} = 8.5$ - $\sigma_s = 0.66 \text{ nm}^{-2} = 10.62 \text{ } \mu\text{C/cm}^2$, $\text{pH} = 9.3$ - $\sigma_s = 1.39 \text{ nm}^{-2} = 22.26 \text{ } \mu\text{C/cm}^2$, $\text{pH} = 10.0$ - $\sigma_s = 1.495 \text{ nm}^{-2} = 23.92 \text{ } \mu\text{C/cm}^2$.

In treatment by the slaked lime pH of the solution reached the value of 10-12. Precipitation of both colloidal and monomeric silica took place, however stability of monomeric silica was much higher than the colloidal (Table. 2). Practically all colloidal silica precipitated already at CaO concentration of 80-100 mg/kg, which was critical at 20°C - 96°C . Monomeric silica concentration started decreasing at CaO concentration over 400 mg/kg at 20°C , and over 700 mg/kg at 96°C . Decrease of the total content C_t of silica at 94 - 96°C because of the higher content of monomeric silica occurred slower than at 20°C . At

high lime CaO concentrations (1000 and 1500 mg/kg) total silica SiO₂ amount reduced to 24 and 1.6 mg/kg correspondingly.

A series of experiments on treatment by slaked lime with seawater injection were conducted. Seawater showed pH level of 8.3 and concentrations of cations Ca²⁺ = 210 mg/kg and Mg²⁺ = 699 mg/kg. Treatment was carried out at lime concentration lower than the critical one CaO = 70-40 mg/kg, seawater concentration amounted 15-100 cm³/kg. For stable precipitation of silica it was necessary to inject the following volumes of seawater: 15-20 cm³/kg of seawater – at CaO concentration of 70 mg/kg, 25-30 cm³/kg of seawater – at CaO concentration of 60 mg/kg, and about 40 cm³/kg of seawater – at lime concentration of 40-50 mg/kg. Total content of SiO₂ reduced to 140-190 mg/kg, which corresponded to almost complete precipitation of colloidal silica. The smallest value of CaO/SiO₂ ratio 0.006 was obtained in the sample precipitated at lime CaO concentration of 40 mg/kg and seawater discharge of 40 cm³/kg. Mg/Ca ratio in this sample being 2.513. At such a treatment regime about 65 mg/kg of cations Ca²⁺ and Mg²⁺ was injected into the solution. Thus, additional intake of seawater allows to reduce lime consumption and obtain the material with a smaller calcium amount.

Results of the experiments on silica precipitation with addition of seawater have showed that seawater acted as a coagulant. Colloidal silica precipitation and reducing of C_t concentration to the values of 160-190 mg/kg occurred already after addition of 100 cm³/kg.

Table 2

Results of separate treatment with addition of slaked lime (C_t - residual total content of silica, C_s - residual concentration of monomeric silica, Ca²⁺ - amount of calcium cations injected into solution with lime).

CaO mg/kg	Ca ²⁺ , mg/kg	20°C			96°C		
		pH	C _t , mg/kg	C _s , mg/kg	pH	C _t , mg/kg	C _s , mg/kg
0	0	9.29	697.0	150.3	9.26	718.8	135.0
100	71.4	10.10	158.1	158.1	9.73	344.9	244.4
150	107.1	10.48	158.0	158.0	n.d.	n.d.	n.d.
200	142.8	10.82	158.0	158.0	9.76	329.8	273.0
300	214.2	11.42	153.0	153.0	9.88	315.0	275.0
400	285.6	11.68	137.5	131.9	10.32	345.0	322.5
500	357.0	11.6	75.6	73.8	10.1	339.0	334.4
600	428.4	12.07	75.0	71.3	10.16	307.8	307.8
700	499.8	12.12	69.0	67.0	10.48	260.9	260.9
800	571.2	12.16	41.3	36.3	10.92	229.7	217.2
1000	714.0	12.25	24.0	24.0	11.16	203.1	203.1
1500	1071.4	12.25	1.6	1.6	12.24	6.3	6.3

Concentration of hydrolyzed salts of calcium, magnesium, copper, cobalt, lead, aluminium and ferrum varied within 0-10000 mg/kg. pH of the

solution decreased because of hydrolysis of metal cations injected into solution during salt treatment. Hydrolysis is accompanied by the formation of colloidal particles of metal hydroxides. Low-soluble hydroxide molecules form the aggregates on the surface of which ions adsorb from the solution and form electrically charged micelle nucleus which pulls up counter ions of opposite charge from the solution. Multicharge colloidal particles of hydrated metal cations or their macrocomplexes as flake are sorbed by the surface of colloidal silica particles. This resulted in colloidal silica coagulation and precipitation from the solution.

Experiments on silica precipitation by electrocoagulation are carried out in the regime of direct current and represented in of Potapov V.V., Serdan A.A. (2002). Experiments on silica precipitation by electrocoagulation were carried out in direct current regime. Electrodes of aluminium, copper and ferrum were used. In this case coagulant added to the solution as a result of metal anode dissolution and following hydrolysis of metal cations. Silica precipitation by electrocoagulation had its peculiarities. Colloidal and monomeric silica precipitated simultaneously and gradually. Decrease of the total silica content at electrocoagulation on aluminium electrodes passed three stages. Colloidal silica in hydrothermal solution was more stable with respect to the gradual coagulant addition than to the quick one, as at the treatment by Al₂(SO₄)₃·18H₂O.

Electric power consumption for treatment reduced while temperature increased because the specific conductivity σ of hydrothermal solution increased: at I=1.0 A and 20°C-σ=1.28·10⁻³ S·cm⁻¹, at 99°C- σ=2.92·10⁻³ S·cm⁻¹, at 130°C- σ=3.85·10⁻³ S·cm⁻¹. Ions contributed to the conductivity of the solution most of all are Na⁺-33.24%, K⁺-6.82%, Cl⁻-39.85%, SO₄²⁻-13.23%, HCO₃⁻-2.04%, CO₃²⁻-2.73%. At current density j=30-200 A/m² and current strength I=0.5-1.5 A per 1 kg of water solution, distance between electrodes h_{el}=8-10 mm, treatment duration t_{el}=10-40 min consumption of electric energy per 1 kg of treated solution accounted for Q_{EL}=0.0009-0.0033 kW·h/kg and per 1 kg of precipitated silica - Q_{Si}=1.8-6.0 kW·h/kg.

After treatment by calcium chloride pH of the solution reduced to the value of 8.2 (Table 3). In a result, obviously, negative electric charge of the colloid particles decreased, sorption capacity of the surface became worse with respect to metal cations and, as the result, rate of coagulation processes, flake-formation and silica precipitation at high CaCl₂ concentrations decreased.

During the hydrothermal solution treatment by easily hydrolyzed salts decrease of pH is more considerable.

After treatment $\text{Al}_2(\text{SO}_4)_3 \cdot 18\text{H}_2\text{O}$ pH reduced to 3.5-4.0, after treatment $\text{AlCl}_3 \cdot 6\text{H}_2\text{O}$ to pH = 3.6, $\text{CuSO}_4 \cdot 5\text{H}_2\text{O}$ - to pH = 4.6, $\text{CoSO}_4 \cdot 7\text{H}_2\text{O}$ - to pH = 5.0, $\text{Pb}(\text{NO}_3)_2$ - to pH = 5.12. The largest decrease of pH was observed at solution treatment by ferric chloride $\text{FeCl}_3 \cdot 6\text{H}_2\text{O}$: in this case pH reduced to 1.96. In a result, not only the sorption capacity of silica particles surface became worse, but also the solubility of hydrated charged complexes of metal cations increased. Aluminium hydroxide stopped to precipitate at pH = 4.0, $\text{Cu}(\text{OH})_2$ - at pH = 6.2, $\text{Fe}(\text{OH})_2$ - at pH = 2.3, $\text{Co}(\text{OH})_2$ - at pH = 7.6, $\text{Pb}(\text{NO}_3)_2$ - at pH = 7.4. Therefore, at acidification of the solution up to the pH values less than mentioned above formation of charged cation complexes was difficult. Precipitation of complexes and coprecipitation colloidal silica became worse, coagulation slowed down. In treatment by hydrolyzed salts monomeric silica did not precipitate even at the highest coagulant concentration up to 10000 mg/kg.

Table 3
Results of the hydrothermal solution probe treatment by hydrolyzed salts at 20°C (CC – coagulant concentration, Ca, Al, Fe – quantity of Ca^{2+} , Al^{3+} , Fe^{3+} cations introduced to solution by addition of calcium chloride CaCl_2 , aluminium sulphate $\text{Al}_2(\text{SO}_4)_3 \cdot 18\text{H}_2\text{O}$, ferric chloride $\text{FeCl}_3 \cdot 6\text{H}_2\text{O}$ correspondingly).

CC, mg/kg	CaCl_2		$\text{Al}_2(\text{SO}_4)_3 \cdot 18\text{H}_2\text{O}$		$\text{FeCl}_3 \cdot 6\text{H}_2\text{O}$	
	pH	C_t , mg/kg	pH	C_t , mg/kg	pH	C_t , mg/kg
0	8.90	687.5	9.22	725.0	9.45	725.0
250	n.d.	n.d.	4.96	146.9	3.73	187.5
500	8.70	468.8	4.36	161.25	2.75	178.1
1000	8.54	131.25	4.02	153.1	2.36	665.6
2000	8.41	129.4	3.78	158.1	2.10	725.0
3000	8.46	131.25	3.73	158.1	2.52	725.0
4000	8.34	129.4	3.72	153.1	2.08	725.0
5000	8.37	135.6	3.70	156.0	2.17	725.0
6000	8.36	135.6	3.66	151.8	2.14	725.0
10000	8.29	130.6	3.56	128.1	1.98	728.1

Because of the pH decrease and sorption capacity of the silica surface being worse the fraction of total mass of metals in the material precipitated by injection of hydrolyzed salts was not large. Thus, in calcium chloride treatment CaO/SiO_2 ratio increased from 0.0163 at CaCl_2 concentration of 1500 mg/kg to 0.0755 at CaCl_2 concentration of 10000 mg/kg. In the material precipitated by aluminium sulphate injection Al/SiO_2 ratio was within a range from 0.0412 to 0.0285 and decreased when coagulant concentration increased to 10000 mg/kg. During lime treatment pH, on the contrary, increased, therefore, CaO/SiO_2 ratio in the precipitated material increased from 0.0196 at CaO concentration 80 mg/kg to 1.50 at CaO

concentration 1500 mg/kg.

The series of experiments with addition of hydrolyzed salts and simultaneous alkalization of hydrothermal solution by alkali was carried out to improve coagulation and silica precipitation and reduce coagulant consumption. Alkalization allowed: 1) to precipitate silica with coagulant concentration less than the critical one; 2) to speed up coagulation and precipitation processes; 3) to increase quantity of precipitated colloidal and monomeric silica; 4) to vary concentration of metal in the precipitated material.

Table 4.
Results of experiments on colloidal silica extraction using membrane filters with pores diameter $d_p=0.2$ microns, 20 °C. CC-concentration of coagulant added to the solution prior to filtration through membrane.

$\text{Al}_2(\text{SO}_4)_3 \cdot 18\text{H}_2\text{O}$				$\text{AlCl}_3 \cdot 6\text{H}_2\text{O}$			
CC, mg/kg	C_t , mg/kg	C_s , mg/kg	Al/SiO_2	CC, mg/kg	C_t , mg/kg	C_s , mg/kg	Al/SiO_2
170.0	145.3	112.5	0.0173	110.0	112.5	112.5	0.0179
165.0	210.9	118.75	0.0161	105.0	114.0	112.5	0.0170
160.0	153.1	125.0	0.0141	100.0	115.6	112.5	0.0149
155.0	215.6	118.75	0.0215	90.0	139.4	134.4	0.0148
150.0	209.4	134.4	0.0188	80.0	171.9	137.5	0.0123
140.0	239.0	128.1	0.0132	70.0	175.0	134.4	0.0136
130.0	400.0	134.4	0.0168	65.0	206.25	128.1	0.0125
120.0	375.0	118.75	0.0137	60.0	209.4	131.25	0.0100
110.0	383.1	121.9	0.0136	55.0	390.6	118.75	0.0165
100.0	437.5	123.75	0.00921	50.0	337.5	115.6	0.0125
90.0	531.25	118.75	0.0123	45.0	406.25	112.5	0.00993
80.0	571.9	118.75	0.0108	40.0	518.75	115.6	0.0151

The results of experiments on colloidal silica extraction by using of membrane filter are shown in the table 4. The diameter of filters pores used in experiments was 0.2 microns. Two types of coagulants were added to solution prior filtration: $\text{Al}_2(\text{SO}_4)_3 \cdot 18\text{H}_2\text{O}$ and $\text{AlCl}_3 \cdot 6\text{H}_2\text{O}$. The concentration of coagulants was lower than critical. Cations Al^{3+} added to solution with coagulants were sorbed by the surface of colloidal silica particles provided aggregation of silica particles and formation of aggregates with the sizes more than 0.2 microns. Aggregated particles were extracted from solution by filter pores. Practically all colloidal silica was extracted at the concentration of $\text{Al}_2(\text{SO}_4)_3 \cdot 18\text{H}_2\text{O}$ 150-170 mg/kg and concentration of $\text{AlCl}_3 \cdot 6\text{H}_2\text{O}$ 60-110 mg/kg. Concentration of cations Al^{3+} was 12.1-13.7 mg/kg when $\text{Al}_2(\text{SO}_4)_3 \cdot 18\text{H}_2\text{O}$ added to the solution and 6.6-12.2 mg/kg when $\text{AlCl}_3 \cdot 6\text{H}_2\text{O}$ added. The concentration of Al in the material extracted by using of membrane filters was lower than in the material precipitated by addition of metal salts with concentrations more than critical: the value of Al/SiO_2 in the material extracted with addition of

$\text{Al}_2(\text{SO}_4)_3 \cdot 18\text{H}_2\text{O}$ was from 0.00921 to 0.0215 and it was from 0.00993 to 0.0179 in the material extracted with addition of $\text{AlCl}_3 \cdot 6\text{H}_2\text{O}$ (table 4).

In experiments the regime of treatment was developed that allowed to obtain a precipitate which passed into silicates of metals after thermal treatment at 900-1000°C. Precipitation in this regime was carried out by introducing metal cations and simultaneous increase of pH to the value of 10-12 and higher. Under such conditions a sufficient quantity of H_3SiO_4^- and HSiO_3^- ions appeared in the solution which were able to form low-soluble compounds with metal cations. Thus, cobalt, magnesium and calcium silicates (Co_2SiO_4 , Mg_2SiO_4 и CaSiO_3) were obtained. Metal silicates can be used in ceramics, glass, paint and anticorrosion material production.

4. DEVELOPMENT OF METHODS OF UTILIZATION OF SILICA PRECIPITATED FROM THE HYDROTHERMAL SOLUTION IN INDUSTRY

4.1. Utilization of silica as a sorbent for purification of water from oil products

We worked out an utilization method of silica precipitation by freezing out dispersed hydrothermal solution for making sorbent which can be used for the purification of sewage of different fields of industry and polluted waters of natural reservoirs from oil products.

Capacity to absorb of organic liquids of silica precipitated from the hydrothermal solution in some cases is 1.5–2.0 times larger than capacity of synthetic amorphous dioxide of silicon obtained by another methods with expenses of reagents. Capacity of geothermal silica to absorb of petrols reaches 160 – 200 g/100g of silica, capacity to absorb of diesel fuel is 190 – 200 g/100g of silica.

Material precipitated by freezing out after drying turned into dispersive powder, surface of which was modified using silicic organic modifiers in such a way, that to change coefficient of surface tension of water on the boundary with silica and add hydrophobic properties to the surface. At the same time coefficient of surface tension of organic liquids on the boundary with silica after modification provided moistening of silica surface and absorption of liquid by powder. One of the oil products (petrol, diesel fuel, etc.), or mixture of several oil products with any ratios of mixing can be tested as organic liquid. Modified silica can be used to eliminate consequences of oil products spilling to the natural reservoirs, including extraction of undissolved filmy formations on the water surface. To remove dissolved oil products, volume of water is filtered through the layer of modified sorbent. Amount of sorbent

required for removing oil products from the given volume of polluted water is determined from the condition of saturation of modified silica with organic liquid in accordance with the capacity of sorbent to absorb this liquid.

Experiments were done on extraction of oil products from water using silica precipitated by freezing out of dispersed hydrothermal solution. Silica was modified according to the method presented in the work Il'inskii V.V., Komarova T.I., Koronelli T.V., Lisichkin G.V., Serdan A.A. (1998). At the first stage silica was dried in toluene. Dry distilled morpholine and then modifier gexadethildimethylchlorsilan $\text{C}_{16}\text{H}_{33}\text{Si}(\text{CH}_3)_2\text{Cl}$ were added to SiO_2 dried at the first stage. Mixture was boiled during 8 hours. Then mixture was washed in the following order: 1) with toluene in filtering vessels twice; 2) with acetone (or isopropanol); 3) with mixture acetone-water-acetic acid with the ratio 2:1:1 according to the volume twice; 4) with mixture acetone-water with the ratio 1:2 three times; 5) with acetone twice. Mixture was dried to powder state, when drying temperature was slowly increased from 70°C up to 120°C.

After modification experiments were done on silica use for purification of distilled water from impurity of petrol A-76 with density 0.758 g/cm³ and diesel fuel with density 0.817 g/cm³. Amount of oil product added to the water before purification was from 4 to 20 ml/l. Consumption of sorbent to remove undissolved oil products was 100 g/(195 - 211)g of petrol and diesel fuel. During the experiments on removal of dissolved oil products volume of distilled water was filled up with diesel fuel up to the concentration 10 microliters/l (less than 1 weight part per 100000). Then, volume of polluted water was filtered through the layer of sorbent modified by the indicated method. Residual total concentration of oil products in the filtered water was 0.19 microliters/l = 0.16 mg/l, that is 98 % of oil products dissolved in water was removed.

4.2. Utilization silica in gas chromatography

Experiments were done on using silica precipitated by freezing out the hydrothermal solution as a sorbent in chromatographic columns to separate mixtures of organic liquid and gaseous substances. Utilization of silica as a sorbent for gas chromatography makes it possible to use sorption properties of precipitated silica surface. That extends fields of utilization of silica material, increases its cost and makes use of hydrothermal heat-carrier more effective. This very method excludes costs of expensive reagents on production of traditional synthetic dispersive amorphous silicas which serve as the initial material for making sorbents for chromatography.

Experiments were done on separating the components of mixture of organic compounds in two chromatographic columns. One column was filled with silica precipitated from the hydrothermal solution and another one – with commercially produced sorbent silochrome C-80. Sizes of fraction of silochrome C-80 particles was within 0.315 – 0.5 mm, specific powder surface – 80.0 m²/g, average pore diameter – 40.0 – 50.0 nm, specific pore volume – 1.3 cm³/g. Both columns had the same preparation and worked simultaneously. The length of columns was 1.8 m, inner diameter – 2.0 m, mass of sorbent in the column filled with silochrome C-80 was 4.67 g, in the column filled with geothermal silica – 1.45 g. Analyzed components were eluted through the columns by gas-carrier – helium. Helium consumption through each column was 0.2 ml/s. Temperature of the experiments was 130°C. To register chromatographic peaks flame-ionization detector was used. Consumption of hydrogen in detector was 0.5 ml/s, air consumption was 5.0 ml/s.

Table 5
Comparative time of retainment of different components in the columns (length of columns – 1.8 m, diameter – 2.0 mm) filled with silica, precipitated from the hydrothermal solution, and silochrome C-80.

Component	Volume of sample, microliters	Time of retainment, t _R	
		Silochrome C-80	Geothermal silica
Isobutan	200.0	44.0 s	53.7 s
Hexane	0.1	1 min 11.0 s	1 min 30.2 s
Heptane	0.1	1 min 43.0 s	2 min 13.0 s
Benzene	0.1	1 min 22.5 s	3 min 22.3 s
Toluene	0.1	2 min 26.0 s	6 min 33.5 s
O-xylol	0.1	4 min 36.9 s	13 min 08.7 s

Table 5 contains experimental results on obtaining the chromatograph peaks of isobutan and vapours of organic liquids: hexane, heptane, benzene, toluene, o-xylol. The evaporator temperature at which vapours of liquids were obtained was 200°C. As it can be seen from the Table 4, time of retainment t_R of each component is larger in the column filled with geothermal silica. The experiments with mixture of these components also showed larger time of retainment of the components for the column with silica precipitated from the hydrothermal solution. That indicated better adsorption activity of geothermal silica surface in comparison with silochrome C-80.

4.3. Addition of silica to cement for increasing of concreat strength

Experiments were done on studying the influence of small silica addition to cement on strength of the concrete product made on the basis of cement. Silica was added to portland cement of the allitic type. Tests were carried out according to the following method. Slurry of normal thickness was prepared from 200 g of cement. It was laid with rodding in two metal forms, each of them had six cells to make bricks with the size 20x20x20 mm. Each brick was rodded ten times, then forms were placed on the shaking table. Forms were shaken 25 times and closed with screwing up lids. Then form was placed in the bath with hydraulic back-pressure valve at the temperature 20 ± 2°C. Samples were subjected to compression by the press to determine concrete strength after 7 and 28 days.

Experiments showed, that addition of silica precipitated from the hydrothermal solution to cement led to the increase in concrete strength. A method of utilization of silica precipitated by lime addition in order to increase concrete strength was proposed. Precipitation is carried out after ageing of the solution and completion of polymerization and formation of the colloidal silica particles. CaO consumption must be within a range of 100 – 1000 mg/kg. Weight fraction of silica with respect to cement must be within a range from 1 to 6-7 %, water-cement ratio – from 0.25 to 0.38. In other regime the silica precipitated by freezing out the dispersed hydrothermal solution is added to the cement. In this case quantity of silica added to cement must not be more than 5 weight %.

4.4. Utilization of silica for liquid glass production

By freezing out the hydrothermal solution the samples of finely dispersive powder were obtained with large weight fraction of dioxide of silicon from 95 to 99 %, amorphous structure, high density of surface hydroxyl groups – 4.9 OH/nm² at 200 °C, high reflectivity of light by the surface – up to 91 – 95 %, oil absorption capacity – up to (159 - 218) g/100g and low Ca, Al, Fe. Concentrations of Ca, Al, Fe are totally not more than 0.6 weight %.

By the method of low-temperature nitrogen adsorption pore characteristics of samples of dispersive silica precipitated by freezing out the hydrothermal solution were measured. Isotherms of adsorption-desorption of nitrogen of IV-type were obtained for the samples of silica powder. Silica samples are characterized by high specific surface area – from 50 to 300 m²/g, porosity – up to 1.1 cm³/g, average values of pore diameters d_p = 12.7 – 16.6 nm, low fraction of area (9 – 10.7 %) and volume (0.5 – 0.856%) of micropore. The largest part of the pores of geothermal silica is concentrated in a rather small range of diameters: 60.9 % of total area and 79.8 % of total pore volume were in the the pores with diameters d_p from 5.18 to 26.47 nm.

Using silica precipitated from solution the samples of liquid sodium silicate glass were produced by autoclave method with heat supply from the waste hydrothermal heat-carrier. Amorphous structure and large specific surface of silica provided its rapid and homogeneous dissolution and reaction acceleration with formation of sodium silicate. That reduced duration of the process and energy expenses for its conducting. Different technical characteristics of glass, such as density, concentrations of combinations, silicate magnitude up to 4.0, satisfying norms for high-quality glass were obtained. Rather low content of calcium, ferrum and aluminium in initial silica provided necessary low contents of these impurities in the final product.

5. TECHNOLOGICAL SCHEME OF SILICA PRECIPITATION FROM THE HYDROTHERMAL SEPARATE

The experiments allowed to reveal physical-chemical properties of the solution which influenced the process of colloidal particle coagulation and determined the technology of silica precipitation: 1) total content SiO_2 $C_t = 300\text{-}1500$ mg/kg; 2) average radius of colloidal silica particles $R = 3.0\text{-}16.0$ nm and specific area of particle surface $A_s = 500\text{-}2000$ cm^2/cm^3 (30-300 m^2/g); 3) density of the surface electric charge of silica particles $\sigma_s = 10.62\text{-}23.92$ $\mu\text{C}/\text{cm}^2$; 4) solution pH before treatment - from 9.4 to 7.0; 5) mineralization $M_h = 1000\text{-}2500$ mg/kg; 6) ionic strength of the solution $I_s = 10\text{-}20$ mmol/kg; 7) a ratio between the concentrations of basic cations (Na^+/K^+) and anions ($\text{Cl}^-/\text{SO}_4^{2-}$).

Technological scheme of colloidal and monomeric silica precipitation at a temperature from 20 to 140–160° C from hydrothermal solution was developed based on the experiment results. It included the following stages: (1) monomeric silica polymerization with the formation of colloidal particles; (2) addition of precipitant (coagulants, flocculants, primary colloidal particles) in a certain moment of polymerization process to form a microstructure of the silica particle complexes without silica precipitation from the solution; (3) injection of a precipitant or mixture of precipitants (coagulants, flocculants, recirculation of precipitated sludge or solution with polymerized silica) for silica coagulation and precipitation; (4) adjusting pH of the solution by adding reagents on the stage of silica coagulation and precipitation to control kinetics of the process and Ca, Mg, Al, Fe content in the precipitated material; (5) separation of flakes of precipitated material and clarification of the solution; (6) dehydration and drying of precipitated material. Dispersity of precipitated material was adjusted by the temperature of solution during the process of silica nucleation and polymerization and also by a

composition, amount and time of precipitant(s) addition during polymerization and precipitation processes.

Increasing the effectiveness of using hydrothermal heat-carrier is determined by a number of factors including elimination of downtime at the geothermal electric power stations, obtaining of additional heat and electric energy in binary cycle with organic liquid having low-boiling temperature and extraction of minerals as amorphous silica (Potapov V.V., Povarov K.O., Podverbny V.M., 2003).

CONCLUSIONS

1. It was shown, that nucleation and polymerization of silicic acid molecules in hydrothermal solution actively developed at the temperature lower 120–150°C. The order n_p of silicic acid polymerization reaction in hydrothermal solution equaled 1.0. Polymerization rate constants $k_p = 0.485$ h^{-1} and $\tau_p = 123.6$ min at 20°C were determined, values of these constants at increased temperature were calculated. Radii of colloidal silica particles measured by photon correlation spectroscopy were distributed within 1.0–50.0 nm, average radius $R = 7.0\text{-}20.0$ nm, diffusion coefficients $D = 2.9 \cdot 10^{-7}$ cm^2/s .

2. Physical-chemical properties of hydrothermal solution essential for the process of coagulation and silica precipitation technology were revealed: 1) total content C_t of silica in the solution; 2) average radius, surface area of colloidal silica particles; 3) electric charge of particle surface; 4) concentration of basic cations (Na^+ , K^+) and anions (Cl^- , SO_4^{2-}); 5) pH; 6) mineralization of the solution M_h ; 7) ionic strength I_s .

3. Experiments showed the possibility of utilization of silica material precipitated from the hydrothermal heat carrier in the following industries: 1. as mineral raw material for production of sorbent for purification of water from oil products; 2. for production of sorbent for gas chromatography; 3. for addition to portland cement for increasing concrete strength; 4. for liquid glass production.

4. The technological scheme of silica precipitation from liquid phase of hydrothermal heat carrier was developed. In this scheme silica precipitation was combined with production of electric and heat energy on geothermal power station. The principles of increasing the effectiveness of using hydrothermal heat-carrier were grounded: 1. elimination of downtime at the geothermal electric power stations and expenditures on drilling of new reinjection wells; 2. obtaining of additional heat and electric energy in binary cycle with organic liquid having low-boiling temperature; 3. recovering of mineral raw material which can be utilized in industry; 4. extraction of valuable chemical compounds (Li, B, As and others).

REFERENCES

Crerar D.A., Anderson G.M. (1971), Solubility and solvation reactions of quartz in dilute hydrothermal solutions. *Chem. Geol.* No. 8. P.107-122.

Fleming B.A. (1986), Kinetics of reaction between silicic acid and amorphous silica surfaces in NaCl solutions. *J. Coll. Interf. Sci.* V. 110. No. 1. PP. 40-64.

Iler R.K. (1975), Coagulation of colloidal silica by calcium ions, mechanism, and effect of particle size. *J. Coll. Interf. Sci.* V. 53. No. 3. P. 476-488.

Iler R. (1982), *The chemistry of silica*. Moscow: Mir. V.1, 21127 P.

Marshall W.L. (1980), Amorphous silica solubilities. I. Behavior in aqueous sodium nitrate solutions: 25 – 300^oC, 0-6 molal. *Geochimica et Cosmochimica Acta.* V 1. 44. P. 907-913.

Weres O., Yee A., Tsao L. (1980), Kinetics of Silica Polymerization. Report LBL-7033. Lawrence Berkeley Laboratory. Berkeley. 256 P.

Weres O., Yee A., Tsao L. (1981), Kinetics of Silica Polymerization. *J. Coll. Interf. Sci.* V. 84. No. 2. P. 379-402.

Potapov V.V. (2003), Colloidal silica in hydrothermal solution. Vladivostok: Dalnauka. 216 P.

Potapov V.V., Serdan A.A. (2002), Silica precipitation from hydrothermal heat-carrier by electrocoagulation. *Chemical technology.* № 9. P. 2-9.

Potapov V.V., Povarov K.O., Podverbny V.M. (2003), Methods of increasing of effectiveness of binary blocks' at geothermal electric power station. *Teploenergetica.* № 10. P. 41-48.

Il'inskii V.V., Komarova T.I., Koronelli T.V., Lisichkin G.V., Serdan A.A. (1998), Sorbent for Elimination of Oil Products from the Water Surface. InCom'98, International Symposium on Instrumentalized Analytical Chemistry and Computer Technology. Duesseldorf (Germany). P. 323

Attendee List

30th Workshop on Geothermal Reservoir Engineering, Jan.31, Feb. 1-2, 2005

Jorge A. Acuna

Unocal
1160 N Duttona Ave Suite 200
Santa Rosa, CA 95401
USA
TEL:707-521-7616
FAX:707-521-7604
jacuna@unocal.com

Michael C. Adams

EGI - University of Utah
Research Park
423 Wakara Way, Ste. 300
Salt Lake City, UT 84108
USA
TEL:801-585-7784
FAX:801-585-3540
madams@egi.utah.edu

Serhat Akin

Petroleum & Natural Gas Engineering Dept
Inonu Bulvari, Ankara 06531
Turkey
TEL:+90 312 210 4892
FAX:+90 312 210 1271
serhat@metu.edu.tr

Laurent Andre

University of Neuchatel
Centre of Hydrogeology
Rue Emile Argand, 11
NEUCHATEL, 2000
SWITZERLAND
TEL:+41 (0)32 718 26 08
FAX:+41 (0)32 718 26 03
laurent.andre@unine.ch

Miklos Antics

Geoproduction Consultants (GPC SA)
Paris Nord 2
Rue de la Perdrix, 14
BP 50030
France
TEL:33148630808
FAX:33148630889
geofluid@rdslink.ro

Nilo Alvarez Apuada

PNOG Energy Development Corporation
PNPC Complex, Merritt Rd.,
Ft. Bonifacio, Makati City
TAGUIG Metro Manila 1201
PHILIPPINES
TEL: (63-2) 8936001 LOCAL 4246
FAX: (63-2) 840-1580
niloapuada@yahoo.com

Brian Arcedera

Unocal Philippines, Inc.
12/F Citibank Tower,
8741 Paseo de Roxas
Makati City
Metro Manila, 1226
Philippines
TEL:+63 2 845 8530
FAX:+63 2 845 8597
barcedera@unocal.com

Yvette Arcedera

Unocal Philippines, Inc.
12/F Citibank Tower
8741 Paseo de Roxas
Makati City
Metro Manila, 1226
Philippines
TEL:+63 2 845 8400
FAX:+63 2 845 8597
yvette.ontoy@unocal.com

Rick Baars

New Mexico Tech
801 Leroy Place
Socorro, NM 87801
USA
TEL:406-249-3059
rmbaars@nmt.edu

Benjamin J. Barker

237 Dartmouth Way
Windsor, CA 95492
USA
TEL:707-838-0238
FAX:707-838-0265
benbarker@earthlink.net

Stephen Bauer

Sandia National Laboratories
MS1033, Dept. 6211
Albuquerque, NM 87108
USA
TEL:505-844-9116
FAX:505-84403952
sjbauer@sandia.gov

Clement Baujard

Ecole Nationale Supérieure des Mines de Paris -
Centre d'Informatique Géologique 35 rue Saint Honoré
Fontainebleau, 77300
France
TEL:01 64 69 47 36
FAX:01 64 69 47 03
clement.baujard@ensmp.fr

Attendee List

30th Workshop on Geothermal Reservoir Engineering, Jan.31, Feb. 1-2, 2005

Ashish Bhat

Kansas State Univ.
309, Rathbone Hall,
Manhattan, KS 66502
USA
TEL:785-532-2621
FAX:785-532-7057
ashish@ksu.edu

David D. Blackwell

Southern Methodist Univ
Dept. of Geo Sciences
217 N.L. Heroy Hall
Dallas, TX 75275
USA
TEL:214-768-2745
FAX:214-768-2701
blackwel@passion.isem.smu

Kevin K. Bloomfield

INEEL
PO Box 1625
Idaho Falls, ID 83415-3830
USA
TEL:208-526-5250
FAX:208-526-0969
blookk@inel.gov

P. Gordon Bloomquist

Washington State Energy Office
925 Plum St SE, Town Square Bldg 4
PO Box 43165
Olympia, WA 98504-3165
USA
TEL:360-956-2016
FAX:360-956-2030
bloomquistr@energy.wsu.edu

Cheryl Blume

Schlumberger
PO Box 81222
Bakersfield, CA 93380
USA
TEL:661-864-4722
cblume@slb.com

Tonya Boyd

Geo-Heat Center
Oregon Institute of Technology
3201 Campus Drive
Klamath Falls, OR 97601
USA
TEL:541-885-1750
FAX:541-885-1754
boydt@oit.edu

Chris John Bromley

Institute of Geological & Nuclear Sciences
Karetoto Rd, Wairakei
Taupo, North Island, Bag 2000
NEW ZEALAND
TEL:64-7-374-8211
FAX:64-7-374-8199
C.BROMLEY@GNS.CRI.NZ

Dominique Bruel

Paris School of Mines
35 rue St honoré
Fontainebleau, 77300
France
TEL:33 01 64 69 47 54
FAX:33 01 64 69 47 03
dominique.bruel@ensmp.fr

Steven Butler

Geothermex
5221 Central Ave., Suite 201
Richmond, CA 94804
USA
TEL:510-527-9876
FAX:510-527-8164
mw@geothermex.com

Wendy Calvin

University of Nevada - Reno
Geological Sciences, MS172
Reno, NV 89557
USA
TEL:775-784-1785
wcalvin@unr.edu

Jean Charlety

EOST-ULP Strasbourg
5, rue René Descartes
STRASBOURG, 67000
France
TEL:+33 3 90 24 00 62
FAX:+33 3 90 24 01 25
jean.charlety@eost.u-strasbg.fr

Chih-Ying Chen

Stanford University
Petroleum Engineering Department
Green Earth Sciences Bldg., Rm. 155
Stanford, CA, 94305-2220
USA
TEL:650-725-0840
FAX:650-725-2099
alnchen@pangea.stanford.edu

Attendee List

30th Workshop on Geothermal Reservoir Engineering, Jan.31, Feb. 1-2, 2005

Andrew Chiasson

Geo Heat Center
Oregon Institute of Technology
3201 Campus Dr
Klamath Falls, OR 97601
USA
TEL:541-885-1750
FAX:541-885-1754
chiassoa@oit.edu

Bruce Christenson

Geological & Nuclear Sciences.
30 Gracefield Road
Lower Hunt
PO Box 31312
NEW ZEALAND
TEL:644-570-4640
FAX:644-570-4657
b.chrisenson@gns.cr.nz

Jim Combs

Geo Hills Associates
2395 Catamaran Drive
Reno, NV 89509-5731
USA
TEL:775-827-1960
FAX:775-827-1960
jimjeany@ix.netcom.com

Mark Coolbaugh

Great Basin Center for Geothermal Energy
259 LMR, ms 172
Reno, NV 89557-0138
USA
TEL:775- 784- 1415
FAX:775- 327- 5801
mfc@unr.nevada.edu,
sereno@dimensional.net

Robert J. Creed

US Department of Energy
Idaho Falls Operations Office
850 Energy Drive, MS 1225
Idaho Falls, ID 83401-1563
USA
TEL:208-526-9063
FAX:208-526-5964
creedrj@id.doe.gov

Nicolas Cuenot

EOST-ULP Strasbourg
5, rue René Descartes
STRASBOURG 67000
France
TEL:+33 3 90 24 00 70
FAX:+33 3 90 24 01 25
cuenot@east.u-strasbg.fr

William Cumming

Geothermal Geoscience
4728 Shade Tree Lane
Santa Rosa, CA 95405
USA
TEL:707-546-1245
FAX:707-568-4260
wcumming@cablone.com

Aysegul Dastan

Stanford University
Petroleum Engineering Department
Green Earth Sciences Building, Rm.103
Stanford, CA 94305
USA
TEL:650-725-0718
FAX:650-725-2099
ayseguld@pangea.stanford.edu

Nicholas Davatzes

U.S. Geological Survey
345 Middlefield Road, MS 977
Menlo Park, CA 94025
USA
TEL:650-329-4024
FAX:650-329-5143
ndavatzes@usgs.gov

Birol Demiral

Middle East Technical University
Petroleum & Natural Gas Engineering Dept
Inonu Bulvari, Ankara 06531
Turkey
TEL: +90 312 210 4892
FAX:+90 312 210 1271
serhat@metu.edu.tr

Jerry Fairley

University of Idaho
7th and Line Sts
Moscow, Idaho, 83844-3022
USA
TEL:208-885-9259
FAX:208-885-5724
jfairley@uidaho.edu

Attendee List

30th Workshop on Geothermal Reservoir Engineering, Jan.31, Feb. 1-2, 2005

David D. Faulder

SAIC
405 Urban Street, Ste. 400
Lakewood CO, 80228
USA
TEL:303-969-6053
faulderd@saic.com

Daisuke Fukuda

Geothermal Engineering Co
101 Hosoyachi
Takizawa mura, Iwate 020-0172
Japan
TEL:81-19-684-4114
FAX:81-19-684-6231
fukuda@geothermal.co.jp

Sabodh K. Garg

SAIC
10260 Campus Point Drive
Mail Stop A-3
San Diego, CA 92121
USA
TEL:858-826-1615
FAX:858-826-5115
gargs@saic.com, sabodh@aol.com

John Garnish

28 Charbrough Way
Struminster Way, Struminster Marshall
Wimbome
Dorset Bh21 4DH
United Kingdom

Ahmad Ghassemi

University of North Dakota
Department of Geology & Geological Engineering
Box 8358
Grand Forks, ND 58202
USA
TEL:701-777-3213
FAX:701-777-4449
ahmad_ghassemi@mail.und.nodak.edu

Shekhar Gosavi

Kansas State University
302 Rathbone Hall
Dept. of Mechanical Engineering
Manhattan, KS 66506
USA
TEL:785-341-2477
shekharg@ksu.edu

Jeremy Griggs

Unocal
14141 Southwest Freeway
Sugar Land, TX 77006
USA
TEL:2811.287.5594
jeremy.griggs@unocal.com; jgriggs@lsu.edu

Saibi Hakim

Laboratory of Geothermics, Kyushu University
6-10-1 Hakozaki, Higashi-ku
Fukuoka, Fukuoka 812 - 8581
JAPAN
TEL: (81) 092 - 642 - 3645
FAX: (81) 092 - 642 - 3614
saibi-hakim@mine.kyushu-u.ac.jp

Stephen Hickman

US Geological Survey
M/S 977
345 Middlefield Rd.
Menlo Park, CA 94025
USA
TEL:650-329-4807
FAX:650-329-5143
hickman@usgs.gov

Roland Horne

Stanford University
Petroleum Engineering Department
Green Earth Sciences Building, Rm.64
Stanford, CA 94305-2220
USA
TEL:650-723-9595
FAX:650-725-2099
horne@pangea.stanford.edu

Allan Jelacic

US Department of Energy
Geothermal & Wind Technologies
EE-12
1000 Independence Avenue
SW Washington, DC 20585
USA
TEL:202-586-6054
FAX:202-586-8185
allan.jelacic@hq.doe.gov

Attendee List

30th Workshop on Geothermal Reservoir Engineering, Jan.31, Feb. 1-2, 2005

Egill Juliusson

Stanford University
Petroleum Engineering Department
Green Earth Sciences Building, Rm. 129
Stanford, CA 94305
USA
TEL:650-725-0813
FAX:650-725-2099
egillj@pangea.stanford.edu

Reinhard Jung

Leibniz Institute for Applied Geosciences (GGA)
Two-Phase Engineering & Research
Stilleweg 2
Hannover
Lower Saxony, D 30655
Germany
TEL:49-(0)511-6432820
FAX:49-(0)511-6433665

Stephen Karner

Idaho NEEL
PO Box 1625
Idaho Falls, ID 83415-2107
USA
TEL:208-526-6292
FAX:208-526-0875
karnsl@inel.gov

Dennis Kaspereit

California Energy Operating Group
7030 Gentry Rd.
Calipatria, CA 92233
USA
TEL:760-348-7044
FAX:760-348-4022
dennis.kaspereit@calenergy.com

Burton Kennedy

Lawrence Berkeley National Lab
1 Cyclotron Road, MS 70A4418
Berkeley CA, 94720-8179
USA
TEL:510-486-6451
FAX:510-486-5496
bmkenney@lbl.gov

M. Ali Khan

CA Dept. of Conservation
Div of Oil, Gas & Geothermal Rscs
50 D Street, #300
Santa Rosa, CA 95404-4772
USA
TEL:707-576-2385
FAX:707-576-2611
akhan@consvr.ca.gov

Tsuneo Kikuchi

Department of Geothermal Research
Geological Survey of Japan
AIST 1-1-1
Higashi Tsukuba
Japan
TEL:81-29-861-3983
FAX:81-29-861-3703
t-kikuchi@aist.go.jp

Thomas Kohl

GEOWATT AG
Dohlenweg 28
ZÜRICH, 8050
Switzerland
TEL:+41 1 242 1454 / +41 79 435 6612
FAX:+41 1 242 1458
kohl@ig.erdw.ethz.ch

Katherine Kovac

Energy and Geoscience Institute
423 Wakara Way
Salt Lake City, UT 84102
USA
TEL:801-585-7971
kkovac@egi.utah.edu

Jennifer Lewicki

Lawrence Berkeley National Lab
1 Cyclotron Rd
Berkeley, CA 94720
USA
TEL:510-495-2818
FAX:510-486-5686
jllewicki@lbl.gov

Kewen Li

Stanford University
Petroleum Engineering Department
Green Earth Sciences Building, Rm.77A
Stanford, CA 94305-2220
USA
TEL:650-723-5377
FAX:650-725-2099
kewenli@pangea

John Lund

Geo-Heat Center
Oregon Inst. of Technology
3201 Campus Dr
Klamath Falls, OR 97601
USA
TEL:541-885-1750
FAX:541-885-1754
lundj@oit.edu

Attendee List

30th Workshop on Geothermal Reservoir Engineering, Jan.31, Feb. 1-2, 2005

Imtiaz Majid

Verrillon, Inc
15 Centennial Drive
North Grafton, MA 01536
USA
TEL:508-890-7100
FAX:508-839-6688
rogers@verrillon.com

Sullivan Marsden

Stanford University
Petroleum Engineering Department
Green Earth Sciences Building, Rm. 49
Stanford, CA 94305-2220
USA
TEL:650-723-3570
FAX:650-725-2099

Jess McCulloch

Coso Operating Company
P.O. Box 1690
Inyokern, CA 93527-1690
USA
TEL:760-764-1300
FAX:760-764-2220
jmcculloch@cenyc.com

David Meade

Geothermal Program Office, U.S. Navy
429 E. Bowen Rd.,
Mail Stop 4011
China Lake, CA 93555-6108
USA
TEL:760-939-4046
FAX:760-939-2449
David.Meade@navy.mil

Thomas Megel

GEOWATT AG
Dohlenweg 28
ZÜRICH, 8050
Switzerland
TEL:+41 1 242 1454
FAX:+41 1 242 1458
megel@geowatt.ch

Michael Mella

EGI at the University of Utah
423 Wakara Way Suite 300
SLC, UT 84108
USA
TEL:801-585-9177
FAX:801-585-3540
mmella@egi.utah.edu

Roy Mink

Geothermal Energy Program
1000 Independence Ave.
Washington,DC 20585-0121
USA
TEL:202-586-5463
FAX:202-586-8185
roy.mink@ee.doe.gov

Francis C. Monastero

U.S. Navy
U.S. Navy Geothermal Program Office
429 E. Bowen Road, Mail Stop 4011
China Lake, CA 93555
USA
TEL:760-939-4046
FAX:760-939-2449

Joseph N. Moore

EGI, University of Utah
Research Park
423 Wakara Way, Ste. 300
Salt Lake City, UT 84109
USA
TEL:801-585-6931
FAX:801-585-3540
jmoore@egi.utah.edu

Paul Moya Rojas

Instituto Costarricense de Electricidad
Apartado Postal 10032
San José 1000
Costa Rica
TEL: 506- 673-0146
FAX: (506) 673-0132
pmoya@ice.go.cr

Shinsuke Nakao

Geological Survey of Japan, AIST
AIST Central 7
Tsukuba Ibaraki 305-8567
Japan
TEL:81-29-861-3955
FAX:81-298-61-3736
sh-nakao@aist.go.jp

Gopi Nalla

Idaho National Eng. and Env. Lab
PO Box 1625
Idaho Falls, ID 83412
USA
TEL:208-526-3395
FAX:208-526-0875
nallg@inel.gov

Attendee List

30th Workshop on Geothermal Reservoir Engineering, Jan.31, Feb. 1-2, 2005

Jay Nathwani

US Department of Energy
850 Energy Dr., MS 1225
Idaho Falls, ID 83401
USA
TEL:208-526-0239
FAX:208-526-5964
nathwaj@id.doe.gov

Gregory Newman

Lawrence Berkeley National Laboratory
1 Cyclotron Road, NS 90-1116
Berkeley, CA 94720
USA
TEL:510- 486 6887
FAX:510- 486 5686
ganewman@lbl.gov

Kim Niggemann

Nevada Geothermal Power Inc.
Suite 900 - 409 Granville Street
Vancouver, British Columbia
V6C 1T2
Canada
TEL:604-688-1553
FAX:604-688-5926
kim@nevadageothermal.com

Gerry Nix

National Renewable Energy Laboratory
1617 Cole Blvd, MS 1732
Golden, Colorado 80401
USA
gerald_nix@nrel.gov

David I. Norman

New Mexico Tech
Dept. of Earth and Environmental Science
801 Leroy Place
Socorro, NM 87801
USA
TEL:505-835-5404
FAX:505-835-6436
dnorman@nmt.edu

Randy A. Normann

Sandia National Labs
1515 Eubank
Albuquerque, NM 87185-1033
USA
TEL:505-845-9675
FAX:505-844-3952
ranorma@sandia.gov

Volker Oye

NORSAR
Instituttveien 25
Kjeller, 2007
Norway
TEL:0047 63805932
FAX:0047 63818719
volker@norsar.no

Susan Petty

Black Mountain Technology
16 W. Harrison St Ste 204
Seattle, WA 98119
USA
TEL:206-217-5960
FAX:206-285-0425
blackmountaintech@earthlink.net

John W. Pritchett

SAIC
10280 Campus Point Drive
San Diego, CA 92121
USA
TEL: 858-826-1628
FAX:858-826-1652
john.w.pritchett@saic.com

Karsten Pruess

Lawrence Berkeley National Lab
Earth Sciences Division
One Cyclotron Road
MS 90-1116
Berkeley CA, 94720-0001
USA
TEL:510-486-6732
FAX:510-486-5686
K_Pruess@lbl.gov

Marshall Reed

U.S. Geological Survey
MS-977345 Middlefield Road
Menlo Park, CA 94025
USA
TEL:650-329-5620
FAX:650-329-5163
mjreed@usgs.gov

Joel Renner

INEEL
PO Box 1625
Idaho Falls, ID 83415-3830
USA
TEL:208-526-9824
FAX:208-526-0969
rennerjl@inel.gov

Attendee List

30th Workshop on Geothermal Reservoir Engineering, Jan.31, Feb. 1-2, 2005

Ann Robertson-Tait

GeothermEx, Inc.
5221 Central Avenue, Suite 201
Richmond, CA 94804
USA
TEL:510-527-9876
FAX:510-527-8164
art@geothermex.com

Marco Rodriguez

Comisión Federal de Electricidad
km. 26.5, Carret. Pascualitos Pescadero
Mexicali, Baja California 21700
Mexico
TEL: (MEX) + 686 523-8156
FAX: (MEX) + 686 523-8146
marco.rodriguez01@cfe.gob.mx

Peter E. Rose

EGI - Univ. of Utah
Research Park
423 Wakara Way, Ste. 300
Salt Lake City, UT 84108
USA
TEL:801-585-7785
FAX:801-585-3540
prose@egi.utah.edu

Andrew Sabin

Innovative Technical Solutions, Inc.
2730 Shadelands Ave., Suite 100
Walnut Creek, CA 94598
USA
TEL:925.946.3121
FAX:925.256.8998
asabin@itsi.com

Jerry Salera

Coso Operating Company
P.O. Box 1690
Inyokern, CA 93527-1690
USA
TEL:760-764-1300
FAX:760/764-2220
jsalera@cenyc.com

Fernando Samaniego V.

UNAM
Div. of Estudios de Posgrado
Facultad de. Ingenieria
DF 04250
Mexico
TEL: 525-550-8717
FAX:525-622-3039
fsamaniegov@smx.pep.pemex.com
ance@servidor.unam.mx

Subir K. Sanyal

GeothermEx, Inc.
5221 Central Ave., Suite 201
Richmond, CA 94804
USA
TEL:510-527-9876
FAX:510-527-8164
mw@geothermex.com

Kei Sato

JMC Geothermal Engineering Co. Ltd.
101-1, Hosoyachi, ukai
Takizawa-mura Iwate, 020-0172
Japan
TEL:81-19-684-4114
FAX:81-19-684-4114
ksato@geothermal.co.jp

Umran Serpen

Istanbul Technical University
Petroleum and N. Gas Eng. Dept.
Maslak, Istanbul, 34469
Turkey
TEL:90-212-2856280
FAX:90-212-2856263
serpen@itu.edu.tr

Chunmei Shi

Stanford University
Petroleum Engineering Department
Green Earth Sciences Building, Rm.109
Stanford, CA 94305-2220
TEL:650-725-0752
FAX:650-725-2099
cmsshi@pangea.stanford.edu

Michael Shook

Idaho Natl Engineering Lab
P.O. Box 1625, MS-2107
Idaho Falls, ID 83415-2107
USA
TEL:208-526-6945
FAX:208-526-0875
mike.shook@inl.gov

Robert Stacey

Stanford University
Petroleum Engineering Department
Green Earth Sciences Building, Rm.150
Stanford, CA 94305
USA
TEL:650-725-0831
FAX:650-725-2099
rstacey@ pangea.stanford.edu

Attendee List

30th Workshop on Geothermal Reservoir Engineering, Jan.31, Feb. 1-2, 2005

Mitchel Stark

Calpine Corporation
10350 Socrates Mine Road
Middletown, CA 95461
USA
TEL:707-431-6101
mits@calpine.com

Mario-Cesar Suarez Arriaga

Michoacan University - ECFM / UMSNH
School of Mathematical and Physical
Sciences Patzimba 438, Vista Bella Morelia
Michoacan, 058090
Mexico
TEL:443-316 7257
FAX:443-3167257
msuarez@zeus.umich.mx

Mituhiko Sugihara

Geological Survey of Japan, AIST
Central 7, 1-1-1,
Higashi Tsukuba Ibaraki, 305-8567
Japan
TEL:+81-29-861-3700
FAX:+81-298-61-3736
m.sugihara@aist.go.jp

Daniel Swenson

Kansas State University
MNE Department
Room 302 Rathbone Hall
Manhattan, KS 66506
USA
TEL:785-532-2320
FAX:785-532-7057
swenson@ksu.edu

Chuanhai Tang

University of North Carolina at Chapel Hill
Department of Geological Sciences,
CB#3315
Chapel Hill NC, 27599-3315
USA
TEL:919-8435846
FAX:919-9664519
ct24@duke.edu

Cenk Temizel

University of Southern California (USC)
925 Bloom Walk,
Petroleum Engineering Building
Los Angeles, CA 90089-1211
USA
temizel@usc.edu

Pierre Ungemach

Geoproduction Consultants (GPC SA)
Paris Nord 2
Rue de la Perdrix, 14
BP 50030
France
TEL:33148630808
FAX:33148630889
pierre.ungemach@geoproduction.fr

Keisuke Ushijima

Kyushu University
Earth Resources Engineering Department
Graduate School of Engineering
Hakozaki, Fukuoka, 812-8581
JAPAN
TEL:81-92-642-3639
FAX:81-92-642-3639
ushijima@mine.kyushu-u.ac.jp

Ilkay Uzun

Middle East Technical University
Petroleum & Natural Gas Engineering Dept.
Middle East Technical University,
Inonu Bulvari , Ankara, 06531
Turkey
uilkay@metu.edu.tr

Anson Villaluz

Stanford University
Petroleum Engineering Department,
Green Earth Sciences Building, Rm.159
Stanford, CA 94305
USA
TEL:650-725-0851
FAX:650-725-2099
villaluz@pangea.stanford.edu

Philip E Wannamaker

University of Utah/EGI
423 Wakara Way, Suite 300
Salt Lake City, UT 84108
USA
TEL:801-581-3547
FAX:801-585-3540
pewanna@egi.utah.edu

Masato Watanabe

Geothermal Engineering Co
1-101 Hosoyachi, Ukai
Takizawa-mura, Iwate-gun
Iwate-ken, 020-0172
Japan
TEL:81-19-684-4114
FAX:81-19-684-6231
watanabe@geothermal.co.jp

Attendee List

30th Workshop on Geothermal Reservoir Engineering, Jan.31, Feb. 1-2, 2005

John H. Weare

Univ of CA, San Diego
9500 Gilman Drive, Mail Code 0340
La Jolla CA 92093-0340
USA
TEL:858-534-3286
FAX:858-534-7244
jweare@ucsd.edu, pedwins@ucsd.edu

Yusaku Yano

AIST (Advanced Industrial Science and Technology)
1-1-1 Higashi
Tsukuba Ibaraki, 305-8567
Japan
TEL:+81-29-861-2412
FAX:+81-29-861-3717
y.yano@aist.go.jp

Colin F. Williams

U.S. Geological Survey
Mail Stop 977
345 Middlefield Rd.
Menlo Park, CA 94025
USA
TEL:650-329-4881
FAX:650-329-4876
colin@usgs.gov

David Wilson

Mighty River Power
160 Peachgrove Road
Hamilton
New Zealand
TEL:0064 7 8570 199
FAX:0064 7 8570 195
david.wilson@mightyriver.co.nz

Michael Woods

California Division of Oil, Gas, and Geothermal
1855 West Main Street, Suite E
El Centro, CA 92243
USA
TEL:619-353-9900
FAX:619-353-9594
mwoods@consvr.ca.gov

Xingru Wu

The University of Texas at Austin
3452 Lake Austin Blvd, Apt C
Austin, Texas 78703
USA
TEL:512-471-6186
FAX:512-471-1006
Xingru_Wu@mail.utexas.edu

Tianfu Xu

Lawrence Berkeley National Lab
One Cyclotron Road
Berkeley, CA 94720
USA
TEL:510-486-7057
tianfu_xu@lbl.gov

Author List

Acuna	245	Demiral	253	Jung	306
Adams	340	Dilley	370	Karner	312
	362		385	Kehrer	306
Akin	93	Dobroskok	207	Kennedy	101
	212	Dorbath, C.	412	Kiryukhin	229
	253	Dorbath, L.	412	Kohl	320
Antics	21		420	Kornilova	510
Apuada	403	Dyer	291	Kotanaka	145
Arai	172	Ehara	427	Kovac	486
Arcedera	245	Eker	212	Kratt	106
Asanuma	145	Fairbank	129	Kueperkoch	291
	172	Faulds	106	Lees	464
	291	Fujimitsu	427	Lewicki	377
Axelsson	72	Fukuda	145	Li	58
Baria	291		172	Linkov	207
Barker	101	Gasperikova	443	Lund	10
Bauer	35	Ghassemi	207	Lutz	486
	129	Gorbach	494	Mansure	35
Baumgaertner	291	Gosavi	222	McCulloch	340
Bertin	253	Goshavi	194		362
Bhat	194	Grant	53		370
Bjornstad	362	Griggs	501		385
Blackwell	435	Gronewald	35	McKenna	435
Boyd	5	Haessler	420	Mégel	320
Bruel	186	Hamilton	35	Mella	340
	299	Hettkamp	291	Mizunaga	456
Buck	340	Hickman	111	Moller	328
	362	Hishi	145	Moore	362
Calvin	106		172		385
Camacho	153	Horne	43	Moya	64
Charléty	412		58		259
	420	Hoversten	101	Mustopa	456
Chen	43		443	Nalla	72
Chiasson	200	Hubner	80	Newman	443
Cuenot	412	Izgec	253	Nicholls	291
	420	Jatho	306	Nishijima	427
Davatzes	111	Jotaki	456		

Norman	370	Suárez	136
	385	Swenson	194
Normann	80		222
Oldenburg	377		435
Olivar	403	Tagomori	456
Omiya	237	Tang	464
Orzol	306	Thompson	464
Oye	448	Tischner	306
Papachristou	21	Tsutsumi	172
Petty	129	Ungemach	21
Pope	178	Ushijima	456
Potapov	494	Uzun	93
	510	van Soest	101
Pruess	335	Vasco	472
	346	Vereina	229
	352	Verma	394
Pulido	153	Vuataz	283
Ramírez	153	Wannamaker	443
Ratchina	510	Watanabe	172
Rial	464	Weare	328
Richards	435	Williams	101
Rivera	153		479
Rose	340	Wu	178
Roth	448	Xu	352
Saibi	427	Yavuzturk	200
Sakagawa	237	Yock	64
Samaniego	136	Zhang	335
	153		352
Sánchez	259		
Sanyal	85		
Sato	237		
Serpen	274		
Shan	346		
Shook	72		
	166		
	178		
Snyder	80		
Soma	291		
Srinivasan	178		

Subject List

3D magnetotellurics	443	cyclic-heat production	306	fracture	111
adsorption	93	Dachny	229	fracture network	420
alcohol	145	decline analysis	53	fracture propagation	207
aluminosilicate minerals	328	density driven flow	186	fractured reservoirs	178
analytical solution	346	district heating	21	fractures	43
aromatic compounds	172	Dixie Valley	435		370
Beowawe	166	drift flux	245		456
BHTV	111	economics	129	friction factor	245
binary plant	200	effective heat transfer area	346	geochemical modeling	340
binary power production	10	Enhanced Geothermal System (EGS)	283	geodetic data	472
brine	283		306	geophysical imaging	435
calcite	362		312	geopressured aquifers	501
calcite scaling	253		328	geopressured brine	501
calcium	362		349	geopressured-geothermal energy	501
caldera	172	electric power generation	10	geostatistics	377
carbon dioxide	377	exploitation	64	gravity change	427
chemical models	328	exploration	377	groundwater	427
chemistry	362	fault type	229	HDR	186
classification	85	production zone			291
clay swelling	352	F-C diagrams	166		299
CO ₂	93	first moments	166	heat capacity	394
coagulants addition	510	first temporal moment	178	heat flow	479
coal mines	200	flow modeling	435	HFR	352
combined heat and power production	10	flow structure	43	hidden geothermal systems	377
concentrations of anions and cations	494	fluid flow	111	high temperature grouts and plugs	35
conductivity	494	fluid inclusions	370	high-temperature electronics	80
Coso	443		385	holdup	245
	486	FMS	486	hot fractured rock	346
Costa Rica	64	focal mechanism	111	hydraulic fractures	306
	259	Fort Bidwell	420	hydraulic stimulation	340
coupled simulation	222	fractal	101		
CSAMT	456		212		

hydromechanical coupling	299	Miravalles	64	SiC	80
hydrothermal chemistry	328	Mori	172	silica	362
hydrothermal solution	494	mudlogs	385	silica precipitation	510
hydrothermal system	510	multiphase flow	43	silica utilization	510
hydrothermal vents	427	Mutnovsky	229	silicate hydrates	35
Iceland	136	naturally fractured reservoirs	153	single pore model	93
	72	non-condensable gases	259	sodium silicate	35
	464	numerical modeling	320	software	394
imaging	443	numerical simulation	194	SOI	80
IMPES	186		222	sorbing tracer	346
infrared spectroscopy	106		237	Soultz-sous-Forêts	283
injectate mitigation	352		335	source scaling	448
injection	362	one well systems	377	spectral ratios	448
injectivity enhancing	352	overpressure	306	spinner	245
inverse methods	472	Pacific Ocean	274	stimulation	186
isotopes	377	permeability reduction	136		291
Japan	172	precise leveling	253	stress modeling	222
	237	quartz	403	stress tensor	420
	427	reinjection	362	submarine hydrothermal chimneys	136
	456	relative permeability	274	sustainability	21
Kakkonda	237	relative permeability	43	Takigami	456
Krafla	464	repeat gravity	58	temporal moments	72
Lattice-Boltzmann	212	reservoir management	403	thermodynamics	328
Laugaland	72	resistivity	21	thermoelastic load	207
liquid tracer	237	resource assessment	58	thermo-hydraulic-chemical modelling	283
liquid-dominated	172	reverse circulation	479	tight rocks	306
lost circulation	35	rough fracture	129	tomography	412
	129	Russia	212	tortuosity	43
Matsukawa	145	scaling	229	TOUGH2	222
Mexico	136	seismic imaging	352	TOUGH2	229
microseismic monitoring	448	shear migration	299	tracer	145
microseismicity	291			tracer test	172
	299			tracer tests	237
	412				72
	420				153

tracers	166
	178
	340
two-phase	145
two-phase flow	178
	245
two-phase tracer	237
Unzen volcano	427
upscaled	299
permeability	
vapor-dominated	145
velocity structure	412
water shut off	35
waterfrac technique	306
web sites	5
well bore integrity	35
well monitoring	80
well testing	53
wellbore heat	335
transmission	
wellbore simulation	194